DEVELOPMENT OF ITM OXYGEN TECHNOLOGY FOR INTEGRATION IN IGCC AND OTHER ADVANCED POWER GENERATION

(ITM Oxygen)

Final Scientific/Technical Report

For the period

1 October 1998 – 31 March 2015

Phillip A. Armstrong, Ph.D.

July 2015

DE-FC26-98FT40343

Air Products and Chemicals, Inc.
7201 Hamilton Blvd.
Allentown, PA 18195

DISCLAIMER

This report was prepared as an account of work sponsored by an agency of the United States Government. Neither the United States Government nor any agency thereof, nor any of their employees, makes any warranty, express or implied, or assumes any legal liability or responsibility for the accuracy, completeness, or usefulness of any information, apparatus, product, or process disclosed, or represents that its use would not infringe privately owned rights. Reference herein to any specific commercial product, process, or service by trade name, trademark, manufacturer, or otherwise does not necessarily constitute or imply its endorsement, recommendation, or favoring by the United States Government or any agency thereof. The views and opinions of authors expressed herein do not necessarily state or reflect those of the United States Government or any agency thereof.

Neither Air Products and Chemicals, Inc. nor any of its contractors or subcontractors nor any person acting on their behalf:

1. Makes any warranty or representation, express or implied, with respect to the accuracy, completeness, or usefulness of the information contained in this report, or that the use of any information, apparatus, method or process disclosed in this report may not infringe privately owned rights; or
2. Assumes any liabilities with respect to the use of, or for damages resulting from the use of, any information, apparatus, method or process disclosed in this report.

TABLE OF CONTENTS

ABSTRACT

EXECUTIVE SUMMARY

PHASE 1 TASKS

- **1.0 Materials Development**
- **2.0 Engineering Development**
- **3.0 Membrane Module Development**
- **4.0 ITM Oxygen Performance Testing**

PHASE 2 TASKS

- **6.0 Materials Development**
- **7.0 Engineering Development**
- **8.0 Ceramic Processing Development**
- **9.0 Module Performance Testing**
- **10.0 Design, Construction and Commissioning of the SEP Test Facility**
- **11.0 Design of the Pre-Commercial Demonstration Facility, pCDF**

PHASE 3 TASKS

- **14.0 Materials Development**
- **15.0 Engineering Development**
- **16.0 Process Vessel Design Engineering**
- **17.0 Ceramic Processing Development**
- **18.0 Module Performance Testing**
- **19.0 Design, Construction and Commissioning of the ISTU**
- **20.0 Intermediate-scale Test Unit (ISTU) Operation**
- **21.0 Management and Reporting Phase III**

PHASE 4 TASKS

- **23.0 Process and Economic Evaluation**
- **24.0 Reaction-Driven ITM Materials**
- **25.0 Membrane and Module Development**

PHASE 5 TASKS

- **28.0 Ceramic Materials and Manufacturing Development**
- **29.0 Engineering Development for Industrial and CCS Applications**
- **30.0 Ceramic Membrane Module Fabrication Facility**
- **31.0 Ceramic Component Testing**

LIST OF ACRONYMS AND ABBREVIATIONS

ABSTRACT

Ion Transport Membrane (ITM) technology is based on the oxygen-ion-conducting properties of certain mixed-metal oxide ceramic materials that can separate oxygen from an oxygen-containing gas, such as air, under a suitable driving force. The "ITM Oxygen" air separation system that results from the use of such ceramic membranes produces a hot, pure oxygen stream and a hot, pressurized, oxygen-depleted stream from which significant amounts of energy can be extracted. Accordingly, the technology integrates well with other high-temperature processes, including power generation.

Air Products and Chemicals, Inc., the Recipient, in conjunction with a dozen subcontractors, developed ITM Oxygen technology under this five-phase Cooperative Agreement from the laboratory bench scale to implementation in a pilot plant capable of producing power and 100 tons per day (TPD) of purified oxygen. A commercial-scale membrane module manufacturing facility (the "CerFab"), sized to support a conceptual 2000 TPD ITM Oxygen Development Facility (ODF), was also established and operated under this Agreement.

In the course of this work, the team developed prototype ceramic production processes and a robust planar ceramic membrane architecture based on a novel ceramic compound capable of high oxygen fluxes. The concept and feasibility of the technology was thoroughly established through laboratory pilot-scale operations testing commercial-scale membrane modules run under industrial operating conditions with compelling lifetime and reliability performance that supported further scale-up. Auxiliary systems, including contaminant mitigation, process controls, heat exchange, turbo-machinery, combustion, and membrane pressure vessels were extensively investigated and developed. The Recipient and subcontractors developed efficient process cycles that co-produce oxygen and power based on compact, low-cost ITMs. Process economics assessments show significant benefits relative to state-of-the-art cryogenic air separation technology in energy-intensive applications such as IGCC with and without carbon capture.

EXECUTIVE SUMMARY

Ion Transport Membrane (ITM) technology is based on the oxygen-ion-conducting properties of certain mixed-metal oxide ceramic materials to separate oxygen from an oxygen-containing gas, such as air, under a suitable driving force. The oxygen in air is ionized on the surface of the ceramic and diffuses through the membrane as oxygen ions in an electrochemical process. A net flow of pure oxygen can be driven through the material by an oxygen activity (partial pressure) gradient to transport oxygen molecules from one side of the material to the other side, such that it operates as a membrane air separation device. Impurities such as nitrogen are rejected by the membrane. In addition, a class of these materials conducts electrons as well as ions, meaning that no external source of electrical power is required. The "ITM Oxygen" air separation system that results from the use of such ceramic membranes produces a hot, pure oxygen stream and a hot, pressurized, oxygen-depleted stream from which significant amounts of energy can be extracted.

Air Products and Chemicals, Inc., the Recipient, in conjunction with a dozen subcontractors, developed ITM Oxygen technology under this Cooperative Agreement from a laboratory bench scale to implementation in a pilot plant capable of producing power and 100 tons per day (TPD) of purified oxygen. A commercial-scale membrane module manufacturing facility, sized to support a conceptual 2000 TPD ITM Oxygen Development Facility (ODF), was also established and operated under this Agreement.

The work was divided into five phases pertaining to the stages of development of the technology. It is notable that the technology development was carried out in two parallel paths: one focused on development of the membrane modules, and a second focused on the development of the processes that use the modules for air separation. Table 1 summarizes the phases, associated tasks, and specific development initiatives within each phase. Phases 1-3 and 5 were focused on developing technology for tonnage oxygen production, while Phase 4 was focused on extending these concepts to explore the potential for "reaction-driven" systems to support, for example, direct oxidation of hydrocarbons on the membrane surface.

Table 1. Description of Development Phases 1-5

Phase	Tasks*	Development Scale and Objectives
1	1-5	Establish feasibility: identify materials, membrane architecture and production methods and develop test equipment at 0.1 TPD scale.
2	6-13	Test concepts: develop membrane module production methods for commercial-scale ceramic devices; establish prototype test equipment at the 5 TPD scale.
3	14-21	Proof of concept: develop processes for and produce quantities of commercial-scale ITM Oxygen ceramic modules on a prototype ceramic manufacturing line; produce tonnage quantities of oxygen in a 100 TPD Intermediate-Scale Test Unit (ISTU) that co-produces power and provides scale-up data for the 2000 TPD ODF.
4	22-26	Test concepts: establish materials property data and conceptual processes for using reaction-driven ITMs for syngas production.
5	27-31	Demonstrate ceramic module production: implement full-scale processes and produce membrane modules in a first-of-a-kind, commercial-scale facility; develop the process design basis for scale-up to 2000 TPD ODF.

*Tasks 5, 13, 21, 22, 26 and 27 were program management-related tasks.

A summary of the key accomplishments is presented below, followed by a discussion of progress against the major development initiatives in materials, engineering, ceramic processing, and performance testing, which are discussed by phase. Detailed descriptions of the work performed are presented by task in the body of the report.

Key Accomplishments

1. (Phase 1) Developed a stable, high-flux material and achieved the commercial flux target under anticipated commercial operating conditions.

   Air Products chose the AP2K formulation, a proprietary perovskite oxide ceramic with significant oxygen non-stoichiometry, for forward development work. With this material, Ceramatec, Penn State, and Air Products compiled a materials property database, produced planar wafers, developed ceramic joining technology and performed flux tests from prototype membrane modules that produced high-purity oxygen at target rates under high-temperature (800-900°C), high-pressure (150-250 psig) conditions.

2. (Phases 1-3, 5) Produced thousands of commercial-size ITM wafers and used them to build commercial-scale ceramic modules in a prototype manufacturing process.

   This effort was based on path-finding work in Phase 1 that established a planar wafer architecture to support thin membranes and pioneering ceramic joining technology that enabled connection of multiple sintered wafers to form all-ceramic, high-capacity modules. Ceramatec scaled up the Process Development Facility (PDF), a prototype manufacturing line, and established standard processes for making large quantities of ceramic wafers and modules. The team produced over 100 1 TPD –scale modules for testing in Phase 3.Ceramatec implemented over 100 quality assurance (QA) steps and used statistical process control (SPC) to improve yields in the PDF. Sustained wafer yield reached 70% and achieved >90% in peak periods, demonstrating the commercial feasibility of the manufacturing approach.

3. (Phases 1-5) Established process designs, methods for integration with turbo-machinery, contaminant mitigation and heat exchange strategies, and developed a pressure vessel design concept to house ceramic membrane modules.

   Air Products, McDermott Technology (SOFCo EFS), NovelEdge Technology, Siemens, Williams International, and Becht Engineering advanced engineering developments in conjunction with various suppliers to enable ITM-based oxygen production processes that support power/steam co-production and/or integration with energy-intensive processes.

4. (Phases 1-3, 5) Established costing for ITM Oxygen process economic evaluations and developed meaningful comparisons with competing cryogenic air separation technology for a variety of energy-intensive applications, illustrating the substantial benefits of the ITM technology.

   Air Products collaborated with the Department of Energy, Concepts NREC, Electric Power Research Institute (EPRI), Texaco Gasification (GE Energy), NovelEdge Technology and Siemens in various studies that established excellent benefits for ITM Oxygen in IGCC, IGCC with carbon capture, decarbonized fuel, and oxy-combustion

applications. In all cases, ITM provided a significantly lower-cost oxygen production technology than state-of-the-art cryogenic air separation.

5. (Phases 1-5) Established the performance of ITM modules based on hundreds of laboratory-scale tests that established expected membrane wafer oxygen flux, purity, reliability, resistance to environmental contaminants, and the effectiveness of both contaminant mitigation steps and ceramic-to-metal seals.

   Air Products designed, built and operated laboratory apparatus that probed performance under high-temperature and high-pressure conditions. Ceramatec supplied hundreds of test articles from subscale wafers to modules based on 12-wafer submodules composed of full-size wafers, an end cap, and a base piece. Air Products ultimately operated a 12-wafer submodule that met target flux and purity for over 12,800 hours. Results of performance tests were used to refine the planar wafer architecture.

6. (Phases 1-3, 5) Qualified proprietary ceramic-to-metal seal designs with demonstrated low-leak performance over multiple cycles, sealing ceramic test articles and full-size modules in high-temperature/pressure tests.

   Air Products, McDermott, and Ceramatec collaborated to create and refine high-temperature designs specific to the expansive AP2K material to enable full-size components to reach and maintain target leakage over 10+ thermal/pressure cycles. Air Products demonstrated repeatedly high oxygen purities (95+%) in flux tests and achieved as high as 99.9+% oxygen purity in multiple tests at the SEP and smaller apparatus.

7. (Phases 2, 3, 5) Determined critical levels of gas-phase impurities and mitigation techniques allowing for contaminant-free operation of membrane modules. Demonstrated pilot-scale operation of such systems with good performance in contaminant removal by getters and particulate filters.

   Air Products established the required removal efficiency for contaminant mitigation processes by assessing the effects of various airborne contaminants, such as chromium and sulfur compounds, on oxygen flux in small-scale apparatus. The team developed getters and process design approaches that reduce the contaminant levels below those

that allow reaction with the AP2K material. These techniques were successfully implemented in the 5 TPD and 100 TPD pilot units.

8. (Phase 4) Successfully advanced Reaction-Driven ITM technology by addressing commercial integration issues, purge gas generation, enhanced performance, forward technical challenges and high-probability solutions to key risk areas of the technology.

   Air Products, Ceramatec, and Penn State identified alternative ceramic materials, and developed and tested representative membrane devices under the operating conditions expected for reaction-driven conditions. Advanced ITM wafer designs with enhanced oxygen flux, improved mechanical strength and higher expected reliability were manufactured and tested in an existing unit at Air Products. Experimental testing of Reaction-Driven ITM devices progressed sufficiently to justify continued scaled-up testing to assess commercial readiness. Air Products identified process routes that enable Reaction-Driven ITM to reduce the cost of syngas generation.

9. (Phase 2 with operation in Phases 2,3,5) Completed the design, construction, and operation of a 5 TPD Subscale Engineering Prototype (SEP) facility for testing full-size ITM modules. The SEP enabled flux and purity data to be gathered from individual modules in a prototype ITM pressure vessel.

   Air Products operated the 5 TPD SEP cumulatively for over 1,100 days in 45 separate campaigns; commercial flux targets were achieved or surpassed, and product purity exceeded 99%. The team demonstrated repeated thermal/pressure cycling of full-size module and performed numerous qualifying tests of key balance-of-plant equipment required for scale-up. These tests included demonstrating effective chromium getter performance, advanced process control schemes, hot flow duct design and insulation schemes, and hot automatic shutoff valves capable of isolating failed modules.

10. (Phase 3) Completed the design and construction of a 100 TPD Intermediate-Scale Test Unit (ISTU) for testing arrays of full-size ITM modules with power co-production. The ISTU includes many of the critical process design and equipment features required for scale-up to large and commercial systems.

Air Products developed the ISTU process design to enable independent production of oxygen and power, and constructed the ISTU at an Air Products ASU site in Convent, Louisiana, with excellent safety performance. Air Products, assisted by Becht Engineering, designed and built a proprietary ITM pressure vessel housing an array of modules with integral getter and particulate removal systems. The ISTU includes a vacuum permeate system with an associated steam system for cooling hot oxygen, a compact recuperator to heat process air, an indirectly fired heater that minimizes contaminants and maximizes oxygen recovery, a hot gas expander fired on oxygen-depleted non-permeate gas (designed and built by Williams International), and a robust process control system enabling independent production of oxygen and power.

11. (Phase 3) Operated the ISTU, demonstrating successful tonnage oxygen production from an array of 1 TPD-scale ITM Oxygen modules supplied by Ceramatec and implemented in a commercial-scale flow duct.

Air Products achieved design operating conditions in the unit, and performed experimental runs with ceramic modules installed that proved the efficacy of the flow duct and pressure vessel design, chromium getter and particulate removal technology, heat exchange steps, and the control system. The unit, loaded to ¼ capacity with 1 TPD-scale modules, performed flawlessly in a final, two-week test in which all modules reached operating conditions and produced oxygen, with overall productivity exceeding predictions for the module array and purities of individual modules reaching as high as 99%. Rated facility power generation from the hot gas expander was demonstrated during commissioning.

12. (Phase 5) Based on the development work with the prototype membrane module production process at Ceramatec, Air Products and Ceramatec collaborated to design, build, and operate a commercial-scale ceramic membrane module fabrication facility (the "CerFab") capable of supplying a 2000 TPD ITM Oxygen plant.

Air Products completed site selection, permitting, and building modification for the CerFab, located in Tooele, Utah, and, with Ceramatec, completed the conceptual and detailed design engineering for the facility. The team specified, procured and commissioned equipment for the facility that comprised all the major operations required

for commercial manufacture of ceramic modules based on the tape casting and lamination approach developed at Ceramatec in Phase 3. Air Products and Ceramatec operated the CerFab, producing tens of thousands of feet of green tape and thousands of finished parts, and also demonstrated full-size module production. Final efforts were successful in transitioning the CerFab process to a new green formulation that enhances wafer reliability.

13. (Phase 5) Air Products developed a process design and preliminary costing for the 2000 TPD Oxygen Development Facility (ODF) with equipment available for implementation by 2020.

Air Products development and engineering teams collaborated on a dual-train ITM Oxygen plant based on either a 2x1 configuration with a Siemens SGT-800 gas turbine and steam turbine or a hot gas expander-based cycle featuring a staged, intercooled air compressor. In a gas-to-liquids application, for example, the 2000 TPD ITM plant can be coupled with a 3000 TPD cryogenic ASU that co-produces 80 MW of net power.

Summary of Phase 1 Accomplishments (Tasks 1-5)

Air Products developed three materials for assessment as potential membrane materials: AP96 (developed prior to this Agreement), AP98 and AP2K, all members of the same family of ceramic perovskites that has significant oxygen non-stoichiometry (vacancies) that enable oxygen transport.

Air Products first selected the AP98 composition under Phase 1 for ceramic process development and scale-up at Ceramatec. AP98 originated from an in-depth statistical property/composition study of ITM Oxygen materials, and also included Ceramatec's laboratory-scale assessments of membrane fabricability. The AP98 composition was selected based on improved strength, creep resistance, chemical resistance and fabricability compared to AP96. Ceramatec developed fabrication processes based on the AP98 material.

A third material, AP2K, was also evaluated based on physical, chemical, and mechanical properties, against an ITM Oxygen performance target developed through process economic studies, and ceramic processing criteria. Air Products, Ceramatec and the Pennsylvania State University (Penn State) collaborated to measure the chemical and physical property data,

including mechanical strength, SO_2 reactivity, thermal and chemical expansion, oxygen transport properties, and high-temperature creep behavior. AP2K was found to have superior oxygen transport properties compared to the AP98 composition, including roughly twice the oxygen ionic conductivity. Air Products selected the AP2K material for further development work as the optimized ITM Oxygen material.

During Phase 1, the team developed and instituted several new material characterization methods, including installation of a new dilatometer, development of a proprietary transient dilatometry technique, and the installation of a rig for high-pressure oxygen thermogravimetric analysis (TGA). Air Products also developed models to determine oxygen transport parameters from the transient response. The new TGA enabled high-pressure oxygen non-stoichiometry to be measured directly for AP2K at elevated oxygen partial pressures representative of ITM Oxygen process conditions. This additional (and pre-existing) infrastructure generated the essential material property databases required to support the development of detailed engineering models (Task 2) that were used to predict the performance of AP2K membranes during steady-state and transient operation.

Air Products revised its models for oxygen non-stoichiometry and thermal and chemical expansion. Both models were based on analysis of extensive in-house experimental data sets developed for AP2K. Experimental oxygen non-stoichiometry data were measured by TGA. The AP2K expansion data were obtained with the new improved-accuracy dilatometer. The thermal and chemical expansion model predicted the expansion behavior of AP2K as a function of temperature and oxygen partial pressure. Both models closely predicted the experimental data and were fundamental in developing detailed engineering models.

Penn State's significant advances in experimental equipment and technique enabled creep rates meeting the Phase 1 target value to be measured at low stress. As a result, Penn State successfully completed qualitative creep rate measurements for the ITM Oxygen materials AP98 and AP2K using bend-bar samples fabricated at Ceramatec. Penn State has further extended its creep rate measurement capabilities for ITM Oxygen materials by developing a quantitative tensile testing method using a new type of tensile creep sample fabricated by Ceramatec. Long-term testing was begun to build the high-quality database needed to calculate accurate maximum allowable stress and membrane operating lifetime. The design stress for creep rate evaluation

was refined later in Phase 2 (Task 6) following thermal and mechanical analyses of the full-size wafer by McDermott Technology.

Air Products completed thermal aging experiments on AP2K test samples to measure grain growth and to determine the activation energy of sintering. Models developed from these data predicted that the AP2K material and ITM Oxygen membrane structure exceed targets set to meet the desired in-service lifetime of ITM Oxygen membrane modules.

Ceramatec investigated the basic parameters that governed tape casting and lamination with the AP98 and AP2K materials. Green material properties were assessed throughout. Path-finding wafer lamination and sintering studies were performed, enabling process development that was successful in producing the first square wafers and then the first square wafers at the target size. Processes were developed to enable manufacture of a multi-layer structure in which the thin separating layer represents the "skin" over a ceramic composite wafer. The layers within the wafer support the skin. A porous layer is placed directly under the thin separating layer, while slotted layers residing below the porous layer provide structural stability as well as a pathway for permeate-side oxygen to find its way to a central hole through which the oxygen product is discharged.

In parallel, Ceramatec began to establish the Process Development Facility (PDF), a prototype manufacturing line featuring full-scale manufacturing equipment where possible. A Class 10,000 clean room was established and a tape caster was installed. A high-speed laser cutter was commissioned for featuring the internal layers. Powder processing equipment and methods were scaled up.

An 'on-line process' (OLP) was established which governed the operation of the PDF and under which the sanctioned processes for wafer production were managed and improved. Ceramatec began producing subscale wafers and tracking quality assurance statistics. As the new wafer designs were qualified, intermediate- and then full-size wafers were produced in the PDF. The team produced over 1,200 wafers during Phase 1. Wafer quality statistics gathered from this population were fed back to the OLP, which led to OLP modification through a rigorous process and ultimately an improvement in production yields. Toward the end of the work, a significant improvement in the assessment of wafer leak locations promised to lead to insights that would

drive up yield considerably. Figure 1 shows the progression in wafer size achieved by the team, culminating in a testable submodule complete with an end cap and base piece.

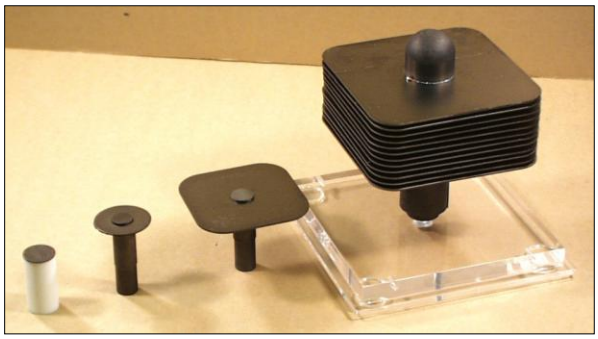

Figure 1. Evolution of wafer size and joining during Phase 1.

Ceramatec also pioneered the joining of sintered ceramic parts. Path-finding efforts with transient liquid-phase (TLP) processing methods led to near-flawless joints between previously sintered parts. Additional tape-based methods also proved successful. These efforts were critical in enabling the production of modules from fully sintered module subcomponents. In addition, Ceramatec demonstrated that it could join a wafer and a spacer in the green state and fire them to produce a unitary body, thus reducing by half the number of ceramic-to-ceramic seals required to make a module.

Ceramatec proposed and developed a two-step process for making membrane modules. Once a population of low-leak wafers was established, wafers could be joined in a first step to make a 12-wafer submodule. Following qualification of a population of these submodules, multiple submodules could be joined together in a second step along with a ceramic base piece and end cap. The two-step process was designed to increase the overall yield of modules from a finite set of wafers and from processes with non-optimized yields.

Air Products collaborated with Concepts NREC to identify suitable gas turbines for integration with ITM Oxygen processes as a step to establish the engineering development challenges of and benefits from machinery integration. With Texaco Gasification (GE Energy), the team carried out a study of IGCC contrasting a state-of-the-art cryogenic air separation unit (ASU) with ITM Oxygen. The work indicated that the capital and operating costs of the oxygen production part of the plant can be reduced by one-third when the supply is based on ITM Oxygen in place of the

cryogenic ASU-based process. Similar benefits were obtained when studying a decarbonized fuel plant with Parsons Engineering.

Figure 2 illustrates a typical integration scheme between and ITM Oxygen process and a gas turbine. The ITM process benefits when a significant portion of the compressed air in the machine is extracted. The ITM removes a portion of the oxygen but returns the remainder of the oxygen and all of the inert species in the non-permeate stream, which is reintroduced to the gas turbine with only a modest pressure reduction and ideally at the ITM operating temperature (800-900°C). The energy in the non-permeate stream is thereby recovered in the gas turbine.

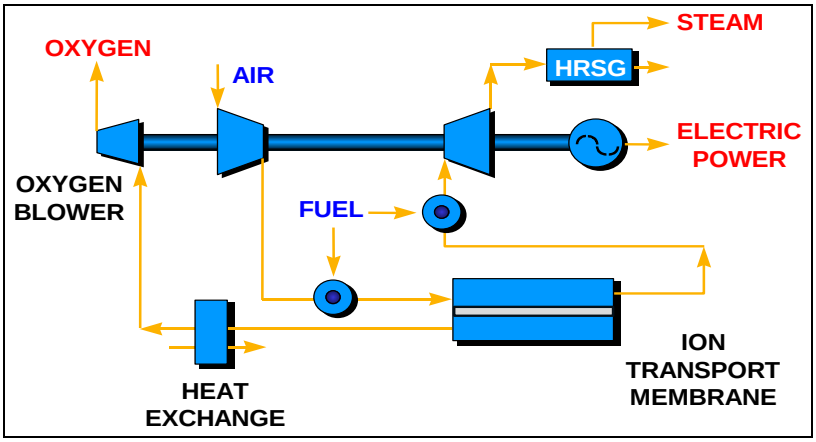

Figure 2. ITM Oxygen integration with a gas turbine.

McDermott Technology provided finite element analysis (FEA) capability to assess membrane wafer architecture stresses and reliability. These approaches were extended to help address chemical expansion-driven stresses and to make recommendations for ceramic-to-metal seal designs.

McDermott also developed the formative concepts framing the approach to house membrane modules in a pressure vessel. Figure 3 illustrates a conceptual ITM Oxygen vessel in which modules are housed in an internally insulated flow duct such that the process heat stays mainly inside the duct – the vessel walls are relatively cool. Hot, high pressure air passes over the rows of modules and is successively depleted in oxygen as it passes over each row. Pressure equalization ports in the duct ensure that the cold walls of the pressure vessel provide the primary pressure containment. The oxygen passes into the modules and out through the ceramic base piece into an oxygen header which dumps into a common manifold. Oxygen is withdrawn

from the vessel through a port, while the oxygen-depleted non-permeate gas exits the duct and vessel through a separate port.

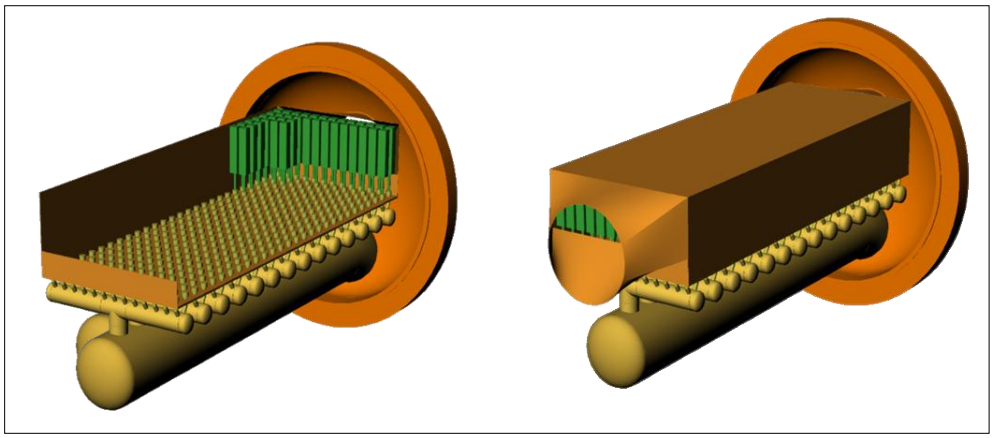

Figure 3. Conceptual design of ITM pressure vessel internals. Left: modules (green) partially loaded into an insulated flow duct base. Right: insulated flow duct fully assembled and housing a full load of modules.

Air Products designed, built and commissioned a new experimental test platform, the Vacuum Permeate Short Loop Test Rig (VP-SLTR), to measure the oxygen flux of subscale wafer modules. The VP-SLTR test platform can perform four independent membrane module tests in parallel. Subscale wafers were tested under steady-state conditions with a pressurized air-feed and a vacuum permeate. These units achieved the full oxygen partial pressure driving force representative of ITM Oxygen process conditions at a feed air pressure of ~200 psig.

Air Products achieved the target oxygen flux set by the objective of cutting the cost of oxygen production by approximately one-third compared to conventional technology. The subscale AP2K wafer membrane test was performed in a VP-SLTR unit at a feed-air pressure of 190 psig, at the full operating temperature, and at oxygen partial pressures typical for commercial process conditions.

Subsequent tests under a variety of smaller and larger driving forces and with a variety of wafer thicknesses provided sufficient information to confirm the feasibility of achieving the flux target with a full-size wafer. Air Products repeatedly demonstrated the flux target with subscale, supported thin-film membranes at feed air pressures of 200-250 psig in the VP-SLTR units, conditions representative of a commercial process. Air Products also exceeded the flux target by 25% at a feed air pressure of 200 psig. Two tests with subscale membranes were operated in

excess of 1950 hours and 2350 hours at the full operating temperature targeted for commercial operations.

Air Products updated a model for predicting the oxygen flux of ion transport membranes formed from AP2K. The material properties were extracted by a statistical analysis of the oxygen flux database measured at oxygen partial pressure ranges representative of ITM Oxygen process conditions. Only oxygen flux data measured with subscale membranes were used for this model revision. The subscale membrane tests were performed in the Vacuum Permeate-Equipped Short Loop Test Rigs. The oxygen flux model supports process engineering and economic evaluations of ITM Oxygen applications.

Air Products has performed ceramic-to-metal seal tests in the pre-existing SLTR test platform. Seal tests have been complemented with an oxidation study on several candidate materials of construction under aggressive conditions. Specific alloys were identified as clearly superior in this service. As a result, Air Products developed a baseline ceramic-to-metal seal design based on U-rings composed of the leading alloy and fitted to an oxygen ceramic flow tube.

Summary of Phase 2 Accomplishments (Tasks 6-13)

Air Products, Ceramatec and Penn State collaborated to expand the material property database for the AP2K material, focusing on establishing parameters to enable membrane module design and reliability prediction based on FEA stress modeling. The team established design values for all major parameters, but focused mainly on developing detailed understanding of stress, creep, and slow crack growth. Penn State built and operated a Chemical Expansion Verification Unit (CEVU) that, coupled with FEA models developed by McDermott Technology (SOFCo), established the model parameters to enable stress modeling and reliability prediction in response to the oxygen vacancy distribution in the material. In addition, the team showed that slow crack growth is not an operative degradation mechanism under operating conditions. The team also showed that the porous wafer layers were stable over a projected 15-year operating life.

Air Products, recognizing that high chemical expansion stresses may dictate allowable thermal cycle times in module manufacturing and process transients in module operation, developed iso-control techniques in which the local oxygen partial pressures around components are controlled to directly influence the oxygen content and oxygen vacancy gradients within the module

materials. The techniques can be used to maintain the materials in a specific stress state during process transients. Dilatometry was used to establish characteristic equilibration times of specific materials. Direct experimentation with full-size wafers demonstrated that iso-control techniques enable a full thermal cycle from ambient to operating temperature and back to ambient conditions within 24 hours. Air Products also carried out a study that established the effects of oxygen impurities in dilution gas used during iso-control.

Ceramatec expanded the PDF and established on-line processes (OLPs) for wafer, submodule, and module production. The team expanded wafer production by a factor of five relative to Phase 1. Wafer production peaked at ~500 wafers per month during Phase 2. The revolutionary ceramic-to-ceramic joining techniques developed in Phase 1 were refined and implemented in the OLP. Over 500 submodules were produced during Phase 2.

By tracking and addressing the effects of key processing parameters on product quality, Ceramatec made substantial progress in improving production yields of both wafers and submodules. Yields of sintered, thin-membrane wafers based on leak rate and corresponding to the target commercial grade-purity oxygen (99.5 vol. %) climbed from near zero to 50% on a sustained basis. Yields of wafers with leak rates corresponding to 97+% oxygen purity (vol.) climbed to >80%. Sustained submodule yields ranged from a low of 33% to as high as 100%, averaging 69% during Phase 2. Both the wafer and submodule yields include experimental lots and indicate the feasibility for achieving high yields in a commercial operation.

Ceramatec developed a conical base piece and flat end cap and utilized ceramic-to-ceramic joining technology to produce all-ceramic modules for testing in laboratory-scale test units and the 5 TPD subscale engineering prototype (SEP). By joining multiple submodules, a base piece and end cap, the team produced fifteen 0.5 TPD-scale modules for testing at the SEP. In a demonstration of the future of the technology, Ceramatec extended their joining efforts to produce the first 1.0 TPD-scale ITM Oxygen module, the full commercial scale. Figure 4 shows an early 0.5 TPD-scale module.

Figure 4. Intact 0.5 TPD-scale, all-ceramic module.

Ceramatec developed techniques to predict the reliability of AP2K ceramic articles. With use of the database of material properties and FEA, Ceramatec and McDermott predicted stress in test pieces, ceramic composites and wafers, and applied CARES or other analysis packages to predict reliability. This work guided the selection of allowable process transients in operating laboratory pilot units and the SEP, as well as wafer architecture refinements.

Air Products tested subscale wafers for oxygen flux to extend the flux database. Work with the VP-SLTRs achieved record oxygen fluxes during Phase 2. Subscale wafers were purposely dosed with chromium during the flux tests, but without effect on the flux.

The Recipient designed, built and commissioned the flux verification units (XVUs) for testing the performance of single, full-size wafer modules. The purpose of these units in Phase 2 was to establish the flux performance of full-size wafer modules and compare it with that of the reference subscale wafers. The team tested 15 full-size wafer modules in the XVUs at full operating conditions of high temperature and pressure, achieving at least 90% oxygen purity in all tests and as high as 99.9% oxygen purity (achieved twice), a record purity for a single-wafer module. Figure 5 shows a photograph of the three XVUs installed during Phase 2.

Figure 5. Three XVUs for single, full-size wafer flux tests.

The work with the XVUs complemented on-going work with the TDU in testing multi-wafer modules. Multiple tests with 2- to 12-wafer modules established the effects of process parameters, including feed flow rate, on flux. During the course of module testing in both the XVUs and TDU, the effect of chromium was observed to have a deleterious effect on flux, in contrast to the results with the subscale wafers in the VP-SLTRs. In parallel, the team identified and developed a MgO-based getter material, which was implemented in both the TDU and XVU1. Fluxes in those units improved, and the flux target was achieved and exceeded in the TDU. Analysis of the TDU getter showed that the chromium in the feed air was removed below detection limits upstream of the module.

Complementary work to getter development included analysis of coating materials for hot metallurgy, which indicated that chromium evolution could be reduced drastically by pretreating the metals.

The Air Products team also investigated and improved ceramic-to-metal seals. The double U-ring seal developed in Phase 1 was found to have some limitations in thermal cycling, mainly caused by the high expansion of the AP2K relative to the constituent metals. McDermott designed an I-ring seal to operate at lower temperatures. Leak tests in the SLTRs of AP2K parts fitted with the I-ring seals showed some improvement over the straight U-rings in successive thermal/pressure cycles, but only modestly. A composite gasket-type seal against the bottom end of the base piece proved to be a much more effective design. Air Products demonstrated 11

consecutive thermal/pressure cycles over 4500 hours with modest and steady leakage under full pressure at 700°C from an AP2K part fitted with a composite gasket seal.

With success in the TDU in producing high-purity oxygen at target or near-target fluxes with up to 12-wafer modules, Air Products designed and built the 5 TPD SEP. The SEP was intended to enable performance tests of 0.5-1.0 TPD-scale modules in a prototype duct based on the vessel concepts developed in Phase 1. The system was based on a recycle loop in which hot, high-pressure gases are re-circulated through the system, and make-up gases are added to maintain the oxygen content and pressure in the loop. The system could reach design operating conditions for temperature, pressure, and gas velocity expected in eventual commercial operation.

McDermott oversaw the design and construction of the SEP pressure vessel and flow duct. A CAD drawing of the vessel is shown in Figure 6. Each module (in green) is connected to an independently operated permeate system with a dedicated vacuum pump and flow and purity diagnostics so individual module performance could be assessed. Air Products oversaw a study of alloy oxidation in pure-oxygen environments to support materials selection in the oxygen permeate system.

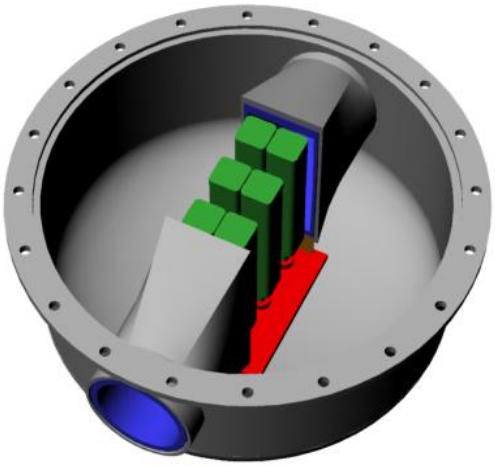

Figure 6. CAD drawing of the inside of the SEP pressure vessel, showing the main duct disassembled and the green modules inside.

An Air Products-led engineering team built the skid-mounted unit next to an Air Products air separation facility in Sparrows Point, Maryland, as shown in Figure 7. The unit is approximately 60 feet long by 30 feet wide.

Figure 7. Photograph of the 5 TPD SEP installed at Sparrows Point, Maryland. The ITM pressure vessel is in blue in the upper right-hand corner of the photo.

Air Products commissioned the unit over a series of four commissioning tests. During the third commissioning trial, the team produced the first oxygen from a 0.5 TPD-scale ITM Oxygen module. Purity reached as high as 95% during the run. Once the unit was commissioned, the team conducted four experiments, each with two 0.5 TPD-scale modules installed. The early trials were characterized by attempts to create a thermal gradient at the base of the modules so that the ceramic-to-metal seals could operate within their elastic ranges. By the end of this work, it was clear that the ITM ceramic was not able to withstand the thermal gradients required, and that further development on a hot seal would be required. Despite these findings, the team was successful in meeting expected fluxes for thick-membrane modules, and reaching as high as 99% purity from a single module. The work also validated the hot flow duct/cold pressure vessel design concept and provided a basis for further scale-up.

Concepts NREC and Air Products collaborated on designs for the 25 TPD pre-Commercial Design Facility (pCDF), an early notion for the Phase 3 test facility that later was expanded to become the 100 TPD Intermediate-Scale Test Unit (ISTU). Based on discussions with Siemens, the team chose the GT35P machine as the basis for the power cycle because it afforded a great

deal of air extraction. The team estimated that the GT35P could support up to 1000 TPD of oxygen production. A larger version of the machine, the GT140P, was identified that could support 4500 TPD oxygen production. The pCDF cycle was based on the GT35P and produced nominally 25 TPD oxygen, but could be expanded to produce ~150 TPD depending on the configuration. Concepts NREC developed a pre-combustor design for the pCDF, establishing the feasibility of its stable operation.

Concepts NREC further developed start-up process control scenarios for a 150 TPD version of the ISTU, which was similar to the pCDF process design. Specific control steps were envisioned to control temperature and pressure ramps to ensure stable flames in the pre-combustor and robust membrane performance.

Air Products and Siemens collaborated to study the ITM-gas turbine integration problem in detail. The team selected the Siemens SGT6-6000G (formerly the W501G) for the study (Figure 8). Siemens considered only modifications of the combustion section of the gas turbine to avoid redesign of the compression and turbine sections. Siemens calculated that ~55% of the total air flow could be extracted from the outlet of the compression section and sent to the ITM as feed flow; the ITM non-permeate stream was returned to the inlet of the combustion section and augmented for mass flow. Special plenums were designed to enable gas flow in and out of these regions.

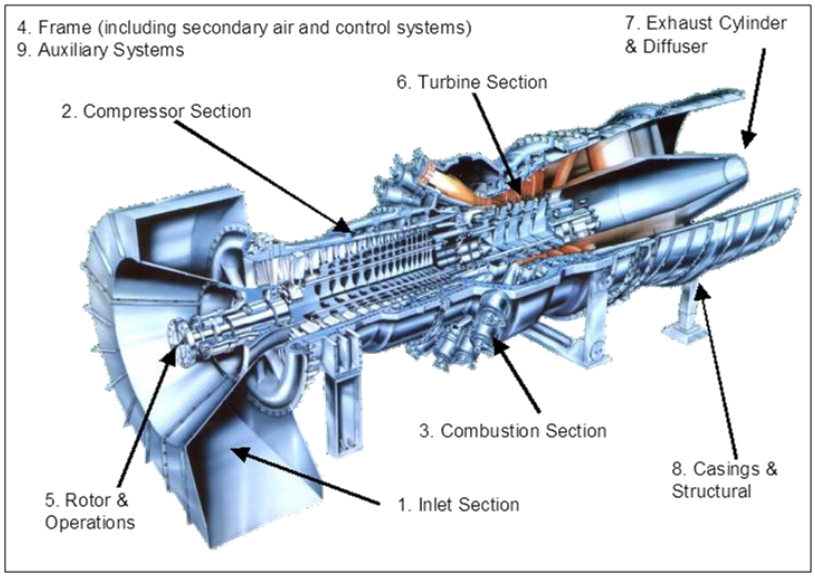

Figure 8. Siemens SGT6-6000G gas turbine functional areas.

Siemens and Air Products carried out a study of the power block and ITM system and contrasted the efficiency and capital costs of various configurations, showing that the system could be designed to give the benefits described in the IGCC study carried out with Texaco Gasification and Concepts NREC in Phase 1. The team also conducted an operability assessment for a fully integrated SGT6-6000G and ITM Oxygen plant.

Finally, Air Products collaborated with NovelEdge Technology to develop a process design that supports integration with unmodified gas turbines. The process features modest air extraction from GE 7EA gas turbines for ITM feed air, which is augmented with air from a supplementary main air compressor, and co-produces nitrogen diluent and power from a dedicated hot gas expander. Studies in an IGCC application showed a 9% reduction in the specific capital cost of an IGCC and 7% lower cost of electricity (COE) in the ITM cases relative to state-of-the-art cryogenic ASU technology.

Summary of Phase 3 Accomplishments (Tasks 14-21)

Ceramatec developed a detailed FEA model based on a five-wafer module, complete with an end cap, spacers and base piece, which produced stress fields representative of larger structures. Studies of stress development in this module during simulated thermal and pressure cycles, characteristic of an operating environment, were used to identify preferred geometries for end caps and base pieces and helped to guide selection of process cycles. This work ultimately led to a redesign of the standard wafer, producing "advanced architecture" wafers with superior reliability under process transients.

Air Products supported module component redesign work with small- and large-frame dilatometry studies that established the relative expansion (strain) between components of different morphology within the module. Relative expansion during transients of temperature and oxygen partial pressure was measured and augmented component strength data gathered by Ceramatec. Improved spacer and base piece designs were produced based on this work.

Penn State and Ceramatec expanded the component reliability database with advanced high-temperature testing of creep phenomena and component failure analysis. Ceramatec implemented *in situ* acoustic emission measurements of thermally cycling wafers with simultaneous IR and visual imaging to correlate failures with specific stresses identified by

modeling. Ceramatec augmented the stress models used to describe the expansion of materials and composites with measurements of the surface exchange coefficient for oxygen on the AP2K, and subjected wafers to thermal gradients to compare with modeling results. The five-wafer model was used to predict stresses in modules subjected to axial gradients and compared with data from the SEP. All of this work supported reliability predictions for full size-parts. A model was ultimately developed for the ISTU which tracked the strain in the materials as various process control schemes were implemented and refined to react to process transients, including unplanned trips.

Ceramatec significantly expanded the PDF to produce modules for eventual ISTU testing by adding kiln and tape casting capacity. The team reduced cycle times in the kilns significantly to increase productivity while maintaining or improving yield, and implemented a Wafer Assembly Machine (WAM) which automated the wafer lamination process to reduce labor costs and increase production uniformity. With the expanded PDF, Ceramatec successfully ramped production rates, producing 74,500 kg of AP2K powder and 720,000 feet of tape during Phase 3. Air Products supported powder production with tests of ~1300 lots, 99.5% of which were within specification for cation stoichiometry in the AP2K powder. From the powder, Ceramatec produced 790,000 featured parts and sintered over 110,000 wafers, 4400 submodules and over 213 modules. Over 100 of these modules were 1 TPD-scale, with the balance at the 0.5 TPD scale. This work provided a substantial database to support of further scale-up of membrane module manufacturing.

During this phase and in addition to the requirement to produce a large number of finished articles for testing, Ceramatec improved all of the components in the module. Beyond their work described above in which end caps, spacers, and base pieces were improved, the team implemented a porous protective layer on the wafers to protect the membrane during fabrication, and also modified the internal wafer slot pattern to reduce internal pressure drop in the interior oxygen flow. Air Products supported those changes with analysis and specific flux tests that showed that the porous protective layer was either neutral or enhanced flux, and with pressure drop testing that showed the improvement in the interior pressure drop brought on by the slot pattern changes. In mid-Phase 3, Ceramatec implemented the advanced architecture wafer and improved its production yield to 50-70%, on a par with standard wafers. Over 90% of the 1 TPD-

scale modules pmade during Phase 3 were produced from advanced architecture wafers, which enabled good joining yields for larger modules. Figure 9 shows four 1 TPD modules built from advanced architecture wafers and ready for shipment to the ISTU.

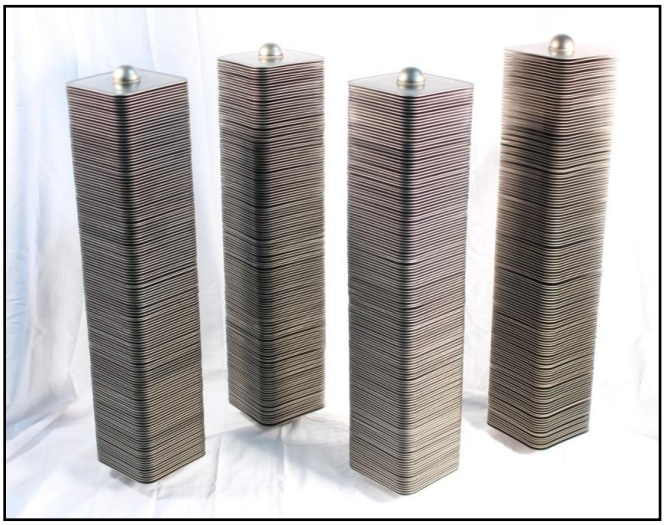

Figure 9. 1 TPD-scale ITM Oxygen modules made with advanced architecture wafers.

Air Products evaluated the redesigned ceramic components with flux and reliability testing in laboratory pilot units that operated at full process conditions. In addition, Air Products completed a 7925 h flux test of a 2-(standard) wafer module in the TDU over a variety of conditions, including planned and unplanned transients (full thermal cycles). The module produced steady flux and purity during the test without degradation. A chromium getter in the TDU maintained the surface of the module chromium-free.

To establish the performance of the redesigned components in larger modules and to qualify various hot-service components for use in the ISTU, the team carried out a total of 21 module performance tests in the 5 TPD SEP. Including the work in Phase 2, by the end of Phase 3 the cumulative on-stream time spent testing modules in the SEP exceeded 1000 days over a total of 31 test campaigns. The performance testing was focused on establishing the reliability of modules during transient operation (start-up/shutdown cycles). Tests were conducted on groups of two to six modules, including the first tests of both 1 TPD-scale modules and advanced architecture modules. The team implemented iso-control techniques and was able to cycle

modules multiple times without degradation in flux or purity. An example data set is shown in Figure 10.

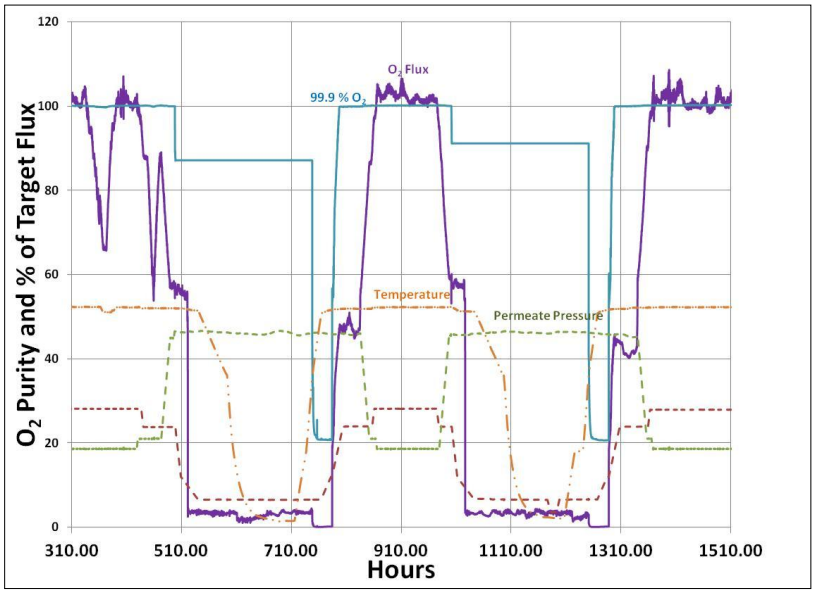

Figure 10. Process data, purity and flux from SEP Run 27, showing performance through multiple cycles.

The SEP was used to qualify a number of components for implementation in the ISTU. Air Products worked with a supplier to scale up production of a MgO-based chromium getter developed in Phase 2 by using a ceramic monolith material as a substrate (such getters were successfully demonstrated in the SEP). Tests with modules fitted with ceramic-to-metals seals selected from extensive laboratory testing were implemented on prototype seal sub-assemblies fitted with Automatic Shutoff Valves (ASOVs) that allowed for remote valve activation. Test results indicated the ASOVs to be reliable and to provide a positive and definite isolation of a damaged module without causing peripheral damage to adjacent modules in the array. These tests were conducted with prototype flow ducts (see example in Figure 11) in the SEP pressure vessel which comprised insulation materials that had first been screened by extensive hot flow path testing in laboratory apparatus to ensure minimal off-gassing of potential contaminants during operation. The successful tests in the SEP directly led to the insulation specification for the ISTU. Finally, the team developed module handling equipment and procedures that allowed for reliable installation and removal of modules from the vessel. All of these technologies were ultimately implemented in the ISTU.

Figure 11. Two examples of SEP flow ducts: an older design during assembly (left) and a newer prototype (right).

Air Products executed the design, construction and commissioning of the 100 TPD ISTU at its Convent, Louisiana, air separation site. The project engineering team that executed the project consisted of project management and process, mechanical, systems, machinery, operations and construction engineering experts supported by the ITM R&D team, site personnel, and EH&S professionals. The ISTU was designed to incorporate the major unit operations expected in a commercial-scale ITM Oxygen facility that co-produces power. The intent of the plant was to provide process design verification and scale-up data to support a subsequent ODF or other demonstration-scale facility. Referring to the ISTU block flow diagram shown in Figure 12, the process included hot recuperative heat exchange, an indirectly fired air pre-heater, an ITM pressure vessel housing an array of modules, oxygen cooling by raising steam, and a hot gas expander fired with natural gas to recover the energy from the oxygen-depleted, high-pressure/high-temperature non-permeate stream.

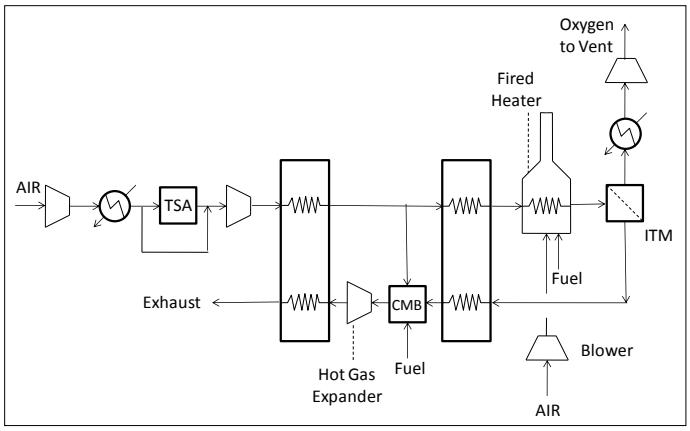

Figure 12. Block flow diagram of the Intermediate-Scale Test Unit (ISTU).

Air Products and Becht Engineering designed the ISTU ITM pressure vessel based on the concepts developed in Phase 1 and trialed successfully in Phases 2 and 3. The vessel included an internally insulated flow duct, individual oxygen permeate piping for each module and connected to one of four common oxygen manifolds within the vessel, an internal getter for chromium upstream of the modules, and was configured for research purposes to enable direct access to all rows of modules to enable implementation of instrumentation and customization of the module environment. Each permeate pipe was out-fitted with a seal sub-assembly fitted with a sample tap for monitoring the oxygen purity from each module as well as an ASOV. The dimensions of the vessel were chosen to give a maximum module array-width within a road-shippable envelope. A photo of the vessel during installation at the Convent site is shown in Figure 13.

Figure 13. ITM pressure vessel being positioned at the ISTU.

Other notable equipment in the ISTU includes a custom hot gas expander built by Williams International. The Williams team, Concepts NREC and Air Products conducted extensive combustor performance experimentation prior to Williams finalizing the design of the integral combustor. The expander components were based on Williams' existing turbo-jet technology used in its commercial aircraft engine product lines. Air Products also developed particulate removal technology that was implemented downstream of the fired heater and upstream of the ITM vessel to protect the modules from any metal oxide spall from the hot metallurgy. Air Products' control system was customized based on the unique requirements of the unit to co-produce or independently produce power and oxygen, and incorporated learnings from the SEP and laboratory apparatus.

Air Products conducted the site work over a 2.5-year period, which included a significant pause in the construction schedule for late equipment delivery. The team completed the unit with 96,500 man-hours of construction engineering and site labor with excellent safety performance (a single first aid case). The finished ISTU is shown in Figure 14.

Figure 14. Photograph of the completed ISTU at Convent, Louisiana.

The ISTU team commissioned the unit over a series of three trials. Prior to commissioning, the ITM vessel was fully equipped with non-fluxing modules that imparted the pressure drop and heat transfer behavior of fully functioning modules to enable characterization of the thermal and hydraulic performance of the flow duct. The commissioning trials were successful in demonstrating that the plant could meet full operating conditions and made the rated power output of the hot gas expander. Moreover, the good thermal performance of duct with the non-

fluxing modules validated the vessel design approach to enable future scale-up of the pressure vessel in the axial direction, allowing for much larger single-vessel production capacities in future implementations.

Ceramatec was successful in developing low-cost shipping containers to house and ship ITM Oxygen modules. Approximately 75 modules were successfully shipped to the SEP and ISTU during the course of Phase 3. The final shipment consisted of 32 1 TPD modules in a single shipment for the ISTU by commercial carrier; all modules were received without damage. The shipping containers feature integral leak-testing and handling provisions to allow installation with minimal module manipulation.

To conclude Phase 3, Air Products carried out two tests in the ISTU with active membrane modules installed and producing oxygen. Run 1 was designed purposefully to put a small number of modules through severe service by subjecting the system to process upsets. The trips included simulation of an electrical failure and loss of the vacuum permeate system. Additional system anomalies resulted in significant thermal gradients developing at times during the run. Some modules were lost during these events, which caused their ASOVs to close appropriately to isolate them. However, at least one of the modules continued to produce 95% pure oxygen throughout the run.

ISTU Run 2 was designed to produce oxygen from an array of ITM Oxygen modules in two rows spanning the entire width of the vessel. The installed modules intentionally represented a range of module production lots and quality; only a few met specification for leakage. Each of the modules was equipped with sample taps to enable individual module product purities to be monitored during the run. Two different ceramic-to-metal seals were used as well. Figure 15 shows the first row of modules installed inside the ISTU prior to re-assembly of the internal flow duct.

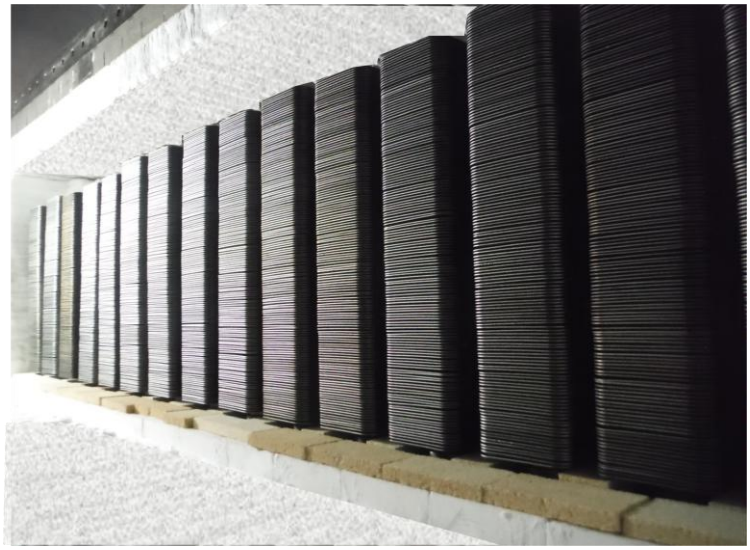

Figure 15. View of the first row of modules installed in the ISTU ITM vessel prior to Run 2.

Air Products operated the ISTU smoothly over a 2-week test; all modules started up successfully and produced oxygen. During the run, 17 of the modules produced >90% oxygen purity; the best module produced 99% oxygen purity. The product purity of the combined module array ranged from 80-85%. Productivity exceeded the expected oxygen output of the installed modules by ~10%, producing 16 TPD oxygen net of any leakage. The run was highly successful in demonstrating tonnage oxygen production from an array of ITM Oxygen modules and supported on-going testing and module refinements in anticipation of a larger-scale demonstration.

Summary of Phase 4 Accomplishments (Tasks 22-26)

In Phase 4, Air Products investigated a "Reaction-Driven" ITM approach in which oxygen from low-pressure air permeates as oxygen ions through the ceramic membrane and is consumed through chemical reactions, thus creating a chemical driving force that pulls oxygen ions across the membrane at high rates. The oxygen reacts with a hydrocarbon fuel in a partial-oxidation process to produce a hydrogen-carbon monoxide mixture known as synthesis gas (syngas). The technology has significant potential to improve the economics for gas-to-liquid facilities and hydrogen plants, especially when carbon dioxide capture is required.

Ion Transport Membranes offer the potential for a substantial reduction in the capital cost associated with syngas production. In this technology, the air separation plant and the high-temperature, partial-oxidation plant are conceptually combined into a single-unit operation,

thereby resulting in a substantial reduction in capital costs. The main technical risks addressed in Phase 4 involve the very high-temperature operation of such systems and the related effect on materials. The work focused on expanding the partial-oxidation scope of ITM technology beyond natural gas feed, specifically investigating the potential for Reaction-Driven ITM technology to be used in conjunction with gasification and pyrolysis technologies to provide more economical routes for producing hydrogen and synthesis gas.

Air Products explored several concepts for integrating Reaction-Driven ITM technology with solid-fuel power and/or syngas production. Of these concepts, integration with a low-temperature gasifier, such as a Sasol-Lurgi dry-ash, fixed-bed gasifier, was the most promising. In this scheme, the ITM unit served as an autothermal reformer, converting residual hydrocarbons in the gasifier syngas product and enabling a high degree of carbon capture in downstream operations such as power generation. No additional air separation unit was required in this scheme.

The team also identified economic solutions for nitrogen production from ITM technology. A comparison of nitrogen gas production processes for making a purge and transport gas stream was completed with good progress in understanding how reaction-driven membrane technology can be used to produce nitrogen at specific maximum oxygen contents.

Air Products and Ceramatec identified alternative ceramic materials, and developed and tested representative membrane devices under the operating conditions expected for reaction-driven processess. Advanced ITM wafer designs with enhanced oxygen flux, improved mechanical strength and higher expected reliability were manufactured and tested in an existing Air Products unit. Experimental testing of Reaction-Driven ITM devices progressed sufficiently to justify continued scaled-up testing to assess commercial readiness.

Summary of Phase 5 Accomplishments (Tasks 27-31)

Air Products investigated literature data published since the development of the AP2K material for potential ITM material improvements. Criteria for selection of materials for further analysis included better strength, better resistance to reaction with CO_2, higher flux and/or lower operating temperature at the same flux. Air Product considered over 200 materials presented or suggested by the published literature, ultimately focusing on <20 materials for experimental assessment. Materials were synthesized and exposured to air and to CO_2-in-air at elevated

temperature. Only two materials exhibited relatively little reaction with CO_2 or phase stability in air at prolonged periods at high temperature. Air Products fabricated thin membranes from these two compounds, demonstrating that they have good potential to be processed to form wafers with conventional ceramic processing techniques.

Air Products worked with a supplier to specify and have built a high-pressure (HP) dilatometer that could accommodate large parts and sustain oxygen partial pressures of ~3 atm. The unit was commissioned and operated. The dilatometry data obtained with the HP dilatometer indicated that the models based on data taken at up to 1 atm oxygen partial pressure somewhat underpredict the expansion at 3 atm.

Air Products, Penn State and Ceramatec expanded the database for porous materials. Dilatometry was used to elucidate the relationship between material open porosity and equilibration time with the gas phase for a variety of composite parts and materials. Air Products applied a Voronoi tessellation technique to analyze porous layer micrographs for quantification of characteristic diffusion lengths within the material. Ceramatec and Penn State developed compressive creep data for both wafers and modules; the data were compared to creep modeling results.

Ceramatec modified the five-wafer stress model developed in Phase 3 to include advanced architecture wafers (AAWs). The modeling indicated that stresses arising during a typical oxygen production cycle, which includes start-up, steady-state operation, and controlled shutdown, are much lower for the AAWs than for the standard wafers. The team augmented this understanding by collecting macroscopic wafer strength data with several techniques that impart different stress states to the wafer. A study comparing AAWs directly with standard wafers showed the AAWs to be much more robust during thermal cycling.

Ceramatec improved AAW manufacturing yield within the PDF. Powder processing was improved, with tightened specifications for AAW pre-cursor powder. A statistical analysis of One Step and Two Step processes for AAW membrane layer fabrication indicated that the Two Step process was superior. Ceramatec also identified an improved formulation for the green material, the so-called “poly” formulation, and recommended modifications to the process steps to enable “poly wafers” to be fabricated in the PDF and the CerFab. Poly wafers are expected to

be stronger than the conventional AAWs while still equilibrating rapidly with the gas phase during sintering, joining, and operation, thus resulting in a higher-yield part that is more reliable.

The team identified the parameters required to produce submodules and modules from improved "OD2" spacers and AAWs. Experimental work also led to improvements in the parallelism of wafers within a module and in maintaining the overall dimensional envelope during joining. Measurements of module dimensions made with a Faro® arm metrology tool were conducted to track progress against a dimensional envelope specification.

In parallel, Air Products carried out an extensive test campaign with AAWs. Twenty-two single-AAW modules were tested in the XVUs; the parts showed good thermal/pressure cycling ability and expected fluxes. Work with the TDU was focused on longevity. A 12-AAW module was tested for a record 8000+ h on-stream at high flux and purity and with no flux or purity degradation during this time period (this module ultimately reached 12,800 h of on-stream time). Another reliability test in the Transient Test Rig (TTR) indicated that the AAWs could withstand severe process transients without failure. Both these tests, conducted under realistic operating conditions, and the modeling and test work carried out by Ceramatec validated the design of the AAWs and the manufacturing methods used to make them.

Much of the Phase 5 effort was devoted to developing specifications for the Ceramic Membrane Module Manufacturing Facility (CerFab) process and equipment. Ceramatec assessed vendor technology by running trials at vendor sites to develop an understanding of available tape casting, milling, and vision system technology. The team performed studies on kiln furniture cleaning, tape- and sintered component-recycling (to improve overall process yield), and reduced the thermal cycle duration for submodule and module joining. Ceramatec also analyzed the material handling process and improved labor efficiency during submodule assembly. All of this information was fed to the CerFab engineering team developing specifications for equipment purchases.

Air Products, with support from Ceramatec, executed the CerFab project in which a membrane module manufacturing facility was designed, built and commissioned, with the capability to supply a 2000 TPD ITM Oxygen plant. The team developed a process scheme based on work completed in the PDF. Figure 16 shows a simple material flow diagram of the CerFab process.

Raw powders are milled and calcined to produce the AP2K material, which is further processed to produce the desired powder size distributions for the various downstream uses. Wafers are made by laminating cast tapes together. Interior layers are featured with slots to allow oxygen transport, with the thin, dense membrane layer toward the outside, sandwiched between porous layers for support and protection. Wafers are sintered to form dense parts, then successively joined to form submodules and then modules. Each of the steps in the figure was trialed with similar equipment at the PDF prior to specification for the CerFab.

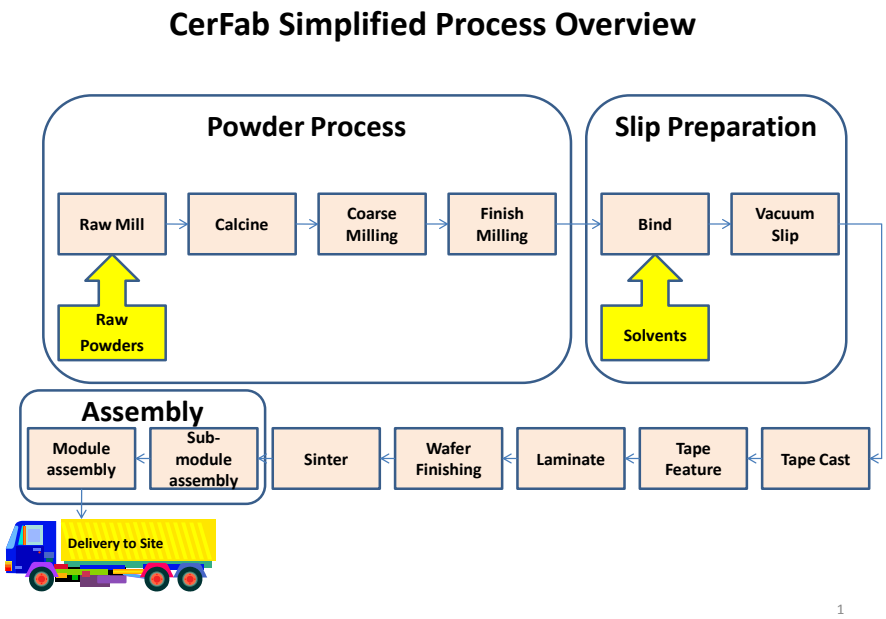

Figure 16. CerFab simplified process overview.

After extensive evaluation, the team chose to construct the CerFab in an existing 100,000+ sq. ft. building in Tooele, Utah, and planned the building retrofits and equipment layout. Competitive bids were obtained for all the major equipment, and all necessary environmental permits were received for operation of the facility. With DOE approval of the budget, the team executed the procured and installed the equipment and began the building retrofits. Figure 17 shows installation of the powder processing room within the CerFab building. The construction and commissioning of the facility were completed within the 24-month schedule allocated.

Figure 17. Cerfab powder processing room during construction.

Commissioning of the facility occurred in two phases with total duration of three months. In the first phase, individual equipment items were commissioned. In the second phase, the process was commissioned as a total ensemble. During commissioning, the team produced 3700 kg of AP2K powder and used that in downstream processes.

A team from Air Products and Ceramatec successfully operated the CerFab, producing advanced architecture wafers, submodules, and modules. In first quarter of operation, the team made 5900 kg of AP2K powder from which 9300 meters of tape were produced. Many in-spec wafers were built, and the team constructed the first intact 1 TPD modules (Figure 18). During the operating period of the facility, 7000+ wafers were produced from 40,000+ featured parts, and yields of testable parts climbed above 50%. Test parts were also produced. Air Products demonstrated that the CerFab-generated wafers produced steady flux and were robust during unplanned transients in XVU tests.

Figure 18. The first 1 TPD module produced at the CerFab.

Toward the latter period of operation, the team transitioned the CerFab operations to investigate the production of poly wafers and to assess process variability with the new formulation. Figure 19 shows the CerFab in operation inside the cleanroom facility where wafers are laminated. The work with the CerFab proved that the ceramic processes developed by Ceramatec in the PDF are scalable, and that ITM Oxygen wafers and modules can be produced in a manufacturing environment with high potential for success in commercial production.

Figure 19. Inside the completed CerFab cleanroom during operation.

To lay the ground work for the next scale-up step beyond the ISTU, the Air Products team developed process options at the 2000 TPD scale. A number of commercial applications were considered in which the ITM Oxygen process could enable low-carbon emissions. These include coupling the ITM with NGCC, gasification of vacuum residue streams, ammonia and GTL/MeOH operations. Most notably, Air Products developed the concept of the *hybrid* ITM

Oxygen-cryo ASU facility in which the ITM Oxygen process provides its excess power to the ASU. One attractive variant is the case in which the power requirements of the ASU are exactly met by the ITM, such that the overall facility requires no import electricity. The team developed two variants of the ITM process based on turbo-machinery selection and compared them for different scenarios.

Ultimately, Air Products chose an ITM process cycle based on the Siemens SGT-800 gas turbine, then formulated a scheme in which a 2000 TPD ITM Oxygen facility is coupled with a 3000 TPD cryo ASU plant to supply a conceptual GTL plant in the U.S. Gulf Coast. Net power production from this *hybrid* facility was estimated to be 80 MW. The team developed a detailed process flow diagram, equipment specifications, plant layout, construction estimate, and overall budgetary costs. The Air Products team devised a dual-train ITM Oxygen system with each train utilizing a fired heater, recuperative heat exchange, and boiler system to cool the oxygen and raise steam. The process contemplates a 2x1 gas turbine/steam turbine configuration for the plant. Siemens conducted an experimental study of low O_2 content combustion and modeled the combustor and core engine design specifically for the SGT-800. With Air Products, Siemens assessed process integration and controls challenges and factors affecting the reliability and maintenance of the resulting system. The results of this work provide a basis for the 2000 TPD Oxygen Development Facility (ODF) envisioned for future scale-up/demonstration of ITM Oxygen technology (Figure 20).

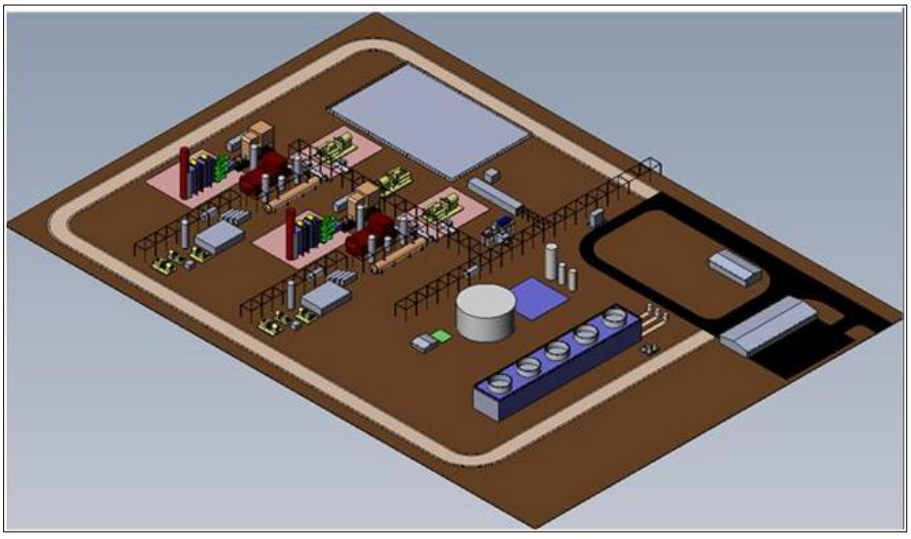

Figure 20. Oxygen Development Facility (ODF) proposed plot plan.

PHASE I RESULTS AND DISCUSSION

TASK 1.0 MATERIALS DEVELOPMENT

1.0 Scope

Under Task 1.0, Air Products selects suitable materials with improved high-temperature properties and ease of fabrication using a statistically designed property/composition data base. Material selection is in part based on lifetime testing in pre-existing and new apparatus under steady-state, simulated process conditions to establish projected oxygen flux and purity results. Additional minor optimization or change in specification due to the engineering evaluations is donee to select a final composition for scale-up. Eltron Research carries out specific evaluations of optimized materials to enable comparisons to be made with the final specification, and to facilitate the selection of final compositions. Penn State University evaluates the compositions for long-term effects on mechanical properties.

Optimize ITM Oxygen Materials

ITM Material Selection: Overview

Air Products proposed its scope of work based on a perovskite ITM material designated "AP96." Work prior to the 'pre-award' period of the contract identified an improved ceramic "AP98" perovskite composition. Selecting AP98 involved experimental verification of chemical and physical properties of four AP98-candidate compositions, and also included a laboratory-scale assessment of membrane fabricability at Ceramatec. The AP98 composition was used for initial membrane fabrication scale-up under Tasks 3.2 and 3.3.

The four AP98 candidates originated from an in-depth statistical property/composition study of ITM Oxygen materials. AP98 is the superior composition, with demonstrated improved properties and fabricability compared to the preceding ITM Oxygen composition (AP96). Strength, creep resistance, and chemical resistance are all enhanced, and AP98 retains bulk ionic conductivity similar to that of AP96.

The high-temperature creep data measured with laboratory-scale samples of AP98 in pre-award work indicated sufficient creep resistance at the envisaged full process operating conditions for ITM Oxygen. Since physical properties may be influenced by the ceramic fabrication method,

further property data were measured for AP98 samples fabricated under Task 3.2. Experiments are also continuing to more fully define the chemical resistance of AP98 to feed gas components. Chemical resistance data was used to determine the engineering requirements for feed gas processing (Task 2.2).

The selection process for the final optimized ITM Oxygen material (AP2K) commenced in August 1998. The first proposed AP2K candidate, AP2Ka, evolved from the statistical property/composition database and the improved membrane fabricability observed to date for AP98. A laboratory-scale assessment of AP2Ka membrane fabricability was initiated at Ceramatec, and measurements of chemical and physical properties began. The second AP2K candidate, AP2Kb, was investigated starting in September 1998. Ultimately, AP2Ka, henceforth referred to simply as AP2K, was chosen in May 2000 based on superior stability and flux.

Material Creep

AP98

Ceramatec generated bend bar creep data at 825°C, 875°C and 925°C at stress levels of 0.5-8 ksi with a known method (Cranmer and Richerson, 1998). The data are plotted in Figure 1-1 as a normalized creep rate against stress in ksi (1 ksi = 1000 psi). Significant advances in experimental equipment and techniques have allowed creep rates less than the 10-year ITM Oxygen target value to be measured at a stress of 0.5 ksi at 875°C. The reported stress is the maximum outer-fiber stress as determined by Penn State under the assumption that compressive and tensile creep obey the same constitutive law. More development of experimental techniques and equipment is necessary to obtain quantitative data for design purposes. Bend bar data can be used to roughly estimate the maximum allowable stress at a given temperature.

A power law expression for creep rate is given by

$$\dot{\varepsilon} = A_{creep}\sigma^{n}e^{-E_{creep}/RT}$$

where A_{creep} is the pre-exponential factor, σ is the stress, n is the stress exponent, E_{creep} is the activation energy and T is the temperature. Fitting the creep data to this expression allows the model parameters to be obtained, which are plotted in Figure 1-1 along with the data. The fit of the model to the data is good.

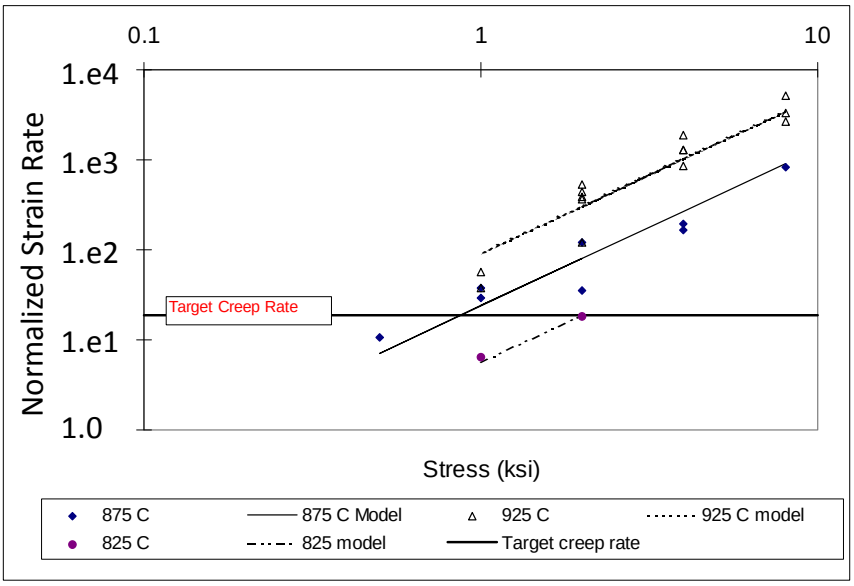

Figure 1-1. AP98 creep data and model predictions.

Using the model derived above, the maximum allowable stress at a given temperature can be estimated. At 875°C, the value is 874 psi for the target 10-year creep life. However, the 95% confidence interval is wide (560 – 1660 psi), indicating a need to obtain more high-quality data to tighten the confidence interval. However, a comparison of data obtained earlier at 925°C to the more recently obtained 875°C data shows significant progress on improving sample-to-sample reproducibility.

AP2Ka

Ceramatec generated a set of bend bar creep data for AP2Ka material using the same method and similar conditions as used for the AP98 material. Figure 1-2 is a plot of the normalized strain rate against stress in ksi. The data were fit to the creep strain model presented above to generate the curves shown.

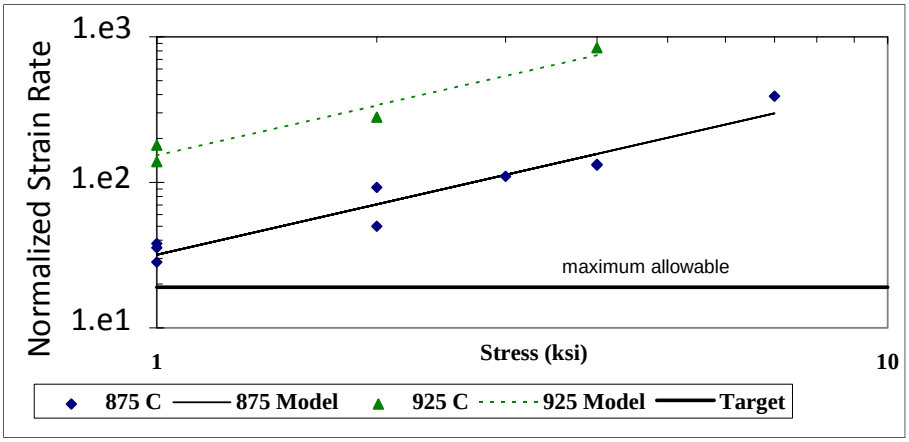

Figure 1-2. AP2Ka creep data and model predictions.

The model derived above can be used to estimate the maximum allowable stress at a given temperature. At 875°C, the value is 637 psi for the target 10-year creep life – a lower value than the maximum tensile stress predicted for a full-scale wafer under Task 2. However, the 95% confidence interval is 437 - 1040 psi. The impact of these stress levels on wafer lifetime will be evaluated in light of the improved wafer geometry developed under Task 3.

Material Expansion

Air Products used thermogravimetric analysis (TGA) to determine the oxygen non-stoichiometry of candidate ITM materials. The data were fit to a non-stoichiometry model for oxygen in perovskites. Figure 1-3 shows the predicted vacancy fraction data, x_v, plotted against the actual values for the AP2Ka material. The x_v data were collected over a range of temperatures and oxygen partial pressures. Similar data and fits were obtained for the AP98 material.

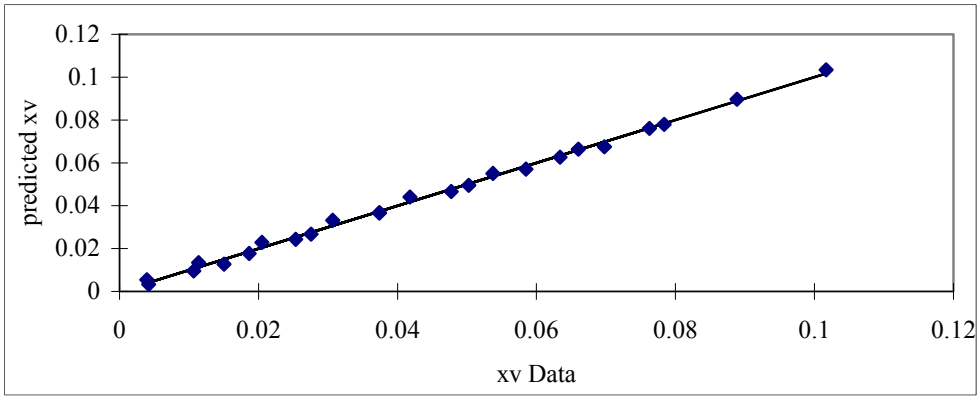

Figure 1-3. Predicted vacancy fraction in AP2Ka versus actual. Predicted values are based on an oxygen non-stoichiometry model for perovskites.

Dilatometry experiments were carried out on samples of AP98 and AP2Ka over a range of oxygen partial pressures (P_{O2}) between 0.005 and 1.0 atm. The data were fit to the following equation:

$$\delta_\varepsilon(T, P_{O2}) = (CCE^0 + CCE^1\ (T-T^0))(x_v-x_v^0) + CTE^0\ (T-T^0)$$

where δ_ε is the fractional expansion, x_v^0 is the vacancy fraction at 300°C/(P_{O2}= 1 atm) and T^0= 573 K. In general, the constants CCE^0, CCE^1, and CTE^0 are a function of temperature and P_{O2}; in practice, the data can be fit well with two equations, one for lower P_{O2}, and one for higher P_{O2}. Figure 1-4 shows the difference between the expansion model and the data for a range of P_{O2}.

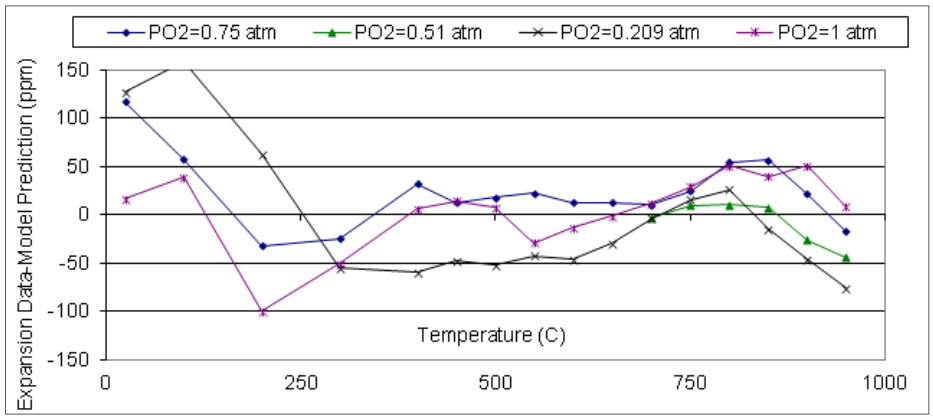

Figure 1-4. Difference between expansion data and model prediction as a function of temperature and oxygen partial pressure for $P_{O2} \geq 0.209$ atm.

AP2Ka was found to expand more than AP98 under similar conditions. Figure 1-5 shows the trend with temperature at a P_{O2} of 0.209 atm.

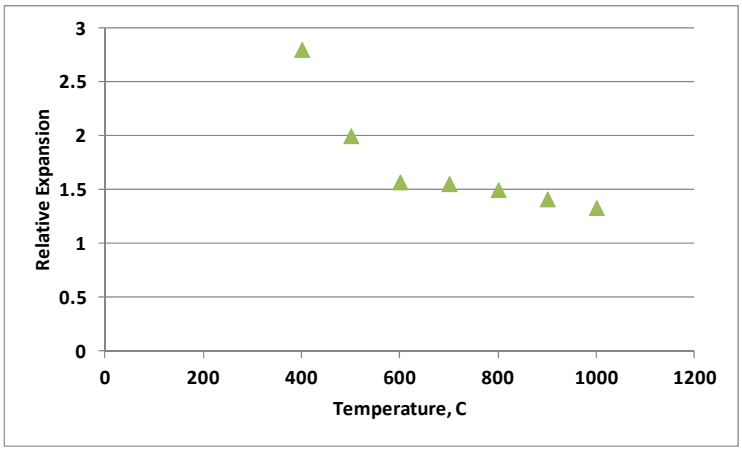

Figure 1-5 Relative expansion of AP2Ka to AP98 over the temperature range of interest at P_{O2} of 0.209 atm.

Under typical operating conditions of 15+ bar air pressure on the feed side of the membrane, the oxygen partial will likely exceed 2.5 atm. Since the process feed P_{O2} is greater than the P_{O2} where the non-stoichiometry and dilatometry data for the models were obtained, predicting the expansion requires extrapolating the models. The high-pressure TGA data are required to confirm or refine the oxygen non-stoichiometry model.

SO_2 Tolerance

AP98, AP2Ka, and AP2Kb samples were exposed to three SO_2 partial pressures ranging over two orders of magnitude at 850°C, 875°C and 925°C. A loose powder sample and a dense piece of each composition were placed into an alumina crucible and held at the atmosphere for 3, 5, and 10 days for the SO_2 partial pressures in decreasing order of magnitude. Atmospheres were prepared by flowing air and a certified mix of SO_2 in air at known mass flow rates over the heated samples. After the given hold time, the unit was quenched to 25°C and the samples were removed and analyzed. XRD was performed on the powder samples and SEM/EDS was done on the dense samples. Runs with SO_2 partial pressure Level 2 at 925°C were repeated twice; runs at 875°C were repeated three times.

SEM analysis, which was found to be more sensitive than XRD, showed that AP98, AP2Ka, and AP2Kb had no reaction at Level 3 (lowest P_{SO2}) at 850°C and 875°C. Reaction was detected at Level 2 at 850°C for all three compositions. At 875°C, reaction was detected only at Level 1 for all compositions. At 925°C, all samples reacted at Levels 1 and 2. This was surprising, since no reaction was detected at 875°C at Level 2. Due to this unusual result, these materials were re-exposed to the same conditions (875°C, Level 2). The same result was obtained. In the first run, AP98 showed a second phase that was concentrated at the grain boundaries and found by EDS to be sulfur-rich. The second run under the same conditions showed very similar results. The first run of AP2Ka also showed an S-rich second phase, which was again detected in a second run. An S-rich second phase was detected in both AP2Kb runs, although in the second run the sulfur coverage was less extensive. Although the concentration of the S-rich phase seems to vary somewhat from sample to sample, all samples did react. Tables 1-1 through 1-3 summarize the data for each of the materials exposed to SO_2. Table 1-4 summarizes the safe operating P_{SO2} at each temperature for all compositions according to SEM results.

Table 1-1. Sulfur reaction data for AP98 composition.

AP98	850°C		875°C		925°C	
Powder # RC12-42A Dense # AMA3-36	**XRD**	**SEM**	**XRD**	**SEM**	**XRD**	**SEM**
Pso_2 Level 3	No Reaction	No Reaction	No Reaction	No Reaction	X	X
Pso_2 Level 2	No Reaction	S at Grain Boundaries	No Reaction	No Reaction	No Reaction	S at Grain Boundaries
Pso_2 Level 1	B-rich phase	S Coating on Surface	S-rich phase	S at Grain Boundaries	No Reaction	S at Grain Boundaries

Table 1-2. Sulfur reaction data for AP2Ka composition.

AP2Ka	850°C		875°C		925°C	
Powder #AMA3-37 Dense # AMA3-37	**XRD**	**SEM**	**XRD**	**SEM**	**XRD**	**SEM**
Pso2 Level 3	No Reaction	No Reaction	No Reaction	No Reaction	X	X
Pso2 Level 2	No Reaction	S at Grain Boundaries	No Reaction	No Reaction	No Reaction	S at Grain Boundaries
Pso2 Level 1	B-rich phase	S Coating on Surface	B-rich phase	S at Grain Boundaries	No Reaction	S Coating on Surface

Table 1-3. Sulfur reaction data for AP2Kb composition.

AP2Kb	850°C		875°C		925°C	
Powder # RC12-44A Dense # RC12-44A	**XRD**	**SEM**	**XRD**	**SEM**	**XRD**	**SEM**
Pso2 Level 3	No Reaction	No Reaction	No Reaction	No Reaction	X	X
Pso2 Level 2	No Reaction	S Coating on Surface	No Reaction	No Reaction	No Reaction	S at Grain Boundaries
Pso2 Level 1	Hexagonal phase detected	S Coating on Surface	B-rich phase	S at Grain Boundaries	No Reaction	S Coating on Surface

Table 1-4. Safe operating SO_2 partial pressures at temperature for compositions according to SEM results.

Composition	AP98	AP2Ka	AP2Kb
925°C	Pso_2< Level 2	Pso_2< Level 2	Pso_2< Level 2
875°C	Pso_2= Level 2	Pso_2= Level 2	Pso_2= Level 2
850°C	Pso_2= Level 3	Pso_2= Level 3	Pso_2= Level 3

Runs were repeated with AP98 and AP2Ka at 875°C with an improved experimental procedure. Samples of AP98 and AP2ka were exposed to Level 2 SO_2 partial pressure and 2.5X Level 2 atmospheres at 875°C by the blending procedure described above. A dense piece of each composition was placed into an alumina crucible and held at temperature for seven days for the

experiment at the 2.5X Level 2 partial pressure. For the Level 2 partial pressure experiments, exposure times of 7 and 14 days were used. After the given hold time, the unit was quenched to 25°C and the samples removed and analyzed by SEM. Prior to exposing the samples to actual test conditions, another set of samples was run at temperature for one week in air with no SO_2 flowing. SEM analysis on these samples confirmed no S was present in the unit at the start of the experiment. The units were thoroughly cleaned between runs.

No SO_2 was detected on the samples exposed to Level 2 partial pressures (875°C) at 7 or 14 days, consistent with the results reported above. The samples exposed to a 2.5X Level 2 partial pressure at 875°C showed extensive reaction with the SO_2. The majority of the reaction products were concentrated at the grain boundaries in the AP98 sample. The surfaces of the AP2Ka samples were completely covered with SO_2.

Oxygen Flux

Flux data were taken from laminate samples of AP98 and AP2Ka. Laminates are disc-shaped ceramic composites ~35 mm in diameter that are made up of multiple layers that represent one half of a wafer, including a membrane layer and porous and slotted support layers. The laminate is brazed to a structural ceramic tube. Feed air is supplied from the top of the assembly inside a furnace; the interior of the ceramic tube is subjected to a vacuum to effect a relatively low partial pressure of oxygen on the permeate side. The assembly is heated, and the permeate flow rate and its oxygen concentration are measured to determine the rate of oxygen flux.

Oxygen Flux Studies with AP98 Laminates

Table 1-5 summarizes the structure of the AP98 laminate membranes tested at 875°C. The membrane structure was chosen as part of a statistically designed experiment to probe the effects of membrane structure on membrane performance. Membranes with and without porous protective (A') layers were tested. The composition and processing conditions of the A' layers also varied from membrane to membrane. Tested laminate porous layers fell into one of three different levels of porosity. The thickness of the membrane layer varied by a factor of >2, as did the porous layer thickness.

Table 1-5. Description of AP98 membrane laminates tested at 875°C.

Membrane	Structure (see Note)	A' characteristics		Porosity	Normalized thickness	
		Composition	Processing		Membrane	Porous layer
AMA2-50-21	A'AB	Comp 1	Treatment 1	High	1.15	0.45
AMA3-8-3	A'AB	Comp 2	Treatment 2	Low	1.15	0.35
AMA2-50-25	ABB	-	-	High	1.02	0.80
AMA3-12-7	A'AB	Comp 2	Treatment 4	Low	1.88	0.32
AMA2-50-33	AAB	-	-	High	1.47	0.39
AMA2-50-35	AAB	-	-	High	1.47	0.39
AMA3-25-6	A'AB	Comp 1	Treatment 3	Low	0.79	0.35
AMA3-25-11	A'AB	Comp 1	Treatment 3	Low	0.85	0.36
AMA3-45-2	AB	-	-	Med	0.72	0.22
AMA3-45-4	AB	-	-	Med	0.78	0.29
AMA3-45-3	A'AB	Comp 1	Treatment 3	Med	0.51	0.25
AMA3-45-13	AAB	-	-	Med	1.91	0.21
AMA3-45-18	AAB	-	-	Med	1.96	0.23
AMA4-12-57	A'ABB	Comp 1	Treatment 3	High	0.93	0.57
AMA4-12-28	A'AABB	Comp 1	Treatment 3	Low	2.04	0.60
AMA4-12-72	AABB	-	-	High	2.20	0.44

Note: A' represents a porous protective layer; A represents a membrane layer; B represents a porous layer; all laminates had slotted layers.

Table 1-6 shows the correlation coefficients between the independent membrane structure variables of the lamimate membranes tested to date. In an orthogonal experimental design, the correlation coefficients between the independent variables will be zero. However, due to the difficulty in making and testing some of the structures, it was not possible to achieve a perfectly orthogonal set. Only the A' layer is significantly confounded with the porosity level. Most importantly, the membrane thickness is not confounded with any of the other variables. Because of the slight confounding of the A' layer with the porosity level, the correlation of the membrane performance will be examined carefully with regard to these two variables.

Table 1-6. Correlation coefficients of the independent variables.

	Porosity Level %	Porous layer thickness	A' (1=A' layer, 0=none)	1/(membrane thickness)
Porosity Level %	1	0.245	-0.565	0.088
Porous layer thickness		1	0.030	0.175
A' (1=A' layer, 0=none)			1	0.367
1/(membrane thickness)				1

Table 1-7 summarizes the flux data obtained from these membrane laminates. Measurements were attempted to establish fluxes through all membranes at feed oxygen partial pressures of 0.209 atm, 0.6 atm and 1 atm. At least three permeate pressures were also to be used at feed pressures of 0.6 and 0.209 atm. However, some laminates began to leak excessively before all measurements could be completed; there are fewer data points for those membranes.

Table 1-7. AP98 membrane laminate test summary.

Laminate	Temp. (°C)	Feed O_2 Partial Pressure (atm)	Permeate Pressure[1] (Normalized)	Ionic Flux (Normalized)	Permeate Purity (%)
AMA2-50-21 A'AB	900	0.209	3.8	0.13	83.1
	875	0.209	3.8	0.11	80.8
		0.209	1	0.34	91.1
		0.209	0.38	0.44	92.3
		0.209	0.038	0.60	94.0
		0.40	0.038	0.77	94.1
		0.40	0.38	0.66	91.0
		0.40	1	0.59	80.0
		0.40	3.8	0.47	63.0
AMA3-8-3 A'AB	875	0.209	3.8	0.10	79.9
		0.209	1	0.32	90.2
		0.209	0.38	0.44	93.7
		0.209	0.042	0.59	94.7
		0.40	0.042	0.72	95.4
		0.40	0.38	0.60	94.9
		0.40	1	0.50	94.7
		0.40	3.8	0.27	93.8
		0.60	3.8	0.37	94.3
		0.60	1	0.59	96.5
		0.60	0.38	0.70	97.6
		0.60	0.042	0.82	98.4
		0.80	0.042	0.91	98.6
		0.80	0.38	0.83	98.0

Table 1-7. AP98 membrane laminate test summary (cont.).

Laminate	Temp. (°C)	Feed O_2 Partial Pressure (atm)	Permeate Pressure[1] (Normalized)	Ionic Flux (Normalized)	Permeate Purity (%)
AMA2-50-25	875	0.209	3.8	0.09	84.5
ABB	875	0.209	0.38	0.37	95.1
		0.209	0.042	0.52	97.3
		0.60	0.042	0.85	98.4
		0.60	0.39	0.81	93.8
AMA3-12-7	875	0.209	3.8	0.10	92
A'AB	875	0.209	0.39	0.40	97
		0.209	0.040	0.51	99
		0.209	0.040	0.55	100
		0.60	0.040	0.86	100
		0.60	0.38	0.79	100
		0.60	3.8	0.45	100
		1.0	3.8	0.49	100
		1.0	0.39	0.85	100
AMA2-50-33 AAB	875	0.209	3.8	0.09	91
		0.209	0.39	0.40	97
AMA2-50-35 AAB	875	0.209	3.8	0.09	85
AMA3-25-6	875	0.209	1	0.39	97.9
A'AB	875	0.209	0.38	0.51	98.5
		0.209	0.042	0.63	98.6
AMA3-25-11	875	0.209	3.8	0.15	88.97
A'AB	875	0.209	0.38	0.49	94.08
AMA3-45-4	875	0.209	3.8	0.09	85.9
		0.209	1.00	0.37	94.5
		1.0	4.9	0.66	100
		0.80	3.9	0.69	96.7
		0.60	3.8	0.66	84.6
		0.60	2.9	0.59	95.9
		0.60	0.38	1.34	86.3
		0.60	0.20	1.55	84.9
AMA3-45-2	875	0.209	3.8	0.11	83.6
		0.209	1.00	0.30	84.8
		1.0	4.9	0.71	100
		0.80	3.9	0.79	100
		0.60	3.9	0.71	97.4
		0.60	2.9	0.64	93.6
		0.60	0.38	1.17	96.6
AMA3-45-3	875	0.209	3.8	0.15	83.6
		0.209	1.00	0.52	96.1

Table 1-7. AP98 membrane laminate test summary (cont.).

Laminate	Temp. (°C)	Feed O_2 Partial Pressure (atm)	Permeate Pressure[1] (Normalized)	Ionic Flux (Normalized)	Permeate Purity (%)
AMA3-45-3	875	1.0	4.8	0.73	100
		0.80	3.8	0.77	97.8
		0.60	3.8	0.63	97.1
		0.60	2.9	0.69	97.2
		0.60	0.38	1.24	99.1
		0.209	0.20	0.89	94.7
		0.209	0.38	0.81	93.2
		0.209	3.8	0.30	82.1
AMA3-45-13	875	0.209	3.8	0.09	85.8
		0.209	1.00	0.25	90
		0.60	2.9	0.44	96.6
		1.0	4.9	0.41	100
		0.80	3.9	0.55	99.8
AMA3-45-18	875	0.209	3.8	0.11	84.8
		0.209	1.00	0.26	87.5
		1.0	4.9	0.33	100
		0.80	3.8	0.34	96.2
		0.60	3.8	0.29	94.6
		0.60	0.38	0.59	96.6
		0.60	0.20	0.68	96.3
		0.209	0.20	0.48	94
		0.209	0.38	0.44	94.4
AMA4-12-57	875	0.209	3.8	0.10	91.1
		0.209	1.00	0.32	96.8
		1.0	4.88	0.54	100
		0.80	3.9	0.60	99.1
		0.60	3.9	0.54	98.5
		0.60	0.38	0.84	100
		0.60	0.20	0.97	100
AMA4-12-28	875	0.209	3.8	0.08	85.8
		0.209	1.0	0.26	92.1
		0.60	2.9	0.31	94.7
		1.0	4.9	0.32	100
		0.80	3.8	0.34	95.3
		0.60	3.8	0.29	93
		0.60	0.38	0.56	96.3
		0.60	0.20	0.63	96.1

[1] This is not corrected for the laminate pressure drop.

Table 1-8 summarizes the pertinent structural data from all the membranes along with the flux data measured at the leading edge driving force with a feed oxygen partial pressure of 0.21 and 0.6 atm. The flux data were linearly interpolated to the same driving force for all membranes.

Table 1-8. Performance of AP98 membranes at the same driving force.

Laminate	Structure (See Note)	Porous Layer Comp.	Porosity	Membrane thickness (normalized)	Normalized flux interpolated to constant driving force of:	
					P'=0.21 atm	P'=0.60 atm
AMA2-50-21	A'AB	Comp 1	High	1.15	0.46	
AMA3-8-3	A'AB	Comp 2	Low	1.15	0.43	0.48
AMA3-12-7	A'AB	Comp 2	Low	1.88	0.37	0.59
AMA2-50-33	AAB	Comp 1	High	1.47	0.39	
AMA3-25-6	A'AB	Comp 2	Low	0.78	0.54	
AMA3-25-11	A'AB	Comp 2	Low	0.84	0.50	
AMA2-50-25	ABB	Comp 1	High	1.02	0.25	0.59
AMA3-45-2	AB	Comp 3	Med	0.72	0.47	0.55
AMA3-45-4	AB	Comp 3	Med	0.78	0.31	0.52
AMA3-45-3	A'AB	Comp 3	Med	0.51	0.47	0.64
AMA3-45-13	AAB	Comp 3	Med	1.91	0.70	0.73
AMA3-45-18	AAB	Comp 3	Med	1.96	0.28	0.28
AMA4-12-57	A'ABB	Comp 4	High	0.93	0.47	0.63
AMA4-12-28	A'AABB	Comp 2	Low	2.04	0.36	0.32
AMA4-12-72	AABB	Comp 4	High	2.20	0.26	0.33

Note: A' represents a porous protective layer; A represents a membrane layer; B represents a porous layer; all laminates had slotted layers.

Table 1-9 presents the correlation coefficients between the measured oxygen flux and the membrane structure properties. The correlation is made at feed oxygen partial pressures of 0.21 atm and 0.6 atm to see if the correlations change with the feed oxygen partial pressure. Table 1-9 shows that the flux is highly correlated with the inverse of the membrane thickness at both $P_{O2}^{Feed} = 0.21$ and 0.6 atm. Both correlation coefficients are significantly different than zero to the >95% confidence level, indicating that bulk ionic resistance is a leading resistance to oxygen transport. At a feed oxygen partial pressure of 0.21 atm, the presence of porous protective layer is positively correlated with the flux. This indicates that the porous protective layer has a positive effect on the flux at $P_{O2}^{Feed} = 0.21$ atm. However, at $P_{O2}^{Feed} = 0.6$ atm, the correlation of the porous protective layer with the oxygen flux is very weak and not statistically significant.

There is no statistically significant correlation between oxygen flux and neither the thickness nor porosity of the porous layer. However, the porosity level was tested over only a narrow range. Changing porosity level to a value outside this range could have an effect on the flux.

Table 1-9. Correlation coefficient and probability that correlation coefficient is zero between membrane features and O_2 flux at the leading edge driving force conditions.

	Correlation coefficient, R /Probability R=0	
Variable	**Feed PO_2=0.21 atm**	**Feed PO_2=0.6 atm**
1/(membrane thickness)	0.72/0.044	0.80/0.017
Porosity	-0.35/0.39	0.34/0.41
Porous layer thickness	-0.24/0.57	0.14/0.74
Porous protective layer	0.78/0.022	-0.024/0.95

The analysis of the independent variables indicated that porosity level is confounded with the porous protective layer. It was expected that the porous protective layer and porosity levels would be positively correlated with the flux. However, at P_{O2}=0.21 atm., the porosity level has slightly negative correlation coefficients, while the porous protective layer has a strong positive correlation. Therefore, the confounding of the porous protective layer with the porosity level does not appear to be an issue.

The information in Table 1-9 indicates that any model of the oxygen flux as a function of membrane structure will have the inverse membrane thickness as the primary variable. The effect of a porous protective layer (as a surface kinetic term) would then be included in the model to see if the mean square error is reduced and if the surface kinetic parameter is statistically significant. Since the effects of the porous layer properties (thickness and porosity level) could not be correlated with the flux, the effect of these variables on the flux is masked by the dominating effect of the membrane thickness. The porous layer pressure drop would be best included by independently measuring the pressure drop through model structures.

Oxygen Flux Studies with AP2Ka Laminates

Table 1-10 summarizes the structure of the AP2Ka laminate membranes tested at 875°C. The composition and processing conditions of the A' layers were the same for all membranes. Tests were conducted on laminates with and without porous protective (A') layers and with one of three different levels of porosity in the porous layer. The thicknesses of the membrane layer and

porous layer each varied by a factor of >2. The structure of the laminates was chosen to be part of a statistically designed experiment to probe the effects of wafer structure on membrane performance.

Table 1-10. Description of AP2Ka laminates tested at 875°C.

Laminate	Structure (see Note)	Porous Layer Composition	Porosity	Normalized thickness	
				Membrane	Porous layer
AMA3-38-12	A'AB	Comp 1	Low	1.01	0.37
AMA3-38-18	A'AB	Comp 2	Med	1.14	0.37
AMA4-28-7	A'AAB	Comp 1	Low	2.80	0.45
AMA4-28-8	A'AAB	Comp 1	Low	2.76	0.39
AMA4-28-16	A'ABB	Comp 1	Low	1.42	0.82
AMA4-21-16	A'AB	Comp 1	Low	2.44	0.30
AMA4-28-21	A'AB	Comp 3	High	1.32	0.30
AMA4-21-31	AAB	Comp 3	High	2.18	0.36
AMA4-28-23	A'AB	Comp 3	High	1.35	0.32
AMA3-45-21	AAB	Comp 3	High	2.03	0.31
AMA3-45-12	AAB	Comp 3	High	1.03	0.28
AMA3-45-22	A'ABB	Comp 1	Low	1.92	0.32
AMA4-21-3	ABB	Comp 1	Low	1.00	0.42

Note: A' represents a porous protective layer; A represents a membrane layer; B represents a porous layer; all laminates had slotted layers.

Table 1-11 shows the correlation coefficients between the independent structure variables of the laminates tested to date. In an orthogonal experimental design, the correlation coefficients between the independent variables will be zero. However, due to the difficulty in making and testing some of the structures, it was not possible to achieve a perfectly orthogonal set. Only the porous layer thickness is significantly confounded with the porosity level. Most importantly, the membrane thickness is not confounded with any of the other variables. Because of the slight confounding of the porous layer thickness with the porosity level, the correlation of laminate performance will be examined carefully with regard to these two variables. In any event, these two variables will only affect the pressure drop through the porous layer, which is best measured independently of flux.

Table 1-11. Correlation coefficients of the independent variables.

	Porosity	Porous layer thickness	Porous Protective Layer (1= layer present, 0=none)	1/(membrane thickness)
Porosity	1	-0.41	-0.12	0.23
Porous layer thickness		1	0.0073	-0.021
Porous protective layer			1	-0.091
1/(membrane thickness)				1

Table 1-12 summarizes the flux data obtained from these membranes. It was our intent to measure the flux through all membranes at feed oxygen partial pressures of 0.209 atm, 0.6 atm and 1 atm. At least three permeate pressures were also to be used at feed pressures of 0.6 and 0.209 atm. However, some membranes began to leak excessively before all measurements could be completed and there are fewer data points for those membranes.

Table 1-12. AP2Ka membrane summary for tests at 875°C.

Membrane	Feed O_2 Partial Pressure (atm)	Permeate Pressure[1] (Normalized)	Ionic Flux (Normalized)	Permeate Purity (%)
AMA3-38-12	0.209	3.8	0.16	88.1
	0.209	1.0	0.43	92.0
	0.6	2.9	0.64	96.9
	1	4.9	0.77	99.5
	0.8	3.9	0.74	97.5
	0.8	3.9	0.76	96.5
AMA3-38-18	0.209	3.8	0.18	85.9
	0.209	1.0	0.45	89.6
	1	4.9	0.92	100.0
AMA4-28-7	0.209	1.0	0.10	93.9
	0.209	0.38	0.34	98.8
	1	0.040	0.40	99.6
	1	0.040	0.45	100.5
	0.6	0.38	0.34	99.6
	0.6	1.0	0.38	99.9
	0.6	3.8	0.47	100.0
AMA4-28-8	0.209	3.8	0.09	93.0
	0.209	1.0	0.27	98.8
	1	4.9	0.36	101.6
	1	3.8	0.41	102.2
	0.6	3.8	0.29	101.9

Table 1-12. AP2Ka membrane summary for tests at 875°C (cont.).

Membrane	Feed O_2 Partial Pressure (atm)	Permeate Pressure[1] (Normalized)	Ionic Flux (Normalized)	Permeate Purity (%)
AMA4-28-8	0.6	2.9	0.32	99.4
	0.6	1.9	0.39	102.1
	0.6	0.97	0.46	102.3
AMA4-28-16	0.209	3.8	0.14	96.6
	0.209	1.0	0.38	98.3
	0.60	2.9	0.53	98.9
	1.0	4.9	0.60	100.0
AMA4-21-16	0.209	3.8	0.10	97.2
	0.209	1.0	0.30	99.8
	0.60	2.9	0.40	100.0
	1.0	4.9	0.46	100.0
	1.0	3.9	0.53	100.0
	0.60	3.9	0.39	100.0
AMA4-28-21	0.209	3.8	0.13	95.5
	0.209	1.0	0.40	100.0
	0.60	2.9	0.55	100.0
	1.0	4.9	0.58	100.0
	1.0	3.9	0.64	100.0
	0.60	3.9	0.50	100.0
	0.60	1.9	0.68	99.2
AMA4-21-31	0.209	3.8	0.11	89.4
	0.209	1.0	0.37	99.6
	0.60	2.9	0.50	100.0
	1.0	4.9	0.56	100.0
	1.0	3.9	0.64	100.0
	0.60	3.8	0.50	97.7
AMA4-28-23	0.209	3.8	0.21	94.0
	0.209	1.0	0.51	96.0
	0.60	2.9	0.69	98.1
AMA3-45-21	0.209	3.8	0.19	84.9
	0.209	1.0	0.43	91.7
	0.60	2.9	0.59	98.3
	1.0	4.9	0.66	100.0
	1.0	4.5	0.72	100.0
	0.60	3.8	0.53	97.9
	0.60	1.9	0.68	98.1
	0.60	0.97	0.82	98.7

Table 1-12. AP2Ka membrane summary for tests at 875°C (cont.).

Membrane	Feed O_2 Partial Pressure (atm)	Permeate Pressure[1] (Normalized)	Ionic Flux (Normalized)	Permeate Purity (%)
AMA3-45-12	0.209	3.8	0.17	100.1
	0.209	1.0	0.50	100.0
	0.60	2.9	0.69	100.0
	1.0	3.9	0.73	100.0
AMA3-45-22	0.209	3.8	0.12	97.4
	0.209	1.0	0.34	98.0
	0.60	2.9	0.42	98.4
	1.0	5.0	0.45	100.2
AMA4-21-3	0.209	3.8	0.16	84.1
	0.209	1.0	0.35	87.4
	0.60	2.9	0.54	95.4
	1.0	4.9	0.77	100.0
	1.0	3.9	0.85	100.0

[1] Not corrected for pressure drop through the component.

Table 1-13 presents the correlation coefficients between the measured oxygen flux and the AP2Ka laminate structure properties. The correlation is made at feed oxygen partial pressures of 0.21 atm, 0.6 atm and 1 atm to see if the correlations change with the feed oxygen partial pressure. The table shows that the flux is highly correlated with the inverse of the membrane thickness (1/L) at all P_{O2}^{Feed} conditions. All three correlation coefficients are significantly different than zero to the >95% confidence level, indicating that bulk ionic resistance is a leading resistance to oxygen transport. At a $P_{O2}^{Feed} = 0.21$ atm, the presence of a protective porous layer is ***negatively*** correlated with the flux. However, at $P_{O2}^{Feed} = 0.6$ or 1 atm, the correlation of the protective porous layer with the oxygen flux is very weak and not statistically significant. Neither the porous layer thickness nor porosity level is correlated with the oxygen flux to any degree of statistical significance. However, the porosity level was varied only modestly within the experimental design; changing the porosity level to more extreme values could have an effect on the flux. Analysis of the independent variables indicated that porosity level is confounded with the porous layer thickness. Neither of these variables is correlated with the flux.

Table 1-13. Performance of AP2Ka membranes at the same driving force.

						Permeate pressure (atm) of normalized flux:		
Laminate	**Structure (See Note)**	**Porous Layer Comp.**	**Porosity**	**Porous Protective Layer**	**Membrane thickness (Normalized)**	**0.21**	**0.60**	**1**
AMA 3-38-12	A'AB	Comp 1	Low	yes	1.01	0.41	0.64	0.77
AMA 3-38-18	A'AB	Comp 2	Med	yes	1.14	0.43	0.92	0.92
AMA 4-28-7	A'AAB	Comp 1	Low	yes	2.80	0.33	0.38	0.40
AMA 4-28-8	A'AAB	Comp 1	Low	yes	2.76	0.27	0.32	0.36
AMA4-28-16	A'ABB	Comp 1	Low	yes	1.42	0.38	0.53	0.60
AMA 4-21-16	A'AB	Comp 1	Low	yes	2.44	0.30	0.40	0.46
AMA4-28-21	A'AB	Comp 3	High	yes	1.32	0.40	0.55	0.58
AMA4-21-31	AAB	Comp 3	High	no	2.18	0.37	0.50	0.56
AMA4-28-23	A'AB	Comp 3	High	yes	1.35	0.50	0.69	0.00
AMA3-45-21	AAB	Comp 3	High	no	2.03	0.42	0.59	0.66
AMA3-45-12	AAB	Comp 3	High	yes	1.03	0.50	0.69	0.73
AMA3-45-22	A'ABB	Comp 1	Low	yes	1.92	0.34	0.42	0.45
AMA4-21-3	ABB	Comp 1	Low	no	1.00	0.33	0.54	0.77

Note: A' represents a porous protective layer; A represents a membrane layer; B represents a porous layer; all laminates had slotted layers.

The information Table 1-14 indicates that any model of oxygen flux as a function of membrane structure will have the inverse membrane thickness as the primary variable. The effect of a porous protective layer (as a surface kinetic term) would then be included in the model to see if the mean square error is reduced and if the surface kinetic parameter is statistically significant. Since the effects of the porous layer properties (thickness and pore former level) could not be correlated with the flux, the effect of these variables on the flux is masked by the dominating effect of the membrane thickness. The pressure drop would be best included by independently measuring the pressure drop through model structures.

Table 1-14. Correlation coefficients and probability of a 0 correlation coefficient between AP2Ka laminate features and the oxygen ionic flux at the leading edge driving force conditions.

	Correlation coefficient, R /Probability R=0		
Variable	**Feed PO_2=0.21 atm**	**Feed PO_2=0.6 atm**	**Feed PO_2=1.0 atm**
1/(membrane thickness)	0.64/0.025	0.75/0.005	0.60/.039
Porosity	0.011/0.97	0.47/0.12	-0.10/0.75
Porous layer thickness	0.01/0.97	-0.10/0.76	0.096/0.77
Porous protective layer	-0.61/0.036	-0.090/0.78	-0.24/0.45

Oxygen Flux Studies with Catalyzed Materials

Eltron Research carried out flux and characterization tests of alternative formulations of materials in the general family of perovskites $Ln_{x1}A_{x2}'A_{x3}''B_{y1}B_{y2}'B_{y3}''O_{3-z}$, in which Ln is a *f* block lanthanide; A' is selected from Group 2 of the periodic table; A" is chosen from Group 1, 2, 3, and the *f* block lanthanides; B and B' are chosen from the *d* block transition metals; and B" is chosen from the *p* block Metals. In addition, Eltron prepared and studied catalysts on both the sides of the membranes to determine effects on overall oxygen flux.

Eltron prepared tubes of various formulations of the general family described above. Catalysts were prepared separately and either dip-coated or painted onto the surfaces of the tubes. In general, the same catalyst was applied to both the inner (feed) side of the tubes and the outer side of the tubes, or on only one side or the other.

Table 1-15 summarizes the tube and catalyst preparations studied. Tube wall thicknesses and catalyst loadings were determined by SEM. All but three samples had catalysts, and one sample was catalyzed on only one side (Q12-30-20).

Table 1-15. Summary of catalyzed tube samples for permeation flux testing.

				Catalyst Coating (μm)	
Sample No.	**Tube Type**	**Catalyst Type**	**Tube Wall Thickness (mm)**	**Inner**	**Outer**
Q12-21-6	ER15-1	PM-L-d	0.54	6-9	14-17
Q12-21-19	ER15-1	PM-L-d	1.10	4-7	5-8
Q12-21-1	ER15-1	PM-L-d	0.94	5-8	1-7
Q12-21-5	ER15-1	PM-L-d	0.64	1-3	<1
Q12-21-30	ER15-1	PM-L-d	1.05	5-6	8-13
Q12-20-16	ER15-1	PM-L-d	0.71	10-13	14-21
Q12-20-15	ER15-1	PM-L-d	0.74	1-3	2-3
Q12-20-17	ER15-1	PM-L-d	1.09	2-3	8-10
Q12-20-26	ER15-1	PM-L-d	1.17	3-5	6-16
Q12-20-6	ER15-1	PM-L-d	0.65	1-2	1-3
Q12-22-6	ER15-1	PM-L-d	0.65	1-2	3
Q12-22-15	ER15-1	PM-L-d	0.73	<1	<1
Q12-22-20	ER15-1	PM-L-d	0.55	8-10	8-18
Q12-22-21	ER15-1	PM-L-d	0.58	1-4	8-13
Q12-22-9	ER15-1	PM-L-d	0.84	1	2-4

Table 1-15. Summary of catalyzed tube samples for permeation flux testing (cont.).

				Catalyst Coating (μm)	
Sample No.	**Tube Type**	**Catalyst Type**	**Tube Wall Thickness (mm)**	**Inner**	**Outer**
Q12-22-16	ER15-1	PM-L-d	0.84	1	2-4
Q12-22-19	ER15-1	PM-L-d	0.50	3-7	7-12
Q12-22-12	ER15-1	PM-L-d	0.84	3	5-9
Q12-22-22	ER15-1	PM-L-d	0.48	3-5	6-8
Q12-18-7	ER15-1	PM-L-t	1.10	1-2	4-5
Q12-18-6	ER15-1	PM-L-t	1.18	3-4	7-9
Q12-23-5	ER15-1	PM-L-t	0.48	1	4-7
Q12-23-4	ER15-1	PM-L-t	0.40	<1	4-8
Q12-21-17	ER15-1	PM-L-t	1.02	6-7	4-8
Q12-21-9	ER15-1	PM-L-t	0.52	4-7	4-9
Q12-20-18	ER15-1	PM-L-t	1.14	4-7	4-8
Q12-16-19	ER15-1	L15	1.03	2-6	2-6
Q12-16-17	ER15-1	L15	1.23	2-6	2-6
Q12-16-24	ER15-1	L15	0.93	2-6	2-6
Q12-16-9	ER15-1	L15	0.58	2-6	2-6
Q12-21-14	ER15-1	PM-L-d	1.09	Not measured	Not measured
Q12-21-22	ER15-1	PM-L-d	1.06	Not measured	Not measured
Q12-21-3	ER15-1	PM-L-d	0.51	Not measured	Not measured
Q12-21-11	ER15-1	PM-L-d	0.43	Not measured	Not measured
Q12-20-18	ER15-1	PM-L-t	1.14	Not measured	Not measured
Q12-21-31	ER15-1	PM-L-t	1.04	Not measured	Not measured
Q12-21-6	ER15-1	PM-L-d	0.54	Not measured	Not measured
Q12-30-20	ER15-1	PM-t	0.58	Not measured	None
Q12-18-2	ER-15-1	none	1.10	None	None
Q12-18-13	ER-15-1	none	1.26	None	None
Q12-18-15	ER-15-1	none	0.62	None	None
Q12-5-5	ER55-1	L55	1.25	2X	X
Q12-5-6	ER55-1	L55	0.985	2X	X
Q12-5-7	ER55-1	L55	1.25	2X	X
Q12-3-4	ER37-1	L55	0.875	2X	X
Q12-3-3	ER37-2	L55	1.20	2X	X
Q12-3-4	ER37-2	L55	1.11	2X	X
Q12-3-5	ER37-2	L55	1.28	2X	X

Tubes were placed in the apparatus shown in Figure 1-6 and sealed to an alumina holder by means of a Pyrex® seal. The ceramic zone of the apparatus was placed in a tube reactor (not shown). Helium was passed over the outside of the sample while air was introduced to the inside of the tubes as shown; oxygen-depleted air was withdrawn by a centrally located tube. All experiments were carried out at 1 atm. Permeation rates were measured by analyzing the exhaust compositions. Typical oxygen concentrations in the permeate gas were 3-5% by volume.

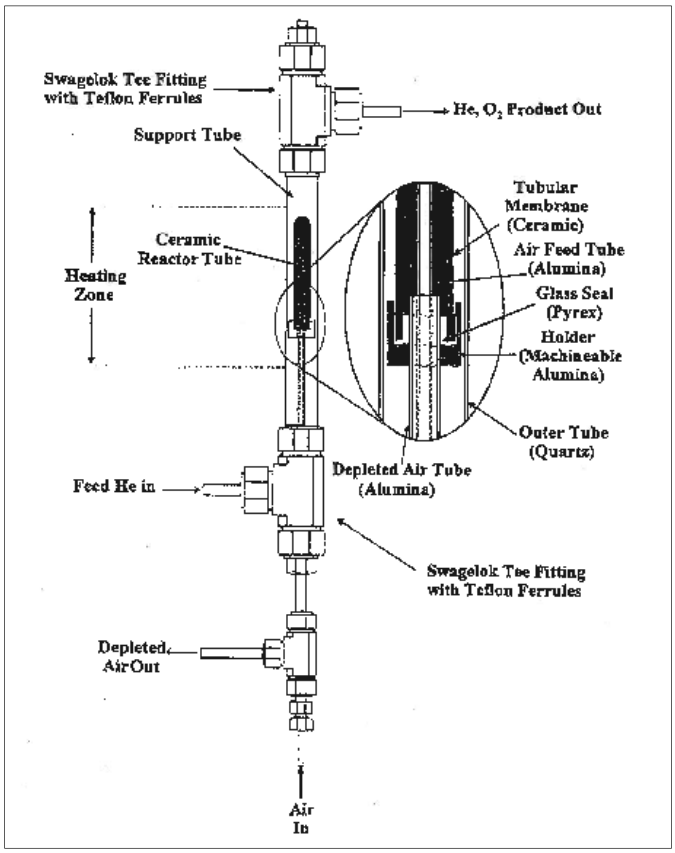

Figure 1-6. Schematic of the permeation flux test apparatus for testing catalyzed tubes.

Permeation data for the catalyzed tube samples are presented in Table 1-16 and plotted in Figure 1-7. All catalyzed samples showed significantly higher flux than the three uncatalyzed samples. In general, the trend of decreasing flux with increasing tube thickness agrees with expectations. Within the scatter of the data, it is not clear if the flux exactly follows the inverse of the tube wall thickness, but if surface kinetics are important (as evidenced by the addition of catalyst) it is possible that the inverse tube wall dependence is not exactly followed for these samples. For the ER15-1 tube, none of the three catalysts appears to be the clearly superior material from the

standpoint of flux performance. For the ER55 tubes catalyzed by L55, flux appears higher based on a limited dataset. Based on these studies, Air Products concluded that none of the samples warranted further work under Task 1.2.

Table 1-16. Oxygen flux data for catalyzed tubes at 875°C.

Sample No.	Tube Type	Catalyst Type	Tube Wall Thickness(mm)	Oxygen Flux (sccm/cm_2)
Q12-21-6	ER15-1	PM-L-d	0.54	0.686
Q12-21-19	ER15-1	PM-L-d	1.1	0.461
Q12-21-1	ER15-1	PM-L-d	0.94	0.491
Q12-21-5	ER15-1	PM-L-d	0.64	0.446
Q12-21-30	ER15-1	PM-L-d	1.05	0.446
Q12-20-16	ER15-1	PM-L-d	0.71	0.756
Q12-20-15	ER15-1	PM-L-d	0.74	0.543
Q12-20-17	ER15-1	PM-L-d	1.09	0.426
Q12-20-26	ER15-1	PM-L-d	1.17	0.315
Q12-20-6	ER15-1	PM-L-d	0.65	0.476
Q12-22-06	ER15-1	PM-L-d	0.65	0.636
Q12-22-15	ER15-1	PM-L-d	0.73	0.375
Q12-22-20	ER15-1	PM-L-d	0.55	0.559
Q12-22-21	ER15-1	PM-L-d	0.58	0.681
Q12-22-9	ER15-1	PM-L-d	0.84	0.569
Q12-22-16	ER15-1	PM-L-d	0.84	0.423
Q12-22-19	ER15-1	PM-L-d	0.5	0.698
Q12-22-12	ER15-1	PM-L-d	0.84	0.439
Q12-22-22	ER15-1	PM-L-d	0.48	0.736
Q12-18-7	ER15-1	PM-L-t	1.1	0.404
Q12-18-6	ER15-1	PM-L-t	1.18	0.357
Q12-23-5	ER15-1	PM-L-t	0.48	0.868
Q12-23-4	ER15-1	PM-L-t	0.4	0.632
Q12-21-17	ER15-1	PM-L-t	1.02	0.413
Q12-21-9	ER15-1	PM-L-t	0.52	0.595
Q12-20-18	ER15-1	PM-L-t	1.14	0.377
Q12-16-19	ER15-1	L15	1.03	0.334
Q12-16-17	ER15-1	L15	1.23	0.311
Q12-16-24	ER15-1	L15	0.93	0.252
Q12-16-9	ER15-1	L15	0.58	0.531

Table 1-16. Oxygen flux data for catalyzed tubes at 875°C (cont.).

Sample No.	Tube Type	Catalyst Type	Tube Wall Thickness(mm)	Oxygen Flux (sccm/cm_2)
Q12-21-14	ER15-1	PM-L-d	1.09	0.421
Q12-21-22	ER15-1	PM-L-d	1.06	0.382
Q12-21-3	ER15-1	PM-L-d	0.51	0.393
Q12-21-11	ER15-1	PM-L-d	0.43	0.409
Q12-20-18	ER15-1	PM-L-t	1.14	0.413
Q12-21-31	ER15-1	PM-L-t	1.04	0.388
Q12-21-6	ER15-1	PM-L-d	0.54	0.686
Q12-30-20	ER15-1	PM-t	0.58	0.506
Q12-18-2	ER-15-1	None	1.1	0.107
Q12-18-13	ER-15-1	None	1.26	0.037
Q12-18-15	ER-15-1	None	0.62	0.067
Q12-5-5	ER55-1	L55	1.25	0.368
Q12-5-6	ER55-1	L55	0.985	0.659
Q12-5-7	ER55-1	L55	1.25	0.372
Q12-3-3	ER37-2	L55	1.2	
Q12-3-4	ER37-2	L55	1.11	0.593
Q12-3-5	ER37-2	L55	1.28	0.668

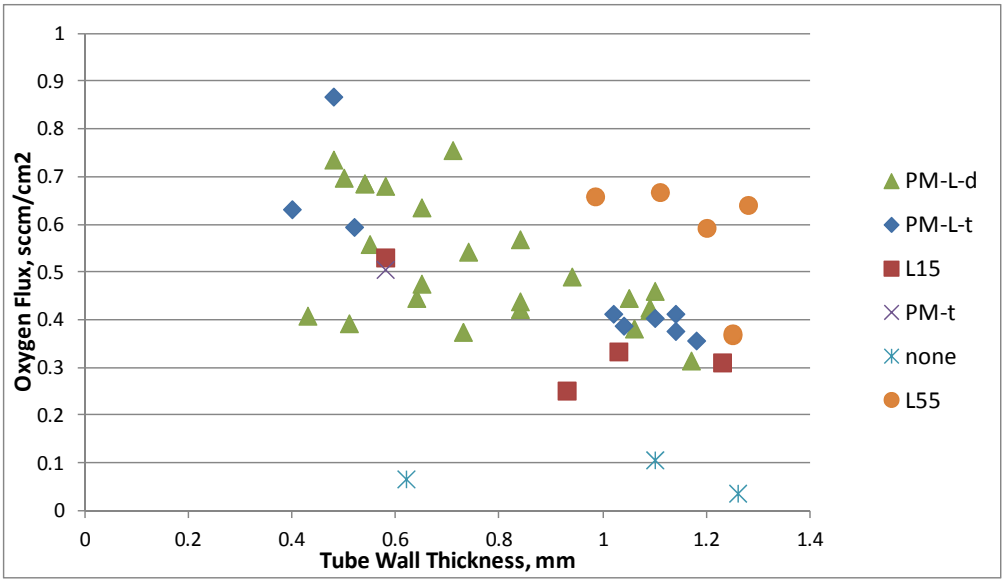

Figure 1-7. Oxygen flux from catalyzed tubes as a function of wall thickness and catalyst type.

Task 1.2 Lifetime Testing of the Optimized ITM Oxygen Materials

Vacuum Permeate – Short Loop Test Rig Retrofit

Air Products retrofitted four of the eight short loop test rigs (SLTRs) with vacuum permeate systems to enable lifetime flux testing with subscale wafers. The SLTRs, originally designed to measure tube seal effectiveness, are composed of simple tube furnaces housing a hot-wall pressure vessel taking a pressurized air feed and exhausting through a back-pressure regulator. All heating occurs in the tube furnace. The pressure vessel is mounted vertically with its large flange on the bottom side out of the heated zone. The ceramic tube sample is mounted to a metal tube connected with a leak-tight seal to a bulkhead fitting in the vessel flange. The tube sample is inserted up into the pressure vessel, and the flange seal is made. Leakage from the test piece or its joint passes into the metal tube, through the flange, and out through connected tubing through flow meters used to assess leak rate.

Air Products designed a vacuum permeate system that could be added to the existing SLTR infrastructure to enable flux experiments with planar, subscale wafer modules at the full oxygen driving force expected in commercial applications. The new Vacuum Permeate-Short Loop Test Rigs (VP-SLTRs) would further comprise larger-diameter vessels and associated tube furnaces. The new system was designed with the capability to test subscale wafer modules at up to 885°C, 250 psig feed air pressure, and 100 Torr permeate pressure to accommodate up to 250 sccm of 100% oxygen flow from individual test pieces.

Figures 1-8 and 1-9 show the process flow diagrams for feed/non-permeate and permeate systems of the VP-SLTRs, respectively. Referring to Figure 1-8, air is sourced from an air compressor (not shown) with associated PSA drier system and feeds all eight SLTRs, including the four VP-SLTRs represented in the top branch of the figure. Mass flow to each VP-SLTR vessel is set by individual mass flow controllers, while back pressure is provided by dedicated back pressure control valves. Feed air passes through the bottom flange of the vessel which is inserted vertically into its tube furnace. The air passes to a ceramic housing located inside the vessel that is supported on a metal pipe fixed to the base vessel flange. The ceramic housing contains the subscale wafer module which is sealed to the metal pipe by means of a ceramic-metal seal. Air passes over the wafer within a controlled gap and exits into the free space inside the vessel, then out through a sideport in the vessel to the back pressure control valve. Permeate

oxygen passes from the interior of the wafer to the module ceramic tube to metal pipe, where it is withdrawn from the vessel through the vessel flange. Figure 1-10 (a) shows photographs of the VP-SLTR vessel next to a module flow housing supported on the vessel flange, and a typical subscale wafer module (b).

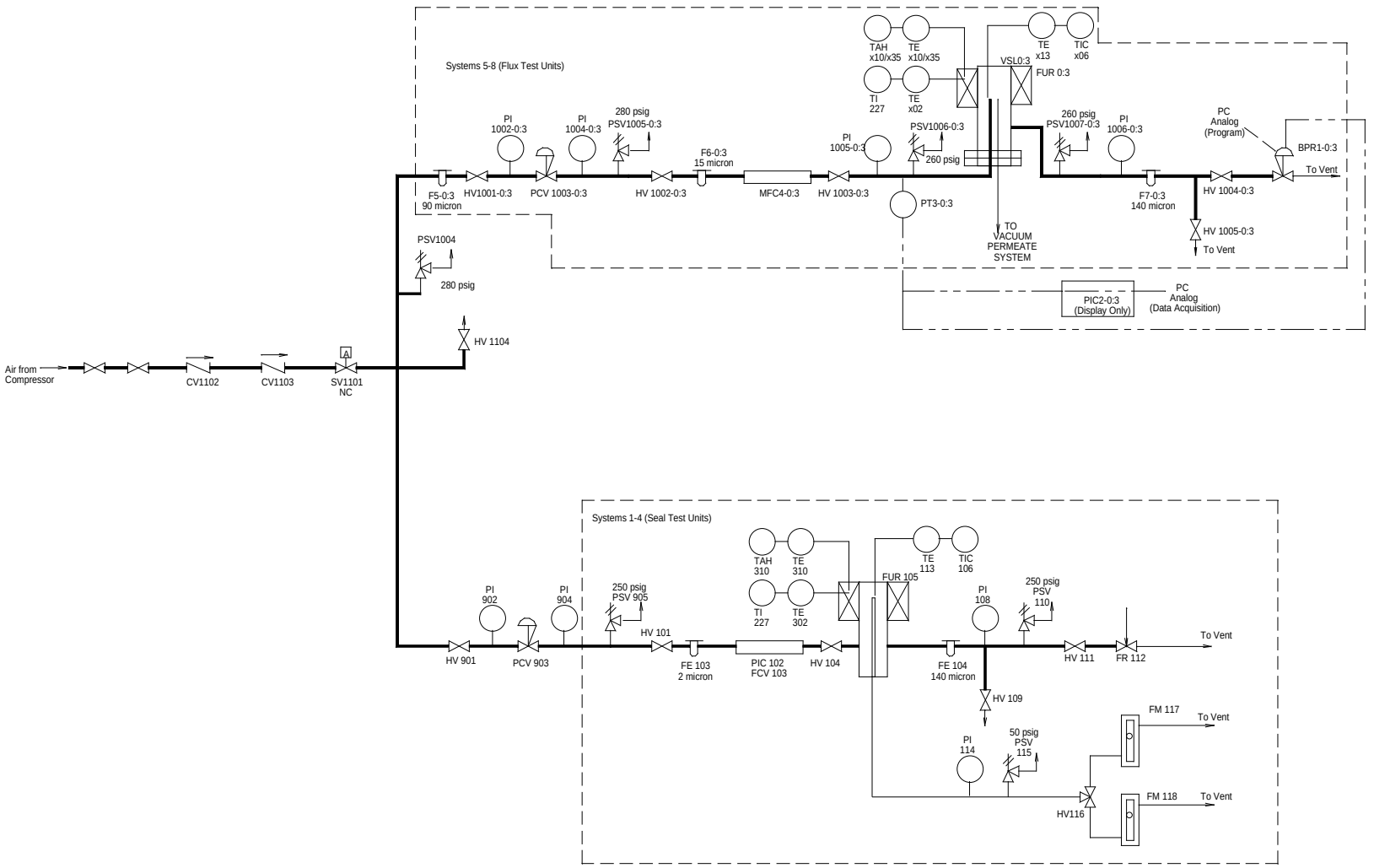

Figure 1-8. Process flow diagram of the feed and non-permeate section of the modified Short Loop Test Rig (SLTR) system. Top branch is the newly modified VP-SLTRs. Bottom branch is the Seal Test SLTRs (unmodified). There are 8 units in all.

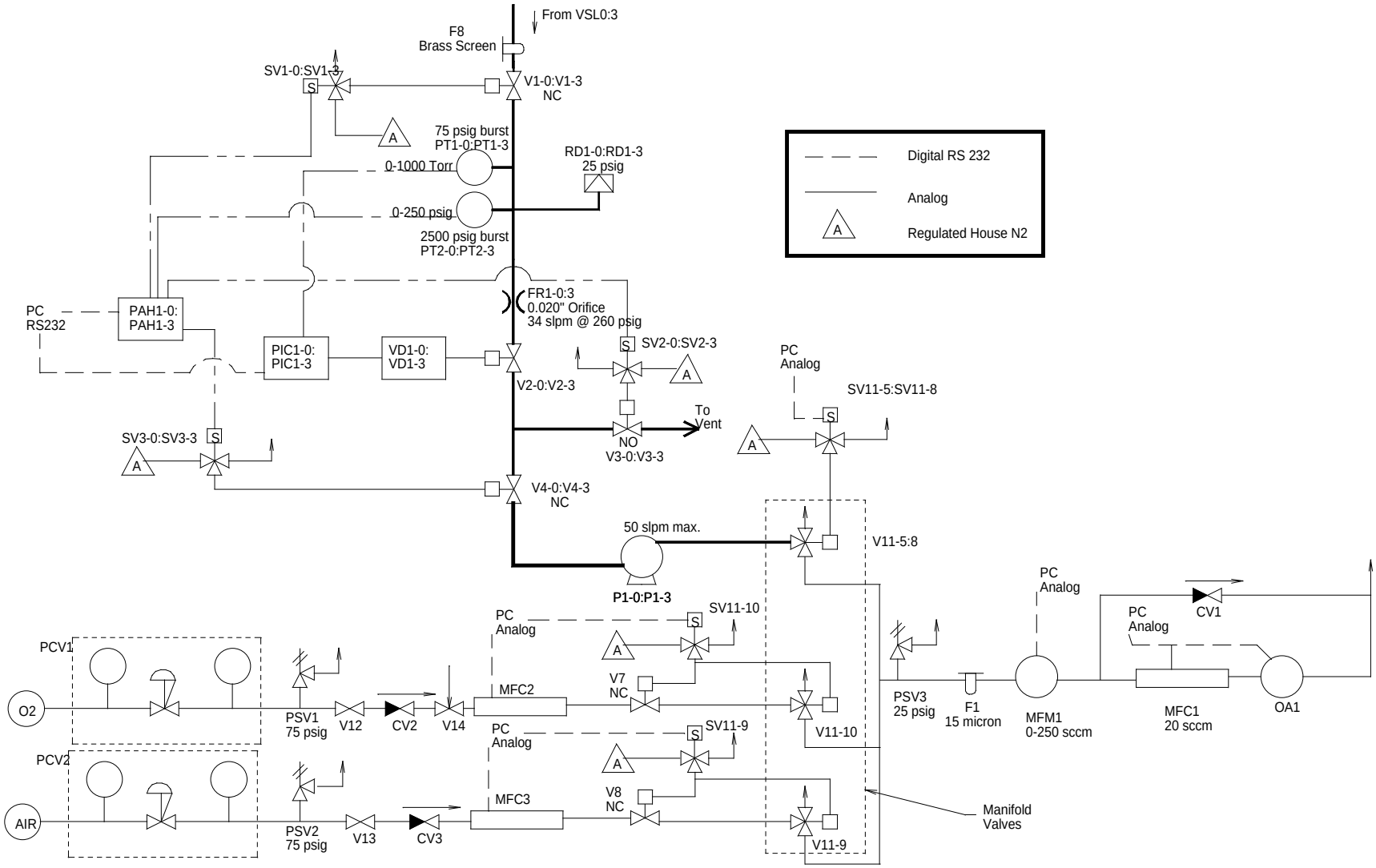

Figure 1-9. Process flow diagram of the permeate section of the VP-SLTRs.

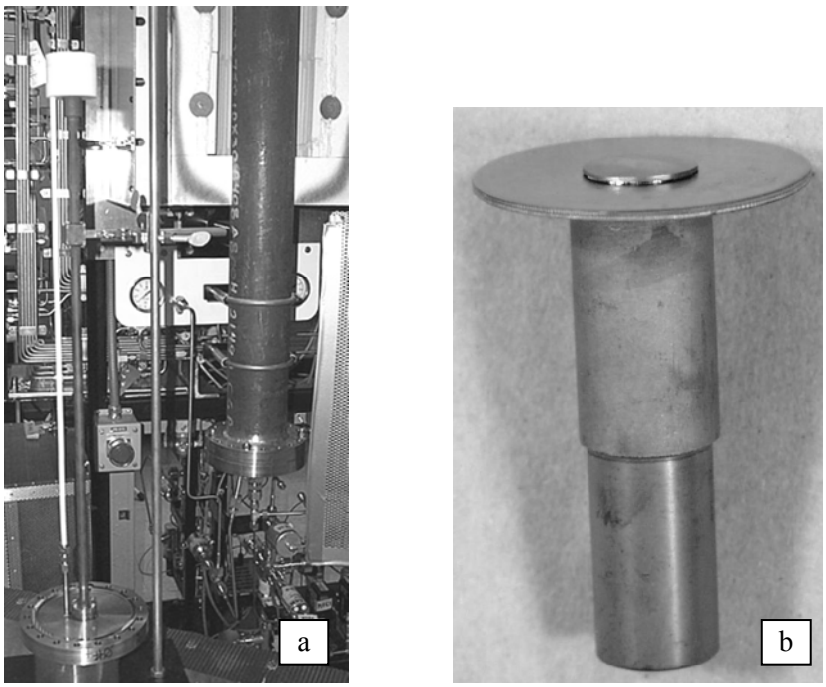

Figure 1-10. a) VP-SLTR vessel in furnace (opened to show vessel) on right side of photo; subscale wafer is housed in the ceramic housing (white) shown on left side of photo supported on a dark metal permeate tube; feed air is provided through the ceramic tube (white) passing up from the flange. b) Close-up of subscale wafer module showing wafer, flat end cap, and tube.

Referring to Figure 1-9, permeate oxygen leaving the vessel in Figure 1-8 first passes through valves that control the permeate-side pressure, then to a dedicated vacuum pump which provides a low ultimate pressure. The vacuum pump discharges at slightly above 1 atm through a selector valve which sends the flow to either a system vent or to a mass flow meter and oxygen analyzer, then to a system vent. A calibration gas supply system is shown on the lower left-hand side of Figure 1-9. The selector valve system rotates through the four VP-SLTRs during operation to provide data for each system at set intervals. Daily calibrations are performed automatically.

Flux and Life Testing of Subscale Modules

Air Products tested a number of subscale wafer modules for flux and flux stability under Task 1.2. All module components were supplied by Ceramatec; Air Products assembled the components to make the modules and fitted them to holders for insertion into the VP-SLTR vessel. A discussion of two VP-SLTR tests is presented here in detail, followed by a summary of flux data obtained during the task.

1. Test of Modules 1, 2, and 10

The three modules were tested with an identical procedure. After the module was assembled and mounted on an alloy seal cup supported by a tube sealed to the inside of the VP-SLTR vessel flange, the ceramic housing and air supply tube were fitted around the module and the module assembly was inserted into the vessel. A thermocouple was inserted into the support tube/permeate line to monitor temperatures at the wafer level in the interior of the module.

Once the vessel was sealed, feed air flow was brought into the alumina chamber, and a temperature ramp was initiated with the furnace temperature controller. The vessel wall was the temperature control point. Once temperature was established, a pressure ramp was initiated with the back-pressure regulator control software. When the vessel pressure reached ~100 psig, the permeate tubing was connected to the permeate system. The set point of the permeate pressure controller initially was set to >760 Torr, causeing the permeate pressure control valve (V2-x) to close. The vacuum pump was turned on, and permeate data acquisition was initiated. The feed pressure ramp was then resumed. When feed pressure was established at its final setpoint, the permeate pressure ramp was initiated. The above procedure was reversed for shut down.

Samples. AP2K Modules 1 and 10 were successfully flux-tested in the VP-SLTRs during early stages of testing. When AP2K Module 2 was tested, it had excessive leakage at 5 psid applied pressure, so the flux test was abandoned. Table 1-17 breaks down the modules by component and lists the leak rate as measured prior to making the ceramic-to-metal seal in the holder.

Table 1-17. VP-SLTR test data for Modules 1, 2 and 10.

Module	Wafer #	Tube #	End Cap #	Module Leak Rate (sccm) at 21° C
1	RC13-18-8	17120-71-52A	D0-8	0.120
2	AMA4-36-5	17120-72-54A	D0-8	0.713
10	WL009 -EX4	17120-98-110A	C1-6	0.578

Results and Discussion. Results described here include the specific conditions of the testing, including ramp rates of temperatures and pressure, the measured flux results, and relevant post-analyses of the modules. A discussion of the results and of future work follows.

Experimental Conditions. The target conditions for steady-state flux measurements were chosen to simulate typical conditions in a commercial ITM Oxygen vessel. A permeate pressure of 350 Torr was used; the feed side pressure was adjusted to obtain the appropriate driving force, given that the feed is air at 20.9% oxygen. Testing was performed at a feed-side pressure of 200 psig.

Module #1 Conditions. Module #1 was tested in SLTR#6. Temperature and pressure ramping followed proscribed schedules estimated to produce a <1% failure rate based on tensile stress testing of bend bars. Process condition schedules are plotted in Figure 1-11. The feed rate was steady at 1.6 SLPM.

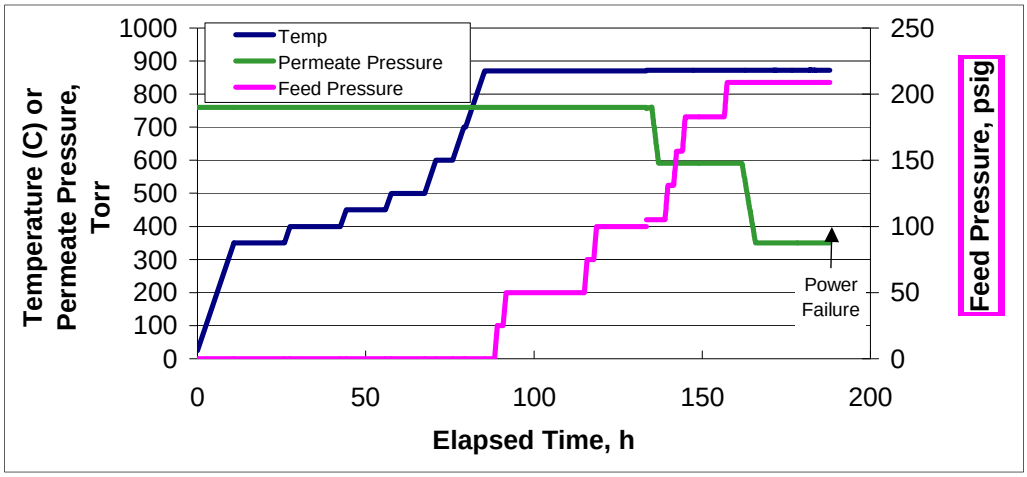

Figure 1-11. Experimental conditions for test of Module 1.

Module 2 Conditions. Module 2 was tested in SLTR#5. The temperature ramp was identical to that used for Module 1. Module 2 was held at 870° C for ~12 h before applying pressure. The feed flow rate was steady at 8 SLPM, and pressure was ramped to 5.4 psig. Leakage to the permeate tube was excessive. Pressure was ramped to 0 psig, and the temperature ramp was followed in reverse down to room temperature.

Module 10 Conditions. Module 10 was tested in SLTR#7. Initial temperature and pressure ramping is shown in Figure 1-12. Feed flow rate was steady at 6 SLPM, except for a controlled excursion at 450 h on-stream which is discussed below. A ½" alumina tube was used as the feed tube to carry air into the flow chamber. The ½" tube was filled with alumina beads (3/32" diam.) to act as a heat transfer medium to preheat the incoming air. Neither of the other two tests had this feature.

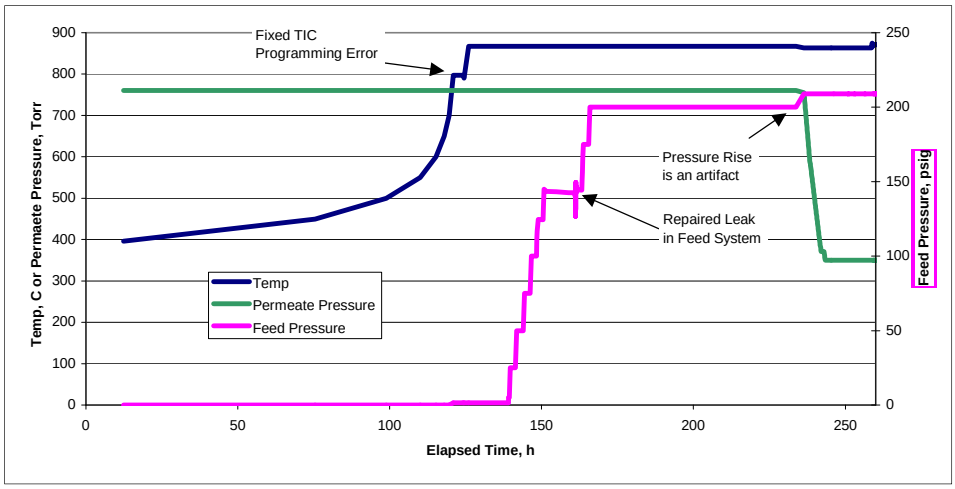

Figure 1-12. Initial experimental conditions for Module 10 testing.

Two anomalies in the ramps for Module 10 are notable: 1) mis-programming of the temperature ramp caused a premature pause in the ramp, and 2) a leak in the air feed tubing interrupted the feed pressure ramp. The latter was caused by a fitting that was not completely tight. The maximum pressure attainable in the system with the leak was ~145 psig. The feed pressure controller was re-set to 144 psig, and the fitting was slowly tightened. Despite the care taken to tighten the fitting slowly, the pressure dropped to 134 psig over 10 seconds, and further to a low of 129 psig after one minute. With further tightening of the fitting, the pressure then climbed to 144 psig over two minutes. Ramping resumed from that point.

Steady-state flux measurements during testing of Module 10 were interrupted by three system failures. As shown in Figure 1-13, the feed pressure underwent sudden drops at ~272 h and ~460 h on-stream. The first was caused by a compressor trip that occurred when the building power was briefly interrupted. The second was caused by another building power failure that caused the feed flow controller to lose power and fail to a no-flow condition. The feed flow controller had been inadvertently connected directly to the power feed rather than through a back-up power supply; this condition was corrected. Neither of these power failures caused changes in the temperature or permeate pressure. The third system failure was caused by a high-temperature alarm in the furnace at ~545 h on-stream due to a thermocouple failure. The module broke during the ensuing (rapid) drop in temperature.

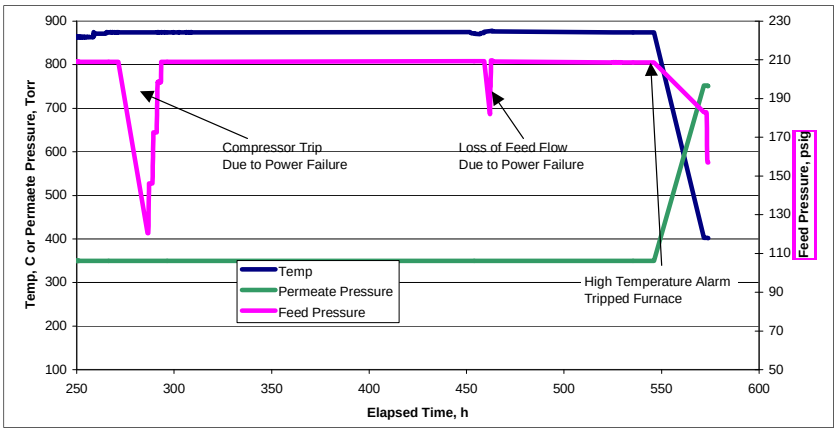

Figure 1-13. Experimental conditions during tests of Module 10 illustrating moments of system trips.

Results: **Oxygen Production.** Oxygen production was measured as the raw measured oxygen flow rate in the permeate stream minus any oxygen introduced through leakage. The total leak rate was calculated assuming that the composition of the stream entering the various leak points in the module was an arithmetic average of the inlet and outlet oxygen composition on the feed side of the module. Oxygen production rate was taken as the difference between the observed permeate flow rate of oxygen minus the calculated leak rate.

Module #1 Oxygen Production Figure 1-14 is a plot of oxygen production rate from Module #1 taken as flux versus elapsed time at temperature. The two pressures in the system, the feed and permeate pressures, are plotted with the flux data for reference; all measurements were made at constant temperature. As seen in Figure 1-14, flux responded proportionally to changes in either feed or permeate pressure and reached a maximum during a 20- hour period at steady-state operating conditions when feed pressure was maximized and permeate pressure was minimized.

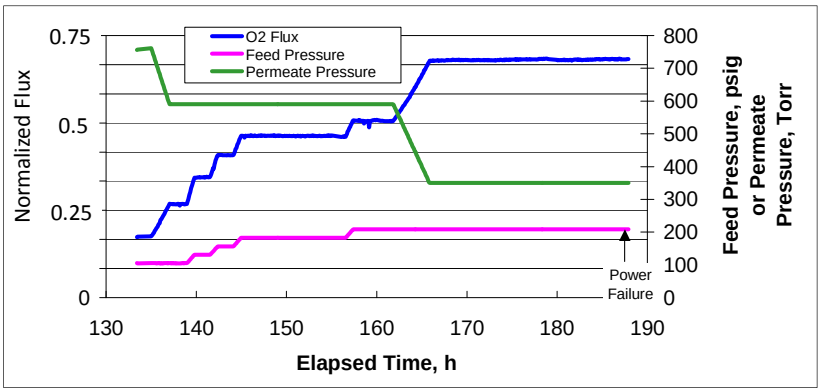

Figure 1-14. Module 1 oxygen production (as normalized flux) versus time.

Though not evident in Figure 1-14, the flux increased slightly over the 20-hour operating period at steady state. This behavior can be rationalized by examining the leak rate during that time. Figure 1-15 is a plot of leakage versus elapsed time at temperature. Leakage rose exponentially starting at ~150 h on-stream. Leak rate curves of this type have been observed before in testing of ITM laminates and have been interpreted as arising from slow degradation of the silver braze(s). As shown in Figure 1-16, the effect of leakage is to decrease the oxygen concentration on the permeate side. Assuming the leakage to be local to and homogeneous within the module, the reduced permeate-side oxygen flux would increase the driving force at constant permeate pressure. The result would be increasing flux with time. Unfortunately, Module 1 was damaged when a power failure caused a rapid drop in temperature and pressure after 188 h on-stream, and further flux testing with Module 1 was abandoned.

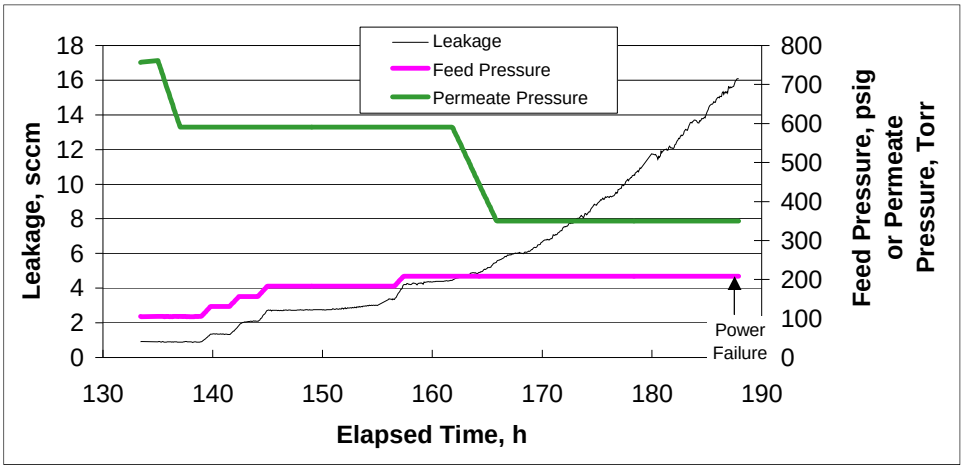

Figure 1-15. Leak rate measured versus time during flux test of Module 1.

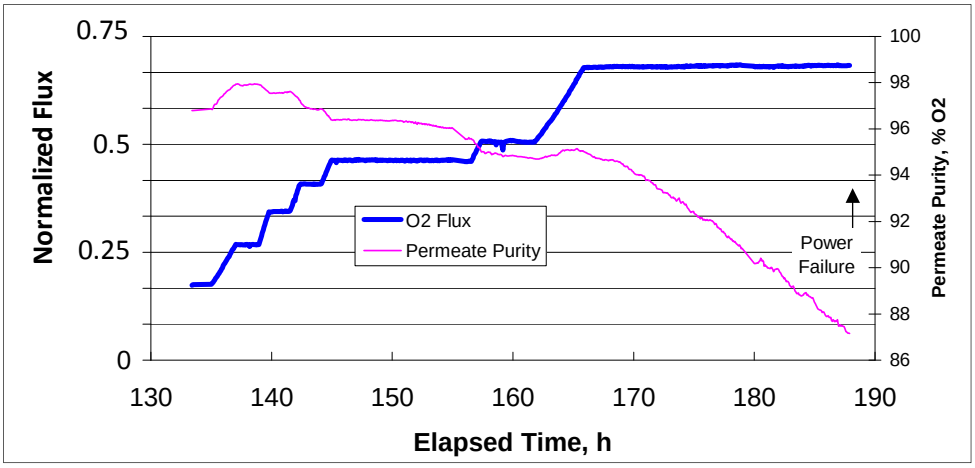

Figure 1-16. Flux and purity versus time during flux test of Module 1.

Module 2 Oxygen Production. No flux data were collected with Module 2. After equilibrating at temperature, it had an excessive permeate-side leak when 5 psig was applied to the feed side.

Module 10 Oxygen Production. Figure 1-17 is a plot of the oxygen production rate from Module 10 taken as flux vs. elapsed time at temperature. The two pressures in the system, the feed and permeate pressures, are plotted with the flux data for reference. Flux initially rose as permeate pressure was reduced to a steady 350 Torr, then leveled out. Flux rose again as the temperature was increased ~12° over eight hours starting at the 268 h on-stream point (temperature data not shown). The flux reached a maximum upon stabilizing at 190 psig feed pressure and 350 Torr on the permeate side of the wafer.

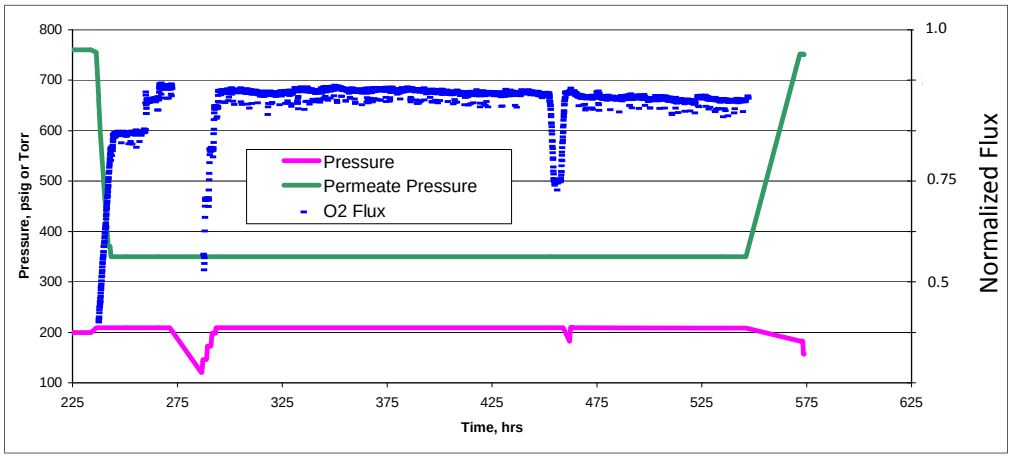

Figure. 1.17. Normalized flux, feed pressure and permeate pressure versus time at temperature during test of Module 10. (Digital noise in the flux signal was later eliminated.)

Following feed pressure losses at 272 h and 460 h, the flux can be seen to recover almost completely. Unlike results obtained with Module 1, however, there was a slight decrease in flux with time. Examination of the leak rate (Figure 1-18) shows that leakage increases exponentially starting at ~350 h on-stream. Thus, despite the increased leakage which would cause an increase in flux at a constant driving force, the overall flux declined. And, while it is possible that the leak path was located downstream of the wafer, such that no real driving force increase could be expected, no mechanism for *decreasing* the driving force is evident. It is possible, though speculative, that the slight decrease in flux (at 545 h on-stream) may have arisen from accumulation of damage to the wafer from the unplanned pressure excursions.

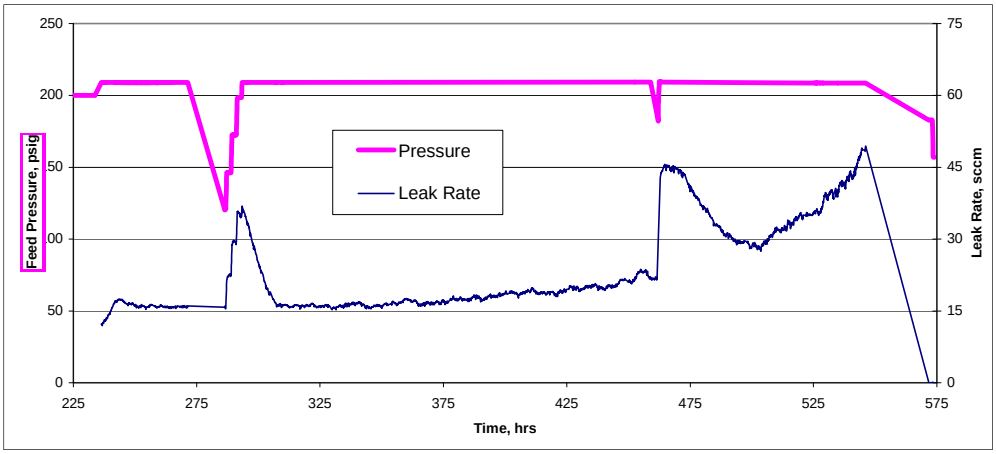

Figure 1-18. Leak rate measured versus time during flux test of Module 10.

Post-Test Analysis of Modules 1, 2, and 10

Module 1. Module 1 was removed from the pressure vessel following cool-down. A long, visible hairline crack ran across the downstream side of the top of the wafer, tangential to the end cap braze. Three visible hairline cracks radiated from the end cap braze on the bottom of the wafer, also on the downstream side. The tube was cracked circumferentially ~10 mm below the wafer-to-tube braze and again below the ceramic-metal seal location.

Module 2. Module 2 was removed from the pressure vessel following cool-down. Three visible pin holes, one was much larger than the other two, were observed in the silver braze between the end cap and the wafer. The end cap was noted to be tilted to a significant degree; silver braze had extruded out from beneath the end cap on one side. The module leak was retested and found to be isolated mainly to the end cap region, as noted by the severe reduction in the system pressure when an O-ring gasket and flat rubber disk were placed completely over the end cap.

Module 10. Module 10 was removed from the pressure vessel following cool-down. The base of the tube broke when the tube was removed from the alloy seal cup. The tube was fitted with an Ultra-Torr™ fitting and placed on the leak-test apparatus. Leakage was found to be excessive (430 sccm). The portion of the braze between the end cap and wafer that had flowed onto the wafer surface was noted to have lifted off of the surface of the wafer over 2/3 of the circumference of the braze. Coating both the end cap and tube brazes with hydrocarbon grease did not change the leak rate.

Discussion

The measured fluxes indicated that the commercial target fluxes were attainable, as discussed in the next section. These results were the first experiments with the VP-SLTR apparatus; subsequent experiments were conducted with improvements in control and feed flow rate, as well as in subscale module quality. Despite the positive flux data, however, it should be noted that the product purity fell quickly below 90% oxygen in both experiments, and point to the limitations of silver as a braze material.

2. Summary of Flux Test Results During Task 1.2

Using the VP-SLTRs and techniques outlined above, Air Products successfully measured oxygen production during tests of 19 subscale modules under Task 1.2. Table 1-18 summarizes the maximum flux data and the elapsed test time for each module. Flux and membrane thickness are reported as normalized quantities relative to commercial targets; the corrected flux is the normalized flux adjusted to be on a consistent membrane thickness basis. Note that no significant degradation in flux rate was observed over any of the test periods when all experiments were considered as a whole.

The data in Table 1-18 are plotted in Figures 1-19 and 1-20 against module count (i.e., the module numbers as listed in table, renumbered 1-19). Two observations stand out: 1) the corrected fluxes generally meet or exceed the target; and 2) the thicker membranes tend to give rise to the higher corrected fluxes. Stated another way, the correction based on membrane thickness alone tends to over-correct when membranes are thicker and under-correct when membranes are thinner. This suggests that, while membrane thickness is a major parameter in dictating the flux, resistances to oxygen transport through the membrane (other than simple bulk diffusion) are likely important in determining the overall flux of oxygen through the membranes.

Table 1-18. Summary of flux and lifetime testing of subscale wafer modules under Task 1.2.

Module	Normalized quantities, %			Time On Stream*, h
	Flux	Membrane Thickness	Corrected Flux	
1	67	190	127	13
10	88	120	106	285
12	38	443	166	350
15	84	120	102	170
16	97	120	116	203
17	87	118	102	480
18	92	110	101	2360
19	77	123	94	710
22	68	150	102	315
24	78	160	125	2756
31	75	145	109	1734
32	78	145	114	620
34	91	115	104	1800
28	125	70	88	466
39	83	125	104	60
29	38	435	163	625
51	93	85	79	3280
52	102	90	92	2100
56	103	105	109	3180

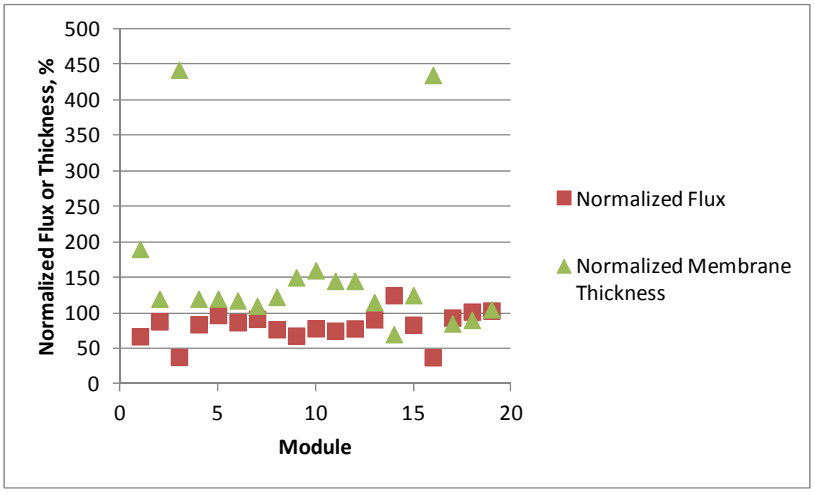

Figure 1-19. Normalized flux and membrane thickness for each module in Table 1-18.

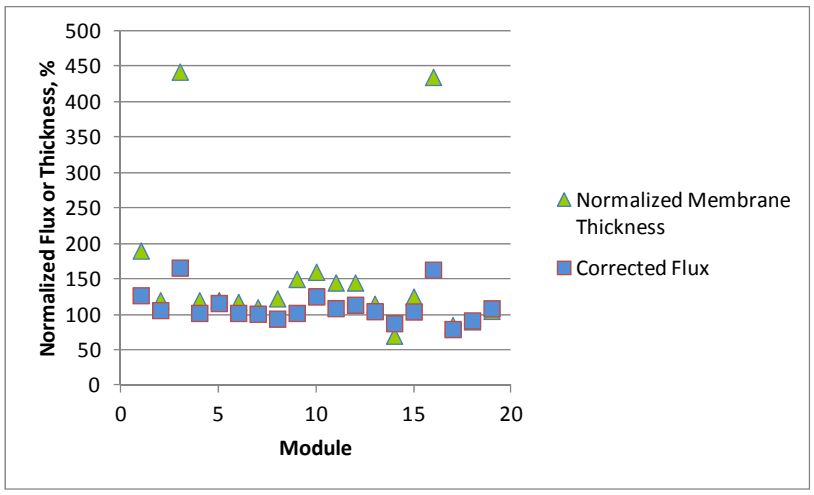

Figure 1-20. Normalized membrane thickness and corrected flux for each module in Table 1-18.

In addition to maximum attainable fluxes, measurements of oxygen production over a range of temperatures and feed and permeate pressures were taken to establish a database of performance for model wafer composite systems. This work represents the baseline testing of wafer performance against which full-size wafer performance can be compared.

References

Cranmer, D.C. and Richerson, D.W., "Mechanical Testing Methodology for Ceramic Design and Reliability," Marcel Dekker, Inc.,1998.

PHASE I RESULTS AND DISCUSSION

TASK 2.0 ENGINEERING DEVELOPMENT

2.0 Scope

Northern Research and Engineering Corporation (NREC) evaluates the critical technical and economic issues associated with integration of the ITM Oxygen technology with a commercially available gas turbine system for IGCC applications. McDermott carries out structural, thermal and mechanical analysis of ITM Oxygen membranes to facilitate their scale-up and improve performance. McDermott also performs a conceptual design and budgetary costing of a commercial ITM Oxygen process vessel using ASME codes to consider design and safety aspects. Texaco prepares case studies for the use of ITM Oxygen technology in an IGCC power production plant. Air Products, with DOE's review and advice, evaluates additional advanced applications of ITM Oxygen technology emerging from CRADA No. PC96-007, titled, "Ion Transport Membranes (ITM) for Oxygen-Blown IGCC Systems and Indirect Coal Liquefaction." Air Products also develops process economics to assess the commercial viability of the selected applications.

Task 2.1 Gas Turbine Integration

2.1.1 Preliminary Cycle Analysis and Design Study

Large-Frame Turbine Integration: Engine Selection

Air Products and Concepts NREC (hereafter NREC) evaluated the technical and economic issues associated with integrating ITM Oxygen technology with a combustion gas turbine. The integration involves physically interfacing with the existing engine flow path structure to extract the required quantity of pressurized air and return the hot, vitiated, non-permeate stream to generate the necessary output power (Figure 2-1). NREC's principal goals in this first task were to obtain a preliminary evaluation of the integration requirements and define conceptual system configurations for application of ITM Oxygen technology to several potential engine models.

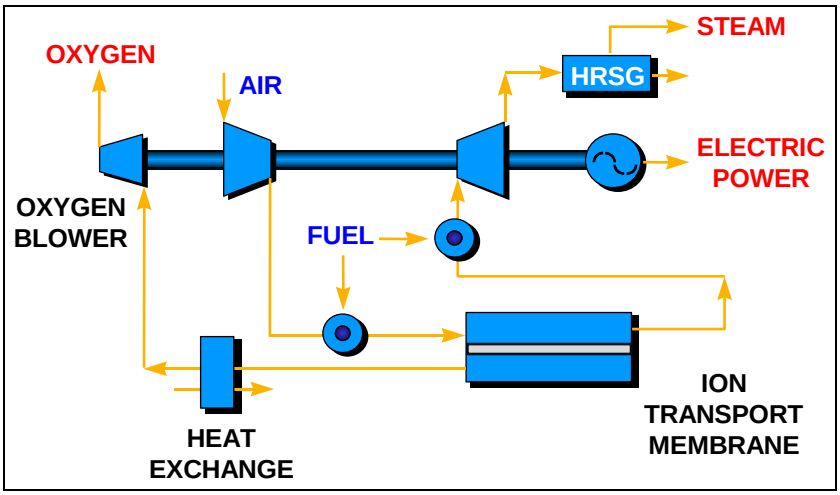

Figure 2-1. ITM Oxygen integration with a combustion gas turbine.

NREC completed a literature search on existing 100+ MW-class engines, then developed a spreadsheet cycle analysis model to investigate the effects of parametric changes in key system variables associated with the integration of ITM components with the gas turbine engine and bottoming cycle. The model was calibrated and then used to conduct an extensive series of parametric cycle calculations for the eight candidate engine models shown in Table 2-1. The calculations were aimed at determining the relative effects of the individual parameters and configuration choices on system design and performance. NREC also analyzed the selected candidate engine models using GateCycle™ software. These results and corresponding results obtained by Air Products using the GT PRO software were compared with NREC's overall system spreadsheet model. Differences among the three models were found to be relatively minor, providing confidence in the accuracy and utility of the spreadsheet model for evaluating the design and performance of the integrated ITM Oxygen system.

Table 2-1. Summary of selected candidate engine models.

	Engine Company		Siemens Westinghouse			GE Power Systems			ABB	
	Model No.		V84.3	W501G	W501H	7EA	7FA	7H	GT11N2	GT24
	Speed	rpm	3600	3600	3600	3600	3600	3600	3600	3600
Simple	ISO Output	MW	153	252	n/a	85	172	n/a	115	183
Cycle:	Heat Rate	kJ/kW-hr	9970	9210		10990	9940		10320	9400
	Efficiency	%	36.1	39.1		32.8	36.2		34.9	38.3
Combined	ISO Output	MW	n/a	367	420	130	263	400	166	271
Cycle:	Heat Rate	kJ/kW-hr		6210	6000	7180	6420	6000	7130	6180
	Efficiency	%		58.0	60.0	50.2	56.0	60.0	50.5	58.3
Compressor:	Air Mass Flow	kg/sec	425	569	544	292	432	558	375	383
	Pressure Ratio		16.1	19.2	27	12.6	15.5	23	15.1	30
	No. of Stages		17	17	19		18	18	16	22
Combustor:	Number		2	1	1	1	1	1	1	2
	Configuration		Silo	Annular	Annular	Annular	Annular	Annular	Silo	Annular
	Number of Cans			16	16			12	37	30/24
Turbine:	Inlet Temp	deg C	1290	1430	1500	1100	1300	1430		1240
	No. of Stages		4		4		3	4		5
	Exhaust Temp	deg C	550	600	590	540	600	610	520	640

NREC also completed a preliminary investigation of the transient operating modes of typical large gas turbines to ascertain the characteristic time intervals for each step in the sequence. Total startup time to full load requires nominally 30 minutes; shutdown sequences last ~10 minutes. These findings confirmed the need for isolation valves, bypass ducting, and controls around the ITM vessel to minimize thermal and chemical expansion effects caused by operating transients.

NREC and Air Products solicited non-confidential input from gas turbine suppliers based on the preliminary analyses. For the models in Table 2-1, 20% air extraction is readily obtainable with virtually no modification of the existing engine structure, which is adequate for IGCC systems integrated with high-recovery cryogenic ASUs. However, the highly integrated, passively controlled bleed air cooling limits further extraction without extensive modifications. Air extraction in excess of 50% of compressor discharge air is required for typical values of oxygen recovery in an ITM Oxygen system (Figure 2-2). Air extraction in excess of 50% is feasible with some older engine models because of different casing configurations and less sophisticated bleed air cooling designs. In addition, engine configurations under development in the APFBC (DOE) program will allow much greater air extraction and return of a hot, vitiated stream to the

combustor. These developments, including both early and current 100+ MW models, provide capabilities that are more than sufficient to satisfy ITM Oxygen integration requirements.

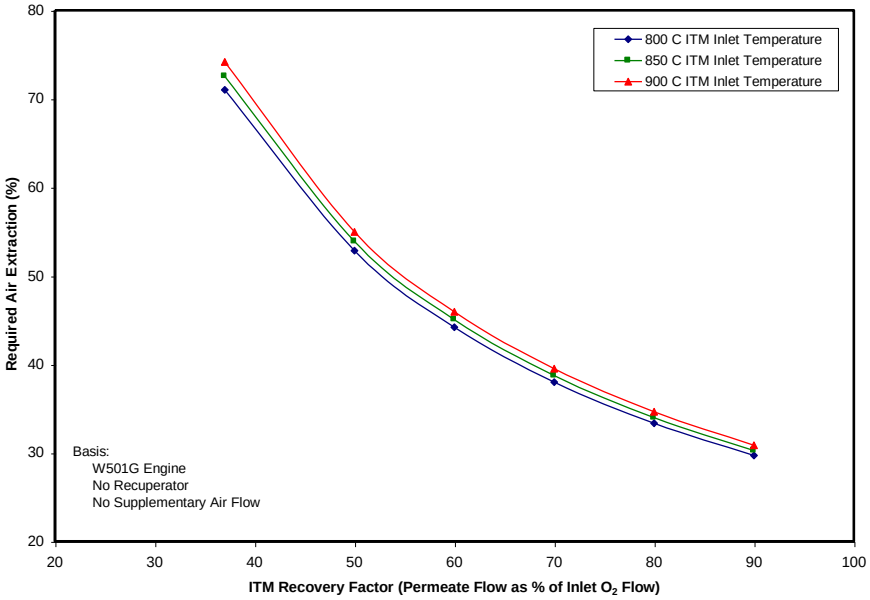

Figure 2-2. Variation of air extraction equirements.

Large-Frame Turbine Integration: Process Integration

The piping difficulty associated with distributing the various streams to a large number of individual combustor cans on a large-frame gas turbine is a disadvantage common to all engine models that use a can-annular combustor design (Figure 2-3). A much simpler configuration is obtained if air is extracted from a single point in the compressor discharge plenum and the non-permeate stream is returned to a single point in a second common plenum feeding all of the combustor cans. This approach has been used successfully in the past for recuperated engine models and would be particularly amenable to engines that use a silo combustor design, as shown in Figure 2-4.

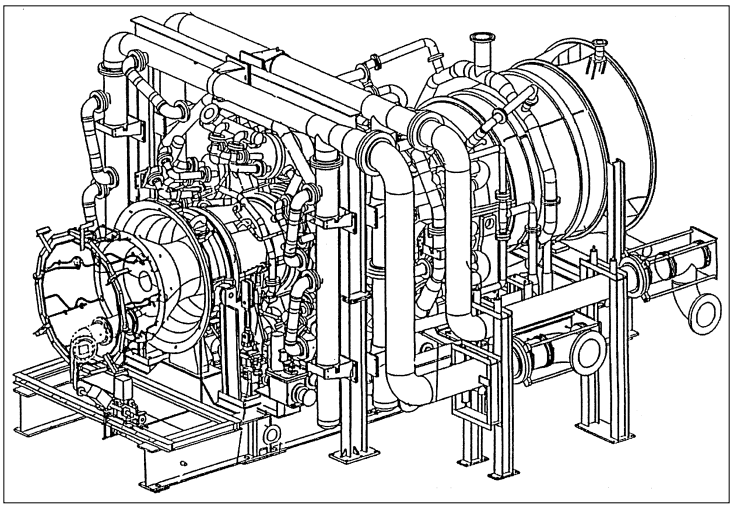

Figure 2-3. Piping arrangement for extraction with GE 6FA engine at Pinon Pine IGCC installation.

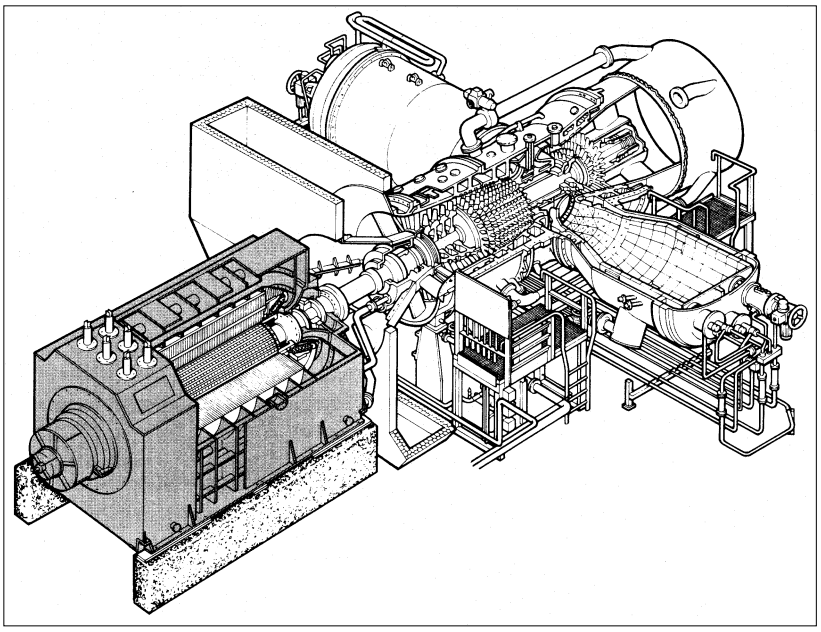

Figure 2-4. Siemens Westinghouse V84.3 engine with silo combustors.

NREC and Air Products identified two important issues associated with the non-permeate gas return to the engine: 1) the increased temperature, and 2) the reduced oxygen concentration compared to the design inlet values for the existing combustors. In a conventional gas turbine combustor, the inlet air cools the internal liner and protects it from the hot flame. Because of the higher inlet temperature in the ITM Oxygen system, cooling the liner using standard techniques will be more difficult. In addition, the reduced oxygen content of the non-permeate stream, in

combination with the relatively low heating value of the syngas fuel, could make it more difficult to achieve acceptable combustion stability and efficiency. However, the high inlet temperature and typically high concentration of extremely flammable hydrogen in the syngas fuel will help considerably in this regard. Consequently, the vitiation effect is likely to offer less of a design challenge than originally expected for syngas fuels, although it remains an issue for natural gas.

The additional system pressure losses associated with the integration of ITM components reduce both power output and cycle efficiency. Air Products determined that, for reasonable design values of the component pressure loss, the decreases are moderate and within acceptable bounds. This finding provided a fair degree of freedom in selecting the design conditions for the ITM system components.

Small-Frame Turbine Integration: Engine Selection

NREC also conducted a parallel review of candidate gas turbine engines in the 0-50 MW size range for potential use in stand-alone oxygen/power co-production applications. They collected and analyzed available design and performance data for 39 engines manufactured by seven different vendors. NREC also performed parametric calculations to estimate achievable oxygen production rates for various engine models, assuming full air extraction (excluding turbine cooling air) and 50% oxygen recovery. In addition, Air Products completed a survey of trends in cost, air flow rate, pressure ratio, and turbine inlet temperature for all currently available >5 MW gas turbines, based on GT PRO's gas turbine model library (November 1999 release).

Small-Frame Turbine Integration: Process Integration

In addition to the issues identified above for large-frame gas tubines, small-frame gas turbines are likely to be fired on natural gas (methane). Flammability data from NREC indicate that the combustor downstream of the ITM requires a minimum inlet oxygen concentration for sustained combustion of methane. For a case when direct firing preheats the ITM feed air to membrane operating temperature results in a feed oxygen concentration of ~16% (mol.), ITM Oxygen system performance is constrained to operate between a relatively low inlet concentration and the minimum inlet oxygen concentration for methane combustion. This can limit oxygen recoveries. For gas turbines up to 125 MW, air flow (lb/s) is reasonably approximated by 7.0×MW. This relationship sets the maximum oxygen production to power ratio at 22 TPD O_2

per MW, assuming 100% air extraction, which is not strictly viable because of turbine cooling requirements. Notably, flammability limits for syngas are somewhat more relaxed because of the combustion characteristics of hydrogen.

2.1.2 Selection of Engine for IGCC Economic Study

Air Products and NREC identified GE's 7EA engine, capable of 55% air extraction, as the basis for a near-term integration of ITM Oxygen with a large-frame gas turbine. It has a strict upper limit of 950°F on the combustor inlet temperature, which would require the use of a high-temperature recuperator to cool the non-permeate return stream.

Based on a dialogue with Siemens Westinghouse, Air Products and NREC recommended that Texaco Inc. (the Gasification Division, hereafter Texaco) proceed with the W501G and/or W501H engines for the IGCC economic study. This recommendation was consistent with Siemens Westinghouse's development activities and proposed configurations for the APFBC application. Air Products and NREC further recommended that Texaco construct the ITM Oxygen and cryogenic ASU base cases around the W501G (Figure 2-5), with the intention of running the W501H in at least one case in the future. Starting with the W501G had the following advantages: it enables upfront comparison with previous work; it offers the best economies of scale with the largest (by >20%) non-H-class single-train capacity; NREC could simulate this engine reasonably well with public information (e.g. GT PRO) while receiving limited help from Siemens Westinghouse; and it uses a pressure ratio historically used in Air Products' designs. Running the W501H later would provide an exciting look at future possibilities for DOE, and the opportunity to evaluate the effects of operating the ITM at a much higher pressure ratio. Texaco concurred with this recommendation.

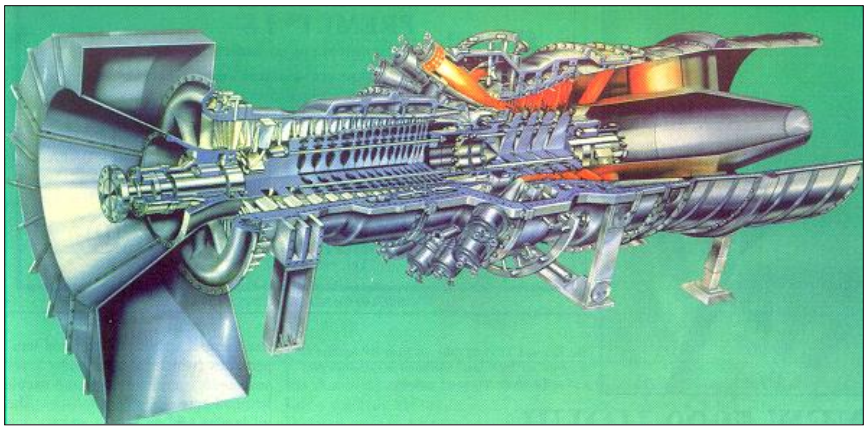

Figure 2-5. Siemens Westinghouse W501G engine.

2.1.3 Economic Assessment of Integrated System

NREC provided support for the Task 2.6.1 study carried out jointly with Texaco and Air Products. NREC calculated performance of the W501G engine in both ITM Oxygen and cryogenic ASU cases to converge on the compositions and properties of the different fuel streams and to finalize the design conditions for each case. NREC upgraded their cycle analysis model to include the effects of fuel-sensible heat on system performance and efficiency. The model was also modified to provide capabilities for simulating the integration of a cryogenic ASU with the engine system (see Task 2.6.1 for a more detailed description of this analysis).

NREC also completed modifications to their combustor design models for syngas fuels and performed calibration calculations to adjust the accuracy of the NO_x and CO prediction procedures. NREC used the updated models to conduct parametric design calculations for the ITM preheat combustor, based on the final conditions selected for the W501G-integrated system. These calculations confirmed the need to use a modular approach to obtain a practical combustor configuration, which is consistent with a modular vessel approach for very large plants. NREC also estimated the size and cost of the recuperator that would preheat the extracted air stream by heat exchange with the non-permeate stream. The estimated component costs for the pre-combustors and recuperator were incorporated into the ITM system costs submitted to Texaco.

Task 2.2 Development and Demonstration of Trace SO_2 Adsorption

Air Products carried out an assessment for the need to control sulfur dioxide (SO_2) in feeds to the ITM. In general, SO_2 will be present in the feed to an ITM Oxygen membrane because it is present in ambient air. Furthermore, if the feed air is preheated by direct firing in a fuel stream,

SO_2 will be a combustion product of the sulfur-containing species in the fuel (e.g., H_2S, COS, mercaptans). Some ITM Oxygen membranes have been shown to react with SO_2 at low SO_2 concentrations in the gas phase, which can have a deleterious effect on oxygen flux and membrane morphology (see Task 1).

A representative kinetic expression to describe the reaction of a perovskite with SO_2 includes terms containing the equilibrium partial pressure of SO_2, P_{SO2}*. At SO_2 pressures less than P_{SO2}*, no reaction will occur and the perovskite will be stable. At SO_2 partial pressures greater than P_{SO2}*, the perovskite will react. P_{SO2}* is expected to be a function of temperature, oxygen partial pressure, and membrane composition.

The partial pressure of SO_2 in the feed air to an ITM, P_{SO2}, will be a function of the ambient concentration of SO_2 and the pressure ratio supplied by the feed air compressor, as well as the sulfur content of the preheat fuel and the fuel to air ratio of the pre-combustor. Figure 2-6 shows P_{SO2} as a function of air feed pressure ratio for 1 ppm total sulfur in the fuel and various ambient SO_2 concentrations (e.g., the yearly maximum three-hour time weighted average (TWA) SO_2 concentration is <200 ppb at 90% of EPA-measured sites). The calculation assumes a 20:1 molar air:fuel ratio typical of a gas turbine burning syngas, and the symbols at the bottom indicate the operating pressure ratios of several state-of-the-art gas turbines. Given 1 ppm total sulfur in the fuel and a 20:1 molar air:fuel ratio, the fuel contributes the equivalent of 50 ppb SO_2 before compression.

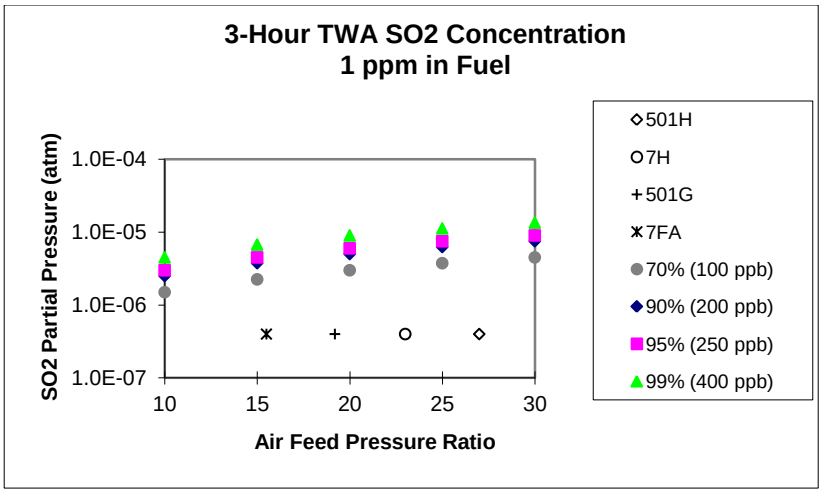

Figure 2-6. SO_2 concentration in the ITM Oxygen feed.

Figure 2-6 shows that for 1 ppm sulfur in the fuel and pressure ratios up to 20:1, the feed P_{SO2} will remain below 10^{-5} atm at 99% of EPA-measured sites (400 ppb ambient SO_2 for a 3-hour TWA). Air Products pursued a better definition of P_{SO2}* under Task 1 in light of these requirements, but concluded that at least for combinations of some sites and available fuels, a SO_2 cleanup system will be required.

Air Products devised a method for integrating sulfur-removal processes with ITM cycles and applied for a U.S. patent. The application stresses the importance of the critical equilibrium partial pressure of SO_2, P_{SO2}*, for reaction with the ITM and its use as a material design parameter to improve the flexibility of the overall system design. For example, Air Products determined that proper material design can obviate the need to employ Rectisol® to treat the fuel stream to <1 ppm total sulfur (such technology has the disadvantages of both high capital cost and undesired removal of carbon dioxide). Furthermore, this invention clearly teaches for the first time that capital cost savings can be achieved by treating only the pre-combustor fuel stream – more than 30% of the total fuel stream in a typical gas turbine integration – to the sulfur specification required by the ITM.

Task 2.3 Thermal and Mechanical Analysis of Membranes and Seals

Wafer and Module Development through Stress Modeling

Air Products, McDermott, and Ceramatec collaborated on Task 2.3 to understand the thermal, structural, and hydrodynamic issues associated with scale-up of the ITM Oxygen wafer from

subscale to full-size dimensions. McDermott began this effort by formulating a method to solve the oxygen transport equations using a heat transfer analogy to determine the distribution of vacancy concentration (and hence, chemical expansion). Chemical expansion is caused by the reversible loss of oxygen from ITM Oxygen materials during changes in temperature or atmospheric environment. McDermott retrofitted existing heat transfer models to calculate chemical expansion as a function of position and time for sub-structures like the dense membrane layer or manifold tubes near the seal region. This method included surface kinetics, transient pressures and temperatures, and simultaneous heat transport. McDermott calculated that the time for equilibration with the gas phase is ~0.1 seconds for the membrane layer thickness scale, compared to six minutes for the tube wall thickness.

McDermott devised a simple method of using the calculated oxygen vacancy distribution and the thermal/chemical expansion model to determine the stress profiles in thick-walled AP98 tubes. This method was used for several applications involving the permeate flow tube, including evaluation of the following: stresses at design conditions; stresses caused by pressure and temperature transients during startup; stresses caused by time/temperature processing cycles; and scale-up of the tube diameter and wall thickness. For example, a transient temperature analysis indicated that significant stresses developed during the existing cooling cycle used in the fabrication of ITM tubes. This type of analysis could be extended to determine the ramp rate necessary to hold the stress below an allowable value, or to determine the best cooling schedule (with minimum stress) for a given cycle time. McDermott also analyzed the chemical expansion effects suspected of causing the manifold tube failure during past PDU tests. They predicted that the ramp in permeate pressure from 90 Torr to 15 Torr caused a dramatic increase in failure probability – from <1% to 37%.

McDermott then developed a suite of modeling tools to complete their thermal and mechanical modeling of the baseline wafer design. First, McDermott developed a three-dimensional "solid" finite element model to evaluate the localized pressure-only capability of the membrane and porous layers over an underlying slot. Using a 300 psi pressure load and the baseline set of AP98 properties, calculated peak stresses in the membrane layer were approximately 790 psi in tension and 840 psi in compression, compared to an "allowable" design stress of 2,700 psi, based on a failure probability of $1x10^{-10}$. Peak stresses in the porous layer were 570 psi in tension and 800 psi

in compression, which are borderline compared to an allowable limit of 530 psi. These calculations agree with handbook calculations of similar geometries with correction for appropriate boundary conditions. McDermott's calculations identified an appropriate slot width limited by the porous layer strength, which matched the experimentally derived existing wafer design.

McDermott also developed a similar solid finite element model for the slotted layers. A 300 psi pressure load caused peak tensile stresses of 410 psi for the layers, as well as compressive stresses of 730 psi to 850 psi. Since all of these results remained well within the allowable stress limits for AP98, some potential existed for opening up the slot width, which helps to decrease the required slotted layer thickness and hence the wafer cost.

Finally, McDermott developed a global "shell" model of the complete baseline wafer structure, including the outer rim, inner rim, and central manifold tube. In this model, the slotted layers are characterized by composite properties determined by subjecting unit cell models of each layer to deformations in two dimensions. McDermott calculated stress fields that show that a saddle-shaped deformation pattern is imposed on the wafer when subjected to an external pressure load, and arises from the slotted layer geometry. The global deflection pattern can be applied as boundary conditions to detailed local models of stress.

Incorporation of thermal and chemical expansion effects into these finite element models yielded calculated peak tensile stresses of ~20,000 psi in the membrane layer. At steady state, other dense structures (e.g., outer rim) experience significant but lesser peak stresses because of their thicker dimensions. This result clearly exceeded the "allowable" design stress determined by Weibull failure probability and seemed to contradict the successful structural performance of wafers in test apparatus. The allowable failure probability depends on several far-reaching factors, including purity requirements, vessel design, overall plant design, overall plant economics, and the number of features per repeat unit (i.e., each module contains many slotted features, but only one manifold tube). However, even the worst-case calculated stress was only ~60% of the characteristic strength of dense AP98. For a typical Weibull modulus (e.g., m=9), the failure probability is $1x10^{-2}$ for this case, which is completely consistent with wafer test results.

McDermott performed sensitivity analyses on some simple concepts to reduce the stresses in the membrane layer, including decreasing the membrane layer thickness, increasing the operating temperature, and decreasing the stiffness of the slotted layers. Of these concepts, decreasing the membrane layer thickness showed the most promise. The chemical expansion-induced stresses decreased in rough proportion to the membrane layer thickness because the oxygen partial pressure driving force undergoes a comparable reduction to maintain the same flux.

In addition, McDermott introduced plastic behavior into their modeling efforts for the first time by including creep calculations in their simple one-dimensional model of stress in a tube. The results clearly showed gradual creep relaxation of stress over several hours, but also demonstrated that creep does not effectively relax stress over short (<1 hour) transients.

In support of the wafer redesign/scale-up effort under Task 3.1, McDermott modified their existing wafer models to incorporate new slot layer thicknesses and slot patterns. Their calculations allowed for alterations of slot dimensions within the allowed stress limit by more than a factor of two. However, the peak membrane layer stresses also increased by about a factor of two, under pressure-only loading. The peak porous layer stresses increased by 20-30%. Sensitivity analyses indicated that the widening the slots in the slotted layer designs increased the stress in the outer layers. Since the fabrication cost analysis indicated that some additional permeate-side pressure drop would not cause extraordinary cost penalties, the slots in the slotted layer were limited to keep the upper-layer stresses closer to acceptable limits. McDermott then updated their local finite element model of the full-size wafer structure to include the new slotted layer slot patterns. Compared to the previous design, the new slot pattern reduced the maximum principal stresses by 15-30% in all layers.

Using their global "shell" model of the full wafer structure, McDermott also evaluated the stresses incurred by moving from round to square geometry, including sensitivity to radius of curvature and overall outside dimensions, under pressure-only loading. As expected, the maximum stresses increased only marginally (~10%) with outer dimension and square geometry. The peak stresses occurred near the inner rim, as the edges of the wafer deflected in a saddle-shaped pattern because of the slotted layers. Including models for the spacers above and below the wafer stiffened the overall structure near the inner rim and greatly decreased the stresses in this region.

In addition, McDermott completed sensitivity studies to determine the effect of porous layer thickness on the stress distribution imposed by pressure-only loading. Their analysis suggested that increasing the thickness of the porous layer would significantly decrease the maximum principal stresses in the wafer. For example, increasing the porous layer thickness by 100% reduced both the membrane and porous layer stresses by ~33%. Further increasing the thickness by another 100% (400% overall) further reduced the porous layer stress by an additional 33% while reducing the membrane layer stress by another 17%.

McDermott then modified their global wafer model by calculating new effective properties for the new slot patterns. The results from this global model were applied as boundary conditions to the local model in the first integration of these two modeling techniques. Results from this integrated approach indicated that the entire wafer is in compression during pressure-only loading. This result is generally favorable except in the porous regions, which are expected to have relatively poor compressive strength. McDermott completed sensitivity modeling to explore potential wafer design modifications to decrease the compressive stress in the porous layer. Improving the slotted layer stiffness by halving its slot length caused a 22% decrease in compressive stress, while increasing the porous layer thickness by 50% caused only a 10% decrease.

One proposed module design concept is to add a spacer to the edge of the rim to maintain wafer-to-wafer spacing in a module during fabrication and operation. McDermott assessed the effect of adding such an "edge spacer." Calculations indicate that adding the edge spacer has approximately the same effect as decreasing the wafer size; that is, an improved compressive stress (reduced by <5%) in the center of the active region. However, the effect was more significant near the outer rim, which has positive implications for volume-weighted reliability assessments. Even without the edge spacer, the stress in the porous layer decreased near the outer rim. In addition, modestly increasing the slot width did not significantly increase the stress in the porous layer.

McDermott also modeled the intermediate-size wafer to determine its viability as a test vehicle for the full-size structure. Their analysis indicated that the stress in the critical region within the porous layer matched the full-size wafer simulation within 3%. This result suggested that

pressure collapse testing data from the intermediate-size wafer could be directly applicable to the full-size wafer.

Effects from Flow-Induced Vibration

McDermott calculated the effects of flow shear, noting that vortex shedding off the trailing edge of the membrane would tend to stress the membrane in an oscillatory fashion. Figure 2-7 shows a wafer deflected because of these stresses, where the effect has been magnified by 10^6 times.

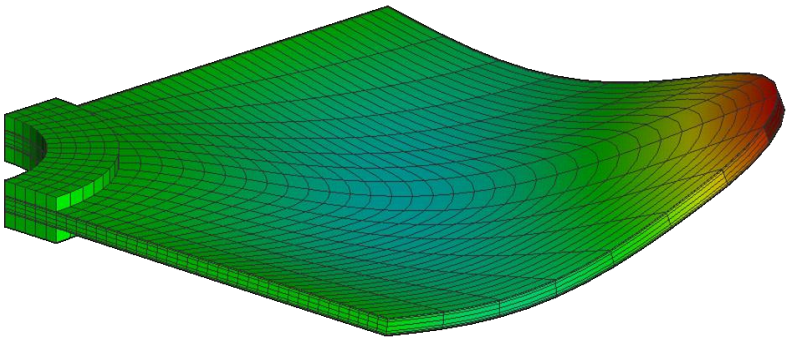

Figure 2-7. Finite element analysis (FEA) of a quarter section of a wafer with imposed boundary conditions of vortex shedding off the trailing edge (right) of the wafer. Deflections are magnified by 10^6 times. Color variation is indicative of the local stresses.

McDermott initiated efforts to perform vibration tests on intermediate-size wafers shipped from Ceramatec. The three-fold purpose of these tests was to determine the potential for a vibration-based quality control test, continue to validate analytical models of the full-size wafers; and provide natural frequency and damping data to assess the potential for flow-induced vibration. Close agreement between model predictions and measured frequencies and mode shapes are used to confirm the suitability of the model stiffness properties used in other structural models to assess thermal, mechanical, and chemical expansion stresses.

McDermott successfully tested several wafers over a bandwidth of 0- 5000 Hz using shaker excitation and miniature accelerometers for response measurements. Manufacturing variations (e.g., mass, thickness, linear dimensions) evident in these wafers appeared to influence the frequency response enough to prohibit distinguishing hermetic wafers from leaking wafers via vibration testing. As manufacturing methods and tolerances improve, however, this conclusion could change.

McDermott also completed parallel FEA modeling of the natural frequencies and mode shapes of intermediate-size wafers. Their analysis predicted that an unconstrained ceramic wafer would have a first natural frequency of 720 Hz. Since this frequency is lower than the wafer's vortex shedding frequency, the possibility of flow-induced vibration exists; McDermott will calculate the response amplitude of the wafer to determine the potential severity. McDermott also modeled and tested an aluminum "dummy" wafer of the same dimensions to verify the experimental boundary conditions. These analyses indicated that the mode shapes and natural frequencies are sensitive to the assumed boundary conditions.

McDermott then completed vibration testing of wafers that include added mass to counterbalance accelerometer mass effects, as well as modified boundary conditions. These tests showed encouraging results. However, adding the mass did affect the frequencies and mode shapes, effectively creating a new structure that departs from the actual wafer response. As a result, McDermott decided to proceed by using a microphone rather than accelerometers for response measurements. Future vibration testing will focus on full-size wafers with tubes attached.

Chemical Expansion Verification

Air Products, McDermott, Ceramatec, and Penn State devised an experiment to verify the chemical expansion-induced strain under oxygen fluxing conditions. The test configuration comprised an AP98 disk sealed to the end of a chamfered alumina tube with a glass seal. Modeling of the glass seal design indicated good deflection and acceptable stress (~2 ksi) for a AP98 disk joined to an alumina tube. McDermott also recommended detailed calibration conditions and test procedures for the chemical expansion verification test, including repeatability checks and recommended transient times.

McDermott then completed additional finite element analyses that included AP2K properties, to support the shakedown of the chemical expansion verification test assembly. Modeling results indicated that the transducer loading at the center of the disk would significantly affect disk deflection. For a 10 Torr total pressure differential, the predicted (downward) deflection increased by 60% with the addition of a 20 gram transducer load. For a disk subjected to an oxygen partial pressure differential of 0.19 atm between the top and bottom surfaces, the predicted (upward) deflection decreased from 138 µm to 119 µm as the transducer loading

increased from 0 gm to 20 gm. As a result, the structural analysis of each test result must necessarily incorporate the measured transducer load.

McDermott completed analyses of several differential pressure shakedown runs on the chemical expansion verification test assembly at Penn State. Finite element modeling predicted a 22 μm deflection at a pressure differential of 10 Torr, which matched the experimental response rather well. For larger pressure differentials, however, the experimental response fell between the wide bounds predicted by simply-supported vs. rigidly-fixed boundary conditions. This result indicated that the glass seal provides significant resistance to disk deflection. Room-temperature tests using vacuum grease as a sealant matched model predictions using a simply-supported boundary condition to within the uncertainty in the model input data. Trial runs at higher temperatures were expected to decrease the restraint imposed by the glass seal by reducing its viscosity, thereby decreasing the difference between experiment and analysis with a simply-supported boundary condition. However, the higher-temperature runs did not reconcile the difference between the analysis and the experiment. McDermott then developed a model that simulates the seal restraint, showing that seal "stiffness" could be adjusted to empirically match experimental results.

Ceramic-to-Metal Seal Stress Modeling

Modeling of the ceramic-to-metal seal proceeded along two paths. McDermott first built a solid axisymmetric finite element model of the permeate flow tube, including a two-dimensional oxygen vacancy profile superimposed on various temperature profiles. The temperature profiles corresponded to several design options: a "hot" seal at process temperature (short tube ~2"); a "warm" seal simply buried in the vessel insulation (long tube); and a "warm" seal with an internal liner for insulation (long tube). The "warm seal with liner" design caused tube stresses that roughly equated to the "hot seal" stresses. While the insulating liner may be difficult to apply in practice, other options would cause similar temperature profiles, such as a metallic sheath surrounding the tube to conduct heat away.

McDermott also built a solid axisymmetric finite element model of the entire seal assembly, including the permeate flow tube, U-rings, and seal holder. This detailed seal model quantifies the contact pressure between the U-rings and the ceramic tube during assembly, pressurization, heat-up, and operation. Initial results indicated that the U-rings would creep significantly after

1000 hours of operation at temperature. McDermott will further refine the model and benchmark it against the ongoing laboratory seal tests before examining more complex scenarios (e.g., thermal cycling).

Task 2.4 Conceptual Process Vessel Design Engineering

Concept Development

McDermott began exploring design options for a 100 TPD process vessel by developing some basic design tools, including integrated one-dimensional heat transfer models of the vessel and all internal components and pressure drop models for both the air side and the oxygen flow path. McDermott used existing empirical models for pressure drop in square-finned tube arrays to estimate the air-side pressure drop as a function of the number of ITM Oxygen modules per row in series. For various spacings between wafers, the models indicate that maximum pressure drop through the vessel can be maintained below 5 psi, which is consistent with expectations of the gas turbine suppliers as ascertained by NREC.

McDermott developed concepts for several possible design configurations. The principal goal during the evolution of these designs was to maintain straight ceramic manifolding tubes between the modules and their ceramic-to-metal seals while moving the oxygen header piping out of the hot zone of the vessel. Building on those themes, additional concepts included provisions to access the stacks and outlet tubes for isolation, repair, or replacement; reduce the ceramic-to-metal seal temperatures; and minimize bypass flow. Using these guidelines and design tools, McDermott developed a conceptual design for a 100 TPD vessel with modules, including insulation requirements and sizing of the oxygen manifolds and piping. Drawings and specifications were suitable for cost estimates. Figure 2-8 shows one early vessel concept (at 350 TPD nominal capacity) in which an insulated flow duct is housed inside a “cold-wall” pressure vessel. In the left side of Figure 2-8, modules (shown in green) are loaded into the base of the duct; the duct receives each module via a dedicated permeate withdrawal pipe that exhausts into a manifold below which then connects to an oxygen header located outside of the duct. Once the base of the duct is fully loaded with ITM modules, the sides and top of the duct are assembled, and the entire apparatus can be loaded into a pressure vessel to make a seal against the vessel head, which supports the duct and piping. This approach allows for the hot feed gases to stay

within the insulated duct so that the shell of the pressure vessel can be fabricated from standard materials.

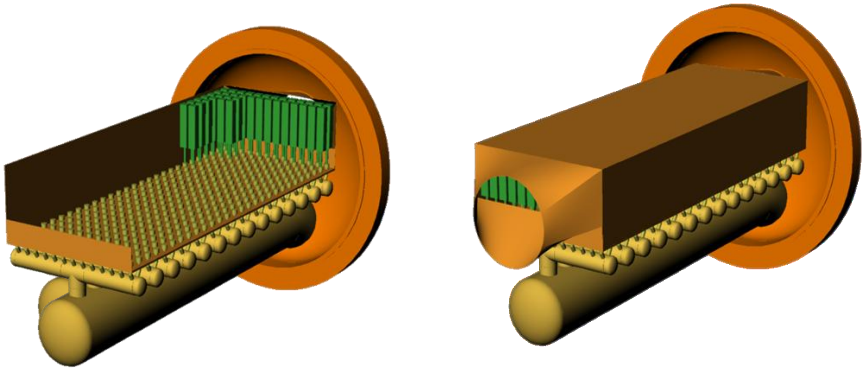

Figure 2-8. Conceptual design of ITM pressure vessel internals. Left side shows modules (green) partially loaded into an insulated flow duct base; right side shows the insulated flow duct fully assembled and housing a full load of modules.

Insulation Development

McDermott also investigated insulation materials and selected a very low-silica, dense, molded alumina fiber material for insulating the hot gas duct and oxygen piping. The insulation allows the carbon steel vessel components to operate below 500°F. Since virtually every practical "low-silica" insulation contains 1-3% silica, McDermott worked with Air Products to develop an allowable silica specification for vessel insulation. In ceramic fiber-based insulations, the silica exists in either an amorphous mixture with alumina or in mullite, a crystalline form of alumina-silica. These forms should significantly inhibit silica transport and loss, but vapor pressure calculations for silica in mullite indicated that the silica would vaporize and contaminate the ITM surfaces in only a few days. However, the equations used to describe the vapor pressure were developed from experiments at conditions considerably different from the ITM Oxygen operating envelope. Experimental measurements at actual operating conditions are required as part of future work.

Vessel Design Screening

McDermott determined an initial cost estimate for the 100 TPD vessel design that contained sufficient detail about the underlying calculations and assumptions to suggest appropriate areas for cost savings. For example, the design included a full-diameter closure flange that contributed 24% of the total cost. Because of other internal details, this flange may not be required for

access and may be replaceable with a full-seam weld. McDermott also utilized a recent advances in gas erosion of fiber insulation to justify increasing the oxygen velocity by a factor of 2.5 (at sub-atmospheric pressure) inside the permeate piping. This design change allowed a significant reduction in manifold and header pipe sizes that also reduced the vessel diameter. Further refinements to the base reduced the estimated vessel cost by 37%. McDermott also completed an evaluation of high-pressure effects on the thermal conductivity of insulation, which was now one of the largest cost components of the commercial vessel designs. The results suggested that relatively low-density insulation is suitable up to 50 atm, potentially reducing insulation costs by 50%.

The 100 TPD vessel was redesigned for the full-size wafers developed under Task 3.1, using the refined costing methods. The vessel diameter was reduced by 26% through this exercise. McDermott also sized a 500 TPD vessel based on the full-size wafers, the 500°F metal temperature limit, and the desired air-side and oxygen-side pressure drop requirements. Modules were arranged inside two parallel air ducts. The resulting vessel design was 140" in diameter by 27' long. The air-side pressure drop constraint imposed by gas turbine integration limits the number of modules arranged in series, forcing large vessels to grow in diameter rather than length. McDermott also completed a design and cost estimate for an intermediate-size (350 TPD) ITM Oxygen vessel and incorporated some additional scalable cost-saving design features. This design allowed for one duct and one oxygen header centered below the duct, as shown in Figure 2-9.

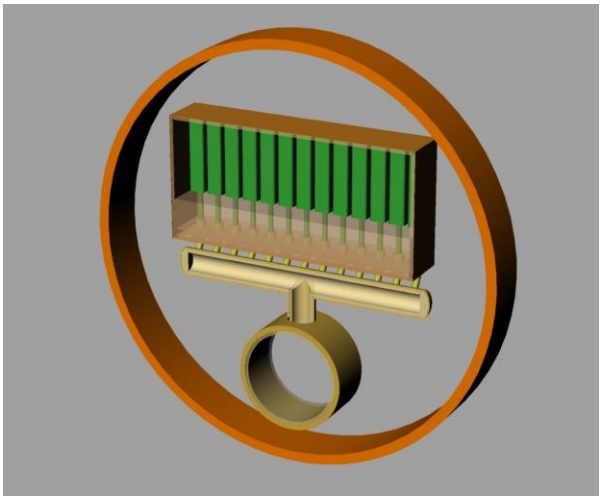

Figure 2-9. Cross-section of 350 TPD vessel design.

Task 2.5 Mass Transfer Modeling of Membrane Wafers

Air Products developed a calculation method wafer, module, and vessel (modules-in-series) performance based on data from tests of AP98 and AP2K materials. The method included a staged calculation of the oxygen profile within a vessel, incorporation of gas-phase mass transfer resistance to more accurately simulate the performance of individual modules (or banks of modules), and a more accurate description of oxygen transport through the membranes.
The inclusion of gas-phase mass transfer resistance into the vessel performance model represents a particularly useful refinement, although no test data currently exist for multi-wafer modules in cross-flow to benchmark against the model. According to the current model, however, even when the inter-wafer gas velocity is slow enough to permit 70% oxygen recovery over a typical vessel configuration at standard operating conditions, the gas-phase mass transfer resistance imposes a performance penalty of just over 5%. Test data from the TDU is expected to help to verify or challenge this result.

As expected, the vessel performance model indicated that inter-wafer spacing also affects gas-phase mass transfer. For a vessel operating at 50% oxygen recovery, the overall performance difference is about 1.6% per mm in the range of practical interest. At 70% oxygen recovery, the difference increases to about 2.7% per mm.

Task 2.6 Process Engineering and Economic Evaluation

2.6.1. Process Engineering and Economic Evaluation for the IGCC Application

Texaco and Air Products collaborated on Task 2.6.1 to produce an updated process engineering and economic evaluation of ITM Oxygen technology in an IGCC power plant. Texaco and Air Products constructed the ITM Oxygen-integrated base case (Case #1) and the cryogenic ASU-integrated base case (Case #2), in addition to identifying potential candidates for up to two additional cases. The scope of study included a block flow diagram, process description, performance summary, emissions comparison, and cost estimate for each case. The cost estimate was subdivided into the following major categories: 1) gasification, including feed preparation, gasification/scrubbing, solids handling, and low-temperature gas cleanup; 2) gas cleanup, including acid gas removal, a sulfur recovery unit, and a tail gas treatment unit; 3) a combined cycle unit; 4) an air separation unit; and 5) the balance of the plant.

Both IGCC designs were based on a Texaco high-pressure quench gasifier, a raw syngas expander turbine, conventional fuel gas cleaning, a sulfur recovery unit, gas turbine integration with either an ITM or cryogenic ASU, and a high degree of steam cycle thermal integration. The combined cycle power plant included a Siemens Westinghouse W501G gas turbine (as discussed in Task 2.1) with maximum output set at 272 MWe, a heat recovery steam generator (HRSG), and a reheat steam turbine with operating conditions of 1800 psig/1050°F. The Texaco high-pressure quench gasifier operates at nominally 950 psig. The primary gasifier fuel was Pittsburgh #8 coal containing 2.5% sulfur.

Texaco took initial screening results supplied by NREC and estimated dry syngas compositions for both the ITM Oxygen-integrated base case (Case #1) and the cryogenic ASU-integrated base case (Case #2). Notably, for Case #1, Texaco proposed treating the syngas for the ITM pre-combustor to a different sulfur level than the syngas for the engine power combustor. Because of the different process steps required, the pre-combustor fuel was available at only 100°F and therefore could be humidified without further heating. The higher-sulfur syngas for both Cases #1 and #2 was available at 300°F and, if appropriate, could be humidified to add mass flow.

For Case #2, NREC helped to examine engine performance assuming return of the waste nitrogen stream to maintain mass flow and boost power output. NREC did calculations with and without recuperation of this nitrogen return stream against the extracted air stream as a means to improve cycle efficiency. Other variations included both dry and humidified fuel, with and without return of CO_2 recovered from the sulfur-removal step. When the syngas was saturated with water, in combination with the available nitrogen and CO_2 return, the W501G produced its maximum output with a reasonable surge margin. Given this performance, there was no need to add a supplemental air compressor (100% air integration with the gas turbine) and or to saturate the return nitrogen. This scenario was transmitted to Texaco as the preferred result. The foundation for a dry syngas case was available, but power output would need to be increased with supplemental air and/or humidified nitrogen.

For Case #1, NREC helped to examine performance differences between dry and humidified fuel for the engine power combustor for fixed pre-combustor fuel conditions. Air Products and NREC found that by assuming the syngas was saturated with water, the added mass flow enabled

the turbine to operate at its maximum output. As a result, four cases of the gas turbine performance, based on various water saturation and recuperation levels, were transmitted to Texaco. NREC also investigated the use of a supplemental air compressor as an alternative to fuel humidification for increasing engine power output.

Air Products provided the cost estimate for the cryogenic ASU producing 3,040 sTPD (contained) at 95% oxygen purity and 1125 psig delivery pressure. This specific cost ($/sTPD) matched the low end of a range of cases published in a recent IGCC study by Texaco, GE, and Praxair. Air Products also developed the ITM Oxygen cost estimate for a unit to produce 3,200 sTPD (contained) of oxygen at 99.5% purity. A detailed description of this work follows and has previously been presented as a Topical Report.

IGCC Study: Process Description

The overall IGCC plant includes four main process areas, which are described in detail in the following sections: 1) the air separation plant consisting of an ITM Oxygen unit or a cryogenic ASU; 2) the gasification plant; 2) the combined cycle power plant; and 4) the balance of the plant.

ITM OXYGEN PLANT / CRYOGENIC AIR SEPARATION UNIT (ASU)

ITM Oxygen Plant

The ITM Oxygen process uses nonporous, mixed-conducting, ceramic membranes that have both electronic and oxygen ionic conductivity when operated at high temperature, typically 1500-1650ºF. The mixed conductors are inorganic mixed-metal oxides that are stoichiometrically deficient of oxygen, which creates oxygen vacancies in their lattice structure. Oxygen from the air feed adsorbs onto the surface of the membrane, where it dissociates and ionizes by electron transfer from the membrane. The oxygen anions fill vacancies in the lattice structure and diffuse through the membrane under an oxygen chemical-potential gradient, applied by maintaining a difference in oxygen partial pressure on opposite sides of the membrane. At the permeate surface of the membrane, the oxygen ions release their electrons, recombine, and desorb from the surface as oxygen molecules. Since no mechanism exists for transport of other species, the separation is 100% selective for oxygen, in the absence of leaks, cracks, or flaws in the membrane.

To minimize the mechanical load imposed by the driving force, the process operates with a medium-pressure air feed stream, typically 100-300 psia, and a low-pressure oxygen permeate stream, typically at less than one atmosphere, although higher air feed pressures or oxygen product pressures may be used. Since oxygen ion transport is thermally activated, the basic process cycle must also include the means to heat the pressurized air feed to the membrane operating temperature, either by indirect heat exchange, direct firing with fuel, or a combination of both. The membrane's chemical stability in high concentrations of carbon dioxide and water allows the use of a cost-effective, direct-heating step.

To achieve a suitable cycle efficiency, the energy associated with the hot, pressurized, non-permeate stream is recovered by integrating the ITM Oxygen membrane with a gas turbine power generation system (Kang, D, et al, 1996 & 1997). This is accomplished by extracting air from the compressor discharge, withdrawing a portion of the oxygen by permeation through the membrane, and returning the vitiated, non-permeate stream to the turbine inlet. The operating temperature of the ceramic membrane is above the compressor discharge temperature, but below the syngas firing temperature characteristic of most gas turbine engines. As a result, the cycle requires two separate heating steps. A direct- or indirect-fired heater upstream of the ITM Oxygen vessel raises the air stream temperature to the membrane operating value by burning a portion of the gas turbine's usual fuel input. Downstream of the ITM Oxygen vessel, the gas turbine combustor achieves the required turbine inlet temperature by burning the remainder of the fuel in the vitiated non-permeate stream, which still contains excess oxygen.

In this application, the gas turbine integration occurs within the IGCC plant's combined cycle unit. In the direct-fired ITM Oxygen case (Figure 2-10), the extraction air is partially preheated against the hot non-permeate stream before final preheating by direct combustion with clean syngas. This combination preheating step improves the partial pressure driving force across the ITM while minimizing the design requirements of the gas-gas economizer. In the indirect-fired ITM Oxygen case (Figure 2-11), the extraction air is again partially preheated against the hot non-permeate stream. Final indirect preheating occurs at the HRSG inlet against turbine exhaust that has been fired with clean syngas in a duct burner. This configuration maximizes the partial pressure driving force across the ITM and eliminates supplementary syngas cleanup (as described in the acid gas removal section), while requiring a duct burner and a high-temperature

gas-gas heat exchanger at the HRSG inlet. In addition, the duct burner requires supplemental air to sustain combustion of syngas in the vitiated turbine exhaust stream.

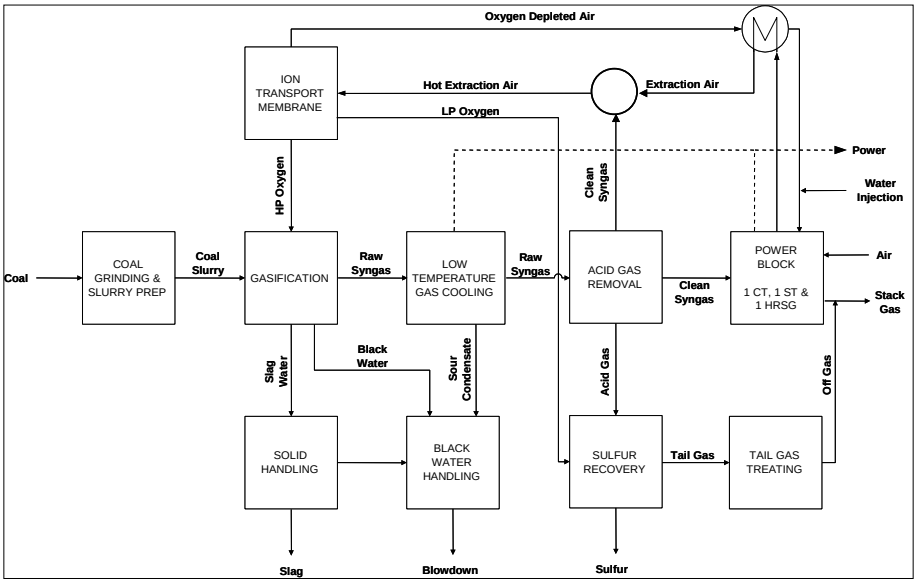

Figure 2-10. IGCC with direct-fired ITM Oxygen.

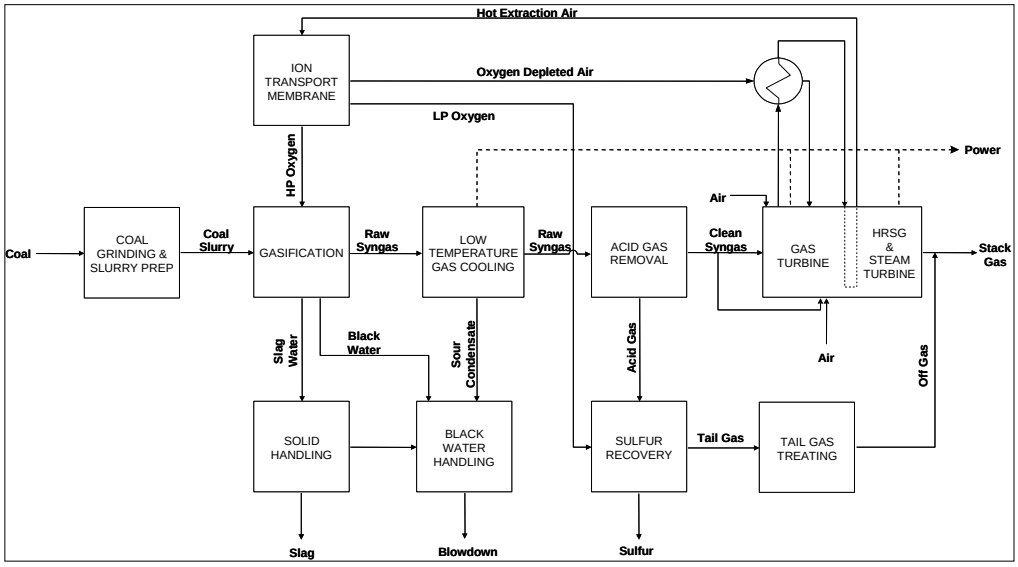

Figure 2-11. IGCC with indirect-fired ITM Oxygen.

The hot, low-pressure oxygen permeate stream is cooled by raising medium-pressure steam, along with other low-level heat integration, before compression to a low-pressure oxygen product stream for delivery to the Claus sulfur recovery unit, and a high-pressure oxygen product stream for delivery to the gasifier.

Cryogenic ASU

The cryogenic ASU employs an elevated-pressure, partially pumped, liquid oxygen (LOX) design that is fully air-integrated. Full air integration means that, like the ITM Oxygen plant, all air for the ASU is supplied via gas turbine extraction; there is no source of supplemental compressed air within the ASU. Elevated-pressure operation indicates that all of the product streams from the ASU cryogenic heat exchange and distillation section (cold box) leave at pressures substantially above atmospheric pressure. This approach reduces ASU power consumption and capital cost when most or all of the by-product nitrogen is required for re-injection into the gas turbine. Partial pumping (internal compression) of LOX removed from the distillation section results in increased suction pressure and reduced volumetric flow, which allows the use of a single-casing compressor to deliver oxygen at its final pressure.

The hot extracted air from the gas turbine is cooled against compressed nitrogen from the ASU (Figure 2-12). This step allows high-level heat to be recovered from the extraction air and returned to the gas turbine via the injected nitrogen stream. The partially cooled air is then expanded to an intermediate pressure level. Work recovered from the expansion step generates power and reduces the net ASU power consumption. Expansion of the air recovers intermediate-level heat from the extracted air and permits the ASU to operate at an optimum pressure that is independent of gas turbine pressure fluctuations that occur at off-design or minimum-power output conditions (Smith and Woodward, 1996 & 1997). The air is further cooled before entering the pretreatment area, where water, carbon dioxide, and hydrocarbons are removed by a cyclical adsorption process. Low-level heat contained in the expanded air can be recovered by heat exchange with the nitrogen stream used to regenerate the adsorption system (Smith and Woodward, 1996).

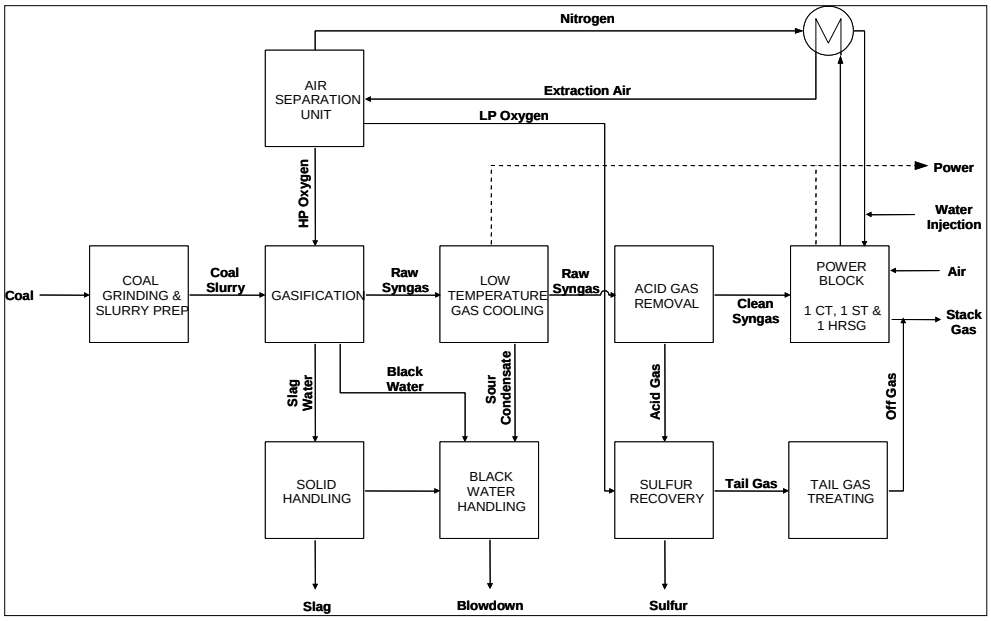

Figure 2-12. IGCC with cryogenic ASU.

The clean, dry air enters the cryogenic heat exchange and distillation area, where it is separated into oxygen and nitrogen product streams. A proprietary, multi-column distillation process is used for the efficient separation of the feed air. The warm product oxygen stream that exits the cryogenic heat exchanger at 95% purity is separated into a low-pressure oxygen product stream for delivery to the Claus sulfur recovery unit, and a high-pressure oxygen product stream that is compressed prior to delivery to the gasifier. Nitrogen exiting the cryogenic heat exchangers is used to regenerate the air pretreatment system either prior to or after being compressed. The compressed nitrogen is heat exchanged against the extracted air stream and returned to the gas turbine. The estimate scope contains no provisions for liquid backup storage or vaporization.

GASIFICATION PLANT

Gasification and Scrubbing

Each design employs a single, oxygen-blown, high-pressure (950 psig) Texaco quench gasifier. High-pressure operation allows the generation of medium-pressure steam against the syngas scrubber overhead, as well as the recovery of pressure energy with a syngas expander.

The Texaco quench gasifier is a downward, entrained-flow gasifier consisting of a reaction chamber followed by a quench chamber. High-purity oxygen and coal slurry are fed to the reaction chamber at the top of the gasifier. There they react at high temperature to produce raw

syngas, molten slag, and particulates that all discharge out the bottom of the reaction chamber into the quench chamber. Quench water cools and saturates the syngas by direct contact. Molten slag rapidly solidifies, disengages from the syngas and settles to the bottom of the quench water pool for removal by a lockhopper system situated directly underneath the gasifier. In addition, many contaminants, such as alkalis and halides, are captured by the quench water and are thus removed from the syngas. Once the saturated syngas leaves the gasifier quench chamber, it passes to the water scrubber for a final stage of particulate removal.

Low-Temperature Gas Cooling (LTGC)

The saturated raw syngas is cooled further by raising medium-pressure steam and by exchanging heat with the clean syngas before its export to the gas turbine. The moisture in the raw syngas is condensed and returned to the scrubber. Next, a turbo-expander recovers energy from the syngas by expanding it from the gasifier operating pressure to the lower gas turbine operating pressure. After expansion, the residual heat in the raw syngas is recovered for use in low-pressure steam generation, clean syngas saturation in the saturator heater, and condensate heating. After heat recovery, the raw syngas is trim cooled to the desired temperature for the acid gas removal (AGR) process.

Acid Gas Removal and Sulfur Recovery

The AGR unit removes sulfur compounds from the raw syngas before its combustion in the gas turbine and the ITM preheat combustor. The MDEA process, which uses methyl di-ethanol amine as the chemical solvent, was chosen for this study because of its low cost and minimal removal of carbon dioxide. In the direct-fired ITM Oxygen case, some of the clean syngas from the MDEA absorber is further treated to remove trace sulfur compounds before going to the ITM preheat combustor. In the indirect-fired ITM Oxygen case, no further cleanup is required because the preheat combustion products do not contact the membrane. The remaining clean syngas goes to the saturator heater in the low-temperature gas-cooling section before passing on to the combustion turbine.

The sour gas (H_2S) from the AGR unit reacts with oxygen supplied by the air separation plant to produce elemental sulfur in the multi-stage Claus reactor. The tail gas from the Claus unit passes to a hydrogenation reactor that converts SO_2 to H_2S for recycle back to the raw acid gas stream.

COMBINED CYCLE POWER PLANT

The conventional combined cycle power plant has high efficiency and excellent operability. In addition, its integration with an oxygen-blown Texaco gasification and cleanup system enables it to operate efficiently on syngas with minimum impact on the environment. The steam cycle is integrated with the gasification and gas cleanup operations to achieve minimum cost per unit of electrical output and maximize thermal efficiency. It is designed for operating simplicity, high reliability, and convenient maintenance.

Gas Turbine

The Siemens Westinghouse W501G gas turbine was developed specifically for combined cycle applications. It also has features that enable it to be integrated with a gasification system. High combined cycle efficiency results from the high specific power of the gas turbine, which is achieved by its efficient compressor and turbine, operating at a high pressure ratio and high turbine inlet temperature. The gas turbine also supplies all of the compressed air for the ITM Oxygen plant or cryogenic ASU and uses all of the available non-permeate or nitrogen to increase power output and reduce NO_x emissions.

Heat Recovery Steam Generator

The heat recovery steam generator (HRSG) is a three-pressure, reheat, and natural circulation-type unit with horizontal gas flow. It consists of a high-pressure (HP) superheater, HP steam drum, HP evaporator, and HP economizer; intermediate-pressure (IP) superheater, IP reheater, IP evaporator, IP steam drum, and IP economizer; and low-pressure (LP) superheater, LP steam drum, LP evaporator, and LP economizer. In the indirect-fired ITM Oxygen case (Figure 2-11), the HRSG inlet includes a duct burner with supplemental air and a high-temperature gas-gas heat exchanger to indirectly preheat the ITM feed against fired turbine exhaust.

Steam Turbine and Condenser

The reheat condensing turbine operates at 1800 psig/1050°F and includes an integral HP/IP opposed flow section. The reheat design assures high thermal efficiency and excellent reliability based on a large experience base. The main steam condenser cools and condenses steam turbine exhaust against circulating cooling water. Makeup water to the condensate system is added through a stripper de-aerator to remove dissolved oxygen.

BALANCE OF PLANT

Major components of the balance of plant systems include a cooling water system, a fresh water supply, relief and blowdown, interconnecting piping, compressed air, auxiliary fuel, electrical equipment, and instrumentation and controls.

DESIGN BASIS SUMMARY

The following list recaps the design basis for this study, which was constructed for low installed capital cost, reasonable efficiency, and high reliability with an eastern U.S. coal as feedstock:

1. ISO ambient (59°F, 14.7 psia, 60% relative humidity)
2. Eastern U.S. coal (14,089 BTU/lb HHV), 2.5% sulfur
3. Single-train, high-pressure quench gasifier (950 psig)
4. Siemens Westinghouse W501G turbine @ 60 Hz (272 MW maximum power output)
5. 100% air/N_2 integration of gas turbine and oxygen plant
6. 68°F cooling water temperature
7. 99.5% oxygen purity from ITM Oxygen; 95% oxygen purity from cryogenic ASU

IGCC Study: Performance Results

Table 2-2 shows the performance comparison for the ITM Oxygen-integrated IGCC facilities and the cryogenic ASU comparative case with equivalent output from the W501G gas turbine.

Table 2-2. IGCC performance comparison.

Case Designation	Direct-fired ITM Oxygen	Cryo ASU	% Change	Indirect-Fired ITM Oxygen
Fuel HHV (MMBtu/hr)	3704	3539		4365
HP O_2 to Gasifier (sTPD)	3153	3012	+4.7	3715
LP O_2 to Claus SRU (sTPD)	43	24	+4.7	51
Nominal O_2 Plant Size (sTPD)	3200	3040		3770
O_2 Plant Power (kWh/ton O_2)	147	235	+5.3	147
W501G MWe	**272**	**272**	**-37**	**272**
Steam Turbine MWe	189	172	---	250
Syngas Expander MWe	14	13		16
IGCC Gross MWe	475	457		538
IGCC Power Consumption MWe	37	48	+3.9	43
IGCC Net MWe	**438**	**409**		**495**
Net IGCC Efficiency (HHV)	40.4	39.5	**+7.0**	38.7
Net IGCC Efficiency (LHV)	41.8	40.9	+2.3	40.1
Sulfur (sTPD)	77	74		91
Solid Waste (sTPD)	474	453		558

Note: sTPD = short tons per day

All cases are economically optimized by driving the gas turbine to its maximum power output. With this parameter fixed, the direct-fired, ITM Oxygen-integrated facility generates 29 additional MWe, or 7% higher power output than the cryogenic case. Approximately 2% (relative) of the difference arises from an improvement in overall plant efficiency caused by the 37% improvement in the oxygen plant power requirement; the balance of the difference results from increased coal throughput. The ITM Oxygen process adds pressure drop to the gas turbine air path and removes some sensible heat by extracting oxygen, which is compensated by increasing the flow of syngas fuel to achieve maximum power output. This requires a slightly larger gasification system which consumes more coal and oxygen. The steam cycle recovers this additional energy input through heat recovery from the oxygen, as well as the increased thermal energy of the gas turbine exhaust. Thus, when both cases are optimized by maximizing *gas turbine* output, the net power production from the direct-fired ITM Oxygen-integrated facility increases by 7%.

By the same token, the indirect-fired ITM Oxygen-integrated facility generates yet another 57 MWe because of all the additional syngas required to indirectly preheat the ITM feed. However,

since all of the surplus output is contributed by the less-efficient steam cycle, the overall IGCC efficiency actually falls below the comparative cryogenic case.

IGCC Study: Economic Results

Table 2-3 shows the economic comparison for each case in this study. All costs include project contingency. Both the performance and cost values for each of the oxygen plant designs are strongly case- and scope-specific. While absolute numbers for other cases can certainly vary, the comparison shown here does represent the typical relative improvement that ITM Oxygen is expected to bring to the IGCC application.

Table 2-3. IGCC Installed Cost Comparison

Area Description	Direct-Fired ITM Oxygen	Cryo ASU	% Change	Indirect-Fired ITM Oxygen
Oxygen Plant	41,600	61,200	-32	45,500
Gasification Unit	97,000	95,200	+1.9	109,800
Gas Cleanup Unit	41,600	34,300	+21	42,100
Combined Cycle	233,600	224,400	+4.1	279,300
Balance of Plant	33,200	32,900	+0.9	36,700
Overall Total IGCC	447,000	448,000	---	513,400
$/kW	1,020	1,094	**-6.8**	1,037
Oxygen Plant $/sTPD O_2	13,000	20,132	**-35**	12,069

Note: All costs represented in thousands of U.S. dollars (including project contingency)

The economic benefit of ITM Oxygen technology for the IGCC application results in a 7% reduction in overall plant-specific cost to $1,020/kW for the direct-fired case. The ITM Oxygen plant, including the preheat recuperator, preheat combustors, ITM Oxygen modules, oxygen coolers, and oxygen blower, saves 35% of the installed specific cost ($/sTPD) for air separation equipment. For this comparison, the savings in air separation equipment allow the plant owner to build the larger IGCC facility (in terms of coal throughput) for essentially the same overall cost. As a result, the direct-fired ITM Oxygen case produces its 29 additional MWe at no additional capital cost; this 7% higher power output converts directly into a 7% improvement in overall plant-specific cost ($/kW). The overall improvement is especially significant given that the oxygen plant comprises less than 14% of the total plant capital cost in the base case. The

efficiency increase also produces an associated reduction in carbon dioxide and sulfur emissions. As a result, integration with ITM Oxygen technology offers IGCC the benefits of better environmental performance and lower costs.

The indirect-fired ITM Oxygen plant saves an additional 5% of the installed specific cost ($/sTPD) for air separation equipment, as expected because of the enhanced inlet oxygen concentration. In addition, the specific cost of the gas cleanup unit decreases because the supplemental sulfur-removal step is eliminated. However, these savings are outweighed by the increased cost of the ITM preheater equipment, raising the overall $/kW from $1,020 to $1,037/kW. This result confirms the benefits of direct-fired preheating, even when factoring in the cost of the fuel cleanup.

Notably, while the coal throughput increases by ~5% for the direct-fired ITM Oxygen case, the cost of the gasification unit is only 2% higher than the cryogenic case, which contributes to the nearly equal total capital cost. This subtlety arises from the difference in oxygen purity between the cases. The cryogenic ASU is optimized at ~95% oxygen purity for a gasification application, since incrementally higher purity adds significant cost. However, ITM Oxygen suffers no appreciable cost penalty for oxygen purity in excess of 99%. As a result, the gas volumes for the direct-fired ITM Oxygen case are approximately 5% smaller than for the cryogenic ASU because of the reduced flow of inerts. This feature reduces the cost impact of the increased coal throughput. Conversely, the gas cleanup unit cost grows by more than just the percentage increase in coal throughput because of the lower sulfur specification for direct-fired ITM Oxygen. Nevertheless, the savings in air separation equipment more than compensate for this added cost, in addition to compensating for the larger IGCC facility.

The IGCC example illustrates the benefits arising from effective integration of ITM Oxygen technology with gas turbine engines.

2.6.2 Process Engineering and Economic Evaluation for Advanced ITM Oxygen Applications

Decarbonized Fuel Plant Study

Air Products completed a process engineering and economic analysis for the integration of ITM Oxygen with a decarbonized fuel plant flowsheet developed by Parsons. A key feature of ITM Oxygen technology originates from the need to expand the non-permeate stream to efficiently recover its stored energy. For this reason, ITM Oxygen technology is ideally suited to

integration with power generation processes that require oxygen as a feedstock for combustion or gasification, or to any oxygen-based application with significant power requirements or opportunities for power export. As a result, the proposed integration with the dcarbonized fuel plant involved the "classic" ITM Oxygen configuration, packaged with its own gas turbine set. The result is a unique facility, consistent with DOE's Vision 21, that co-produces hydrogen and ultra-clean electric power from coal.

Air Products determined that, through the use of ITM Oxygen technology, adding an extra 124 MW of electric power generation to the product slate requires the modest addition of $31 MM in capital, or less than 9% of the original facility cost, and consumes only 42% of the original hydrogen product. Excluding the capitalized cost of hydrogen fuel, this incremental installed cost of power equates to a very low $250/kW. To achieve a head-to-head comparison with cryogenic oxygen generation, the "Baseline" decarbonized fuel plant scope was modified to include the same combined cycle power plant used by the ITM. Based on equivalent product slates, the ITM Oxygen case saves 37% of the installed cost for air separation equipment and more than 6% of the total facility cost. Furthermore, the incremental installed cost of additional power for the base case rises to $57 MM or $460/kW.

These results apply to a case with maximum hydrogen production from the ITM Oxygen facility while co-producing ultra-clean electric power. Other choices for gas turbine equipment could further decrease the cost of the ITM components and increase power output while decreasing the hydrogen available for sale from the facility. In the extreme, the turbine could be sized to produce only ultra-clean power from coal. This alternative "Max Power" case offers a 46% savings in the installed cost of the ITM vs. the cryogenic ASU.

For the ITM Oxygen base case ("H_2/Power"), a W401 gas turbine, rated at 85.9 MW on natural gas fuel, provides the required air flow while minimizing hydrogen consumption. For the ITM "Max Power" case, a V84.3A gas turbine, rated at 182 MW on natural gas, maximizes hydrogen consumption to produce power. The corresponding ASU cases use the same combined cycle equipment as the ITM cases. Cost and performance information on the W401 and V84.3A combined cycle equipment was obtained from the November 1999 release of GT PRO. All relevant mechanical, gear box, and generator losses were factored into the net power values for the new power generation equipment.

Table 2-4 summarizes the results. All costs are for installed equipment. Excluding the cost of the gas turbine, the installed cost of air separation equipment decreases by 37% for the ITM-integrated co-production case ("H_2/Power"). In terms of total plant cost, the ITM-integrated facility saves more than 6% of the cost to modify the ASU base case with an equivalent combined cycle ("ASU H_2/Power"). For the larger turbine, consuming most of the available hydrogen, the increased air flow further decreases the size and cost of the ITM by increasing the average driving force for oxygen permeation ("ITM Max Power"). In this case, the installed cost of air separation equipment decreases by 46% compared to the ASU cost.

Table 2-4. ITM Oxygen cost savings for decarbonized fuel plant integration.

	ASU Base	**ITM H_2/Power**	**ASU H_2/Power**	**ITM Max Power**	**ASU Max Power**
Total Net Power Prod'n (MW)	18	142	142	300	278
H_2 Production (lb/hr)	35,205	20,369	20,369	1,682	3,805
Cost of Air Sep'n Equip. ($000)	70,960*	44,800	70,960	38,448	70,960
Cost of W401/V84.3A CC ($000)	---	57,120	57,120	91,583	91,583
Air Sep'n + Power Gen. ($000)	70,960	101,920	128,080	130,031	162,543
Total Facility Cost ($000)	349,735*	380,695	406,855	408,806	441,318

* Parsons Report, 1999

In an effort to minimize hydrogen consumption in the co-production case, no attempt was made to replace the mass flow removed by the ITM. Injection of water, steam, or supplementary air into the non-permeate stream would better utilize the additional capital investment for the gas turbine, but this type of measure would further shift the product slate to increase the power-to-hydrogen ratio. For the "Max Power" case, steam injection provided mass flow compensation to return the combined cycle power output to its rated value.

In summary, integration with ITM Oxygen shifts the product slate of the decarbonized fuel plant toward co-production of ultra-clean electric power. However, if the power is valued reasonably, this scenario should produce a more economical hydrogen co-product. If the cryogenic ASU base case is modified to produce an equivalent product slate, the ITM Oxygen case saves 37% of the installed cost for air separation equipment. By further shifting the product slate toward power, the ITM savings can increase up to 46%.

H_2 with CO_2 Sequestration and Coal-Bed Methane Recovery

Air Products also completed an evaluation for ITM Oxygen integration with a National Renewable Energy Laboratory (NREL) flowsheet for "Hydrogen from Western Coal with CO_2 Sequestration and Coal-bed Methane Recovery." ITM Oxygen technology is ideally suited to integration with NREL's "Hydrogen/Power Co-production" case because of the existing gas turbine in the flowsheet. Although the NREL flowsheet was not designed around a particular model of gas turbine, a V84.3A, rated at 167.8 MW on natural gas fuel, provided the closest fit to the available fuel flow (only slightly exceeding it). This turbine then allowed a very straightforward integration with ITM Oxygen.

Table 2-5 summarizes the results. All costs are for installed equipment. The installed cost of air separation equipment decreases by 39% for the ITM-integrated "Hydrogen/Power Co-production" case. Because the V84.3A gas turbine already "existed" in the baseline flowsheet, the product slates between the cryogenic ASU and the ITM Oxygen cases are essentially identical, providing a good basis for cost comparison.

Table 2-5. ITM Oxygen Cost Savings for NREL Plant Integration

	ITM H_2/Power	**ASU H_2/Power**
Total Net Power Prod'n (MW)	227	228
H2 Production (lb/hr)	17,622	17,622
Coal-bed Methane Combusted (lb/hr)	82,852	82,894
Cost of Air Sep'n Equip. ($000)	31,062	50,681
Cost of V84.3A CC ($000)	91,426	91,426
Air Sep'n + Power Gen. ($000)	122,488	142,107

The underlying cost and power values for the cryogenic ASU originated from an Air Products budgetary quote for a single-train pumped LOX plant. The scope followed that of the Parsons decarbonized fuel plant study and included storage and vaporization capacity for an 8-hour backup supply of oxygen, spare parts, and the same multiplier used by Parsons to convert the "bare erected cost" to a "total plant cost." Cost and performance information on the V84.3A combined cycle equipment was obtained from the November 1999 release of GT PRO. All

relevant mechanical, gear box, and generator losses were factored into the net power values for the power generation equipment.

In the ITM Oxygen case, steam injection provided mass flow compensation to the gas turbine. However, the steam flow rate was chosen to match the fuel consumption of the original, unmodified unit, leaving the combined cycle power output slightly decreased but the net power production coincidentally about the same. In reality, to best utilize the large capital investment for the gas turbine, the entire front end of the plant should be resized to produce the extra fuel required to maximize power output. However, the resulting changes to the flowsheet were beyond the scope of this comparison. Nevertheless, ITM Oxygen contributes to a unique facility design, consistent with DOE's Vision 21, that co-produces hydrogen and "clean" electric power from an abundant domestic resource, with a 39% decrease in the installed cost for air separation equipment.

References

Kang, D, et al., "High Temperature Oxygen Production with Steam and Power Generation," U.S. Patent 5,565,017, October 15, 1996.

Kang, D, et al., "Integrated Production of Oxygen and Electric Power," U.S. Patent 5,657,624, August 19, 1997.

Parsons Report, Decarbonized Fuel Production Facilities Base Case Comparisons, Appendix C, June 1999.

Smith, A. R. and Woodward, D. W., "Pressurized Feed Air Expansion in Air Separation Processes," Research Disclosure, pp. 207-211, March 1996.

Smith, A. R. and Woodward, D. W., "High Pressure Combustion Turbine and Air Separation System Integration," U.S. Patent 5,666,823, September 16, 1997.

Smith, A. R., et al., "Next-Generation Integration Concepts for Air Separation Units and Gas Turbines," Journal of Engineering for Gas Turbines and Power, Transactions of the ASME, Vol. 119, pp. 298-304, April 1997.

PHASE I RESULTS AND DISCUSSION

TASK 3.0 MEMBRANE MODULE DEVELOPMENT

3.0 Scope

Ceramatec and Air Products utilize the structural and mechanical analysis from McDermott (Task 2) to improve the design of the membrane and select the full-size wafer and module design. Ceramatec scales up the fabrication of membranes to the full commercial size, and fabricates modules for performance testing in the TDU. Critical factors in the fabrication process that support production yield improvement are identified through use of statistical process control techniques. Based on this understanding, Ceramatec installs a pilot membrane fabrication line. Ceramatec also prepares test parts for testing membrane performance under Task 4.

Membrane Wafer Design and Fabrication

Ceramic Process Development

Ceramatec focused on developing ceramic composites comprising dense, porous and slotted layers of AP98 or AP2K. Early work successfully produced laminates for testing under Task 1. Wafer designs were initiated with a circular planar design incorporating a thin membrane, a permeable porous layer to support the thin membrane, and a rectilinear-cut channel layer to facilitate the flow of oxygen to a central tube. Processes based on tape-casting technology were developed to allow formulation of the various layers using the same ITM ceramic throughout the composite.

Tape Development

Early tape development work focused on the use of AP98 powder exclusively. Ceramatec studied the use of dipersants for the AP98 powder in the tape slip. An oleic diethanolamide (DEA) at a concentration of 0.5 wt. % was contrasted with an alternative dispersant, a modified polyvinyl butyral (PVB), at a lower level (0.3%). Figure 3-1 shows that PVB is a better dispersant and that low levels are effective in dispersing AP98.

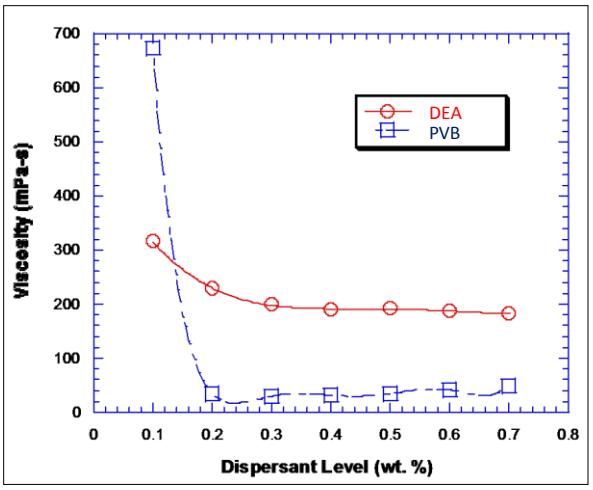

Figure 3-1. Viscosity measured at 100 rpm for AP98 slips as a function of wt. % dispersant (based on AP98) added.

Figure 3-2 shows the solubility characteristics of binder materials of differing molecular weights in the slip solvent system.

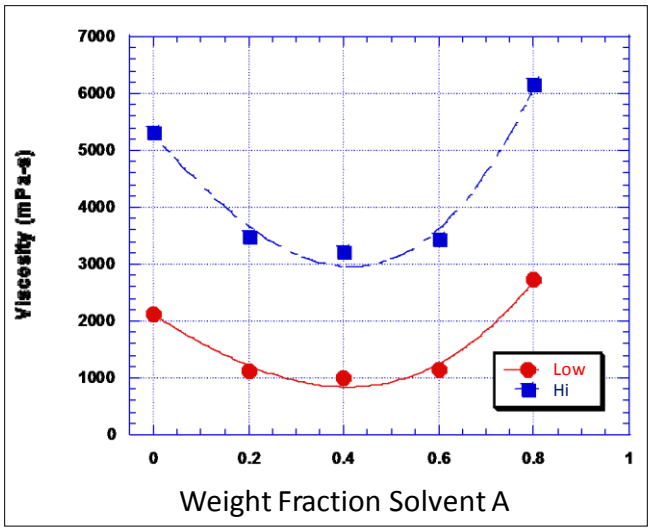

Figure 3-2. Viscosity of constant volumes of binder (14.3 vol. %) plus liquid as a function of liquid composition for two molecular weight binders.

Slips were made at a content of 62 vol. % solids with various solvent systems. All tapes were nominally 0.25 mm thick after drying. Solvent system composition was more important than slip density or binder molecular weight (MW) in making crack-free tapes using the same binder chemistry in the slips. A substantial cost savings in solvent (up to 30%) arises from using lower molecular weight materials. However, both low and high molecular weight binders were tape

cast to a dried thickness of 0.25 mm without cracking. The tapes looked excellent under the microscope.

High-MW and functional group-content binders were compared to low-MW and functional group-content binders for both AP98 and AP2K. Figure 3-3 shows the solvent/binder ratio for the AP98 tapes as a function of solids content for slips with viscosities of ~2500 mPa-s. As expected, these same curves are valid for AP2Ka, since it has similar surface area and particle morphology. The fits to the data allow the entire range of 60-75 vol.% solids to be easily accessed.

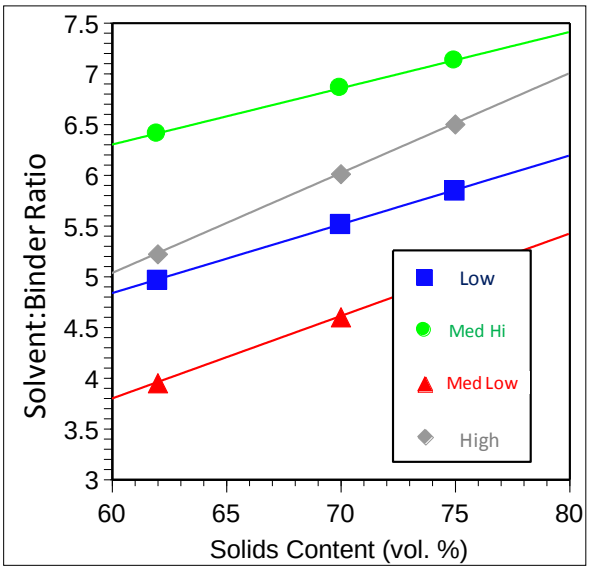

Figure 3-3. Solvent-to-binder ratios for four different binder molecular weights and functional group contents as a function of volume fraction of AP98. These same relationships hold for AP2Ka at the same volume fractions.

Figure 3-4 shows the green density of AP98 tapes. Not surprisingly, the total porosity increases as the solids content increases. Figure 3-5 contains SEM micrographs of a 62 vol. % tape. The binder at the surface is more visible at lower accelerating voltages since the electron beam evaporates the binder. As expected, there is more binder on the supporting substrate side of the tape since the binder is soluble in the moving front of liquid that flows towards the polymer substrate side of the tape as drying continues. Figure 3-6 can be compared with Figure 3-5 to show the higher packing of perovskite particles achieved with increased solids content. This can also be observed on the fracture surface. Backscattered imaging (Figure 3-6) shows darker

regions for the binder, compared to the brighter perovskite. It is still difficult in the backscattered mode to distinguish between the surface porosity and the binder.

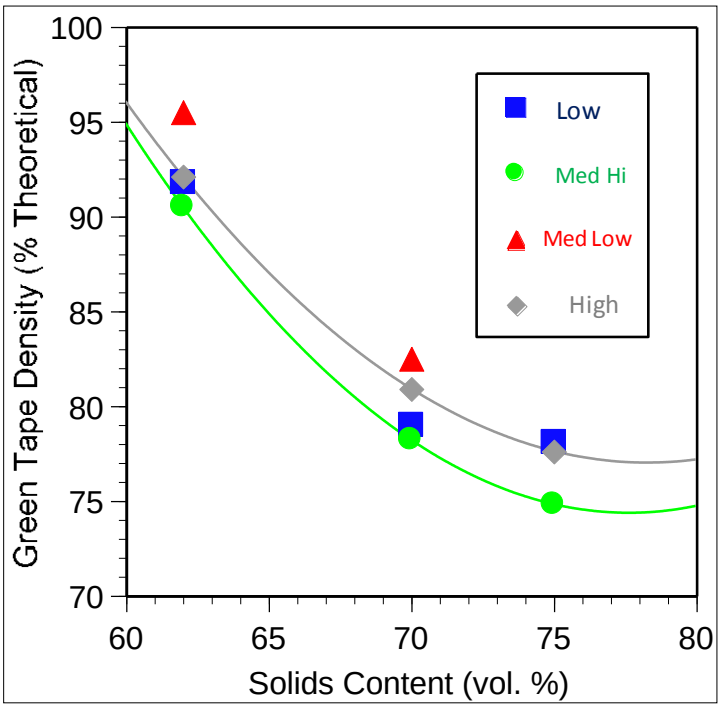

Figure 3-4. Green density of tapes as a function of solids content for binders of various molecular weights. Total porosity is calculated as 100 minus % theoretical density. Curve fits should not be extrapolated beyond data points.

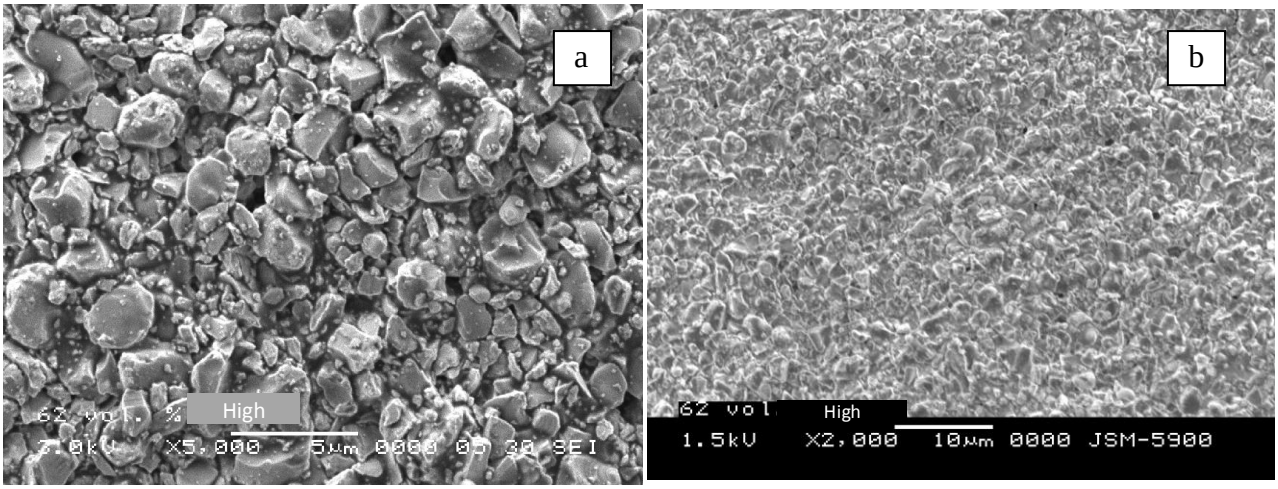

Figure 3-5. SEM micrographs of air side (with respect to casting) of green tape of AP98 cast at 62 vol. % solids using high-MW binder. (a) 3 kV accelerating voltage showing grains (5000X), (b) 1.5 kV accelerating voltage showing binder surrounding grains (2000X).

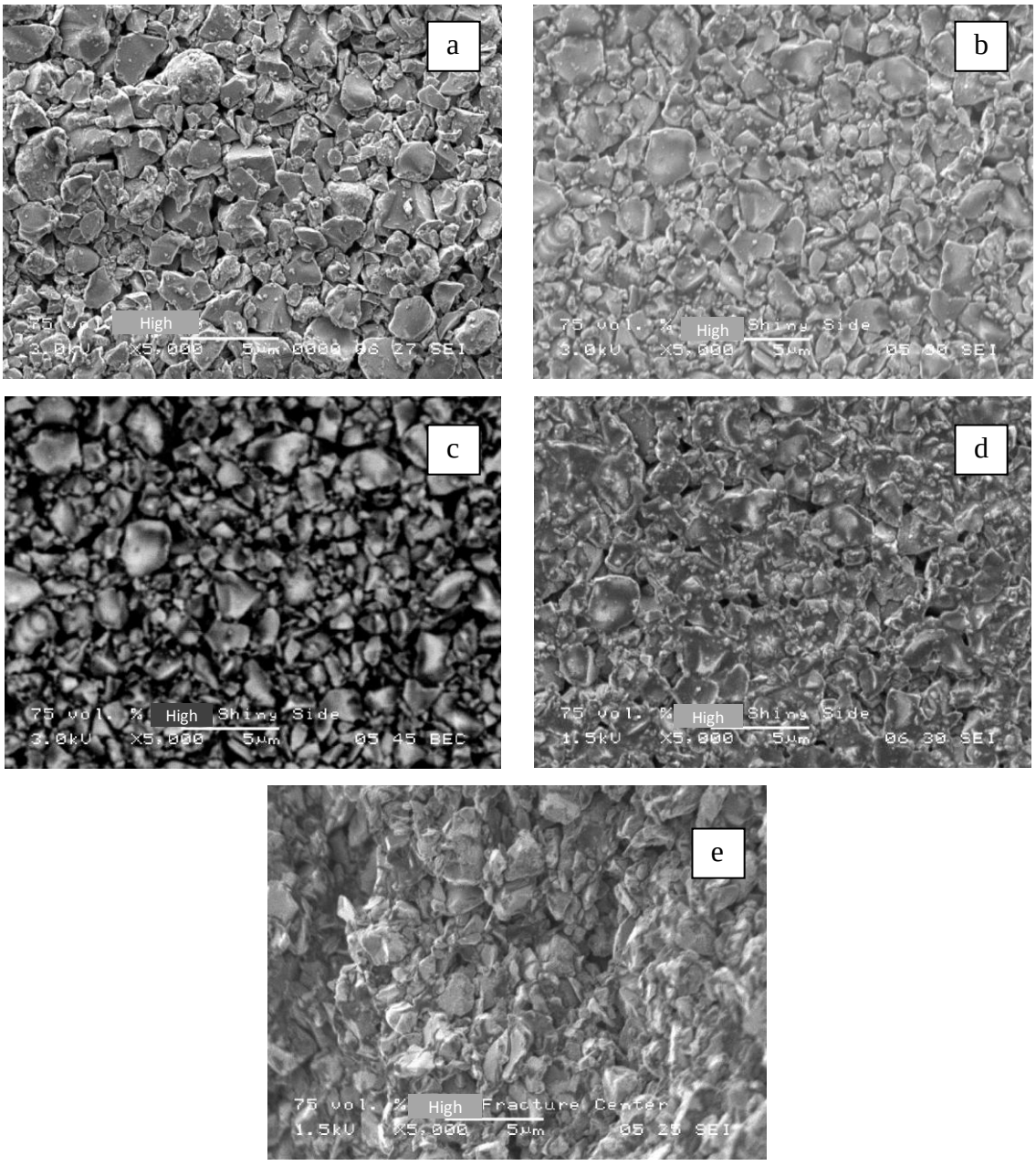

Figure 3-6. Micrographs of green AP98 tape cast at 75 vol. % solids viewed in the SEM with an accelerating voltage of 3 kV (5000X). a) Air side; b) side in contact with polymer substrate; (c) backscattered image of b) with dark regions being polymer or porosity; d) secondary electron image of tape at 1.5 kV [compare with a) and b)]. Both c) and d) suggest that there is polymer on the tape surface; e) fracture surface of tape [compare with d)].

Figure 3-7 displays the tensile properties of the cast tapes. The medium low MW binder was not cast at 75 vol. % solids simply due to its problem with cracking at higher solids content. As expected, the tensile strength of the tapes decreases with decreasing binder content and increasing porosity. It is not evident whether porosity or binder content controls the strength of

the unpressed tape. The medium high MW tapes appear to be more dependent on the total binder content in the tape than on the porosity, although this is not as clear for the low and high cases (compare Figures 3-4 and 3-7). It is the plasticizer character of the binder that gives the tape its strength and flexibility. The main difference with the low- and medium low-case binders is their lower yield strength. The modulus of tapes containing high MW binder drop with only moderate increase in temperature.

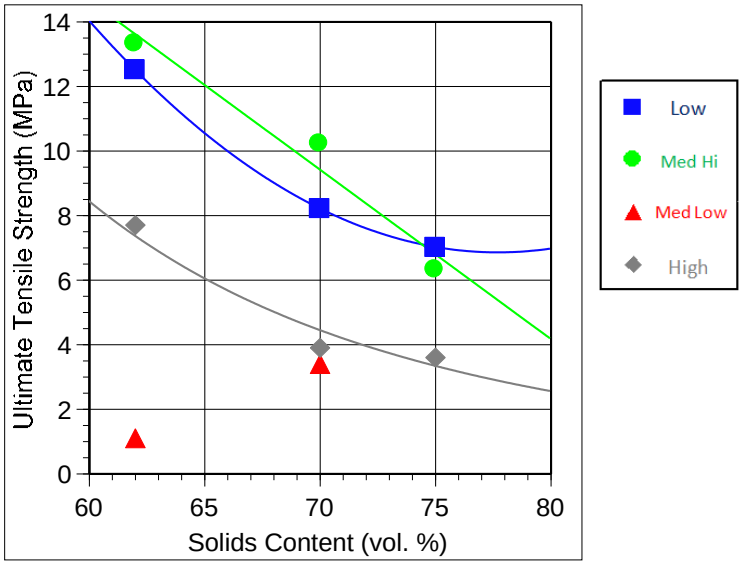

Figure 3-7. Ultimate tensile strength of green, unannealed tapes as a function of solids content for tape formulations with different molecular weight binders. Note that curve fits are shown only to help see data trends, realizing that curves will not be valid over wide ranges in binder content. The low strength of the medium low MW case is due to cracks in the tape.

The main concern with increasing solids content was that higher solids content would result in less binder at the surface to help with layer-to-layer bonding. Surprisingly, the higher solids-content materials appear to bond nearly as well as those with lower solids content, and perhaps bond better without pressure.

Literature (H. Hellebrand, 1996) suggests that total porosity in the 25-35% range is desired for interlocking laminates. The 70-75 vol. % (solids) compositions are close to the optimum range as described by Hellebrand.

Figure 3-8 shows the fixture designed for measuring the strength of bonded tapes. Figure 3-9 shows that bonding is a linear function of binder content in the range investigated. It is

necessary to get the binder to flow properly before the laminated part approaches the tensile strength of the tape. Bonding at higher temperature was better for the three solids loadings studied. The data show that there is no advantage to using the any of the binders in this regard. Furthermore, lamination pressure is a function of the solids content, since higher solids content tapes will not be able to support as much pressure during green lamination as lower solids content tapes.

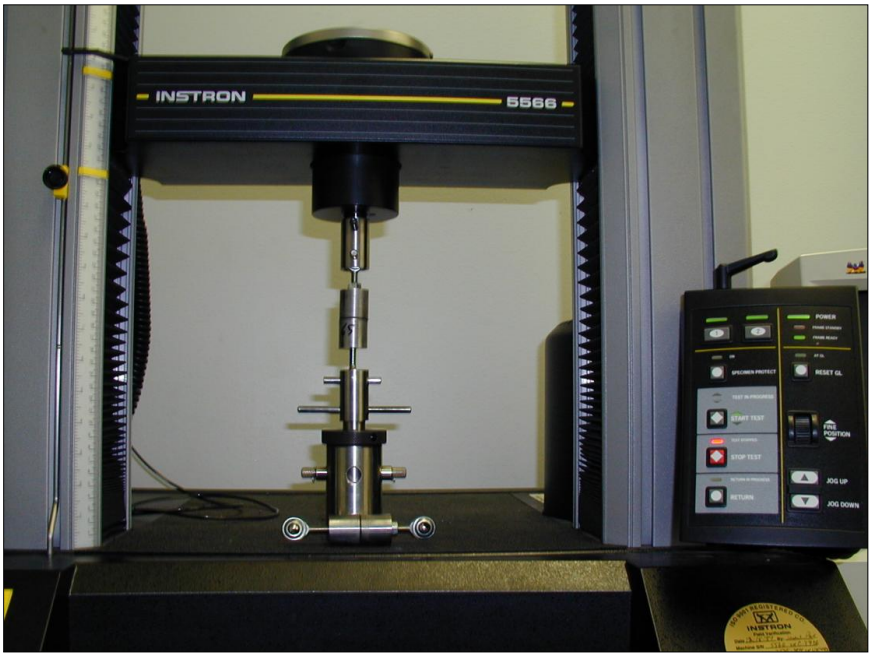

Figure 3-8. Uniaxial pull test for assessing bond strength. Test fixture with rod-ends, allowing triaxial swiveling for alignment, is shown unattached from Instron at bottom.

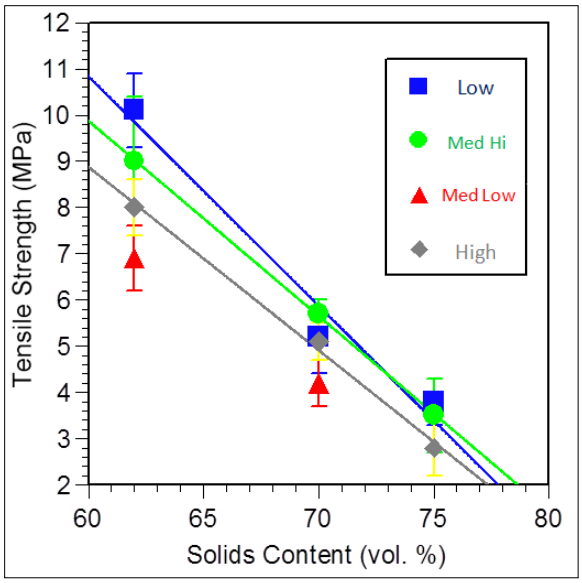

Figure 3-9. Tensile pull strength of laminated bi-layers of AP98 tape using the fixture shown in Figure 3-8. Note that linear fits are meant to be illustrative only and are not to be extrapolated outside of the data range.

Figure 3-10 gives data for sintered disks made from the three binder levels for the four binder types studied. As expected, there is a general correlation between green density and shrinkage. It is not known why the medium high MW binder did not behave in a similar manner. The sintered densities were between 96.8 % and 98.2 % of theoretical density, with slightly higher density achieved with higher solids content due to better packing in the green state.

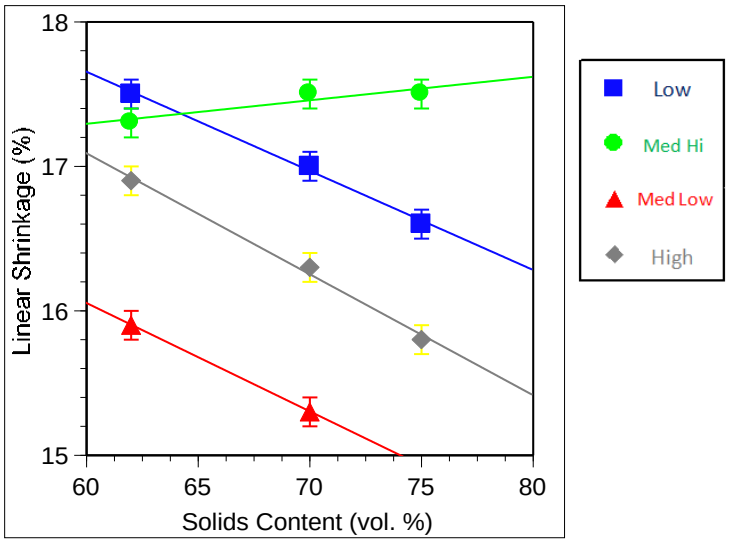

Figure 3-10. Linear shrinkage for sintered AP98 tapes. Note that the shrinkage generally is a function of the green density of the tape.

Figure 3-11 shows the relative costs of the slurry systems used in tape casting as a function of solids content. The costs were calculated using current costs for binder, plasticizer, and solvents. It is instructive to see that the relative cost to produce one square meter of green tape drops linearly as a function of the volume of binder/plasticizer. It is also instructive so see that the cost is dependent on the type of binder chosen. This is due to the ability to solvate the binder.

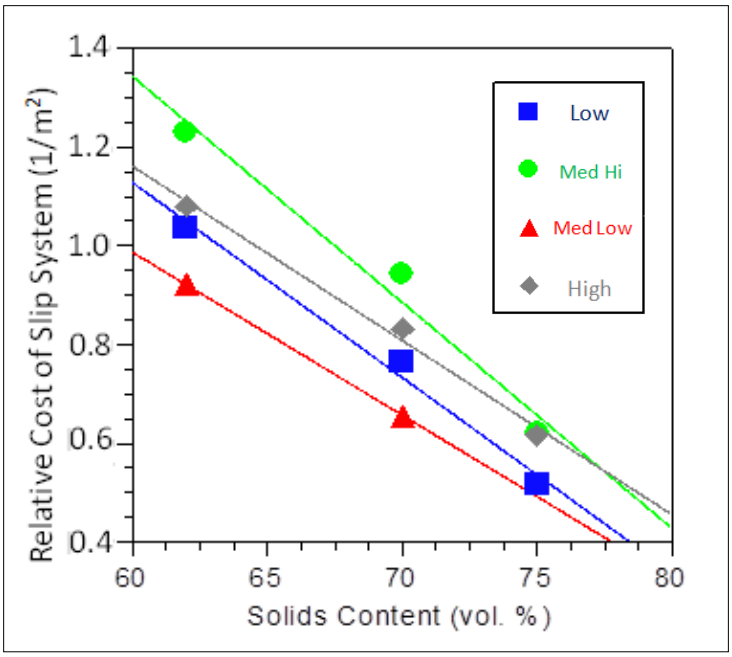

Figure 3-11. Relative cost of organics required to cast one square meter of green tape as a function of the solids content. Note that the cost is highly dependent on the binder chosen.

Choosing the optimized binder system involves a number of factors, since the quality of the finished product must come into consideration. Yield is one of the factors that enters into evaluating how different tapes behave during lamination. Costs of environmental compliance and raw materials drive toward using higher solids content, which allows for easier removal of organics and results in fewer organics to deal with from a pollution control perspective. Moving to a 70-75 vol. % solids tape will result in substantial cost savings when high quantities are used.

The low MW binder appears to be the binder of choice when considering the ability to process high solids-content tapes economically. Considerable works remains to determine what solids content can be reasonably achieved in practice and whether there are unforeseen advantages for using a higher molecular weight binder.

AP2K Tape Development

Table 3.1 gives the properties of AP2Ka tapes cast at 75 vol. % solids. These tapes were prepared by using procedures similar to those developed for the AP98 powder.

Table 3.1 Room-temperature tensile tape property comparison of AP2Ka tapes cast at 75 vol. % solids using low MW binder.

Tape Code	Solvent	Young's Modulus (GPa)	Yield Stress (MPa)	UTS (MPa)	Energy/Area (mJ/mm^2)	Max. Strain (%)
BK6-14A	41-P	0.31	0.8	6.4	25	15.9
BK6-14B	41-S	0.29	0.9	6.1	27	13.9
BK6-14C	23-S	0.35	1.3	6.4	15	7.3
BK6-14D	01-S	0.34	1.0	6.7	19	9.7

Some observations from preparing AP98 and AP2Ka tapes:

1. Binder content and type have a strong influence on the properties of both AP98 and AP2Ka tapes. Higher solids content results in greater green density, which in turn gives slightly lower shrinkage. The strength of both uncompacted and compacted tapes decreases with increasing solids content, since the strength is controlled by the volume fraction of binder.
2. The cost of organics, coupled with the expense of disposing of these vapors in an environmentally friendly way, will push toward use of higher solids contents for any tapes that are produced in large quantities. Low MW binder appears to be the binder of choice at high solids content because it is able to survive drying, requires less solvent to achieve the same viscosity, has high strength after lamination (i.e., lower cost), and is amenable to different bonding approaches.
3. Crack-free tapes were cast with low and high molecular weight binders under different conditions – a more controlled tape casting environment enables better drying and a wider range of options. Use of different solvent systems resulted in comparable tensile properties of the green tapes, suggesting that this substitution should be evaluated on a larger scale.
4. Adequate bonding appears feasible using any of the binders. Bonding at high solids contents does not appear to be of concern.
5. The green tensile strength of laminated joints is controlled primarily by the binder content. except for the medium low molecular weight binder, the other three binders show similar

bond strengths when tested at the same solids content. There is no clear choice and all three of these binders are acceptable.

6. The room-temperature tensile strength of green tapes decreases with solids content. This represents a concern for pressing slotted structures without interior support and will result in lower loads at higher solids contents. Tensile strengths at 75 vol. % solids are roughly half as strong as they are at 62 vol. % solids.
7. It is difficult to see the binder using the SEM due to volatilization of the binder by the electron beam. Low accelerating voltages allow one to sense the surface morphology, but it was not possible to get quantitative data of surface binder content using this approach.

Strength of Sintered AP98 and AP2K

Ceramatec adapted a uniform pressure-on-disk test (Chao and Shetty, 1991) to assess the tape strength of as-sintered disks, and compared these results to data obtained prior to this cooperative agreement. The main advantage of the uniform pressure-on-disk (UPD) technique is that a much larger volume of material is under test than, for example, the ball-on-three-ball (BTB) tests used previously (Kristein and Woolley, 1967). Figure 3-12 shows the results of the comparison. The characteristic strengths were 185 and 245 MPa for the UPD and BTB techniques respectively. The respective mean strengths were 170±35 and 237±18 MPa for the same two techniques. The Weibull moduli were, respectively, 5.8 and 15.8 for the UPD and BTB tests.

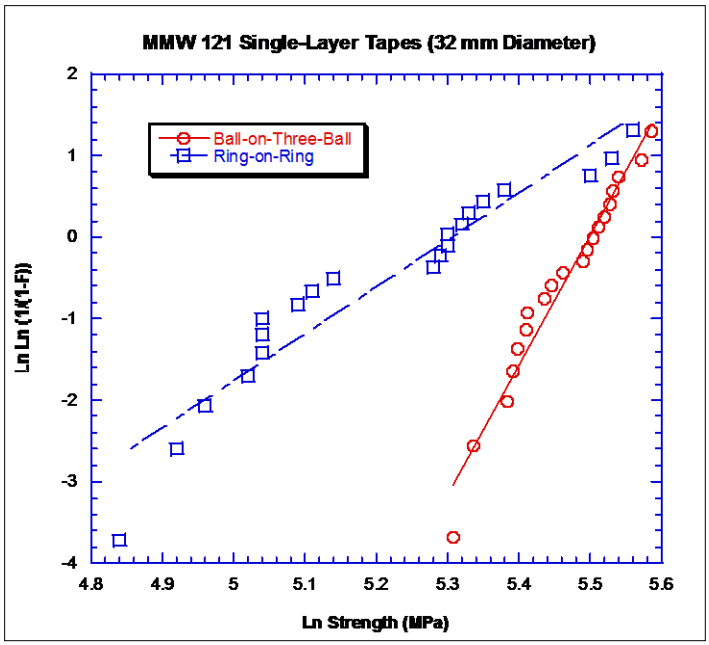

Figure 3.12. Weibull plots for disks loaded with setter-side in tension, comparing biaxial flexure strength from sintered AP98 tapes loaded using the ball-on-three-balls test with the uniform-pressure-on-disk apparatus.

If the same flaw populations were being measured in both cases, the strength difference expected would be given by

$$\sigma_1/\sigma_2=(A_2/A_1)^{1/m} \qquad (3.1)$$

where A is the effective area of the disk under stress, m is the Weibull modulus, and subscripts 1 and 2 refer to the BTB and UPD tests respectively. The effective area is given by (Batdorf, 1997)

$$A=2\pi r_{eff}^2 m^{0.45} \qquad (3.2)$$

where r_{eff} is taken at t/10 (t = disk thickness) for the BTB or 0.35r (r = support radius) for the UPD test, such that the material within that radius experiences 90% of the peak stress (Shetty, et al, 1983). Plugging these effective areas into Equation 3.1 results in a predicted σ_1/σ_2 of 1.7 if m=15.8 and 4.3 if m=5.8, versus the measured values of ~1.35. The strength decrease is therefore not as severe as predicted. This suggests that the same flaw populations are not being sampled between the two tests. It is probable that multiple flaw populations are sampled by the UPD test due to the larger volume of material under test. These results are in accord with data from other researchers (Simpatico,Cannon, and Matthewson, 1999).

The effect of AP98 grain size and setter interaction was investigated by sintering the material at three different temperatures, resulting in grain size increasing from 4-5 μm to 10-12 μm with a 50°C increase (Figure 3-13). All samples were at least 98% of theoretical density. The biaxial strength was independent of grain size (i.e., sintering temperature) in the range investigated (Figures 3-14 and 3-15). An increase in characteristic strength from 108 to 131 between the air and setter side was offset by a decrease in the Weibull modulus (m=6.9 for the air side and m=4.1 for the setter side). The fracture toughness of AP2K was calculated to be 0.87±0.13 MPa√m based on flaw size measurements.

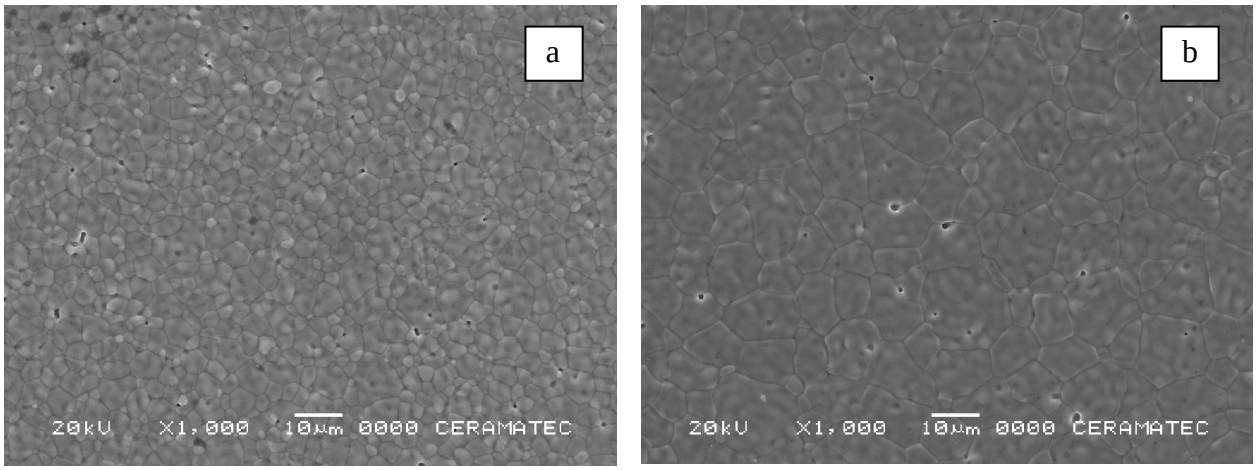

Figure 3-13. SEM micrographs of as-fired setter-side surfaces of AP98 disks showing how grain size increases with increasing temperature. (a) baseline, (b) baseline plus 50°C.

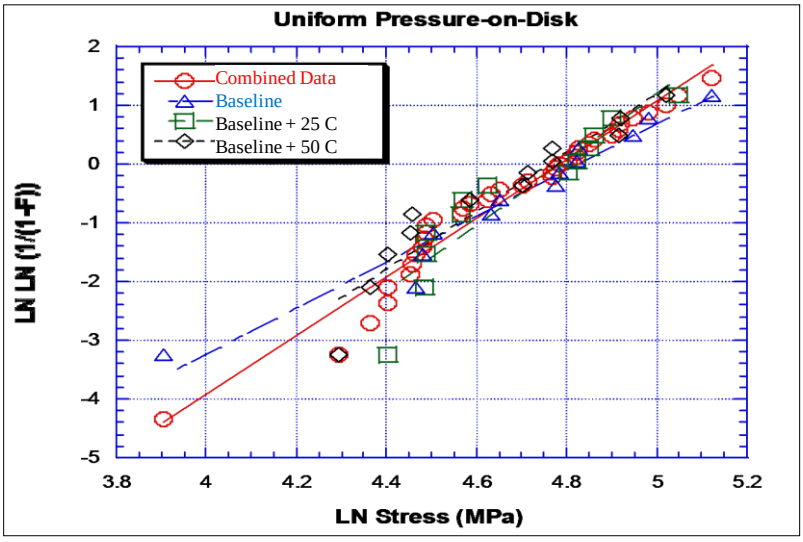

Figure 3-14. Biaxial strength data for baseline AP98 tapes. Strength as a function of sintering temperature showing no effect of grain size.

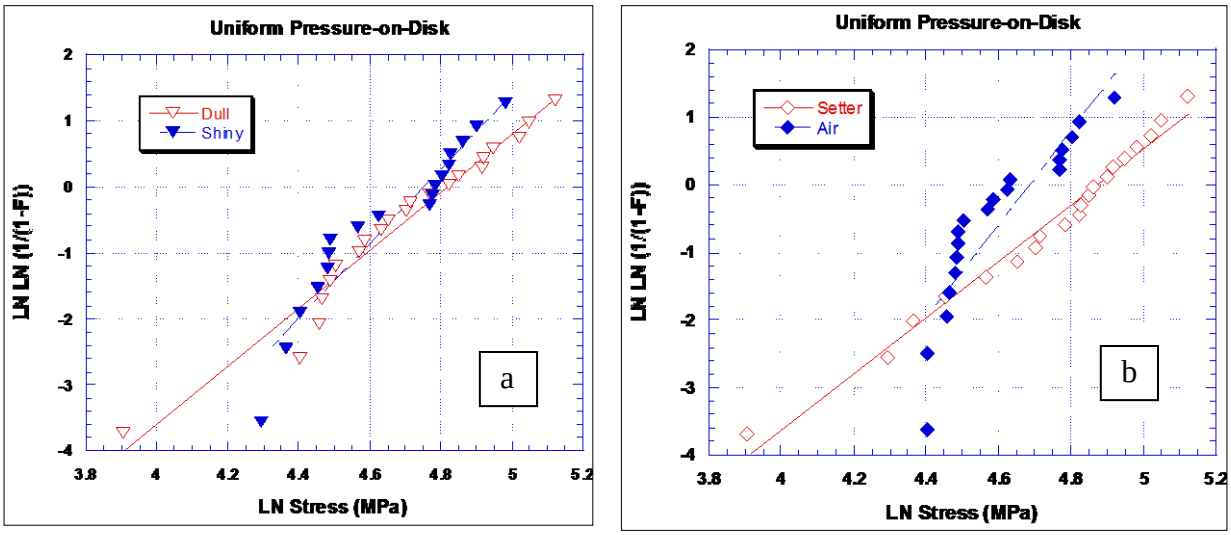

Figure 3.15. Biaxial strength data for baseline AP98 tapes. (a) Strength as a function of cast orientation showing no effect of surface texture on tensile failure; (b) and setter side in tension compared to air side of tape in tension. Increase in strength is offset by decrease in Weibull modulus.

Strength measurements were made to determine the compressive strength of both dense and porous AP2K. The AP2K was three times stronger in compression than it was when tested in bending regardless of the porosity level (up to 50% porosity). The implication of this path-finding work is that unless the compressive stresses are expected to exceed the bending stresses by a factor of three, measurements of biaxial stress in tension have merit. Measurements have indicated that these materials are susceptible to flaws inherent in the structure, and that stresses must be kept low in order to avoid brittle fracture. This implies that modules will be very sensitive to thermal and chemical shock due to transients in temperature and pressure. In order for a module to operate successfully, these transients need to be minimized through engineering design.

Wafer Fabrication

Design of the full-size wafer required information developed under Task 2 on internal pressure drop and costs (Air Products) and mechanical stress modeling (McDermott Technology). Scale-up proceeded from subscale (round) to intermediate-scale (rectangular) to full-size (rectangular) wafers. Internal layers were added as necessary to accommodate the increased stiffness and internal oxygen flow required in the scaled-up structures. Ceramatec focused on developing

prototype wafer production processes and methods to join spacers to wafers and ultimately wafers to wafers.

Prototype Wafer Fabrication

Ceramatec carried out path-finding work toward scaled-up wafers. One of the most difficult challenges was obtaining an internal porous layer that had sufficient porosity and was well-bonded to the surrounding layers. Shrinkage control between porous and dense layers was possible by varying the green density in the green tape and reactivity of powder particles. Both variation in binder/plasticizer content allowed tapes to be developed for different surface area powders. This approached was employed in small trials to tailor the properties of the different tape layers to allow simultaneous shrinkage during sintering. In addition, a series of polymethyl methacrylate (PMMA) dies were cut to constrain the lateral expansion of the tapes during lamination to accommodate both the increased size and in going from the more natural circular discs shape to the rounded square shape required for low cost.

Figure 3-16 shows the end result of the path finding work performed by Ceramatec that resulted in testable full-size square wafers. Ceramatec demonstrated that such wafers could be fabricated out of the 62 – 75 vol. % solids tapes.

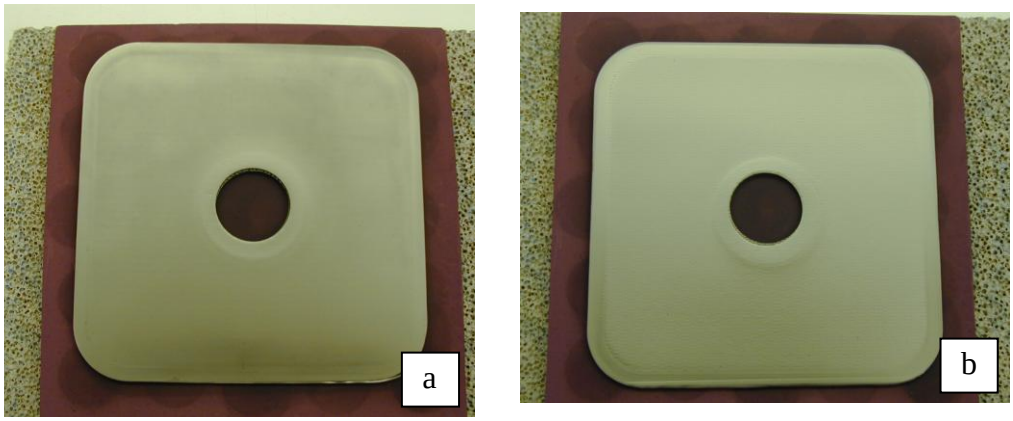

Figure 3-16. Full-size wafer with fully integrated dense, slotted and porous layers made using PMMA die to demonstrate that square wafers can be successfully fabricated. The dense layers were made from 62 vol. % solid tapes with low MW binder. (a) setter side, (b) air side.

The porous layers were made using a different powder stream from the dense layers. Scanning electron micrographs showed that unconstrained controls were a good indicator of the porosity in constrained wafers (see Figure 3-17).

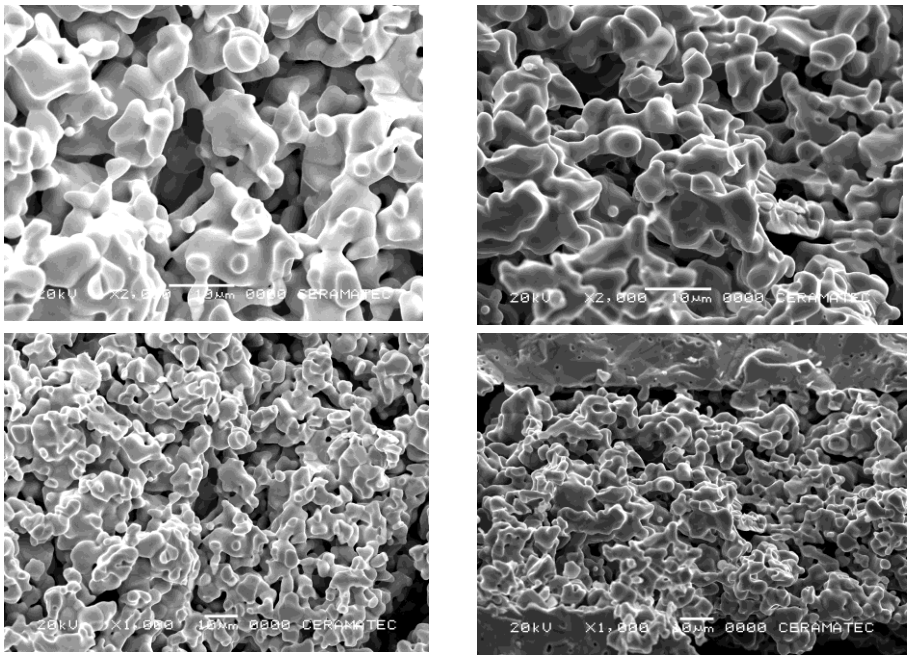

Ex-sagger control Ex-sagger wafer

Figure 3-17. SEM micrographs showing that controls (left-hand side) accurately predict the morphology/porosity in the porous layers in sintered wafers (right-hand side), where the porous layer is constrained by the surrounding dense layers.

Path-finding bonding trials with slotted layers addressed the challenge of green tapes flowing under stress during production of multilayer laminates. One approach was explored for putting a fluid in the channels to keep them open during bonding; further work is needed to see if this technique has merit. Another tested method involved dropping the temperature to increase tape stiffness, then locally solvate the surfaces to be bonded with a low-vapor-pressure solvent, using pressure to locally bond the layers together. Acceptable bonding was achieved with solvent amounts between $8x10^{-6}$ and $1x10^{-5}$ g/mm^2 with pressures ranging between 2 and 8 MPa. Since tapes were not uniform, it was necessary to use higher pressures than what can be achieved with better control of the tape casting process. As expected, a pressure-transmitting polymer or crushable cardboard could be used to obtain the same result at lower pressures (1-2 MPa) by more evenly distributing the pressure. Figure 3-18 shows the internal structure of the wafers. These structures, while imperfect, demonstrated that the full-size wafers could be fabricated.

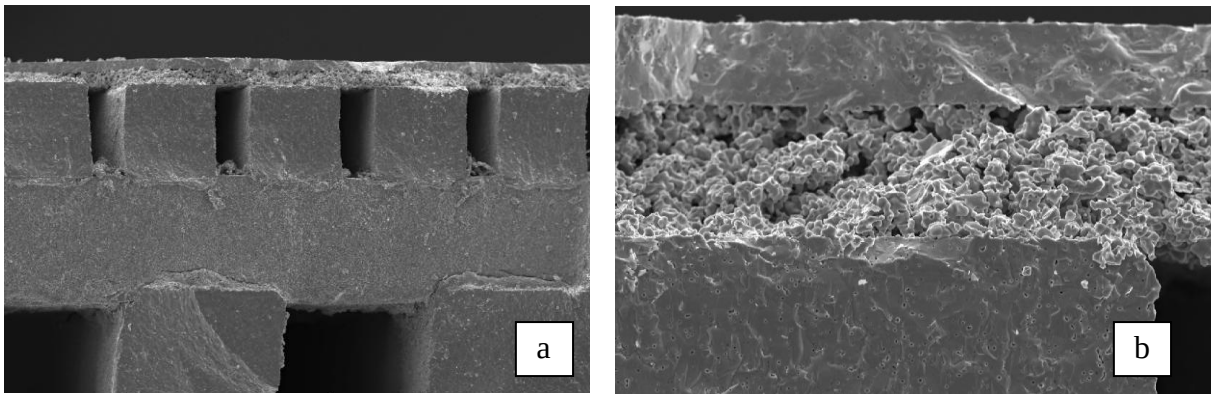

Figure 3-18. Cross-sections of wafers made during prototype path finding work. (a) Dense/porous/slotted structure showing some cracking around slots as a result of high bonding pressure, (b) dense/porous/slotted fracture cross-section showing excellent bonding.

The prototype wafer fabrication effort was an iterative process, learning about binder removal and how to eliminate cracking due to porosity formation. The wafer fabrication process was conducted concurrently with the tape development discussed above. The prototype wafer fabrication effort was replaced by more sophisticated work with metal dies and punches. Much of what was learned during the prototype work, however, was relevant to efforts to scale-up the process.

Bonding of Sintered Wafers Using a Transient Liquid Phase

One of the main challenges in making stacks is to seal a large number of wafers, because one bad seal will impact the entire stack of wafers. Silver seals have been successfully used in joining. While a ductile metal is advantageous for relieving stress, silver volatizes and will not create a stable, long-term seal, and cost may be an issue. Ceramatec investigated ceramic-ceramic joining techniques to make robust, low-cost joints out of materials similar to the ITM ceramic.

A transient liquid phase (TLP) that could be incorporated into the perovskite structure was evaluated as a potential route to a seal. Several metal oxide-based systems were investigated to see if joining was possible. Ground AP2K tubes were successfully joined to ground AP2K disks at high temperature by applying low pressure to a transient liquid phase composed initially of an ABO compound, and oxide in which A is an alkaline earth metal and B is a transition metal. EDS mapping showed that these elements diffused away from the interface during a 4-hour hold at elevated temperature, presumably allowing solidification at that temperature. Both tube

assemblies pumped down to an effective He leak rate of $8x10^{-10}$ cc/s in the absence of He, but were not leak-tight to He. SEM observation showed porosity at the interface and regions of B-site excess oxides. It was suggested that equimolar ratios of BO and ABO be used to minimize the B-site excess. It is presently not understood why the some ABO systems are effective in forming a seal, whereas others are not.

AP2K was joined at elevated temperature for one hour using ABO-precursor inks. Leak rates as low as 0.001 sccm were observed for joints formed by sealing one AP2K tube to an AP2K disk. Microscopy showed that metals in the AP2K diffuse away from the joint as a front, leaving a band of material dissimilar to AP2K. The concentration of transition metals in the AP2K is lower on either side of these bands, which are located hundreds of microns away from the interface. These regions are susceptible to cracking upon grinding due to the expansion mismatch between the two phases. The width of the region is proportional to the amount of A added, and the band forms even when no A is in the ink. Despite the fact that A is the culprit leading to the transition metal concentration gradient, there is no evidence that A concentrates in the bulk of the AP2K.

AP2K was joined at elevated temperature for one hour by first screen printing an ABO ink on the end of a tube and then joining it to an uncoated disk. Nine out of nine assemblies were hermetic to He at room temperature using this first trial with smaller amounts of ink. An ink amount corresponding to a thickness of 13±1 μm upon melting gave better bonding than a screen-printed layer of half the thickness. Subsequent experiments showed that it is imperative that the disk and tube surfaces be in intimate contact if hermetic seals are to be consistently achieved. Figures 3-19 and 3-20 show interfaces for AP2K that are hermetic to He at room temperature after joining.

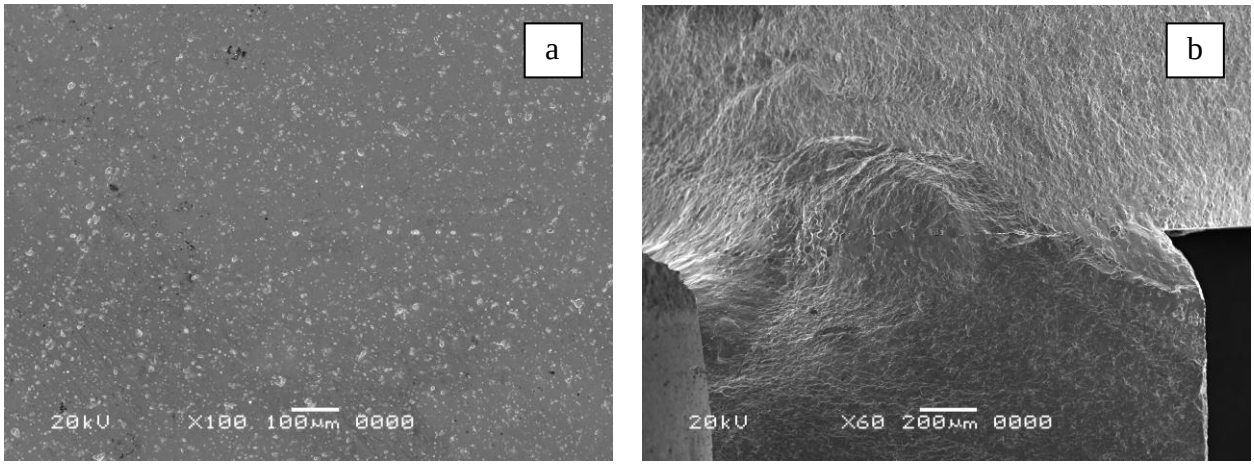

Figure 3-19. Cross-sections showing well-bonded interfaces formed using transient liquid phase joint. (a) Polished cross-section, (b) fractured cross-section showing disk (top) bonded to unground tube (bottom).

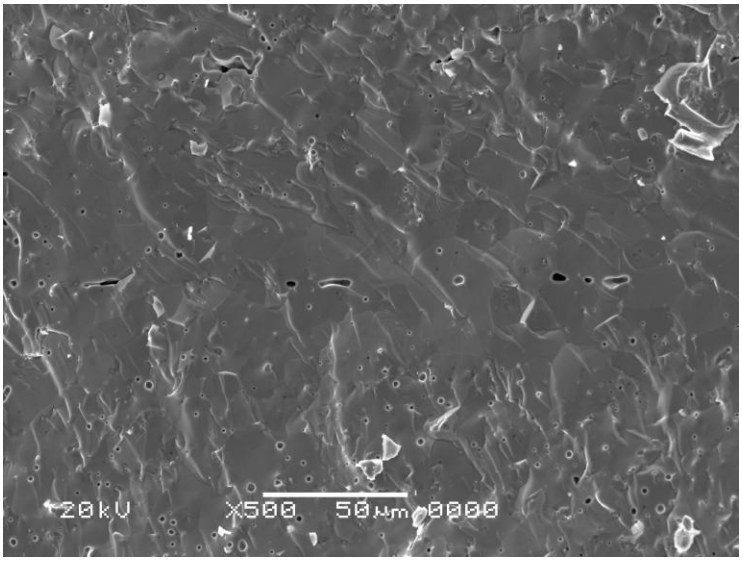

Figure 3-20. Cross-section showing well-bonded interface formed using transient liquid phase joint. Fracture cross-section shows closed pores at interface (see center horizontal line in micrograph).

There is no evidence of the liquid phase after joining, and these joints can be thermally cycled without damage. The porosity in the porous layer is maintained by limiting the joining time and temperature. Because the liquid phase not only wets the surface of the ceramic but also spreads due to a low contact angle, it is necessary to have flat surfaces for joining. Currently, a 20 μm diamond wheel is used to grind the two surfaces prior to joining. In order to allow grinding of the inner rim of the wafer, a concept was developed that allows for supported sintering of a

sacrificial outer layer (Figure 3-21). The inner rim of this structure is dense to allow bonding, while the area over the active wafer is primarily (75 %) open with porous networks allowing air access to the active area. It is anticipated that this approach would cut down the flux slightly, but it would also protect the outer surface of the wafer from setter interaction. Further efforts are needed to show that the joining has high reliability, but initial trials were very promising in this regard once it was realized that the cations in the AP2K do not diffuse at the same rate. Limiting the amount of transition metal cations introduced by the TLP is consistent with strength measurements discussed above.

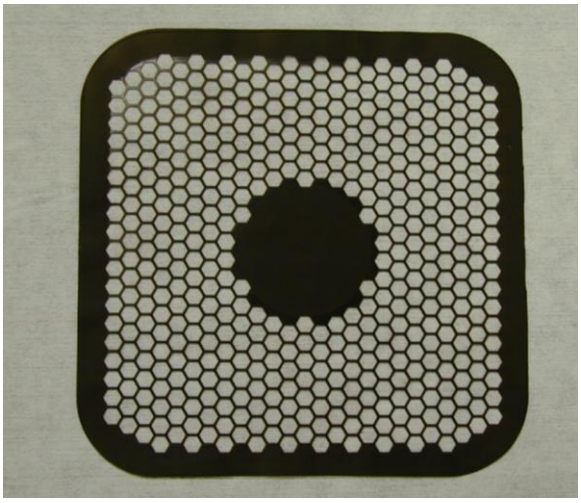

Figure 3-21. A' protective layer for wafers made from dense outer and inner rims, with a porous network of honeycombs. The A' layer provides for an inner rim for sealing (the outer rim can be porous) and protects the setter side of the part during sintering.

Intra-wafer Pressure Drop

Air Products assessed the radial pressure drop incurred in the flow of oxygen as it moves toward the center collection port inside the ITM Oxygen wafer. This pressure drop can impede the flux through the membrane by decreasing the partial pressure driving force. However, easy flow through the wafer interior must be balanced against the mechanical strength required to support the thin separating membrane. The radial pressure drop in a channeled wafer was approximated as a simple function of flux, wafer dimensions, and channel geometry. PDU results collected previously are "corrected" by this relationship, yielding a straight-line plot of oxygen flux vs. log(P'/P")-driving force (Figure 3-22).

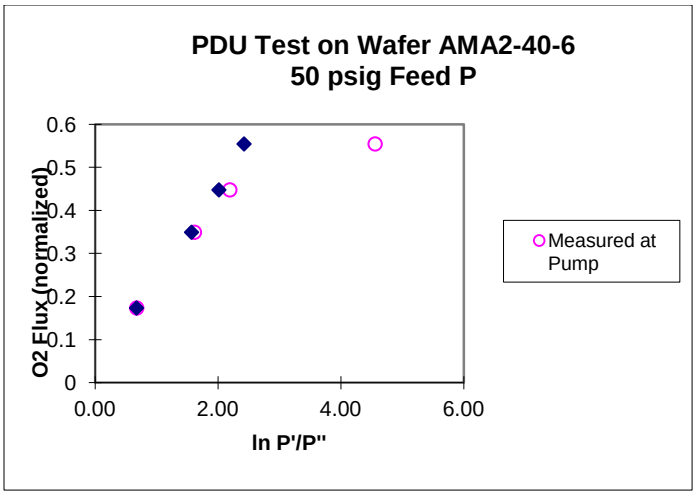

Figure 3-22. Radial pressure drop "correction" of PDU data.

Based on engineering models for fluid flow, Air Products calculated radial pressure drop for subscale wafers at expected process conditions to be ~10 Torr, which would not significantly impede the flux. In contrast, a wafer with a characteristic dimension 2.9 times larger under the same conditions would exhibit a pressure drop exceeding 120 Torr (for equivalently scaled center port dimensions). These results demonstrated the need to accommodate the greater flows in the wafer interior. Preliminary calculations have recommended larger and more frequent slots in the slotted layer. Initial selection of the slotted layer channel arrangement and dimensions was based on qualitative mechanical considerations. The recommended channel pattern for the larger wafers increased the slotted open area by 50%.

The required slotted layer thickness depends on the overall wafer dimensions, the flux, and the target pressure drop. For a 2.9X circular wafer (i.e., 2.9X larger than a subscale wafer) at expected process conditions, the required thickness can be set based on a target pressure drop. For the same pressure drop in a 4.3X wafer at the same conditions, the thickness must roughly double.

McDermott analyzed stress in the slotted layers and showed that they could be opened up to improve radial oxygen flow and decrease the layer thickness. Ceramatec then evaluated manufacturing thickness requirements as a function of slot width to help determine a new optimized design for the slotted layers that McDermott could model more rigorously. As a target for the new design, the thicknesses were adjusted by 50-100%, resulting in a further increase in slotted layer open area by over 35%. New slot patterns were devised to accommodate these new

dimensions. The radial pressure drop model was then used to calculate slotted layer thickness requirements for the new design over a range of wafer sizes. In addition, the radial pressure drop model was modified to include calculations for square wafer geometries. Nominal slotted layer thickness requirements decreased significantly for the 2.9X and 4.3X wafer sizes.

Full-size Wafer and Module Sizing

Using results from the radial pressure drop model (with the new slot pattern), the wafer/stack performance calculation method developed under Task 2.5, and a previous cost estimate for wafer fabrication (obtained independently of this cooperative agreement), a spreadsheet was developed to estimate the incremental cost of wafer/stack fabrication as a function of wafer size and shape. Sensitivity analyses were included for materials recycling, labor rate, center port size, fabrication yield, and allowable permeate-side pressure drop. The calculations indicate that a strong optimum wafer size exists, and the exact optimum shifts to smaller or larger sizes within that range depending on the various sensitivities. The optimum exists because labor costs favor larger wafers, while material costs favor smaller (thinner) wafers. A full-size square wafer dimension with specified thicknesses of the slotted layers was chosen for future development (and eventual commercialization) based on this analysis. McDermott's FEA work under Task 2.3 supported the selection made for the full-size wafer specification.

Air Products developed a framework to determine the optimum ITM Oxygen module size for a fixed value of pressure drop in the tube, including the portion of the "tube" made up of wafer holes and central spacers. The process involved calculating the number of wafers required to produce the target pressure drop in a range of tube diameters, and then calculating the specific cost ($/TPD) of that module. In reverse, as the module size (number of wafers) grows, the required tube diameter grows, thereby decreasing the active area of each wafer (because the outside wafer dimension is fixed). For a typical set of performance parameters, operating criteria, and components costs, preliminary results indicated that an optimum module cost ($/TPD) does exist with a specified tube ID and a number of wafers to produce ~1 TPD.

Wafer Processing

To respond to the need to produce parts sufficient for testing and to develop processes that could subsequently be scaled up to support future activities, Ceramatec initiated development of a

prototype manufacturing process and equipment in the Process Development Facility (PDF), created especially for the purpose of developing and producing ITM wafers. The execution of the project will occur in two parts, with the first part completed during Task 3 and the second part completed in subsequent Tasks under the cooperative agreement.

Ceramatec and Air Products assembled a task force to develop and manage execution of the PDF project, describing the organization, size, utilization, unit operations, equipment, and siting for the facility. Line sizing, wafer scaling and throughput models were developed to produce an initial estimate of the ultimate capacity of the facility. Ceramatec installed a high-speed laser cutter in a soft-wall cleanroom; the new unit is the baseline for full-size wafer processing.

Ceramatec significantly advanced the PDF Stage II installation. The long-lead-item ceramic processing tools were selected and ordered, including a high-speed laser cutter for featuring ceramic green tapes, a Class 10,000 clean room from a turnkey cleanroom manufacturer, a continuous tape caster, and other wafer processing equipment such as punching and lamination tooling. Installation of the large Stage II cleanroom was commissioned in 3Q FY01. Additional sintering furnace capacity was installed at Ceramatec to support wafer processing, and further capacity is being procured for membrane module development.

Ceramatec scaled up its powder processing facility, first to make AP98 ceramic powder and then to make AP2K. The approach was to use scaleable process steps wherever feasible or practical. This established a reproducible powder supply for subsequent development steps. Powder production exceeded 300 kg per quarter. The following equipment was added in this effort:

- Pre-calcine mixing & particle size reduction mill (scaleable)
    - Ball mill
    - Attrition mill
- Post-calcine particle size reduction mill with classifier and baghouse (scaleable)
    - Jet mill
- Calcining kilns
- Powder binder mixer

Ceramatec reformulated the ceramic tape as described in the sections above, utilizing a series of statistically designed experiments, and implemented its production on larger-scale equipment. To this end, Ceramatec added and commissioned the following:

- Fixed blade bench type batch tape caster (installed)
- Continuous tapecaster (scaleable) (planned)

Additional tooling was designed, built and utilized for each progression of the wafer from subscale to full-size to prepare the parts and to laminate them together consistently. Layer featuring equipment figured prominently in this activity. The following equipment was brought into use to facilitate these processes:

- Punch presses
- High speed laser cutting station
- Part coating and washing stations
- Lamination presses
    - Auto part transfer into press

Finally, the team extensively adjusted the thermo-processing schedules in newly added batch kilns. Multi-part lots were generated during which statistical process control (SPC) charting was initiated to understand the repeatability of the processes, identify process shifts, and identify areas where improved methods were required to better control the processes.

The PDF coordinates and houses the new equipment and processes, comprising two clean rooms (one for tape production, the other for laminating and featuring):

- PDF1 Clean room – Class 10,000, approximately 1,000 square feet (installed)
- PDF2 Clean room – Class 1,000, approximately 8,000 square feet (newly installed)

Figures 3-23 and 3-25 show a continuous tape caster located in the clean room, a laser cutter that features slots in the inner wafer layers, and a laminating press used to join the wafer layers together.

Figure 3-23. Continuous tape-caster in the clean room of the Process Development Facility located at Ceramatec, Inc., Salt Lake City, Utah.

Figure 3-24. Laser cutter used for featuring layers in the Process Development Facility (PDF) located at Ceramatec, Inc., Salt Lake City, Utah.

Figure 3-25. Lamination press used for making wafers in the Process Development Facility located at Ceramatec, Inc., Salt Lake City, Utah.

Yield Progression

In Q2FY00, Ceramatec shifted from producing small (round) subscale wafers to intermediate square wafers where the active area increased ~6X, and additional featured layers were added for internal gas flow. In Q4FY00, the transition was made ultimately to the square full-size wafer with ~20X more active area than the subscale wafers. These transitions required process modifications as well as considerable scale-up in the amount of ceramic powder and ceramic tape processed and also in thermo-processing capacity. Once the full-size process was stable, it was scaled up in terms of numbers of wafers processed. Figure 3-26 indicates the relative scale-up showing the wafers expressed as membrane area per month. The chart also shows an additional type of wafer built for the purpose of module development – the "Full-Size Wafer – thick." These were non-functional, full-size wafers fabricated without a permeable porous layer so the leak rate would be very low. These were useful for the development of modules. To serve as a process monitor and also to provide a vehicle for continued flux testing at Air Products, a modest level of baseline subscale wafers continued to be processed, even after full-scale wafers began to be produced.

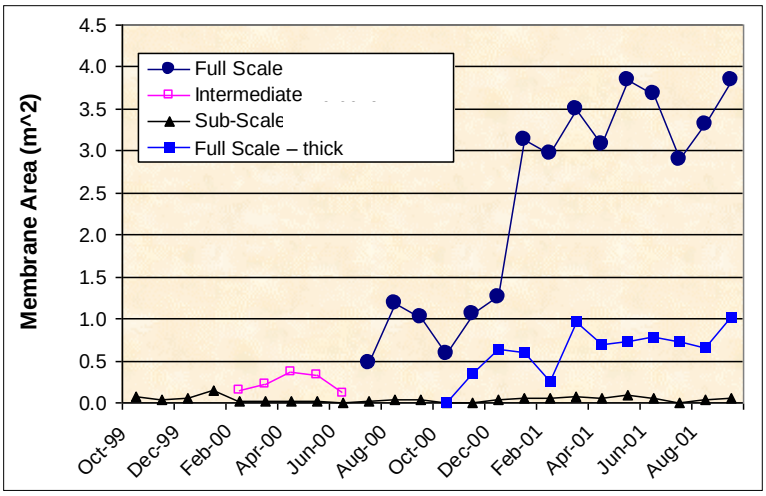

Figure 3-26. Wafer production by month during Task 3 for the four wafer types produced.

During Task 3, three types of yield were monitored: sintering, delaminating, and leak rate. Sintering yield is the fraction of intact wafers coming out of thermo-processing relative to the number of green wafers entering the kilns. There are several failure modes where the wafers crack during the course of thermo-processing. Figure 3-27 shows the split between cumulative cracked wafers and cumulative intact full-size wafers. By the end of Task 3, improvements were implemented that resulted in some dramatic yield increases. For example, the sintering yield improved to 100% in the final two lots produced under this task. Chemical expansion stresses, inherent with the AP98 and AP2K materials, are being addressed by techniques that Air Products is developing to increase thermal processing time and yields by adjusting the kiln atmosphere during cooling.

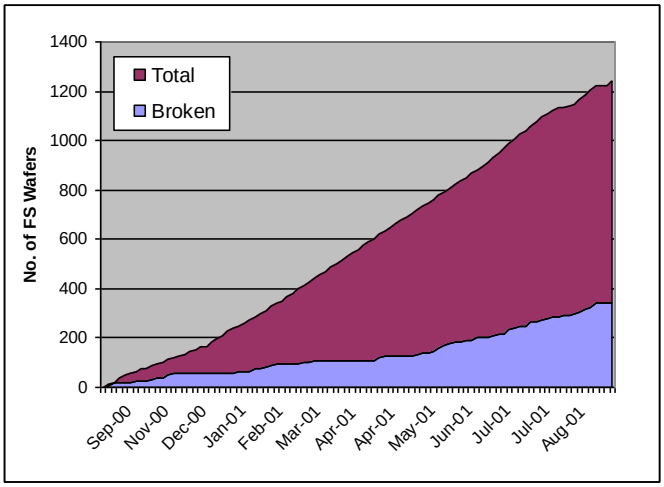

Figure 3-27. Cumulative number of wafers built and broken in thermal processing.

Delamination of adjacent wafer layers is a known defect leading to high leak rates. Delamination arose as process changes were introduced during the task to address other problems. While delamination has occurred between each layer interface, delaminating between the inner layers of the wafer was the most prevalent situation (Figure 3-28). The defect was mostly non-existent for 63 lots of wafers, then became a major failure mode in the latter part of Task 3. [Note: this defect was eliminated under subsequent tasks.] Several experiments were underway at the end of Phase 1 to eliminate the failure mode. The experience highlights the need to document and control processes.

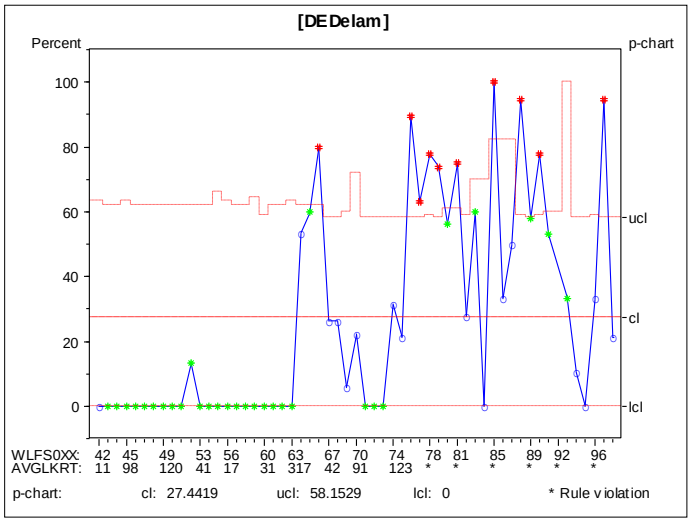

Figure 3-28. P-chart of delamination defects between the inner wafer layers by lot number. Note that this defect was rare until approximately Lot 63.

Another type of yield relates to the measured leak rate of free intact wafers. By pulling a vacuum on the central hole of the wafer, air leaks through the wafer membrane defects at measurable rates. The leak rate of air with the wafer interior under vacuum must reach a specified points corresponding to various grades of oxygen purity attainable under operating conditions.Three major categories were tracked: 1) testable wafers; 2) 95% wafers; and 3) in-specification wafers. Testable wafers could be expected to produce 90% oxygen, suitable for testing requirements during the program. The 95% wafers produce 95% pure oxygen, while the "in-spec" wafers can be expected to produce at least 99.5% oxygen.

Figure 3-29 shows the yield progression of "testable" wafers during Task 3, while Figure 3-30 shows the yield progression of "95% wafers" during Task 3. Note that the yield curves are a composite of experimental trials. Factors affecting the outcome of the trials are statistically

assessed in planning future work. Defect analysis is a critical part of the overall effort to improve leak.

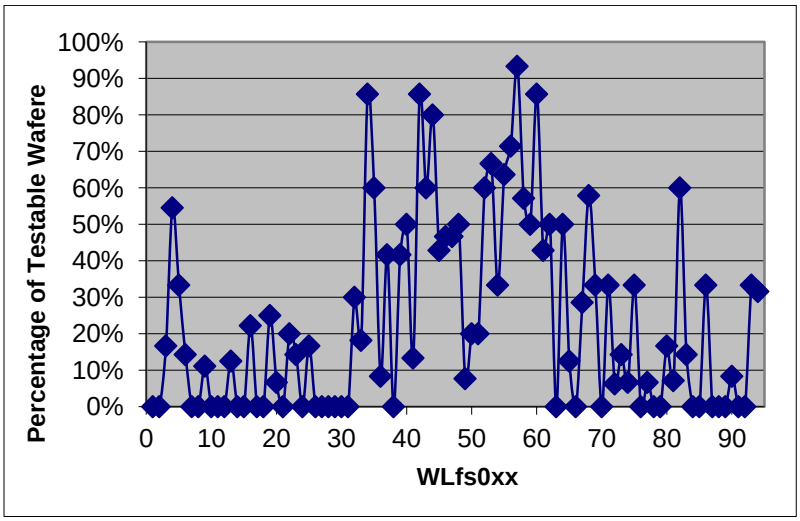

Figure 3-29. Testable wafer yield by lot number during Task 3.

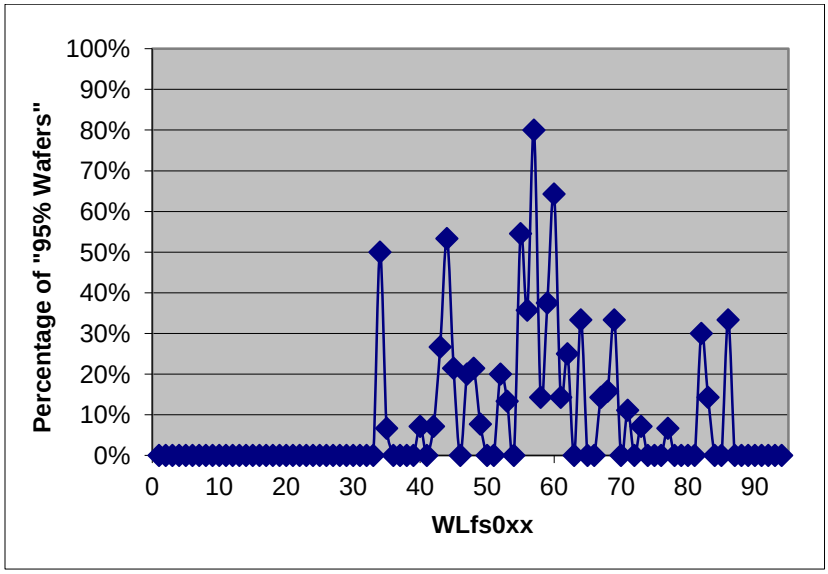

Figure 3-30. "95% wafer" yield by lot number during Task 3.

The surface defects affecting the leak rate are microscopic, but not all such defects leak. Air Products developed a method to locate leaks on the wafer surface so they may be marked and observed microscopically. The method is also able to distinguish between the relative magnitude of the leaks. Ceramatec used this method to rank the defects affecting leak rate and prioritized work to systematically reduce them. The work has produced improvements in sintering yield toward the end of Task 3 and is likely to lead to improvements in leak yield going forward.

Module Fabrication

Fabrication of subscale modules from subscale (round) wafers was performed by Air Products using tubes, wafers, and end caps produced at Ceramatec. The wafers were joined to the tube and end cap using metal brazes. The techniques were then transferred to Ceramatec, where all single- and multi-wafer modules of full-size wafers were fabricated. The largest module consisted of a full-size tube, 12 full-size wafers, and an end cap. In addition to the 12 full-size wafer modules, several 1-, 2-, and 3-wafer modules were fabricated and delivered for testing. Modules with intermediate-sized wafers were not fabricated because there was not a testing window for them in the TDU.

To reduce the number of joints necessary to ultimately fabricate a full-size module, the spacer between wafers was redesigned to enable lamination of the green spacer to a green wafer and subsequent co-sintering. As each wafer was tested for leakage after sintering, the wafer/spacer joint was verified to be leak tight. Co-sintering the wafer and spacer reduces by half the number of ceramic-ceramic joints required to make a full-size module. This reduction in the number of joints dramatically increases the probability of successfully making a low-leak module.

A two-step strategy was developed to further increase the probability of successfully making a full-size module,. First sub-modules consisting of 12 wafers each are fabricated, then multiple sub-modules along with end cap and bottom flow tube are joined make a full-size module. By leak testing sub-modules before assembling them into full-size modules, the overall yield of wafers successfully incorporated into full-size modules is expected to be higher. Since sub-modules will have only 12 wafers each, it was relevant to build a 12-wafer sub-module and test it in the TDU. Figure 3-31 shows the evolution of the wafer sizes and modules produced during Task 3.

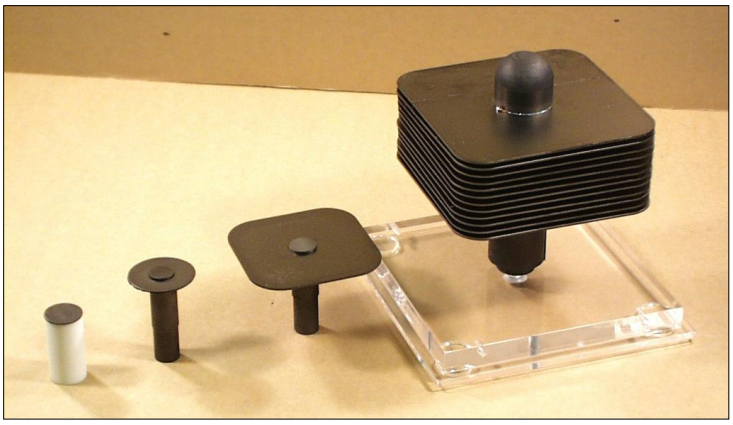

Figure 3-31. Evolution of wafer size and joining during Task 3, culminating in a testable 12-wafer module shown at right in the photo. Shown are a laminate, subscale wafer, intermediate-scale wafer, and 12 full-size wafers in a module with end cap and flow tube.

Brazing processes for joining were adopted while Ceramatec developed all-ceramic joining techniques. To enable Ceramatec to have a two-step assembly process, Air Products developed brazing processes compatible with the AP2K wafers which process at two different temperatures. In this way, the sub-modules could be brazed using the higher-temperature braze but would not be affected when subjected to the second, lower-temperature brazing process.

In parallel, Ceramatec began work to develop a ceramic joining process. Such a process would offer several advantages over braze-type joints, primarily stability in the operating environment and lower material cost. While promising results were obtained with ceramic joining, brazes remained the "on-line" joining process at the end of Task 3.

In addition, during execution of Task 3, Ceramatec developed fixtures used in the joining processes that do not introduce contaminants to the surface of the membranes.

Improved Wafers and Modules

Ceramatec proposed and made and several improvements to the wafers and modules. The team reduced the width of the outer dense rim to reduce stresses from changes in chemical expansion during temperature transients. Making this change increased the amount of precision required during the lamination process. However, without changing thermo-processing ramp rates, yield increased in both the initial thermo-processing of the wafers and subsequent subscale module thermo-processing. The other benefit was a 9% increase in active area without increasing the size or material requirements of the wafer.

Another enhancement to the wafer was the addition of the flow tube spacer, which provides a joining surface between the wafer and the flow tube at the base of the module. Initially, the flow tube spacer was a simple section of flow tube, fabricated and thermo-processed separately from the wafer. To reduce the number of joints in the module by one half, a laminated ceramic tape spacer was designed that is conducive to lamination to the green wafer. By incorporating features into the spacer, the characteristic length remained small while improving the spacer aspect ratio, increasing module stability and making it more conducive to manufacturing. Adding the flow tube spacer to the wafer considerably simplified module assembly.

During Task 3, Air Products and McDermott Technology recommended increasing wafer-to-wafer spacing by 25% to ultimately reduce pressure drop through a vessel containing several rows of modules. The height increase from taller spacers was offset by reducing the number of wafers in a module, while the decrease in the number of wafers was offset by the increased active area of each wafer made possible by decreasing the rim width. Ceramatec implemented the spacer height increase successfully, and also eliminated the concept of an edge spacer in the module design pending future verification of wafer creep.

Work toward developing ceramic joints to replace brazed joints enjoyed early positive results with AP2K surfaces that were ground flat. Efforts to develop more compliant joints to avoid the need for machining is planned for future work.

References

Batdorf, S.B., "Some Approximate Treatments of Fracture Statistics for Polyaxial Tension," Int. J. Fract., 13[1] 5-11 (1977).

Chao, L.Y. and Shetty, D.K., "Reliability Analysis of Structural Ceramics Subjected to Biaxial Flexure," J. Am. Ceram. Soc., 74[2] 333-44 (1991).

Hellebrand, H., "Tape Casting," pp. 189-265 in Materials Science and Technology, Vol. 17A, Ed. by R. J. Brook (VCH, Weinheim, 1996).

Kristein, A.F. and Woolley, R.M., "Symmetrical Bending of Thin Circular Elastic Plates on Equally Spaced Point Supports," J. Res. Natl. Bur. Stand., 71C[1] 1-10 (1967).

Shetty D.K., et al., "A Biaxial Flexure Test for Evaluating Ceramic Strengths," J. Am. Ceram. Soc., 66[1] 36-42 (1983).

Simpatico A., Cannon W.R., and Matthewson, M. J., "Comparison of Hydraulic-Burst and Ball-on-Ring Tests for Measuring Biaxial Strength," J. Am. Ceram. Soc., 82[10] 2737-44 (1999).

PHASE I RESULTS AND DISCUSSION

TASK 4.0 ITM OXYGEN PERFORMANCE TESTING

4.0 Scope

The Recipient carries out upgrades of existing apparatus and scales up laboratory-scale pilot units for membrane module oxygen flux performance testing with full-size wafers. Air Products designs and installs a combustor upstream to complete the capabilities for a process system validation. In addition, Air Products designs and constructs a Technology Development Unit (TDU) comprising a prototype ITM Oxygen pressure vessel integrated with a pre-combustor to simulate commercial operating conditions. The TDU features instrumentation to enable a total mass balance for the process with capability to fully characterize the performance of multi-wafer membrane modules operating with a high-pressure feed and vacuum permeate system. Air Products demonstrates the achievement of high-purity oxygen production utilizing an air feed preheated by direct-fired combustion at the full process pressure and the stability of module oxygen performance. The Recipient demonstrates the achievement of high-purity oxygen at the target flux range.

Testing Capability Upgrades

Combustor Design and Installation

Air Products developed a high-pressure burner for use upstream of the existing Process Development Unit (PDU) and for subsequent use in the Technology Development Unit (TDU). The challenges of burner development included lighting the burner at pressure and operating it with a fuel:air ratio appropriate to create the desired process chemistry in the feed air stream to the ITM modules.

Table 4-1 indicates the range over which the combustor operation is targeted based on the desired outlet temperature from an upstream, in-line combustor. In Case 1, air discharging from a gas turbine compressor section or dedicated air compressor reaches 300°C through the compression process and must be heated to 900°C entirely by an in-line burner. In Case 2, the compressed air is subsequently heated by recuperative heat exchange steps or other indirect heating means to 700°C and is finally heated to 800°C by in-line combustor. Because heat leak is

expected to be appreciable with lab pilot-scale equipment, the role of the combustor is to create the desired process chemistry upstream of the ITM modules.

Table 4-1. Desired adiabatic flame temperature range (ITM inlet condition) and corresponding required fuel:air mix.

Case	Combustor Inlet Air Temperature (°C)	Combustor Exit Gas Temperature (°C)	Fuel:Air (vol./vol.)
1	300	900	0.0254
2	700	800	0.00419

Burner Development

Initial work focused on identifying a suitable burner head. Because flow in the combustor was expected to be downward, the combustor could be located above process heaters and vessel of the PDU. Therefore, the burner head must contain a suitable flame holder to stabilize the flame against the buoyancy forces that would otherwise reverse the hot flame and combustion zone gases. The vessel housing the burner head should be rated at ≥300 psig MAWP.

An early burner head design featured a perforated plate located in the head of the pressure vessel. Fuel entered the top of the hemispherical head and passed through the perforations in the plate. Air was fed through the side of the head. This burner did not achieve a stable flame. The following observations were noted:

- The perforated burner was tested under an extensive set of fuel flow, air flow, and pressure conditions. No conditions could be identified under which the burner ignited.
- The perforated burner was modified through the removal of an air baffle (intended to direct air through the burner air inlets). Once removed, the burner did ignite and burn at pressures up to 30 psig. However, the flame was extremely fuel-rich and produced unacceptable amounts of soot. The flame always extinguished when the operating pressure was increased above 30 psig.

The burner was modified by installing of a number of different torch nozzles taking natural gas feed from the side of the burner head and redirecting the feed air flow inlet vertically. These nozzles are based on commercially available propane burner designs and feature significantly smaller fuel apertures and an integral fuel/air mixer design. Several different aperture sizes were tested. Static tests of these burners outside of the combustor indicated that they can sustain a

stable methane flame. These burners did ignite (as indicated by UV emission and thermal transients), but did not sustain a flame under the air and fuel flow conditions tested.

A number of configuration options were considered as shown in Figure 4-1. Except for Version 1, each of these options features a torch nozzle burner with air flow directed around the burner. Tests of Version 1 are described above and didn't sustain a flame during normal air flows.

A test of the Version 3 burner was carried out. At the outset, a baffle electrode was placed just downstream of the torch nozzle to allow for better flame attachment (see Figure 4-2). Fuel and air flow rates varied over a wide range (1-10+ scfh CH_4 and 36-150 scfh air), but a flame signal occurred only during 7-second ignition sequence. Visual observation through the upper header peeper port showed a flame coming down and spraying outward against baffle. Visual observation from side peeper showed little flame making it around the baffle.

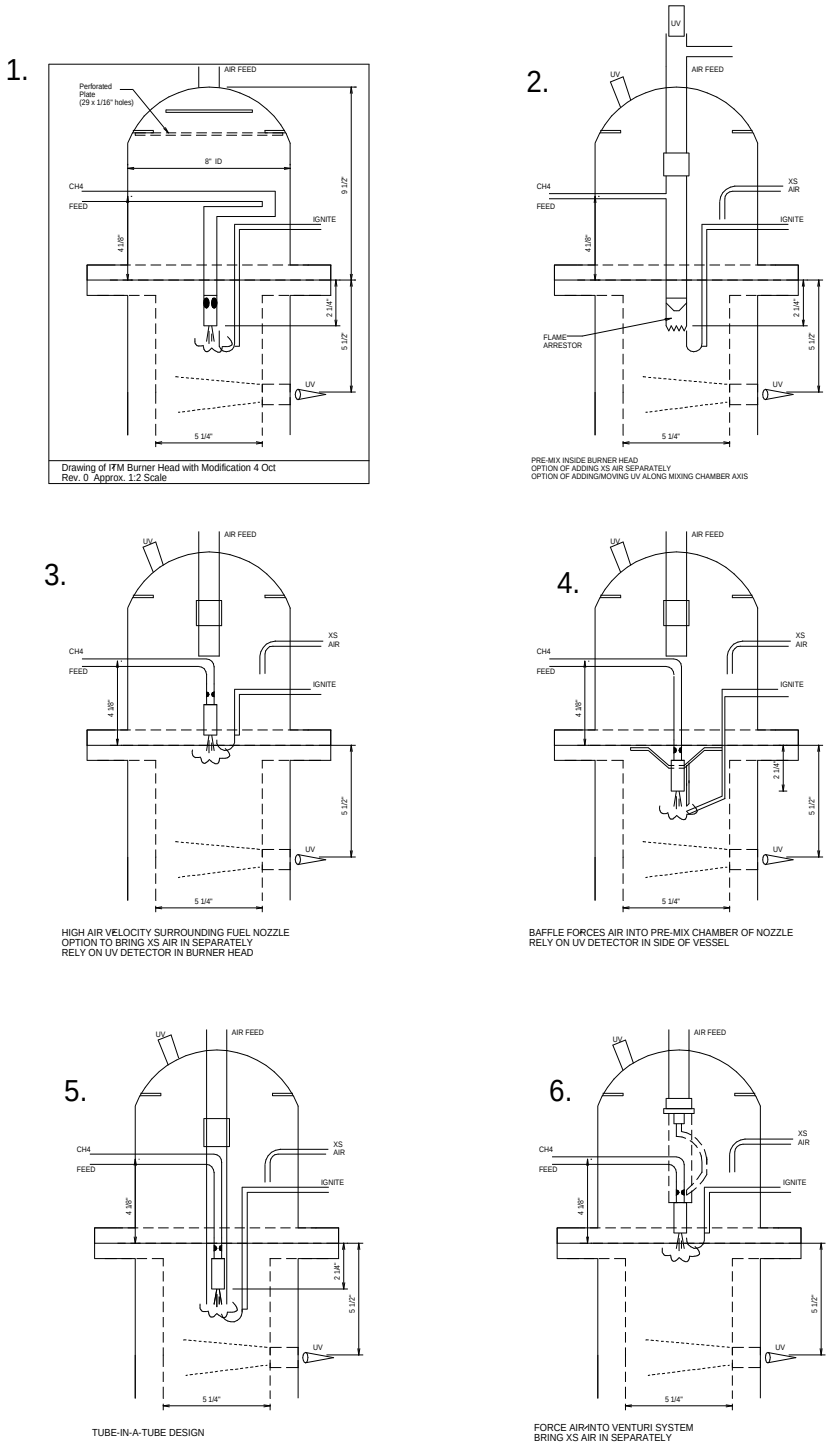

Figure 4-1. Optional burner types considered. 1. Simple torch. 2. Pipe burner with arrestor. 3. Torch with directed flow. 4. Torch with baffle. 5. Torch in a pipe. 6. Forced venturi air and directed air flow.

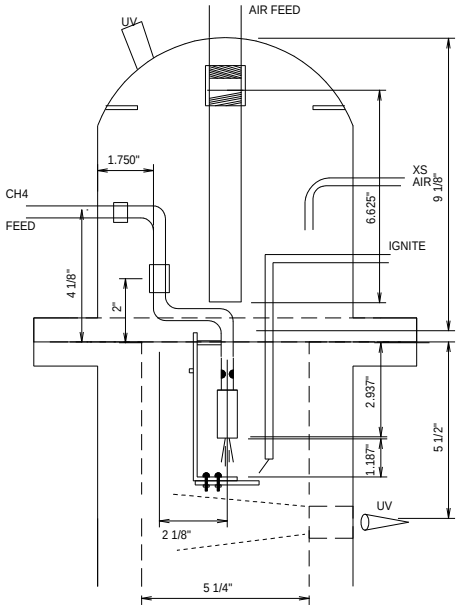

Figure 4-2. Version 3 burner showing two ignitor electrode positions as tested.

The baffle electrode was removed and replaced with welding wire electrode, and the ceramic feed-through insert on the ignitor was replaced. Table 4-2 lists ignition trials conducted at atmospheric pressure.

Table 4.x2. Ignition test results for the Version 3 burner.

Fuel Flow (scfh)	**Air Flow** (scfh)	**Result**
9	90	Flame observed for ~1-5 minutes
10+	90	Flame observed for ~1 minute
10+	178	Flame observed for <1 minute
8	180	Flame observed for ~1 minute
10+	225	Flame observed for ~1 minute
2.4	77	Flame observed for >2 hours (did not go out)
2.4	50	Flame observed for ~1-5 minutes
2.4	26	Flame observed for 1-10 minutes

The following visual observations were made from the side peeper port:

- At fuel/air ratios of 9/90, 10+/90, 10+/178, 8/180, 10+/225, the flame had a bright blue, luminous central core (the "pre-mixed" flame) and a dark blue outer region ("post-mixed" flame). Occasional luminous streaks were seen in the flame. The flame would initially be steady, with little or no buoyancy. Unsteady oscillations from side to side would begin to grow until one of these oscillations finally caused the flame to blow out.

- The pre- and post-mixed flame regions were observed at fuel/air ratio of 2.4/77. The oscillations still occurred, but with lower amplitude and frequency. This flame was steady for >2 hours and did not go out (except by operator intervention).
- At fuel/air ratio of 2.4/50, the pre-mixed (bright blue) flame was seen only intermittently from the side peeper port. The flame had very large amplitude oscillations and appeared to be more buoyant near its ends, with a lot of flickering.
- At fuel/air ratio of 2.4/26, the flame was short and very buoyant and the blue region very infrequently appeared in the field of view. Side-to-side oscillations were large but slow.

Two conclusions arose from this work:

1. Gas velocity at 100 psig is about one sixth of what it is at 0 psig at the same mass flow rate. A burner working at 0 psig must work at low feed flow rates to be scaleable to high-pressure operation.
2. Turbulence oscillations are limiting flame stability --- the burner-in-tube design (Version 5) is likely to better control turbulent oscillations.

Air Products implemented the burner-in-tube design (Version 5) in the combustor and installed it in the PDU. Combustion was achieved and sustained under high-pressure conditions (200 scfh air, 5.5 scfh methane, 100 psig). Stable flames were demonstrated with fuel:air ratios of 1:4 to 1:40 and firing rates up to twice the design rate. Soot formation was negligible under stoichiometric and fuel-lean conditions. The combustor was commissioned following separate operating campaigns of 24 and 42 hours at 200 scfh air, 5.5 scfh methane, and 100 psig feed pressure. The measured combustion gas composition was consistent with near-complete combustion of the methane; 5.6 ppm of methane and 4.0 ppm carbon monoxide were detected. A minimal amount (<1 g) of soot was recovered collectively from the combustor head, the PDU pressure vessel, and from a downstream filter. Analysis of the soot indicated two types of particles differing by composition: one type was predominantly composed of carbon and represents the majority of the powder; the second type consisted of metals including titanium, chromium, manganese, tungsten and iron.

The combustor was re-fitted with a modified sight glass window to enable them to better withstand the thermal stress in the unit. In addition, excess air flow piping was re-routed to better disperse the hot combustion gases. The system was tested for one week at a 100 psig feed

pressure. At feed rates of 200 scfh for air and 5.5 scfh for methane, the combustor vessel wall and sight glass temperatures were well within the vessel ratings. Post-combustion stream composition is consistent with expectations, including very low CO (<1 ppm downstream of the ITM membrane vessel). Soot formation was very low and was restricted to light accumulations in the head of the vessel.

Air Products fitted the combustor with a retractable ignitor system (NAO, Inc.) during the TDU modifications; the ignitor works well under high pressure conditions and removes the ignitor head from the flame region when it's not in use.

Technology Development Unit (TDU) Design and Construction

Air Products carried out design of the TDU to test full-size, planar membrane modules. The existing apparatus, the PDU, was originally designed to operate with tubular membranes and was adapted to run subscale planar membranes, but was not configured to operate with full-size planar membrane structures. The design goal of the TDU was to operate modules comprising multiple full-size wafers to produce oxygen under commercially relevant experimental conditions.

The TDU comprises a feed air compressor, high-pressure combustor (see section above), line heaters, a hot-walled pressure vessel housing the ITM module, a non-permeate gas cooling system, a permeate gas cooling system, a permeate-side vacuum train, oxygen analyzers in the permeate system, a control system with burner management system, and a combustion gas analyzer. A simple flow schematic of the TDU is shown in Figure 4-3. Table 4-3 lists the operational characteristics of the TDU as designed.

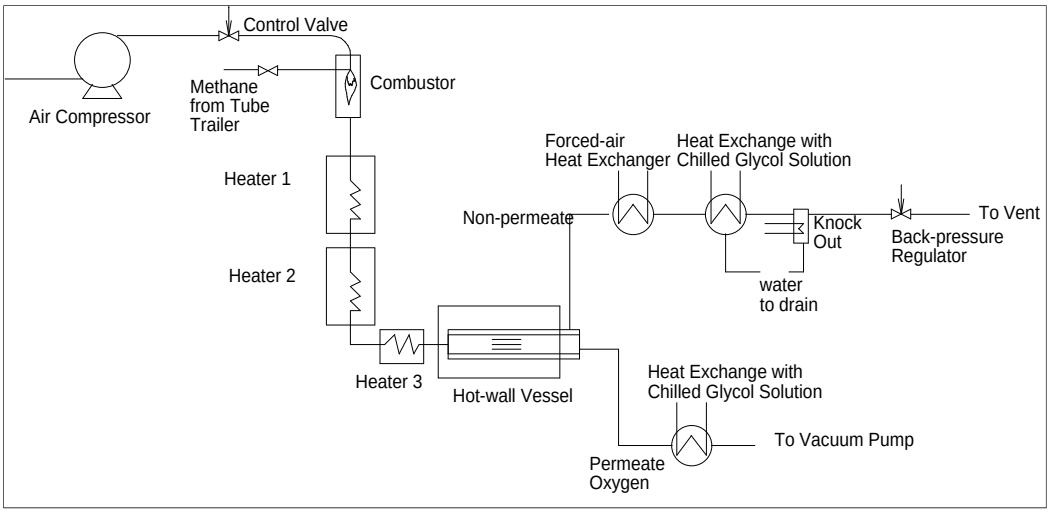

Figure 4.x3. A simple process flow diagram of the TDU. The ITM modules are housed in the hot-wall vessel during operation.

Table 4-3. TDU design control ranges of key operating parameters.

Feature	Control Range	Unit
Air Feed Flow Rate	200-4000	scfh
Air Feed pressure	0-300	psig (MAWP)
Methane Flow Rate	0-100	scfh
Methane Pressure	0-300	psig
Oxygen Product Flow Rate	0-100	scfh
Oxygen Product Pressure	100-760	Torr
Operating Temperature	25-900	°C

The TDU was built using some equipment that had been used in the PDU. The combustor, Heaters 1 and 2, the chilled heat exchangers on both the permeate and non-permeate sides of the process, and the vacuum pump were removed from the PDU and adapted for use in the TDU.

New equipment that was designed, built/purchased, and installed included the air compressor (to achieve higher flows and pressures) with a PSA dryer system, the trim heater (Heater 3), the hot-wall pressure vessel specially designed to accommodate multiple full-size planar wafers, the vessel heater, and the forced-air heat exchanger to add capability to cool the much larger volumes of non-permeate. The PDU vacuum train heat exchanger and pump had been over-sized

for the PDU, so modifications of those systems were not required; however, knock-out pots were added to condense and capture water in the non-permeate stream. The knock-out pots were fitted with timed drains to enable long-term operation with the combustor running.

Hot-Wall Pressure Vessel

The hot-wall pressure vessel and associated tube furnace were supplied by PDC Machines, Inc. (Warminster, PA). The vessel was designed to accommodate the insertion of ITM wafer modules horizontally, with the permeate gas exiting through a flange located in one end of the vessel and the non-permeate exiting through a nozzle located just downstream of the module location. Figure 4-4 shows a schematic of the vessel, which sits inside an electrically heated tube furnace. The non-permeate nozzle and main vessel flange sit outside the heated zone. The interior of the vessel was treated by Alon Processing (Leechburg, PA) to reduce chromium evolution during operation. A photograph of the vessel during fabrication is shown in Figure 4-5.

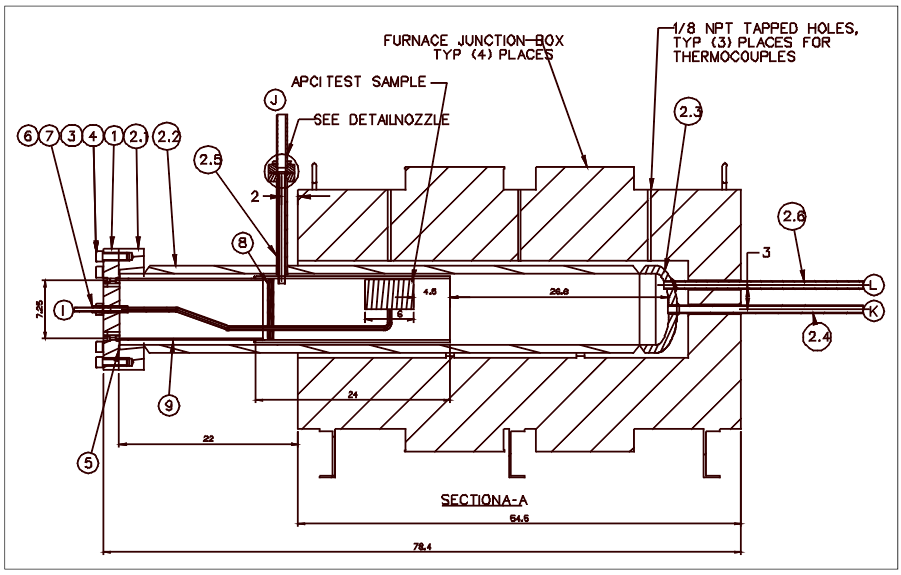

Figure 4-4. Engineering drawing of the TDU hot-wall pressure vessel housing the module and associated furnace. (Side view) Nozzle J is the non-permeate nozzle; Nozzle I is the permeate nozzle; Nozzle K is the feed air nozzle; Nozzle L is a spare and was capped.

Figure 4-5. Photograph of the TDU hot-wall pressure during fabrication.

Project Execution

The TDU construction project was initiated in Q1FY99. Table 4-4 presents a timeline of the work through completion.

Table 4-4. Timeline for TDU construction/commissioning.

Date	Item	Status
Dec. 1999	System Design Targets	Established
Jan. 2000	Compressor	Ordered
Feb. 2000	Compressor Shed	Underway
	ITM Vessel/Heater	Ordered
May 2000	Non-permeate forced-air cooler	Ordered
	Compressor	Received/Installed
	Compressor Shed	Completed
July 2000	ITM Vessel/Heater	Received
	Non-permeate forced-air cooler	Received
	Preliminary Hazards Review	Completed
	Piping stress analysis	Completed
Aug. 2000	Non-permeate forced-air cooler	Installed
	Vessel furnace	Installed
Sept. 2000	Compressor	Commissioned
	Design Hazards Review	Completed

Table 4-4. Timeline for TDU construction/commissioning (cont.).

Date	Item	Status
Dec. 2000	ITM Vessel interior treatment	Completed/Received
	ITM Vessel	Installed
	Hot piping welding	Completed
	Insulation	Installed
	Combustor Retractable Igniter (see above)	Installed
Jan 2001	Mechanical Systems	Complete
	Operational Readiness Inspection	Complete
	Safety System PLC	Installed
	System Shakedown	Underway
Mar. 2001	Vessel internals	Received
May 2001	Combustor Retractable Igniter	Successful ignition test at 100 psig
July 2001	System Commissioning	Complete

Vessel internal treatment proved to be problematic because of the alloy used for the vessel. Air Products determined that a pre-plating step was necessary, which was carried out before sending the vessel to Alon Processing. The tubing leading up to the vessel was also treated by Alon Processing. The vessel internals, precision-machined ceramic that supports the ITM module and its alloy seal cup and permeate pipe, were fabricated by CoorsTek (Oak Ridge, TN) and also proved to be difficult items to manufacture. Shakedown required six months to address flow and temperature anomalies, heater tuning, combustor ignition trials at elevated pressure, and various system safety checks having to do with the combustor system. Figures 4-6 to 4-10 are photographs of the completed unit. Figure 4-11 is a photograph showing the configuration of the TDU, vessel furnace and combustor system.

Figure 4-6. TDU ITM vessel furnace (blue) and line heater, air inlet end.

Figure 4-7. TDU ITM vessel, flange end (behind safety barrier). The forced air non-permeate cooler can be seen in the background (grey vertical box).

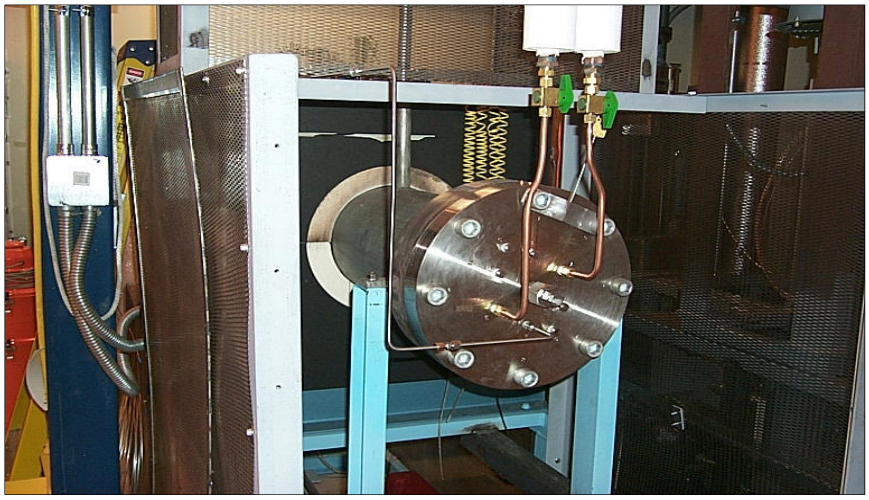

Figure 4-8. Head of the TDU vessel. Permeate exits through the center port.

Figure 4-9. TDU heaters 1 and 2 (vertical cylinders) with inlet to ITM vessel in foreground.

Figure 4-10. Permeate cooling system (skidded). A partial view of the combustion analyzer can been seen on the left (blue).

Figure 4-11. The TDU, showing the vessel furnace (foreground behind ladder) and combustor system overhead (rear mezzanine, located over Heaters 1 and 2).

PDU Testing with Combustor

With the combustor configured as described above but without the retractable ignitor installed, Air Products tested an AP98 subscale wafer module (with two wafers on a single tube) in the PDU vessel during run M32. Because the PDU vessel allows downward flow normal to the plane of the wafers, mass transfer resistance in the gas phase was relatively high during the test. The system was brought to 850°C, 100 psig and 300 Torr permeate pressure; two temperature trips occurred during the temperature ramp. Despite these excursions, a total permeate flow rate was established at ~40 ccm (70°F/1 atm) at a product oxygen purity of ≥90%. Through a software programming error, the system then underwent eight consecutive controlled permeate pressure excursions between 300 Torr and 760 Torr. Flux was re-established and remained steady for over 18 hrs. Feed pressure was then ramped to 0 psig, and the combustor was ignited to achieve 15.5% oxygen feed to the wafer. Pressure was ramped to 75 psig, but the flame was lost when attempting to ramp to 100 psig. Pressure was ramped to 0 psig in preparation for re-ignition, but the unit shut down because of an electrical equipment failure.

Upon removal from the PDU vessel, the module was found to be in excellent shape, with its silver-plated U-ring seal remaining tightly in its holder.

TDU Testing with the Combustor

Air Products carried out the first experiment with the TDU, which was also the first flux test of a full-size wafer. Ceramatec supplied the single-wafer AP2K module (FS-2). Air Products pressed the module into an alloy seal cup with a U-ring-type ceramic-metal seal and loaded the assembly into the TDU.

During heat-up, the module underwent two temperature excursions: 1) a mild (20°C) rise and fall at 440° C caused by an ambient temperature excursion, and 2) a 180°C drop from 780°C over seven hours caused by an unanticipated shutdown of the main vessel furnace at the end of a temperature ramp. During pressurization, the module underwent three sudden pressure losses caused by trips during start-up of the vacuum system. System pressure dropped from 100 psig to 60 psig, 100 psig to 83 psig, and 200 psig to 120 psig on the three occasions. Ultimately, the module was brought to steady conditions at 200 psig feed pressure and 350 Torr at >800°C. Oxygen flux was recorded within 10% of the expected flux at experimental conditions and reached a maximum purity of 75%. These conditions were maintained for 100 hours, at which

point the sample was cycled to ambient pressure conditions (0 psig feed, 760 Torr permeate) and then back to 200 psig, 760 Torr. Following this cycle, oxygen purity fell to ~46%.

The combustor was lit off subsequently with a stoichiometric fuel:air ratio to effect ignition. The ignition caused a sudden pressure wave that burst the rupture disc in the system (rated at 300 psig) and shut down the unit. The module failed at that point. The system was cooled, and the module was inspected. The wafer cracked in many places though remained assembled. Darkened areas were noted along the wafer edges and on the wafer on the trailing side of the tube/end cap, which make patterns consistent with the anticipated velocity profile. The tube was also fractured at the U-ring level.

Air Products examined the wafer of this module with SEM/EDS. The darkened areas, which appeared consistent with regions of lower air flow velocity, had porous surfaces, while lighter areas were only slightly pock-marked. The pores in the darker areas were roughly 0.2 μ in breadth. Particulate impurities on the wafer surface include Cr and S. No significant quantities of carbon were found. The bottom of the wafer was uniformly darkened, while only the top of the module showed the light and dark areas.

Achievement of the Target Flux

Air Products operated the VP-SLTRs as described under Task 1.2 with a number of subscale modules over various operating conditions. One goal of the experiments was to obtain the target flux rate, which was achieved with AP2K submodules. Selected data from Table 1-18 are reproduced here in Table 4-5. Three subscale modules exceeded the flux target without correcting the flux for membrane thickness. The membrane thicknesses of Modules 28 and 52 were below the target. With Module 56, however, the membrane exceeded the target thickness, yet the flux still exceeded the target. These data completed the milestone and clearly demonstrated that commercial oxygen fluxes are achievable with the AP2K material at a manufacture-able membrane thickness.

Table 4-5. Subscale wafer module flux data obtained with the VP-SLTRs.

	Normalized quantities, %			
Module	**Flux**	**Membrane thickness**	**Corrected Flux**	**Time on stream*, h**
28	125	70	88	466
52	102	90	92	2100
56	103	105	109	3180

TASK 6.0 TABLE OF CONTENTS

6.0 MATERIALS DEVELOPMENT 3

6.1 MEASUREMENT OF ITM OXYGEN MATERIAL PROPERTIES 3

Creep Testing 3

Tensile Creep Testing 3

Compressive Creep of Dense AP2k Discs 7

Flexural creep of dense AP2k 10

Stress Rupture Testing of AP2k Tensile Samples 12

AP2k Slow Crack Growth Testing (SCG) 15

Chemical Expansion Verification Unit (CEVU) 20

Background 20

Apparatus and Experimental Method 20

Results 22

Materials Summary 24

Elastic Modulus 24

Hardness 24

Fracture Toughness 25

Strength 25

Tensile creep 29

Compressive creep, preliminary data 30

Slow crack growth, 4-pt flexure, at operating temperature 30

Expansion as a function of temperature and oxygen vacancy fraction 31

6.2 SPECIFICATION OF ALLOWABLE PROCESS GAS COMPOSITION 31

Background 31

Contaminants 31

6.3 DEVELOPMENT OF ITM OXYGEN MATERIALS 33

Catalyst Coating 33

Protective Layer Specification 36

Nitrogen Bisque 38

Porous Layer Life 40

Background 40
Experimental Procedure 40
Results 41

TASK 6.0 MATERIALS DEVELOPMENT

6.1 Measurement of ITM Oxygen Material Properties

Creep Testing

Tensile Creep Testing

Results

Penn State conducted creep assessments of AP2k in air. The samples were tested at three temperatures using applied stresses of 1, 2, 3, and 4 ksi. Figure 6-1 shows the stress/strain relationship at the three temperatures.

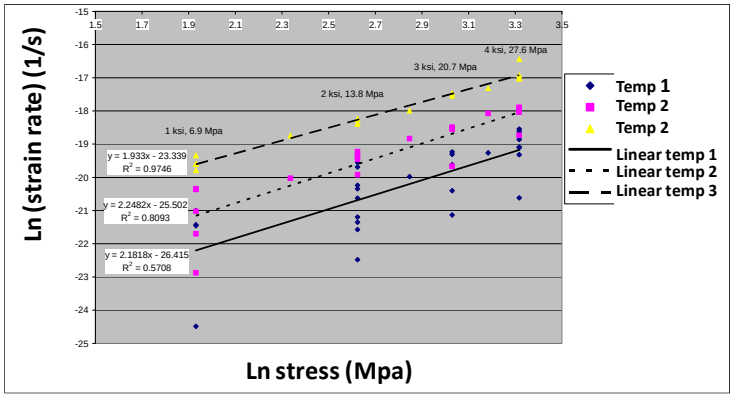

Figure 6-1. AP2k stress/strain relationship at three temperatures.

Tests conducted at the highest temperature showed little scatter in the data, while results for the lower-temperature tests show much more scatter. Some of the scatter may be attributable to differences in grain size. The average stress exponents were 1.87±0.32, 1.96±0.25, and 1.94±0.27 for the three lowest temperatures. A stress exponent of around two is typically attributed to an interface reaction that is slower than diffusion and thus controls the creep rate.

Tensile creep models were regressed against the tensile creep data from Penn State. The models differed in the value of the stress exponent used. The first model regressed the stress exponent, while the second and third models assumed stress exponents of 1 and 2 respectively. The power law creep model fits the data well.

Figure 6-2 shows the predicted allowable tensile stress as a function of allowable strain for a 10-year membrane life. For a 10% allowable tensile strain, the allowable stress is >2,000 psi.

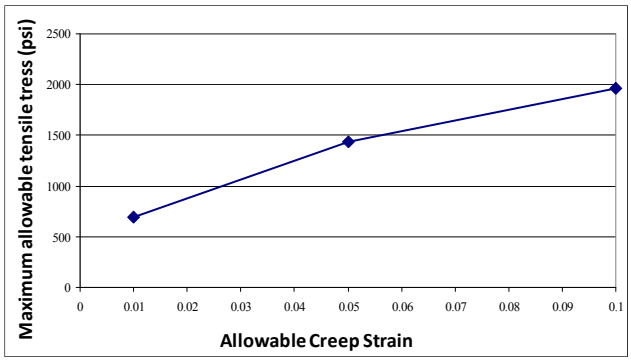

Figure 6-2. Predicted allowable stress for 10 year membrane life.

Grain size was investigated. The grain size of an untested sample was found to be equiaxed with respect to all three axes. The grain size of three samples was measured in the hot zone and the cold zone. The grains in the hot zone were slightly larger than in the cold zone and increased with strain. Grain growth during creep should decrease the strain rate for the duration of the test. The extent of this was minimal in the strain ranges experienced during the tests.

In an extension of this work, Penn State evaluated creep as a function of oxygen partial pressure (P_{O2}). Samples were tested using partial pressures ranging from 20 ppm to 100% at an elevated temperature under an applied stress. A slope of -0.30 was obtained for the oxygen dependence of creep strain rate for AP2k tensile samples (Figure 6-3). This was substantially less than the 0.09 slope estimated by Air Products based on TGA studies.

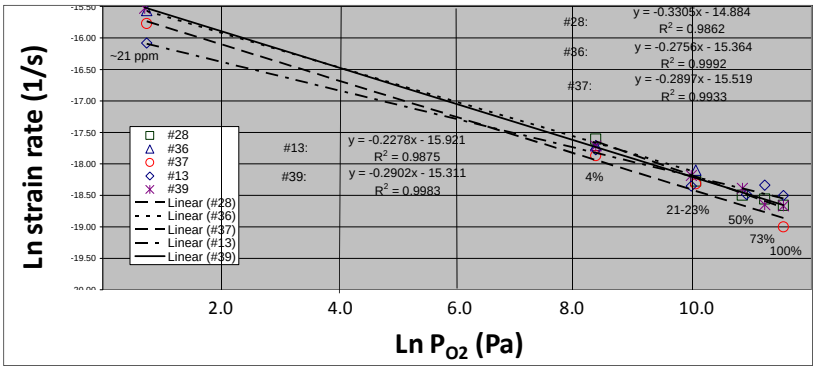

Figure 6-3. Tensile creep strain rate as a function of oxygen partial pressure for AP2k at elevated temperature under an applied stress

One possible explanation for the discrepancy was that the creep of AP2k is controlled by an interface reaction, such that the Po_2 dependence on the formation and annihilation of grain boundary defects is controlling the creep. Penns State conducted a grain boundary slide

experiment to investigate this hypothesis. A reduced gage section of an AP2k sample was polished, then scratches were introduced using both 6 μm and 15 μm diamond paste. The scratches were applied both parallel and perpendicular to the tensile axis of the sample. The sample was creep tested in tension at until failure occurred. Evidence of grain boundary sliding will appear as jogs or separations in the scratches with respect to adjacent grains. Figure 6-4 shows the resulting tensile creep curve (regions of primary, secondary, and tertiary creep).

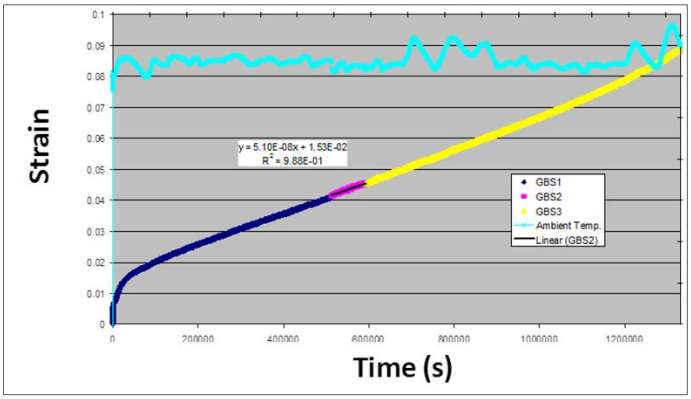

Figure 6-4. Tensile creep curve for an AP2k sample used for a grain boundary sliding test.

The primary creep in the sample could have been due to sample preparation. The sample experienced an elongation that equates to 6.6% strain. The fracture surface showed that fracture occurred along grain boundaries (Figure 6-5).

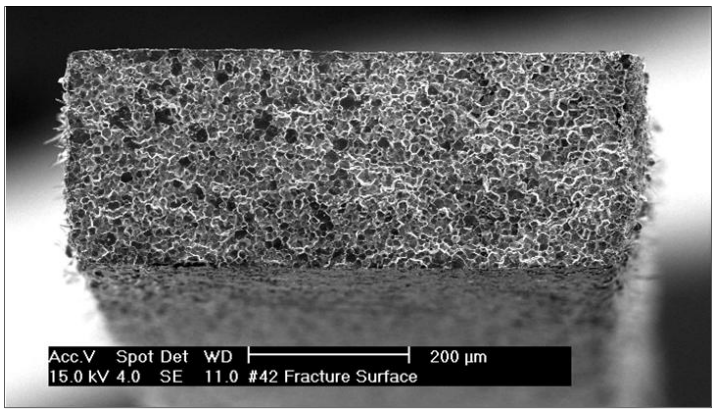

Figure 6-5. Fracture surface.

Lenticular cavities perpendicular to the tensile stress occurred throughout the reduced gage section of the sample (Figure 6-6)

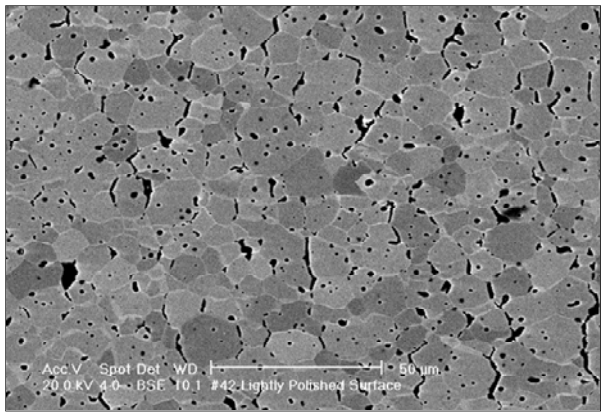

Figure 6-6. Cavitation along grain boundaries generally perpendicular to stress axis.

SEM images were analyzed to determine if grain elongation occurred during creep. Results from three fields of view indicate that there could be some grain elongation. The aspect ratio was determined by measuring the average linear intercept grain size parallel and perpendicular to the stress direction. The measured cavitation was much less than the total creep strain experienced by the sample. Sample analysis suggested that grain boundary sliding and grain rotation are likely occurring during the creep process. However, a quantitative measurement of the contribution of grain boundary sliding to the total creep strain could not be obtained.

Additional experiments assessed primary creep at an elevated temperature and under higher applied stress. Figure 6-7 shows the entire creep curve for two samples.

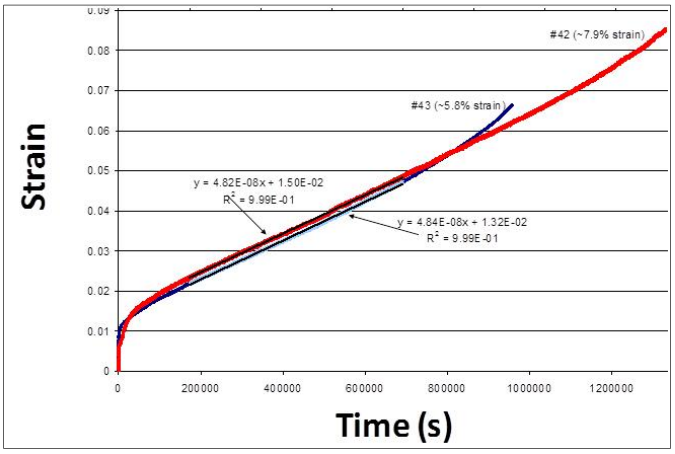

Figure 6-7. Creep curve for Ap2k tensile tested to failure.

Both samples exhibited all three creep regimes: primary, state-steady, and tertiary. While the steady-state creep rates for the two samples are essentially the same, one sample experienced

more total strain. It was conjectured that significant primary creep occurs only at higher temperatures and stresses. The impact of water partial pressure on creep was also investigated. No influence was found.

Compressive Creep of Dense AP2k Discs

Apparatus and Experimental Method

Penn State prepared AP2k sample discs for compressive creep experiments. A hole was drilled through a rod of aluminum that was sectioned in half to form a crescent shape to help align a stack of AP2k discs. The aluminum form was temporarily glued to a loading platen. The AP2k discs were stacked within the semi-circle of the aluminum form, and two thin lines of glue were run along the stack of AP2k discs to hold them in place while putting the sample into the furnace. After the glue dried, the aluminum form was removed and a small amount of glue was placed around the circumference of the AP2k discs and the alumina loading platen. After drying, the AP2k discs/alumina platen was inverted, placed on the center of a second alumina loading platen and glued in place around the circumference of the AP2k discs.

A small V-notch was cut from the platen at its outer diameter to permit a fused silica push rod to contact the bottom alumina loading platen. This fused silica push rod measured the expansion/contraction of the loading system via a length transducer mounted above the furnace. Directly across from the V-notch, a section of the outer diameter of the alumina loading platen was reduced in thickness. A second fused silica push rod rested against the thinned section of the alumina loading platen and tracked the deflection of the AP2k discs from length transducers mounted above the furnace.

The assembly was placed in a furnace. The upper loading ram was then lowered against the upper alumina loading platen and a small preload was applied to the discs. The system transducer/push rod was positioned against the lower alumina platen, followed by the sample transducer/push rod on top of the upper alumna loading platen. Figure 6-8 shows a schematic of the compressive creep test rig.

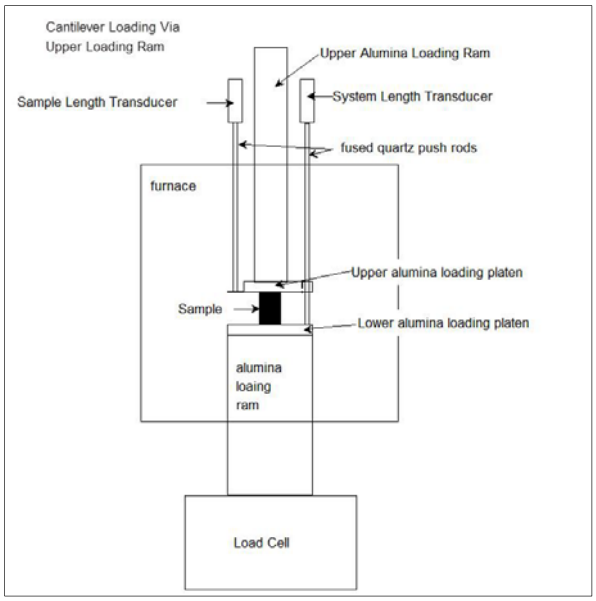

Figure 6-8. Compression creep test rig.

The sample was heated to the desired test temperature and held overnight to thermally and chemically equilibrate. The following day, the desired load was applied to the sample to achieve applied stresses ranging from 1 to 4 ksi. Data was logged to a computer.

Results

The tests were conducted at three temperatures at stresses of 1, 2 and 4 ksi. A total of 26 tests were completed. Figure 6-9 is a Ln stress/strain plot of the data.

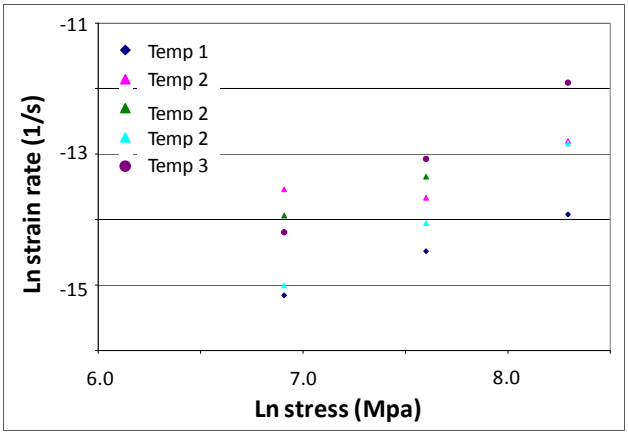

Figure 6-9. Compressive creep strain rate as a function of applied stress for AP2k dense discs.

The compressive creep data was regressed using a multi-variable regression package. The power law expression for creep rate is given by

$$\dot{\varepsilon} = A_{creep}\sigma^{n}e^{-E_{creep}/RT}$$

Three cases are considered: the best fit value of n, n=1, and n=2. Plots comparing the data to the three models are presented in figures 6-10, 6-11 and 6-12.

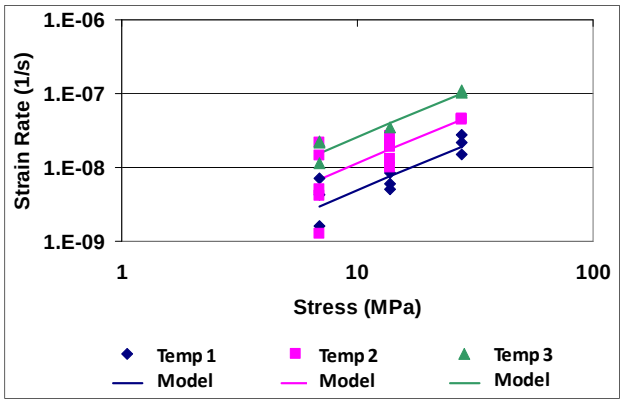

Figure 6-10. Data and model predictions for power law compressive creep model for dense AP2k (all parameters regressed).

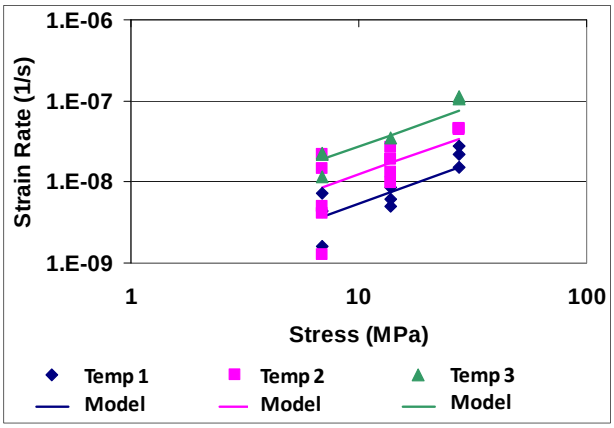

Figure 6-11. Data and model predictions for power law compressive creep model for dense AP2k, n=1.

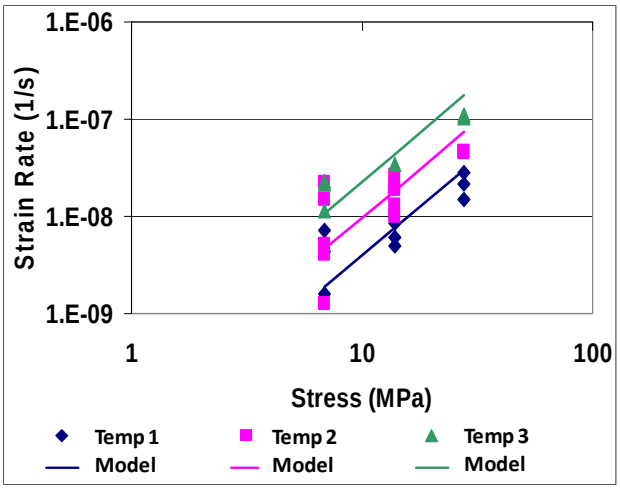

Figure 6-12. Data and model predictions for power law compressive creep model for dense AP2k, n=2.

Flexural creep of dense AP2k

Results

Penn State completed flexural creep testing at applied stresses of 1 to 4 ksi at three elevated temperatures on eight samples. Figure 6-13 is an example of a strain/time plot.

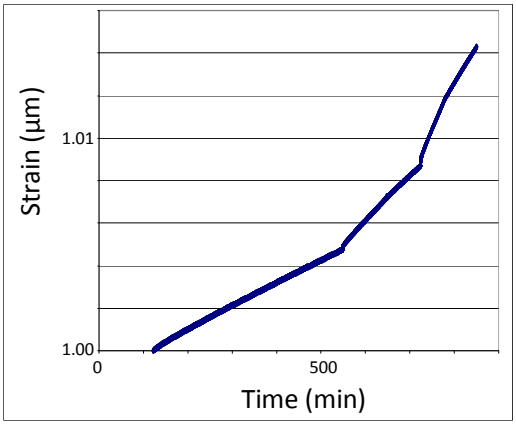

Figure 6-13. Flexural creep strain as a function of time for AP2k Sample #1.

Figure 6-14 plots the data used to obtain the creep stress exponent.

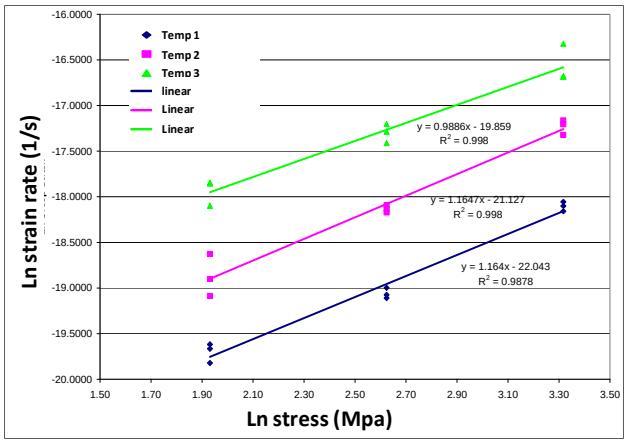

Figure 6-14. Ln creep strain rate (1/s) as a function of ln stress (MPa) for the test temperatures for AP2k flexure bars.

Based on the eight samples tested for flexural creep, the average stress exponent is 1.11±0.18. The average flexural creep activation energy is equivalent to that obtained from tensile testing. The flexural creep stress exponent is lower than that for tensile creep (i.e., 1.84±0.05).

Additional flexural creep testing was done to determine the impact of the AP2k material stoichiometry. Eight samples were tested at three stress levels. It was concluded that the modest stoichiometric shifts does not impact creep rate.

Penn State studied the effect of grain size on creep rate for AP2k samples tested at an elevated temperature in air via four-point flexure. Figure 6-15 presents the results.

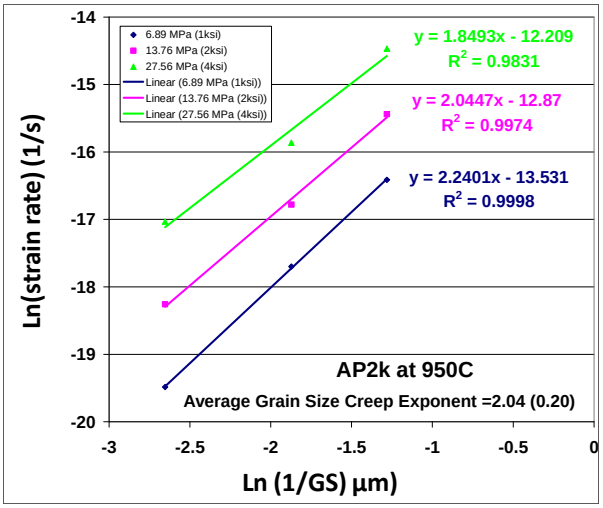

Figure 6-15. Ln-Ln plot of creep strain rate versus inverse grain size for AP2k bend bars tested at an elevated temperature in air.

The creep grain size exponent for AP2k appears to be 2.04±0.20. This indicates that Nabarro-Herring creep or lattice diffusion is controlling the creep rate, although the stress exponent is consistently greater than one.

Stress Rupture Testing of AP2k Tensile Samples

Penn State conducted an extensive and lengthy study into the stress rupture characteristics. Samples were stressed at 90%, 75%, and 50% of the average fast fracture strength. The average tensile fast fracture strength of 75 MPa at elevated temperature was determined by performing a volume-based Weibull statistical scaling of the strength distribution of AP2k bend bars. The preliminary predicted time-to-failure, based on tensile creep data and at 75% of the average fracture stress, was about 43 days and 90 days at 37.5 MPa (50%). Figure 6-16 is an example creep versus time plot.

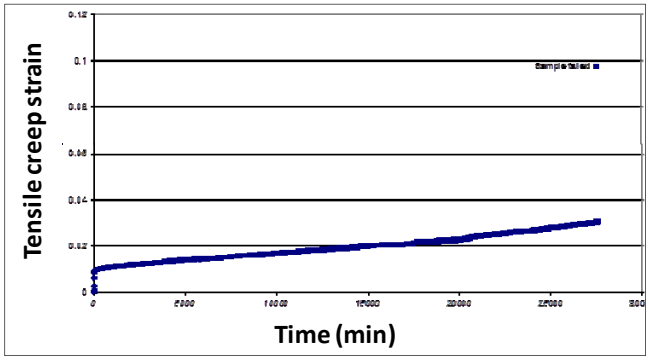

Figure 6-16. Tensile creep strain versus time plot for AP2k stress rupture Sample #154 at75% of average fracture stress.

Significant difficulties in obtaining valid data were encountered during the study. Numerous equipment modifications were made that increased the probability of a successful test, but the majority of trials were unsuccessful. Table 6-1 is a listing of all the test data. A "Y" indicates valid data and a "N" indicates invalid data.

Table 6-1. Stress rupture experimental data.

Sample #	Rig #	Stress Level	Time-to-Failure	Valid Test	Comments
		% of Ave FS	(min)	Y or N	
122	**9**	**90**	**20.9**	**Y**	**0.98% Strain to failure**
124	**10**	**90**	**3.1**	**Y**	**1.25% Strain to Failure**
125	**11**	**90**		**N**	**Failed during loading at top hole in tab region**
126	**12**	**90**		**N**	**Failed loading in gage length**
130	**9**	**90**		**N**	**Failed loading in gage length**
133	**10**	**90**		**N**	**Failed loading in gage length**
134	**11**	**90**		**N**	**Failed loading in gage length**
135	**12**	**90**		**N**	**Failed during loading at top hole in tab region**
160	**9**	**90**		**N**	**Failed loading in gage length**
162	**10**	**90**		**N**	**Failed during loading at top hole in tab region**
163	**11**	**90**		**N**	**Failed loading in gage length**
164	**12**	**90**		**N**	**Failed loading in gage length**
89	9	75	0.0	N	Failed Loading Sample
85	9	75	23125.5	Y	16.05 days,2.5% Strain to failure
90	10	75	180.3	N	Failed at retaining ring
86	10	75	162.0	N	Failed at Upper Retaining ring
107	10	75	540.0	?	
109	10	75	0.0	Y	Failed during loading within GL
140	10	75	12.7	?	
143	10	75	138.9	Y	
147	10	75	0.2	Y	
91	11	75	0.0	N	Failed at retaining ring
88	11	75	405.0	N	Failed from hole in end of sample
111	11	75	2.1	N	Epoxy Failed
113	11	75	26.9	?	
141	11	75	3.2	N	Failed at lower retaining ring
144	11	75	0.0	N	Failed loading sample at retaining ring
148	11	75	112.8	Y	
92	12	75	0.0	N	Failed just after loading, retaining ring
89	12	75	0.0	Y	Failed in GL at lower end
112	12	75	7.0	N	Failed from hole in tab region
114	12	75	4.9	N	epoxy failed
142	12	75	0.0	N	Failedloading from hole in tab region
146	9	75		N	epxoy failure, New in-line loading desgin
145	12	75	0.0	N	Failed loading the sample
150	9	75	22641.3	Y	15.7 days, 2.77% Strain to failure
151	10	75	335.0	N	Failed from hole in top tab region
149	10	75	423.0	N	Failed from hole in top tab region
152	11	75	30106.0	Y	20.9 days, 25.8% Strain to Failure
153	12	75	0.0	Y	Failed loading within gage length
154	12	75	33225.7	Y	23.1 days, 29.4% Strain to Failure
115	9	75	27520.9	Y	19.1 days, 3.04% Strain to Failure
116	10	75	35288.7	Y	24.5 days, 3.22% Strain to Failure
118	9	75	16237.1	Y	11.3 days, 2.80% Strain to failure
119	10	75	0.4	Y	Failed just after loading
120	11	75	32302.6	Y	22.4 days, 3.33% Strain to failure
121	12	75	37231.3	Y	25.9 days,4.14% Strain to failure
75	13	50	211104.0	Y	146.6 days, 3.03% Strain to failure
93	13	50	73128.5	N	Failed in gage length, 50.8 days, TC problems
105	14	50	201458.6	Y	139.9 days, 4.04% Strain to fail
101	15	50	62.0	N	Epoxy Failed
104	15	50	0.0		Failed Loading
106	15	50	170831.9	Y	118.6 days, 7.14% Strain to failure
98	16	50	6470.0	N	Failed after 6470min at hole in top tab

Based on the limited amount of stress rupture data, the preliminary stress rupture analysis using the Larson-Miller method yields a Larson-Miller parameter (LMP) of 24.48. The LMP is related to the stress rupture relaxation energy (Qr) and the rupture strength (Sr) of the material via the expression:

$$\ln Sr = 2.3E-(B/R)\ Qr \qquad [1]$$

where E and B are empirical constants derived from the best fit to the data based on an Arrhenius plot. R denotes its usual meaning: the ideal gas constant. The stress rupture relaxation energy (Qr) is related to the time-to-failure (t_f) via the expression:

$$Qr = RT\ (\ln t_f + C) \qquad [2]$$

where T is temperature in Kelvin and C is effectively a constant.

Substituting Equation 2 into Equation 1 and plotting ln Sr versus ln t_f yields a slope of -0.1295 and thus, B and E were estimated to be 148.7 and -2.38E+05 respectively. C was estimated to be 13.3. Figures 6-17 and 6-18 illustrate the results of a Monkmann-Grant and Larson-Miller stress rupture analyses respectively.

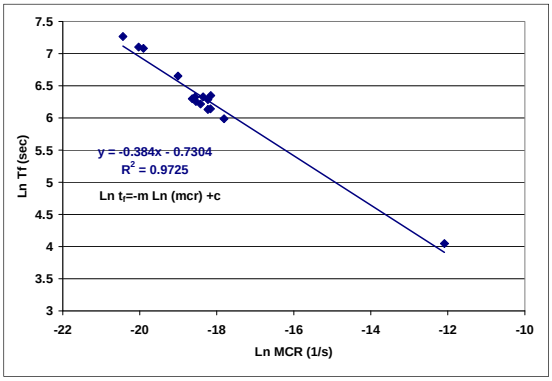

Figure 6-17. Stress rupture results for AP2k via Monkmann-Grant analysis.

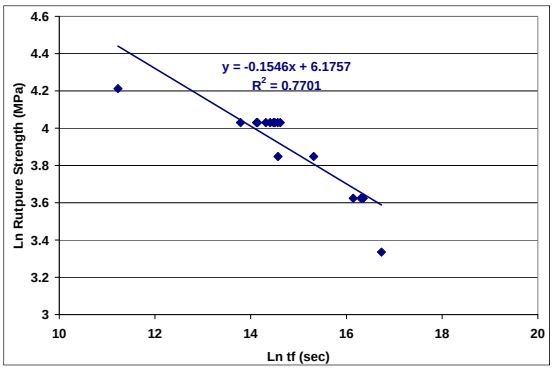

Figure 6-18. Stress rupture results for AP2k via Larson-Miller analysis.

Unlike the Larson-Miller method, the Monkmann-Grant method does not yield a master stress rupture creep curve for all temperatures, but rather an individual linear slope at different temperatures (Figure 6-19). For the higher-temperature data, both the stress rupture and the two tensile creep data sets fall on the same slope.

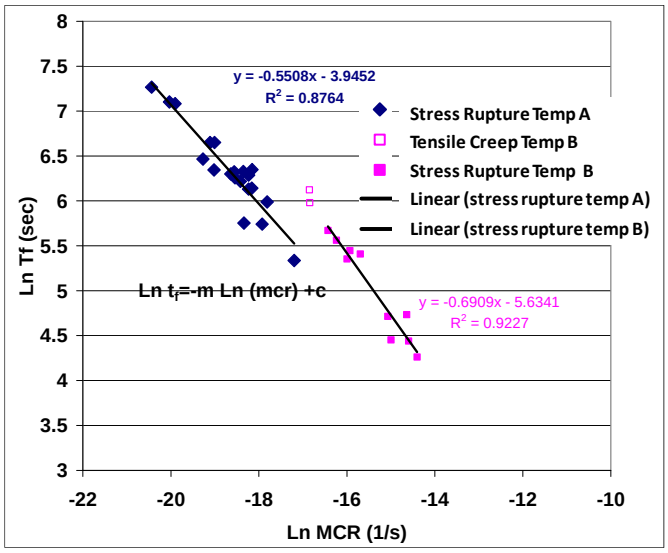

Figure 6-19. Monkmann-Grant plot of stress rupture data tested at two temperatures.

AP2k Slow Crack Growth Testing (SCG)

Penn State determined the strength properties of AP2k bend bars as a function of temperature and stressing rate to assess the susceptibility of AP2k to slow crack growth at various temperatures. Four-point flexural strength tests were conducted using strain rates that span four orders of magnitude.

Slow Crack Growth at Elevated Temperature

Figure 6-20 shows representative stress versus time plots at three strain rates at an elevated temperature.

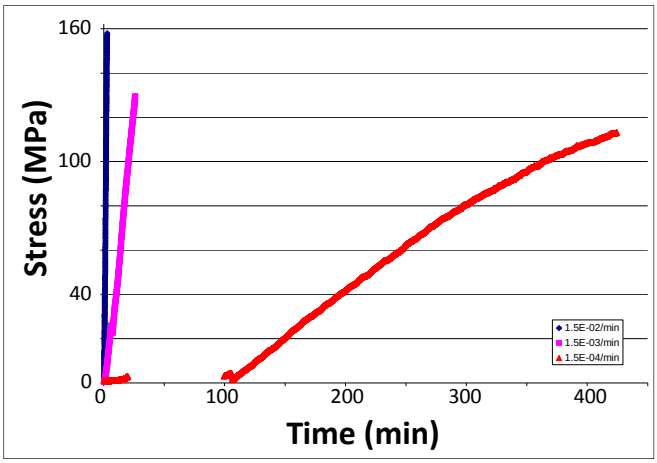

Figure 6-20. Stress as a function of time for AP2k flexure bars tested at three different strain rates.

Based on the above and other data, the slow crack growth susceptibility parameter AP2k at elevated temperatures is 286. Thus, AP2k is not susceptible to slow crack growth at these temperatures.

Slow Crack Growth of AP2k at 275ºC

As a first step in performing the threshold stress intensity testing, the sample was subjected to a 10N Vicker's indent in the center of the tensile surface of the AP2k bend bar. The sample was then loaded onto a 4-point bend fixture, placed a furnace and on top of the Instron lower loading ram. A 1-2N preload was applied to the sample, and the Instron was placed in load control to maintain the preload during heating and thermal equilibration. Next, the Instron was switched over to rate control and the sample was loaded. Upon reaching the desired load, the Instron was switched back to load control to maintain the desired load for 4-8 hours. If the sample survived the 4-hour hold, it was loaded to failure using the rate control mode.

Slow crack growth (SCG) testing of AP2k bend bars at 275ºC in air predicted a SCG susceptibility parameter of 67, which indicated that very little SCG occurs at this temperature. Additional experiments were conducted to determine the onset of SCG at temperature near 275ºC. Table 6-2 presents the data, including other temperatures, and Figure 6-21 plots the data.

Table 6-2 Strength and SCG susceptibility comparison for AP2k bend bars as a function of temperature.

Lot	Temp. (C)	# of samples	tressing Rate (MPa/sec	Ave Str (StDev)	N
Previous	RT	10	451	75.1 (13.9)	14
		10	45.1	69.9 (3.7)	
		10	4.51	61.5 (10.2)	
		10	0.451	46.8 (5.8)	
Current	RT	5	451	77.6 (12.1)	17
		5	45.1	69.1 (11.3)	
		5	4.51	61.1 (9.3)	
		5	0.451	53.0 (6.7)	
Current	175	5	451	52.9 (7.1)	304
			45.1		122^
			4.51		
		5	0.451	50.0 (8.2)	
		5	0.0451	52.0 (4.8)	
Previous	275	10	451	51.7 (12.0)	67
		10	45.1	48.4 (12.7)	
		10	4.51	53.2 (13.2)	
		10	0.451	44.8 (8.3)	
Current	275	5	451	76.5 (20.9)	27
		5	45.1	72.1 (16.2)	
		5	4.51	63.5 (6.4)	
		5	0.451	60.6 (12.1)	
Current	375	5	451	75.0 (10.6)	
			45.1		
			4.51		
		5	0.451	76.4 (6.7)	
^ - N value based only on the two fastest stressing rates)					

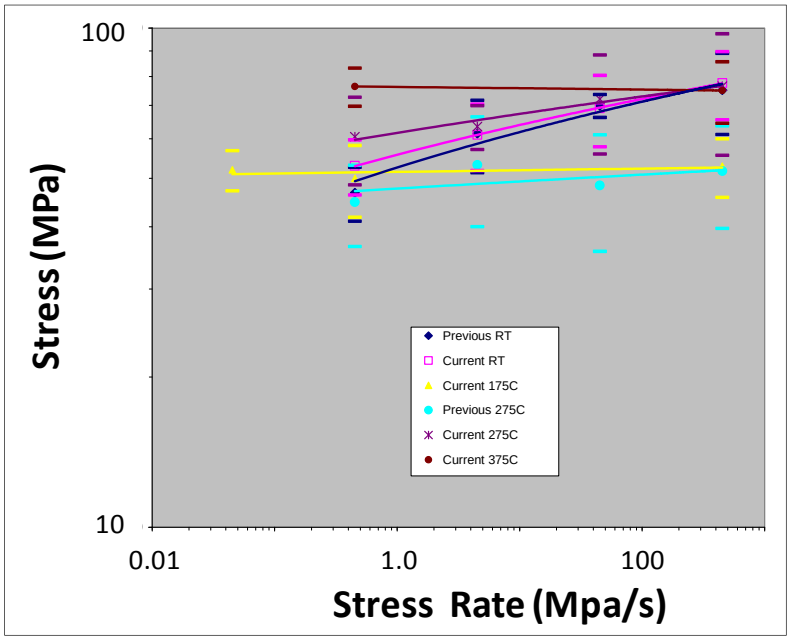

Figure 6-21. Strength versus stressing rate plot for AP2k as a function of temperature

The slope (used to determine N) of the two lots is not that different when taking into account the standard deviations of the strength data. Thus, the difference between the N values of 27 and 67 is not as dramatic and the numbers suggest.

Room Temperature Slow Crack Growth (SCG) of AP2k Bend Bars

Based on the stress rate/time data, AP2k at room temperature has a SCG susceptibility parameter (N) of 13.9, which is similar to glass. The lower the value of N, the more susceptible the material is to SCG behavior. The source of the SCG behavior could be environmentally induced (e.g., from humidity as in glasses) or from residual stress.

Penn State performed a series of static hold tests with a 10N indent to determine the threshold stress intensity for slow crack growth at room temperature. A sample was subjected to one of a series of loads which produced a certain percentage of the fracture toughness stress. The sample was held at load for either four or eight hours. If it survived, it was loaded to failure. The resulting strength was compared to the fast fracture indented sample strengths. A reduction in strength indicated that the sample underwent SCG during the static hold, but it was not sufficient to cause failure. The stress at which SCG is observed is defined as the threshold stress intensity. All samples survived, and the results indicated that the threshold stress intensity was approximately equal to 27% of fracture toughness, which is below the threshold for SCG.

Additional indentation-strength tests were conducted on AP2k bend bars at room temperature in air and in water. Five different stressing rates were used which ranged from 335 to 0.00335 MPa/s with each rate decreasing by an order of magnitude. Figure 6-22 plots the data. The results show that AP2k does exhibit significant slow crack SCG at room temperature, and the measured SCG susceptibility parameter (N) for both air (15.9) and water (19.4) are very similar.

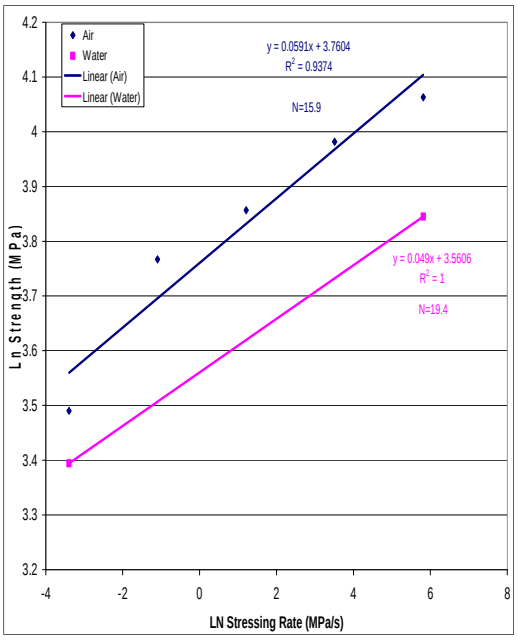

Figure 6-22. Indentation-strength of AP2k tested at room temperature in air and water as a function of stressing rate.

Elastic Moduli of AP2k as a Function of Temperature

Figure 6-23 summarizes the Young's and shear moduli data for iso-pressed AP2k samples as a function of temperature.

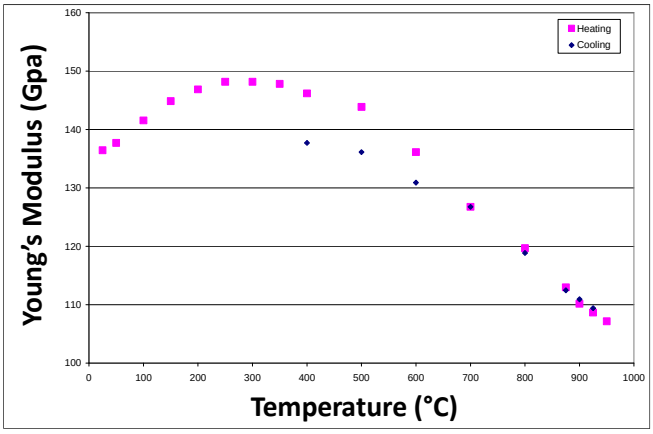

Figure 6-23. Young's moduli of iso-pressed AP2k samples as a function of temperature from 25ºc to 950ºC.

There was a gradual increase in the Young's modulus from room temperature to 250ºC. From 250ºC to 350ºC, both the Young's and the shear moduli remained constant. At temperatures above 350ºC, a gradual decrease with temperature was observed. No hysteresis behavior was observed on cooling.

Biaxial Strength of 55mm Dense AP2k Disks at Elevated Temperature

Biaxial flexure strength tests were conducted by Penn State. An average strength of 123.5±37.8 MPa was obtained at elevated temperature, which was slightly greater than that measured at room temperature (90.4±30.4 MPa). Weibull analysis of the strength distribution (Figure 6-24) obtained at an elevated temperature yielded an unbiased Weibull modulus and characteristic strength of 3.41 and 135.99 MPa respectively.

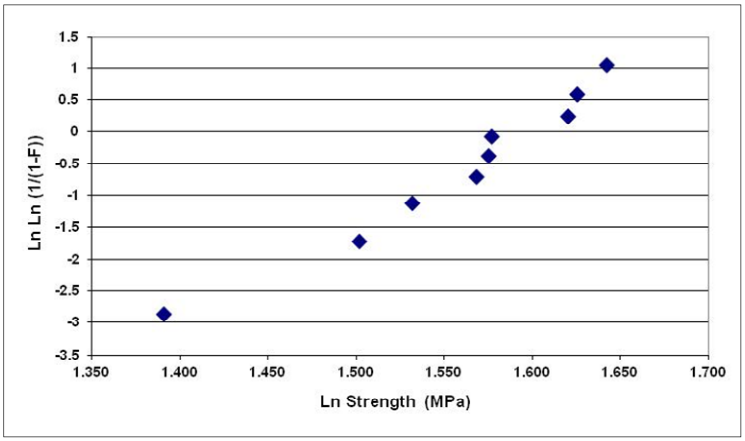

Figure 6-24. Weibull plot for dense AP2k biaxial flexure disks tested at elevated temperature.

Chemical Expansion Verification Unit (CEVU)

Background

A Chemical Expansion Verification Unit (CEVU) as described under Task 7 was constructed by Penn State to determine whether the non-stoichiometry and expansion constitutive relations determined on simple specimens were applicable in regions with vacancy gradients. A mechanical model of the disk membrane was used to fit the deflection data and extract the chemical expansion parameters of the material.

Apparatus and Experimental Method

The CEVU in part consisted of an ITM ceramic disk on top of an inert tube (Figure 6-25).

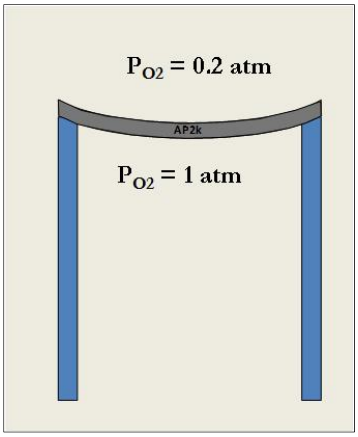

Figure 6-25. Simple schematic of the proposed chemical expansion measurement. An oxygen partial pressure gradient is applied to a thin disk of ITM material (grey), supported on an inert tube (blue).

The atmosphere beneath the disk (within the tube) and above the disk (outside of the tube) are independently controlled. The disk is simply supported at the radial position of the tube inner surface. The premise behind the apparatus is to take advantage of the expansion properties of the ITM ceramics to enable measurement of the degree of expansion. ITM material expands as the P_{O2} decreases. Thus, applying a P_{O2} gradient across an unconstrained disk membrane composed of ITM ceramic will result in a measurable deflection. Deflections of the disk created by the chemical expansion response to different applied atmospheres were transmitted to measurement electronics by a push rod located at the center of the disk. A schematic of the concept is shown in Figure 6-26.

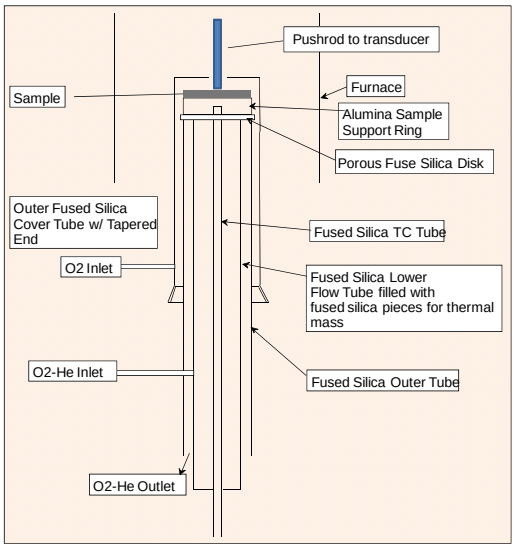

Figure 6-26. Schematic of the CEVU experiment.

The apparatus is placed in a furnace, and a transducer measured the deflections through a push rod. One end of the push rod is connected to the transducer, while the other rests against the membrane, as shown in Figure 6-27. Separate gas mixes are prepared and metered into the apparatus outside and inside of the tube supporting the membrane.

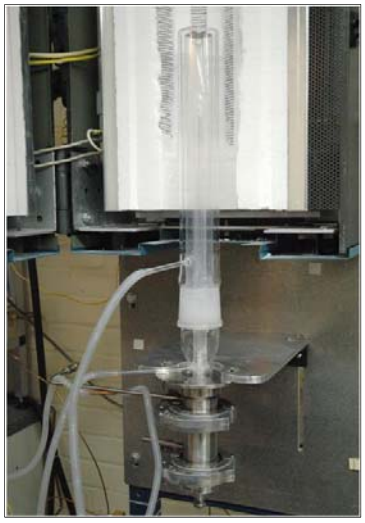

Figure 6-27. Photograph of the working CEVU experiment at the Penn State laboratory.

McDermott/SOFCo and Ceramatec modeled the response of the disk in the CEVU experiment for a range of experiments (see Task 7.3). Under Task 6, Penn State improved the CEVU experiment and developed the experimental methods.

Results

For reference, the deflection was measured as a function of mechanical loading. Deflection at different oxygen partial pressures P_{O2} across the disc was measured at various temperatures. Penn State conducted extensive experimentation and incorporated significant modifications to ensure that the data were accurate.

Residual Stress

A sensitivity study was conducted on the effects of residual stresses. Two scenarios for warped disks were considered. Scenario 1 was for a warped but stress-free disk, where the degree of warping was characterized by the center deflection (e.g., curvature). Scenario 2 was for a disk warped by residual stresses. It was found that for Scenario 1, as long as a warped, stress-free disk has a small initial deflection, mechanical loading yields realistic results. However, for Scenario 2,

a critical level of residual stress is needed to cause a disk to warp. Below the critical level for residual stress, up to an 85% increase in the deflection response is possible. When residual stresses are greater than the critical level, residual stresses tend to decrease deflections when the initial deflection is downward. Things get even more complicated when the initial deflection is upward. For a disk with a critical or greater level of residual stress, there exists a mechanical load level that can make the disk response unstable – a phenomenon known as snap-through. If the mechanical load exceeds the threshold for snap-through, then the disk will bow in the opposite direction (assuming the disk can survive this event). Large deflections were predicted for mechanical load levels less than the threshold for snap-through.

As a result of this work, a new testing protocol was instituted whereby room-temperature loading and unloading experiments are conducted to see if equivalent deflections result for both sides of the wafer. If the deflections are within 10% for the two sides, the sample is deemed suitable for chemical loading tests. If deflections are >10% for the two sides of the wafer, the sample is rejected.

Ferroelastic Behavior

Deflection data at temperatures below ~700°C suggested that the AP2k may exhibit ferroelastic behavior. A study determined that AP2K does not appear to be ferroelastic above 400ºC, which suggested that there is a Curie temperature below 400ºC.

Temperature Measurement

An analysis was conducted to determine the effect of temperature on deflection from chemical loading. The predicted deflection ranged from 351 μm at 875ºC to 158 μm at 800ºC for the assumed conditions of the test. The decrease in predicted deflection with temperature results from the decreasing vacancy gradient due to the increasing relative surface resistance. It was observed that deflection increases with increasing flow at low flow rates and decreases with increasing flow at high flow rates; this was qualitatively consistent with a competition between gas-phase mass transfer and disk cooling. Given the sensitivity of deflection to temperature, it was decided to baffle the top and bottom surfaces of the disk and measure the baffle temperature. Also, preheating of the incoming gas streams was improved.

Additional Improvements

Two additional modifications were made to the CEVU. An in-situ oxygen monitoring system was installed to measure any reduction in the actual oxygen partial pressure on the top side of the disc due to gas blow-by from below the sample and the support tube. The second modification was the addition of a second length transducer to measure deflection from the bottom side of the disc.

Materials Summary

Ceramatec compiled a database of AP2k materials properties. Elastic modulus, hardness, fracture toughness, strength, creep, slow crack growth rates, thermal diffusivity, thermal conductivity, thermal expansion, and chemical expansion were measured and compiled as discussed below.

Elastic Modulus

The elastic modulus was measured by two different methods: acoustic resonance and strain gauge bars loaded in four-point bending. Acoustic resonance measurements were performed at Penn State, and strain gauge measurements were performed at Ceramatec, Inc. The results are in good agreement with each other. All measurements were made on samples at room temperature that were pressed from powders.

Hardness

The hardness of AP2K was measured using indentation methods at Penn State and the University of Minnesota (through a consultancy agreement). Measurements at Penn State were made on a sample of dense AP2k formed by pressing powders by polishing to a 1 μm finish using diamond paste followed by 0.05 micron β-alumina using a felt type polishing pad in preparation for indentation. A LECO model V-100-C1 hardness tester was used with a dwell time of 15 seconds and a 0.3 kg load. The testing machine automatically calculated the hardness value. The University of Minnesota measured the hardness by using indentations with a Vickers-shaped indenter on the rim of full scale wafers. The hardness, H, was calculated from:

$$H = P/2a^2$$

where P is the peak load and $2a^2$ is the projected contact area estimated for the peak load. The measurements taken at the University of Minnesota spanned a range of -5%/+43% of the average measurement taken by the Penn State team.

Fracture Toughness

The fracture toughness of AP2K was measured by indentation measurements. The following equation was used to calculate the fracture toughness T (Pa√m):

$$T = \xi(E/H)^{1/2}(P/c_o^{3/2})$$

where ξ is a geometric constant, E is Young's modulus (GPa), H is the hardness (GPa), P is the indenter force (N), and c_o is the measured crack radius. Measurements around a mean value spanned a range of -33%/+25%.

Strength

Weibull Parameters, Four-Point Flexure

The strength of AP2K was measured numerous times as material properties evolved during development of manufacturing processes. The strength of AP2k specimens that were formed by tape casting and lamination was measured. In addition, the strength of AP2K was measured in air at elevated temperature. Typically, the strength of AP2k bar-shaped specimens was measured in flexure by four-point bending. The flexural strength of the bars, σ_{max}, was calculated from:

$$\sigma_f = 3/4(P_{max}\, l_O)/(b\, h^2)$$

where P_{max} is the maximum load at failure, l_O is the distance between the outer and inner loading points, b is the width of the bar, and h is the thickness of the bar. It is important to note that strength is not a material property. Strength is dictated, according to Griffith's theory of brittle failure, by defect size according to:

$$\sigma_{max} = Y\, T\, c^{-1/2}$$

where σ_{max} is the stress at failure, Y is a constant that accounts for the load geometry, T is the fracture toughness, and c is the size of the defect responsible for failure. For specimens with residual stresses, however, the residual stress state must be accounted for by the principal of superposition. For example, if there is a residual tensile stress of 20 MPa acting on a 10 μm flaw, in a material with a toughness of 1 MPa-$m^{1/2}$, then even though the strength of the material should be 90 MPa it would only appear to be 70 MPa from a calculation based upon the maximum applied load. Therefore it is critical to understand residual stresses in strength specimens.

Weibull parameters were calculated for AP2K bend bars in two different studies. The bars were formed by pressing powders in one study, and from laminating tape cast layers in the other.

Weibull parameters are dependent on the specimen size and stress state. The stress for a given probability of failure can be calculated from the Weibull parameters, σ_0 and m, for one specimen and loading geometry if the defect population is the same and the loading factor is known, i.e.:

$$\sigma_1(P_{F1})/\sigma_2(P_{F1}) = (K_1V_1/K_2V_2)^{1/m}{}_1$$

where $\sigma_i(P_{F1})$ represents the stress for a probability of failure of P_{F1}, K_i represents the loading factor for a particular geometry and stress state, V_i represents the volume of the component, and the index i indicates either component 1 or 2 (the Weibull parameters for component 1 are measured by experiments).

The data for mean strength, characteristic strength and Weibull modulus for AP2K specimens are given in Table 6-3. In general, the results for the strength of AP2K specimens measured at room temperature are in good agreement with each other.

Table 6-3. Strength of AP2K: four-point bending.

Specimen Type	**Characteristic Strength Relative to Baseline**	**Weibull Modulus**
RT, uniaxially pressed powders (PSU)	1.0	8.7
875ºC, air, uniaxially pressed powders (PSU)	1.44	5.1
RT, laminated tape* (CI)	0.98	6.1

Strength as a Function of Stoichiometric Ratio, Four-Point Flexure

The flexural strength of AP2K as a function of AP2K stoichiometry was also measured by using four-point bending. The results are shown in Table 6-4. The values of strength depend on the stoichiometry of the compound.

Table 6-4. Strength of AP2K: effect of stoichiometric ratio.

Relative Stoichiometric Ratio	No. of Bars Tested	Normalized Mean Strength
0.98	12	0.92±0.16
0.99	13	0.92±0.12
0.99	11	0.84±0.18
1	11	1.00±0.086
1.005	13	1.04±0.10
1.01	11	1.18±0.16
1.02	14	1.24±0.095
1.02	10	1.22±0.11

Strength as a Function of Porosity, Four-Point Flexure

The strength of AP2K as a function of porosity has also been measured by using four-point bending. Samples were made from laminating tape cast layers. Thirty specimens were tested for each value of porosity and Weibull parameters were calculated. The strength, σ, decreased with increasing porosity, P.

The results are summarized in Table 6-5. It should be noted that since experiments were performed with a limited range of values of porosity, ±4 percentage points, it is not advisable to make extrapolations to other porosity values well outside the range of values tested.

Table 6-5. Effect of porosity on AP2K strength for 25 mm specimens.

Porosity	Mean Strength Normalized	95% CI Normalized	Characteristic Strength Normalized	Weibull Modulus
0	1.00	0.85-1.15	1.0	5.6*
-4% pts	0.32	0.30-0.34	0.31	7.4
Baseline	0.21	0.19-0.22	0.22	6.2
+4% pts	0.17	0.15-0.18	0.17	4.0

* calculated from 9 specimens.

Strength as a Function of Grain Size, Biaxial Flexure

The strength of AP2K as a function of grain size was measured by using uniform pressure on disk measurements. The disk radius was ~16 mm and the inner support radius was 12.5 mm. The results are summarized in Table 6-6. Interestingly, the strength was not a strong function of the grain size. It is possible that the density plays a more important role in determining the strength

in materials with grain sizes smaller than the size of strength-limiting defects (on the order of 20 μm).

Table 6-6. Effect of grain size on AP2K strength.

Relative Grain Size	Relative density (%TD)	Mean Strength Normalized	95% CI Normalized
0.24	92.3	0.86	0.70-1.02
0.59	96.7	0.91	0.80-1.01
1.0	97.8	1.00	0.88-1.12
2.3	98	1.08	0.94-1.14

* measured on the surface of the samples.

Strength as a Function of Cooling Rate, Four-Point Flexure

The strength of AP2K materials of differing stoichiometry as a function of cooling rate and environment was measured by using four-point bending of specimens formed by pressing powders. The objective of the experiments was to determine whether the amount of residual tensile stress in AP2K components after cooling could be decreased either via slower cooling or controlling the environment such that oxygen concentration gradients were minimized. The data shown in Tables 6-7 and 6-8 indicate that the strength of AP2K increases as the cooling rate decreases, in agreement with the hypothesis that slower cooling rates lead to smaller oxygen gradients and tensile residual stresses on the surfaces of components. Samples that were cooled in controlled environments were 35-65% stronger than similar bars cooled in air at the same rate of 1°C/minute (Table 6-9). The bars cooled in controlled environments, however, were not stronger than the as-annealed bars cooled at 0.5°C/minute. Air Products later found that these experiments were dependent on the ultimate purity of the inert gas employed in the controlled atmosphere. Therefore, the strength data are provisional.

Table 6-7. Strength of 0.98 stoichiometric AP2K: effect of cooling rate.

Sample	Cooling Rate (°C/min)	No. of Specimens	Mean Strength ormalized	Std. Dev. Normalized
as-ground	50	15	1.28	0.16
ground then cooled	60	4	0.49	0.23
	30	5	0.73	0.082
	15	6	0.96	0.082
	3	6	1.07	0.11

Table 6-8. Strength of 0.99 stoichiometric AP2K: effect of cooling rate.

Sample	Cooling Rate (°C/min)	No. of Specimens	Mean Strength Normalized	Std. Dev. Normalized
as-ground	50	7	0.83	0.047
ground then cooled	60	3	0.21	0.035
	30	4	0.16	0.023
	15	4	0.33	0.082
	3	5	0.55	0.11

Table 6-9. Strength of AP2K: effect of controlled atmosphere during cooling.

Treatment	Strength Normalized	Std Dev. Normalized
cooled at 50°C/hr to 600°C, 5°C/hr 600-400°C, 50°C/hr 400-20°C, ground after cooling	1	0.11
ground, annealed at joining temp, cooled at 60°C/hr to 600°C, 30°C/hr 600-20°C	0.73	0.090
ground, annealed at joining temp, cooled at 60°C/hr to 20°C	0.47	0.15
ground, annealed at joining temp, cooled in air to 850 °C, then isocompositionally at 60°C/hr 850-20°C with T*=400°C (old model)	0.72	0.14
ground, annealed at joining temp, cooled in air to 850 °C, then isocompositionally at 60°C/hr 850-20°C with T*=400°C (new model)	0.63	0.041
ground, annealed at joining temp, cooled in air to 850 °C, then isocompositionally at 60°C/hr 850-20°C with T*=500°C (new model)	0.73	0.090
ground, annealed at joining temp, cooled in air to 850 °C, then isocompositionally at 60°C/hr 850-20°C with T*=600°C (new model)	0.77	0.069
ground, annealed at joining temp, cooled in air to 850 °C, then isocompositionally at 60°C/hr 850-20°C with T*=500°C (new model variation)	0.69	0.15

Tensile Creep

The creep of AP2K was measured at Penn State by using dog bone-shaped specimens, applied stresses ranging from 7-30 MPa, temperatures ranging from 900º to 950ºC, and oxygen

concentrations ranging from 21 ppm to pure oxygen. The creep rate, $\partial\varepsilon/\partial t$, was assumed to fit a modified Dorn equation,

$$\partial\varepsilon/\partial t = A_0\sigma^n P_{O2}{}^r \exp(-Q/R_B T)$$

where A_0 is a constant, s represents the applied stress, n is the stress exponent, P_{O2} is the partial pressure of oxygen, r is the oxygen concentration exponent, Q is the thermal activation energy, R_B is the gas constant, and T is the absolute temperature. A series of constant load experiments, as a function of temperature and stress level, were conducted at Penn State. The results are summarized in Table 6 -10.

Table 6-10. AP2K tensile creep parameters.

	900ºC	**925ºC**	**950ºC**
stress exponent , n standard deviation	1.87 0.32 (6 samples)	1.96 0.25 (4 samples)	1.94 0.27 (4 samples)
activation energy standard deviation	520 kJ/mole 49 kJ/mole (18 samples)		
exponent for oxygen concentration (Pa)		-0.3	

Compressive Creep, Preliminary Data

The creep of AP2K in compression was measured by using stacks of disc-shaped specimens, applied stresses ranging from 7-30 MPa, and temperatures ranging from 925º to 975ºC, in air. Preliminary results are summarized in Table 6-11.

Table 6-11. AP2K compressive creep parameters.

	925ºC	**950ºC**	**975ºC**
stress exponent, n	1.15	1.13	1.26

Slow Crack Growth, Four-Point Flexure, at Operating Temperature

The strength of AP2K, at operating temperature in air, was measured as a function of strain rate to determine whether slow crack growth could be detected. If slow crack growth occurs in a material, its strength will decrease as the strain rate decreases since there is more time for crack growth to occur. The results are summarized in Table 6-12. Under the conditions investigated, there was no evidence of slow crack growth.

Table 6-12. Effect of strain rate on AP2K strength.

Strain Rate (min-1)	Strength Normalized	Std Dev. Normalized (5 Specimens)
1.5 x 10-1	0.96	0.17
1.5 x 10-2	0.96	0.13
1.5 x 10-3	0.93	0.17
1.5 x 10-4	1	0.20

Expansion as a Function Of Temperature and Oxygen Vacancy Fraction

Air Products measured the combined thermal and chemical expansion of AP2K using dilatometry and thermogravimetric analysis. The expansion was found to be described by:

$$\text{Expansion (ppm)} = \text{CTE}(T-299K) + \text{CCE1}\ x_v\ (T-299K)$$

where CTE represents the coefficient of thermal expansion, T represents absolute temperature, CCE1 represents the coefficient of chemical expansion, and x_v represents the oxygen vacancy fraction. The oxygen vacancy fraction can be obtained by solving the Gibbs energy equation with an expression for the chemical potential temperature dependence of the oxygen in the solid.

6.2 Specification of Allowable Process Gas Composition

Background

The composition of the feed gas to the ITM system is not purely atmospheric gases (i.e., O_2, N_2, Ar). Compounds can be released into the feed stream from the materials in the ITM flow duct via desorption, decomposition, or as the result of chemical equilibrium-driven mass transfer. Some of these compounds can contaminate the ITM ceramic, resulting in a loss of performance. These contaminant materials must be minimized and/or removed from the feed stream to ensure oxygen flux is maintained for the projected life of the ITM modules.

The primary sources of contamination are the insulating materials and metal components in the flow duct. Studies determined the rate of contamination associated with various and metal alloys.

Contaminants

Numerous metal components of a working ITM Oxygen system contact high-temperature feed gas. At these temperatures, chromium may volatilize and contaminate the ITM material/module.

The primary contaminant gas from metals in contact with the feed gas is CrO_3. Flow path testing was conducted to determine the amount of chromium evolved from candidate alloys.

Flow Path Testing Experimental Procedure

Figure 6-28 is a schematic of the working portion of the experimental apparatus. Dry, clean air at 1 atm is introduced to a quartz tube located in a tube furnace. The tube is maintained at high temperature and contains samples of the material of interest followed by an AP2K 'witness piece.' In this case, various alloy chromium sources (foils) were studied as the test sample. Air passes over the sample, which evolves chromium into the gas phase. Any gas-phase chromium is deposited onto the AP2k target, which is later analyzed with surface techniques or fully by elemental analysis.

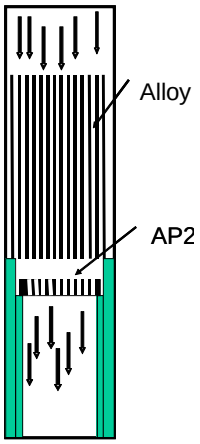

Figure 6-28. Flow path testing apparatus.

To study the evolution of chromium from metal foils, Air Products carried out runs of 168 hours' (1 week) duration, after which the AP2k witness piece was replaced with a new witness piece and the run repeated five more times. The witness pieces were examined with a scanning electron microscope and by EDS to determine the level of chromium contamination. Figure 6-29 is an example of an SEM image of one of the alloys before being tested and after six weeks at temperature.

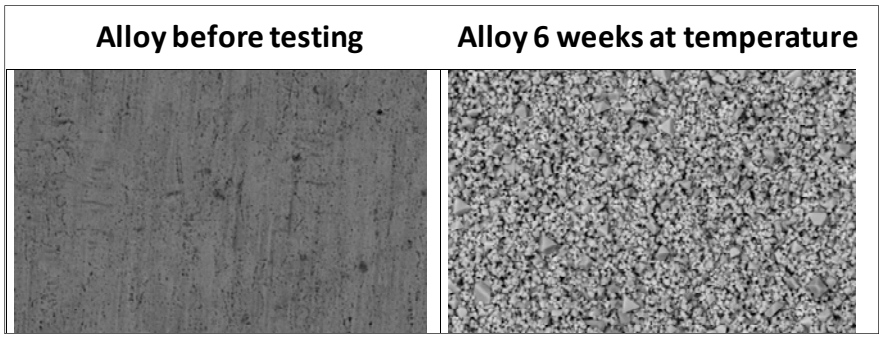

Figure 6-29. Alloy surface before testing and after six weeks at temperature.

Figure 6-30 is an example of an SEM image of an AP2k witness piece contaminated with chromium.

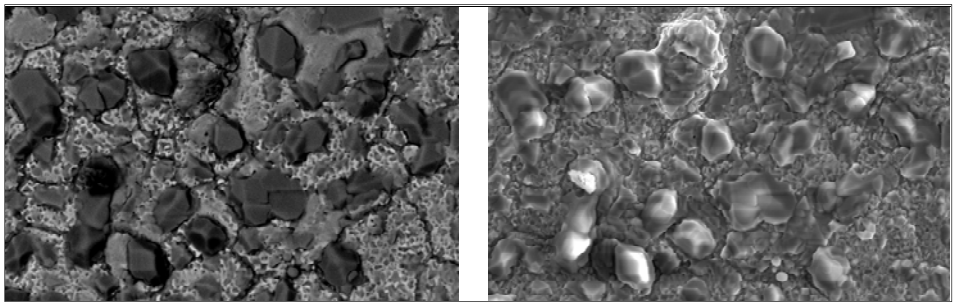

Figure 6-30. AP2k witness piece surface contamination.

Three alloys were tested with and without an applied coating. Alloy 1 cause chromium contamination. Chromium volatization was greatly minimized by the coating. Alloy 2 also caused chromium contamination, but less than Alloy A. The performance of the coated sample was only slightly better than the uncoated sample.

Alloy 3 had a higher level of contamination that Alloy 1 or 3. However, the coated Alloy 3 was very effective at minimizing chromium volatization. A 50-week test of a coated Alloy 3 sample was conducted at a higher-than-typical temperature. There was minimal chromium breakthrough.

6.3 Development of ITM oxygen materials

Catalyst Coating

Eltron Research investigated the impact of grain and particle sizes of powders used in catalyst coating on membrane oxygen permeability (flux). Batches of powder of an alternative membrane material were prepared by solid-state synthesis and the combustion reaction processes. Ceramic

disc membranes were prepared by pressing. Catalyst slurries were prepared and applied to the ceramic disks. Catalyst was applied by the dip coating procedure, where the withdrawal rate was varied.

Nine coarse-grain disks were prepared at two thicknesses. The average density, as determined by mass and geometric measurements, was measured at 87% theoretical density. Similarly, 11 fine-grain disks at two thicknesses were sintered and had an average density of 88%.

No discernible difference in permeation was observed between disks pressed from coarse powder that had been polished green and those polished after sintering. However, for disks pressed from fine powder, the permeation of disks polished green exceeded that of sintered polished disks. These results suggested a correlation between surface treatment and permeation for disks made with fine powder.

Fine-grain membranes had a slightly higher average oxygen permeation than course membranes among the thick membrane samples. The coarse-grain membrane performed better among the thinner membrane samples. There was no indication that the small particles improved catalytic performance, for example, by increasing catalytic surface area. The data suggest that the particle size of the catalyst powder applied by a dip coating procedure has little influence on the oxygen permeation rate of coarse grain-membranes. Membranes with fine grain and fine catalyst showed the highest performance

Tests were conducted to assess the performance differences between membranes that are ground to thickness before and after sintering. These tests were carried out on disks which did not have a catalyst coating applied to either surface. Tests were done on coarse-grain and fine-grain disks of different thicknesses. Figure 6-31 is a SEM of the sample sintered at 1,200°C; Figure 6-32 is the sample sintered at 1,175°C. Results suggest that the process of grinding and polishing the membranes before sintering leads to greater uniformity of surface roughness between membranes.

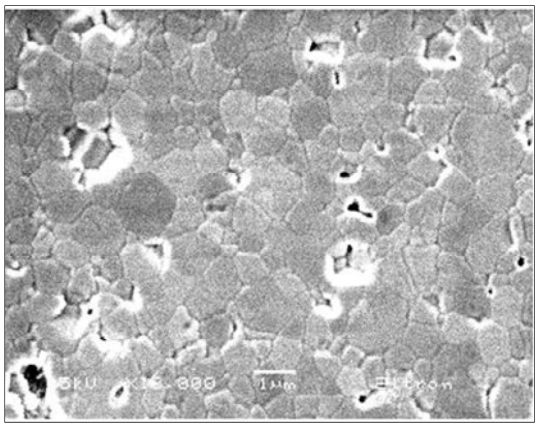

Figure 6-31. SEM image of thermally etched cross section of sample sintered at 1200°C.

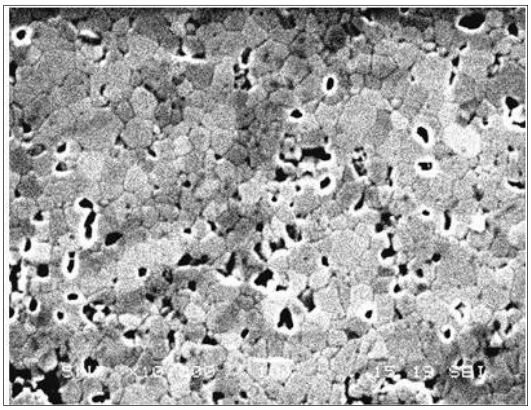

Figure 6-32. SEM image of thermally etched cross section of sample sintered at 1175°C.

The shrinkage of the tapes varies as a function of solids loading and powder particle size. It has been previously found that tapes made with coarse powder shrink by ~50% during the drying stage. With the fine powder, tapes were observed to shrink significantly more.

In order to improve the densification and sintering of the tapes, thermal analysis was performed by both TGA and TMA. These tests were performed on samples taken from the second tape cast described here with 5% dioctyl phthalate added. Test results are shown in Figure 6-33.

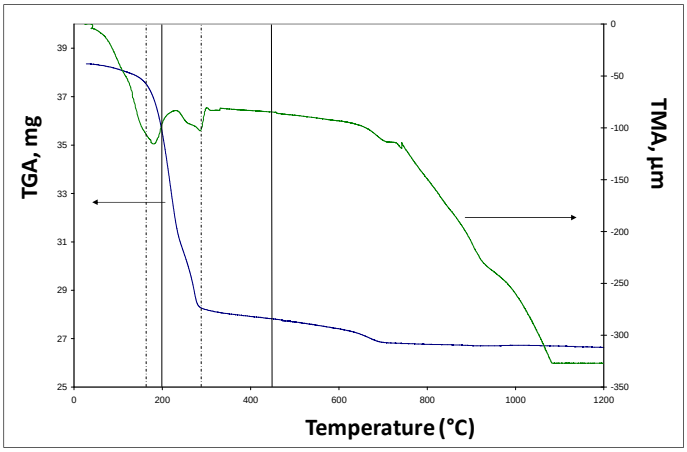

Figure 6-33. TGA and TMA of tape cast film with 5% dioctyl phthalate added.

The TGA curve (y-axis on the left) shows a sharp weight loss associated with binder burnout, mostly occurring below 300°C, with additional weight loss up to nearly 800°C. Some of this higher-temperature weight loss may be associated with loss of carbon dioxide from residual carbonate. The TMA curve (y-axis on the right) shows both contraction and expansion during the burnout of organic binders. It then remains fairly constant until densification begins at ~700°C. The signal bottomed out above 1000°C due to limitations of the range of the instrument and does not reflect the completion of densification. The solid vertical lines indicate the temperatures at which the ramp rate is changed. It starts at 30°C/h up to 200°C, slows to 10°C/h up to 450°C, and above 450°C the membranes are heated at 30°C/h to the sintering temperature. The results of the current tests show that a more appropriate heating rate might be represented by the dashed lines – where the 10°C/h range might begin at ~150°C and end at 300°C, as this is the range over which most of the binder burnout occurs.

Protective Layer Specification

The addition of a protective layer to the outside of a wafer was proposed as a means of reducing setter-side wafer defects. The thickness, tortuosity and porosity of the protective layer had to be determined to avoid introducing a significant gas-phase mass transfer resistance on that side of the wafer.

Air Products utilized an oxygen flux model to calculate the flux through a membrane at baseline operating conditions. The flux model was then used to calculate the mole fraction of oxygen needed at the membrane surface to achieve a given percent decrease in wafer flux relative to the

normal operating condition. Given the calculated mole fraction of oxygen at the membrane surface and the mole fraction of oxygen at the protective layer surface, the thickness, tortuosity and porosity of the protective layer can be determined using the equation for diffusion through a stagnant film:

$$J_{O2}=(cD_{O2\text{-}N2}\varepsilon/(\tau*L))\ \ln((1-y_{O2}'')/(1+D_{O2\text{-}N2}/D_K))/(1-y_{O2}'/(1+D_{O2\text{-}N2}/D_K)))$$

where J_{O2} is the molar flux of oxygen, c the total concentration of the gas, y_{O2}' and y_{O2}'' are the feed- and permeate-side oxygen mole fractions respectively, $D_{O2\text{-}N2}$ is the molecular diffusivity of oxygen in nitrogen, D_K is the Knudsen diffusivity, ε is the porosity, τ is the tortuosity and L is the thickness of the protective layer. Figures 6-34 and 6-35 show the results from one calculation.

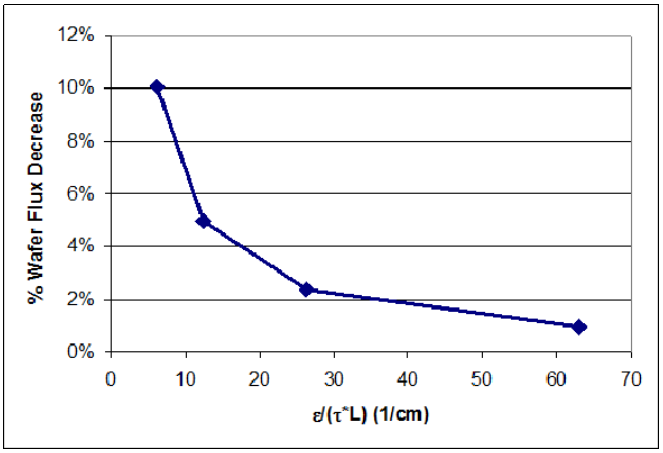

Figure 6-34. Percent decrease in wafer flux as a function of porous layer parameter, ε/(τ*L).

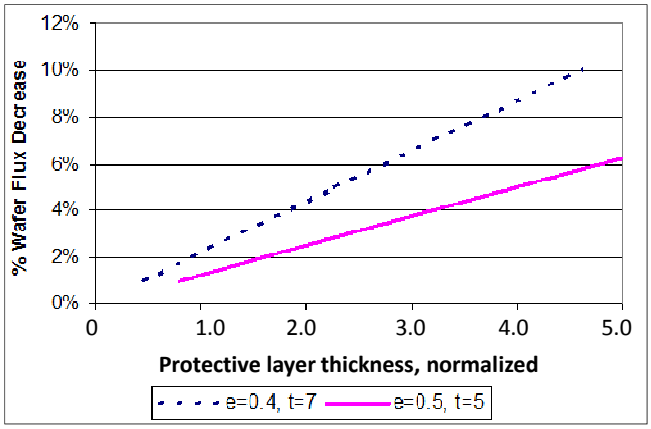

Figure 6-35. Allowable protective layer thickness.

To minimize the loss of flux, the protective layer should be as porous and as thin as possible while still achieving the desired ceramic yield increase. Different configurations were investigated. Figure 6-36 is an example of the calculated flux loss for three variations on one configuration.

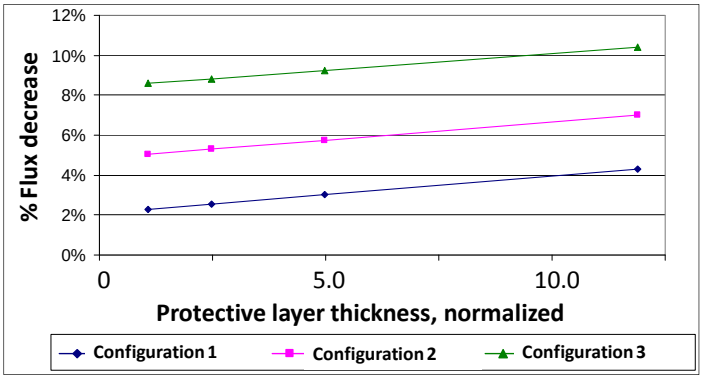

Figure 6-36. Flux loss for three variations of a configuration.

Ceramatec initiated work to develop methods to fabricate wafers with a protective layer. Early efforts resulted in wafer cracking due to differential chemical expansion during cooling caused by faster surface kinetics on the wafer surface (Figure 6-37). A slower cooling rate below 600°C was required to reduce the chemical expansion differential.

Figure 6-37. Wafer cracking due to differences in protective layer and membrane differential chemical expansion.

Nitrogen Bisque

It was hypothesized that bisqueing in nitrogen would aid wafer sintering during the binder removal phase of the thermal cycle. Two full-size wafers with a protective layer were bisqued

and partially sintered to determine the benefits of bisqueing in nitrogen. The wafers were identified as 402-1 and 402-2. Wafer 402-1 was bisqued and partially sintered in air. Examination of the sintered wafer revealed it had broken into several pieces. Wafer 402-2 was bisqued in nitrogen to 350°C, cooled to room temperature, and then sintered in air. Wafer 402-2 survived the nitrogen bisque with no visible cracks. A number of small hairline cracks were visible on the air side of the wafer after the air sintering step, along with two larger cracks that went all the way through the wafer. The results of bisqueing Wafer 402-2 in nitrogen and sintering in air were much improved over the air-bisqued and sintered Wafer 402-1.

In another experiment, a full-size wafer with a protective layer was nitrogen bisque, then sintered at a slower cooling rate. The wafer survived the nitrogen bisque with no visible cracks. Examination of the sintered wafer revealed it had fractured in several locations, with the cracks extending from the center hole and the rim of the wafer. Figure 6-38 shows the bisqued wafer, and Figure 6-39 shows the wafer after sintering.

Figure 6-38. Wafer with protective layer after a bisque in nitrogen.

Figure 6-39. Nitrogen-bisqued wafer with protective layer after sintering.

Porous Layer Life

Background

A reduction in the open porosity of the internal porous layer due to sintering over long periods at operating conditions would increase the pressure drop through the wafer and lower the flux rate. Air Products conducted a sintering study to provide data to estimate parameters in an equation that predicts the operational life of the porous layer at operating conditions. The equation

$$\ln(\Delta L/L_0)=\ln(k)+n(\ln(t)), \text{ where } k=k_o\exp(-E/RT)$$

was used, where $\Delta L/L_0$ is the relative sintering shrinkage, k is the sintering constant and follows the Arrhenius functionality, t is time at the sintering temperature T, and n is the sintering exponent. The y-intercept of a ln-ln plot identifies the sintering constants (k) at a specific temperature, and the slope of the lines identifies the sintering exponent (n).

Experimental Procedure

Porous layer tape was pressed into bars and sintered, which yielded a nominal open porosity in the target range for bars 1-5. Figure 6-40 shows the microstructure of Bars 4 and 5.

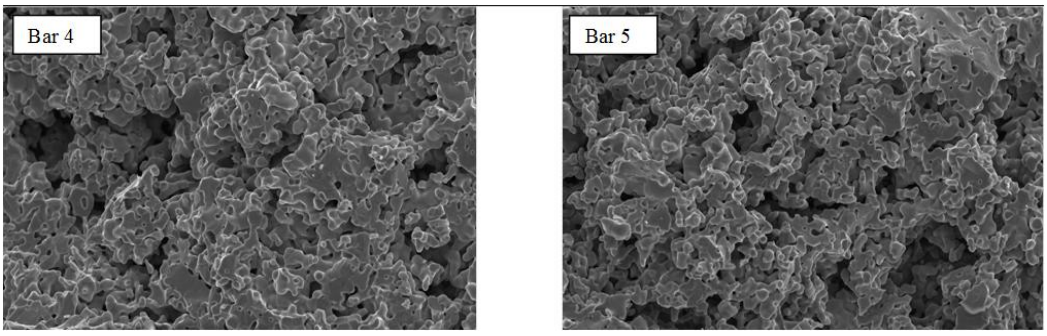

Figure 6-40. Porous layer microstructure of Bars 4 and 5 before aging.

The bars were then aged in a dilatometer at the joining temperature for 9 and 22 days (Bars 3 and 5 respectively), joining temperature 50ºC for six days (Bar 2) and joining temperature +100ºC for one day (Bars 1 and 4). Figure 6-41 shows microstructure of the bars aged for nine days (Bar 5) and 22 days (Bar 3).

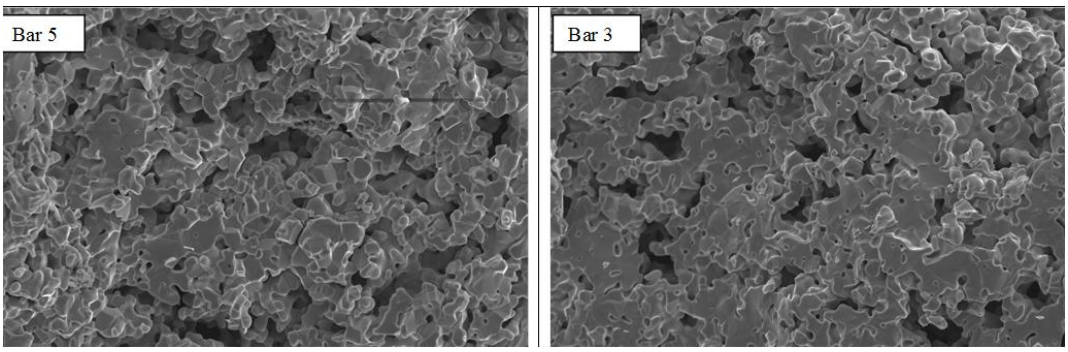

Figure 6-41. Porous layer microstructure of Bars 5 and 3 after aging nine days.

Results

Figure 6-42 is a plot of the expansion data.

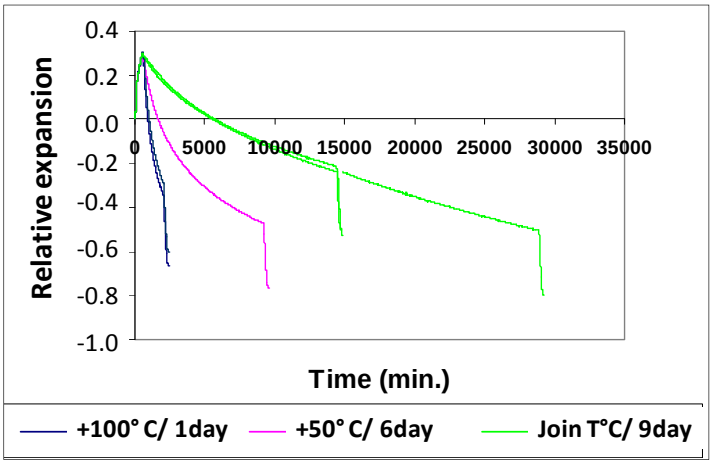

Figure 6-42. Porous sample expansion at time and temperature.

The first 0.2 of relative shrinkage was used to estimate the equation parameters. Figure 6-43 identified the sintering constants (k) at each of the temperatures, and the slope of the lines identified the sintering exponent (n). Figure 6-44 is a plot of k for the three temperatures; the slope of the line identified the activation energy for sintering.

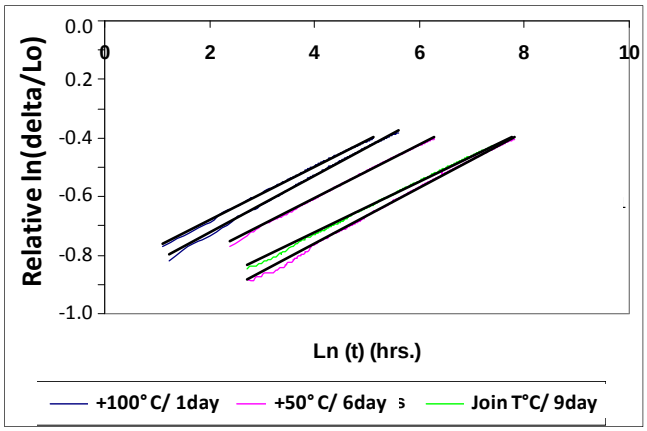

Figure 6-43. ln-ln plot of linear shrinkage (0 to 0.2).

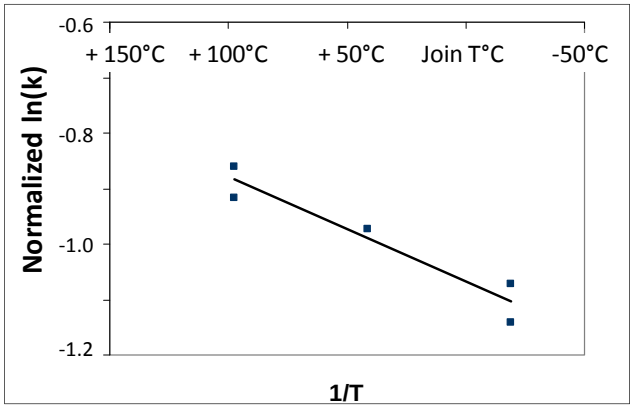

Figure 6-44. Arrhenius plot showing sintering constant (k) in terms of temperature.

Figure 6-45 plots the sintering shrinkage data and the equation predictions for each sintering temperature.

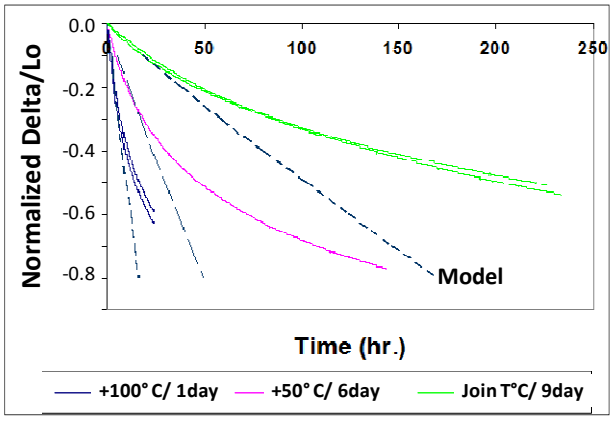

Figure 6-45. Sintering shrinkage data plotted with equation predictions for each temperature.

The equation predicts faster shrinkage beyond the 0.2 shrinkage point, making it very conservative. The equation predicts a shrinkage of 0.2 and a 5.3% reduction in open porosity after 15 years at operating temperature.

To test the model with an actual part, Air Products carried out a sintering study to artificially age porous layers and measure their effective permeability to gas flow in the aged state. Laminate disks of porous material were aged at the joining temperature for two hours and 40 hours. The latter condition represents an aging (and densification) of the porous layer by 15 years.

A batch of porous laminates prepared by Ceramatec were obtained and examined. Porous layer thicknesses were measured by optical microscopy. The pressure drop across the laminates was measured using helium and a Dwyer manometer series 475 Mark III. This manometer measured the pressure drop in units of inches of water (W.C) with a range and accuracy of 0.00-40.00/ 0.5%. The permeate flow was measured using a Brooks 1000 sccm mass flow meter at a pressure drop of 1.2 W.C/2.24 Torr across the laminate. After baseline permeation testing, the laminates were heated to joining temperature for two hours. After permeation testing, they were heated again to joining temperature for 40 hours, followed by final permeation testing.

Figure 6-46 shows the permeation results after the two aging treatments. The more aged samples had a slightly higher permeability then the baseline. This unexpected result might have been caused by pore coarsening. The open porosity of control parts accompanying the laminates changed by 20% after the 40 hour treatment. This porosity change was not seen in the laminate layers, suggesting that the laminates, which are constrained by adjacent layers, do not change porosity to the degree that unconstrained porous layers change. Figure 6-46 presents the results.

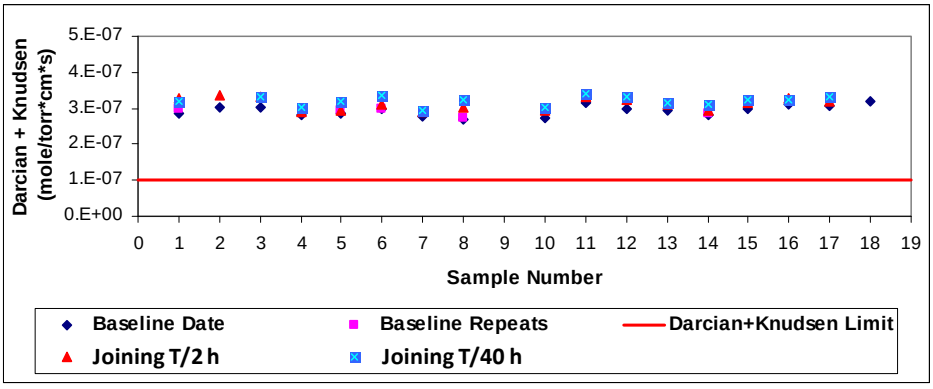

Figure 6-46. Permeation results for thermally aged porous laminates (2 h and 40 h at joining temperature), relative to baseline results.

PHASE 2 RESULTS AND DISCUSSION

TASK 7.0 ENGINEERING DEVELOPMENT

7.0 Scope

In Task 7.0, Air Products collaborates with Ceramatec, Concepts NREC, McDermott Technology, NovelEdge Technologies, and Siemens to develop approaches to design scaled-up membrane modules and the vessels that house them, to integrate the membrane vessel system with other flow-sheet components, to integrate the overall ITM system with gas turbine engines and assess control requirements, and to design and establish costs and reliability of the ITM Oxygen system components to enable further scale-up.

7.1 Gas Turbine and Air Flow-Path Integration

Large Gas Turbine Integration Study with Siemens and Concepts NREC

Air Products and Siemens Energy, Inc., (SEI) executed a detailed study of the integration of a large-frame gas turbine with the ITM Oxygen process. The focus of the study was to explore some of the assumptions made in the IGCC study discussed in Task 2 (Phase I), and to establish feasibility of the integration approach. Details of the work were presented in a Topical Report (December 2009), some of which are reproduced here. Concepts NREC supported Air Products in this work with heat exchange calculations.

The SGT6-6000G (W501G) was chosen for the Task 2 (Phase I) study because it was the largest, most advanced Siemens gas turbine contemplated for IGCC service at the time. That study assumed a scenario of 80% air extraction from the gas turbine compressor. Since that work, Air Products has determined that reducing the air extraction to 60% increased the membrane area requirement by only 4.5%.

The SEI work scope focused on:

1. Identifying any major obstacles for the proposed integration and potential solution paths for those issues. (SEI Task 1)
2. Developing conceptual designs for the solution paths. (SEI Task 2)

In SEI Task 1, the assessment approach was to do the following: define the operational characteristics of the ITM process that affect the gas turbine; identify any significant mismatches

between ITM process requirements and conventional gas turbine capabilities; define the turbine modifications needed to accommodate ITM integration; and identify design and development activities that can be addressed either within the scope of this contract or as part of a subsequent effort. SEI Task 2 focused on a detailed conceptual design for the gas turbine system, including the turbine components and their configuration, air flow patterns, piping and valve systems, and procedures for system startup and shutdown.

SEI Task 1: Major Obstacles

Integrated ITM-Gas Turbine Concept

Figure 7-1 is a simplified block flow diagram for the integrated ITM-gas turbine portion of an IGCC plant showing the interface between the ITM system (APCI scope) and the SGT6-6000G (W501G) gas turbine combined cycle (SEI scope). The ITM-IGCC plant includes a gasification block with water quench and gas cleanup (not part of this study), a syngas saturator block, an ITM block, and a combined cycle block. For ease of historical comparison, the gasification block is based on typical Texaco gasification performance values, but any oxygen-blown gasifier could be used with an ITM-gas turbine configuration. The combined cycle block includes a modified SGT6-6000G (W501G) gas turbine, a heat recovery steam generator (HRSG), and a steam turbine cycle. The gas turbine is modified to accommodate air extraction to the ITM and the combustion of gasifier syngas, oxidized by hot, oxygen-depleted air from the ITM (known as "retentate" or "vitiated air").

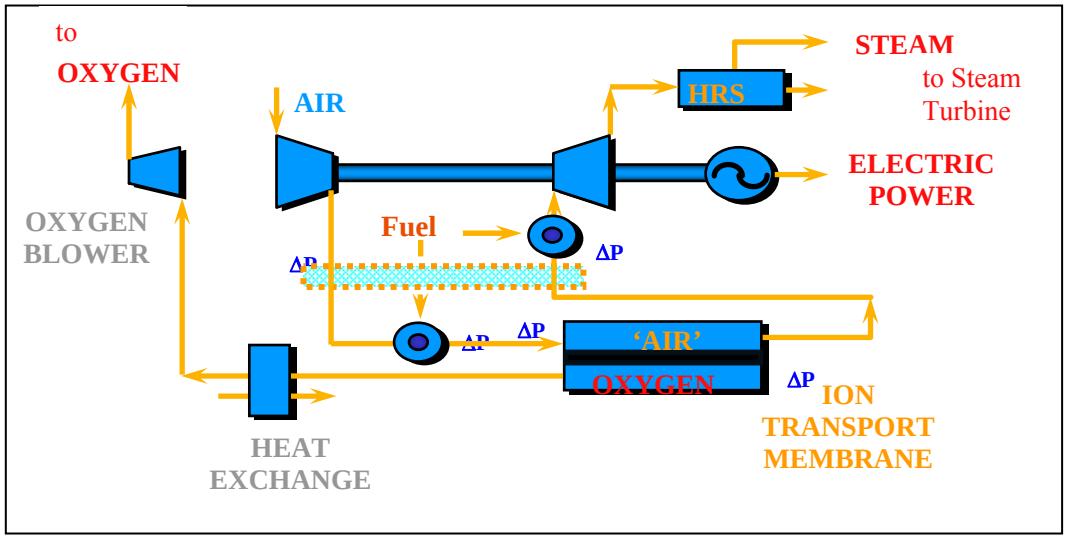

Figure 7-1. Simplified ITM-gas turbine block flow diagram.

Gas Turbine Modification Assessment Approach

The modification assessment approach used in this task involves four steps:

- Define the operational characteristics of the syngas and the ITM process, such as temperatures, pressures, flows, compositions, and other relevant parameters that affect the design and/or operation of the gas turbine.
- Compare these characteristics with the operational characteristics and operating limits of the SGT6-6000G (W501G) gas turbine, and identify any significant mismatches between ITM process requirements and conventional SGT6-6000G (W501G) capabilities.
- Define the turbine modifications needed to accommodate the ITM and/or syngas requirements.
- Identify design and development activities that can be addressed either within the scope of this contract or as part of a subsequent effort.

Adjustments, modifications, and re-designs of gas turbine components identified in this study are located in one or more of nine functional areas identified in Figure 7-2.

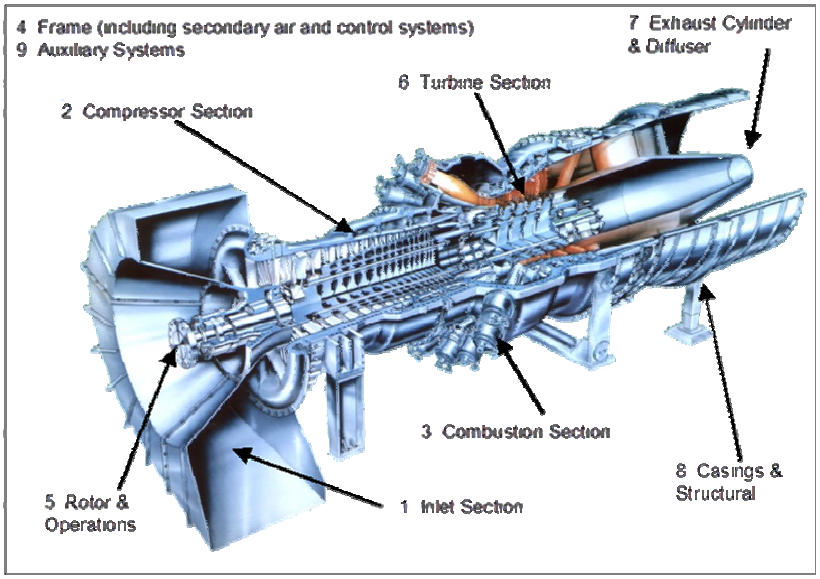

Figure 7-2. Gas turbine functional areas.

Combustion of Syngas with Vitiated Air

The gas turbine for the ITM-IGCC application burns syngas instead of natural gas and uses vitiated (oxygen-depleted) air, possibly at a high temperature, instead of compressed ambient air to provide the oxygen for combustion. The oxygen content of the ITM vitiated air is about 50%

of the oxygen content of compressed ambient air, so additional "fresh" air might be needed to provide oxygen and cooling to the combustion system.

Extraction of Large Amounts of Compressed Air

The gasifier in the ITM-IGCC plant requires oxygen in proportion to the amount of syngas fuel consumed in the ITM pre-burner and the gas turbine combined cycle. In the ITM-integrated scenario, that oxygen is separated from air extracted from the gas turbine compressor, and this extracted air represents a significant portion of the total compressor air flow. In simple terms, the oxygen production of the ITM is equal to 21% of the extracted compressed air flow (air is 21% oxygen) multiplied by the ITM separation fraction (or oxygen recovery). The best combination of air extraction and ITM separation fraction is the result of design trade-offs between ITM requirements and gas turbine requirements.

Pressure Losses Through ITM System

The ITM system introduces pressure losses in the gas path between the compressor exit and the burner inlet. This reduces both the available pressure ratio through the expander, and the power per unit mass flow that the expander can produce.

Hot Gas Piping, Manifolding, and Valves

The ITM Oxygen separation unit for an ITM-IGCC plant requires a large array of membrane modules, which are contained in separate pressure vessels connected to the gas turbine by hot gas piping. A conceptual arrangement of major equipment might resemble the preliminary plot plan shown in Figure 7-3. (Note that the use of two ITM vessels was chosen for convenience and does not reflect a true equipment breakpoint; a single ITM vessel could have been used.) Compressed air is collected in a manifold and ducted to preheaters at the entrance to the ITM vessels. Vitiated air leaving the ITM vessels is ducted to the vitiated air manifold, from which it is distributed to the gas turbine combustors.

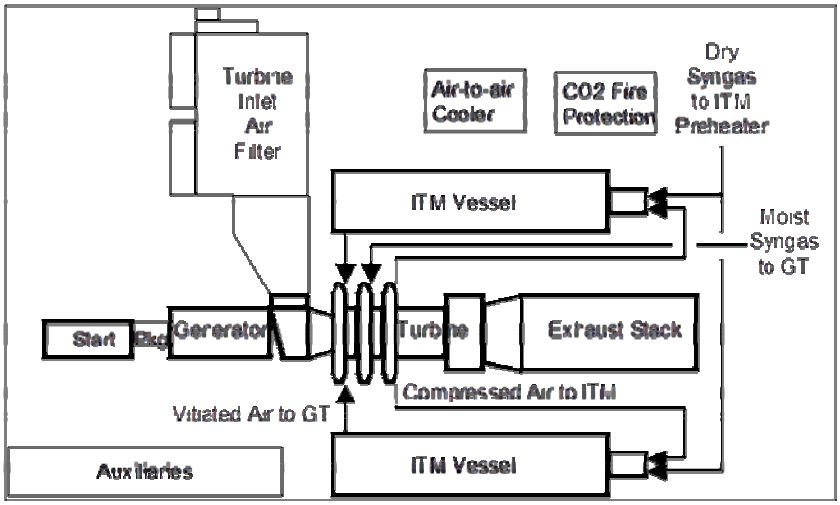

Figure 7-3. Possible arrangement of ITM vessels with gas turbine.

Syngas and natural gas (for startup) are also ducted to and distributed from their own manifolds, although the temperature and flow requirements of syngas and natural gas piping and manifolds are considerably less demanding than those of the compressed air and vitiated air piping and manifolds. This layout was updated and modified somewhat during SEI Task 2, as shown later (Figure 7-10).

Operation of Integrated System

Use of ITM technology may add a certain amount of complexity to the normal operating procedures of an IGCC plant. This is due to the high degree of integration of the ITM system with the gas turbine, along with at least a moderate degree of integration between the gas turbine combined cycle and the gasification island.

Conclusions from SEI Task 1

Siemens concluded that some design and development work is needed to integrate the gas turbine with the ITM Oxygen system, but no significant barriers to development were discovered.

SEI Task 2: Gas Turbine System Conceptual Design

Figure 7-4 is a simplified block flow diagram for the complete IGCC plant showing the interface between the ITM system and the SGT6-6000G (W501G) gas turbine combined cycle. The modified gas turbine features air extraction for ITM use and syngas burners designed for ITM operating conditions. Electric power is produced by the main gas turbine combined cycle and

the syngas expander, and auxiliary power is consumed by the extracted-air boost compressor and oxygen compression.

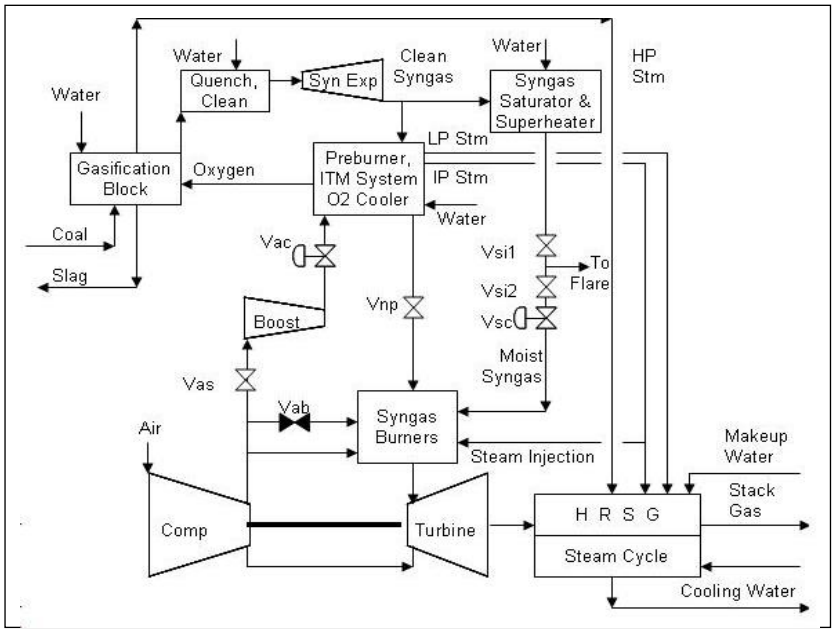

Figure 7-4. Simplified ITM-IGCC block flow diagram.

Selection of Preferred Configuration

APCI and Siemens jointly identified and evaluated 11 sensitivity cases representing various plant configurations with and without an extracted-air boost compressor, with and without a recuperator, and at several vitiated air return temperatures. The boost compressor counteracts pressure losses through the ITM system, but requires additional auxiliary power and capital cost. The recuperator heats the air entering the ITM system and cools the vitiated air leaving the ITM system to enter the gas turbine, but incurs additional pressure loss through the gas turbine circuit as well as additional capital cost. In many cases, however, the net effect of adding a recuperator was to reduce the overall plant's specific capital cost ($/kW). Concepts NREC supported the study with heat exchange network calculations within the ITM sytem.

The estimated plant net efficiencies and total plant costs for these 11 cases are summarized in Figure 7-5 and Table 7-1. Each case is identified by the following CC-RR-TTT code:

CC (compressor): BC = with boost compressor; NB = no boost compressor

RR (recuperator): wR = with recuperator; NR = no recuperator

TTT (temperature): temperature (°C) of vitiated air entering the gas turbine

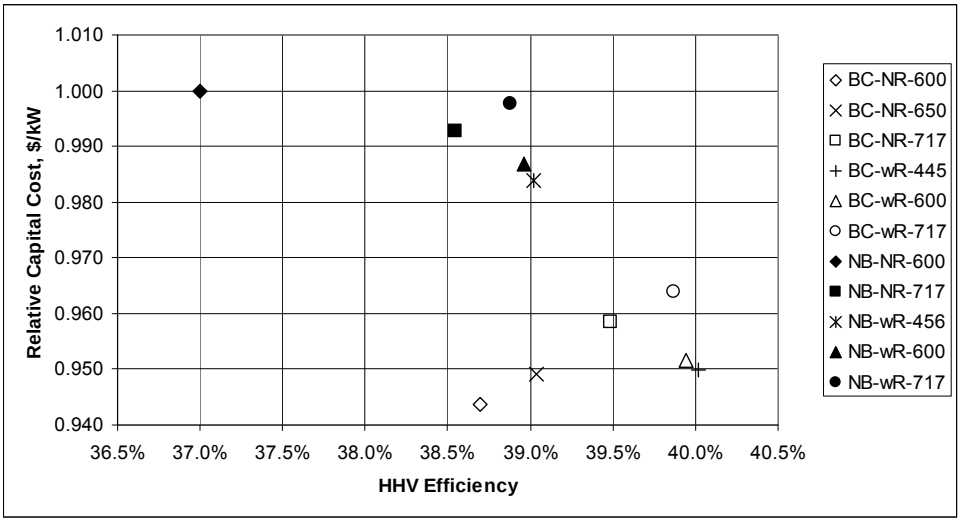

Figure 7-5. ITM-GT configuration comparison.

Table 7-1. ITM-GT configuration comparison.

Case	Eff(HHV)	Relative $/kW	Boost?	Recup?	T(vit.air), °C
BC-NR-600	38.7%	0.944	Yes	No	600
BC-NR-650	39.0%	0.949	Yes	No	650
BC-NR-717	39.5%	0.958	Yes	No	717
BC-wR-445	40.0%	0.950	Yes	Yes	445
BC-wR-600	39.9%	0.952	Yes	Yes	600
BC-wR-717	39.9%	0.964	Yes	Yes	717
NB-NR-600	37.0%	1.000	No	No	600
NB-NR-717	38.5%	0.993	No	No	717
NB-wR-456	39.0%	0.984	No	Yes	456
NB-wR-600	39.0%	0.987	No	Yes	600
NB-wR-717	38.9%	0.998	No	Yes	717

The LHV efficiency for each case can be estimated as 1.04 times its HHV efficiency because coal fuels the IGCC. Detailed plant-wide simulations and cost estimates of each case were not performed in this study; parameters contributing to the results in Figure 7-5 and Table 7-1 were scaled from the Task 2 study completed by Air Products, Texaco Power and Gasification, and Concepts NREC.

These comparative results indicate that plants with a boost compressor and recuperator have higher efficiencies and lower specific capital costs than plants without these two components. These plants were selected for further consideration even though the addition of a boost

compressor may cause the perception of increased plant complexity. Within this group of study cases, the variations in efficiency and cost were small compared with the uncertainties involved in the calculations. Therefore, the results should be considered comparative rather than definitive.

Although Case BC-wR-445 showed the highest efficiency and the lowest specific capital cost, it was discarded because the large amount of recuperated heat transferred from the vitiated air to the ITM inlet air raised the ITM inlet air temperature above acceptable limits for the ITM preheater. Case BC-wR-600 featured the highest acceptable level of recuperation and was identified as the most promising choice. In this case, HHV and LHV efficiencies were 39.9% and 41.4% respectively, and vitiated air returned to the gas turbine at an acceptable temperature of 601^{o}C (1114^{o}F).

Effects of Recuperator Designs

For cases with a recuperator, increasing the size of the recuperator (decreasing the vitiated air return temperature) improves specific cost ($/kW) with essentially no change in efficiency. Compared to each corresponding NB-wR case, each BC-wR case is about 1% more efficient, with specific cost about 4% lower.

For cases without a recuperator (all vitiated air cooled by water injection), increasing water injection decreases efficiency. For the BC-NR cases, water injection should not exceed the value at which the compressor inlet guide vanes (IGVs) begin to close to avoid choked flow through the turbine. With a 650^{o}C (1202^{o}F) vitiated air return temperature, Case BC-NR-650 represents the maximum water injection case and approximates the theoretical maximum, with inlet air flow and turbine temperature converging to within 1% of design values. It may be possible to inject more water by raising the boost compressor discharge pressure, thereby increasing the mass flow at the turbine choke condition. However, such an adjustment might require redesign of the gas turbine compressor and combustor shell to accommodate the higher pressure. The effects of using a higher-pressure boost compressor are discussed in a subsequent section.

The best cases overall are the BC-wR cases, with lower vitiated air return temperatures favored. However, more recuperation results in higher inlet temperatures to the ITM pre-combustor,

which causes liner cooling issues. One option would have been to trade water injection against recuperation, but increasing water injection decreases efficiency.

Effects of Higher-Pressure Boost Compressor

The capital cost and performance of ITM systems tend to improve with increased operating pressure, so a sensitivity study was performed to assess the effects of higher boost compressor exit pressure on overall plant cost. The analysis was based on Case BC-wR-600, except that the pressure rise across the boost compressor was increased by 10 bar (145 psi), which increased the ITM feed pressure by the same amount.

The boost compressor required to compress the necessary air flow an additional 10 bar is estimated to cost about $3.2M more than the base boost compressor and use an extra 26.5 MW of compressor power. The cost of the ITM in this higher-pressure case would be reduced by about $3M, but this cost savings would be eliminated by the estimated $3.2M increase in boost compressor cost, as well as undetermined cost increases for two higher-pressure components that would be required (gas turbine shell and recuperator). Based on these results, the higher-pressure boost compressor option was removed from further consideration.

Selected Configuration

As described previously, 11 cases representing a matrix of configurations were evaluated in terms of the total plant's specific capital cost ($/kW) and net efficiency. Case BC-wR-600 was identified as the most promising current choice. Key performance parameters for this selected case are listed in Table 7-2.

Table 7-2. Performance of ITM-IGCC Case BC-wR-600.

Parameter	Quantity	Unit
GT Net Power	282.6	MW
Steam Turbine Net Power	186.4	MW
Syngas Expander Power	13.8	MW
Plant Gross Power	482.7	MW
Air Booster Power	8.0	MW
O_2 Compression Power	19.8	MW
Other Plant Auxiliaries	16.4	MW
Plant Net Power	438.5	MW
Plant Net Efficiency (HHV)	39.9%	%(HHV)
Plant Net Efficiency (LHV)	41.4%	%(LHV)
Vitiated air temp to GT	601 (1114)	^{o}C (^{o}F)
Recuperator Effectiveness	0.414	-

Concepts NREC showed that the recuperator design may require a high inlet temperature to the pre-combustor which might reduce the life of the combustor liner. This issue would be addressed by the using a thermal barrier coating.

ITM-Integrated Gas Turbine Combustor

The properties of the boundary streams of the SGT6-6000G (W501G) gas turbine in the selected cycle are summarized in Table 7-3.

Table 7-3. Gas turbine boundary streams for case BC-wR-600.

		GT Inlet Air	GT Air to ITM	Recup Vitiated Air to GT	Fuel GT Burner Syngas	GT Exhaust
Mass Flow	Lb/s	1,291	710	676	142	1,399
Pressure	psia	14.7	303.7	286.0	364.7	15.2
Temperature	F	59	833	1,114	440	1138
Mass Flow	Kg/s	585	322	307	64	634
Pressure	bar	1.01	20.94	19.72	25.14	1.05
Temperature	C	15	445	601	227	615
Mol %						
Ar	%(mol)	0.9%	0.9%	-	-	0.4%
CH_4	%(mol)	-	-	-	0.1%	-
CO	%(mol)	-	-	-	44.8%	-
CO_2	%(mol)	0.03%	0.03%	2.5%	9.5%	9.2%
H_2	%(mol)	-	-	-	32.3%	-
H_2O	%(mol)	1.0%	1.0%	6.7%	12.9%	10.4%
N_2	%(mol)	77.3%	77.3%	81.1%	0.5%	72.3%
O_2	%(mol)	20.8%	20.8%	9.8%	-	7.7%
Mol %		100.0%	100.0%	100.0%	100.0%	100.0%
Syngas HHV	MJ/kg				11.08	
Syngas HHV	Btu/lb				4763	
Syngas HHV	MJ/Nm^3				9.79	
Syngas HHV	Btu/scf				249.1	
Syngas LHV	MJ/kg				10.36	
Syngas LHV	Btu/lb				4453	
Syngas LHV	MJ/Nm^3				9.15	
Syngas LHV	Btu/scf				232.9	

The design of the ITM-integrated gas turbine combustor has two main aspects: the diffusion-flame burner for the actual combustion, and the surrounding passages that guide the compressed

air, vitiated air, and fuels to their proper locations. Each aspect is described in more detail in the following sections.

Combustion Engine Burner Conceptual Design

The conceptual ITM-integrated syngas combustor for the engine is a diffusion-flame burner with oxygen supplied by vitiated air from the ITM, supplemented by compressed ambient air not needed for extraction or for cooling the blades, vanes, or rotor. Diffusion-flame combustion was chosen over lean-premix combustion – typically used for dry low-NOx burners – in order to remove the potential for flashback caused by the relatively high hydrogen content of the syngas.

Bypass flows around the combustor are needed to cool blades, vanes, and the rotor. The remaining air is either extraction air for the ITM or combustion air. The air available for the combustor for selected Case BC-wR-600 contains enough oxygen to enable syngas combustion with over 40% excess oxygen, as summarized in Table 7-4.

Table 7-4. Oxygen sources and uses (totals for 16 burners).

Reagent	Syngas	Vitiated Air	Compressed Ambient Air	Totals
Mass flow	64.4 kg/s (142.0 lb/s)	306.7 kg/s (676.2 lb/s)	144.4 kg/s (318.4 lb/s)	515.5 kg/s (1136.5 lb/s)
Molecular weight	19.85	28.13	28.86	-
Molar flow	7.15 mol/s	24.03 mol/s	11.18 mol/s	-
Stoich. O_2 needed	2.77 mol/s	-	-	2.77 mol/s
O_2 mol%	-	9.77%	20.78%	-
O_2 provided	-	2.35 mol/s	2.32 mol/s	4.67 mol/s
Excess O_2	-	-	-	40.7%

Combustor Flow Rates

The physical configuration of the diffusion-flame syngas combustor for the ITM-integrated gas turbine is based on the design of a conventional natural gas-fueled combustor in an SGT6-6000G (W501G), with adjustments made to accommodate the vitiated air from the ITM unit and the substitution of syngas for natural gas.

Replacement of natural gas with syngas and combustion air with higher-temperature vitiated air results in volumetric flows through the burner that are a manageable 17% higher than the flows

in a conventional gas turbine combustor. The standard SGT6-6000G turbine is designed to operate with syngas, but not with the flow of hot, vitiated air.

Hot Gas Connections to Turbine

From the standpoint of physical design, the main combustion zone differences between the ITM-coupled gas turbine and a conventional syngas-fueled turbine are the compressed air extraction ports and vitiated air inlets near each combustor.

Since the volumetric flows through the combustor in the ITM case are roughly equivalent to the volumetric flows through a conventional natural gas combustor, the dimensions at the combustor – ITM turbine interface are similar to the corresponding interface dimensions in a natural gas-fueled turbine. Key interface dimensions for both turbines are within 5% of each other, including the distance between adjacent combustor penetrations.

While the combustors in the ITM gas turbine are similar to combustors in conventional turbines, the air extraction and vitiated air return flows are unique to ITM applications. Significant air flow must be extracted from the compressor exit flow, and similar flows of hot, vitiated air must be ducted back into the combustors. The conceptual design approach to accommodate these ITM-specific features uses the flow characteristics of the compressed air within the shell of a conventional turbine.

In a conventional turbine, high-velocity air leaving the last compressor stage flows against the outside of the compressor shell, where it reverses direction and flows to the combustors (see Figure 7-6).

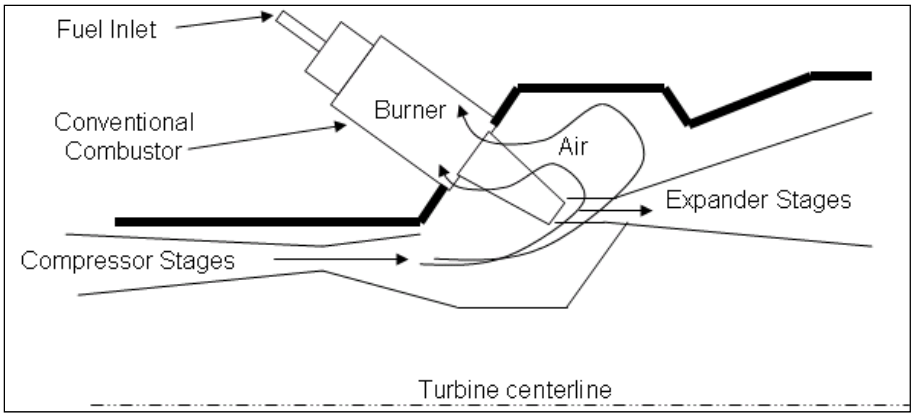

Figure 7-6. Air flow pattern in conventional turbine shell.

The air extraction and vitiated air flow paths in the ITM turbine are designed to be compatible with these conventional flow paths. Air is extracted through the compressor shell at the normal flow reversal site through circumferentially-arranged holes through the shell and into a circular plenum. These holes are connected to larger compressed-air piping leading to the boost compressor inlet. Vitiated air returning from the ITM in large pipes enters its own circular plenum, enters the shell through another set of circumferentially-arranged holes, mixes with some compressed air, and enters the combustors. The compressed air and vitiated air flows for this arrangement are shown in Figure 7-7.

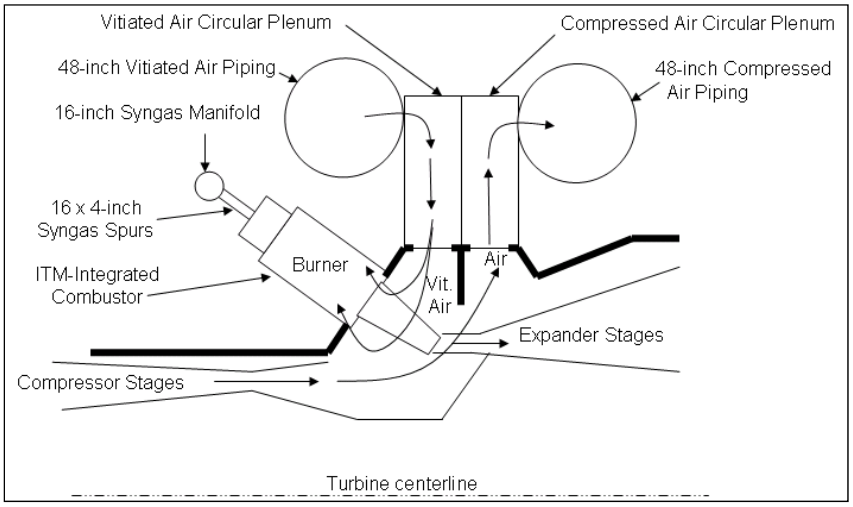

Figure 7-7. Air flow patterns in ITM-GT shell.

The flat, ring-shaped divider on the inside circumference of the shell between extraction air and vitiated air is needed only near the shell because the high-velocity jet of air leaving the compressor will not mix with the vitiated air. Compressed air that is not extracted, however, will reduce velocity, turn, and mix with the vitiated air to provide oxygen and some cooling before entering the burner.

The syngas nozzles in each combustor are connected to a toroidal ("ring") manifold that encircles the gas turbine combustion zone. Figure 7-8 is a more complete depiction of the piping, plenums, and turbine.

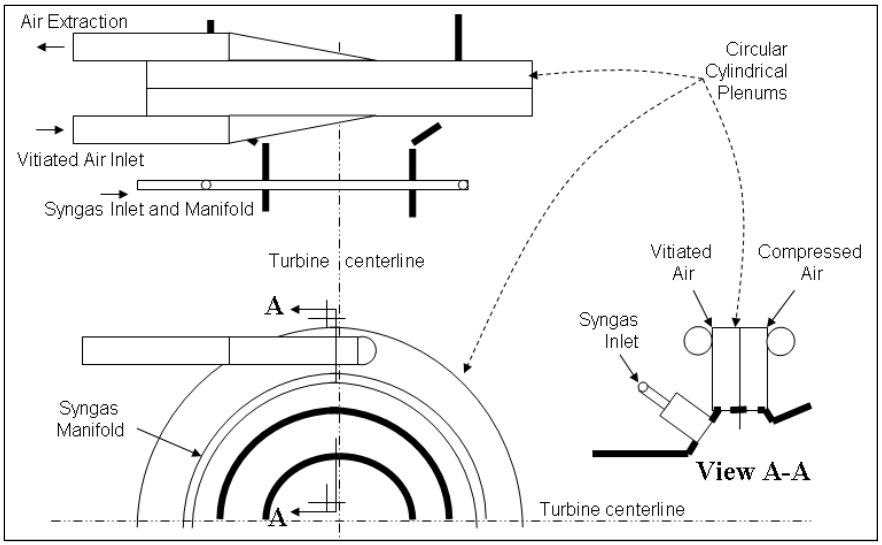

Figure 7-8. Hot gas connections to gas turbine.

Estimated Turbine Exhaust NOx Emissions

The diffusion-flame syngas burner used in this ITM-coupled gas turbine is expected to produce between 35 and 40 ppm(v) of NOx, corrected to conditions of 0% moisture and 15% oxygen. This range of emission levels is similar to that of diffusion-flame burners operating on syngas in a conventional SGT6-6000G turbine.

NOx emission levels can be reduced somewhat by water or steam injection. Direct injection of water is a proven, effective technology that reduces the peak flame zone temperature in the combustor, thereby reducing the production of thermal NOx. Injecting water at a water:fuel mass flow ratio of 1:1 reduces NOx levels to about 20% of levels without water injection (dry). The upper limits of possible water injection rates are usually determined by compressor surge limits or combustor instability. Eventual testing of the ITM-coupled gas turbine combustor would include the exploration of those limits.

Steam injection for NOx control works by the same principle as water injection, except that the cooling effect of the heat of vaporization for water is not available. Therefore, about 1.4 kg (~3 lb) of steam is needed to accomplish the same level of NOx reduction as 1.0 kg (2.2 lb) of water. As with water injection, the upper limits of steam injection rates are set by compressor surge limits or by combustor instability.

Figure 7-9 shows the expected NOx emissions for a range of injection steam/fuel ratios.

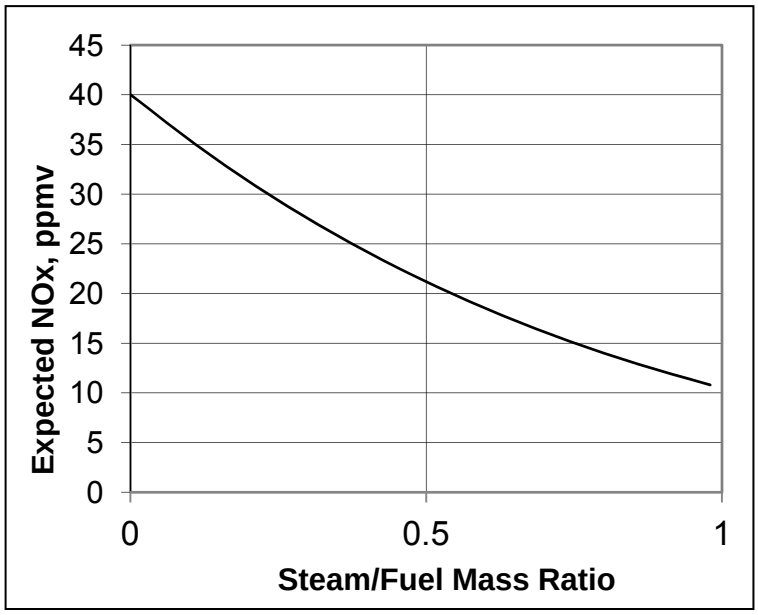

Figure 7-9. Expected NOx reduction from steam injection.

The emission levels in Figure 7-9 are preliminary estimates, based on typical emissions trends with steam injection. Detailed design and testing of the ITM-coupled gas turbine combustor will determine the actual effects of steam injection on NOx emission levels.

Gas Turbine and Accessories

The gas turbine connected to the ITM system is based on a conventional gas turbine modified to accommodate air extraction, syngas fuel, and vitiated air return to the combustors. The nominal performance parameters of this turbine are listed in Table 5.

Table 7-5. Gas turbine nominal performance.

Parameter	Metric Unit	English Unit
Net power output	282.6 MWe	
Syngas flow	64.4 kg/s at 227 ^{o}C	(142 lb/s at 440 ^{o}F)
Vitiated air inlet flow	307 kg/s at 601 ^{o}C	(676 lb/s at 1114 ^{o}F)
Extraction air flow	322 kg/s at 445 ^{o}C	(710 lb/s at 833 ^{o}F)
Gas turbine exhaust flow	635 kg/s at 517 ^{o}C	(1,399 lb/s at 963 ^{o}F)
Pressure ratio	19.2:1	

Equipment Arrangement: Gas Turbine

The modified SGT6-6000G (formerly W501G) gas turbine consists of three basic elements: an axial-flow compressor, a combustion system, and a turbine expander. These three elements are combined into a single assembly with a horizontally-split and sectionalized casing, a two-bearing rotor support, a turbine air cooling system, a compensating alignment system and axial-flow exhaust.

The axial-flow compressor has 16 stages, with advanced-profile airfoils and a nominal 19.2:1 pressure ratio. To avoid compressor surge during startup, a single-variable inlet guide vane (VIGV) assembly is used, and the compressor bleed valves are opened. The VIGV is also modulated to improve combined-cycle part load efficiency.

Although some compressed air is reserved for cooling various gas turbine components, about 55% is extracted for the ITM separation process. The air is extracted through orifices arranged circumferentially around the turbine to ensure uniform air flows within the turbine.

For the ITM application, the SGT6-6000G incorporates 16 dual-fuel syngas combustors. Syngas from the gasifier provides the fuel for the combustor. Exhaust gas from the ITM system (from which the oxygen has been partially removed) is the vitiated air that provides oxygen for combustion.

Syngas, vitiated air, and compressed ambient air flow to each combustor as shown previously in Figure 7-7. Compressed air leaves the compressor and enters the circular plenum through holes located around the shell. Vitiated air enters the shell through a separate set of entry holes, then combines with some compressed air to form the oxidizing mixture for combustion. Syngas (or natural gas during startup) is injected into each burner nozzle, and the products of combustion are delivered to the gas turbine expander through individual transition ducts.

The SGT6-6000G turbine uses a 4-stage turbine to optimize efficiency. The first three stages are air-cooled. The turbine uses advanced materials such as directionally-solidified castings for the first two turbine rows and state-of-the-art, electron-beam, vapor-deposited thermal barrier coatings.

Rotor cooling air is provided by compressor discharge air extracted from the combustor shell. This provides a blanket of protection from hot blade path gases and eliminates excessive contaminants that could block critical cooling passages to the rotor blades. Other compressor air is used to cool the turbine blade ring cavities and vane segments.

Equipment Arrangement: General

The bill of materials for the basic gas turbine system includes the gas turbine assembly previously described, together with the following equipment and assemblies:

- generator
- starting package
- lube oil system
- inlet air system
- ccmpressor water wash
- cooling assemblies
- isolated phase bus (optional)
- static excitations & voltage regulator system
- electrical package
- gas fuel system
- exhaust gas system
- pipe packages
- fire protection system
- auxiliary transformer (optional)

The hydrogen inner-cooled generator is equipped with integral lube oil, cooler piping and necessary instrumentation. The design uses a shaft-mounted axial blower to circulate cooling hydrogen through the generator. A solid coupling connects the generator directly to the compressor at the cold end of the combustion turbine.

The major equipment components in the gas turbine plant are listed in Table 7-6, along with their approximate shipping weights.

Table 7-6. Gas turbine plant equipment weights.

	Weight	
Item	**kg**	**(lbs)**
gas turbine	272,000	(600,000)
generator	247,000	(545,000)
collector	5,000	(11,000)
starting package	38,600	(85,000)
electrical package	1,400	(3,000)
lube oil reservoir	7,300	(16,000)
lube oil pump skid	8,200	(18,000)
turbine piping package	15,900	(35,000)
excitation skid	8,300	(18,200)
excitation transformer	7,600	(16,700)
generator seal oil skid	10,000	(22,000)
fuel oil/water inject. skid	9,100	(20,000)
fuel oil pump skid	8,200	(18,000)
water injection pump skid	6,800	(15,000)
boost compressor	4,000	(8,900)

The heaviest piece lifted during construction is the generator, with a weight of 247,000 kg (545,000 lbs). The heaviest piece lifted after construction is the bladed gas turbine rotor (53,500 kg /118,000 lbs).

Figure 7-10 is a plan view showing a conceptual arrangement of the gas turbine, ITM vessels, boost compressor, and recuperator. (The number of ITM vessels chosen does not represent a true equipment breakpoint; a single ITM vessel could have been used.) The enclosures, piping, wiring, fuel system, and the bypass system are not included because they would obscure the view of the major equipment. The ITM-gas turbine complex occupies a space approximately 46 m X 43 m (150 ft X 140 ft).

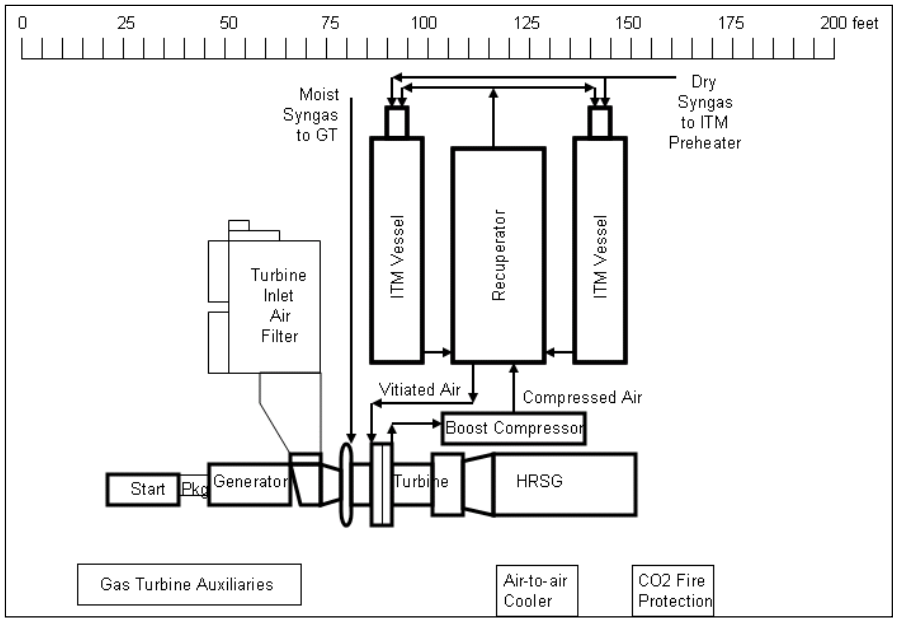

Figure 7-10. Plan view of ITM-gas turbine complex (vitiated air quench unit not shown).

Conclusion from SEI Task 2

Air Products and Siemens developed a conceptual design for an ITM Oxygen–gas turbine integrated system for IGCC based on the SGT6-6000G (W501G) platform, and considered a matrix of cases to determine the appropriate equipment and conditions at the interface between the two sub-systems. Following are the specific conclusions from this work:

- To achieve minimal design impact on the highly pre-engineered gas turbine sub-system while providing the best opportunity to minimize specific capital cost ($/kW) and maximize efficiency, the team determined that the optimal arrangement should include an extracted-air boost compressor, a recuperator between the ITM feed and non-permeate streams, and a vitiated air return temperature to the gas turbine of 600 °C.

Siemens developed conceptual designs for the required modifications to the gas turbine, primarily in the combustion section. Key conclusions from this work included:

- Designs enable air extraction of up to 55% of the compressor discharge air prior to it entering the combustors, as well as returning the 600°C vitiated air and mixing it with the fresh, unextracted air as it enters the combustors.
- Despite changes in temperatures and molecular weights, the volumetric flow rates through the combustors match within a manageable 17% to flows through the

conventional combustor design. Key dimensions at the combustor–turbine interface match within 5%.

- The team also developed a notional plot layout and required footprint, leading to a conclusion that the ITM Oxygen plant requires about half the plot space of a comparable cryogenic air separation unit.

Integrations with Small Gas Turbines (<100 MW)

Concepts NREC built on its activity under Task 2 to identify gas turbine engines suitable for integration with ITM Oxygen process cycles at smaller scale than is typical for IGCC applications. That work identified desired tubine operating parameters which enabled discussions with gas turbine suppliers regarding potential integrations in the pCDF and (later) the ISTU. Through such discussions, Siemens identified their GT35P and GT140P gas turbines as integration-ready candidates for ITM Oxygen.

The GT35P was developed in the 1990s specifically for integration with pressurized fluidized bed combustion (PFBC) of coal. As such, it has operated at five commercial plants in this mode with near-100% air extraction. The GT35P produces 17 MW, operating with a pressure ratio of 12:1 and a turbine inlet temperature in the range of the ITM Oxygen operating temperature, thereby avoiding the need for post-combustion of the non-permeate stream. Because of its large air flow, it would be capable of supporting an ITM Oxygen plant of >1,000 sTPD. The GT140P is the dimensionally equivalent larger cousin of the GT140P, producing 70 MW with a pressure ratio of 18:1 and the same turbine inlet temperature. It is currently operating in one commercial PFBC plant and would be capable of supporting an ITM Oxygen plant of >4,500 sTPD.

GT35P and GT140P Gas Turbines

Air Products, aided by Concepts NREC, conducted a literature search on the GT35P and GT140P turbines. The GT35P is a two-shaft, intercooled turbine in which the LP compressor and LP turbine are on a free-wheeling shaft, while the HP compressor and turbine are on a constant-speed shaft connected to the generator (Almhem, 1996). The GT35P has an overall pressure ratio of 13:1 (Fulton, 1996) and produces 17 MWe (Nilsson, June 1998). Figure 7-11 shows a cutaway view of both the GT35 and the GT35P gas turbine.

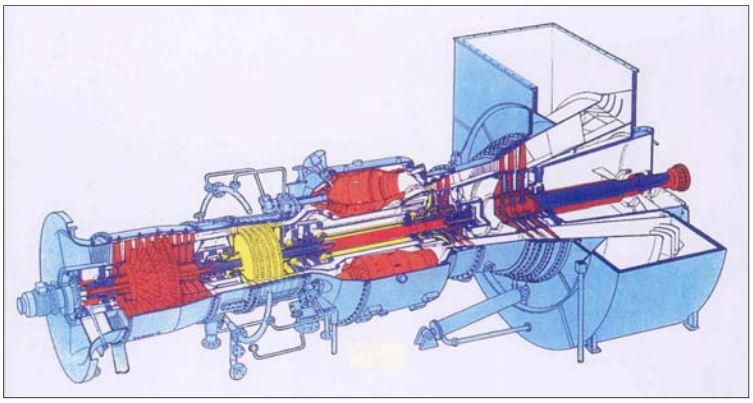

Figure 7-11. GT35 and GT35P gas turbines.

The GT140P is a scaled-up version of the GT35P (Nilsson, June 1998). The GT140P has an 8-stage LP compressor and a 12-stage HP compressor with an overall pressure ratio of 18:1; a 3-stage HP turbine; and a 1-stage LP turbine. The GT140P produces 70-80 MWe of electric power. (Fulton, 1996). The intercooler between the LP compressor and the HP compressor keeps the temperature of the HP exit air below 300 ^{o}C (572 ^{o}F). The compressed air is cooled by condensate from the steam cycle (Fulton, 1996). Key design parameters for the GT35P and GT140P gas turbines are compared in Table 7-7.

Table 7-7. Design performance of PFBC gas turbines (Fulton, 1996).

Gas Turbine	GT35P	GT140P
Output, MWe	14-17	70
Air flow, ISO kg/s (lb/s)	85 (187)	370 (816)
Air flow range	40-100%	40-100%
Pressure ratio	13:1	18:1
Vitiated air flow, kg/s (lb/s)	96 (212)	420 (926)
Turbine entry temperature, ^{o}C (^{o}F)	850 (1562)	850 (1562)
LP shaft speed, rpm	2850-6560	1250-3150
HP shaft speed, rpm	6100	3600
Generator speed, rpm	1500/1800	3000/3600
LP compressor stages	11	8
HP compressor stages	12	12
HP turbine stages	4	3
LP turbine stages	1	1

The GT35P and GT140P share a common arrangement, which is depicted in Figure 7-12.

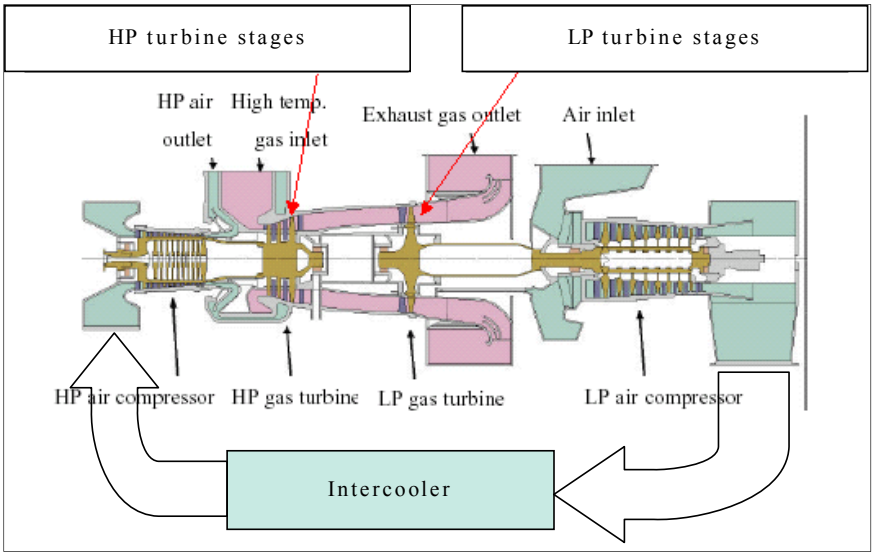

Figure 7-12. GT35P and GT140P general arrangement.

The profile of the GT140P gas turbine with alternator/motor measures 34 meters (112 feet) long and 10 meters (33 feet) high above the foundation, with an additional 9 meters (30 feet) below the foundation required for the intercooler (Fulton, 1996).

GT-P Gas Turbines in PFBC Applications

Turbine blades in the GT35P and GT140P are designed to accept the PFBC's ash-laden vitiated air (Fulton, 1996; Evett, 1998). As shown in Table 7-8, there are six GT36P turbines and one GT140P turbine operating in PFBC applications (ca. 2005).

Table 7-8. Gas turbines at pfbc power plants (Wright et al, 2003).

PFBC Plant	Gas Turbine	Startup	PFBC Pressure, bar
Vartan	2 x GT35P	1989	12 [a]
Tidd	1 x GT35P	1991 [d]	11.6 [b]
Escatron	1 x GT35P	1991	12 [a]
Wakamatsu	1 x GT35P	1994	
Cottbus	1 x GT35P	1998	
Tomatouatsuma	1 x MW-151P	1998	
Ohsaki	1 x GE F7EA	1999	
Karita	1 x GT140P	1999	16 [c]

[a] Bed pressures from Jansson, 1991.
[b] Bed pressure from McDonald, 1992.
[c] Bed pressure from Omata and Anderson, 1997.
[d] Tidd plant operation was started in November 1990 (McDonald, 1992) and shut down in March 1995. (Wright et al, 2003)

The GT140P is connected to the PFBC by coaxial cross-over piping with an intercept valve. High-pressure (HP) compressed air flows in the outer annulus, and vitiated air returns in the inner pipe. The intercept valve is located at the HP compressor exit and is used to connect and disconnect the compressor from the PFBC during startup, normal operation, and shutdown (Fulton, 1996).

PFBC Plant Startup Sequence with GT140P

The alternator for the GT35P/GT140P gas turbine acts as a motor driving the HP compressor during startup, with the induced air flow through the LP compressor also turning the LP rotor. Starting the GT140P requires about 15 MWe of power (Fulton, 1996). During startup, the compressor provides air to fire a preheater and ignite the coal in the PFBC. Once the coal is burning, the temperature of the vitiated air entering the gas turbine increases, reducing the power requirements of the starting motor until the unit becomes self-sustaining without the need for the motor (McDonald, 1992).

Combustor Configuration Methods for Integration with Gas Turbine Engines

Concepts NREC undertook an analysis of the design approach of gas turbine combustors to address the challenge in ITM-integrated systems posed by return of hot oxygen-depleted non-permeate stream to the combustor. Three options were considered:

Option A (Figure 7-13): The baseline case, in which a sufficient fraction of the compressor discharge stream bypasses the ITM to satisfy the combustion and line cooling requirements. The non-permeate stream is introduced solely to provide the require dilution of the flow from the primary combustion zone of the combustor.

Option B (Figure 7-14): A portion of the bypass stream is mixed with the non-permeate to reduce its temperature sufficiently so that it can be used for liner cooling and dilution. Option B has the potential to simplify the thermo-mechanical design of the piping.

Option C (Figure 7-15): This approach reverses the process and mixes a portion of the non-permeate with part of the by-pass stream. The resulting stream is used for premixing with the fuel and subsequent combustion. The intent of Option C is to reduce the fuel concentration by dilution with the vitiated non-permeate stream sufficiently to provide a degree of NOx control.

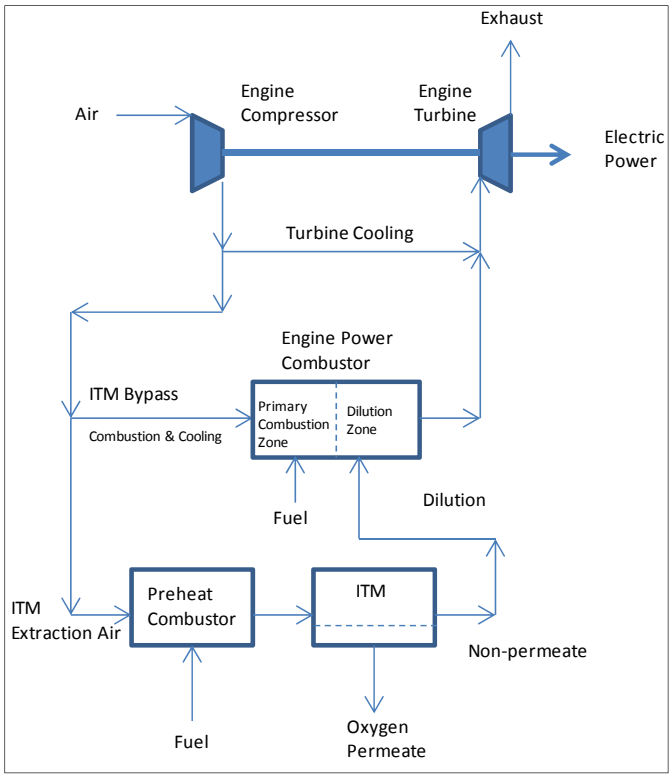

Figure 7-13. System Option A: non-permeate is used for dilution.

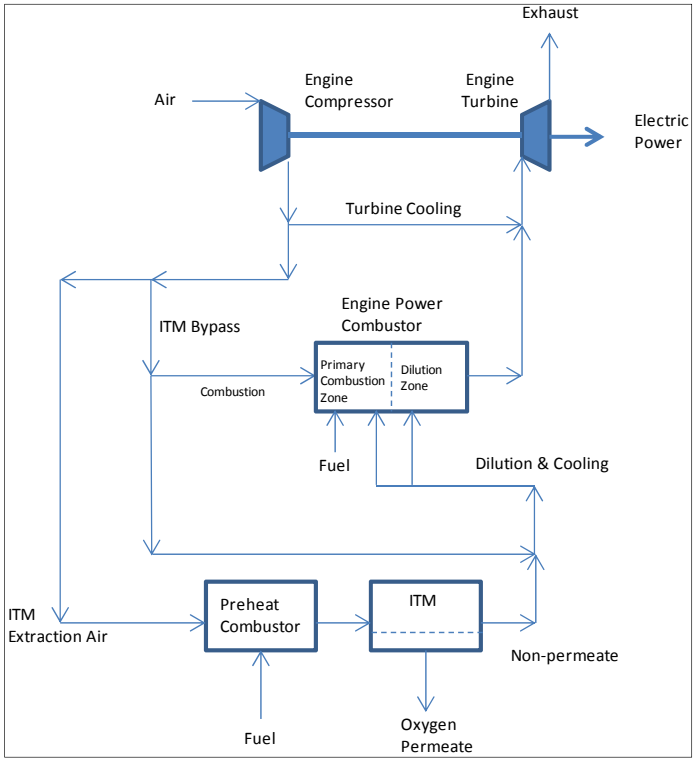

Figure 7-14. System Option B: Non-permeate, mixed with air, is used for dilution and cooling.

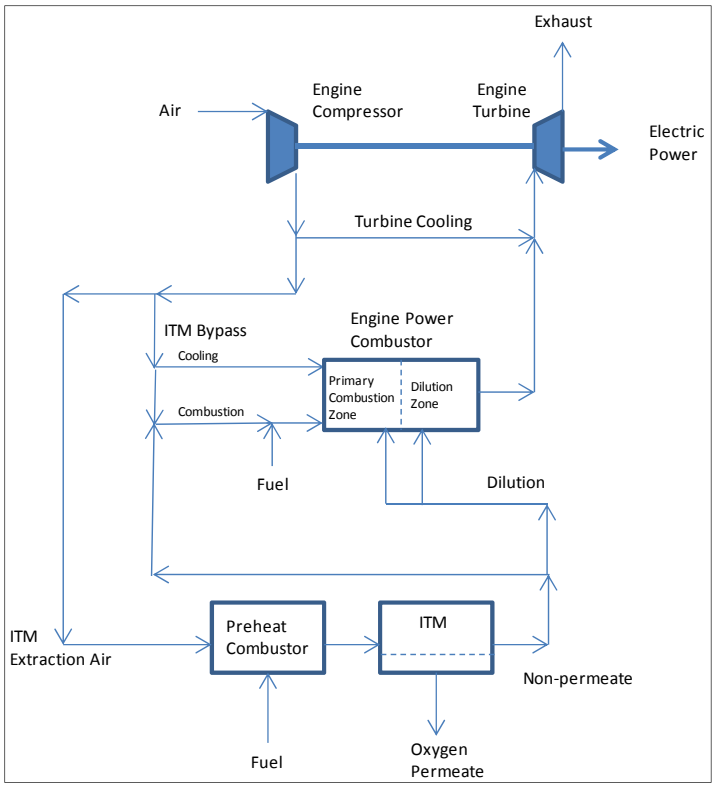

Figure 7-15. System Option C: Non-permeate used for NOx control in combustion zone.

Design Basis

Table 7-9 details the parameters chosen for the study. The gas turbine engine is a model of the FT8 (Pratt & Whitney) and is scaled to a net power output of 50 MW.

Table 7-9. Design basis summary.

Parameter	Value	Units
ITM Operating Temp.	850	° C
ITM Oxygen Recovery	50	%
Machine Parameters:		
Pressure Ratio	20:1	
Air Flow Rate	344	lbm/sec
Turbine Inlet Temp	2200	° F
Overall Air/Fuel Ratio	50:1	
Compressor Efficiency	85	%
Turbine Efficiency	90	%
Turbine Cooling Flow	10	%

Benchmark System

Concepts NREC analyzed the performance of an idealized integrated system with minimum constraints on air extraction. For this benchmark case, the amount of air extraction was adjusted to provide an oxygen content to the inlet of the power combustor of 14% (vol.). The benchmark system flowsheet is shown in Figure 7-16.

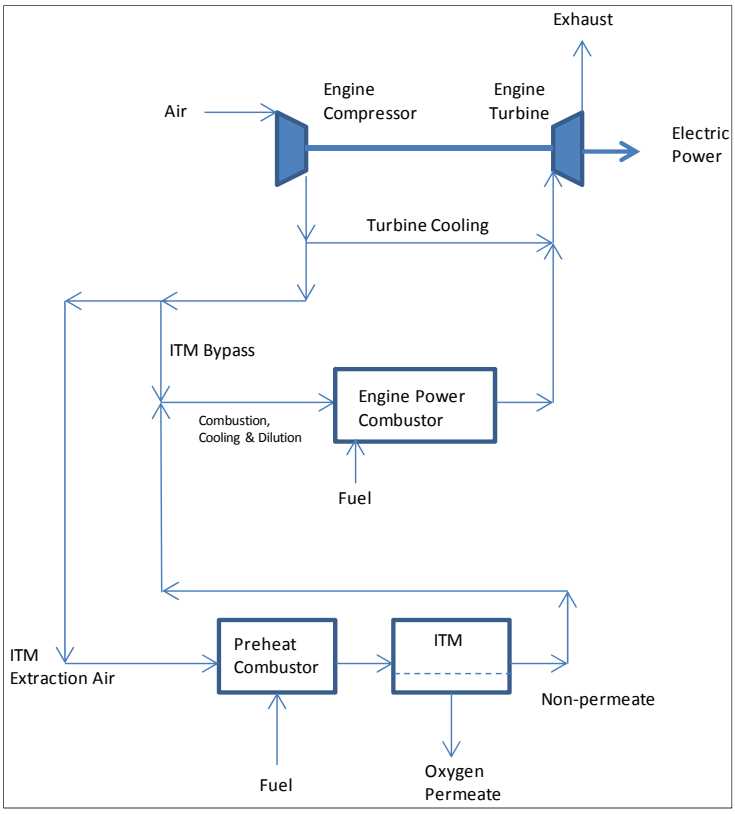

Figure 7-16. Idealized benchmark system.

Results and Discussion

Table 7-10 summarizes the overall results of the study. Option B maximizes power make, while minimizing oxygen make. The benchmark maximizes oxygen make, while minimizing power make. The cases are discussed in more detail below.

Table 7-10. Production summary for the study cases.

System	O_2 Conc. (vol. %) at Combustor Inlet	Liner Cooling Air Temp. (° F)	Electric Power Output (MWe)	O_2 Production Rate (TPD)
Base Engine	20.8	854	50	0
Benchmark	14.0	1278	34	800
Option A	20.8	851	40	480
Option B	20.8	1100	43	300
Option C	14.0	851	38	600

Analysis of Option A Results

The achievable system performance for this option is primarily a function of the required air flow split for combustion and liner cooling. For a conventional engine, the liner cooling is typically in the 10-40% range of the total mass flow in the combustor. The amount of air needed for combustion depends on how lean a primary combustion zone is desired. For dry low-NOx (DLN) combustors, a lean primary zone equivalence ratio (e.g., 0.5) is necessary. If another method of NOx control is used (e.g., water injection) an equivalence ratio as high as 1.0 is likely. The corresponding range of combustion air required is on the order of 30-60% of the total mass flow. Based on these considerations, Concepts NREC chose the following nominal air flow distributions in conducting the analysis:

- Liner cooling flow = 25%
- Combustion air flow = 45%
- Dilution air flow = 30%

Option A enjoys no deviations from standard operation in the inlet oxygen concentration or liner cooling ability, and provides a balanced power and oxygen production.

Analysis of Option B Results

Option B allows the non-permeate return to be used for both dilution and liner cooling. The temperature of the mixed stream limits the extent to which the non-permeate can be used in this capacity. Figure 7-17 is a plot of the outputs versus the mixed stream temperature. The upper limit on allowable mixed stream temperature is 1200°F based on cooling requirements, with 1100°F a more practical upper limit.

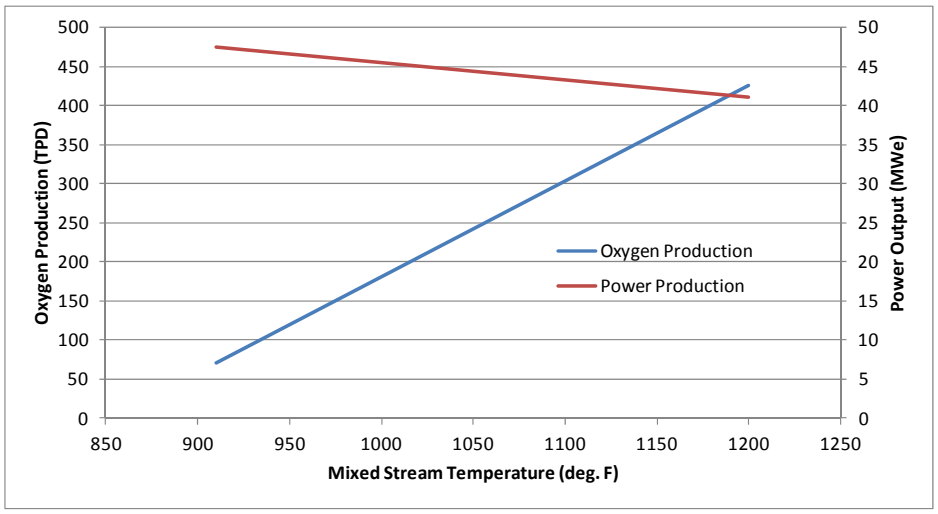

Figure 7-17. Effect of adjusting return stream temperature on output tradeoffs for Option B systems.

Analysis of Option C Results

DLN combustors control NOx emissions by premixing the fuel with a sufficient quantity of air to obtain a low equivalence ratio (φ, defined as fuel/air ratio devided by the stoichiometric fuel/air ratio) in the combustion zone. Typically, values on the order of φ = 0.3-0.5 are required to achieve single-digit NOx (ppm) levels. Flame stability is a problem at these low equivalence ratios. The stability situation can be improved by increasing the inlet air temperature. The effect is demonstrated by the data plotted in Figure 7-18, which shows the lean blowout (LBO) equivalence ratio trend with temperature for premixed methane/air flames.

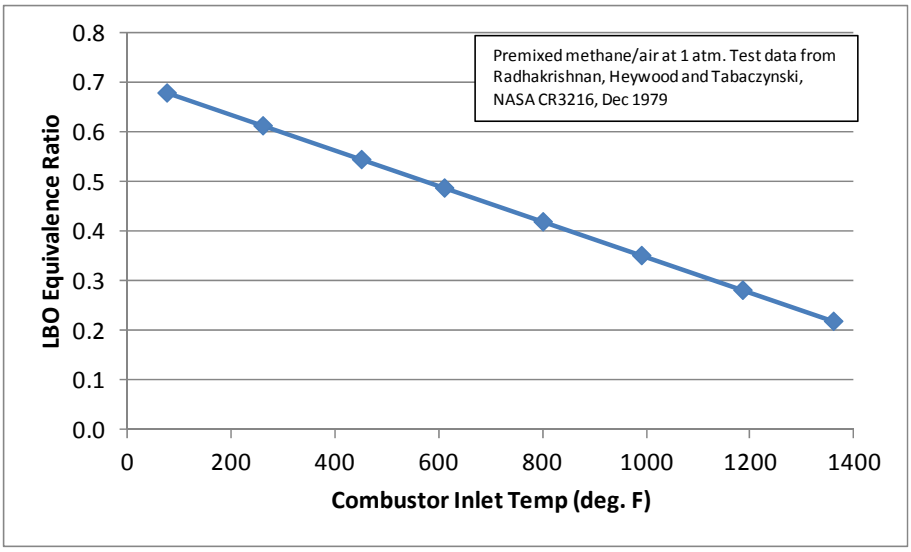

Figure 7-18. Effect of combustor inlet temperature on Lean Blowout (LBO) equivalence ratio.

Addition of hot, vitiated non-permeate to the combustion air before premixing is intended to provide assistance in producing low NOx combustion. The addition of the hot gas should aid flame stability, while the reduced oxygen content should aid NOx reduction.

Figure 7-19 shows the results of calculations with a range of non-permeate/air mixtures with liner cooling flow fixed at 25% of the total mass flow and with all of the non-permeate stream used for premixing. Equivalence ratios of 0.3-0.4 are achievable with this approach. In this study, equivalence ratio was a minimum of 0.35 to maintain 14% oxygen in the inlet stream.

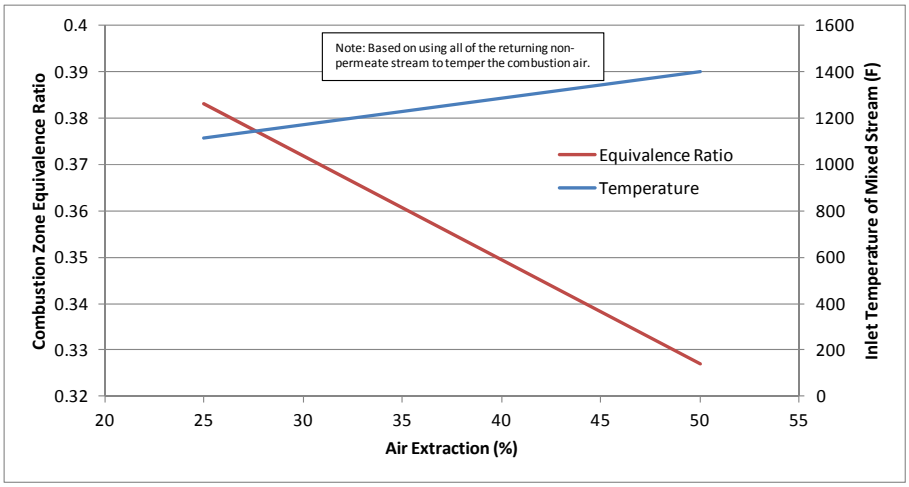

Figure 7-19. Effect of combustor inlet temperature on lean blowout (LBO) equivalence ratio

Conclusions

Option A is the simplest of the options to implement and provides reasonable levels of both power and oxygen production. It has no compromises on oxygen inlet concentration or liner cooling gas temperature. Option B represents an increase in power at the expense of oxygen make, but has a marginally acceptable cooling gas temperature. Option C is useful primarily as a means of assisting NOx control in a DLN configuration. Options B and C could be improved if coupled with water injection and/or recuperative heat exchange.

Pre-combustor Design for ITM Oxygen Systems

The pre-combustor may be used as an in-line combustor upstream of the ITM unit to provide process heat by direct combustion of a fuel with the compressed air feed to the ITM system. Such pre-combustors had been investigated by Concepts NREC in Task 2; a conceptual design based on a gas turbine combustor design was studied.

Initial work under this Task was focused on determining the limits of such pre-combustors. Concepts NREC determined that the fuel turndown limit at full air flow is 20-25% of the full fuel flow rate, limited by the lean blowout threshold. In principle, the pre-combustor can turn down even lower with an equivalent turndown in air flow (i.e., maintaining constant air to fuel ratio). Concepts NREC determined that, ultimately, the degree of control over exit temperature depends on the degree of control over the fuel flow rate (i.e., valve control range(s) and available pressure drop). These designs were applied to both the IGCC flowsheet and the pCDF flowsheet, the latter of which is under development in this Task.

IGCC Pre-Combustor Design

Concepts NREC investigated pre-combustor designs for the model IGCC system that was the basis for the gas turbine integration with Siemens and Air Products described above. A model flow sheet (Figure 7-20) was developed to enable the study.

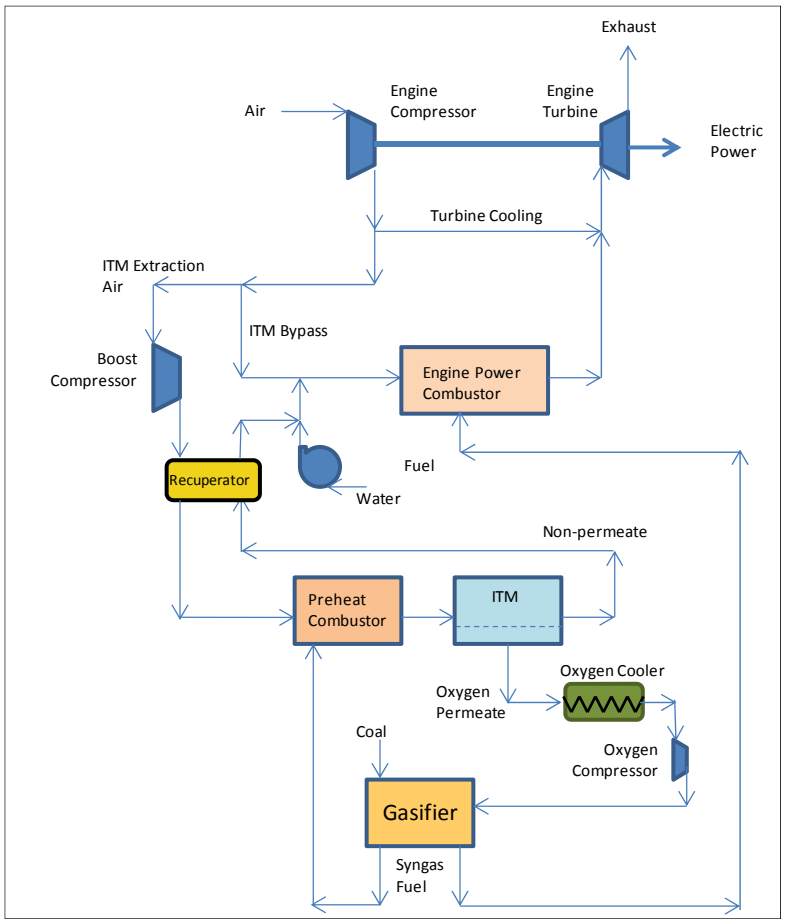

Figure 7-20. Model IGCC flowsheet for the basis of the pre-combustor design study.

Concepts NREC chose as the design basis inputs the parameters shown in Table 7-11. The BC-WR-600 case was considered here (that case was described above in the gas turbine integration section). As in the turbine integration study, two ITM vessels and their dedicated pre-combustors were assumed with a syngas fuel specified by Texaco (266.45 BTU/ft^3 LHV).

Table 7-11. Preheat combustor design conditions, IGCC case.

Parameter (per combustor)	Value	Units
Air Flow Rate	355	lbm/s
Inlet Air Temp	1172.5 (634)	F (C)
Inlet Air Pressure	322	psia
Fuel Flow Rate	9.58	lbm/s
Inlet Fuel Temp	110	F
Inlet Fuel Pressure	354	psia
Fuel Lower Heating Value	5027.6	BTU/lbm
Combustor Outlet Temp	1607 (875)	F (C)
Temperature Rise	434	F
Overall Air/Fuel	37.1:1	mass:mass
Targets:		
Combustor Pressure Loss	2	%
Max NOx level	50	ppm
Max Liner Wall Temp	1472 (800)	F (C)
Max Exit Temp Deviation	± 18 (10)	F (C)
Exit Traverse Quality	~0.04	

Concepts NREC chose a baseline combustor design comprising primary, secondary, and dilution zones, and a diffusion flame burner as shown in Figure 7-21. The combustor is lined so that dilution air and air for film-cooling the liner is provided in an annulus around the three combustor sections.

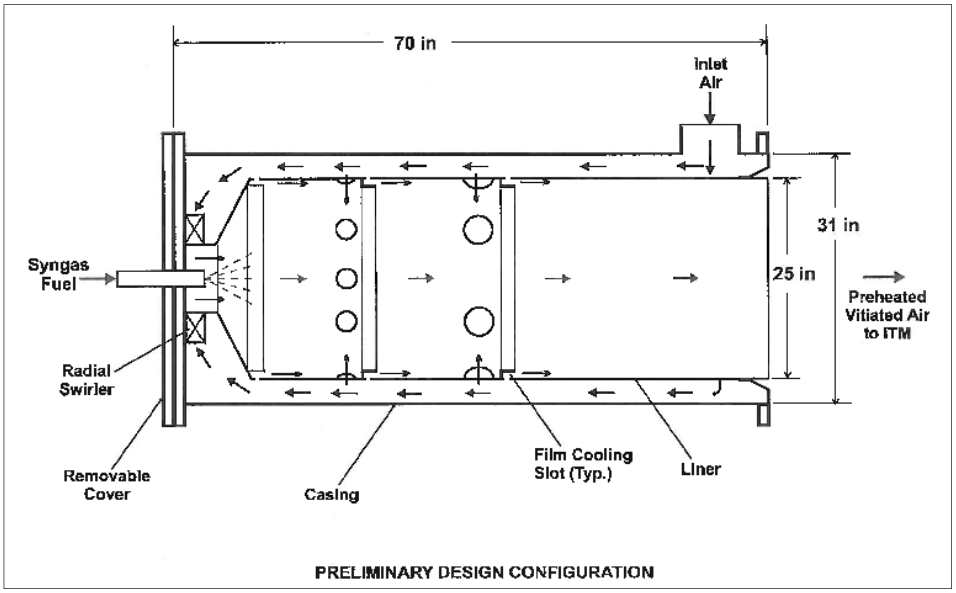

Figure 7-21. Design configuration for the preheat combustor.

Concepts NREC performed a series of parametric studies on dimensions of the combustor. Effects including liner diameter, air distribution, and dilution zone length were studied for their influence on combustion efficiency, mixing, emissions, flame stability, and temperature uniformity. The axial liner temperature profile was studied for several cases and analyzed for its likely influence on durability and life of the combustor. A representative axial liner temperature distribution is shown in Figure 7-22.

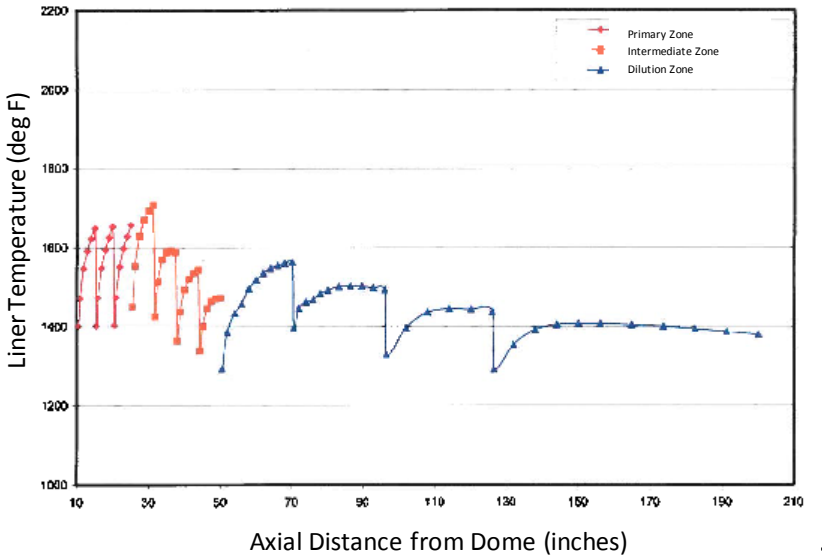

Figure 7-22. Axial liner temperature profile for one design case.

Concepts NREC determined an optimal combustor geometry during the work and made the following conclusions based on the study:

- A lean, well-mixed primary combustion zone is required for control of the liner temperature and NOx.
- Combustion stability is a concern.
- Liner cooling is challenged by high inlet temperatures; a thermal barrier coating may be required.
- Target exit temperature uniformity requires increased pressure drop, for example by a downstream mixing device.

pCDF Pre-Combustor Design

Similar to the IGCC case discussed above, Concepts NREC carried out a design exercise for the pCDF pre-combustor. As of the date of this work, the pCDF, nominally a 25 TPD ITM Oxygen pilot unit, was in the conceptual design stage. The GT35P gas turbine platform, discussed above, was chosen as the basis in some scenarios. Concepts NREC considered the case of GT35P integration in the pCDF flowsheet, as shown in Figure 7-23.

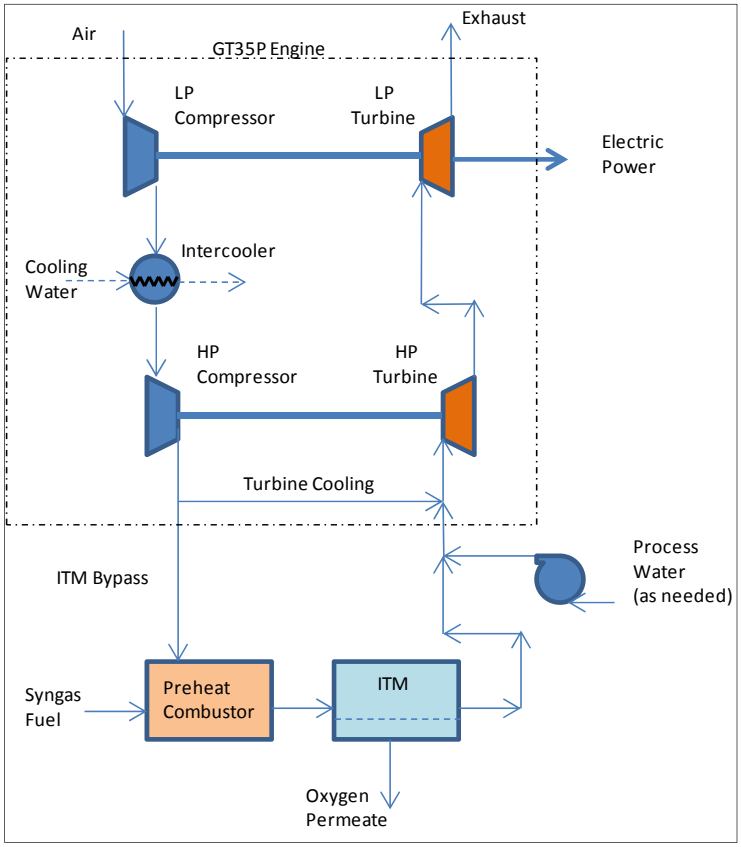

Figure 7-23. Model pCDF flowsheet based on the GT35P engine for the precombustor design study.

Table 7-12 shows the parameters that Concepts NREC chose as the design basis inputs. A syngas fuel identical to the one used in the IGCC case precombustor study (i.e., 266.45 BTU/ft^3 LHV) was used in the pCDF case precombustor study so the two cases could be compared. The pCDF precombustor must increase the air temperature by 1035°F, in contrast with the IGCC precombustor, which has only to increase the air temperature by 434°F. Thus, the air/fuel ratio in the pCDF precombustor is 16.3:1, or more than 2X richer than in the IGCC case. The mass flow rate and combustor pressure in the pCDF case are quite a bit lower, as can be seen by comparing Table 7-11 with Table 7-12.

Table 7-12. Preheat combustor design conditions, pCDF case.

Parameter (per combustor)	Value	Units
Air Flow Rate	177	lbm/s
Inlet Air Temp	572 (300)	F (C)
Inlet Air Pressure	189	psia
Fuel Flow Rate	10.83	lbm/s
Inlet Fuel Temp	110	F
Inlet Fuel Pressure	208	psia
Fuel Lower Heating Value	5027.6	BTU/lbm
Combustor Outlet Temp	1607 (875)	F (C)
Temperature Rise	1035	F
Overall Air/Fuel	16.3:1	mass:mass
Targets:		
Combustor Pressure Loss	2	%
Max NOx level	50	ppm
Max Liner Wall Temp	1472 (800)	F (C)
Max Exit Temp Deviation	± 18 (10)	F (C)
Exit Traverse Quality	~0.02	

Starting with a design concept as shown previously in Figure 7-21, Concepts NREC again performed a series of parametric studies on dimensions of the combustor with the design basis summarized in Table 7-12, focusing on critical performance factors to establish the appropriate dimensions.

The final dimensions are shown in Figure 7-24. These dimensions were arrived at after considering the relationships between the combustor features and various performance parameters. Figure 7-25 shows that large liner diameters favor combustion efficiency. In contrast, pressure-loss factor increases with liner diameter (Figure 7-26). An intermediate point was chosen. The number of dilution holes was optimized based on traverse quality, a measure of the temperature uniformity at the combustor outlet. An example is shown in Figure 7-27.

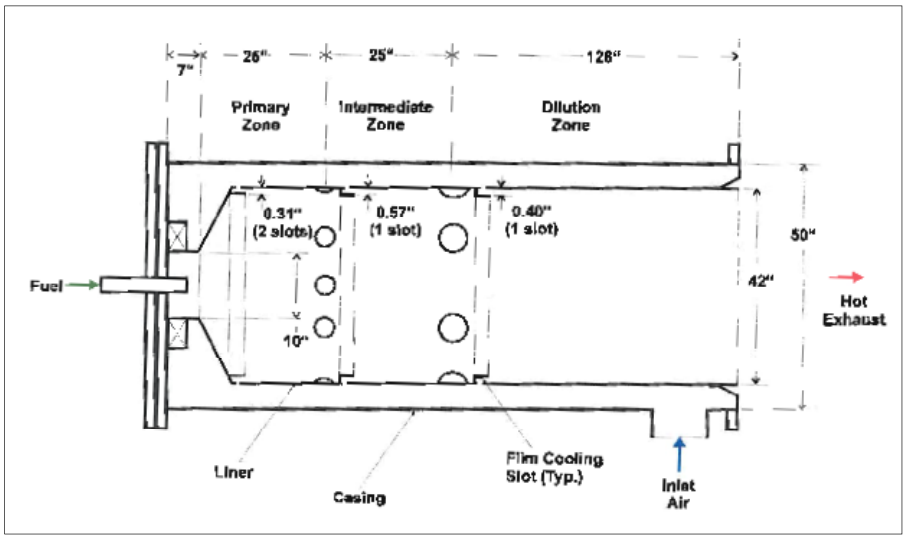

Figure 7-24. pCDF preheat combustor nominal dimensions.

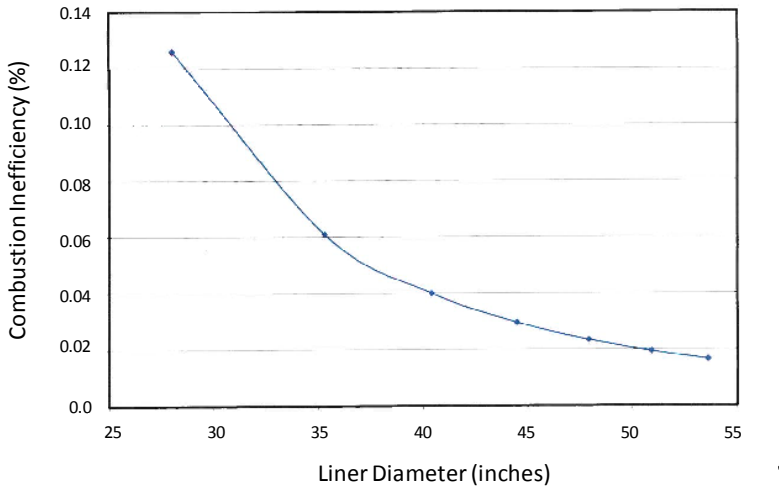

Figure 7-25. pCDF preheat combustor inefficiency as a function of liner diameter.

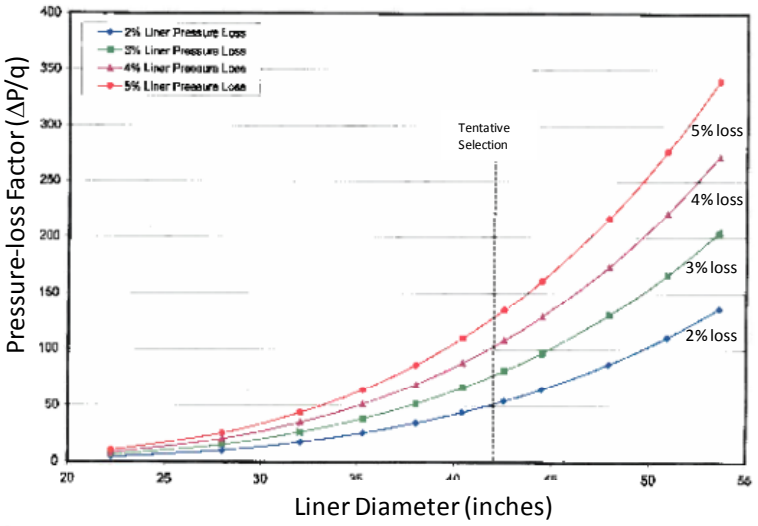

Figure 7-26. pCDF preheat combustor pressure-loss factor as a function of liner diameter.

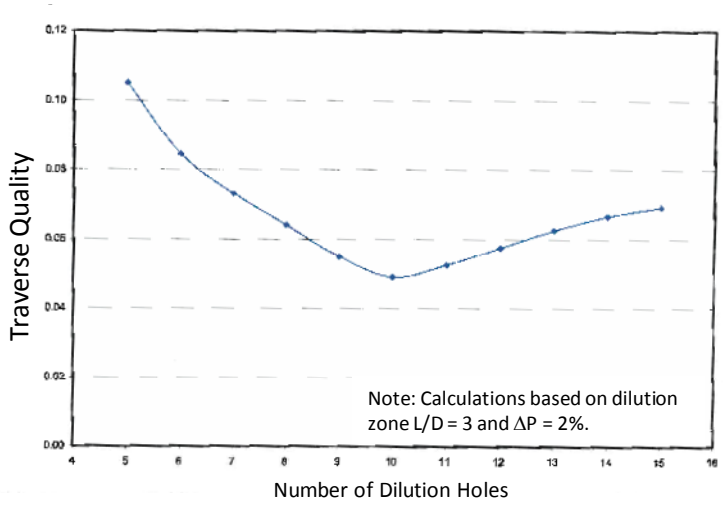

Figure 7-27. pCDF preheat combustor traverse quality as a function of number of dilution holes in the dilution zone.

Figure 7-28 shows the calculated liner temperature variation along the length of the combustor for the chosen design. The equivalence ratio at lean blowout (LBO), a measure of combustion stability, is shown in Figure 7-29. The design point of 0.6 is appropriate for the low inlet temperature of the air and is in a stable regime. NOx calculation results for a range of equivalence ratios is shown in Figure 7-30. The 50 ppm NOx level at 0.6 equivalence ratio meets the study target level

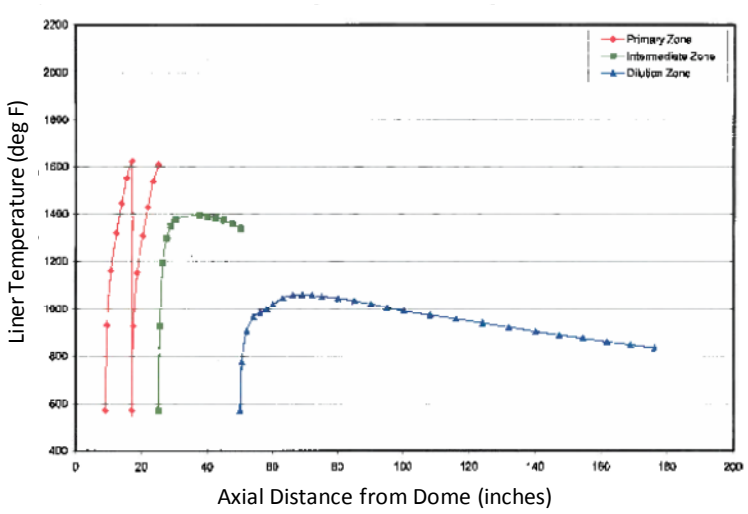

Figure 7-28. pCDF preheat combustor axial liner temperature variation.

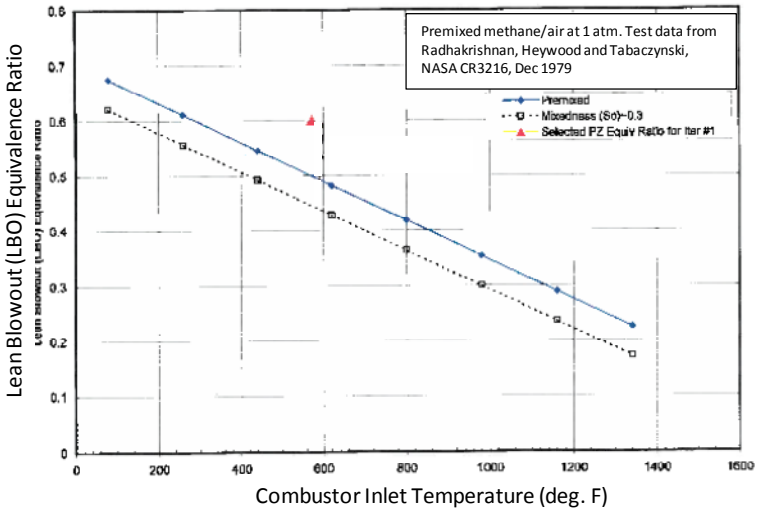

Figure 7-29. pCDF Preheat Combustor equivalence ratio at lean blowout point, variation with inlet temperature. The design point is the red triangle.

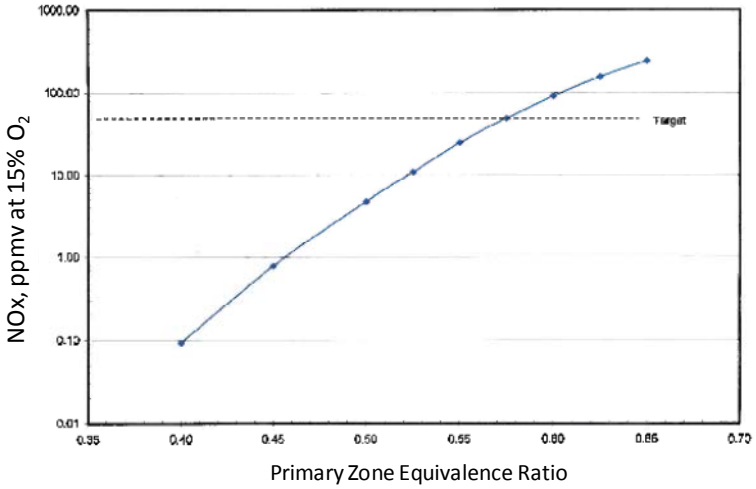

Figure 7-30. pCDF preheat combustor NOx levels relative to primary combustion zone equivalence ratio.

Concepts NREC made the following conclusions based on the study of the pCDF precombustor:

- Relative to the IGCC case precombustor, the high equivalence ratio helps to mitigate stability concerns.
- Liner cooling is straightforward.
- Target exit temperature uniformity requires attention and may require a downstream mixing device.

7.2 Oxygen Circuit Design

Air Products carried out work under this task in the context of Tasks 7.1 and 7.7, where results are summarized. The key efforts focused on identification of large-scale oxygen blowers for applications to large oxygen trains. Select suppliers were contacted and provided input to the process economic studies with price and performance information.

A study was carried out with the information provided by the vendors to establish operating limits for the oxygen circuit. Lower oxygen (permeate) pressures on the membrane side of the circuit enhance the driving force of oxygen through the membranes, leading to less required membrane surface area in the ITM vessel. Lower pressures lead to high actual gas velocities in the circuit, with the concomitant challenges of higher pressure drop and greater likelihood of an oxygen fire. Designs of piping systems and heat exchange equipment at very low pressures therefore require larger equipment to reduce local oxygen gas velocity to meet pressure drop and

oxygen safety requirements. In addition, lower oxygen circuit pressure requires more stages of oxygen compression and greater power requirement. Air Products determined that an optimum in vacuum permeate pressure exists depending on membrane costs and oxygen circuit equipment costs and relative power costs; Air Products generally designed for those optima in process cycle selection activity under Tasks 7.1 and 7.7.

In addition, Air Products gathered oxygen flammability data for various alloys that might be used in oxygen service in the oxygen circuit. A list of some alloys and the conditions of test are shown in Table 7-13. Based on this work, alloy selections were made for the oxygen circuits as well as test apparatus built under this Cooperative Agreement.

Table 7-13. Summary of high temperature test conditions of oxygen flammability.

Alloy	Max Temp, F	O2 Pressure (100% O2) [psig]
446	1380	35-185
316	1575	25
Incoloy 800	900-1800	21-1000
Inconel 617	1800	20-190
Inconel 600	2000	190
HR 160	2000	190
Monel	900	1000

7.3 Engineering Analysis of Membrane Module Components

McDermott Technology, Inc., (MTI) was the original subcontractor under this task and completed some of the work described here. MTI spun off a new company, SOFCo-EFS Holdings, LLC, (SOFCo) during the course of Task 7. The subcontract was moved to SOFCo, who executed the remainder of the tasks. MTI/SOFCo performed a number of analyses during Task 7 to support ceramic architecture development under Task 8 and testing under Tasks 6, 9, and 10.

CEVU Modeling

The Chemical Expansion Verification Unit (CEVU) was constructed by Penn State to determine whether the non-stoichiometry and expansion constitutive relations determined on simple specimens were applicable in regions with vacancy gradients. The CEVU consisted of an ITM ceramic disk on top of an inert tube (see Section 7.6). The atmosphere beneath the disk (within

the tube) and above the disk (outside of the tube) were independently controlled. The disk is simply supported at the radial position of the tube inner surface. Deflections of the disk created by the chemical expansion response of the part to different applied atmospheres were transmitted to measurement electronics by a pushrod located at the center of the disk.

The model (see Figure 7-31a) utilized axisymmetric elements in a coupled diffusion-structural analysis. The pushrod load is applied as a uniform pressure in the center. A model for expansion and transport of the oxygen within the ITM material was coded into the input deck to obtain the no-flux surface vacancy concentration for the specified surrounding oxygen partial pressure. The actual surface vacancy concentration, a function of the flux, was determined by using the surface exchange coefficient (in a manner analogous to a heat transfer coefficient). Since the disk was assumed isothermal, the chemical expansion was calculated by multiplying the change in vacancy concentration relative to the initial condition by the chemical expansion coefficient for that temperature (analogous to multiplying the change in temperature by the thermal expansion coefficient).

Figure 7-31b is an example calculation of the deflection of the disk with an applied oxygen gradient. The deflection data match the experimental data collected by Penn State (see Section 7.6).

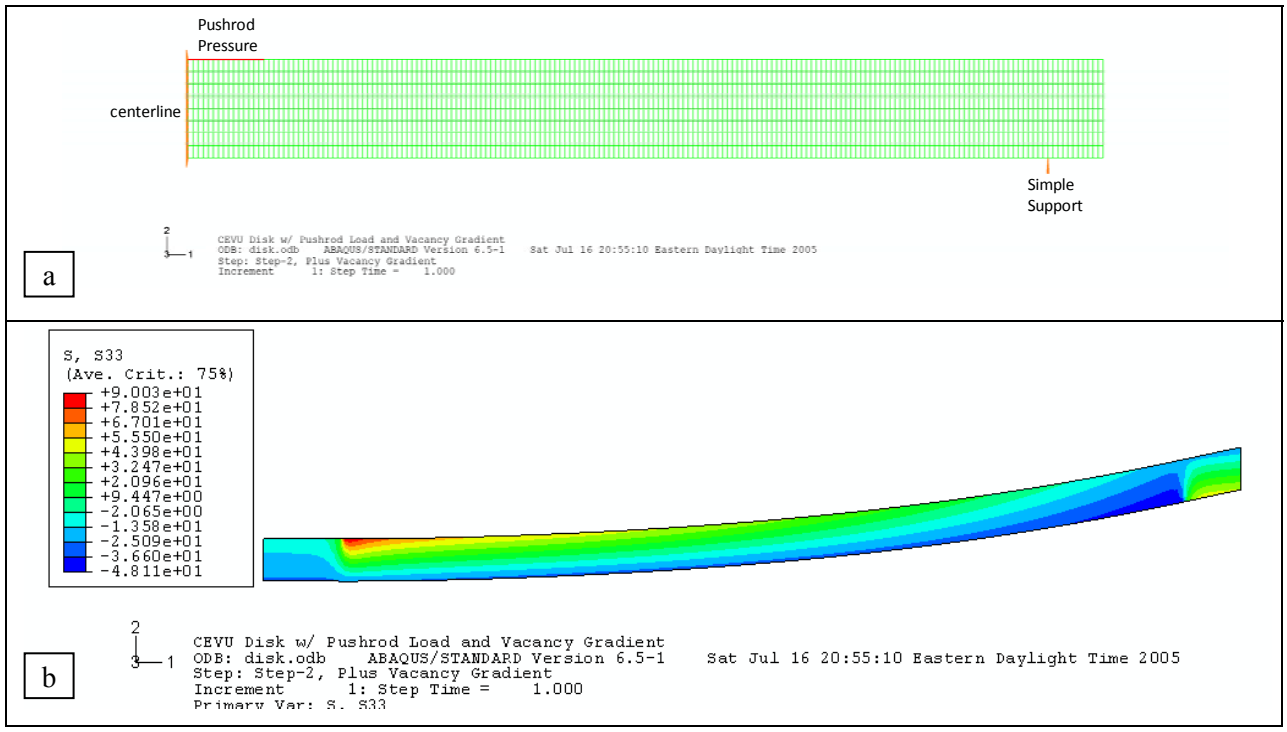

Figure 7-31. a) CEVU model geometry; b) Hoop stresses (MPa) in a simulated disk with an oxygen gradient applied.

U-Ring Seal Modeling – Asymmetric Loading

SOFCo generated a model to determine the U-ring seal response to lateral loading, for example that caused by the hydrodynamic drag on the module from the feed flow. One-half (circumferentially) of a U-ring was modeled with shell elements (see Figure 7-32). The tube and holder were modeled as analytical rigid surfaces. Hard contact was assumed between the U-ring and the tube and holder surfaces. The analysis first resolved the specified interference fit and then considered the specified lateral loading. The interference generated at operating temperature and the lateral loading due to drag were separately calculated. This exercise established limits for the gas velocities when using a seal of this type.

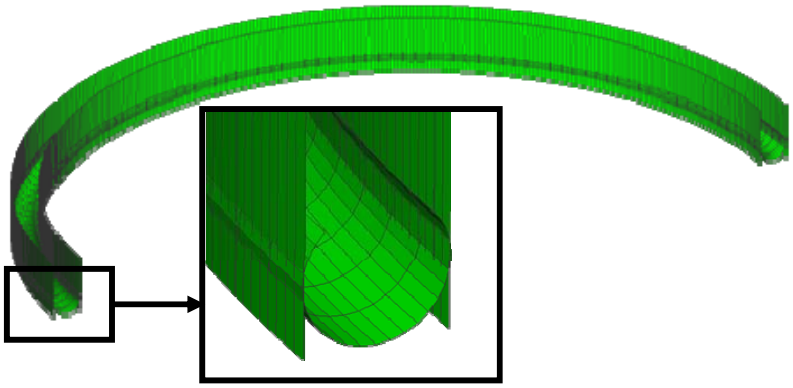

Figure 7-32. Model geometry for a U-ring ceramic-to-metal seal.

U-Ring Seal Modeling – Axisymmetric Loading

SOFCo generated a model to determine the response of a U-ring seal and the adjacent ceramic tube to interference resulting from differential thermal/chemical expansion of the tube, seal, and holder. A submodel was also generated of the tube which explicitly considered a circumferential crack of specified size and location within this stress field. The model and submodel consisted of axisymmetric elements (see Figure 7-33a). The global model utilized first-order elements and assumed hard contact; the interference generated at operating temperature was calculated separately. The submodel considered only the tube and utilized second-order elements with a focused mesh and nodes near the crack tip. The displacements on the OD of the tube from the global model were used as boundary conditions on the submodel. The model was used to calculate crack tip stress intensities, which are shown in Figure 7-33b.

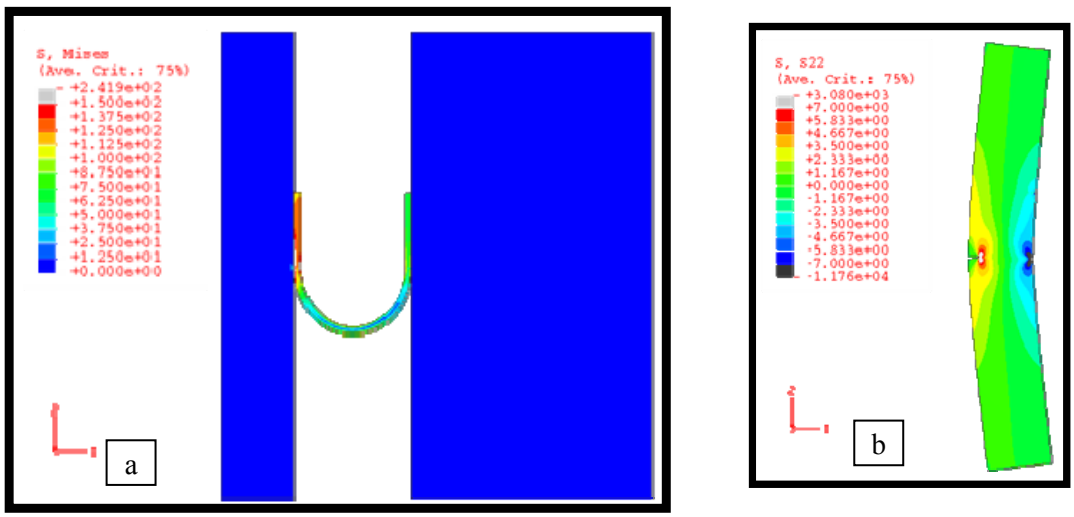

Figure 7-33a. a) Axisymmetric U-ring tube model and calculated stress field; b) submodel of the U-ring tube model, showing stresses near a tube crack.

I-Ring Seal Modeling

SOFCo determined the response of an I-ring seal and the base of the ceramic tube during an operational cycle by calculation. Axisymmetric elements were used (see Figure 7-34a). Yield and creep of the alloy I-ring and gasket were considered. Pressure and differential thermal expansion were considered (chemical expansion was neglected). Soft contact was assumed. Figure 7-34b shows accumulated creep strain in the I-ring element after a simulated 50,000 h at operating temperature.

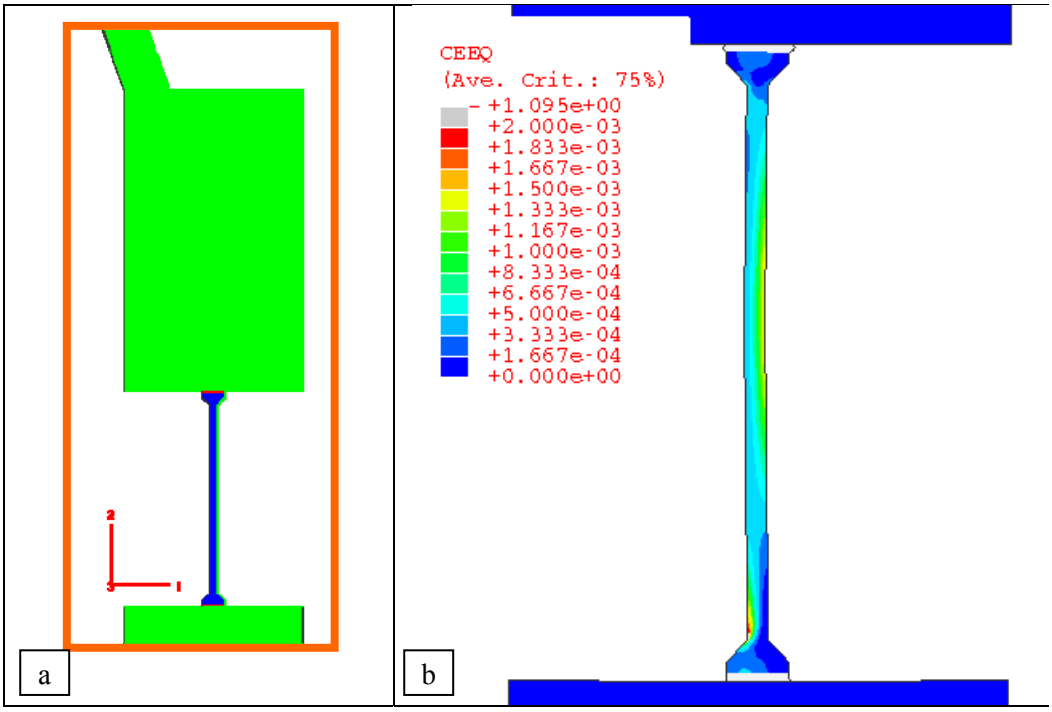

Figure 7-34. a) Geometry of the I-ring seal model; ceramic conical tube "foot" section is shown; b) . Model results of creep strain in the I-ring seal after 50,000 h at temperature.

Flow Tube Modeling

A model was generated to determine the effect of preload, seal load, pressure, and drag on the ceramic flow tube. The model used an axisymmetric element mesh generated with Patran that was modified with a script to handle non-axisymmetric loads. Figure 7-35 shows stresses in a cross-section of a conical flow tube (base piece) showing the effects of drag causing an asymmetric flow field at the point of overturning of the module. Seal loads are shown as point loads.

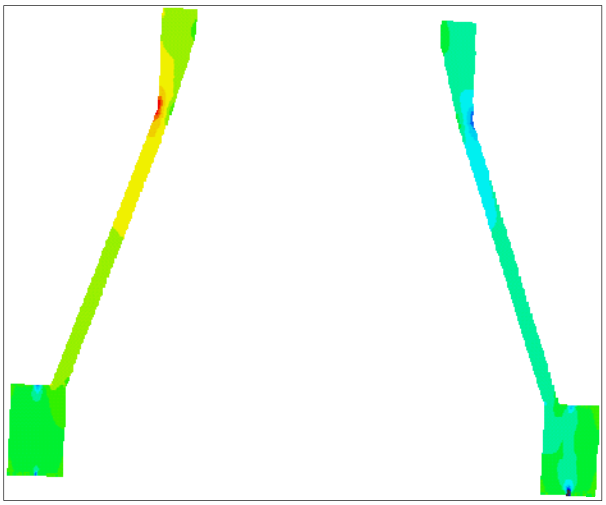

Figure 7-35. Stresses in a cross-section of a 3D model of a conical ITM basepiece.

Transient Dilatometry Modeling

SOFCo built a model to determine the response of a dense bar to an oxygen partial pressure transient to determine transport properties. The one eighth-scale symmetry model consisted of 3D, second-order, reduced integration elements (see Figure 7-36). The diffusion and structural analyses were sequentially coupled. The AP2K expansion properties were written into a subroutine. These results were used to verify material properties.

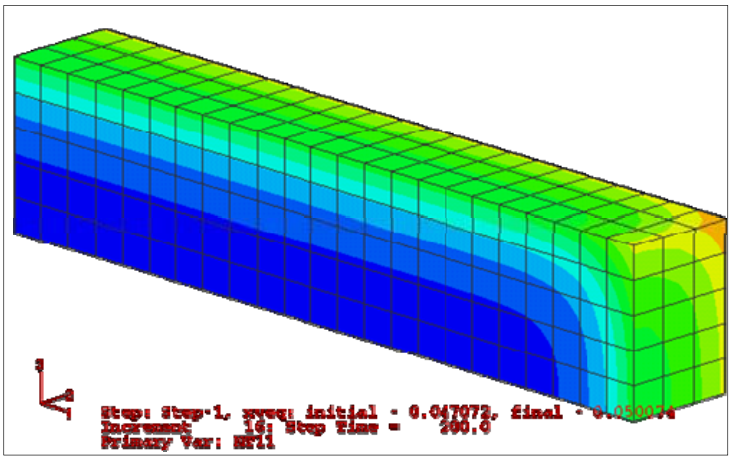

Figure 7-36. Oxygen vacancy fraction in ITM material dilatometry bar during simulated temperature transient.

Flow Tube Creep Collapse Modeling

SOFCo developed a model to determine the potential for creep collapse of an externally pressurized ceramic flow tube (base piece). A quarter-symmetry model of a tube with ovality

and a half-symmetry model of a tube with non-concentric ID and OD were constructed. The models used 2D, second-order, generalized plane strain elements (Figure 7-37). The ITM ceramic material creep properties were implemented with a subroutine. The pressure load was applied on the outer diameter and also simulated axially. Two cases are shown for two times during the evolution of stress and creep, with the starting case shown as an all-green stress field. This work established allowable eccentricity tolerances for base piece fabrication.

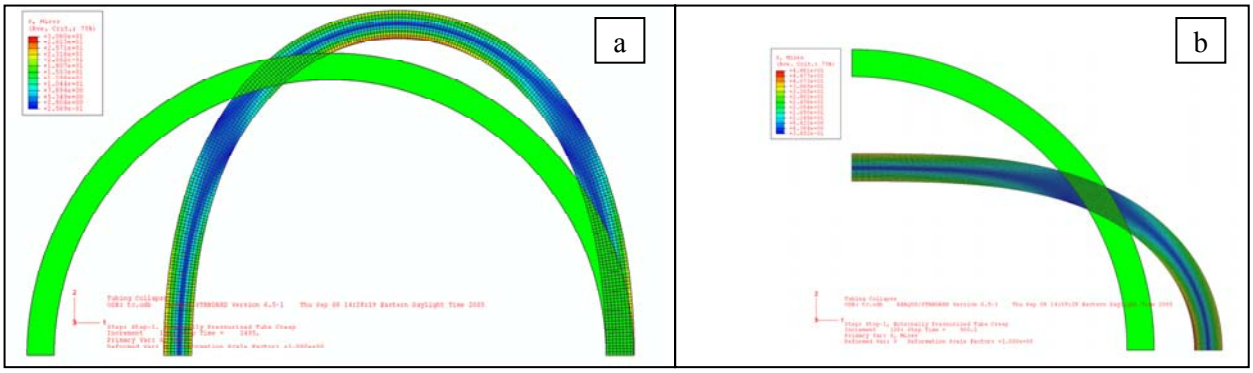

Figure 7-37. a) Tube collapse model with externally applied load, t=900 h; b) Tube collapse model with externally applied load, t=2495 h.

Wafer Modeling for Pressure Loading

Wafer stresses were modeled based on the external pressurization. A quarter-symmetry model of a wafer and half-spacers above and below was constructed. Also, submodels of the region near the outer rim were constructed and implemented on second-order, 3D meshes (Figure 7-38). SOFCo used effective properties in the slotted and porous regions of the global model. Pressure was applied to the external surfaces. The axial symmetry surfaces of the spacers in the global model were forced to stay in plane and were subjected to axial pressure loading. The cut surfaces of the submodels were subjected to the displacements from the corresponding coarse model.

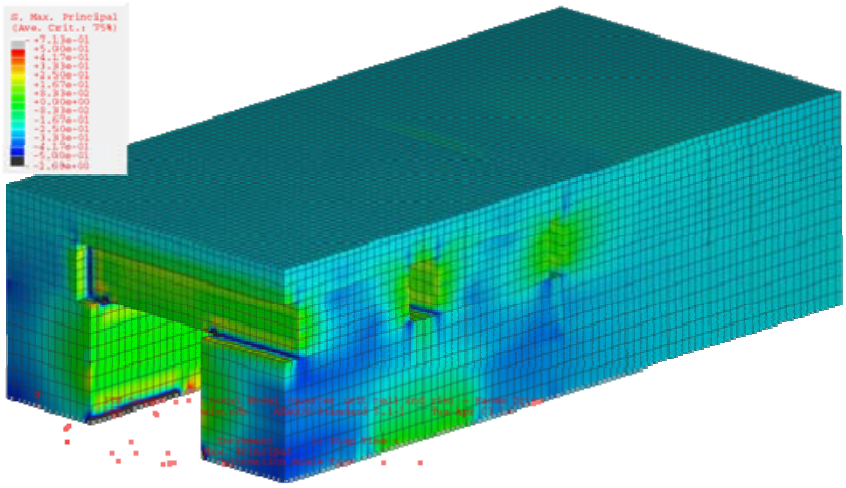

Figure 7-38. Geometry of a slotted region near the wafer edge showing principal stresses caused by applied external pressure load. Local stresses were subjected to boundary conditions determined with a global wafer model.

Unit cell models were also generated solely of the slotted layers to obtain effective properties for the global analysis. SOFCo used a mesh consisting of second-order, 2D, solid elements. The in-plane effective properties were obtained by stretching the model in the two in-plane directions and shearing the model in plane. The response was used to generate a set of effective material properties that were used to represent the interior of the wafer in a global wafer model.

Flow-Induced Vibration in a Wafer

SOFCo generated a quarter-symmetry, 3D, second-order mesh (Figure 7-3.9) to consider the forced vibration resulting from vortices being shed from the wafer's trailing edge. A model was implemented that allowed for stress calculations resulting from vortex shedding frequencies coinciding with the wafer natural frequencies up to the full flow conditions. A typical damping coefficient was assumed. Separate analyses were conducted for each possible symmetry boundary condition to consider all possible modes (asymmetric – asymmetric shown in the figure). The analysis first applies the loading in phase to the trailing edge of the model (consistent with the first two modes). In the second step, loading is applied of opposite sign to those regions moving in opposite directions for the third mode.

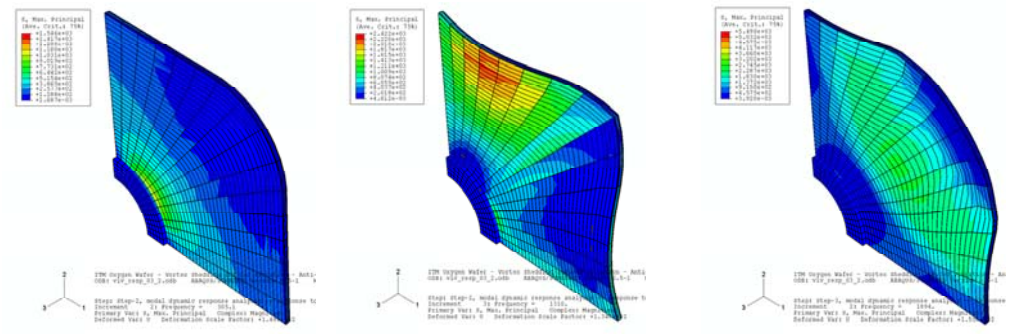

Figure 7-39. Results from flow-induced vibration stress analysis at the resonant frequencies of the wafer. Three frequencies are shown for asymmetric modes.

7.4 Process Vessel Design Engineering

This task focused on developing vessel concepts to house ITM modules that could be implemented and tested in the Subscale Engineering Prototype (SEP) and ultimately scaled up to subsequent pilot-scale apparatus.

SEP Vessel Conceptual Development

McDermott developed two design concepts for the ITM Oxygen SEP vessel, both of which included an air flow duct housing an array of modules (two wide by three in series), as well as individual penetrations through the vessel shell for each of the six module connections. The latter feature allowed for performance analysis of each individual module. McDermott developed two major variations: 1) a commercially prototypical horizontal vessel shell arrangement (see Task 2); and 2) a vertical vessel shell arrangement which allows easy field access to the flow duct and modules, as well as short, straight oxygen permeate piping that could drop directly into a quench tank positioned beneath the vessel. Figure 7-40 illustrates the concept.

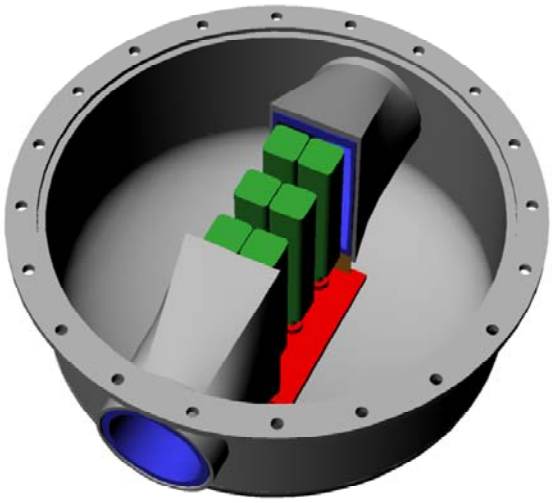

Figure 7-40. Isometric view of a conceptual, vertically oriented vessel to house modules in the SEP. Modules are shown in green. An insulated flow duct, partially disassembled in the figure, houses the modules and maintains the high temperatures away from the vessel walls.

As discussed under Task 7.3, McDermott completed finite element analyses of various flow tube designs subjected to preload, external pressure, and drag loading. Based on that work, McDermott proposed a tapered-tube, passively-cooled C-ring seal design and integrated that approach into the conceptual SEP vessel design. The design relies on the C-ring seal to take all axial loads and positions the C-ring in-line with both the preload and the tube taper. The C-ring is expected to have an operating life greater than five years. Based on these analyses, McDermott determined that fixturing at the top of the module is not necessary to withstand the drag loads at SEP and commercial operating conditions. However, fixturing at the ceramic-to-metal seal to support the module at its base may be required. McDermott's analysis showed that the tapered ceramic flow tube is predicted to have unacceptably high stress levels during cooldown. This occurs due to differential radial contraction of the flow tube and C-ring. An alternate metal sealing element with greater radial compliance was investigated as an alternative.

McDermott also completed a computational fluid dynamics (CFD) analysis of the air flow profiles through the ITM vessel flow duct with a 90° elbow immediately upstream of the inlet nozzle. This configuration is likely because of the close-coupling of the preheater with the ITM vessel. As shown in Figure 7-41, the flow profile is significantly distorted in the inlet section and much of the transition piece, but the flow is reasonably well-redistributed by the time it reaches the first bank of modules.

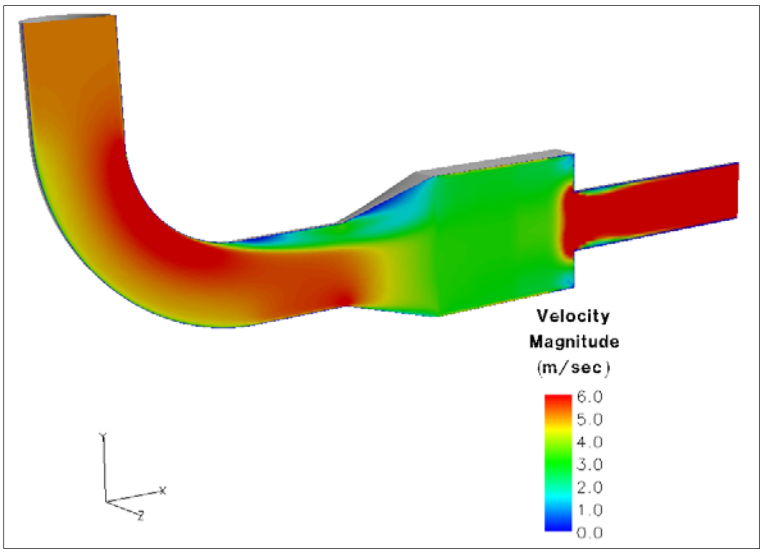

Figure 7-41. Central slice of a calculated flow field of air feed into a conceptual design for the SEP vessel.

McDermott completed a quarter-symmetry, 3D model of the SEP vessel (Figure 7-42) to determine the temperature distribution within the vessel and perform thermal-stress analysis of the ceramic flow tube. The oxygen permeate stream was modeled with convective-diffusive elements. The stagnant gas within the vessel was modeled with shell elements adjacent to all exposed surfaces within the vessel, which were constrained to have uniform temperature and coupled to the adjacent surfaces with the appropriate convective heat transfer correlations. The radiation heat transfer within the vessel was also explicitly modeled.

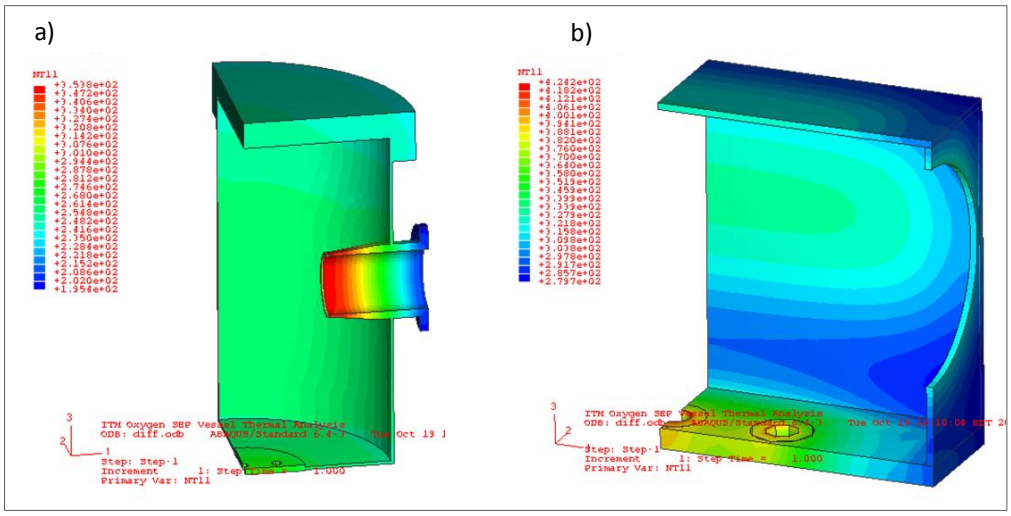

Figure 7-42. Calculated thermal profiles in a conceptual SEP vessel. a) internally insulated inlet nozzle; b) interior flow duct (insulated).

The thermal stress analysis was accomplished with a first-order mesh. The ceramic tube thermal distribution was mapped first onto a second-order thermal mesh and then onto a second-order structural mesh. Only thermal loading was considered in the structural analysis. The model includes natural convective behavior in the insulation region around the seals to capture the possibility of convective heat leak there. The model also includes provisions to simulate natural convection in the annular air space between the flow duct and the walls of the vessel.

Ceramic-to-Metal Seal Sub-Assembly for ITM Oxygen Modules

McDermott and Air Products developed concepts to support ITM Oxygen modules within the ITM pressure vessel/flow duct. One concept entails preassembling the module with a metallic fixture outside the vessel. The fixture holds the seal cup, short pipe stub, and a compact flange. A metal-to-metal seal at the top of the seal cup enables change-out of the sealing surface and re-use of the sub-assembly. The sub-assembly also might provide an appropriate base from which to build a protective enclosure for handling and perhaps shipping. The aim of the sub-assembly is to minimize precarious handling of the ceramic modules inside the vessel shell. The general aim of the effort is to connect the ceramic base piece of the ITM module with the manifold piping within the vessel through an appropriate intermediary element.

The team investigated a specific embodiment of the concept. The sub-assembly was designed wtih a metallic seal cup that houses the base of the ceramic tube and the sealing element(s), and a short metallic pipe stub terminating in a flange that can connect to a metallic element within the vessel. The pipe stub can provide a mounting point for hardware (e.g., tie rods, clamping collars, springs, etc.) used to pre-load the ceramic-to-metal seal as necessary.

This concept allows individual pre-assembly of ceramic-to-metal seals remotely in a controlled environment, with tightly spaced field connections relying only on simple bolted joints. This feature is especially advantageous if the ceramic-to-metal seal involves complicated pre-load fixturing and/or shorter turnaround time is important.

McDermott performed a thermal analysis of the sub-assembly with the assumption that it is buried in insulation and is internally insulated as well, up through the ITM ceramic conical base piece. Results are presented in Figure 7-43, showing a cross-section of the sub-assembly on the left, and details of the ceramic conical base piece surface temperatures on the right. Such

calculations were useful in establishing the thermal gradients that the ceramic conical base piece must withstand.

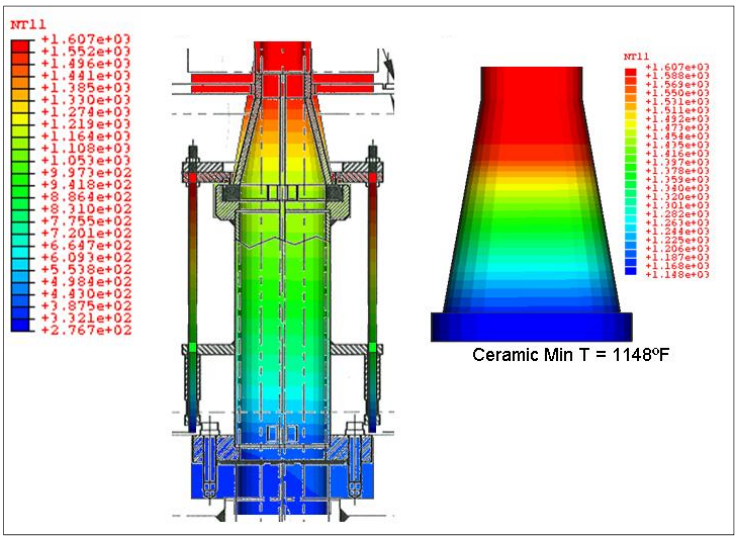

Figure 7-43. Calculated thermal profile of the sub-assembly supporting an ITM module with a conical base piece. Left: cross-section of subassembly. Right: surface temperatures of conical basepiece.

Figure 7-44 shows a first prototype of the sub-assembly, fitted with a conical ceramic base piece that has been fitted with a ceramic end cap for ceramic-to-metal seal testing. Tie rods provide proper tensioning of hold-down clamps and/or ceramic-to-metal seal elements. The flange at the base would clamp to the vessel piping and make a metal-to-metal seal. Note that additional features can be introduced to this design, including a means of sampling the gas stream, pressure and/or temperature measurement, insulation, and gas introduction and valving. Such units were ultimately included in the Subscale Engineering Prototype (SEP) design and operation (Task 10).

Figure 7-44. Photograph of an early prototype of the sub-assembly.

7.5 Controls System Design

Gas Turbine Protection and Plant Operation Conceptual Design

Air Products and Siemens collaborated to evaluate the process control requirements of an integration between a gas turbine and an ITM system. Both the large frame (SGT6-6000G) for IGCC and a small-frame machine (GT35P) for the ISTU were considered. Flowsheets were developed and operating procedures were conceptualized.

1. **IGCC Integrated Gas Turbine-ITM System Control, Siemens SGT6-6000G**

IGCC Flowsheet development: Hot Gas Piping Conceptual Design

The interconnections between the SGT6-6000G gas turbine and the ITM systems are shown schematically in Figure 7-45. The major equipment and piping identified in the figure are further specified in Table 7-14.

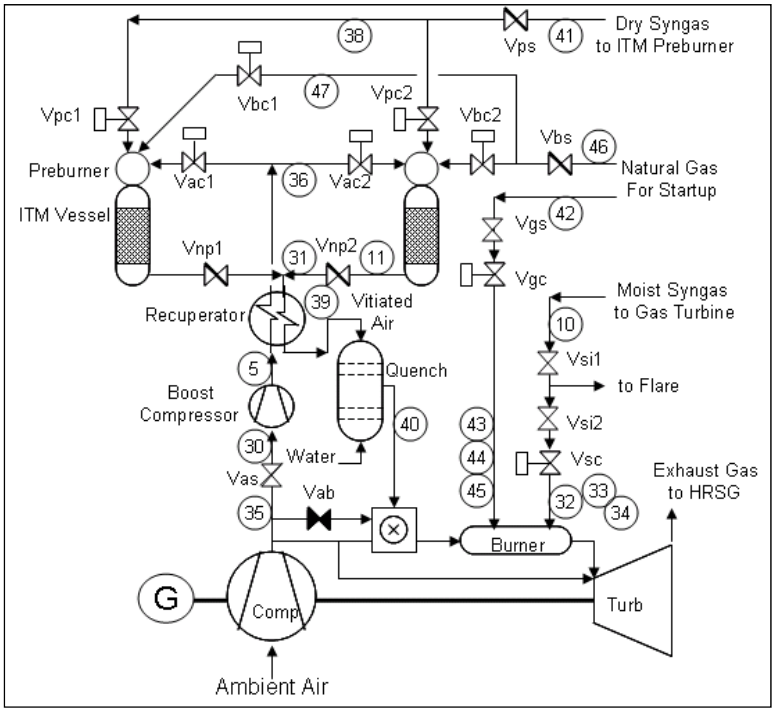

Figure 7-45. ITM gas turbine interconnection diagram, SGT6-6000G.

All line sizes, design pressures, and design temperatures in the table are based on design-point conditions. Startup fuel flow rates and line sizes are based on the assumption that the fuel enthalpy flows for the ITM preheater and gas turbine are the same during startup as during steady-state, design-point operation.

Table 7-14. ITM gas turbine interconnection components, SGT6-6000G.

Item	No.	Description	Size
5	1	Extraction air pipe, carbon steel, 370 psig, 850 ^{o}F	42 inch (nominal)
10	1	Syngas pipe, carbon steel, 450 psig, 455 ^{o}F	18 inch (nominal)
11	2	Vitiated air pipe, alloy steel, 350 psig, 1130 ^{o}F	28 inch (nominal)
30	1	Extraction air pipe, carbon steel, 370 psig, 850 ^{o}F	36 inch (nominal)
31	2	Vitiated air pipe, alloy steel, 350 psig, 1130 ^{o}F	32 inch (nominal)
32	1	Syngas pipe, carbon steel, 450 psig, 455 ^{o}F	16 inch (nominal)
33	1	Syngas manifold, carbon steel, 450 psig, 455 ^{o}F	14 inch (nominal)
34	16	Syngas manifold spurs, carbon steel, 450 psig, 455 ^{o}F	4 inch (nominal)
35	1	Extraction air pipe, carbon steel, 370 psig, 850 ^{o}F	48 inch (nominal)
36	2	Extraction air pipe, carbon steel, 370 psig, 850 ^{o}F	28 inch (nominal)
38	2	ITM Preburner syngas pipe, carbon steel, 450 psig, 455 ^{o}F	6 inch (nominal)
39	1	Vitiated air pipe, alloy steel, 350 psig, 1130 ^{o}F	42 inch (nominal)
40	1	Vitiated air pipe, alloy steel, 350 psig, 1130 ^{o}F	42 inch (nominal)
41	1	ITM Preburner syngas pipe, carbon steel, 450 psig, 455 ^{o}F	8 inch (nominal)
42	1	Natural Gas (startup) pipe, carbon steel, 730 psig, 75 ^{o}F	6 inch (nominal)
43	1	Natural Gas (startup) pipe, carbon steel, 730 psig, 75 ^{o}F	6 inch (nominal)
44	2	Natural Gas (startup) manifold, carbon steel, 720 psig, 75 ^{o}F	6 inch (nominal)
45	16	Natural Gas (startup) spurs, carbon steel, 720 psig, 75 ^{o}F	2 inch (nominal)
46	1	Natural Gas preburner (startup) pipe, carbon steel, 720 psig, 75 ^{o}F	4 inch (nominal)
47	2	Natural Gas preburner (startup) pipe, carbon steel, 720 psig, 75 ^{o}F	2 inch (nominal)
Boost	1	Boost Compressor	37 ft. Long x 6.4 ft. Wide x 10 ft. High
Burner	16	SGT6-6000G Combustor	-
Comp.	1	SGT6-6000G Compressor	-
ITM Vessel	2	ITM Oxygen Separation Vessel	11.5 ft Dia x 56 ft. Long

Table 7-14. ITM gas turbine interconnection components, SGT6-6000G (cont).

Preburner	2	ITM Preburner	4.5 ft. Dia x 10 ft. Long
Quench	1	Vitiated Air Quench Cooler	TBD
Recup.	TBD	ITM Recuperator, ~90,000 sq,ft, active surface area	TBD
Turb	1	SGT6-6000G Expander	-
Vac	2	ITM Inlet Air Control Valves, 370 psig, 850 ^{o}F	28 inch (nominal)
Vas	1	ITM Inlet Air Shutoff Valve, 370 psig, 850 ^{o}F	36 inch (nominal)
Vab	1	ITM Bypass Air Shutoff Valve, 370 psig, 850 ^{o}F	36 inch (nominal)
Vbc	2	Natural Gas preburner (startup) Control Valve, 730 psig, 75 ^{o}F	2 inch (nominal)
Vbs	1	Natural Gas preburner (startup) Shutoff Valve, 730 psig, 75 ^{o}F	4 inch (nominal)
Vgc	1	Natural Gas (startup) Control Valve, 730 psig, 75 ^{o}F	6 inch (nominal)
Vgs	1	Natural Gas (startup) Shutoff Valve, 730 psig, 75 ^{o}F	6 inch (nominal)
Vnp	2	Vitiated air Shutoff Valve, 350 psig, 1130 ^{o}F	28 inch (nominal)
Vpc	2	Preburner Syngas Control Valve, 450 psig, 455 ^{o}F	6 inch (nominal)
Vps	1	Preburner Syngas Shutoff Valve, 450 psig, 455 ^{o}F	8 inch (nominal)
Vsc	1	GT Syngas Control Valve, 450 psig, 455 ^{o}F	18 inch (nominal)
Vsi	2	GT Syngas Isolation Valves, 450 psig, 455 ^{o}F	18 inch (nominal)

IGCC Flowsheet development: Syngas Piping and Valve System

Compared to natural gas piping, syngas piping is larger in diameter because the syngas contains fewer combustible compounds and is moving through the piping at a higher temperature. The syngas produced by the gasifier contains only ~22% of the heating value of natural gas, so in this application the gas turbine requires a syngas mass flow rate ~4.8 times greater than that of natural gas. Also, the temperature of the syngas entering the gas turbine is almost 400^{o}F, hotter than the nominal 60^{o}F temperature of natural gas. Therefore, this syngas has, respectively, a specific volume and volumetric flow rate 1.5X and 7X greater than natural gas. The STG6-6000G turbine is designed to operate with this type of warm syngas, but a separate piping system for this syngas is needed to complement the existing natural gas fuel piping.

Clean syngas leaving the gasification island flows through two isolations valves and a syngas gas control valve before entering the gas turbine. These valves regulate or shut off the flow of fuel to the gas turbine combustors in the event of a plant upset, change of load, or loss of load. The syngas piping and valves are about three times the diameter of natural gas piping.

IGCC Flowsheet Development: Bypass Piping and Valve Systems

The sudden loss of electrical load causes rapid acceleration of the gas turbine, which must be stopped in order to prevent catastrophic damage to the gas turbine and other equipment shown in Figure 7-45. At the first instant of load loss, the fuel gas valve (Vsc) quickly closes to interrupt gas flow to the turbine, bypassing the fuel gas to flare. Also, the preburner syngas control valves (Vpc1, Vpc2) close to stop the flow of syngas to the ITM preburners, while vitiated air valves (Vnp1, Vnp2) close to isolate the ITM system from the gas turbine.

The system of air bypass valves shown in Figure 7-45 is required to ensure overspeed protection for the gas turbine. Because of the large inventory of hot, pressurized air in the ITM system and piping, merely shutting off the fuel is not sufficient for overspeed protection. The considerable amount of pressurized air and thermal energy that exists in the ITM system – from the compressor discharge to the gas turbine combustor inlet – must be controlled to prevent excessive overspeed of the gas turbine/generator unit and subsequent catastrophic failure.

Upstream of the ITM, the air bypass system prevents air from entering the ITM system. The compressed air bypass valve (Vab) opens as the compressed air supply valve (Vas) closes, interrupting the flow of air through the ITM system to the turbine and sending cooler, compressed air directly to the gas turbine combustor. By adjusting the air bypass valve (Vab), the compressor pressure ratio is elevated, increasing compressor work to aid in the deceleration process.

IGCC Plant Start Up

The startup of an ITM-IGCC plant involves interactions among four main plant subsystems: the gas turbine, the combined cycle, the ITM Oxygen separator, and the coal gasification unit.

- The gas turbine provides power generation, compressed air for the ITM Oxygen separator, and waste heat for steam generation

- The combined cycle provides steam for steam turbine power generation, coal gasification, syngas cleaning, purging, and NOx abatement during gas turbine operation on natural gas
- The ITM Oxygen separator uses compressed air to provide oxygen to the coal gasification unit.
- The coal gasification unit includes coal gasification and syngas conditioning, which may include the addition of N_2 and H_2O to reduce the heating value from about 9 MJ/kg down to about 4 MJ/kg.

The main plant startup steps are listed in Table 7-15.

Table 7-15. Plant start sequence.

Step	Activity	Valve Lineup
1	Start combined cycle with natural gas	Vab, Vgs open; Vgc at setpoint; All other valves closed
2	Start air extraction from gas turbine to ITM	Open Vnp1, Vnp2, Vas Gradually open Vac1, Vac2 while closing Vab
3	Start ITM with natural gas	Open Vbs; Gradually open Vbc1, Vbc2 through preburner ignition.
4	Start oxygen supply from ITM to gasification unit	(Not shown)
5	Start main systems of gasification unit (coal preparation, gasification, waste heat boiler system, syngas desulfurization, sulfur recovery)	(Not shown)
6	Start of saturator system	(Not shown)
7	Start clean syngas supply from gasification unit to combined cycle (gas turbine)	Open Vsi1, Vsi2; Gradually open Vsc while closing Vgc
8	Switch off natural gas to gas turbine	Close Vgs; Vsc at setpoint
9	Start clean syngas supply from gasification unit to ITM preburner	Open Vps Gradually open Vpc1, Vpc2 while closing Vbc1 and Vbc2
10	Switch off natural gas to ITM preburner	Close Vbs; Vbc1 and Vbc2 at setpoint
11	Integrate part-load operation with 75% gasification load	Modulate Vsc, Vac1, Vac2 as needed
12	Operate combined cycle on syngas with 75% gasification load (after water/steam side coupling)	Modulate Vsc, Vac1, Vac2 as needed
13	Operate combined cycle on syngas at full load	Modulate Vsc, Vac1, Vac2 as needed

IGCC Normal Plant Shutdown

The normal plant shutdown sequence is listed in Table 7-16.

Table 7-16. Normal plant shutdown sequence.

Step	Activity	Valve Lineup
1	Reduce combined cycle operation to 75% load by reducing syngas feed rate while closing the GT guide vanes to maintain constant exhaust gas temperature. Reduce gasifier coal, oxygen, and steam feeds while maintaining normal operating temperature.	Modulate Vsc, Vac1, Vac2 as needed; (Other valves not shown)
2	Reduce syngas feed rate to reduce GT power output to about 16% GT load. (Since GT power is above 15%, the transition cooling medium does not need to change from steam to air.)	Same as in previous step
3	Open natural gas flow to GT to enable GT operation after syngas is shut off.	Open Vgs; (Vgc still closed)
4	Ramp down coal, oxygen, and steam feeds to gasifier. Ramp down ITM operation.	Gradually close Vpc1, Vpc2, Vac1, Vac2, and other valves not shown.
5	Switch GT to natural gas operation	Open Vab; Open Vgc to setpoint; Close Vas, Vps, Vsi2
6	Ramp down steam turbine system.	(Not shown)
7	Shut off natural gas to GT, stopping GT	Gradually close Vgc, then close Vgs

IGCC Abnormal Plant Shutdown

The steps listed in Table 7-17 must be executed simultaneously for the fastest plant shutdown.

Table 7-17. Plant abnormal shutdown sequence.

Step	Activity	Valve Lineup
1	Shut off syngas	Close Vsi2, Vps; Flare syngas
2	Shut down gasifier	(Not shown)
3	Isolate ITM	Close Vas; Open Vab; Close Vnp1, Vnp2

ISTU Integrated Gas Turbine-ITM System Control, Siemens GT35P

ISTU Plant-Integration Concept Description

The proposed ISTU comprises the functional subsystems shown in Figure 7-46 as a process flow diagram. This facility produces 150 short tons of oxygen per day. The streams and equipment in the diagram are identified in Tables 7-18 and 7-19 respectively. The figure and tables include

streams for both an indirect-fired preheater and a direct-fired preheater. One or the other of these options might be selected for the actual plant, or both may be included in parallel for technical risk management.

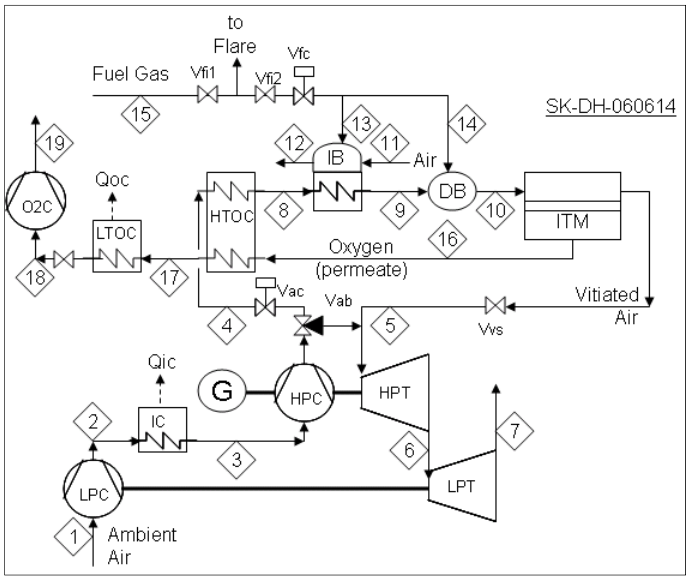

Figure 7-46. 150-TPD ITM test facility process flow diagram.

Table 7-18. 150-TPD ITM test facility streams.

Stream	Fluid	Location
1	Air	LP compressor inlet
2	Air	LP compressor exit / intercooler inlet
3	Air	Intercooler exit / HP compressor inlet
4	Air	HP compressor exit
5	Vitiated air	HP turbine inlet
6	Vitiated air	HP turbine exit / LP turbine inlet
7	Vitiated air	LP turbine exit
8	Air	High-temp O2 cooler exit
9	Air	Indirect burner exit
10	Vitiated air	Direct burner exit / ITM inlet
11	Air	Indirect burner inlet
12	Vitiated air	Indirect burner exit
13	Fuel gas	Indirect burner inlet
14	Fuel gas	Direct burner inlet
15	Fuel gas	Total plant inlet
16	Oxygen	ITM exit
17	Oxygen	High-temp O2 cooler exit
18	Oxygen	Low-temp O2 cooler exit
19	Oxygen	O2 compressor exit

Table 7-19. 150-TPD ITM test facility equipment.

Item	Description
DB	Direct burner (if used)
G	Generator
HPC	High-pressure compressor
HPT	High-pressure turbine
HTOC	High-temperature oxygen cooler
IB	Indirect burner (if used)
IC	Intercooler
ITM	ITM Oxygen separator
LPC	Low-pressure compressor
LPT	Low-pressure turbine
LTOC	Low-temperature oxygen cooler
O2C	Oxygen compressor
Vab	Air bypass valve
Vac	Air control valve
Vfc	Fuel control valve
Vfi1	Fuel isolation valve
Vfi2	Fuel isolation valve
Vos	Oxygen shutoff valve
Vvs	Vitiated air shutoff valve

ISTU Start Procedure

The basic ISTU system is shown schematically in Figures 7-47 through 7.55. Valves Vvi and Vab are the "intercept valves" incorporated within the current configuration of the GT35P engine. Valve Vvi consists of two butterfly-type shutoff valves located in the inner passage of the coaxial piping connecting the engine to the ITM pressure vessel and external combustion system. As these valves will likely leak because of their severe service, an additional valve, Vvs, provides positive shutoff to isolate the turbine from the large volume and thermal mass of the ITM system. Valve Vab consists of four independently-actuated, piston-type shutoff valves located in the outer annular passage of the coaxial piping. In the “open” position, the valves divert the flow from the HP compressor to the external ITM system. In the alternate “closed” position, they bypass the external ITM system and divert the compressor discharge flow directly to the inlet of the HP turbine.

The "ASU bypass" valve, Vbp, will control the portion of compressed air bypassing the entire ASU system and mixing with the ITM exit (non-permeate) stream before entering the HP

turbine. This bypassing capability is necessary to maintain stable operation of the gas turbine during startup conditions, as well as to moderate the turbine inlet temperature slightly below the ITM operating temperature during normal operation.

The "ITM bypass" stream shown in the schematic consists of a portion of the combustor exhaust stream diverted around the ITM modules and mixed with the exiting non-permeate stream. In the current concept, this bypass would be provided passively by fixed orifice rather than by an adjustable control valve. This design feature allows simple adjustment of the air flow through the ITM modules as appropriate for different oxygen production capacities. For a larger plant (e.g., 500 TPD), the entire balance of plant, including pre-heater, would remain the same; only a change to the orifice and additional ITM modules would be required.

A very small auxiliary compressor will provide the capability of pressurizing the ITM system as part of the startup procedure. The vent valve Vav, mounted on the vessel shell will ensure positive flow through the auxiliary compressor (i.e,. no dead-heading) if necessary. In addition, it will provide emergency depressurization if Vvs and Vvi should fail or leak during a gas turbine trip. Valve Vfc will control the fuel flow to the preheat combustor during start-up and full operation of the system. Valve Vos will control the flow of oxygen by controlling permeate pressure. It may actually consist of a variable frequency drive (VFD) on the oxygen compression equipment.

The main purpose of the valve arrangement is to:

- control air flow to the ITM pressure vessel during start and trip sequences;
- instantly isolate the gas turbine from the ITM pressure vessel on both air and flue gas sides during a gas turbine trip situation;
- depressurize the ITM vessel after a gas turbine trip, if necessary;
- control air flow to the ITM pressure vessel for different plant loads.

Valve Descriptions

Vab	Cold Intercept Valve	Open	By-pass	One controllable, three digital
Vvi	By-pass Valve	Open	Shut	Digital
Vbp	Hot Intercept Valve	Open	Shut	Controllable
Vav	Cold Blow Off Valve	Open	Shut	Controllable

Vfc	Fuel Control Valve	Open	Shut	Controllable
Vos	ITM Oxygen Valve	Open	Shut	Controllable
Vvs	Vitiated Air Shut-off Valve	Open	Shut	Digital

The plant start procedure is described in the following series of steps. Note that the times shown for the ITM system start-up (steps 6 through 9) are durations currently practiced in the laboratory and pilot plant; they are expected to improve with operating history and advanced control methods (to about one full day for all steps combined).

Step 1 - Baring

Vab By-pass
Vvi Shut
Vbp Shut
Vav Shut
Vfc Shut
Vos Shut
Vvs Open

Baring the LP and HP rotor at 108 and 150 rpm, respectively, for 30 minutes.
The term "Baring" refers to a motor turning the turbine shaft to prevent it from deforming during cooldown. Two motors are needed – one motor for the HP shaft and another for the LP shaft – because the speed of the HP rotor is too low to generate enough air flow to rotate the LP shaft. All valves are closed except Vvs. Valve Vab is set in the closed (bypass) position which diverts any flow from the HP compressor to the inlet of the HP turbine (Figure 7-47).

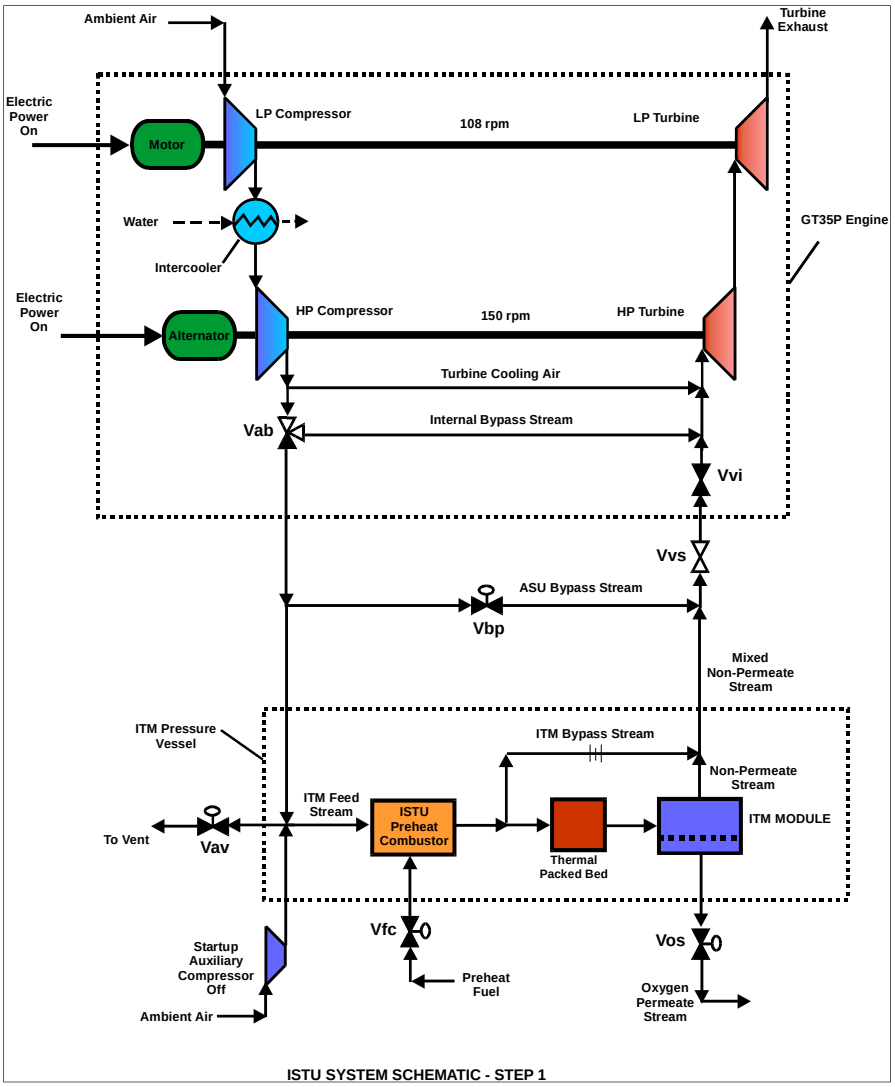

Figure 7-47. Baring (30 minutes).

Step 2 - HP Rotor Acceleration

Vab By-pass
Vvi Shut
Vbp Shut
Vav Shut ===> Open (if necessary)
Vfc Shut
Vos Shut
Vvs Open

When the start sequence begins, the baring is stopped and the generator on the HP shaft is used as a motor by means of special start equipment (frequency converter). When the HP shaft is accelerated, the HP rotor generates enough air flow to rotate the LP rotor. The HP

rotor speed is increased to 2500 rpm, causing the LP rotor to increase its speed to 500 - 700 rpm. This sequence takes 15 – 20 minutes.

Meanwhile, a separate auxiliary start-up compressor system pressurizes the ITM pressure vessel to 0.5 bar(g) (7.5 psig) back to the cold intercept valve (Vab). This pressurization ensures that the compressor always works with sufficient backpressure to avoid "windage" which might damage the compressor. If necessary, valve Vav is opened and adjusted to allow positive flow through the auxiliary compressor to avoid dead-heading it (Figure 7-48).

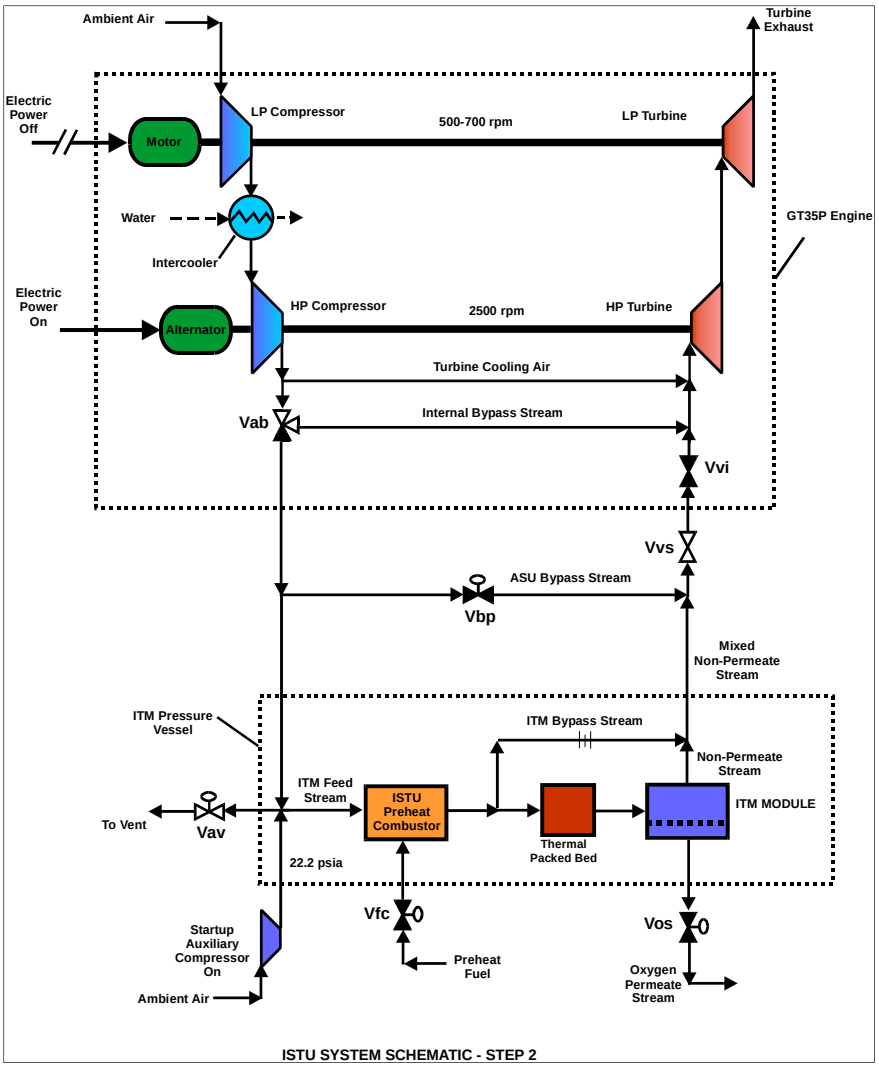

Figure 7-48. HP rotor acceleration (15-20 minutes).

Step 3 - Synchronizing

Vab By-pass
Vvi Shut
Vbp Shut
Vav Open (if necessary)
Vfc Shut
Vos Shut
Vvs Open

The HP rotor speed is increased to synchronization speed (6107 rpm) and the generator is connected to the grid, which takes 15 – 20 minutes. During this time the LP rotor speed is increased to 1500 – 1700 rpm (Figure 7-49).

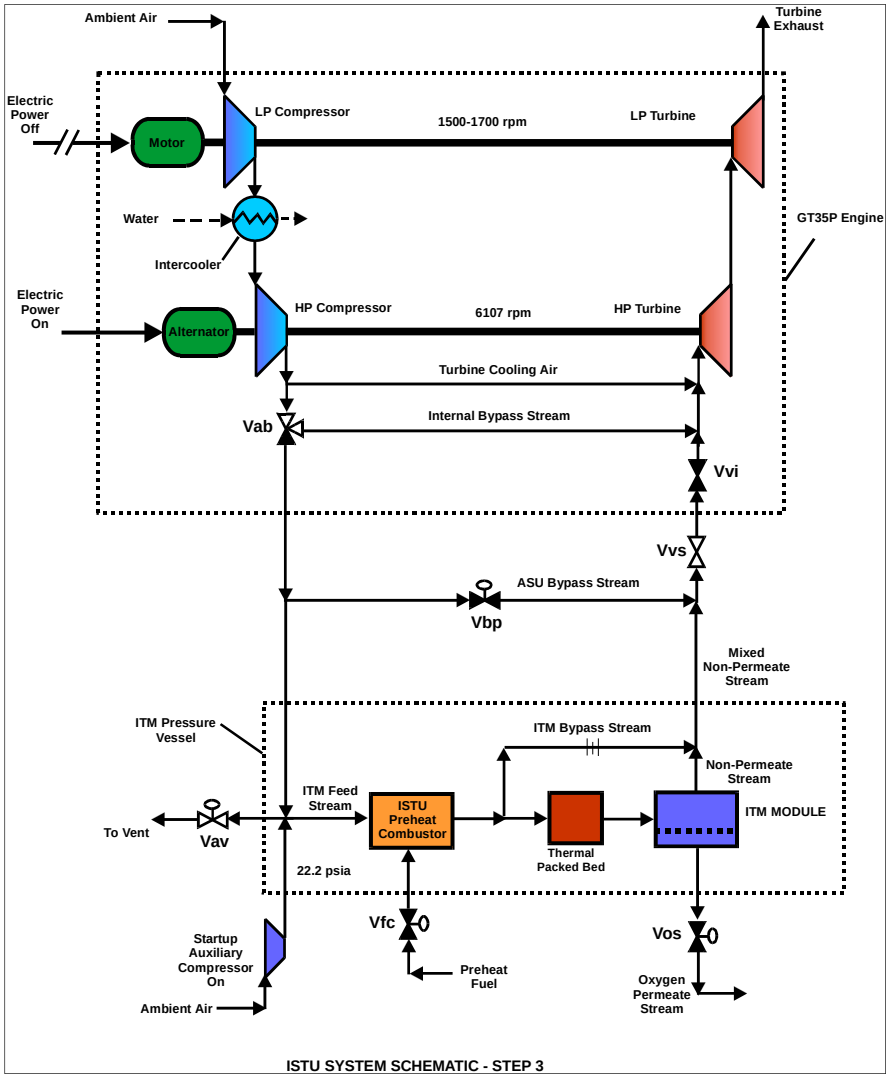

Figure 7-49. Synchronizing (15-20 minutes).

Step 4 - Ventilation

Vab By-pass ===> Open
Vvi Shut ===> Open
Vbp Shut ===> Open
Vav Open===> Shut
Vfc Shut
Vos Shut
Vvs Open

The controllable cold intercept valve is carefully opened, and as the differential pressure stabilizes, the rest of the intercept valves (Vab and Vvs) to the ITM pressure vessel are opened and air flows from the compressor through the pressure vessel and back to the turbine expander. At the same time, the ASU bypass valve (Vbp) opens fully, to limit the rate of heat input to the ITM pressure vessel. If open, vent valve Vav is closed, and the auxiliary compressor is turned off (Figure 7-50).

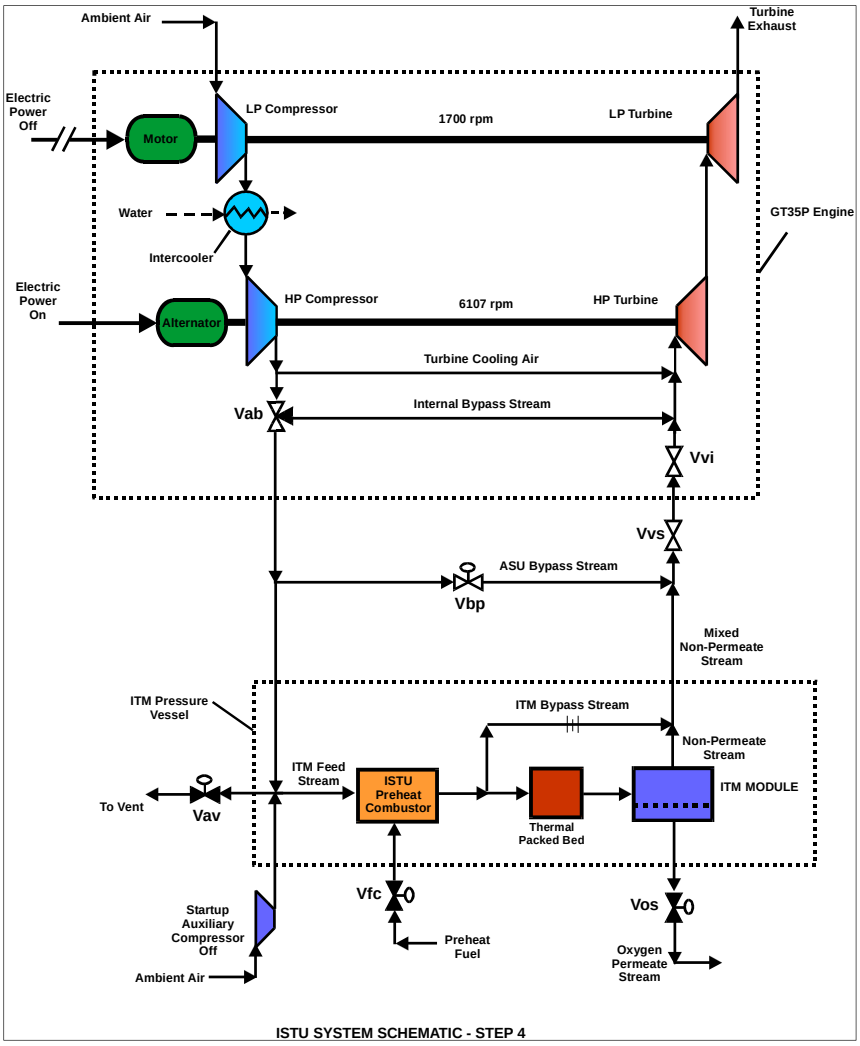

Figure 7-50. Ventilation (5 minutes).

Step 5 - LP Rotor Acceleration

Vab Open
Vvi Open
Vbp Open
Vav Shut
Vfc Shut
Vos Shut
Vvs Open

The LP rotor speed is almost continuously increased to 3000 rpm at the end of this step by controlling the angle of the LP turbine inlet guide vanes (IGVs). The LP rotor speed will be maintained at 3000 rpm from here until the last step of the start-up sequence.

The generator, used as a motor, provides power to the HP shaft until the ITM system produces enough hot gas flow to make the gas turbine generate power instead of consuming it. The generator-motor turning the GT-35P consumes as much as 4 MWe during some periods of the start sequence (Figure 7-51).

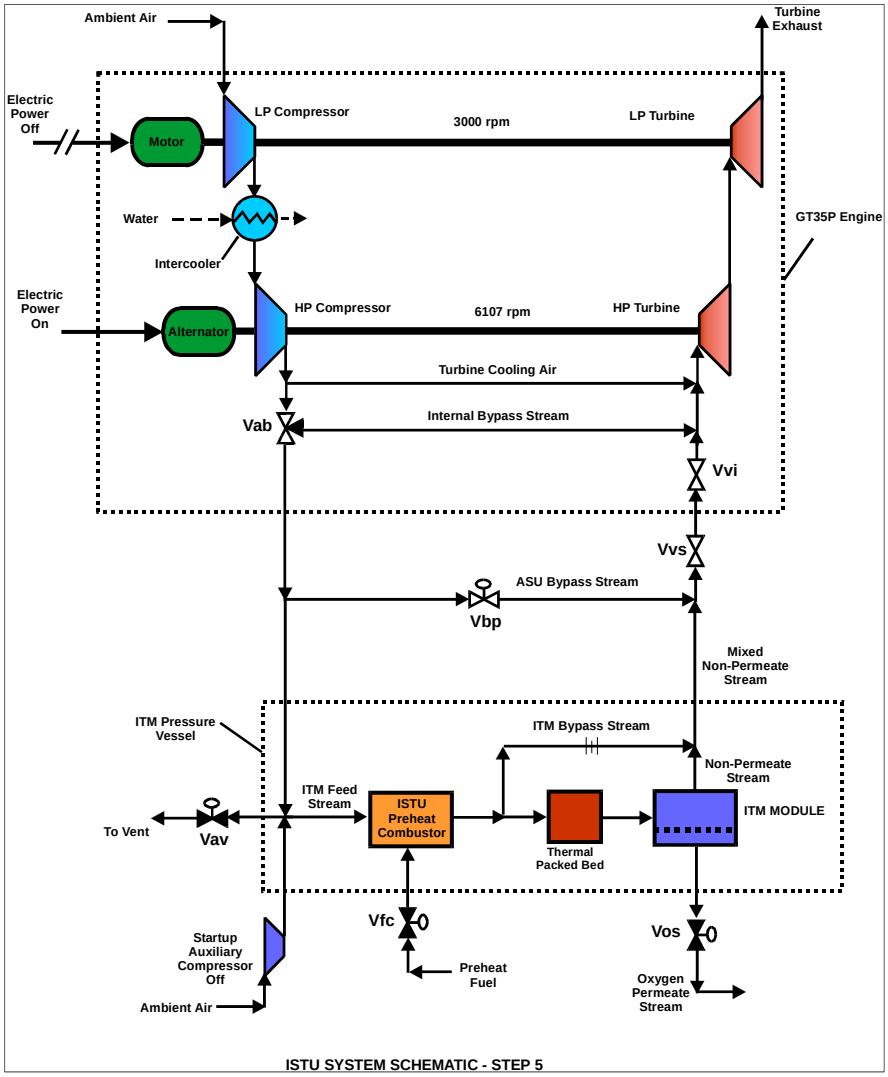

Figure 7-51. LP rotor acceleration.

Step 6 - Initial Vessel Heating and Pressurization

Vab Open
Vvi Open
Vbp Open===> Controlled
Vav Shut
Vfc Shut
Vos Shut
Vvs Open

The ASU bypass valve (Vbp) is controlled (closing slowly) to increase air flow through the ITM vessel and control the heat up rate. At the end of this step, the ITM vessel is pressurized to 2.9 bar (42 psia) at a compressor discharge temperature of 154 ºC (310 ºF; Figure 7-52).

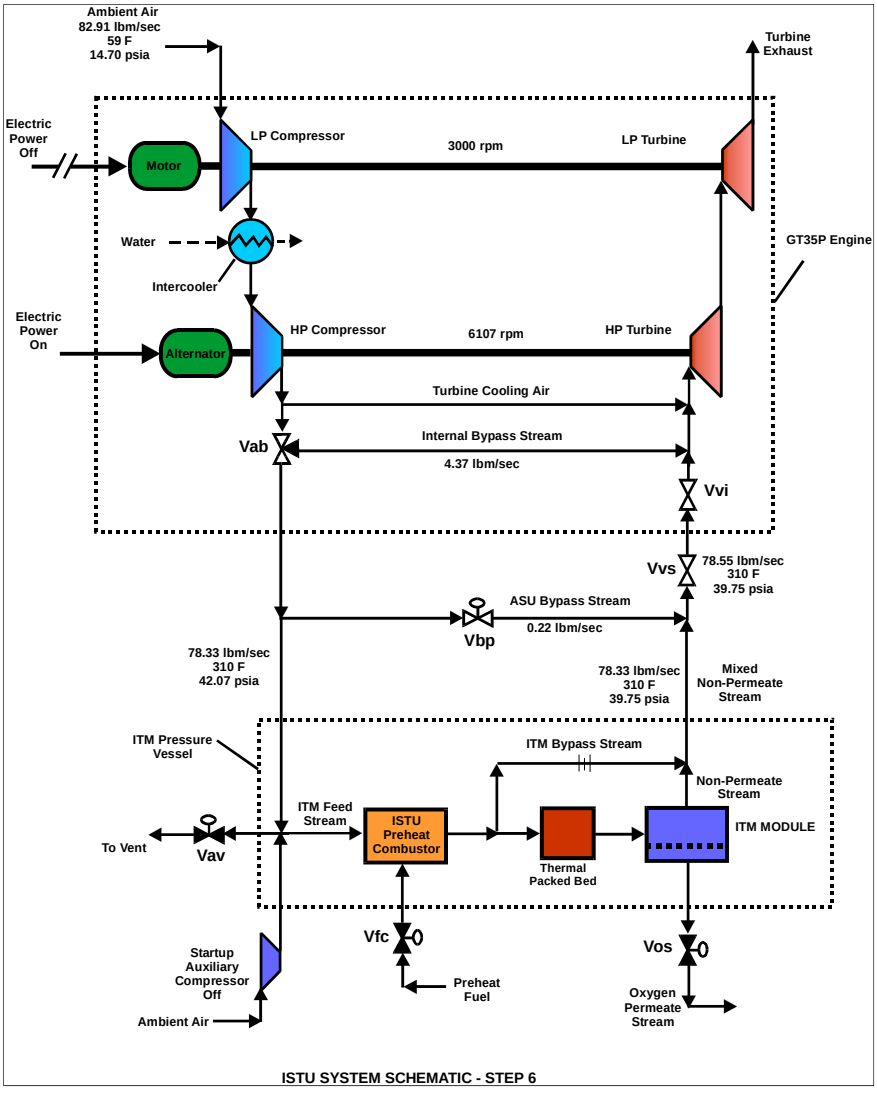

Figure 7-52. Initial vessel heating and pressurization (up to 1 day).

Step 7 - ITM Combustor Ignition and Membrane Heating I

Vab Open
Vvi Open
Vbp Controlled
Vav Shut
Vfc Shut ===> Controlled
Vos Shut
Vvs Open

The ITM ISTU preheat combustor is started to heat the ITM system at a slow rate for up to 2.5 days, with the LP rotor speed maintained at 3000 rpm. During this step, the valve V_{fc} is opened and adjusted to provide increasing fuel flow to the combustor (Figure 7-53).

As the air to the ITM heats up, the loading on the turbine increases, and the compressor discharge pressure increases accordingly. The ITM vessel is pressurized to 3.3 bar (47 psia) by the time the membrane temperature reaches 450 ºC (842 ºF). The LP rotor speed is maintained at 3000 rpm by controlling the angle of the LP turbine IGVs.

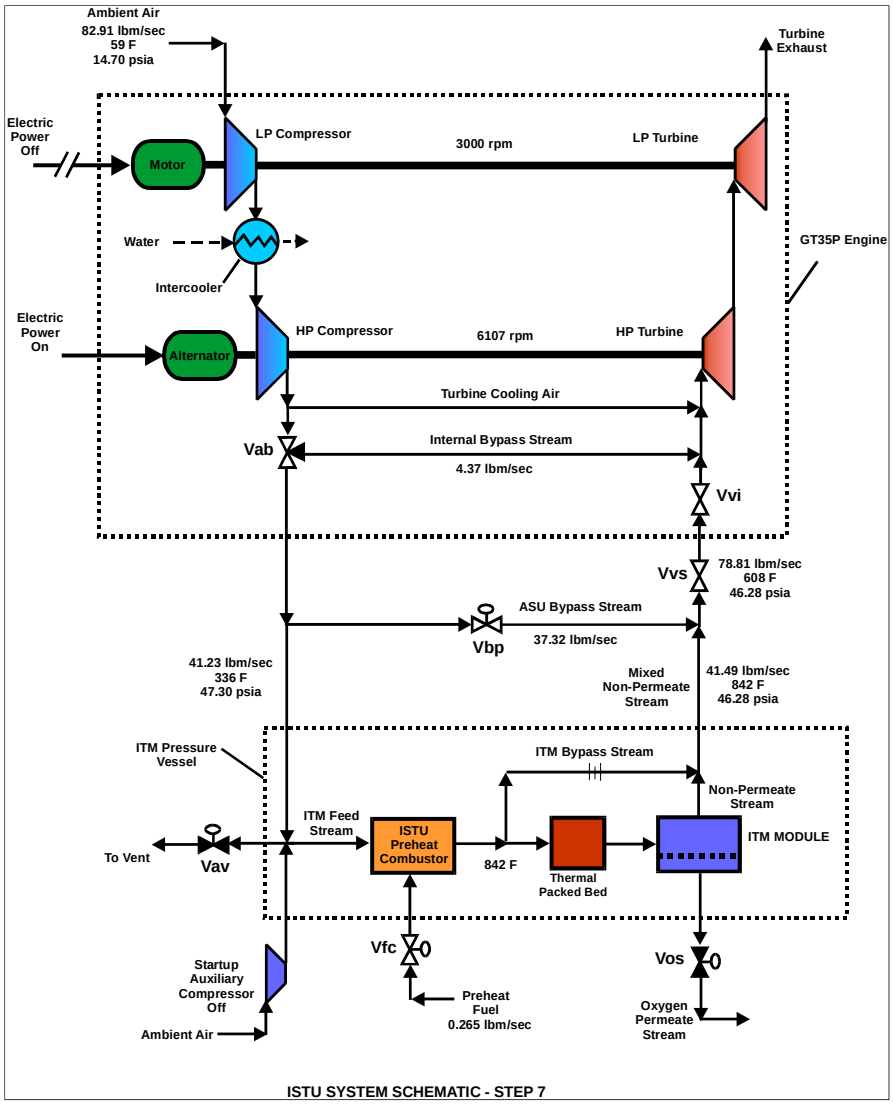

Figure 7-53. ITM combustor ignition and membrane heating I (up to 2.5 days).

Step 8 - ITM Membrane Heating II

Vab Open
Vvi Open
Vbp Controlled
Vav Shut
Vfc Controlled
Vos Shut
Vvs Open

The ITM membrane heating rate is increased for up to one day, with the LP rotor speed maintained at 3000 rpm. During this step, the ASU bypass valve Vbp is adjusted to control the amount of bypass flow as necessary to maintain the LP turbine discharge temperature below

the specified maximum allowable value of 398 ^{o}C (748 ^{o}F) and/or to maintain the LP turbine IGVs within a controllable range at 3000 rpm.

The ITM vessel pressure increases to 3.9 bar (56 psia) by the time the membrane temperature reaches operating conditions (800-900^{o}C or 1472-1650^{o}F; Figure 7-54).

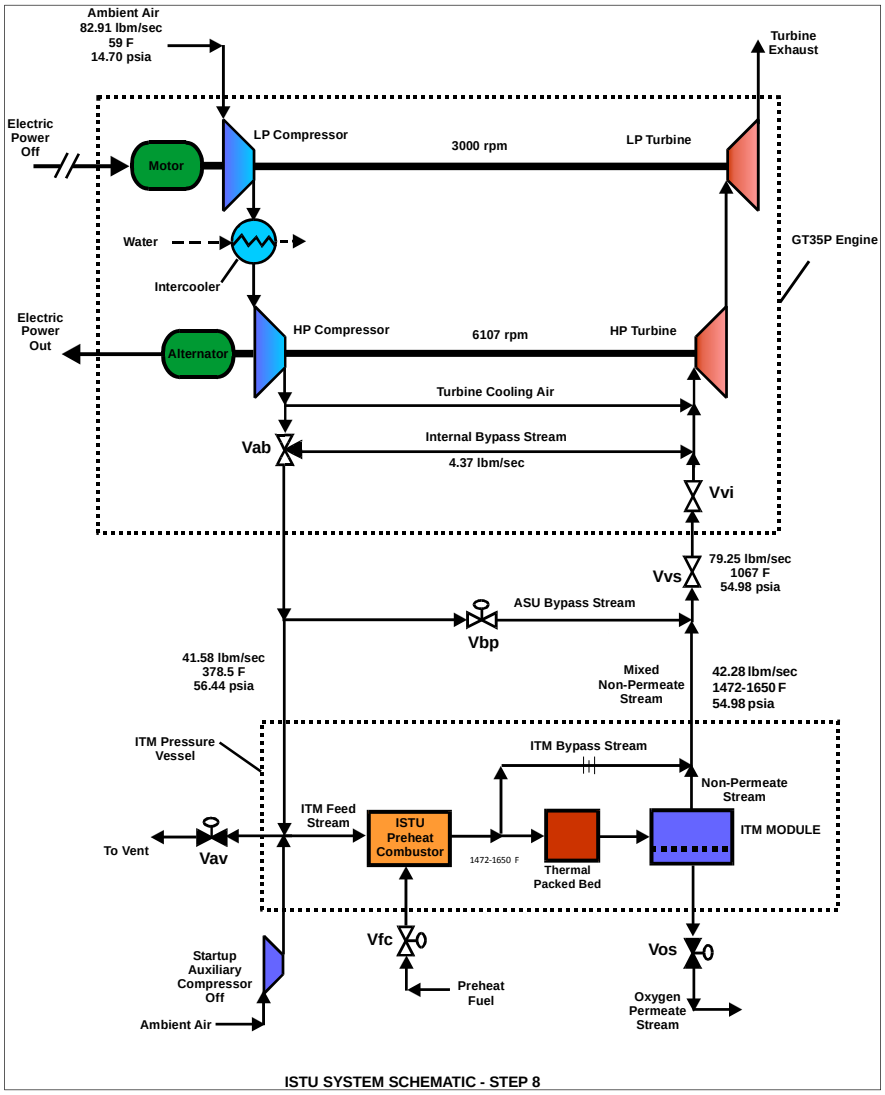

Figure 7-54. ITM membrane heating II (1 day).

Step 9 - ITM Pressurization

Vab Open
Vvi Open
Vbp Controlled
Vav Shut
Vfc Controlled
Vos Shut ===> Controlled
Vvs Open

Once the ITM vessel has reached operating temperature, pressure is increased at 10 psi/hr to about 11 bar (160 psia) by increasing the LP rotor speed to 5450 rpm through IGV control. This is the design point for the GT35P gas turbine. Some small ASU bypass flow is still required to maintain the design turbine inlet and/or exhaust temperatures with the ITM vessel operating at 800-900ºC. Valve Vos is opened to initiate and control oxygen generation. Finally, the pressure downstream of valve Vos will be decreased until full oxygen production (150 sT/D) is reached (Figure 7-55).

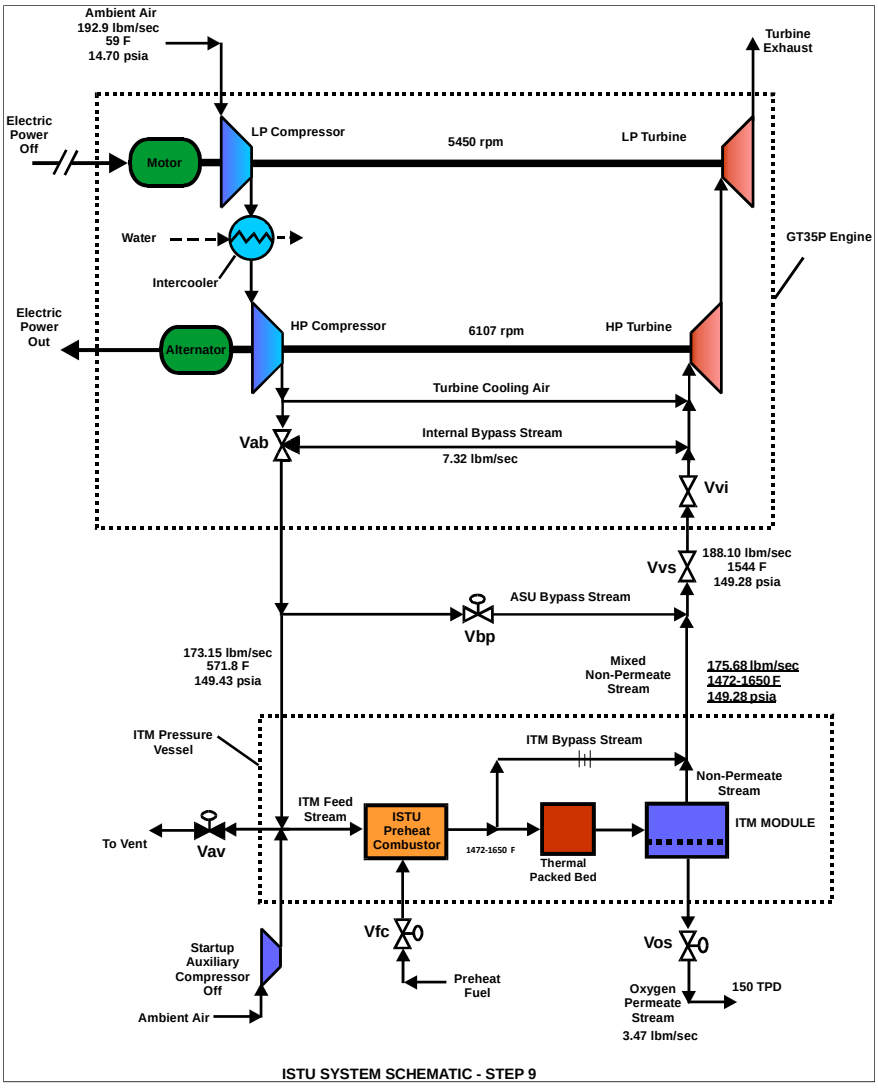

Figure 7-55. ITM pressurization (up to 1 day).

Summary of Control Sequences for ISTU

Table 7-20 lists preliminary estimates for values of key parameters at the end of each step in the start-up sequence. The ITM preheat burner heats the compressor exit air beginning with Step 7, and ASU bypassing is required in Steps 8 and 9 in order to cool the HP turbine inlet stream and maintain LP turbine exit temperatures below 398°C. Table column headings are explained in notes following the table.

Table 7-20. ITM – GT interface stream conditions during plant start (preliminary estimates)

Step	P(ITM), bar	T(hpco), °C	Burner MW(t)	T(ITM), °C	ASU Bypass	T(hpti), °C	T(lpto), °C
1	1.08	20	-	20	-	20	20
2	1.08	20	-	20	-	20	20
3	1.08	20	-	20	-	20	17
4	1.08	20	-	20	-	20	17
5	1.08	20	-	20	-	20	17
6	2.9	154	-	154	-	154	106
7	3.3	169	5.7	450	0.48	320	220
8	3.9	193	Var.	800-900	0.47	575	354
9	10.3	300	Var.	800-900	0.07	840	394

Notes: P(ITM) ITM vessel pressure, bar
T(hpco) = HP compressor exit temperature, °C
Burner = Fuel thermal input to burner, MW(t)
T(ITM) = ITM vessel temperature, °C
ASU Bypass = Bypasses air / HP compressor exit air
T(hpti) = HP turbine inlet temperature, °C
T(lpto) = LP turbine exit temperature, °C (Max = 398 °C)

2. IGCC Integrated Gas Turbine-ITM System Control, ITM Preheat Considerations

Concepts NREC considered process control aspects of the IGCC flowsheet with a preheat combustor, focusing on preheat combustor design considerations.

Figure 7-56 shows the system considered. Valves and heat exchange units have been explicitly shown for purposes of consideration and discussion.

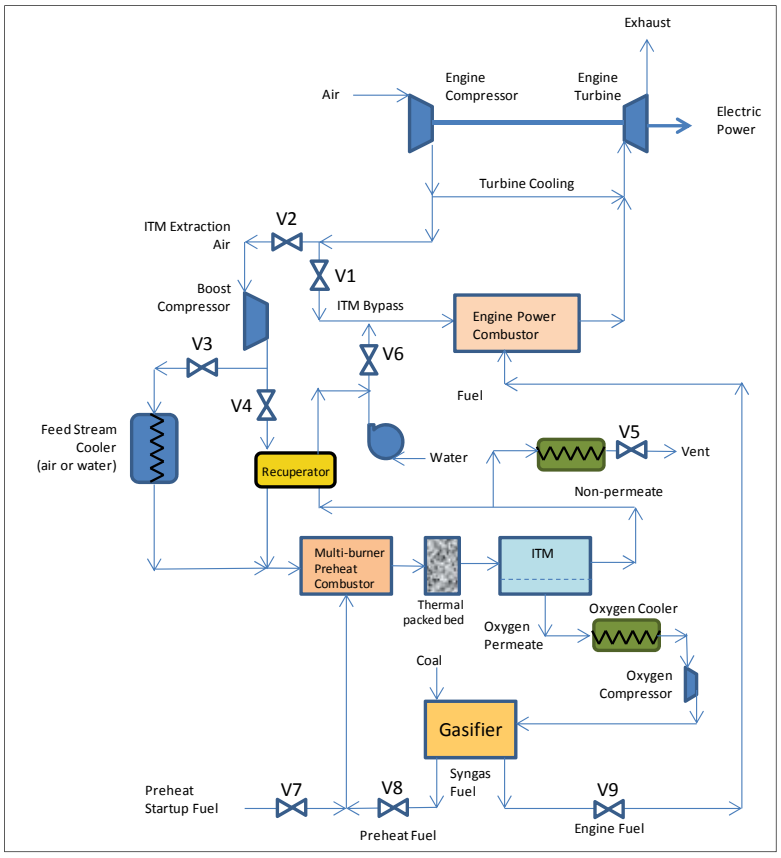

Figure 7-56. IGCC process scheme for process control development.

Concepts NREC made the assumption that the engine is started and brought up to full power before the ITM system is brought on-line. It is also assumed that the boost compressor has a wide operating range to handle the low initial flow through the ITM system. If not, then a separate by-pass around the booster would be required (not shown).

Key features of the process design include:

- A feed stream cooler to control the temperature of the ITM feed, allowing it to rise gradually over the initial portion of the warm-up period.
- An exceptionally large preheat combustor turndown to provide a sufficiently gradual warm-up to the full ITM operating temperature (800-900°C). A practical design approach to achieve the turndown is to use multiple burners that could be turned on sequentially. This approach increases temperature from an initially low value to the final design value in a number of steps, with each step representing a relatively small increment in the total

fuel flow and corresponding overall temperature rise. The stepwise process would be reversed to achieve a gradual shutdown of the ITM system.

- A multi-burner approach, which may exacerbate the problem of achieving a uniform combustor exit temperature. For example, when the first burner is turned on, it represents a localized hot spot in the flow surrounded by the unlit burners. When all burners are operating, the uniformity would likely be good. To facilitate good temperature uniformity at low temperature, the addition of a packed bed of ceramic material at the outlet of the combustor would promote mixing and minimize temperature non-uniformities in the flow. (Air Products noted that the packed bed could also be used for thermal dampening during transients.)
- An optional non-permeate vent cooler, which is used to reduce the temperature of the stream prior to venting so as to reduce the temperature requirements of the vent control valve (V5). The cooler may have to operate even when V5 is completely shut off to protect it from thermal damage. A jacketed design for V5 might be required to avoid the need to continually operate the vent cooler.
- A startup fuel circuit, provided for when the syngas isn't available at start up.

Preheat Combustor Design

In the case in which the startup fuel is natural gas, the preheat combustor must be designed for both fuels. From the standpoint of combustion performance, the two most relevant fuel properties are:

Z_{st} = stoichiometric air/fuel ratio by mass

LHV = lower heating value, BTU/lbm

The values of these parameters for two representative fuels are given in Table 7-21.

Table 7-21. Fuel properties.

Fuel	Z_{st}	LHV (BTU/lbm)
Syngas	3.04	5,028
Natural Gas	16.0	20,500

For each burner, a relationship can be derived between equivalence ratio (φ = actual fuel/air ratio divided by stoichiometric fuel/air ratio) and temperature rise (ΔT):

$$\Phi \sim (Z_{st}/LHV)\ \Delta T$$

Comparing the two fuels gives the following:

$$(\Phi_{NG}/\ \Phi_{SG}) = 1.29\ (\Delta T_{NG}/\Delta T_{SG})$$

where the subscripts NG and SG refer to natural gas and syngas, respectively.

The expression $\Phi_{NG} = 1.29\ \Phi_{SG}$ is used to keep temperature rise constant, or, equivalently, $\Delta T_{NG} = 0.775\ \Delta T_{SG}$.is ued to keep equivalence ratio constant. In terms of fuel flow rate, m_f, the relative values for constant temperature rise, are $m_{NG} = 0.245\ m_{SG}$, and for constant equivalence ratio $m_{NG} = 0.19\ m_{SG}$. Either option is acceptable, although the constant ΔT approach is preferable.

These results are encouraging and confirm that a dual-fuel design is reasonable. One can design for syngas and run slightly richer on natural gas to get the same temperature rise. During the initial warmup period, operation at even higher ΔT could be followed because the inlet temperature will be below the ultimate design value and therefore would pose less risk of overheating.

Critical Valves

Valves V1 and V2 adjust the split of compressor discharge air between the ITM bypass and ITM feed. Valves V3 and V4 are used during the initial warm-up period prior to lightoff of the preheat combustor. In combination, they control the temperature of the air entering the ITM vessel.

Valve V6 initially isolates the ITM system from the engine hot section (power combustor and turbine). Valve V5, in combination with the upstream valves, controls the flow rate through the ITM system and the backpressure on it. Valves V5 and V6 operate in combination to phase in the full integration of the ITM system with the engine. Valves V7 and V8 combine to initiate the flow of startup fuel and phase in the syngas as it becomes available for the preheat combustor. Valve V9 serves the same purpose for the engine fuel.

Startup Procedure

The major steps involved in starting the integrated system and bringing it to its full design-point operating conditions are nominally as follows:

1. The engine is started and brought to full-power operation with valve V2 closed and V1 fully open. Note: Use of utility natural gas is assumed adequate for this purpose.
2. Valves V1 and V2 are adjusted to start flow through the ITM system. The feed stream cooler is activated. Valves V3 and V4 are adjusted to control the temperature of the ITM feed stream. Valve V6 is closed and V5 is open to vent flow to the atmosphere.
3. Valves V1, V2, V3, V4 and V5 ar adjusted in combination to gradually increase the temperature and flow rate of the ITM feed stream and the backpressure on the ITM system. The final value of temperature in this step will be the maximum achieveable with just uncooled (V3 closed) compressor discharge air (nominally 870°F). The final values of flow rate and backpressure will be preselected conditions for initial lightoff of the preheat combustor.
4. Valve V7 is opened and startup fuel is directed to one of the multiple burners of the preheat combustor. The burner is ignited, providing a predetermined temperature rise in the ITM throughflow stream.
5. There are three optional procedures for this final step of the startup and integration process:
    a. Valve V5 and the upstream valves, V1, V2 and V4, are adjusted to gradually increase the ITM flow rate up to the full design value. During this process, the individual burners are lit off either one at a time or in groups until all are operating. The pressure level is maintained at the maximum value acceptable from an ignition pressure-pulse standpoint. Therefore, the engine speed and power output will drop off and the temperature of air entering the preheat combustor will be below the design value because no recuperation will be occurring. Once steady-state is established, valve V5 is gradually closed down to increase the backpressure above the power combustor inlet value. At this point, valve V6 can be opened and V5 closed completely, allowing all of the non-permeate to return to the engine. Note: the disadvantage of this approach is that a considerable amount of mass flow will be initially diverted from the engine, which may cause operating stability problems. Also, handling that amount of flow through the venting system may be difficult.

b. An alternative is to adjust valve V5 and the upstream valves, V1, V2 and V4, so as to gradually increase the backpressure to a high enough value above the pressure at the inlet to the power combustor. At this point, V6 can be opened and V5 closed to allow all of the non-permeate flow to be returned to the engine. At this point, V6 and the upstream valves are adjusted to gradually increase flow rate and the individual burners are lit off sequentially until full flow conditions are achieved. Note: The potential problem with this approach is that the ignition pressure-pulse associated with lightoff of each burner may be excessive.
c. Another alternative is a variation of the procedure described in Step 5b above. The variation is that the engine is first brought down to an idle or low-power operating condition. This reduces the engine pressure level to a value which may be more acceptable from the standpoint of preheater ignition pressure pulse. With the engine operating at this condition, valves V5, V1, V2 and V4 are adjusted to increase the backpressure above the power combustor inlet value. When this is achieved, V5 is closed and V6 is opened until all of the non-permeate flow is returned to the engine. Then the valves are adjusted to gradually increase the flow rate, light off the individual burners and increase engine power level until full design-point conditions are achieved. Note: The potential disadvantage of this approach is that it will require very close and active coordination between the engine controls and the ITM system controls.

Based on the preceding considerations, it is clear that the preheat combustor will have to operate for a considerable length of time during the startup period at conditions quite different from the full design-point conditions. This operation will also be with a startup fuel which is unlikely to be syngas. The actual operating range will depend on which startup scenario is selected. The design of the preheat combustor will be driven not only by the final operating conditions, but also those which are encountered over the course of the warm-up, startup and integration processes.

7.6 Evaluation of System Reliability

Reliability Approach

The reliability of the ITM Oxygen technology is a function of the reliability of the individual components that make up the technology performing under the required conditions. Establishing

the feasibility of achieving adequate ceramic component reliability is a critical goal, as the least was known about the ITM materials and structures derived thereof in the early stages of the technology's development.

Ceramatec established the primary objective of the ceramic component reliability task: to develop and validate the experimental and analytical methodology required for the prediction of 1) the probability of survival of membrane components (e.g., wafers, etc.) and devices (e.g., modules) operating under various expected conditions such as startup, shutdown, steady state, and unexpected transients; and 2) changes in probability of survival occurring over time due to time-dependent phenomena including slow crack growth, creep, and deleterious environmental reactions. The reliability methodology was based primarily on the well-established weakest link concept, which describes failure in terms of both the largest defect present within the component as well as changes in the defect population arising from various time-dependent processes. In areas where stress concentrations control failure, a fracture mechanics approach was required to supplement this overall approach. The reliability methodology allows one to 1) predict reliability for existing process control protocols, 2) optimize these protocols with respect to maximizing the reliability, and 3) quickly assess the effects of changes in wafer/stack design on reliability. A secondary goal is to evaluate nondestructive (NDE) techniques capable of measuring key properties such a stress state and temperature distribution, which can be used to validate the reliability methodology. These same NDE techniques may ultimately be used to monitor selected wafers during module operation, thereby providing an additional level of control of the reliability.

Figure 7-57 illustrates the flow chart used for the reliability effort. Performance targets are defined and preliminary materials identified, then the two main activities, Data Collection and Validation and Ceramic Component Design (wafer, cone, spacer, etc), are initiated. The goal of the first task is to generate the key property data required for finite element analysis and model development. This task involved the use of standardized test specimens and testing protocols. When non-standard tests are required, such as the Chemical Expansion Verification Unit (CEVU) described below, those tests must be established as valid. The second main task involved developing the specific designs for the membrane wafer and associated supporting components.

As the database was developed, Ceramatec began to implement the Reliability Model Development and Validation effort as shown in Figure 7-57. This work focused on developing the analytical models defining the mechanisms which control reliability (e.g., fast fracture, time-dependent behavior, creep, chemical expansion, etc.) in terms of the key controlling variables. To a large extent, the selection of the appropriate model and associated model parameters was based on observations made during data collection and analysis.

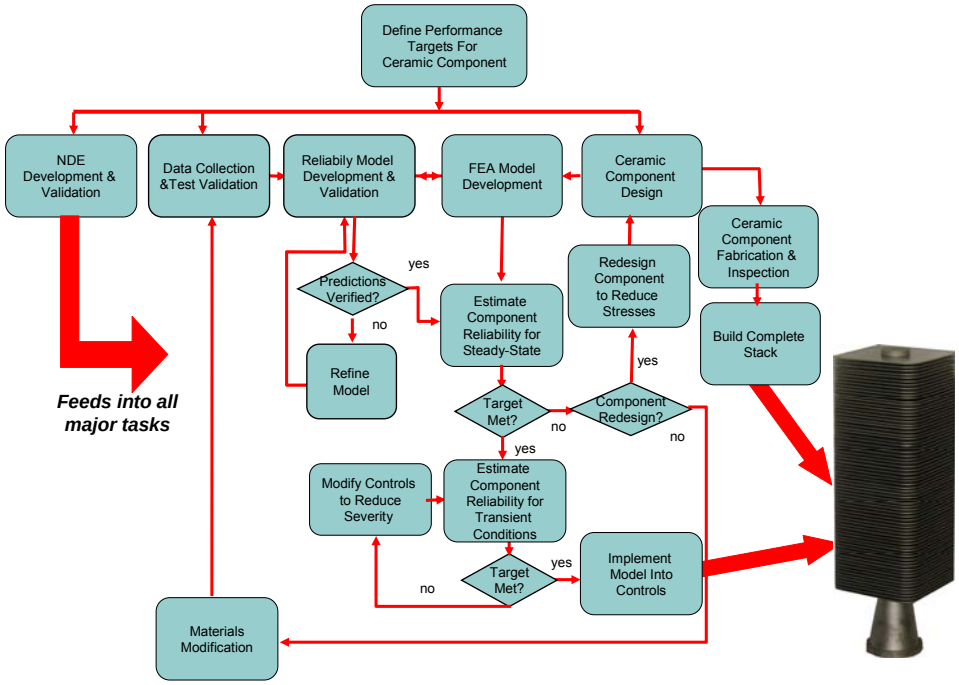

Figure 7-57. General approach for establishing ceramic reliability.

The creation of the base component design served as a starting point for the finite element analysis (FEA). A key requirement is that the FEA model must capture the complexity of the component in question (wafer, spacer, base piece, etc) and also predict the chemical, thermal, and mechanical stresses and temperatures within the component which arise during testing. This aspect required that the analytical expressions discussed previously be incorporated into the FEA model.

Once an adequate database was compiled, models developed, and FEA activities resolved, Ceramatec implemented a reliability verification activity in which the models were used to predict behavior for other types of tests. As shown in Figure 7-58, these tests included 1) prediction of fracture in featured flexure bars and biaxial disks, 2) verification of chemical

expansion, 3) prediction of creep deformation in single-wafer creep tests, 4) prediction of fracture of wafers exposed in the transient reliability rig, and 5) component failures arising from thermal gradients.

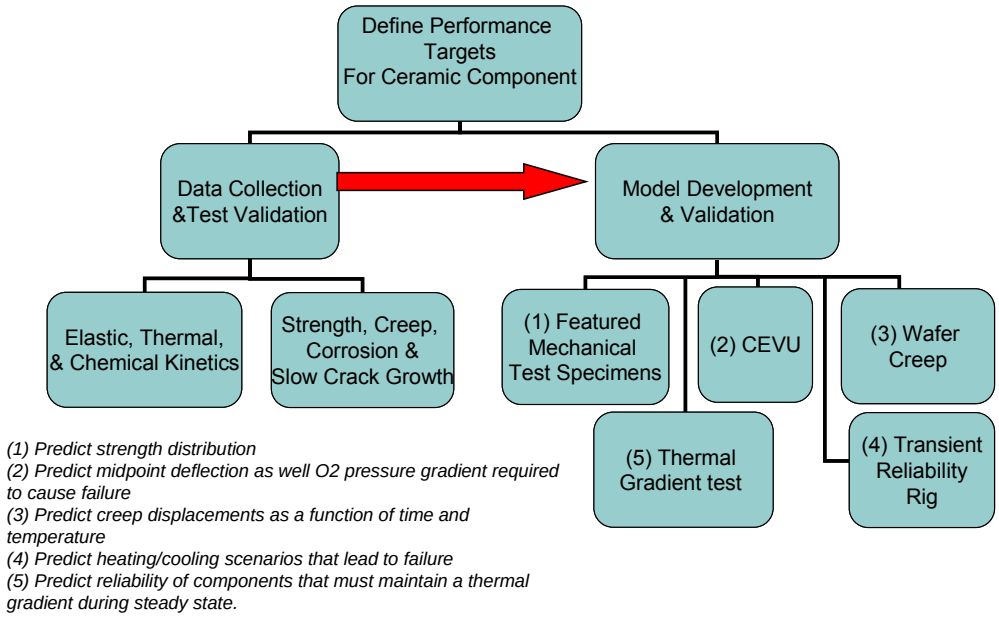

Figure 7-58. Ceramic reliability verification approach.

Although not illustrated in Figure 7-58, another approach for validating the failure models is to mechanically (or thermally) interrogate specimens fabricated directly from the wafers. This method has the advantage of capturing the true effects of laminate architecture. Furthermore if wafers are subsequently recovered from TDU/SEP tests, the same techniques can be used to compare changes in mechanical behavior arising from the test with those predicted from the models describing time-dependent response. One may also use the specimens fabricated from the components to evaluate the response to micro-mechanical testing. This approach may be particularly relevant for evaluating the mechanical reliability of membrane layers located over slots (Figure 7-59).

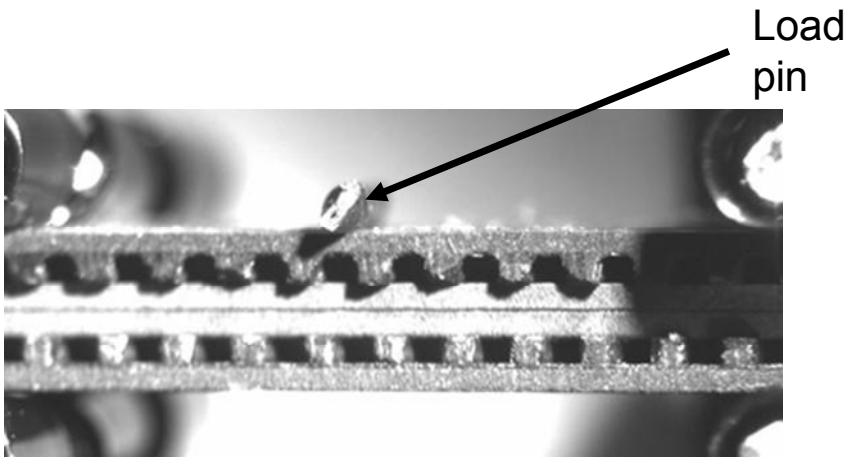

Figure 7-59. Example of a targeted test of strength of a microchannel body.

Once the reliability model is validated, it can be used to predict the reliability of the module operating under steady-state conditions. If time-dependent strength degradation processes are operative, the reliability will be a function of time. In this case, the module reliability (expressed as the desired probability of survival) must not drop below the target value within the expected operating life of the module. If this condition is not met, there are two options. First, minor changes to the component design may be made to further minimize stresses and thus increase reliability. If this approach is not successful, then the materials may be modified to improve mechanical properties such as Weibull modulus or average strength. Once the steady-state reliability target is satisfied, the reliability model can then be used to predict module reliability operating under transient conditions. If the transient conditions (shutdown, startup, etc.) are too severe, they will have to be modified until the reliability target is met.

The final key activity shown in Figure 7-57 is non-destructive evaluation (NDE) development and validation. One goal of this work is to identify and validate those NDE techniques that can be used to rapidly implement acceptance tests for components prior to fabrication of the module. These techniques include those capable of defining internal structures (dimensional inspection) and identifying critical defects (damage inspection). A second goal of this effort is to identify NDE methods for measuring critical properties, which can be used to validate the reliability and FEA models. An example is resonant ultrasound spectroscopy (RUS), which can be used to measure the resonant frequencies of actual components. The resulting data can then be compared with the frequencies predicted from an FEA model.

Once validated, many of NDE techniques can be used to periodically examine stacks during routine inspections. The resulting information, which includes characteristics such as residual stress level, surface phase content, and damage, would ultimately be used to assess the remaining life of the module. Ceramatec evaluated the possibility these techniques being integrated into the control system such that measurements could be made in real time.

In summary, work with ITM ceramics has led to an understanding of the long-term effort required to establish expectations of ITM devices operating in a commercial environment. As with all ceramics, reliability depends on flaws and the stress field around those flaws, and flaws are dependent on the processing history of the parts. It is therefore expected that reliability will evolve as manufacturing techniques and scale evolve; it is further expected that reliability will depend on the operational history of components to the extent the flaw population changes with time on stream.

An approach which addresses the evolution of flaws with time is illustrated in Figure 7-60, which presents two conceptual plots. The plot on the left side shows failure probability of a population of manufactured parts against time in service. Failure probability is relatively high initially, as the population of weaker parts dominates the probability statistics. Many of these parts do not pass the normal quality assurance process (i.e., these failures would be reflected in the manufacturing yield statistics); NDE and proof testing can be used to identify the remaining weaker or flawed parts. Once the weaker/flawed parts are eliminated, the population may meet commercial targets for reliability for a period of time.

The mechanisms leading to failure include the fast fracture -type mechanisms discussed above and as shown on the right side plot of Figure 7-60. These phenomena are subject to quantification through Weibull statistics and reliability prediction using techniques such as CARES and those discussed above. However, time-dependent mechanisms such as creep and slow crack growth affect modules with time in service, as does the accumulation of part damage leading to stress rupture; these can be studied and understood, but ultimately controlled only through part stress management. With time, as shown in the left plot, the failure probability will begin to climb again as a result of these long-term mechanisms. Commercial life targets must be set with the knowledge that the long-term degradation mechanisms will ultimately determine the useful life of components.

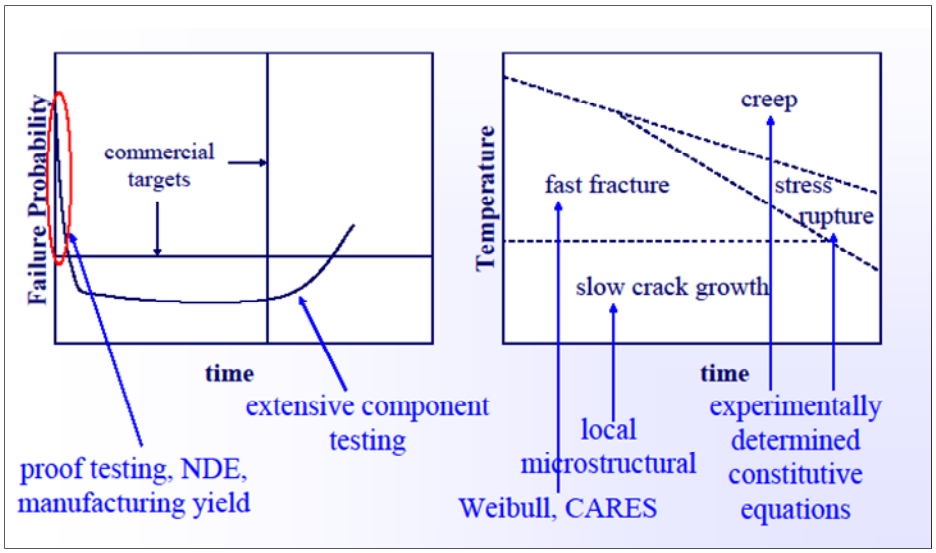

Figure 7-60. Conceptual plots illustrating (on the left) manufactured component population failure probability with time in service and (on the right) mechanisms leading to short term and long-term degradation.

Structural-mechanical Modeling

Creep

Norton's creep law model was applied by first estimating the stress, temperature, and PO_2 dependency of the creep rate using data previously generated at Penn State. A multi-linear regression analysis of these data yielded an expression for tensile creep rate of the form:

$$de/dt\ (1/s) = A\ \sigma^{n}\ PO_2^{\alpha}\ \exp(-Q/RT) \qquad [1]$$

where de/dt is the creep rate, A is a pre-exponent factor in [1/s], σ is the tensile stress in MPa, PO_2 is the oxygen partial pressure in atm, n is the stress exponent, α is oxygen partial pressure exponent, Q is the activation energy, T in the absolute temperature, and R is the universal gas constant. In order to predict creep of full-sized wafers, a multi-axial generalization of Norton's creep law was incorporated into an FEA model. This generalization assumes that the creep strain rate tensor, $(de/dt)_{ij}$, is proportional to the stress deviator s_{ij} in accordance with the expression,

$$(d\varepsilon/dt)_{ij} = 3/(2\ \tau)\ (\sigma_e/\sigma_c)^{n-1}\ s_{ij}\ \exp(-Q/RT) \qquad [2]$$

where σ_e is the von Mises effective stress, τ is a time constant, σ_c is a creep stress constant (τ and σ_c are used to avoid material data with unconventional units), n is the stress exponent for

creep, T in the absolute temperature, R is the universal gas constant, and Q is the activation energy. Note that Equation 2 is valid only for steady-state creep.

This model was verified by using it to predict 1) the tensile creep rates previously measured at various temperatures at 900°C and above; and 2) the extent of steady-state stress relaxation (redistribution) occurring in a flexure bar exposed at elevated temperature and pressure. The latter case was considered because an analytical solution (Chen and Chuang, 1990) is available for comparison. As shown in Figures 7-61 and 7-62, the predicted data were in excellent agreement with the expected results. The model was then used to predict the creep of edge loaded wafers (Figure 7-63). A 2D geometry was used represent the loading configuration. To simplify the preliminary analysis, the differences in creep behaviors of the porous and dense layers were ignored. As shown in Figure 7-64, the predicted deflection-time curve (blue line) greatly underestimated the time-dependent changes in deflection particularly for times <336 h. This discrepancy could in part be a result of neglecting the effects of primary creep. To address this issue, a primary creep component, which was based on tensile creep curves generated as part of the stress rupture testing of the AP2K, was added to Equation 2. The resulting prediction (red line) was in better agreement with experimental results.

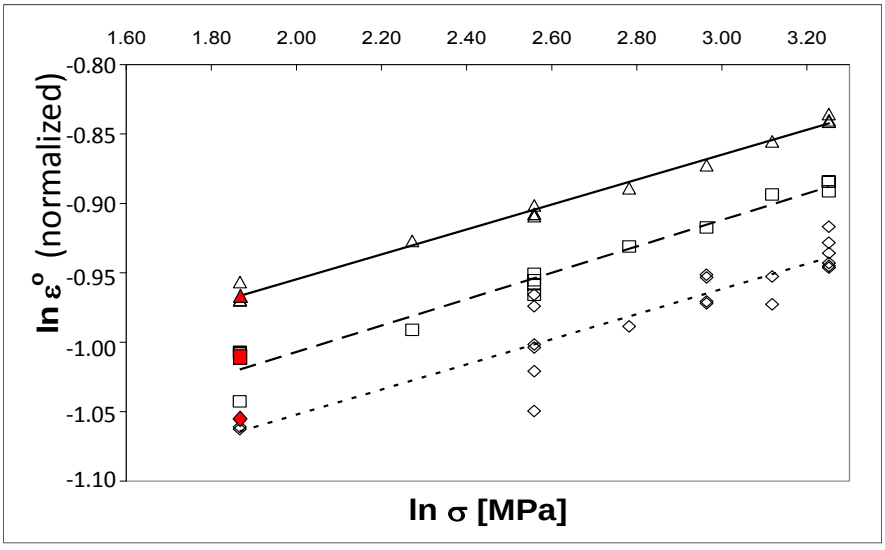

Figure 7-61. Comparison of experimental and predicted (red symbols) tensile creep rates associated with the AP2K material.

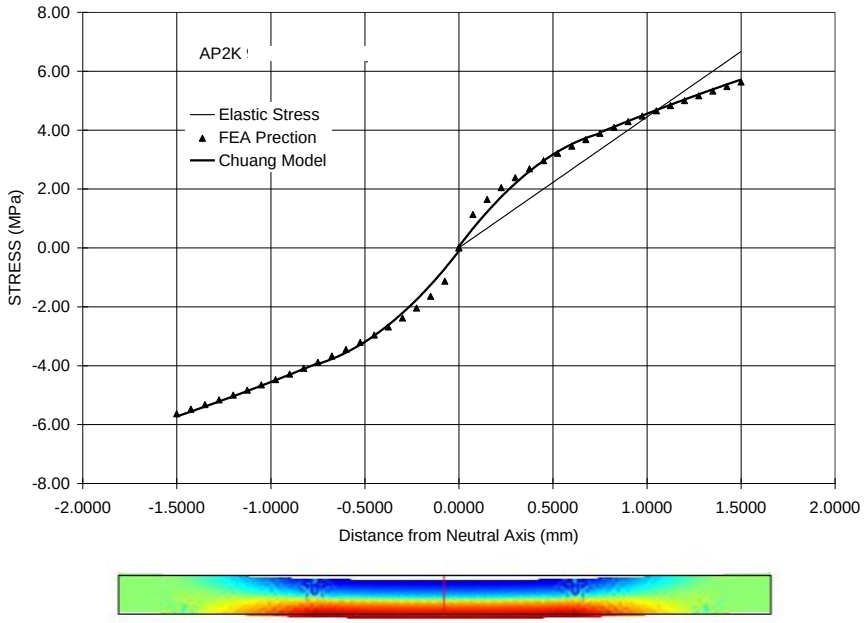

Figure 7-62. Steady-state stress profiles in flexure specimen at elevated temperature and pressure. Creep eventually causes the stresses to deviate from the linear profile. The symbols are the results predicted from the FEA while the solid line is predicted by Chuang.

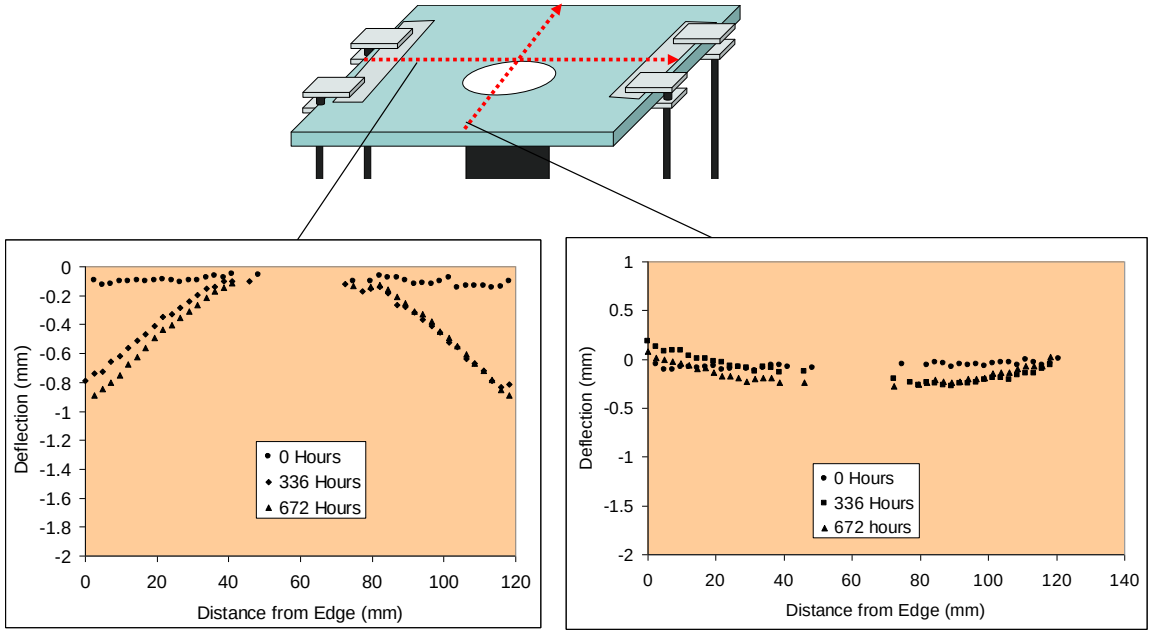

Figure 7-63. Schematic representation of edge loaded wafer used to experimentally measure measure creep at elevated temperature. The deflection in the vicinity of the applied loads was determined from laser profilometery measurements.

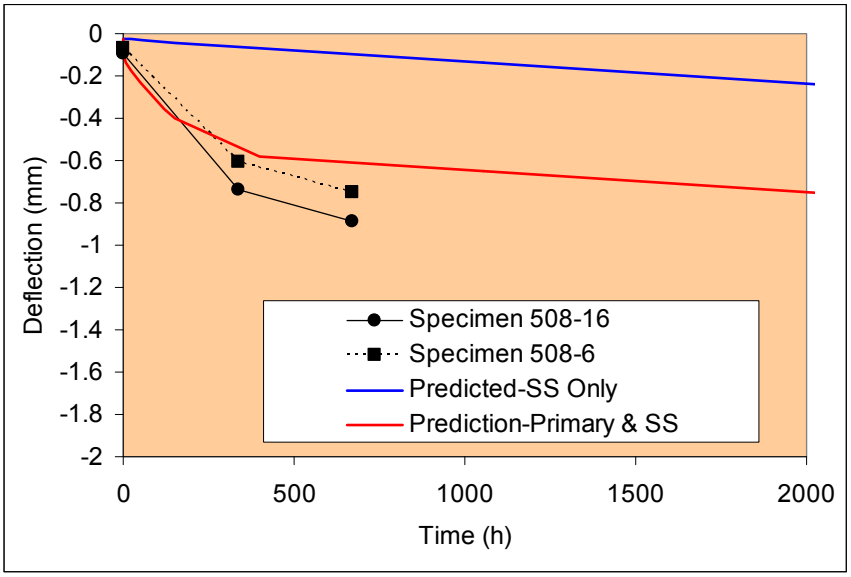

Figure 7-64: Comparison of wafer creep (as determined from profilometer measurements) with model predictions.

Wafer Strength

Ceramatec further developed the wafer FEA model with "smeared" properties representing the interior slotted layers, and extended the analysis to the case in which the wafer has differing stiffness in two directions owing to specific slot patterns. This necessitated the determination of the effective properties of the interior layer. To obtain the effective elastic modulus in various directions im the unit cell, it was displaced while constraining specific faces in the cell sequentially. The constrained faces were allowed to contract due to the Poisson effect.

The effective Poisson's ratios, ν_{12} and ν_{13}, were found using the same loading as was used to find the elastic modulus in the 1-direction. Ratio ν_{23} was found using the same loading as was used to find the elastic modulus E_2.

To obtain the effective shear modulus G_{12}, the top face of the unit cell was displaced in the 2-direction while the bottom face was constrained to zero 2-displacement. Also, the right and left faces were constrained to zero 1-displacement. Finally, the back face was constrained to zero normal displacement and the front face was forced to stay in plane. G_{13} and G_{23} were determined similarly.

The effective elastic modulus for each load case was found by taking the effective normal stress on the displaced face and dividing by the effective strain of the unit cell normal to that face. The effective normal stress is defined as the total reaction force acting normal to the face divided by the area of that face if no slots were present. The effective normal strain is defined as the imposed displacement of the face divided by the length of the unit cell in the direction normal to the face. The effective Poisson's ratio ν_{12} was found by taking the negative of the effective strain in the 2-direction divided by the effective strain in the 1-direction for the load case used to find the elastic modulus in the 1-direction. Ratios ν_{13} and ν_{23} were calculated in a similar way.

The effective shear modulus for each load case was found by taking the effective shear stress on the displaced face and dividing by the effective shear strain of the unit cell. The effective shear stress is defined as the total reaction force acting along the face divided by the area of that face if no slots were present. The effective shear strain is defined as the imposed displacement of the face divided by the length of the unit cell in the direction normal to the face.

The smeared wafer model for slotted layers was subsequently used to assess the reliability of the centrally loaded wafer as a function of orientation. In this analysis, symmetric boundary conditions are applied on the left and bottom sides of the wafer. These supported regions are restrained from moving up and down. Load is distributed uniformly over the ring area, which represents the spacer region. As a preliminary check of the model, the maximum displacement under a specified load was predicted for each orientation. As indicated in Table 7-22, the predicted deflections tended to be a bit lower than the experimental values. This difference could easily be explained by load train compliance, which would cause the experimentally measured deflections to trend larger.

Table 7-22. Comparison of experimental measurements and theoretical predictions of wafer displacement under load.

	Orientation 1	**Orientation 2**
Measurement (in)	0.726	0.475
Prediction (in)	0.664	0.429
Relative error (%)	8.5	9.6

Conical Base Piece Strength

Ceramatec developed a 2-D axi-symmetric finite element model of the conical base piece. This model accounted for the evolution of both chemical and thermal stresses during heatup of the cone. To simplify the analysis, the cone was assumed to consist of three layers: an outer layer of slotted material, a dense middle layer, and a slotted inner layer (Figure 7-65). Further it was assumed that the slotted layers were able to quickly equilibrate with the inside and outside conditions. These values were derived from an operating temperature/pressure profile specified by Air Products. Given these assumptions the highest stresses were generated in the dense layer since it had to accommodate a relatively steep gradient in oxygen concentration.

The stress profiles occurring within the cone were calculated as a function of time for two cases. For Case 1 the cone temperature was uniform and the temperature-time profile followed that of the wafer while for Case 2 the temperatures at the top and bottom of the cone were equal during the initial heating. At 600°C the top of the cone continued to follow the specified wafer temperature while temperature at the bottom remained at 600°C. Normalized versions of the temperature gradients calculated by Air Products were used to define the axial temperature profile (see Figure 7-66).

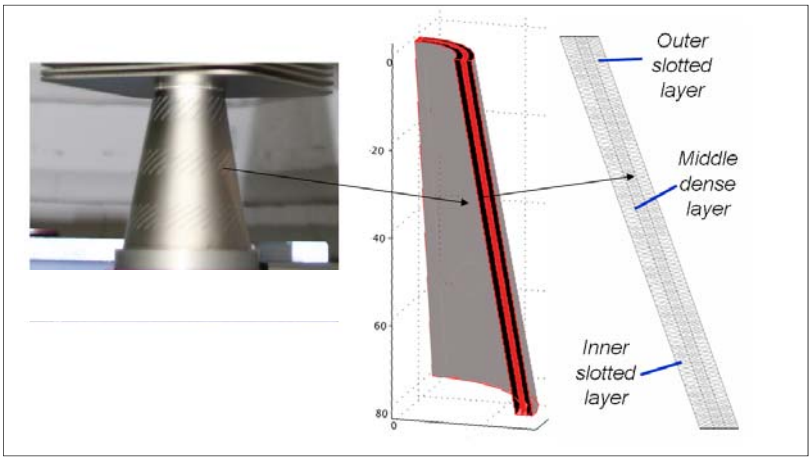

Figure 7-65. The cone was modeled using simple 2D axi-symmetric geometry and assuming that the cross-section was composed of three layers.

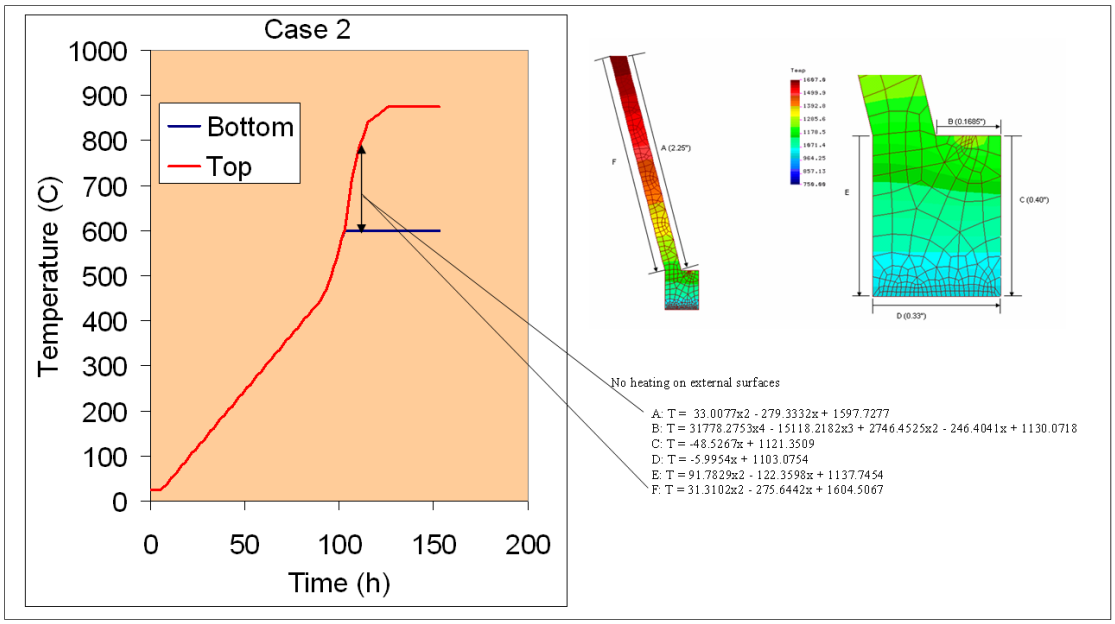

Figure 7-66. Case 2 of the cone modeling: the temperature of the bottom of cone remained at 600°C while the temperature at the cone top continued to follow the wafer temperature progression. Normalized versions of the temperature profiles were calculated by Air Products and represented as polynomials to describe the axial temperature profile.

The chemical and thermal strains were determined using the expression

$$e(T,Xv) = (CCE0 + CCET1\ (T-T0))(Xv-Xv0) + CTE0\ (T-T0) \qquad [3]$$

where $e(T,X_v)$ is the strain, CTE^0 is the thermal expansion coefficient, CCE^0 and CCE^1 are first and second order terms in the polynomial expression relating strain to X_v only, $CCET^1$ is the expansion cross term, T^0=26°C, and X_v^o=0. The resulting stresses in the dense layer determined from the finite element analysis were subsequently used to estimate the reliability of the cone as a function of time (as described in the "Reliability Prediction" section below).

Reliability Prediction

a. Strength and reliability of AP2K

Ceramatec modified the NIKE (finite element) code obtained from Lawrence Livermore National Laboratory so that it would generate neutral files for analysis with CARES (CARES, Software package) software. An FEA model of a bend bar loaded in ¼, four-point bending and an accompanying neutral file was created and used to generate the CARES input parameter file. The neutral and input files were used to perform CARES analysis of the reliability of a model

bend bar at several different stresses. Raw bend bar strength values were used as input to CARES, which was used to generate Weibull distribution parameters and failure probabilities associated with each stress. A comparison of the failure probabilities measured by CARES and those estimated experimentally is shown in Figure 7-67.

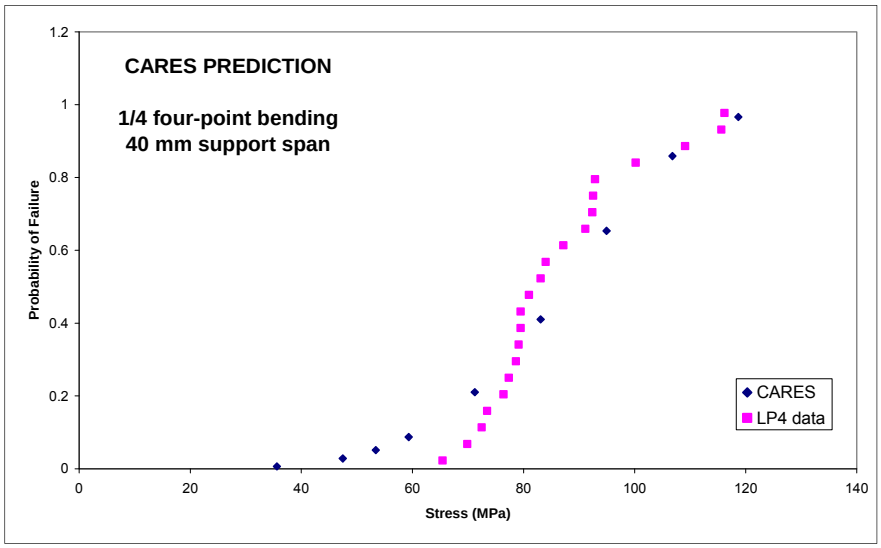

Figure 7-67..A comparison of failure probabilities predicted by the CARES code and estimated experimentally for simple bend bars.

The results indicate that the CARES prediction generally agrees with the experimental data. This agreement is best at the higher failure probabilities. The CARES predictions are for a bend bar with fixed dimensions, whereas the data come from bend bars that each has slightly different dimensions. Furthermore, the experimental data provide only an estimate of the population failure probability.

b. Reliability of Various Layer Types

Based on the FEA work to predict stress distributions the and CARES modeling approach discussed above to predict reliability, Ceramatec modeled the reliability of the various layer types and composite structures built from the layers. Strength data were generated at Penn State and Ceramatec. The strength data and reliability predictions are shown in Figure 7-68. In general, agreement is quite good for the straight porous and dense layers and is reasonable for the various combinations of porous, dense, and slotted layers tested as composite structures. This work served to validate the overall approach for assessing wafer and, ultimately, module reliability.

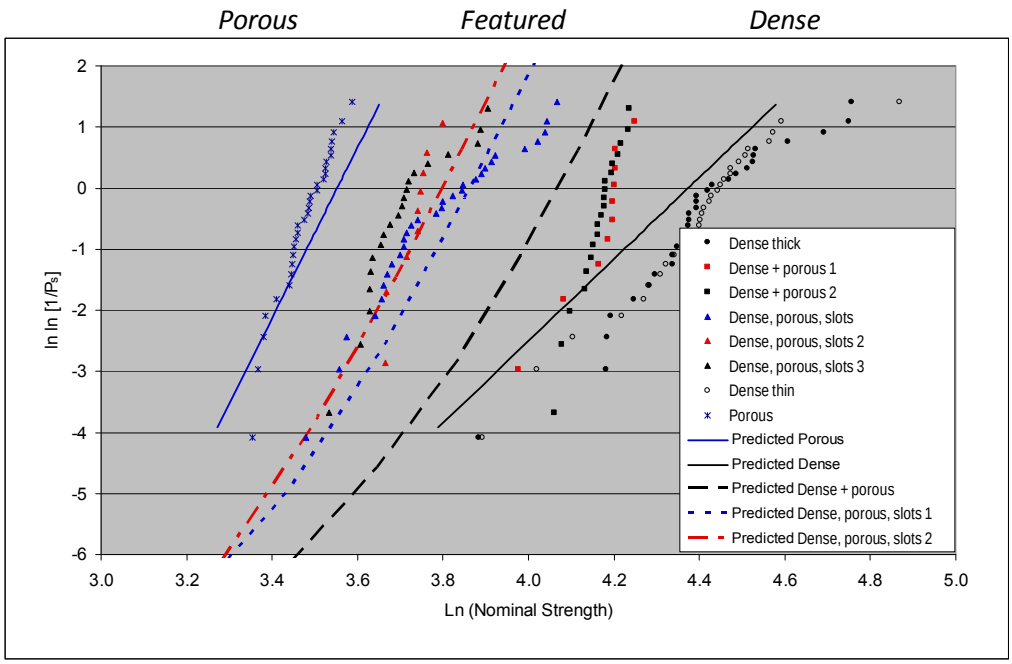

Figure 7-68.A comparison of failure probabilities predicted by the CARES code and estimated experimentally for various wafer layer types and composites.

c. Reliability of Wafers

A subroutine calculating the reliability of the wafer was developed and subsequently used to calculate the reliability of the centrally loaded wafer (i.e., the "wafer strength" data discussed above); Weibull parameters were generated using information for the porous and dense layers in the wafer. The model accounted for the differences in stiffness of the wafer depending on slot orientation. Figure 7-69 presents the experimental data and theoretical predictions. It shows the discrepancy in reliability estimation between Orientation 1 and Orientation 2. For each orientation, the deviation between experimental data and predictions is about 20%. The main reason that the prediction is relatively conservative is that the boundaries used in the modeling tend to give higher stresses.

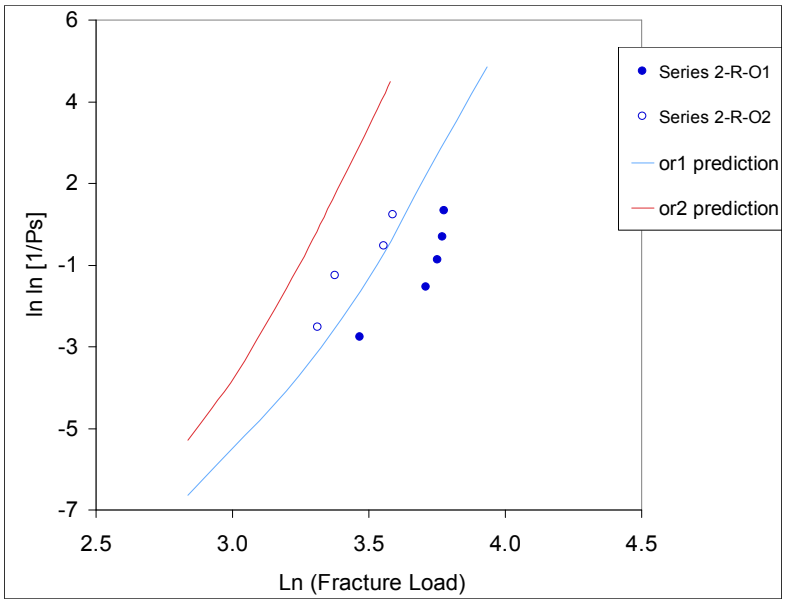

Figure 7-69. Weibull plots for wafer fracture loads (O1=Orientation 1 and O2 = Orientation 2).

Experiments were repeated using a ring-on-ring stress test and comparing standard slotted wafers with those that have a slot pattern designed to give a lower internal pressure drop. The reliability models do a better job of predicting failure based on the ring-on-ring testing, as shown in Figure 7-70. A separate model for stress in the low pressure drop wafers was generated to make the comparison.

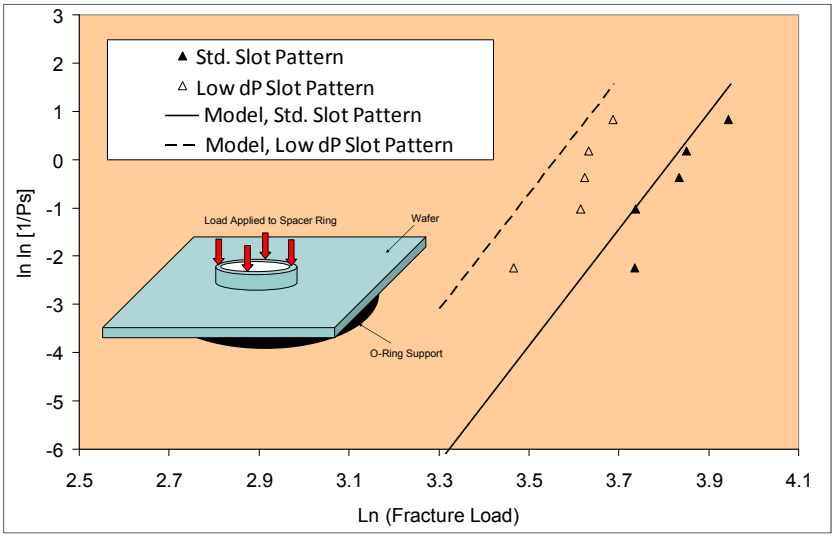

Figure 7-70. Comparison of predicted and experimental Weibull plots for standard and low-pressure-drop wafers fractured using the ring-on-ring fixture (shown in the inset schematic).

d. Reliability of Conical Base Piece

Figure 7-71 shows the probability of survival of the conical base piece dense layer as a function of time for Cases 1 and 2 (discussed above), based on a similar approach as was used to analyze the bend bar and wafer reliability above. The drop in Probability of Survival, Ps, for both cases at approximately 105 h is a result of the formation of gradients in oxygen along the inner and outer surfaces of the dense layer as the initial oxygen concentration in the dense solid begins to equilibrate with the respective surface values. The lowest value of Ps occurs as the steady-state gradient in oxygen concentration is established across the dense layer. Normally, the high stresses that caused the low reliability would be expected to relax somewhat due to creep; however, creep was not considered in this analysis. Because the oxygen concentration inside is smaller than the oxygen concentration outside under steady-state conditions, the inside of the dense layer attempted to expand with respect to the outer portion, causing the stresses to be tensile in this outer region. The inclusion of the axial temperature gradient for Case 2 did induce additional stresses in the lower portion of the inside slotted layer, but these stresses were relatively modest. The primary effect of the gradient was to reduce the severity of the chemical strains in the lower portion of the cone due to the diminishing contribution of the CCET term in Equation 3.

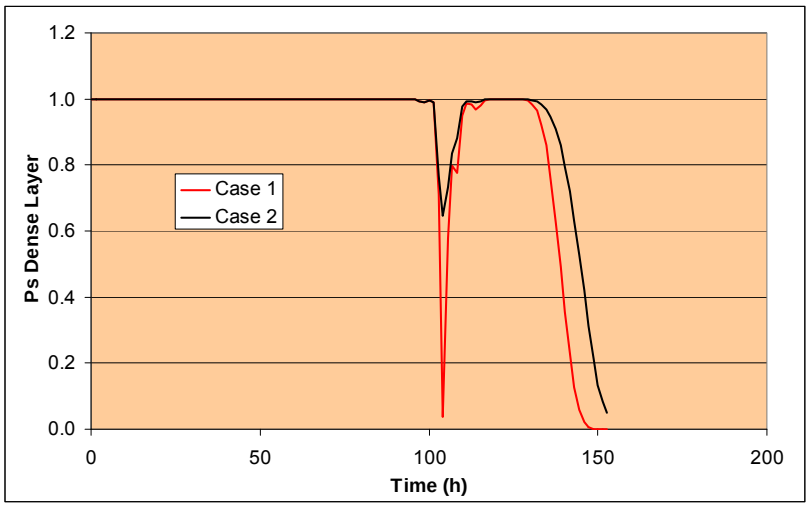

Figure 7-71. Probability of survival of the dense layer within the cone as a function of time.

Development Of The Chemical Expansion Verification Unit (CEVU)

Air Products and Penn State collaborated to design a test unit to verify the chemical expansion properties of the ITM ceramic materials under high-temperature conditions. The unit was ultimately built and operated by Penn State. As this was a new type of test for chemical expansion, the apparatus was extensively trialed to assess accuracy and precision of the measurements.

The premise behind the apparatus is to take advantage of the expansion properties of the ITM ceramics to enable measurement of the degree of expansion. The materials tend to expand as the P_{O2} decreases. Thus, applying a P_{O2} gradient across an unconstrained disk membrane composed of ITM ceramic will result in a measurable deflection. A mechanical model of the disk membrane can be used to fit the deflection data and extract the chemical expansion parameters of the material. A schematic of the concept is shown in two dimensions in Figure 7-72.

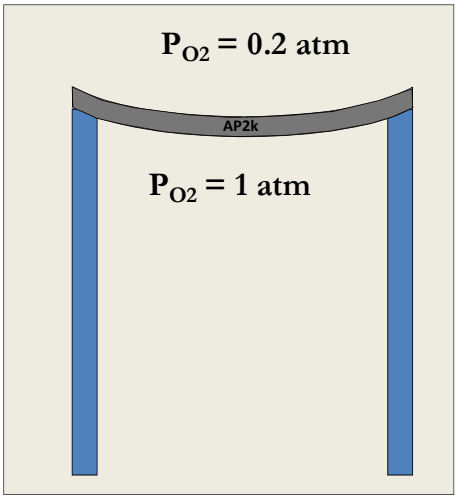

Figure 7-72. Simple schematic of the proposed chemical expansion measurement. An oxygen partial pressure gradient is applied to a thin disk of ITM material (grey), supported on an inert tube (blue).

A "Chemical Expansion Verification Unit" (CEVU) was devised in which the disk deflection concept could be implemented in a furnace, with a transducer measuring the deflections through a push rod. One end of the push rod is connected to the transducer, while the other rests against the membrane (Figure 7-73). Separate gas mixes are prepared and metered into the apparatus outside and inside of the tube supporting the membrane.

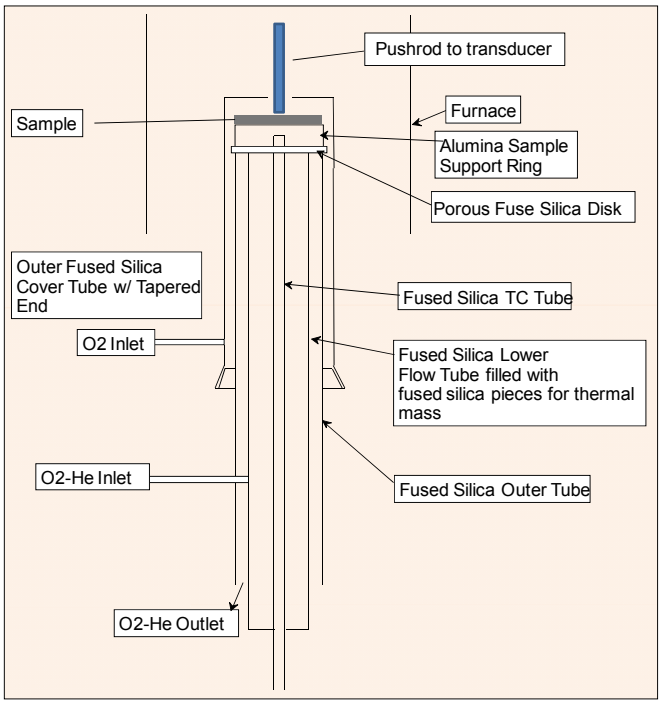

Figure 7-73. Schematic of the CEVU experiment.

Initial attempts to implement this concept revealed some challenges. Gas-phase mass transfer resistance caused uncertainty in the local oxygen partial pressure on both sides of the disk. The resistances were minimized by using a pure oxygen environment on the top of the membrane and a helium-oxygen mix on the bottom of the membrane. Thermal gradients were also found to cause problems in the apparatus; these were minimized by good flow rate control. Finally, numerous challenges arose in the detection of small deflections. These challenges were successfully addressed by Penn State. A photograph of the working apparatus is shown in Figure 7-74.

Figure 7-74. Photograph of the working CEVU experiment at the Penn State laboratory.

Penn State carried out measurements with the CEVU over a range of operating conditions at elevated temperature. One example is shown in Figure 7-75, where an AP2K disk deflection was measured with a maximum P_{O2} difference of 0.8 atm between the top and bottom sides of the disk. The top-side oxygen concentration was cycled to show the reproducibility of the test, and a range of top-side gas flow rates were demonstrated to illustrate the lack of mass transfer resistance.

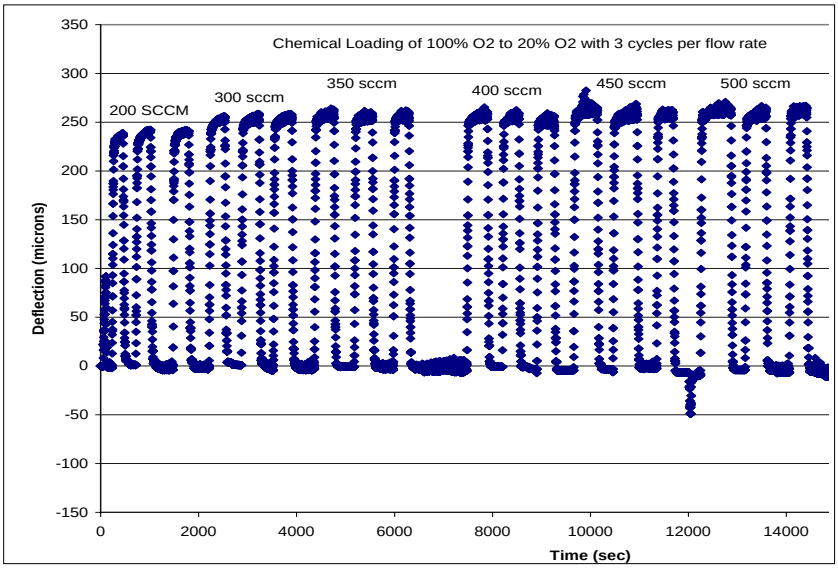

Figure 7-75. Deflection of an AP2K disk in the CEVU, cycled between 100% oxygen and 20% oxygen on the top side of the disk (with air on the bottom side). All experiments were conducted at elevated temperature and atmospheric pressure.

McDermott/SOFCo and Ceramatec modeled the response of the disk in the CEVU experiment (Figure 7-76) for a range of experiments (a half disk was modeled, assuming symmetry.) Good fits to the data were enabled by the modeling work, and chemical expansion coefficients were determined accordingly. The obtained chemical expansion coefficients from this experiment agree with independently obtained coefficients from dilatometry, thus validating the CEVU test.

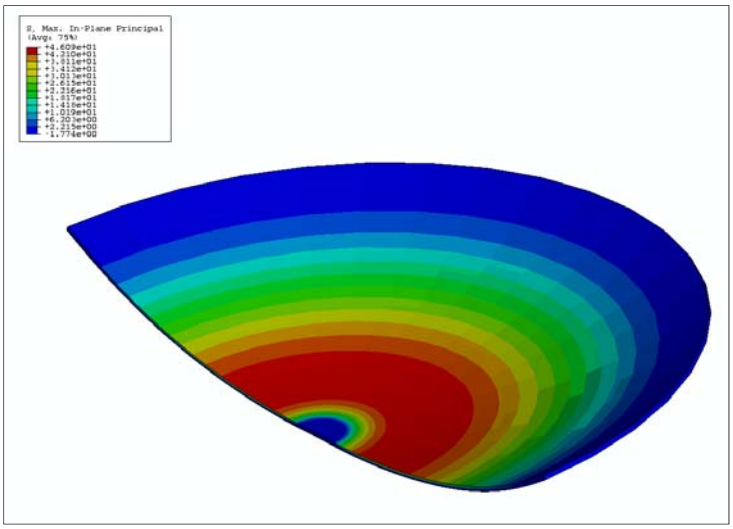

Figure 7-76. Calculated deflection of an AP2K disk in the CEVU experiment, showing contours of principal stress in the disk.

Methods To Control Chemical Expansion Stresses

ITM ceramics expand and contract depending on the amount of oxygen present in the sample. This is the property known as chemical expansion. The presence of gradients of oxygen concentration within an ITM ceramic part leads to stress arising from the chemical expansion differences between regions of lower and higher oxygen concentrations. These stresses may exist independently of the presence or absence of any stresses arising from thermal gradients in the parts.

Under Task 7.6, Air Products devised a means for controlling the oxygen concentration gradients in the parts so as to control the level of stresses that are allowed to develop. Conceptually, the method seeks to eliminate the driving force for oxygen transport both inside and outside of a wafer. This approach is implemented when no oxygen production from a wafer is required, for example during process transients such as starting up or shutting down an ITM Oxygen process or during manufacturing of ITM wafers. The method requires that the equilibrium partial

pressure of oxygen be maintained in the gas phase adjacent to the ceramic materials. Different equilibrium oxygen partial pressures may be required on the outside and inside of the wafer, if, for example, the wafer had been previously at steady-state operating conditions. The equilibrium oxygen partial pressure is a function of temperature and the amount of oxygen in the ceramic part.

Air Products named one such method "iso-compositional control." During iso-compositional control, the gradients within the part are eliminated by fully equilibrating the part with the gas phase. When cooling the part, following, for example, the sintering step of wafer fabrication, the material throughout the wafer is exposed to the gas-phase oxygen partial pressure. At a sufficiently high temperature, the oxygen content in the part is in equilibrium with the oxygen in the gas around the part. As the part is cooled, the oxygen partial pressure in the gas phase must be adjusted to maintain the oxygen content in the part constant throughout the part. This will entail reducing the oxygen partial pressure in the gas phase to eliminate the driving force that would otherwise drive oxygen into the part. During part cooling, this can be carried out, for example, by diluting the atmosphere around the part with an inert gas such as nitrogen. As the part is fully cooled, depending on the starting temperature and oxygen content in the part, the oxygen partial pressure in the gas phase may be reduced by several orders of magnitude. By utilizing such iso-control techniques, ITM parts can be heated and cooled much quicker than if the parts are simply cycled in air because chemical expansion stresses are minimized.

Experimental Verification of Iso-compositional Control

Air Products conducted experimental trials with simple bar samples of AP2k and with full-size wafers to verify the effectiveness of the iso-compositional control concept.

a. Dense and porous AP2k samples were cooled in a dilatometer under various isocompositional cooling profiles. Air Products used a relationship determined under Task 2 between the temperature, the partial pressure of oxygen, and the equilibrium oxygen concentration within AP2k. Thus, for each starting value of temperature and oxygen concentration in the part, a corresponding cooling schedule can be generated that prescribes how the oxygen partial pressure should be adjusted with temperature. A family of such curves is shown in Figure 7-77 where the oxygen partial pressures have been normalized based on expected starting values. Each of the curves represents a unique

quantity of oxygen in the part (corresponding to the starting temperature) that will remain fixed as the part is cooled and oxygen partial pressure around the part is adjusted according to the curve.

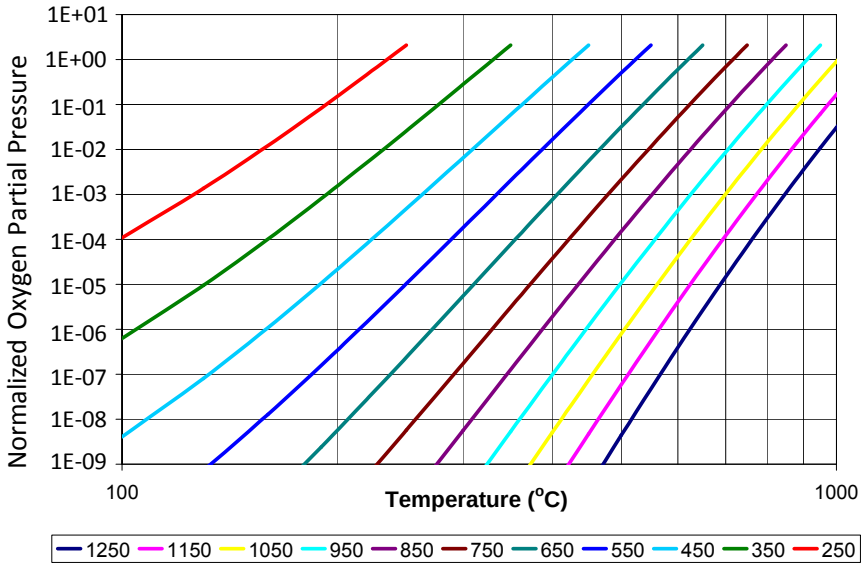

Fig. 7.77: Normalized P_{O_2} as a function of temperature, for a variety of isocompositional temperatures.

The isocompositional starting temperature needs to be chosen at a point where the solid-state mobility of oxygen has slowed and yet where concentration gradients have not had a chance to develop. One possibility is a point where the dominant limiting resistance has changed from the surface exchange reaction to bulk diffusion. This can be characterized by the dimensionless factor L (Crank,1975).

$$L = \left(\frac{t}{2}\right)\left(\frac{K_{ex}}{D_v}\right) \qquad [4]$$

where t is the thickness of the sample (t/2 is the diffusional path length), K_{ex} is the surface oxygen exchange rate, and Dv is the chemical diffusivity of the oxygen vacancies. When L > 1, the dominant limiting resistance is vacancies diffusion, and if L < 1, the dominant limiting resistance is the surface exchange reaction. These parameters have been determined for the AP2K material, thus indicating the appropriate isocompositional cooling temperature range.

Experiments were carried out in a dilatometer connected to a gas blending unit. A porous bar was used to represent the equilibrium expansion of AP2k, and a solid bar cut from the

dense rim of full-sized wafer was used to represent the maximum diffusional path length of an AP2k component. The samples were heated in air to 850°C and cooled to room temperature under controlled ramps. The P_{O_2} control from the gas blending unit was operational only during cooldown and began affecting the atmosphere over the sample once the isocompositional temperature has been reached.

The gas blending unit consists of three mass flow controllers (MFCs), one 0 – 500 sccm MFC to control the flow of nitrogen, one 0 – 500 sccm MFC to control the flow of air and one 0 – 10 sccm MFC to control the flow of air (Figure 7-78). The two MFCs controlling the flow of air allow control of P_{O_2} over approximately four orders of magnitude. This is important because the relationship between P_{O_2} and temperature is approximately log - normal (see Figure 7-77). Based on the thermocouple reading, the PC calculates the desired P_{O_2} and adjusts the MFC set points to obtain the correct P_{O_2} entering the dilatometer. The P_{O_2} entering (or leaving) the dilatometer is measured directly with an oxygen analyzer.

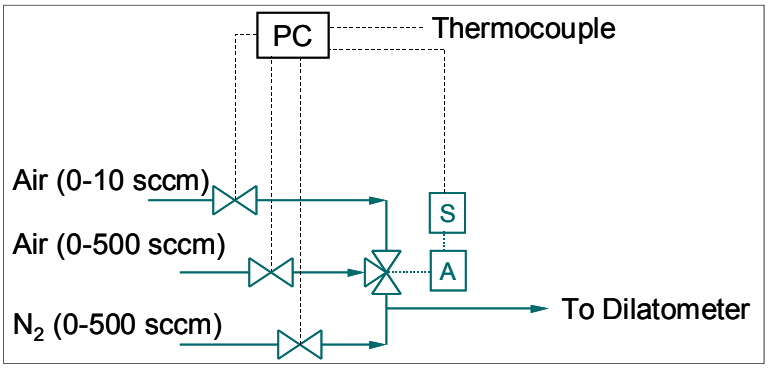

Fig. 7.78. Gas blending unit schematic.

Figure 7-79 shows a plot of differential strain between the dense and porous bar for three different isocompositional control starting temperatures. Negative differential strains represent a condition of residual compression on the surface of the dense bar, and vice versa for positive differential strains. Also plotted is the strain differential if there were no gas blending unit, only flowing air (black curve). The isocompositional temperature of 600°C gives the lowest strain differential when cooled to room temperature, and therefore the least amount of residual surface tensile stress. The reduction in strain among the isocompositionally cooled bars relative to the black curve representing no iso-control

indicates that oxygen transport into and out of the samples has been greatly reduced in the iso-control cases.

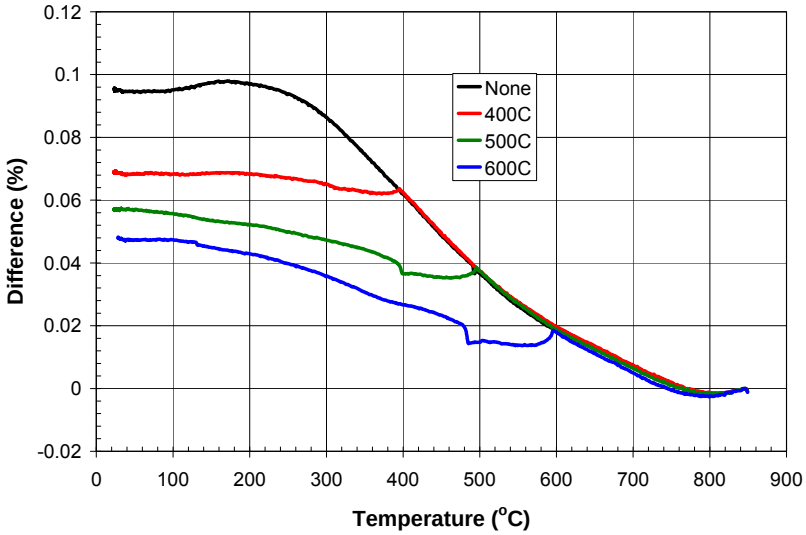

Fig. 7.79. Effect of isocompositional temperature on differential strain.

b. The advantage of using isocompositional cooling is that it should be possible to dramatically increase the cooldown rates of full-size parts. Therefore, Air Products heated full-scale wafers to 850°C, and aggressively cooled them 1) under air and 2) under an isocompositional cooling composition profile. The entire temperature cycle, from ambient to operating temperature and back to ambient, required only 24 hours.

The goal was to determine if a qualitative difference (i.e., wafer failure) could be shown between the wafers. The results are shown in Table 7-23. Wafer failure occurred when no isocompositional cooling was used, or an isocompositional cooling temperature of 400°C was used. The wafer did not fail when isocompositional temperatures of 500°C and 600°C were used. These results are consistent with the bend bar iso-compositional cooling data, which showed that the lowest strains were observed at higher iso-compositional temperatures.

Conclusions from this study are that the iso-control techniques can serve to allow faster thermal/pressure cycles and increase the reliability of parts through reduction of local stresses.

Table 7-23. Results from cooling full-size wafers.

Isocompositional Temp, °C	Result
400	Fractured
500	Intact
600	Intact
None	Fractured

7.7 Process Engineering and Economic Evaluation

IGCC Study of ITM Oxygen with Nitrogen Diluent Production

Under this Task, Air Products carried out a study of an IGCC system with NovelEdge Technologies, LLC. The study focused on utilizing available gas turbine technology and compared ITM Oxygen technology with state-of-the-art cryogenic air separation technology. Cases were also studied which made use of steam system improvements to reduce the specific capital cost and increase efficiency. The study was presented at the PowerGen International conference in November 2006 (Armstrong et. al., 2006). Previous studies had shown significant advantages of the integration of ITM Oxygen with the IGCC plant flowsheets (see Task 2). Those studies had included 1) substantial air extraction from the GT compressor, for which there exist few offerings from GT original equipment manufacturers (OEMs); and 2) air heating by direct-firing in a combustor upstream of the ITM unit, which consumes some of the oxygen content in the ITM air supply. The work described here eliminated those two potential drawbacks to the application of ITM Oxygen.

An OEM gas turbine requires a diluent fluid in addition to fuel and air to operate successfully in an IGCC plant. The diluent is pre-mixed with the syngas fuel available in an IGCC facility, and its use suppresses the formation of NO_x in the GT combustors. Although water and steam have been utilized in natural gas-fired applications, for IGCC many developers prefer nitrogen as the diluent. When oxygen is provided by a cryogenic ASU, a stream of nitrogen containing only small concentrations of oxygen (e.g., ≤ 2 mol. %) is readily available. In previous studies, when oxygen is supplied by the ITM Oxygen process, the residual oxygen-depleted (non-permeate) stream typically contains approximately half of the oxygen in the supplied air stream (e.g., ~10 mol. %).

Process Modifications

Basic changes to the ITM configuration were devised to provide not only the necessary oxygen for the gasification process, but also the necessary diluent at low oxygen concentration for the GT. In previous ITM Oxygen IGCC application studies, the air feed flow to the ITM system was sufficient from which to extract enough oxygen for the gasifier to produce the required fuel for the GT, while leaving significant amounts of oxygen in the non-permeate stream. In the case in which both oxygen and diluent must be produced, the ITM system is over-constrained by the unique requirements of the GT. In general, the GT requires fuel and diluent in specific proportions. For coal gasification-derived syngas fuel, the ratio of the oxygen to the diluent gas (nitrogen) required by the GT is more than the ratio of oxygen to nitrogen in air. Thus, once sufficient oxygen is extracted from the air in an ITM system to produce the fuel for the GT, the resulting non-permeate stream will be insufficiently depleted in oxygen to be used as diluent. Additional oxygen extraction from the non-permeate to produce a low oxygen-content diluent will require additional membrane area and will result in additional (unneeded) oxygen production.

To avoid these drawbacks while producing both sufficient oxygen for the gasifier and a non-permeate stream low enough in oxygen content to meet GT OEM diluent specifications, a scheme was devised in which two or more ITM systems could be placed in series with one or more intermediate streams of oxygen-depleted gas removed and expanded to make power. A simple schematic of such a scheme is shown in Figure 7-80. A heated air stream is first passed through an ITM vessel from which the majority of oxygen is produced. The resulting (non-permeate) vitiated air stream is depleted in oxygen, but not sufficiently so to be used as the diluent stream to a GT. A portion of the vitiated air stream is expanded to make power (optionally the vitiated air stream is fired with a fuel prior to expansion as shown). The exhaust from the expansion step can be sent to a heat recovery steam generator (HRSG), for example, for additional energy recovery.

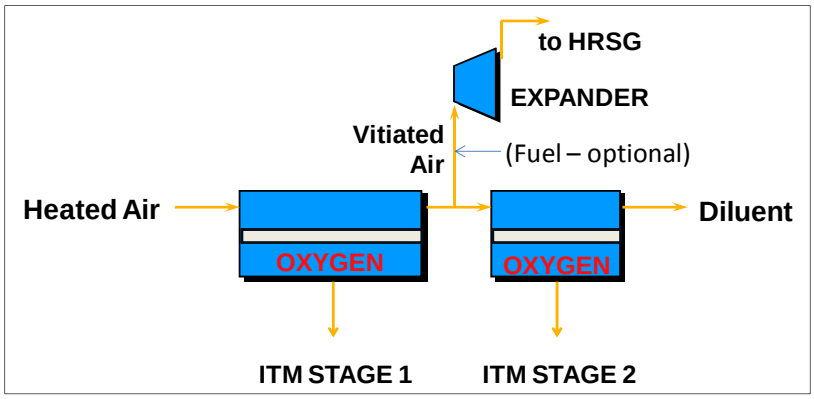

Figure 7-80. Simple scheme for producing oxygen and diluent.

The second portion of the non-permeate stream is passed to a second ITM vessel, which pulls out the remainder of the oxygen to create a diluent stream suitable for a GT. For example, the diluent stream may contain <2 mol. % oxygen and represent sufficient mass flow so that the fuel is appropriately diluted in the GT, and the GT can make its rated power output.

In this approach, the main role of first ITM vessel is to produce oxygen. Accordingly, the feed flow rate to the first vessel should be relatively large so that the oxygen partial pressure throughout the vessel remains sufficiently high to sustain high oxygen fluxes throughout the ITM module array in the first ITM vessel. In contrast, the main role of the second ITM vessel is to produce diluent gas for the GT, which in general will require less diluent mass flow than is represented by the non-oxygen species in the feed flow to the first ITM vessel. Thus, it is advantageous to divert a portion of the non-permeate stream before it enters the second ITM vessel. This scheme results in a smaller required membrane area than if a single ITM vessel were used and sized to make the oxygen flow and diluent flow. This scheme produces only required flows of oxygen and diluent – the vitiated air stream removed from between the two vessels is used directly for power generation without further, unnecessary processing.

To address the limited air extraction capability from an OEM GT, a standalone air compressor was added to the process. The ITM system therefore simultaneously utilizes air from both the standalone air compressor as well as a modest amount of air extracted from the GT.

To avoid the consumption of oxygen in direct combustion operations adding heat to the ITM feed, the team included some process design features developed previously by NovelEdge Technologies. The NovelEdge^{TM} combined cycle process and ITM Oxygen system can be

integrated together in the IGCC process. This is accomplished by adding significant amounts of low-cost power generation capacity through the use of supplemental firing in the HRSG. This feature reduces the specific cost of the power island.

Because the NovelEdge™ process utilizes substantial supplemental firing in the HRSG, all of the air heating for the ITM system can be achieved in a special section within the HRSG. This configuration eliminates the need for a direct-fired air preheat process, thereby providing a heated pure air supply to the ITM modules with higher oxygen content.

Figure 7-81 illustrates this new system configuration for the NovelEdge™ system integrated with ITM Oxygen in an IGCC application. Air is extracted from the gas turbine compressor section and boosted slightly to overcome pressure drop in the system. Additional air sourced from the supplementary air compressor and combined with the extracted air from the gas turbine compressor section is subsequently fed to a heat exchange coil in the duct-fired HRSG. Pure air exits the indirect heating section at a controlled temperature in the range of 800 to 900°C (1475° to 1650°F) and proceeds to a 2-stage ITM system.

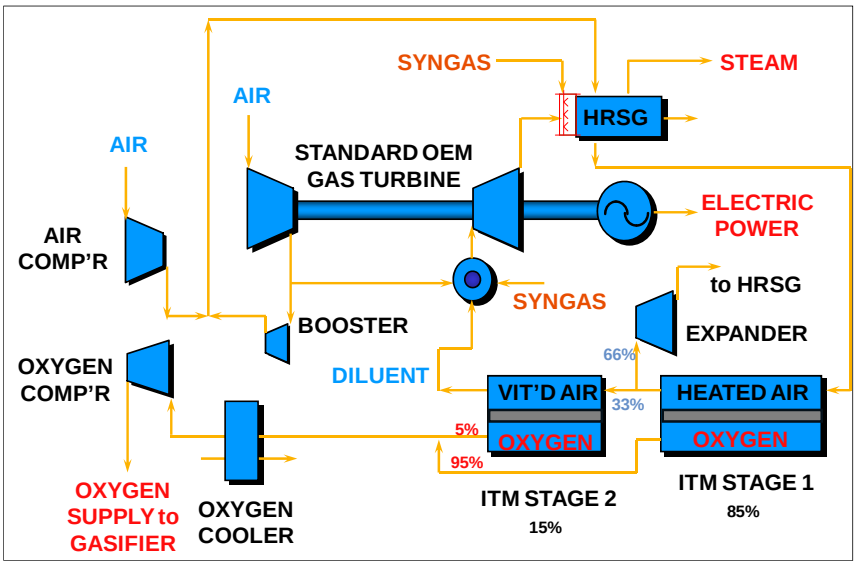

Figure 7-81. Process flow diagram of IGCC process integrating ITM Oxygen and NovelEdge™ technology.

The first stage of the ITM system produces ~95% of the oxygen required by the facility. The non-permeate stream exiting the first section is split into two streams: two-thirds of the stream is directed to a hot gas expander and is expanded to make power; exhaust from the expander is

directed to provide additional steam in the HRSG. The other one-third of the non-permeate stream exiting the first ITM stage is directed to the second ITM stage, where it is further processed to provide the final ~5% of the oxygen required by the facility as well as all of the diluent stream. The diluent stream, containing less than 2 mol.% oxygen, is directed to the combustion section of the GT. A heat recovery step (not shown) cools the diluent to raise HP steam for the HRSG prior to the introduction of the diluent to the GT combustor.

The oxygen from ITM stages 1 and 2 is combined, cooled by raising HP steam, compressed and sent to the gasification island (not shown). Syngas from the gasifier is used to fire the gas turbine combustor and the duct-fired section of the HRSG.

System Performance and Cost

Air Products and NovelEdge Technologies collaborated to determine the process and financial performance of three systems built from progressively adding features to the flowsheet described under Task 2, and culminating in the flowsheet shown in Figure 7-81. The cases consisted of combinations of conventional IGCC with cryogenic air separation, IGCC with ITM Oxygen, and IGCC integrated with the NovelEdge approach to HRSG implementation and ITM Oxygen. A GE 7EA gas turbine was used as the power turbine in each of these studies.

Table 7-24 details the process performances in the three cases. Replacing the cryogenic air separation unit (ASU) with an ITM Oxygen system resulted in a 1.2 percentage points increase in efficiency. Adding duct firing and additional features in the HRSG as recommended by NovelEdge Technologies resulted in a 4.5 percentage point increase in efficiency over the baseline and a 3.3 percentage point increase over the system with just the ITM Oxygen system replacing the cryogenic ASU. Adding both the ITM Oxygen and the NovelEdge™ technology increases the overall power output of the plant; despite that, the system efficiencies increase with each addition of these technologies.

Table 7-24. Study cases considered

Case	Plant Configuration	Power Output (MW)	Efficiency Change, HHV (% pts.)
1	Conventional IGCC with Cryo ASU	543	baseline
2	Conventional IGCC with ITM Oxygen	627	+1.2
3	NovelEdge™ IGCC with ITM Oxygen	820	+4.5

The team developed budgetary estimates of capital costs for the three cases above and determined operating costs leading to an overall cost of electricity (COE) for each of the cases. These are summarized in Table 7-25, which includes costs from another study (Heaven and Rollins, 2004) for a case with cryogenic ASU oxygen supply and NovelEdge™ technology in the HRSG.

The data show a 9% decrease in specific capital cost ($/kW) and a 7% decrease in COE for the ITM-based IGCC (Case 2) relative to the cryo ASU case (Case 1). When ITM is compared against cryogenic ASU case in the cases when the NovelEdge™ treatment of the plant is considered (Case 3 against the case provided previously (Heaven and Rollins, 2004)) the specific capital cost of the ITM case is 6% lower and the COE is 5% lower. Case 3 is fully 18% lower in specific capital cost than the base case, and 16% lower in COE.

Table 7-25. Summary of financial performance of study cases.

Case	*Plant Configuration*	*Power Output (MW)*	*Capital Cost ($/kW)*	*Fuel Cost ($/kwh)*	*Capital Cost ($/kwh)*	*O&M Cost ($/kwh)*	*Total COE ($/kwh)*
1	***Conventional IGCC with cryo ASU***	543	1500	.0133	.0214	.0110	**.0457**
2	***Conventional IGCC with ITM Oxygen***	627	1368	.0132	.0195	.0098	**.0425**
	NovelEdge™ IGCC with cryo ASU	785	1305	.0131	.0186	.0088	**.0405**
3	***NovelEdge™ IGCC with ITM Oxygen***	820	1224	.0126	.0175	.0083	**.0383**

Note: Based on $1.50 per MMBtu for fuel and 80% capacity factor.

The following conclusions were reached based on this study:

- Process performance and economic analyses of integrated ITM Oxygen and NovelEdge™ technologies in IGCC application indicate substantial cost savings in both the specific cost of installed power and the cost of electricity. The use of both ITM Oxygen and NovelEdge™ technologies provides synergies that result in over 15% savings in *both* specific plant capital cost ($/kW) and cost of electricity (COE) relative to conventional, state-of-the-art methods.
- The combined ITM Oxygen and NovelEdge™ technologies enable over 50% additional power production.
- These results have been obtained assuming the use of gas turbine machinery that is available today, without further modification.

References

Almhem, Par, and Anderson L., "Cottbus Opts for PFBC Repowering," *Modern Power Systems*, September 1996.

Armstrong P.A, Repasky J.M., Rollins W.S., Stein V.E., "Integrated Oxygen Supply Technology for Gasification," presented at POWER-GEN International 2006, (28-30 Nov 2006), Orlando, Florida

Ceramic Analysis and Reliability Evaluation of Structures (CARES)" Software package. NASA Glenn Research Center

Chen C.F, and Chuang T.J., "Improved Analysis for Flexural Creep will Application to Sialon Ceramics," J. Am. Ceram. Soc., 73 [8] 2366-73 (1990).

Conway, A., "FBC Powering into the Year 2000," *Modern Power Systems*, April 1992.

Crank J., *The Mathematics of Diffusion*, 2nd Edition, pp60 – 61, Oxford University Press, New York, NY, 1975.

Evett, B., "Driven by Necessity," *Int. Power Generation*, **21**(4) (May 1998) p. 23.

Fulton, K., "GT 140P Clean Coal PFBC Plant Rated 425 MWe and 45% Efficiency," *Gas Turbine World*, November-December 1996.

Heaven D. and Rollins W., "The NovelEdge IGCC Reference Plant: Cost and Emissions Reduction Potential," presented at the 2004 Gasification Technologies Conference, October 2004.

Jansson, S. A., "Developments in PFBC," *International Power Generation*," March 1991.

McDonald, D.K., PFBC Plant Operations – TIDD, Presented at *PowerGen '92*, Orlando, Florida, 1992.

Nilsson J.C, Anderson J., Thőrnblad P., "The GT140 P-machine is Extensively Tested for Commercial Application," Presented at the *International Gas Turbine & Aeroenge Congress and Exhibition*, Stockholm, Sweden, 2-5 June 1998.

Omata, K., and Anderson L., "Karita 360 MWe PFBC an Imminent Prospect," *Modern Power Systems*, April 1997.

Wright, I. G., Stringer J., and Wheeldon J.M., "Materials Issues in Bubbling PFBC Systems," *Materials at High Temperatures*, **20**(2) (2003), 219-232.

8.0 CERAMIC PROCESSING

8.1 Full-Size Wafer Yield

Ceramic Joining

Building on the success in ceramic joining under Task 3, Ceramatec performed extensive trials to define the appropriate material characteristics and operating parameters for ceramic joining of sintered spacers to sintered wafers. The optimization parameters included tape surface area, pressure, time and temperature. Figure 8-1 is an example of the relationship between leak rate and pressure. Three-wafer modules and spacer-wafer couples were typically fired to assess leak performance. A significant number of runs were completed to determine the repeatability of the joining process.

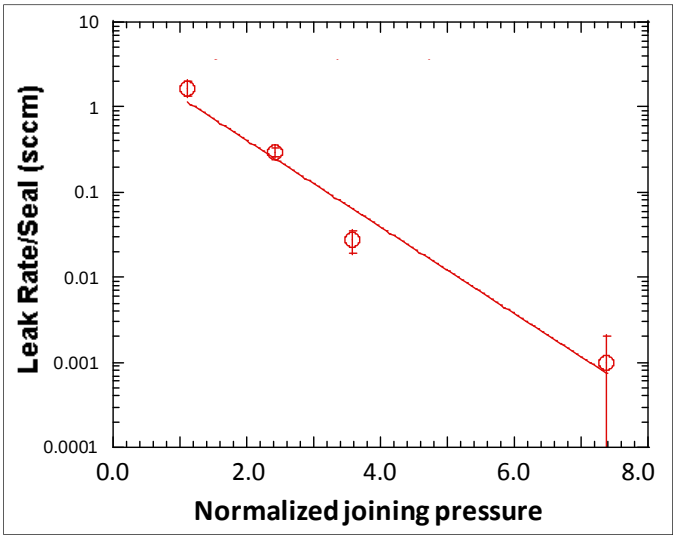

Figure 8-1. Effect of joining pressure on leak rate of AP2k spacers.

The joining process was clearly repeatable; only two out of 60 seals had unacceptable leaks during tests conducted over a one-year time period. Joining tape with a smaller surface area produced the best results.

Additional work was conducted to determine if unground spacers could be joined (i.e., with low leak rates). Six assemblies made with unground spacers had leak rates of 1 sccm or less. Leak rate decreased markedly with pressure. Figure 8-2 compares joints made with ground and unground spacer assemblies. It was concluded that the tape used to join unground spacers produced joints with acceptable leak rates.

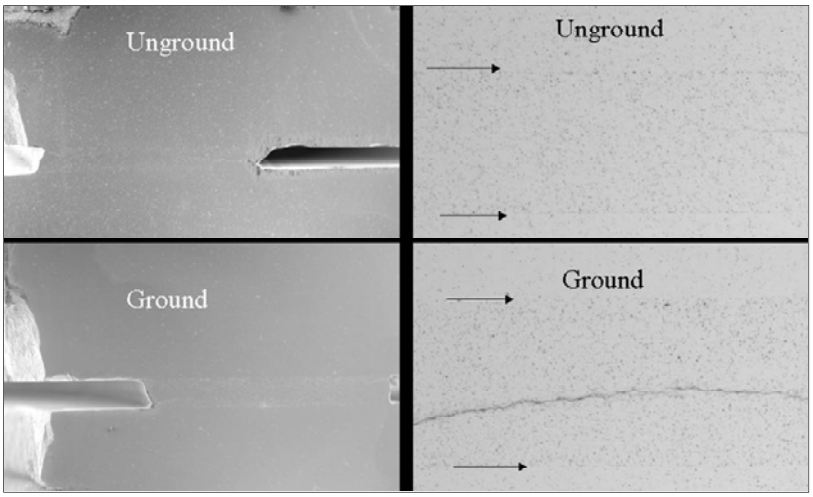

Figure 8-2. Comparison of joints made on ground and unground spacer assemblies. *Left:* Images at 50-55X in SEI; *Right*: images at 300X in BEI. Arrows show interface between sintered parts and joined tape. Cracks were observed to begin at the outer edge and propagate inward.

Additional work was conducted to minimize cycle time through the use of higher-surface-area tape and pressure. Twenty-one spacers were joined at a faster cycle time with higher-surface-area tapes. All had leak rates below 0.1 sccm.

The first ceramic seal attempt on a one-wafer module yielded a testable module. Twelve wafers were joined to 24 half-spacers under pressure. One half-spacer was joined to the spacer side of a wafer and the other to the wafer side of the wafer. This resulted in 19 of 22 seals with a leak rate of <1 sccm and 13 of 22 seals with leak rates <0.1 sccm.

Conical Tubes

Fabrication

McDermott specified a conical tube as the basepiece on full-size modules. The conical tube allows the transition between the module ID and an internally insulated pipe. The inside of the cone is expected to be thermally insulated as well to allow the ceramic-to-metal seal to operate at temperatures below its plastic deformation temperature.

Ceramatec developed manufacturing techniques for the conical base piece. Fabrication of a conical tube from tape cast with AP2k was successful. Internal featured layers were designed to accommodate the chemical expansion of AP2k, and a flexible program was written to generate

code for the laser cutting. Tapes were cut and laminated into a tape-wrapped tube. The cone was successfully sintered (Figure 8-3).

Figure 8-3. First AP2k tape-wrapped tube, successfully laminated and sintered.

Thermal Gradient

Two conical tube thermal gradient tests were conducted. The tubes had a silver helical stripe painted on the surface to act as an electrical conduction path that would be broken if the tube failed. Surface thermocouples contacted the cones at the top, bottom and three equally spaced places in between. The cones were placed between two electrically heated plates in a heated kiln. One plate was heated to a higher temperature than the other plate.

The first test fractured the tube with a crack running in the circumferential direction. The thermal gradient at the time of fracture was unknown because the crack did not run through the silver stripe. The maximum temperature difference between the top and bottom of the tube was 241°C (Figure 8-4)

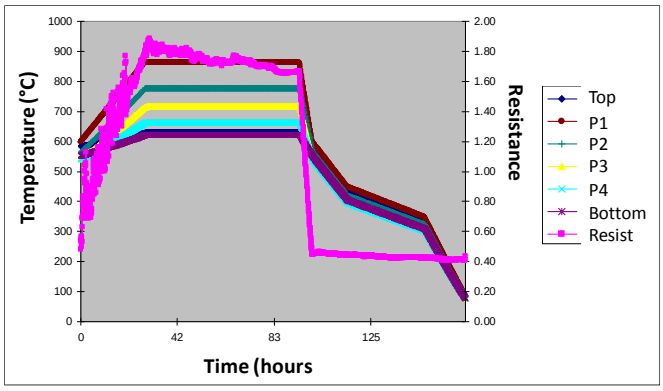

Figure 8-4. Thermal and resistance data for the first conical tube thermal gradient test.

The second test was a repeat of the first test, but the tube did not break. As shown in Figure 8-5, the maximum temperature difference between the top and bottom of the tube was 262°C.

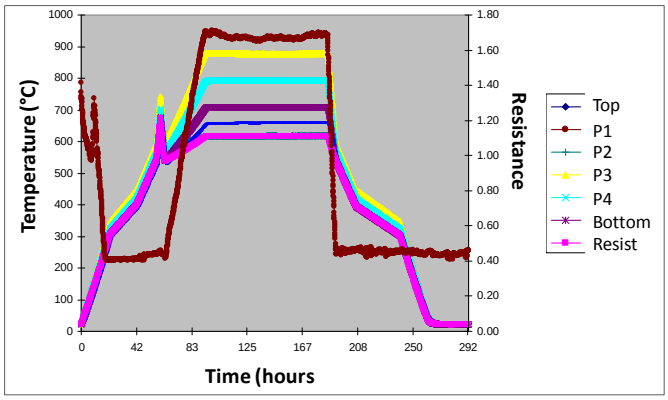

Figure 8-5. Thermal and resistance data for the second conical tube thermal gradient test.

These tests indicate that the ceramic cone base piece can withstand a significant thermal gradient in the absence of an applied pressure difference between the outside and inside of the cone.

8.2 Module Processing Development

Wafer Production

Ceramatec operated the PDF with the following goals:

- Implement processes developed to the conceptual level under Task 8.1 to establish higher production volume manufacturing statistics;
- Improve manufacturing yields;
- Produce wafers and modules for the VP-SLTR, XVUs, TDU, TTR, and SEP.

Manufacturing steps included powder production, slip preparation, tape casting, featuring, lamination, sintering, and joining. Spacers, end caps and base pieces were manufactured in addition to wafers. The standard manufacturing methods that were established, taken together, formed a standard "on line process" (OLP). Any changes to the process were measured against the performance of the OLP. If the changes resulted in a statistically significant improvement in yield, or saved costs in the form of materials, processing time, or labor at the same yield, the changes were adopted according to a rigorous methodology. The changes became part of the revised OLP. In this way, Ceramatec was able to gradually improve yields while maintaining a standard process.

Wafer production rates were adjusted during Task 8 to meet the requirements of the SEP test plan. A population of experimental wafer lots was also continually fabricated to improve yield. Figure 8-6 shows the relative membrane area produced in the green state in the PDF through much of Task 8. In general, production levels are 5-6X those maintained during Phase 1 (Task 3).

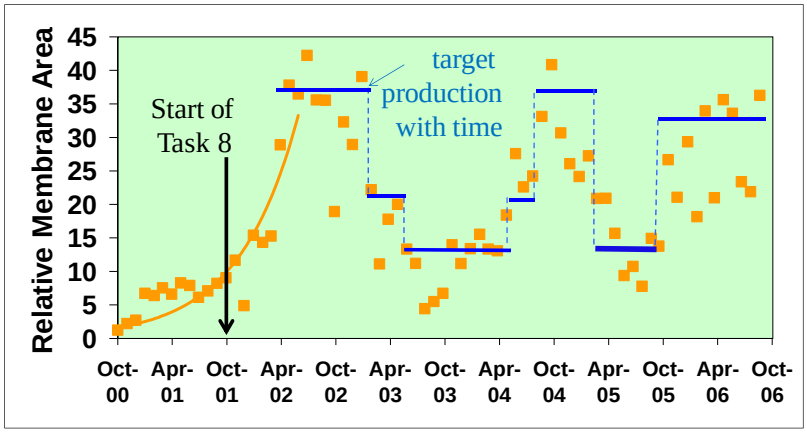

Figure 8-6. Production rate (orange squares) as membrane area versus time. Task 8 started in October 2001. Target production rate (blue lines) was adjusted during the Task.

Wafer yields were tracked using three metrics: delaminations, intact/broken, and leak rate. Delaminations were an early defect indicating poor layer-to-layer bonding during the lamination steps. The number of intact or broken wafers was an indication of the numbers of wafers surviving the thermal cycles while structurally sound, if not leaky. Leak rate was the most stringent test, and ultimately the measurement on which wafer specifications for produced oxygen purity were ultimately based.

Figure 8-7 is a plot of the numbers of total wafers produced as well as the number that were intact, broken or delaminated. As shown, delamination defects were eliminated early in Task 8. The fraction of intact wafers also increased markedly during the Task, resulting from steady improvements to many of the individual processing steps that went into making the wafers.

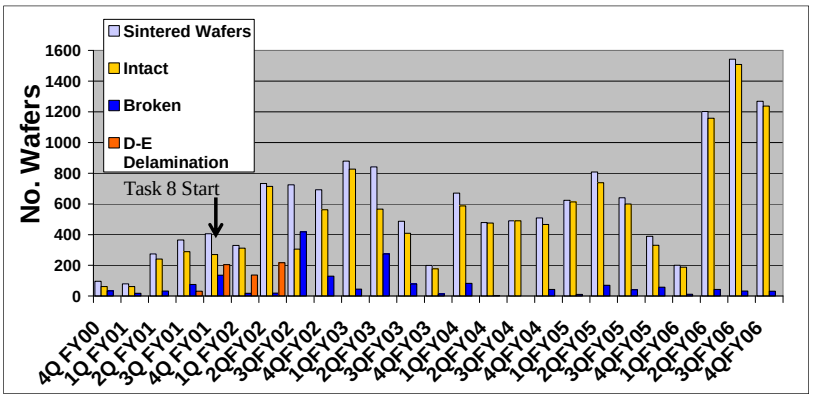

Figure 8-7. Numbers of wafers produced by government fiscal year quarter. Of those, intact, broken and delaminated wafer populations are also plotted.

Ceramatec produced both thick- and thin-membrane wafers. Thick-membrane wafers were used to assess yield improvement early in process development, when yields were relatively low and uncertainty in yield improvement was therefore high compared to the absolute value of the yield. As processes improved, Ceramatec switched to making thin-membrane wafers that would yield the target oxygen production from a membrane module. Figure 8-8 shows the trends of wafer production by membrane thickness during Task 8.

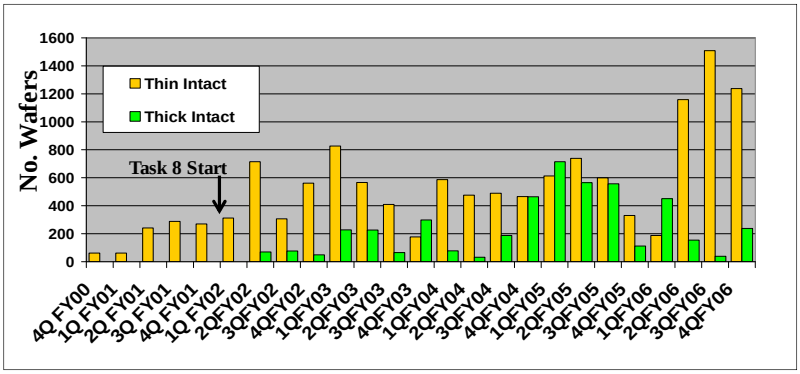

Figure 8-8. Numbers of wafers produced by membrane thickness during Task 8.

Leak rate yields were tracked for the thin-membrane wafers. Using the leak rate of a wafer measured with a standard test, the resulting oxygen purity from that wafer can be projected. Figure 8-9 shows the leak rate yield of thin-membrane wafers during Task 8. Yields were tracked

separately for wafers that meet specifications to produce 99.5% oxygen (so called "in-spec" wafers), and those that were projected to yield lower-purity oxygen. Improvement in processing steps could be monitored by assessing the relative levels of in-spec wafers to those producing 97% or greater oxygen purity and 90% or greater oxygen purity. The number of intact wafers indicates a population, by difference with the other leak rate grades, of highly leaky wafers.

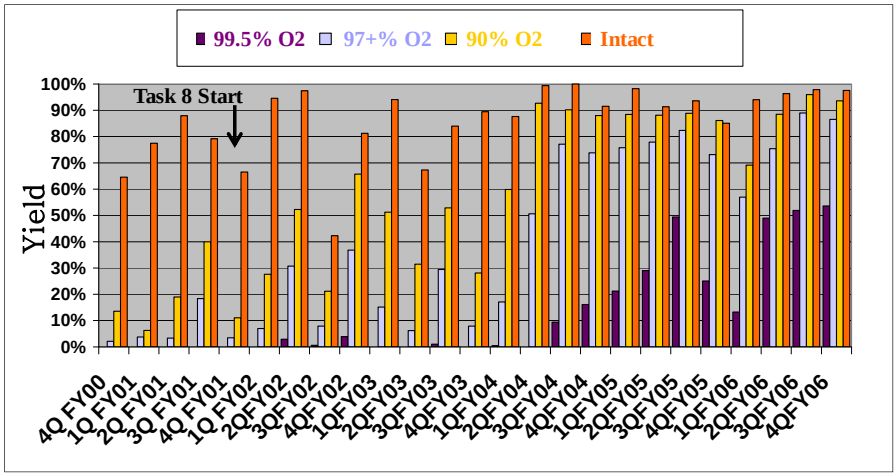

Figure 8-9. Yield by expected oxygen production purity based on leak rate for *thin*-membrane wafers produced during Task 8, by government fiscal year quarter.

As can be seen in Figure 8-9, by the end of the Task wafer yields of in-spec, thin-membrane wafers were steadily at 50%, while those producing 97+% oxygen or better were in the range of 80-90%. This improvement enabled Ceramatec to produce an inventory of wafers from which significant quantities of submodules and modules were built.

Thick-membrane wafer yields were also tracked. Figure 8-10 shows the trends with time during Task 8. In general, leak rate yields are higher for thicker membranes because the thicker membranes are stronger and resist stresses caused by defects. However, resulting purities from thick-membrane wafers are lower because the flux through a thick wafer membrane is lower. In general, yields from thick-membrane wafers were demonstrated consistently at 70+% during Task 8 for the lowest leak rate category, which is consistent with production of 99% pure oxygen.

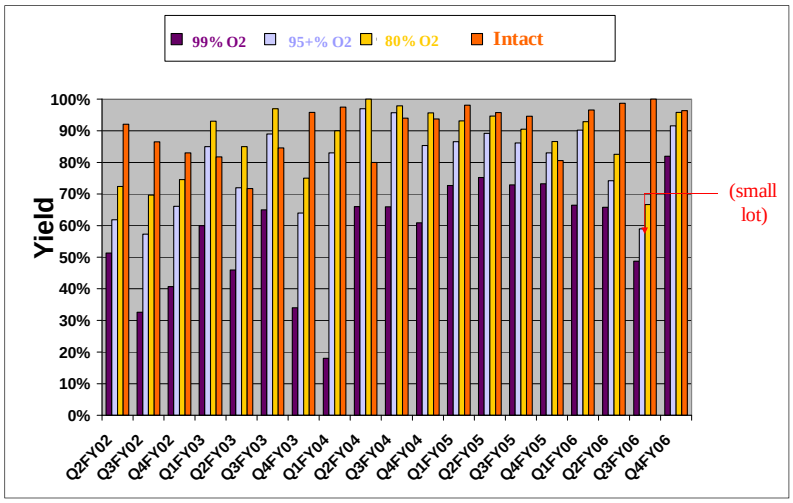

Figure 8-10. Yield by expected oxygen production purity based on leak rate for *thick*-membrane wafers produced during Task 8, by government fiscal year quarter

Ceramatec performed a study to assess the effect of membrane thickness on yield. Figure 8-11 shows the relationship between yield based on leak rate and membrane thickness. On a relative basis, the yield falls off at a membrane thickness of roughly half of the thick-membrane thickness. The steepness of the curve in the relative thickness range of 0.75-1.0 indicates that the yield is very sensitive to membrane thickness below a critical level.

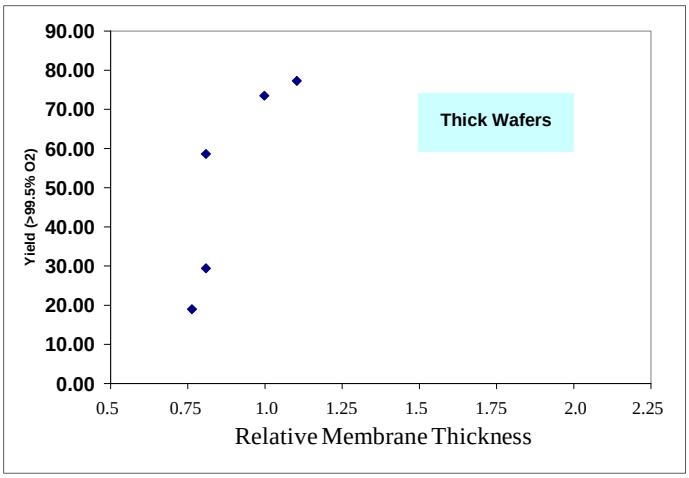

Figure 8-11. Yield of high-purity wafers based on leak rate as a function of membrane thickness. Thick wafers occupy the blue band. Data points represent small sample populations.

Ceramatec further explored this phenomenon by lowering its membrane thickness target in experimental lots over six months during 2006. Figure 8-12 shows the trend of yield and

membrane thickness as a function of time. For thicknesses <1.0 (relative scale), the yields fall substantially below the yield of 65+% established initially for a wafer with a membrane of 1.0 relative thickness. This figure indicates the critical nature of maintaining good thickness control on the membrane layer.

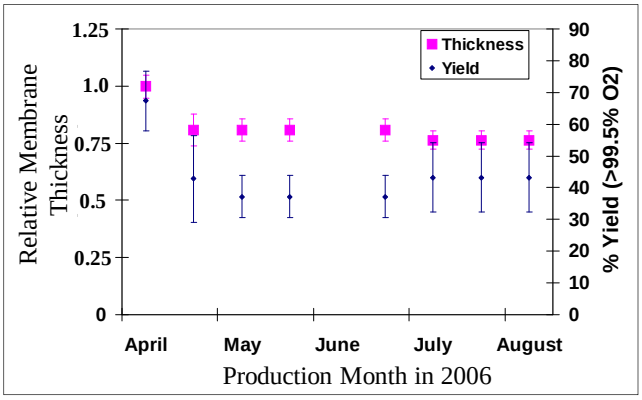

Figure 8-12. Yield and membrane thickness of high-purity wafers (in experimental lots) based on leak rate as a function of production month.

Ceramic Sealed Submodules

Ceramatec developed a manufacturing approach in which wafers were first joined to each other to form a submodule. Following submodule joining, leak rates of individual submodules were assessed and compared against leak rate threshold corresponding to the expected oxygen production purity. Submodules meeting the leak rate threshold were then joined to make modules. The two-step process was developed as a means to maximize leak yield from a full size module. Defects at the submodule scale could be isolated and excluded from the population of wafers that went into a full size module build. Figure 8-13 illustrates the process schematically.

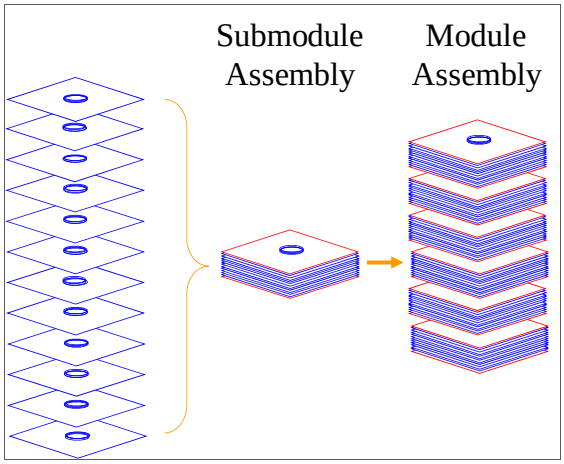

Figure 8-13. Schematic representation of module construction. Submodules are constructed from 12 single, sintered wafers with acceptable leak rates. Modules are constructed from multiple submodules with acceptable leak rates. The two-step process improves yield of modules relative to a single-step process.

Ceramatec's ceramic-to-ceramic seal work transitioned from test specimens to submodule assembly in the PDF as described below. The first trials combined the typical spacer-wafer-spacer test specimen and three-wafer submodules in parallel in the same run. The results (Table 8-1) were encouraging.

Table 8-1. Submodule leak rates.

Type	Lot	No.	Normalized Leak initial	Normalized Leak final	
Wafer-Spacer-Wafer	WLfs353	36	4.1677	3.1752	
Wafer-Spacer-Wafer	WLfs353	37	3.4344	3.3614	
Wafer-Spacer-Wafer	WLfs353	38	3.6584	2.9151	
Wafer-Spacer-Wafer	WLfs353	39	4.7985	7.1159	
Wafer-Spacer-Wafer	WLfs353	23	3.7081	2.3159	
Wafer-Spacer-Wafer	WLfs353	28	4.1400	3.1481	
Sub-module	WLfs353	30	3.8823		
	WLfs353	32	3.5189	6.5705	Measured Leak rate
	WLfs353	33	3.5160	10.9172	Expected Leak Rate
Sub-module	WLfs353	34	3.7426		
	WLfs353	35	3.1505	7.1135	Measured Leak rate
	WLfs353	15	4.8767	11.7698	Expected Leak Rate
Sub-module	WLfs353	16	3.6119		
	WLfs353	17	3.4062	6.3983	Measured Leak rate
	WLfs353	18	4.6664	11.6845	Expected Leak Rate

The next two tests were done in parallel in separate kilns including three 12-wafer submodules each. Different joining conditions were used. Five of the six submodules had significantly lower leak rates relative to the initial leak rates of the wafers. The one submodule that failed had a broken wafer.

Techniques were continually improved to positively affect yield. Primary efforts were focused on improving the ceramic-to-ceramic joint.

Significant breakthroughs were made during development trials which enabled Ceramatec to assemble 15 all-ceramic, 12-wafer submodules using an optimized tape. The results were very favorable. Six of the nine thick-wafer submodules were within specification. Only two of the 15 submodules exhibited defects. Table 8-2 documents the results.

Table 8-2. All-ceramic submodule leak rate performance.

Submodule ID	Normalized Wafer Leak Rate	Normalized Module Leak Rate	Membrane Layer
SMFS048-1	7.84	1.18	Thick
SMFS048-2	7.40	2.62	Thick
SMFS048-3	6.39	3.00	Thick
SMFS049-1	67.22	55.32	Standard
SMFS049-2	68.78	61.40	Standard
SMFS049-3	45.68	107.8	Standard
SMFS050-1	48.85	32.79	Standard
SMFS050-2	61.30	34.41	Standard
SMFS050-3	91.61	60.12	Standard
SMFS051-1	34.61	23.67	Thick
SMFS051-2	31.97	3.63	Thick
SMFS051-3	41.52	4.37	Thick
SMFS052-1	26.26	17.33	Thick
SMFS052-2	21.34	2.12	Thick
SMFS052-3	28.39	44.16	Thick

Based on this progress, Ceramatec moved production to the PDF, having established an OLP for all-ceramic submodules. Table 8-3 is a summary of the submodule production and yield in the PDF following the optimization of joining techniques described above. Table 8-3 includes a combination of thick- and thin-wafer submodules. The inventory of submodules was used to test methods for and ultimately produce full-size modules.

Table 8-3. Production and yield of 12-wafer submodules in the PDF during Task 8

Quarter	No. in spec.	Yield
Q2FY04	5	83%
Q3FY04	6	33%
Q4FY04	34	81%
Q1FY05	13	72%
Q2FY05	49	60%
Q3FY05	38	83%
Q4FY05	67	100%
Q1FY06	39	81%
Q2FY06	40	58%
Q3FY06	90	59%
Q4FY06	72	65%

Wafer Module

Ceramatec developed fixtures to join multiple submodules to form modules. Initial trials were conducted using a brazing technique. Once the fixtures were proven in trials with brazed submodules, Ceramatec attempted to produce modules with ceramic-to-ceramic joints. Each module consisted of multiple submodules, an end cap, and a base piece at the scale necessary to produce 0.5 TPD oxygen in the SEP.

Ceramatec was successful in producing a first-of-a-kind, all-ceramic module at the 0.5 TPD scale using high—leak-rate submodules. The attempt yielded an intact module (Figure 8-14).

Figure 8-14. Intact 0.5 TPD-scale, all-ceramic module produced from high-leak submodules.

Subsequently, Ceramatec began using submodules that had passed leak rate specifications in an OLP for module production. Module production was carried out at a rate of four modules per month when the SEP test schedule required module inventory. Table 8-4 summarizes the production activity with all-ceramic modules during Task 8. Testable yields reflect the yields of modules that produce 90+% oxygen.

Table 8-4. Production and yield of all-ceramic modules produced with the OLP during Task 8.

Quarter	# intact	Testable Yield
Q4FY04	**1**	**100%**
Q1FY05	**0**	**0%** (of 1)
Q2FY05	**4**	**100%**
Q3FY05	**na**	**na**
Q4FY05	**4**	**44%**
Q1FY06	**7**	**88%**
Q2FY06	**-**	**n/a**
Q3FY06	**-**	**n/a**
Q4FY06	**0**	**0%** (of 7 attempts)

Yield data were inconsistent and pointed to the need to do more module fabrication development work. Nonetheless, a number of modules were produced and delivery to the SEP commenced. Figure 8-15 is a photograph of four 0.5 TPD-scale modules produced under Task 8 and awaiting shipment to the SEP for testing. Each is fitted with a flat end cap and conical base piece.

Figure 8-15. 0.5 TPD-scale all-ceramic modules awaiting shipment for testing at the SEP.

Based on techniques developed for 0.5 TPD-scale modules, Ceramatec attempted to build the first 1 TPD-scale module and achieved an intact module on the first attempt. Figure 8-16 shows the first such module produced in the program upon removal from the joining kiln.

Figure 8-16. The first 1 TPD-scale ITM Oxygen module produced.

8.3 Optimization of the Ceramic Process Development Facility (PDF)

Kiln Uniformity

Ceramatec optimized the sintering kiln operation for temperature uniformity. The initial temperature difference between the top and center of the kiln was over 20°C versus the requirement of <5°C. Five thermocouples were added to the kiln to control individual zones. This reduced the sensitivity to changes in loading. All heat leak points were identified and closed. To aid the kiln in maintaining ramps, larger-wattage elements were added to the bottom of the kiln. A run of 120 wafers and 60 setters was conducted after the modification. All wafers were intact and the temperature spread in the kiln was ~8°C.

Web Coater

Ceramatec investigated a process in which a polymer layer is used to coat featured layers to minimize the residual ceramic fines left on the part. Three coating methods were tested: gravure roll coating, immersion coating, and Mayer rod coating. Roll coating was trialed at a vendor site.

The coater vendor ran sample strips of a wafer layer through a double-sided roll coater with good success. The coating thickness achieved was very uniform. Figure 8-17 displays photographs of the vendor coating as compared to the original coating method.

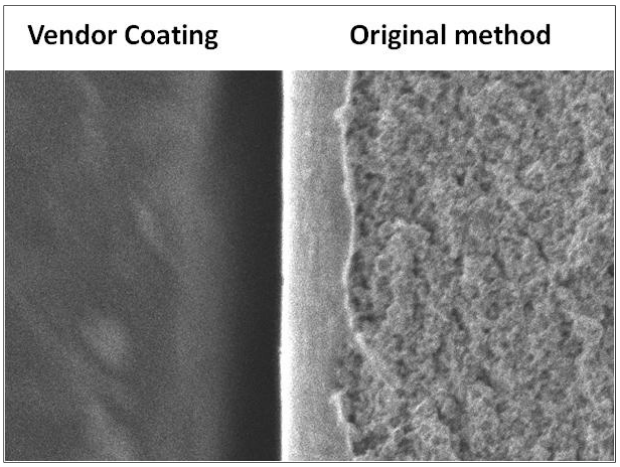

Figure 8-17. Coating comparison.

The drying time of the vendor's samples was much faster than the drying time for the original method. The coating was much easier to wash off because it was uniform across the entire surface. With the original method, the coating dried non-uniformly and left regions of thicker and thinner coating.

Lamination

Ceramatec investigated alternative pre-lamination methods. A test was conducted where a lot of cast tape was split by using the reel-to-reel slitting and punching machines on part of the tape and processing the rest via the on-line process. Based on trials in which lamination quality was assessed, the reel-to-reel process was adopted. This semi-automated process reduces the labor required to prepare layers for lamination.

Nitrogen Blanketing and Iso-compositional Cooling

Ceramatec investigated the use of iso-control in manufacturing wafers to decrease kiln/wafer cooling time. Initial testing used only a nitrogen blanket without feedback control.

Two trials were run. In one trial, 20 wafers were cooled under a nitrogen blanket from an intermediate temperature at a high cooling rate. Six of the wafers met leak rate specification. This yield was lower than the on-line process.

A second trial with 20 thick wafers were fired and then cooled under a nitrogen blanket from an intermediate temperature at a higher cooling rate. Only one of the wafers was in spec for leakage. These results can be compared to the other half of the same wafer lot, which were fired using the

online process and yielded 50% wafers in spec for leakage. This indicates that the straight nitrogen blanketing process was damaging the wafers. Two possible causes are that the kiln P_{O2} is not low enough, or the nitrogen blanket places too high of a chemical gradient in the part.

The kiln was modified to control the partial pressure of oxygen as a function of temperature. A paramagnetic oxygen analyzer was used to provide the concentration to the controller. The target concentration was input in a piecewise linear curve in 25° increments. Figure 8-18 shows the results compared to the target.

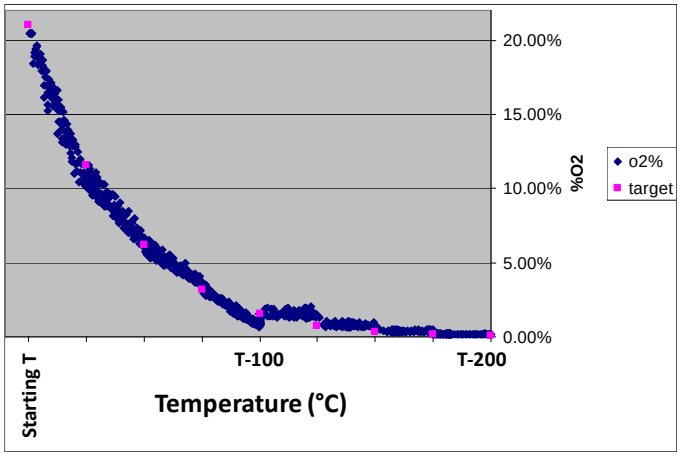

Figure 8-18. Iso-compositional cooling test.

Air Products and Ceramatec completed calculations indicating that trapped nitrogen gas in the insulation of the kiln may limit the ultimate nitrogen purity attainable over reasonable time scales within the kiln during iso-control. Accordingly, Air Products performed dilatometry experiments to compare the residual strain in AP2K parts caused by impure nitrogen employed during iso-cooling.

Ceramatec supplied AP2k bars cut from a rim of a full-size standard wafer. A bend bar prepared for mechanical testing with a microstructure similar to the internal porous layer was used as the reference bar.

A two-stage Linsies dilatometer was used to measure both bars simultaneously in the same atmosphere. The parts were initially heated in air to 900°C at 0.5°C/min, held at 900°C for 30 minutes, and isocompositionally cooled at 0.5°C/min to room temperature. The onset of

isocompositional cooling was 600°C, which means that the oxygen vacancy fraction was maintained at the value in equilibrium with 1 atm air at 600°C.

During subsequent runs, the parts were isocompositionally heated such that the atmosphere switched to 100% air at 600°C, heating continued to 900°C in air, the parts were held at 900°C for 30 minutes, and then the parts were isocompositionally cooled at 0.5°C/min to room temperature. Isocompositional cooling was performed in pure nitrogen and in a "ppm O_2"-in-N_2 blend. The measured outlet concentration of oxygen using pure nitrogen was 52 ppm, and the measured outlet concentration of oxygen using the O_2/N_2 blend was 212 ppm.

Some non-idealities in the experiments resulted in residual strain occurring for the pure nitrogen case. However, the results for the two types of gases can be compared as a relative assessment of the effects of impure gas on residual strain following iso-compositional cooling.

The result of this experiment is given in Table 8-5. The differences between the dense and porous bars for the two cases were 612 and 816 ppm, respectively, resulting in an additional 200 ppm of chemical contraction in the impure N_2 case as compared to the pure N_2 case. Figure 8-19 shows that this extra contraction of the porous bar occurred between 380°C and 300°C. Over this temperature range, the target P_{O2} for isocompositional cooling decreased well below the inert gas P_{O2}. Apparently, oxygen mobility in the porous bar is sufficiently high at these temperatures to allow the porous bar to take up oxygen.

Table 8-5. Measured contraction differences (cm/cm) at ambient temperature, after isocompositional cooling from 900°C between pure N_2 (52 ppm O_2) and 212 ppm O_2/bal N_2.

Porous Bar Difference, ppm	Dense Bar Difference, ppm	Differential in Dense-Porous Bar Difference (ppm)
236	32	204

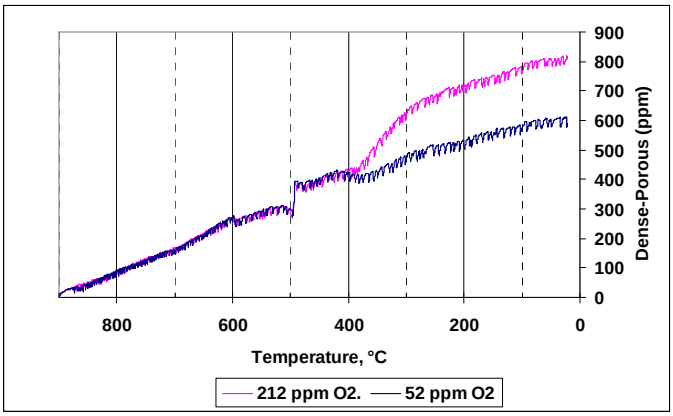

Figure 8-19. Comparison of the difference between the contraction of the dense and porous bars using either a 212 ppm O_2 inert gas or a 52 ppm O_2 inert gas. Above 380°C, there is no difference between the contractions produced from the two inert gas sources. However, between 380°C and 300°C, the porous bar contracts an additional 200 ppm in the 212 ppm O_2 gas compared to the 52 ppm O_2 gas.

Different approaches could potentially be used to address the residual strain caused by using impure "inert" gas. For example, the cooling schedule might use faster cooling rates above 300°C to allow less time for oxygen uptake by the shorter-length scale parts when the P_{O2} is above the isocompositional target. Alternatively, a lower onset temperature for iso-cooling could be used such that the actual P_{O2} levels do not exceed the target P_{O2} levels until the temperatures is <300°C. This would require using a longer, slower temperature ramp in air to a lower temperature (such as 450°C or 500°C) before beginning iso-cooling.

TASK 9.0 MODULE PERFORMANCE TESTING

9.0 Scope

*Air Products conducts module testing and demonstrations to (i) evaluate lifetime performance against target values, and (ii) obtain membrane module performance data to validate and support the development of engineering models used to predict the performance of membrane modules. The Recipient tests modules of full-size wafers and full-size ceramic-to-metal seals at full operating pressures and temperatures to establish flux and lifetime performance data. Air Products designs and builds getter systems to mitigate system contaminants in small, pilot-scale units. Air Products extends long-term oxygen flux tests, and builds the Flu**x** **V**erification **U**nits (XVUs) equipped with vacuum permeate systems and non-vitiated air feed flowing at commercially relevant velocity. Performance tests of candidate ceramic-to-metal seal configurations are conducted in the Short Loop Test Rigs (SLTRs) to support the selection of the ceramic-to-metal module seal for SEP and the subsequent ISTU testing.*

9.0 MODULE PERFORMANCE TESTING

Background

Work under Task 9 expanded upon the success achieved under Tasks 1 and 4 in which target oxygen fluxes and purities were first achieved. Air Products carried out tests designed to maximize the flux from a wafer in the VP-SLTRs, then set about establishing a database of flux and lifetime performance by putting into service the XVUs and testing multiple submodules in the TDU. Contaminant testing, as described under Tasks 1 and 6, paralleled these activities and provided supporting means for the creation of contaminant mitigation devices that were introduced to the performance testing apparatus.

Ceramatec-to-metal seals were also improved upon. Limitations of the seals developed under Task 1 and 4 were exposed during this Task, and alternatives were developed which reflected a shift in philosophy to a lower-temperature seal. These notions led to a successful redesign of the seal. The data from the work with submodules, getter technology and seals was directly applicable to the ultimate design and operation of the SEP under Task 10.

Flux and Lifetime Testing

1. Flux maximization in the VP-SLTR

Test of Module P87

SLTR No. 6 was loaded with sub-scale Module P87, and the system was brought to operating conditions. The module operated for over 1000 hours, with a full set of process conditions successfully tested at in the range 800-900° C. A record normalized flux of 1.6 was measured. Figure 9-1 shows the process variables during the run and the resulting flux behavior of the module.

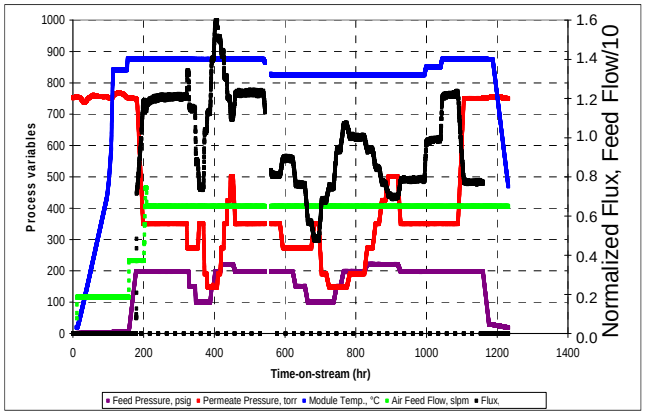

Figure 9-1. Process variables and flux during VP-SLTR test of Module P87.

Measured oxygen purities ran in the 97-98% (vol.) range early in the run. The leak rate began to increase starting at 725 hours onstream and became larger with time, resulting in purities dropping below 90% at 1075 hours. The run was shutdown as purity continued to decline. Figure 9-2 shows the purity performance and leak rate during the experiment.

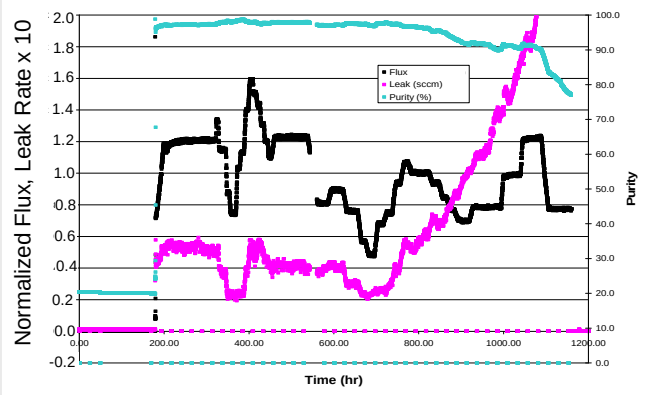

Figure 9-2. Flux, purity and leak for Module P87.

Post-test analysis of Module P87 by SEM/EDS showed a relatively high level of chromium on the wafer surface. The chromium collects as an impurity compound predominantly located at the grain boundaries of the AP2K, as shown in Figure 9-3. The source of chromium in the VP-SLTR during this experiment was unidentified. Nonetheless, flux performance appeared unaffected despite its presence.

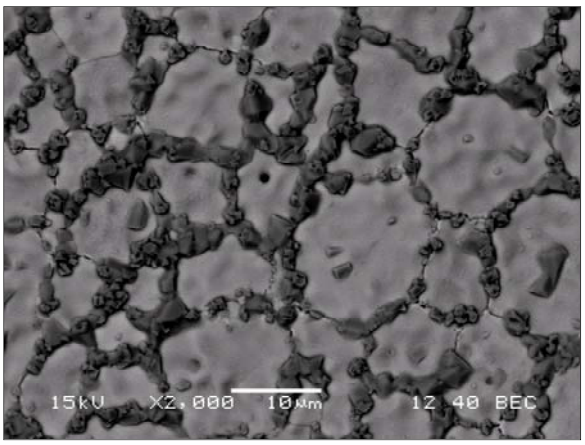

Figure 9-3. SEM image of top surface of wafer P87.

A sample of the fluxing area of the wafer was ground and analyzed using X-ray fluorescence spectroscopy. The results of this bulk analysis (as opposed to the surface analysis noted above) are compared with AP2K powder and an unexposed wafer from the same batch in Table 9-1. The table compares ratios of cations in the sample. Cation "B" represents the transition metals in the AP2K material. Cation "C" represents a typical impurity cation present during ceramic processing.

Table 9-1. Cation ratios in AP2K samples

Sample number	1055-59	P78	P87
Sample type	AP2K powder	unexposed	SLTR run
Analysis method	XRF	ICP	XRF
C/B	0.00707	0.003092	0.01384
Cr/C	0.202373	0.240552	0.156626
Cr/B	0.00143	0.000744	0.002167

Elevated levels of chromium relative to Cation B are noted in the flux test sample. These results do not appear to agree with a hypothesis that the source of the chromium contamination is the manufacturing process.

Test of Modules P73 and P76

In light of the results of the Module P87flux test, Air Products studied the effects of Cr deposition on flux in the VP-SLTR. Two modules were intentionally contaminated with Cr in the VP-SLTR by first saturating the feed air stream with Cr by passing it over a bed of alloy turnings held at operating temperature, then passing the air across the module. The modules fluxed oxygen normally at target rates. Both such modules, P73 and P76, were analyzed by SEM/EDS. The micrographs and EDS spectra were very similar to each other, indicating that two additional phases are present: a Cr-rich phase and another rich in an AP2K constituent compound. Total coverage of non-AP2k phases by image analysis was 32% (top) and 19% (bottom) for the P76 wafer. These results confirm that this module was successfully contaminated with Cr as intended. It is not clear why this level of contamination did not affect the measured flux in the VP-SLTR experiment.

2. Flux Performance with Full-Size Wafers

2.1 Construction of the fluX Verification Units (XVUs)

The ITM Oxygen fluX Verification Units (XVUs) were designed to verify the oxygen flux capability of a module consisting of a single, full-size wafer. The units operate at target conditions of up to 900°C, 250 psig feed pressure, and down to 0.2 atm absolute permeate pressure. Air Products executed the design, procurement and construction of three XVUs during Task 9. The conceptual design was created under Task 4. After XVU1 was built and tested, XVU2 and XVU3 were built according to an identical design. All three units take compressed air from a common source. Each unit comprises:

- a hot wall pressure vessel that houses the ITM sample,
- a feed air preheater,
- a vacuum permeate system in which the oxygen product from each vessel is throttled, compressed to atmospheric pressure, metered and analyzed;
- a non-permeate heat exchanger and vent system.

The XVU vessel is “T” shaped and is constructed of high-nickel alloy. The coded vessel is dually rated at 250 psig/1650°F, 450 psig/1525°F. The feed air preheater is constructed of alloy tubing wrapped around the horizontal section of the vessel in the heated zone, and welded to the inlet nozzle of the vessel. Figure 9-4 shows a picture of the vessel inside a clamshell-style electric furnace.

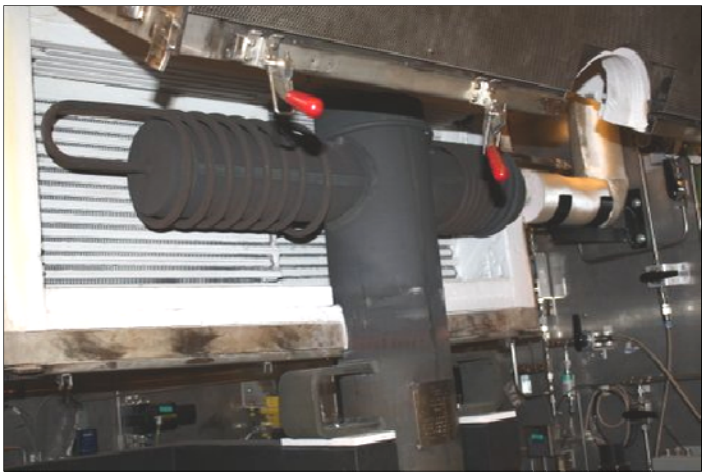

Figure 9-4. FluX Verification Unit (XVU) Vessel. Feed air enters the vessel from the left in the photo.

A flange attached to the bottom of the vertical section of the vessel allows for installation and removal of membrane modules. The flange is fitted with three TC ports and a tube for oxygen permeate removal. The entire vessel and the preheater are enclosed in the 35kW electric resistance heater.

Compressed air is delivered to the system from a remotely located compressor at 500 psig. The air is passed through a bypass valve for venting, then through several check valves and finally a pressure control valve before being distributed to each unit. At the unit level, the compressed air passes through a flow control valve and into the preheater coil.

In the preheater coil, the air is heated to the required process temperature before entering the horizontal inlet section of the pressure vessel which houses the ITM module. After passing through the inlet section, the high-pressure air passes through to a channel which directs the air into the central vertical section of the vessel that houses the ITM wafer (Figure 9-5).

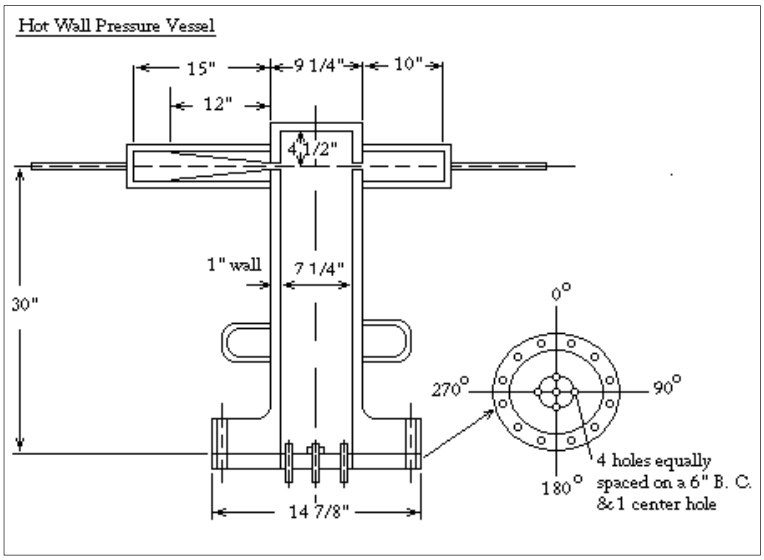

Figure 9-5. Schematic of the XVU vessel. Air enters the horizontal inlet arm on the left, passes through the central portion of the vessel over the wafer (not shown), and exits through the horizontal outlet arm on the right.

The ITM module is positioned in an alumina housing such that the wafer is located in line with the air flow coming from the channel, and the air passes through a narrow passageway above and below each wafer. The housing serves to channel the flow to create appropriate air velocities over the wafer surface. Each wafer is supported on a metal pipe assembly that houses a ceramic-to-metal seal at the base of each module. The pipe carries the oxygen down to the flange below and out of the vertical section of the vessel through the flange. Figure 9-6 shows photographs of the wafer mounted on the permeate pipe, as well as the wafer entirely enclosed in the alumina housing,

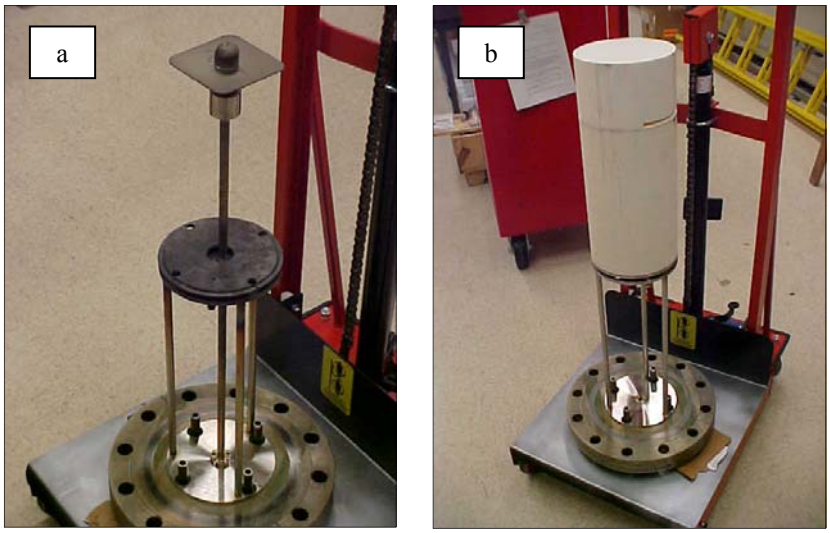

Figure 9-6. a) Single-wafer module mounted on a permeate tube attached to the XVU vessel flange; b) Single-wafer modules housed in the alumina housing prior to installation in the XVU. The narrow through-channel visible on the right side of the housing allows flow over the wafer.

The oxygen-depleted (non-permeate) air then flows out of the vessel through an identical channel 180º opposite the first. The non-permeate flows through the horizontal outlet section of the vessel and exits through tubing that carries it to a jacketed heat exchanger. The heat exchanger is a tube-in-a-tube design: cooled glycol solution is carried in the outer annulus of the exchanger and cools the non-permeate below 50ºC. A portion of the non-permeate is passed to an analyzer for purity measurement; the remaining gas is then exhausted to vent.

High-nickel alloy tubing carries the oxygen permeate at high temperature and sub-atmospheric pressure to a section of exposed tubing located outside the vessel and of sufficient length so the stream is cooled to <50º C. The oxygen then flows to a vacuum pump where it is compressed to slightly more than 1 atm. The stream then passes into an oxygen analyzer and is exhausted to vent.

The system is PLC-controlled. All field devices are wired to a remote I/O unit. The I/O is connected to a process control module, which is linked to PC for control. The system is UPS powered and backed up by emergency power.

Figure 9-7 is a photo of the three XVUs, completed and ready for operation.

Figure 9-7. Three complete XVUs.

2.2 XVU Testing of Single-Wafer, Full-Size Modules

Test of FSM 037-01

FSM 037-01, a fully ceramic module with a single standard wafer, was tested in XVU1 for 118 hours prior to a compressor-related shutdown. The normalized flux at leading-edge conditions was stable, but low, at 0.46. The recovered module was cracked into several pieces because of the rapid drop in pressure and temperature, but the orientation of the pieces was identified with respect to the flow path.

The used wafer was examined by SEM/EDS for Cr content and also to investigate whether there is a Cr concentration gradient across the wafer in the direction of the flow path. As expected, the wafer surface had extensive Cr contamination, as indicated by the presence of a second phase by the SEM images. The second phase was concentrated at the AP2k grain boundaries but also decorated the interior of the grains. Moreover, contamination was observed on all wafer surface regions examined (leading edge, middle, and trailing edge on both top and bottom). Image analysis software was employed to quantify the coverage of the second phase. Table 9-2 shows the SEM image analysis results for the various locations on the wafer. The average surface coverage was 18.1% and coverage was comparable on the top and bottom of the wafer. Also, there does not appear to be a significant Cr gradient across the wafer in the direction of flow.

Table 9-2. Image analysis results: % coverage by chromium-rich phase.

	Position w.r.t flow direction		
	Leading	**Middle**	**Trailing**
Top surface	18.1%	12.2%	18.8%
Bottom surface	20.0%	23.3%	16.2%

Test of FSM055-1 with Iso-Gradient Heating and Cooling

Single-wafer module FSM055-1 was loaded into XVU3 using a variant of the composite ceramic-to-metal seal in conjunction with a U-ring seal as described in the seal development section below. The module was started successfully; initial normalized flux at full operating conditions was 0.66, decreased slightly, and leveled out to 0.64 after about two weeks at steady conditions. Purity was stable at ~97%. Before commencing iso-controlled heating and cooling trials, limited studies of driving force were done in an attempt to shed some light on the reason(s) for the low flux observed for full-size modules in the XVU relative to the flux observed of samples tested in the VP-SLTRs.

After the driving force studies, the module was cooled and then heated back up. Flow and composition were controlled by an iso-control gas feed control unit designed according to the theories discussed in Tasks 6 and 7 for managing stresses in materials with high chemical expansion. The unit regulates the O_2 concentration of the air and permeate sides of the module in the XVU by blending air and N_2 using electronic flow controllers, which get their set points from a control computer. The target O_2 concentration for each side is determined by the module temperature in a feedback mode. The composition control algorithm works to regulate the O_2 concentration to maintain a constant oxygen vacancy concentration on each side of the module. Thus, the control used here is actually iso-gradient, i.e., a constant gradient of vacancy concentration is maintained during heating and cooling. This differs from iso-strain operation, which would control composition on each side to maintain a constant strain gradient by using a material expansion model that accounts for the effect of thermal expansion as well as the effect of temperature on chemical expansion. Also, note that the introduction of gas on the permeate side is done via a tube that extends into the interior of the module, terminating just below the wafer. The gas introduced at this point may not have a large effect on the composition inside the wafer because of the effectively narrow and long diffusion path length. Thus, the gas introduced on the permeate side likely maintains the vacancy concentration only in the cylindrical tube. For simplicity, and also due to the limited pressure of the house N_2 supply, the cooling/heating cycle was done at an air-side pressure of 50 psig.

One cycle of cooling and heating was successfully achieved. The module was cooled from operating temperature to 80°C in 40 hr, held at 80°C for 20 hr, and then heated back up over

~40 hr. After heatup, operating conditions were re-established and flux and purity measured. Table 9-3 shows the flux and purity before and after the iso-gradient cooling/heating cycle.

Table 9-3. Effect of iso-gradient cycle on flux and purity

	O_2 Flux Normalized	**O_2 Purity (%)**
Before cooling/heating cycle	0.63	96.7
After cooling/heating cycle	0.52	93.3

The modest purity change after the cycle indicates that, at worst, the module survived largely intact (the ceramic-to-metal seal may also contribute to the leakage change). The reason for the decrease in flux is unclear; the flux was quite stable during the initial two weeks after operating conditions were first established.

A second cycle of iso-gradient cooling/heating was attempted, but upon cooling to 80°C the leak rate to the permeate side became so excessive that it exceeded the capacity of the vacuum control system, thereby forcing that system to shut down. Upon removing the sample for inspection, the wafer was found to be intact with no visible cracks; however, the tube was cracked at the U-ring level.

XVU#1 Modification: Addition of Guard Bed for Cr

Following experimentation with the XVUs, the TDU (described below), and VP-SLTRs in which chromium was observed on wafers examined following flux testing and/or expected fluxes were not achieved, Air Products modified XVU1 to fit it with a guard bed for chromium. The XVU1 pressure vessel was modified so that the horizontal feed section was extended outside the furnace and fitted with a terminal flange. The feed air entered the horizontal feed section through a tee located within the heated zone. The flange allows access to the horizontal feed section for the installation of getter materials downstream of the tee. Figure 9-8 shows a view of the flange opened during inspection of a porous getter material, and closed prior to operation.

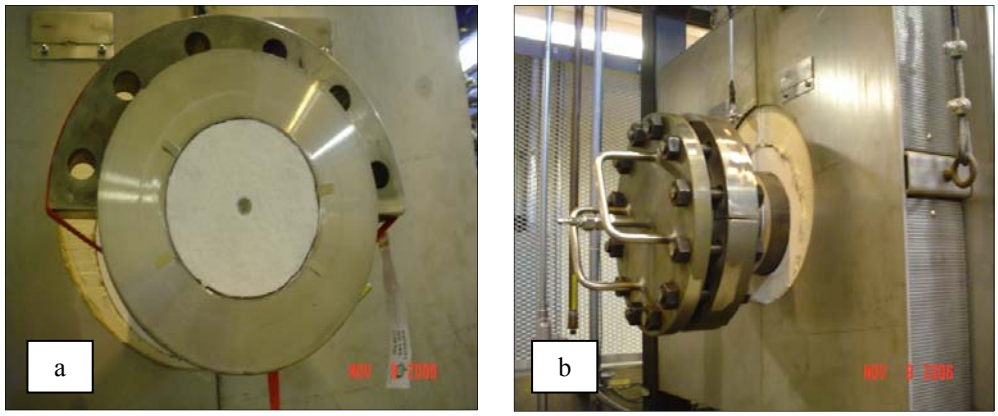

Figure 9-8. a) View of modified XVU1 feed section, showing inspection of getter material; and b) modified XVU1 feed section, showing closed access flange.

Air Products constructed a pressure drop test unit to evaluate the pressure drop of candidate getter systems. The unit was designed to measure pressure drop across 1" diameter samples of up to 6" in length and at air feed flow rates of 1500 scfh at atmospheric pressure. A ceramic foam sample with 30 pores per inch (ppi) was investigated. Bed lengths of 2", 4", and 6" were used at flows between 100 and 700 scfh. Initial tests were inconsistent, but improvements were made to eliminate flow bypass at the wall resulted in reproducible results. The pressure drop data for all three bed lengths was fit to the Forchheimer equation for compressible fluids:

$$\frac{P_i^2 - P_o^2}{2P_oL} = \frac{\mu}{k_1 g_c} v_s + \frac{\rho}{k_2 g_c} v_s^2$$

in which P_i and P_o are the inlet and outlet pressure, L is the bed length, v_s is the superficial velocity, μ is viscosity, ρ is density, and k_1 and k_2 are the Darcyan and non-Darcyan permeabilities. The parameters v_s, μ, and ρ were evaluated at the outlet conditions. The range of v_s tested was 5-36 ft/sec. The values of the permeabilities that gave the best fit to the experimental data are:

$$k_1 = 1.3746 \times 10^{-7}\ ft^2, \quad k_2 = 1.8537 \times 10^{-3}\ ft.$$

Test of FSM061-2 with Cr Guard Bed in XVU#1

Air Products tested full-size, all-ceramic, single-wafer Module FSM061-2 (with a low-pressure-drop wafer design and a thin membrane layer) in XVU1 following installation of a Cr getter in the modified feed section. The start-up of FSM061-2 was successful, thus marking the first successful startup in this vessel since the modification to incorporate the guard bed. The module reached full

flow at operating conditions; normalized flux was 0.78 at an oxygen purity of 99.6%. The flux was the highest ever recorded at these conditions in XVU#1. Normalized flux declined slightly to 0.76 during the two-week period, but purity stayed high (Figure 9-9). The gaps in data in the figure were when the module was operated at different driving forces. The module was run for only two weeks, after which a scheduled facility power outage required the module to be depressurized and cooled.

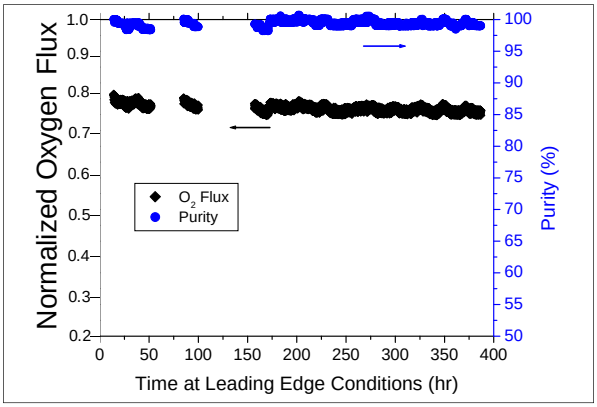

Figure 9-9. Flux and purity vs time for Module FSM061-2

A limited number of driving-force conditions and flow rates were run on FSM061-2 during the short time on stream. The results were compared to model predictions. Figure 9-10 compares measured and predicted flux for FSM061-2 as well as for Module FSM037-1, which was run in XVU1 before installation of the guard bed (see above). For FSM061-2, the measured flux falls short of predicted flux by a significant gap. However, the measured values are much closer to prediction than those for FSM037-1, thereby indicating that the installation and use of the guard bed had a significant positive effect.

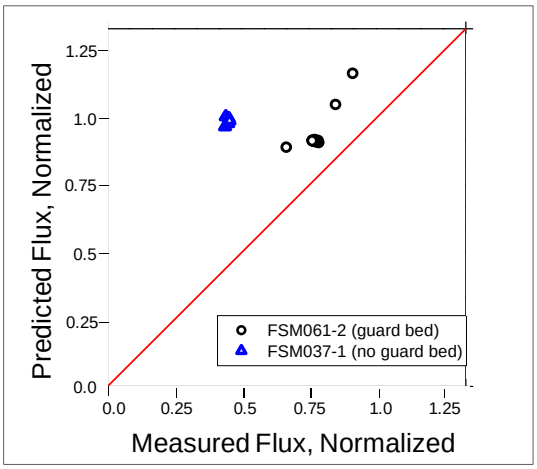

Figure 9-10. Comparison of measured and predicted flux.

SEM analysis of the FSM061-2 wafer surface shows that Cr contamination occurred. In fact, comparison of the surfaces of FSM061-2 (tested with guard bed) and FSM037-1 (tested without guard bed) indicates that FSM061-2 has only slightly less prevalence of a Cr-containing second phase. However, it should be noted that FSM061-2 was on-stream 3X longer than FSM037-1.

XVU Flux Test Summary

Air Products completed a number of flux tests with the XVUs under Task 9 as summarized in Table 9-4. Many of these runs included process variable scans that helped build a database of flux as a function of conditions. All tests likely had some level of chromium contamination.

Table 9-4. Summary of flux tests completed with the XVUs during Task 9.

Test	Module	Wafer Type	XVU #	Norm. Flux	Purity %	Comments
1	FSM 012-01	Ph I, Standard	1	0.65	98.6	process variable scans done (31 conditions), feed flow rate varied, declined to 0.67 (97% purity) after 1 month
2	FSM 015-02	Ph I, Standard	1	0.58	99.6	flux decreased to 0.52 (99.3% purity) after 170 hr
3	FSM 023-01	Low dP Type 1	1	0.53	97.4	Analyzed by SEM/EDS and found to be contaminated with Cr.
4	FSM 023-03	Low dP Type 1	1	0.47	91.7	
5	FSM 029-01	Ph. II, Standard	2	0.44	92.1	Flux decreased slowly with time
6	P54	sub-scale module	1	0.78	98	V. high driving force, wafer found to be contaminated with Cr
7	FSM 030-02	Low dP Type 2	2	0.61	92	Rapidly lost purity
8	FSM 032-02	Ph. II, Standard	1	0.52	97	Gradually lost purity, <90% at ~300 hr
9	FSM 037-01	Ph. II, Standard all-ceramic	1	0.46	99.9	System trip shortened run.
10	FSM037-3	Ph. II, Standard all-ceramic	3	0.78	90	Flux decreased to 0.75 over the first approx. 250 hr; used for iso-strain heating/cooling shakedown run.
11	FSM055-1	Low dP Type 2 all-ceramic	3	0.64	97	Gasket type ceramic-metal seal
12	FSM055-2	Low dP Type 2 all-ceramic	3	0.60	98.3	Heater trip after 40 hr shortened run.
13	FSM060-1	Low dP Type 2 all-ceramic thick membrane	3	0.54	98.5	Gasket type ceramic-metal seal
14	FSM061-2	Low dP Type 2 all-ceramic	1	0.78	99.6	First MgO guard bed installed.
15	FSM061-3	Low dP Type 2 all-ceramic	1	0.78	99.9	MgO guard bed installed.

2.3 Flux tests with the TDU

The TDU was constructed under Task 4. The TDU can accommodate full-size membrane modules composed of one to 12 wafers.

Test of FSM017-01

Twelve-wafer Module FSM017-01 was loaded into the TDU and brought to operating conditions. Figure 9-11 shows the process variable changes and resulting flux performance. Figure 9-12 shows the purity and leak trends.

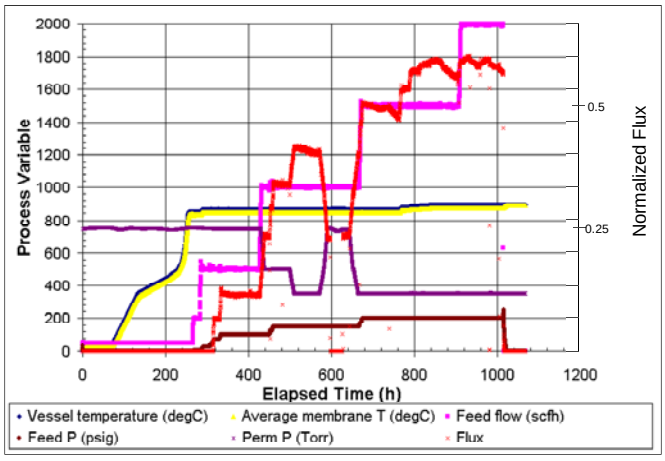

Figure 9-11. Flux results and operating conditions for FSM017-01.

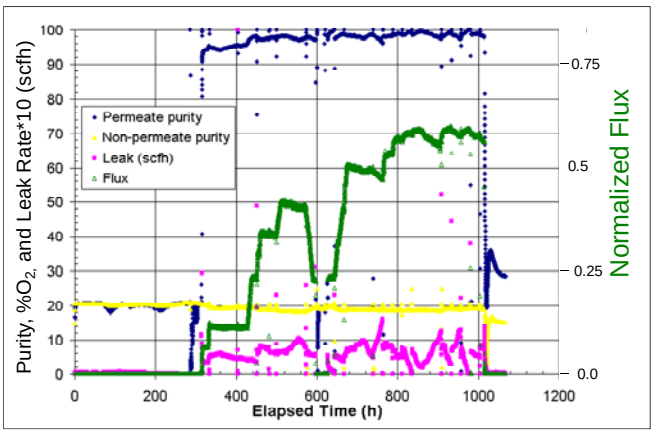

Figure 9-12. Purity and leak results for FSM017-01.

A steady operating condition was maintained for 100 h, over which time the flux appeared to be declining slightly. However, it is not clear if this was related to the increased level of O_2 analyzer drift or not.

The run was ended when the house air failed, leading to a sudden stoppage of feed flow. The furnaces in the preheater section of the unit tripped due to overtemperature alarms. The vessel slowly depressurized over a 10-hour period, during which time feed air drained through the non-permeate O_2 analyzer. The module failed during this process upset.

The maximum flux achieved was 0.58 on a normalized basis at 98.6% purity. The flux appeared to be degrading toward the end of the run, Under the same conditions described above, the flux had decreased to 0.57 over a 24-hour period. The reason for this is unclear. Module FSM017-01 was fluxing for just under 700 hours.

Test of FSM021-01

Two-wafer module FSM021-01 was brought to full pressure conditions at an operating temperature ~14°C below target. Under these conditions, the module achieved a maximum flux of 0.62 on a normalized basis at 97.4% purity. The maximum purity achieved in this run was 98.5% under the same conditions. Module FSM021-01 was fluxing for more than 850 hours, but flux degradation was significant in this run (60% decline in 450 hrs).

The data were regressed against two different feed-side gas-phase mass transfer resistance models. However, due to the overwhelming dominance of the time-dependent degradation, it was not possible to evaluate a feed-side gas-phase mass transfer model with this data set. Chromium contamination of the membranes was the primary suspect for the flux degradation.

Figure 9-13 documents conditions and flux during the run. Figure 9-14 documents leakage.

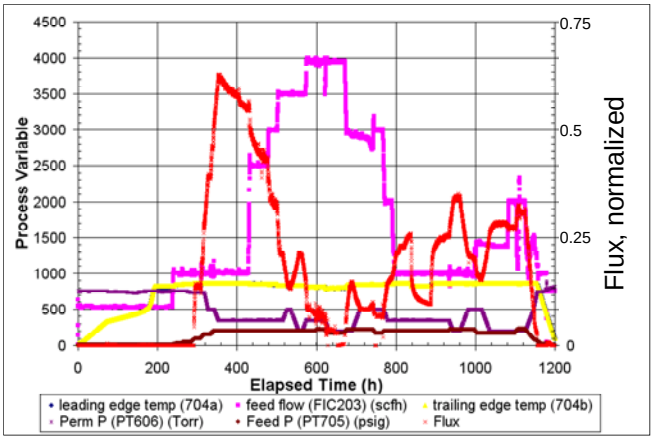

Figure 9-13. Flux results and operating conditions for FSM021-01.

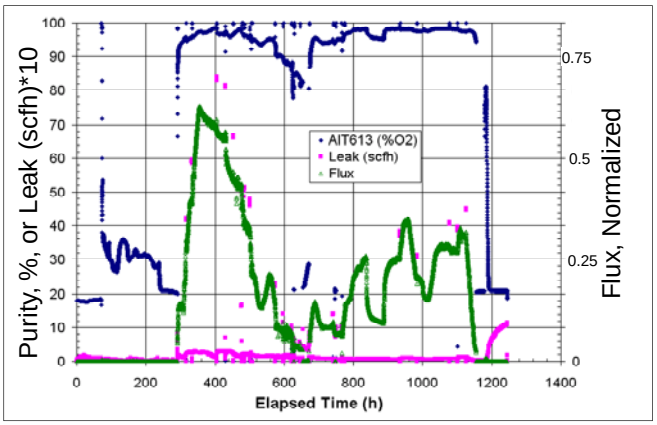

Figure 9-14. Purity and leak results for FSM021-01.

Test of FSM024-02 with Foam Getter

A ceramic foam getter section was added to the inlet section of the TDU to remove chromium, similar to the material used in the XVU1 inlet section as described above. FSM024-02, a 12-wafer module, was loaded and brought to full operating pressure at a temperature 17°C below the operating target. Flux data are presented in Figure 9-15. The maximum normalized flux of 0.69 was achieved at 98% purity. The module fluxed for 600 hours and then was shut down in anticipation of a facility power outage. Flux degradation was significant in this run, as observed through the fluxes recorded during periodic returns to the starting conditions. For example, at full operating conditions (-17°C relative to target) the normalized flux decreased from 0.68 at 370 hrs to 0.59 at 620 hrs. It is noteworthy that the flux was the same at 780 hrs. The decline was not as significant as the previous run (with FSM021-01), which suggests that the foam getter helped mitigate some of the Cr contamination.

As shown in Figure 9-16, the leak from the module remained remarkably constant throughout this run.

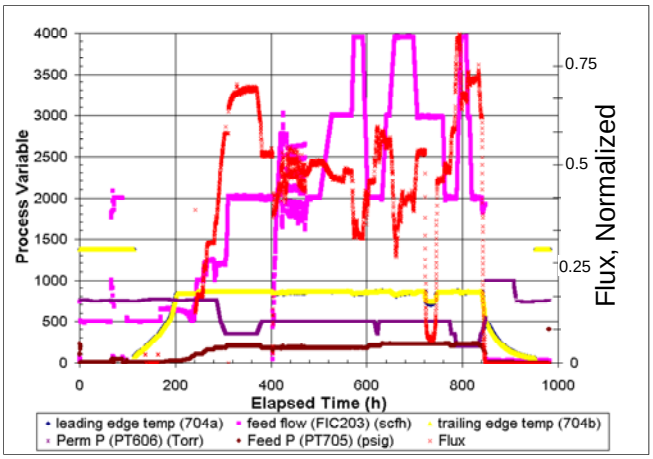

Figure 9-15. Flux results and operating conditions for FSM024-02.

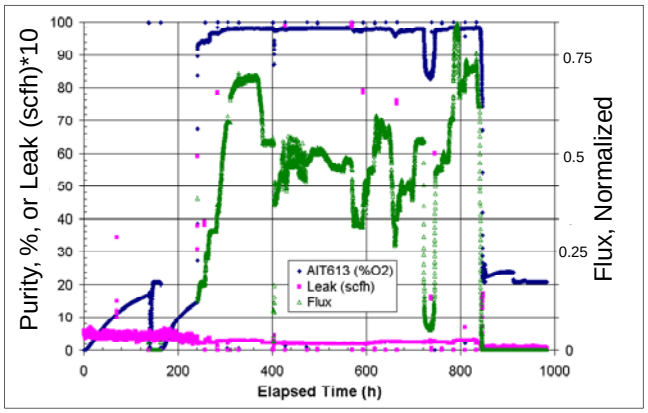

Figure 9-16. Leak and purity results for FSM024-02.

Test of FSM043-2 with a Tube Bundle Getter

The foam getter was replaced with a getter comprising a bundle of MgO tubes located upstream of the module position in the TDU vessel and oriented parallel to the feed flow. A brief run had shown this to be a more effective getter than the foam getter attempted previously.

FSM043-2, a two-wafer module, was loaded into the TDU immediately downstream of the MgO tube bundle getter. The getter consisted of two bundles of ¼’ OD, low-density MgO tubes in series with respect to the flow direction. The first and second bundles were 3” and 6” long respectively. The 3” tubes were new, while the 6” tubes had been used in a prior TDU run. The module was brought up to temperature and pressure and accumulated a total of 730 hr of total run

time at various conditions. The run ended when a preheater shut down because of a blown fuse, causing a rapid temperature transient that fractured the module.

The module was operated at ~4°C below target, but at full operating pressure. The measured flux under these conditions was 0.9 on a normalized basis, the highest measured to date. Over 500 hr of operation, the flux degradation rate was only 2%.

The team assessed air-side mass transfer influence by varying the flow rate at maximum driving force. Figure 9-17 shows the effect of flow rate at fixed conditions over the range of 1000 to 2000 scfh (500 to 1000 scfh per wafer). Based on this limited data, it appears that the effect of increasing flow rate levels off at a~1000 scfh per wafer.

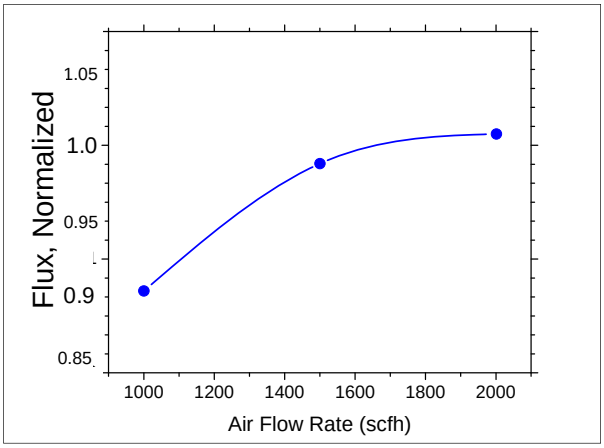

Figure 9-17. Effect of air flow rate on flux for TDU run with FSM043-2.

Following the run, wafers from FSM043-2 were analyzed by SEM/EDS. The analysis indicated that this module was, in fact, contaminated with Cr, although the extent of the contamination was less than that typically observed for modules tested in the XVUs or in the TDU without the guard bed. A second Cr-rich phase was observed.

Table 9-5 summarizes the results of the SEM image analysis for the Cr-rich phase coverage, along with the measured membrane thickness, for each of the four membranes in the two-wafer module. The significant Cr-rich phase coverage observed indicates that gas-phase Cr may have broken through the guard bed. Also consistent with the observed Cr contamination is the fact that there was evidence of flux decay during the course of the TDU testing, although the rate of decay was much less than previously experienced.

Table 9-5. SEM/EDS analysis of FSM043-2.

Wafer	Surface	% Coverage by Cr-Rich Phase	Mean Membrane Layer Thickness, Normalized
Top	Top	14.9	0.86
Top	Bottom	6.4	0.94
Bottom	Top	9.8	0.96
Bottom	Bottom	3.6	0.85

Air Products investigated the Cr profile in the tube bundle getter. The results obtained for analysis of individual MgO tubes in the guard bed indicate that that Cr breakthrough is a possibility.

The guard bed used during the test of FSM043-2 in the TDU consisted of two bundles of ~800 tubes each, a 3" long section followed by 6" long section of tubes in series parallel to the flow. After the test, which lasted 915 total hours, 3" tubes were removed at selected radial positions in the bed and cut up into 1" pieces, recording the orientation with respect to the flow path. Each 1" piece was analyzed (after digestion) by ICP/AES for Cr content. In addition, fresh tubes were analyzed to provide the background Cr level in the MgO tubes as-received. Nine 1" sections of fresh tubes were analyzed and showed a overall mean Cr content of 23.0 ppm with a standard deviation of 1.9 ppm.

Table 9-6 summarizes the results for the MgO tube analyses. Based on the observed radial distribution of Cr, flow was unevenly distributed and focused toward the center. This is not at all surprising since flow entered the bed through a feed pipe located at the center. The analytical evidence indicated that Cr likely broke through the 3" bundle of tubes. However, based on the steep gradient measured through the three sections, it appears that the MgO tubes are a very efficient getter. Tubes from the 6" bundle were not analyzed because the results would be ambiguous since they had been used in previous runs. The use some type of a flow distributor on the feed end would improve the effectiveness of the bed.

Table 9-6. ICP/AES analyses of used MgO guard tubes in the 3" bed. Background Cr level is 23.0 ppmw +/- 1.9 ppmw.

		1" section		
Radial Position	**Tube 19945-73-#**	**Leading (ppmw Cr)**	**Middle (ppmw Cr)**	**Trailing (ppmw Cr)**
Center	003	238	80	55
	006	310	106	65
	009	207	45	41
1.25" from the center	3/0	100	26	31
	3/3	97	29	26
	3/6	139	53	45
	3/9	48	26	26
One tube diameter from wall	0	23	23	25
	3	26	23	23
	6	26	23	23
	9	25	22	22

Test of FSM056-2 with a Tube Bundle Getter

Prior to this run, Air Products built and installed a new MgO guard bed in the TDU vessel consisting of two bundles of tubes 0.25" in diameter. Tube length was 6" in the first bundle and 3" in the second. In addition, the team installed an alloy perforated plate distributor and an alumina funnel-shaped piece downstream of the guard bed for flow direction to the module. Two-wafer module FSM056-2 was then installed. The module reached full operating conditions with a product purity of 99.6% oxygen.

Flux for this module reached 0.88 (normalized) at full operating conditions and showed no degradation over nearly 1000 hours onstream. Process studies were carried out over a range of flow rates, feed and permeate pressures, and temperatures. The flux measured under these process conditions compares well to the values predicted, as shown in Figure 9-18.

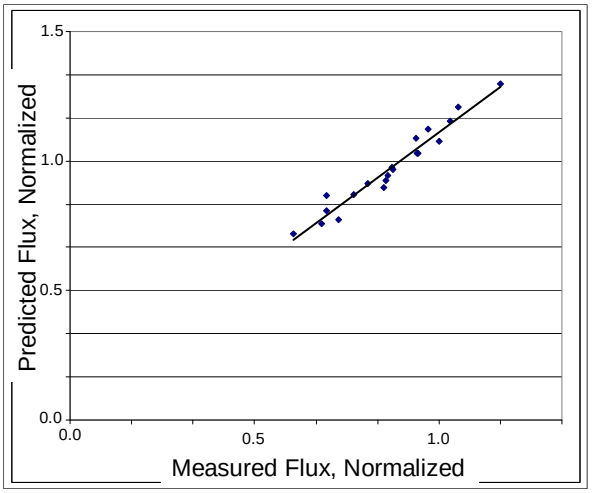

Figure 9-18. Measured versus predicted values for flux for TDU run with FSM056-2.

The MgO getter tubes were removed from the TDU and analyzed following the run. The getter bed comprised of a bundle of tubes with a total length of 9", with 6" tubes followed by 3" tubes. Chromium levels were measured using ICP and normalized to the measured Mg level for each sample. Duplicate samples of fresh tubes were also analyzed, and the background levels of chromium (18.7 ppm and 27.7 ppm for 6" and 3" tubes, respectively) were subtracted from the measured values. Tubes were sampled from various positions within the bed; Tubes 8 and 9 represent replicate samples from the center of the bed. Each sampled tube was cut into 1" sections, and half of each section was analyzed while the other half was retained. Only Tube 8 was analyzed along the entire length; the analysis of the other tubes considered only the three samples closest to the entrance of the bed.

The chromium concentration profiles are presented in Figure 9-19. A prediction by a mass transfer model was compared against the data: the Cr concentration fell off quickly and was essentially zero by the 3" position in the bed. Results in the previous run with a tube bundle getter bed without a distributor plate showed the central area of the bed had much higher Cr levels than the perimeter of the bed. In this run, all tubes sampled had a similar profile and total Cr level, so it appears that the distributor plate was effective.

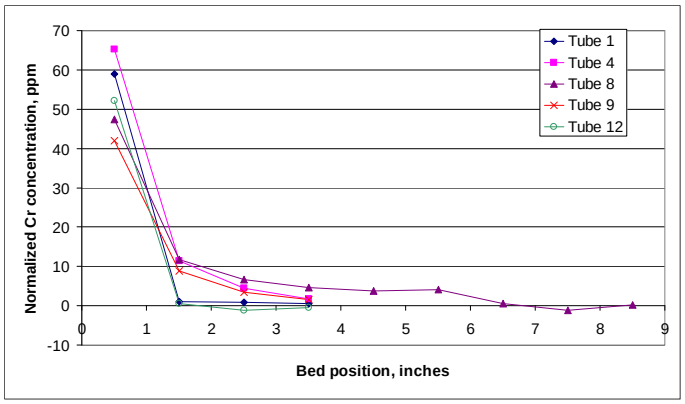

Figure 9-19. Chromium levels in MgO tubes used in the getter during the TDU test of module FSM-056-2.

Summary of TDU Tests

Air Products completed a number of TDU tests of oxygen flux from multiple-wafer modules produced by Ceramatec during Task 9. As with the XVU testing, the effects of chromium as a contaminant appeared to be important. Modules run in the TDU without the MgO getter bed consistently showed lower flux and a higher degradation rate than those with the getter bed installed. Importantly, measured fluxes with the getter bed installed approached the target level and were steady for hundreds to thousands of hours of operating time.

In contrast, the flux results after intentional contamination of the SLTR modules as described above were at odds with the TDU results. If Cr contamination was the primary reason for low flux for full-size wafers, then the SLTR modules intentionally contaminated with Cr should have fluxed at a low rate, but they did not. It is necessary to find an explanation for these SLTR results before drawing any definitive conclusions on the effect of Cr. The consideration of other potential influences on flux in sub-scale and full-size modules is likely important.

Wafer Internal Pressure Drop Measurements

Ceramatec devised variations of the wafer slot geometry in an effort to reduce the pressure drop that the oxygen flow undergoes as it passes through the wafer's interior channels and flows toward the central hole. Such wafers are referred to here as "Low dP" wafers, of which there are two types. This pressure drop could be important in dictating the flux through the wafer, because it sets the permeate-side partial pressure of oxygen at the interior surface of the membrane.

Air Products investigated the pressure drop across a Type 1, Low dP wafer by removing the rims from sample wafers and measuring the pressure drop from the outside of the wafer through the slots to the central hole, which is the maximum distance that oxygen would have to travel once it passes through the membrane to the wafer interior before entering the vertical central core of the module. Air Products used helium as the working fluid in atmospheric pressure experiments. Results were compared against a standard wafer slot geometry developed during Phase 1 (Task 3) and an improved standard wafer slot geometry developed during Phase 2 (Task 8).

The pressure drop results are summarized in Figure 9-20. The Low dP wafers have a 30% lower projected pressure drop than the Standard Phase 2 wafers, and a 60% lower projected pressure drop than the Standard Phase 1 wafers. These results suggested that additional wafers be made for flux testing in the XVUs.

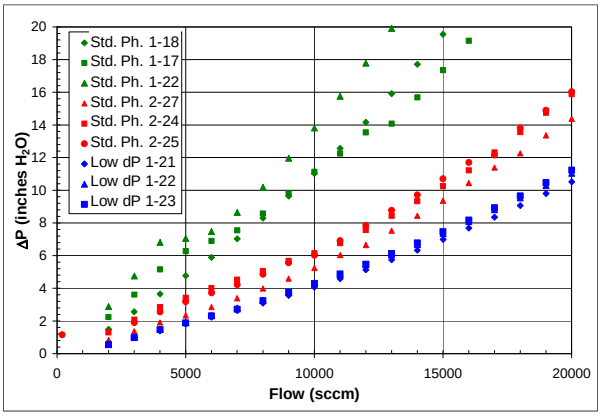

Figure 9-20. Pressure drop results for standard wafers (Ph. 1 and 2) and Low dP Type 1 wafers**.**

Ceramic-to-Metal Seal Test Results

Background

Air Products invented a ceramic-to-metal seal during Task 1 based on U-rings that fit on the outside of the base piece tube to form an annular seal with a metal receiver. These seals showed excellent capability to form an initial seal, but had limited effectiveness in temperature/pressure cycling experiments with AP2K parts operating at the ITM operating temperatures. During execution of Task 2, McDermott recommended an I-ring type seal that would be operated well below the plastic deformation (creep) regime of the metal I-ring, requiring that the ceramic base piece withstand a significant thermal gradient during operation. This approach is based on the concept that, by keeping the I-ring in the temperature range in which its stress-strain behavior

remain elastic, the I-ring seal may withstand temperature/pressure cycles without permanent deformation. Additional seal concepts were developed during Task 9, including the packed powder seal and the gasket-type seals.

Experiments were conducted in the SLTRs to assess the effectiveness of the seals. The SLTRs consist of a vertically oriented heated pressure vessel in which ceramic parts fitted to a metal tube are inserted, supported off of the horizontal bottom flange of the vessel. The interior of the vessel is pressurized and heated and the leak rate through the metal tube is measured outside the vessel.

Results

1. I-ring Seal Tests

SLTR #3 was loaded with an I-ring seal sample. The seal included silver gaskets between it and both the AP2k closed end tube and the metal receiver. As shown in Figure 9-21, the seal was tested over 5000 hr and 11 thermal cycles. The maximum temperature of the seal during the test was 600°C.

Initial performance was quite good, with a leak rate below 200 sccm under a pressure of 200 psig for the first temperature/pressure cycle, and a leak rate of below 500 sccm for the second and third temperature/pressure cycles. For the fifth and sixth cycles, the leak rate climbed to 800 sccm, and was 750 sccm for the seventh cycle. For the eighth and ninth cycles, the leak climbed to 850 and 925 sccm respectively. Ultimately, the leak reached 1000 sccm for the tenth and eleventh cycles (Figure 9-21). This experiment was then shut down.

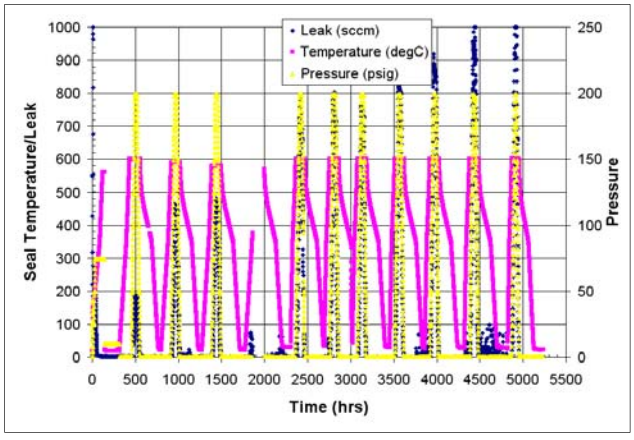

Figure 9-21. SLTR #3, I-ring seal with silver gaskets.
(Every fifth data point shown)

2. Packed Powder Seal Tests

Exploratory work was done to investigate the potential to use a packed powder seal with the AP2k base piece. Non-reactive powders were prepared and/or purchased. A fixture was developed to allow a known mass of the powder to be delivered to the annular region between an AP2K tubular base piece and a metal receiver. The powder was compressed by tightening a bushing down against the powder with a known torque, after which the bushing was removed. The assembly was placed in SLTR3 and heated. Pressurization was performed slowly and the leakage recorded.

Several variations of the basic packed powder seal concept were investigated. Gasket materials were introduced in an attempt to reduce the stress on the base piece. Figure 9-22 displays the results.

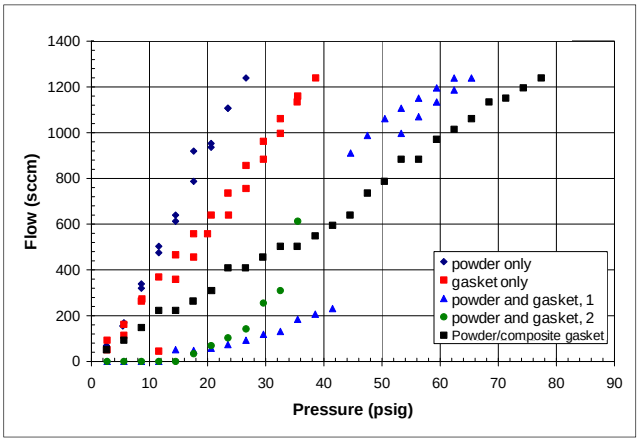

Figure 9-22. Seal test results with packed powder seal variations and AP2K tubes at operating temperature.

Leak rates were quite high even at mild pressure differentials. Use of a gasket improved the initial seal effectiveness, but leak rates were approximately 10 times higher than target in the best seal. These concepts were abandoned.

Tests of Gasket-type Seals with U-rings

Simple Gasket

Air Products tested a simple gasket-type seal in conjunction with a double-U ring on the annulus of AP2k sealed tubes in SLTR4. The sample consisted of closed-end tube No. 533 mounted in metal receiver with with two U-rings and two simple gaskets. Five temperature cycles and six pressure cycles were completed as shown in Figure 9-23. The sample was subjected to lower

temperatures during each successive thermal cycle. Leak rate during pressurization to 200 psig was initially very low, then climbed to >700 sccm after the third thermal cycle.

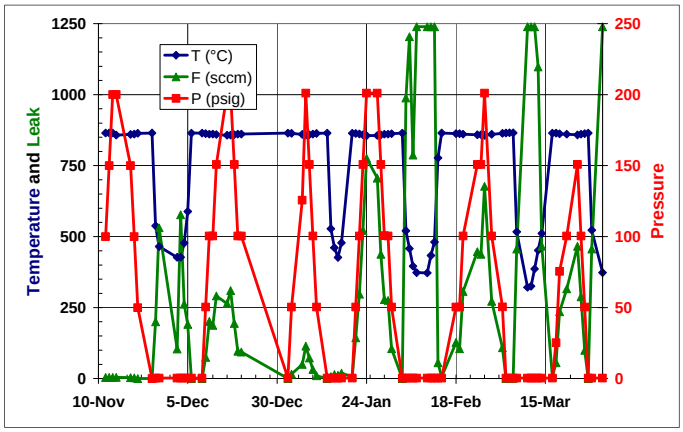

Figure 9-23. Process conditions and leak rate during the test of a simple gasket seal on an AP2K closed end tube (No. 533).

a. Dual-Material Gasket Seal with U-rings

SLTR2 was loaded with a sample consisting of a metal receiver holding a closed-end AP2k tube with a double U-ring seal around its circumference and a dual-material gasket at its base. One material was specifically chosen to interface with the metal receiver; the second material was specifically chosen to interface with the AP2k part. The dual-material seal configuration performed well over four temperature and pressure cycles to room temperature and ambient pressure as shown in Figure 9-24. This work suggests that improvements in the gasket approach may lead to seals that can be cycled multiple times without degradation in performance.

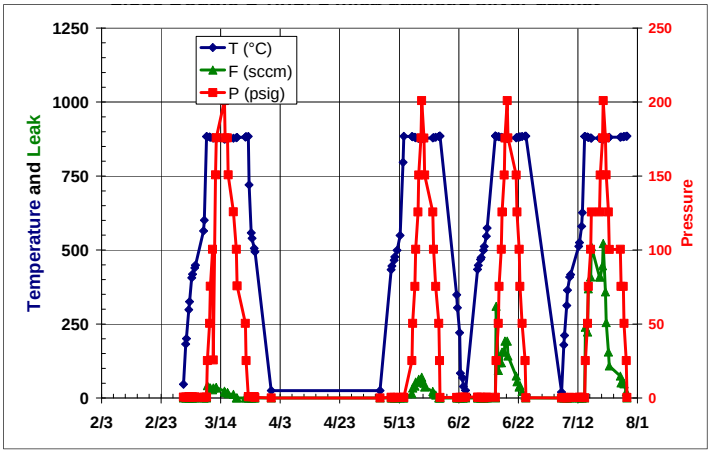

Figure 9-24. Process conditions and leak rate during the test of a dual-material gasket seal on an AP2K closed end tube.

b. Composite Gasket Seal with U-rings

A closed-end AP2k tube was fitted with double U-rings and inserted into a metal receiver in which a composite gasket had first been placed. The assembly was loaded into SLTR1. Two temperature-pressure cycles were completed without measureable leak. The maximum temperature in the test was 700°C. Nine additional temperature and pressure cycles were completed, during which time the leak did not reach 200 sccm at a differential pressure of 200 psi (Figure 9-25).

This work suggests that gasket-type seals have considerable promise to be useful seals for full-size ITM Oxygen modules.

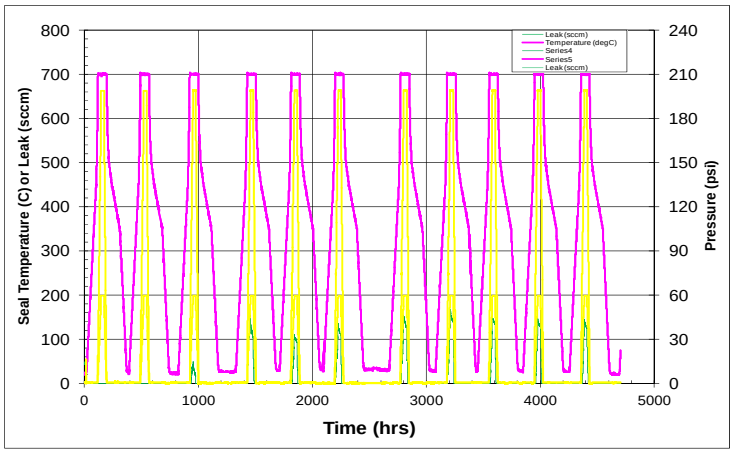

Figure 9-25. Process conditions and leak rate during the test of a composite gasket seal on an AP2K closed-end tube. Temperature is in pink, pressure is in yellow, and leak rate is in green.

PHASE II RESULTS AND DISCUSSION

TASK 10.0 DESIGN, CONSTRUCTION AND COMMISSIONING OF THE SEP TEST FACILITY

10.0 Scope

Air Products designs, constructs, and commissions the Subscale Engineering Prototype (SEP) test facility with an oxygen capacity of approximately 5 TPD. The SEP facility enables testing of key design features of commercial ITM Oxygen systems, including the ability to manifold multiple subscale or full-size ITM Oxygen modules;operate at relevant temperatures, pressures, oxygen purities, oxygen flow rates, and feed gas velocities; and assess the performance of individual modules to assess module design and manufacturing performance. The SEP design facilitates the acquisition of design, engineering, cost, and scale-up data for the subsequent development facilities. Air Products identifies and sites the SEP test facility at an existing domestic host site and provides the overall project management for the activity, including the overall project schedule and budget. Air Products provides coordination of the activities of the participants including McDermott/SOFCo, and provides process engineering and overall process safety analysis to the project. In addition, Air Products includes contaminant mitigation systems in the SEP design or retrofits the SEP with such systems depending on results.
As the final activity under this Task, Air Products will test subscale (0.5 TPD) modules with a target to produce 1 TPD of oxygen, and will test multiple full-size (1 TPD) modules.

SEP Design, Construction and Commissioning

Air Products executed the SEP project through the product supply team that supplies its commercial plants. The project was divided into the following phases:

1) Conceptual Process Design
2) Site Selection
3) Equipment Design and Process Design Selection
4) Budgetary Bid Phase
5) Detailed Design
6) Firm Bid Phase
7) Procurement
8) Site Prep and Construction
9) Commissioning

Process Conceptual Design

The overriding design concept for the SEP facility was that it had to be integrated into an existing Air Products facility which would act as a host for several of the process requirements. With the host-site concept in mind, the team mainly considered two cycle options: 1) a recycle case with high-pressure makeup air and oxygen, heat recovery between feed and non-permeate, and electrical trim heating for the feed air; and 2) and a once-through case with high-pressure air supplied by the host site, no heat recovery between feed and non-permeate, and natural gas-fired heating for the feed air because of the increased duty required. Important factors in the evaluation included: equipment availability (e.g., high-temperature heat recovery exchanger, high-temperature electrical heater); replacement value for any parasitic high-pressure air usage; estimates of total evaluated cost; quality of temperature control attainable through the entire startup and shutdown ramps; staying under 10 MMBtu/hr for each natural gas-fired unit in the flow sheet to avoid triggering permitting issues; and maintaining electrical loads below practical limits for a particular site.

Site Selection

Air Products identified a number of potential locations within its commercial operations that could be used as the host site. The sites were evaluated on the basis of available utilities, ease of integration of one or both of the conceptual SEP process designs with the host site, operating staff availability, proximity to R&D personnel, and overall cost. The Sparrows Point, Maryland, site emerged as the preferred choice. Air Products' Sparrows Point air separation plant had a supply of high-pressure, clean, dry air that could be used as feed or make-up air, as well as power tie-ins and plot space. In addition, Sparrows Point is only a 3-hour drive from the Pennsylvania-based R&D team.

Equipment Design and Process Design Selection

Three main equipment considerations in the conceptual process design involved the ITM vessel, heat addition requirements, and heat exchange requirements. The conceptual vessel design work was carried out by McDermott/SOFCo and is described in the Task 7.4 section. The team concluded that the vertical vessel design concept afforded flexibility and ease of loading/unloading modules, ideal for the development stage of the technology. The heat addition

requirements of the recycle process design case were determined to be achievable, given the availability of electrical trim heating equipment (Indeeco, St. Louis, Missouri).

The heat exchange strategy of the recycle process design required an oxygen cooling system and a recuperative heat exchanger that could handle the non-permeate stream maximum temperature. Oxygen cooling options were developed in conjunction with Air Products' safety experts to identify suitable alloys for the oxygen train (see Task 7.2). A combination water-cooled trim cooler and air-cooled finned tube section was chosen to cool the hot, sub-atmospheric oxygen prior to its compression. Among the anticipated conditions in the SEP are upset conditions in which the process flow would be stopped and the gas pressure maintained; the upset conditions were the most severe for the recuperator. A suitable solution was identified working with the supplier (Brown Fintube, Houston, Texas).

As a result of the favorable feedback from equipment suppliers and the amenability of the Sparrows Point site to support the selection, the team chose the recycle process design. A schematic of the concept is shown in Figure 10-1. The electric process heater passes electrical current through the pipes that contain the process gas to directly heat them. Oxygen produced in the process is vented and made up in the loop by introduction of high-pressure air or oxygen. A vent (not shown) avoids the accumulation of inerts in the loop.

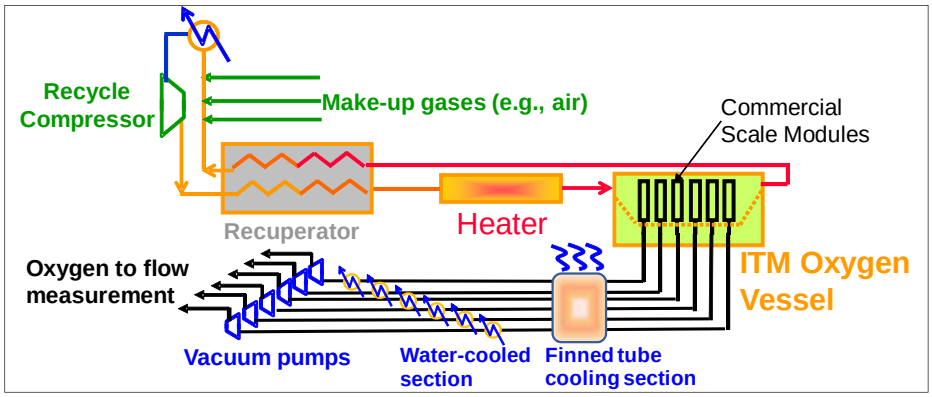

Figure 10-1. Schematic process flow diagram of the SEP recycle process design.

Detailed Design

Air Products determined the operating design targets for the unit as summarized in Table 10-1. These targets represent expected commercial operating conditions. The air flowrate range was

chosen to create the local gas velocity range that ITM modules are expected to experience in commercial applications.

Table 10-1. SEP design operating targets.

Parameter	Design Target	Units	Comment
Temperature	900	°C	Max. Allowable Working Temperature; operation is at least 15°C lower
Feed Pressure	215-285	psia	Vessel MAWP 300 psig
Feed Flowrate	0-150,000	scfh	
Permeate Pressure	300-350	Torr	
Permeate Flowrate	0-5	TPD	Limited by oxygen cooling capacity
Permeate oxygen concentration	20-100	% (vol.)	Sets material selection

Air Products developed a detailed process flow diagram, conducted a design hazards review (DHR), developed equipment specifications and a control/data acquisition strategy for the unit. Details of the vessel design were executed by McDermott/SOFCo as described below. A CAD drawing of the SEP was generated to enable piping design layout details to be finalized (Figure 10-2). In the figure, the pressure vessel is shown in the foreground (vertical vessel with flat lid).

The SEP was designed to be skid-mounted as shown in the figure. One skid (on the left in Figure 10-2) supports the electric heater, recycle compressor, and control room. The second skid supports the ITM vessel, recuperator and trim cooler, oxygen cooling train, and vacuum pumps. This approach allowed the unit to be almost entirely shop fabricated and assembled.

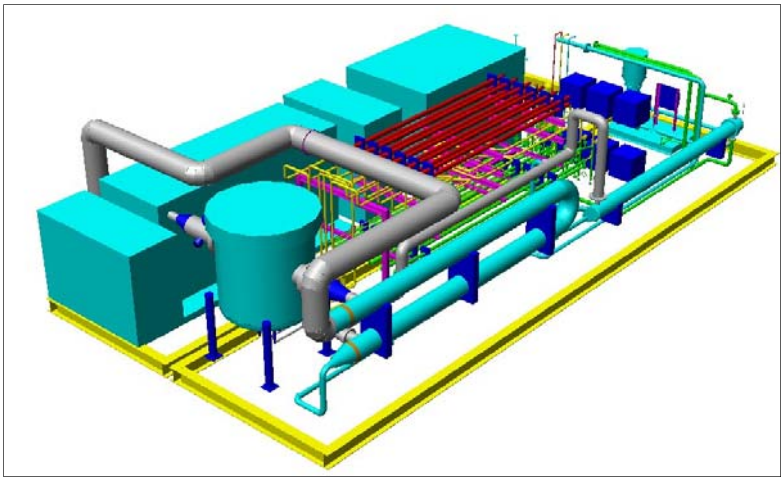

Figure 10-2. CAD drawing of the SEP equipment layout.

With the parameters in Table 10.1 in mind, McDermott/SOFCo executed the detailed engineering vessel design package and oversaw the construction of the ITM vessel. As described in Task 7.4, the design includes a flow duct contained within a pressure vessel. The flow duct houses the ITM modules and is configured for testing purposes, allowing access to modules for inspection and change-out and use of instrumentation.

Modules are arrayed in a 2x3 arrangement within the flow duct. Each of the modules is connected to a separate vacuum pump via permeate line piping so that the performance of individual modules can be assessed. Figure 10-3 shows a side cutaway view of the vessel and duct; module locations are represented by the green rectangles. Feed flow is from left to right in the figure, and the permeate lines exit the vessel at the bottom. The arrangement allows for access by personnel standing inside the vessel with the lid removed. The vessel is shown with a flat lid on the top; the lid was later changed to a hemispherical dome.

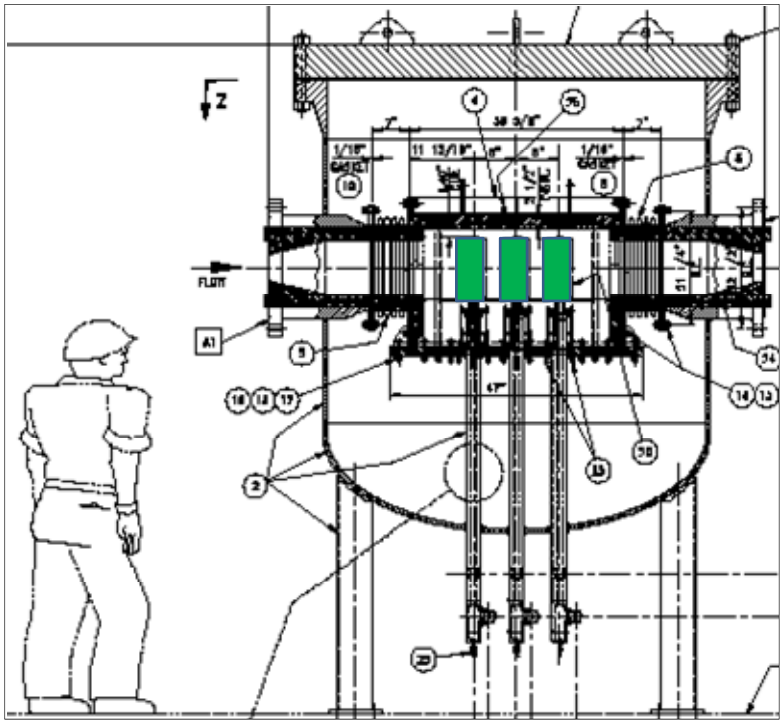

Figure 10-3. Engineering drawing of the SEP vessel. Module positions are shown as green rectangles.

For the first embodiment of the vessel, the flow duct was designed to accommodate 0.5 TPD-scale modules with provision to allow a duct to be designed later to accommodate 1.0 TPD-scale modules. The flow duct design was a removable three-sided enclosure; a flow baffle was

included to direct flow through the modules. Nozzles for thermocouple pass-through accommodated approximately 80 thermocouples and other sample/test lines.

Air flow through duct (across modules) was provided for by two through-wall vessel nozzles. The nozzles, flow duct and all six permeate pipes were internally insulated. The vessel walls itself were not insulated. Vent hole(s) in the duct base plate provided for pressure equalization between the inside and outside of duct. The operating pressure is entirely maintained by the vessel, which was designed for 300 psig MAWP at 700°F.

McDermott/SOFCo also included in the vessel design the ceramic-to-metal seal sub-assemblies described in Section 7.4 to accommodate sealing to the base of the ITM modules.

Procurement, Site Prep, and Construction

Once the design was finalized and approved, the team purchased the required equipment and delivered it to a shop fabricator who performed the final assembly. Figure 10-4 shows the vessel in transit from the vessel supplier to the shop fabricator. Figures 10-5 and 10-6 show intermediate stages of fabrication of the SEP.

Figure 10-4. ITM SEP vessel in transit to the shop fabricator.

Figure 10-5. SEP vessel (blue) in place during skid fabrication. The recuperator is shown at right.

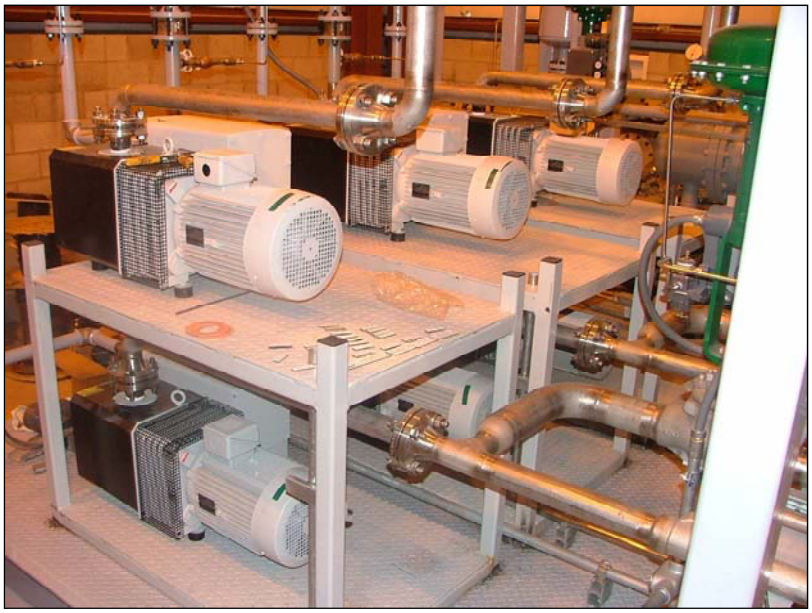

Figure 10-6. SEP permeate vacuum pumps in place during skid fabrication.

Site preparation at the Sparrows Point facility was a modest effort – the skids were to be located in a previously prepped section of the facility that provided access to the required utilities, signal wiring and gas piping. Footers were dug to accept the skids.

Once the skids were completed and shop tested, they were shipped to Sparrows Point and placed on the site. All piping and electrical connections were completed within a week, a testament to the utility of the skid-mounted approach.

Figure 10-7 shows an aerial view of the SEP during installation at the Sparrows Point facility.

Figure 10-7. The SEP in place at Sparrows Point during installation and tie-in.

Commissioning

Commissioning Trial No. 1. Air Products loaded the ITM vessel with two ceramic test pieces that simulate the bottom conical base portion of 0.5 TPD-scale modules and initiated air flow and heating. During the first trial, the unit was operated at a maximum pressure of 255 psig with robust control. Air temperature to the ITM vessel reached a maximum value of 865ºC at about half of the design air flow rate. The shortfall on temperature was attributable to three factors: current primary voltage of 456V at the site vs. 480V design (resulting in ~10% reduction in electric heater output); control hardware limitations within the electric heater that limited the output; and shop wiring of the heater transformer to the tap with the lowest secondary voltage (resulting in a 38% reduction in heater output). The unit achieved a maximum air flow rate of 117,000 scfh, or ~70% of the design flow rate of 150,000 scfh. The shortfall in flow rate was caused by excessive pressure drop across the strainer at the suction of the recycle compressor.

Air Products observed that temperatures near the ceramic-to-metal seals of the test pieces were higher than design target during the first commissioning run. Otherwise, the flow duct insulation design worked well, and vessel wall temperatures remained well below design limits throughout the run. The ceramic test pieces were examined post-run and found to be intact, though significantly contaminated with chromium. Air Products also demonstrated both consistent manned and unmanned operation, and demonstrated that the unit could be controlled remotely per design.

Following the trial, Air Products cleaned and replaced the compressor suction strainer, which appeared to have accumulated some insulation from the ITM flow duct. The electric heater transformer was rewired to the second of three taps to increase heater output. In addition, the temperature control scheme was modified to enable better control in the heater. A storage trailer was installed on-site immediately adjacent to the ITM skids.

Air Products redesigned the insulation system at the base of the modules to restrict convective flow. The conical ceramic test pieces were replaced with alloy test pieces of the same basic design to permit much more rapid adjustment of process conditions to more quickly assess important plant performance issues.

Commissioning Trial No. 2. At the beginning of this trial, the compressor suction strainer plugged several times shortly after starting the compressor. The mesh screen on the strainer was then replaced with a more course screen. This change allowed slightly longer run times, but the strainer continued to plug. Again, the culprit was primarily material from the flow duct, but it was impossible to determine whether the material was new or still within the system from the first commissioning trial. The new temperature control scheme allowed the system to reach 875°C at 60% of design air flow rate. Tests at higher flow rates were inconclusive because of the plugging strainer.

Following completion of the second commissioning trial, the team designed a parallel strainer arrangement for the compressor suction, and the on-site contractor fabricated the replacement piping section. This arrangement will allow for on-line cleaning of one strainer after switching the parallel strainer into service. The contractor also cut the existing piping at a low point downstream of the cooling water exchanger to insert the new piping, and found that section to be

dry and clean with no evidence of either a tube leak in the exchanger or an accumulation of old material.

Temperature measurements taken during the first and second commissioning trials indicated that the insulation system in the flow duct at the base of the modules performed significantly poorer than design. Thus, the team decided to replace the insulation scheme with a more conventional approach. In addition, an inlet radiation shield, composed of a reticulated porous alumina piece, was removed from the system to eliminate a potential source of pressure drop that might cause hot inlet air flow to divert downward into the seal region within the insulation box. Finally, the electric heater transformer was rewired to the third of three taps with the highest secondary-side voltage.

To provide an early test of oxygen production, the team successfully loaded two testable 0.5-TPD-scale modules into the SEP vessel, retaining the two conical alloy test pieces in place to permit continued commissioning of the unit in the event of module failure during operation. A photograph showing reassembly operations of the SEP duct is shown in Figure 10-8.

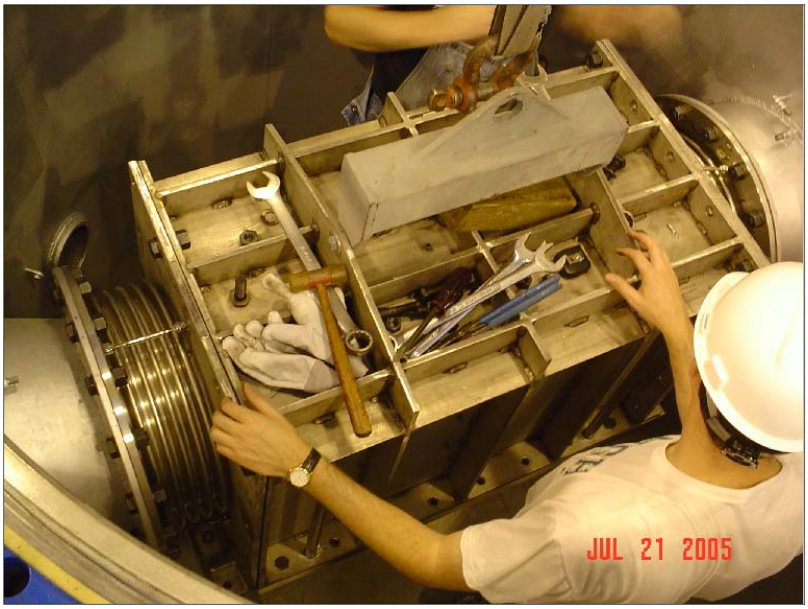

Figure 10-8. View down into the SEP vessel during reassembly of the flow duct.

Commissioning Trial No. 3. Air Products brought the system up in temperature under a slight back-pressure. Both modules remained leak tight to at least 525ºC, as measured by bubble testing the permeate vents. At 550ºC, the electric heater tripped when an over-temperature controller

failed in one of the heater zones. While troubleshooting the problem, flow and pressure were ramped down to minimize the cooling rate. Despite this measure, vessel temperature decreased linearly at ~40ºC/hour throughout the four hours required to diagnose and fix the problem. As flow rate and pressure increased after the heater came back on-line, the temperature inside one module spiked up to match the air-side temperature. A bubble test of the permeate vents confirmed a substantial leak in this module, while the other module remained leak-tight at low pressure.

Because of the low air feed rate, the air feed temperature reached only 730ºC. At this point, flow and pressure were ramped up, with the flow rate reaching 70,000 scfh and the pressure reaching 200 psig. Temperature was raised to operating temperature (800-900ºC).

With the permeate lines still venting to atmosphere, the vacuum pumps were started, pressure control valves cracked open, and pressure control set in automatic at 765 Torr, so that air was now drawn into the permeate vents as ballast for the vacuum pumps. The permeate analyzer began showing an increase in oxygen purity, indicating that the intact module had begun to flux oxygen. The permeate pressure ramp was started, and the vent/ballast valve for the intact module was closed completely; at 615 Torr, oxygen purity was 91.6% with a total flow rate of 240 scfh. When the permeate system reached 350 Torr permeate pressure, it produced 320 scfh of total flow at 94% purity, which increased to 350 scfh at 95% purity. This result corresponds to approximately 75% of expected productivity. The other module, while leaking significantly, still produced 47% purity oxygen at this same condition.

After slightly more than two days of steady-state operation (other than increases in air feed flow), the electric heater experienced a significant excursion which caused the current draw to drop by 10% and the outlet temperature in a heater zone to drop by 125ºC. As a result, the air feed temperature to the ITM vessel dropped by 25ºC. Then the recycle compressor shut down, failing both modules almost immediately, as evidenced by failure of the rupture disks in the permeate lines. Later investigation showed that the compressor shutdown was caused by a loose terminal block in the motor control center, which was subsequently fixed. Inspection of the electric heater revealed breakthrough oxidation of the upper tier of stainless steel buss bars that carry current from the transformers to the pipes.

The electric heater supplier agreed to a warranty replacement of the upper tier of buss bars, The nickel-alloy material for the upper tier was ordered and received.

Prior to material receipt, the entire upper tier of buss bars was cut out of the system. With improved access to the middle tier, further inspection revealed catastrophic, high-temperature-induced oxidation of those buss bars, particularly in the section which exhibited the steep loss in performance at the end of the Commissioning Trial No. 3. Notably, the oxidation appeared to begin suddenly along the length of the bars; the buss bars appeared to be in good shape at the cooler end. The nickel-alloy pipe bends and buss bar lugs looked good, lending confidence to the proposed change-out to nickel-alloy buss bars.

The local contractor and insulation sub-contractor completed the warranty repair of the SEP electric heater.

Commissioning Trial No. 4. The Air Products team subsequently completed a week-long heater performance test, including a stretch of >100 hours at the design operating temperature. Achieving operating air temperature in the ITM vessel required the maximum pipe temperatures of 918ºC in each heater zone. At 250 psig pressure in the vessel, the maximum achievable flow at these conditions was 136 Kscfh, or ~91% of design flow, and heater output in Zone 3 was the limiting factor. Primary line voltage varied between ~450 and 460 V during this test, which is a major factor impacting the shortfall in heater performance. At 200 psig pressure in the vessel, the maximum achievable flow at these conditions was ~120 Kscfh, and compressor flow was the limiting factor. Throughout the performance test, the heater control system smoothly handled numerous, small perturbations caused by changes in weather, precipitation, and modest swings in line voltage. Based on the results of the heater performance test, the SEP facility was considered fully commissioned.

10.1 SEP Demonstration

Air Products carried out four experimental runs and one system trial with the SEP during this task. All modules tested were 0.5 TPD-scale modules produced by Ceramatec under Task 8 with a variety of wafer types and leak rates; all were testable modules likely to yield 90% oxygen purity in a successful SEP oxygen production test. Table 10-2 provides a summary of the run data; a discussion of each run follows the table with more details.

Table 10-2. Summary of SEP module testing under Task 10.

Run	Modules, Scale	Max. O_2 Purity	Max. Flux (Norm.)	Comments
4	FSM-050-1 FSM-051-1	n/a 99.2%	n/a 0.81	Thick membranes; one broke during heat-up; produced O_2 for 14 days; did not survive thermal/pressure cycle. Power outage ended run.
5	FSM050-4 FSM052-3	98.0% 95.1%	0.93 1.07	Thick membranes; 13 days operation; heater trip (caused by rain infiltration of electronics) ended the run.
6	FSM-050-3 FSM-052-1	40%	0.86 0.99	Thick membranes; lower temperatures at module base; lost purity during heat up
7	Dry run			Iso-control system trialed
8	FSM065-1, thick FSM-065-7, thin	N/a N/a	N/a N/a	FSM065-1 failed during heat-up; thermal gradients observed. Returned to ambient.

The highlights of the table include demonstration of 99+% oxygen purity and fluxes that met expected levels. Run 5 produced ~0.5 TPD oxygen. Runs 4-6 and 8 progressively demonstrated lower temperatures at the base of the module, such that a significant thermal gradient existed across the wafers at the bottom of the modules (especially) in Runs 6 and 8. This trend was the result of targeted efforts to reduce the temperature of the ceramic-to-metal seal elements so that the operating temperature was out of the creep regime for the metal elements of the seal. At the end of this work, based mainly on the failure rates of the modules experiencing high thermal gradients in Runs 6 and 8, it was concluded that the temperature gradients in the ITM ceramic led to stresses that were not tenable. This suggested that an isothermal system with the ceramic-to-metal seal operating at the ceramic temperature was desirable.

SEP Run 4

Two 0.5 TPD-scale modules were loaded and heated to operating temperature. One module (FSM-050-1) showed excessive leak rates during the startup and was isolated to prevent possible damage to the seal region in the adjacent module (FSM-051-1). The intact module ultimately produced 99.2% oxygen purity during 14 days of operation.

Figure 10-9 shows a sample of the run data. Oxygen flux (normalized for membrane thickness) is plotted in red. Several process conditions were run during the 14 days of operation at

temperature. Some of the flux variability was the result of loss of high-pressure oxygen makeup gas. This outage occurred two separate times during maintenance work at the plant for periods of nearly 10 hours and 6 hours. During each outage, the oxygen level in the loop decreased from 20.95% to less than 19% over 20-30 minutes. Increased fresh air feed helped to stabilize the system, and the oxygen content in the loop was successfully ramped slowly back to its original level. No apparent effect was seen on the module during either of these abrupt changes.

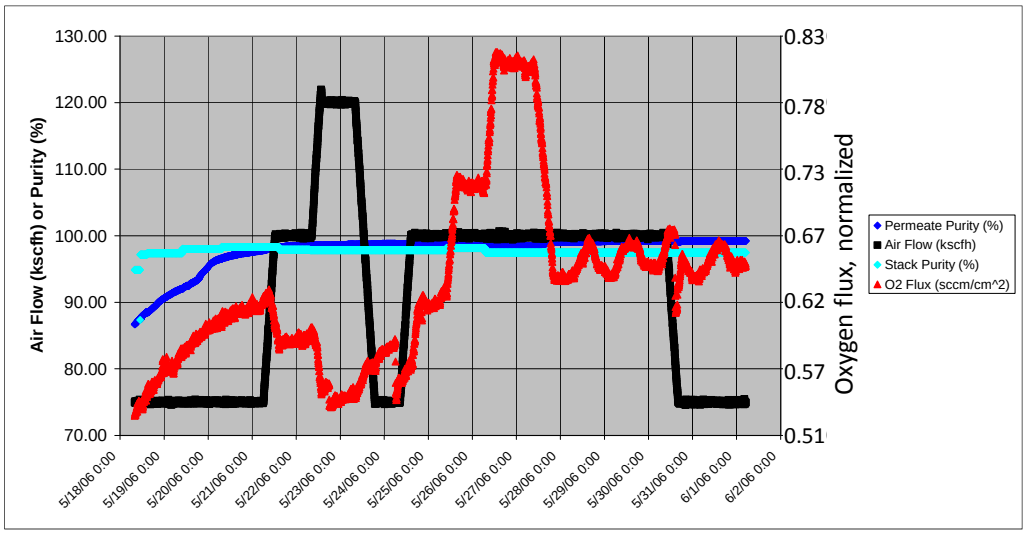

Figure 10-9. Oxygen purity, flux and feed flow rate during SEP Run 4.

The full process variable trends are shown in Figure 10-10. The period of 5-15 June was used to ramp the modules down slowly in temperature. Minimum temperature reached was 275°C.

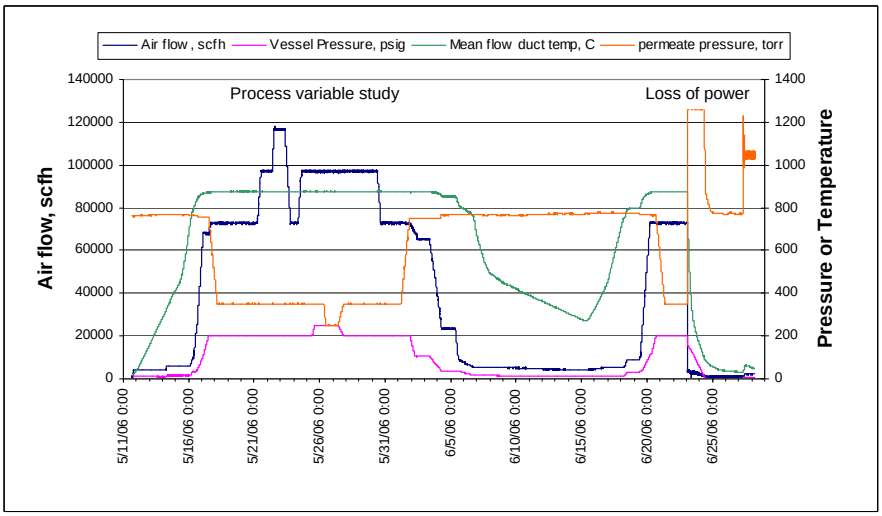

Figure 10-10. Process variable trends during SEP Run 4.

During the cooldown, several distinct jumps in the temperature measured inside the module were noted, suggesting an increased flow due to opening of the seal or a crack in the module. The modules were returned to full operating conditions, but purity levels for both modules were low, at roughly 35% for module FSM-050-1 (previously isolated) and 50% for module FSM-051-1 (which gave 99%+ during the first cycle). The flux values for both modules during the second cycle were similar to values to the first cycle. Analysis of the run data after recalibrating the air analyzer with a certified standard and correcting the temperature compensation on several flowmeters allowed both the total flow balance and the oxygen balance to close within about 2%.

Following the power outage and sudden shutdown of the unit, the modules were inspected and found to be heavily damaged by the rapid thermal transient. Analysis of wafer surfaces from one of the modules showed chromium contamination on most wafers, with second-phase coverage ranging from 11% to 27%.

SEP Run 5

Prior to Run 5, a new insulation scheme for the flow duct was implemented with tighter-fitting, less-friable material with a lower k value than the previously used material. This effort was carried out to reduce the temperature at the base of the module to enable better performance from the ceramic-to-metal seal during temperature cycling.

Two 72-wafer modules (FSM050-4 and FSM052-3) with thick membrane layers and low starting leak rates were tested in Run 5. Module 50-4 had wafers with the standard internal slot pattern, and Module 52-3 had wafers with the low-pressure-drop slot pattern.

The process started up well and ran fairly uneventfully for 13 days. Figure 10-11 shows the flux/purity trace for Module FSM052-3 during the run by calendar day. On 30-31 August, the high-pressure oxygen supply was interrupted twice due to high transient demand for oxygen from the associated ASU. The run terminated after a ground fault tripped the heater, which was ultimately traced to rainwater infiltration of the heater control electronics. The modules had failed based on the very high flow rates through the permeate system.

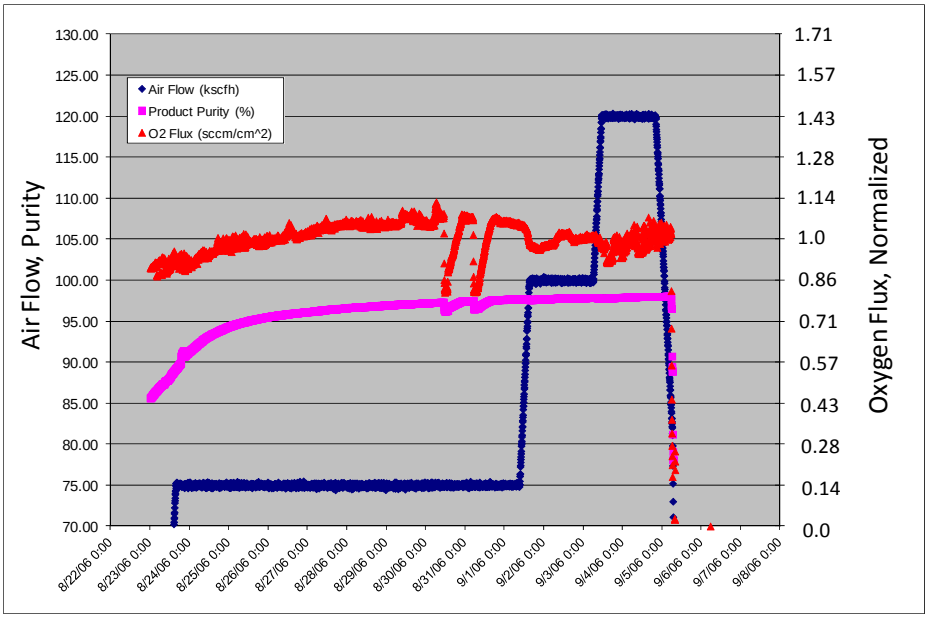

Figure 10-11. Purity and flux performance of Module FSM052-3 during SEP Run 5.

Flow duct temperatures near the seals did not improve in this run. Seal cup temperatures were similar to previous runs, but portions of the seal sub-assembly ran significantly hotter (100°C) than in run 4. The seal temperatures were still significantly higher than design.

SEP Run 6

To address the high temperatures at the seal cup sub-assembly, Air Products devised means to actively cool the seal region. An initial design was drafted for a split collar with a helical channel for cooling air flow. Thermal modeling of this design suggested that a low-flow design like this would result in large temperature gradients around the circumference of the seal cup. Instead, efforts were directed toward a high-flow, single-channel design that minimizes the air side temperature change and thus the deformation of the seal region.

Some effort was spent examining the predicted cooling performance of the seals and verifying the sizing of components based on a 1D heat transfer analysis. Figure 10-12 shows the predicted outlet temperature and heat removal rates given an inlet temperature of 150°C for two different operating pressures representing the two ends of the range to be used. Two different correlations for the convective heat transfer coefficient were used (for developing and fully developed flow, h') which give different results, especially for the heat flow. The simulations predict that there is a sizable range of heat removal rates accessible by varying the airflow rate.

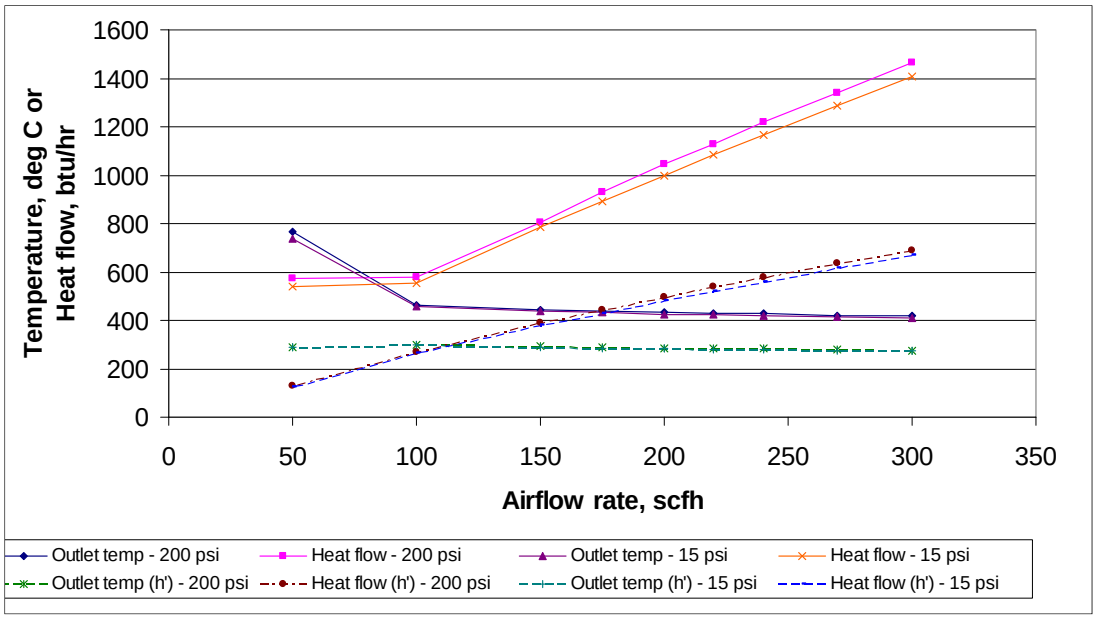

Figure 10-12. Heat transfer predictions for active seal cooling as a function of flow rate.

Thermal modeling also suggested that high stresses would be seen at the weld between the sub-assembly's bottom flange and the central pipe. Inspection of the weld by dye pen uncovered cracking in the high-stress region. An alternate weld method was suggested and used during the modification of the sub-assemblies.

The team performed a management of change (MOC) on the SEP, subsequently installing the cooling air loop was and tying it into the DCS with feedback control from the seal cup temperature. Cool air was piped into the vessel through the vessel wall fittings previously used to route thermocouples. The air was routed through the cooling channel and up through the floor panels of the flow duct, then exhausted into the process stream downstream of the modules. In addition, the team constructed a roof over the heater cabinet to minimize rain infiltration into the heater control electronics.

Full-scale modules FSM-050-3 and FSM-052-1 were pressed into the modified seal sub-assemblies and loaded into the vessel. The insulation box was returned to the Run 4 insulation scheme with the addition of a layer of Saffil insulation around the conical base pieces on the modules to protect them from reacting with the base insulation.

During heatup, two “events” were seen in which a sudden rise in the module internal temperature was noted. These events occurred at temperatures between 140°C and 200°C (Figure 10-13).

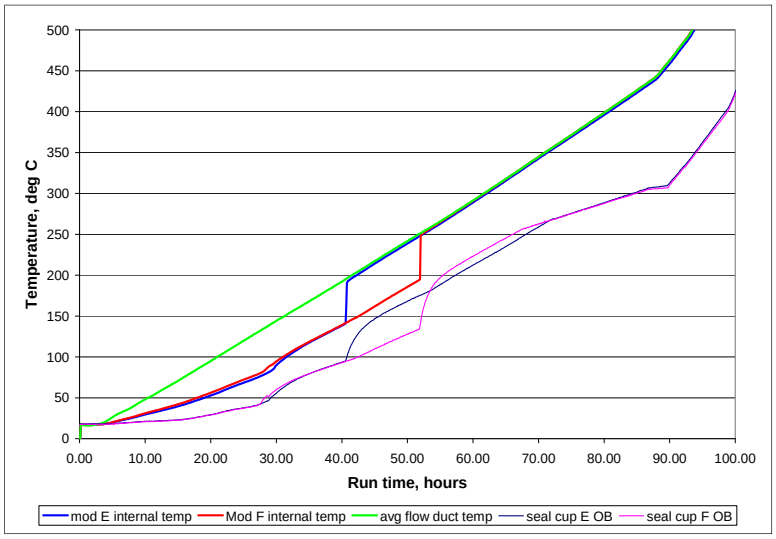

Figure 10-13. Module and seal temperature trends during Run 6. (Module E is 50-3, Module F is 52-1.)

The modules were brought to full operating conditions, but permeate purity did not exceeded 40%. Fluxes were as expected for thick membrane layers. Control of the seal temperatures was good. Initially, a flow of 25 scfh was used to minimize any abrupt changes if flow were turned on during the run. As the flow duct temperature increased, the difference between the internal module temperature and the seal temperature increased beyond that seen in previous runs, and led to concern that the gradient on the cone was becoming too large. The flow to the seal was turned off at 28 hours into the run; the rate of change of the temperature increase for both the seals and the internal module temperatures is evident in Figure 10-13.

After the module temperature reached 300°C, the seal temperature was set proportionally, and flow was adjusted automatically to control temperature.

After several days at operating conditions, it was apparent that no further purity improvement would occur. The temperature on the seal for module FSM-052-1 was ramped first to 700°C and then to 800°C to see if purity would improve at higher seal temperature, but no improvement was seen. The maximum cooling flow used was less than 200 scfh, less than predicted.

Following Run 6, the modules were found to be largely intact. The only damage immediately apparent was broken wafers at the bottom of both modules. Upon closer inspection, some evidence of cracking in the cones was also noted.

SEP Run 7

Run 7 focused on ambient-temperature operation to test the gas blending system to prepare for the contingency that the main source of air would not be available. A test of the isocompositional control system was also done during this run. An algorithm built into the DCS adjusts the air and N_2 flows to adjust the O_2 level as a function of temperature to keep a constant oxygen vacancy fraction in the ceramic. The algorithm was tested using dummy inputs for temperature; the system appeared to calculate the desired O_2 level correctly and adjusted the flow controllers to match this setpoint.

SEP Run 8

Modules FSM065-1 (thick membranes and low-pressure-drop wafers) and FSM-067-4 (thin membranes and low-pressure-drop wafers) were pressed into spool pieces in preparation for SEP Run 8. Modifications were made to the piping for the seal cooling system, adding metering valves to allow very slow, controlled introduction of cooling air to the seals and avoid abrupt temperature changes to the module. This run used a number of relocated thermocouples in the flow duct to provide data about temperature distribution near the base of the module after the observed failures of the lowest wafers in Run 6.

This run showed slower heatup than normal, with a larger temperature differential between the module and the flow duct that was attributed to cold ambient temperatures. Temperature differences between the internal module thermocouple and the seal thermocouples were also larger than desired, and the heating ramps were paused three times for several hours each time in order to reduce this gradient. Figure 10-14 shows the module/seal gradients for Run 8 relative to previous runs. The orange curves show the gradients for Run 8, which were kept in line with previous successful runs.

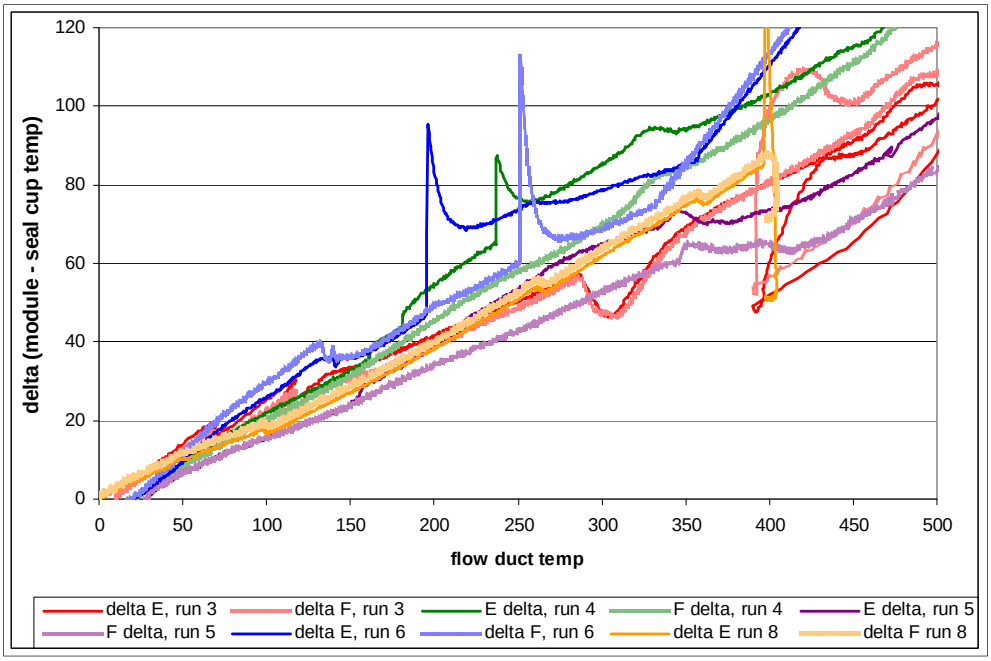

Figure 10-14. Module to seal gradients for SEP runs. "E" and "F" refer to two module positions in the flow duct that have been used in all runs.

Module FSM-065-1 failed during heatup just after a flow ramp was started. The failure point was 315° C, higher than previous runs where early failures were seen. Both axial and lateral temperature gradients were observed around the modules.

After the module failure occurred, process cooldown was begun to preserve the condition of the modules. Upon complete cooling and inspection, the failed module looked very similar to the failures in Run 6 – with the lowest two wafers cracked and broken. No radial cracks were observed in any of the wafers looking up into the center manifold. A dye penetrant, sprayed onto the cone region before the module was removed, was found to penetrate in multiple places into the interior of the cone. Multiple cracks became apparent in the cone as the module was removed from the flow duct. The module failed during removal just above the cone, with portions of slotted layers remaining attached to the cone.

The team concluded that the primary hypothesis for low-temperature failures of wafers located near the base piece is the temperature gradient across the wafers, particularly at the lower module level. Newly located thermocouples in this run measured temperature differences from upstream to downstream of the module at the lowest wafer level of 15°C at the time of failure.

PHASE II RESULTS AND DISCUSSION

TASK 11.0 DESIGN OF THE PRE-COMMERCIAL DEMONSTRATION FACILITY, PCDF

11.0 Scope

Air Products selects the site, defines the scope and process, and prepares descriptions of long-lead items for a pre-Commercial Design Facility (pCDF) to operate under anticipated commercial conditions. The facility has an oxygen capacity of approximately 25 TPD and includes the major elements of a commercial ITM oxygen facility. The final design, procurement, completion of construction, commissioning, operation and de-commissioning of the pCDF will occur in Phase III. As part of this work, Air Products assesses conceptual project development work of Phase III test facilities that produce in excess of 50 TPD oxygen, up to 250 TPD oxygen.

pCDF Process Design and Site Selection

Air Products developed a conceptual pCDF process design based on dialogues with Siemens' gas turbine division. The philosophy behind the design would be to integrate the ITM process with a gas turbine that could be used for subsequent scale-up activities. Other potential gas turbines, such as the 2 MW machine operating as part of the Power Systems Development Facility (PSDF) (Southern Co., Wilsonville, Alabama) were considered, but ultimately rejected for integration because they do not provide high potential for scale-up. Siemens identified the GT35P machine described under Task 7 as a candidate machine, capable of integration with the ITM through air extraction and enabling scale-up of the ITM process. Air Products developed a conceptual process flow diagram based on this machine, as shown in Figure 11-1 (identical to Figure 7-23).

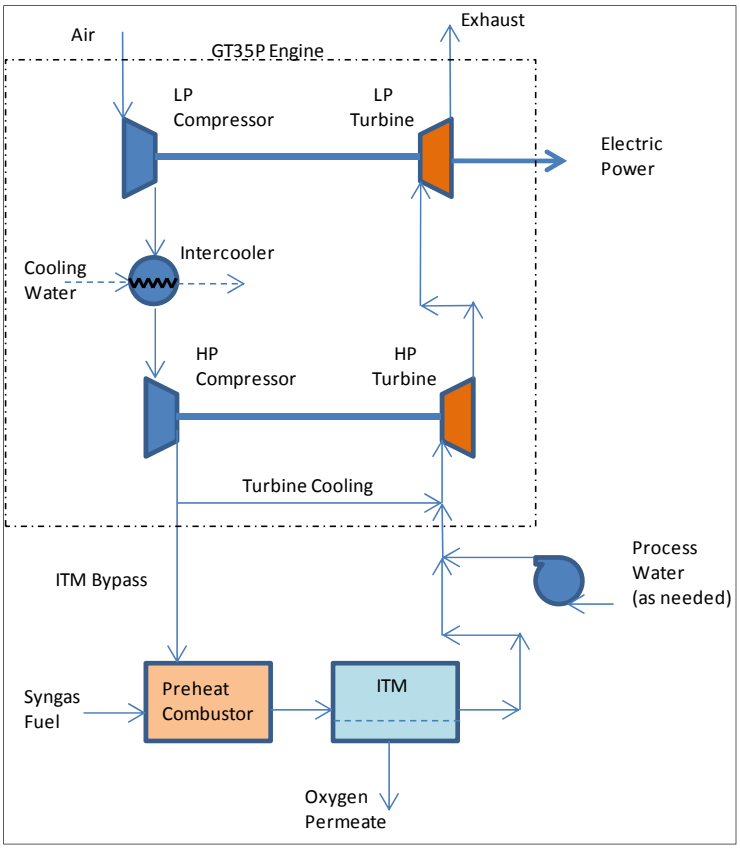

Figure 11-1. Conceptual pCDF flowsheet based on the GT35P engine.

The two-shaft GT35P is configured for a high degree of air extraction and a turbine inlet temperature is 850°C, ideal for the ITM non-permeate exhaust. The process could be operated with syngas or another fuel (syngas is shown in Figure 11-1). The process was configured in simple cycle mode and would produce ~17 MW net power (compression of 25 TPD oxygen would require ~0.1 MW). The oxygen cooling train was not specified in the conceptual work, but was expected to be dictated by site issues. Options include a quench system or steam cooling.

The ITM vessel system for the pCDF was based on the designs shown in the description of Task 2.4, in which an array of modules is housed in an insulated flow duct. The high flow rates of feed air extractable from the GT35P required that the layout of modules accommodate a relatively shallow bed aspect ratio. Design considerations included use of considerably more modules than required for the 25 TPD production, use of flow elements to act as baffles, and/or by-pass of a considerable amount of the process gas around the ITM vessel to reduce velocities there.

Modules were expected to be accessible as an ensemble rather than individually, as in the SEP design (Task 10).

The team identified the gas turbine and ITM vessel as the long-lead items in this flowsheet. The gas turbine, typical of rotating equipment, requires ~30-36 months of lead-time, while the ITM vessel was estimated to require 18 months lead time including engineering development.

The simplicity of the process enables it to be sited at an Air Products facility and supply either grid power or power to offset site use while operating. Air Products tentatively identified the Sparrows Point facility as an amenable location for the pCDF, although other sites among the Air Products' facility locations could also be suitable. Scale-up studies were conducted for adding oxygen-production capacity to the cycle in the form of a larger ITM vessel housing more modules. These factors weigh heavily on the final choice of pCDF location.

As mentioned in Task 7, the GT35P could enable over 1000 TPD of oxygen production. This capacity is attractive for future ITM scale-up activities. Air Products considered two alternative pCDF cycles, one in which the air extracted from the GT35P is fired directly with fuel prior to entering the ITM (as in Figure 11-1) and another in which the air is indirectly heated prior to entering the ITM. Consideration was given only the cases in which air sufficient for oxygen production was directed to the ITM; the remaining extracted air was assumed to bypass the ITM and be re-injected at the turbine inlet. Air Products also considered two permeate pressures (250 and 350 Torr).

Oxygen production was calculated as a function of the amount of extracted air directed through the ITM vessel, taking into account mass transfer resistances in the gas phase and the membrane, as shown in Figure 11-2. These cases assume a fixed number of modules for the two permeate pressures considered. As shown, the system could provide over 150 sTPD oxygen at 20% of available flow at a permeate pressure of 250 Torr with indirect firing in the air preheat step. The effect of the preheating choice is about 30% of the oxygen production.

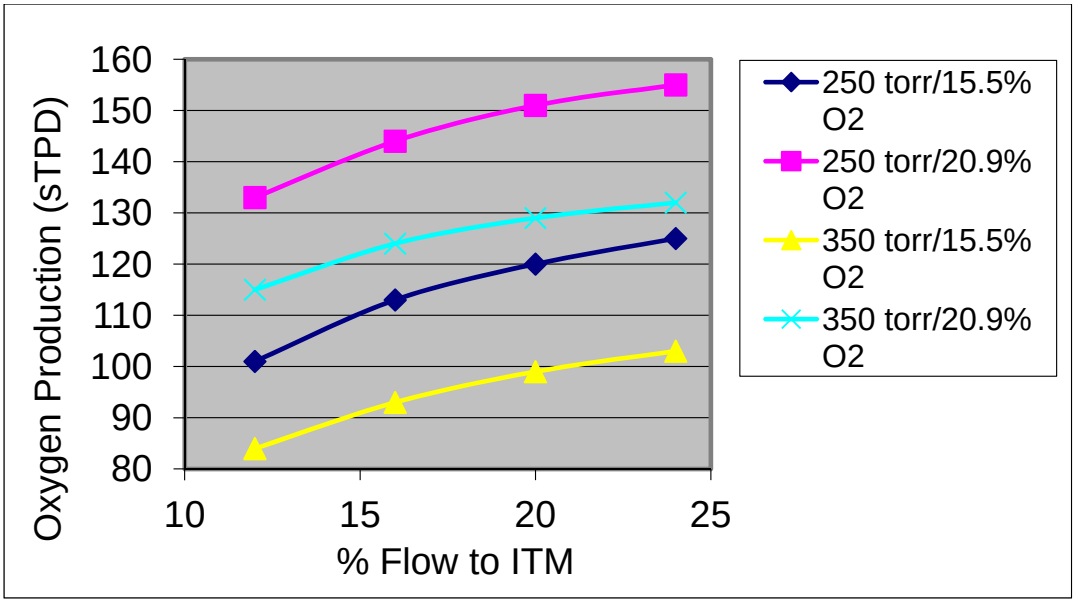

Figure 11-2. Effect of air flow to a fixed bed of modules on oxygen production for two different permeate pressures and two different preheating options.

TASK 14.0 TABLE OF CONTENTS

TASK 14.0 MATERIALS DEVELOPMENT 4

14.0 SCOPE 4

14.1 MEASUREMENT OF ITM OXYGEN MATERIAL PROPERTIES 4

POWDER CHARACTERIZATION 4

Background 4

Quality Control Methodology 5

Results and Conclusions 5

EXPANSION CHARACTERISTICS 8

Background 8

Thermal and Chemical Expansion 8

Dilatometry 9

Experimental Methods 10

Standard Wafers 12

Base Piece 15

Improved Spacers 18

Domed End Caps 21

Cooling Cycle 23

Parts Testing (Dilatometry at Constant Temperature) 24

Experimental Method 24

Bars 25

Wafer Bars/Sections 29

Advanced Architecture Wafer Bars 31

Experimental: Gas Switch Time and Bell Housing Development 32

Base Piece 35

Spacer 39

Parts Testing (Effect of Water on Expansion) 40

Experimental Method 40

Porous bars 43

MECHANICAL PROPERTIES 46

Background *46*
Flexural Strength 46
Burst 48
Seal Torsional Friction 48
Creep 48
Elastic Properties 49
Experimental Methods *49*
Flexural Strength *55*
Burst *56*
Base Piece 56
Wafer 58
Seal Torsional Friction *59*
Creep *63*
Compressive Creep 69
Elastic Properties *72*
14.1.2 SPECIFICATION OF ALLOWABLE PROCESS GAS COMPOSITION 73
Background *73*
Contaminants 74
Refractory: $Si(OH)_4$ from Silica (SiO_2) *74*
Experimental Method 74
Results 76
Flow Path Testing of Refractories 76
SO_2 Adsorption 77
Recommendation for SO_2 Monitoring in the ISTU 80
Metal: Chromia *82*
Flow Path Testing 82
Coatings 84
Chromium Effect on Flux 85
Moisture and Carbon Dioxide *86*
Getter development *89*
Sulfur Dioxide Getter 89

Chromium Getter 90
14.1.3 DEVELOPMENT OF ITM OXYGEN MATERIALS 92
Setter Material 92
Background 92
Results 92
Stability of ITM Ceramics 93
Background 93
Phase Stability of Perovskites 94

PHASE III RESULTS AND DISCUSSION

TASK 14.0 MATERIALS DEVELOPMENT

14.0 Scope

In Task 14.0, Air Products, Ceramatec Inc., and the Pennsylvania State University (Penn State) collaborate to (i) conduct the materials development required to support materials selection for the various components of the ITM Oxygen system, (ii) measure properties of the ITM Oxygen Ceramic to support further development and refinement of the engineering models used to predict the performance of ITM Oxygen Ceramic membrane modules, and (iii) to refine the thermodynamic models of the ITM Oxygen Ceramic. The thermodynamic models are used to predict reactivity of the ITM Oxygen Ceramic with various potential feed-air impurities and poisoning chemistries, and complement experimental testing of the effects of poisons on membrane material chemistry. Tools and methods for the assessment of parts intermediate in the production process are also investigated, as are promising new ITM Oxygen materials identified under Task 6.

14.1 Measurement of ITM Oxygen Material Properties

Powder Characterization

Background

The ITM ceramic perovskite formulation, "AP2k," belongs to the material family described in Claim 1 of U.S. Patent No. 6,056,807 as $Ln_xA_x'A_x''B_yB_y'O_{3-z}$, in which Ln is a *f* block Lanthanide, A' is selected from Group 2 of the Periodic Table, and A" is chosen from Group 1, 2, 3, and the *f* block Lanthanides, and B and B' are chosen from the *d* block Transition Metals, with the exception of titanium and chromium. For the purposes of description, AP2k will be generalized here as having the formula $(AA')(B)_yO_{3-z,}$ where y is between 1 and 1.1 and z is chosen for charge neutrality. The performance of the ITM ceramic is sensitive to the A/A' ratio, and the (A+A')/(B+C+D) ratio where C and D are metal impurities such as chromium and other transition metals. The maximum acceptable deviation in the ratios is plus/minus four percent; thus it is important that the starting materials such as the transition metal oxides (BOx's) have low levels of impurities. Ceramatec produced the powders for ITM component fabrication (e.g., wafers, end caps, etc).

Quality Control Methodology

Air Products and Ceramatec instituted quality control measurements to ensure the powder and the metal oxide blends were within specification. Wavelength dispersive X-ray fluorescence (WDXRF) spectroscopy was used to analyze powder samples and metal oxide blends. WDXRF is a variation of X-ray fluorescence (XRF) spectroscopy, in which X-rays incident on a sample excite photons with energies characteristic of the atoms in the sample. The WDXRF technique further splits the photon emission into characteristic wavelengths for broader and more rapid simultaneous elemental analysis of solid samples.

Air Products performed a study to determine the repeatability of the WDXRF technique by re-analyzing a test sample prepared in July 2008. Figure 14-1 shows the ratio of the measured cation ratios to the target cation ratio from repeated measurements of the sample.

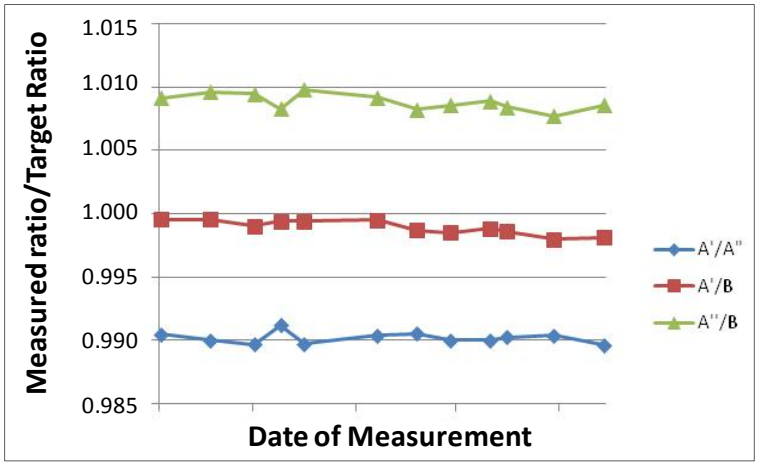

Figure 14-1. The measured cation ratios to the target cation ratios from the July 2008 sample.

There was little variation, thereby validating the technique. This "standard" bead was reanalyzed with each new batch of samples as a means to track the repeatability of the WDXRF technique. The standard bead was also used to correct changes in cation sensitivity. Air Products also analyzed BO_3 samples to determine impurity levels.

Results and Conclusions

Ceramatec generated samples of powder batches during each powder preparation conducted in the Process Development Facility (PDF) under Task 17. Contaminant levels in the transition metal oxide (BOx) blends proved to be very low and are not reported here.

Figure 14-2 is a typical graph showing the A/A' ratio relative to the target ratio for a set of samples of the AP2k powder samples.

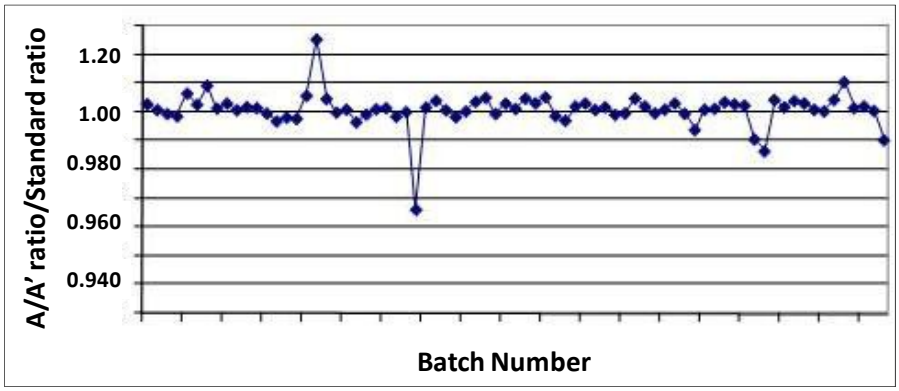

Figure 14-2. The A/A' ratio of samples versus the standard ratio.

Figure 14-3 graphs the number of samples, the rejected sample and the control samples analyzed by quarter. Table 14-1 documents the reported number of samples analyzed by Quarter and the reject rate.

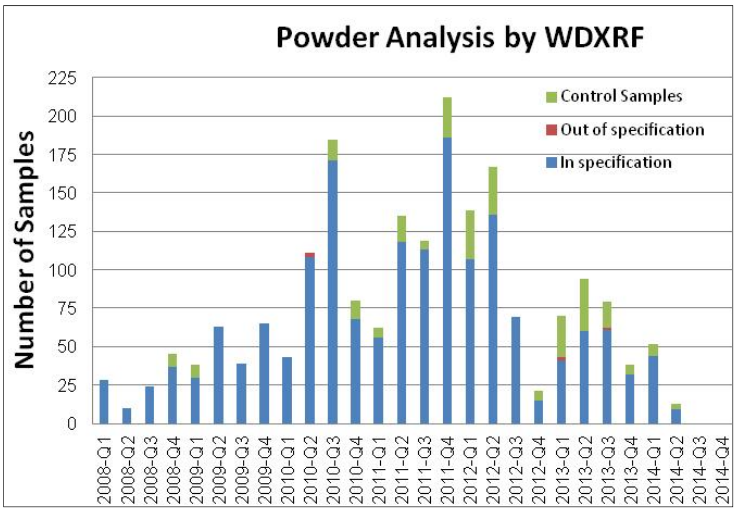

Figure 14-3. Samples analyzed by WDRXF by quarter, accepted, rejected and controls.

Table 14-1. Number of WDXRF samples analyzed by quarter.

Quarter	Samples Analyzed	Samples rejected	Control Samples
2008-Q1	28	0	0
2008-Q2	10	0	0
2008-Q3	24	0	0
2008-Q4	27	0	8
2009-Q1	30	0	8
2009-Q2	63	0	0
2009-Q3	39	0	0
2009-Q4	65	0	0
2010-Q1	43	0	0
2010-Q2	114	3	0
2010-Q3	171	0	14
2010-Q4	68	0	12
2011-Q1	56	2	6
2011-Q2	118	0	17
2011-Q3	113	0	6
2011-Q4	186	0	26
2012-Q1	107	0	32
2012-Q2	136	0	31
2012-Q3	69	0	
2012-Q4	15	0	6
2013-Q1	43	2	27
2013-Q2	60	0	34
2013-Q3	62	1	17
2013-Q4	32	0	6
2014-Q1	44	0	8
2014-Q2	9	0	4
2014-Q3	0	0	0
2014-Q4	0	0	0
Total	**1734**	**8**	**262**

More than 1,700 samples were analyzed during the period 2008-Q1 through 2014-Q4. Fewer than eight batches where rejected and the source of contamination of two of the batches was quickly determined. The data clearly establishes that the quality control of power production is excellent (i.e., 99.5% within specification). It is further expected that the control will be tighter at the Cerfab facility given the larger batch size.

Expansion Characteristics

Background

Thermal and Chemical Expansion

As is typical with other materials, ITM components expand with an increase in temperature. The change in length due to thermal expansion is related to temperature change by the "linear expansion coefficient" α_L. The fractional change in length per degree of temperature change can be written as:

$$\alpha_L = \frac{1}{L}\frac{dL}{dT}$$

Where L is a length measurement and dL/dT is the rate of change of that linear dimension per unit change in temperature. An estimate of the amount of thermal expansion can be described by the material **strain** given by $\epsilon_{thermal}$ and defined as:

$$\epsilon_{thermal} = \frac{(L_{final} - L_{initial})}{L_{initial}}$$

Thus, the change in either the strain or temperature can be estimated by:

$$\epsilon_{thermal} = \alpha_L \Delta T$$

Conversely, α_L can be estimated by measuring the strain and temperature differential. The control of thermal expansion in brittle materials is a key concern. For example, both glass and ceramic are brittle. A temperature gradient will cause uneven expansion which induces thermal stress which can lead to fracture. Figure 14-4 shows an example of a drinking glass that has fractured due to uneven thermal expansion after pouring of hot liquid into the otherwise cool glass.

Figure 14-4. Example of brittle fracture caused by a thermal expansion stress.

The same holds true for ITM ceramic. If a temperature gradient within a part is of sufficient magnitude to give rise to differential stresses that exceed the ITM material strength, a fracture may occur. This is true for temperature gradients within a single part as well as between joined parts. The thermal gradient within a part (and thus the induced stress) generally arises from the boundary conditions around the part and depends on the material thermal diffusivity.

The ITM perovskite material loses or gains oxygen from its crystal structure to maintain internal charge balance, and therefore maintains a population of vacancies in its oxygen sub-lattice. In the case of AP2k, loss of oxygen within the crystal structure causes the material to expand, giving rise to a property known as "chemical expansion." By analogy, the equation below describes the equilibrium strain due to oxygen vacancy changes in the material:

$$\varepsilon = \alpha \, \Delta O_v$$

where α is the "oxygen vacancy expansion coefficient" and ΔO_v is the change in oxygen vacancy fraction. O_v is a function of temperature and the oxygen available in the system. When the temperature of the material is changed, the equilibrium O_v value also changes. Oxygen will tend to diffuse in or out of the part to satisfy the new equilibrium requirement. For finite rates of oxygen transport, an Ov gradient will develop in the material, causing differential stain and internal stress. The O_v gradient (and strain gradient) is reduced through the transport of oxygen.

In general, the oxygen transport rate in or out of a part composed of perovskite is a complex function of the part geometry, temperature, and prevailing boundary conditions. Gas-phase mass transfer resistance may be reduced in practice, for example, by effecting good mixing around the part or by working in a pure oxygen environment.

Dilatometry

Dilatometry is a technique in which a dimension of a material (or part) under negligible load is measured as a function of changing conditions. Dilatometry has been used to determine the expansion behavior of the ITM membrane material and components as a function of temperature, oxygen partial pressure and gas composition.

When the temperature in the dilatometer is changed, a non-equilibrium strain condition will occur unless the rate of temperature change is infinitely slow. The differential between the

specimens' equilibrium thermal strain and actual strain is influenced by its dimensions/geometry, structure (e.g., density) and thermal conductivity. The same is true for the expansion/contraction associated with oxygen vacancy fraction where oxygen diffusivity and surface kinetics depend on temperature and the prevailing oxygen partial pressure in the gas phase around the part.

Because the ITM materials and parts have a relatively low resistance to thermal conduction, significant thermal gradients in parts typically do not arise during dilatometry experiments. However, oxygen transport resistances in the parts can be appreciable. Thus, experiments in which either the temperature is changed with time at constant oxygen partial pressure P_{O2} (giving rise to gradients of oxygen vacancy fraction) or P_{O2} is varied with time at constant temperature can result in time-dependent dimensional changes in parts and lead to understanding of transport properties of specific samples. Manipulation of gas-phase conditions can give insight into surface resistances relative to bulk diffusive resistance to oxygen transport. In addition, the effects of chemical expansion can be isolated relative to those of thermal expansion by measuring the expansion characteristics of ITM test parts relative to an ITM reference part of known (and generally rapid) transport properties.

Experimental Methods

Air Products conducted dilatometry experiments to determine the differential strain between a "reference bar" and ITM component parts at various rates of temperature increase (e.g., 30°C/hr). The data were used to identify differences in component behavior, refine finite element analyses and assess changes in component geometries and structure to minimize stress. The work was instrumental in specifying the joining cycle and ISTU startup temperature ramp rate and the design of the ITM component parts.

Several small- and a large-scale dilatometers were used to conduct the experiments. Figure 14-5 is a photograph of one of the small-scale dilatometers. A porous reference bar is on the left and the test specimen is on the right. Figure 14-6 is a photograph of an experimental setup in the large-scale dilatometer showing the test specimen (i.e., a stack of spacers) and a porous reference bar in the background.

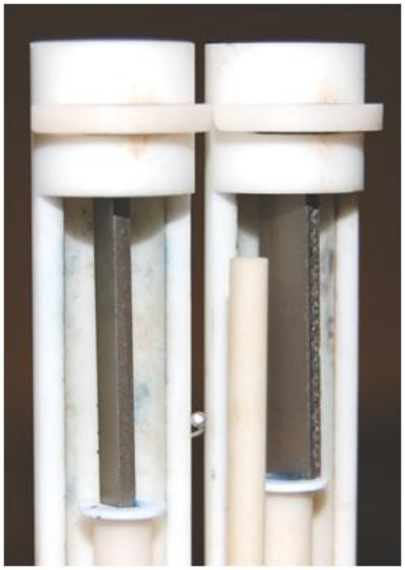

Figure 14-5. Photograph of a bar cut from active area of wafer (right stage) and a porous bar (left stage) used in the transient dilatometer experiment.

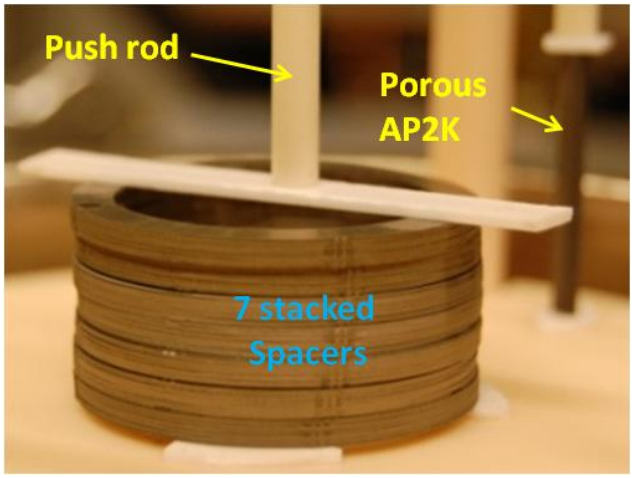

Figure 14-6. Photograph of the large dilatometer experimental setup. Stacked spacers are the test specimen (foreground) and the reference bar is in the background.

The dilatometer is fitted with a gas-purged sample cell and a heating stage to perform a full temperature cycle (ambient to operating to ambient) while maintaining a constant oxygen partial pressure around the part.

After the test specimen and reference bar were placed underneath the measuring rods, a flow of gas with a specific composition (typically air, 100% nitrogen or 100% oxygen) was started. The gas was then heated at a specific rate (e.g.,30°C/hr). The expansion of the test specimen and reference bar were measured as a function of temperature and the strain rate was calculated

based on the appropriate length. The reference bar strain was subtracted from the specimen strain (i.e., differential strain) and plotted as a function of temperature.

Air Products carried out dilatometry for various parts and subcomponents in atmospheres of constant composition and pressure. In all experiments, the temperatures of the sample and reference parts were substantially the same at any one time, thus eliminating any contribution of differences in thermal expansion in the results. Moreover, based on previous work, the parts were known to reach rapid thermal equilibrium with the dilatometer stage.

Standard Wafers

Dilatometry measurements were conducted on a standard ¼ wafer. Figure 14-7 shows the experimental setup.

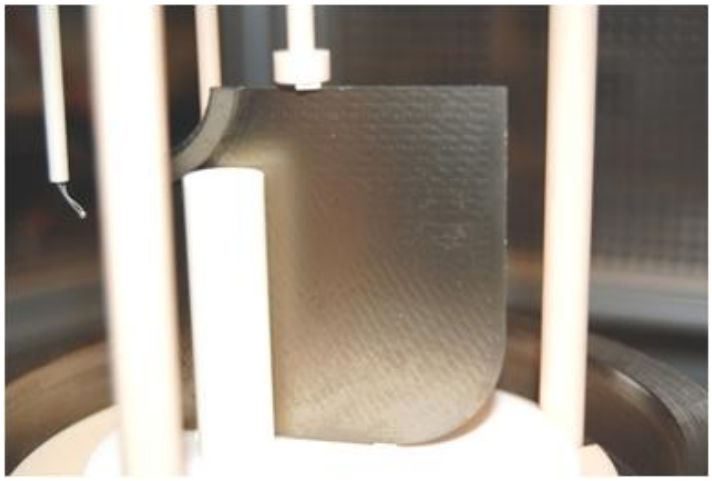

Figure 14-7. Dilatometer set up showing a standard ¼ wafer positioned in the large-scale dilatometer. The reference bar is behind the wafer.

The sample was heated and cooled at 0.5C/min. along with the reference bar. The ¼ wafer cracked during testing. Figure 14-8 shows the expansion of the wafer and reference bar and the differential. A wafer strip from the active area of a Slot Pattern #1 wafer and a porous bar (Figure 14-9) were heated to elevated temperature and then cooled at 30°C/hr in 100% O_2. Figure 14-10 shows the differential strain between the parts during cooling.

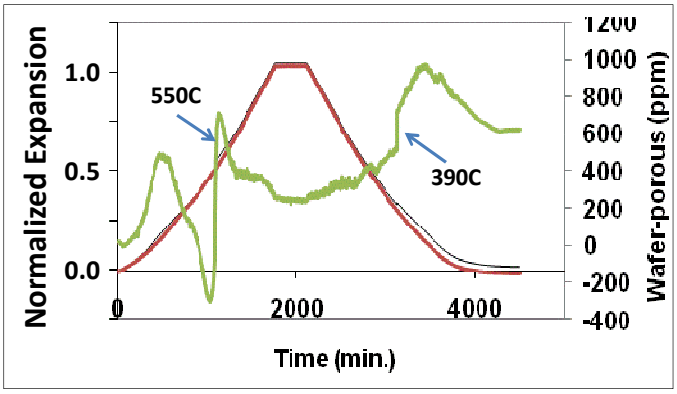

Figure 14-8. Expansion of ¼ standard wafer compared to a reference bar. Normalized expansion on the left axis is plotted against time for the porous reference bar and wafer section. The difference between the two curves is shown on the right axis (green curve).

Figure 14-9. Wafer strip (*left*) and a reference bar (*right*) loaded in the dilatometer.

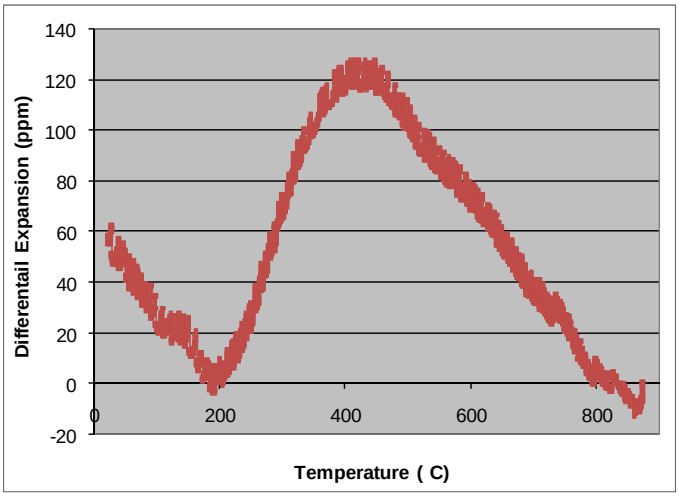

Figure 14-10. Differential strain of wafer strip–porous bar during cooling at 30°C/hr in oxygen.

The magnitude of the differential strain was very small, indicating the wafer strip is able to stay equilibrated or nearly equilibrated with the gas phase at this cooling rate.

Tests were conducted to measure the locked-in vacancy concentration of a wafer as a function of the radial distance from the center of the wafer. Differential strains of bars cut from various locations of the wafer are shown in Figure 14-11.

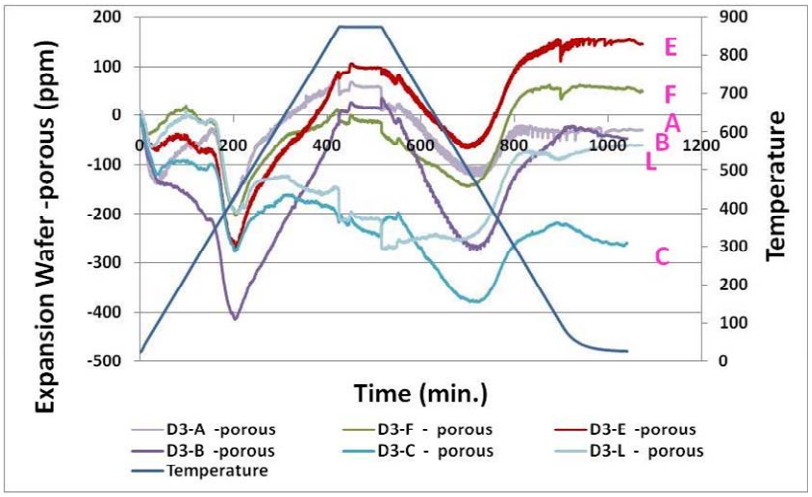

Figure 14-11. Differential strain of wafer bars relative to a porous reference.

Bar A was closest to the center wafer hole, and bar L was closest to the wafer corner. It was expected that these bars would have the most difference. There was no apparent correlation between residual strain and bar position. Figure 14-12 shows the expansion of bars B and C after two consecutive cycles.

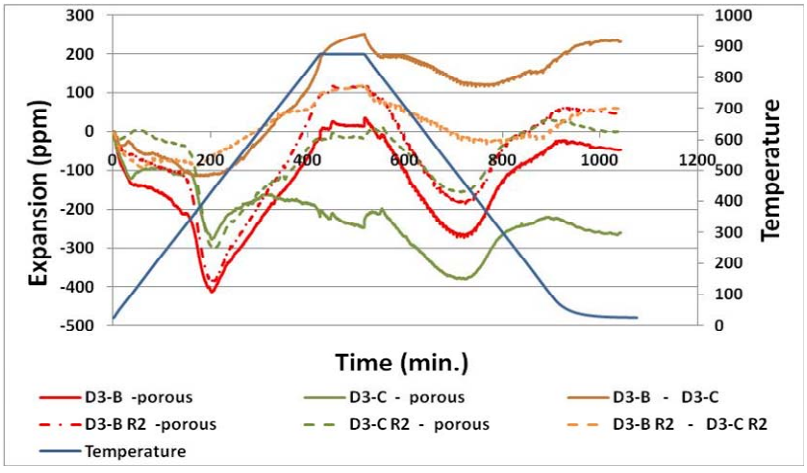

Figure 14-12. Differential strain of wafer bars B and C over two consecutive thermal cycles.

The overall residual strain between the bars ranged from 125 to -250 ppm. The bar expansions matched closely after the second cycle, suggesting that some residual strain was relieved during the first cycle.

Base Piece

Air Products measured the differential expansion of a base piece diameter at heating rates of 10ºC/hr, 15ºC/hr. and 30ºC/hr. Figure 14-13 shows the experimental setup in the dilatometer.

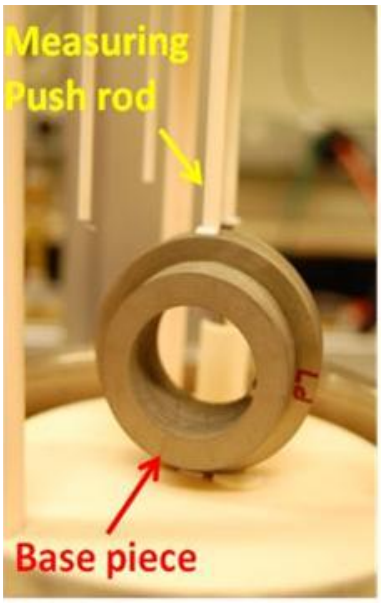

Figure 14-13. Dilatometer setup showing a base piece sample positioned on its side to enable the expansion of its diameter to be measured. The reference bar is behind the base piece.

The base piece is oriented on its side to enable an expansion study of the larger diameter at its base. Figure 14-14 shows the differential strain of the base piece diameter during initial and repeat tests.

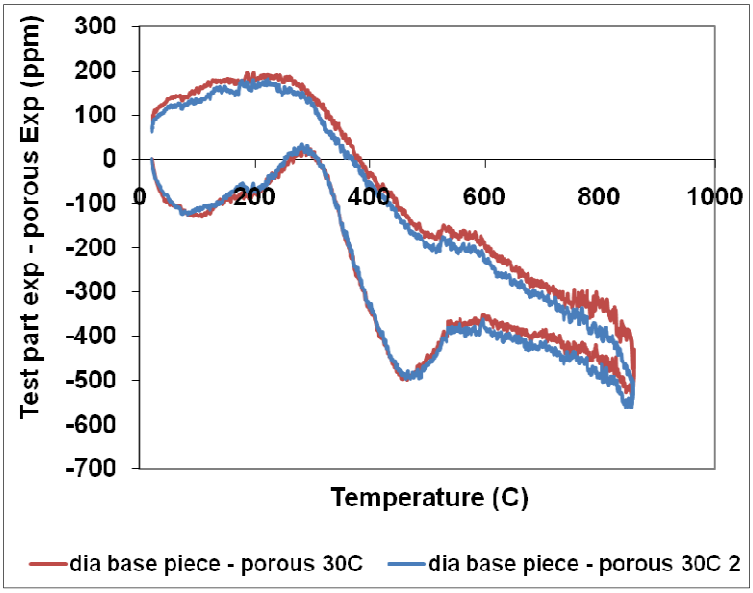

Figure 14-14. Base piece expansion differentials for two experiments heated and cooled at 30ºC/hr. Graph shows good repeatability between the runs.

During heating the expansion difference between the base piece and the reference bar reach a high of -510ppm+-50ppm.

Figure 14-15 shows the result for heating rates of 10ºC/h and 15ºC/hr.

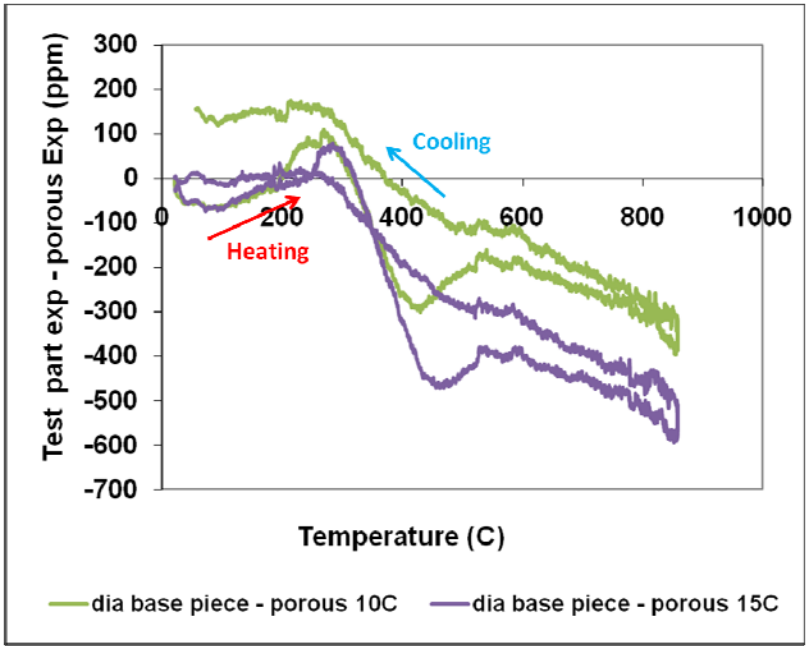

Figure 14-15. Base piece expansion differentials at heated rates of 10ºC/hr and 15ºC/hr.

The base piece heated to 10ºC/hr accumulated less strain compared to the sample heated at 15ºC/hr. It is speculated that some of the difference may be due to the different thermal histories that the part had at the beginning of each experiment (i.e., residual strain).

The height differential strain of a base piece was measured at heating rates of 15ºC/hr and 30ºC/hr. Figures 14-16 and 14-17 show the differential strain results of the height and the previous results (above) for the diameter at heating rates of 15ºC/hr and 30ºC/hr respectively.

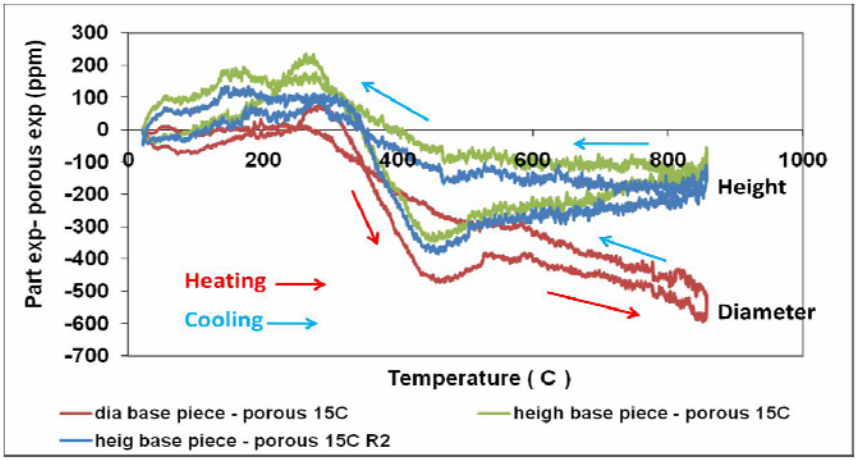

Figure 14-16. Base piece height and diameter differential strain at a heated rate of 15ºC/hr.

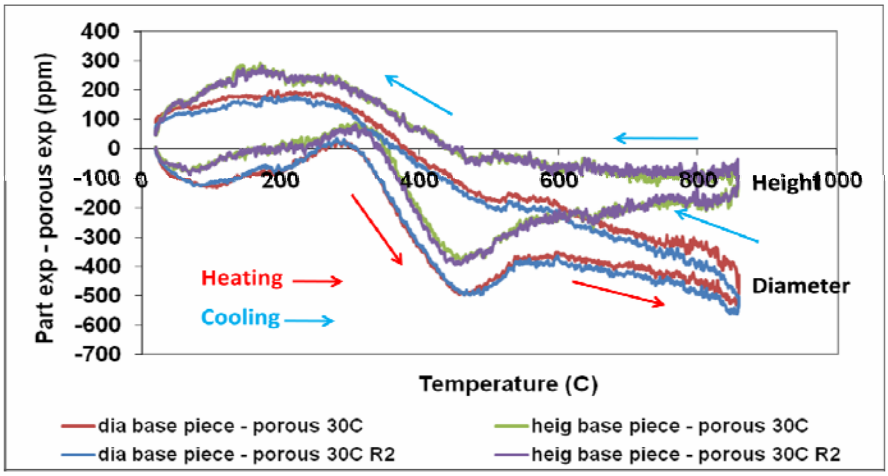

Figure 14-17. Base piece height and diameter differential strain at a heated rate of 30ºC/hr.

The differential strain in the diameter was greater than that of the height. This means there was more residual strain in the diameter at room temperature. This expansion anisotropy could have been caused by the anisotropic microchannels in the base piece.

In the above work, the gas oxygen concentration was 21%. Additional work was completed in an atmosphere of 100% oxygen (P_{O2} = 1.0 atm) to eliminate any gas-phase mass transfer resistance. Figure 14-18 shows the differential strain of a base piece height in oxygen.

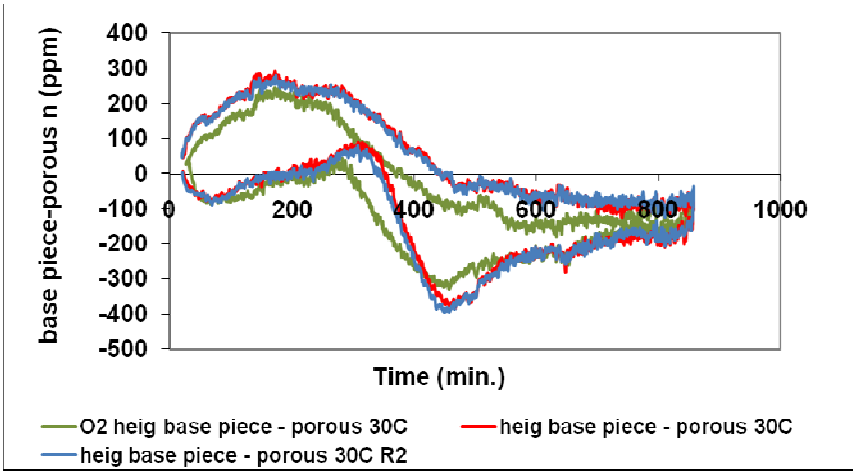

Figure 14-18. Base piece height differential strain in oxygen and air (from above).

During heating in oxygen, the part became active at a lower temperature compared to heating in air, indicating that gas-phase mass transfer resistance is most appreciable at low temperature. Such activity is to be expected for transport in and out of slotted parts. It is important to note that the parts were preconditioned in oxygen at elevated temperature and cooled in oxygen before they were used in the oxygen expansion experiment; doing so would rid the "trapped" gas (residual nitrogen) in the part.

Improved Spacers

The diameter differential strain of an improved "OD2" spacer design was measured. The new spacer was made of slotted layers that communicated with the inner diameter surface. Figure 14-19 shows the results.

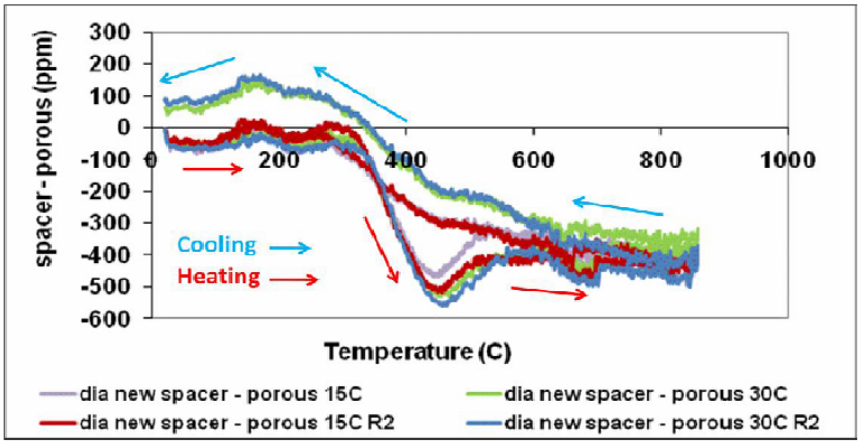

Figure 14-19. Diameter differential strain of the OD2 spacer design.

These results show good resolution and repeatability between runs. The expansion result was similar to the diameter base piece expansion as shown in Figure 14-20. The base piece was made from the same slotted layers as the spacer.

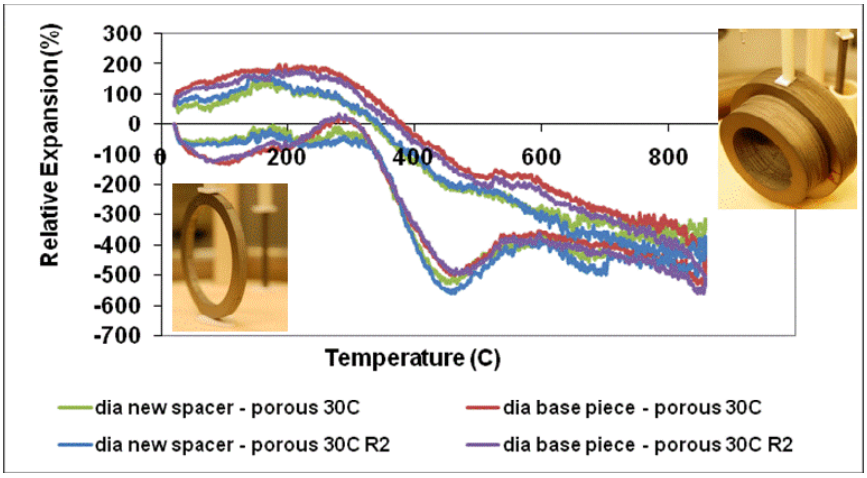

Figure 14-20. Diameter differential strain of OD2 spacer design and a base piece.

In the above work, the gas oxygen concentration was 21%. Additional work was completed in in an atmosphere of 100% oxygen (P_{O2} = 1.0 atm).

Figures 14-21 shows the differential strain of the spacer diameter in oxygen and includes the data from Figure 14-20 taken in air as reference.

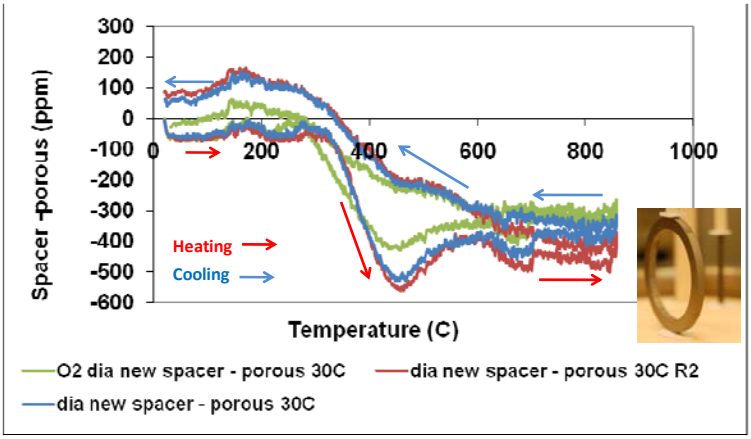

Figure 14-21. OD2 spacer diameter differential strain in oxygen and air.

During heating in oxygen, the ITM Oxygen ceramic (AP2K) became active at a lower temperature compared to heating in air, indicating that gas-phase mass transfer resistance is most appreciable at low temperature. Such activity is to be expected for transport in and out of slotted parts. It is important to note that the parts were preconditioned in oxygen at elevated temperature and cooled in oxygen before they were used in the oxygen expansion experiment; doing so would rid the "trapped" gas (residual nitrogen) in the part.

Standard-design (OD) spacers were heated at 30°C/hr, 80°C/hr, 120°C/hr and 180°C/hr. Figure 14-22 shows the differential strain relative to that of a prototype advanced architecture wafer at each of the heating/cooling conditions.

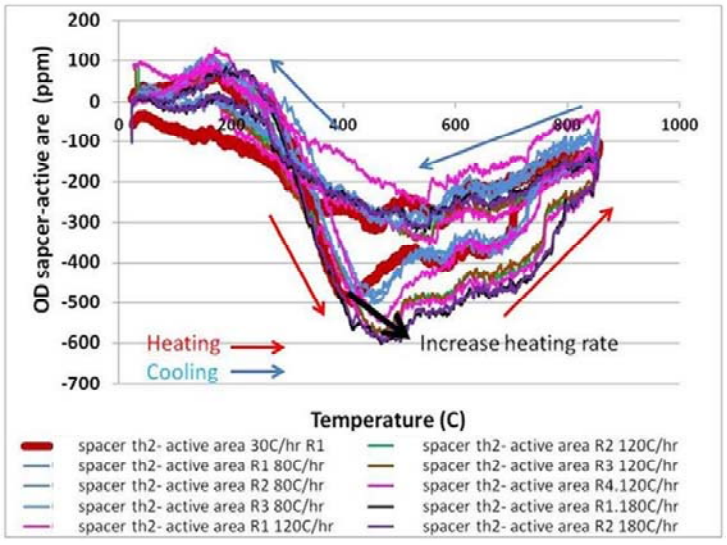

Figure 14-22. Differential strain between a standard (OD) spacer and a prototype advanced architecture wafer at various heating cooling rates.

Initial wafer expansion was faster compared to the OD spacer, resulting in a large negative differential at 425°C-450°C. The magnitude increased slightly as the heating rate increased. The maximum shifted to a higher temperature as well. It was concluded that there is no advantage in heating modules faster through the kinetically slower/lower temperatures to minimize stress.

Domed End Caps

Figure 14-23is a photograph of the experimental setup of a domed end cap and reference bar loaded in the large sample dilatometer.

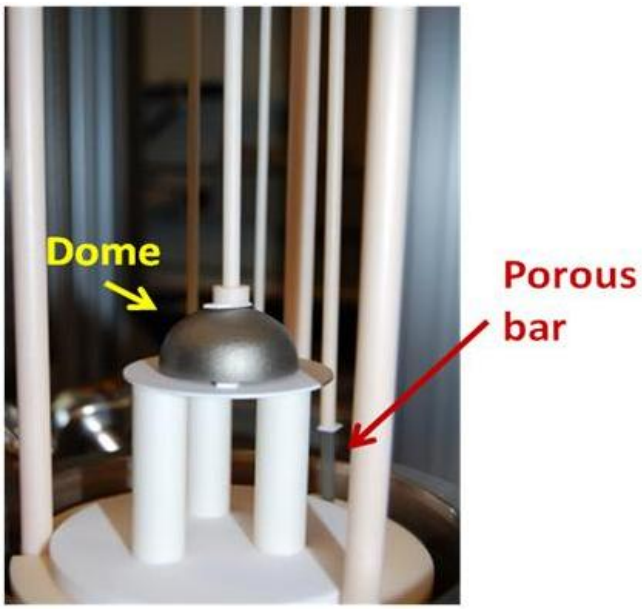

Figure 14-23. Experimental setup in the large-scale dilatometer to measure differential strain relative to a reference bar.

Figures 14-24 and 14-25 are data from tests conducted on End Caps #30 and #34.

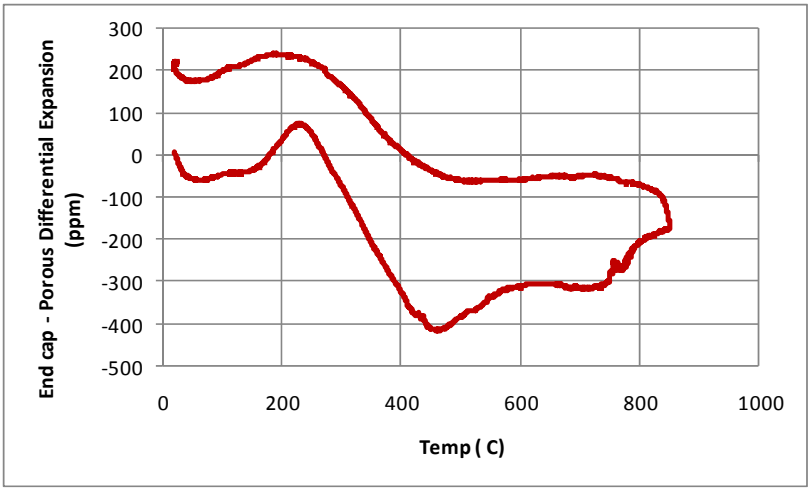

Figure 14-24. Differential expansion of End Cap #30 when heated and cooled at 10°C/hr in air.

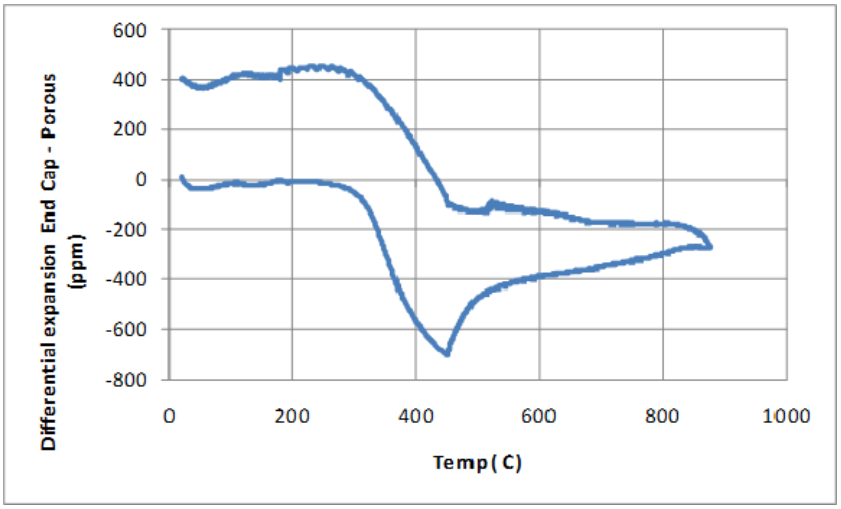

Figure 14-25. Differential expansion of End Cap #34 when heated/cooled according to a temperature ramp used in module testing.

End Cap #30 was heated at 10°C/hr. During heating, significant differential expansion begins to occur around 275°C as the reference bar is able to lose oxygen and expand faster than the end cap. At 450°C, the differential expansion starts to decrease for the remainder of the heating, as the end cap becomes more equilibrated with the gas phase. During cooling, there is little differential expansion until the temperature decreases to <450°C, at which point the end cap can no longer stay equilibrated with the gas phase at this cooling rate.

The strain differential upon cooling did not return to zero. This indicates that the end cap had "residual" or non-equilibrium strain and non-equilibrium oxygen vacancies. This residual strain can be relieved by increasing the temperature and apply a very slow cooling rate.

In the testing of End Cap #34 (Figure 14-25), the system temperature was increased according to the typical temperature ramp. The behavior is similar to End Cap #30. During heating, significant differential expansion begins to occur ~300°C. At 450°C, the differential expansion starts to decrease for the remainder of the heating, as the heating rate is decreased. During cooling, there is little differential expansion until the temperature decreases to <450°C, at which point the cooling rate increases and the end cap can no longer stay equilibrated with the gas phase.

As seen with End Cap #30, the strain differential upon cooling did not return to zero, indicating that the end cap had "residual" or non-equilibrium strain and non-equilibrium oxygen vacancies.

Cooling Cycle

Differential dilatometry experiments were conducted to determine the difference in strain rate of a standard wafer rim, a spacer, standard wafer active area as compared to a porous bar at various cooling rates (Figures 14-26, 14-27 and 14-28). The changes in differential strain were minimal, and it was concluded that stress would not be materially increased at the faster cooling rate.

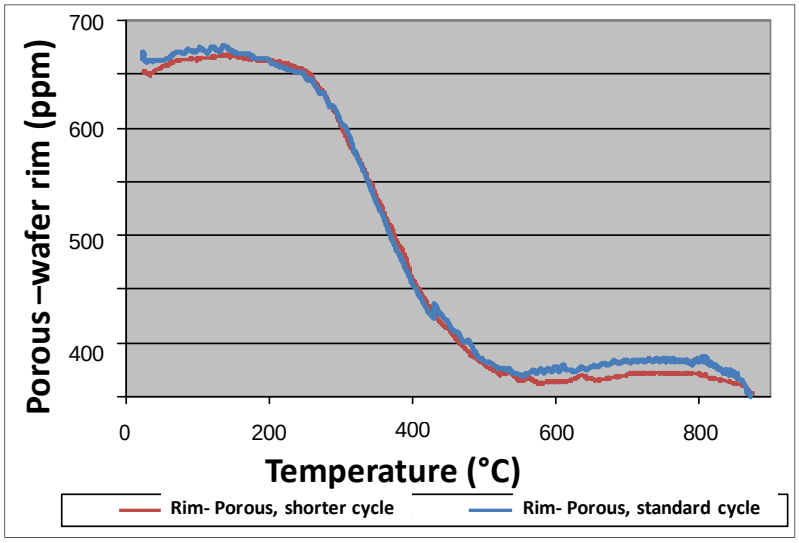

Figure 14-26. Comparison of the differential expansion of a wafer rim versus a porous bar during cooling at either the standard or shorter schedules.

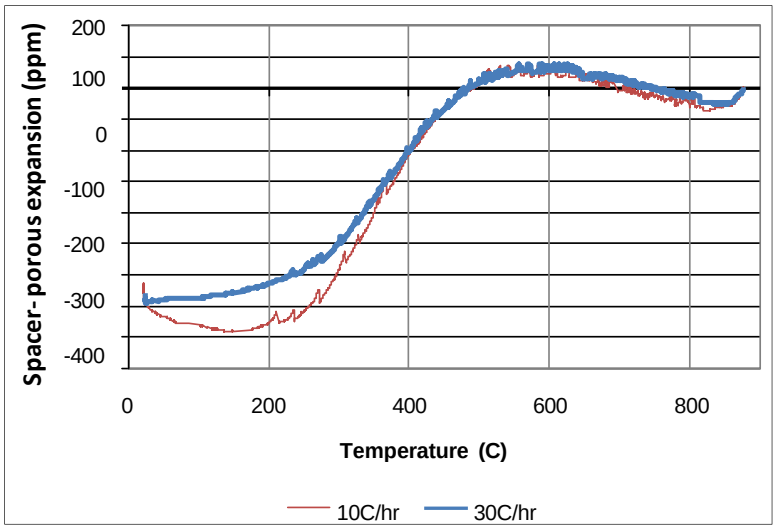

Figure 14-27. Differential expansion of a section of a spacer and a porous bar during cooling at constant temperature ramp rates in air.

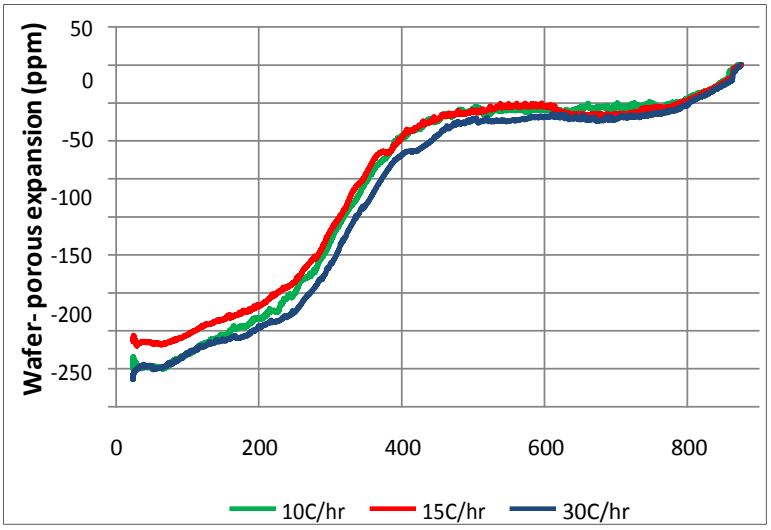

Figure 14-28. Differential expansion of an active wafer section and a porous bar during cooling at constant temperature ramp rates in air.

Parts Testing (Dilatometry at Constant Temperature)

Experimental Method

Air Products also conducted dilatometry experiments to determine the differential strain between a "reference bar" and ITM component parts during step changes in oxygen partial pressure. The data were used to identify differences in component behavior, to refine finite element analyses and assess changes in component geometries and structure to minimize stress. This work was

instrumental in specifying the ISTU startup pressure and permeates ramp rates and the design of the ITM component parts.

Both small- and large-stage dilatometers were fitted with the capability to test the effects of atmosphere on expansion. After the test specimen and reference bar were placed underneath the measuring rods, a flow of gas with a specific composition (typically air, 100% nitrogen or 100% oxygen) was started. The flow was continued and the temperature was increased to a specific (and constant) value. The specimens where allowed to reach their equilibrium expansion. The gas composition was then changed, and the change in strain was measured as a function of time. The data are used to determine the impact of pressure on the ITM material and component parts and to assess diffusivity.

Bars

The small-scale dilatometer was used to measure expansion of a dense bar relative to a porous reference bar of the same material composition. The dense ceramic can be slow to achieve oxygen equilibrium levels relative to the reference bar because of slower oxygen diffusion in the dense part. The part will expand or shrink during a partial pressure change depending on the temperature and amount of oxygen in the part.

Figure 14-29 displays data collected during the transient dilatometry experiment at 450°C when the gas was switched from 0.5% O_2 to 100% O_2.

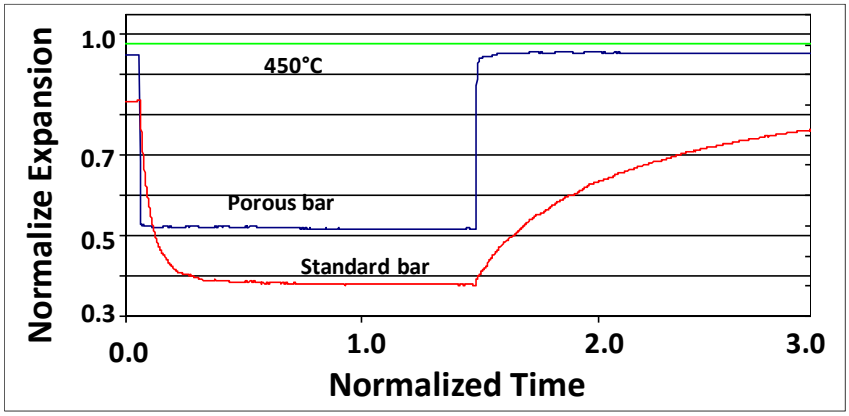

Figure 14-29. Transient diffusion response of a dense ITM ceramic bar at 450°C.

The response of the dense bar is much faster when switching from 0.5% O_2 to 100% O_2 than from 100% O_2 to 0.5% O_2. This indicates that there is an additional resistance when oxygen diffuses out of the bar than when oxygen diffuses into the bar. This resistance is likely the resistance of the surface reaction. Fitting the data to the transient diffusion solution indicates that the surface kinetic resistance is not significant for the 0.5% O_2 to 100% O_2 switch, at least at the relatively low fluxes achieved for this part. However, the transient diffusion equation does not fit the reduction curve well, possibly indicating that the surface resistance changes during the course of the experiment.

Figure 14-30 presents data from a dilatometer experiment performed on dense AP2K bars at low temperatures relative to normal operating temperatures. The data were compared to an expansion and stress model developed by Ceramatec and to provide relevant data for thermal cycling.

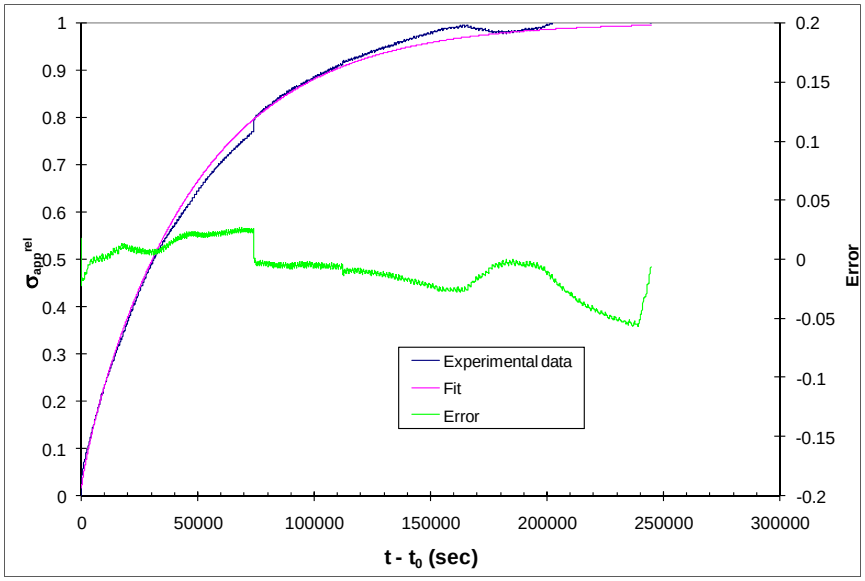

Figure 14-30. Normalized transient response of the dense bar at 400°C during the switch from PO_2=0.005 atm to PO_2=1 atm, along with the fitted response.

Two AP2k dense bars were subjected to the following series of transients at 400ºC: 100% O_2 → 0.5% O_2 → 100% O_2 → 21% O_2 → 100% O_2 → 3% O_2 → 100% O_2 → 0.5% O_2 → 100% O_2. The experiments were done in the small-scale dilatometers 1 and 4. Figures 14-31 and 14-32 show the responses of the dense bars during the four oxidation steps compared to a porous bar.

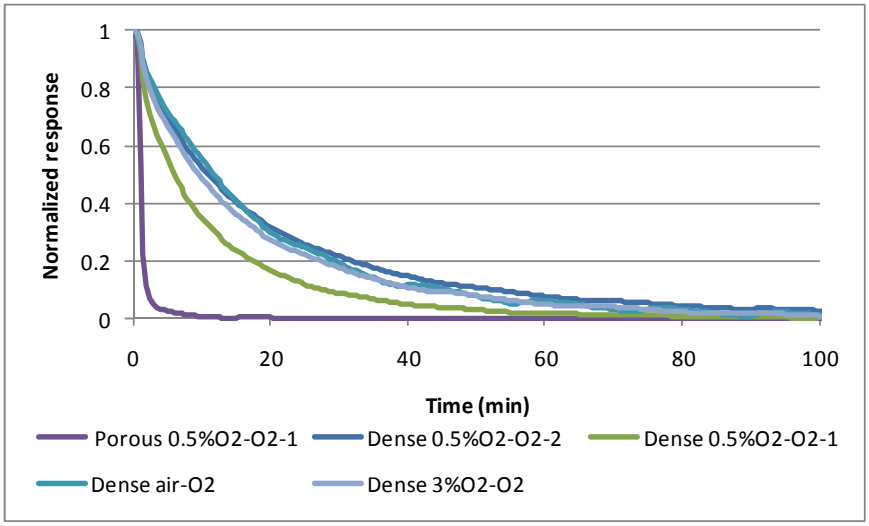

Figure 14-31. Transient response of a dense AP2k bar following step changes in P_{O2} to 100% O_2. Dilatometer 1 at 400°C.

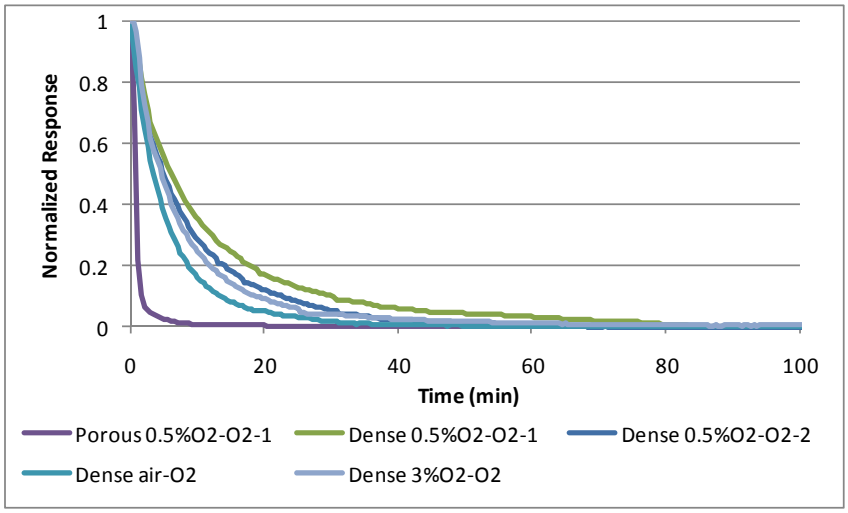

Figure 14-32. Transient response of a dense AP2k bar following step changes in P_{O2} to 100% O_2. Dilatometer 4 at 400°C.

The response times of the two dilatometers are very similar and do not depend on the initial P_{O2} before the step change. Figures 14-33 and 14-34 show the responses of the dense bars in Dilatometers 1 and 4 during four reduction steps.

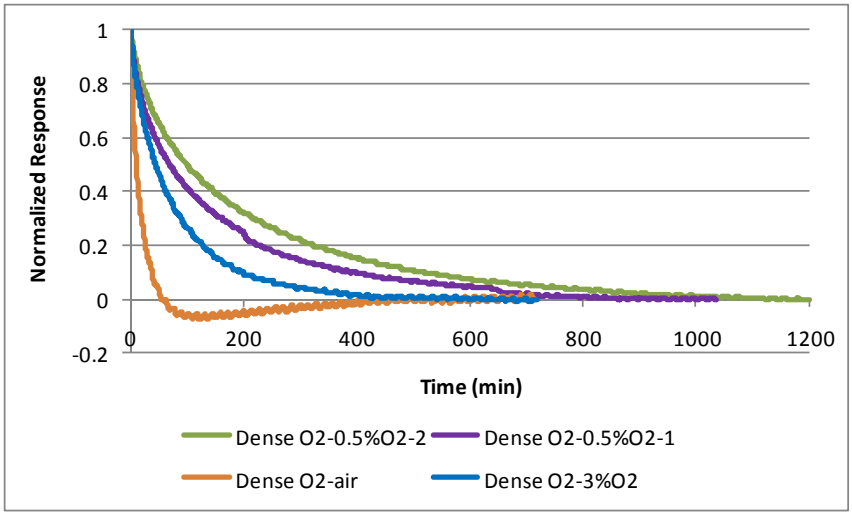

Figure 14-33. Transient response of a dense AP2k bar following step changes in P_{O2} from 100% O_2 to a gas of the given P_{O2}. Dilatometer 1 at 400°C.

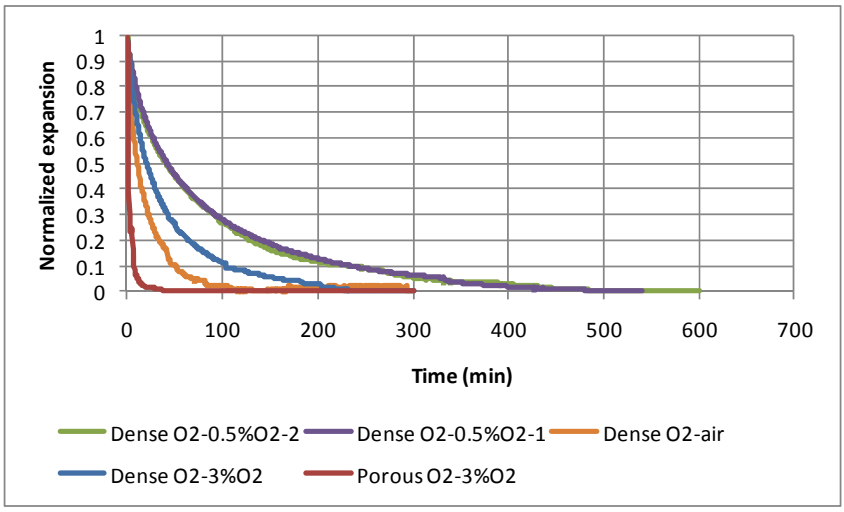

Figure 14-34. Transient response of a dense AP2k bar following step changes in P_{O2} from 100% O_2 to a gas of the given P_{O2}. Dilatometer 4 at 400°C.

The response times of the dense bars during the reduction step were inversely proportional to the P_{O2} of the reducing gas. The response times of the first and last reduction steps with 0.5% O_2 were identical for the sample in dilatometer 4, demonstrating that the surface kinetics of the bar did not degrade during the course of the experiment.

There was a small change in the response times for the bar in Dilatometer 1 during the first and last reduction steps using 0.5% O_2. Dilatometer 1 had a peculiar response for the P_{O2}=0.21 step.

This data was not used for curve fitting. The rate constant is proportional to $\approx P_{O2}^{0.5}$, which is consistent with a reaction mechanism involving oxygen atoms in the rate-determining step.

Wafer Bars/Sections

Air Products sectioned full-size ITM Oxygen wafers to produce specimens that could be used in the small-scale dilatometer to measure the relative equilibration rates during PO_2 transients. The rim was cut from a wafer, and a section of the wafer encompassing the featured layers was cut. After the wafer was cut into the bars, the bars were "resintered" to restore the cut surfaces to a microstructure similar to an as-sintered surface. A porous AP2k bar and the wafer rim bar were then loaded into the dilatometer, heated to 600°C in air, held at 600°C in air until equilibrated,. At that point, the gas in the dilatometer was switched to 100% oxygen, the bars were held in oxygen until equilibrated, and the gas was switched to air. After equilibrating in air, the bars were cooled to 550°C and the gas-switching steps were repeated. The experiment was then repeated with the active wafer section.

The following figures show the transient response upon switching from air to oxygen for the porous bar and the wafer rim (Figure 14-35) and a porous bar and the wafer section (Figure 14-36).

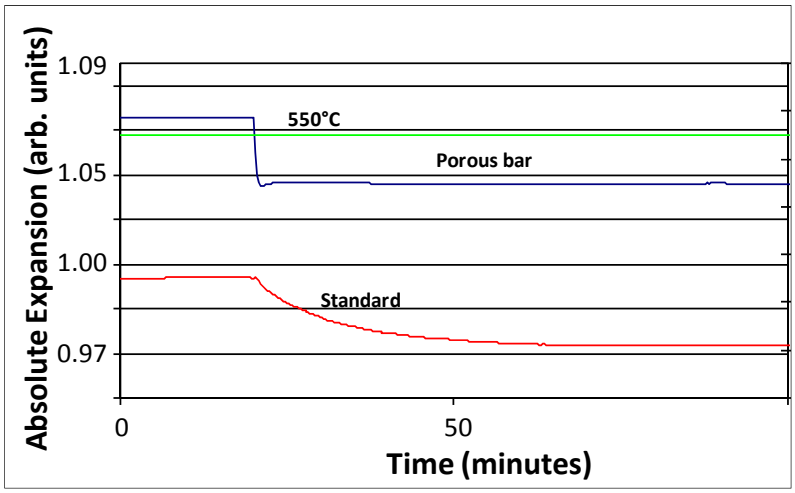

Figure 14-35. Comparison of the transient response of a standard wafer rim and a porous bar during a PO_2 transient from air to 100% oxygen at 550°C.

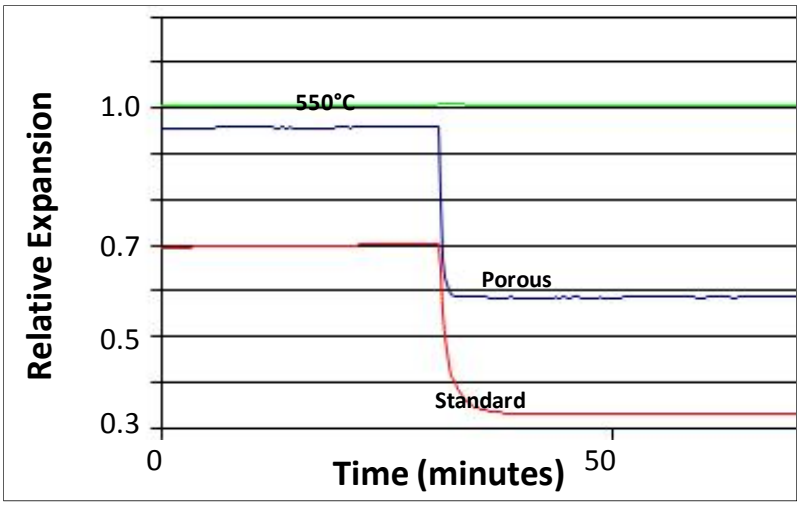

Figure 14-36. Comparison of the transient response of an active standard wafer section and a porous bar during a P_{O2} transient from air to 100% oxygen at 550°C

The transient response of the wafer rim is much slower than the porous bar, whereas the active area wafer bar equilibrates quickly. The slower equilibration of the rim relative to the active area could produce stresses during thermal and oxygen partial pressure transients.

Air Products investigated the surface kinetics of oxygen transport in additional experiments with wafer rim sections. Rims were cut from a wafer, followed by "re-sintering" the parts to establish a typical microstructure on the cut surface by taking the rims through a simulated sintering cycle. Figures 14-37 and 14-38 shows the transient responses measured at 500°C.

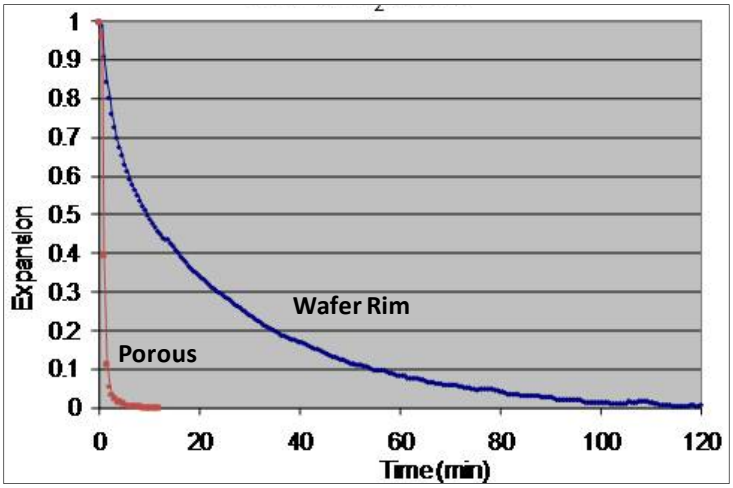

Figure 14-37. Transient response of an AP2k wafer rim and a porous bar at 500°C during step changes in P_{O2} from 1.0 atm O_2 to air.

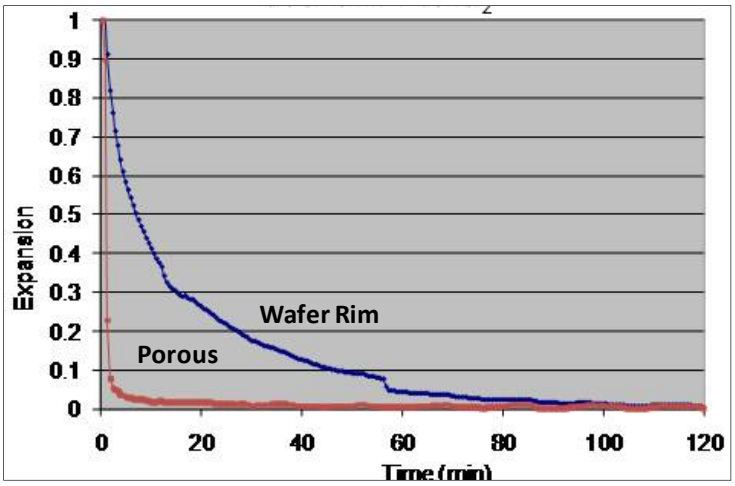

Figure 14-38. Transient response of an AP2k wafer rim and a porous bar at 500°C during step changes in P_{O2} from air to 1.0 atm O_2.

The response time of the wafer rim is nearly the same in both transients, which is an indication that surface kinetics are not a significant resistance relative to bulk oxygen diffusion through the rim at 500°C.

Advanced Architecture Wafer Bars

Air Products initiated transient oxidation experiments with bars made from various exploratory wafer formulations to assess the advanced architecture concepts. These parts were designed to have more rapid equilibration with the gas phase. The transient oxidation response of bars derived from four wafer formulations was measured at 300ºC because the kinetics are too fast at temperatures >400ºC. Figure 14-39 shows the transient response during oxidation.

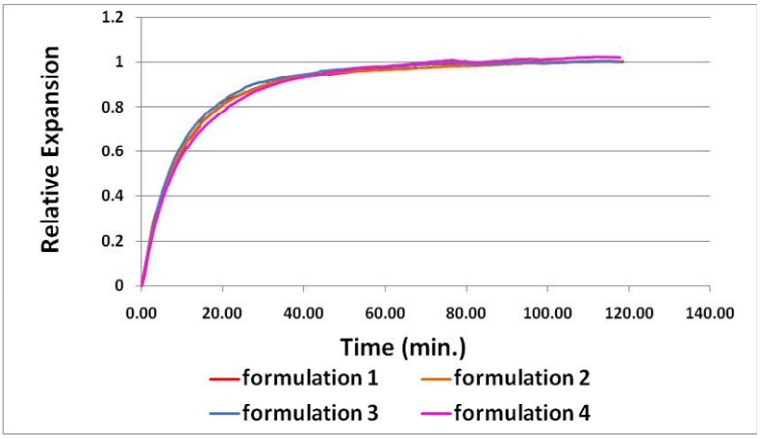

Figure 14-39. Oxidation of bars of various advanced architecture formulations at 300ºC from 0.5% oxygen/nitrogen to 100% oxygen for four different starting powder formulations.

All samples showed similar responses and came to equilibrium within 60 minutes.

Large-Scale Dilatometer Gas Switch Time

Experimental: Gas Switch Time and Bell Housing Development

Prior to testing part responses to gas switching in the large-stage dilatometer, Air Products carried out a series of experiments for comparison with predictions to assess the effect of stage size on the transient response. Figures 14-40 through 14-42 document the results.

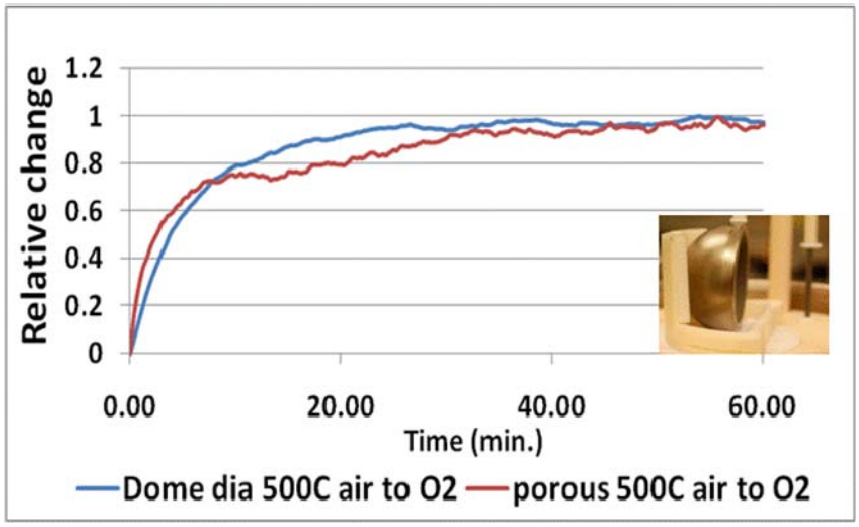

Figure 14-40. Expansion response of the dome diameter after the gas was changed from air to oxygen.

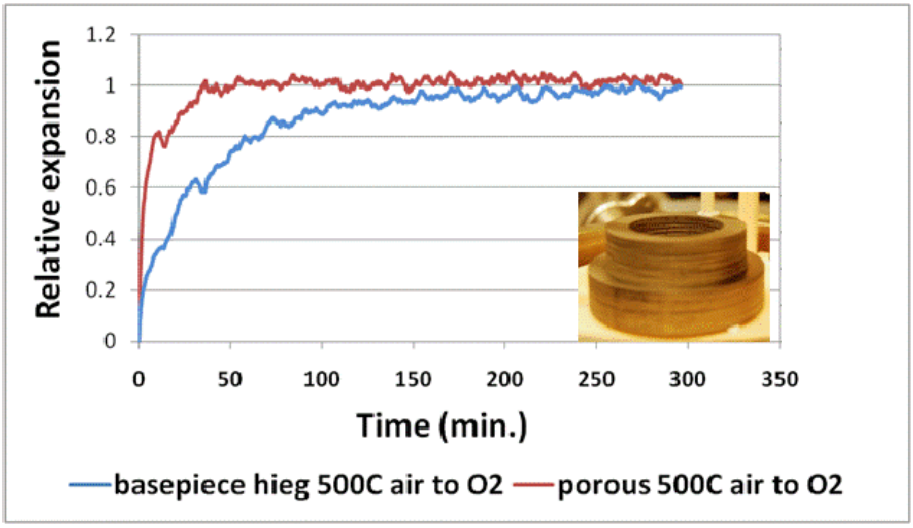

Figure 14-41. Expansion response of a laminated base piece height after the gas was changed from air to oxygen.

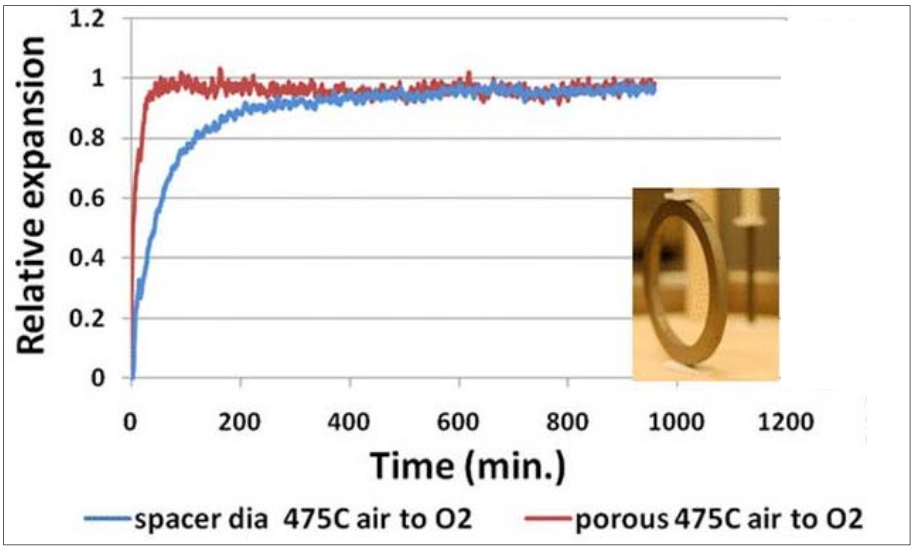

Figure 14-42. Expansion response of a standard spacer diameter after the gas was changed from air to oxygen.

The predicted response of the base piece was compared to the dilatometry data to check the accuracy of the predicted response. The predictions made use of the response times measured with the smaller dilatometers. The predictions were compared to an experiment in which the atmosphere was switched from 0.5% O_2 to 100% O_2 at 600ºC. The calculations assumed that the gas-phase P_{O2} change is described as a linear change with time, and the total switching time was assumed to be 10 seconds. The calculations predicted a faster transition than occurred in the experiment. It was suggested that the actual switch time in the dilatometer was substantially greater than 10 seconds. A second calculation was done assuming a 2-minute switch time. Again, the calculations predicted a faster transition than occurred in the experiment. Ideally, the gas switching should occur instantaneously for the best transient expansion measurement.

A study was conducted to determine the actual gas switch time in the large-scale dilatometer. The gas switching response was measured using an oxygen sensor positioned on the dilatometer outlet. The gas switch occurred over one hour, and the response time for the porous sample occurred slightly faster. This switch time was too slow to meet the needs for transient dilatometer measurements.

To shorten response time, a quartz bell housing was designed with a substantially lower internal volume than the large-stage dilatometer and three holes for the push rod, thermocouple and the gas delivery tube, as shown in Figure 14-43.

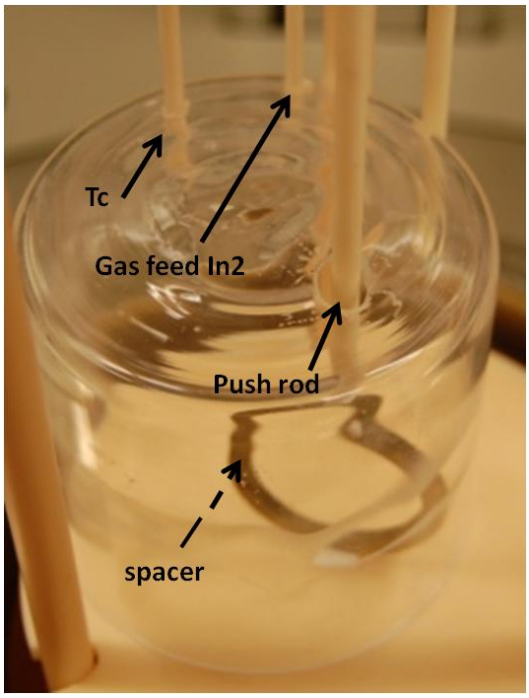

Figure 14-43. Quartz bell housing for the large-scale dilatometer.

The housing is designed to fit inside the dilatometer; the sample and atmosphere preparation occurs in the housing. Figure 14-44 is the calculated change in gas composition for the full volume, large-scale dilatometer and for the quartz bell housing as a function of time.

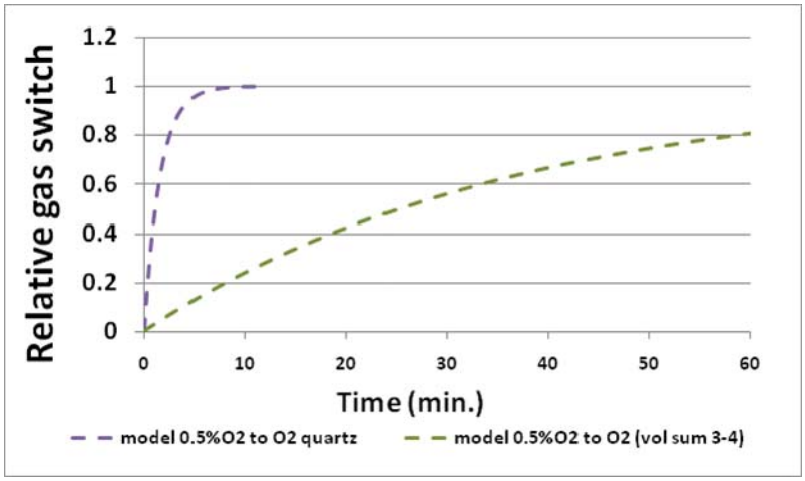

Figure 14-44. Predicted change in gas switching time for the quartz bell housing and the full-volume, large-scale dilatometer volume.

The predicted gas switch time for the quartz bell housing was eight minutes. Experiments were conducted to determine the actual gas switch time. Figure 14-45 presents the results.

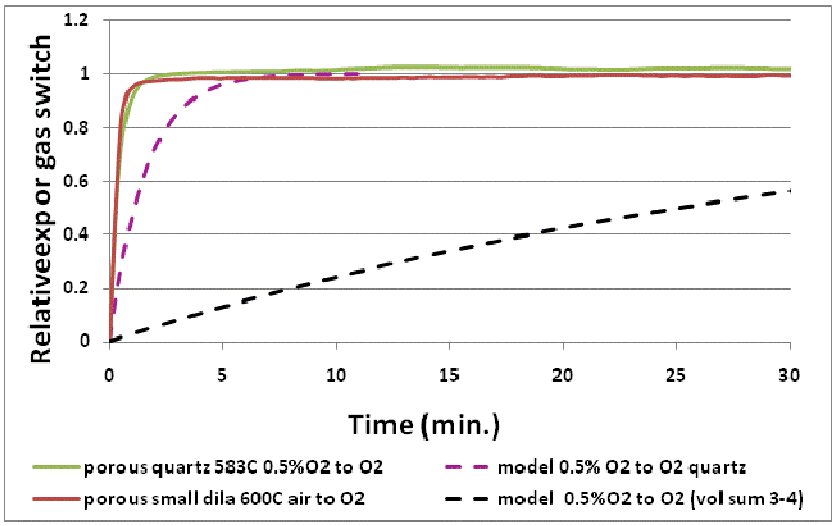

Figure 14-45. Actual respond/gas switching time for the quartz bell housing and small-scale dilatometer. Predicted gas switch time (dashed line) for quartz bell housing and full-volume, large-scale dilatometer.

The porous bar in the quartz bell changed faster than the predicted gas change, roughly 2 min instead of 8 min. The prediction assumes the gases are mixing uniformly, which probably does not happen. Mixing would be poor at the onset of the gas change, causing the initial gas to be swept out at a richer concentration than what would be predicted assuming ideal mixing.

The quartz bell housing response time was similar to the small scale dilatometer response time. All further gas composition dilatometer work used the quartz bell housing in the large-stage dilatometer.

Base Piece

Air Products performed experiments that assessed the gas-phase mass transfer limitations in the quartz bell housing during an oxidation experiment of a laminated base piece. The transient response of a ¼ base piece is documented in Figure 14-46, along with the response of full-size base pieces and spacers.

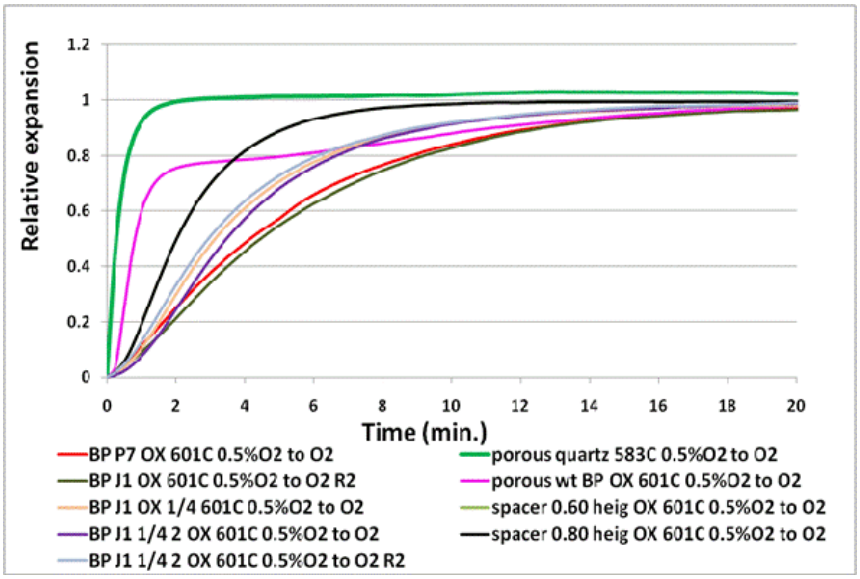

Figure 14-46. Oxidation transient response at 600°C of full-size and ¼ section of a laminated base piece. Included are wafer sections and spacers. The pink curve represents the porous bar response without the quartz bell housing present.

The ¼ section responded faster compared to the full-size base piece. This data confirms that the transient response was gas-phase mass transfer-limited in experiments in which the quartz housing was not used. A lower temperature would decrease the solid-state diffusivity and increase the gas-phase mass transfer time. Calculations indicated that during oxidation, a base piece would reach chemical equilibrium in slightly less than two hours at a temperature of 500ºC. The time at 600ºC is approximately 10 minutes.

The transient oxidation temperature was decreased from 601ºC to 502 ºC to reduce the effect of gas-phase mass transfer resistance relative to bulk diffusion during the oxidation of a ¼ base piece. Figure 14-47 shows the transient oxidation response.

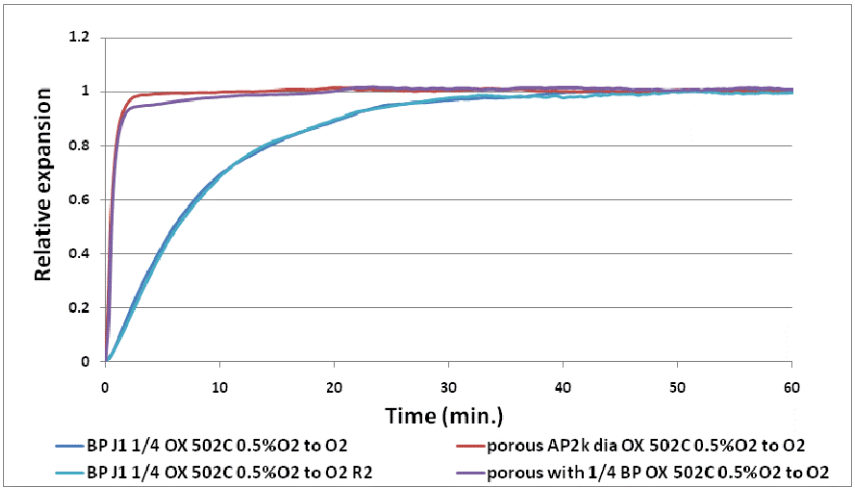

Figure 14-47. Oxidation response at 502ºC of a ¼ section of a base piece and a porous AP2k bar with and without a ¼ section base piece in the quartz bell housing.

The graph also shows the transient response of a porous AP2k bar with and without a ¼ base piece. The similarity of response indicated the gas-phase mass transfer resistance was low. At these conditions, the porous bar achieved chemical equilibrium between three and six minutes, whereas the base piece achieved equilibrium in 50 minutes. This difference added confidence that the transient response of the ¼ base piece was controlled by length scale and diffusion kinetics.

Air Products also conducted experiments with J1 and Rev 1 base pieces at 450ºC. Figure 14-48 plots the data sets for the J1 at 500ºC and the J1 and Rev.2 base piece at 450ºC.

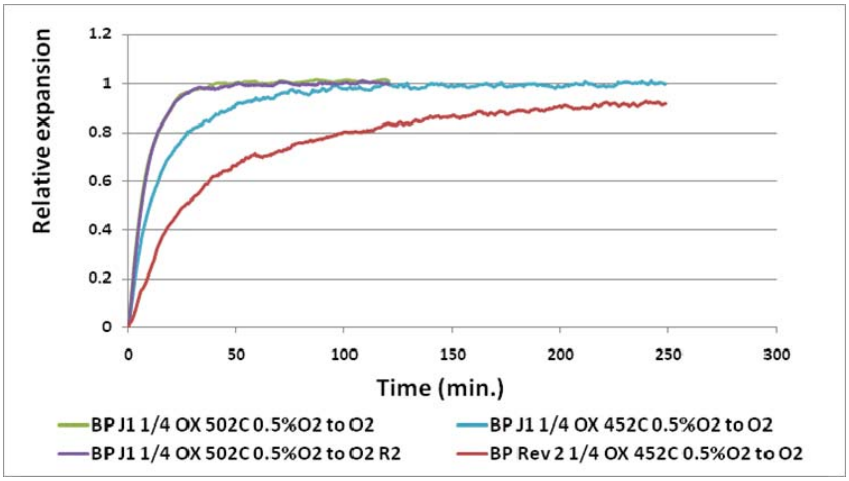

Figure 14-48. Oxidation response of J1 and Rev. 2 base piece at 450ºC and 500ºC

At 450ºC, the differences between the Rev. 2 base piece and J1 (the older base piece design) are apparent. The Rev. 2 transient response was slower, suggesting that the diffusion path length in the Rev. 2 base piece was longer than the older design.

Additional transient oxidation experiments at 450 and 500ºC for the Rev.2 (OD2) spacer and the Rev. 2 laminated base piece were conducted. Figure 14-49 shows the results for the Rev. 2 (OD2) spacer, and Figure 14-50 shows the results for the Rev. 2 base piece.

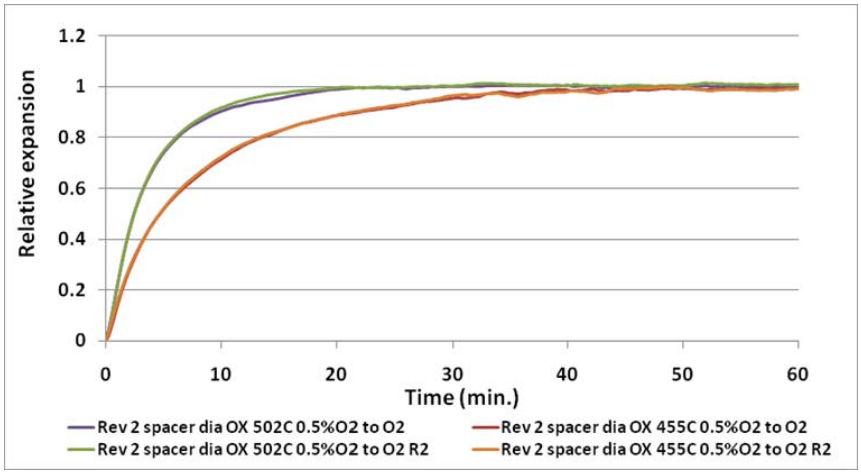

Figure 14-49. Oxidation response of the Rev. 2 (OD2) spacer at 455 and 502ºC.

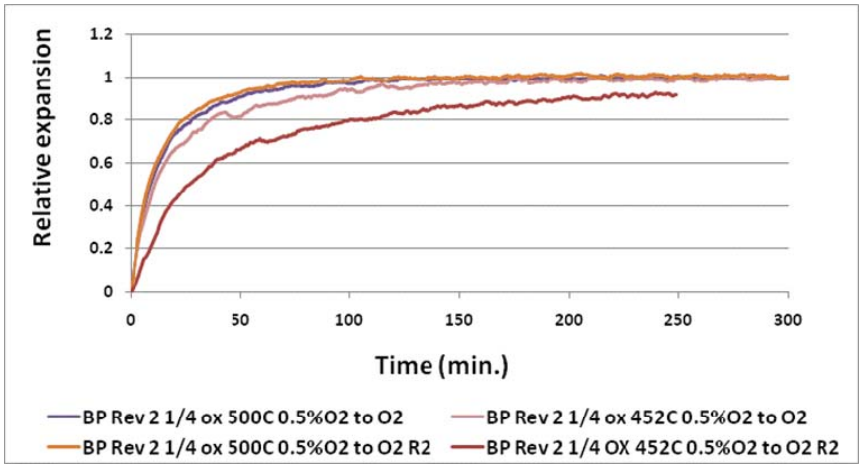

Figure 14-50. Oxidation response of the Rev. 2 (OD2) base piece at 450 and 502ºC.

The run-to-run repeatability for the base piece at 450°C was poor, indicative of sample-to-sample variation in these prototype parts.

Spacer

Air Products assessed the transient oxidation response of a new Rev. 2 (OD2) spacer and a (OD) spacer stack with different joint thicknesses. These results are shown in Figures 14-51 and 14-52 respectively.

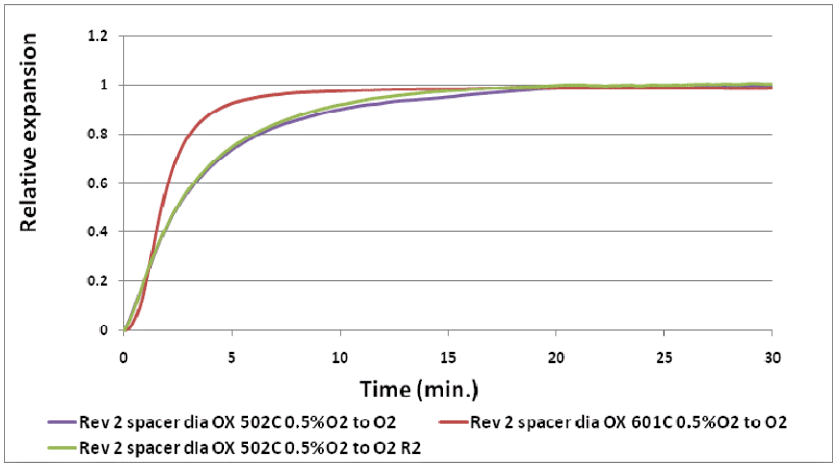

Figure 14-51. Oxidation response of a Rev. 2 (OD2) spacer diameter at 502ºC and 601ºC.

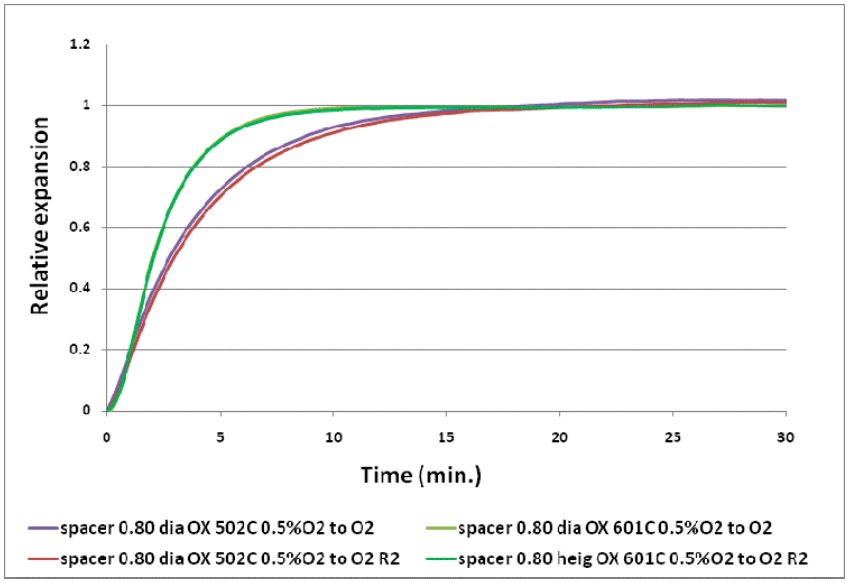

Figure 14-52. Oxidation response of stacked (OD) spacers (height) at 502ºC and 601ºC.

Figure 14-53 plots the data set for the stacked spacer, and Rev. 2 (OD2) spacer samples at 500ºC on a single graph.

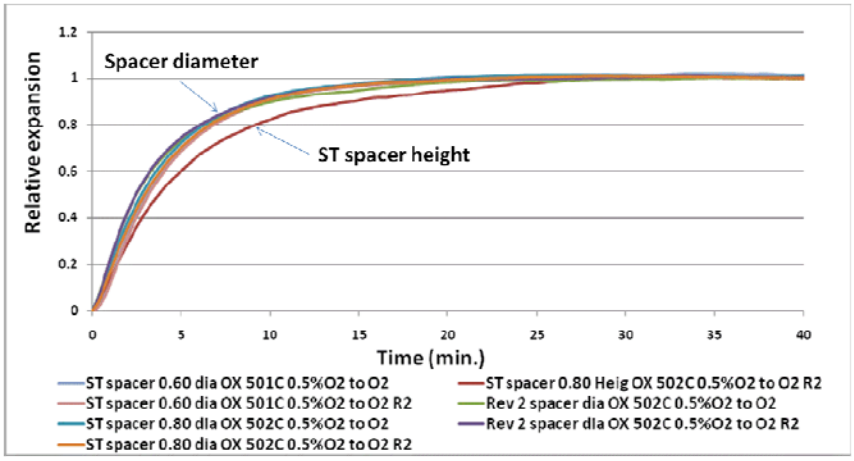

Figure 14-53. Oxidation response of stacked OD and Rev. 2 (OD2) spacers at 502ºC.

At 500ºC, the transient responses of the stacked spacer height and OD2 spacer diameters were roughly the same. The transient response of the stacked spacer height was slower than the transient response of the diameter. In comparison, there was no difference for the same parts at 600ºC.

Parts Testing (Effect of Water on Expansion)

The presence of water over the ITM ceramic has been observed to affect the sealing characteristics of ITM modules during oxygen flux experiments. The influence of water vapor partial pressure on the expansion characteristics of the ITM ceramic was identified as a potential cause. Penn State conducted dilatometry experiments to establish the effect of wafer vapor partial pressure on the expansion characteristics of the ITM ceramic.

Experimental Method

Penn State designed and constructed a steam dilatometry system. A schematic is shown in Figure 14-54.

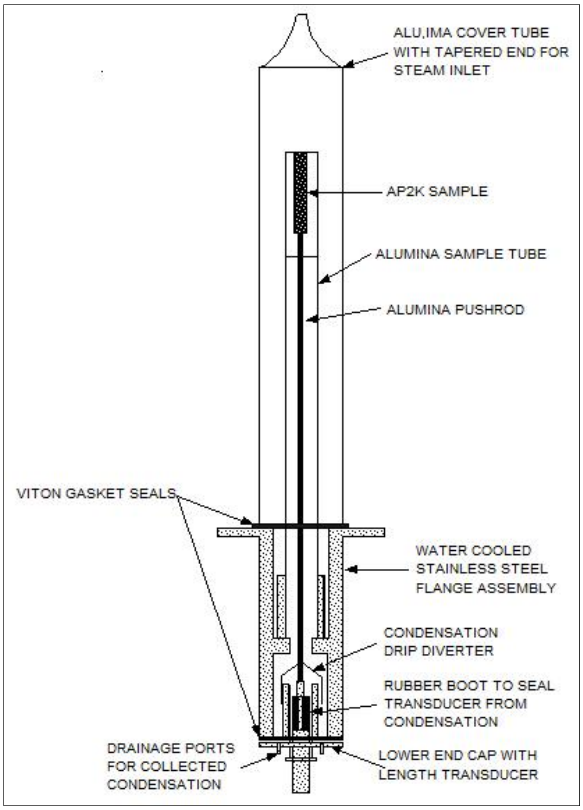

Figure 14-54. Schematic of steam dilatometer developed by Penn State.

The system consists of an alumina cover tube that houses the ITM ceramic sample and allows steam to flow into the unit. The sample is supported by an alumina push rod that is affixed to a length transducer at its base. The base is water-jacketed to cool and condense the steam. Special care is taken to direct condensing away from the push rod and the transducer.

Figure 14-55 is a photograph of the system inserted into a tube furnace. The steam preparation and delivery system is located above the apparatus and is not shown in the photo.

Figure 14-55. Photograph of the steam dilatometer developed by Penn State, showing the furnace housing the sample and the water-cooled transducer section.

The experimental procedure was:

a) Flow 500 sccm of air (20.9% O_2-N_2) through the dilatometer and raise the temperature to a specific value (e.g., 850°C).

b) Continue flowing 500 sccm until the alumina system and ITM specimen achieve strain equilibrium (typically several hours). This initial state was set as the zero value.

c) Change the gas flow from 500 sccm of air to 250 sccm at 36.7% O_2-N_2. Allow the system to equilibrate and document the strain.

d) Introduce a steam flow of 189 sccm for a total flow of 439 sccm, 20.9% O_2 and 43% water vapor. Allow the system to equilibrate and document the strain.

e) Remove the steam flow, thus returning the gas to 250 sccm at 36.7% O_2-N_2. Allow the system to equilibrate and document the strain.

f) Switch the gas from 250 sccm at 36.7% O_2-N_2 to 500 sccm of air. Allow the system to equilibrate and document the strain.

g) Switch the gas flow from 250 sccm at 36.7% O_2-N_2 to 104.5 sccm at 100% O_2. Allow the system to equilibrate and document the strain.

h) Introduce a steam flow of 395.5 sccm for a total flow of 500 sccm, 20.9% O_2 and a water concentration of 79.1%. Allow the system to equilibrate and document the strain.

i) Remove the steam flow, thus returning the gas flow to 104.5 sccm of 100% O_2. Allow the system to equilibrate and document the strain.

j) Switch the gas flow from 104.5 sccm at 100% O_2 to 500 sccm of air. Allow the system to equilibrate and document the strain.

The specimens' strain rate is determined by subtracting the system strain (i.e., alumina push rod, see Figure 14-54) from the total strain. Tests were conducted to determine the system strain at the above gas flows and compositions. Figure 41-56 documents the results at 750°C.

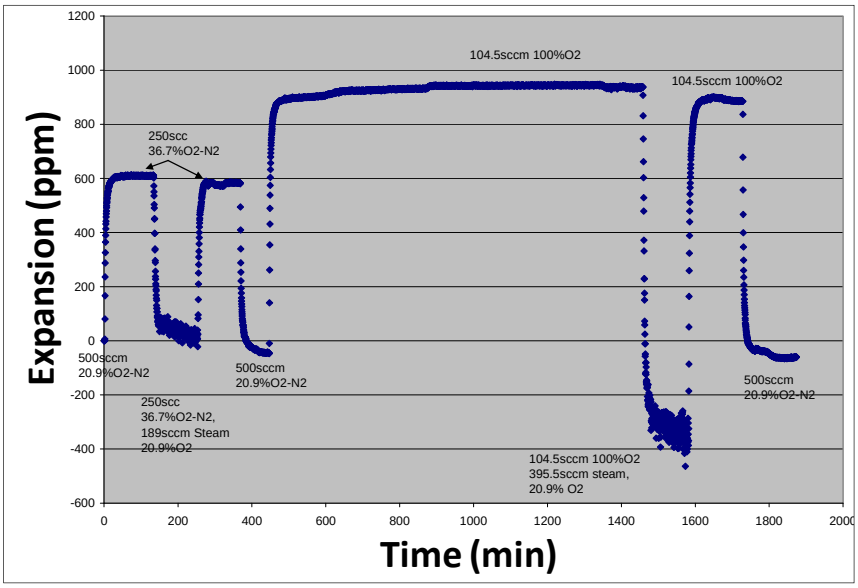

Figure 14-56. Alumina standard and system expansion for steam dilatometry tests conducted at 750°C as a function of gas compositions and gas and steam flow rates.

Porous bars

A number of issues developed which impacted the accuracy of the specimen strain measurement, including poor temperature control and a noisy length transducer signal. A number of actions were taken to resolve these issues. The computer program was changed to average the

temperature and length transducer signals. The surface of the length transducer was coated with a silicon gasket sealer to shield the metal body of the length transducer from moisture and ensure electrical isolation while steam is flowing in the dilatometer. The temperature controller was tuned. After the system was optimized, a second test was conducted to determine the system strain at the various gas flows and compositions and temperatures (i.e., 750°C, 800°C and 875°C). These data were used as the baseline system strains.

A more serious issue was identified when the data from the initial experiments were reviewed. The repeatability of the results was poor and in many instances did not agree with theoretical values. It was decided to conduct a second round of system calibration tests at 750°C, 800°C and 875°C. The results at 875°C (Table 14-2) were compared to the original calibration test.

Table 14-2. System (alumina rod) expansions from two tests and their differences.

Gas Composition	Gas (sccm)	Steam (sccm)	Oxygen Conc.	Strain Old (ppm)	Strain New (ppm)	Delta New-Old
20.9% O_2-N_2	500	0	20.9%	Set to 0		
20.9% O_2-N_2 to 36.7% O_2-N_2, no steam	250	0	36.7%	-564	-571	-7
36.7% O_2-N_2 to 36.7% O_2-N_2, with steam	250	189	20.9%	+656	-+883	+227
20.9% O_2-N_2 to 100% O_2	104.5	0	100%	-856	-789	+67
100% O_2 to 100% O_2 with steam	104.5	395.5	20.9%	+1340	+1467	+127

The delta between the old and new measurements was of the same order of magnitude as the specimens' strain, and thus the potential for error was high. As a result, Penn State designed and built a large double pushrod steam dilatometer with two length transducers and a dual pushrods system (i.e., a differential dilatometer) to reduce scatter in the thermal expansion measurements and decrease the time and amount of gas needed to assess the effects of steam on strain behavior.

The results presented below are from experiments using the original dilatometer. Figure 14-57 is a representative plot of the experimental data; the tables that follow document some of the results. It is important to note that much of the data was within reasonable agreement with predicted strain rates.

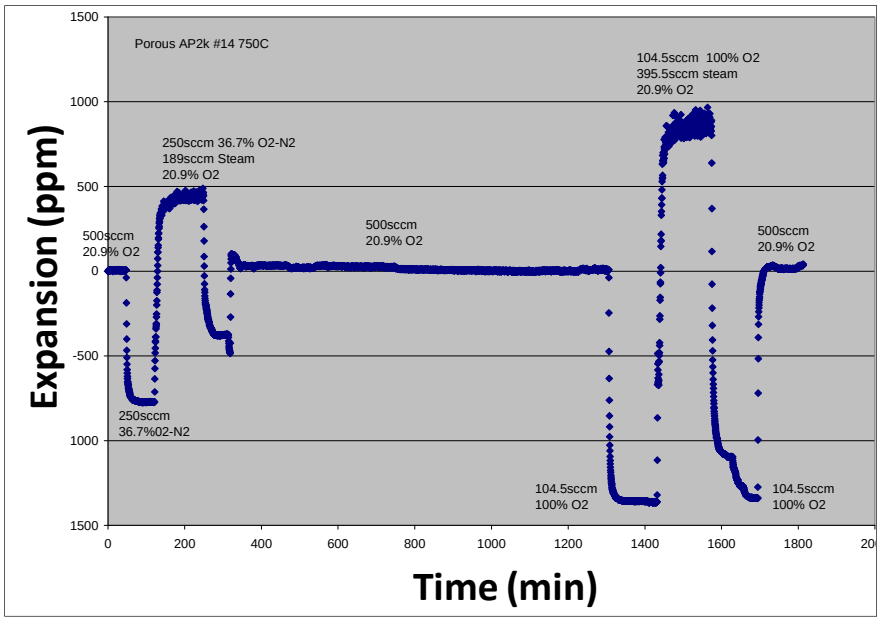

Figure 14-57. Expansion versus time plot for porous ITM Oxygen Ceramic Sample #14 as a function of gas and steam flow rates and percent oxygen at 750°C.

Table 14-3. Measured expansion changes as a function of gas and steam flow rates and percent oxygen for porous AP2K sample #18 tested at 750°C.

Gas Composition	Gas (sccm)	Steam (sccm)	Oxygen Conc.	Net Expansion (ppm)
20.9% O_2-N_2	500	0	20.9%	Set to 0
20.9% O_2-N_2 to 36.7% O_2-N_2, no steam	250	0	36.7%	-3566
36.7% O_2-N_2 to 36.7% O_2-N_2, steam	250	189	20.9%	+1020
20.9% O_2-N_2 to 100% O_2	104.5	0	100%	-3637
100% O_2 to 100% O_2 with steam	104.5	395.5	20.9%	+902

Table 14-4. Measured expansion changes as a function of gas and steam flow rates and percent oxygen for porous AP2K sample #17 tested at 800°C.

Gas Composition	Gas (sccm)	Steam (sccm)	Oxygen Conc.	Net Expansion (ppm)
20.9% O_2-N_2	500	0	20.9%	Set to 0
20.9% O_2-N_2 to 36.7% O_2-N_2, no steam	250	0	36.7%	-4399
36.7% O_2-N_2 to 36.7% O_2-N_2, with steam	250	189	20.9%	234
20.9% O_2-N_2 to 100% O_2	104.5	0	100%	-4973
100% O_2 to 100% O_2 with steam	104.5	395.5	20.9%	+855

Table 14-5. Measured expansion changes as a function of gas and steam flow rates and percent oxygen for porous AP2K sample #20 tested at 875°C.

Gas Composition	Gas (sccm)	Steam (sccm)	Oxygen Conc.	Net Expansion (ppm)
20.9% O_2-N_2	500	0	**20.9%**	Set to 0
20.9% O_2-N_2 to 36.7% O_2-N_2, no steam	250	0	36.7%	-7802
36.7% O_2-N_2 to 36.7% O_2-N_2, with steam	250	189	20.9%	3291
20.9% O_2-N_2 to 100% O_2	104.5	0	100%	-7760
100% O_2 to 100% O_2 with steam	104.5	395.5	20.9%	+2897

Table 14-6 is a summary of the above results.

Table 14.1-6. Measured expansion changes as a function of gas and steam flow rates and percent oxygen for porous AP2K sample #18 at 750°C, #17 at 800°C and #20 tested at 875°C.

Gas Composition	Gas (sccm)	Steam (sccm)	Oxygen Conc.	Expansion #18-750°C	Expansion #17-800°C	Expansion #20-875°C
20.9% O_2-N_2	500	0	20.9%	Set to 0		Set to 0
20.9% O_2-N_2 to 36.7% O_2-N_2, no steam	250	0	36.7%	-3566	-4399	-7802
36.7% O_2-N_2 to 36.7% O_2-N_2, with steam	250	189	20.9%	+1020	+234	+3291
20.9% O_2-N_2 to 100% O_2	104.5	0	100%	-3637	-4973	-7760
100% O_2 to 100% O_2 with steam	104.5	395.5	20.9%	+902	+855	+2897

Mechanical Properties

Background

Flexural Strength

Flexural strength, a mechanical parameter for brittle material, is defined as a material's ability to resist deformation under load. When an object formed of a single material, like a steel rod, is flexed parts of the body undergo compressive stress while other parts undergo tensile stresses. The two stress balance each other in the material (Figure 14-58).

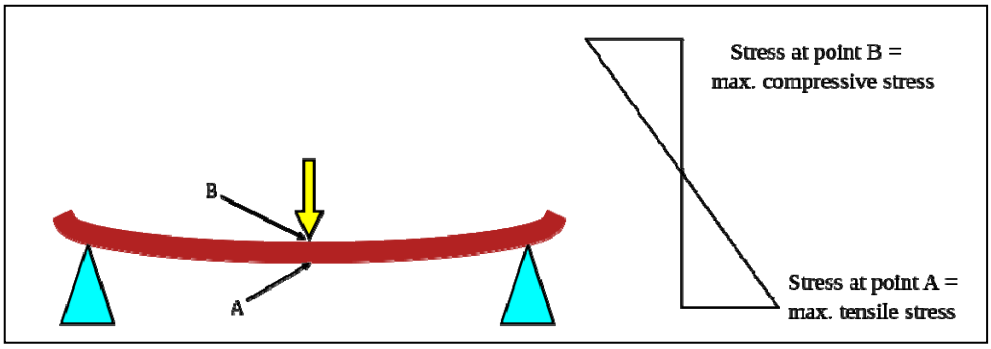

Figure 14-58. Schematic of an applied load causing flexural stress in a body.

At the edge of the object on the inside of the bend (concave face) the *compressive* stresses will be maximized, while at the edge of the object on the outside of the bend (convex face) the *tensile* stresses will be maximized. Most materials fail under tensile stress before they fail under compressive stress, so the maximum tensile stress value that can be sustained before the beam or rod fails is its flexural strength. For a rectangular sample, the resulting stress under four point bending force (see Figure xxx) is given by the following formula:

$$\sigma = \frac{3FL}{4bd^2}$$

where the stress (σ) is related to the dimensions of the body (Figure 14-59) and b is the width of the body. Note that this equation is for the special case in which L_i is ½ of L.

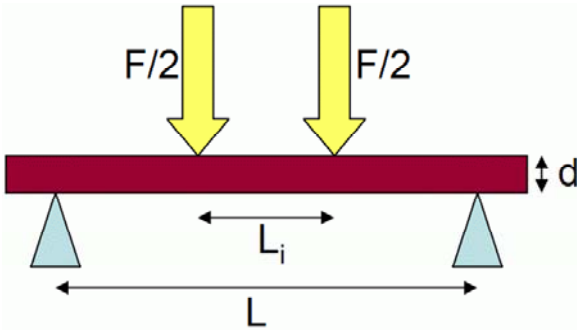

Figure 14-59. Four-point bending for flexural strength measurement.

Knowledge of the flexural strength is critical when designing ITM structural components such as end caps and base pieces and when predicting stresses in and reliability of ITM ceramic parts, components and modules.

Burst

Burst testing is a means of characterizing the strength of parts under a uniform, hydrostatically imposed stress. Parts with internal volumes are typically pressurized with air or another fluid to the point of failure.

Seal Torsional Friction

The coefficients of expansion of the ITM ceramic and the seal material are different. During temperature transients, the materials will try to expand/contract at different rates; static and kinetic friction will resist this movement. Therefore, the friction behavior (coefficient of friction) of ceramic-metal seal materials under transient and operating conditions is needed to assess the behavior/performance of seals.

Creep

Creep is the tendency of a solid material to deform permanently under the influence of mechanical stress. It can occur as a result of long-term exposure to a stress that is below the yield stress of the material. Creep is more severe in materials that are subjected to high temperature for long periods. Strain accumulates as a result of long-term stress. Therefore, creep is a "time-dependent" deformation.

ITM components (e.g., wafers) experience stress due to the combination of chemical expansion stresses and the hydrostatic load differential between the feed and permeate sides of the membrane. Creep deformation may limit the life of operating ceramics by causing excessive creep strain, leading to tensile failure. Accumulated creep damage, caused by repeated thermal and/or pressure cycles, may also weaken ITM materials leading to premature failure. Thus, determining the creep behavior of the ITM ceramic and module components is required to assess long-term performance.

ITM components experience both flexural stresses (leading most importantly to tensile creep) and compressive stresses (leading to compressive creep). Thuerefore, both flexural and compressive creep studies were carried out.

Elastic Properties

The "primary" material properties of the ITM ceramic are required to determine its behavior under a load. These three primary properties are:

- Young's modulus (E), which describes tensile elasticity or the tendency of an object to deform along an axis when opposing forces are applied along that axis. It is defined as the ratio of tensile stress to tensile strain and is often referred to simply as the *elastic modulus*.
- The shear modulus (G or μ), which describes an object's tendency to shear when acted upon by opposing forces. It is defined as shear stress over shear strain.
- The bulk modulus (K), which describes volumetric elasticity, or the tendency of an object to deform in all directions when uniformly loaded in all direction. It is defined as volumetric stress over volumetric strain.

Experimental Methods

Burst

Penn State designed and constructed a burst test facility to test the burst strength of ITM components. The system (see Figure 14-60) consists of a pressure control and gas handling equipment, a steel test chamber, and a computer system for data acquisition and programmable pressurization.

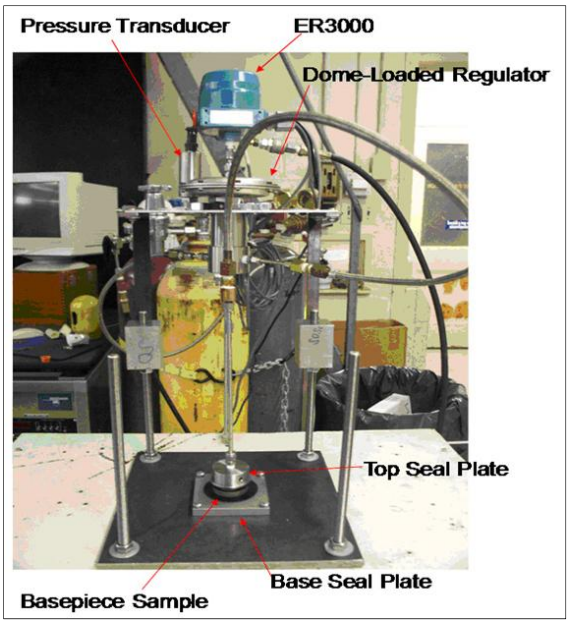

Figure 14-60. Photo of burst test rig for ITM Oxygen base piece samples.

The pressure control system uses a pneumatic actuator. Gas pressure is measured using a pressure transducer. The outlet port of the actuator is connected to the inlet port of the dome-loaded gas regulator. A tank of compressed nitrogen is connected to the gas inlet port of the dome-loaded gas regulator. The gas outlet from the dome-loaded gas regulator is connected to a top face plate seal (Figure 14-61).

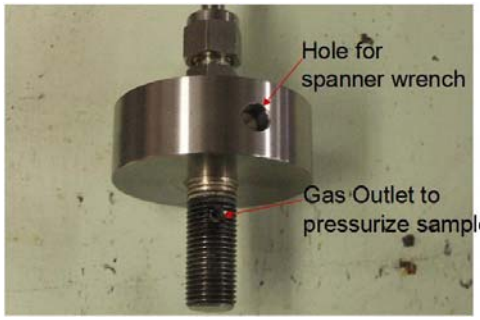

Figure 14-61. Photo of top seal plate with holes drilled through thread rods for gas outlet to pressurize test samples.

Soft rubber gaskets are used to seal base piece samples. The bottom of the sample sits on a bottom face seal plate equipped with a gas outlet port. The outlet port then transitions to tubing connected to the pressure transducer. Threaded rods are used to close a top cover plate over a metal containment ring that surrounds the test sample (Figure 14-62).

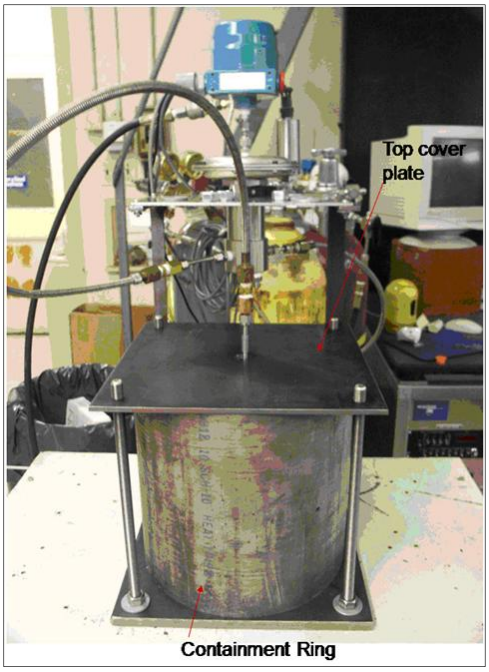

Figure 14-62. Photo of burst test rig cylindrical containment ring and cover lid.

The ring is filled with padding to capture the fragments of the base pieces upon failure due to internal gas pressure. The pressure is controlled by either a set point profile signal from a computer or an external analog signal provided by data acquisition board equipped with two analog output channels. The data acquisition board was configured via a Labview program.

A second burst test method was also used. In this method, the samples are filled with a rubber compound that is allowed to cure. A force is applied to the rubber until the sample breaks.

Flexural Strength

The Penn State measured the flexural strength of porous bars using a 4-point bend test over a range of temperatures. Photographs of the 4-point bend bar test are shown in Figure 14-63.

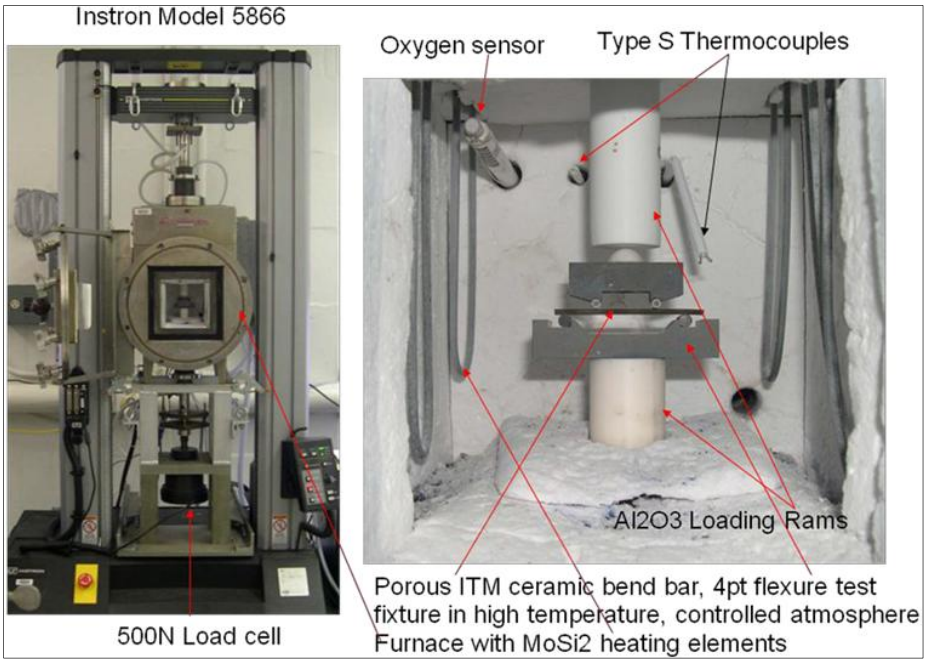

Figure 14-63. High-temperature, 4-point bend test apparatus at Penn State.

A small furnace sits in the test cavity of a standard Instron machine. The load rams pass through apertures in the furnace to apply load to the sample located inside. The system is fully temperature- and atmosphere-controlled.

Seal Torsional Friction

Penn State built a test rig to assess the friction behavior of gasket materials at temperatures ranging from room temperature to 875°C and gasket stresses ranging from 100 to 3,500 psi. The

compression-torsion test rig can apply a rotational movement while subjecting the test specimen to an axial compression load applied by an Instron testing machine. Figure 14-64 is a photograph of the lower portion of the compression-torsion test rig mounted to the actuator of the Instron 1332 testing machine.

Figure 14-64. Photograph of the lower portion of the compression-torsion test rig.

A thrust bearing is used to isolate the compressive load from the torque sensor. Two roller bearings were installed on the loading ram to maintain vertical alignment. Figure 14-65 is a photograph of the entire system.

Figure 14-65. Photograph of the entire compression-torsion test rig.

A brace was installed to span the support columns of the Instron 1332 and surround the outside diameter section of the thrust-roller bearing housing (Figure 14-66).

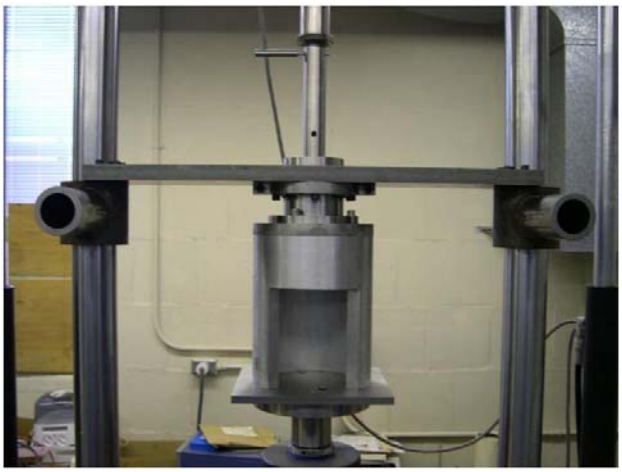

Figure 14-66. Photographs of the horizontal brace mounted to the support columns to the Instron 1332.

After initial testing, a number of modification were made to enhance the accuracy of the data. Once there was confidence in the basic measurement, the furnace was attached to the system (Figure 14-67).

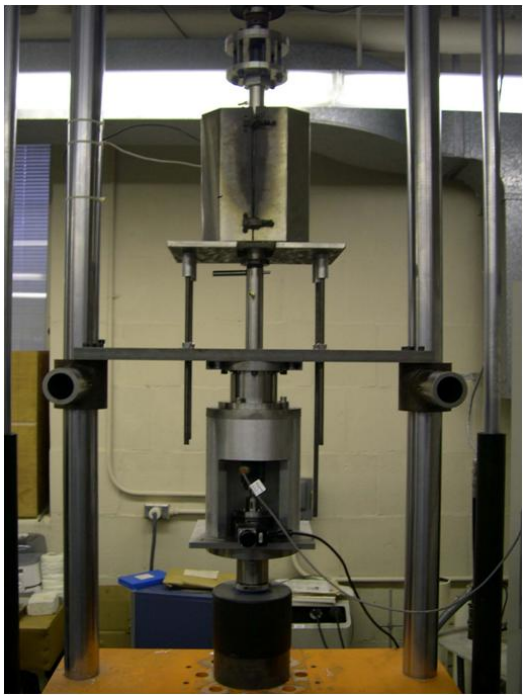

Figure 14-67. Compression-torsion test rig with the furnace mounted to actuator brace.

After insertion of the gasket, the experimental procedure was:

a) Apply a specific axial load.
b) Heat the system to a specific temperature.
c) Rotate the loading ram by +10° (at a specific rate) and document the torque.
d) Rotate the loading ram back to 0° and document the torque.
e) Rotate the loading ram by -10° and document the torque.
f) Rotate the loading ram back to 0° and document the torque.

Creep

Ceramatec used the pneumatic test system shown in Figure 14-68 to conduct 4-point flexural creep studies.

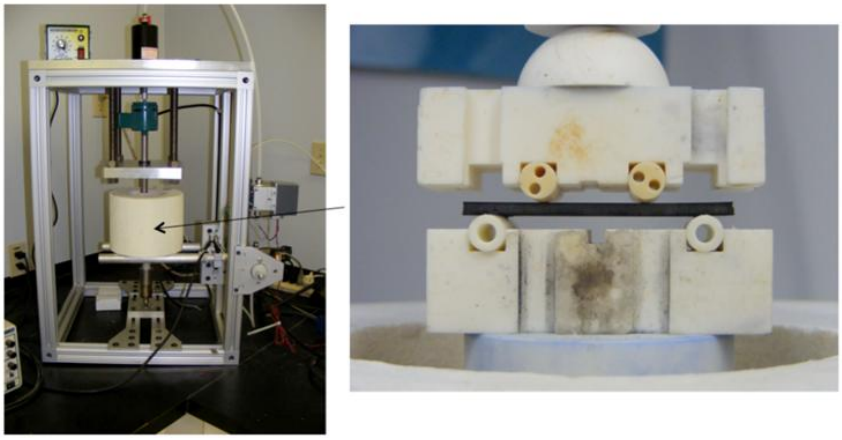

Figure 14-68. Pneumatic test frame used to measure creep deflection of flexure bars (right) at elevated temperatures.

This system consists of an air cylinder for generating the mechanical load, a load cell for measuring the loads, and 2 LVDTs for measuring ram and specimen deflection. A computer was used to control the applied load via an electric to pneumatic actuator. The studies were conducted by applying a flexural load onto the specimen at a specific temperature and then documenting it creep behavior. Penn State also conducted flexural creep studies using the same equipment shown in Figure 14-68.

Elastic Properties

An Instron machine (Figure 14-69) with a furnace surrounding the test specimen was used to determine ITM material properties (e.g., Young's modulus) as a function of temperature.

Figure 14-69. Photograph of the Instron 4206 testing machine at Penn State.

Flexural Strength

Penn State measured stress to failure of porous bend bars. The tests were conducted at two stress rates that differed by a factor of 1,000 over a range of temperatures. Several samples were measured for each condition and average values were calculated. In general, the strength is higher for the samples that were stressed rapidly, indicating a slow degradation mechanism is active for some temperatures. In addition, a minimum in the strength occurred between 275°C and 375°C. Analysis of the strength distribution at 375°C indicated a mixture of both high and low strength failures. SEM fractography of samples tested at both temperatures indicates that the fracture surfaces of both the low- and high-strength samples for both fast and slow stressing rates did not have any pronounced differences in failure origins.

One sample was allowed to come to temperature and equilibrate, after which the 4-point bend test was conducted. The strength of the sample with the 2-hour hold improved dramatically, suggesting that the hold enables more residual stresses from chemical gradients to be relieved prior to testing.

Ceramatec examined the relationship between porosity and the elastic modulus of bend bars. The porosity level was controlled by casting porous tapes with 0, 5, 10 and 20wt% fines added to the classified powder. Figure 14-70 shows the porosity level and elastic modulus as a function of the % fines. The elastic modulus was calculated from time-of-flight measurements made with the scanning acoustic microscope. The strength of the bars with 20% fines is also significantly greater than that for standard porous tape.

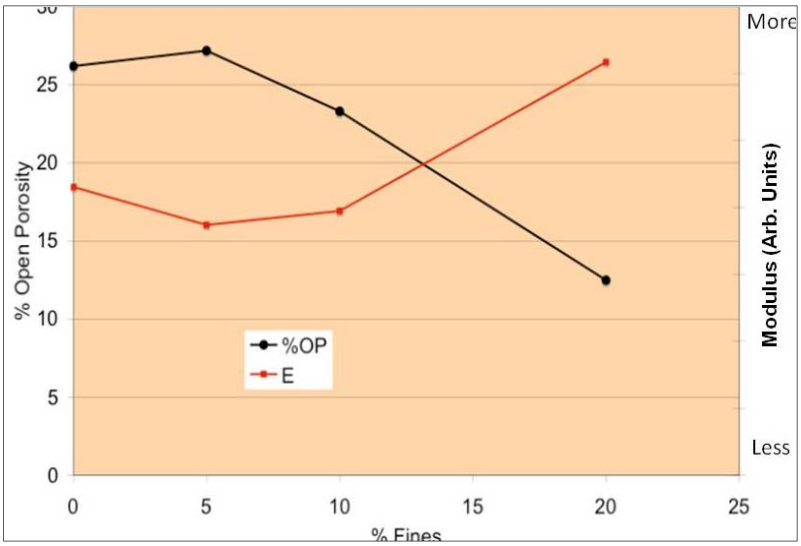

Figure 14-70. Effect of % fines on open porosity and modulus.

Burst

Base Piece

Penn State tested three conical base pieces, which failed at internal pressures of 203, 216 and 232 psig. The inside surface of the cone base piece that failed at 216 psig is shown in Figure 14-71. The results indicate that the burst pressures are highly reproducible.

Figure 14-71. Re-constructed fragments of an ITM Oxygen cone sample that was internally pressured via nitrogen gas to a maximum pressure of 216 psig.

Penn State also burst a prototype cylindrical basepiece design sample "I7" using internal gas. The burst pressure was 672 psig. Based on the equation for an internally pressurized, thick-walled tube, the calculated burst strength of the smaller and larger outside diameters were 12.08 MPa (1750 psig) and 8.07 MPa (1170 psig) respectively. The high burst strengths indicate that the cylindrical base piece is a stronger part than the conical base piece.

Penn State tested two prototypes of the improved (cylindrical) base piece using the rubber compound method (Figures 14-72 and 14-73).

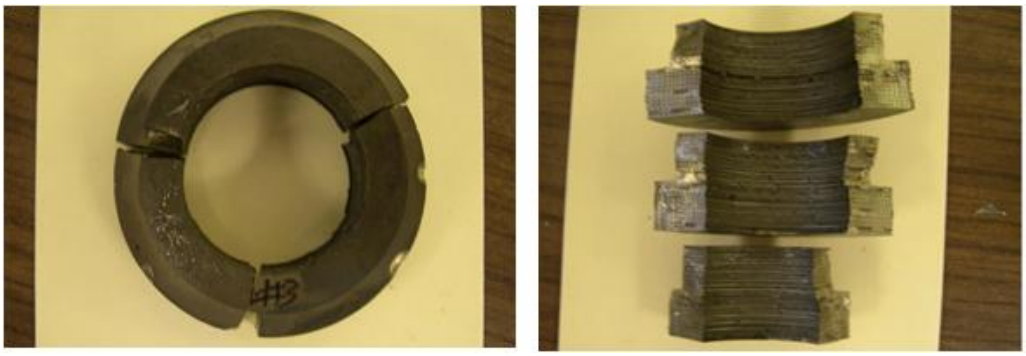

Figure 14-72. Photographs of prototype base piece Sample #3 burst tested at room temperature by the axially compressed rubber method.

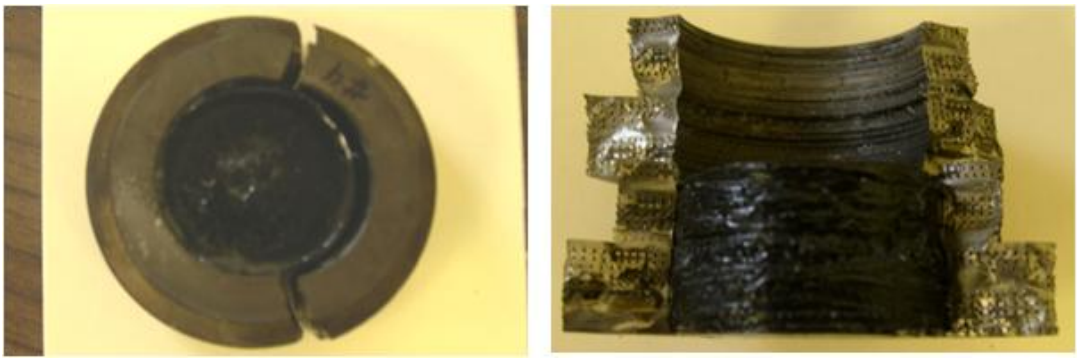

Figure 14-73. Photographs of prototype base piece Sample #4 burst tested at room temperature by the axially compressed rubber method.

For base piece Sample #3, the calculated fracture stresses for the small and large outside diameter regions were 9.40 and 6.18 MPaS respectively. For basepiece Sample #4, the fracture stresses were 3.39 and 2.30 MPa.

Wafer

Penn State also measured the burst of 24 wafers. Figure 14-74 are photographs of a wafer ready for testing before and after the steel containment shell is placed around the assembly.

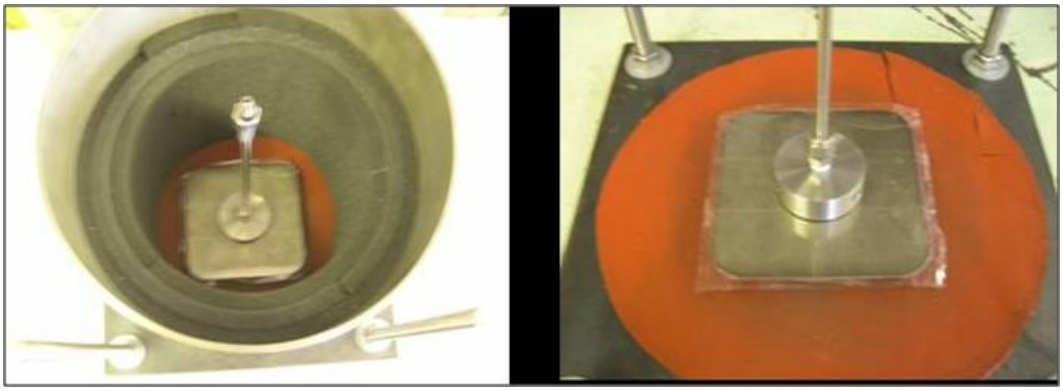

Figure 14-74. Photos of taped wafers ready for burst strength testing with and without the surrounding steel shell.

The leak initiation pressure was identified in 20 of the trials. All but one initiated leakage at 1,200 psig or higher, with a few wafers first leaking at over 2,000 psig. Analysis of the leak initiation site in the 20 wafers indicated that the wafers had leak initiation sites located just inside the outer rim of the modules, coincident with a particular slot pattern internal to the wafer there.

Seal Torsional Friction

Penn State conducted the first friction tests on candidate seal materials. A 50 mm mica gasket with a 9.6 mm diameter hole in the center was placed between two loading rams. The Instron was placed in load control mode, and the furnace was heated to 200°C at a rate of 5°C/min. After system thermal equilibrium was reached, a series of friction tests were conducted (see experimental procedure above) by rotating to +10°, then -10° and then ending the cyclic back at 0°. A rotation speed of 0.5° per second was used. Two 0° to +10° to -10° to 0° degree cycles were performed per applied load. The applied load was increased in 25 lb increments until a 225 lb load was reached. At this load, the torque reading was nearing the limit of the sensor.

Figure 14-75 plots rotational torque as a function of rotational position as a function of applied compressive load.

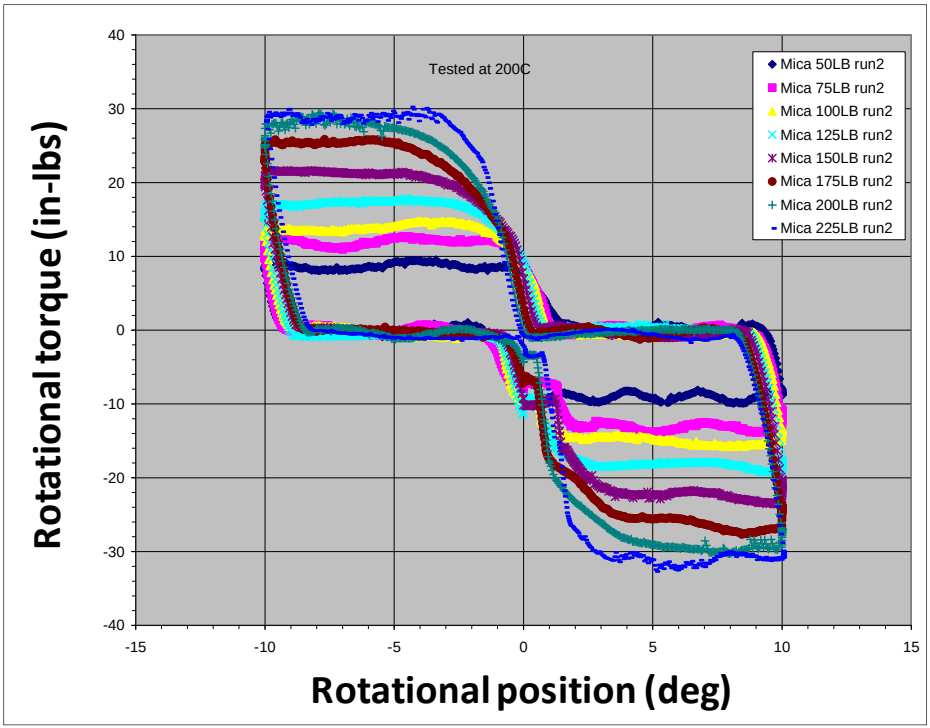

Figure 14-75. Rotational torque versus rotational position for a 50 mm OD by 9.6mm ID mica gasket tested at 200°C as a function of applied compressive load.

With the exception of the first tests at 50 lbs applied load, no significant differences were observed between repeated tests. The magnitude of the torque is important, not the sign. The sign simply refers to the direction of rotation.

There is about a 1°- 3° region where the torque sensor remains unchanged. This was believed to be due to a slight misfit between the connections where the torque sensor is attached to the rotational stage and thrust-bearing loading ram.

The general shape of the curves does not change significantly with increasing applied load, but, as expected, the magnitude of the torque increases. The torque increased from 8-10 in-lbs for an applied load of 50 lbs to 30-32 in-lbs for an applied load of 225 lbs.

The torque (τ) of an axially loaded disk is related to the coefficient of friction (μ) via the following relationship:

$$\tau = \frac{2}{3} F \mu R$$

where F is the applied force and R is the radius of the disk. Since the gasket is not a solid disk, but has about a 3/8" (9.6 mm) diameter hole in the center, the above equation is re-arranged and expressed as:

$$\mu = \frac{3\tau}{2F}\left(r_o - r_i\right)$$

where r_o is the outer radius and r_i is the inner radius of the gasket.

Figure 14-76 shows a curve for the coefficient of friction as a function of rotational position and applied load for the gasket tested at 200°C.

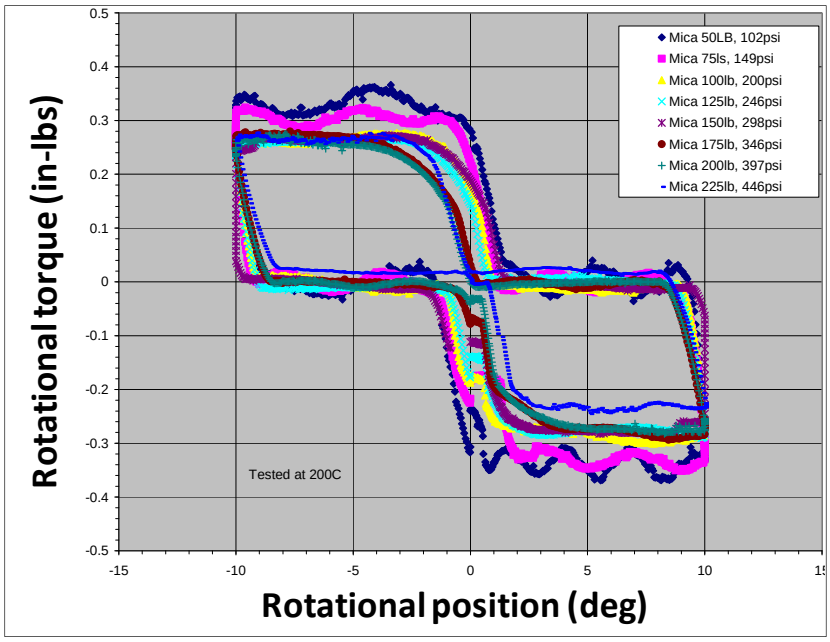

Figure 14-76. Coefficient of friction versus rotational position for a 50 mm OD by 9.6 mm ID mica gasket tested at 200°C as a function of applied compressive load.

As with the torque data, the + or – sign simply reflects the direction of the rotation. The highest coefficient of friction (0.28 to 0.35) occurred for the first two tests performed using the 50 and 75 lb loads. Following these two tests, there was a slight decrease in the coefficient of friction (0.27 to 0.3) for tests perform using applied loads of 100 to 200 lbs. For an applied load of 225 lbs, the coefficient of friction decreased again to 0.22-0.24.

The coefficient of friction tended to decrease slightly with continued friction tests at higher compressive loads. As the compressive load is increased, a greater force is needed to compress and align the platelets of the mica gasket. Thus, as the load ram is rotated, the platelets that are protruding can be pushed over and aligned in the direction of rotation. When the ram is rotated in the opposite direction, some of these plates may pop back up, while others may be broken off (i.e., wear). Therefore, a combination of platelet alignment (e.g., pushing over vertically aligned platelets in the direction of rotation), along with wear of the mica platelets, can lead to a reduction in the coefficient of friction as the compressive load is increased.

Additional tests of the 50mm OD by 9.6 mm ID gasket were conducted at 22°C, 400°C, 600°C, 800°C, and 875°C. The coefficient of friction tends to increase with increasing temperature. At 22°C, the maximum coefficient of friction was 0.4 to 0.46. At 400°C, the coefficient of friction

decreased slightly to 0.16 to 3.4. At 600°C, the coefficient of friction increased back up to 0.4 to 5.2. At 800°C, the coefficient of friction increased further to 0.36 to 0.64. Finally, at 875°C, the coefficient of friction was 0.60 to 0.76.

It was concluded that:

a) The measured torque tends to increase with increasing applied compressive load, as expected.
b) For a given temperature, the coefficient of friction tends to decrease with increasing applied compressive load, especially for loads of 150 to 200 lbs.
c) The coefficient of friction tends to increase with temperature; however, this may be due to continuing wear of the gasket.

Experimental Error

A 2- to 3- degree misfit (or backlash) was evident in all of the friction measurement tests. Three areas were identified as sources of misfit in the rotational load train. Modifications were made to the test rig to minimize the misfit. Figure 14-77 shows the rotational torque versus rotational position plot for an applied compressive load of 50 lbs after the modifications.

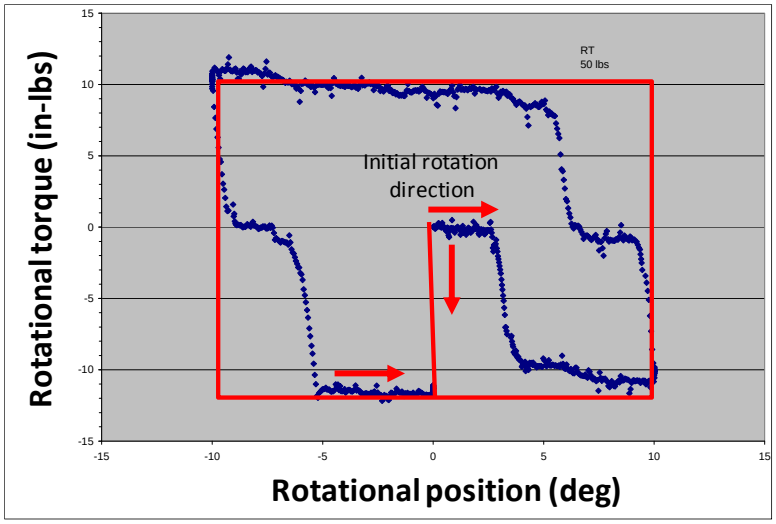

Figure 14-77. Rotational torque versus rotational position plot after design modifications. Red rectangle is theoretical response.

For an applied compressive load of 50 lbs, which is an applied compressive stress of 97 psi, a coefficient of friction of 0.4 was measured.

In regards to Figure 14-77, if the system response were perfect and the coefficient of friction were constant, the data would follow the red rectangle. While some of the misfit (or backlash) was removed from the test rig, there still seemed to be an initial 2-3° of low torque response as the stage begins to rotate from 0° to +10°. However, as the stage is rotated from +10°, the torque reading decreases rapidly and yields a near zero response for about the same 2-3°, and then increases. The near-zero reading lasts almost until the stage returns to near 0°. Based on these results, it seems that the test rig has significantly more than 2-3° of misfit while the stage is rotating.

Although the system response is not perfect, it was agreed that the current design yields a tolerable amount of misfit (2-3°) that is reproducible and does not significantly affect the coefficient of friction measurements for the gaskets.

Creep

Ceramatec studied the bars that were used to determine the relationship between fines added to the starting powders and elastic modulus (Figure 14-70) to measure flexural creep. Figure 14-78 summarizes the creep rate-stress curves measured at 900°C.

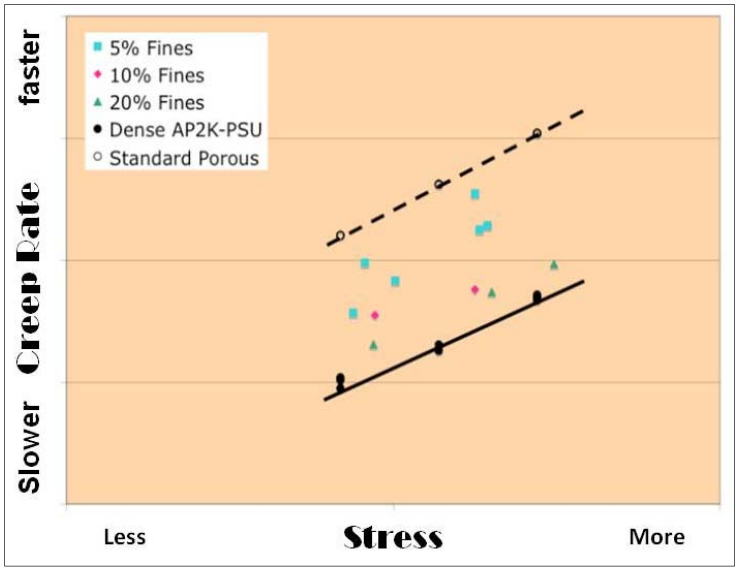

Figure 14-78. Creep rate-stress curves measured at 900°C for the porous bars with 5, 10, and 20% fines.

For a given stress, the creep rate decreases as the porosity decreases (% fines increases). In fact, the behavior of the bars with 20% fines is comparable to the creep response measured previously

for the dense AP2K. The strength of the bars with 20% fines is also significantly greater than that for standard porous materials. Both observations lead to the conclusion that the mechanical performance can be dramatically improved by lowering the porosity.

Table 14-7 summarizes the tensile creep strain rate data and creep stress exponents for eight porous AP2k bend bars tested by the Penn State at 850°C, 875°C, and 900°C .

Table 14-7. Summary of 4-point flexural creep for porous AP2k.

Tensile Creep of Porous AP2k Summary							
Sample#	**Test Rig#**	**Temp.(C)**	**Applied Stress (MPa)**	**Strain Rate (1/s)**	**Ln Stress**	**Ln Rate**	**Stress Exponent n**
11	1	850	6.89	3.70E-09	1.93	-19.41	1.93
			13.79	9.10E-09	2.62	-18.52	
			27.58	5.41E-08	3.32	-16.73	
12	2	850	6.89	2.14E-09	1.93	-19.96	2.02
			13.79	5.57E-09	2.62	-19.01	
			27.58	3.51E-08	3.32	-17.16	
3	2	875	6.89	3.81E-09	1.93	-19.39	2.53
			13.79	1.94E-08	2.62	-17.76	
			27.58	1.28E-07	3.32	-15.87	
5	2	875	6.89	4.30E-09	1.93	-19.26	2.12
			13.79	1.86E-08	2.62	-17.80	
			27.58	2.22E-07	3.32	-15.32	
8	1	875	6.89	9.68E-09	1.93	-18.45	1.83
			13.79	1.48E-08	2.62	-18.03	
			27.58	1.23E-07	3.32	-15.91	
4	1	900	6.89	1.93E-08	1.93	-17.76	2.07
			13.79	8.12E-08	2.62	-16.33	
6	1	900	6.89	1.93E-08	1.93	-17.77	2.00
			13.79	4.28E-08	2.62	-16.97	
			27.58	3.10E-07	3.32	-14.99	
7	2	900	6.89	1.81E-08	1.93	-17.83	
						Ave	**2.07**
						stdev	**0.22**

Figure 14-79 plots the Sample #3 creep strain versus time for the three applied stresses.

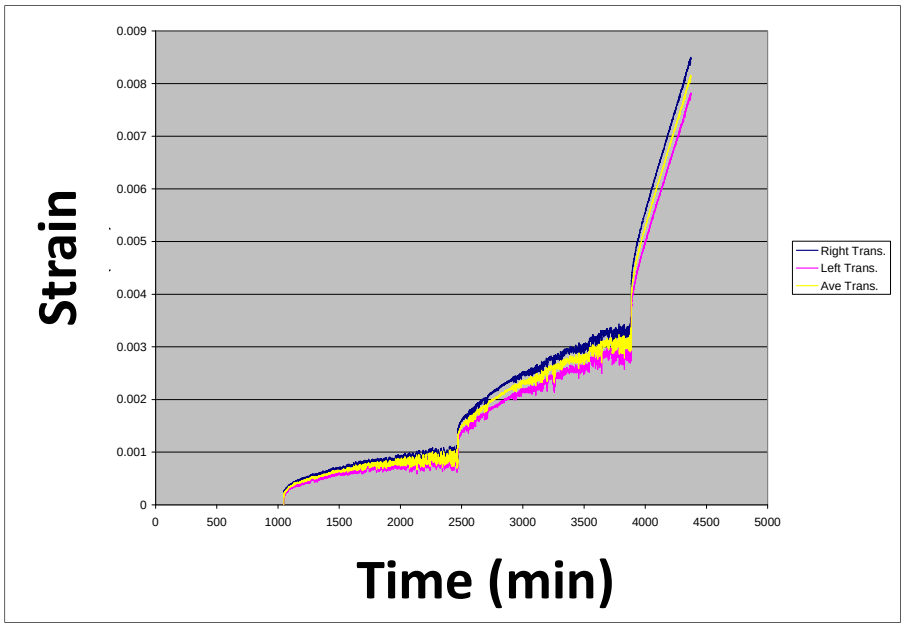

Figure 14-79. Flexural (4pt) creep strain versus time plot for porous AP2k sample #3 tested at 875°C with applied stresses of 6.84MPa (1ksi), 13.79 MPa (2ksi), and 27.58MPa (4ksi).

Figure 14-80 shows a summary log-log plot of the strain rate versus applied stress with linear regression fits of the data at each temperature.

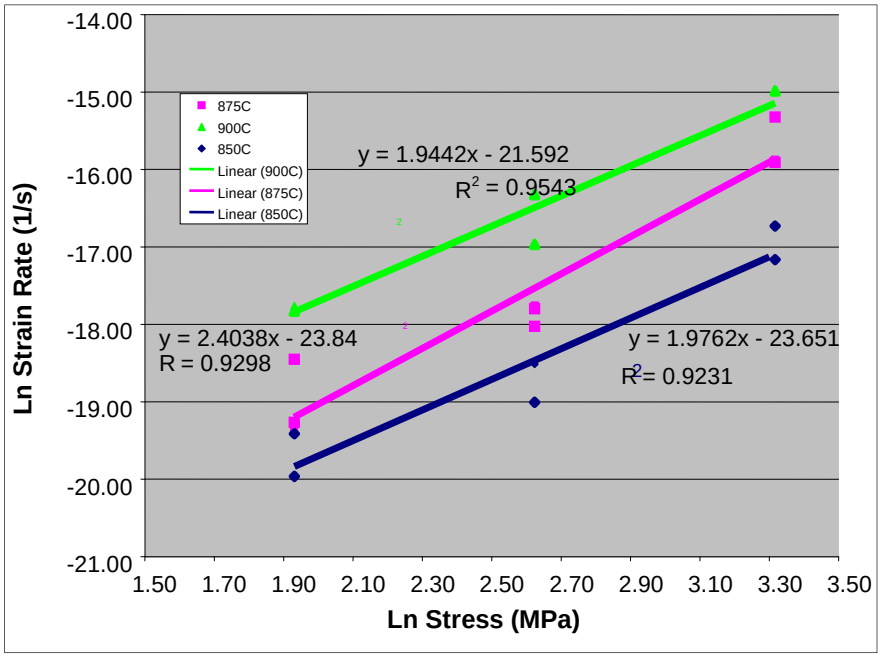

Figure 14-80. Log-log plot of the flexural creep strain rate versus applied stress for a porous AP2k tested at 875 and 900°C.

The slope of the regression fit was used to determine the steady-state creep stress exponent, which was 1.98 at 850°, 2.40 at 875°, and 1.94 at 900°C. If the data for all samples are pooled, then the average creep stress exponent is 2.07±0.22.

The activation energy for flexural creep was determined by plotting the average creep strain rate versus the inverse temperature in degrees Kelvin for each applied stress (Figure 14-81).

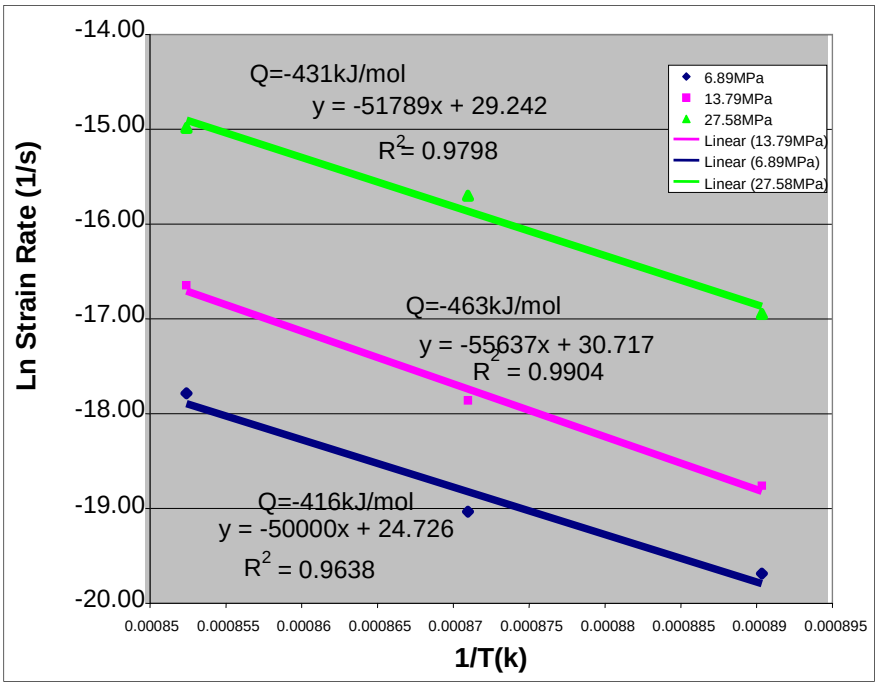

Figure 14-81. Natural log of the flexural creep strain rate versus inverse temperature plot for a porous AP2k tested at 875°C and 900°C to estimate creep activation energy (Q).

The creep activation energies for this porous AP2k sample were -416, -463, and -431 kJ/mol for applied stresses of 6.89, 13.79, and 27.58MPa respectively. The average of the creep activation energies for all the porous AP2k samples is -436±24kJ/mol.

Penn State measured flexural creep of 13 additional bend bar specimens at temperatures of 850°C, 875°C, 900°C, 925°C and 950°C and applied stresses of 6.89, 13.78, and 27.56 MPa. Figure 14-82 is a ln-ln plot of creep strain rate as a function of applied stress for the four materials tested at 900°C (20% fines, 10% fines, 5% fines and standard porous material).

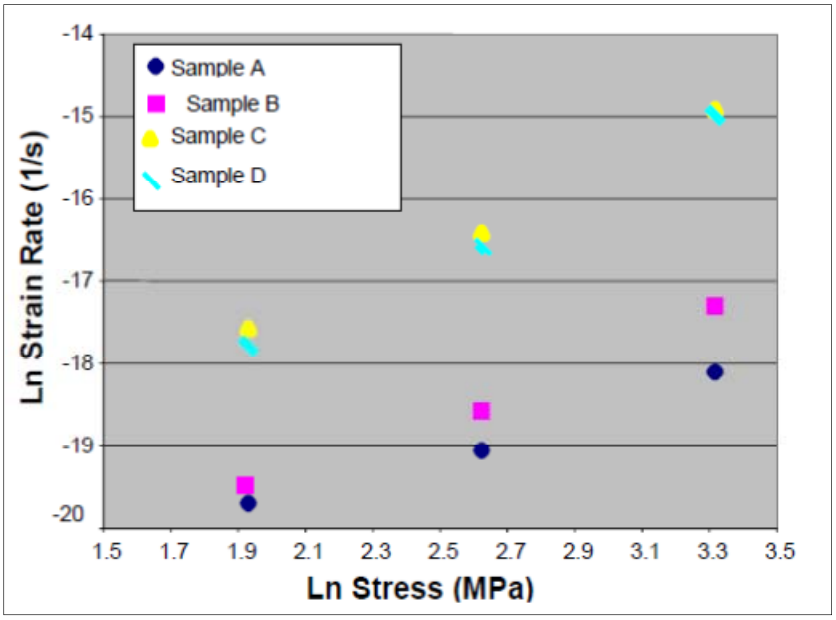

Figure 14-82. Log-log plot of flexural creep strain rate versus applied stress tested at 900°C for four porous materials.

The average creep stress exponent is 1.58±0.22 and the creep activation energies for applied stresses of 6.89, 13.78, and 27.56 MPa are -531, -442, and -430 kJ/mol respectively. Sample A had a slightly lower activation energy at 13.78 and 27.56 MPa relative to the other samples, and a much lower activation energy at a stress of 6.89MPa.

Table 14-8 summarizes the creep results, including creep rate as a function of applied stress and the resulting values for stress exponent (n) and activation energy, Ea.

Table 14.1-8. Flexural creep rates and creep parameters of AP2k samples.

Powder		Average	Flexural	Creep	Rate		Ea (kJ/mol)	Ave. Ea	StDev Ea	Ave n	Stdev n
		(1/s)	(1/s)	(1/s)	(1/s)		per Stress	(kJ/mol)	(kJ/mol)		
	Temp.(C)	850	875	900	925	950					
	Stress (MPa)										
Lot 3	6.89			3.62E-09	2.54E-08					1.86	0.15
Code B	13.78			1.05E-08	1.15E-07						
	27.56			4.69E-08	3.26E-07						
	(Stdev)			2.07E-09	1.01E-08						
	(Stdev)			2.45E-09	3.73E-08						
	(Stdev)			9.75E-09	1.36E-07						
Lot 3	6.89				2.19E-08					1.84	0.05
Code B	13.78				1.11E-07						
	27.56				2.87E-07						
	(Stdev)				1.14E-08						
	(Stdev)				5.21E-08						
	(Stdev)				1.66E-07						
Lot 3	6.89			1.30E-08	1.16E-08					1.73	0.29
Code C	13.78			3.89E-08	4.41E-08						
	27.56			1.07E-07	1.36E-07						
	(Stdev)			4.11E-09	9.48E-09						
	(Stdev)			1.63E-08	2.75E-08						
	(Stdev)			3.19E-08	6.32E-08						
Lot 3	6.89				1.34E-08					1.74	0.30
Code C	13.78				4.33E-08						
	27.56				1.26E-07						
	(Stdev)				1.27E-08						
	(Stdev)				3.89E-08						
	(Stdev)				8.58E-08						
Lot 3	6.89				1.17E-08					2.19	0.30
Code D	13.78				5.65E-08						
	27.56				2.50E-07						
	(Stdev)				9.13E-10						
	(Stdev)				1.68E-08						
	(Stdev)				8.18E-08						
Lot 3	6.89			8.32E-09	9.73E-09					2.10	0.32
Code D	13.78			3.13E-08	5.05E-08						
	27.56			1.16E-07	2.22E-07						
	(Stdev)			3.88E-09	3.44E-09						
	(Stdev)			6.94E-09	1.58E-08						
	(Stdev)			3.68E-08	7.57E-08						

Figures 14-83 and 14-84 plot the Ln strain rate versus Ln applied stress plots obtained at 925°C and 900°C respectively.

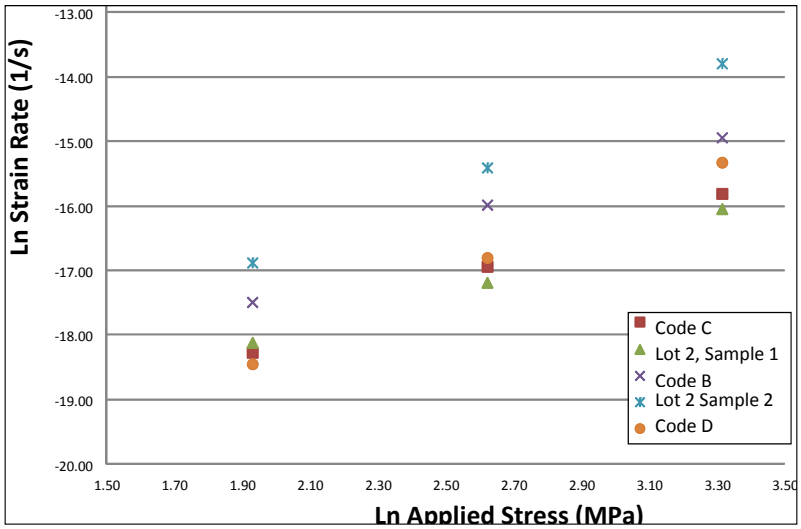

Figure 14-83. Ln strain rate versus Ln applied stress for AP2k samples tested at 925°C.

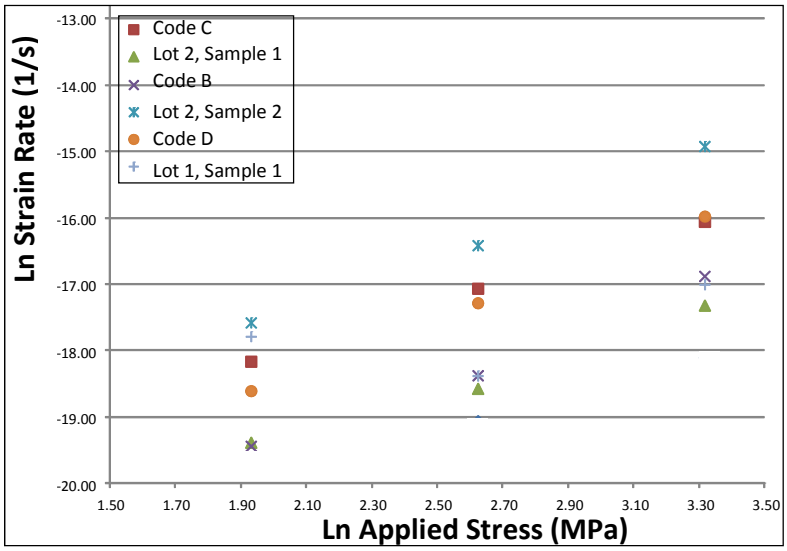

Figure 14-84. Ln strain rate versus Ln applied stress for AP2k samples tested at 900°C.

Compressive Creep

Bars

Compressive creep tests at 925°C were conducted on a laminated, low-porosity AP2k sample. The compressive stress was applied perpendicular to the lamination direction. Figure 14-85 plots strain versus time for applied stresses of 50 MPa, 60 MPa, and 70 MPa. The compressive creep strain rates were 2.80×10^{-8}, 1.87×10^{-8} and 2.6×10^{-8}/sec respectively.

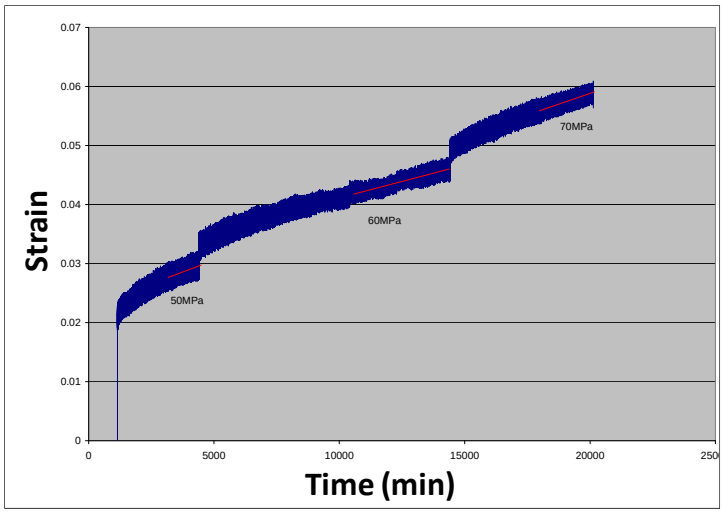

Figure 14-85. Compressive creep strain versus time plot for a laminated low-porosity AP2k sample #8 tested at 925°C with stress applied perpendicular to lamination direction of sample creep strain.

Figure 14-86 shows the results of the compressive creep test on a laminated high-porosityAP2k Sample #3 at 925°C and applied stresses of 10, 20, and 30MPa.

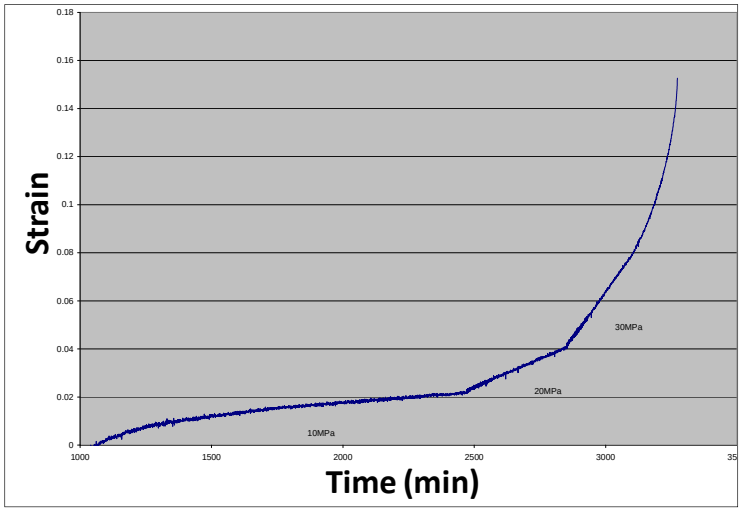

Figure 14-86. Compressive creep strain versus time plot for laminated high-porosity AP2k Sample #3 tested at 925°C with stress applied parallel to lamination direction of sample.

The resulting creep strain rates were 1.59×10^{-7} (10 MPa), 7.87×10^{-7} (20 MPa), and 2.564×10^{-6}/sec (30 MPa). The strain rate increased approximately 200 minutes after increasing the applied stress to 30 MPa. This may be evidence of tertiary creep. When the sample was removed from the

furnace, it was found to have fractured into multiple fragments and fallen off the loading rams. The calculated creep stress exponent for this sample was 2.50 (Figure 14-87).

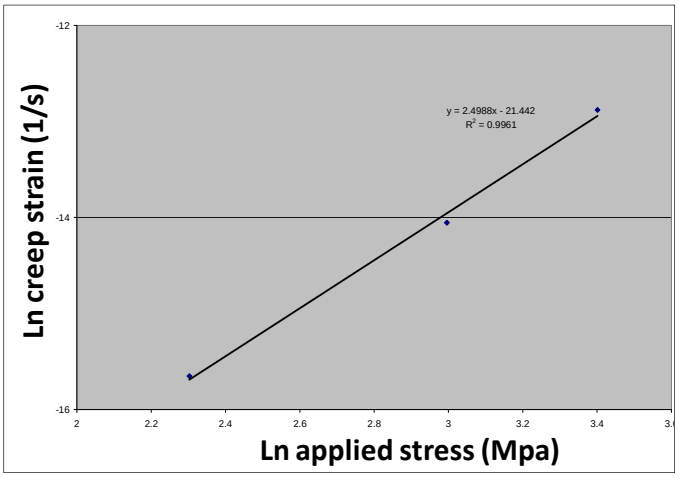

Figure 14-87. Ln creep strain rate versus Ln applied stress plot for laminated, high-porosity AP2k Sample #3 tested at 925°C, yielding a creep stress exponent of 2.5.

At this high temperature, the high-porosity AP2k creep was much faster than low-porosity AP2k. Creep rate differences of 1-1.5 orders of magnitude were measured at significantly lower applied stress.

Penn State conducted additional creep tests on three high-porosity AP2k rod samples at 875°C and applied stresses of 6.89, 13.78, 27.52 MPa (1, 2, and 4 ksi). Table 14-9 summarizes the compressive creep results.

Table 14-9. Summary of compressive creep for high-porosity AP2k cylindrical rods.

Sample #	Temp (C)	Stress (MPa)	Strain rate (1/s)	Ln Stress (MPa)	Ln Strain Rate (1/s)	n
1	875	6.89	1.22E-08	1.93	-18.22	0.53
		13.79	1.76E-08	2.62	-17.85	
		27.58	2.54E-08	3.32	-17.49	
2	875	6.89	3.71E-09	1.93	-19.41	1.25
		13.79	5.57E-09	2.62	-19.01	
		27.58	2.11E-08	3.32	-17.67	
3	875	6.89	5.49E-09	1.93	-19.02	0.86
		13.78	6.46E-09	2.62	-18.86	
		27.56	1.81E-08	3.32	-17.83	
Average		6.89	7.12E-09	1.93	-18.89	0.88
		13.78	9.89E-09	2.62	-18.57	
		27.56	2.15E-08	3.32	-17.66	

The average compressive creep strain rates (1/s) of 7.12×10^{-9}, 9.89×10^{-9}, and 2.15×10^{-8} were measured for the three applied stresses of 6.89, 13.78, and 27.52 MPa respectively. The calculated creep stress exponent is 0.88±0.36. This creep stress exponent is much smaller than that obtained for the flexural creep, which was 2.07±0.22.

Elastic Properties

The Penn State conducted tests to determine the Young's and shear moduli of porous AP2k samples as a function of temperature by using the high-temperature, acoustic-resonant test method. The heating and cooling rate is 30°/hr with dwell times of 30, 15 and 10 minutes. This ensures the samples reach thermal and chemical equilibrium prior to being resonated. Two samples from each lot were tested, one using the flexural mode and the other using the torsional mode. The flexural mode yields the Young's modulus, while the torsional mode gives the shear modulus.

The Young's and shear moduli as a function of temperature are plotted in Figures 14-88 and 14-89 respectively.

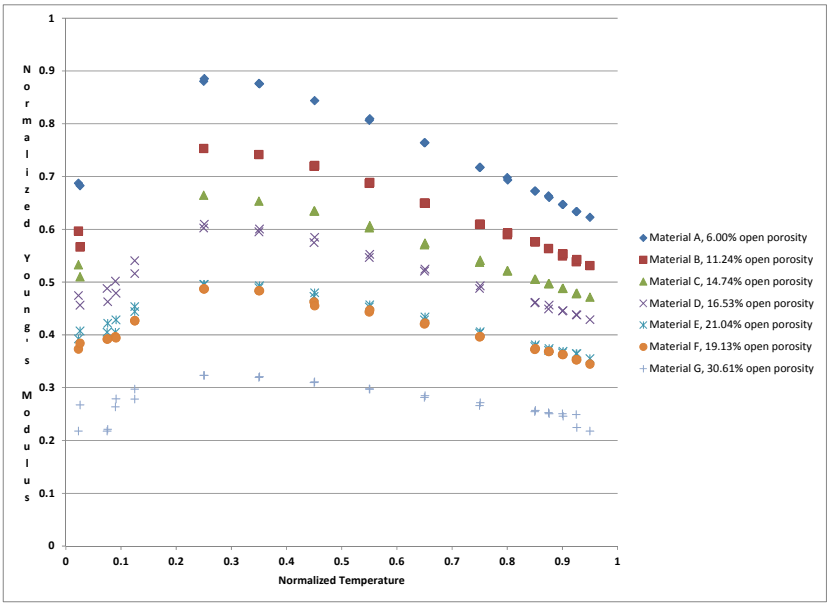

Figure 14-88. Young's moduli of AP2k as a function of temperature.

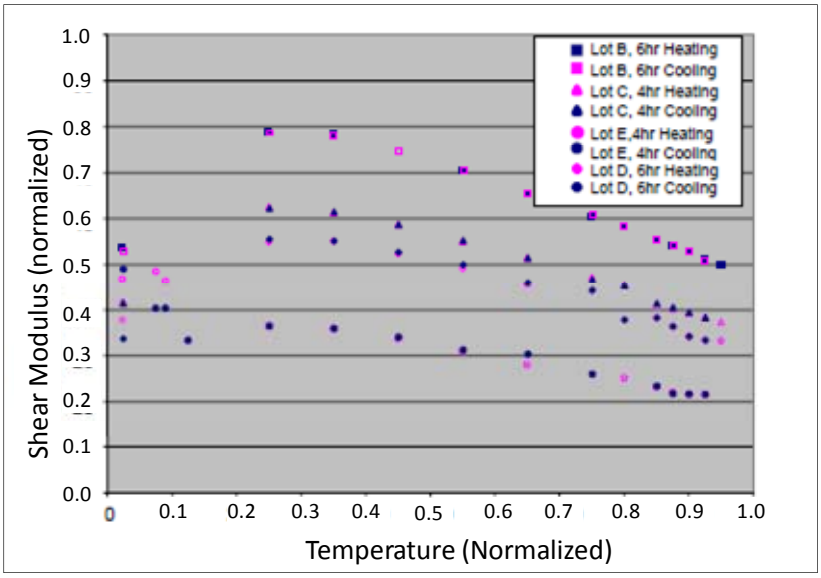

Figure 14-89. Shear moduli of AP2k as a function of temperature.

14.1.2 Specification of Allowable Process Gas Composition

Background

The composition of the feed gas to the ITM system is not purely atmospheric gases (i.e., O_2, N_2, Ar). For example, water and carbon dioxide will be present if the feed gas is heated by direct firing with methane. Compounds can be released into the feed stream from the materials in the ITM flow duct via desorption, decomposition, or as the result of chemical equilibrium-driven mass transfer. Some of these compounds can contaminate the ITM ceramic, resulting in a loss of performance (i.e., oxygen flux). These contaminant materials must be minimized and/or removed from the feed stream to ensure oxygen flux is maintained for the projected life of the ITM modules. Air Products completed thermodynamic stability calculations and experiments to determine the impact of various contaminants on the ITM ceramic composition and flux.

The primary sources of contamination are the insulating materials and metal components in the flow duct. Studies determined the rate of contamination associated with various insulating materials and metal alloys. The information was used to specify the insulating materials and the material of construction for components contacting the feed air. The impact of feed gas carbon dioxide and water partial pressure on oxygen flux was also investigated.

The concentration of two contaminants, SO_2 and $CrO_3(g)$ needs to be reduced to levels below those achievable simply through a judicious choice of materials. Air Products evaluated candidate getter materials experimentally to determine their ability to remove contaminants from the feed gas and to design a getter system which would ensure the ITM modules maintain an acceptable flux rate for their projected life.

Contaminants

Refractories

$Si(OH)_4$ from Silica (SiO_2)

Silica is a typical component in refractories. Silicon tetrahydroxide, $Si(OH)_4$, is the most thermodynamically favored gas phase species in equilibrium with silica.

Sulfur Dioxide (SO_2) from Sulfur

Sulfur is a trace element in refractories which can evolve as sulfur dioxide (SO_2). It was also determined that refractories can adsorb sulfur dioxide at ambient temperatures and release it as the temperature increases.

Metals

Numerous metal components of the ISTU system contact high-temperature feed gas. At these temperatures, chromium, molybdenum and tungsten in the metal alloy may volatilize and contaminate the ITM material/module. Physical contamination through the spallation of metal oxidation can also occur.

Refractory: $Si(OH)_4$ from Silica (SiO_2)

Experimental Method

A steam/air mixture was flowed through a candidate refractory at elevated temperature for a period of seven days. The exit gas then flowed over an ITM ceramic "witness" piece immediately downstream of the refractory. The gas had a water partial pressure of 0.75 atmospheres, which is characteristic of the case when feed air is heated by direct firing of methane. Figure 14-90 is a schematic of the experiment.

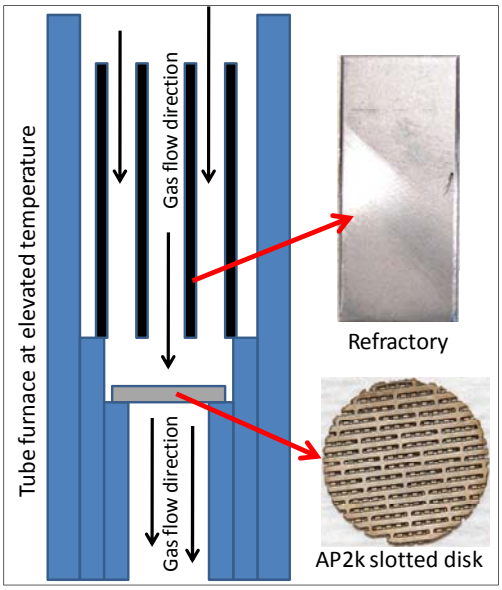

Figure 14-90. Experimental set up showing an AP2k slotted disk positioned downstream of the alloy plates within tube furnace.

The witness piece was examined in a scanning electron microscope and analyzed by EDS to determine the level of silica species contamination. Figure 14-91 shows micrographs of four witness piece after being exposed to the candidate refractory exit gas.

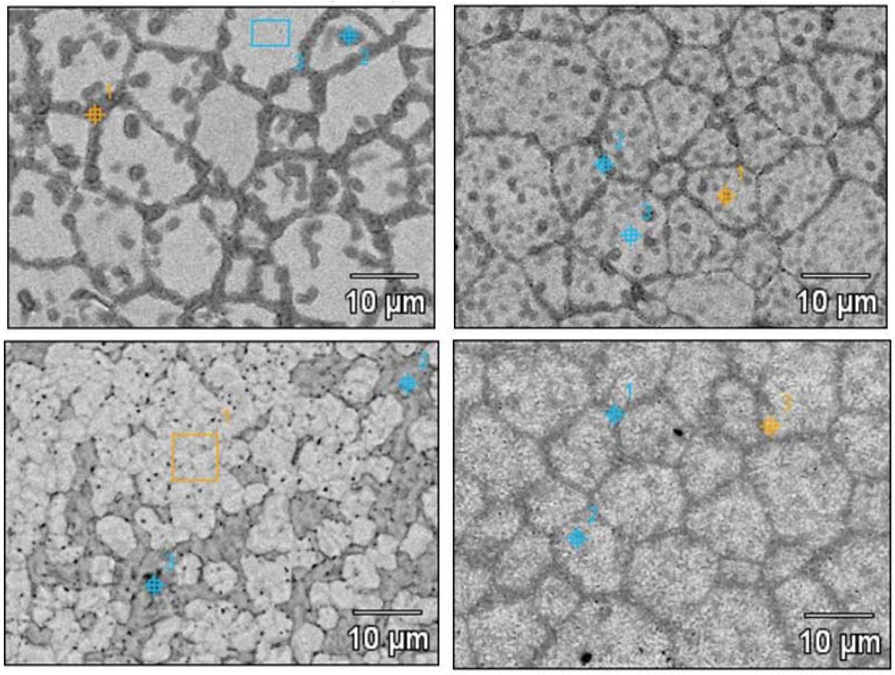

Figure 14-91. SEM micrographs of ITM ceramic witness pieces downstream of candidate insulations after exposure to flowing air and steam.

Results

Table 14-10 is a listing of the refractory materials testing for silica and/or sulfur contamination. Seventeen refractories were specifically tested for silica contamination. Two refractories caused substantial silica contamination.

Table 14-10. Tested refractory materials.

Refractory Material		
Insulation A	Insulation H	Blanket C
Insulation B	Insulation J	Blanket CW
Insulation C	Insulation K	Insulation Z
Insulation D	Insulation M	Insulation ZR
Insulation E	MgO brick 1	Loctite C5A
Insulation F	Alumina foam	Ceramic Paper
Insulation G	MgO foam	MgO brick 2
Castable I	Blanket "U"	

Refractory: SO_2

The SiO_2 micrographs were also examined for sulfur contamination. Nine of the 17 refractories caused sulfur contamination of the witness piece. This was unexpected, as the sulfur content of the tested refractories was <0.1 wt%. Also, when refractory D was used in the SEP flow duct, the initial SO_2 concentration in the outlet air went off-scale. The evolution rate was ~10X higher than one of the blanket refractories. This was inconsistent with the refractory sulfur contents. Refractory D contained 0.0019 wt % sulfur compared to 0.0054 wt % sulfur in the blanket material. It was speculated that the refractories were adsorbing sulfur dioxide at ambient conditions and desorbed the SO_2 at elevated temperature.

Flow Path Testing of Refractories

The experimental method to assess sulfur contamination was similar to the SiO_2 methodology. Air Products conducted tests lasting seven days. In this case, the first 7-day test was followed by a second 7-day test with a new witness piece. The second test was conducted to determine if the sulfur contamination was transient. Figure 14-92 shows micrographs from one of the trials.

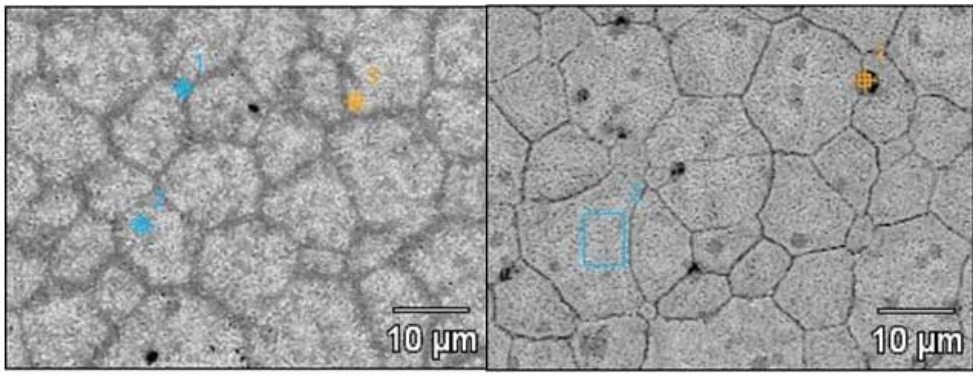

Figure 14-92. SEM micrographs of the surface of two ITM witness pieces downstream of the candidate refractory material after exposure to an air and steam mixture. The image on the left is the witness piece after the first week of exposure. The image on the right is a new witness piece exposed to a second week of flow.

Sulfur contaminated the witness piece during the first week. The witness piece exposed to the gas during the second week did not exhibit sulfur contamination. Tests on other refractories produced the same result, so it was concluded that the sulfur contamination was transient.

SO_2 Adsorption

Experiments were conducted to determine if the evolution of sulfur dioxide from the refractories was, in part, due to the adsorption of SO_2 at ambient temperatures and its subsequent desorption at elevated temperature. Thermal programmed desorption (TPD) was used to determine:

- If the as-received samples evolve SO_2 when heated.
- The temperature at which SO_2 evolves.
- Whether, after being heated to elevated temperature, the materials adsorb SO_2 at ambient temperature from an air stream with a SO_2 content of 50 ppb.
- The temperature at which SO_2 adsorbed at ambient temperature desorbs.

The as-received refractory was ground to a coarse powder and a 4.5 g bed was prepared. A flow of 100 sccm of SO_2-free air was passed through the bed as it is heated to temperature. The SO_2 concentration of the air was measured. The sample was cooled to the ambient temperature, then subjected to an air flow with an SO_2 concentration of 50 ppb for a period of 72 hours. The sample was then tested for SO_2 evolution using the same procedure as above. Figure 14-93 documents the SO_2 evolution from Material D after it was exposed to the 50 ppb SO_2 air.

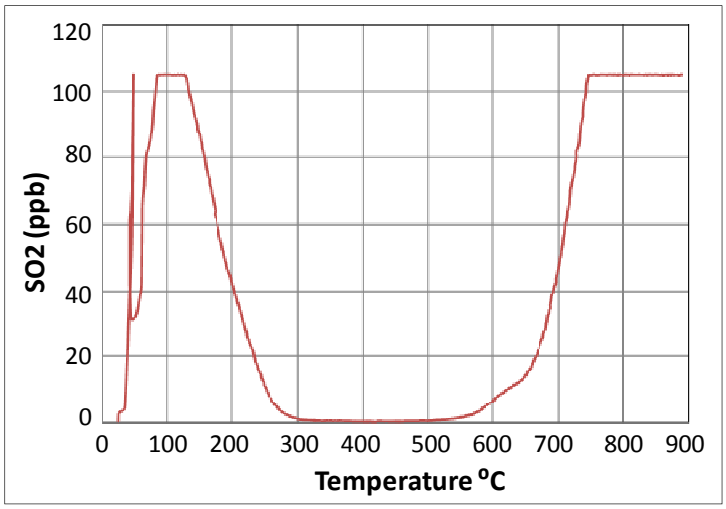

Figure 14-93. Thermal program desorption of Refractory D after 72 hours of exposure to 50 ppm of SO_2.

High levels of SO_2 evolution occurred at low temperatures, presumably from physisorbed SO_2 and again at high temperatures, presumably from either chemisorbed SO_2 or the decomposition of a sulfate compound.

Figure 14-94 is a plot of the SO_2 levels in the effluent air as a function of temperature for a number of as-received samples of refractories.

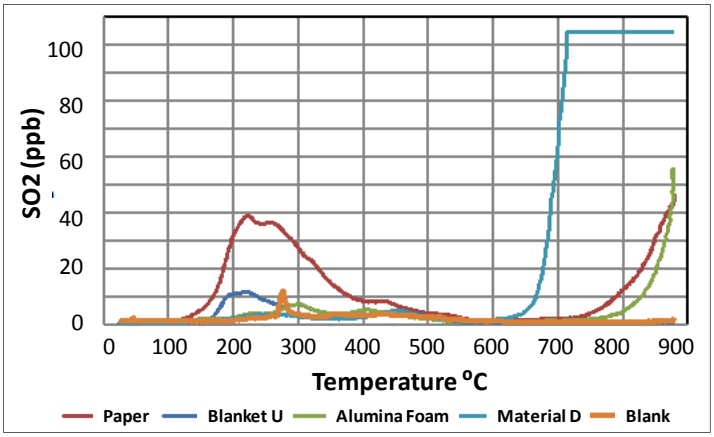

Figure 14-94. Thermal program desorption of various as-received refractories.

All of the refractories evolved SO_2 at high temperatures. However, refractory D evolved substantially more than the other materials. This explained the high levels of SO_2 in the outlet air from the SEP when refractory D was used.

The paper and alumina foam samples were exposed to the 50 ppb of SO_2 air. Figure 14-95 is a plot of the data.

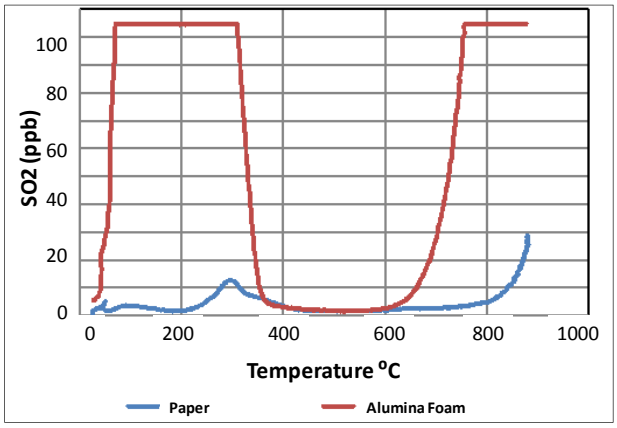

Figure 14-95. Temperature programmed desorption (TPD) results of paper and alumina foam insulation after exposure to 50 ppb air.

The alumina foam evolved very high levels of SO_2 at low temperatures and again at higher temperatures. The ceramic paper evolved modest amounts of SO_2 at elevated temperatures. When Figures 14-94 and 14-95 are compared, it is clear that the alumina foam adsorbs SO_2 at ambient temperature. *Note that the alumina foam is plotted in green in Figure 14-94 and in red in Figure 14-95*

In some cases. the evolution of SO_2 of the as-received sample was greater than the evolution after exposure to 50ppb air. As a result, it was decided to determine the SO_2 evolution rates of all as-received candidate insulating materials. Figures 14-96 and 14-97 document the results from a subset of tested materials.

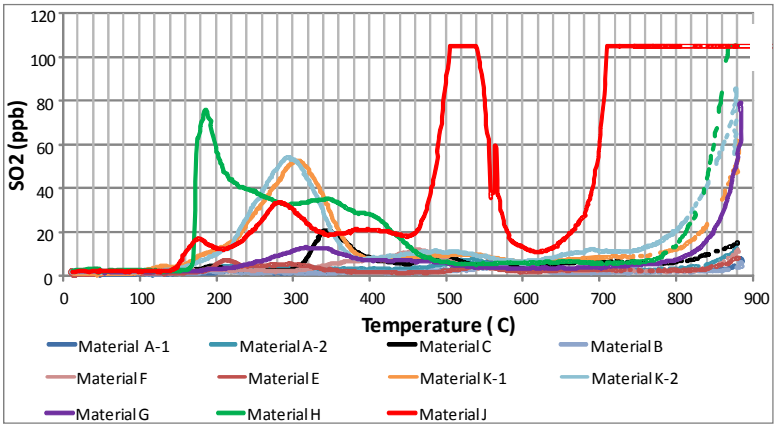

Figure 14-96. Temperature programmed desorption (TPD) results of various as-received insulating materials.

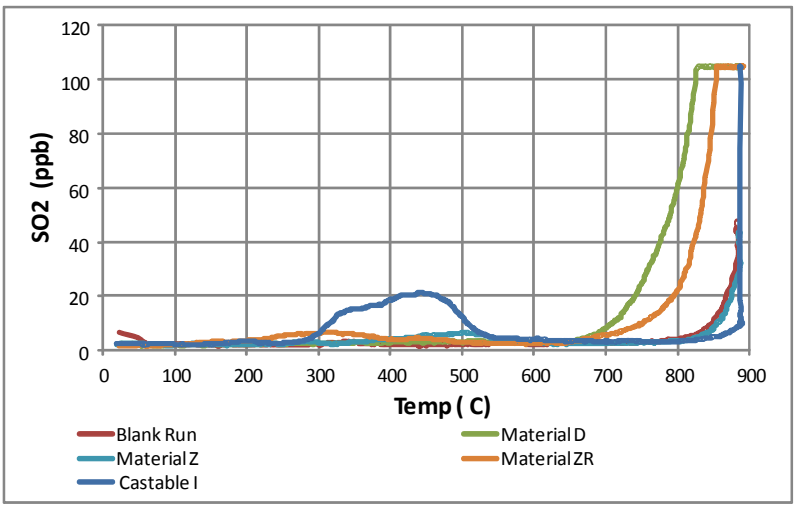

Figure 14-97. Temperature programmed desorption (TPD) results of various as-received insulating materials.

Most materials have very similar desorption curves. There are one or two low-temperature peaks in the SO_2 levels between 200°C and 600°C. This is likely due to pre-existing adsorbed/absorbed SO_2. For materials with two peaks, there must be two types of sorption sites. All materials evolve an increasing amount of SO_2 at high temperature. Some of the SO_2 is due to desorption from the apparatus, especially the stainless steel upstream and downstream of the heated quartz reactor that holds the sample. This can be seen in Figure 14-97 where the blank run (red line) exit gas SO_2 concentration increased when the temperature exceeded 800°C.

Materials that evolved high levels of SO_2 at high temperature likely contain sulfur in a chemical form, such as a sulfate, which decomposes above 800°C. Refractory J evolved more SO_2 than any other material tested. Its evolution rate peaks at 500°C, a temperature where all other materials did not evolve SO_2. It also evolved high levels of SO_2 at high temperature. This is consistent with the WDXRF results that showed that Refractory J had high total sulfur content.

Recommendation for SO_2 Monitoring in the ISTU

The work discussed above verified that some of the refractory materials being used in the ISTU will initially emit measureable SO_2, but the emission rate is expected to drop off rapidly with time at elevated temperature.

Given the potential evolution of SO_2, it was decided to include an SO_2 analyzer in the ISTU design to track SO_2 levels during initial start-up, ensure that SO_2 evolution has slowed to an

acceptable level before installing membrane modules, and provide ongoing monitoring of SO_2 concentrations in the ISTU flow duct during operation. The initial design specified stainless steel tubing to convey the gas from the ISTU flow duct to the analyzer. The adsorption of SO_2 onto the walls of stainless steel tubing and/or its reaction with adsorbed water was identified as a potential source of erroneous SO_2 data. Experiments were conducted to assess this possibility. The primary objective was to understand the response time and accuracy of the analyzer given various step changes in SO_2 concentrations. The effect of humidity was also investigated, and the impact of ambient temperature was documented.

A 50-foot coil of 316SS tubing (approximately the distance between the ISTU sample point and the analyzer location) was plumbed between a gas blending manifold and an analyzer. The tubing was heated for 20 minutes while 1,000 sccm of air flowed through the tubing to desorb water vapor and other volatile contaminants. A flow of 700 sccm of pure air and 0.0 – 30.0 sccm of air with a known trace concentration of SO_2 was mixed and sent to the analyzer. The coil was, at times, humidified by bubbling 1,000 sccm of pure air through water at ambient temperature and then directing it through the coil. This treatment was done for 30 minutes, followed by three minutes of flow with the feed diverted around the bubbler to purge most of the moist air from the tubing (i.e., leaving only the adsorbed water vapor).

The results clearly established that 316SS tubing will adsorb/desorb SO_2. There was an initially high adsorption rate. Once the tubing had been "pickled," the working capacity for SO_2 was 20X lower, and the time to approach steady state was about 8 hours. The time to reach desorption steady state was at least 20 hours and may have been substantially longer. The presence of adsorbed water greatly increased the capacity for SO_2 adsorption and increased the time to steady state. It was also found that the measured SO_2 concentration (and presumably the adsorption and desorption rate) was quite sensitive to changes in the ambient temperature.

Based on these results, a decision was made to use SilcoNert™ tubing to reduce the propensity for SO_2 adsorption onto the tubing wall, and to heat-trace the majority of the tubing from the flow duct to the analyzer. A small portion of the tubing adjacent to the process (tentatively two feet, based on a process team calculation) was left uninsulated/traced to ensure that the gas cools sufficiently prior to entering the analyzer.

Metal: Chromia

The primary contaminant gas from metals in contact with the feed gas is CrO_3. The vapor pressure of CrO_3 over $MnCr_2O_4$ (s) was determined. The thermodynamic functions were calculated from three different literature sources, and the information was added to the HSC thermodynamic database. Figure 14-98 plots the calculated vapor pressure of CrO_3(g) in 18 bar(a) air over $MnCr_2O_4$(s) using each data source and also over Cr_2O_3(s).

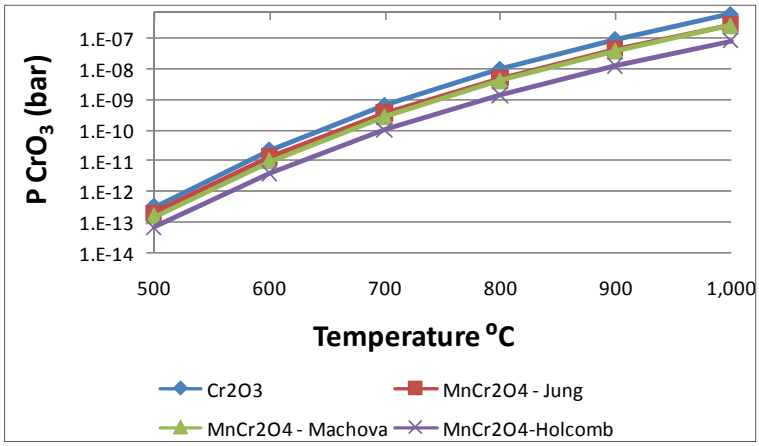

Figure 14-98. Calculated partial pressure of CrO_3 over Cr_2O_3 and $MnCr_2O_4$.

Between 800°C and 900°C, the vapor pressure of $CrO_{3(g)}$ over $MnCr_2O_4$(s) is predicted to be 13-46% of the predicted vapor pressure over Cr_2O_3(s), depending on which thermodynamic data is used. This is in qualitative agreement with experimental data and suggests that the $CrO_{3(g)}$ is in equilibrium with $MnCr_2O_4$(s).

Flow Path Testing

A metal sample was place in a reactor and heated to a specific temperature. Air at the sample temperature and atmospheric pressure flowed over the sample. After a specific time period ranging from zero to five weeks, an ITM witness piece was placed immediately downstream of the coupon and the experiment was continued. After a specific time period (usually 1 week), the witness piece was removed and replaced by a fresh witness piece. This procedure continued until the experiment concluded.

The witness piece was examined in a scanning electron microscope (photomicrographs) and by EDS to determine the level of chromium contamination. Alloys being used in the SEP and prospective alloys for ITM components were tested to determine their propensity to contaminate

the ITM modules. Figure 14-99 is a micrograph from one of these experiments.

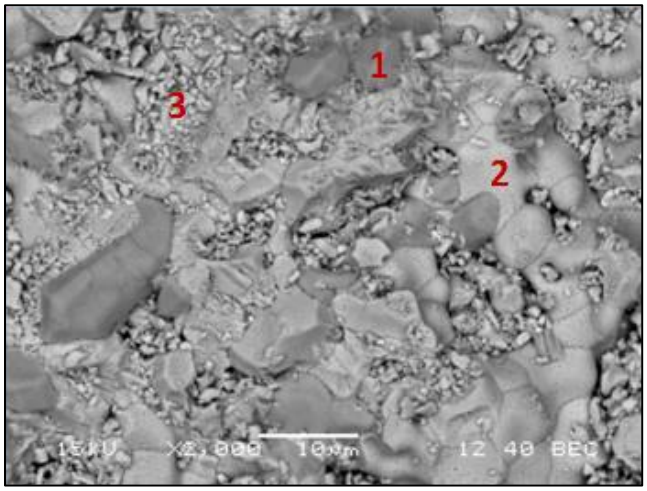

Figure 14-99. AP2k surface located on the downstream side of Alloy A at 815ºC using 39°F dewpoint air. The AP2k was treated at 815ºC for a total of 1 week and the alloy was aged for 1 week.

Table 14-11 documents the result of a subset of tested alloys.

Table 14-11. Alloy AP2k contamination data.

Alloy	Temp. (°C)	Witness inserted, week	Chromium	Molybdenum
A	815	1	√	trace
A	815	2	√	
A	815	3	√	
A	815	4	√	
A	815	5	√	
E	815	4		√
E	815	5		√
F	815	1	√	
F	815	2	√	
F	815	3	√	
F	815	4	√	
F	986	4	√	
F	986	5	√	
G	815	2	√	
G	815	3	√	
X	875	7		√
X	875	8		√
330	875	3	√	
330	875	4	√	

Coatings

Additional experiments evaluated chromium contamination from alloys subjected to a pretreatment and alloys that had a coating applied. The same experimental procedure, as above, was used. Figure 14-100 is a micrograph of a coated alloy F sample. Results indicate that the pretreating and coating the alloys reduces chromium contamination.

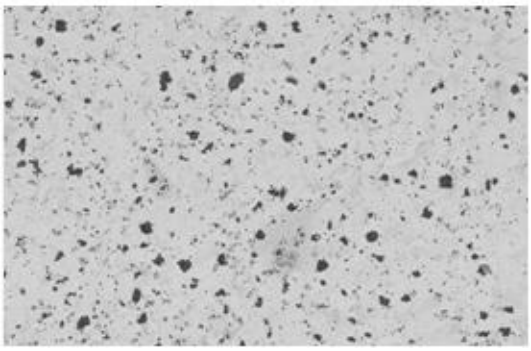

Figure 14-100. SEM image of a coated Alloy F sample.

Thermal cycling of the pretreated and coated alloy samples was conducted to evaluate their performance. Results were assessed using SEM imaging (morphology) and EDS analysis (chemistry). Figure 14-101 shows a series of SEM images of an Alloy A, Alloy A with Coating 1, Alloy A with Coating 2 and Alloy F with Coating 2, following thermal cycling.

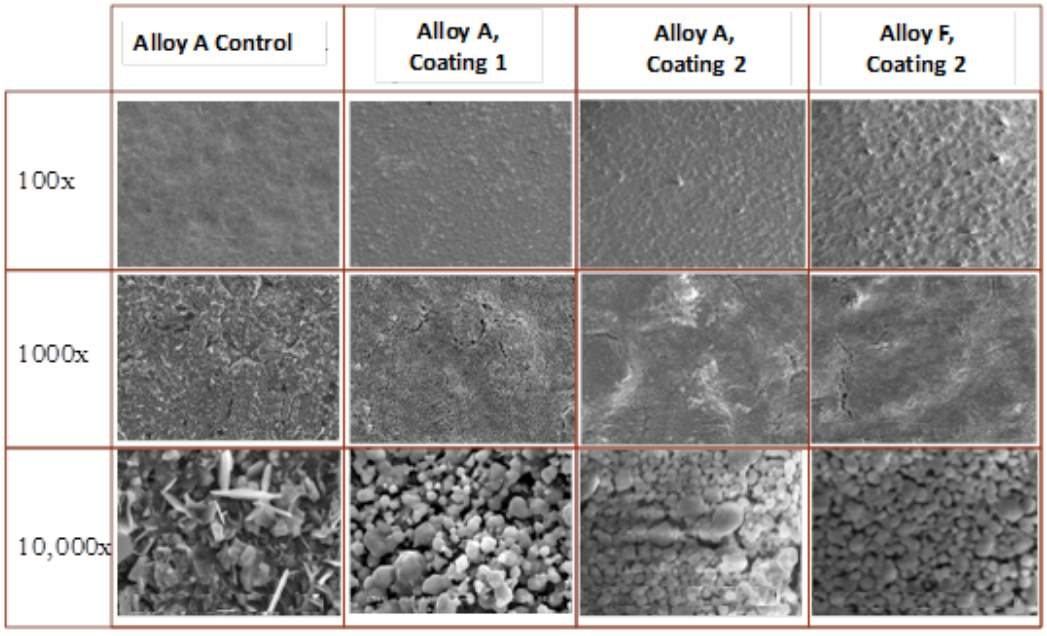

Figure 14-101. Surface SEM images of coated Alloy A and Alloy F coupons.

In a thermal cycling assessment of a coated Alloy A, it was found that coating adhesion to the metal coupon was maintained, but the coating quality deteriorated. Substantial spallation at both the metal-scale and scale-coating interfaces occurred.

Chromium Effect on Flux

An SLTR feed system was modified to determine the effect of chronic and acute chromium contamination on wafer oxygen flux. Acute chromium effects are due to surface competition for adsorption sites. Chronic effects are due to gradual accumulation of chromium on the wafer surface and reactions that form new phases. The modified SLTR feed system is depicted in Figure 14-102.

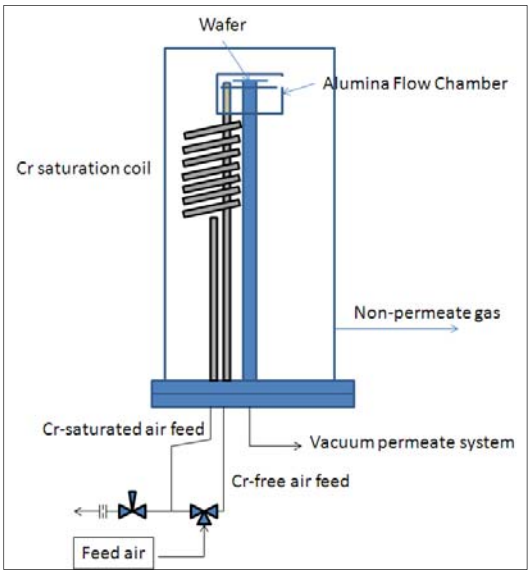

Figure 14-102. VP-SLTR feed system for chromium impact assessments.

Two separate tubes are used to feed air into the flow path of a subscale module. The first feed tube passes air through a coil in the hot zone of the furnace and then enters the flow chamber. The second feed tube terminates with a short length of alumina tubing containing a section of chromium getter. A 3-way valve outside the vessel allows back-and-forth switching between the two feed paths. To minimize the possibility that Cr-rich air might diffuse out of the end of the Cr-saturated feed when Cr-free feed is desired, the Cr-saturated line is designed for backflow through a very small bleed controlled by an orifice and regulating valve. Both feed paths enter the alumina flow chamber at approximately the same location. The Cr-free feed line switches from saturated tubing to the alumina/getter at the point where it enters the bottom of the flow

chamber. Air exits the flow chamber through a slit on the perimeter opposite the feed point, then exits the vessel as non-permeated gas through a line located near the bottom of the vessel.

The experimental procedure is to start up with Cr-free air, establish an oxygen flux baseline, and then switch to a Cr-saturated feed. If there is a decrease in performance, the feed is switched back to Cr-free to determine if any of the effect is reversible. In one experiment, a slow decrease began at hour 275 which is consistent with an irreversible change to the surface morphology/chemistry.

In a separate experiment, an AP2k sample was exposed to chromium for three, six and twelve hours. Dilatometry was used to compare the expansion of this sample (Figure 14-103).

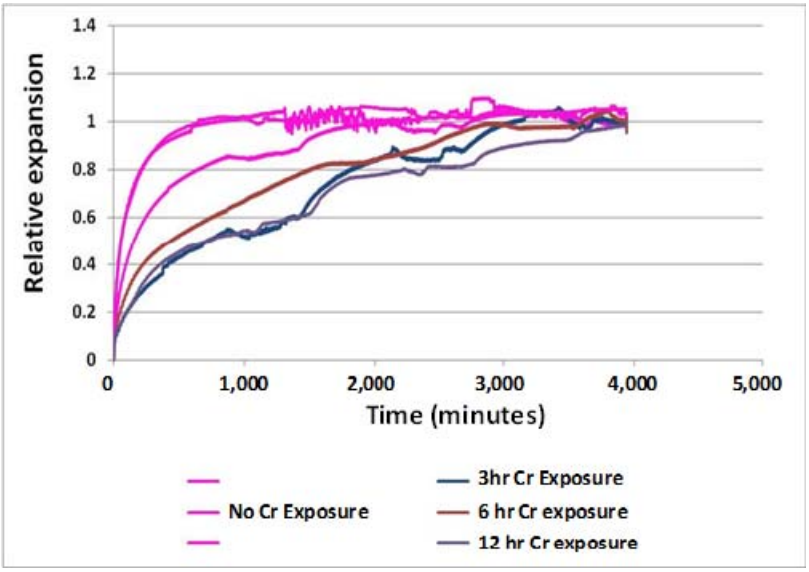

Figure 14-103. Reduction response of chromium exposed and unexposed AP2k samples.

It was expected that a longer transient response would occur with the longer exposure times. This was not the case; the entire sample set showed similar response times.

Moisture and Carbon Dioxide

Water does not react with the ITM ceramic, but does reduce the feed gas oxygen partial pressure through dilution. At levels below a critical level, carbon dioxide behaves similarly. The reduced oxygen partial pressure reduces the oxygen concentration gradient across the ITM membrane and the oxygen flux. Figure 14-104 documents the influence of humidity.

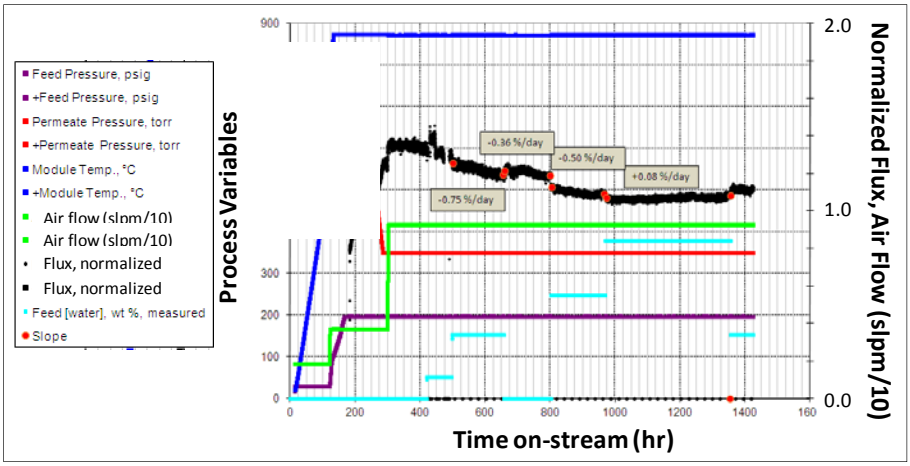

Figure 14-104. Influence of water vapor on subscale module flux.

After an initial period of flux loss, the module flux remained very stable regardless of the water content of the feed air. Figure 14-105 documents the influence of carbon dioxide on flux.

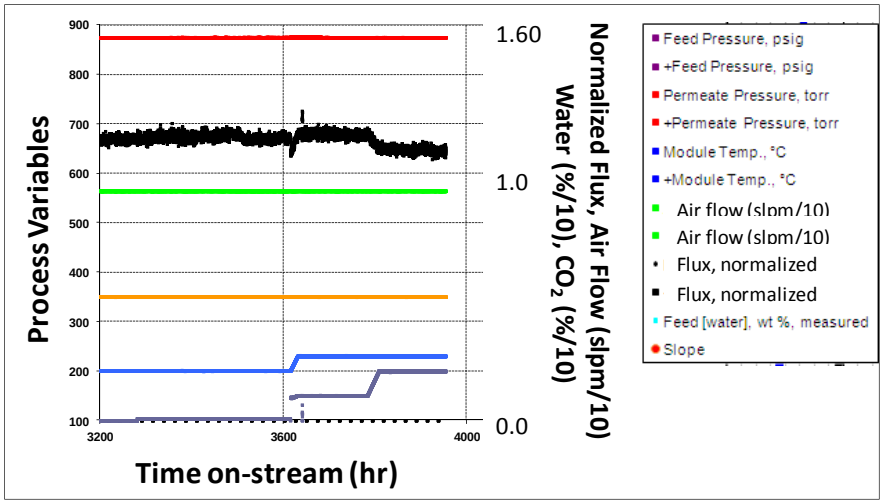

Figure 14-105. Influence of process variables on subscale module flux.

There was no statistical change at the lowest carbon dioxide partial pressure. Operation at a higher total pressure nearly offset the impact of the second carbon dioxide pressure. Increasing the CO_2 partial pressure to the third level decreased the flux.

Air Products conducted additional experiments to determine the impact of water and carbon dioxide on purity and flux; Tables 14-12 and 14-13 summarize the work. The tables reflect a variety of sample wafer formulation types and wafer-architectural approaches to reduce the effects of contaminants on operation.

Table 14-12. Impact of moisture on purity and flux, summary of experiments.

Date	Composition	Comment
03/07	2% H_2O	Drop in flux followed by a recovery. Possible Si contamination Significant water entered the permeate stream then tapered off
05/07	2.1% H_2O	No flux impact. Purity increase
06/07	0.5-3% H_2O	No flux impact Purity decline at 1%
07/07	3% H_2O	Slight flux impact
10/07	0.4% H_2O	No flux impact Purity increase, decayed and then recovered
10/07	2.5% H_2O	No flux impact Significant purity reduction
11/07	2.5% H_2O	No flux impact
12/07	3.0% H_2O	Measurable flux decrease
03/08	3.0% H_2O	Immediate 16% flux drop, recovered to 4% over 120 hours, recovered to baseline at 1,000 hours
08/08	3,0% H_2O	Purity increase to near 100%
08/08	3.0% H_2O	Immediate and long term purity improvement No flux impact
12/08	3.0% H_2O	Immediate flux drop that was not recovered
06/09	$\leq$8.0% H_2O	No flux impact
06/09	$\leq$ 8.0% H_2O	No flux impact

Table 14-13. Impact of carbon dioxide on purity and flux, summary of experiments.

Date	Composition	Comment
08/07	400 ppm CO_2	Measurable flux reduction with recovery to near baseline
11/07	400ppm CO_2	5% decrease in flux with recovery
03/08	3.0% H_2O 400ppm CO_2	No flux impact due to CO_2
08/08	3.0% H_2O 400ppm CO_2	No flux impact due to CO_2 No purity impact due to CO_2
08/08	3.0% H_2O 400ppm CO_2	No flux impact due to CO_2 No purity impact due to CO_2
12/08	400ppm CO_2	No flux impact No purity impact
12/08	400ppm CO_2	No flux impact No purity impact

Getter development

The judicious choice of insulation materials and alloys will minimize the concentration of SO_2 and $CrO_3(g)$ in the feed gas, but will not reduce the concentrations to acceptable levels. Contaminant capture systems/getters are required to remove the trace concentrations of these gases. Air Products identified candidate getter materials and conducted experiments to determine their effectiveness.

Sulfur Dioxide Getter

An SO_2 /air mix at 1000 sccm flows through a powder bed of getter particles sized at 0.841 mm-1.90 mm. The bed is 8 mm long with a diameter of 3.8 mm. The SO_2 concentration of the exit gas was measured using a Teledyne SO_2 detector. The SO_2 adsorption rate was recorded as a function of time. Experiments were conducted at various temperatures to determine the impact on getter performance.

Figure 14-106 is a plot of the results for one of the candidate getter materials at two feed gas SO_2 concentrations without CO_2, and the performance with the addition of CO_2. *The fluctuations in the breakthrough data are likely due to temperature changes in the lab, causing the tubing between the reactor and the analyzer to absorb and desorb SO_2.*

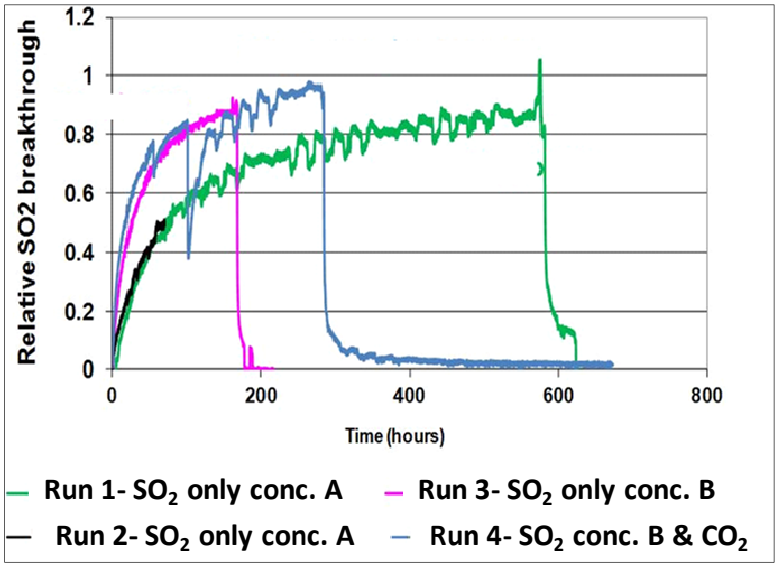

Figure 14-106. SO_2 breakthrough, with and without CO_2. SO_2 Concentration B is higher than Concentration A.

The presence of CO_2 did not impact getter performance.

The deactivation rate of the getter material as a function of time was also determined. Figure 14-107 documents the results from one of the candidate materials, showing breakthrough curves for various inlet concentrations at constant total feed rate.

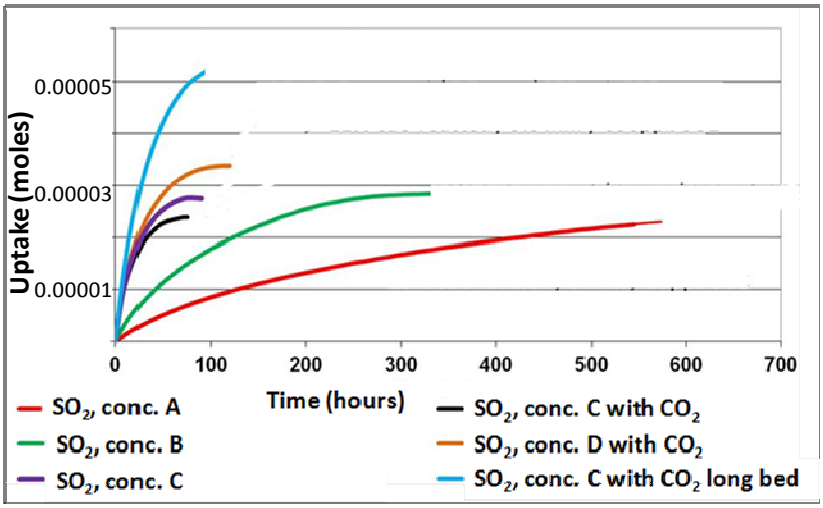

Figure 14-107. Uptake versus time at different SO_2 concentrations for constant total SO_2 feed.

Model predictions did not match results from SO_2 getter tests run under conditions where the model predicts delayed breakthrough. This may be due to kinetic limitations or the bypass behavior of the small test bed. The aspect ratio of the test bed ranged from 1.5 to 6.7 (beds of various lengths were tested). A new, larger bed with an aspect ratio of 16.2 was fabricated at over twice the diameter of the original bed. The test unit gas feed system was also modified to supply mixtures containing air, CO_2, water and SO_2. The modified system was used to assess the efficacy of the SO_2 adsorbent being used in the ISTU.

The results from all of the work described above were used to specify the SO_2 getter material for the ISTU and to design the getter system.

Chromium Getter

Chromium getters are composed of an active "getter" coating bonded to a supporting substrate. Air Products evaluated various materials and bonding methods to determine their adhesion properties under temperature cyclic conditions, and also conducted experiments to determine the reactivity of the getter material with the supporting substrate.

Samples were heated to and cooled from 900ºC at a rate of 5ºC/min. After the first cycle and every subsequent 10 cycles, the samples were evaluated to see if the coating flaked off the sample. The materials were weighed before and after cycling. Figure 14-108 shows the thermal cycling results for the SEP Cr getter supports.

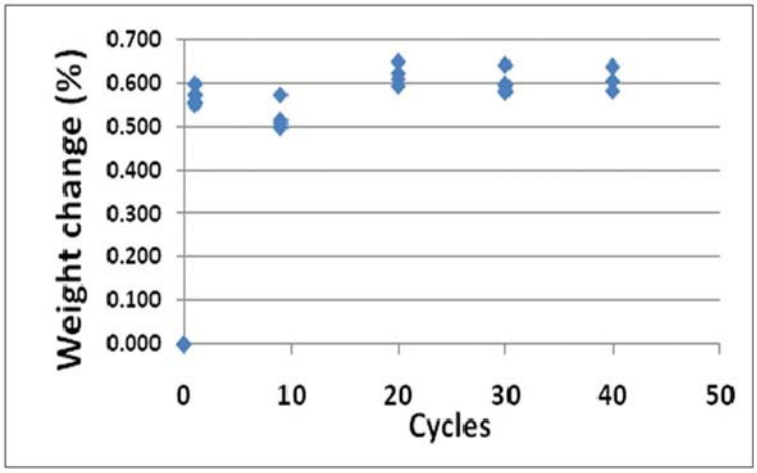

Figure 14-108. Weight loss of Cr-getter materials (used in the SEP) after thermal cycling to 900ºC at 5ºC/min.

The results showed that the evaluated bonding methods produced good adhesion properties under cyclic temperatures. SEM examinations reinforced this conclusion.

Reactivity

Getter/support samples were held at 875ºC, 1000ºC, 1100ºC and 1200ºC for extended periods of time (typically one year) to determine the rate of reaction of the getter material with the substrate and to estimate its operational lifetime. The data followed a parabolic rate law. Figure 14-109 shows the extrapolated active material consumption rate beyond one year at 875ºC.

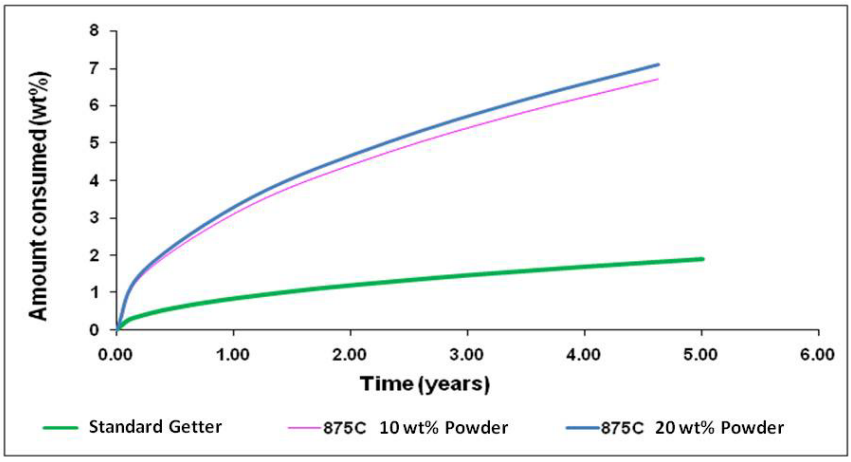

Figure 14-109. Extrapolated getter consumption rate at 875ºC for pressed powders (10 wt% and 20 wt% getter) and standard getter.

The data suggested the reactivity would be minimal at a representative operating temperature over a 5-year time frame.

14.1.3 Development of ITM Oxygen Materials

Setter Material

Background

Setters are used to support ITM Oxygen wafers and modules while they are being fired in kilns. The setter materials are specially chosen for their refractory behavior while in contact with the ITM material. A study was performed to assess alternatives to the current setter material to reduce cost.

Results

Candidate setter materials were examined using energy dispersive X-ray spectroscopy (EDS) and scanning electron microscopy (SEM) to assess their phase-purity. The materials chosen for further examination are documented in Table 14-14.

Table 14-14. Summary of candidate setter materials.

Candidate Material	Description
R	**Oxide ceramic based on dissimilar cations to those in ITM material**
B-doped R	**Material R, doped with cation B, a constituent of ITM material**
C-doped R	**Material R, doped with cation C, which is dissimilar to the constituents of ITM material**
B,C-doped R	**Material R, doped with a mixture of cations B and C**
Incumbent	**The current setter material**
Lite Incumbent	**This is the current material with a modified stoichiometry**

Ceramatec selected compound B-doped R for further development. Setters were fabricated, sintered, and machined. The parts were cycled with dense and porous ITM ceramic control parts to determine if the setters affect the grain structure of sintered ITM ceramic. Five standard wafers were also sintered while on the B-doped R setters with doping levels of 0.5 and 3 mol% B. All five wafers met the leak rate specification.

Stability of ITM Ceramics

Background

A phase diagram in materials science is used to show conditions at which thermodynamically distinct phases can occur at equilibrium. One example is the iron-iron carbide (Fe–Fe3C) phase diagram (Figure 14-110).

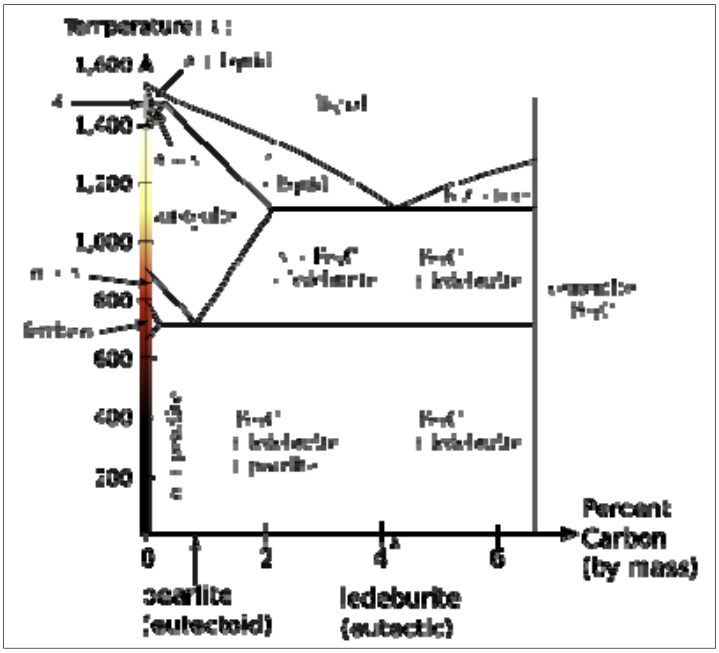

Figure 14-110. Iron-carbon phase diagram.

The percentage of carbon present and the temperature define the phase of the iron-carbon alloy and therefore its physical characteristics and mechanical properties. The percentage of carbon determines the type of the ferrous alloy: iron, steel or cast iron. As clearly seen in the figure, phase diagrams can be quite complex.

The ITM perovskite materials have associated phase diagrams which depend upon their composition. When the ITM powders are sintered and/or annealed, they can experience phase changes. Specific phases are preferred for the ITM ceramic and must be stable.

Phase Stability of Perovskites

Air Products investigated the stability of various perovskites as part of a program to develop a thermodynamic model of a perovskite system. Table 14-15 is a summary of the stability limits of specific perovskite materials in air. In this table, the A and B cations include the constituents of AP2k.

Table 14.1-15. Summary of lower stability limits of perovskite materials in air.

Composition	Temperature (°C)
$(A_{0.9}A'_{x1}A''_{y1}A'''_{z1})(B_nB'_mB''_o)O_{3-d}$	975>T>950
$(A_{0.8}A'_{x2}A''_{y2}A'''_{z2})(B_nB'_mB''_o)O_{3-d}$	875>T>850
$(A_{0.7}A'_{x3}A''_{y3}A'''_{z3})(B_nB'_mB''_o)O_{3-d}$	T<600
$(A_{0.6}A'_{x4}A''_{y4}A'''_{z4})(B_nB'_mB''_o)O_{3-d}$	T<600

Composition $(A_{0.8}A'_{x2}A''_{y2}A'''_{z2})(B_nB'_mB''_o)O_{3-d}$ (in which x2 + y2+ z2 = 0.2) is stable in air at 875°C, but is unstable at 850°C. Anneals of a range of compositions at 500°C indicate that the kinetics of the decomposition reaction are too slow to detect any composition change even after 2,000 hours, even for compositions that should be unstable at that temperature [e.g., $(A_{0.9}A'_{x1}A''_{y1}A'''_{z1})(B_nB'_mB''_o)O_{3-d}$]. Compositions $(A_{0.7}A'_{x3}A''_{y3}A'''_{z3})(B_nB'_mB''_o)O_{3-d}$ and $(A_{0.6}A'_{x4}A''_{y4}A'''_{z4})(B_nB'_mB''_o)O_{3-d}$ were annealed for 2,000 hours at 700°C and 600°C without any sign of decomposition. However, $(A_{0.9}A'_{x1}A''_{y1}A'''_{z1})(B_nB'_mB''_o)O_{3-d}$ decomposed at 700°C and 600°C and for times greater than 2,000 hrs, indicating that the reaction kinetics are fast enough for $(A_{0.7}A'_{x3}A''_{y3}A'''_{z3})(B_nB'_mB''_o)O_{3-d}$ and $(A_{0.6}A'_{x4}A''_{y4}A'''_{z4})(B_nB'_mB''_o)O_{3-d}$ to decompose. Compositions $(A_{0.6}A'_{x4}A''_{y4}A'''_{z4})(B_nB'_mB''_o)O_{3-d}$ and $(A_{0.7}A'_{x3}A''_{y3}A'''_{z3})(B_nB'_mB''_o)O_{3-d}$ are stable at 700°C and 600°C. The ITM ceramic, a subset of the above compounds, was stable at all temperatures tested.

Another series of measurements of the thermodynamic properties of a range of perovskite compositions was conducted in support of the thermodynamic modeling effort. The phase boundaries of a representative perovskite system ($AA'A''BB'B''O_3$) were measured as a function of temperature and P_{O2}. These data were used to refine the thermodynamic model. A set of $AA'A''BB'B''O_3$ perovskites was annealed at a series of temperatures and oxygen partial pressures. The composition of the annealed sample was analyzed by XRD and SEM/EDS to determine the phases present. Table 14-16 below shows the initial and final compositions for each sample for the first three series of samples.

Table 14-16. Initial and final compositions of A-A'-A"-B-B'-B"-O perovskites following annealing at the given temperature and P_{O2}.

				Final Composition (weight %)				
Starting Composition	T (°C)	P_{O2} (atm)	Time (days)	% P	% BOx	% TrOx	% A1Ox	%A2Ox
$\mathbf{A_{0.4}(A_x'A_y")_{0.6}B_iB_k'B_l"O_3}$	1300	0.001	3	66.8	4.8	11.5	16.9	
$\mathbf{A_{0.5}(A_x'A_y")_{0.5}B_iB_k'B_l"O_3}$	1300	0.001	3	41.8	14.0	42.3	2	
$\mathbf{A_{0.6}(A_x'A_y")_{0.4}B_iB_k'B_l"O_3}$	1300	0.001	3	13.2	21.7	63.9	1.2	
$\mathbf{A_{0.9}(A_x'A_y")_{0.1}B_iB_k'B_l"O_3}$	1300	0.001	3	74.9	5.7	19.3		
$\mathbf{A_{0.1}(A_x'A_y")_{0.9}B_iB_k'B_l"O_3}$	1100	0.03	7	100				
$\mathbf{A_{0.2}(A_x'A_y")_{0.8}B_iB_k'B_l"O_3}$	1100	0.03	7	100				
$\mathbf{A_{0.3}(A_x'A_y")_{0.7}B_iB_k'B_l"O_3}$	1100	0.03	7	100				
$\mathbf{A_{0.1}(A_x'A_y")_{0.9}B_iB_k'B_l"O_3}$	1300	0.01	3	81.7				18.3
$\mathbf{A_{0.2}(A_x'A_y")_{0.8}B_iB_k'B_l"O_3}$	1300	0.01	3	100				
$\mathbf{A_{0.3}(A_x'A_y")_{0.7}B_iB_k'B_l"O_3}$	1300	0.01	3	96.4			2.5	

Note: P = perovskite; BOx = $B_jB_k'B_l"O_x$; TrOx = $(A,A')_y\ B_jB_k'B_l"O_z$; A1Ox = $A'_mB_jB_k'B_l"O_p$ and A2Ox = $A'_i\ B_jB_k'B_l"O_n$.

In addition, a set of $(A,A")BO_3$ pervoskites was annealed at 1,100 and 1,300°C at a series of oxygen partial pressures. Tables 14-17 and 14-18 show the initial and final compositions for each sample for the initial series of samples.

Table 14-17. Initial and final compositions of $A_{1-x}A''_xBO_{3-d}$ perovskites after annealing at 1100°C at the given PO_2. P=Perovskite, A2BO4=$(A,A'')_2BO_4$

x=	0.1	0.4	0.5	0.6	0.7	0.8	0.9
P_{O2} (atm)							
0.03					P	P	P
0.01	P	P	P	P	P	P	?
0.001	P	A2BO4/ BO	A2BO4/BO/P	P			
0.0003	P	A2BO4/ BO	A2BO4/BO/P	A2BO4/BO/P			
0.0001	A2BO4/BO/P/ A2BO	A2BO4/ BO	A2BO4/BO/P/ A''BO	A2BO4/BO/P/ A''BO			

Table 14-18. Initial and final compositions of $A_{1-x}A''_xBO_{3-d}$ perovskites after annealing at 1300°C at the given P_{O2}. P=Perovskite, A2BO4=$(A,A'')_2BO_4$, S3C2O6=$A''_3B_2O_6$

x=	0.1	0.4	0.5	0.6	0.7	0.8	0.9
P_{O2} (atm)							
0.03	P	P	P	P	P	P	P
0.01	A2BO4/BO/P	A2BO4/ BO	A2BO4/BO/P	A2BO4/BO/P		P	P
0.001	A2BO4/BO/P	A2BO4/ BO	A2BO4/BO/P	A''3B2Ox /A2BO4/BO/P			
0.0003	A2BO4/BO/P	A2BO4/ BO	A2BO4/BO/P	A2BO4/BO/P			
0.0001	A2BO4/BO/P	A2BO4/ BO	A2BO4/BO/P	A''3B2Ox/A2BO4/BO/P			

At 1,100°C, all of the compositions are stable at a P_{O2} =0.01 atmospheres, but decomposition occurs at x=0.4 and x=0.5 at P_{O2} =0.001 atmospheres; at 100 ppm for x=0.1 and at 300 ppm for x=0.6. The phase boundary occurs between 0.01 and 0.03 atmospheres at 1,300°C for x=0.1-0.6. It is important that the model be able to predict these boundaries between single and multiphase areas of the phase diagram.

TASK 15.0 TABLE OF CONTENTS

TASK 15.0 ENGINEERING DEVELOPMENT 2

15.0 SCOPE 2

SUMMARY 2

15.1 GAS TURBINE AND AIR FLOW 2

Results 2

Case 1: Indirectly heating the air feed to the ITM by means of a heat exchanger 2

Case 2: Indirectly heat the air feed to the ITM by means of a fired heater 4

Case 3: Hydrogen-fueled direct fired preheat combustor 8

Hot Gas Expander Development 11

15.2 OXYGEN-CIRCUIT DESIGN 11

Background 11

Results 12

Cyclic Oxidation 12

15.3 ENGINEERING ANALYSIS OF MEMBRANE MODULE COMPONENTS 14

Background 14

Results 15

General 15

Microstructure 18

15.3.1 Wafer Model 21

15.3.2 Ceramic to Metal Seal Region Model 23

15.3.3 Module Model 23

15.3.4 Validation Testing of Engineering Models 28

15.3.5 Ceramic Module Architecture Improvement 35

TASK 15.0 ENGINEERING DEVELOPMENT

15.0 Scope

Under this Task, Air Products works with Siemens, NovelEdge Technologies, Concepts/NREC, and Williams International to develop flow sheets for specific applications at various ITM Oxygen production ranges. The work focuses on general turbo-machinery integrations, which involve general turbo-machinery integrations that depend on the scale and ultimate commercial application of the technology. The work is also focused on integrations with various heat exchange and combustion operations required to add heat to the ITM Oxygen feed stream and to extract useful heat and/or work from the by-product, oxygen-depleted, non-permeate stream and the hot oxygen product stream.

15.1 Gas Turbine and Air Flow

Results

Concepts NREC analyzed a number of system configurations as discussed in detail below. The cases focused on means of heating air and utilizing the hot non-permeate stream. These cases were evaluated as potential ISTU process cycles.

Case 1: Indirectly Heating the Air Feed to the ITM by Means of a Heat Exchanger

In Case 1, combustor air is supplied from a compressor and the products of combustion are mixed with the oxygen-depleted non-permeate stream. The heated non-permeate is cooled against the pressurized air feed stream to the ITM module to achieve the ITM operating temperature. Figure 15-1 illustrates the scheme.

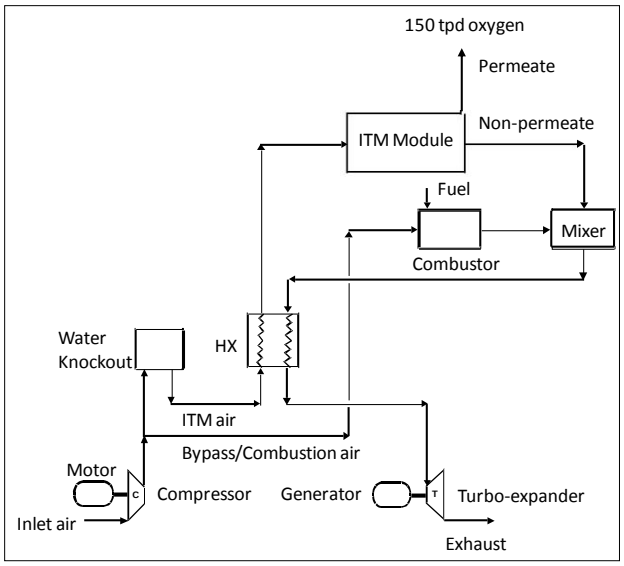

Figure 15-1. Candidate ISTU process cycle showing heating of the air stream by indirect heat exchange with a heated non-permeate stream.

Combustor Performance and Design

Concepts NREC calculated the pressure pulse when an in-line combustor, such as that shown in Figure 15-1, is lighted off under various operating conditions. Results are shown in Figure 15-2.

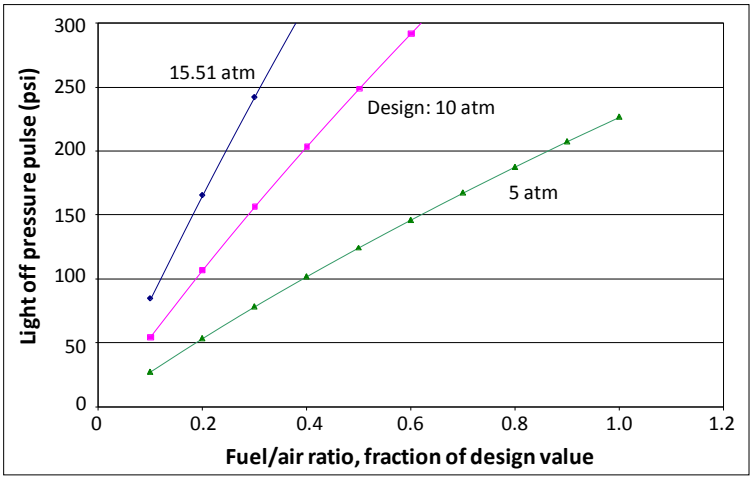

Figure 15-2. Effect of fuel/air ratio on the magnitude of the pressure pulse during light-off of the combustor.

The pulse magnitude increases with increasing operating pressure and fuel/air ratio. The calculated pressure pulse was high and could damage ceramic modules if the pulse propagates backwards to the ITM system. One strategy is to light off the combustor at low pressure to minimize the pressure pulse. The calculated pressure pulse at low pressures are shown in Figure 15-3.

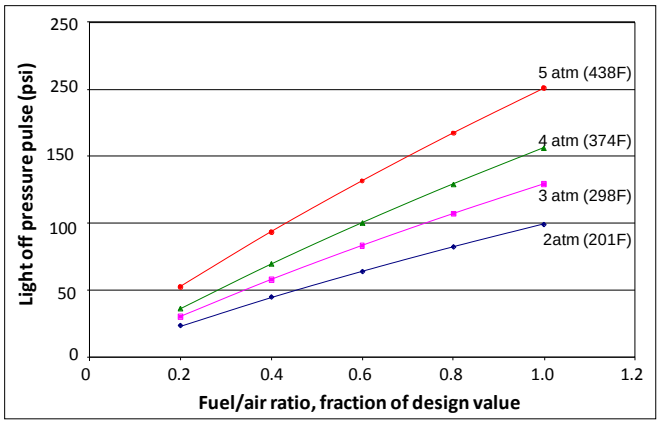

Figure 15-3. Effect of fuel/air ratio on the magnitude of the pressure pulse during light-off of the combustor at low system pressures

The magnitude of the pulse can be brought down by a factor of two or more by lowering overall system pressure and can be reduced by up to four times by lowering the fuel/air ratio during light-off.

Case 2: Indirectly Heating the Air Feed to the ITM by Means of a Fired Heater

In this case, the post-combustor is operated with a mixture of fresh air feed from a compressor and a portion of the oxygen-depleted non-permeate stream. Products of combustion are mixed with a second portion of the oxygen-depleted non-permeate stream and fed to a hot gas expander. A schematic of Case 2 is shown in Figure 15-4.

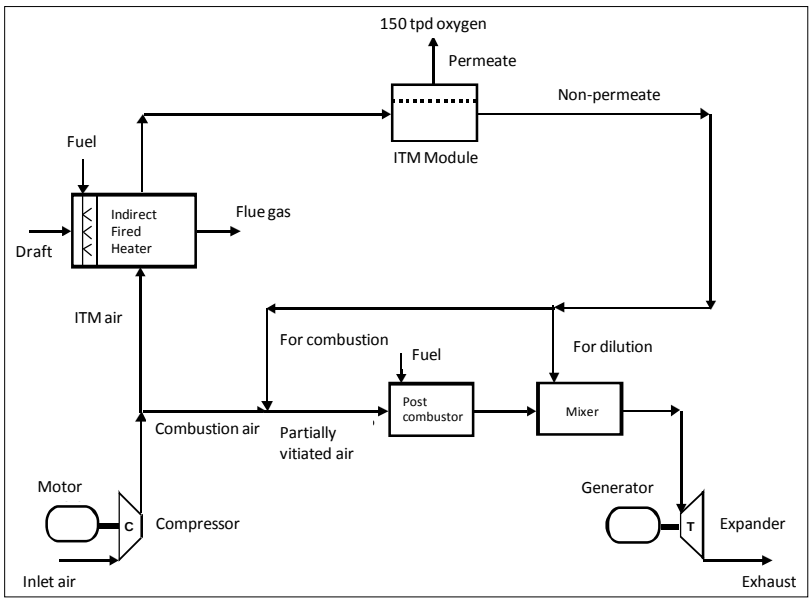

Figure 15-4. Candidate ISTU process cycle; heating of the air stream by an indirectly fired heater with post-combustion of at least a portion of the non-permeate stream.

The fuel flow and hence the oxygen requirement was determined based on an expander inlet temperature of 1900° F. The non-permeate flow (and oxygen flow) to the combustor was varied and the amount of compressed air (and oxygen) required for complete combustion was calculated. The oxygen concentration of the air/non-permeate gas was calculated via a mass balance. Figure 15-5 is a plot of the relationship between gas oxygen concentration and the additional compressor air requirement.

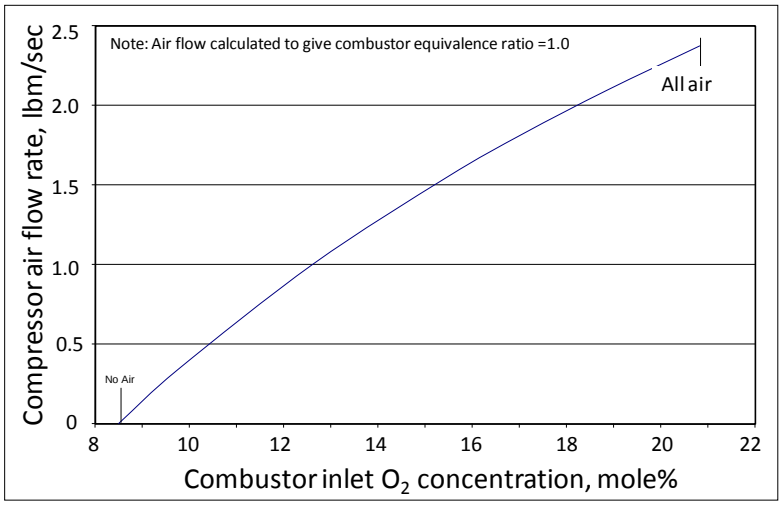

Figure 15-5. Compressed air flow to the post-combustor and resulting combustor oxygen inlet concentration.

At the "no air" end of the curve, all of the non-permeate is used for combustion and none is used for dilution (i.e., there is no mixer). The oxygen concentration is equal to the concentration in the non-permeate stream (i.e., 8.5 mole percent). At the "all air" end of the curve, the reverse is true: all of the non-permeate is used for dilution and none is used for combustion.

The mixed gas temperature is a function of the compressor air and non-permeate flows and temperatures. A maximum gas inlet temperature of 1,037°F to the combustor was chosen based on materials of construction temperature limitations. Assuming a non-permeate temperature of 1,600°F, a compressor air temperature of 290°F and the design combustor inlet temperature of 1,037°F, the required mass flow of each stream can be calculated. Once the mass flows are determined, the gas oxygen concentration can be calculated. At 1,037°F, the inlet oxygen concentration is about 14%. Stable combustion must be achievable at this temperature and oxygen concentration.

At a non-permeate temperature of 1600°F and with 25% of the non-permeate going to the combustor, the flow rate of air required to co-feed the combustor is approximately 4 lb/s.

Combustor Design: Natural Gas with Compressed Air and Non-permeate gas

Concepts NREC conducted a literature review of natural gas combustion with low oxygen containing streams at high temperature. Literature data on flame stability as a function of combustion gas temperature and inlet oxygen concentration were plotted (Figure 15-6).

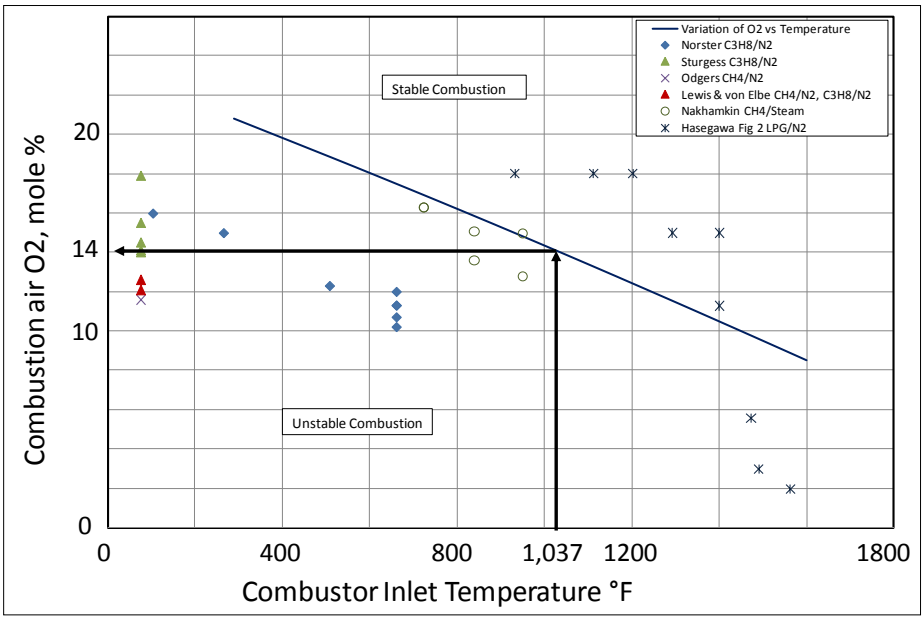

Figure 15-6. Combustion stability plot for vitiated air streams over a range of temperatures. Blue line is the temperature and oxygen concentration for mixtures of compressor air (290°F) and non-permeate gas (1,600°F).

The blue line is the calculated temperature and oxygen concentration that correspond to ratios of compressor air (at 290C) and non-permeate gas (at 1,600F) mass flows needed to achieve full combustion. See above for details on the 1,037°F data. Increasing the pressure helps stabilize the flame in higher shear conditions.

Concepts NREC modeled a combustor that included a combustion chamber contained by a liner. The feed gas flows through an annulus between the liner and the combustor shell to keep the liner cool. The combustion efficiency and pressure drop as a function of combustor liner diameter were calculated (Figure 15.1-7).

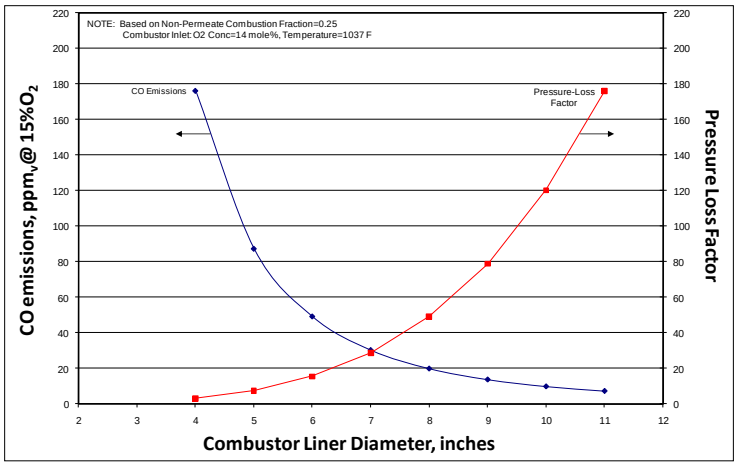

Figure 15-7. Inverse combustion efficiency, as measured by the CO concentration in the flue gas, and pressure loss factor plotted against combustor liner diameter.

Combustion efficiency, as measured by the extent to which carbon monoxide (CO) is fully consumed, increases with increased liner diameter. Pressure drop, as expressed by a pressure loss factor, also increases. A design diameter was chosen by calculating the economic optimum between combustor efficiency and pressure loss.

Mixer Design

Concepts NREC also calculated the performance of a mixer that contains a liner. The cooling gases flowed through an annulus between the liner and the mixer shell. Two issues were critical to the mixer's performance: pressure drop and the temperature variation across the mixer diameter in the outlet stream. Figure 15-8 shows the pressure loss factor for the mixer as a function of the mixer liner diameter. Pressure loss increases with increasing diameter.

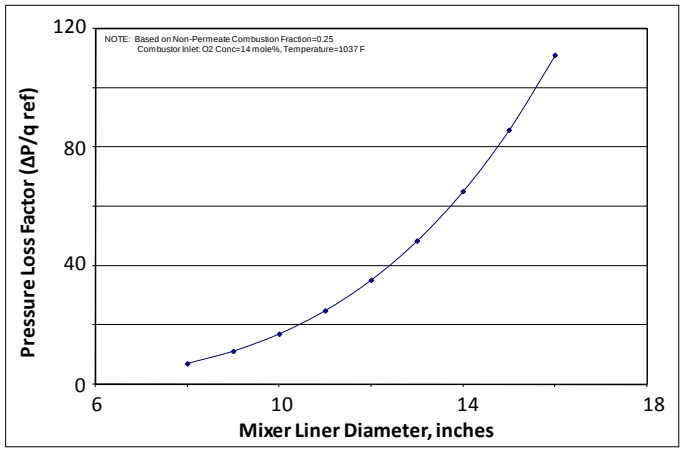

Figure 15.1-8. Effect of mixer liner diameter on pressure loss factor at constant non-permeate flow conditions.

Figure 15-9 shows the deviation of the temperature in the exit gas from the mixer at different liners diameters.

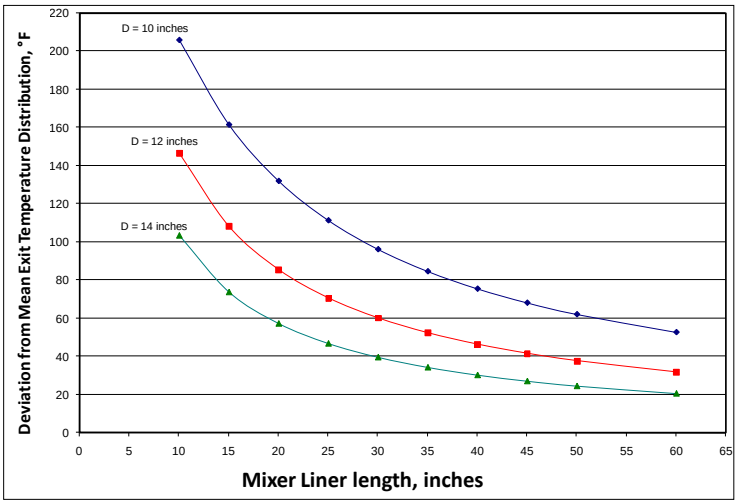

Figure 15-9. Effect of mixer liner length on mixing performance for three mixer liner diameters calculated for constant non-permeate flow conditions.

The deviation decreases with decreasing liner diameter and increasing liner length. These plots, in conjunction with allowable limits determined by the expander supplier on temperature uniformity and the limits of pressure drop in the system, were used to design the mixer.

Case 3: Hydrogen-Fueled Direct-Fired Preheat Combustor

Concepts NREC used a variant of a preheat combustor that uses hydrogen as the fuel to assess combustor requirements (Figure 15-10). The only product of combustion is water vapor, which minimizes the contaminants to the ITM system as compared to a direct-fired, hydrocarbon-based fuel.

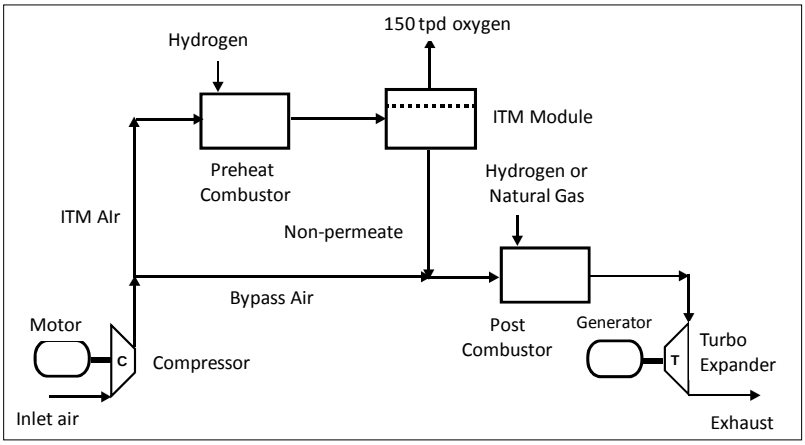

Figure 15.1-10. Hydrogen-fired system configuration.

Combustor Development and Design: Hydrogen Fuel

A literature search was conducted to collect relevant information on hydrogen combustion properties such as flammability limits, auto ignition conditions, ignition delay, flame speed and flame temperature. A parallel search was conducted to gather information on past experience and combustor designs. The design calculations focused on the tradeoffs between the overall nominal dimensions (diameter and length) and the major performance variables: combustion efficiency, NOx emissions, pressure loss and exit temperature uniformity.

Properties were calculated for an in-line preheat combustor firing hydrogen fuel. The combustor consists of a primary combustion zone and one or more dilution zones with an internal, cooled liner. Three primary combustion properties were considered: the pressure pulse upon lightoff, NOx emissions; and combustion stability. The influence of operating conditions on these parameters is shown in Figures 15-11, 15-12 and 15-13 respectively.

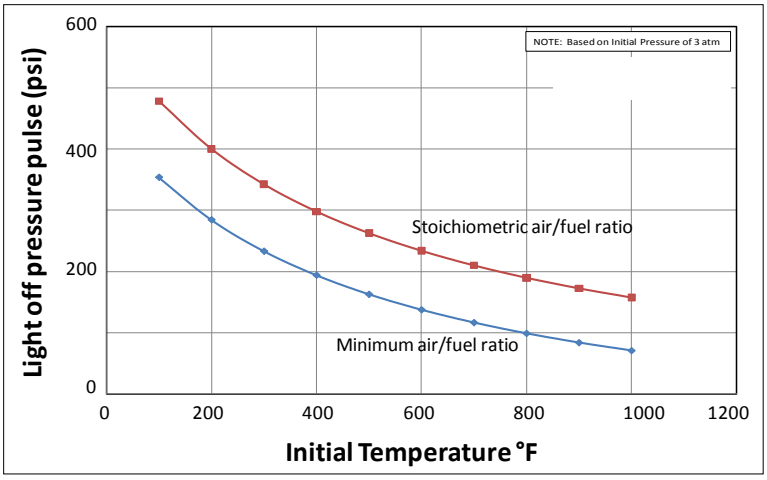

Figure 15-11. Effect of stoichiometry and temperature on lightoff pressure pulse.

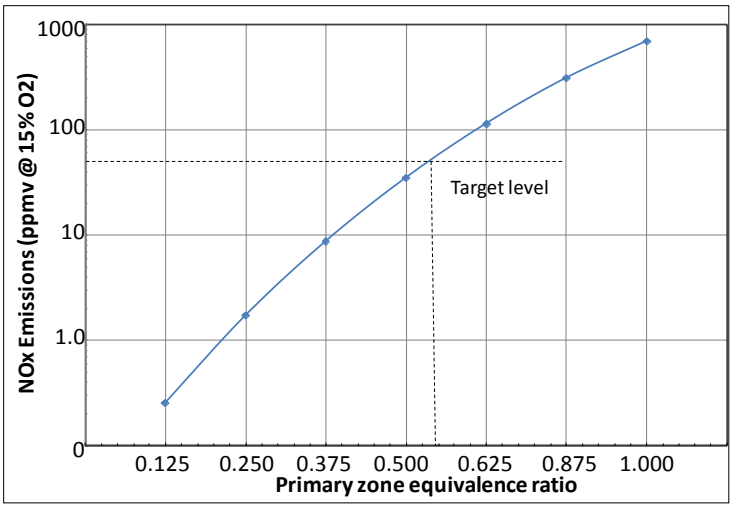

Figure 15-12. Effect of primary zone equivalence ratio on NOx emissions .

The NOx emissions are a measure of the effectiveness of the dilution zones. The overall NOx emissions for the facility are expected to be much lower than what is shown in Figure 15-12. The calculations predict stable combustion.

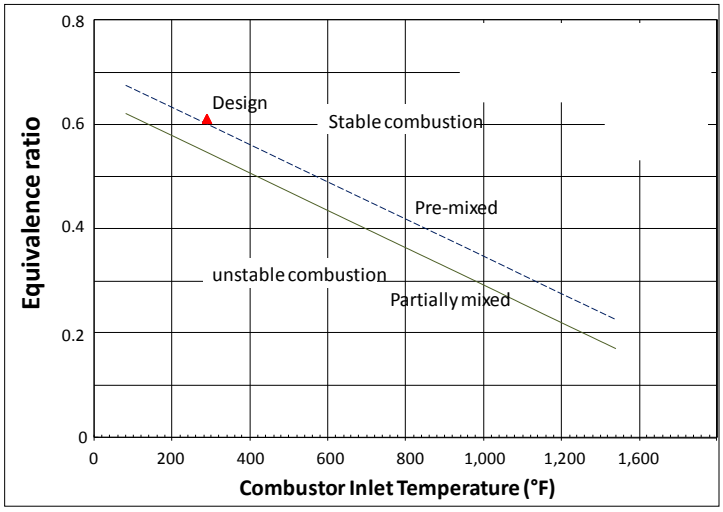

Figure 15-13. Estimated lean blow out (LBO) combustion stability limits for hydrogen combustor.

Conclusions from Process Design Study

Concepts NREC considered three cases for air preheating: direct, post-fired (Case 1), indirect, pre-fired (Case 2), and direct, pre-fired (Case 3). In each case, the ramifications on the combustor design requirements were considered. Air Products used these factors when designing the ISTU under Task 19. Combustor Performance (1/3 scale)

Hot Gas Expander Development

Combustor

Williams International constructed a ⅓-scale combustor test rig to collect operational data and assess performance. The pressure pulse at lightoff was measured at several test conditions. There was no over-pressure spike and only a modest 3 psi pressure step change. There was almost no sensitivity to starting pressure level. The results indicate that the combustor can be lit off without a damaging pressure pulse propagation to the membranes.

Lightoff and lean blowout data were obtained over a range of inlet temperatures and pressures and a feed gas oxygen concentration of 21% (air). The burner lit off very smoothly and predictably, well within all operational and safety parameters. Lightoff and lean blowout improved significantly with increased temperature.

Tests were conducted to determine the minimum oxygen concentration of the feed gas to achieve lightoff. Lightoff could not be achieved at any condition with feed gas oxygen concentrations of 8% and 11%. Two successful lightoffs were achieved at a concentration of approximately 16%. Concepts NREC and Williams estimated that the at-scale combustor would achieve stable combustion at an ~11% oxygen inlet concentration, based upon known scaling laws for combustion. The detailed hot gas expander design was completed under Task 19.

Williams International mapped the operation of various proposed hot gas expander designs based on their turbojet technology. The design for the ISTU expander was finalized based on the data.

A cross-section model of the hot gas expander for the Intermediate-Scale Test Unit (ISTU) was completed. The model comprised a combustion section and a hot gas turbo-expander section. A preliminary flow map was generated that enabled materials selection for the various components. Further work was executed under Task 19.

15.2 Oxygen-Circuit Design

Background

The permeate/oxygen from the ITM system is discharged at high temperature. Methods of cooling this stream to extract heat/work energy are required to maximize thermal efficiency.

Results

Air Products evaluated a number of different means to cool the product oxygen based on process simulations. The information was used to determine the best heat exchange options for the low-pressure, high-temperature oxygen permeate. The best oxygen cooling method was found to depend upon the air-heating method chosen for a given application.

Air Products investigated the conceptual design of a compact heat exchanger to cool high-temperature permeate and heat ITM oxygen feed air. Design considerations included: materials of construction; corrosion; mechanisms and allowance; thermal gradients and cycling; ASME code; supplier modeling/analysis and manufacturing capabilities; testing requirements, protocols and infrastructure; scale-up; and fouling/cleaning. Duty specifications were developed to heat the ISTU feed air from 540°C to 900°C at 3,500 MTPD oxygen capacity at 300 psig pressure.

A list of potential high-temperature materials of construction was identified. Ranking data was collected, including allowable stress, cyclic oxidation resistance, contaminant elution, cost, availability, and manufacturability. Two nickel-based alloys emerged as high-potential material candidates. Literature searches on mechanical design/stress analysis/thermal cycling in core heat exchangers were also conducted.

Cyclic Oxidation

The hot, high-oxygen-concentration permeate stream is in contact with alloy/metals in the heat exchanger. As a result, high oxidation rates can occur in some alloys. Cyclic oxidation testing of alloys at a peak temperature of 732°C in 200 psig air were conducted to determine the suitability of candidate materials of construction. Samples were cycled 40 times. The experimental protocol was:

- Use four samples of each alloy.
- Ramp to 700°C at 1°C/min in cylinder air at 200 psig. 0.5 slpm flow.
- Ramp to 725°C at 0.25°C/min.
- Ramp to 732°C at 0.15°C/min.
- Hold at 732°C, 200 psig, 0.5 slpm air flow for 24 hrs.
- Ramp to 100°C at 10°C/min.
- Repeat for a total of 10 cycles.

- Remove 1 coupon per alloy after each 10 cycles.
- Weigh post-test coupons.
- Repeat for a total of 40 cycles for the last coupon of each alloy.

Figure 15-14 documents the mass change for each alloy tested through 40 cycles.

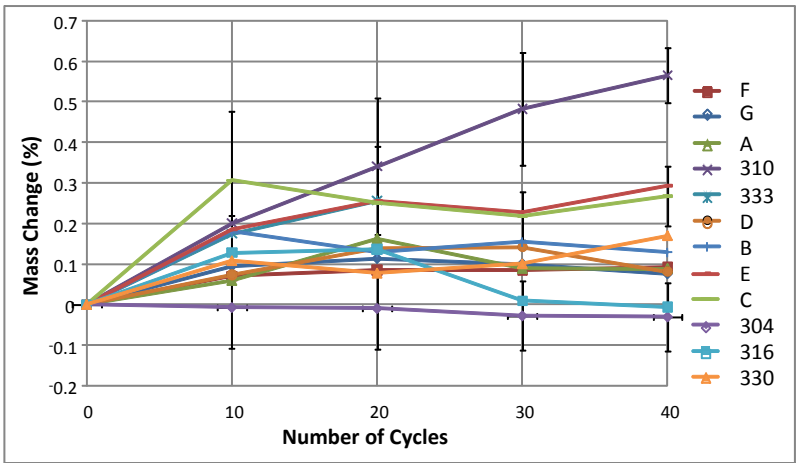

Figure 15-14. Mass change of alloy coupons under thermal cycling.

The resolution of the mass change measurement is approximately 0.03%. Most of the mass changes were above the resolution of the mass change measurement. The sample-to-sample variation in weight change can be a large fraction of the average weight loss. Alloy A and 304 had a very low mass change. Alloy 310, E, 330, and C showed the largest mass loss after 40 cycles. In other work, Alloy H and X had greater than 2% total affected metal. Figure 15-15 documents alloy mass change in a subsequent experiment.

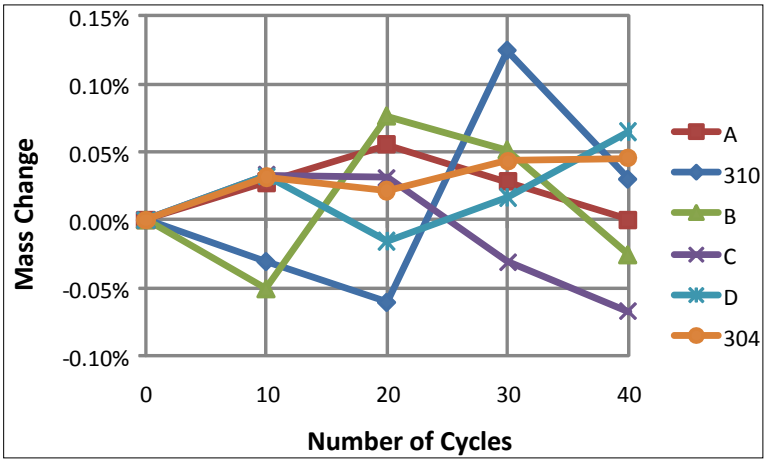

Figure 15-15. Cyclic oxidation behavior of candidate alloys.

The data indicated that the cyclic oxidation behavior of all of the alloys was acceptable at 1350°F (732° C). Figure 15-16 documents the cyclic mass loss of alloys at a temperature of 1450°F (788° C) after 10 cycles.

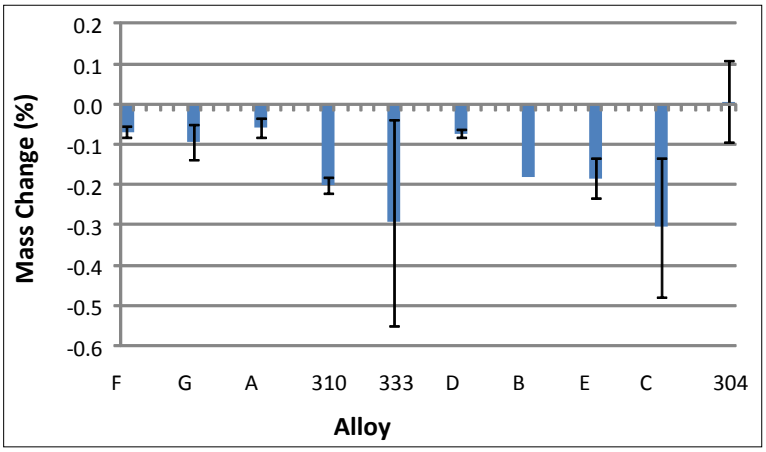

Figure 15-16 Cyclic oxidation behavior of candidate alloys at 1450°F after 10 cycles. Error bars are standard deviation of mass change of four samples of each alloy.

Alloys 333 and C showed the largest mass losses. Alloy C was rejected as a material of construction due to its extreme susceptibility to cyclic oxidation corrosion. The preferred materials are Alloys A, B, J, 333, and F.

15.3 Engineering Analysis of Membrane Module Components

Background

Knowledge of the stresses within ITM component parts and between component parts (typically at the joints) is required to ensure they do not exceed the strength properties of the ITM ceramic. Finite element analyses based on the geometry and structure of the component parts were conducted to predict stress, strain and creep behavior. The induced stresses are primarily caused by differential expansion due to temperature and oxygen vacancy gradients within and between the parts. As discussed in 14.0, Materials Development, the temperature gradient is a function of thermal diffusivity. The oxygen vacancy gradient is related to the equilibrium vacancy concentration, the temperature-dependent oxygen transport properties, surface kinetics, and gas-phase mass transfer resistances. Various component geometries and structures were simulated to determine configurations that limited stress.

The greatest stress occurs during temperature and pressure transients. Ceramatec conducted simulations by initially assuming the module was at equilibrium with a known oxygen-containing atmosphere, and then ramping temperature and pressures according to a scheme developed from experiments with 0.5 TPD modules in the 5 TPD Subscale Engineering Prototype (SEP). Multiple temperature cycles were simulated to determine oxygen concentration profiles. Figure 15-17 is a typical plot of stress as a function of time and transient operations.

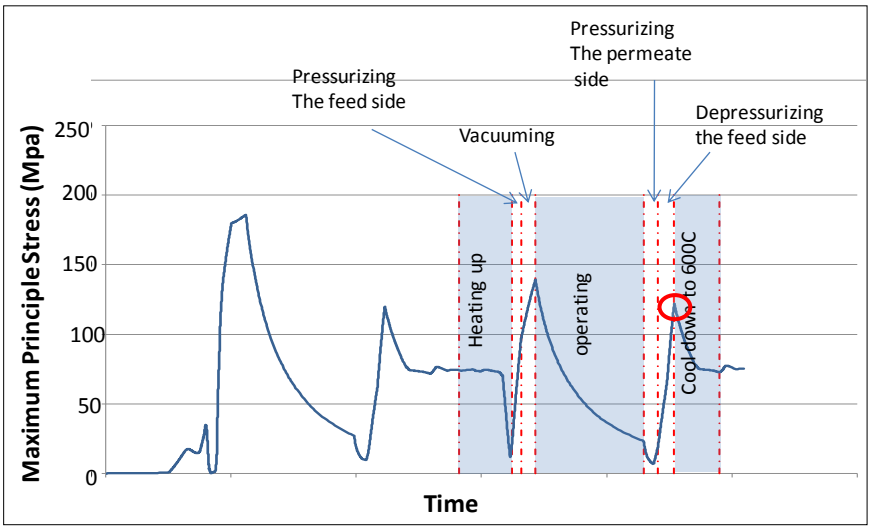

Figure 15-17. A typical FEA principle stress simulation as a function of time and operating conditions.

Transient condition experiments were conducted to validate and refine the FEA models. Additional work was conducted to estimate creep deformation as a function of temperature, time and stress.

The oxygen flux through an ITM wafer is dependent upon the oxygen partial pressure differential across the ceramic. The permeate pressure at the interface will depend upon the vacuum applied and the pressure drop between interface to the vacuum/compressor equipment. Work was performed to predict the pressure drop through porous ITM materials.

Results

General

Ceramatec carried out a study of grid size dependence on the results from Finite Element Analysis (FEA) stress modeling. Larger, more refined grids gave more accurate answers. However, computational time depends non-linearly on grid size. Figure 15-18 shows a two-

dimensional structure of a five-wafer module which is sufficient to approximate the stress field in a full-size 1-TPD module.

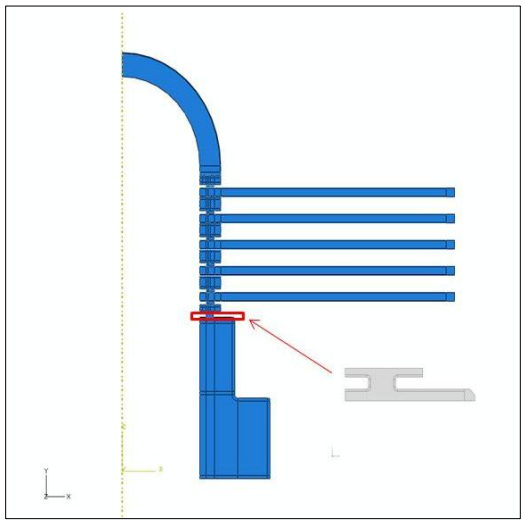

Figure 15-18. Two-dimensional framework of the FEA grid used to calculate stresses in a five-wafer module. The region of interest is shown expanded in the lower right side of the schematic.

The figure shows the seal region between the base piece and a spacer ring as the area of interest in the study. Figure 15-19 shows four grids in the region of interest.

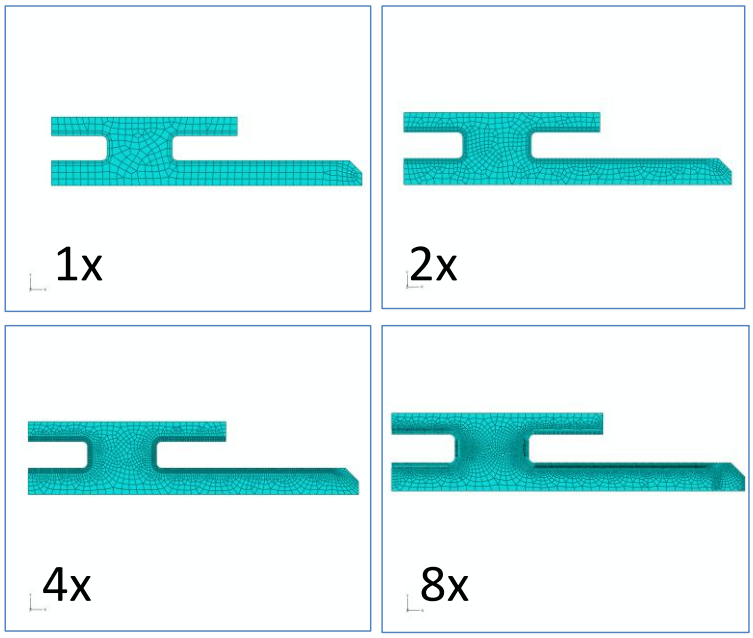

Figure 15-19. Four grids with increasing grid density in the region of interest.

The least dense grid is labeled the "1X". The densest grid is eight times more dense. Figure 15-20 is an example of the stress calculated at the end of a typical operating cycle in the region of interest.

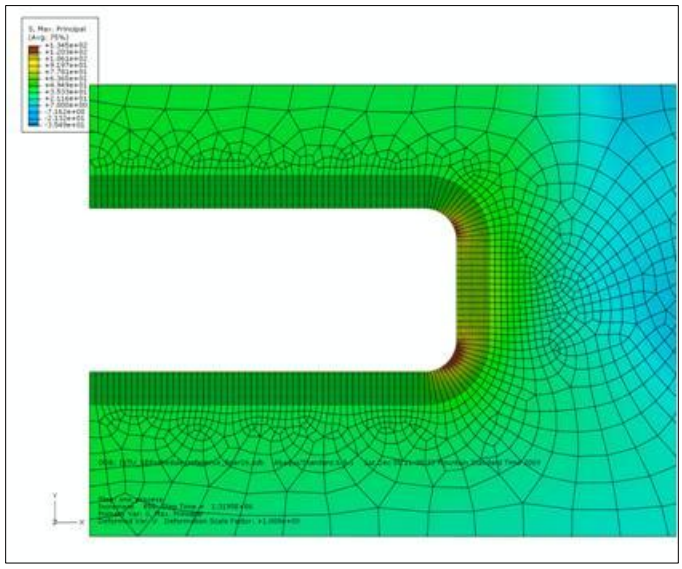

Figure 15-20. Calculated stress profile in the critical section of the seal region after a complete operating cycle.

As expected, the highest stresses (green regions) tend to be near the regions of highest curvature.

Figure 15-21 plots the principal stress versus time during a simulated operating cycle for the four grid densities.

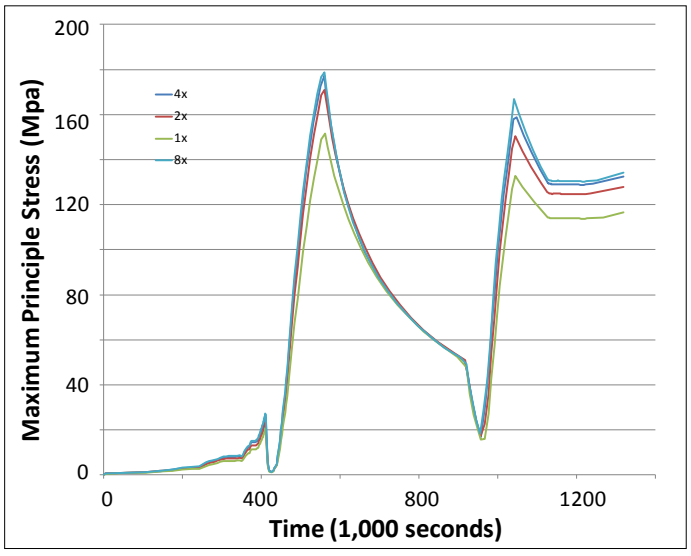

Figure 15-21. Principal stress in the seal region of interest versus time for four grid densities.

The densest grid showed the highest peak stresses. But the lower grid density "4X" and sometimes the "2X" gave very similar results. The "1X" case, while not adequate for precise work, gave a reasonable approximation for screening studies.

Microstructure

A model was developed to predict that behavior of eight ITM ceramic microstructures (Figure 15-22).

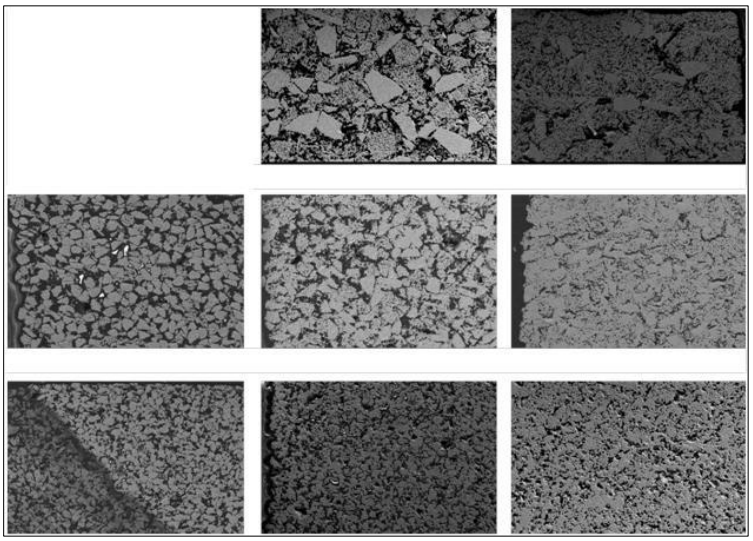

Figure 15-22. Model microstructures.

The microstructures were subjected to a series of constant cooling rate experiments assessed using TGA (Figure 15-23) and dilatometry (Figure 15-24).

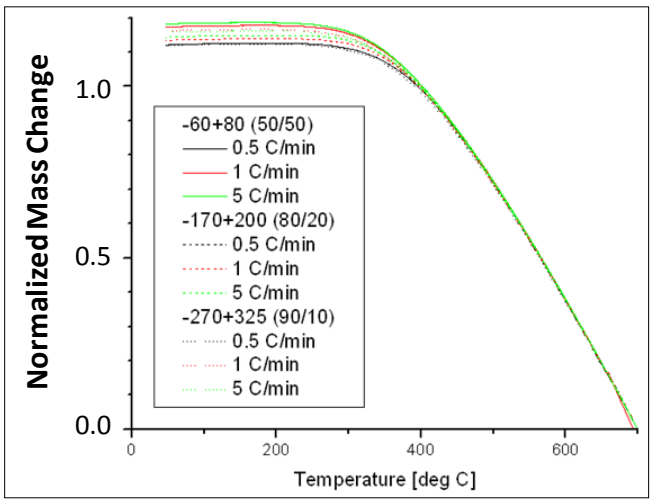

Figure 15-23. TGA data of three model microstructures cooled at three rates.

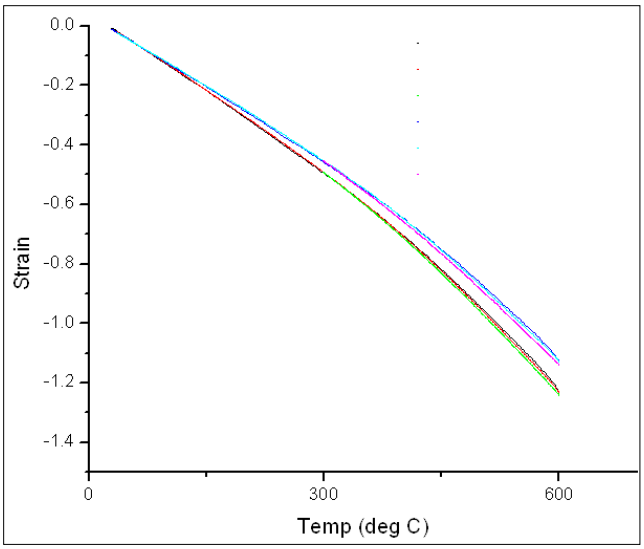

Figure 15-24. Dilatometry traces of two model microstructures at three cooling rates.

The mechanical properties of the model microstructures were also measured (Figure 15-25).

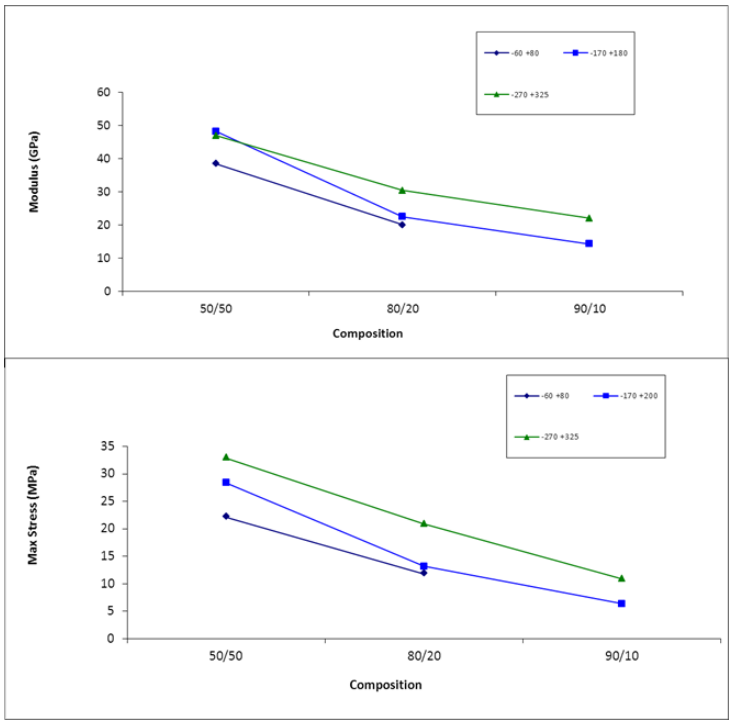

Figure 15-25. Mechanical properties of model structures.

The experimental results were compared to results from a COMSOL model of a spherical AP2k particle. Comparisons of the modeling and experimental TGA and dilatometry results are presented in Figures 15-26 and 15-27.

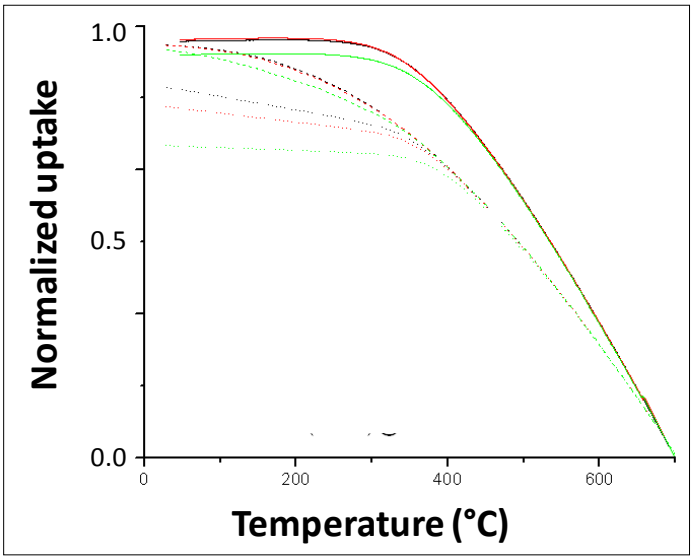

Figure 15-26. Comparison of model and experimental thermo-gravimetric data. Solid lines are the experimental data.

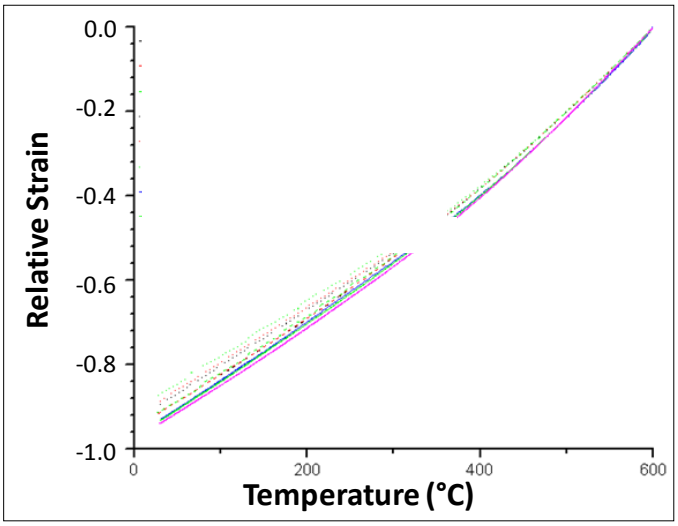

Figure 15-27. Comparison of the model and experimental dilatometric data.

The model did a good job of capturing the total mass gain, but the temporal match is poor. The model worked well with the shape and magnitude of the change, but the time scale over which the change occurred is different than the model prediction. The model exhibits mass gain all the way down to room temperature, while the TGA experiments suggest mass gain stops at a higher

temperature. This temporal discrepancy in oxygen uptake may be the cause of the discrepancy between the dilatometric data and the model. The discrepancy is likely due to improper values and/or the mechanistic model does not fully describe the phenomena. Combining the modulus data with the differential strain calculated by the model gives a descriptive assessment of the residual stress within an AP2k body.

15.3.1 Wafer Model

Ceramatec used transient dilatometer data generated for standard AP2K bars to estimate the temperature dependencies of the surface exchange (K_{chem}) and vacancy diffusion (D_{chem}) coefficients. FEA models were developed to predict the expansion/contraction behavior of the bars. Table 15-1 documents the evolution of model development from Tasks 7 to 15.

Table 15-1. FEA model development.

2005	Task 7: Based on extrapolation of the flux and limited dilatometer data
2008	Task 15: Derived from additional dilatometer and TGA data
2010a	Task 15: First attempt to include a pressure dependence for K
2010b	Task 15: Transient dilatometer test at <600°C; results indicated that the surface exchange not only became the limiting factor but was also a function of the P_{O2}

The Task 7 model relied heavily on extrapolations to describe the behavior at temperatures below 600°C. The Task 15-2008 model was derived from transient dilatometer data generated at temperatures down to 500°C. However, the model was based on the rather simplistic assumption that K_{chem} was never rate-controlling. This assumption was invalidated by additional dilatometer data, which showed that K_{chem} was not only rate-controlling at lower temperatures, but was also a function of the oxygen partial pressure. The Task 15-2010a model considered these findings by allowing K_{chem} to be a function of the direction of oxygen transport away from (reducing) or into (oxidizing) the surface. One of the assumptions used in generating the Task 15-2010a model curves was that the surface exchange coefficient was only a function of the direction of O_2 transport. However, it was determined that K_{chem} is a function of the P_{O2} level and not just the direction of oxygen transport. This new assumption and additional transient dilatometer data used to estimate the temperature dependencies of K_{chem} and D_{chem} from 800 to 400°C were incorporated into the Task 15-2010b model.

Ceramatec validated the four models using three approaches. First, the predictions were compared to measured thermal expansion/contraction curves obtained at different rates and specimen sizes. Second they were used to predict the reliability of flexure bars cooled from 900°C to room temperature at various rates. The residual strength at room temperature was measured for those bars surviving the thermal cycle. For bars that failed during cooling, acoustic emission was used to determine the temperature at which fracture occurred. Finally, the models were used to predict the TGA data generated from heating and cooling small standard and advanced AP2K samples.

The Task 7-2005 model was not capable of predicting all three metrics. Both the Task 15-2008 and Task 15-2010a models were found to give reasonable predictions of the expansion-contraction curves, as well as the reliability of flexure bars cooled to room temperature at various rates. The Task 15-2008 model yielded the best predictions of the TGA curves. The residual stresses predicted by the Task 7-2005 model far exceeded the expected fracture strength. For the third validation approach, predictions were made of TGA data generated from heating and cooling a small standard AP2K sample between 700 and 100°C. In this case, the Task 15-2008 model yielded the best predictions. The Task 15-2010b model fit the transient dilatometer data quite well and was capable of predicting the reliability of the cooled flexure bars.

The Task 15-2010b model (Figure 15-28), was used to predict the expansion/contraction curves resulting from switching the atmosphere from low to high oxygen content at a fixed temperature.

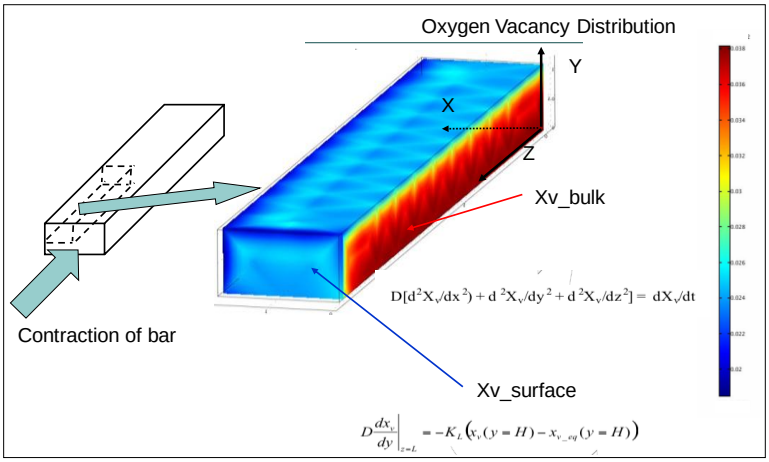

Figure 15-28. 3D FEA model of dilatometer bar used to predict expansion-contraction curve arising from a sudden change in P_{O2} at a fixed temperature.

The values of D_{chem} and K_{chem} were iterated to give the best fit between experimental and predicted curves as dictated by the minimum in the sum of the square of the errors.

A LabVIEW virtual instrument (see Figure 15-29) was created to implement the actual calculations.

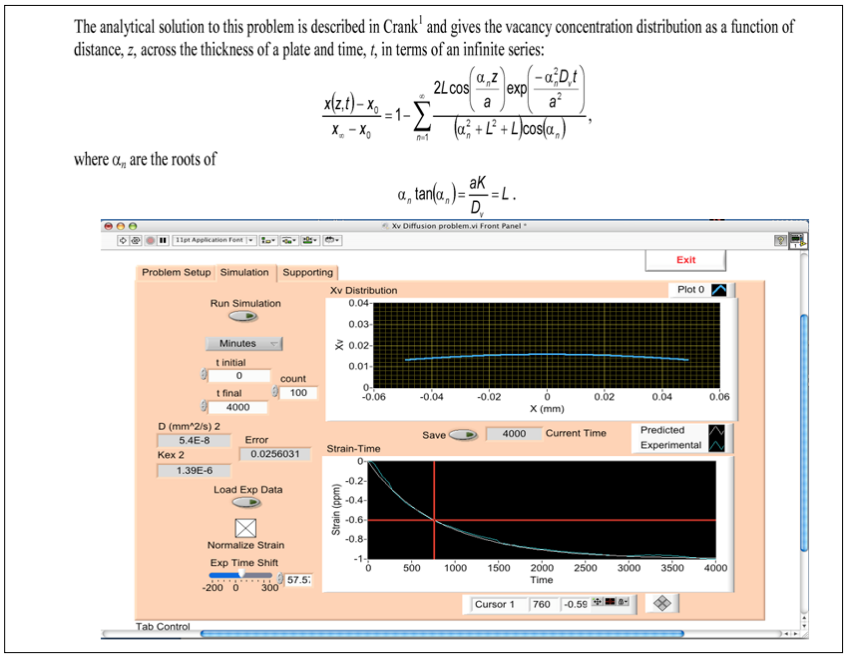

Figure 15-29. Main window of LabVIEW virtual instrument (VI) used to predict expansion/contraction curve arising from a sudden change in P_{O2} at a fixed temperature.

The VI optimizes the D_{chem} and K_{chem} values, calculates the sum of the square of the errors between predicted and experimental strain-time curves and produced a graphical representation of both curves. The 3D FEA required much more time to generate a predicted curve. For fixed values of D_{chem} and K_{chem}, the 3D FEA and VI gave comparable results.

15.3.2 Ceramic-to-Metal Seal Region Model

15.3.3 Module Model

End Caps

A five-wafer FEA model (Figure 15-30) was built to compare the maximum principal stresses of six proposed end cap designs during temperature and pressure cycling.

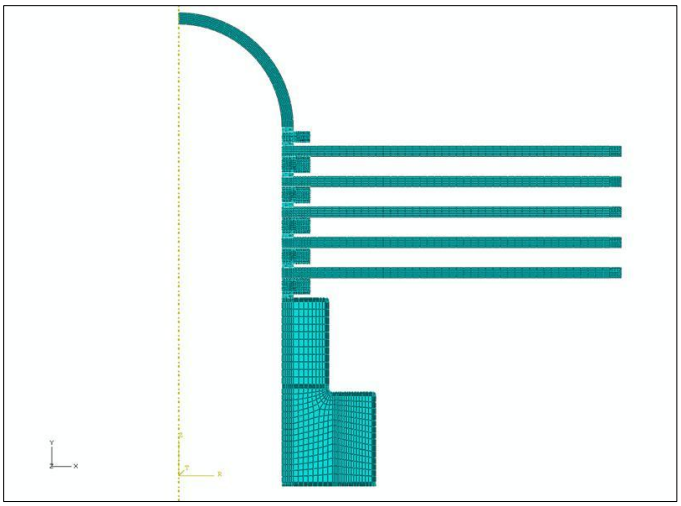

Figure 15-30. A 5-wafer FEA model including end cap, five wafers, spacers, ceramic-ceramic joints and a model base piece.

Figure 15-31 plots the principal stress in six end cap designs for two complete temperature-pressure process cycles. The dome design had the lowest stress.

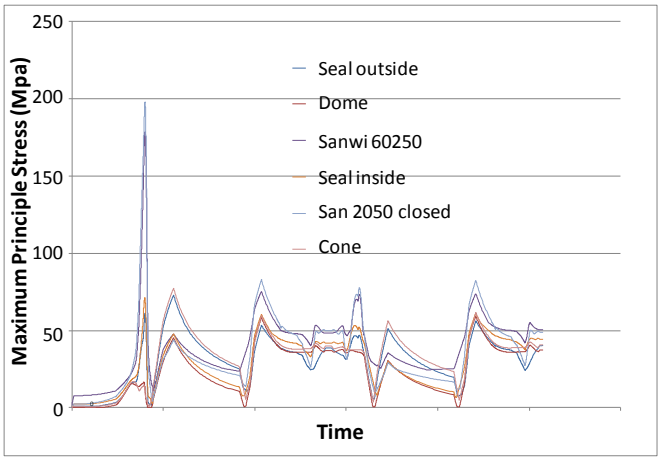

Figure 15-31. Principal stress in six end cap designs over a simulated process cycle.

Figure 15-32 plots the principal stress in the ceramic-ceramic joint between the top wafer and spacer for the same six end cap designs plus one additional. The dome design exhibited the least stress.

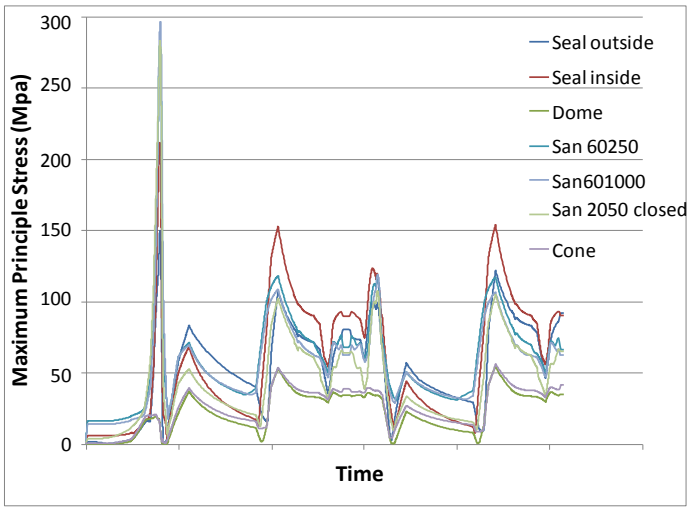

Figure 15-32. Principal stress in the first ceramic-ceramic joint under the top wafer for seven designs during a simulated process cycle.

Six additional designs were evaluated and compared against the low-stress reference design (the dome). The dome design was again the low-stress case. Variations on the dome design were compared (Figure 15-33).

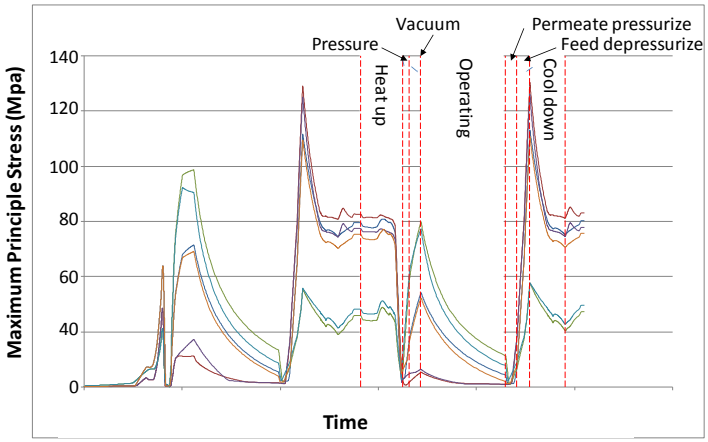

Figure 15-33. Principal stress in variations of the dome end cap design with time and operating condition during a process operating cycle.

Different designs exhibited the lowest stress depending upon the stage in the ITM operating cycle. Depressurization of the feed side causes the highest stresses. Refinements were made to the model from Figure 15-32 to 15-33. As a result, the absolute stress values cannot be compared from one model case to another. However, a relative stress comparison can be made.

Figure 15-34 is a plot of the maximum principal stresses in the ceramic seal between the end cap and the top of the wafer stack for three different seal location designs.

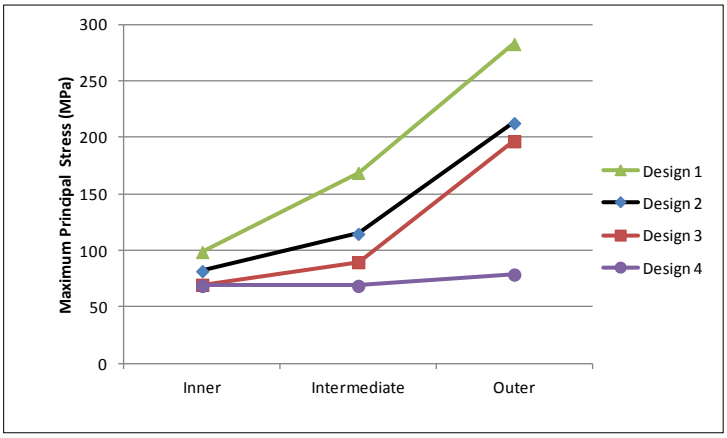

Figure 15-34. Maximum principal stress in the ceramic seal region for three locations of the seal region relative to the module radius for the four end cap design variant cases.

Design 4 yielded the lowest stresses in the seal region and the lowest stress in the end cap. It therefore was chosen for further development.

Spacers

A model of a new spacer was built so that an optimized pressurization schedule could be obtained. A quarter of the geometry was modeled based on the symmetrical conditions, as shown in Figure 15-35. The spacer has several layers. Tie constraints were established between each adjacent layer.

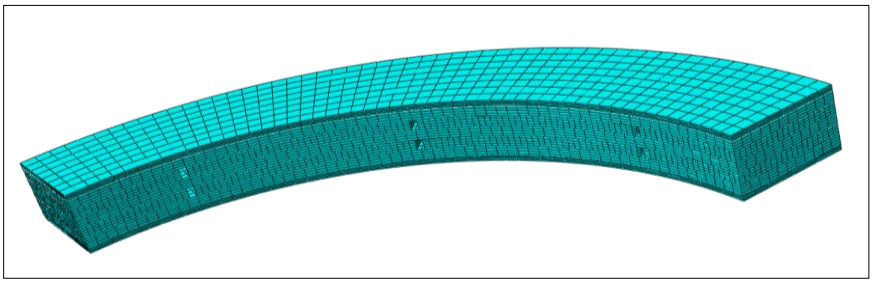

Figure 15-35. A quarter of the modeled spacer.

Flow Resistance

The flow resistance of porous AP2k disks was measured. Table 15-2 documents the measured open porosity of the AP2k samples.

Table 15.3-2. Open porosity of the AP2K samples.

Sample	% Open porosity
Oxygen Porous Disk 1	14.41
Oxygen Porous Disk 2	10.92
Oxygen Porous Disk 3	26.24
Oxygen Porous Disk 4	31.63
Oxygen Porous Disk 5	27.63
Oxygen Porous Disk 6	22.52
Oxygen Porous Disk 7	14.51

A flow of helium was forced through the disks, and the pressure drop across the disk was measured. The Reynolds number of the helium flow spanned the range of Reynolds numbers for expected oxygen fluxes within the wafer. The pressure drop data was fit to the Darcy equation for compressible flow. Figure 15-36 shows the predicted pressure drop as a function of porous layer thickness at the commercial target oxygen flux.

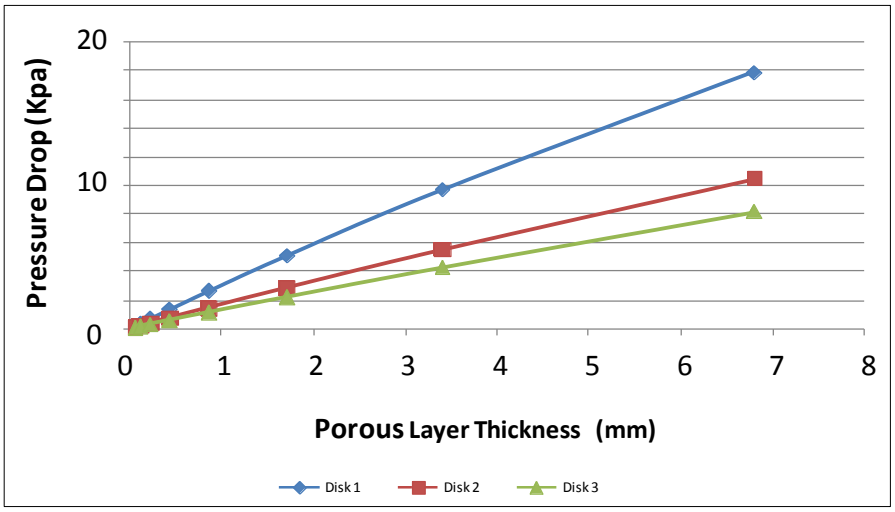

Figure 15-36. Predicted pressure drop through porous bodies.

Disk 3, with the highest porosity, had the lowest flow resistance. However, Disk 1, which had the intermediate porosity, had the highest flow resistance. The data suggests that the pressure drop through the porous bodies can be appreciable.

The measured permeability was used to calculate the pressure drop in porous layers as a function of the dense layer thickness. Transport was modeled using a series resistance, with the flux

model used to calculate the flux through the part and compressible flow through the porous layer. The pressure at the dense-porous interface was an input for the pressure drop calculation through the porous layer. Figure 15-37 plots the calculated pressure drops through the porous layer.

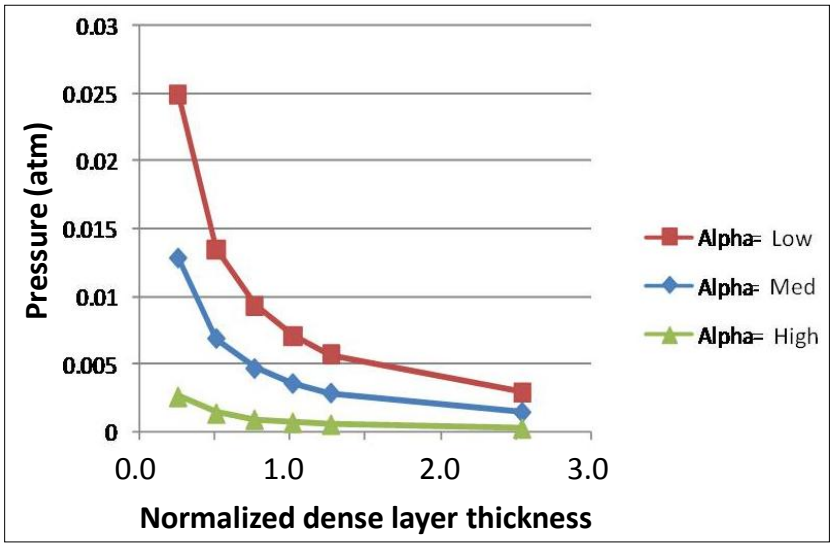

Figure 15-37. Predicted pressure drop through the porous layer under operating conditions for three permeabilities as a function of dense layer thickness.

Even with a thin dense layer, which produces a high flux, the pressure drop for the lowest permeability samples was still very low and thus will result in very little differential chemical expansion through the porous layer.

15.3.4 Validation Testing of Engineering Models

Wafer

Ceramatec constructed a thermal test rig to understand stress development in advanced architecture wafers. The rig included a heating chamber, testing chamber, frame and plumbing. The preheating chamber attached to the testing chamber was formed by two aluminum plates on the top and bottom housings. Ten heaters heated the air to 300°C. Aluminum blocks on each aluminum plate contained the heaters and provided flow channels. Holes in the middle of the two aluminum plates let two cylinder heaters through to contact the wafer spacers to control the vertical temperature gradient through the wafer. Two temperature control boxes were built for the 15 temperature controllers (Figure 15-38).

Figure 15-38. Two control boxes with 15 controllers.

Thermocouples were used to measure the temperature profiles of the wafer and provided input to the control system. Figure 15-39 shows the placement of strain gauges during commissioning.

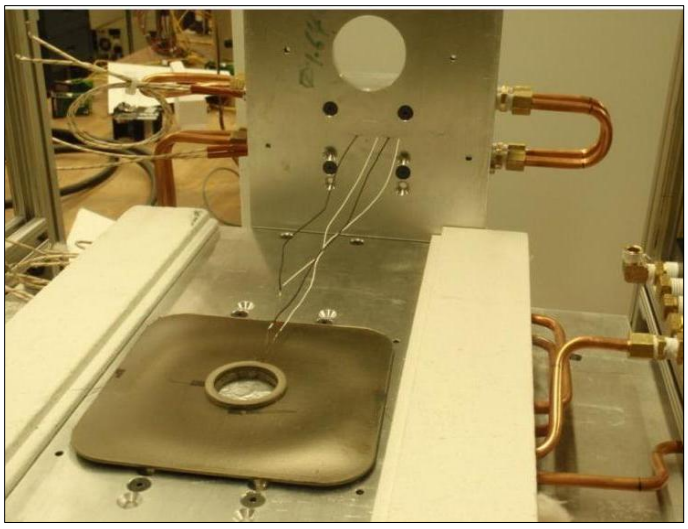

Figure 15-39. Position of the strain-gauged wafer and the lead wires.

A pneumatic loading capability was added to mimic the stack joining process. Figure 15-40 shows the assembled rig.

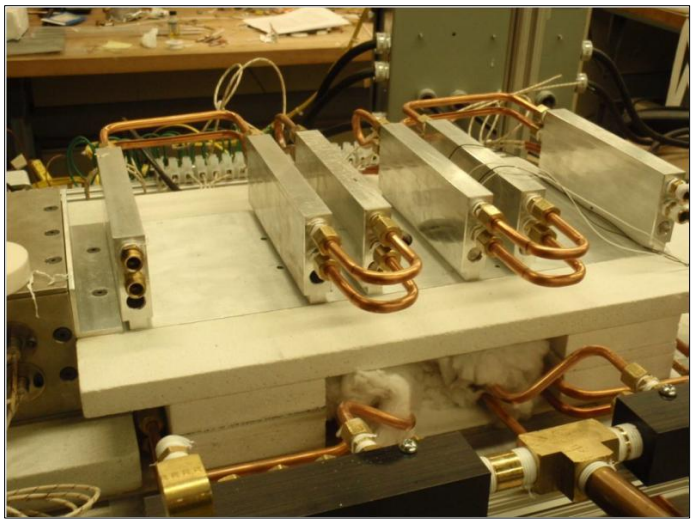

Figure 15-40. Assembled wafer thermal test rig.

Ceramatec conducted simulations to predict velocity fields in the test chamber and wafer temperature profiles. The geometry was created in Solidworks (Figure 15-41).

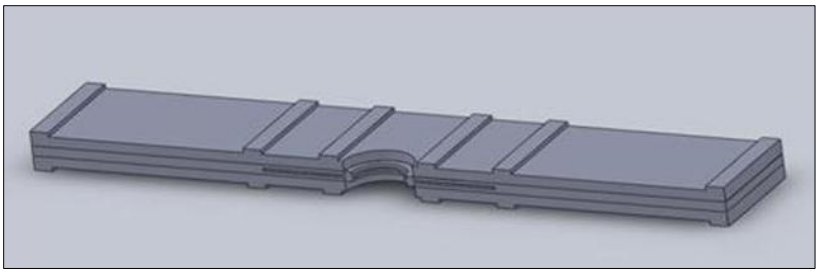

Figure 15-41. Solidworks model of half the testing chamber.

The boundary condition for the flow is a constant velocity inlet of 2m/s at 300°C. Figure 15-42 displays the predicted velocity distribution.

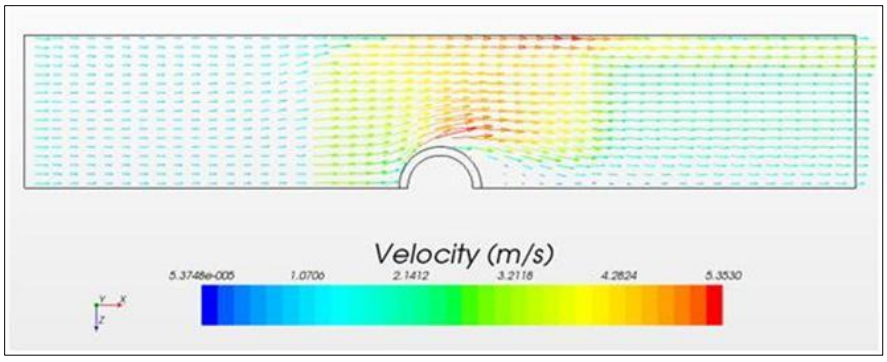

Figure 15-42. Velocity profile in a cross-section of the flow domain above the wafer.

Figure 15-43 shows the predicted temperature distribution in the advanced architecture wafer and spacer.

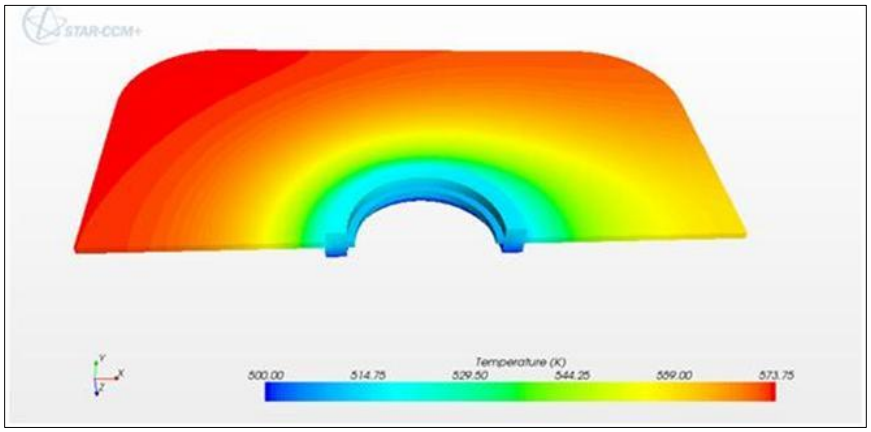

Figure 15-43. Temperature profile in a plane cross-section of the top metal plate.

An ABAQUS model was created to calculate wafer stresses (Figure 15-44).

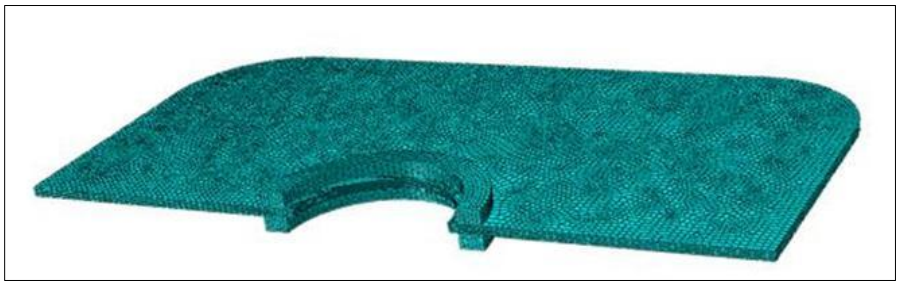

Figure 15-44. ABAQUS wafer stress model.

The wafer spacer assembly temperature field was mapped to the ABAQUS model and the wafer stresses were calculated, as shown in Figures 15-45, 15-46, and 15-47.

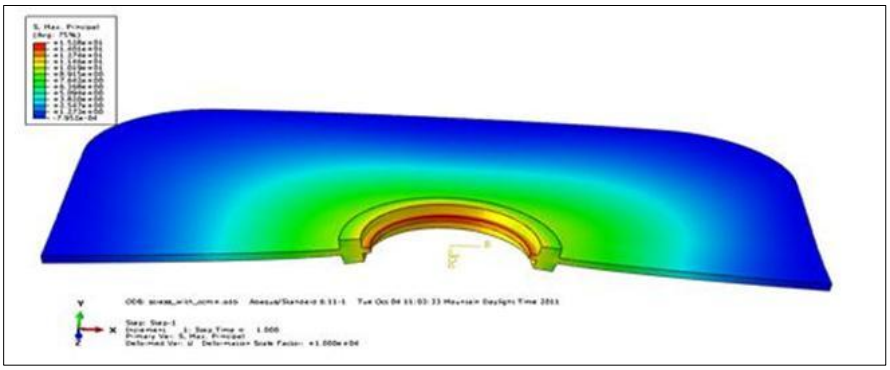

Figure 15-45. Radial stresses in the wafer.

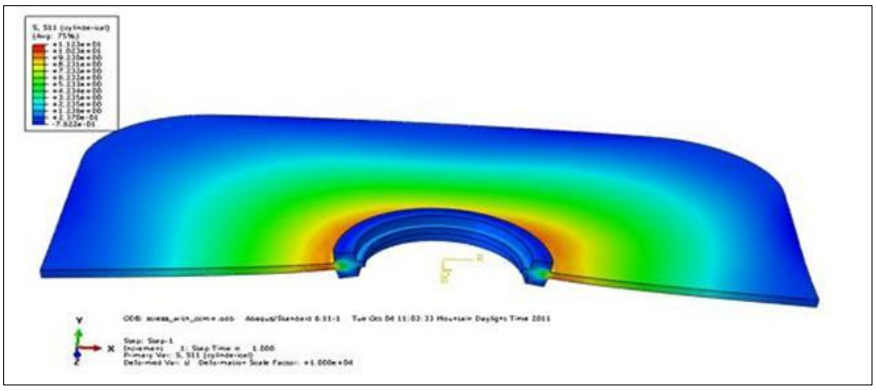

Figure 15-46. Maximum principle stresses in the wafer.

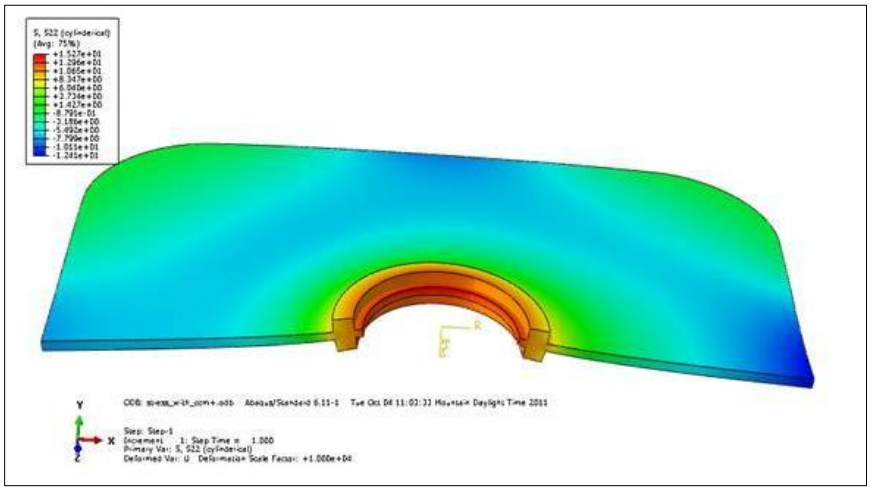

Figure 15-47. Hoop stresses in the wafer.

A stainless steel mockup wafer was used in the initial run to test the setup. Air at 2 m/s and 150°C was blown over the mockup wafer. The corresponding chart of temperature versus time (Figure 15-48) shows that relatively large temperature gradients were generated across the wafer.

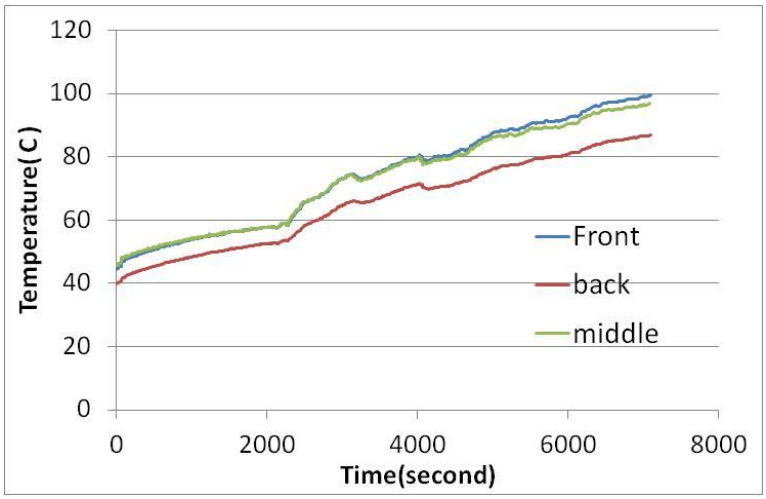

Figure 15-48. Thermal rig initial-run temperatures from the three thermocouples.

This work was used to corroborate thermal gradient modeling in ITM wafer ceramics.

Spacer Development

Mechanical Strength

Figures 15-49, 15-50 and 15-51 document the progression in strength properties of the spacer design.

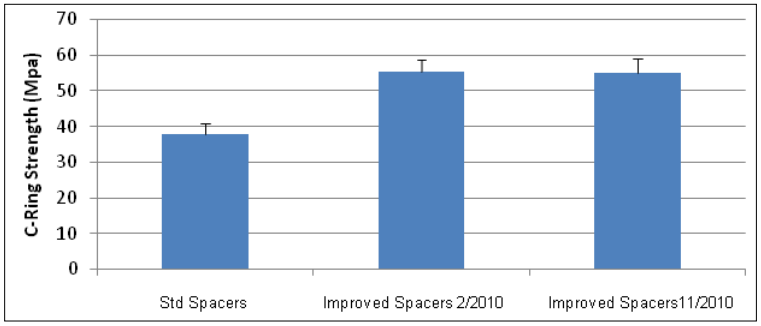

Figure 15-49. C-ring strength of standard (OD) and improved (OD2) spacers.

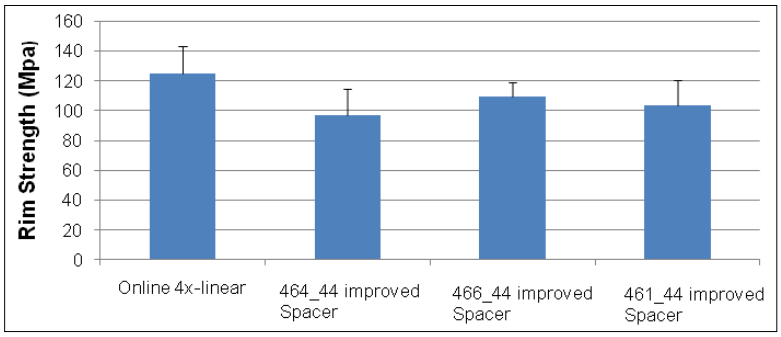

Figure 15-50. Rim strength of standard (OD) and improved (OD2) spacered wafers.

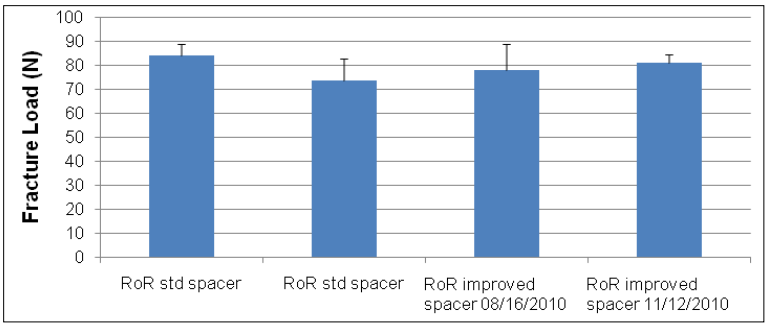

Figure 15-51. Ring on Ring fracture loads of standard (OD) and improved OD2) spacered wafers.

Module Alignment

One challenge with building a module is maintaining straightness. One possible cause for a deviation of straightness is misalignment of the joint. The misalignment can be non-concentric alignment of adjacent parts with respect to themselves, or to the vertical axis of the module (eccentric joining surfaces). During sintering, the joint will deform because of the external load and densification. An initial misalignment will cause the spacer to tilt, which will lead to a crooked module.

Ceramatec developed a model to validate the impact of misalignment and to improve the joining process. A widely used sintering model proposed by Skoroho-Olevsky is described by the following expression:

$$\boldsymbol{\sigma_{ij}} = \frac{\boldsymbol{\sigma(W)}}{\boldsymbol{W}}\left(\boldsymbol{\varphi}\dot{\boldsymbol{\varepsilon}}'_{\boldsymbol{ij}} + \boldsymbol{\mu}\dot{\boldsymbol{\varepsilon}}_{\boldsymbol{kk}}\boldsymbol{\delta_{ij}}\right) + \boldsymbol{P_L}\boldsymbol{\delta_{ij}}$$

where $\boldsymbol{\sigma(W)}$ is the effective stress, $\boldsymbol{W}$ is the equivalent strain, $\boldsymbol{\varphi}$ is the normalized shear viscosity modulus, $\boldsymbol{\mu}$ is the normalized bulk viscosity modulus, $\boldsymbol{P_L}$is the effective Laplace pressure (sintering stress) and $\boldsymbol{\delta_{ij}}$ is the Kronecker delta. This expression was incorporated into ABAQUS program through a USER defined subroutine.

Ceramatec used the model to define the important parameters that lead to an improved joining process with better module alignment. Results are presented under Task 17.

15.3.5 Ceramic Module Architecture Improvement

Ceramatec developed a FEA model to optimize the wafer design for creep deformation resistance. It includes two standard joints and a central wafer region, which has the same size as the spacer (Figure 15-52).

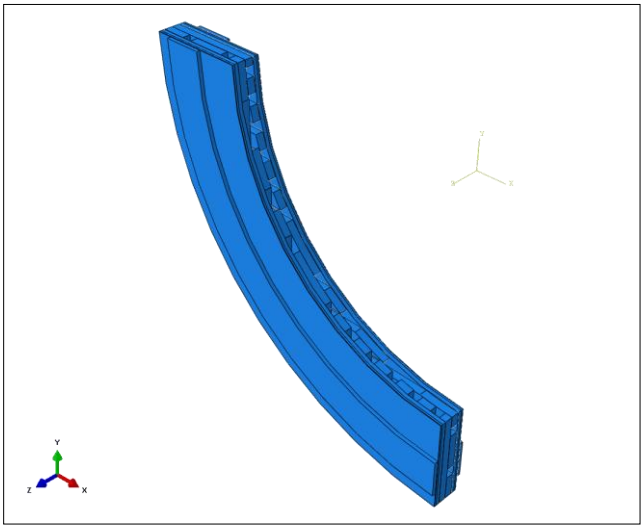

Figure 15-52. A unit cell ABAQUS model for design optimization.

Four different designs were considered. Eight MPa pressure was loaded on the top joint, and the bottom joint was fixed from moving up and down. The temperature was held at operating temperature for 100,000 seconds. A plot of typical displacement in the axial direction is shown in Figure 15-53.

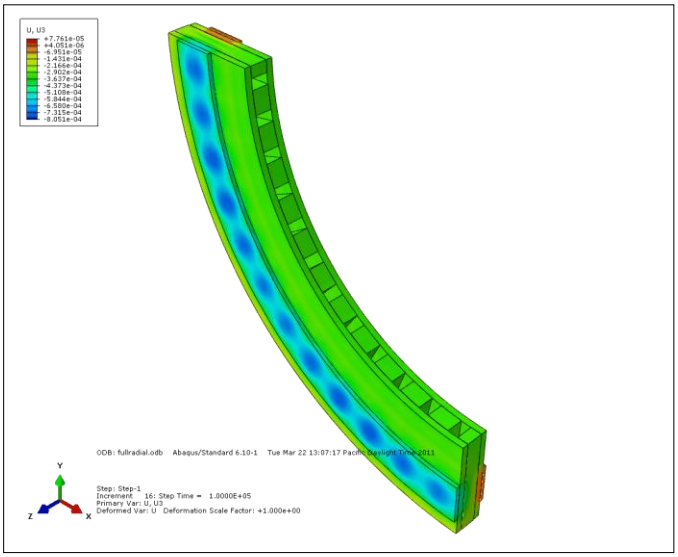

Figure 15-53. Vertical displacement plot in the unit cell for design D.

The creep deformation in the axial direction with time is plotted in Figure 15-54.

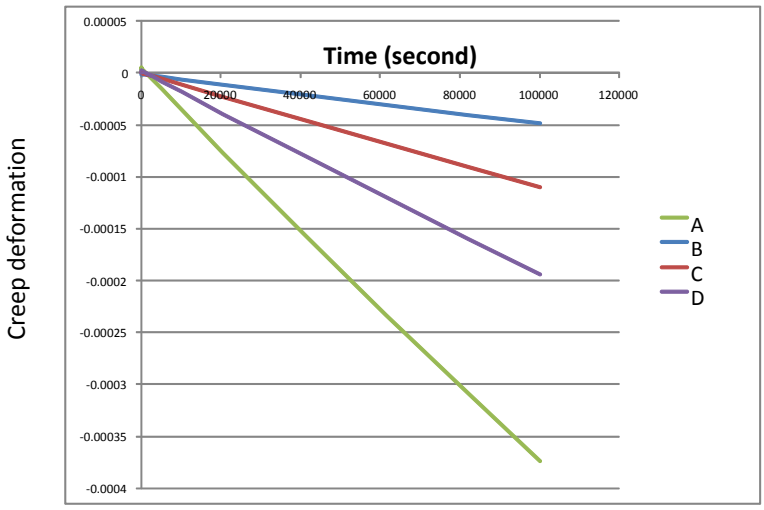

Figure 15-54. Creep deformation in the vertical direction for all four designs.

The model predicts that the creep displacement of Design A is about seven times that of Design D after 28 hours (100,000 sec). The creep deformation of Design A is about twice that of Design B. Testing shows the difference to be about six times (Figure 15-55), which indicates that the model is fairly accurate.

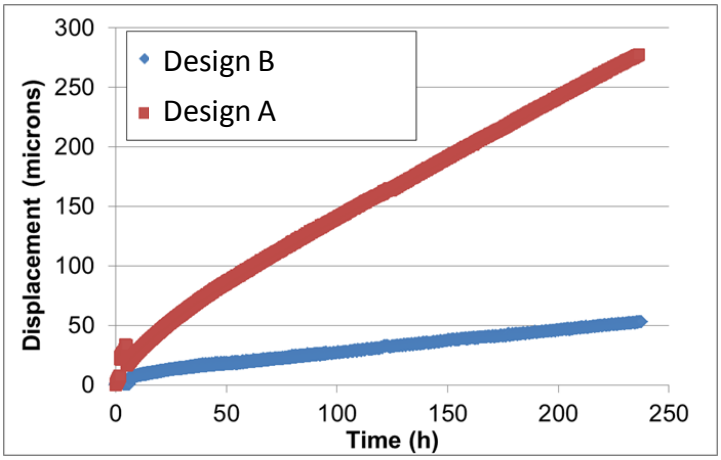

Figure 15-55. Creep deformation with time of two types of central core structures.

TASK 16.0 TABLE OF CONTENTS

TASK 16.0 PROCESS VESSEL DESIGN ENGINEERING 3

16.0 SCOPE 3

16.0 PROCESS VESSEL DESIGN ENGINEERING 3

Permeate Piping Train: Background 3

Results 4

Metal-to-Metal Seal in Permeate Piping Train: Validation Testing 4

Permeate Piping Train: Automatic Shutoff Valve 5

16.1 CONTROL SYSTEM DESIGN 6

Background 6

Results 6

Development of Improved Pressurization Schedules 6

Unplanned Transient (Loss of Electricity) 12

SEP Operations 14

16.2 EVALUATION OF SYSTEM RELIABILITY 16

Background 16

Ceramic Component Strength 17

Measurement Techniques 17

Results 17

End Cap Reliability 17

Wafer Reliability 21

Prediction of Oxygen Uptake Data 21

Iso-controlled Cooling Studies of Module Components 37

Reliability Model of SEP Modules 42

Reliability during ISTU Operation 44

Auto Shutoff Valve (ASOV) Reliability 47

16.3 PROCESS ENGINEERING AND ECONOMIC EVALUATION 48

Power Generation with Carbon Capture and Storage 48

Oxy-Combustion 48

Integrated Gasification Combined Cycle (IGCC) with Carbon Capture 50

16.4 CONTAMINATION MITIGATION SYSTEMS 52
Chromium 52
Background 52
Equipment and Test Method 52
Results 53
Sulfur Dioxide 65
Background 65
Equipment and Experimental Method 66
Results 66
Particulate Removal 68
Background 68
Results 68

TASK 16.0 PROCESS VESSEL DESIGN ENGINEERING

16.0 Scope

Air Products completes the conceptual design of representative commercial ITM Oxygen process vessels, sized to match appropriate machinery selections. This design effort is applied with the detailed design and fabrication of the ISTU vessel under Task 19.0. Elements of the design include internal and auxiliary device aspects such as the oxygen permeate train hardware selections.

Based on early conceptual work for the ISTU vessel design, Air Products identifies vessel design concepts that can be tested in a repeatable environment in the ISTU and in subsequent tests at a larger scale. Air Products works with Becht Engineering to develop these concepts for testing applications during this Cooperative Agreement and beyond. Critical factors for scale-up are identified, and specific design criteria established. The overall design effort supports the detailed design and fabrication of the ISTU vessel under Task 19.0.

In addition, Ceramatec, Air Products and Penn State collaborate to assess component reliability to guide membrane module architecture designs. The work supported the development of advanced architecture components under Task 17.

Air Products developed additional auxiliary technology, including process control and contaminant mitigation. Novel getter systems were identified, developed and tested in the SEP and specified for the ISTU. Particulate removal systems were also developed.

Finally, process economic cases were defined and advanced.

16.0 Process Vessel Design Engineering

Permeate Piping Train: Background

Under Task 19, Air Products developed the detailed design for the vessel to house the ceramic membrane modules in the Intermediate-Scale Test Unit (ISTU) based on concepts developed under Tasks 2 and 7. The design approach included an insulated duct to house the modules with a supporting system of oxygen permeate piping below. Besides supporting the modules, the piping system is to perform other functions, including the accommodation of a ceramic-to-metal seal and an automated shutoff valve that acts to isolate a module that has structurally failed. Under Task 19, Air Products and Becht Engineering developed a design for connecting the seal

sub-assembly that houses these components to the permeate piping. The seal sub-assembly may be removed for alterations between operating campaigns of the ISTU. To enable use of the removable seal sub-assembly concept, a flange connection was designed for the area between the seal sub-assembly and the permeate pipe. The flange connection included a metal-to-metal seal to keep the hot, high-pressure feed gas out of the permeate oxygen. Testing was conducted under this Task to assess efficacy of the metal-to-metal seal.

Results

Metal-to-Metal Seal in Permeate Piping Train: Validation Testing

Seal Configuration

Tests of proposed metal-to-metal seal were conducted to determine the best design. A bolted metal flange and gasket were tested under cyclic conditions between ambient and full operating conditions. The assembly was pre-loaded to a known bolt tension to achieve the design gasket compression and inserted into an externally heated pressure vessel. The flange connection was piped outside the vessel through a flow meter so that leakage through the flange could be monitored continuously. Figure 16-1 documents the results from one of the tests.

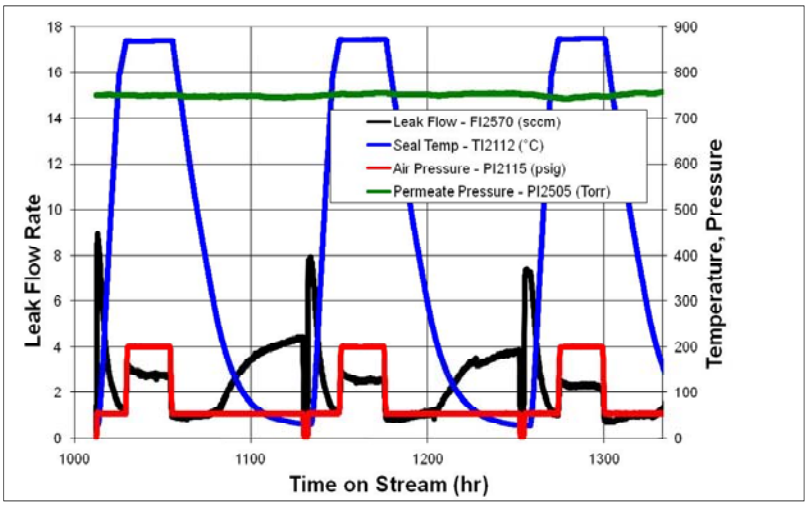

Figure 16-1. Leak rate behavior of a metal-to-metal seal.

The metal-to-metal seal was put through three complete temperature-pressure cycles, with the pressure differential being completely removed at ambient temperature after each cycle.

Various configurations were assessed including bolt material for creep resistance, the number of bolts, gasket material, use/non-use of a washer, surface treatment and tightening torque.

The test showed that a pre-load of 45 in-lb of torque to three bolts results in reliable and excellent performance. The performance was obtained whether or not washers are used on the bolts. In addition, the type of flange surface did does not have a significant impact. These results served to specify the metal-to-metal seals for the ISTU.

Permeate Piping Train: Automatic Shutoff Valve

The automatic shutoff valve (ASOV) utilizes a ceramic pin that fails when a specific pressure drop across the valve is reached. The pin design was based on strength measurements. The likelihood of failure over a stress range was assessed by determining the Weibull modulus that maps the probability of failure of a component at varying stresses.

Three-point bend tests were performed on small-diameter ceramic rods. Twenty samples were tested at room temperature and ten at elevated temperature. Figure 16-2 plots their Weibull strength distributions.

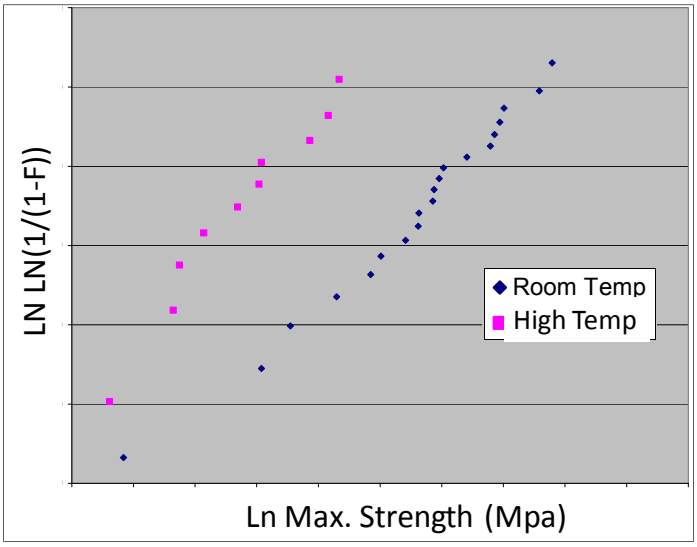

Figure 16-2. Weibull strength distribution plots for ceramic rods tested at room temperature and elevated temperature in three-point bending.

There was a slight decrease in strength at elevated temperature (442.8±23.6 MPa) compared to room temperature (510.4±42.8 MPa). The Weibull modulus was still quite high, which indicates that components can be designed to fail within a fairly narrow operating range. Tests at various operating conditions and varying pressure drops confirmed that the failure distribution (i.e., ΔP) was acceptable.

16.1 Control System Design

Background

Knowledge of the stresses within ITM component parts and between component parts (typically at the joints) is required to ensure they do not exceed the strength properties of the ITM ceramic. The induced stresses are caused primarily by differential expansion due to temperature and oxygen vacancy gradients within and between the parts. As discussed under Task 14, dilatometry experiments were conducted to determine the ITM ceramic material properties. In Task 15, FEA models were developed based, in part, on the Section 14 dilatometry data. In this task, the models were used to optimize the transient (startup and shutdown) operating conditions to minimize both component stress and the time to reach operating conditions.

Calculations were also conducted to determine the time rate of change in operating parameters on the loss of electrical power. This data were then used to estimate module stresses.

Results

Development of Improved Pressurization Schedules

Ceramatec utilized a spacer FEA model to calculate the maximum principal stress for ten pressurization schedules:

1. A slower air side pressurization.
2. An even slower air side pressurization.
3. Two distinct pressurization schedules. The second/slower schedule starts at ~2.5 atm of oxygen partial pressure. The original vacuum schedule was retained.
4. As per 3, but with a faster second schedule.
5. As per 4, but with a slower vacuum depressurization rate.
6. As per 5, but with the second schedule starting at ~2.2 atm of oxygen partial pressure.
7. As per 4, but with the second schedule starting at ~1.8 atm of oxygen partial pressure.
8. As per 7, but with the vacuum depressurization placed on hold three times with a total hold time of 10, 20 and 25 hours.
9. As per 7, but with three permeate depressurization ramps at different ramp rates in the ranges from 760 to 600 Torr, from 600 to 450 Torr, and from 450 to 350 Torr.
10. As per 7, but with one slow permeate depressurization ramp.

Figure 16-3 is an example of a simulated schedule (i.e., #1)

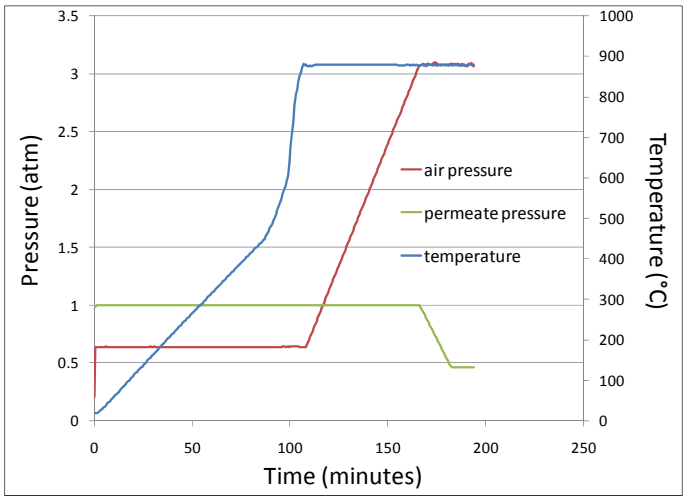

Figure 16-3. Simulation 1 schedule.

The stress results for Schedules 1 and 2 are compared to the original schedule in Figure 16-4.

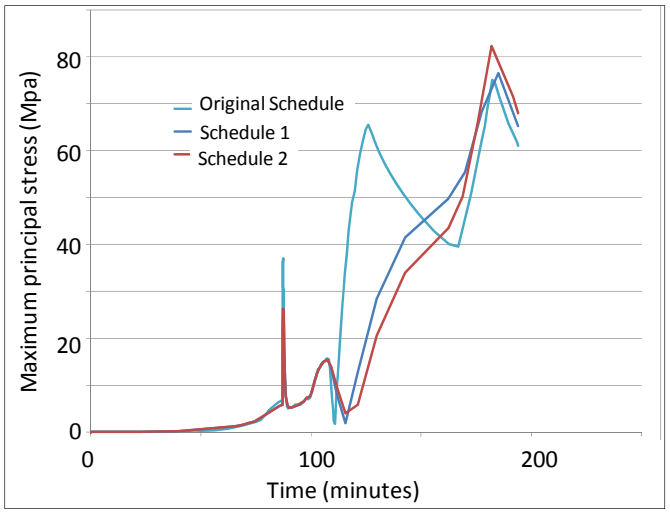

Figure 16-4. Principle stress from the original schedule and Schedules 1 and 2.

It was concluded that Schedules 1 and 2 will not significantly reduce the maximum principal stress. The principal stresses for Schedules 3 and 4 are shown in Figures 16-5.

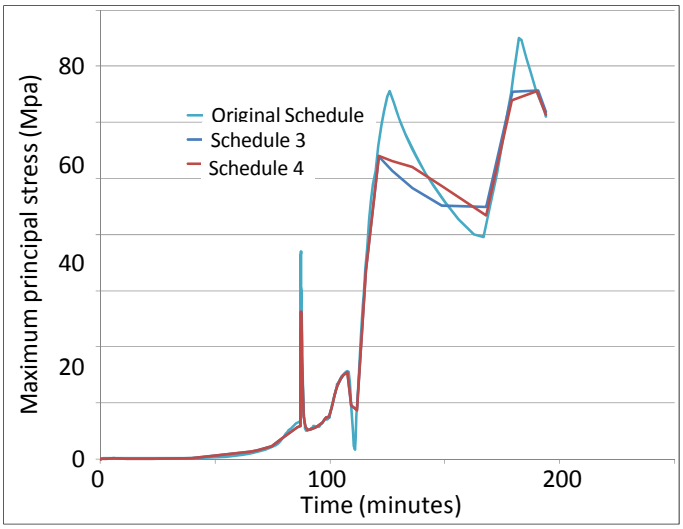

Figure 16-5. Principle stress from the original schedule and Schedules 3 and 4.

The results showed a reduction in maximum principal stress. The principal stress based on Schedules 6 and 7 are shown in Figure 16-6.

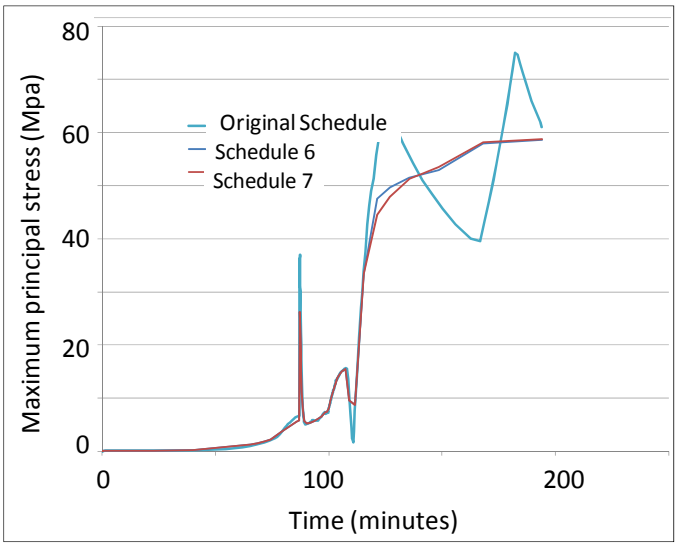

Figure 16-6. Principle stress from the original schedule and Schedules 6 and 7.

Results showed that the principal stress could be reduced through a two-step pressurization schedule where the second schedule is started at 2.2 atmospheres (or less) of oxygen partial pressure. Figure 16-7 shows the Schedule 8 simulation for a total of 25 hours hold.

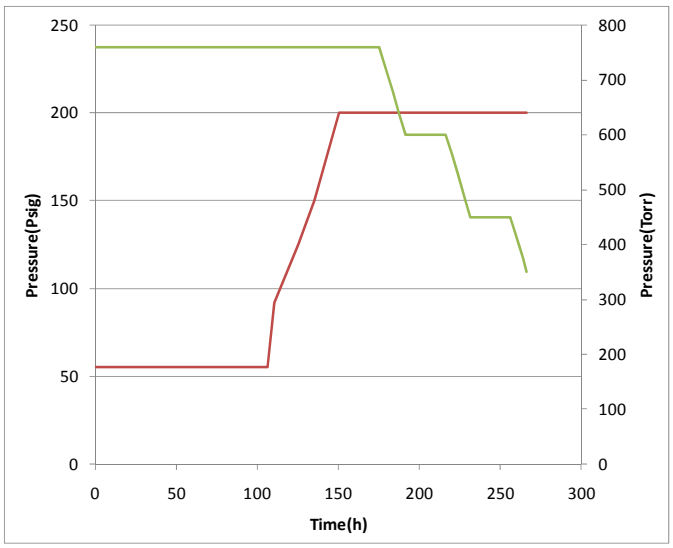

Figure 16-7. Schedule 8 pressurization and vacuum depressurization schedule, 25 hour hold.

The stress plots are documented in Figure 16-8.

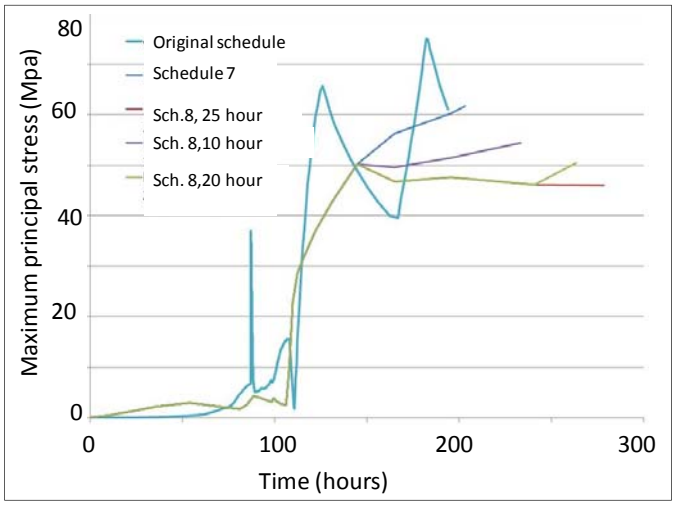

Figure 16-8. Principal stress for Schedule 8 simulation at 10, 20 and 25 hour total hold in permeate depressurization.

The results show that introducing a permeate depressurization holding time can further reduce the peak stress level. Figure 16-9, is the stress plot for Schedules 9 and 10.

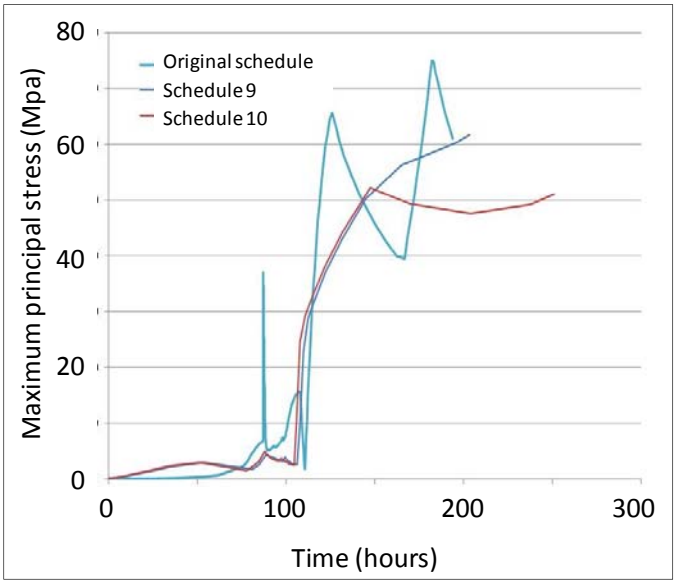

Figure 16-9. Principal stress Schedules 9 and 10.

The results show that Schedule 10, a slow vacuum depressurization in conjunction with a two-step air-side pressurization, will also reduce the maximum principle stress.

The stress field in a newly designed basepiece was modeled based on the original pressurization schedule. The geometry is shown in Figure 16-10.

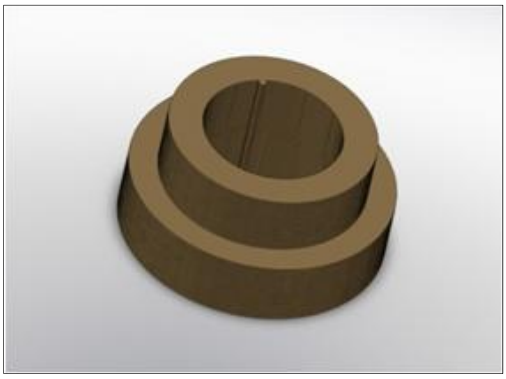

Figure 16-10. A Solidworks drawing of base piece.

The FEA model is shown in Figure 16-11.

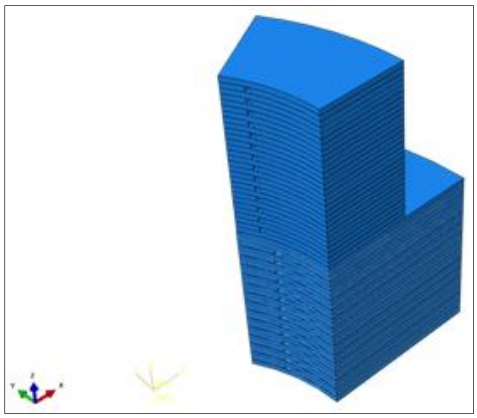

Figure 16-11. FEA model of a repetitive unit base piece.

The stress field based on the original schedule is presented in Figure 16-12.

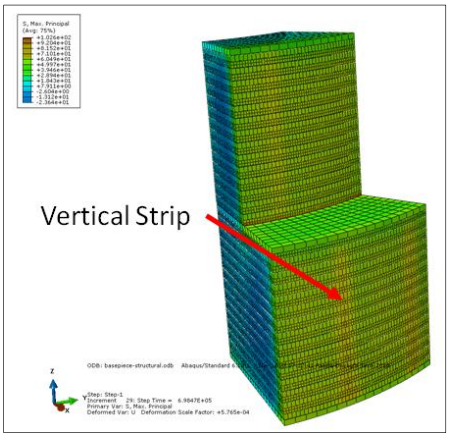

Figure 16-12. Stress field of base piece using the original schedule.

The model predicted high stress in vertical strips of the base piece. Test results (Figure 16-13) verified their existence and validated the model.

Figure 16-13. Base piece showing vertical cracks after testing in the XVUs.

The stress through a number of cross sections (Figure 16-14) was compared to the area of maximum stress.

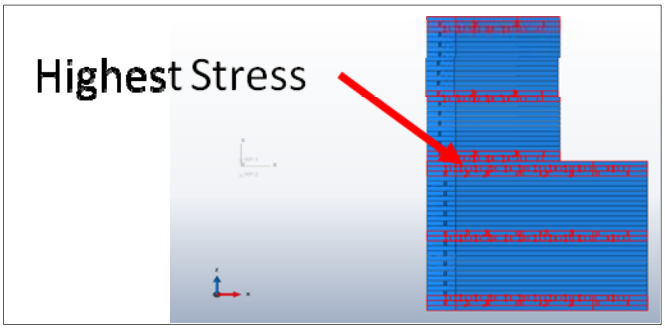

Figure 16-14. A cross section of a basepiece showing the high-stress layers

The joint layer between the top and bottom tube which showed the largest values (Figure 16-15) is the calculated principal stress based on proposed pressurization schedules.

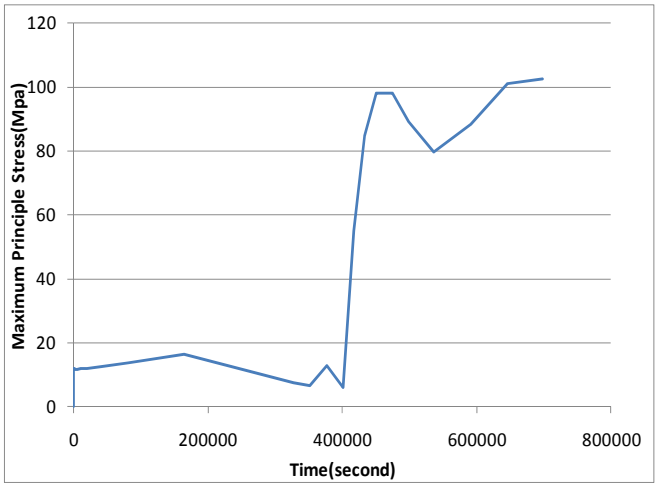

Figure 16-15. The peak stress history in the layer joining the top and bottom tube for the original pressurization schedule.

Unplanned Transient (Loss of Electricity)

Air Products completed a series of time-dependent calculations to assess the performance of a recuperated ITM system and to simulate the effects of a rapid unplanned process transient on the ceramic membrane modules. The ISTU vessel design was used as the basis for the simulation. The event studied was a power outage resulting in a "stand-by" condition. The transient conditions were calculated for the ITM vessel and supporting piping, heat exchangers, oxygen piping, oxygen cooler, oxygen vacuum pump, and fired heater. At the moment of the event, the

process was assumed to react to maintain the pressure on the feed side of the unit. The fired heater and main air flow were assumed to shut down. Because of varying levels of heat leak within the ITM vessel, the banks of modules in series in the vessel operate at different temperatures and begin to cool accordingly. Strain develops in the modules as they cool and equilibrate with the oxygen partial pressures on the feed and permeate sides of the membranes.

Figure 16-16 plots the strain (ppm) in the module banks with time following the simulated power outage.

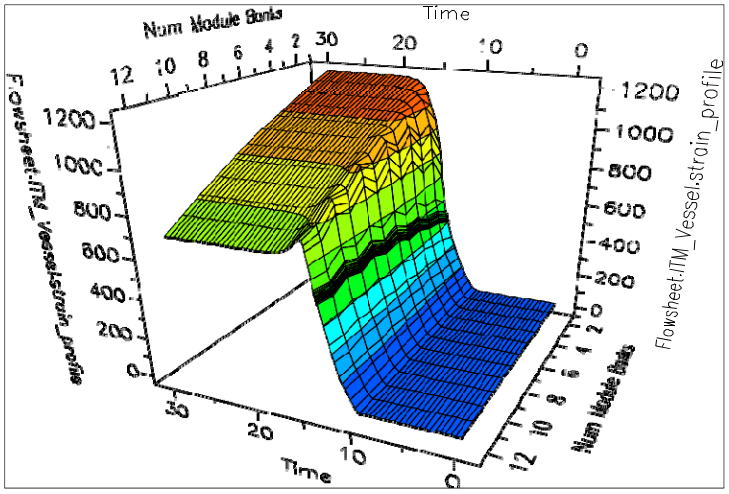

Figure 16-16. Material strain (ppm) as a function of time and module bank number during a simulated power outage (Note that Bank No. 1 is the leading module bank in a series of 12).

Strain was highest in the modules near the front of the vessel (Bank 1) and remained roughly steady as the system slowly cooled.

A system restart was also simulated. The fired heater and air flow are restarted. Temperature transients occur in upstream equipment as system components begin to heat up. Thermal waves move through the bed of modules. The temperature profile for 12 banks of modules in series is shown in Figure 16-17.

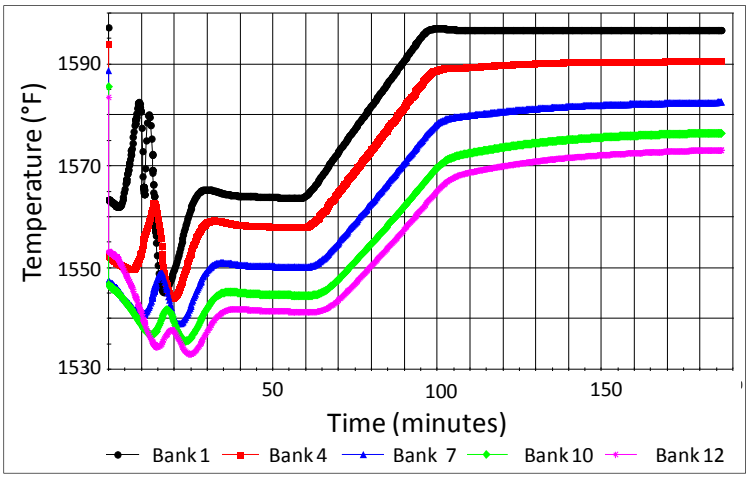

Figure 16-17. Simulated temperature profiles in an ITM vessel following restart of a systemhaving previously undergone a power outage.

A temperature profile develops down the axial length of the vessel. It was estimated that oxygen production could begin 3-4 hours after power is returned to the unit. The information was used to design the Intermediate-Scale Test Unit (ISTU) process control system and in the Section 16.2 "Evaluation of System Reliability."

SEP Operations

Operational data from the SEP was used in developing the design strategy of the ISTU control system. Two examples are presented. In the first case, the ASOV trip is noted to not affect an adjacent module. As a result, the ramifications of such events were not considered under the control system design, nor were modifications made to the seal sub-assembly to accommodate such events. In the second case, the shortcomings of the SEP control system were addressed in the ISTU control system design.

An assessment of the ASOV was conducted. The valve was intentionally tripped by adding an external flow of air to the oxygen product/permeates. Figure 16-18 shows process data before and after the ASOV trip. Modules E and F refer to module locations in the SEP (see Task 18).

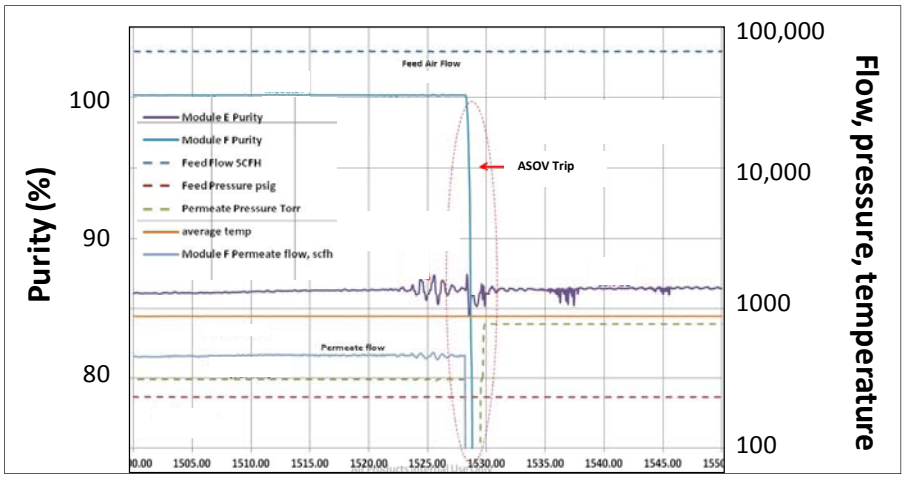

Figure 16-18. Process data before and after ASOV trip.

The product flow from the module immediately stopped following the trip and there was no change to the performance of the other module (O_2 purity and flow remained unaffected).

During a SEP run, the modules were subjected to iso-control heating and cooling cycles using a modified process. Figure 16-19 shows the percent deviation of P_{O2} from the target during the first cycle of iso-cooling and heating.

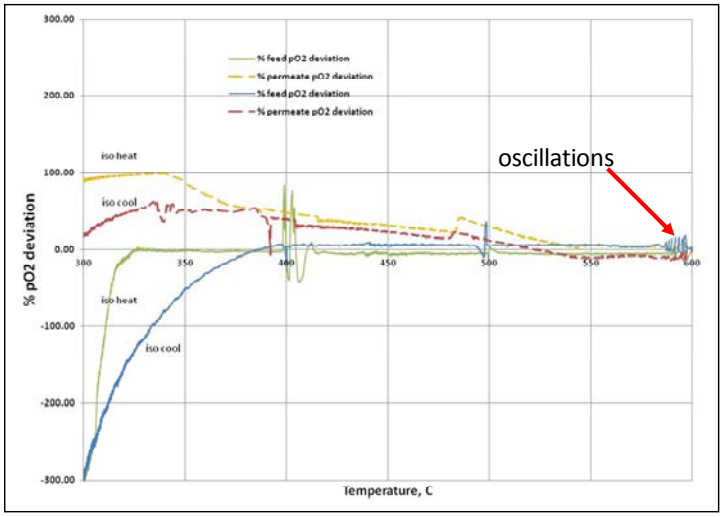

Figure 16-19. Percent P_{O2} deviation during iso cool/heat.

At the start of iso-cooling, oscillations were observed which were stopped by tuning the integral and gain of the feed-side adjustment valve. The feed-side deviation was <5% until about 400°C, but increased rapidly, reaching -300% at 300°C. It was found that the feedback adjustment valve

did not respond below 400°C. During the iso heating, the deviations were almost eliminated above 325°C by fine tuning the adjustment valve. The valve responded very well to minimize deviations from the target P_{O2}.

16.2 Evaluation of System Reliability

Background

The reliability of ceramic articles is usually strongly correlated with their manufacturing histories. Figure 16-20 is a simplified overview of an ITM module fabrication process.

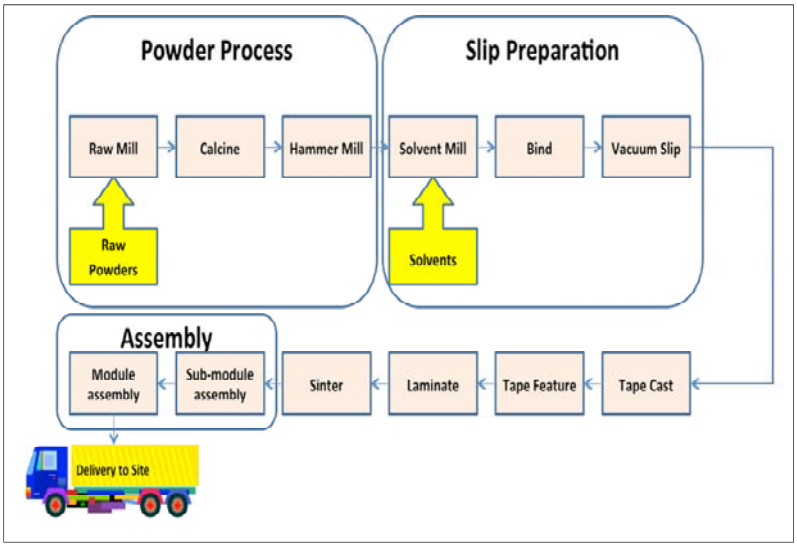

Figure 16-20. Ceramic process overview.

The ITM powder is firstly calcined and milled to a specific size distribution. The milled powder is then mixed with a solvent to produce a "slip," which is a suspension of fine raw materials powder in a liquid with small amounts of secondary materials such as dispersants, surfactants and binders. The slip is sent to a tape caster where sheets of ITM ceramic are produced. The tape is cut and layered/laminated to make the specific component parts, after which the ITM ceramic membrane is applied. This "green" part is then sintered.

The sintering conditions impart specific properties to the part including density, porosity and strength. The sintered parts are assembled into submodules and re-sintered to bond the joins between the parts. The submodules are assembled into modules and sintered again to bond the joins. The quality of the parts, submodules and modules, and specifically their resistance to cracking, is affected by the entire manufacturing processes.

Ceramic Component Strength

A sintered ceramic is brittle and typically contains flaws within its structure. Unlike metals which have distinct fracture strengths, the fracture strength of a ceramic can vary depending upon the number of flaws within the structure and its basic strength properties. When the fracture strength of a group of supposedly identical ceramic bars is measured, a strength distribution is found. This strength distribution is characterized by a statistical parameter called the Weibull modulus. Statistical equations have been developed which use the Weibull modulus to predict the Probability of Survival (Ps) or Failure (Pf) of a ceramic as a function of stress.

Measurement Techniques

Scanning Acoustic Microscope

A scanning acoustic microscope (SAM) is a device which uses focused sound to investigate, measure, or image an object. It is commonly used in failure analysis and non-destructive evaluations. The technique is used to identify subsurface defects in a part.

Acoustic Emissions Testing

Acoustic emission (AE) testing is a non-destructive test method. An AE system monitors acoustic emissions produced within a material caused by internal fractures.

Thermal Gravimetric Analysis

Thermal gravimetric analysis (TGA) is a method of thermal analysis in which changes in physical and chemical properties of materials leading to mass changes are measured as a function of increasing temperature (with constant heating rate), or as a function of time (with constant temperature and/or constant mass change). TGA is commonly used to determine selected characteristics of materials that exhibit either mass loss or gain. In the case of ITM ceramic, oxygen is released from the material as the temperature is increased. The data can be used to estimate the oxygen vacancy concentration.

Results

End Cap Reliability

The original module end cap was designed as a flat disc. A module with this design was tested in the SEP, where it was subjected to six process cycles. Significant cracking occurred (Figure 16-21).

Figure 16-21. Radial and circumferential cracks were observed in the end cap on Module B, Run 12.

Furthermore, SAM analysis of the end cap showed that the subsurface cracking was even more extensive than indicated by the visible cracks seen on the surface. A study was conducted to evaluate the mechanical properties of end caps under the load produced by the feed air pressure. The resulting data (Figure 16-22) showed that the load-carrying capability of the samples was only marginally higher than the end loads expected by pressure loading.

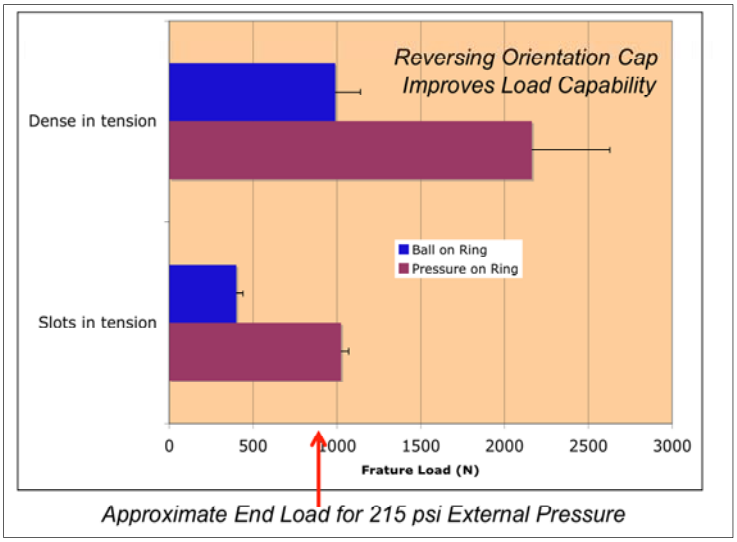

Figure 16-22. Fracture loads measured using two test configurations.

Thermal Cycling Studies

A study was initiated to evaluate and model the reliability of the flat end cap design when subjected to various thermal cycles. Figure 16-23 shows the three temperature-time profiles used in the experimental testing at Ceramatec. The profile designated as "Shortened Cycle" represents the cycle proposed to shorten the overall duration of individual tests.

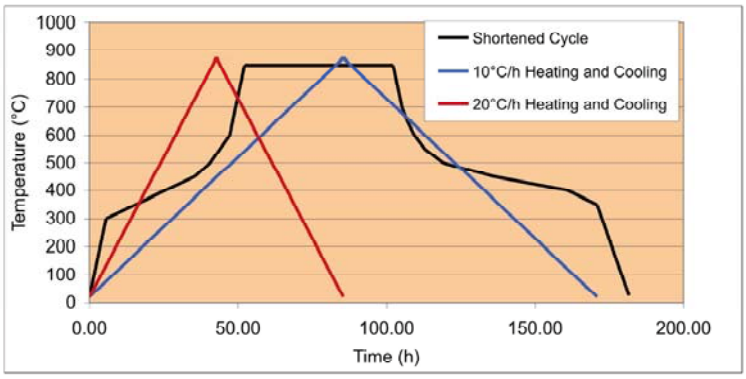

Figure 16-23. Temperature-time profiles used in the experimental end cap testing.

For each of the three cycles, a finite element analysis (FEA) model was used to estimate the probability of survival. Existing Weibull parameters for the ITM ceramic were used as input to the probability of survival (Ps) analysis. Note that a value of 1.0 represents 100% probability of survival. Figure 16-24 is a representative plot which includes the effects of temperature, pressure, loading and creep.

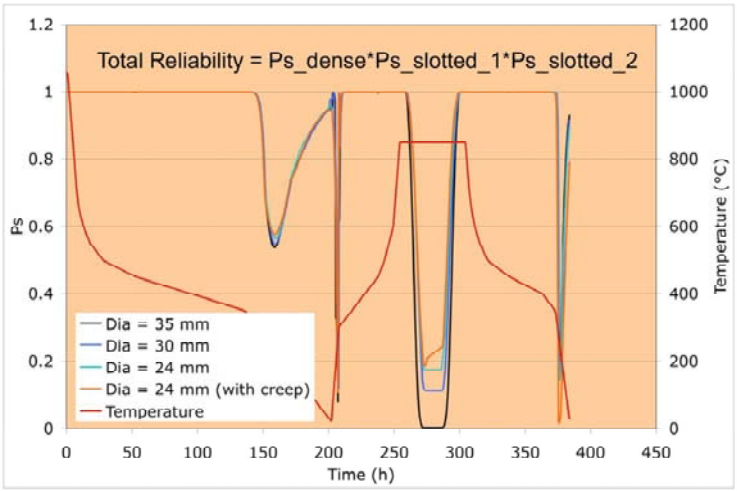

Figure 16-24. Total reliability versus time curves for the inverted end cap subjected to the shortened cycle.

The data predicts nearly complete failure. The predicted results were in qualitative agreement with experimental data collected at both the SEP and laboratory pilot units in tests of end caps in fluxing modules.

Ceramatec also considered another temperature cycle to which unjoined end caps were subjected. The results of an FEA simulation to estimate the Ps is presented in Figure 16-25. Note that the portion of the red curve at times exceeding 200 hours gives the temperature-time profile of interest. The portion of this curve for times <200 hours represents a cooling profile used to simulate pre-processing of the end cap. Its inclusion in the analysis was required to generate reasonable estimates of the stresses expected at room temperature.

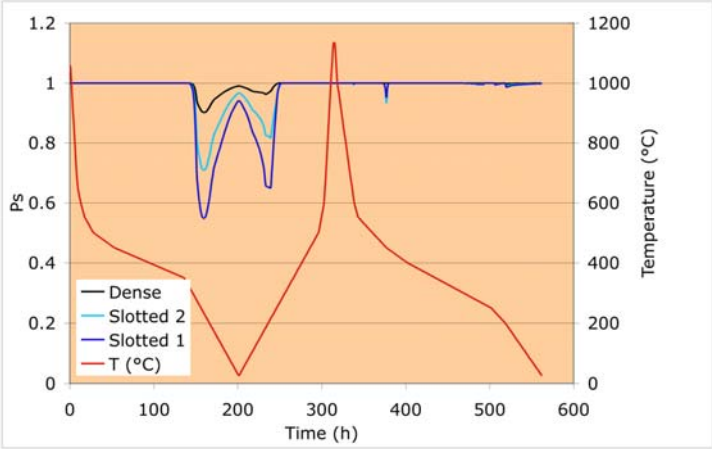

Figure 16-25. Results of the FEA of a thermal cycle applied to end caps.

The end caps were intact after the cycle and SAM inspection showed no internal damage. The FEA model indicated that probability of survival was high throughout the cycle.

The domed end cap design was proposed; prototypes were built by Cerameteac, and Air Products tested the new design in the transient test rig (TTR). The system was started using a modified SEP startup protocol. When the run was concluded, the sample was examined, and several cracks were found in the base piece, but none were observed in the domed end cap. Some of the cracks can be seen in Figure 16-26. It appeared that some of the base piece cracks were associated with the areas of contact with holddown clamps that were used in the experiment.

Figure 16-26. Photo showing cracks in base piece after test.

Wafer Reliability

Prediction of Oxygen Uptake Data

Accurate models of oxygen transport in and out of composite structures made of the ITM ceramic are critical for good modeling of reliability. Ceramatec conducted thermal gravimetric analyses (TGA) to measure the mass change for both dense and porous ITM ceramic bar samples subjected to thermal cycling between 100 and 700°C in air and 1 atmosphere of oxygen (Figure 16-27).

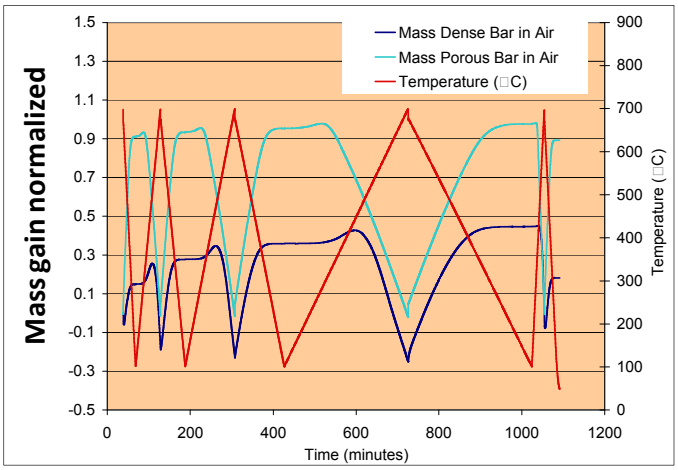

Figure 16-27. TGA results for porous and dense bars of ITM material cycled between 100 and 700°C in air.

A FEA model was used to predict the oxygen vacancy distribution occurring within the specimen as a function of time. At any given temperature, the number of moles of oxygen vacancies is given as

$$n_O = \frac{\rho c}{\mathrm{MW}} \int_{\mathrm{V}} X_v dV$$

where ρ is the density of the material, c is the number of mole of O per mole of the material, and MW is the molecular weight of the material. The spatial distribution of Xv is the vacancy fraction, and n_{O2} is the number of oxygen vacancies. Changes in this vacancy distribution were used to calculate the change in mass occurring as vacancies were either created (during heating) or destroyed (during cooling).

Experimental TGA data for the dense bar cycled in oxygen are shown in Figure 16-28 along with the predicted curve.

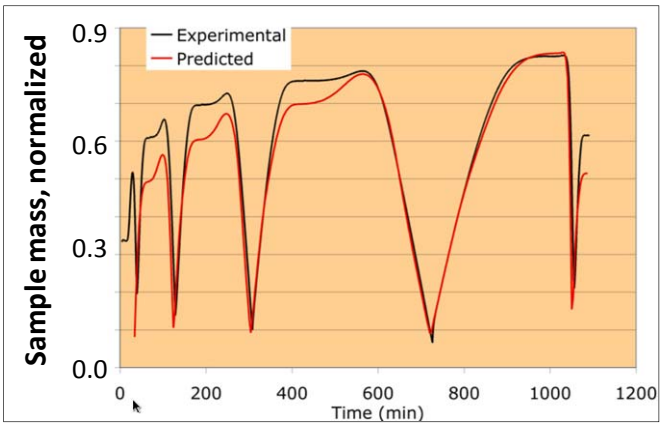

Figure 16-28. Comparison of predicted and measured mass change for dense ITM ceramic bar tested in 1 atmosphere of oxygen.

While model predictions did agree well with the experimental data at the slowest heating/cooling rate, they underestimated the response at the faster heating rates.

A simple particle model was used to represent the porous bar (Figure 16-29).

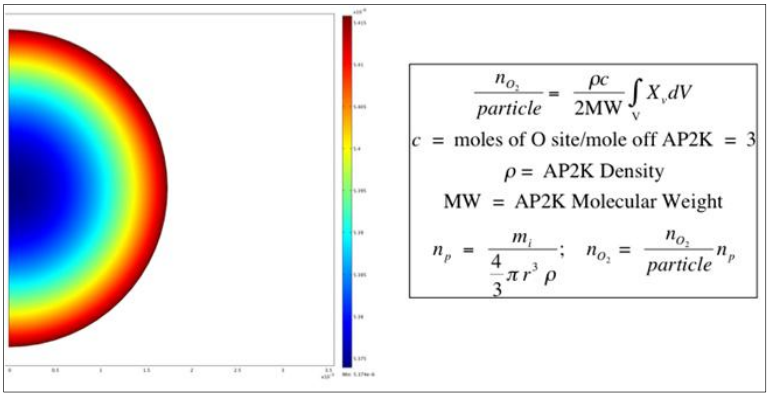

Figure 16-29. Details of single particle model used to represent porous bar. The bar is assumed to be composed of N_p particles of fixed radius.

For this situation, the number oxygen vacancies was calculated from the expression,

$$n_{O_{tot}} = \frac{n_O}{particle} n_p = \frac{n_p \rho c}{\mathrm{MW}} \int_V X_v dV$$

where ρ is the density of dense ITM material, and n_p is the total number of particles:

$$n_p = \frac{m_i}{\frac{4}{3}\pi r^3 \rho}$$

where m_i is the initial mass and r is the particle radius. The predicted mass change is dependent upon the particle radius. A particle radius of 150 μm was the best fit to the experimental data. The initial model predictions captured the shape of the experimental data as the temperature transitioned through its minimum at 100°C. Better agreement was obtained by adding a low segment in the temperature dependence of the activation energy. Increasing the activation energy in the 100°C to 300°C range improved the shape of the predicted peaks, but the overall mass change for the predicted curves became increasingly smaller than that obtained experimentally.

Thermal Cycling Studies

Ceramatec conducted extensive testing to assess the conditions under which components can fail by using rapid thermal cycling. The resulting information was used to optimize the heating and cooling profiles associated with sintering and joining cycles.

One of the issues that arose when attempting to use these data for model development was the inability to exactly determine the point in the thermal cycle when the part failed. Acoustic emission was successfully used to monitor failure in some tests but did not always succeed because ofa low signal-to-noise ratio. In an attempt to address this problem, Ceramatec modified a test system that had been used to thermally cycle wafers joined to conical base pieces in air to evaluate low-temperature failures. A firewire camera system was added along with image acquisition software. The new equipment was integrated into the existing data acquisition package so that images could be collected along with temperature-time data. Figures 16-30 and 16-31 illustrate the various components of the image acquisition system.

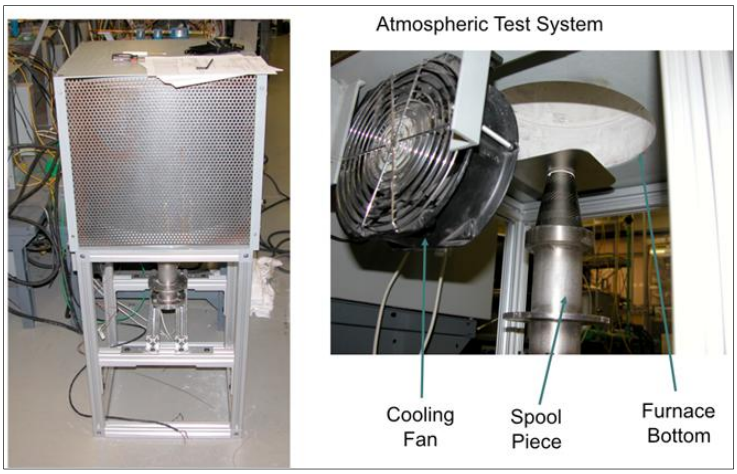

Figure 16-30. Set-up of atmospheric test system used to subject cone-wafer parts to thermal treatment cycles.

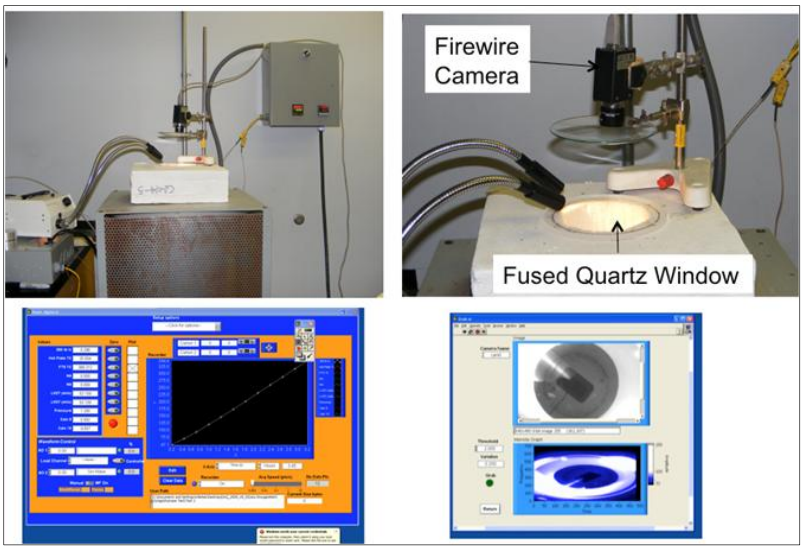

Figure 16-31. System used to visually monitor components during temperature cycling. The software illustrated in the lower left is used for acquiring data from the various thermocouples around the sample, while the screenshot in the lower right shows the system used for the acquisition of images.

A standard wafer was heated to 600°C at a heating rate of approximately 12°C/hour, then cooled at 18°C/hour. An example of the test data is shown in Figure 16-32.

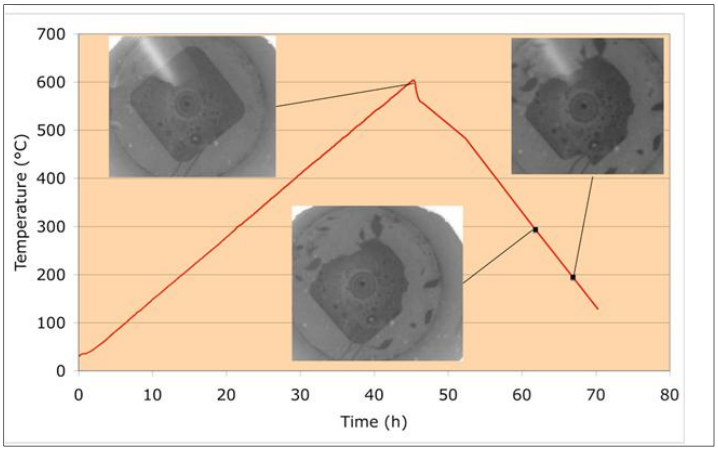

Figure 16-32. Initial results obtained for cycling a single standard wafer at 12°C/h to 600°C and then cooling at 18°C/h back to room temperature.

Based on previous tests, the wafer was expected to survive during heatup but fail during the subsequent cooldown. As shown in Figure 16-32, upon cooling the wafer failed via rim cracking first at about 300°C and then at 200°C. The spots on the wafer occurred due to unintended movement in the furnace lid which caused insulation to be deposited on the surface during heating. A new lid design eliminated this problem.

A series of tests to define critical heating rates was undertaken. For a few of these tests, an acoustic emission (AE) measurement system was used to record the acoustic energy resulting from the fracture. This required the introduction of three solid alumina rods into the bottom of the furnace (Figure 16-33).

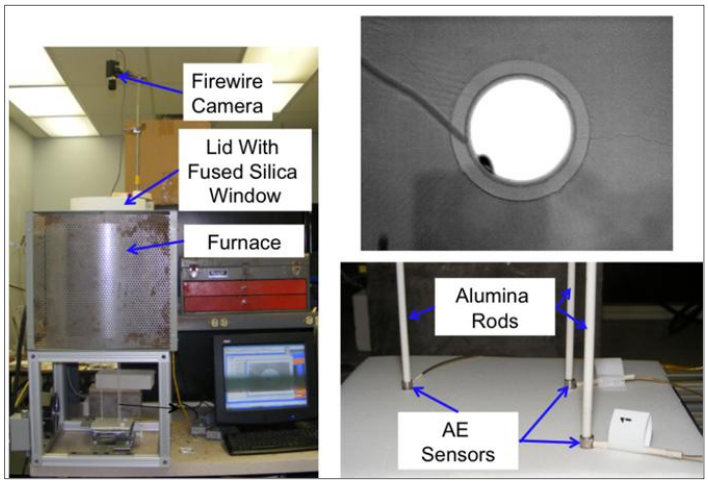

Figure 16-33. Setup for measuring acoustic emission during wafer heating and cooling.

These rods served to support the wafer and transmit the sound out of the furnace and into the acoustic sensors attached to the ends of alumina rods. These sensors were in turn connected to a digital signal processing board located in the same computer used to monitor temperatures and capture images.

In one test, a standard wafer was heated to 475°C at 260°C/hour. It was expected that the wafer would fail at no more than 200°C. While the AE system did pick up a few counts during heating, the wafer remained intact even after rapid cooling back to room temperature.

Later tests showed that that standard wafers could be heated up to 800°C at 60°C/h without inflicting damage in the membrane layer. This conclusion was based on measurement of wafer leak rates before and after heating in the range of 400 to 800°C and then cooling slowly to room temperature. In all of these tests, acoustic emissions were detected in the 350°C to 500°C range on heating (Figure 16-34). The fact that the leak rates did not change appreciably indicates that any damage was confined to an internal portion of the wafer.

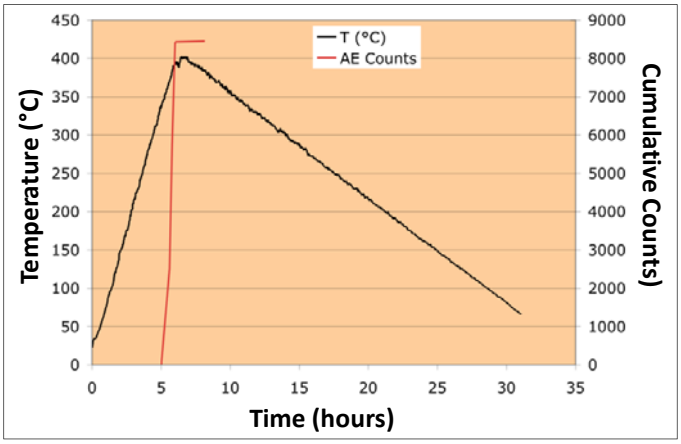

Figure 16-34 Temperature-time profile for a wafer test and acoustic emissions.

Additional studies were conducted to better define the heating-cooling profiles for ¼ wafer sections. Two ¼ Slot Pattern #1 and one ¼ Slot Pattern #2 wafers were heated at 4.8°C/h to 800°C and cooled to 25°C at 10°C/hr (Figure 16-35).

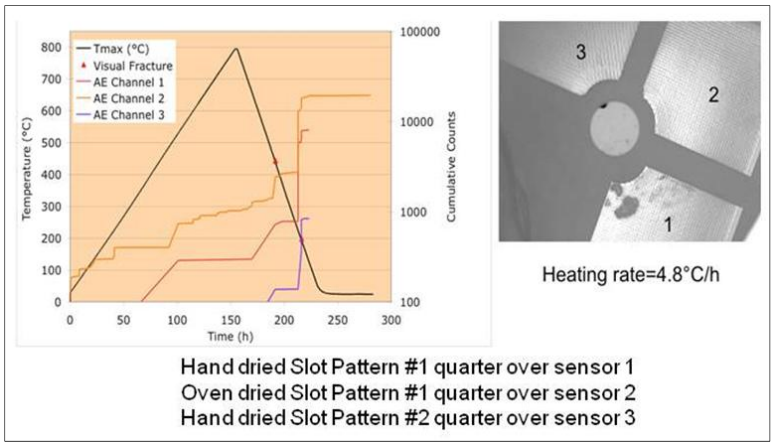

Figure 16-35. Temperature-time and AE results for multiple ¼-wafer sections.

All three wafers survived heating. As shown in Figure 16-36, a fracture was visually detected on cooling in the Slot Pattern #2 wafer at 450°C and in one of the Slot Pattern #1, ¼ wafers at just below 200°C.

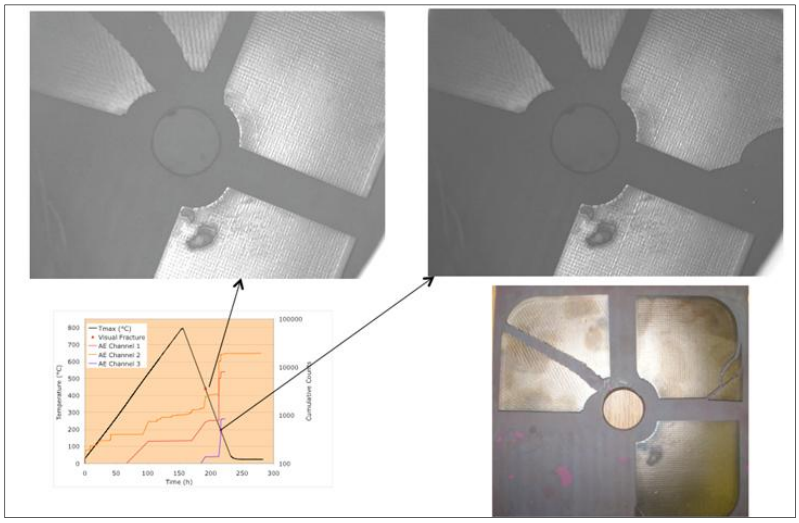

Figure 16-36. Illustration of visible failure conditions observed during cooling. The image in the lower right was taken after the test.

After the test, the second Slot Pattern #1 wafer was found to be cracked as well. With the exception of the Slot Pattern #2 wafer, failures initiated from the cut surfaces.

Additional tests focusing on rim cracking were conducted using the ATS and the box furnace. The results are summarized below:

- A Slot Pattern #1wafer failed on cooling below 400ºC. Most of the failures occurred along the sides of the wafer with the thickest rims.
- Sub-par Slot Pattern #2 sub-modules were examined using a linear heating and cooling cycle. Fracture was detected by acoustic emission and visually on both heating and cooling.
- Tests in the larger furnace showed that air flow did not impact the survival/failure rate.
- Additional tests conducted in a box furnace with air flow showed that all of the Slot Pattern #2 wafers and sub-modules tested could be cycled to 800ºC using heating and cooling rates of 10ºC/h without failure (see Figure 16-37).

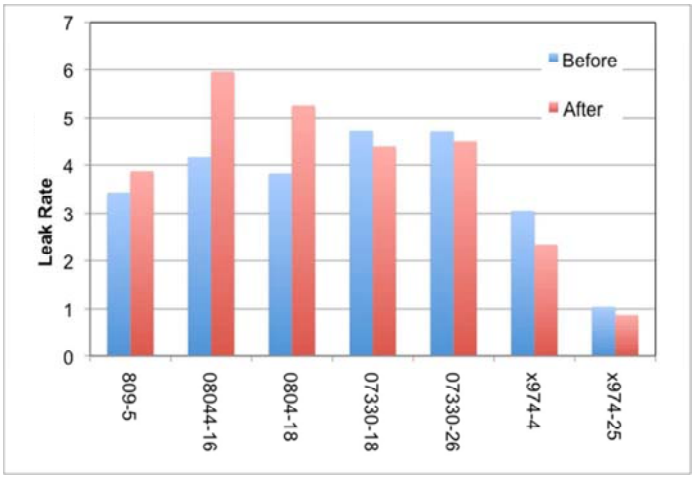

Figure 16-37. Leak rates of Slot Pattern #2 wafers before and after cycling in KBR2.

- Slot Pattern #1 wafers and sub-modules with both Slot Patterns #1 and #2 wafers were cycled in both the large box furnace and in the atmospheric test system using 10°C/h heating and cooling cycles. All wafers except one failed on cooling. Typical failures consisted of corner cracking starting at temperatures at or below 200°C.
- Standard wafers were tested at a heating rate of 30ºC/hr and a cooling rate of 5ºC/hr. No significant AE counts were detected throughout the cycle. All of the components survived, with no increases in leak rate. The data suggested that for temperatures below 300ºC, the critical rate for corner cracking lies between 5 and 10ºC/hr.

Ceramatec acquired an IR camera in order to do wafer thermal gradient testing. Tests were conducted to determine the radial thermal gradients required to cause corner failure of a wafer. A three-zone heater shown in Figure 16-38 was used to heat a wafer.

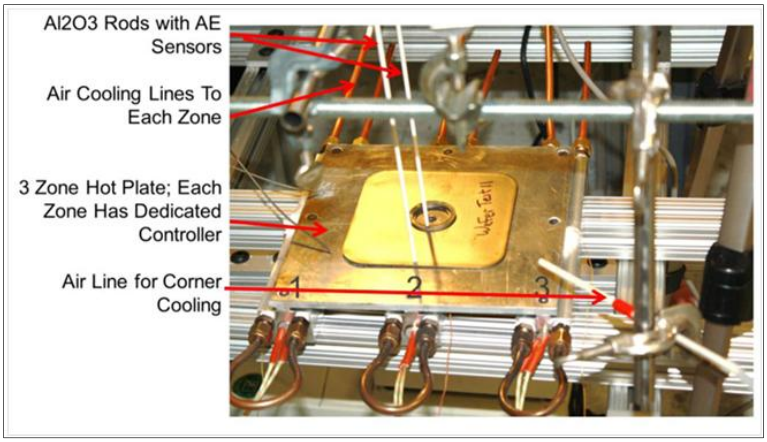

Figure 16-38. Three zone heating system used for wafer thermal gradient testing. The IR camera is located out of the field of view on the upper right side.

The 3-zone system provided independent temperature control of each zone for the application of front to back thermal gradients. Air cooling ports could rapidly cool each heat zone. The wafer was held at temperature, after which a small jet of air was directed toward one of the wafer corners. The temperatures along the wafer surface were recorded with the IR camera during the heatup and the subsequent air cooling process. The acoustic emission (AE)-vision system software acquired the thermal gradient images and data. The system recorded images with a firewire camera. Temperatures were recorded via two thermocouples. Acoustic emissions were detected from a probe attached to the wafer via a long alumina rod.

Dedicated software was developed to display each frame of an IR movie and extract the temperature profile along a specified line on the image (Figure 16-39).

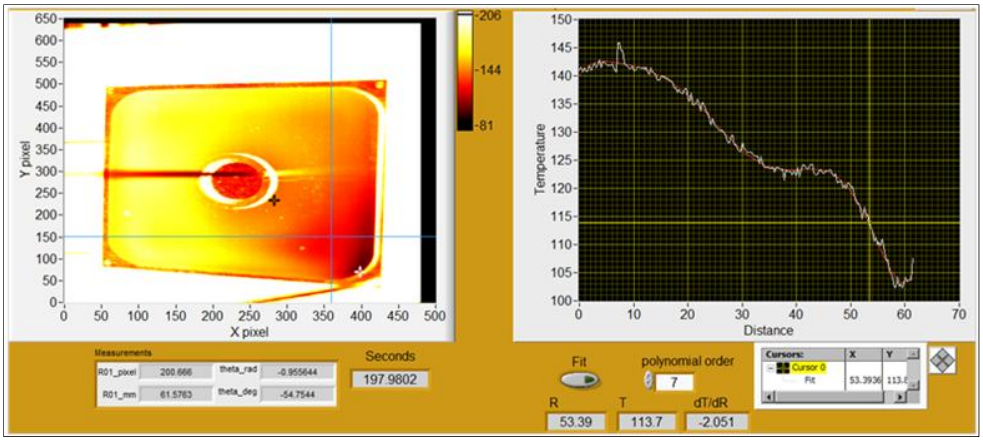

Figure 16-39. Screen shot of IR display software showing a single frame of IR movie on the left and temperature profile on the right. The profile is associated with the line formed by connecting the white and black cursors in the IR image frame. A polynomial fit to the profile allows the user to calculate the temperature gradient at any point along the temperature-distance curve.

Table 16-1 summarizes the data on a lot of standard wafers. All wafers, save one, failed. The one that did not fail saw the smallest temperature gradient. As can be seen in the table, all of the thermal gradients across the wafer were very high.

Table 16-1. Summary of critical thermal gradients required to cause corner cracking in standard wafers.

Test No.	Rate (°C/mm)	Failed (Y/N)	Comment
5	2.2	N	
11	3	Y	
16	3.6	Y	
17	2.9	Y	Failed during soak
18	3.3	Y	
19	3.8	Y	
21	2.3	Y	

One wafer failed during the high-temperature soak because it did not uniformly contact the heating plate, which caused significant temperature gradients during heating. Figure 16-40 demonstrates the three methods of data acquisition, infra-red (IR), firewire (visual) and acoustic emission (AE) for the wafer mentioned above. Note that the AE emissions occurred with a rapid temperature decrease. In a few instances, the cooling air was turned off shortly after the initial formation of the rim crack, which resulted in the formation of a radial crack.

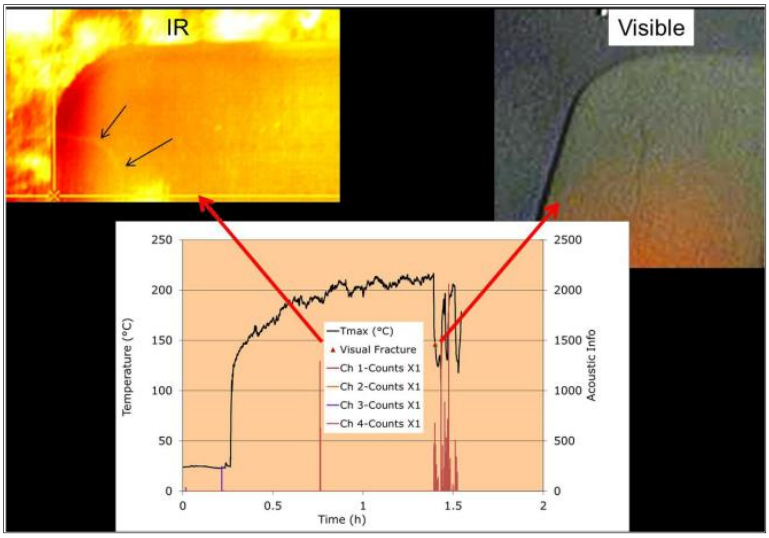

Figure 16-40. Comparison of visual and IR images and AE emissions during Wafer Test 17.

Strength of Alternative Wafer Geometries

ITM Oxygen wafers are fabricated with internal slots that allow the oxygen that permeates through the outer membrane skin to be transported to the central, open portion of the wafer for evacuation to downstream equipment. Ceramatec designed and produced wafers with two types of internal slots that differ mainly in the geometry of the slot pattern. Slot Pattern #2 wafers have slots that tend to allow the oxygen to flow more directly to the inner region of the wafer, while the slots in Slot Pattern #1 wafers cause the oxygen to flow in a more tortuous path. However, the Slot Pattern #2 wafers have a lower strength, as shown in Figure 16-41. The figure is a plot of the average stress applied at fracture for the two wafers types in a standard strength test. The Slot Pattern #1wafers show higher strength by about 10%.

Figure 16-41. Comparison of fracture loads determined from ring-on-ring tests of wafers made with Slot Patternss. 1 & 2.

Wafers of both types were thermally cycled, and leak rates were measured before and after the test. The Slot Pattern #1 wafers were shown with 95% confidence to be significantly less leaky.

Ceramatec applied a fundamental modeling approach to predict the failure probability of the two wafer types. The approach consists of a finite element analysis (FEA) to estimate the stresses in the wafer. The stresses and the Weibull moduli and were used in statistical calculations to estimate the Probability of Survival (Ps). Wafer strengths at failure were measured by using a standard ring-on-ring test (Figure 16-42).

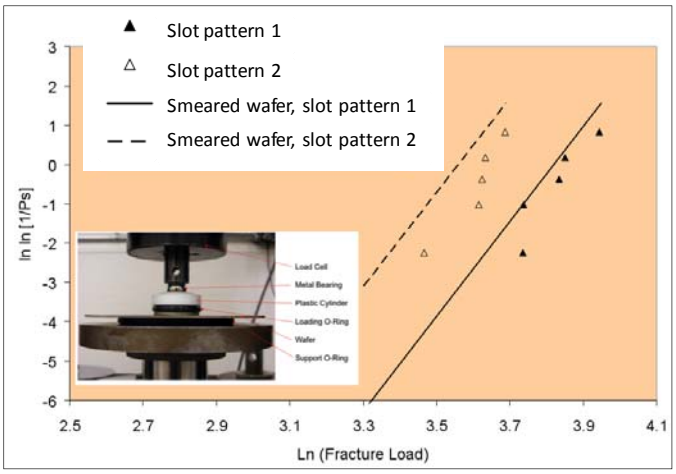

Figure 16-42. Comparison of predicted and experimental Weibull distributions of fracture load for wafer ring-on-ring testing for Slot Pattern 1 & 2 wafers.

The figure shows excellent agreement in both the slope and location of the predicted failure curve based on a Weibull distribution approach. Both the data and the prediction further indicated that the Slot Pattern #1 design is a stronger than the Slot Pattern #2 design.

Sintering Cycle Development

This study focused on the comparison of wafers sintered using a standard versus a shorter sintering schedule. Slot Pattern #1 standard wafers were sintered using either a standard or a shorter sintering cycle. Ring-on-ring testing was used to measure the critical fracture loads for both. After testing, rims were sectioned from the wafers for four-point flexure testing. To evaluate slow crack growth effects, sets of wafers from both standard and shorter wafer cycles were soaked in water for one week. Following exposure, ring-on-ring and rim flexure tests were conducted. As shown in Figure 16-43, the ring-on-ring and rim fracture strengths (loads) were

comparable for the as-sintered standard and short-cycle wafers, indicating that the accelerated shorter cycle does not adversely affect mechanical performance.

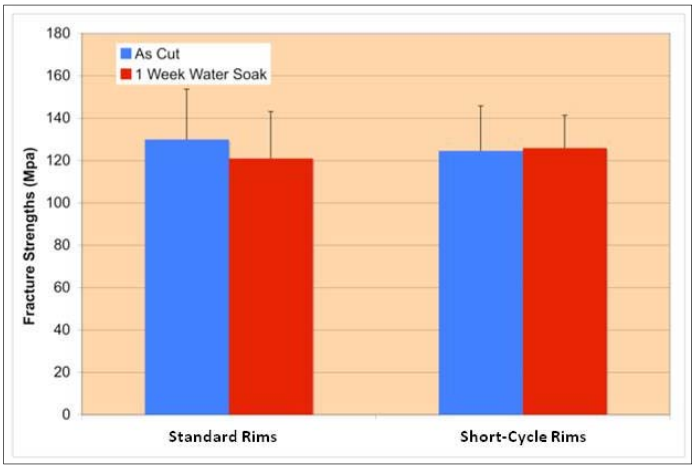

Figure 16-43. Comparison of rim fracture strengths for Slot Pattern #1wafers sintered using standard and shorter cycles.

While slow crack growth effects were found in the ring-on-ring tests, the extent of strength reduction was comparable for the standard and short-cycle wafers. No slow crack growth was indicated by the rim four-point fracture data. This suggests that the level of residual stress within the cut rims was insufficient to promote subcritical crack growth.

Wafer Joining

Testing was conducted to understand damage evolution in wafers subjected to the joining cycle. Four sets of stacked wafers were subjected to the joining cycle (Figure 16-44).

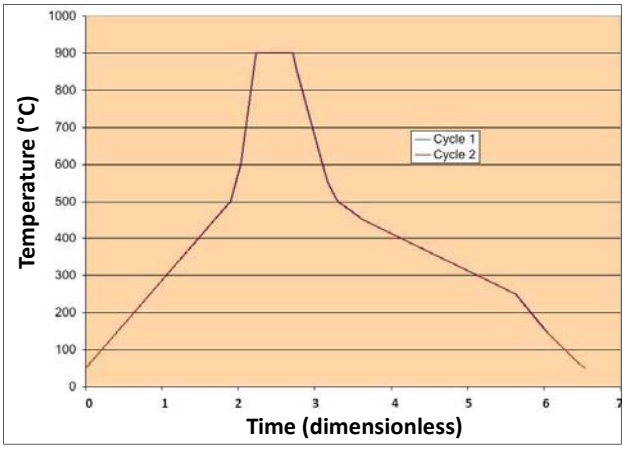

Figure 16-44. Joining cycle used to examine damage evolution in wafers.

Due to limitations of the furnace, the maximum temperature was limited to ~ 900°C. Although the modified cycle did not capture the portion of joining cycle above 900°C, it was felt that the time-temperature segments below 800°C were the primary contributors to the damage processes.

Four sets of stacked wafers were tested (see configuration in Figure 16-45).

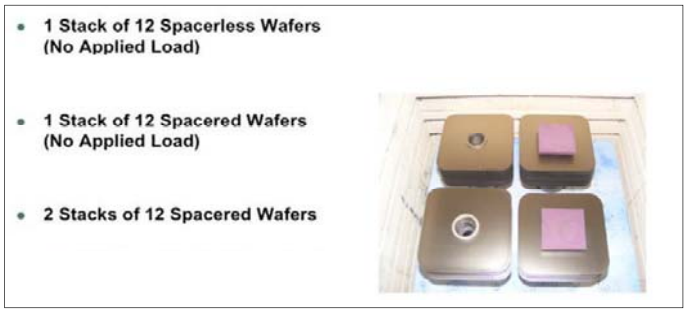

Figure 16-45. Test conditions for a series of thermal cycle tests involving the configuration of stacked wafers pictured on the right. Two stacks were loaded.

High air flow was maintained throughout the first cycle. Figure 16-46 summarize the results.

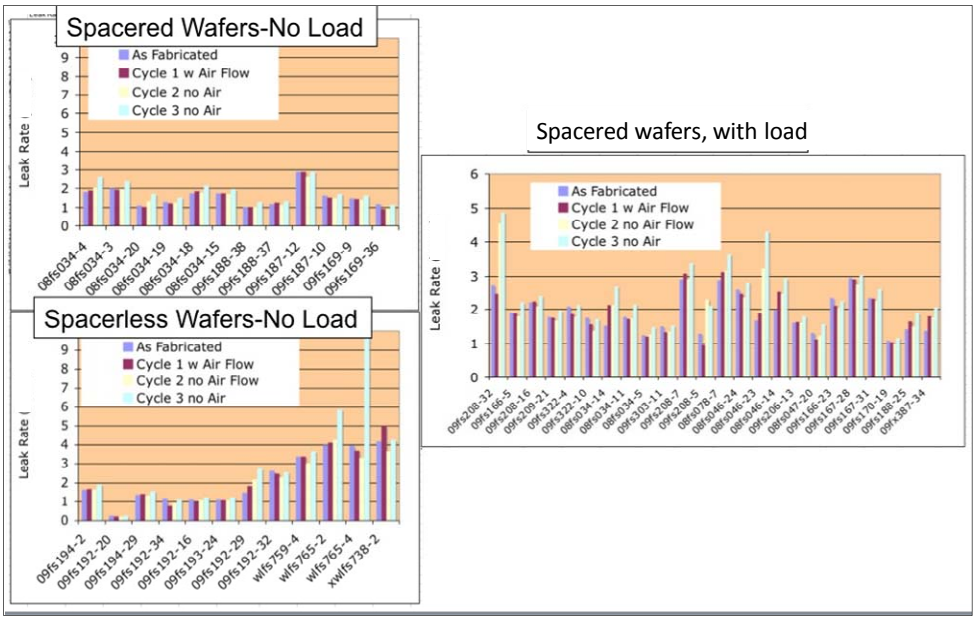

Figure 16-46. Leak rate data for wafer stacks as fabricated and following thermal cycle tests.

The leaks rates for all of the wafers did not change appreciably after the first cycle. The next two cycles were conducted without air flow; the leak rate increased for some of the wafers. The leak rate increases were most prevalent for the spacerless wafers with no load, followed by the

spacered wafers subjected to a load. Bubble tests showed the leak rate increases were due to either new defects occurring in the active area located somewhat away from the center hole (Figure 16-47) or radial cracks originating from the center hole (Figure 16-48).

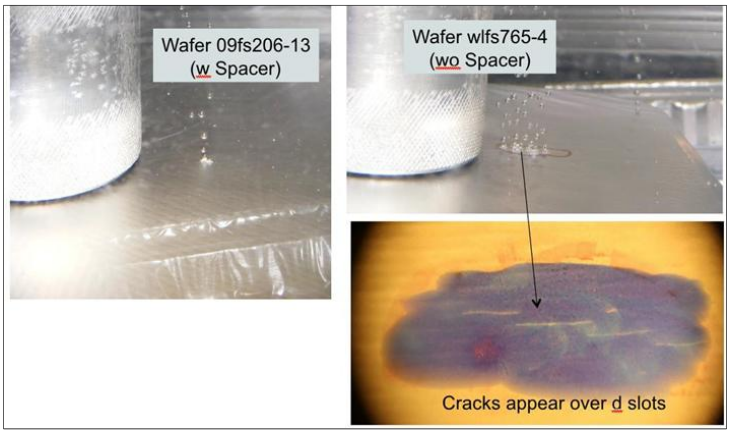

Figure 16-47. Bubble test results for two wafers showing new defects in active area.

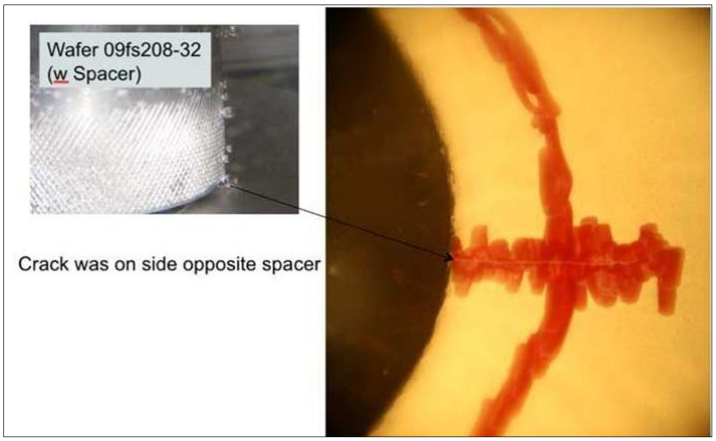

Figure 16-48. Bubble test results for wafer showing radial crack.

The atmospheric test system (ATS) was subsequently used to monitor acoustic activity in a spacerless wafer subjected to the thermal cycle (Figure 16-49).

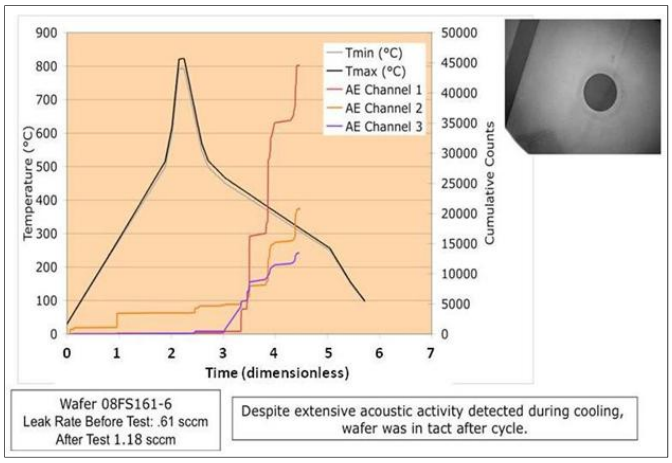

Figure 16-49. Acoustic emission data collected from standard spacerless wafer subjected to a thermal cycle.

Significant acoustic emission (10,000+ counts) was detected during cooling of the wafer below 500°C. In spite of the apparent damage, the wafer was intact after the cycle and exhibited an increase in leak rate from 0.61 to 1.18 sccm.

To further understand the evolution of the radial cracks, the same wafers were subjected to a different thermal cycle. Following the test, the wafer was reexamined. The crack extended by approximately 100%. Based on the acoustic emissions (AE) data, this growth likely occurred during heating at either 50 or 500°.

A second series of thermal cycling tests of wafer stacks was conducted to examine wafer reliability after repeated cycling. The configuration of the stacks was similar to the first test (Figure 16-45), except the stacks included a combination of Slot Pattern #1 and #2 wafers as shown in Figure 16-50. The test conditions differed from the previous test in that air flow was maintained for all cycles.

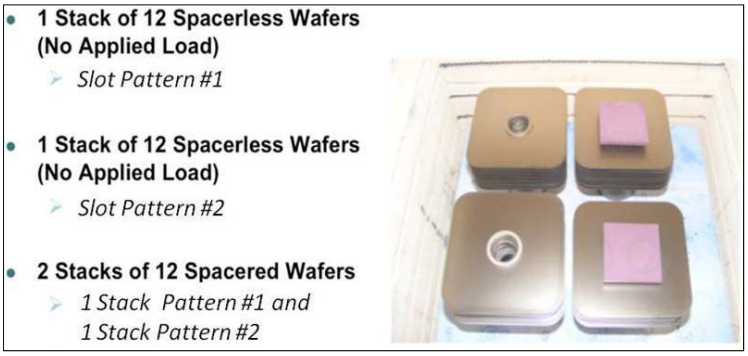

Figure 16-50. Test conditions for two thermal cycle tests involving stacked wafers.

The leak rates of two of the Slot Pattern #2 wafers increased by a factor of three. Changes in leak rates of all of the Slot Pattern #1 wafers were small. Both stacks of the spacered wafers showed increases in leak rate after the first and second cycles. However, the leak rates of all wafers remained modest.

Four cycles were performed in a repeat of this test with fresh wafers. The spacerless Slot Pattern #2 wafers (no load) exhibited the largest increases in leak rate, including one wafer that failed during the third cycle and a second wafer that developed a large defect in the active area after the fourth cycle (Figure 16-51).

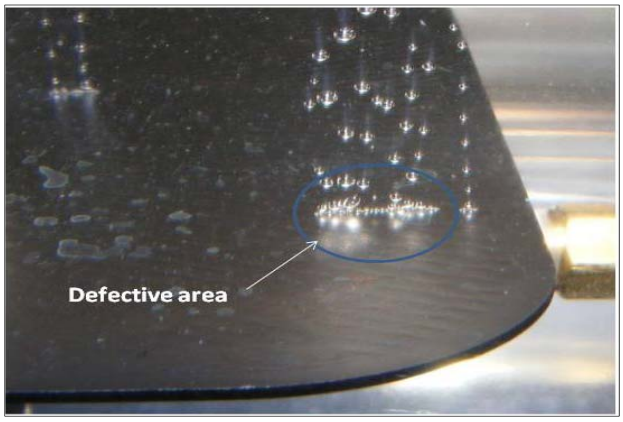

Figure 16-51. Bubble test of Slot Pattern #2 wafer after Cycle 4 showing a large defect in the active area.

Though not as severly as the spacerless Slot Pattern #2 wafers (no load), the leak rates of the loaded Slot Pattern #2 wafers with spacers also increased. Conversely, the Slot Pattern #1wafers showed no significant changes in leak. These results indicate that the Slot Pattern #1 wafers experience very minimal damage during thermal cycles, and that air flow does not seem to have a significant effect on the rate of damage evolution in the Slot Pattern #2 wafers.

Iso-controlled Cooling Studies of Module Components

To determine if air-cooled modules could be added to the ISTU vessel with iso-controlled cooled modules and then heated with iso-control, the differential expansion of a wafer rim versus a porous AP2K sample was measured using a dilatometer during iso-controlled heatup. A dilatometer bar was prepared by cutting a rectangular bar from a wafer rim and re-sintering. The bar was loaded into a dilatometer alongside a porous AP2K bar, and both bars were heated at

0.25°C/min using the iso-compositional protocol, starting with N_2 and transitioning to 100% air by 600°C. Figure 16-52 shows the differential expansion of the two bars.

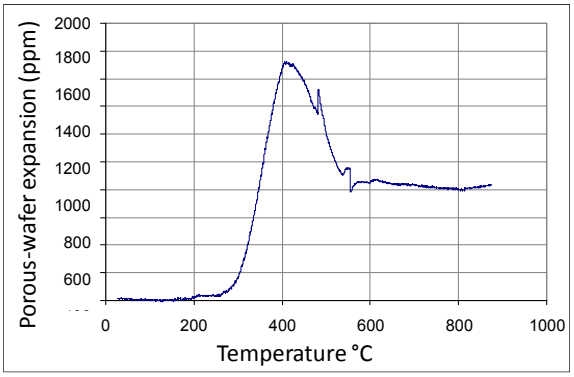

Figure 16-52. Expansion differential of air-cooled porous bar and an air-cooled wafer rim during iso-controlled heating at 0.25°C/min.

Above 300°C, the porous bar expands much faster than the rim, reaching a peak differential expansion of 1,700 ppm at 400°C. The discontinuity observed at 475°C is due to a switch from the low-range to the high-range air mass flow controller. Another discontinuity at 550°C could be due to the rim cracking, although no cracks were visible.

A porous AP2K bar and a rectangular bar cut from a wafer rim were cooled from elevated temperature in a dilatometer. The temperature profile mimicked the SEP temperature schedule. Below 370°C, the atmosphere was 100% nitrogen. To determine the effect of switching from nitrogen to low-purity nitrogen, the atmosphere was switched from nitrogen to air at 250°C, 150°C, 100°C and 50°C during cooling. Figure 16-53 shows the differential expansion between the porous bar and the rim.

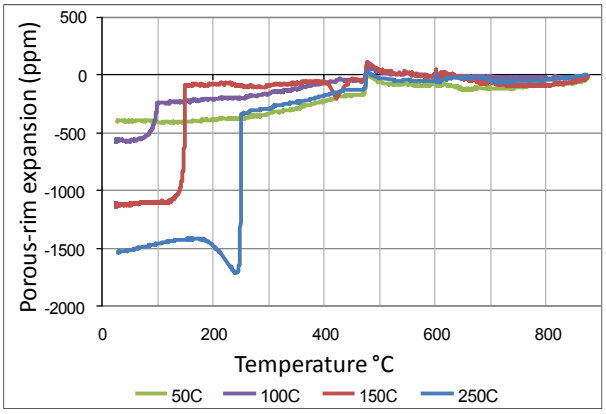

Figure 16-53. Differential expansion of a wafer rim and a porous bar during iso-controlled cooling.

Large differential expansions were observed when the atmosphere was switched at 250°C or 150°C. A smaller differential strain was observed when the atmosphere was switched at 100°C. No differential expansion was measured when the switch was made at 50°C. The data showed that a switch to air can be made at 50°C or at lower temperatures.

Air Products iso-compositionally heated an air-cooled dome and an air-cooled base piece bar, then cooled the parts under iso-conditions to determine if air-cooled modules could be heated under iso-control. After the iso-cycle, the parts were intact with no visible damage, as shown in Figure 16-54.

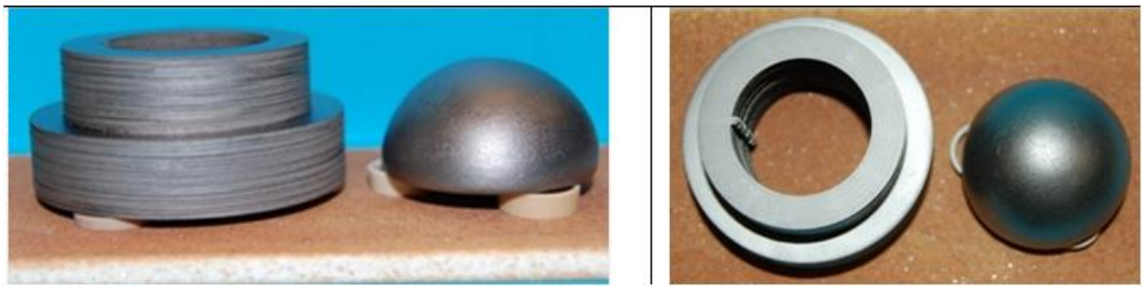

Figure 16-54. Dome and base piece after iso-cycle.

A set of nine air-cooled bend bars were iso-compositionally heated, followed by cooling under iso-control to determine if air-cooled modules could be heated under iso-control. After the iso-cycle, the bars were intact with no visible damage.

A set of air-cooled AP2K bend bars and biaxial flexure disks were heated and cooled under iso-control. A second set of bars and disks was air heated to elevated temperature and air cooled at 15ºC/hr for comparison. Strength testing showed that the parts that were heated and cooled under iso-conditions were much stronger than the as-sintered parts. Subsequent SAM analysis found that two of the air-cooled bars had cracks originating at their ends.

Additional dilatometry work was conducted to measure the expansion of an air-cooled wafer strip and rim during iso-compositional heating (Figure 16-55).

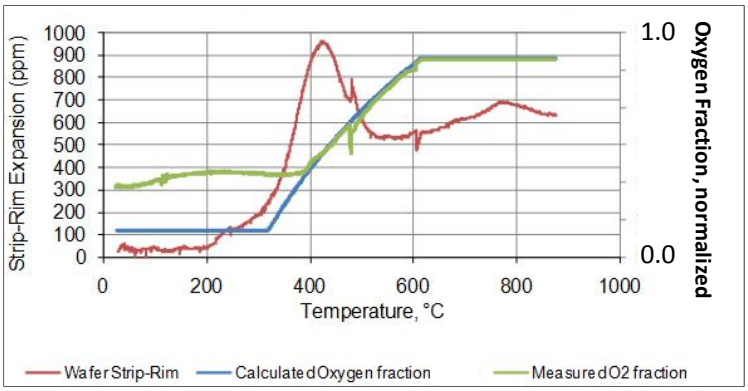

Figure 16-55. Differential expansion of an air-cooled wafer strip and an air-cooled wafer rim during heating in an atmosphere with an iso-compositional P_{O2} trajectory.

The low P_{O2} of the iso-heating atmosphere at low temperatures creates a driving force for oxygen to diffusion out of the air-cooled AP2K parts. The wafer strip, due to its smaller characteristic diffusion length, is able to diffuse a larger fraction of its oxygen than the rim, and hence the strip expands more than the rim at lower temperatures. The peak differential expansion reached 950 ppm. The relative P_{O2} as a function of temperature is given on the right-hand axis, both the measured P_{O2} downstream of the dilatometer, and the calculated value from the MFC inputs. The 600 ppm strain difference at the highest temperature indicates that the rim began with 600 ppm of chemical expansion strain relative to the wafer strip prior to heating. The rim must have locked in 600 ppm of strain relative to the active area when the parts were air cooled.

Evaluation of Stresses from P_{O2} Variations During Iso-cooling

Ceramatec used a 2D tube model (Figure 16-56) to examine the effect of errors in the P_{O2} values used for iso-controlled cooling.

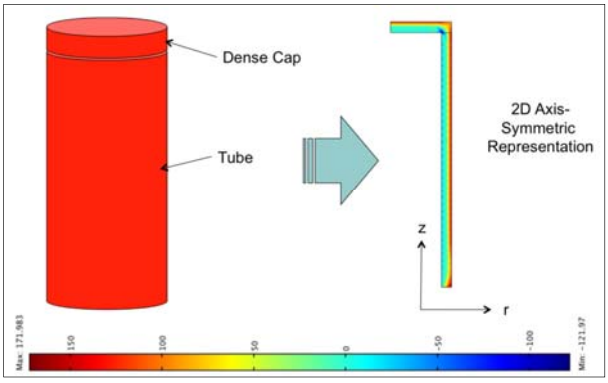

Figure 16-56. FEA model used to examine effects of iso-controlled cooling P_{O2} trajectory errors on stress.

Generally, the P_{O2} values should be chosen such that the vacancy fraction, X_v, is controlled on the air and permeate sides as the temperature undergoes a controlled ramp to ambient conditions. However, the desired P_{O2} values cannot always be maintained, which causes the equilibrium vacancy fraction, $X_{v,eq}$, to deviate from the desired set point. To determine how such variations influence stress generation, the FEA model was first used to estimate stresses for the boundary conditions for the idealized case. The principal stresses generated along the tube OD and ID are shown as functions of time in Figure 16-57.

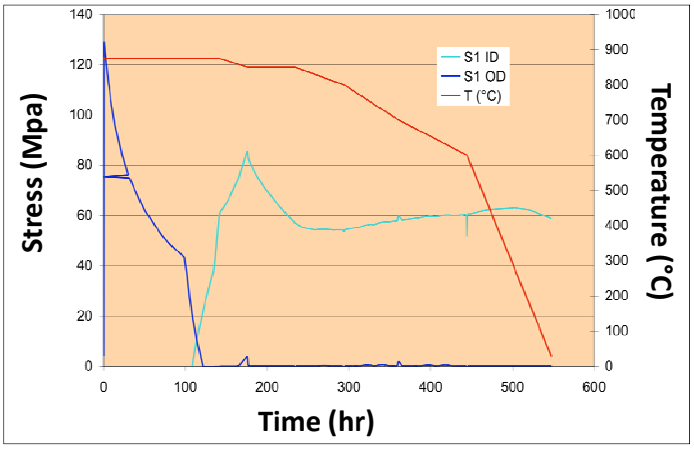

Figure 16-57. Principal stress values as a function of time at the ID and OD of the tube.

Over the 100-hr hold period at steady-state, the high stresses initially generated at the tube OD are quickly relaxed from 130 to 45 MPa. During depressurization, stress reversal causes the OD stresses to become compressive in nature and the ID stresses to become tensile. These ID stresses relaxed somewhat as the temperature is cooled to 600°C. Below 600°C, these stresses remain approximately constant at 60 MPa.

Five additional analyses were conducted in which the $X_{v,eq}$ values were allowed to deviate from the target value. The additional tensile stresses generated for these five cases were found to be proportional to the absolute value of ($X_{eq,permeate}$-$X_{eq,air}$) times a function that depends on temperature and the chemical expansion coefficients. Furthermore, when $X_{eq,air} > X_{eq,permeate}$, the tensile stresses were located along the tube ID, and when $X_{eq,air} < X_{eq,permeate}$, the tensile stresses were located along the tube OD. These stresses must be superimposed on the stresses obtained from the base line case. This lead to additional ID tensile stresses as the temperature approached 25°C.

Reliability Model of SEP Modules

Ceramatec developed a finite element analysis (FEA) model that includes the original end cap design, conical base piece design, wafers, spacers, ceramic joints and ceramic-to-metal seal to optimize the SEP heating and cooling schedule. The model includes the thermal history of the module during assembly to better approximate the initial stress and oxygen vacancy concentration state. Figure 16-58 shows the stress distribution in a five-wafer module after two operating cycles. Stresses throughout the body are mildly tensile.

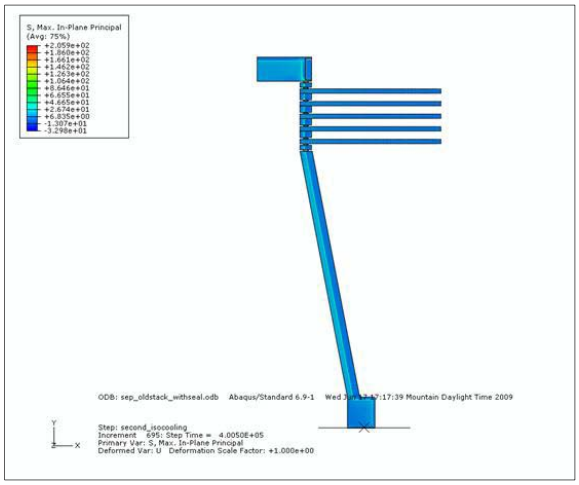

Figure 16-58. Five-wafer module geometry and stress distribution calculated with the FEA model.

Ceramatec used the model to predict the stresses in the modules in SEP Runs 5 and 13 to check the validity of the FEA model. These runs experienced a sudden temperature drop due to a heater trip. There was a catastrophic failure of the ceramic after the heater trip for Run 5, while it appeared that the heater trip in Run 13 had a lesser effect on the modules.

Stress levels were predicted at all the joints, the flat end cap and basepiece during the heater trip of Run 5 and the first and second heater trips of Run 13. The peak maximum principal stresses are plotted by location in the module in Figure 16-59. The location "Tape 0" is the joint at the top of the module between the end cap and the first spacer ring. The location "Tape 7" is at the bottom of the module between the base piece and the bottom spacer ring. As seen in Figure 16-59, the stress levels are highest in Run 5 and lowest in Run 13 during the first heater trip, which is consistent with the observed leak rate observation in the SEP operation.

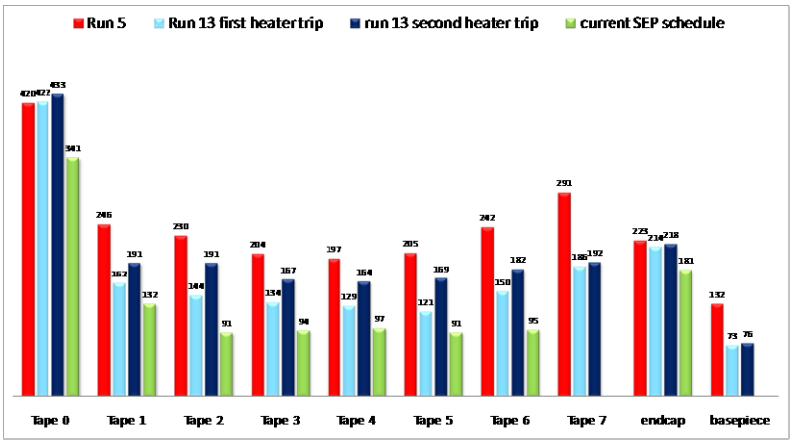

Figure 16-59. Predicted peak stress values at different locations in the modules used in SEP Runs 5 and 13.

The stress levels in the top joint ("tape 0") are very high and seem inconsistent with observation. The high stresses at that joint should have led to failure in all cases. It is likely that the flat end caps used in these modules were damaged previously, which would have released the stresses in the top joint. This was partially verified, as cracks were found in the end caps and near the top joint after the two trials. The high stress expected in the top joint is an artifact of the flat end cap design (since redesigned).

Evaluation of Critical Temperature Gradients during Module Heating

The temperature-time data generated in SEP tests were reviewed to define critical temperatures at which wafers failed on heating. As shown in Figure 16-60, failure was indicated by a sudden increase in the internal temperature (T_{int}) with respect to the flow duct temperature (T_{ext}).

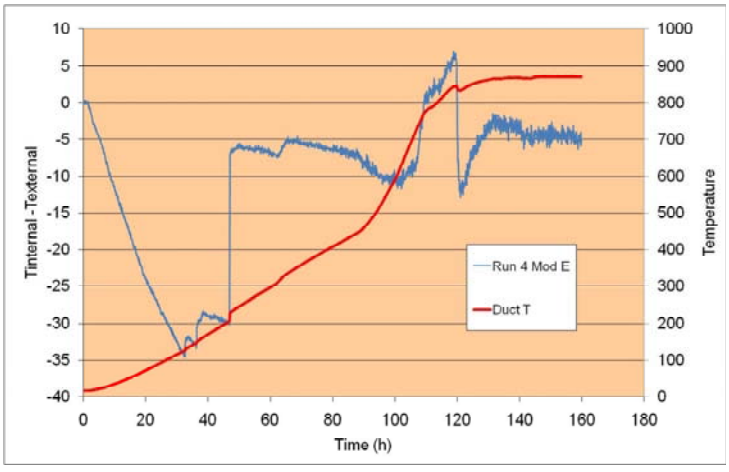

Figure 16-60. Temperature-time data obtained for SEP Run 4 showing sudden increase in internal temperature.

Post-test examinations of several of the wafer modules revealed long radial cracks in one or more of the wafers located at the bottom of the stack.

These data, which are also plotted in Figure 16-61, indicate that the allowable ΔT at which failure occurred increased with increasing temperature. Previous temperature-time data reported for a single wafer and wafer stacks cycled in the atmospheric test system (ATS), are included in the figure for purposes of comparison. The ΔT versus T trends are quite similar. These results show that radial gradients across the wafer must be minimized particularly during the initial stages of heat-up.

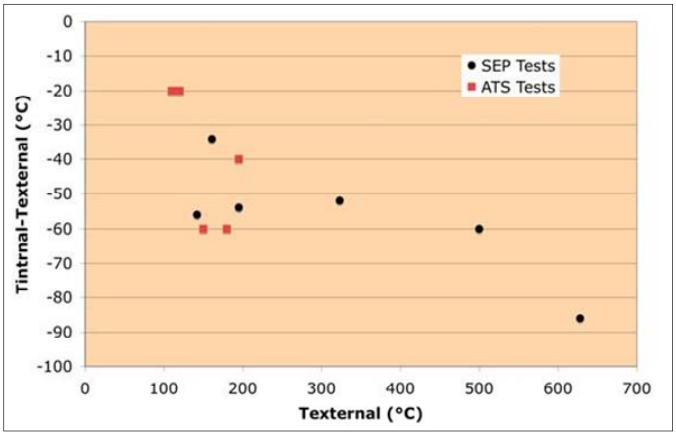

Figure 16-61. Critical values of ΔT (internal – external) measured as a function of temperature in SEP and ATS tests. Temperature-time data obtained for SEP Run 4 showing sudden increase in internal temperature.

Reliability during ISTU Operation

Ceramatec applied the FEA model to the expected module geometry to be used in the Intermediate-Scale Test Unit (ISTU) and used it to evaluate the stress generated during an emergency shutdown. The module geometry is shown in Figure 16-62.

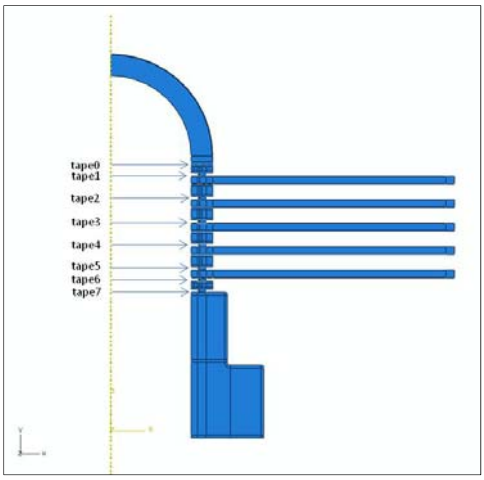

Figure 16-62. A 5-wafer module simulated with the FEA model.

In the emergency scenario, the module is assumed to be operating at steady state under full driving force conditions when an event occurs to necessitate a complete shutdown of operation. The control system is assumed to act in such a way as to isolate the ISTU membrane vessel from flow and to close the permeate section of the piping so that oxygen builds up in the permeate system. The modules continue to flux until the partial pressures of oxygen on the two sides of the membranes equilibrate. This scenario is termed the "standby" scenario. The entire process lasts approximately 15 seconds. The results from the stress calculations are summarized in Figure 16-63. The calculated stresses generated by the standard SEP cooling schedule are also listed for reference.

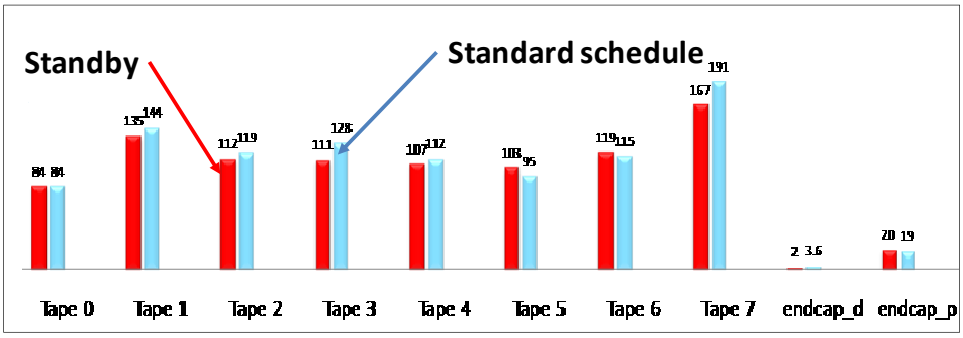

Figure 16-63. Predicted peak stress values (red bars) at different locations of the 5-wafer module shown in Figure 16-62after standby scenario. Stresses predicted for the standard SEP cooling schedule (blue bars) are plotted for reference.

The highest stresses are developed in the ceramic-to-ceramic joints. Base piece and wafer stresses are low and are not plotted. Two locations in the end cap also have low stress as shown. The chart shows that the "Standby" plan is reasonable.

Ceramatec extended the calculations. Heat was assumed to conduct through the base of the module into the permeate piping network over a period of minutes to hours. A temperature gradient develops along the vertical axis of the module that can lead to stresses caused by differential thermal and chemical expansion. The resulting calculated temperature gradient within the module is shown in Figure 16-64.

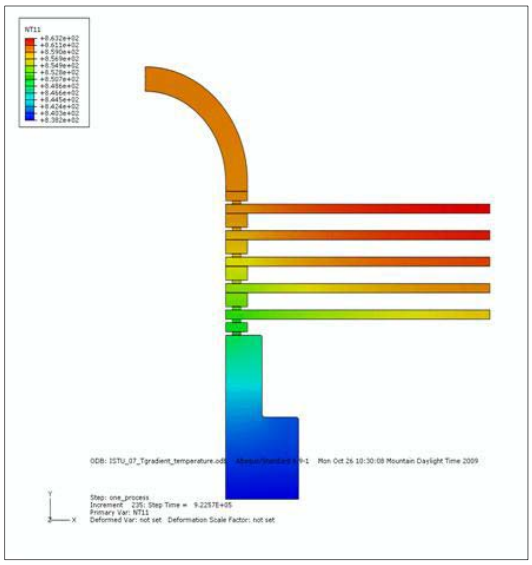

Figure 16-64. Temperature profile in the module based heat flow through the base. The temperature differential is ~25°C.

The highest maximum principal stress occurs at the joint between wafers. Figure 16-65 plots the maximum principal stress profiles at the "Tape 7" joint (see Figure 16-62) in the original simulation and the heat flow simulation. The stress associated with the temperature gradient increased by ~20%.

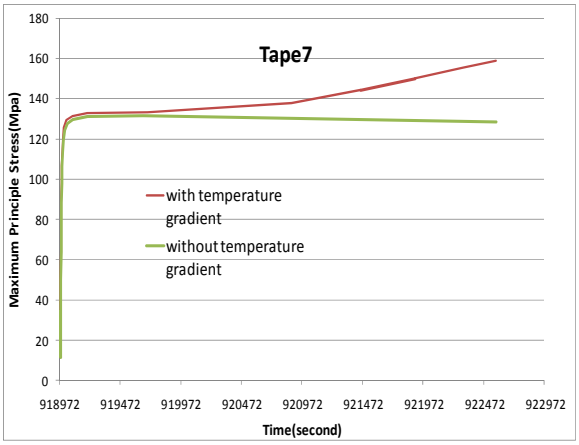

Figure 16-65. Maximum principal stress profiles with time at a joint ("Tape 7") in the module following a "standby" condition with and without heat loss.

Auto Shutoff Valve (ASOV) Reliability

Testing of ASOV assemblies was conducted. Five sample ASOVs (EFV5-1A, -1B,-1C, -1D, and -1E), were tested in a heated pressure vessel and brought to operating temperature and 1 atm total pressure under flowing air. A samples were connected to a downstream piping network with a vent, vent valve, and a branched leg with a flow meter that exhausted to a captured vent.

Air flow was increased across EFV5-1A until the valve sustained a ΔP of ~0.25 psi. After 150 hours, the flow was increased until the sample tripped at <1 psi. The feed pressure was ramped up to measure the leak through the sample. The leak rate was <50 sccm at a feed pressure of 163 psia. There was no measureable leakage after four hours.

Sample EFV5-1E was held in an air flow for 17 hours at operating temperature and 1 atm pressure. The flow was increased until the sample tripped at ~1 psi.. At the 2.25 hour point after the pressure was ramped up, the leak rate was <100 sccm. After four hours, the leak rate was <50 sccm. There was no measureable leakage after 30 hours.

Sample EFV5-1C was trip-tested after maintaining 90 hours of steady air flow at operating temperature and pressure. The air flow was increased until the sample tripped at <1 psi. After 67 hours, the leak rate was <100 sccm. After an additional 28 hours, the leak rate was 65.3 sccm.

The pressure vessel was de-pressurized and put through two thermal cycles. After the first cycle, the pressure was ramped to 200 psig to check the leak rate of the tripped samples. The EFV5-1A & E leak rates were 0.0 sccm; the EFV5-1C leak rate was 44.2 sccm.

After the second thermal cycle, air flow was established across EFV5-1B and EFV5-1D and held for 15 hours. The air flow across EFV5-1B was increased until it tripped at ~1 psi. The vent valve was closed as the vessel pressure was ramped up to 200 psig. The leak rate was 60 sccm after 15 minutes at a pressure of 100 psig. There was no measureable leakage after one hour at 200 psig. The leak rate on all the tripped units was checked again. The leak rate of EFV5-1A, B, & E was 0.0 sccm. The leak rate of EFV5-1C was 32.0 sccm.

The vent valve was closed as the reactor pressure was ramped up. The leak rate of EFV5-1D was 100 sccm after 20 minutes at a reactor pressure of 157 psig, and 50 sccm after 25 minutes at a reactor pressure of 200 psig. There was no measureable leakage after eight hours, 20 minutes. The leak rate on all the tripped units was checked again. The leak rates were all 0.0 sccm except EFV5-1C, which had a leak rate of 16.2 sccm.

A further test was conducted in XVU1, where ASOV sample ASO5-2A was installed. Flow was initiated to the system, and the sample was heated to operating temperature at 1 atm pressure. The sample valve was opened, and flow was established across the assembly to generate the design pressure drop. Flow was increased across ASO5-2A until valve closure was observed within 0.3% of the design trip point. The permeate flow valve was opened, the feed air pressure was ramped up to 200 psig, and the permeate vent valve was closed. The leak rate through the ASO was zero. After ~15 hours, the leak rate had not changed. The system pressure was reduced to 10 psig, and the sample was held for an additional 440 h without observable leakage.

16.3 Process Engineering and Economic Evaluation

Power Generation with Carbon Capture and Storage

Oxy-Combustion

Air Products and EPRI selected the basis for a performance and cost study of a coal-based Greenfield oxyfuel combustion power plant with carbon capture and storage (CCS). The study was based on a boiler operating with recirculated flue-gases to which oxygen has been added. Three cases were evaluated:

1. A standalone cryogenic ASU for oxygen supply.
2. A standalone ITM system for oxygen supply.

3. An integrated ITM system for oxygen supply where the ITM Oxygen system was heat-integrated with the boiler system.

Illinois No. 6 coal was specified. A critical issue was the assumed air leakage into the boiler and other subsystems. A previous DOE study (DOE/NETL-2007/1291) assumed a 2% air infiltration for the overall plant, which is an aggressive assumption reflecting very mature oxygen combustion technology in a new plant. The study used a higher level of air infiltration, consistent with earlier implementations of oxycombustion. Two preliminary design cases, A and B, were considered. Case A assumed a higher level of air infiltration at 23% excess air at the exit of the economizer. Two variants were evaluated: 17% excess oxygen at the burner, and 3.2% (mol., dry basis) oxygen at the burner exit. Case B assumed a lower level of air infiltration, i.e., 19% excess air at the exit of the economizer, with the same two variants for oxygen level at the burner as proposed in Case A. The assumptions are specific to oxycombustion, for which less excess oxygen may be required to achieve complete combustion.

After consultation with DOE-NETL and Air Products, EPRI subsequently modified the oxy-combustion model and added a two-step flash and auto-refrigeration module to purify the CO_2 flue gas to nominally 90% recovery and 95% purity.

Case 1: Standalone Cryogenic ASU for Oxygen Supply

A preliminary set of heat and mass balances (HMBs) and a process flow diagram based on cryogenic oxygen supply were completed. The predicted oxygen requirement for the 800 MW (gross) oxycombustion plant was 1.24 million lb/hr at 100°F and 23.2 psia. The net output power was 563 MW and the net plant efficiency was 29.6% (HHV). The net plant heat rate was 11,536 Btu/kWh (HHV).

Case 2: A Standalone ITM System for Oxygen Supply

In Case 2, the oxygen from the ITM system is required at 100^{o}F, 17.1 psia, and 99.5 % purity

Case 3: An Integrated ITM system for Oxygen Supply

In Case 3, the oxygen from the ITM system is required at 1000^{o}F, 17.1 psia, and 99.5 % purity. The model was run and with the addition of flue gas from the ITM O_2 unit into the CO_2 purification unit.

Results

EPRI sent a draft technical report, "*Plant-Wide Performance and Cost Analysis of Ion Transport Membrane Based Oxy-Combustion Power Generation Systems*," to Air Products. This work was a collaboration between EPRI, DOE and Air Products. EPRI prepared the cost analyses using the DOE template to calculate the cost of electricity and conducted numerous sensitivity studies, included sensitivities to the cost of natural gas and coal over the life of the plant.

The report was divided into the following sections:

- Introduction to Oxycombustion
- Review and update on existing and proposed Oxycombustion projects
- Lessons learned with operating Oxycombustion systems
- Potential considerations when integrating an ITM Oxygen system with Oxycombustion

An abstract was submitted to and accepted by the selection committee of the 2nd International Oxyfuel Combustion Conference, IEAGHG Programme, Yeppoon, Australia, 12-16 Sept 2011. The title was "*Integration of Ion Transport Membrane Technology with Oxy-combustion Power Generation Systems*." The authors were Robert Steele from EPRI, and Phillip Armstrong and John Repasky from Air Products.

Preliminary results included:

- A preliminary cost analyses for a cryogenic ASU with flue gas purification and 73% CO_2 capture.
- An indirect oxy-fired ITM Oxygen cycle was required to achieve 90% CO_2 capture. This also showed a reduction in unit capital (CAPEX per net MW) and COE relative to the ASU case.
- COE comparison results showed modest sensitivity to energy pricing.

The remainder of this work was completed outside of this Cooperative Agreement.

Integrated Gasification Combined Cycle (IGCC) with Carbon Capture

Background

Air Products and EPRI initiated an IGCC study to compare an ASU oxygen supply with an ITM oxygen supply. A generic IGCC system schematic is shown in Figure 16-66.

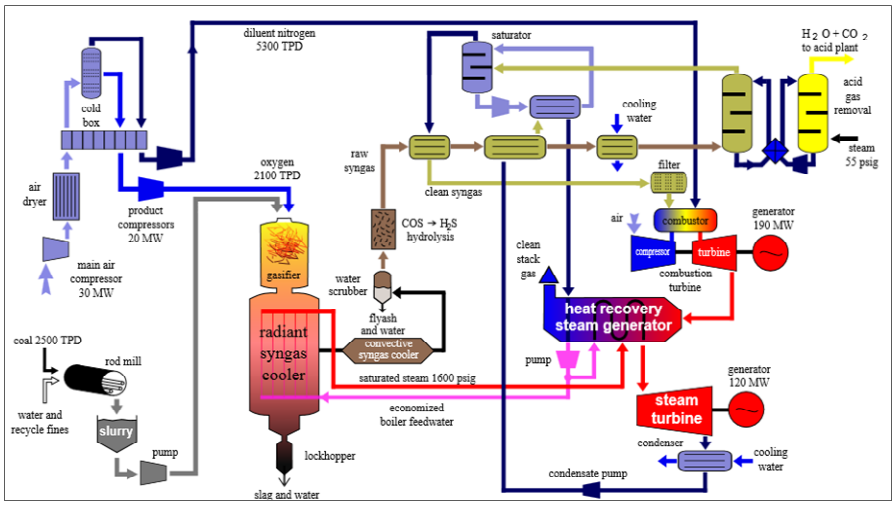

Figure 16-66. Generic IGCC system.

The IGCC configuration included a cryogenic ASU, F-class gas turbine with partial integration, water gas shift, and a two-stage Selexol unit for CO_2 purification. The model included gas-side block flow diagrams (BFD) and heat and material balances (HMB). Preliminary estimates were determined for the auxiliary power requirements and process cooling loads, including the cryogenic ASU. Siemens confirmed the GT assumptions, including integration with the ASU.

Advanced gas turbines such as a G-class, H-class or J-class were further evaluated; EPRI recommended that the Siemens 60 Hz H-class be considered as a first/future choice. The purity specification (by volume) for the CO_2 from the combined acid gas removal (AGR) system streams was:

- CO_2 at 95% dry
- Sulfur at 100 ppmv dry
- CO <2500 ppmv dry
- Minimal H_2

The following parameters were also set:

- Inter-cooling and after-cooling for gas compressors (MAC, N_2, CO_2, tail gas).
- Location of steam injection into the water gas shift unit.
- Location of heat utilization in the low temperature gas cooler.
- Temperature and aux load requirement for the Selexol unit.
- Temperature control of the Claus unit.
- Additional details of the miscellaneous auxiliary loads

Results

The preliminary results were presented at an Air Products-DOE-EPRI meeting on May 4, 2010. The detailed results were published in the paper "*Ceramic and Coal: ITM Oxygen for Power Generation with Reduced CO_2 Emissions, Detailed Engineering Study Results*" authored by John M. Repasky, VanEric E. Stein, Phillip A. Armstrong, Merrill S. Quintrell, Andrew Maxson, and L. Michael Bartone. The paper was presented at the AIChE Spring National Meeting Topical 5: Emerging Technologies in Clean Energy for the Twenty-First Century Session on Carbon Capture, Storage and Utilization Routes to Produce Chemicals, San Antonio, TX April 28–May 2, 2013. The Integrated Gasification Combined Cycle (IGCC) Power Generation with Carbon Capture and ITM Oxygen (case IGCC-2A) study showed a 1.8 percentage point efficiency advantage, a 12% lower specific capital cost, and a 10% reduction in levelized cost of electricity relative to the cryogenic ASU case. The ITM Oxygen technology case also showed a significant increase in net power output, raising the facility power production levels back to the nominal IGCC rating without carbon capture. The remainder of this work was completed outside this Cooperative Agreement.

16.4 Contamination Mitigation Systems

Chromium

Background

Gas-phase chromium species are known to form over chromium-scale-forming metals in the presence of air according to the reaction:

$$Cr_2O_3(s) + 3/2O_2(g) \rightarrow 2CrO_3(g)$$

Previous experiments indicated that high-nickel-content metals form chromia scales that evolve gas-phase chromium species, which deposit on the ITM material and act to retard the oxygen flux. A good approach to solving this problem is to reduce the amount of hot metal that is exposed to flowing air and to remove any gas-phase chromium below the level at which it reacts with the ITM material. Air Products developed suitable materials to act as high-temperature getters to remove chromium species.

Equipment and Test Method

Tests were conducted in the Vacuum Permeate Short Loop Test Rig (VP-SLTR) which consists of a compressed air source, air dryer, air flow metering system, heated pressure vessel, back-

pressure regulator, and vent. Pressurized air is passed into the pressure vessel through a preheater/saturator section to bring the air to operating conditions and saturate it with chromium via Incoloy 800H tubing. The chromium-saturated air passes through the getter sample. A sample of ITM ceramic located downstream of the getter bed serves as a last trap for any chromium species that bypass the getter or that are not taken up by the getter. The tests were typically run for 30 days. The data were compared to a predicted profile based on a mass transfer model. There is some uncertainty in the predicted uptake, as it is based on an estimate of the CrO_3 vapor pressure at run conditions; the actual feed concentration is not known.

Results

Chromium Getter

Experiments were performed to measure the effect of on-stream time on the axial Cr uptake profile with candidate getter materials. The chromium axial profiles and overall content of five samples were measured. Table 16-2 lists the samples and the duration of the experiments.

Table 16-2. Getter sample and time on stream.

Sample ID	Time on stream (days)
Cr getter 3 – 03/11/09	31.1
Cr getter 1 – 06/06/09	30.7
Cr getter 4 – 06/06/09	13.9
Cr getter 2 – 08/19/09	13.8
Cr getter 3 – 08/19/09	6.1

Figure 16-67 shows the measured axial Cr profiles.

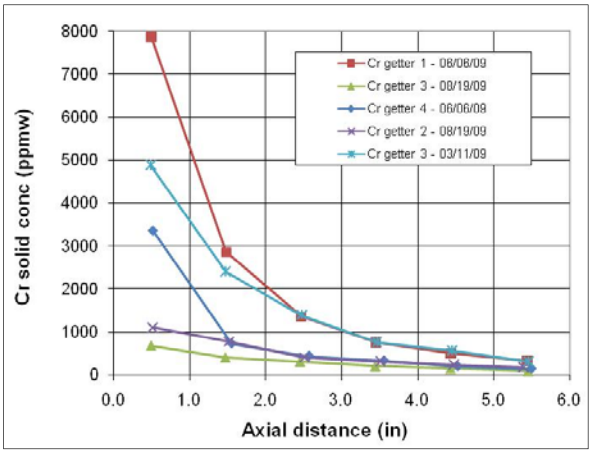

Figure 16-67. Effect of time on stream for Cr getters – axial Cr profiles.

The profiles are generally consistent with expectations, although not as steep as a simple mass transfer model predicted. Figure 16-68 shows the total Cr uptake on each sample as a function of on-stream time. No tail-off in capacity was evident with increasing time on stream.

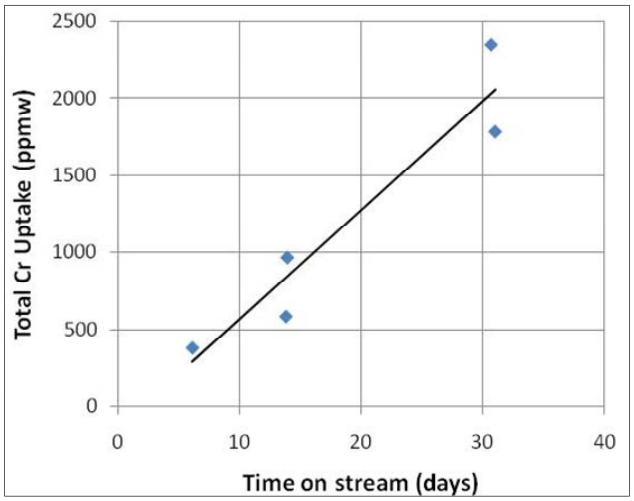

Figure 16-68. Effect of time on stream for Cr getters – total Cr uptake vs. time.

Superficial gas velocities were varied to determine the effect on chromium uptake. Figure 16-69 compares the post-run axial Cr distribution at two velocities.

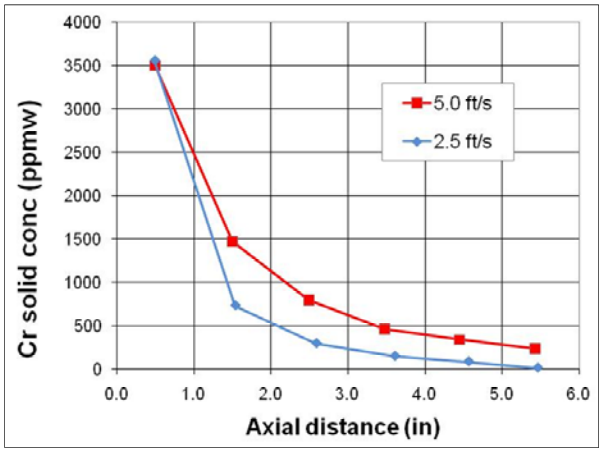

Figure 16-69. Effect of superficial velocity on Cr uptake profile.

As expected, the Cr uptake gradient was steeper for the lower velocity. At the lower velocity, the measured Cr concentration at the end of the sample was very low. Examination of the ITM ceramic witness pieces by scanning electron microscopy – energy dispersive X-ray spectroscopy

(SEM-EDS) showed extensive coverage by a chromium-containing species for the 5.0 ft/s run, but no Cr was detected on the surface of the witness piece for the 2.5 ft/s run.

Comparisons between vendor-supplied and Air Products-produced getters were conducted to assess compositional differences and production methods. Figure 16-70 compares the axial Cr uptake profile obtained for two vendor-supplied samples with profiles obtained from samples produced by Air Products.

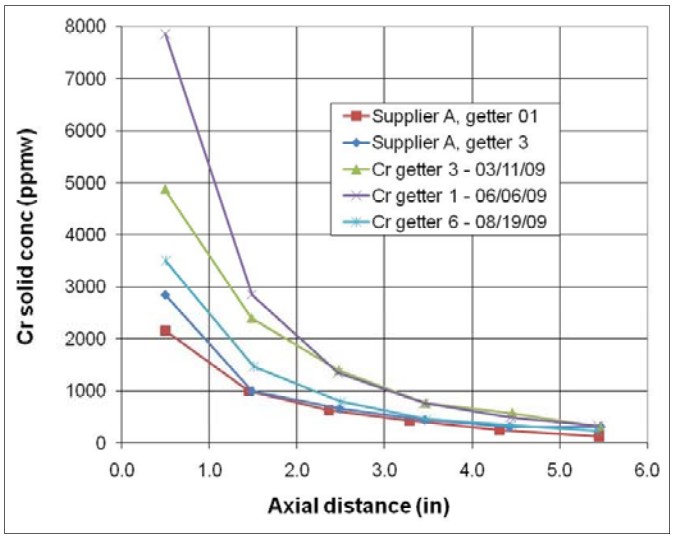

Figure 16-70. Comparison of Cr uptake performance of vendor-supplied and Air Products-produced getter samples.

There was variability in the performance of the Air Products samples notably in the absolute level of the Cr uptake. One possibility reason for the variability is that the source of the chromium is changing in composition with time and thereby producing variable levels of volatile chromium species.

The effects of source variability was mitigated to a large extent by normalizing the concentration gradient where the normalized Cr concentration is the measured Cr concentration divided by the overall average Cr concentration in the entire getter sample. Figure 16-71 compares the normalized Cr concentration gradients of the samples in Figure 16-70.

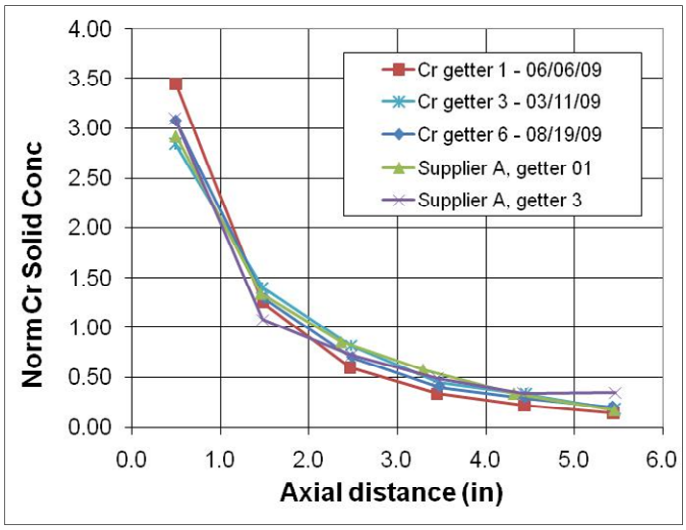

Figure 16-71. Normalized Cr uptake performance of vendor-supplied and Air Products-supplied getter samples.

The data is much more consistent and shows that the vendor-supplied samples performed similarly to the Air Products samples. All further work used the normalized Cr gradient for comparison purposes.

Two banks of getter in series with a gap of a few inches between them were used in SEP Run #19. Post-run SEM analysis of the modules showed no Cr-containing phase on the membrane surface. The ICP-AES results from the SEP Run #19 samples are shown in Figure 16-72.

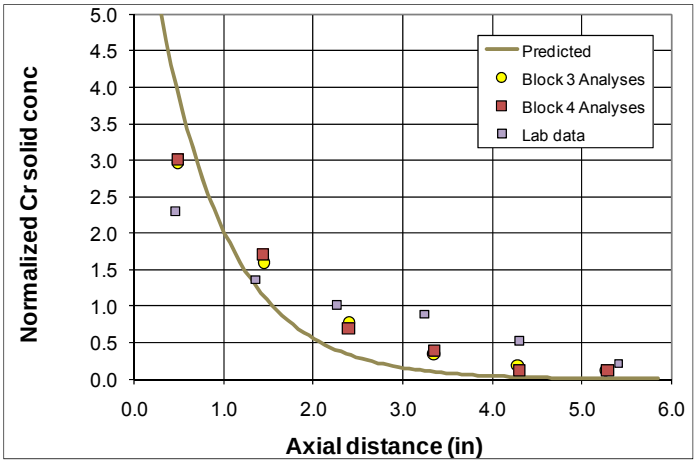

Figure 16-72. Axial Cr profiles from SEP Run #19 and lab getter tests.

The normalized Cr profile for the upstream bank was compared with a theoretical curve and lab data obtained from a sample from the same getter batch. The results were consistent. The SEP

feed concentration of Cr, as back-calculated from the loading on the getter, was roughly an order of magnitude lower than the Cr-saturated stream used in the lab tests. Figure 16-73 plots the Cr profile across both getter banks during Run #19.

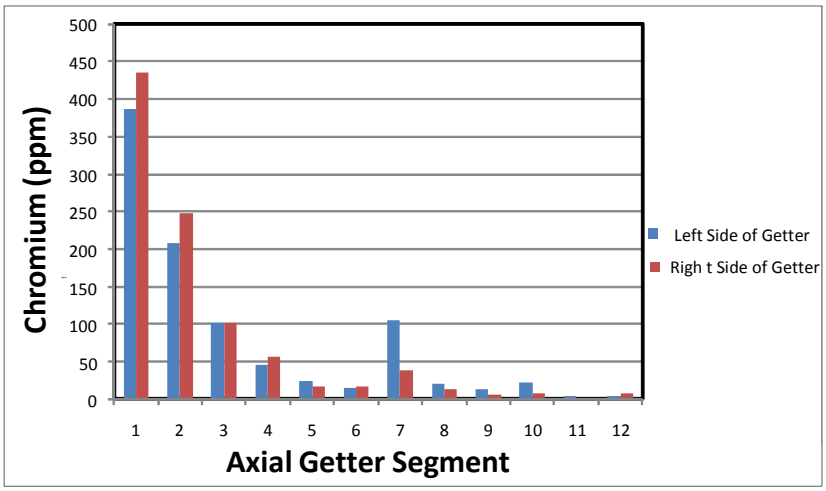

Figure 16-73. Cr analyses for axial getter segments through both banks on the left and right sides of the getter. Segments 1-6 are in Bank #1 and 7-12 are in Bank #2.

The Cr loading on the upstream side of the second bank (Segment 7) increased. The primary source of this Cr was not bypassing of the first bank; the increase was due to Cr evolution from two thermocouples situated in the flow path between the two banks.

The predicted values in the above graphs were based on a simple mass transfer model; a more detailed calculation method was subsequently developed. Data showed the rate of reaction of $CrO_3(g)$ with the getter followed a function of form $Sc_{gp}c_{sp}^{n}$, where S is a rate constant, c_{gp} is the concentration of CrO_3 in the gas phase, c_{sp} is the solid-state loading of Cr, and n is an exponent. This function was incorporated into an Excel model (Table 16-3).

Table 16-3. Equations used in the revised getter model.

	In the gas phase	On the Solid
Gas-phase diffusion limited	Equation (1) $\Delta c_{gp} = \left(c^* - c_i\right)\left[1 - \exp\left(kA\Delta l / V_S\right)\right]$	Equation (2) $\Delta c_{sp} = \frac{142\Delta c_{gp} F_{ch}\Delta t}{m_{ch}\Delta l}$
Solid-state reaction	Equation (3) $\Delta c_{gp} = \frac{m_{ch}\Delta l \Delta c_{sp}}{142 F_{ch}\Delta t}$	Equation (4) $\Delta c_{sp} = \frac{S c_{gp} c_{sp}^n \Delta t}{V_S}$

Where:

Δc_{gp} is the change in the gas phase concentration of CrO_3, over a distance Δl and a time Δt.

Δc_{sp} is the change in the average solid phase loading of Cr, for a given length of getter Δl over a time Δt.

c* is the concentration of CrO_3(g) in equilibrium with $MgCrO_4$(s) at process conditions

c_i is the inlet concentration of CrO3(g), entering a length of getter channel Δl.

k is the laminar mass transfer coefficient, taken as 2.018 cm/s.

A is the area per unit volume in the getter, in cm^2/cm^3.

V_S is the superficial velocity, in/s.

142 is a conversion factor.

Note: F_{ch} is the flow through one flow channel through the getter, in gmol/s, calculated as $d_H^2(2.54V_S/\varepsilon)/22400$. d_H is the hydraulic diameter of a channel and ε is the fraction of open channel area.

m_{ch} is the mass of solid in one flow channel, as calculated from the hydraulic diameter, wall thickness and getter density.

S is a rate constant for the reaction of CrO3(g) with the getter.

c_{sp} is the loading of Cr on the solid, in ppm.

n is the power-law dependence of the reaction rate on the Cr loading, unitless.

The first row, "gas phase diffusion limited," presumes the gas-phase profile is a function of the rate of diffusion of CrO_3 to the getter wall. The rate of reaction is calculated using Equation (1). The solid-phase Cr loading for a given time interval Δt is then calculated using Equation (2) in the column "On the solid." The second row, "Solid-state reaction limited," presumes that the solid-state reaction is the slow step. The rate of reaction is calculated using Equation (4), and

then the corresponding impact on the gas-phase concentration is calculated using Equation (3). The model results are compared, and the one giving the lower rate of reaction is used.

Figure 16-74 documents measured data and the model predictions.

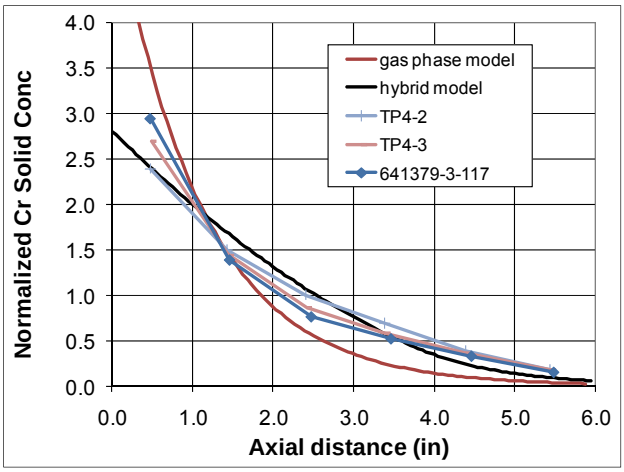

Figure 16-74. Cr concentrations in solid: measured and model predictions.

A better approximation of the observed concentration profile versus the gas-phase model was achieved by adjusting the S-parameter while holding the exponent constant. The breakthrough profiles of CrO_3 from each getter block can be predicted by expanding the time scale and assuming a CrO_3(g) saturated feed (Figure 16-75).

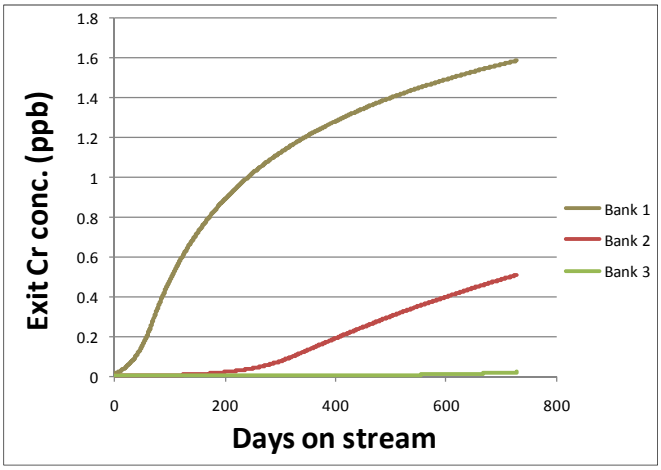

Figure 16-75. Predicted Cr Getter block exit concentrations in solid as a function of time (assumes feed is saturated).

A 3-month test of a getter sample was completed to obtain experimental data on the development of the Cr gradient along the getter bed with extended exposure (Figures 16-76 and 16-77).

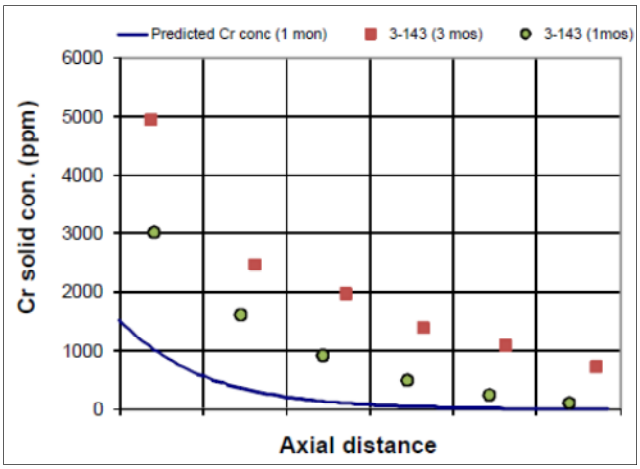

Figure 11-76. Getter 3-143 performance over 3 months.

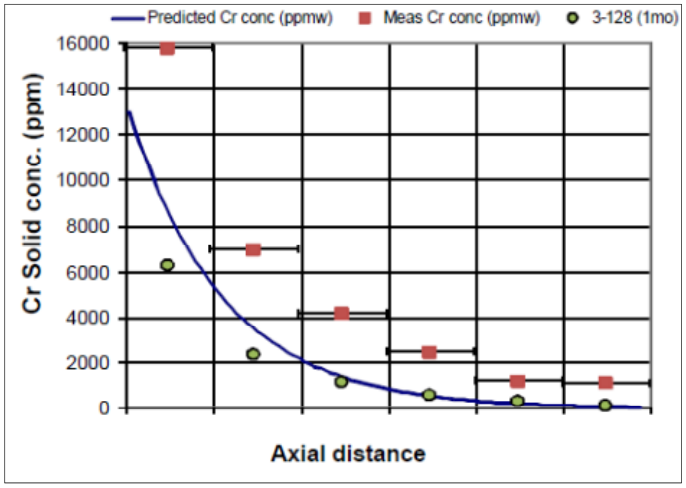

Figure 16-77. Getter 3-128 performance over 3 months.

Note that the Cr solids concentration is not normalized. The flatter, profile of the 3-143 sample in the 3-month test reflects a difference between calculated and the actual measured Cr levels on the gas stream.

A chromium getter was designed for and installed in the ISTU. Several samples of the getter were tested under standard, controlled conditions in laboratory apparatus. There was excellent agreement between the actual and theoretical curve.

A prototype chromium getter having an active loading that was over three times the amount on the ISTU getter material was evaluated. Results of a standard one-month test are shown in Figure 16-78.

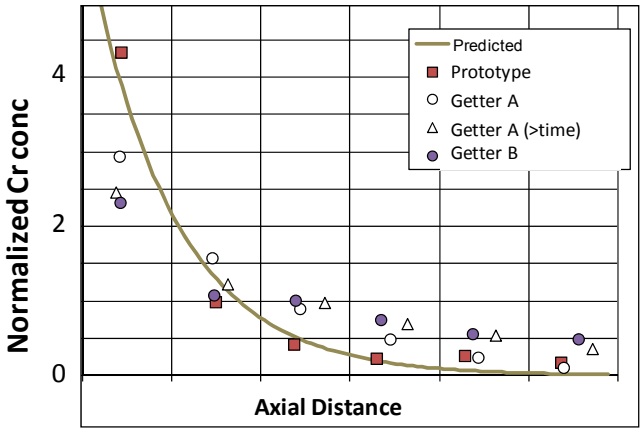

Figure 16-78. Chromium concentration with distance, prototype.

The results were encouraging. The normalized profile was quite sharp and agreed with the theoretical curve based on diffusion of $CrO_3(g)$. The effluent end of the sample contained Cr levels that were just above the baseline.

Getter Substrate

The getter material is mixed with a substrate. Experiments were conducted to determine the rate at which the getter material would react with the substrate phase under ISTU operating conditions. Supported getter samples were prepared at 20 wt% getter and then heat treated at 900º C, 1000º C and 1100º C. The data were fitted to models to estimate the consumption of getter through reaction with the substrate at 875°C and 1000°C (Figure 16-79).

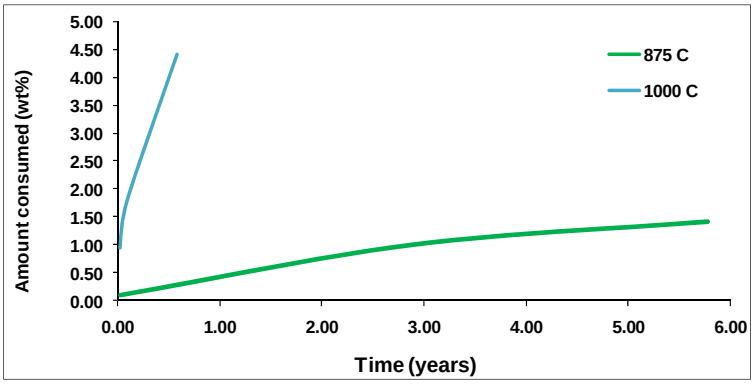

Figure 16-79. Prediction of consumption of getter through reaction with the substrate at 875°C and 1000°C.

The predicted curve is consistent with good getter lifetime in the operating range of the ITM modules.

Getter Support Structure

The getter material is attached to a monolith mounting mat composed of ceramic fibers. Key properties are compression characteristics and gas permeability.

Compression and Permeability Testing

Compression and permeability results are summarized in Figure 16-80. Both compressibility and permeability are presented as functions of mat density, which is termed GBD, or gram bulk density.

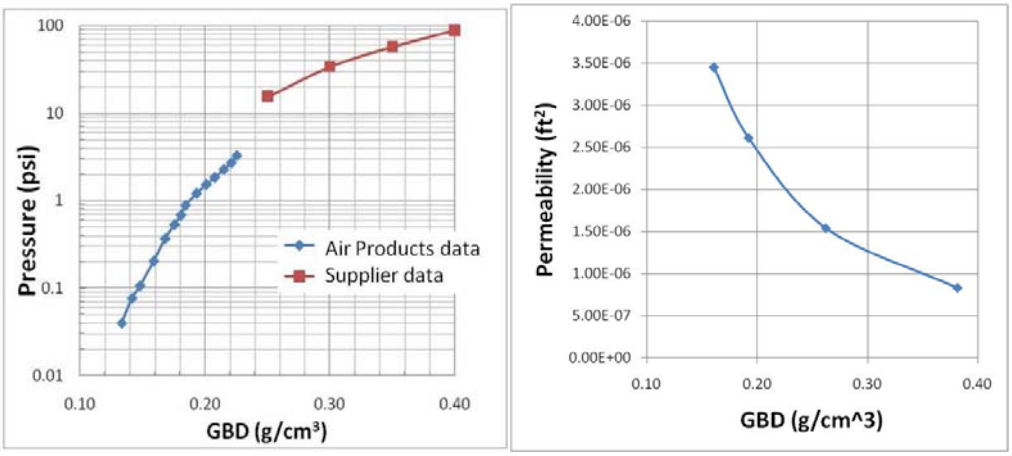

Figure 16-80. Compressibility and permeability of a candidate monolith mounting mat.

The data was used to estimates the bypass flow through the mat using a mat compression of <10 psi. It was found that the bypass flow through the mat would be very low, typically less than 0.05% of the total flow.

Pressure Drop Testing

For the velocities of interest for ITM operating conditions, the flow through the channels of a monolith Cr getter was expected to be laminar. As such, prediction of pressure drop in the straight, square channels should be straightforward because the friction factor (f) for developed laminar flow is simply and directly related to Reynolds number (Re). The pressure drop in the monolith was measured as a function of flow rate to compare the actual and predicted values. Entrance and exit losses were included in the prediction of pressure drop. Figure 16-81 summarizes the results of the measurements and includes a comparison between the measured and predicted values for ΔP.

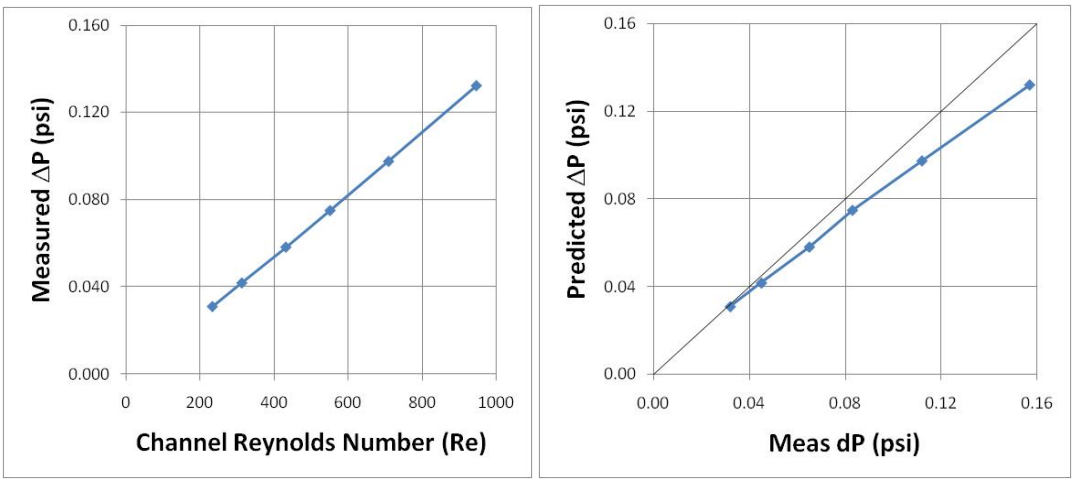

Figure 16-81. Monolith pressure drop – cold flow measurements.

The measured ΔP was greater than that predicted, and the extent of the deviation (in percentage terms) increases with increasing Re. The relative deviation at Re of 246 (the proposed operating condition for the ISTU) is only approx. 4%.

Cement

In the ISTU design, ceramic cement is used to bond some of the getter blocks, similar to mortaring a brick wall, to transfer support through the entire block wall. The cement also seals some of the leak paths between the blocks. The preferred cement would hav the following properties:

- Not crack during curing.
- Have minimal shrinkage.
- Not crack during thermal cycles.

The difference between the coefficient of thermal expansion (CTE) of the cement and the getter is a primary consideration, as it will cause stress within the cement. The dilatometer was used to measure the cure shrinkage and the thermal expansion of four candidate cements. Prior to the expansion measurements, the bars were cured for two weeks at room temperature. The samples were then put through three heating cycles to elevated temperature. Figure 16-82 shows the shrinkage/expansion of the cement bars after the third heating cycle.

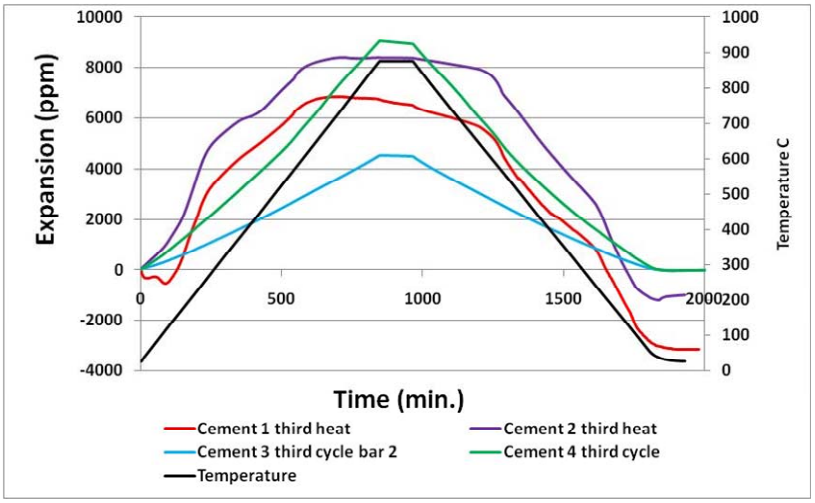

Figure 16-82. Expansion/shrinkage results for Cements 1 through 4 during a third heat treatment to elevated temperature.

Getter blocks bonded by Cement 2 were used in a number of SEP runs. It was found that the joints were still very strong ater the first SEP run. However, the joint ultimately failed after repeated cycling. The failure was a complete loss of adhesion on both joint surfaces, such that the thin layer of cement was loose between the two blocks. This is indicative of a CTE mismatch. The joint experienced over a dozen temperature cycles with several cooldowns back to ambient temperature.

Four-point flexure tests of bonded getters were conducted at the Penn State. It was determined that the joints are sufficiently strong and that the critical challenge is making joints that can tolerate repeated thermal cycling.

Tests were conducted to determine if the addition of a ceramic powder into the cement would improve the thermal cyclability of the cement joints. It was expected that the mixture CTE would more closely matches the CTE of the getter. A set of samples was prepared using four combinations of Cement 2 and ceramic powder. All 16 samples were subjected to three cycles to operating temperature at a rate of 5°C/min, a two-hour hold, and then cooling as quickly as possible. At the end of the three cycles, all of the joints were intact. Penn State conducted 4-point flexure tests on two samples from each composition. No samples failed at the joint, and all had strength of at least 100 psi.

The cement composition chosen for ISTU getter bonding was based on a Cement 1/ceramic mixture. This decision was based on the following experimental results and observations at the SEP:

- Nearly all of the joints prepared for 4-point bend testing at Penn State failed in the getter rather than at the joint. The joints were inherently stronger than the getter itself under these test conditions.
- Pre-wetting the surfaces led to much better spreadability of the cement.
- Pure Cement 1 joints failed on both sides during cycling at the SEP, such that the cement broke away cleanly. There appeared to be a CTE mismatch.
- Follow-up lab tests were performed with the partial substitution of ceramic into Cement 1. There was a clear trend toward higher strength under thermal cycling with ceramic substitution.
- SEP tests indicated that it is valuable to pre-wet both surfaces with activator prior to joining.
- A Taguchi experiment design examined the effects of humidity and setting time before firing on ultimate joint integrity. A humidity-controlled aquarium provided a Louisiana-like environment (90°F and 100% humidity). Both fired and unfired samples were evaluated visually and 4-point bend testing was conducted. No systemic effects were observed. The unfired joints are comparatively strong regardless of curing time or humidity.

Sulfur Dioxide

Background

Sulfur dioxide (SO_2) is present in the atmosphere at low levels, typically <20 ppb. With sufficient operating time, even low levels of SO_2 can adversely affect the performance of the ITM. A typical front-end TSA system in a cryogenic ASU can remove SO_2 to acceptable levels. However, in cases were a TSA is not desired in an ITM cycle, an alternative means for SO_2 removal is required. One option is a getter, operating at the discharge conditions of a gas turbine compression section or air compressor. Air Products focused on identifying suitable materials for this application.

Equipment and Experimental Method

A laboratory system was adapted to mildly heat a candidate adsorbent while simultaneously dosing it with a flow of SO_2 in air. A downstream SO_2 analyzer records the breakthrough characteristics of the candidate adsorbent. A model was used to guide material performance requirements.

Results

A model was constructed that assumed the SO_2 adsorption rate in the adsorption bed is controlled by film and pore diffusion, (i.e., no reaction kinetics impact). A similar model has been used elsewhere to extrapolate lab data to design larger, commercial-scale getters. The model accurately predicted the SO_2 adsorption of a Type I getter material. Model inputs include feed flow rate and composition, SO_2 diffusivity in air, adsorbent bed sizing, adsorption capacity and physical parameters (inter- and intra-particle void fraction, average pore diameter). Two parameters define the pore shape characteristics: Knudsen diffusion tortuosity and molecular diffusion tortuosity. These material characteristics are not readily measured directly. Their values were adjusted until the model predictions fit one of the data sets. These "fixed" parameter values were then placed in the model. It was later realized that the Knudsen and molecular diffusion resistances could be combined into a single effective diffusivity. Thus, any pair of values that results in the same effective diffusivity are equivalent and equally good at fitting the data.

The measured data set in Figure 16-83 was used to fit the two tortuosity parameters and a third parameter, the total adsorption capacity of the getter material.

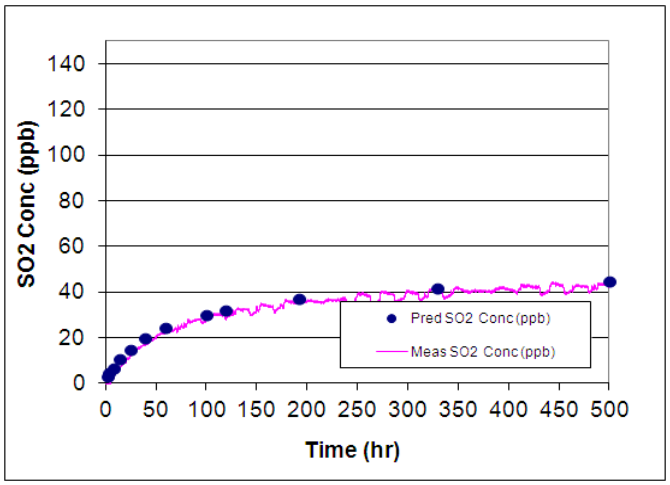

Figure 16-83. SO_2 breakthrough model parameters fitted to measured data.

The values of the two tortuosities strongly indicated that pore diffusion controls the adsorption process. Figure 16-84 plots the model predictions versus measured values for a feed gas SO_2 concentration 3X greater than what was used in the tests shown in Figure 16-83.

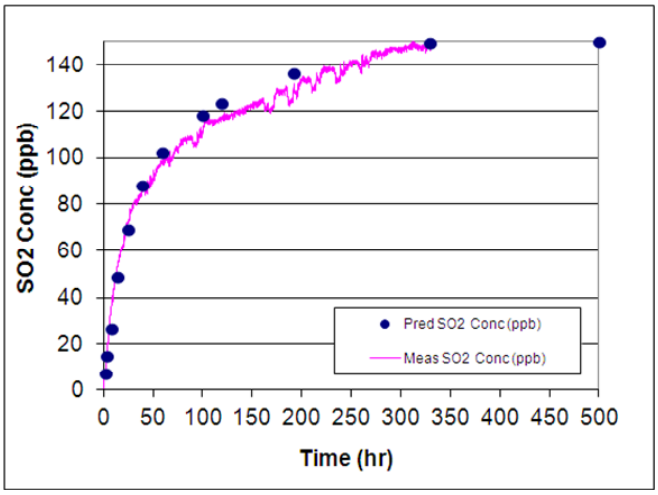

Figure 16-84. SO_2 breakthrough model values versus measured data.

No adjustment was made to the tortuosity parameters. A slight change was made to the total adsorbent capacity. New bed dimensions were input, and the inter-particle void which depends on how the bed was loaded was recalculated. The fit was quite good. An actual versus theoretical comparison was done at an SO_2 concentration that was 12 times that used in the Figure 16-83 tests. The resulting fit of the model was excellent.

To further test the model's robustness, a set of experimental conditions was calculated that predicted 100% capture for 20 hours. Figure 16-85 shows the SO_2 breakthrough and getter deactivation curves for one set of conditions.

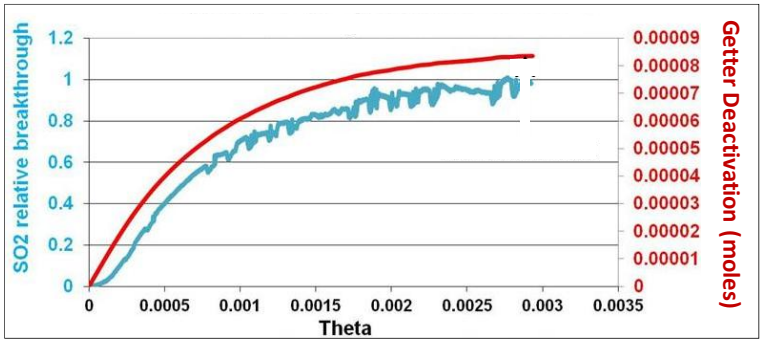

Figure 16-85. SO_2 relative breakthrough and cumulative getter deactivation in the presence of CO_2.

The 100% capture predicted by the model was inconsistent with the experimental results. One possible cause for this inconsistency could be bed bypass, so efforts were undertaken to minimize this. Additional experiments were conducted on an extended bed and smaller particles to determine if the effective diffusivity value that fit the earlier data would accurately predict their behavior. However, the model did not match the measured breakthrough curves, indicating that bypass or channeling in the test chamber was still occurring.

Particulate Removal

Background

In a commercial ITM Oxygen plant, particulates in the air feed could foul the Cr getter. Of particular concern is Cr-bearing oxidative scale from heat exchange equipment and the fired heater. This Cr-bearing scale could infiltrate and penetrate the Cr getter support structure and reduce its effectiveness. Moreover, complete penetration of particles through the support structure could directly impact the modules, contaminating the membrane surface with Cr. As such, a filter is required to remove particulates from the feed air stream. The filter must be capable of removing small particles without adding excessive pressure drop.

Results

A wall-flow filter was installed in the SEP. The filter ran through three complete temperature cycles with only a minor increase in the pressure drop across the filter. A pressure drop equation

for flow through the filter was identified:

$$\Delta P = L(\alpha\mu u_{ch} + \beta\rho u_{ch}^2)$$

where αand β, the Forchheimer coefficients, are calculated as:

$\alpha = aw_s/[0.995 * 4 * L^2\text{k}]$
$\beta = 1.348C_f/\text{a} = 20.09/(\text{Re*a})$

Where

u_{ch} = velocity in the channels	*ft/s*	$2V_s/(\text{cpi}*a^2)$
cpi = cells per square inch		200
a = cell dimension	*inches*	$\text{cpi}^{-0.5}$ - w_s
w_s = wall thickness	*inches*	0.012 inches
L = length	*inches*	12 inches
k = actual permeability	m^2	Est'd: 2E-13
C_f = friction factor	*dimensionless*	14.9/Re
Re = Reynolds number	*dimensionless*	$au_{ch}\rho/\mu$

α and β are only dependent on the nature of the filter, other than the Reynolds number dependence of the friction factor. The predicted ΔP agreed very well with the data at low flow rates but much less so at higher flows, where the model underpredicted the pressure drop by over 40% (Figure 16-86).

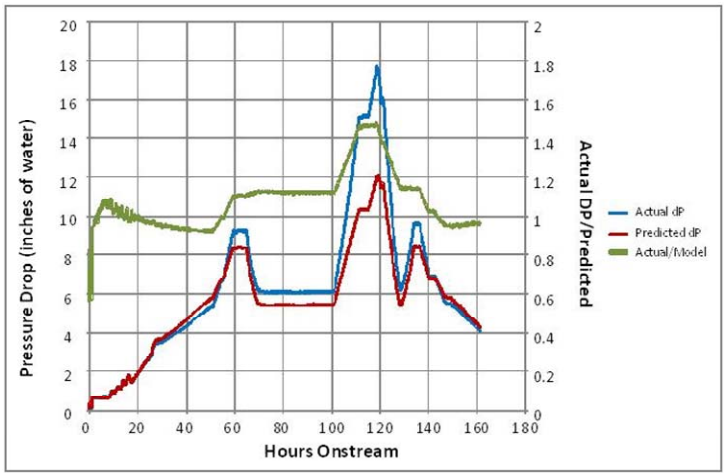

Figure 16-86. Observed ΔP vs. model prediction.

Various modifications to the model were explored. A reasonable correlation was obtained when the model was forced to agree with the observed pressure drop by varying the friction factor C_f, rather than assuming $C_f = 14.9/\text{Re}$ (i.e., laminar flow). Figure 16-87 shows the resulting values

for C_f as a function of Re. The red line is the 14.9/Re curve. The green points are the first 120 hours onstream; the blue points were obtained at low flow.

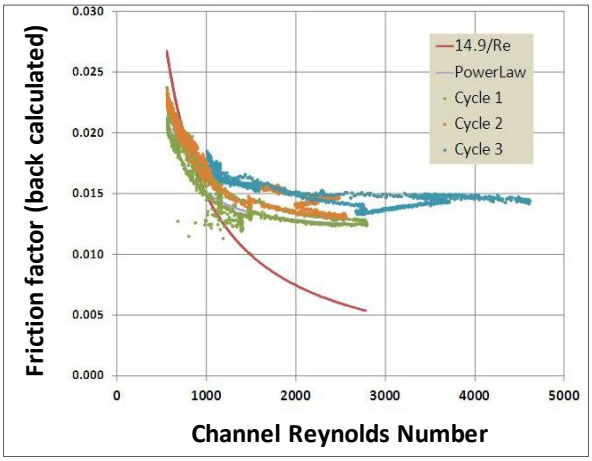

Figure 16-87. Friction factor vs. channel Reynolds number.

These friction factor data show that the explored flow range was much closer to the onset of turbulence than anticipated from the channel Reynolds number. Thus, the laminar relationship (C_f=14.9/Re) is not valid. Above a Reynolds number of ~2,500, C_f appeared to be independent of the Reynolds number, which indicates that the flow is fully turbulent. The back-calculated friction factor increases from cycle to cycle, reflecting the increase in the pressure drop due to accumulation of particles in the filter. There was also some hysteresis in the data within each cycle, suggesting that the model does not perfectly account for variations in the actual temperature, pressure and flow.

The green friction factor points were empirically fit to a simple arithmetic expression ($C_f = 0.012 + 1550/Re^{1.9}$). This revised expression for the friction factor was placed into the original model, with the results shown in figure 16-88.

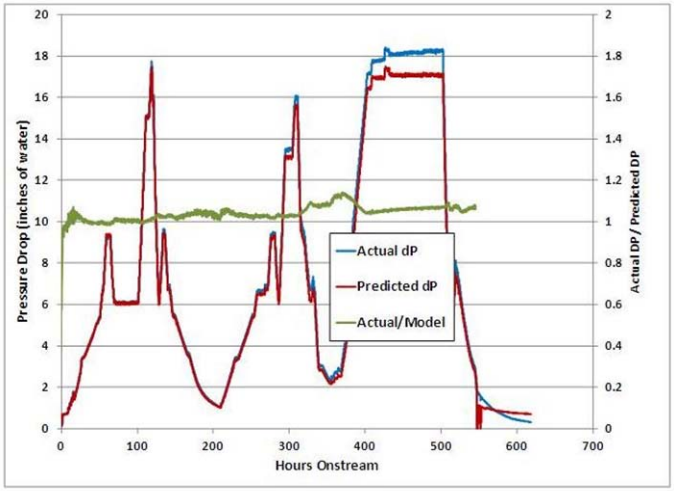

Figure 16-88. Observed ΔP vs. modified model prediction.

The green curve shows the percentage difference between the actual data and the revised model, which generally does not exceed 10%. The slight positive slope of the curve reflects a gradual (and minor) plugging of the filter with particles. This empirical model can determine if there is a measurable increase in pressure drop when comparing similar, but non-equivalent, flow cases.

The particulate filter from previous runs was installed in the SEP for Runs 28 and 29. Figure 16-89 shows the friction factor along the filter in comparison to that measured in earlier runs as a function of the Reynolds number.

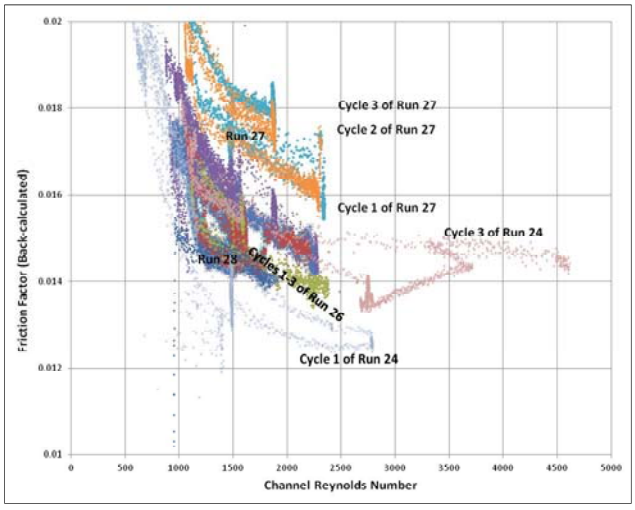

Figure 16-89. Friction factor vs. channel Reynolds number for Runs 24-28.

The friction factor is lower than that observed in Run 27 and slightly higher than in the first run (Run 24). The removal of spall particles prior to the installation helped lower the friction factor.

Wall Filter Characterization

Two types of wall filters were characterized using ImageJ software. The filters have parallel channels that do not go completely through the block; a channel open at one end of the block is closed at the opposite end. Adjacent channels are closed on the opposite side, creating an alternating checkerboard pattern of open and closed channels on each end of the block. Gas entering a channel is filtered through the wall between the channels.

The software identified the open face area, total channel length and wall thickness. Filter A had a smaller open face area than Filter B (Figure 16-90).

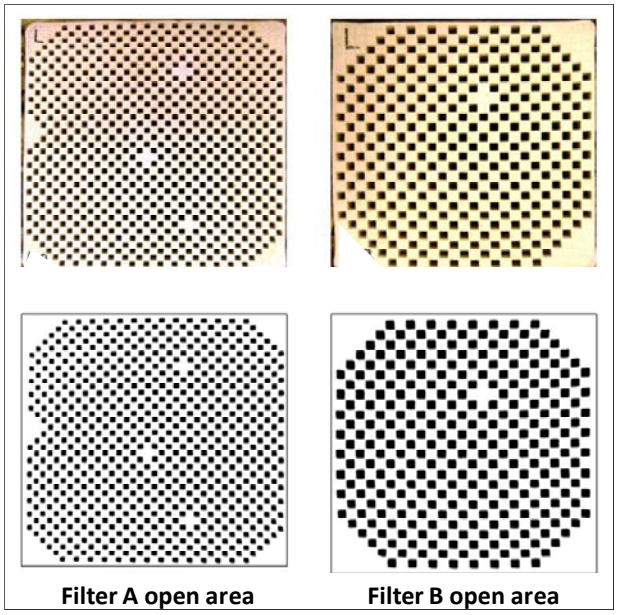

Figure 16-90. Imaging construction to identify the open face area of Filters A and B.

The software identified the channel edge length, a parameter used to determine the functional filter area. Figure 16-91 shows the imaging constructions to determine the edge values.

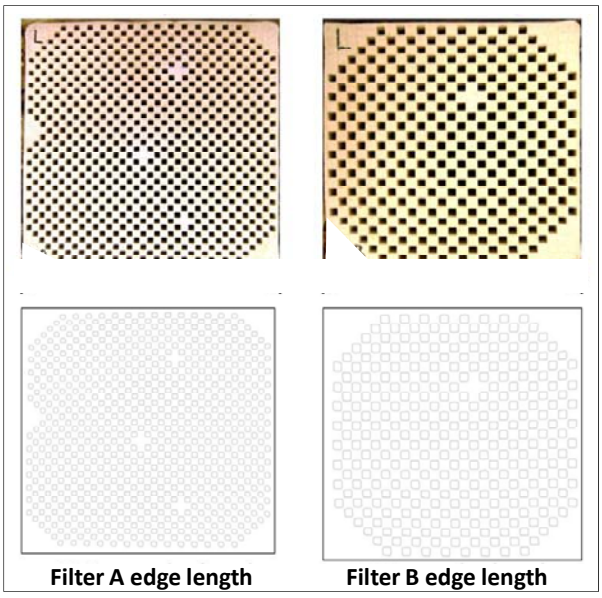

Figure 16-91. Imaging construction to identify the total length of the channel edges.

Filter A had greater edge length. Figure 16-92 depicts the software methodology to identify the wall thickness between the channels.

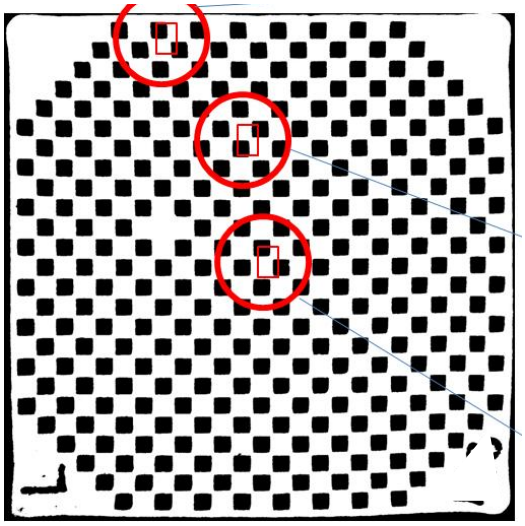

Figure 16-92. Software methodology for identifying the wall thickness between channels.

The software measures the relationship between black areas (open channels) and white areas (wall thickness) within each of the squared boundaries. Both filters had similar wall thicknesses.

Commercially available filter elements with a square cross-section are being considered for particulate removal in commercial designs. The ISTU uses a filter with a circular cross-section, which is installed in the feed piping to the ITM vessel.

An initial assessments were conducted of filter elements suitable for a commercial-scale ITM system. The filters were found to give acceptable pressure drop. However, this work was done using a clean filter. There was some concern that once small amounts of particulate were captured by the filter, the pressure drop might increase rapidly. Tests were completed where small aliquots of dust were added sequentially to the filter, and the resulting impact on pressure drop was measured. The results of the test were satisfactory; there was only a minor increase in pressure drop across the filter under the test conditions. Figure 16-93 presents the experimental data. The observed increase in pressure drop is equivalent to a ~5% decrease in filter permeability.

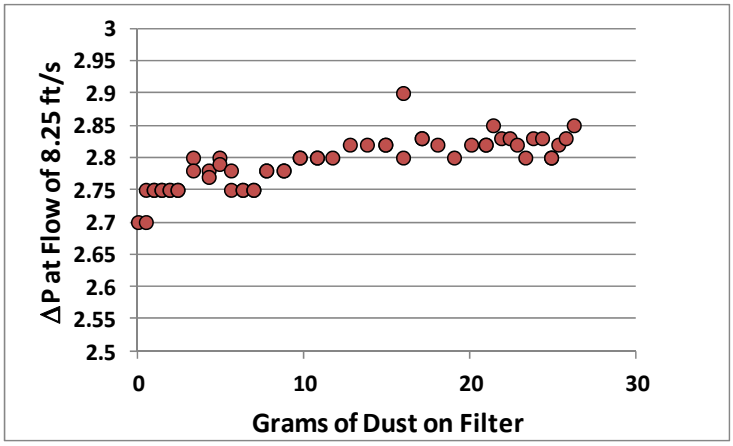

Figure 16-93. Filter pressure drop as a function of filter dust load.

TASK 17.0 TABLE OF CONTENTS

TASK 17.0 CERAMIC PROCESSING DEVELOPMENT 3

17.0 SCOPE 3

17.0 CERAMIC PROCESSING DEVELOPMENT 3

Background 3

Summary 4

17.1 FULL-SIZE WAFER YIELD PROGRESSION 5

General 5

Sintering Thermal Cycle Reduction 6

17.2 FULL-SIZE MODULE FABRICATION 11

Production 11

Powder 11

Tape 11

Module Inventory 13

Component Development 15

Wafers 15

Base Piece 15

End Cap 16

Joining Yield 18

Wafer Flatness 18

Module Alignment 20

Module Conditioning 22

Module Shipping and Handling 23

Advanced Architecture Wafer Modules 26

17.3 OPTIMIZATION OF THE CERAMIC PROCESS DEVELOPMENT FACILITY (PDF) 28

Background 28

Powder Processing 29

Slip Preparation 30

Tape Casting 30

Featuring/Lamination 32

Sintering 35
Submodule Fabrication 40
17.4 CERAMIC PROCESS ENGINEERING AND ECONOMIC EVALUATION 41
17.5 CERAMIC PROCESSING COST AND PRODUCTION ANALYSIS/2000 TON PER DAY CAPACITY CERAMIC MANUFACTURING STUDY 43

TASK 17.0 CERAMIC PROCESSING DEVELOPMENT

17.0 Scope

In Task 17.0, Ceramatec conducts ceramic processing development to (i) fabricate full-size wafers required for full-size membrane module development, (ii) increase the yield of ceramic processing and the efficiency of ceramic processing unit operations, (iii) increase the yield for membrane module processing and determine a preferred procedure for constructing full-size modules, and (iv) increase the scale of production by approximately fivefold to support the expanded testing requirements of the ISTU at 100 tons/day oxygen capacity. Ceramatec will incorporate additional processing tools and equipment in support of wafer and membrane module processing during Phase III, make process modifications to support the larger-scale production equipment, and revise existing equipment as necessary to meet the expanded production demands. This will prioritize processing bottlenecks and key areas requiring further improvements in processing yield.

17.0 Ceramic Processing Development

Background

Figure 17-1 is a simplified overview of the ITM module fabrication process.

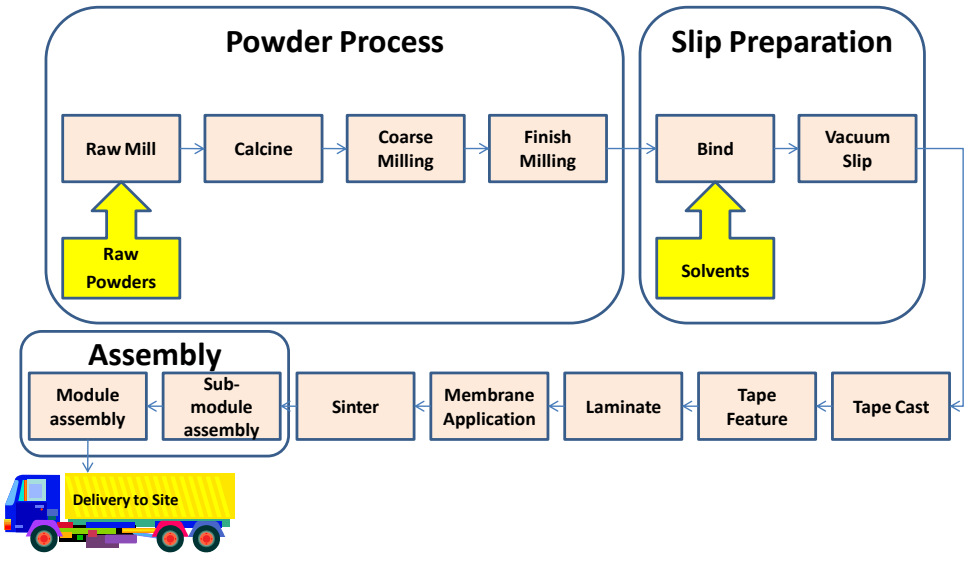

Figure 17-1. Module fabrication as a simplified process overview.

In **Powder Process**, ITM Oxygen materials are prepared by reacting the base constituent powders together in a process known as "calcining." The powder is then milled in various ways depending upon the part to be fabricated. In **Slip Preparation**, the powder is mixed with a solvent and organic binder to prepare a "slip" (slurry). The slurry is sent to a **Tape Caster**. Tape is formed by casting the slip onto a flat surface, then the wet tape is then dried to remove solvents. The physical properties of the tape are critical for the subsequent lamination steps. The tape is **Featured**, which simply means it is laser cut or punched to form the channels necessary for the internal features for the part specification. The featured tape is layered/laminated to make the specific component parts, after which the ITM ceramic membrane is applied. This "green" part is then **Sintered**.

Sintering is the process of compacting and forming a solid mass of material by heat and/or pressure without melting it to the point of liquefaction. In a collection of tightly packed ceramic particles, species diffuse to adjacent particles, fusing the particles together and creating one solid piece.

The sintering conditions impart specific properties to the part including density, porosity and strength. The sintered parts are assembled into submodules and thermally processed to form the joints between the parts. The submodules are assembled into modules and thermally processed again to bond the joints.

The quality of the parts, submodules and modules, and specifically their resistance to cracking is affected by all of the manufacturing processes. Sintering is particularly important, and significant efforts were taken to define the proper operating parameters.

Summary

Under Task 17, significant development has been completed at Ceramatec, Inc. to improve ceramic processing yield and to manufacture commercial-scale modules and small test parts. Improved manufacturing methods were developed for many of the module production steps to enable larger-scale production and higher yields. Equipment was procured, and processing conditions were optimized for several steps including a large-scale tape caster/comma coater, a punch for layer featuring, laser improvements for layer featuring, several larger-scale kilns for wafer and module processing, and tools and fixtures to improve module alignment. Thermal

processing cycle times were reduced without detriment to part reliability, increasing productivity.

Numerous 0.5 TPD modules were produced for testing in the SEP with acceptable yields. Attempts to produce 1 TPD modules resulted in significantly lower yields. A root cause analysis led to the conclusion that the wafer reliability through thermal cycling needed to be increased. A significant effort was undertaken to reduce the path length for oxygen diffusion, since that was seen as a significant improvement in redesign of the modified base piece and end cap. Modified wafers were shown to be much more resistant to damage during thermal and P_{O2} cycling. Two entire processing methods for producing the modified wafer architecture were developed, and one method was chosen based on yields and scalability. A baseline modified wafer was selected and 1 TPD modules were built using this process starting in April 2012.

A test of prototype advanced architecture 1 TPD modules was run at the SEP in May 2012 just prior to the final shutdown of the Sparrows Point ASU. Numerous lab-scale tests on advanced architecture single-wafer modules confirmed similar flux performance and superior reliability to transients, as presented in the quarterly reports. Yield improvement continued throughout this time frame and is again tracking the development yield target trajectory. Sufficient numbers of full-height modules were produced for the first two ISTU runs.

17.1 Full-Size Wafer Yield Progression

General

In early 2009, Ceramatec changed the wafer architecture by adding an A-prime (porous) layer to the wafer to better stabilize the membrane layer. Once the A-prime wafer fabrication process was developed and qualified, a study on the effect of the A-prime layer was conducted. Wafers were constructed using standard techniques and fired in standard kiln runs. The wafer population included standard control wafers without an A-prime layer, wafers with only one side containing the A-prime layer, and wafers with both sides containing the A-prime layers. Following firing, the wafers were tested using standard leak tests. The results of the study are summarized as follows:

- Wafers with A-prime layers on both sides had the highest average (73.6%) leak-rate yield.

- Control wafer average yield was 52%
- Wafers with A-prime layers on only one side had an average yield of 64.3%.
- Wafers without spacers showed a higher average yield.

In Q4-2009 Ceramatec commissioned new equipment to produce slip. The yield of wafers produced with the new equipment/process was statistically indistinguishable from that of the standard process wafers.

Sintering Thermal Cycle Reduction

Ceramatec optimized the sintering thermal cycle to minimize fabrication costs and increase throughput. A range of process times and temperature schedules were studied. Figure 17-2 is an example of a study conducted in Q3-2009.

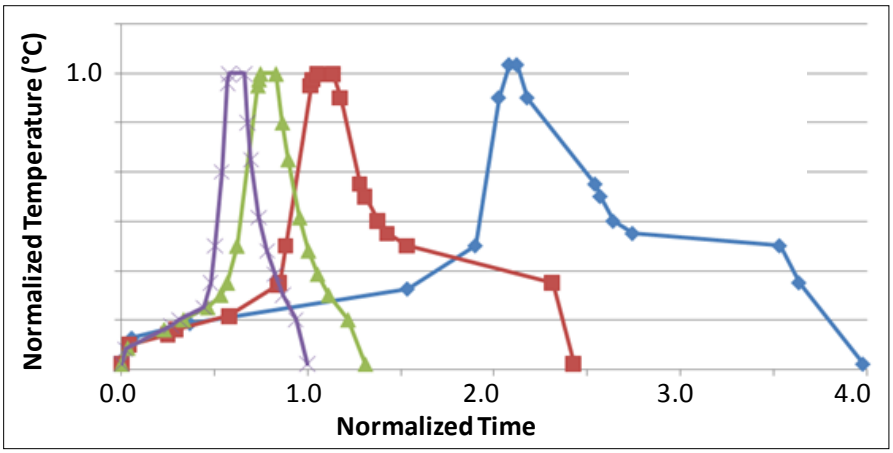

Figure 17-2. Wafer sintering cycle study.

Residual stress develops in the wafer when the oxygen vacancy does not reach equilibrium and can cause failure. This locked-in vacancy is a function of the cooling rate and diffusivity. Experiments were conducted to determine the fastest cooling schedule while maintaining acceptable yields. Wafers are monitored for fracture over a range of cooling rates to create a data set for model validation. The strength of wafers was measured. In one experiment, the oxygen uptake at low temperatures for various samples with a range of oxygen diffusion path lengths was measured by using a thermo-gravimetric analyzer (TGA). Figure 17-3 is a plot of the oxygen vacancies as a function of temperatures below 600°C for a variety of samples with different component thicknesses. The data were used to establish the extent to which a deficit of oxygen remains in a sample after cooling.

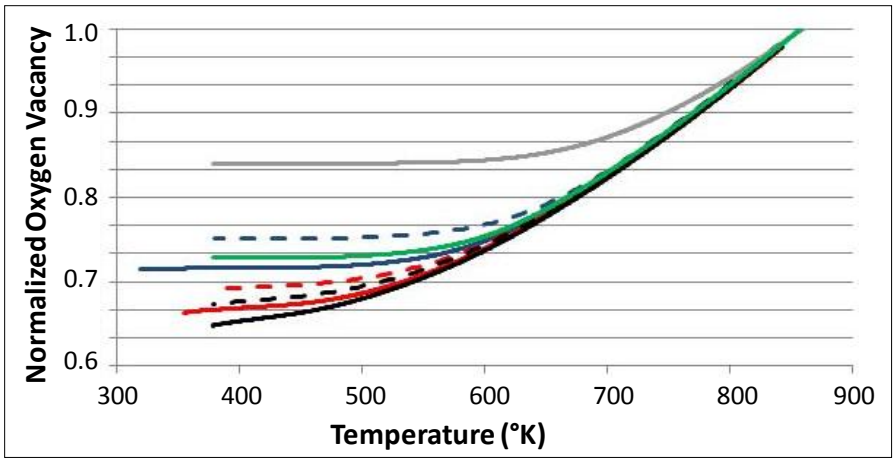

Figure 17-3. Oxygen equilibration data for a variety of sample types.

Thermal cycle time optimization continued in Q2-2010. Figure 17.1-4 plots the leak rate distribution of the original and a shortened thermal cycle.

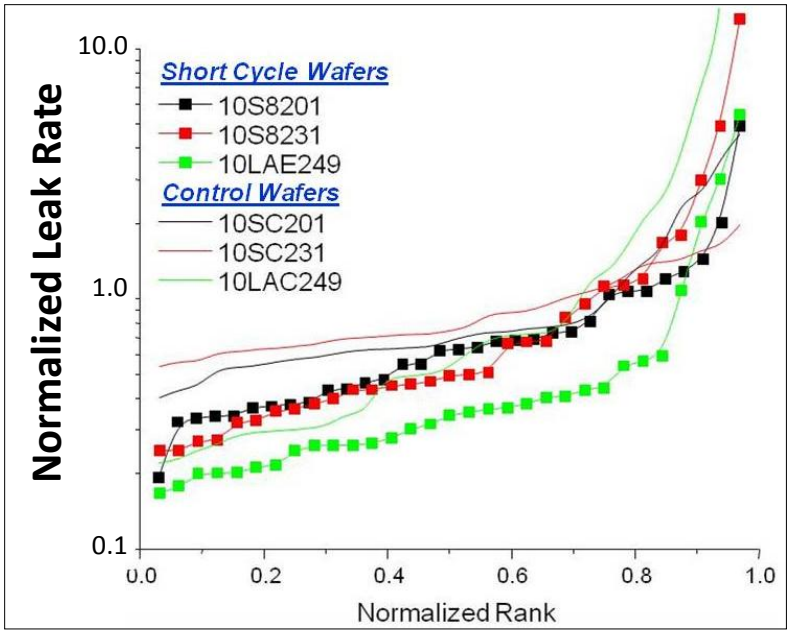

Figure 17-4. Ranked leak rate distribution plot of 3 split wafer lots using the original and shortened thermal cycle.

The data suggested that the shortened cycle actually decreased the average leak rate. An additional set of original and short thermal cycle wafers was inspected by scanning acoustic microscopy (SAM) followed by C-ring mechanical testing. It was concluded that compared to the original cycle wafers, the short cycle wafers had:

- Equivalent strength
- Equivalent or better leak rate yield
- A reduced base leak rate
- Equivalent residual strain in the rim
- Equivalent flatness and parallelism

To further qualify the reduced sintering cycle, two reduced-cycle sintering runs were conducted in the large kiln. The first run (403314) consisted of several small lots which included Slot Pattern #2 wafers. The second run (403474) utilized only Slot Pattern #1 wafers. As shown in Figure 17-5, neither furnace run achieved acceptable leak rate distributions.

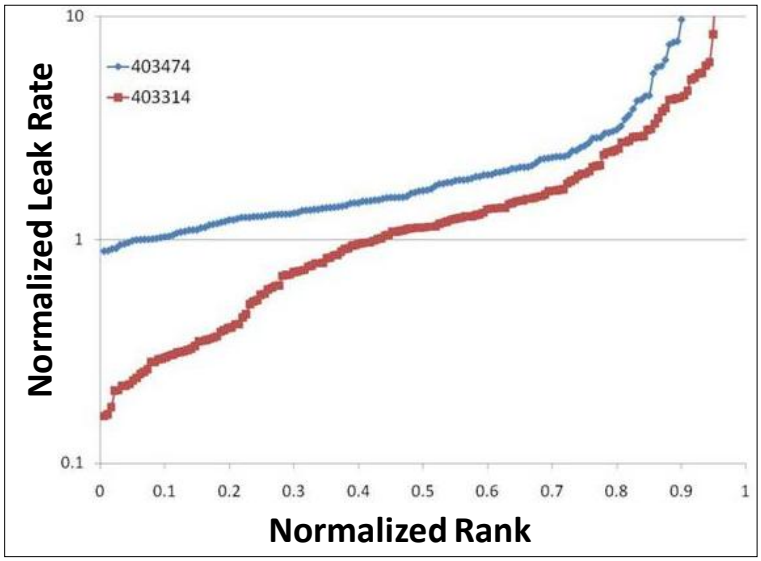

Figure 17-5. Leak rate distributions of the first two short cycle runs in Kiln #104.

Subsequent run yields were similar to those achieved by wafers produced using the original thermal cycle (Figure 17-6). This suggested that the drop in yield seen in Figure 17-4 was due to a factor other than the thermal cycle.

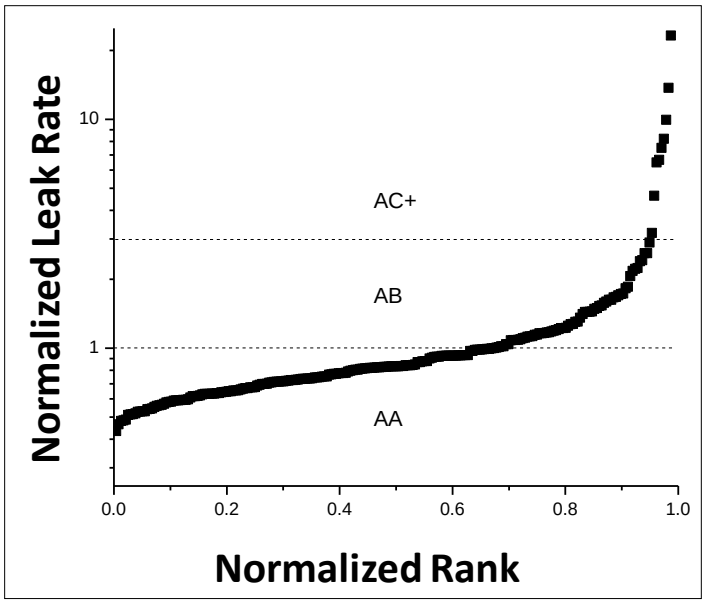

Figure 17-6. Leak rate distributions of subsequent runs in Kiln 104.

These results led to a review of manufacturing tolerances. A survey of tape tile shrinkage was conducted. The data in Figure 17-7 showed that there was significantly more shrinkage in the Y direction (perpendicular to the slots) than in the X direction.

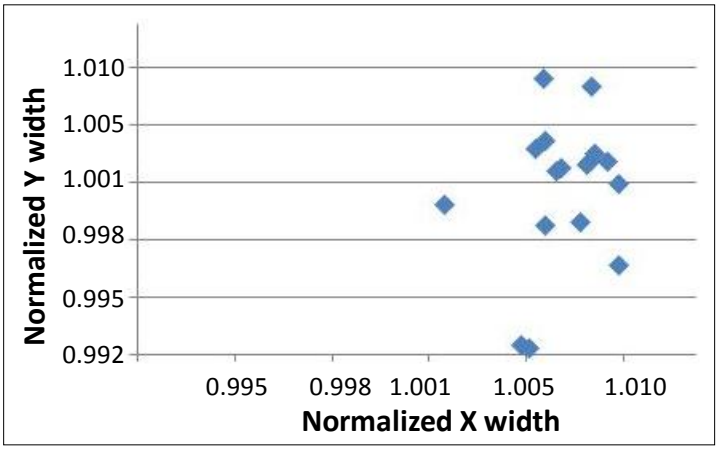

Figure 17-7. Layer tile dimensions from eighteen different lots of tape.

These same tiles were then measured three times over a one-week period (Figure 17-8).

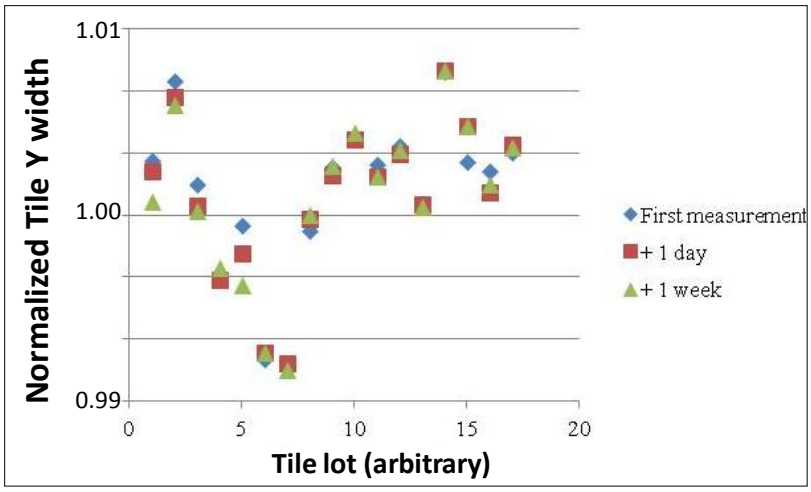

Figure 17-8. Measurement repeatability over 1 week.

The data suggested that the tape does not continue to shrink after washing. The variability within a lot was also checked; results are shown in Figure 17-9.

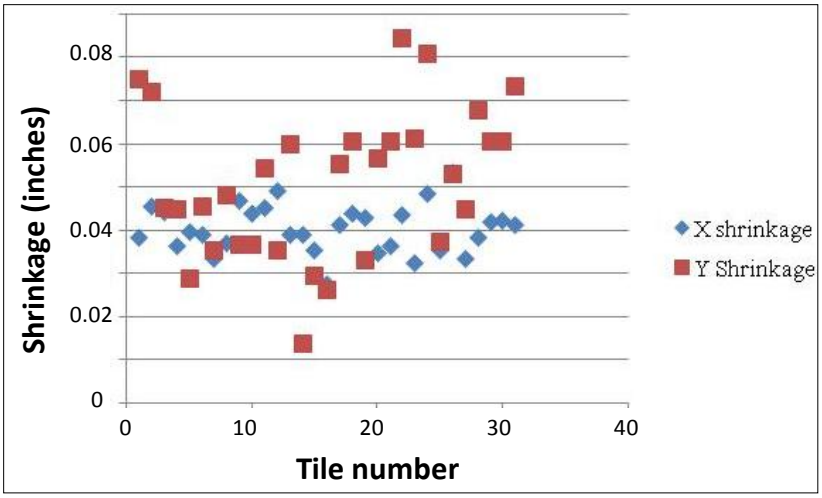

Figure 17-9. Shrinkage within a tape lot (MED100610).

The variability in Figure 17-9 indicated that wafers built with a rim almost certainly have a significant number of wafers with exposed slots. The cause was attributed to registration of the layers from the edge, which results in the laser cut pattern being shifted to one side (i.e., too much rim on one side, not enough on the other). This shift caused the wafer rims to equilibrate differently, leaving the wafer susceptible to residual stress fracture during further processing. This differential was eliminated by using the centers rather than the edges to place the laser pattern.

17.2 Full-Size Module Fabrication

Production

Powder

Figure 17-10 documents the powder production from Q2-2007 through Q2-2015. Note that production was shifting to the ceramic module fabrication facility (Cerfab) in 2014. Over this period, Ceramatec produced over 74,500 kilograms of powder. The production for Phase V (Tasks 28 and 30), which was produced at the CerFab, is included for reference but not included in the total.

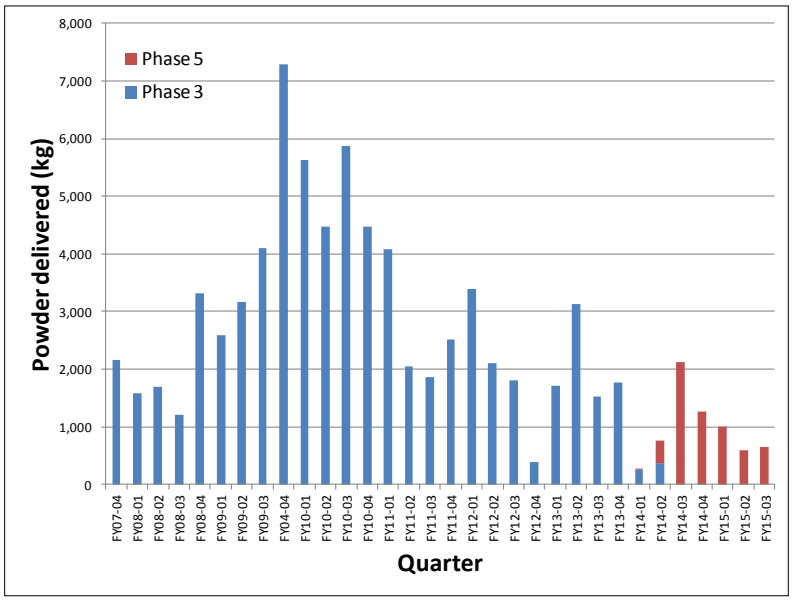

Figure 17-10. Powder production by quarter.

Tape

Figure 17-11 documents the tape production from Q2-2007 through Q2-2015. Over this period, Ceramatec utilized the powder to make over 720,000 feet of tape. The production for Phase V, which was produced at the CerFab, is included for reference but not included in the total.

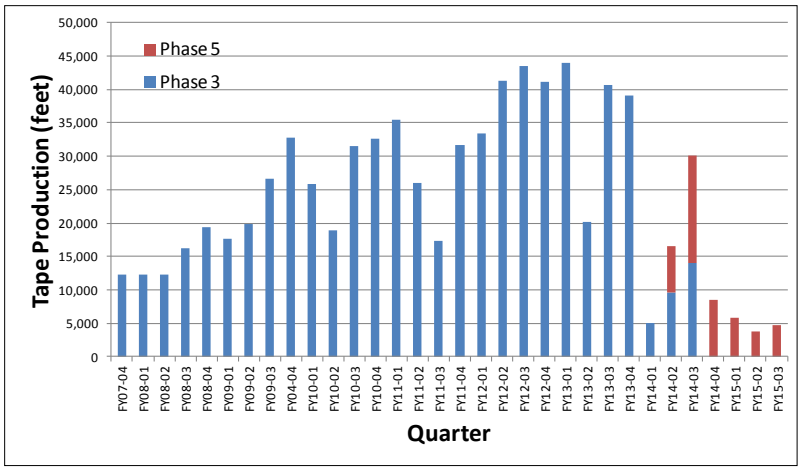

Figure 17-11. Tape production by quarter.

Figure 17-12 documents the featured parts production from Q1-2008 through Q2-2015. Over this period, tape was converted to over 790,000 featured parts. The production for Phase V, which was produced at the CerFab, is included for reference but not included in the total.

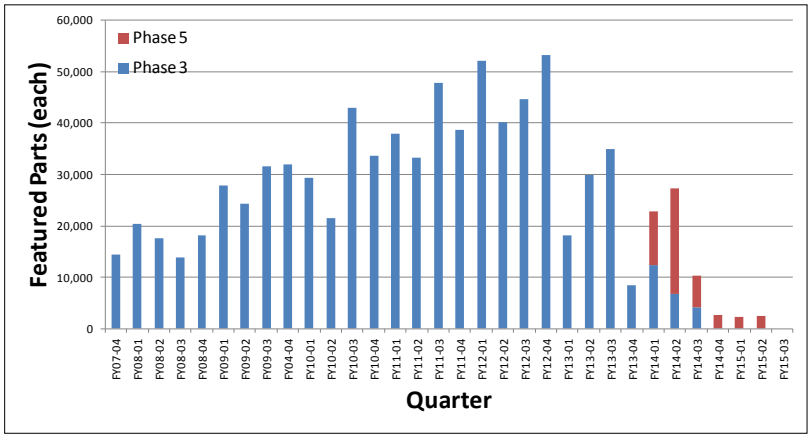

Figure 17-12. Featured parts production by quarter.

Figure 17-13 documents the number of wafers sintered through the time frame of Phase 3. Over this period, a total of nearly 110,000 wafers were sintered. The production for Phase V, which was produced at the CerFab, is included for reference but not included in the total.

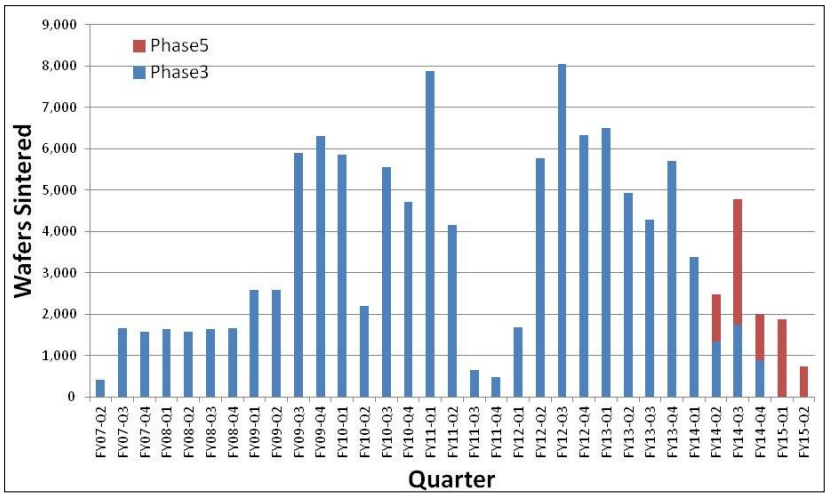

Figure 17-13. Wafers sintered by quarter.

Figure 17-14 documents submodule production from Q2 FY2007 through Q2 FY2014. A total of almost 4,400 submodules were fabricated over this period. The production for Phase V, which was produced at the CerFab, is included for reference but not included in the total.

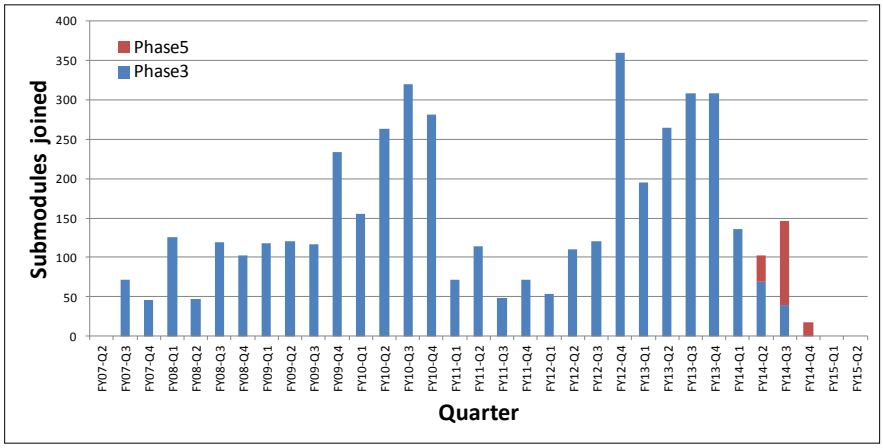

Figure 17-14. Submodule production from Q1-2008 to Q2-2010 by quarter.

Module Inventory

Modules capable of producing 0.5 TPD of oxygen were produced over the time period 2005 – 2012 for testing at the SEP. Full height modules were successfully produced after advanced architecture wafers were developed under Phase V, Task 28.2.1. Figure 17-15 documents total module production from Q2 FY2007 through Q2 FY2015. A total of 213 modules were fabricated over this period. The production for Phase V (Tasks 28 and 30), which was produced at the CerFab, is included for reference but not included in the total.

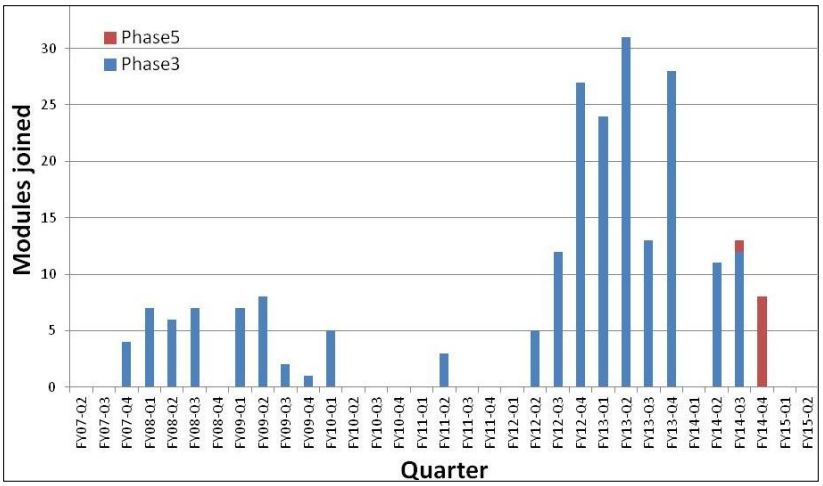

Figure 17-15. Module production from Q2-2007 to Q2-2015 by quarter, combination of 0.5 TPD- and 1 TPD–scale production.

Production of parts capable of >97% purity met the target yield for all but the submodule process. Yields of advanced architecture wafers were initially lower than those for standard wafers. Advanced architecture wafer yields are shown in Table 17-1.

Table 17-1. Wafer Yield % (xx/xx) at: 99.5% purity (first number) and >97% purity (second number).

	Wafer Yield %
ISTU Delivery (Final target)	70
Cumulative FY13 Yield (Oct-Sept)	58/75
Cumulative FY14 Yield (Oct-Sept)	50/74
Commerical development end of phase III	75

Figure 17-16 shows full-height modules with the improved base piece and end caps.

Figure 17-16. Full-height modules.

Component Development

Wafers

Alternative wafer architectures were evaluated by Ceramatec. Wafers made from Slot Pattern #1 and Slot Pattern #2 were cycled under the "worst case" loading conditions (i.e., that produced the highest wafer failure and leak rate increase in the baseline wafers). The sintering yields are shown in Figure 17-17. AA represents the lowest leak rate and HLR represents the highest.

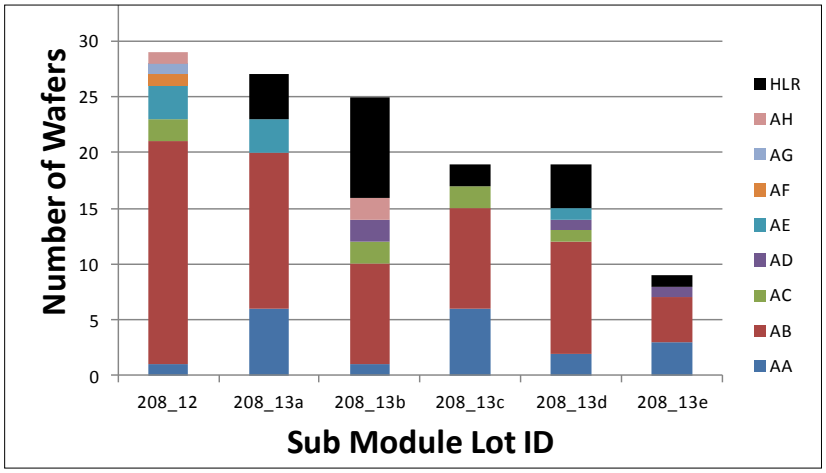

Figure 17-17. Distribution of leak rates from alternate wafer design sintering.

Most AD and higher yields were due to exposed slots on the outer rim. The wafers with internal reinforcement features had the highest sintering yields. The following lists the conclusions based on the above and other work:

- The addition of a compliant layer during submodule joining increased yield.
- Slot Pattern #1 wafers had a higher yield relative to the alternatives.
- A shorter slot design and/or modified wafer rim increased the cyclability of the wafers and reduced the leak rate.
- The cause of leakage for some of the higher leak rate wafers was due to delamination.
- Rim edge leaks were due primarily to exposing internal slots.

Base Piece

In 2009, it was decided to change the design of both the base piece (originally conical) and the end cap (originally flat). Both of these components had shown reliability issues during testing in the laboratory and the SEP. In Q3-2009, Ceramatec completed the fifth design revision of the

improved base piece and produced parts for testing. Three sets of three prototype lab-scale modules were fabricated. The modules incorporated an additional component to relieve stresses between the wafer and the base piece. Figure 17-18 is a photograph of one of the lab-scale modules.

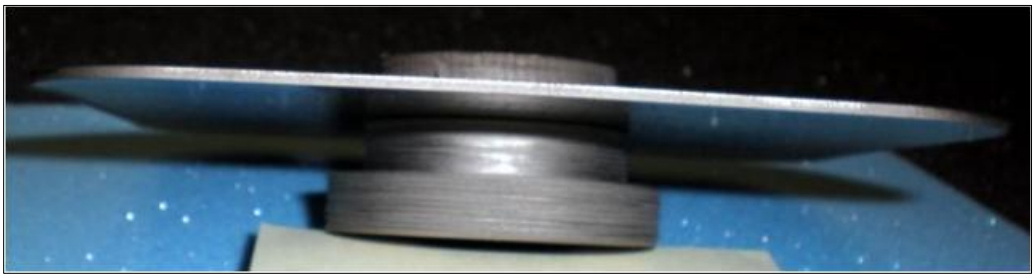

Figure 17-18. Prototype single-wafer, lab-scale module with an improved base piece.

Ceramatec also developed a new fabrication technique in 2009. Figure 17-19 shows a base piece and prototype module produced with the new technique. The new architecture and fabrication method produced significantly more robust parts and lowered manufacturing costs.

Figure 17-19. Base piece and prototype module produced with new fabrication technique.

End Cap

Development of a domed end cap began in 2009. In Q3-2009, fifteen domed end caps were produced and a rough fabrication process was developed. Figure 17-20 shows the prototype end cap.

Figure 17-20. Prototype domed end cap.

The manufacturing technique was refined in Q4-2009 resulting in a more robust outer skin on the end cap. Figure 17-21 shows a sample domed end cap made with the new technique compared to an end cap made in the previous quarter.

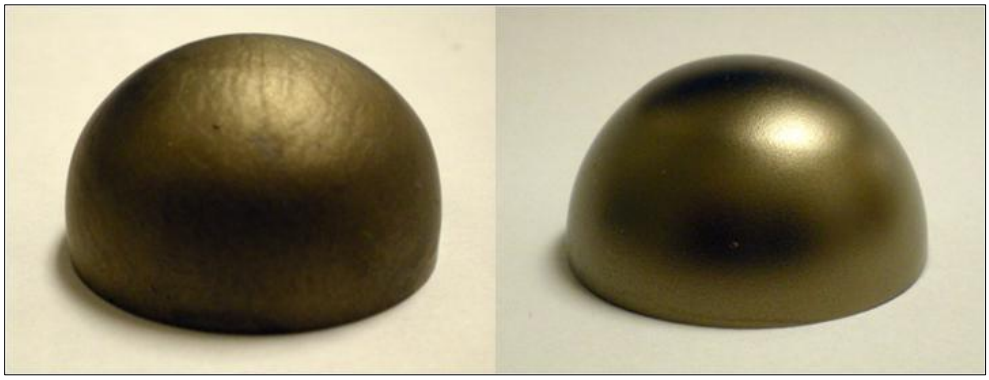

Figure 17-21. Q3-2009 prototype domed end cap (left) and Q4-2009 prototype.

Twelve end caps were produced using the new procedure during Q4-2009. All of the end caps had low leak rates, and one achieved hermeticity (10^{-5} sccm with a helium leak test).

Samples were thermally cycled in air to determine critical heating rates. One sample was subjected to fast cooling. One sample that was bubble checked had only a single small bubble source, indicating very good leak tightness. Another sample was heated to operating temperature at a rate of 1,000°C per hour. The end cap survived intact. This marked a record heating rate for any part composed of ITM ceramic and is much faster than would be encountered in use.

Air Products subjected an end cap to a series of conditions to create stresses in the part and to measure the effects of those stresses. A domed end cap was tested in the fluX Verification Units

(XVUs). The part was heated in air to ISTU conditions and held at steady state conditions for four days.

After the 4-day hold, the part was put through a series of progressively more aggressive P_{O2} transients. The end cap was subjected to seven conditions of increasingly severe compressive stress as shown in Figure 17-22 (trial numbers 1-7). The last six significantly exceed the stresses expected during normal operation. Compressive stress would be expected if the ISTU vessel was rapidly depressurized following the opening of a relief valve. The end cap was then subjected to a series of rapid transients by manipulating the oxygen partial pressure around the part that put the end cap into tension (trial numbers 8-14).

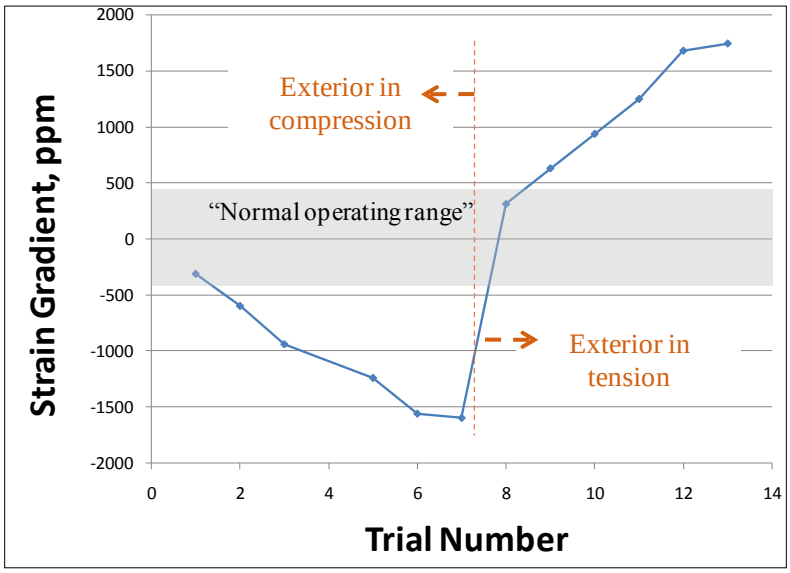

Figure 17-22. Strain gradient applied between the outside and inside of a domed end cap at operating temperature in rapid transients.

The end cap suffered no damage. This result confirmed that the new architecture and manufacturing methods produce much stronger parts.

Joining Yield

Wafer Flatness

The flatness of the surfaces that are mated together to form the joint is a critical parameter. Ceramatec used a laser profilometer to compare the flatness of the joining surface of sintered wafers with and without the use of weights. Figure 17-22 plots the profiles of wafers without an applied weight; Figure 17-23 are the profiles with weight. The x-axis is the azimuthal position

around the wafer in 10^{o} increments for eight ring scans around the periphery of the sealing region. The weighted wafer was substantially flatter.

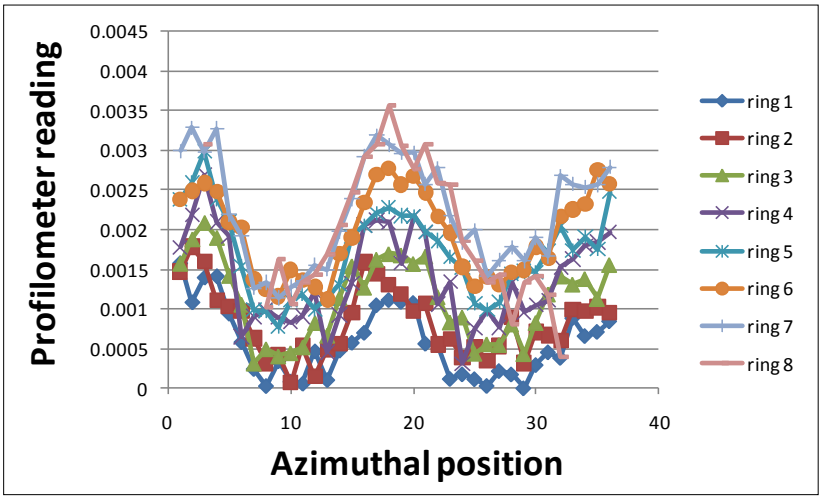

Figure 17-22. Surface flatness of a wafer without an applied weight.

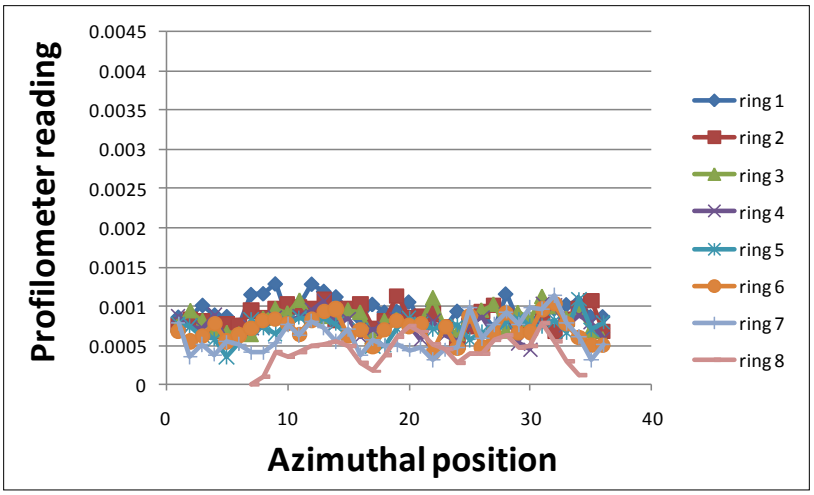

Figure 17-23. Surface flatness of a wafer with an applied weight.

Parallelism

The impact of a wider joining material and preheat on the parallelism of sub modules was conducted in Q2-2010 (Figure 17-24). It was concluded that preheat does not impact parallelism, and that a wider joining material may reduce "out of parallel."

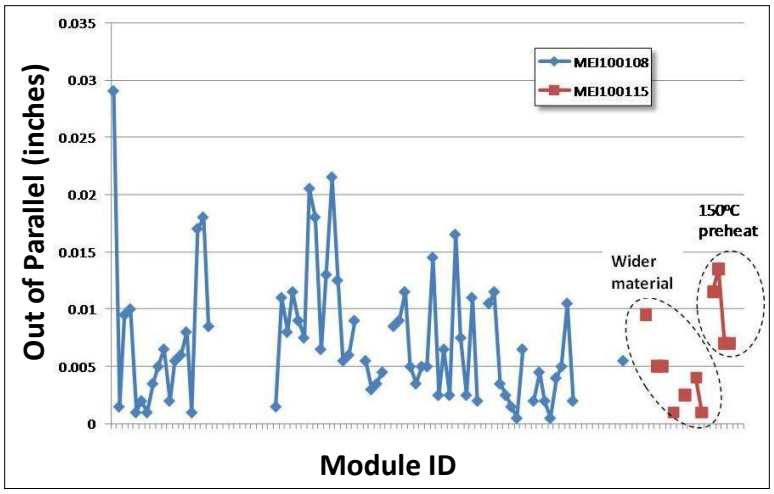

Figure 17-24. Submodule out-of-parallelism measurements.

Module Alignment

In 2010, a new procedure for module assembly and joining was developed that produced straighter modules. Following are the differences between the original and new procedure:

- The module was joined in an alternative joining kiln.
- The module was aligned from the center rather than from the outside.
- The module was assembled using a combination of parts stacked in alternating series.
- The module was thermally cycled to a moderate temperature and back to ambient; the fixture was then changed, and the module was cycled through the full joining cycle.

The alignment data for a module fabricated with the new procedure is shown in Figure 17-25. The alignment data shows the location of wafer edges relative to a target location going up the module. The alignment was substantially better.

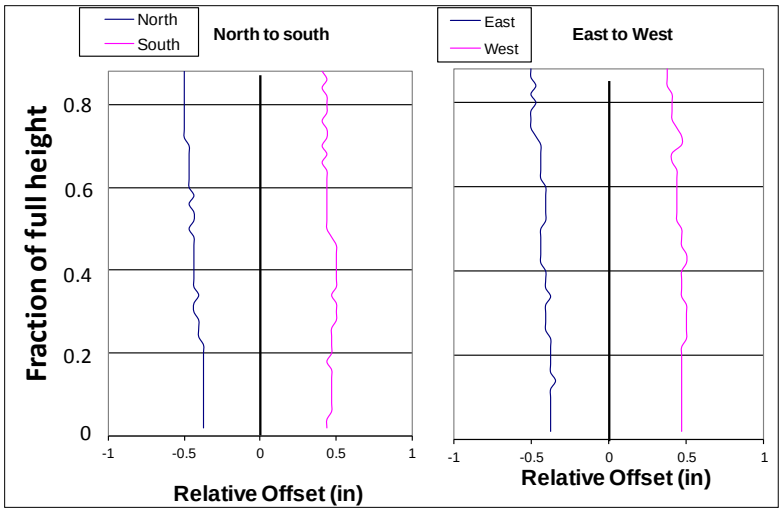

Figure 17-25. Vertical alignment of a module assembled using newly developed procedures.

Additional tests were conducted in another furnace. Two sets of the new alignment furniture were constructed and used to join two modules. Two additional modules were built using the old furniture and loading setup to compare the new joining technique. All four modules were joined using the center-alignment approach. Each module was built and loaded using slightly different conditions to understand the effects of several variables. The conditions and results were as follows:

- Module #1 was built and loaded using the new alignment furniture, the thermally pre-cycled. This module had the best alignment to that date.
- Module #3 was also built and loaded using the new alignment furniture, but was not thermally pre-cycled. This module had a lean of ~0.3" before the module started its joining cycle.
- Module #4 was built and loaded without the new furniture using some baseline methods. The module was built according to the center-alignment approach. The module was remarkably straight compared to modules built with the old tooling.
- Module #2 was built identically to Module #4, but with intentional misalignment by ~1 cm from center. The intent was to re-create a "stepped" module joined previously and hypothesized so due to misalignment. The module was bowed, not stepped.

The results of these experiments were extremely promising. Even the modules loaded by the old method (i.e., not using the new alignment furniture), were much straighter and more aligned than

almost all of the previous modules. The new center-alignment approach clearly led to straighter modules.

Additional runs were conducted to assess the benefits of thermally pre-cycling the modules. Figure 17-26 compares a pre-cycled and non-pre-cycled module and clearly shows the advantage of pre-cycling.

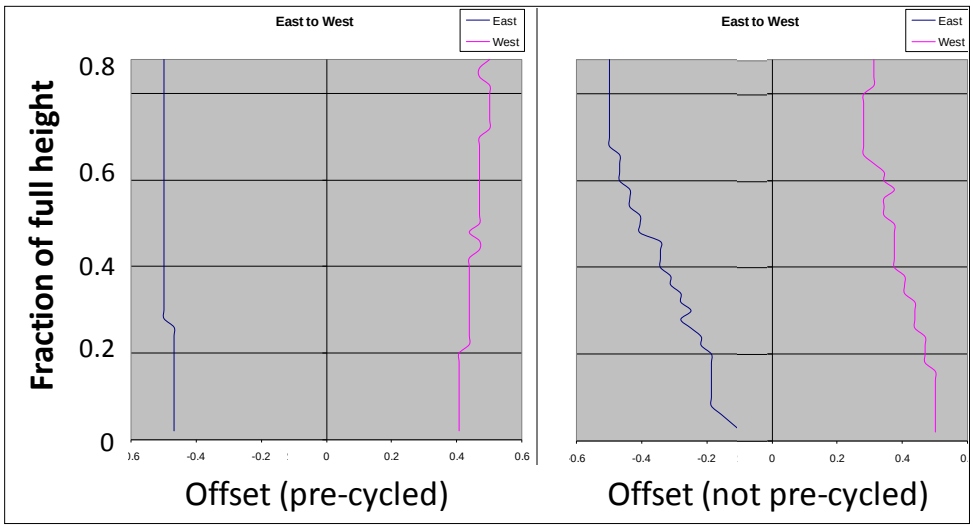

Figure 17-26. Module alignment built with the new alignment approach and pre-cycled (left), and not pre-cycled (right).

In Q2-2013, equipment to be used at Cerfab to ensure module alignment was installed and tested. Eight modules were successfully joined. The module alignments were consistent with previous modules built with the alignment procedure.

Module Conditioning

Air Products and Ceramatec investigated module production strategies that support module testing in the Intermediate-Scale Test Unit (ISTU). The ISTU is likely to be run in campaigns, with interruptions between test campaigns to add modules. One complication with the addition of modules is that the heat-up cycle is tailored to the ceramic modules previously cooled in the vessel. This may cause different stresses in the newly added modules, which have a different oxygen content characteristic associated with their fabrication history.

Air Products conducted experiments to address this potential. Two air-cooled "flat" end caps were subjected to an iso-controlled heating cycle and then cooled with the iso-control technique. Figures 17-27 plots the oxygen partial pressures during the heating part of the cycle.

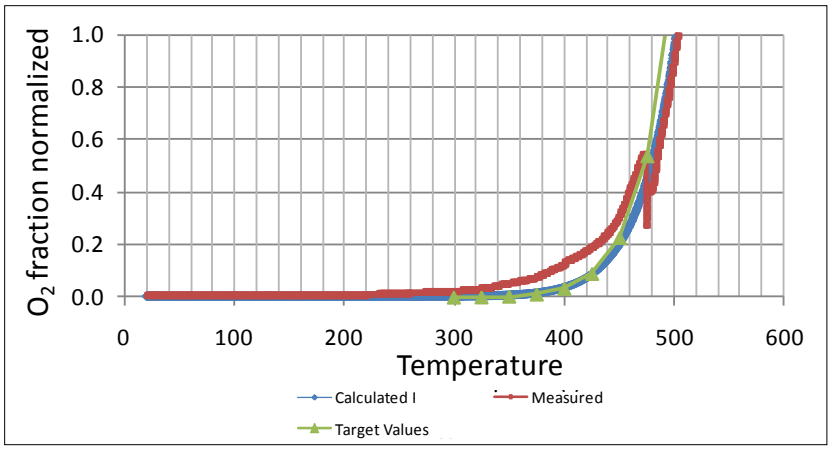

Figure 17-27. Calculated, measured and target P_{O2} during heating.

The blip in the measured P_{O2} at 480°C was due to the switch between two air mass flow controllers. The measured values slightly led the target values at lower temperatures, and slightly lagged the target after switching to a different flow controller. There was no visible damage to the parts.

Cooling experiment was conducted using bend bars. The bend bars were heated in air to operating temperature and then cooled with iso-control techniques to ambient temperature. The iso-controlled bars were stronger than air-cooled bars.

Module Shipping and Handling

Ceramatec developed shipping containers which support the modules and isolates them from forces encountered during shipping by commercial carrier. The original containers were large, with only one module per pallet, and required transfer into a separate installation fixture. Each transfer requires time and risked damage to the module. Additional work resulted in a streamlined container that can fit four modules to a standard pallet and be shipped by commercial carrier. The container can be partially disassembled and then used for installation as a subassembly.

During development, tests were done on a shaker table to characterize the resonant frequency and test the level of damping done by the shipping structure. Figure 17-28 is a photograph of the shaker table.

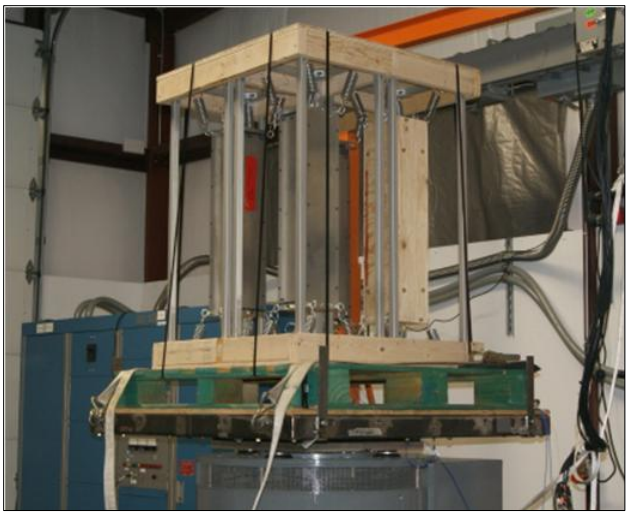

Figure 17-28. Shaker table testing of simulated modules.

In Q2-2010, two modules were shipped, unpacked and loaded into the SEP for run 16. Module 1 was shipped using a new shipping/loading fixture; Module 2 was shipped using a modified shipping/loading fixture that allowed for tighter tolerances without weakening the support (Figure 17-29).

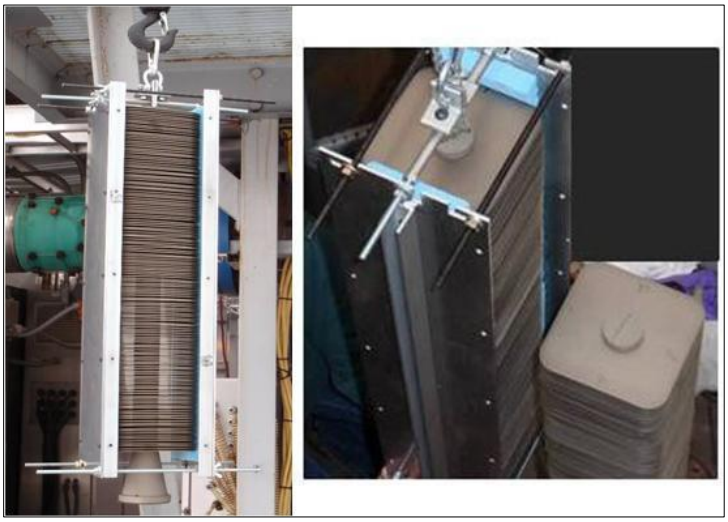

Figure 17-29. Module 1 (left) being lifted into the SEP and Module 2 (right) showing the new side supported fixture.

Accelerometers were attached to containment boxes, and modules were shipped to the SEP in Q3-2014. All six modules were shipped in "Gen. 3.0" containment boxes. The modules arrived in Convent (ISTU site) with leak rates comparable to starting leak rates. Five accelerometers were used, one on each of four modules (including one dummy module) and one mounted on one

of the containment boxes. The recorded accelerations of the four module holders were comparable. Acceleration data for one of the modules and the containment box are shown in Figure 17-30 (vertical direction) and Figure 17-31 (lateral direction).

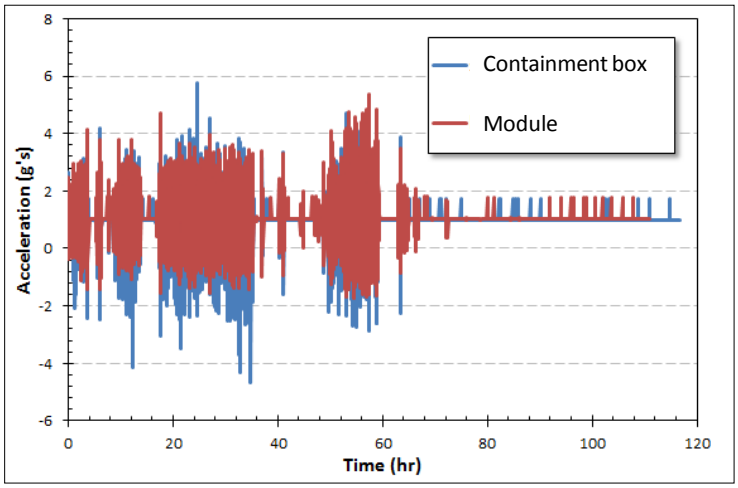

Figure 17-30. Accelerometer data for a module and containment box – vertical.

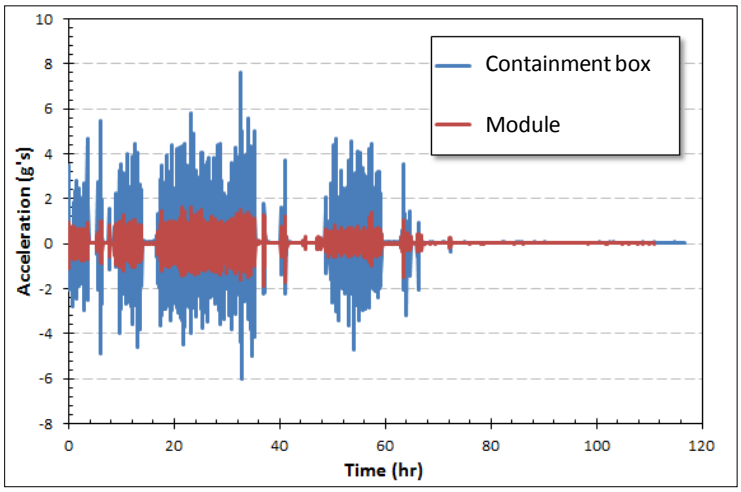

Figure 17-31. Accelerometer data for a module and containment box – lateral.

The forces on the module were more effectively dampened in the lateral direction with the current containment box design. All measured forces were within the allowable levels for safe module shipping.

Ten Version 3.1 module shipping holders were fabricated in Q4-2014 and an additional 40 module holders were ordered. Ceramatec successfully shipped numerous modules to Convent, Louisiana, for testing under Task 20.

Advanced Architecture Wafer Modules

Development of Advanced Architecture Wafer Modules began in 2011.

Finite element analysis (FEA) was used to determine optimum module architectures that would minimize stresses that arise in the structures during operation. In addition to conventional mechanical stress generated by pressure, hydrodynamic flow, gravity, etc., ITM Oxygen materials are susceptible to stresses created by mismatched chemical expansion within the material due to oxygen concentration gradients caused by mass transport limitations. An assumption was made that the greatest overall reliability would be provided by designing structures that evolve minimal stress during unplanned shutdown transients. Although these structures may or may not be optimally designed for start-up conditions, these conditions can be controlled to minimize stress evolution. Controlled start-up and cycling have been demonstrated repeatedly at the Subscale Engineering Prototype (SEP).

Ceramatec provided a FEA-driven analysis that indicated that advanced structures that minimize oxygen concentration gradients experience the lowest stresses during unplanned cooldown scenarios. An illustration of this is shown in Figure 17-32, where the stresses experienced by a 5-wafer module during a typical cycle in the SEP facility are compared for standard and advanced-model architectures.

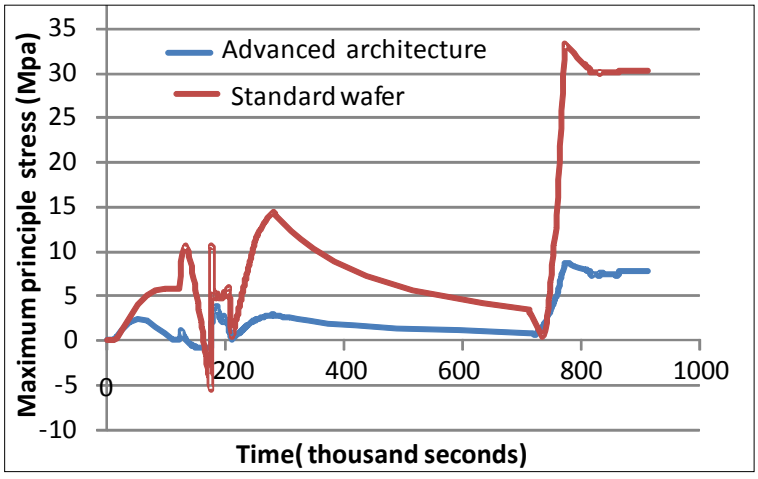

Figure 17-32. Comparison of stresses in standard and advanced modules during an operational cycle.

At the time these results were generated, processing methods for fabricating the advanced components required for ITM Oxygen modules were not practiced at Ceramatec. Subsequently,

a method was developed under this Task to make module structural components that met the requirements of sufficiently low leak rates to be used in modules. Ceramatec utilized the results of the FEA-driven analysis and advanced architecture component performance to guide development of improved components for ITM Oxygen modules. Ceramatec conducted work on wafer, submodule, and module components to reduce module cost, increase module performance, and increase module durability based primarily on advanced architecture designs.

Based on the approaches used to fabricate structural components for ITM modules, similar processes were applied to the fabrication of advanced architecture wafers. There are many similarities between fabricating a standard wafer and an advanced architecture wafer, as well as a few subtle differences. For example, both wafer types involve producing ITM powder by solid-state reaction of precursors, followed by particle size reduction processes to obtain particles capable of densifying via solid-state diffusion (sintering).

The forming methods used for both wafers are identical: tape casting, tape featuring, and lamination. Two parallel approaches for applying the membrane layer to advanced architecture wafers were investigated, one in which the membrane is applied as a single layer (single application), and another in which the membrane is first applied to other layers and then applied to the balance of the wafer. After wafer fabrication, the methods of building submodules and modules from advanced architecture wafers are the same as has been practiced for standard components.

Due to the ability of the advanced architecture components to equilibrate more rapidly with the surrounding environment, much lower stresses are induced in these types of structures due to oxygen concentration gradients within the material. Subsequently, the durability of components made with the advanced architecture is anticipated to be greater than components made with the standard architectures. This durability was also expected to manifest in higher production yields that reduce manufacturing costs and in a broadening of the allowable operating conditions, which improve performance. Another large advantage of this architecture and the fast equilibration times is that modules can be thermally cycled successfully without iso-control.

In the initial work, the submodules appeared to produce good joints, but five of the six assemblies cracked the bottom wafer upon processing. A large dome-shaped warp around the

center hole of the spacerless wafers developed upon processing. A set of wafers was profiled. Figures 17-33 is an example profile.

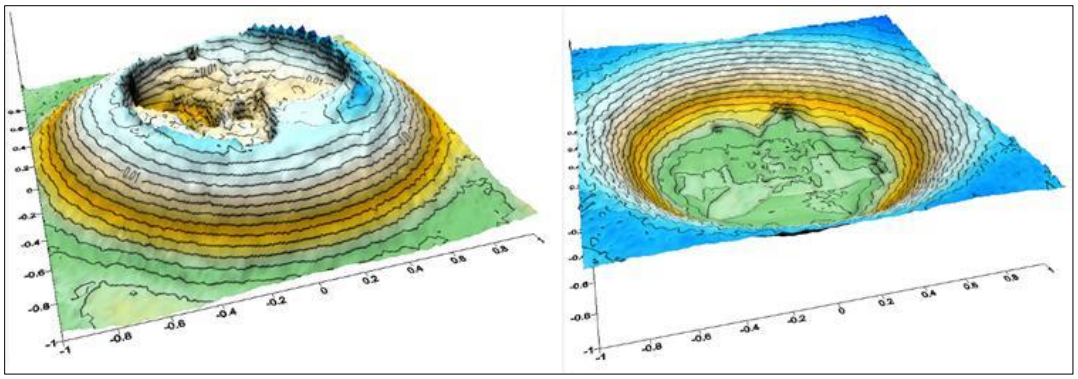

Figure 17-33. Flatness profile of the center region of an advanced architecture wafer (AAW) both top and bottom of the wafer.

The joining surfaces were warped. This distortion appeared to be caused by plastic deformation of the wafer in the green state during processing. It was expected that this warping was the primary cause of the wafer cracking during joining. These results demonstrated that the joining surface of the wafers needed to be flatter to successfully join submodules and modules.

Both domes and base pieces were produced using with a slightly altered fabrication method. The primary difference is in processing of the outer skin. Ceramatec altered the slip preparation, which enabled 18 domes and 10 base pieces to be fabricated in Q1-2012.

17.3 Optimization of the Ceramic Process Development Facility (PDF)

Background

The production capacity of the ceramic process development facility (PDF) was expanded five fold over the course of the program. Equipment was procured and processing conditions optimized for several steps including a large scale tape caster, a punch for layer featuring, laser improvements for layer featuring, several larger-scale kilns for wafer and module processing, and tools and fixtures to improve module alignment. The expansion included three new processing kilns, each having twice the capacity of the largest existing kiln.

In Q3-2009, Ceramatec commissioned a wafer assembly machine (WAM) that laminates green parts automatically. The WAM laminates multiple wafers simultaneously. Several lamination techniques were combined to apply uniform pressure while compressing the wafer layers.

Powder Processing

Calcining

In Q3-2009, Ceramatec modified the kiln architecture to improve powder handling for bigger batch sizes and to reduce contamination of the powder. The results were excellent. During the quarter, 50 thermal cycles were conducted without contaminating the ITM materials.

Milling

In Q3-2009, Ceramatec produced 200 wafers using a scalable milling method. The leak rates from these wafers met or exceeded specifications for production of 99.5% oxygen, and exceeded the yield of the existing milling methods.

Control of powder particle size distribution (PSD) is required to ensure quality parts. A number of milling machines were tested. Figure 17-34 is an example plot of the PSD of one of the tested machines. The difference curves are associated with specific process parameters including time, surfactant type, amount of powder and media type.

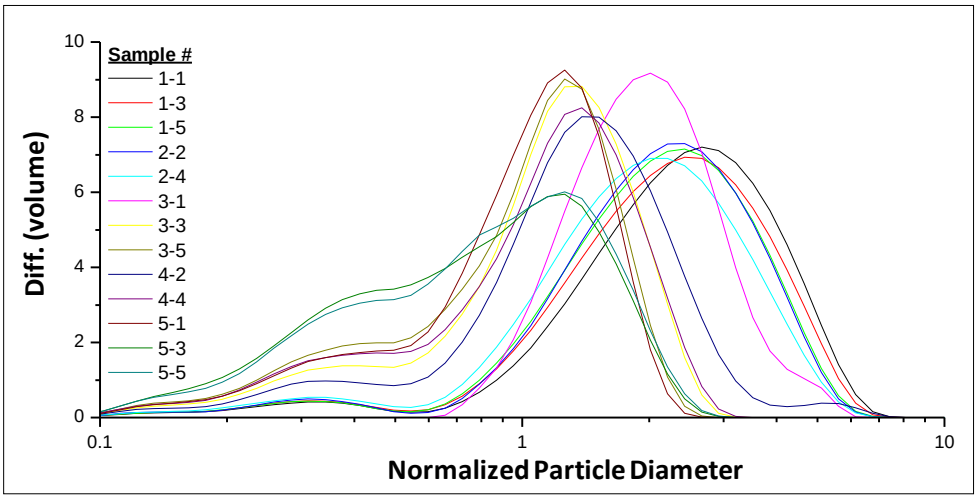

Figure 17-34. PSD results from the high surface mill.

Figure 17-35 compares the suspension PSD made for different mills. The PSDs were very similar.

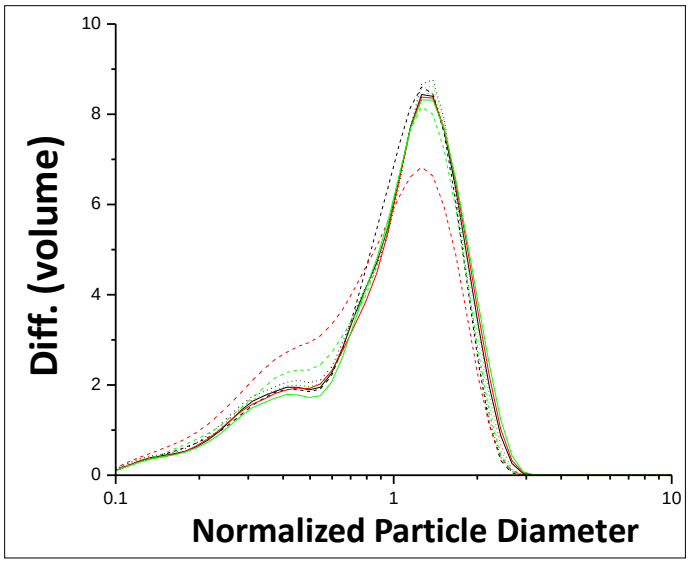

Figure 17-35. Suspension PSDs for different mills.

Slip Preparation

Ceramatec qualified scaled-up slip preparation equipment during this Task. The slip is slurry of ceramic particles, liquids, and the polymeric binder system used to make the cast tape. Slip preparation requires appropriate ceramic powder preparation and intimate mixing of the powder with the liquid/binder phase so that uniform tapes can be cast. Scaled-up equipment was required to meet the overall Phase III requirements for wafers and modules. A process was developed that combines powder milling with solvent/binder mixing.

During Q4-2009, Ceramatec produced lots of wafers from slip prepared using the scaled-up equipment. The yield of wafers from these lots was statistically indistinguishable from that of the standard process, indicating that the scaled-up process was able to produce acceptable slip. The density of dense and porous control parts was monitored. Density of the dense parts met or exceeded targets, while the porosity of the porous parts fell below the target range. The porous particle size distribution was adjusted to meet the control target.

Tape Casting

Quality Control

Ceramatec continuously monitored tape yield. Figures 17-36 is an example showing the yield of porous layer tape after sectioning into “tiles” or groups of individual tape layers cut prior to lamination.

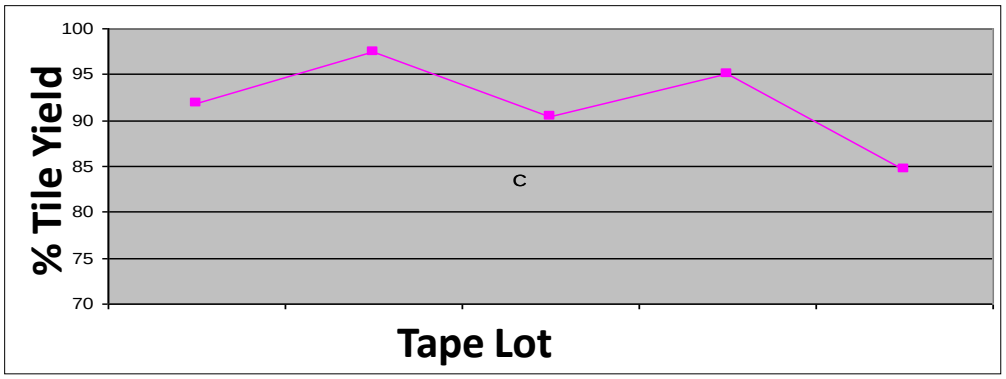

Figure 17-36. Yield of cast porous tape after sectioning into tiles by lot number.

The yield data for these five lots ranged from 85-97%. These high yields are indicative of a well-controlled process that stays in control at high throughput.

The physical properties of the tape are critical for the featuring process and subsequent lamination step. A variety of parameters affect tape properties. Ceramatec varied powder morphology and loading and casting parameters in a number of studies to optimize tape properties. In one study, multiple casts were made on a developmental tape caster at various tape thicknesses. All tapes were successfully cast. The stress-strain behavior was measured and compared to a reference tape lot. The results are shown in Figure 17-37.

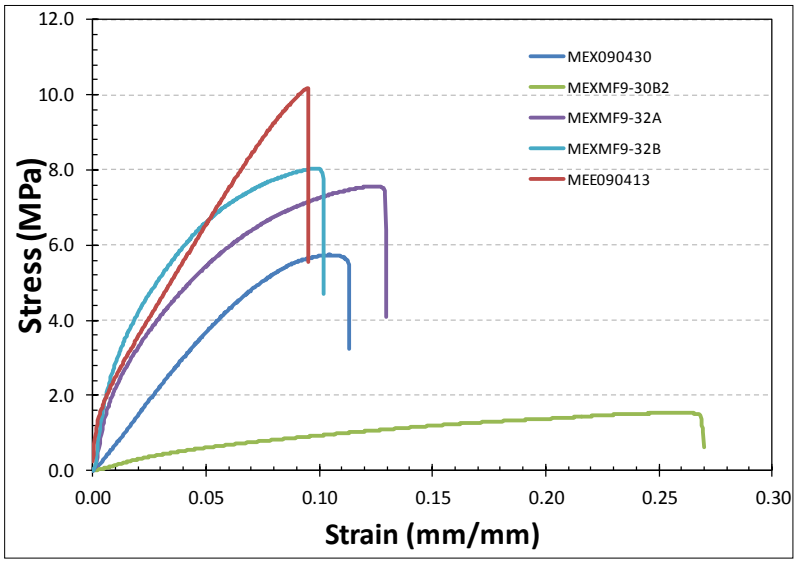

Figure 17-37. Stress-strain of different porous tapes compared with a reference tape.

The first tape cast (green line) was much weaker than the baseline. Reformulating the tapes by changing powder properties resulted in the family of blue and purple lines. The new tapes approach the strength of the reference tape (red line).

Additional work was conducted in Q1-2010. Figure 17-38 documents the results.

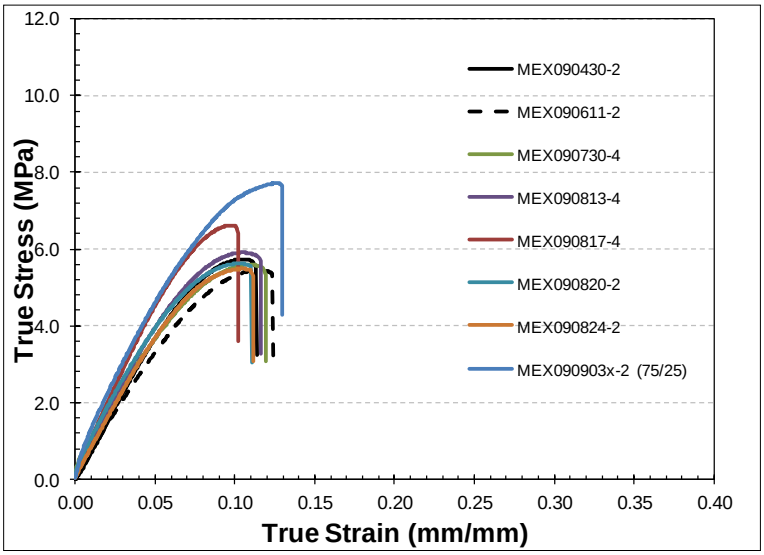

Figure 17-38. Stress-Strain of tapes produced in Q1-2010.

A new caster was installed in Q2-2012 and a new formulation for thick tapes was tested on the new equipment. Two small-scale batches were mixed and cast. The tape from these casts featured well. The mechanical properties were such that featured parts were not damaged by routine handling.

Featuring/Lamination

Earlier work provided the basis for specifying and then building a wafer assembly machine (WAM) which is shown in Figure 17-39.

Figure 17-39. Wafer assembly machine (WAM).

A requirement for Phase III of the ITM Oxygen Program was to develop the processes and machinery to be used for final production manufacturing of the wafers. The original method of assembling the ITM Oxygen wafers was very manual and labor-intensive. The assembly process relied on operator verification for quality control of all processes. Assuming that automation would reduce future manufacturing costs and that wafer assembly and lamination were the most labor-intensive processes in module production, evaluation of the practicality of automating these processes was conducted. A non-proprietary process flow sheet was developed, and processing parameters were specified. This flow sheet and parameters were provided to custom, automated equipment manufacturers who proposed various designs in a competitive process. The result was procurement of an automated WAM that was tested under this Task.

The automated WAM was designed so that ITM Oxygen wafers can be assembled on the machine with a minimal amount of time and effort. This machine is also able to produce spacer assemblies. The machine retrieves the different ceramic layers from preloaded cartridges and prepare them for the assembly process. The WAM thoroughly cleans the layers prior to any assembly activity. After cleaning, the layers are then positioned into either various dies or application for subsequent lamination processes.

In the case of the porous layer assemblies, the WAM peels substrate from the in-process assemblies. After layers are laminated, the WAM then punches registration holes in the assemblies for positioning on subsequent fixtures.

The WAM runs in a “batch” mode, wherein one type of assembly will be processed for an extended period of time before changing over to another type of process. Thus, different parts of the full wafer are assembled at different times and must be stockpiled.

To do this, the machine must be able to retrieve appropriate parts from cartridges, clean the individual layers, prepare the layers, stack the layers in the correct configuration and laminate the components together into a single wafer or subassembly. After assembly, the machine vision system inspects component parts. If a nonconforming part is found, the part is sent to the reject bin of the machine and a message is displayed on the HMI to alert the operator of the reason for failure.

Three wafer lots were made using laminations built on the WAM. Control wafers were made from laminations using the baseline process. All three qualification wafer lots showed no statistical difference between control and experimental wafers with respect to leak rates (Figure 17-40).

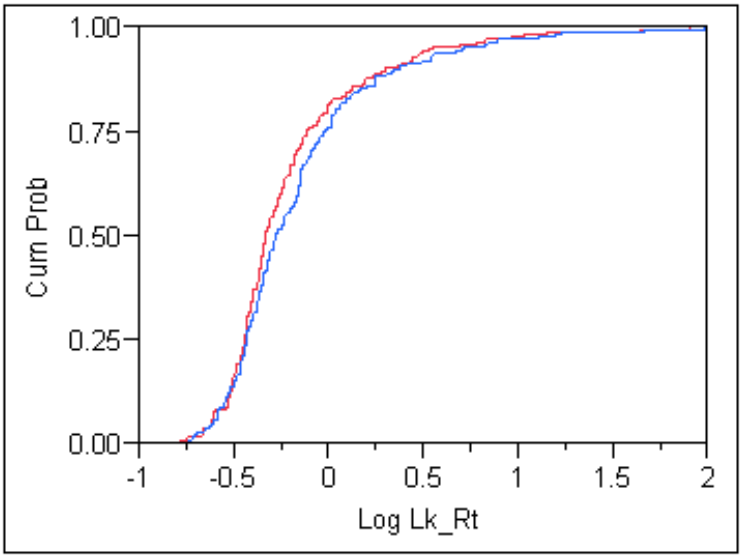

Figure 17-40. Distribution of leak rates for experimental wafer lots built with WAM laminates compared to control wafer lots.

Valuable lessons were learned from using the WAM under this Task. The first was that automated tooling could greatly improve productivity, with process yields equivalent to manual yields. The specific design of the WAM was never able to meet the Takt time specifications provided to the equipment vendors. This was due to attempting to integrate too many individual

processes with disparate cycle times. Therefore, bottlenecks occurred in the machine that were incompatible with ideal process times. Therefore, during specification of the CerFab tools in Phase V (Task 30), lamination steps were semi-automated and separated from the solvent application and inspection processes. The second lesson learned from use of the WAM was that it had limited capability for adapting to continuous process improvements and design changes. Even in Task 17 alone, enough process improvement and changes occurred that many of the later wafers were made entirely by hand. Therefore, processes known to be the least mature were subject to the least automation when specifying the CerFab tools under Task 30.

Sintering

Kiln/Furnace Performance

Process control temperature rings (PCTR) were used to establish the temperature non-uniformity and thermal history of the furnace inventory during sintering runs. The PCTR sinters linearly with time at temperature. Measurements of the ring dimensions made before and after a kiln run correlates with temperature and time. Figure 17-40 is an example of the temperature data derived from the PCTRs.

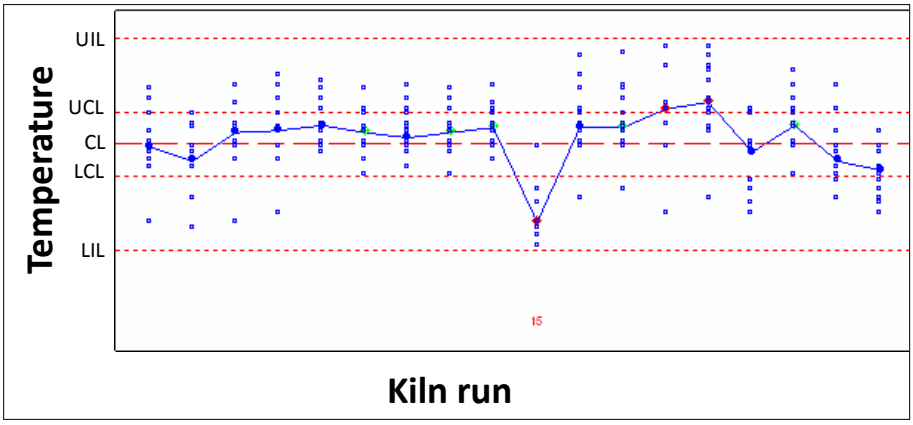

Figure 17-41. Temperature data from PTCRs plotted for several kiln runs.

Ceramatec qualified one of the large sintering kilns in Q3-2009. Qualification was made based on three separate sintering lots of progressively larger size. Leak rate and temperature uniformity data from these lots were significantly better than the existing kilns, which are smaller by a factor of two. Figure 17-42 is a plot of the temperature profile standard deviation in the kiln measured by process temperature control rings for several kiln runs.

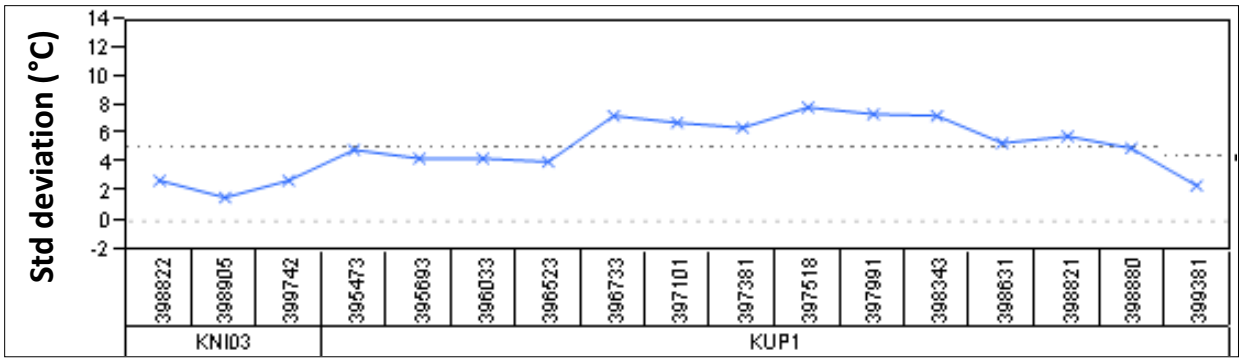

Figure 17-42. Kiln temperature profile standard deviation.

The three data points that fall under the KN103 label are the temperature data for the new (larger) kiln, while those under KUP1 are the temperature spreads in the older (small) kilns. As can be seen by examining Figure 17-42, the standard deviation, the new kiln had a considerably tighter temperature band indicating better uniformity.

A study was conducted in Q3-2010 to statistically determine the dependence of wafer thermal cyclability (leak rate stability over multiple thermal cycles) on kiln operating conditions, placement in the kiln, joining loads, wafer slot pattern, the presence or absence of spacers and the spacer design. Wafers with Slot Pattern #1 and Slot Pattern #2 were evaluated.

Wafers were assembled into multi-wafer stacks. A compliant material was used instead of a ceramic-ceramic seal material during the loading process. In this way, the wafer could be re-inspected for leak rate and damage. Figures 17-43 and 17-44 illustrate the wafer design population, as well as the positioning populations within the kiln.

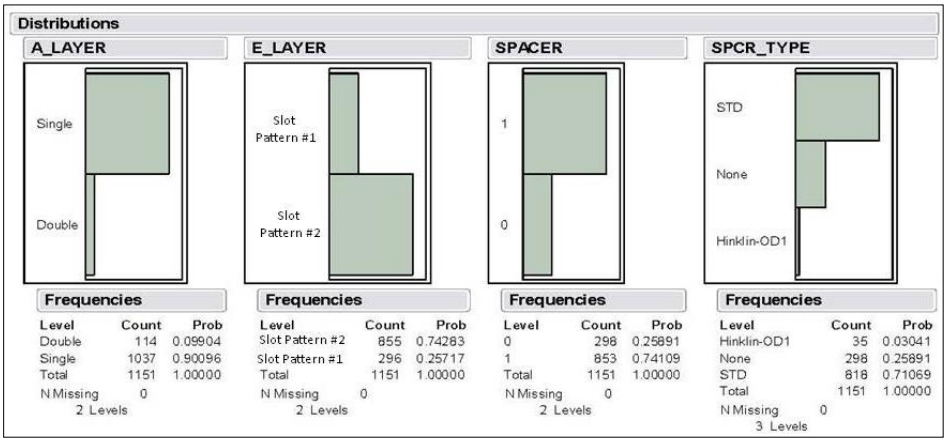

Figure 17-43. Distribution of wafer design population. SPACER =0/1 is binary, 0=Spacerless and 1=Spacer Present.

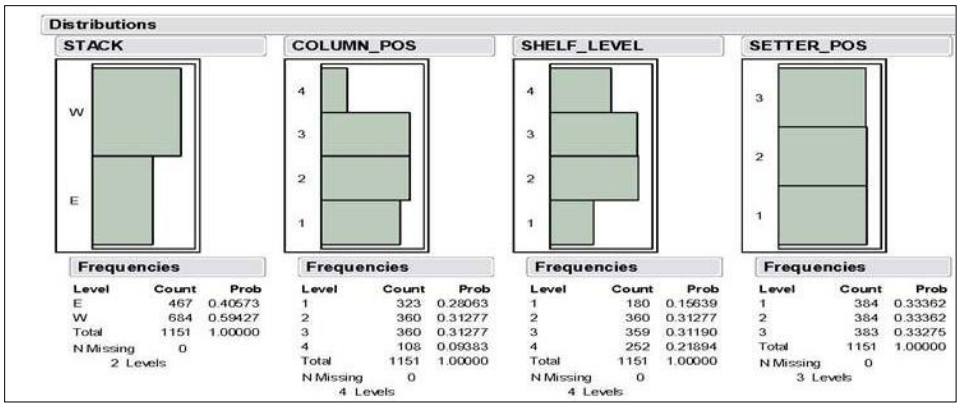

Figure 17-44. Distribution of wafers within joining kiln KNI03 over the five runs.

Approximately 1,150 tests were conducted by varying the wafer design and kiln position. Two primary metrics were used in analyzing the data. The first was whether the wafer had broken or cracked after thermal cycling, and the second was the change in leak rate. The change in leak rate was based on a leak rate grouping number from 1-7. The lower the grouping number change (difference), the more cyclable the wafer. A broken wafer had a leak rate grouping of seven.

The data analysis was presented as a mosaic plot along with the statistics. The mosaic plot was based on leak rate grouping number change. This is the change in grouping number from the starting point (after wafer sintering, typically "1") to the designation after the submodule thermal cycle. Figure 17-45 is an example.

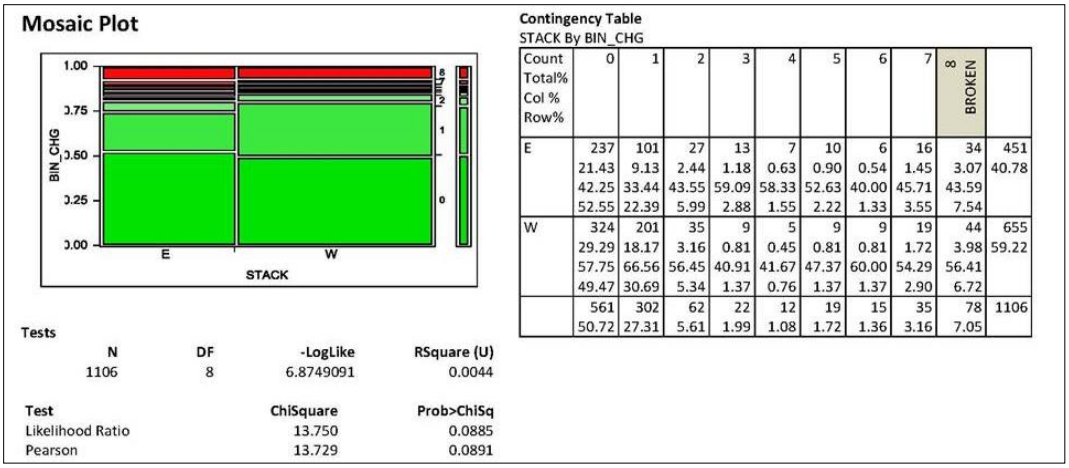

Figure 17-45. Contingency analysis of leak rate grouping number change (leak rate stability) by STACK position within the kiln. 8 = BROKEN.

The left axis indicated the probability of being in a particular grouping number range (height of the colored bar). The right axis indicates the grouping number, 0 - 8. A value of eight means that a crack was observed in the wafer, whereas a large change in leak rate (7) means the wafer was still intact.

The study conclusions were:

- Stack, column, and position in the local arrangement were not statistically significant.
- Column position was not statistically significant.
- Submodule positioning within loading arrangement was not statistically significant.
- Kiln shelf level was statistically significant.
- Slot pattern design was statistically significant.
- Spacer presence and design (STD, New) were statistically significant.

Slot Pattern #1 had significantly improved leak rate stability compared to Slot Pattern #2 wafers. There was no statistical difference between a revised spacer design and the standard spacer design. The data showed that the furnace was very uniform in terms of thermal process operation.

Setter Thermal Cycle Reduction

Ceramatec optimized the thermal cycle times used to fabricate the setter plates that support the wafers during sintering. Techniques previously used to reduce the thermal cycle time for wafers were applied to the setter. The constant weight-loss mode of the thermo-gravimetric analysis (TGA) system was used to guide the cycle time adjustment. The TGA measures the mass of a sample as it is heated; the constant weight-loss mode is a control technique in which the temperature is controlled based on the mass loss rather than the time. Results from a constant weight loss experiment for the standard setter material is shown in Figure 17-46.

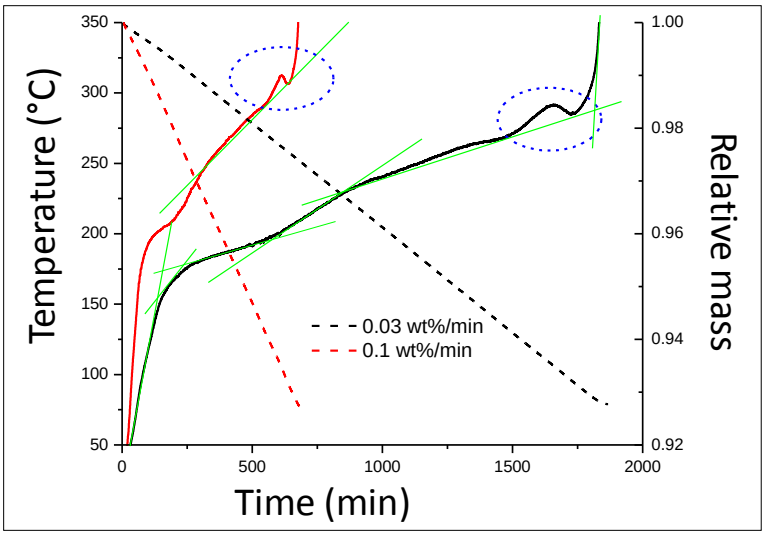

Figure 17-46. Setter powder constant weight-loss for two weight loss rates showing approximated segments (green lines) and exothermic final burnout step (blue circle).

While it is impractical to use the time-temperature profile established by the TGA in an actual kiln, the profile can be converted to a useful temperature-time schedule by approximating the curve to less than a half-dozen linear segments (shown in green in the Figure 17-46). The resulting temperature and binder burnout profiles are shown in Figures 17-47 and 17-48 respectively.

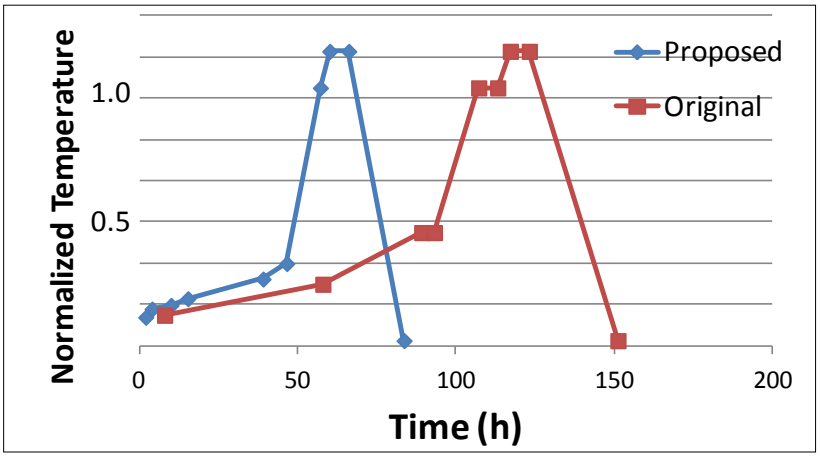

Figure 17-47. Comparison of original and modified thermal cycles for setter sintering.

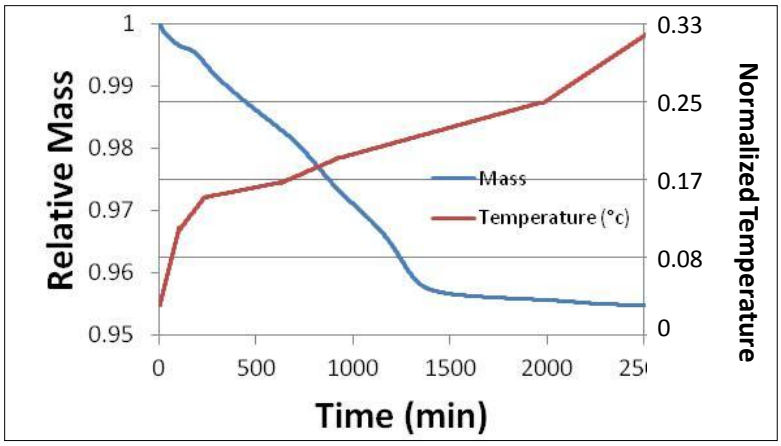

Figure 17-48. Binder burnout based on segmented constant weight loss thermal cycle.

Submodule Fabrication

Construction

In Q3-2009, Ceramatec completed a study of submodule construction techniques. Various building methods were evaluated in an effort to improve the quality of the ceramic to ceramic joint. A total of 272 submodules were manufactured containing various combinations of processing factors. Yield and submodule quality were tracked. The ceramic-to-ceramic seal type showed a statistical significance from the control group.

Joining Cycle

Standard sub modules and modules were joined using various joining cycles (Figure 17-49) to determine yields that could be achieved at extended cycle times.

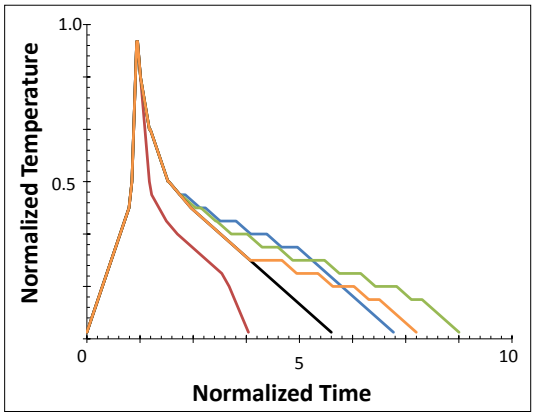

Figure 17-49. Thermal profiles.

The results are documented in Table 17-2.

Table 17-2. Sub-module yields for cooling profiles.

	Yields				
Profile Furnace	**xA**	**xA-xB**	**Testable**	**Cracking**	**Notes**
zA KLL1	14/24 (58.3%)	21/24 (87.5%)	22/24 (91.7%)	2 radial cracks	
	20/24 (83.3%)	22/24 (91.7%)	24/24 (100%)	none	2 power interruptions
C KLL2	27/36 (75.0%)	31/36 (86.1%)	32/36 (88.9%)	3 radial, 5 corner, 1 other	
	8/12 (66.7%)	9/12 (75.0%)	9/12 (75.0%)	1 radial, 2 other	
D KLL1	23/24 (95.8%)	23/24 (95.8%)	24/24 (100%)	none	
	8/12 (66.7%)	10/12 (83.3%)	10/12 (83.3%)	2 radial cracks	
	7/12 (58.3%)	11/12 (91.7%)	11/12 (91.7%)	1 radial crack	

The data confirmed that yields of both submodules and modules could be improved significantly by slowing the cooling rates. Four modules were joined using the Profile B joining cycle (Figure 17-48). Only one of the modules showed signs of a crack. The remaining three showed very good leak rates.

17.4 Ceramic Process Engineering and Economic Evaluation

Ceramatec assessed various pathways for manufacturing ITM membrane modules based on the scale of manufacture and specific processing techniques that could be deployed based on development progress. The starting point for the process design was the PDF.

All basic process designs that were considered included the tape casting/lamination approach to wafer fabrication. Estimates were made for process yields and equipment scale in the areas of powder processing, slip preparation, tape casting, featuring, lamination, sintering, and joining. A time management study was used to evaluate the requirements for automation of each of the steps and as a function of scale of manufacture. Process information from the Wafer Assembly Machine (WAM) was used in the estimate of lamination processing. A scale-up strategy for milling and slip preparation was developed based on data from the PDF.

Ceramatec specifically addressed advances in technology in thermal processing and wafer design to enable specific manufacturing pathways. For production of the standard wafer design, concepts were developed for the use of atmosphere-controlled kilns for thermal processing to sinter and join wafers. Information obtained from kiln suppliers during the procurement of a large-wafer sintering kiln and submodule joining kilns for the PDF was used in the analysis. Atmosphere control requires a heated, flowing air stream to effect good mass transfer with and uniform heating of the ceramic part, while also enabling concentration changes in the flowing gas. Semi-batch equipment-based processes were envisioned with shorter thermal cycles than were in operation with the standard wafers in the PDF. Figure 17-50 is a plot of the relative thermal processing time required for joining modules in the three cases: the baseline (PDF), a conventional semi-batch method based on shorter cycles with advanced architecture structures, and the approach based on atmospheric control and standard architecture.

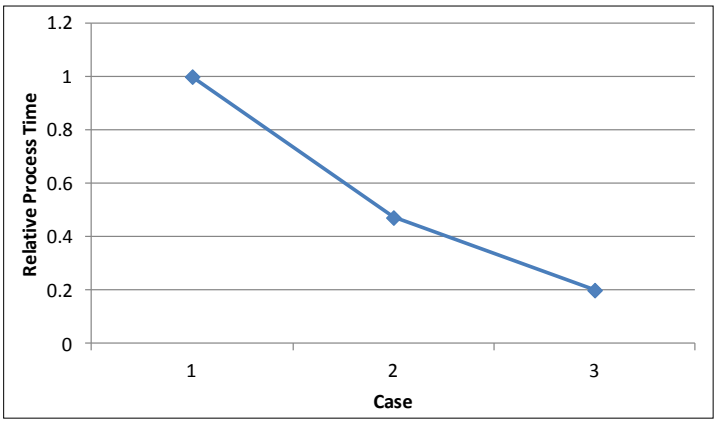

Figure 17-50. Relative thermal process time for three cases: 1) baseline; 2) advanced architecture; 3) baseline with atmospheric control.

For the advanced architecture wafers and modules, Ceramatec also evaluated processes based on tunnel kilns. A model was developed that calculated the size and throughput of associated thermal processing steps based on tunnel kiln technology. Tunnel kilns afford a continuous sintering/joining process and potentially would reduce the unit cost of the ITM module, provided production occurs on a suitably large scale.

17.5 Ceramic Processing Cost and Production Analysis/2000 Ton per Day Capacity Ceramic Manufacturing Study

Based on the concepts developed under Task 17.4, Ceramatec devised a manufacturing process design for next-scale module production beyond the PDF, i.e., that capable of supplying a 2000 TPD ITM Oxygen plant. Specific assumptions in the process design were evaluated with the input of equipment suppliers.

The team met with various suppliers for all of the major equipment items in the manufacturing process. Specific equipment options were identified for each process. Various powder calcining, milling, and classification process options were assessed. Concepts for combined milling and slip preparation were considered. A tape casting technique specifically for thick tapes was investigated. A number of featuring processes were considered for forming the micro-channel slots in the interior wafer layers. Lamination approaches were developed based on the results of operating the WAM and from experimental work under Task 17.1. Sintering and joining strategies were devised based on work under Task 17.2 and with the success in expanding the PDF under Task 17.3. This work was later used under Task 30 to develop the CerFab manufacturing process.

TASK 18.0 TABLE OF CONTENTS

TASK 18.0 MODULE PERFORMANCE TESTING 3

18.0 SCOPE 3

18.1 TESTING OF MODULE COMPONENTS 3

Background 3

Technology Development Unit (TDU) 4

FluX Verification Unit (XVU) 5

Vacuum Permeate Short Loop Test Rigs (VP-SLTRs) 6

Transient Test Rig (TTR) 8

Subscale Engineering Prototype (SEP) 9

Summary 11

18.1.1 Module Quality Assurance Testing with Pure Air Feed 12

Flux measurements under various conditions on subscale modules 12

Spacer 18

Base piece 20

Part Validation 21

18.1.2 Module Flux Performance in Impure Environments 23

SEP Run 17 23

SEP Run 18 23

SEP Run 24 24

SEP Run 26 25

18.1.3 Commercial Seal Design Verification 27

Background 27

Experimental Apparatus 27

Results 29

18.1.4 Module Flux Performance at High Driving Forces 60

Wafers 63

18.1.5 Full-size Module Performance 66

SEP Run 10 67

SEP Run 11 70

SEP Run 12 71
SEP Run 13 75
SEP Run 14 77
SEP Run 15 78
SEP Run 16 81
SEP Run 18 83
SEP Run 19 86
SEP Run 20 88
SEP Run 21 90
SEP Run 27 90
SEP Run 28 93
SEP Run 29 94
SEP Relocation 95
SEP Run 31 at Convent Louisiana 97
Automatic Shutoff Valve, Small Scale Trials 99
SEP Run 20 100
SEP Run 25 101
18.1.6 Advanced Ceramic Component Performance Testing 103
Base Piece 103
End Cap and Base Piece 104
End Cap, Spacer and Base Piece 104
Wafer 105

TASK 18.0 MODULE PERFORMANCE TESTING

18.0 Scope

In Task 18.0, Air Products conducts module testing to (i) evaluate lifetime performance against target values, and (ii) obtain membrane module performance data to validate and support the development of engineering models used to predict the performance of the ITM Oxygen Ceramic membrane modules. Air Products tests performance of full-size wafers and full-size ceramic-to-metal seals fabricated at Ceramatec in the fluX Verification Units (XVUs) and the Short Loop Test Rigs (SLTRs). Short-term quality assurance tests and longer-term tests are performed to extend the performance database and provide quality assurance information about the full-size wafer processing at Ceramatec. In addition, Air Products uses the Technology Development Unit (TDU) and Subscale Engineering Prototype (SEP) to measure performance of larger modules under higher stresses. Air Products uses the SEP to simulate process transients prior to operation of the ISTU.

18.1 Testing of Module Components

Background

Ceramic modules comprising one or more planar wafers, spacer rings between each wafer, an oxygen flow tube and an end cap were built and tested in specially designed pilot-scale rigs for assessing oxygen flux and purity under commercially relevant, high-temperature, high-pressure conditions. In general, the rigs are composed of a heated pressure vessel to house the ceramic module, a compressed air source, an air heater, and an oxygen collection system consisting of an oxygen control valve for controlling the oxygen pressure at the membrane, an oxygen pump, and a downstream flow meter and purity analyzer. A simple pictorial arrangement of these components is shown in Figure 18-1. A variety of rigs are used for different purposes; each is briefly explained in the experimental section of the report.

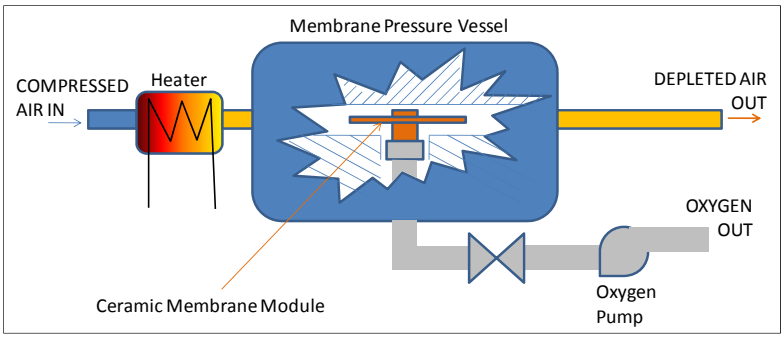

Figure 18-1. Simple schematic of a pilot-scale test rig for assessing oxygen flux performance and purity from ceramic membrane modules.

Technology Development Unit (TDU)

The TDU comprises all the components mentioned above, including a horizontal vessel with an 8-inch internal diameter. The test module can be comprised of one to 12 wafers and is contained in a dense alumina flow duct which channels the flow around the wafers. A chromium getter resides in the inlet of the vessel and is made up of a bundle of getter tubes. Product oxygen exits through a support tube, then passes through the vessel flange where it is cooled. The product flows through a pressure control valve, a vacuum pump and a flowmeter before being vented to atmosphere. Slip streams of product as well as nonpermeate are plumbed to an oxygen analyzer for measurement of oxygen content. The TDU is fitted with a direct-fired combustor upstream of the vessel. Modules capable of producing up to 0.1 ton per day (TPD) of oxygen were tested for flux and purity. Figure 18-2 shows the TDU and the module.

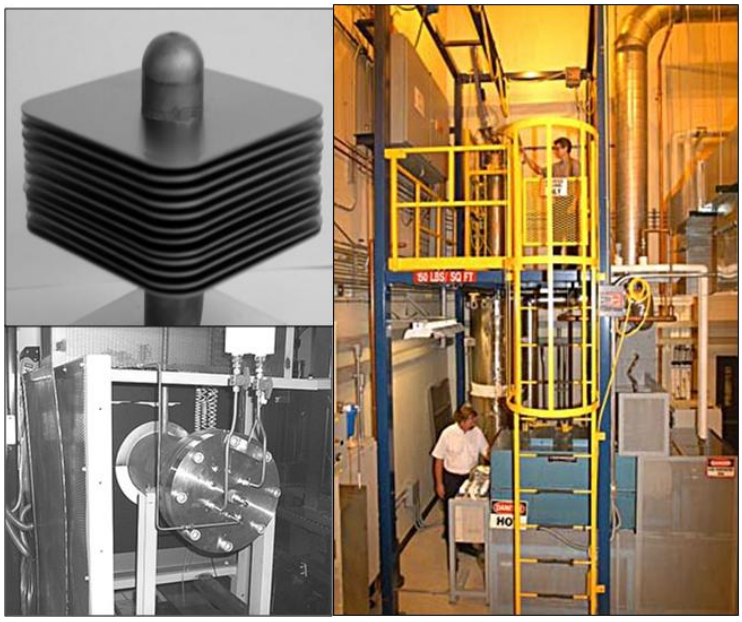

Figure 18-2. The Technology Development Unit (TDU). *Upper left:* Ceramic module capable of producing up to 0.1 TPD. L*ower left:* TDU pressure vessel and associated heater. *Right:* Wide-angle view of the rig; the blue box in the foreground is the TDU vessel heater.

FluX Verification Unit (XVU)

The ITM oxygen Flux Verification Units (XVU1, XVU2, and XVU3) are designed to verify the oxygen flux capability of a full-size single wafer module (Figure 18-3).

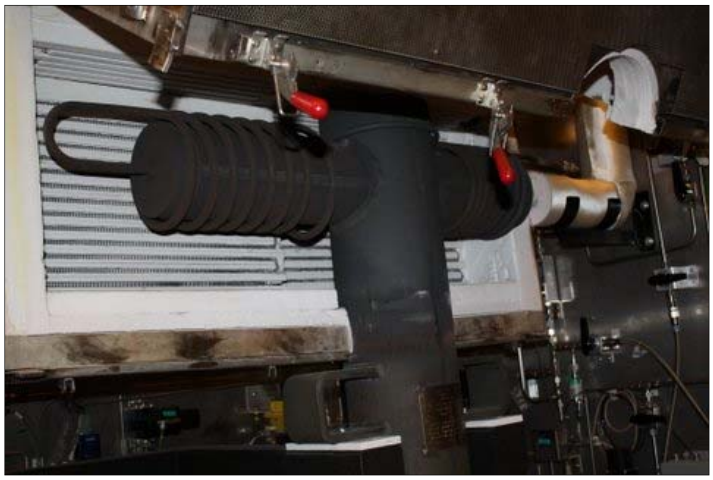

Figure 18-3. FluX Verification Unit (XVU).

Compressed air is supplied to each of the 3 XVUs at 500 psig from a remotely located compressor to a high-pressure manifold located above the XVUs. Air from the manifold is reduced in pressure through a pressure regulator and its flow is controlled via a mass flow controller for each unit. The controlled flow of air then enters a preheater coil that heats the air to the required process temperature before entering the pressure vessel that which houses the ITM module. Both the preheater and the vessel are located inside a large, electrically heated furnace. After entering the vessel, the high-pressure air goes through the horizontal inlet section of the vessel. The inlet section channels flow to a slot located in the wafer. The oxygen-depleted (non-permeate) air then flows out of the vessel through an identical slot 180º opposite the first. The non-permeate then flows through the outlet section of the vessel and exits. A slip stream of the non-permeate is analyzed for O_2 content using paramagnetic oxygen analyzer.

After oxygen permeates through the membrane, it travels down a support tube at 0.2-1.0 atm (absolute) pressure to the bottom of the vessel to the connecting flange. The oxygen product stream cools rapidly by losing heat to ambient air. The oxygen then flows through a dry-seal, diaphragm-based vacuum pump and is exhausted into the vent. A slip stream is sent to a paramagnetic oxygen analyzer for purity measurement.

While the flow systems for XVU1, XVU2, and XVU3 are very similar, the flow systems for XVU2 and XVU3 have special provisions to conduct iso-compositional (or “iso-strain”) thermal cycling. Iso-compositional methods enable changing of the gas composition on both the air and permeate sides of the membrane to manage the composition-dependent chemical expansion that is characteristic of the ceramic material. As such, either XVU2 or XVU3 can be optionally connected to the ISU unit, a cart-mounted flow control system that manages the blending of air and N_2 on the air feed side and O_2 and N_2 on the permeate side.

The XVU vessel is “T” shaped and constructed of high-nickel alloy. The vessel is ASME coded and dually-rated at 250 psig/1650° F and 450 psig/1525° F. The vessel includes a a section of alloy tubing wrapped around the horizontal section which is used as an air preheater. A flange is attached to the bottom of the vertical section. There is also a mating blind flange fitted with three thermocouple ports, and a tube that is inserted inside the vessel and which supports the modules. The tube acts as the permeate flow tube and connects to the permeate system on the outside of the mating blind flange. The portion of vessel that houses the module along with the preheater tubing section is enclosed in a furnace. XVU1 has a slightly different vessel design than XVU2 and XVU3. The upstream side-arm of XVU1 has been extended outside of the furnace, where it terminates at a bolted flange closure. This allows for a guard bed to be loaded into the sidearm to remove impurities from the hot air stream before contacting the ITM module.

Vacuum Permeate Short Loop Test Rigs (VP-SLTRs)

The Vacuum Permeate Short Loop Test Rigs are designed to investigate the oxygen flux response of small prototype membrane modules as a function of time, temperature, pressure, and feed gas composition (Figures 18-4 and 18-5).

Figure 18-4. VP-SLTR housing, closed (L) and open (R) showing subscale wafer.

Figure 18-5. VP-SLTRs showing moisture addition system at bottom.

The four VP-SLTR systems are similarly configured, although they vary somewhat in their feed composition capabilities. The heart of a VP-SLTR system is a furnace, in the hot zone of which a subscale ITM module is mounted inside a magnesium oxide flow path with an integral permeate tube. The subscale ITM module features a single planar disk wafer approximately one twentieth the surface area of a single full-size wafer, which allows meaningful flux results to be obtained at feed air throughputs easily attained at the laboratory scale. The flow duct receives pressurized air as feed, optionally modified with potential contaminants such as water vapor, carbon dioxide, or sulfur dioxide. The oxygen permeate from the membrane and any leak is withdrawn from the interior of the subscale module using a vacuum pump. The permeate flow is measured using a mass flow meter, and its oxygen concentration determined using a zirconia-cell oxygen analyzer. These measurements allow characterization of the oxygen flux during the experiment. Air is fed from the shared compressor system. Using auxiliary feed systems (liquid water feed system, pure CO_2 feed system, ppm-level SO_2 feed system), low percentage-level concentrations of CO_2 and/or water, and ppb-level concentrations of SO_2 can be established in the inlet gas.

In a typical experiment, the oxygen flux is first evaluated at baseline operating conditions, then its immediate and long-term responses to changes in operating conditions are evaluated, typically over a duration of several weeks to months.

Transient Test Rig (TTR)

The Transient Test Rig (TTR) is designed to evaluate the response of ITM-Oxygen modules when subjected to transients in temperature, pressure, and oxygen concentration (Figure 18-6).

Figure 18-6. Transient Test Rig (TTR).

The reactor portion of the TTR consists of an internally-heated pressure vessel. The module is contained within a magnesium oxide-lined, high-nickel alloy retort. The vessel heating element is embedded in a cast ceramic split cylinder unit, and the interior of the vessel (outside of the heating element unit) is filled with vacuum-formed ceramic insulation and is purged with nitrogen during operation.

The process feed gas is a mixture blended from nitrogen, air, oxygen, and CO_2, all at high pressure. These gases have independent pressure and flow controls to permit process feed gas compositions spanning the range from pure nitrogen to pure oxygen at pressures from 0 to 300 psig. In the vicinity of the module, the feed is transitioned to a MgO pre-heater/getter bed to equilibrate the feed gas to the reactor temperature while also acting as a getter to remove

chromium and other contaminants from the process gas feed. The process feed gas is fed across the module through an MgO-lined flow path. The non-permeate stream then exits the reactor.

The vessel is purged with nitrogen, which has independent pressure and flow control. The purge stream enters through the vessel wall and exits through the bottom blind flange. The purge exit stream is combined with the non-permeate stream after exiting the reactor. A back-pressure controller acts on the combined stream to regulate the vessel pressure. A check valve arrangement maintains the purge gas pressure at a slightly higher value than the process gas within the reactor.

The module can be purged, if desired with a purge feed gas mixture blended from nitrogen and oxygen. These gases have independent pressure and flow control to permit module purge feed gas compositions ranging from pure nitrogen to pure oxygen at pressures from sub-atmospheric to ~10 psig. The module purge feed gas enters the reactor through the bottom blind flange. Permeate pressure is regulated by a pressure control valve. The permeate gas stream can be at sub-atmospheric pressure as it runs through a vacuum pump system.

Subscale Engineering Prototype (SEP)

Phase II tasks culminated in the design, construction, and commissioning of a 5 TPD subscale engineering prototype (SEP) facility which produces tonnage-quantity oxygen exceeding 95% purity (see Task 10). Figure 18-7 is a schematic of the system.

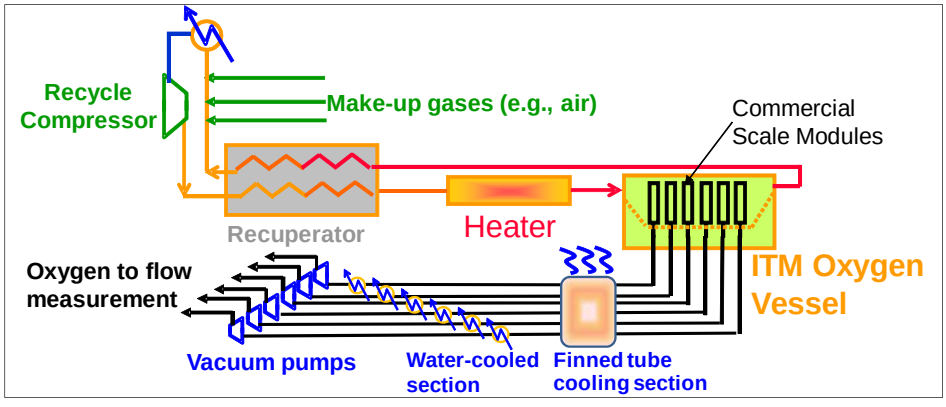

Figure 18-7. Subscale Engineering Prototype (SEP) schematic.

The SEP vessel/duct design approach was configured for R&D testing. The conditions enable operation with incoming high-temperature air at up to 250 psig, allow access to wafer modules

(stacks) for inspection and change-out, and allow operation of modules independently. The design has a high-temperature flow duct contained within a cold wall vessel. Figure 18-8 details the flow duct and module configuration.

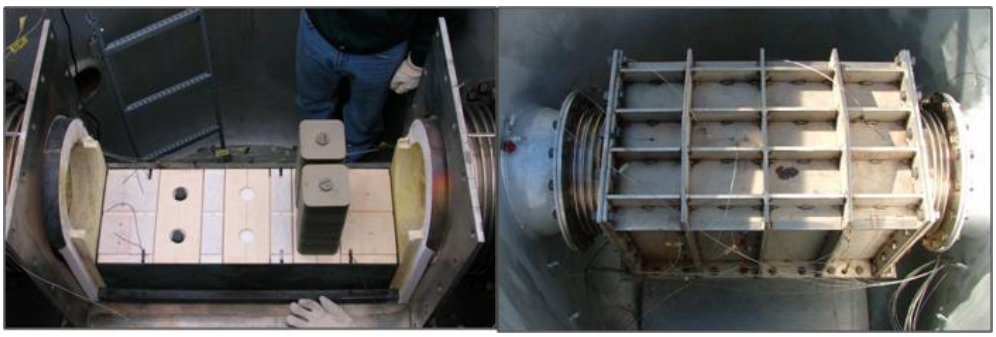

Figure 18-8. *Left*: ITM modules installed in the SEP vessel; *Right* outer flow duct installed.

The flow duct is rectangular with a stationary base plate and removable top and sides. The duct houses six module stacks in a 2 x 3 array. The base design is sized for modules of 0.5 TPD-scale, with the elevation of base plate within vessel chosen to accommodate taller 1.0 TPD-scale modules by using a taller duct enclosure. The module stacks mount indirectly to the base plate with intermediate, removable ceramic-metal sub-assemblies. The module ceramic foot connects to the top of a sub-assembly utilizing U-ring seals in the original design, which was later modified to accommodate different seal designs. The bottom of the sub-assembly attaches to base plate with a bolted vacuum flange.

Six permeate pipes are welded to the base plate and extend through the bottom of vessel to transport oxygen from the modules through the sub-assemblies to the piping network outside of the vessel. Air flow through duct (passing across module wafers) enters and exits through vessel nozzles. The air inlet and outlet nozzles, flow duct and six permeate pipes are internally insulated. The vessel shell is not internally insulated and has a relatively cool temperature. A vent hole in the flow duct equalizes the pressure acting on the inside and outside of duct. The operating pressure is contained by the vessel, not the flow duct. The vessel is vertically oriented with all-welded construction. Four vertical support legs attach to the shell, with base plates to mount the vessel to the skid. The vessel has a removable top head with a bolted flange. Four 6-inch NPS instrumentation nozzles through the vessel shell provide capacity for 80 internal measurement probes including thermocouples and pressure probes.

The flow duct has internally insulated bellows-type expansion joints at the inlet/outlet and uses a bolted flange and gasket joint design. The original design used a removable 3-sided enclosure that accommodated 1-6 module stacks. It includes alumina baffle plates surrounding the modules to direct air flow over the modules and minimize by-pass. Radiation shields are placed at inlet and outlet ends. The SEP was operated in campaigns (runs) to acquire specific data and information.

An aerial photograph of the SEP, which was installed at the Air Products facility in Sparrows Point, Maryland, is shown in Figure 18-9.

Figure 18-9. Aerial view of the SEP installed in Sparrows Point, MD.

Summary

Air Products carried out significant work in Task 18 that has confirmed predicted performance of AP2K wafers and modules and has guided development of new wafer structures in Task 17. Flux testing of subscale modules, single-wafer and multi-wafer modules has been done in lab units to confirm performance of the developmental structures. Tests performed over one calendar year have shown no degradation of flux performance. Flux data has been obtained under a wide variety of conditions to establish correlations for use in engineering designs.

Ceramic-to-metal seals are one challenging area of ITM technology. Task 18 included substantial screening of new seal designs and optimization of designs for effectiveness,

cyclability, and cost. Several lead candidates were identified for ISTU testing, and all aspects of the seal design were optimized. Testing was initially done one at a time. Modification of the test units allowed simultaneous testing of multiple samples, both on a small scale and at full scale. This increased number of samples tested provides increased confidence in results. Results have been confirmed in testing in the larger laboratory units and at the SEP.

Auto shutoff valves (ASOV) were designed to protect product purity in case of module failure. Testing of prototype valves in lab units verified predicted performance. Units were also tested in the SEP and were shown to trip at the desired conditions. Adjacent modules continued to perform without damage after the intentional trip of an ASOV under a fluxing module.

Testing of 0.5 TPD and 1 TPD modules was done at the SEP. Over 1,000 days of cumulative testing have been completed. Flux and purity of commercial-scale modules were confirmed. Advanced process control methods were developed to manage stresses during thermal cycling. The ability of modules to survive temperature and pressure cycles was confirmed, as was the performance of seals, filters, and contaminant getters. Startup and shutdown schedules were tested. The shutdown of the Sparrows Point air separation unit made that location no longer viable for SEP operation, so the unit was relocated to Convent, Louisiana, near the ISTU site.

18.1.1 Module Quality Assurance Testing with Pure Air Feed

Flux Measurements Under Various Conditions on Subscale Modules

Experiments were performed to measure flux data on subscale modules with standard membrane layer wafers under various degrees of feed air dilution with nitrogen and at various permeate vacuum levels. In this way, baseline data was obtained for subsequent testing of subscale modules with a porous protective layer. These runs were successful in this regard. However, some unexpected results were obtained, which led Air Products to explore the effects of feed pressure as well as the use of other diluent gases such as argon and helium.

One objective of these experiments was to understand the impact of the feed oxygen partial pressure on the observed flux. The partial pressure of oxygen was varied by diluting the feed air with various diluents in the VP-SLTRs, and also by using undiluted air at lower pressures. Theoretically, in the absence of any external mass transfer limitations, the flux should be the same at a given feed oxygen partial pressure, regardless of the choice of diluents or total feed

pressure. However, as seen in Figure 18-10, reducing the P_{O2} by reducing the total air feed pressure gave somewhat different results from those obtained by diluting the feed with nitrogen. Air Products was able to model these results qualitatively using a simple boundary-layer model for diffusion of oxygen from the bulk gas to the surface. Lowering the total pressure of the gas phase significantly increases the diffusivity of oxygen in air. For example, to produce 25 psi oxygen partial pressure in the two cases below corresponds to a) feeding air at 105.6 psig and b) feeding 56.8% air and 43.2% nitrogen at 197 psig. Under these two conditions, the predicted oxygen diffusivities are 0.96 ft^2/hr and 0.54 ft^2/hr respectively. This near-doubling of the diffusivity contributes to a 10% higher flux for the low-pressure case versus the diluted feed case at 25 psi oxygen partial pressure.

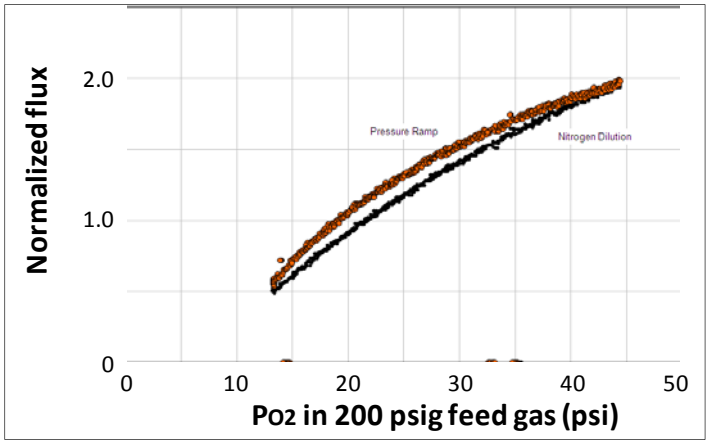

Figure 18-10. Observed flux as a function of the partial pressure of oxygen on the air side. In the pressure ramp, the total pressure was varied from 197 psig to 49 psig.

These VP-SLTR experiments with subscale modules were typically run at feed rates of 8 nplm or greater, with the observation that at that point, the flux no longer increases with increased flowrate. However, these new results indicated that there is still some meaningful impact of mass transfer from the bulk to the surface under those conditions. One concern was that nitrogen may actually be able to compete for surface sites with oxygen. To test this, experiments were also run using argon and helium dilution. These gases are not expected to have any affinity for the AP2k. The argon should have essentially no impact on the oxygen diffusivity, while the diffusivity of oxygen in helium should be markedly higher. The results are shown in the Figure 18-11. Gratifyingly, the argon dilution data is essentially identical to that obtained via nitrogen

dilution. Also consistent with the model, the flux obtained when the feed was diluted with helium was slightly greater than the corresponding nitrogen dilution cases.

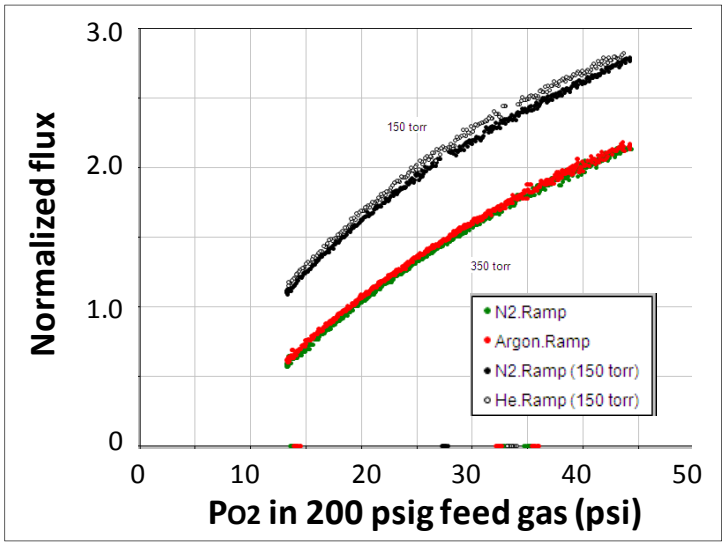

Figure 18-11. Observed flux as a function of the partial pressure of oxygen on the air side using argon and helium as diluents.

Experiments were run in which the feed partial pressure of oxygen was varied by adjusting the total pressure rather than the feed composition. In this experiment, the leak rate from the module decreased as the flux decreased, so that the permeate purity would not be as strongly impacted. However, this approach does introduce other factors, particularly an increase in the diffusivity of oxygen (offset, however, by a decrease in driving force across the bulk gas-phase boundary layer), an increase in the actual gas velocity and a decreased overall flux through the module as the feed pressure is decreased. All of these factors serve to reduce any bulk gas-phase mass transfer effects.

The same effect was seen in a second module, this one with a protective layer (Figures 18-12 and 18-13). The effect clearly was greater at a 150 Torr permeate pressure than at 350 Torr, which is consistent with the notion that when the flux is greater, one expects more impact of bulk gas phase mass transfer. The data at 350 Torr show a crossover point where the flux obtained by nitrogen-dilution exceeds that obtained with a total pressure ramp. This is pretty clear evidence that very poor permeate purity can have some impact on the flux through the membrane layer.

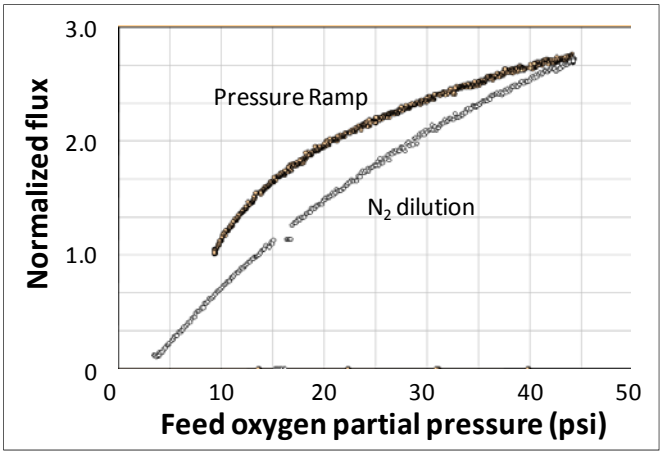

Figure 18-12. Observed flux as a function of the feed oxygen partial pressure via nitrogen dilution at 150 Torr.

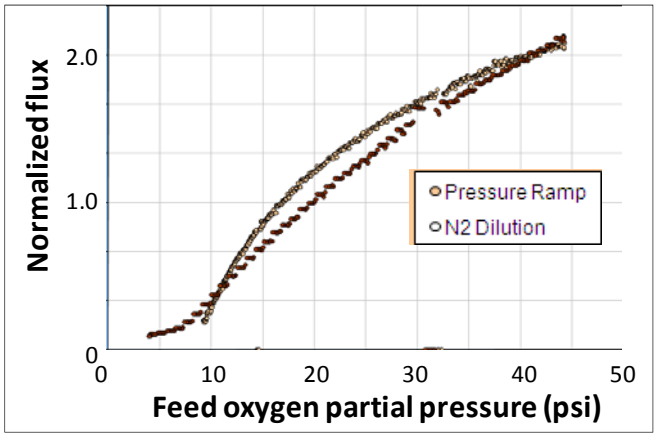

Figure 18-13. Observed flux as a function of the feed oxygen partial pressure via nitrogen dilution at 350 Torr.

If feed-side bulk mass transfer did have an impact on overall flux, one would expect that the impact would be greater with a protective layer present. To assess this, flux values were extracted (by interpolation) from the four datasets at specific feed oxygen partial pressures (Table 18-1). The four datasets used were module P150 (no protective layer) in a nitrogen ramp and in a pressure ramp, and P171 (with a thick protective layer) in the same two ramps. The "P vs. N (no protective layer)" and "P vs. N (with a protective layer)" columns give the percentage increase in flux seen in the pressure ramp experiment over the corresponding data points in the nitrogen-dilution experiment. The N-ramps column tabulates the percentage increase in flux measured in a nitrogen-dilution experiment with the protective layer over that measured without a protective layer. Similarly, the P-ramps column compares the flux measured in a pressure

ramp experiment with and without a protective layer. The data are shown in graph form in Figure 18-14.

Table 18-1. Flux data extracted from the datasets obtained from modules with and without protective layers were tested in nitrogen-dilution and pressure ramp experiments.

P_{O2}	P vs. N (no protective layer)	P vs. N (with protective layer)	N-ramps	P-ramps
44	0.7%	-1.9%	7.6%	4.8%
40	3.3%	1.3%	8.3%	6.1%
35	5.9%	5.1%	6.8%	6.0%
30	8.1%	7.4%	9.8%	9.2%
25	13.0%	13.1%	9.2%	9.3%
20	15.8%	20.6%	10.3%	14.9%
15	16.4%	23.8%	11.8%	18.9%

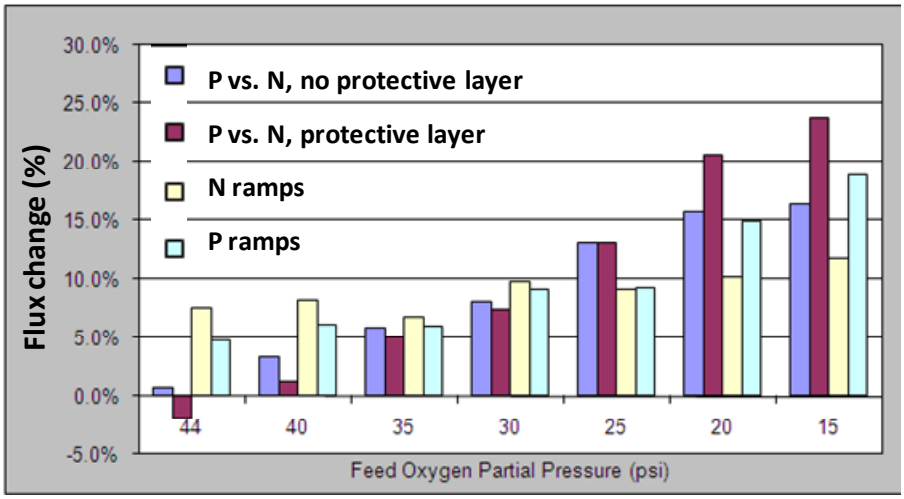

Figure 18-14. The percentage change data from Table 18-1 shown in graphical form to aid in assessing trends.

These data are somewhat scattered, and it is important to recall that the permeate purity effect is also in play. However, the following observations can be made:

- Both with and without a protective layer, there is an increasing enhancement in flux (as the feed oxygen partial pressure is reduced) in a pressure ramp experiment over that measured in a nitrogen-dilution experiment. This is evidence that there is a feed-side, gas-phase oxygen diffusion resistance.
- This effect is greater when a protective layer is present, confirming that the protective layer does further increase the overall mass transfer resistance.

- The nitrogen ramp data shows only a slight dependence on the feed oxygen partial pressure (i.e., feed composition).
- The pressure ramp data show a stronger dependence on feed oxygen partial pressure (i.e. total pressure). The flux obtained with the protective layer decreases less as the total pressure is lowered compared to the case without a protective layer. This is another way of looking at the evidence that the protective layer *does* impose a greater resistance to mass transfer.
- The flux obtained with the protective-layer module was higher than that obtained in the module without a protective layer. This result is specific to this pair of modules, since they may have different physical characteristics. But this is encouraging, since it shows that in spite of the increased bulk gas mass transfer limitation it imposes, the presence of the protective layer has certainly not led to poor flux performance. Similarly, high flux has been measured with other modules with protective layers that have been tested to date.

Experiments were performed to determine whether the presence of a porous protective layer over a standard membrane layer has any impact on flux over the range of relevant feed compositions and temperatures. Data show that the fluxing behavior of a "thick FEL, thin membrane" module can be explained by trade-offs between two effects: enhanced overall oxygen surface transport rates offset by greater resistance to oxygen diffusion from the bulk gas to the membrane layer. The model predictions are based on the flux measurements from subscale module P171 under the following conditions:

- A constant feed pressure of 197 psig, diluting the feed air with nitrogen.
- Undiluted feed air at various feed pressures.
- Constant feed pressure of 197 psig with helium dilution.
- Feeding undiluted Heliox™ (20.9% oxygen in helium) at various feed pressures.
- A constant feed pressure of 197 psig, diluting a Heliox™ feed with helium.

The feed-side diffusional resistances are occurring both in the FEL and in the "bulk" gas phase. The dependence of flux on feed gas flow rate over the entire range of flows used in these experiments is evidence that an oxygen concentration gradient (boundary layer) exists in the bulk gas phase (Figure 18-15).

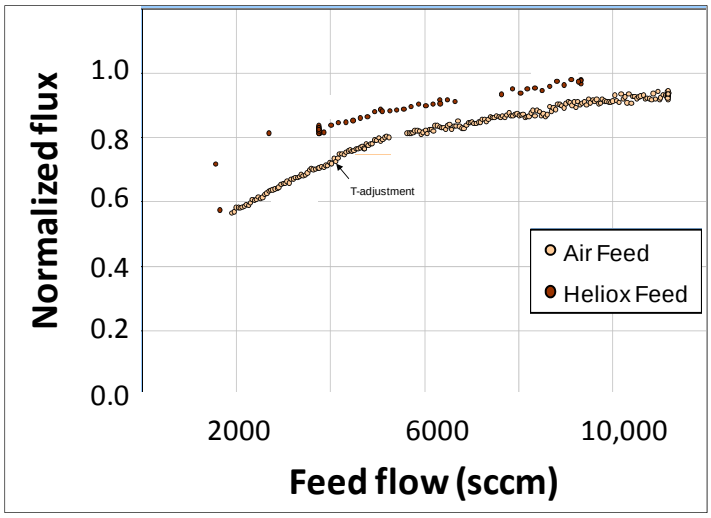

Figure 18-15. Normalized flux with subscale module P171 (thick FEL, thin membrane layer) as a function of feed flow rate at various temperatures.

Spacer

A test of the new OD spacer design was initiated in the Air Products Flux Verification Unit #2 (XVU2). The purpose was to qualify the design by determining if the spacer survived both startup procedures and aggressive run conditions. Figure 18-16 documents the XVU operating conditions and the space performance parameters.

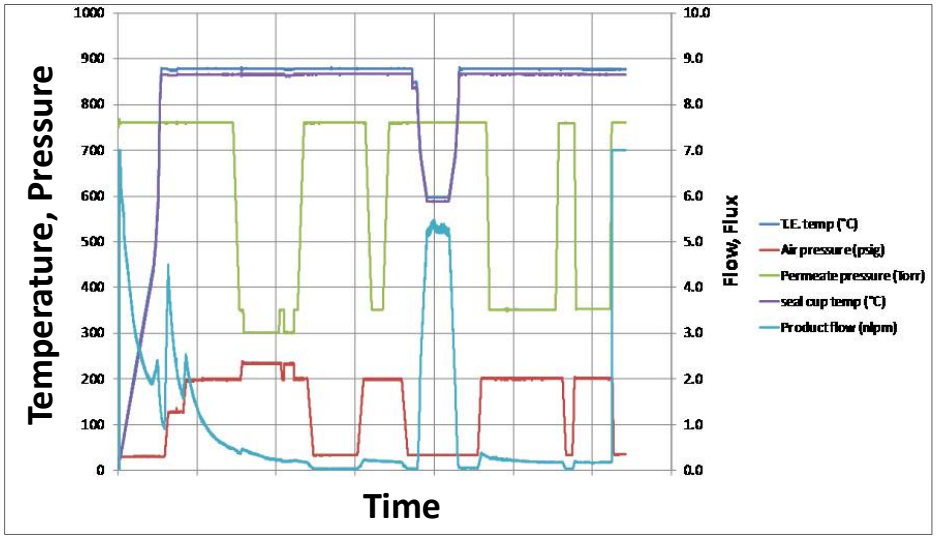

Figure 18-16. OD Spacer test in the XVU#2

The test included cycles at the standard ramp rates, a thermal cycle to 600°C, a pressure cycle at twice the standard rate, and a pressure cycle at four times the standard rate. The part failed at the start of the feed depressurization step of the fastest cycle. Multiple cracks were found on the part

after removal from the reactor, and a small chip adhered to the inorganic material of the seal (Figure 18-17).

Figure 18-17. Spacer pieces after testing.

Six advanced OD spacers joined in a stack were tested in the XVU2. Figure 18-18 documents the XVU operating conditions and the spacer performance.

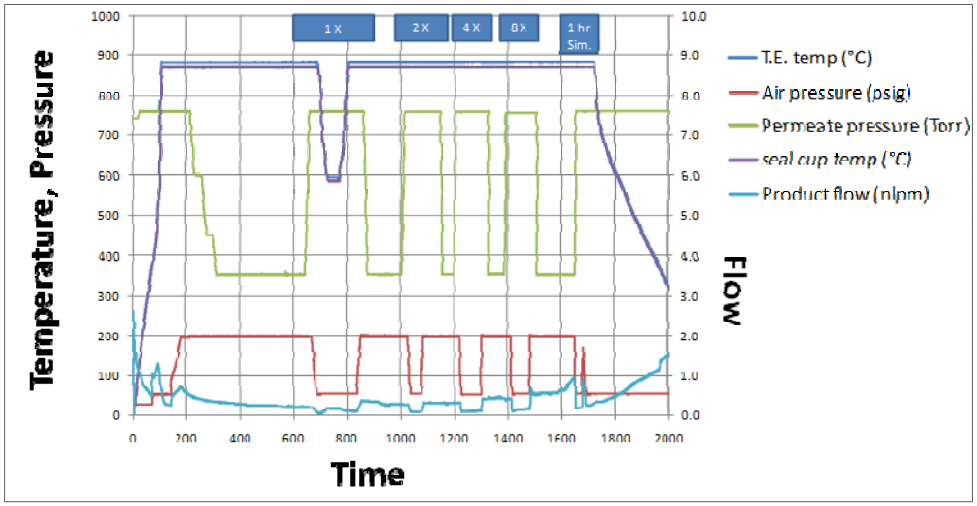

Figure 18-18. Test results for stacked advanced spacer.

The sample assembly had a low leak rate throughout the startup and hold at full conditions. The sample successfully underwent a linear pressure cycle, with a cool to 600°C and back to full temperature while at 55 psig feed air pressure and 760 Torr permeate pressure. There was a slight increase in leak rate observed after completion of the full cycle. After a 5-day hold at conditions, the sample was subjected to a pressure cycle at twice the ramp rate. A slight increase in leak rate was observed after its completion. After a 30- hour hold, the sample was subjected

to a pressure cycle at four times the ramp rate at full temperature. There was a slightly greater increase in leak rate just at its conclusion. An 8X faster cycle was then run. Again, a slight increase in leak rate was observed. After the 8X cycle, a one-hour simultaneous pressure and vacuum cycle was conducted. There was a slight increase in the low-pressure leak rate. The spacer assembly proved to be very robust to rapid pressure changes.

Base Piece

A new base piece design comprising multiple layers was tested in XVU2. Figure 18-19 documents the XVU operating parameters and base piece performance.

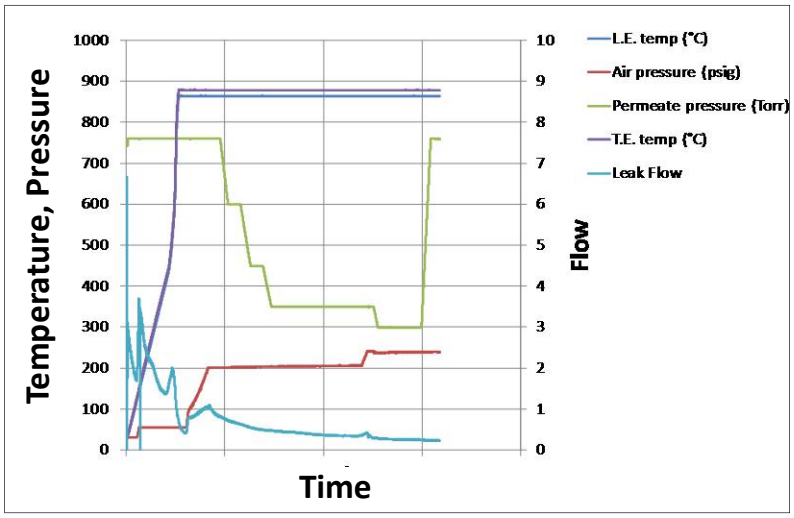

Figure 18-19. Test results for a layered, redesigned base piece in XVU2.

The base piece was successfully started up using a multi-step pressure schedule for the feed and permeate pressures. The leak rate decreased throughout the test, with a minimum leak rate of approximately 0.25 slpm at full conditions.

A second base piece design was tested in XVU3. Figure 18-20 documents the operating conditions and base piece performance.

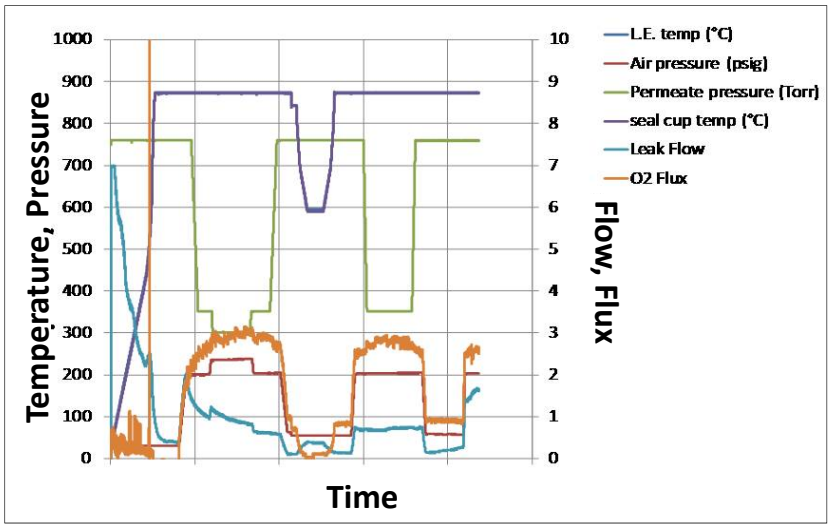

Figure 18-20. Test results for a second base piece design tested in XVU3.

The leak rate steadily decreased during heating. The leak rate increased during the feed pressurization using the standard linear schedule and then decayed during the hold at pressure, reaching a minimum of ~0.6 slpm. The sample was de-pressurized using linear ramps, cooled to 600°C, and then re-heated. The reactor pressures were ramped to operating conditions at twice the standard linear rates. The observed leak rate was slightly higher on this cycle, but was stable over the course of the hold. The reactor pressures were then ramped back to baseline at twice the standard rate. A slow increase in leak rate was observed during this hold at baseline conditions. The reactor pressure was ramped back to operating conditions at four times the standard rate. Upon reaching full pressure, the observed leak was about twice that observed on the second cycle and was increasing with time.

Part Validation

Air Products validated the improved (OD2) spacer design through testing in XVU2. A ceramic-to-metal seal was used at the base of the part. Figure 18-21 summarizes the run conditions and performance data.

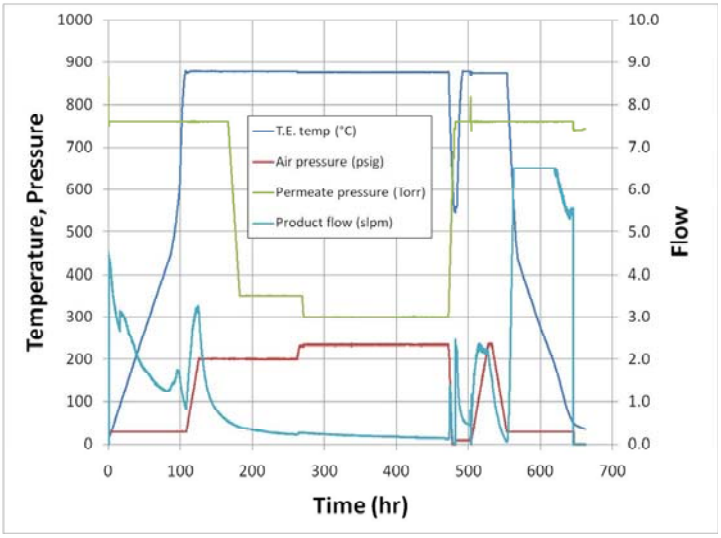

Figure 18-21. Conditions during testing of Spacer #1 in XVU2.

After heat-up and air-side pressurization, the leak rate was slightly more than 3 slpm. The leak rate rapidly decreased to ~0.4 slpm during the short hold at temperature and pressure, and continued to decrease. The leak rate did not change during the permeate-side ramp and continued to improve during steady-state operating conditions. The leak rate dropped to 0.2 slpm, which matches the expected leak rate from the two ceramic-to-metal seals.

A subsequent test was conducted with a replicate part; results were very similar to those documented in Figure 18-21. The second test utilized a revised start-up pressure schedule. The leak rate was quite low throughout the start-up and de-pressurization stages, but increased during the cooling portion of the temperature cycle and returned to approximately the same value at full conditions.

Modules

Air Products validated an ensemble of joined, improved parts in a single module. A single-wafer module consisting of a domed end cap, improved (OD2) spacer, standard wafer, improved (OD2) spacer, and a base piece was tested in an XVU. The leak rate slowly decreased into the range of 0.8 slpm during a 2-day hold at operating conditions. The oxygen driving force was then maximized by adjusting the feed and permeate pressures. The leak rate increased slightly but was still <1 slpm.

18.1.2 Module Flux Performance in Impure Environments

SEP Run 17

The primary purpose of SEP Run 17 was to evaluate the performance of the chromium getter. Two 0.5 TPD modules were loaded into the SEP. The chromium getter was installed to fill the full cross section of the flow duct, using a compressible material to fill gaps between the duct insulation and the getter. The arrangement is shown in Figure 18-22.

Figure 18-21. Run 17 flow duct arrangement showing chrome getter bed.

Significant process fluctuations occurred during Run 17 which caused extensive damage to the wafers. Interestingly, both end caps and both base pieces showed very little damage.

SEP Run 18

The primary objective of Run 18 was to assess the chromium getter and the impact of flow duct modification on thermal gradients. The chromium getter used in Run 17 was re-installed and two 0.5 TPD modules were loaded. The arrangement is shown in Figure 18-22.

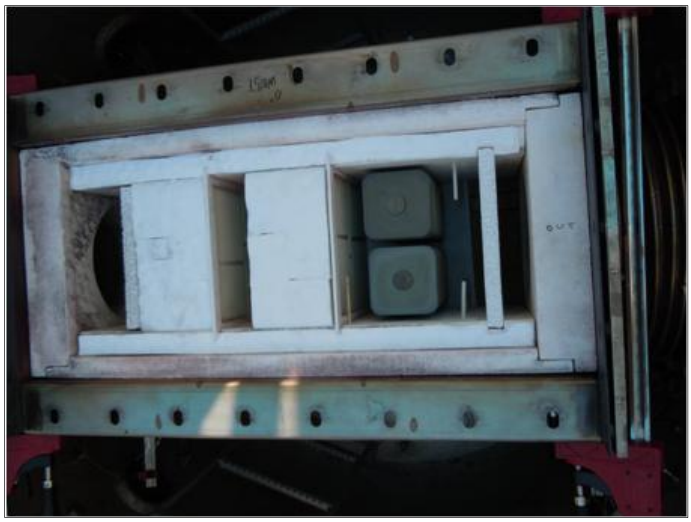

Figure 18-22. Overhead view of flow duct assembly for Run 18.

Flux values for Run 18 were below expectations. Three wafers from each module were analyzed using surface imagining and EDS. Sulfur compounds were observed at the grain boundaries. This observation initialed the testing of both fresh and used insulation samples. Also, a SO_2 analyzer was installed to continuously monitor the process air stream during startup.

The getter in Run 18 was at full operating temperature for a much longer time than in Run 17. The getter bed was analyzed for axial chromium profile by XRF. Samples from the upstream bed were also analyzed using ICP/AES for higher accuracy at the low chromium concentrations. In addition, a sample of as-received chromium getter material was analyzed using both methods to determine the background chromium level. Overall, the chromium concentrations were unexpectedly low. The predicted chromium level in the getter material (based on the predicted vapor phase species) was a few times higher than what was measured. However, there was still a steep chromium axial gradient, indicating that the getter performed well. The ICP results, which are more accurate at these low levels, indicate that the chromium level was close to background after the first section of the bed.

SEP Run 24

A polishing filter was installed just upstream of the modules and used SEP Runs 24, 25 and 26. During this testing, the filter accumulated a total of 1,600+ operating hours over with over 600 hours at leading-edge conditions. The differential pressure across the filter increased by 3% due

to the accumulation of spall particles in the filter. The filter successfully prevented spall particles from entering the flow duct. See SEP Run 26 for more details on the filter performance.

SEP Run 26

Run 26 was completed using the polishing filter previously employed in Runs 24 and 25. The primary objectives of Run 26 were:

- Determine spalling tendency and evaluate the final filter performance.
- Assess chromium getter performance.
- Develop a fully automated iso-control program.
- Obtain chromium deposition data to address the safe handling and disposal of used ISTU modules.

Figures 18-23 show the interior of the flow duct.

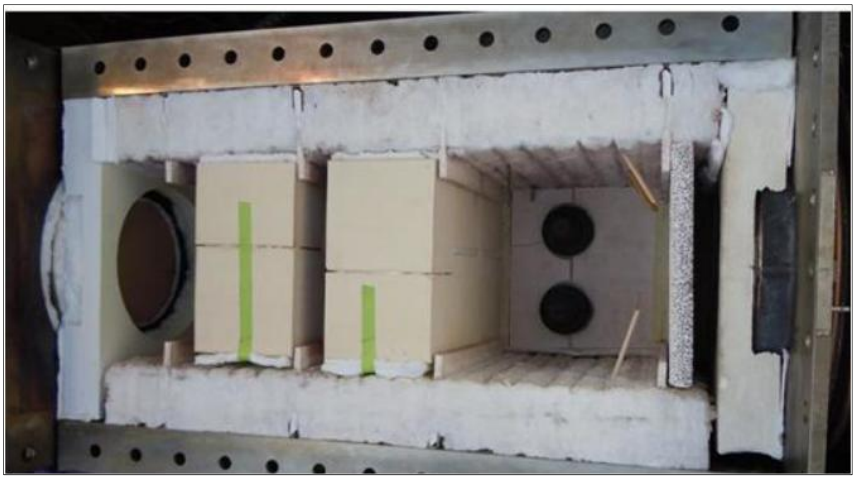

Figure 18-23. SEP Run 26 flow duct configuration.

The flow duct had two rows of chromium getters, but no modules were installed. Samples of unused AP2K wafers (acting as Cr deposition witness plates) were inserted into the insulation on the side panels, protruding into the flow duct at different locations. There was no increase in pressure drop associated with the final filter, and no spall particles were observed in the flow duct after 45 days of operation and three thermal cycles.

Several iso cool/iso heat ramps were performed, which led to the successful evaluation of a fully automated iso-control. Figure 18-24 shows the percent deviation in P_{O2} versus temperature during iso cool ramps 3, 6 and 9. Control improved with successive cycles.

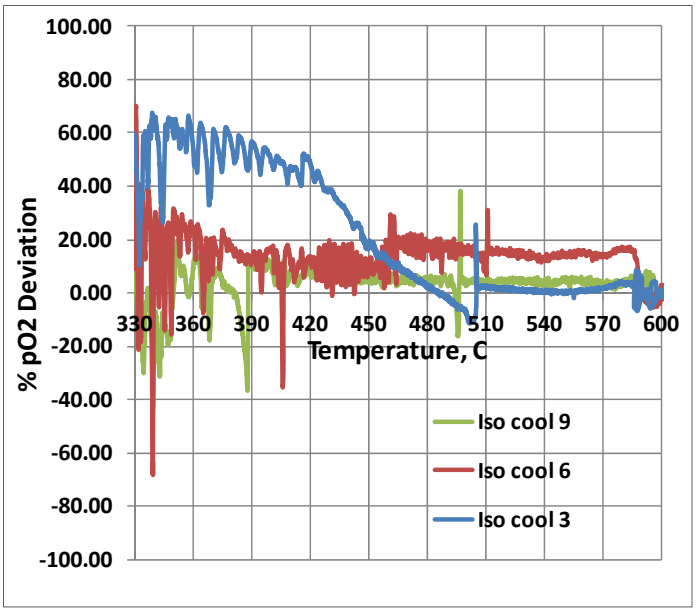

Figure 18-24. Percent P_{O2} deviation versus temperature during iso cool ramp.

The control parameters were tuned manually during the initial runs. In subsequent runs, a fully automated control sequence was used to run iso ramps. Figures 18-25 and 18-26 show both the iso cool and iso heat curves during fully automatic control. The automatic control reduced the P_{O2} deviations considerably.

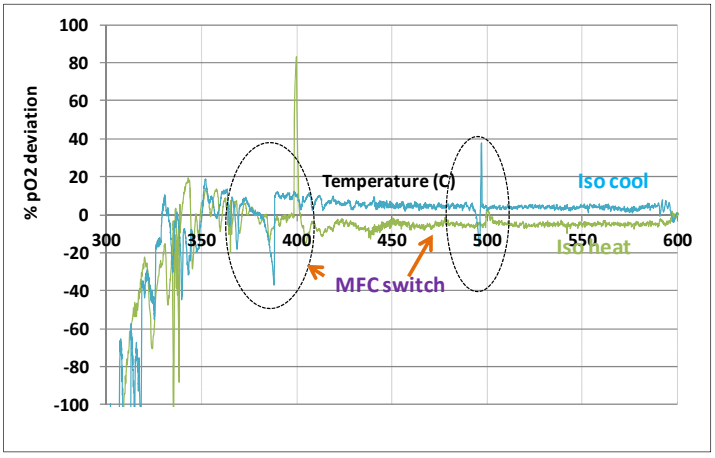

Figure 18-25. Percent P_{O2} deviation during iso cool and iso heat Cycle 9, SEP Run 26.

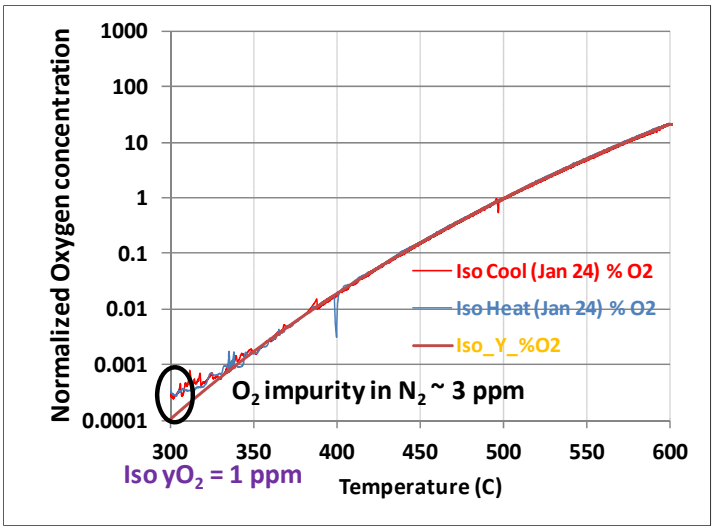

Figure 18-26. P_{O2} versus temperature during fully-automated iso cool and iso heat ramp.

18.1.3 Commercial Seal Design Verification

Background

Air Products developed an improved ceramic-to-metal seal technology. The role of the seal is to reduce or eliminate leakage from the high-pressure feed stream into the permeate system at the interface between the ceramic module and its associated metal piping system. The seal is required to maintain the leakage at a low level, such that the purity of the product oxygen does not fall below the desired product purity specification (i.e., 99.5%). In addition, the seal must not add stresses or contribute contaminants to the ceramic parts leading to stresses that would cause brittle fracture. Because the ITM ceramic expands and contracts relative to the metal system during temperature and pressure cycling, the seal must accommodate the differential expansions while maintaining manageable stresses in the ceramic during these cycles.

Experimental Apparatus

Four Short Loop Test Rigs (SLTRs) were modified to test up to eight seal samples simultaneously under cycling service between operating and ambient conditions (Figure 18-27).

Figure 18-27. Two Short Loop Test Rigs (SLTRs) modified to accommodate up to eight (8) seal specimens simultaneously.

Each seal sample consists of a ceramic part, a seal, and a metal receiver to accommodate the seal. The receiver is connected to a tube that supports the seal sample off the bottom flange of a vertically oriented pressure vessel. The pressure vessel is inserted into a tube furnace. Thermocouples located inside the vessel near the seal samples monitor the temperature near the samples during the experiment. High-pressure air is fed through a flange port to pressurize the inside of the pressure vessel. A small flow of air is maintained into the vessel and exhausts through fixed orifice. Pressure is controlled with an upstream pressure/flow control valve, so the flow rate into the vessel is thereby automatically adjusted to maintain pressure and make up for leak flow. Any leakage that occurs through a seal passes through its tube, through the bottom vessel flange, and then through a flexible hose outside the vessel to a flow meter where the leak rate is measured. The leakage flow is maintained at ~1 atm. Leak rate data is continuously collected. The leakage from all the samples can be monitored during the experiment as the samples undergo process cycles consisting of heating, pressurization, depressurization, and cooling at rates representative of commercial operation. An excess flow valve protects the flow meter from catastrophic failure of the sample. Target performance is to maintain low leak for multiple cycles.

Results

Reproducibility

Eight experimental seal replicates were tested, each consisting of the same metal receiver and seal configuration to gauge reproducibility. The samples were tested by heating to temperature, then applying pressure. After a hold period, the pressure and temperature were decreased to ambient. This constitutes one cycle. Results are presented in Figure 18-28, showing the leak for each of the eight samples after each cycle. Reproducibility was good. It was observed that performance improved for the first several cycles for all of the tests, after which it generally leveled off, and by the sixth cycle, six of the eight tests showed leak rates less than the target value. The tests demonstrate the cyclic durability of the experimental seal.

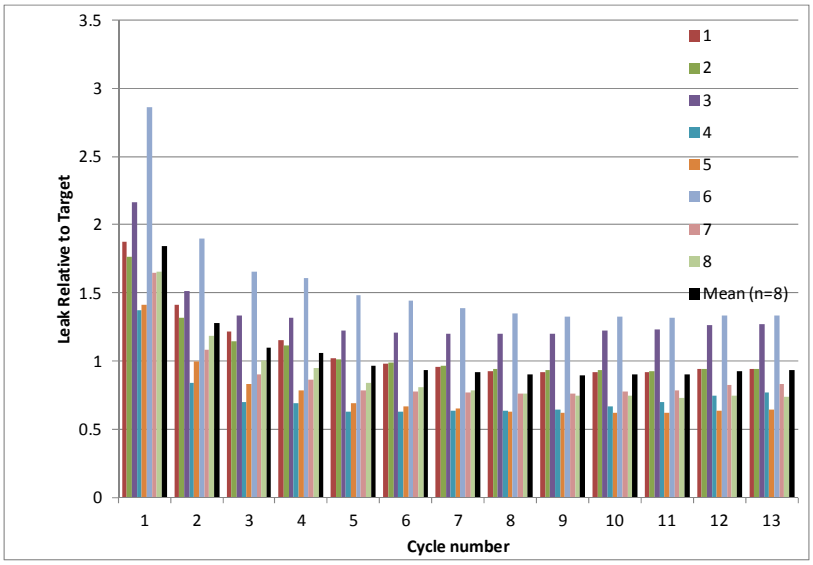

Figure 18-28. Reproducibility of seal testing.

Geometry and Pressure

Tests were conducted to assess the impact of seal geometry on performance under repeated thermal cycling. The force applied to the seal is a combination of the pressure on the ceramic part, any mechanical clamping load, and the seal geometry. The seal geometry was altered to vary the sealing force. Altering the seal geometry also affects the leak path through the seal or the seal interfaces. Three seal geometries were studied. All other parameters for the seals were held fixed.

Figure 18-29 shows the leak rate data for each unit for the highest and lowest seal forces.

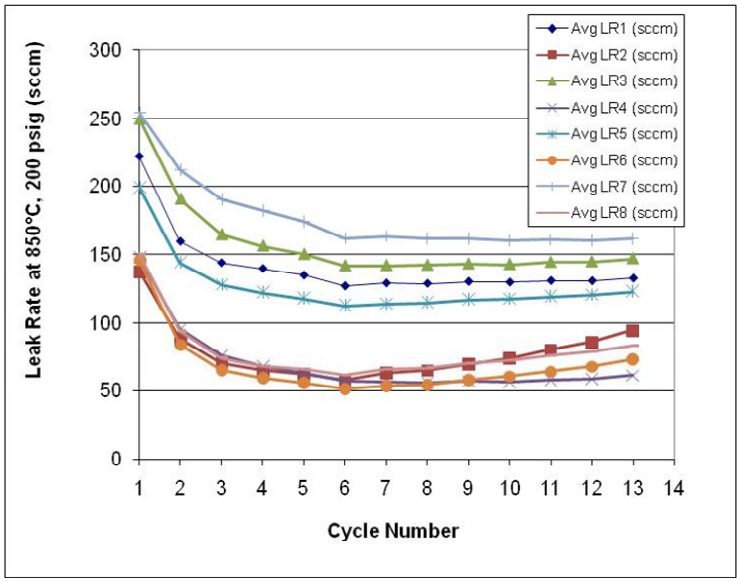

Figure 18-29. Leak rates after successive temperature/pressure cycles at the highest (bottom group) and lowest (top group) applied seal forces.

The lower cluster of lines is data for the highest seal forces. After Cycle 6, the performance of three of the highest-seal-force seals deteriorated much faster than that for the lowest-seal-force seals.

Seals of different dimensions were also compared to confirm their acceptability for subsequent XVU and SEP runs. Figure 18-30 shows the leak rate of the seals over 10 temperature/pressure cycles. Seal A had a lower leak rate and held up better than Seal B. Both Type A seals met the target leak rate through 10 cycles, with no indication of seal degradation.

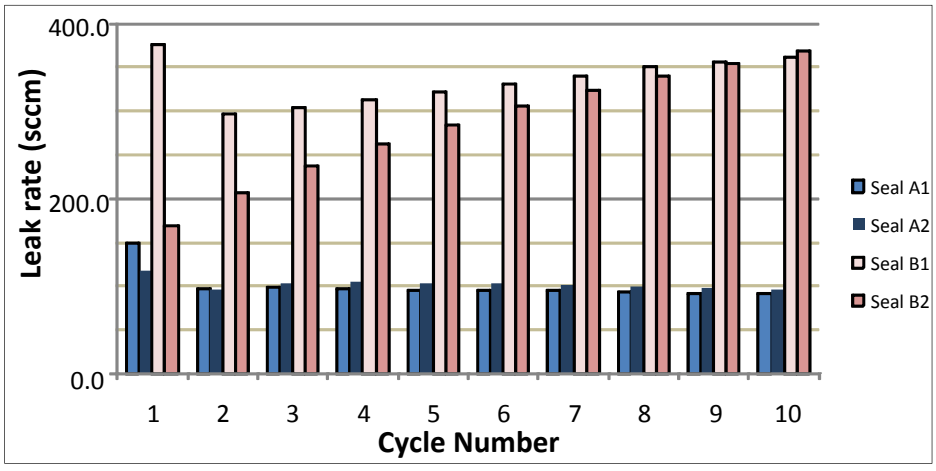

Figure 18-30. Leak rates of Seal A and B over 10 cycles.

Surface Flatness

A study was conducted to determine the surface flatness of the upper sealing surface (in the form of a ceramic disk) and the lower sealing surface (in the form of a metal seal cup). The device used is referred to as the "flatness surface plate." Table 18-2 documents the results.

Table 18-2. Surface flatness of disks and seal cups.

Disks		**Seal Cups**	
Disk ID#	**Flatness (in)**	**Seal cup ID#**	**Flatness (in)**
1	0.0004	1-1	0.0002
2	0.0004	1-2	0.000125
3	0.00035	1-3	0.0002
4	0.00025	1-4	0.00025
5	0.00025	2-1	0.00015
6	0.00015	2-2	0.00015
7	0.0004	2-3	0.0001
8	0.0004	2-4	0.0001
9	0.00055		
10	0.00045		
11	0.00045		
5 (repeat)	0.0004		
7 (repeat)	0.00025		
Mean=	0.000361	Mean=	0.000159
Stdev=	0.000108	Stdev=	0.000053
Min=	0.00015	Min=	0.0001
Max=	0.00055	Max=	0.00025

All parts were very flat. The seal cups were slightly flatter than the disks, likely owing to the machining method used. However, the repeatability was poorer.

Seal C3 and C4

Seal configuration C3 and C4 for advanced architecture AP2k base pieces were evaluated. The same seal designs were also tested using MgO disks. Table 18-3 presents the experimental design.

Table 18-3. Experimental details for run AP2k basespieces and seal C3 and C4.

Unit #	Ceramic Part	Seal Configuration
1- Short	AP2K BP-dome AA41021	C3
2-Tall	AP2K BP-dome XAA41021	C4
3- Short	MgO	C3
4-Tall	MgO	C4

The use of ITM component parts complicates the analysis, as the oxygen flux through the AP2k parts may be significant. Oxygen flow from flux through the part mixes with the leak flow, and the combined flow is measured. This flux needs to be subtracted from the measurement to give an accurate leak rate. In addition, the air near the modules becomes quite vitiated. The oxygen concentration in the gas leaking through non-fluxing samples in the same pressure vessel provides a measurement of the bulk oxygen concentration on the high-pressure side of the parts. The bulk oxygen purity was used to estimate the oxygen concentration in the vicinity of the fluxing part seals. This provided a means of estimating the leak contribution to the permeate flows from "fluxing" Samples 1 and 2. The results of the leak test are documented in Figure 18-31.

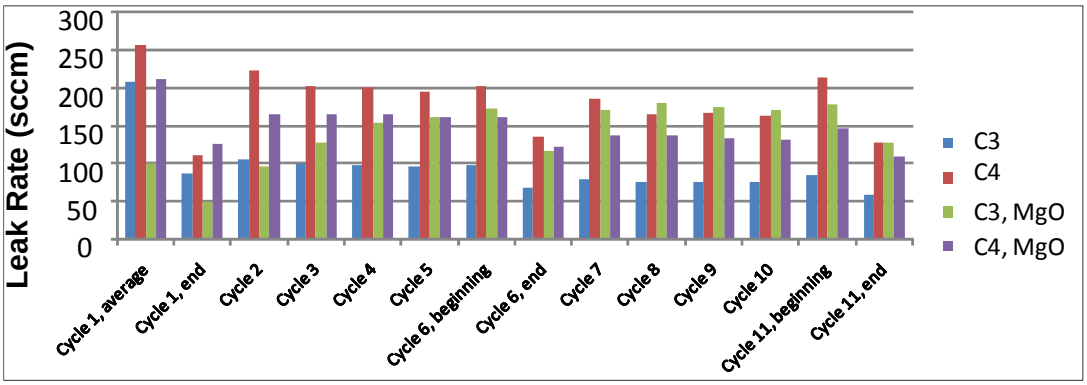

Figure 18-31. Seal leak rates over 12 cycles.

Cycle 1 lasted 23 days at full conditions; Cycle 6 lasted seven days. All other cycles were 50 hours, during which time there was a pressure increase from 30 to 200 psig, a hold at 200 psig and then depressurization to 30 psig. It was observed that:

- Seal configuration C3 achieved the target leak rates. However, it may require as long as two weeks at temperature to achieve this level of sealing.
- Seal configuration C4 did not seal sufficiently when used with the advanced architecture base piece.

- Seal configuration C3 with MgO did not perform as anticipated based on similar experiments with smaller seals.

Seal A4

An advanced architecture base piece with a No. 4 seal was tested in the XVU3. The XVUs are equipped with vacuum permeate systems so samples can experience the full oxygen partial pressure driving force during a seal or flux test. A cap plate was used to cover the opening on top of the base piece. Both the cap plate and seal plate were made from Alloy A. Leakage occurs through the seals at both the seal plate and the cap plate. A communications card failed during testing; it was replaced and the test was restarted. The leak rate was significantly higher on the restart (Figure 18-32).

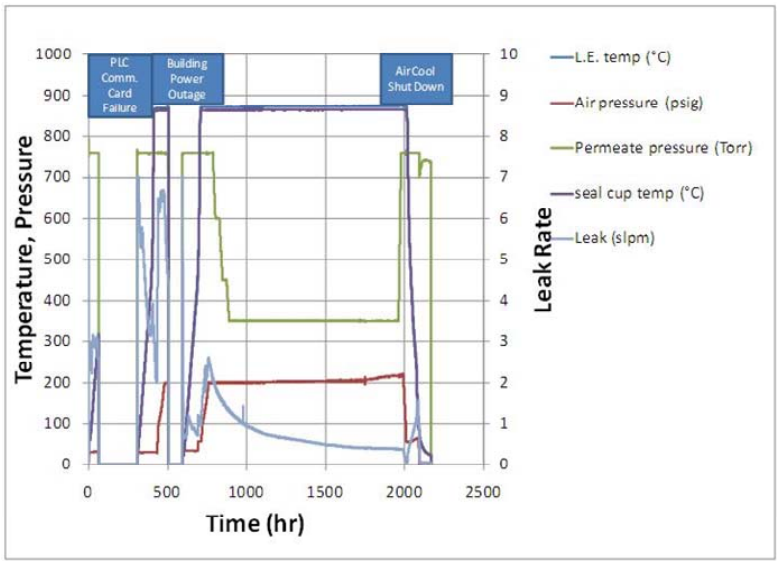

Figure 18-32. Results from base piece testing in XVU3.

A power shutdown tripped the heater during the permeate pressure ramp. After the restart, a relatively low leak rate was observed during the permeate pressure ramp.

Testing continued as shown in Figure 18-33. The sample was subjected to a simultaneous pressure ramp and sequential pressure ramps. The leak rate was consistent. After holding for several days, the permeate pressure control was put into manual mode. The permeate pressure was increased and decreased, then subjected to a series of pressure ramps. The sample exhibited good performance.

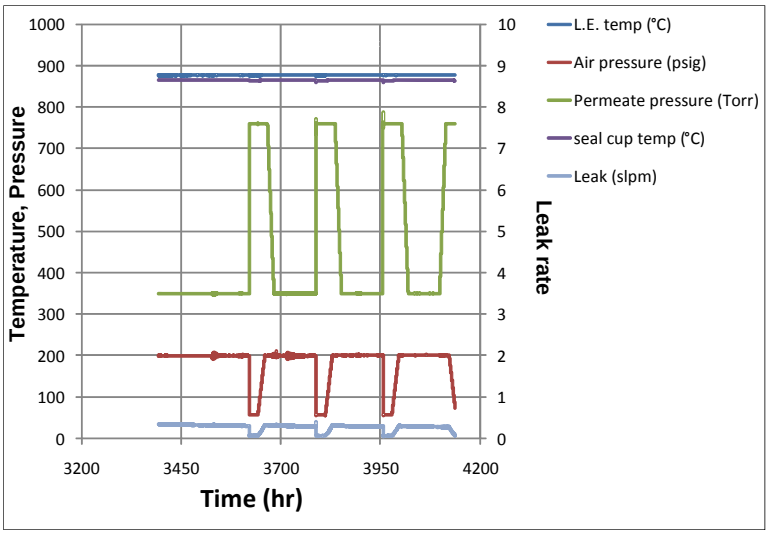

Figure 18-33. Results from continued testing of base piece in XVU3.

Seals, A5, A6, C8 and C9

Testing of seals with MgO disks and various seal configurations were conducted in the SLTRs. Four seal configurations were tests in duplicate: A5, A6, C8 and C9. The experimental objectives were:

- Obtain longevity results for seal configurations A5 and A6.
- Compare the metallurgical interaction of A5 and A6 with the seal plates.
- Obtain Seal C8 performance data.
- Compare the performance of Seals C8 and C9 to A3 and A4.

Table 18-4 documents the experimental design. Each combination of factors was run in duplicate.

Table 18-4. Experiment details for run 9638-SLTR3-20110411.

Position #	Seal Configuration
1	A5
2	A5
3	A6
4	A6
5	C8
6	C8
7	C9
8	C9

The samples were subjected to a 7-day cycle followed by nine 24-hour cycles. Cycles 11 and 12 were each 28 days long. Figure 18-34 details the results. Seal configuration A5 showed no signs of deterioration through a total of over 2,300 hours on stream and 12 temperature-pressure cycles.

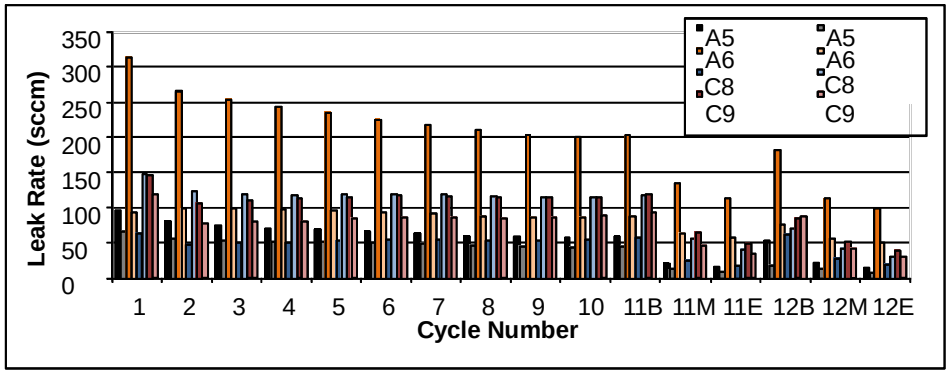

Figure 18-34. Seal leak rates over 12 cycles.

Seal 10

A test was conducted on No.10 seals with an advanced architecture AP2k base piece-dome assemblies Two MgO disks were tested for comparison with the AP2k parts. An Alloy A seal cup was used for all samples. The seal configurations are documented in Table 18-5.

Table 18-5. Experiment details for run 7001-SLTR1-20110923

Unit #	Ceramic Part	Seal Configuration
1- Short	AP2K BP-dome	A10
2-Tall	AP2K BP-dome	A10
3- Short	MgO	A4
4-Tall	MgO	A4

All four seals performed well on start-up, with leak rates of <400 sccm shortly after leading-edge conditions were achieved. After the first one-week cycle, the leak rates were all 170 sccm or lower. The two seals with advanced architecture AP2k parts were leaking at 69 and 112 sccm. During additional time on stream and cycling, Sample 1 developed some noise in its leak data. All samples saw two shorter cycles (roughly one week at full conditions), followed by three cycles of approximately one month each. The seals showed adequate robustness over four months of service with some cycling. Both AP2k samples were able to achieve the leak rate

target once they had been exposed to full conditions for a time period. Figure 18-35 documents the operating conditions and leak rate.

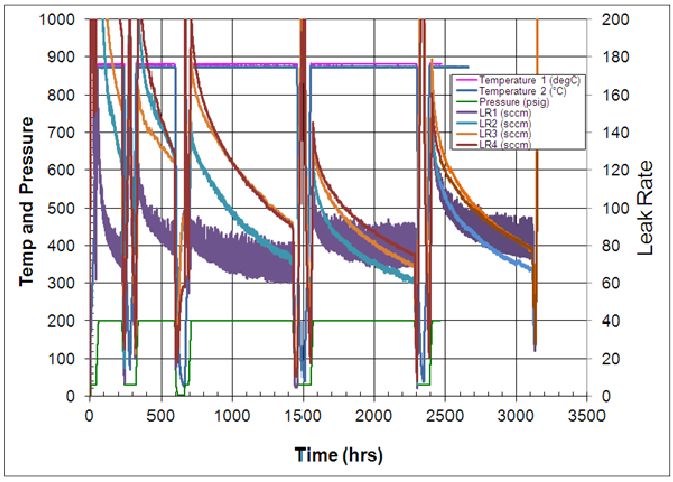

Figure 18-35. Seal A10 leak rate with cycling.

An advanced architecture wafer module with a No.10 seal and an Alloy A seal plate was tested in XVU2 using the standard module start-up protocol. The results are presented in Figure 18-36.

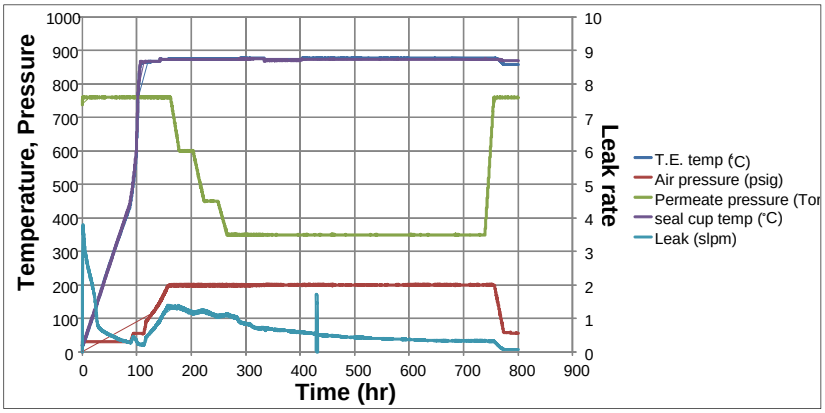

Figure 18-36. Results from test of advanced architecture wafer module with a No.10 seal.

The initial leak rate was higher than typical, but declined over the course of the hold.

Testing of an advanced architecture dome/base piece with an A10 seal was conducted in the TTR. The initial high leak rate decreased by ~50% during heat-up (Figure 18-37). The leak rate increased during the pressure ramp. Once the planned pressure was achieved, the leak rate decayed.

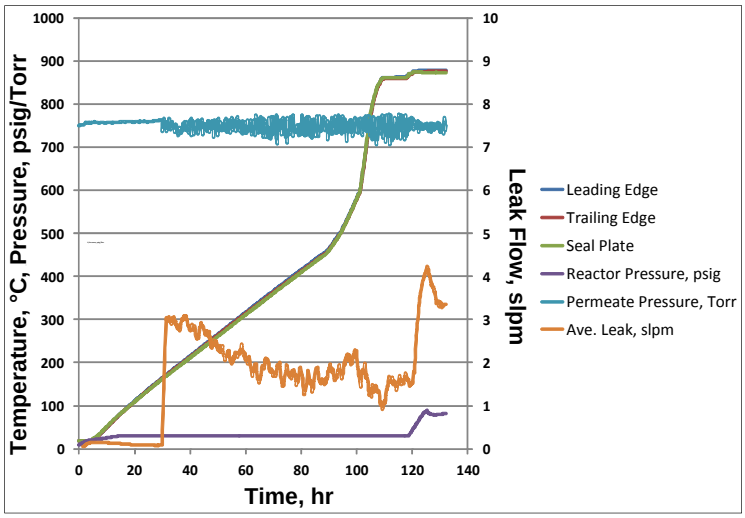

Figure 18-37. Leak rate of Seal A10 with an advanced architecture dome/base piece.

Seal No. 10 was also tested in the SLTR1. The seal configurations are documentes in Table 18-6; seal performance is documented in Figure 18-38

Table 18-6. Sample descriptions for test in SLTR1

No.	Top	Cup Material	Seal Configuration
1	AP2k	A	10
2	AP2k	A	10

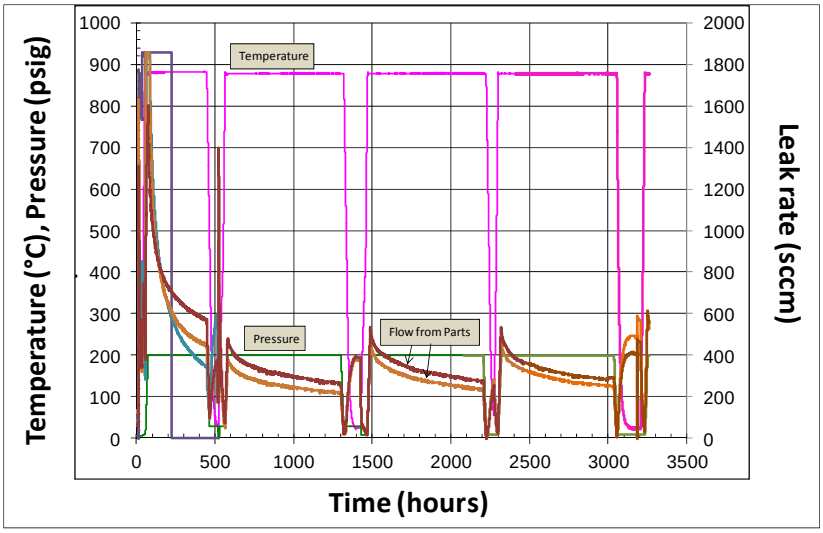

Figure 18-38. Seal 10 leak rate with time (AP2k).

The curves show the total flow (composed of flux, part leak and seal leak) over the course of one two-week cycle and three four-week cycles. The cyclability and longevity of these seals were satisfactory. Seal No.10 was qualified for use at the ISTU.

Seal 11

An investigation was conducted on the performance of alternative seal materials which have low costs and widespread use in other high-temperature research. The initial test of such a seal, Seal No. 11, was carried out in the SLTR and used an Alloy C seal cup and MgO disks. The results are presented in Figure 18-39. For comparison, tests were conducted on two No. 4 seal configurations.

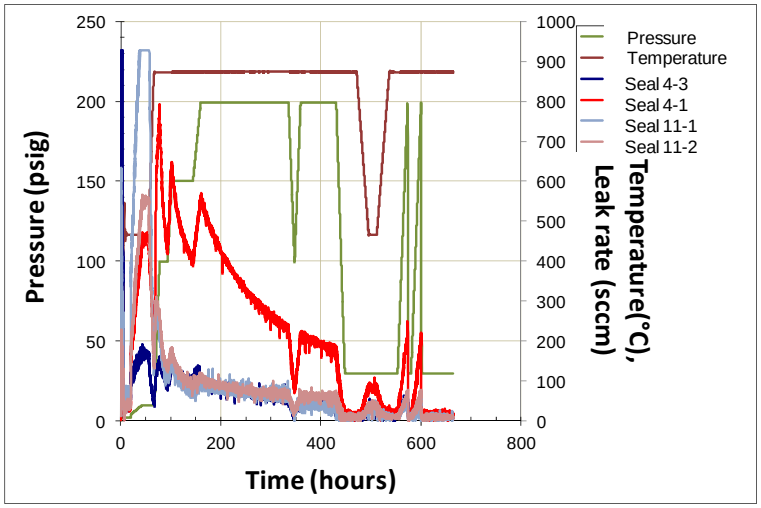

Figure 18.1-39. Performance of Seal Nos.4 and 11.

Another test of two samples, A and B, of Seal No. 11 achieved leak rates of <100 sccm relatively quickly during the two pressure cycles in the first 1150 hour of operation (Figure 18-40).

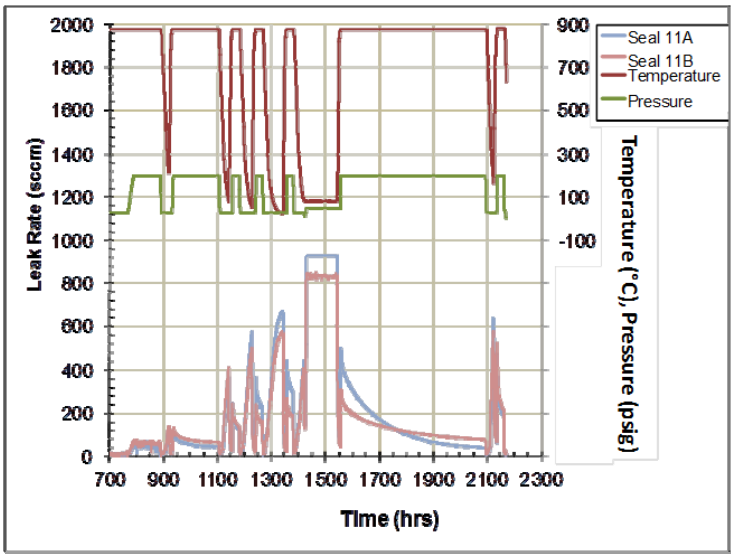

Figure 18-40. Continued performance testing of Seal No. 11.

The seals were then put through a series of 24-hour cycles to full temperature and pressure. Cycling degraded the performance of the seals. However, there was "healing" each time the seal was held at full temperature and pressure. At 1,550 hours on-stream, the seals were held at full temperature and pressure conditions to see if the baseline seal performance could be restored. The leak rate returned to a value below the target. Seal 11A initially had better performance but responded less robustly to cycling. During the extended "healing" period, its performance was better than Seal 11B.

A standard cycle was then initiated to see if the healing process eliminated the cumulative damage that had accrued. While the initial leak following this cycle was similar to the previous cycle and higher than initial cycles, the rate of leak decrease was faster following the extended hold. Figure 18-41 documents the leak rate for Seal 11A as a function of time after reaching full conditions for each cycle.

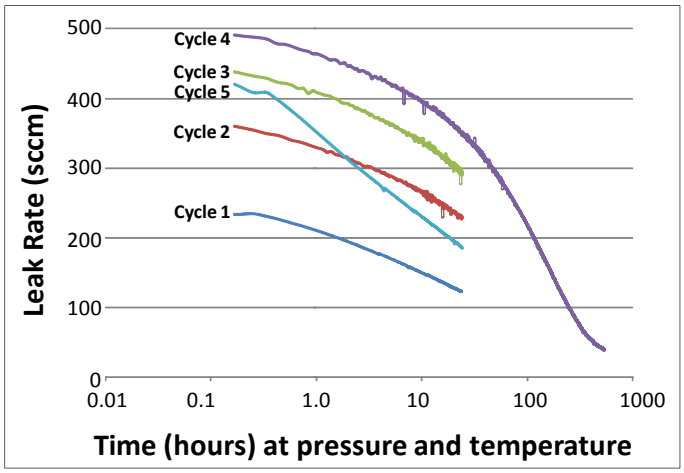

Figure 18-41. Seal 11A leak rate transient with time at full conditions.

Eight identical No.11 seals were tested in SLTR3. All eight samples were placed on an Alloy A seal cup with a MgO disk. The results are presented in Figure 18-42.

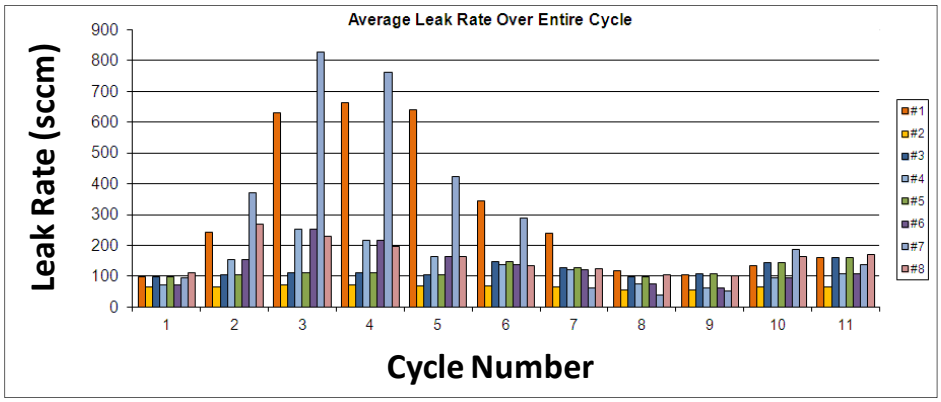

Figure 18-42. SLTR #3 test leak rate test of Seal No. 11.

The samples were started up with a one-week hold at full conditions, and then subjected to three cycles with 24-hour holds at full conditions. Between each cycle, the seals were depressurized and cooled to <60°C. These were followed by a similar series of "day," "week" and "double-week" cycles. Table 18-7 documents the cycle lengths and the calculated purity reduction that the seals would contribute to the expected oxygen production from a 1 TPD module. The expected purity reduction is very small.

Table 18-7. Seal No. 11 leak test conditions and predicted purity reduction.

Cycle #	Duration (hours)	% Purity Reduction
1	168	0.04%
2	24	0.08%
3	26	0.14%
4	24	0.13%
5	71	0.10%
6	168	0.08%
7	168	0.06%
8	328	0.04%
9	336	0.04%
10	336	0.06%
11	325	0.06%

The samples held up quite well over an extensive series of cycles. It is important to note that even in the last cycle, the leak rates were still improving with time. Some of the samples did not perform well under the fast cycles, but even these did not have a major impact on the overall purity of the eight-sample system. Cycle 3 had the highest purity impact. All longer cycles showed much lower leak rates. The experiment showed that this seal design can hold up well under both cycling and 3½-month longevity tests. SEM evaluations were conducted on the best- and worst-performing seals. This evaluation revealed changes to the microstructure and composition, including the formation of new microstructures, void formation, micro-cracking and deposition of chromium-rich phases within the seal.

Full-scale seal tests were conducted in the SLTR2 using a No.10 and No.11 seal between AP2k domed base pieces. The seal configurations are documented in Table 18-8. This test is noteworthy as it was the first test of Seal No. 11 with AP2k parts.

Table 18-8. Seal No.10 and No.11 testing combinations with AP2k.

No.	Top	Cup Material	Seal Configuration
1	AP2k	A	10
2	AP2k	D	11
3	AP2k	D	11
4	AP2k	A	10

The initial results are presented in Figure 18-43.

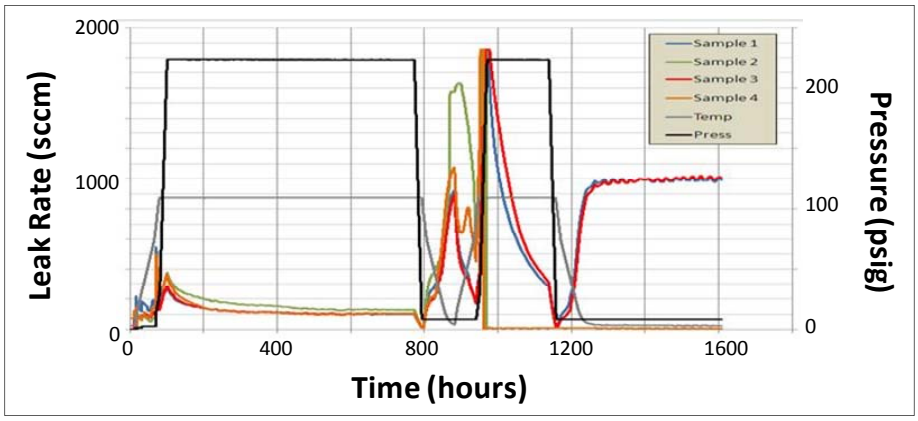

Figure 18-43. Leak performance of Seal No. 10 and 11 with AP2k dome/base pieces.

The initial seal performance was quite satisfactory. All four seals achieved low leak rates very quickly and maintained this performance through the first one-month cycle as shown in Figure 18-44.

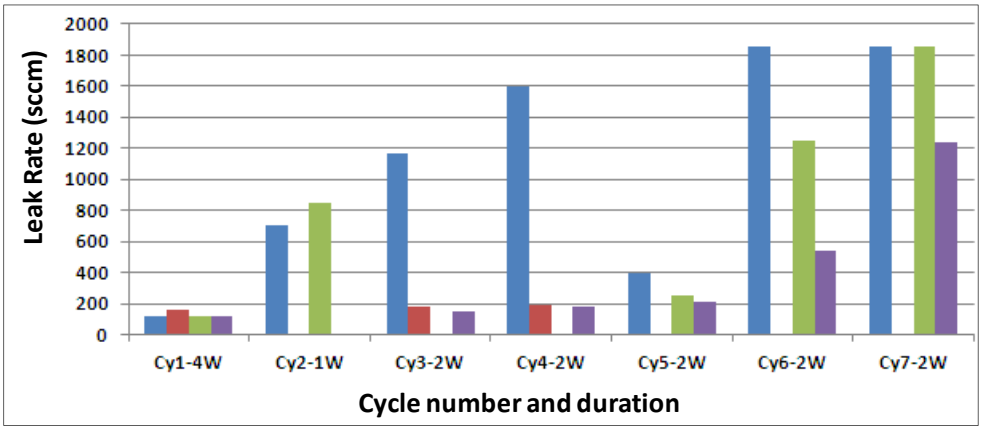

Figure 18-44. Seal No.11 performance.

However, all four seals incurred damage upon cycling followed by 1- or 2-week holds. Two of the seals had to be replaced after failing during the second cycle and again in the third cycle. The new seals were reconfigured with the hope that they would be more robust under temperature-pressure cycling and provide stability for the module. However, the new configuration reduced the local sealing stress. On restart (Cycle 4), the two new seals performed well, but one of the existing two seals did not. One of the samples failed because the AP2k domed base piece had cracked. The leak rates of the two new seals were slightly high, but this reflects both the reduced sealing stress and the higher inherent leak rates of the AP2k parts. The remaining cycles were completed with disappointing results. In every case, the seals initially demonstrated excellent performance but failed after one or two cycles. In many cases, these failures could be attributed to cracking of the seal. It was concluded that this seal arrangement is inadequate for ITM Oxygen applications involving thermal cycling.

Seal A13 and A14

Long-term tests of seals A13 and A14 were conducted (Table 18-9).

Table 18-9. Seal testing combinations including Seal Nos. 13 and 14.

No.	Ceramic Part	Cup Material	Seal Configuration
1	**MgO**	**A**	**13A**
2	MgO	A	13B
3	**MgO**	**A**	**14**
4	MgO	A	14

The test results are documented in Figure 18-45.

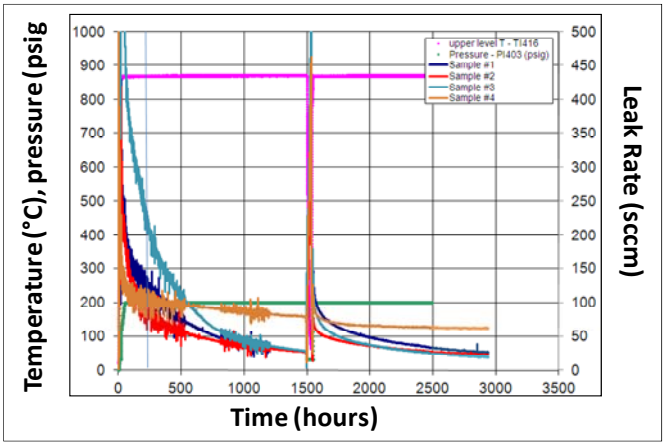

Figure 18-45. Leak rates of Seal Nos.13 and 14 over time, 2 cycles.

The seals were brought to full conditions and held for two months. All four seals continued to improve, although seal Sample 4 did not achieve an excellent seal. Samples 1, 2 and 3 achieved a "reasonable" leak rate at the start of full conditions and achieved the target leak rate in about two weeks. At the end of the first two-month cycle, the seals were depressurized and cooled, then reheated and re-pressurized. Seal performance was similar to the first cycle, with some minor variance in the transients. Seal Sample 2 sealed more rapidly than Sample 1, but the performance of the two converged with time.

Seal No. 16

Testing in SLTR3 assessed the relative performance and robustness of various seal architectures (Table 18-10).

Table 18-10. Seal configurations for SLTR3 tests.

No.	Ceramic	Cup Material	Seal Configuration
1	**AP2k**	**A**	**10**
2	AP2k	A	10
3	**AP2k**	**A**	**4**
4	AP2k	A	4
5	**MgO**	**A**	**16**
6	MgO	A	16
7	**MgO**	**A**	**11**
8	MgO	A	11

It was observed that:

- Seals 10 and 16 had better initial performance.
- Seal 4 has been quite robust.
- One Seal 10 degraded and then failed.
- Both samples of Seal 16 and 11 initially degraded, but healed somewhat during subsequent two-week cycles.
- Cooling to room temperature and full depressurization caused Seal 11 samples to fail, and there was significant damage to both Seal 16 samples.

Seals Nos. 17, 18, 19, 20, and 21

Seal screening tests were conducted in SLTR4 to evaluate other designs (Table 18-11).

Table 18-11. Seal configurations for SLTR4 trials.

No.	Ceramic	Cup Material	Seal Configuration
1	MgO	A	17
2	MgO	A	18
3	MgO	A	19
4	MgO	A	19
5	MgO	A	20
6	MgO	A	20
7	MgO	A	21
8	MgO	A	21

Seal leak performance through three cycles is presented in Figure 18-46.

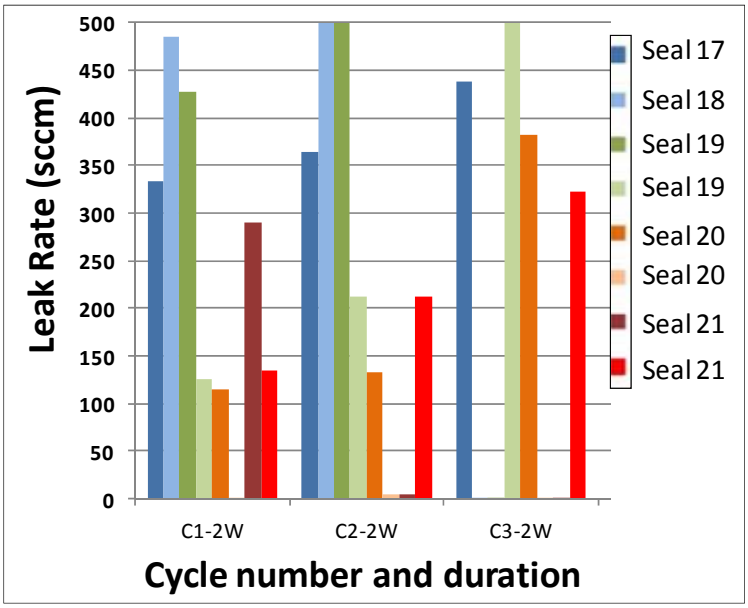

Figure 18-46. SLTR4 Seal performance. Each cycle was followed by a 2-week hold at high temperature and pressure.

One seal No. 19 and one Seal No. 21 failed, and the other sample of each configuration showed mediocre performance. However, some of the leakage is due to how the experiment was conducted. The first cycle was begun at 200 psig and then increased to 225 psig, while the subsequent cycles all went directly to 225 psig. One seal No. 20 (Sample 5) performed reasonably well, while the other (Sample 6) tripped its excess flow valve. The transient performance of the four seals that survived the three cycles is presented in Figures 18-47 though 18-50.

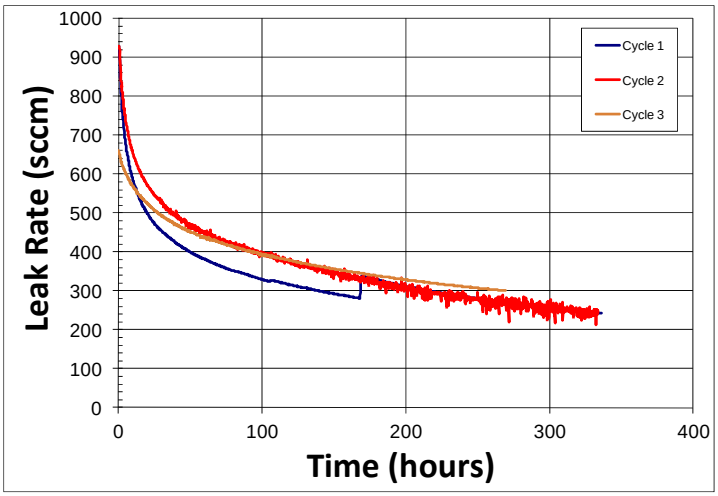

Figure 18-47. Sample 1, Seal No. 17 transient leak rate.

Sample 1 shows essentially identical behavior for all three cycles. Note that the pressure was increased from 200 to 225 psig roughly 170 hours into the first cycle.

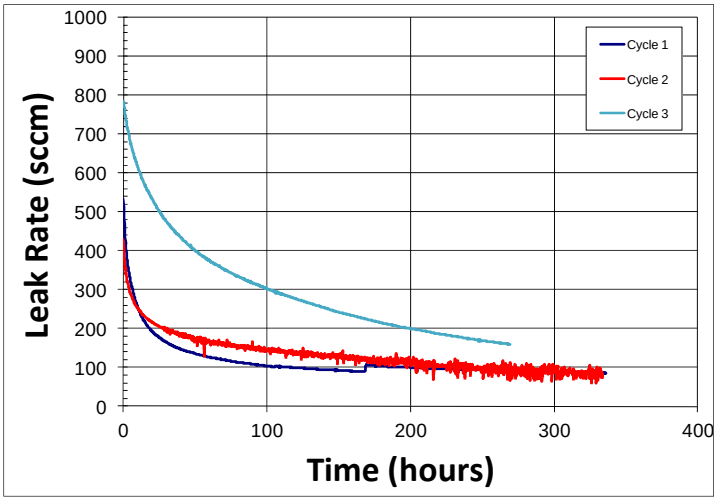

Figure 18-48. Sample 5, Seal No. 20 transient leak rate.

Sample 5, Seal No. 20 also showed very good reproducibility from the first cycle to the second, but performance degraded between the second and third cycles. The vessel was briefly depressurized between those two cycles to replace a relief valve, so it seems likely that this depressurization was responsible for the loss of performance.

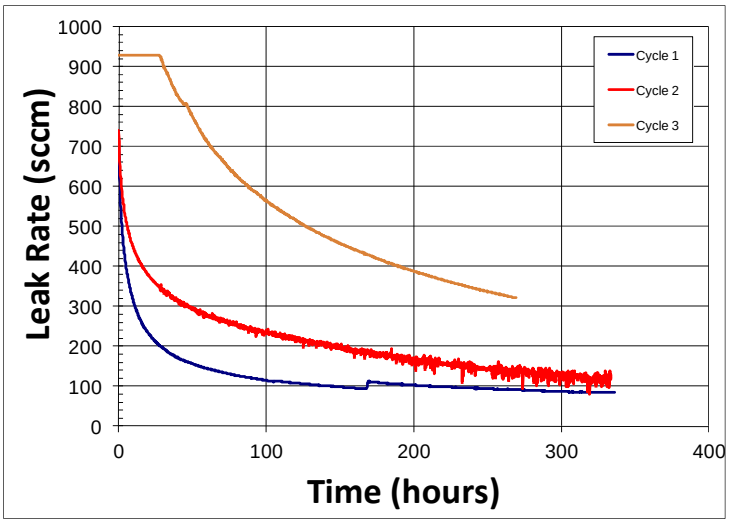

Figure 18-49. Sample 4, Seal No. 19 transient leak rate.

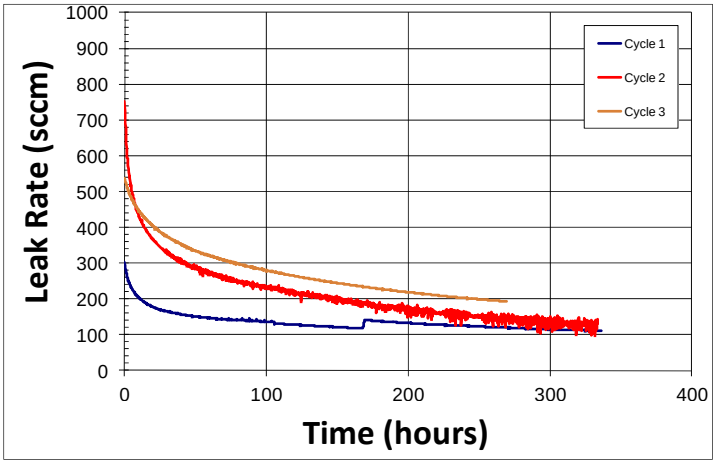

Figure 18-50. Sample 8, Seal No. 21 transient leak rate.

Sample 4, Seal No. 19 and Sample 8, Seal No. 21 had the two lowest leak rates but showed signs of cycle-to-cycle degradation. The expansion of one of the seal materials was measured to support seal development. Figure 18-51 shows the material expansion during heating/cooling.

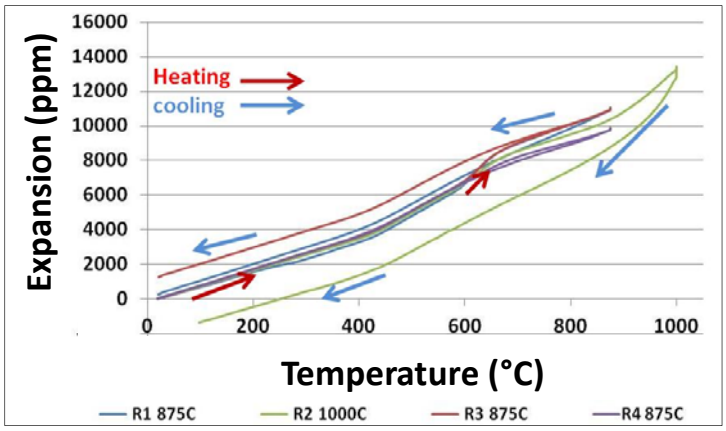

Figure 18-51. Seal material expansion versus temperature.

The sample showed a net contraction, suggesting that it was heated well beyond the softening point. On the next heating cycle, the expansion rate increased sharply at 600°C. This was not seen in other cycles.

Seal No. 23

Testing of two No.10 seals and two No.23 seals were completed in the SLTR2 (Table 18-12). Seal No.10 performed well; Seal No.23 did not perform well.

Table 18-12. Seal configurations tested in the SLTR2.

No.	Ceramic	Cup Material	Seal Configuration
1	AP2k	A2	10
2	AP2k	A2	10
3	AP2k	A2	23
4	AP2k	A2	23

Tests of eight No.23 seals placed between an AP2k sample and an alloy A cup were initiated in the SLTR3. Two seals (Samples 2 and 5) failed early due to faulty setting of the excess flow valve. Figure 18 -52 shows the average "leak" rate over the entire hold period, where "leak" rate refers to the sum of the seal leak, AP2k part leak and flux through the AP2k part. Figure 18-53 documents the average leak rate over the last four hours of the cycle (i.e., when the seal is performing at its best). Each cycle was at full conditions for 168 hours.

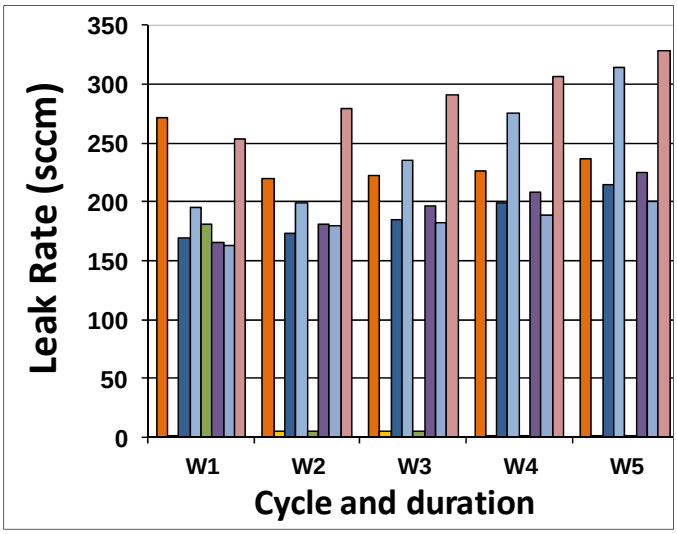

Figure 18-52. Seal No.23 average seal performance over a week at steady conditions following temperature/pressure cycling for successive weeks, 1-5.

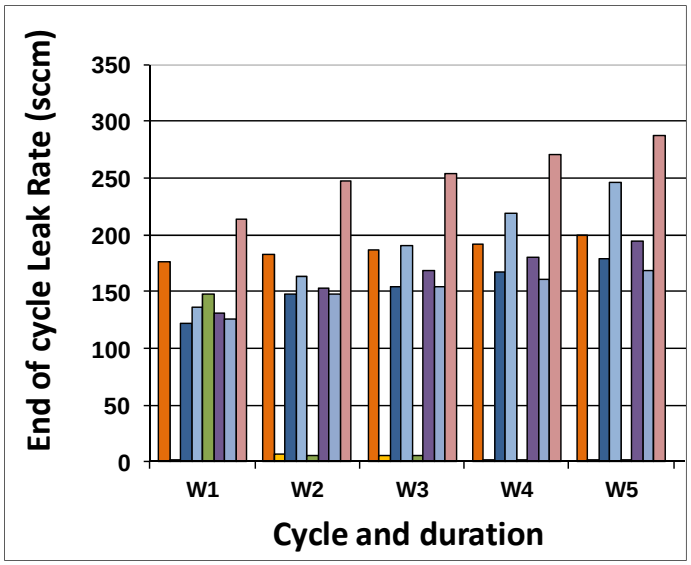

Figure 18-53. Seal No.23 average performance over the last four hours of steady conditions following temperature/pressure cycling for successive weeks, 1-5.

Seal performance was consistent, and the overall leak rates were reasonable. All of the samples showed a gradual increase in leakage from cycle to cycle. The performance of all the seals improved rapidly during each hold at operating conditions.

Given the encouraging cyclic testing shown above, additional testing of Seal 23 was conducted. Eight replicate samples were tested in SLTR3. Figure 18-54 documents the operating conditions and leak rate of all eight replicate samples over the full operating period of the testing.

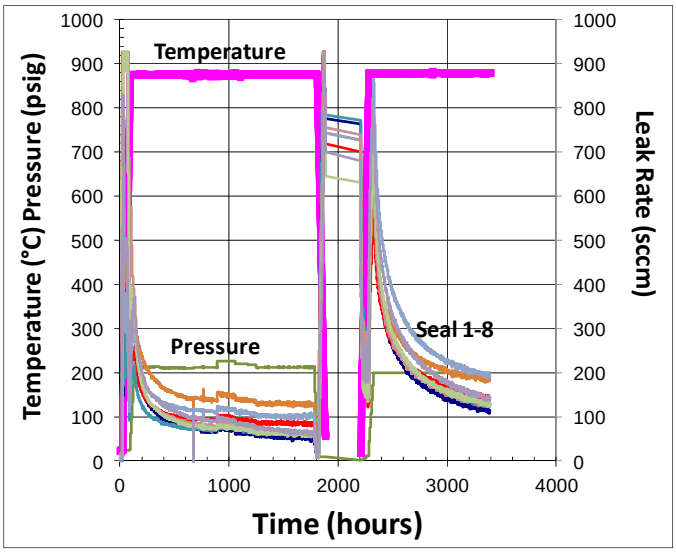

Figure 18-54. SLTR3 operating conditions and seal leak rates.

The samples were exposed to an 1,800-hr cycle, then a two-week outage at room temperature and zero pressure, followed by 1,000 hours at normal operating pressure and temperature. There was some loss of performance from the first cycle to the second, and it took longer for the seals to come to steady state. However, the sample-to-sample performance variation was encouragingly small.

Figure 18-55 documents the leak rate behavior of five of the seals during the depressurization step. This figure confirms that leak behavior is essentially linear with pressure driving force.

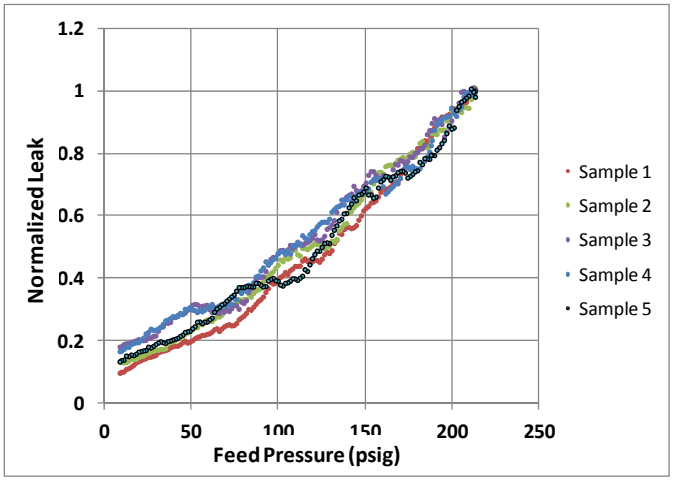

Figure 18-55. SLTR3 seals normalized leak rate versus pressure.

Four No.23 seals with AP2k domed base pieces were evaluated in the SLTR1. Seal Samples 3 and 4 had the same configuration except for a variation in seal element dimensions. Figure 18-56 documents the SLTR1 operating conditions and leak rate of each seal.

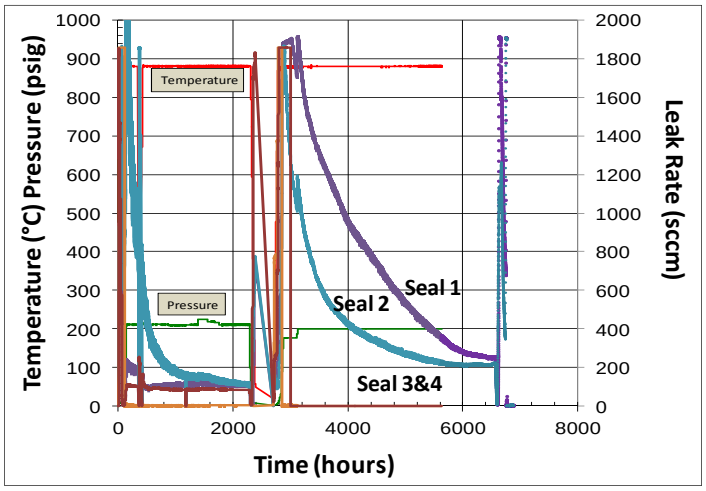

Figure 18-56. SLTR1 operating conditions and seal leak rates of four samples of No. 23 seals. The pressure data are depicted with green data points.

Seal Samples 1, 2 and 4 started up successfully, with fairly similar total leak rates that include some flux through the parts and some part leakage as well. Sample 3 did not seal well and tripped the excess flow valve during the first pressurization. The disturbance at 350 hours on-stream was due to an outage; it did not hinder any of the remaining three samples and actually improved the performance of Sample 1. The slow increase in total leak through Sample 1 gradually leveled out. The samples were on-stream for 2,200 hours before the unit was shut down for a scheduled two-week, building-wide power outage. Sample 4 failed during the start-up of the second cycle. The leak rates of Samples 1 and 2 improved rapidly over the five weeks post-restart. Depressurizing and then cooling the samples a second time led to high leak rates in both seals upon re-heating and re-pressurizing. The run was terminated after about eight months of total time at full conditions. The seals were all easily disassembled. None of them showed any tendency to constrain the AP2k domed base piece by the seal plate.

Seal No. 24

The performance of seal Nos. 10, 15, 23, and 24 were evaluated in SLTR4. All seals have Alloy A seal cups and a MgO disk. Figure 18-57 displays the SLTR4 operating conditions and leak rate data of each seal.

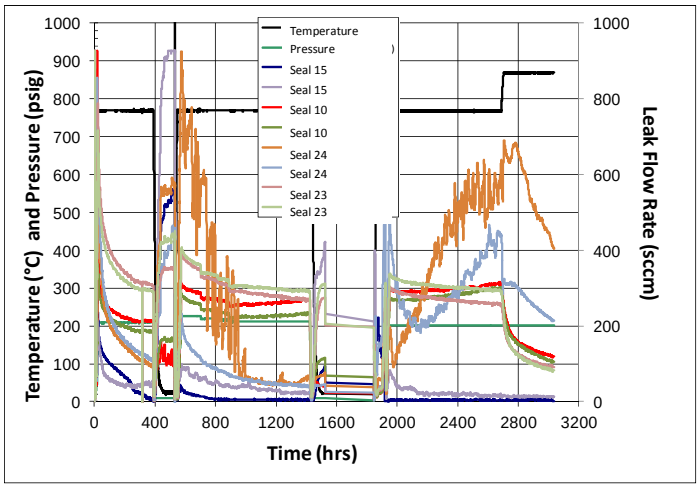

Figure 18-57. SLTR4 operating conditions and seal configuration leak rates.

The data shows good reproducibility between the two samples of each type up to the 400 hour mark of the first cycle. Seals No.15 and No.24 formed superior seals compared to seals No.10 and No.23.

The following occurred during the second cycle:

- One of the No.23 seals showed erratic performance, although it did eventually achieve high seal quality.
- The No.23 seal performance was similar to the first cycle.
- The No.10 seals degraded somewhat.

Seal No. 25

Data from the testing of Seal 25 is presented in Figure 18-58.

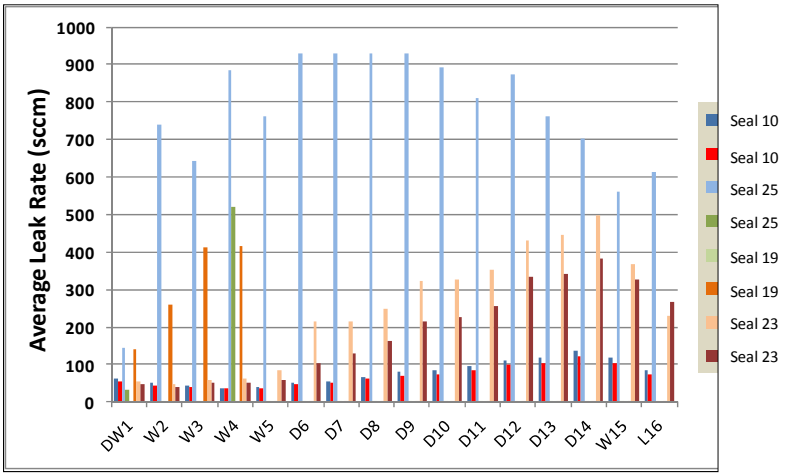

Figure 18-58. Leak rates of various seal configurations, including seal No. 25.

There is evidence of reproducibility between pairs of samples, most notably the seal No.10 and the seal No.23 samples (two each). Based on the revised data, it is concluded that:

- Seal No.19 failed badly.
- The performance of seal No.10 was excellent.
- There was a clear ordering of seal performance: No.10> No.23> No.25> No.19.

Exploratory Seal Concepts

Exploratory seal design concepts were tested in the SLTR3. Figure 18-59 documents the average leak rate over five cycles.

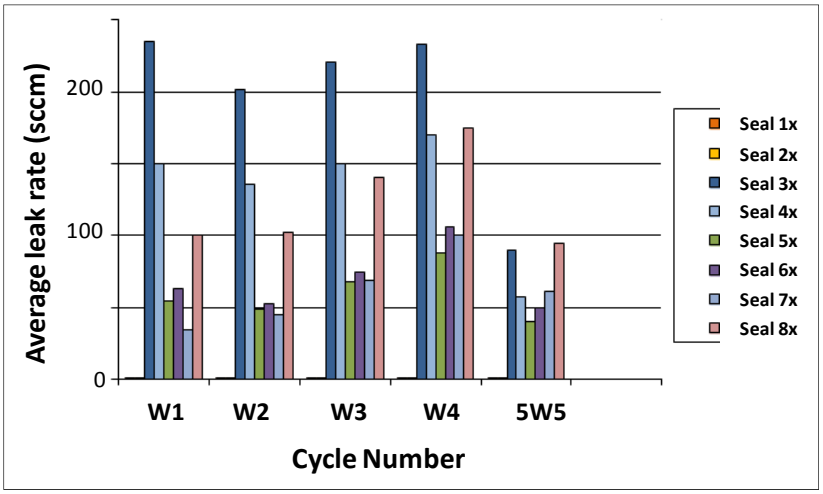

Figure 18-59. SLTR3 exploratory seal average leak rate over 5 cycles.

Seal Nos. 1x and 2x failed on start-up; the performance of seal Nos. 3x and 4x was robust. Seal Nos. 5x and 6x looked good initially, but trended upward in the third and forth cycles. Their performance in the fifth cycle was better.

A second set of experimental seals was tested in the SLTR3. Figure 18-60 documents the average leak rate over five cycles.

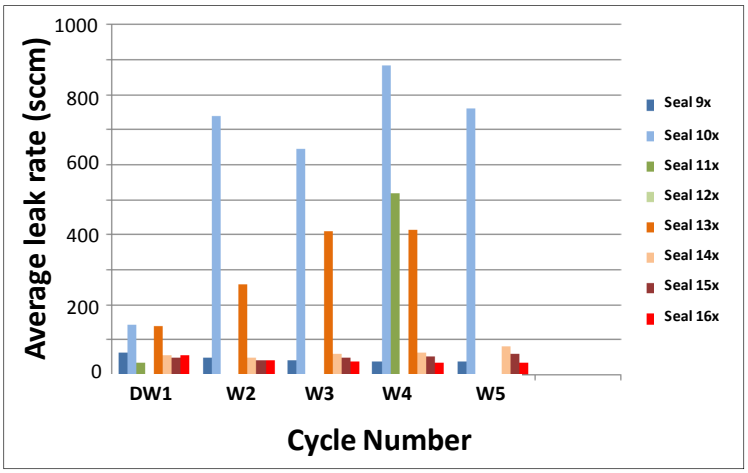

Figure 18-60. SLTR3 exploratory seal average leak rate over 5 cycles.

Seal Nos. 9x and 10x are duplicate seal designs, as were 11x and 12x, 13x and 14x, and 15x and 16x. Seal Nos. 11x and 12x performed poorly, with seal No. 12x failing immediately. Seal No. 11x showed excellent performance through the first cycle. However, during the cooldown, the leak sharply increased and remained at the higher level through the subsequent heatup. When the pressure was raised, the leak rose sharply and tripped the excess flow valve. Seal Nos. 9x and 10x produced inconsistent results, and seal No. 10x had a high leak rate. The data for seal No. 11x on Cycle 4 is an artifact of the excess flow valve performance.

Metal-to-Metal Seal

Unlike the lab units, where the metallic parts used to seal to the ceramic and receive the oxygen product are reconditioned for each test, large-scale ITM units will have permanently mounted piping to the (oxygen permeate) product system. When modules are replaced on a periodic basis, a fresh metal surface will be required at the ceramic-to-metal seal. Designs incorporate a metal seal plate which is bolted onto the permanent product system and provides a flat surface for the ceramic-to-metal seal. A metal-to-metal seal will be required between the permeate piping and the seal plate.

A metal-to-metal seal test was conducted in the XVU1. The assembly was intentionally torqued incorrectly to determine the base leak rate and whether the bolts could be removed and re-torqued without adversely affecting the seal. Figure 18-61 shows the initial results.

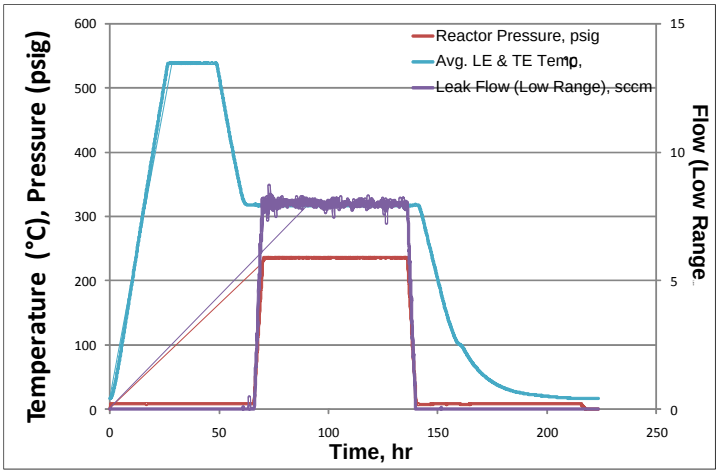

Figure 18-61. Initial metal-metal seal test results.

The seal assembly was taken through a bake-out period at 1000°F (538°C) followed by cooling to 600°F (316°C) and pressurizing to 235 psig. The leak rate under these conditions was low (7.5-7.7 sccm).

Alloy Pretreatment

Seal cups were coated with formulations intended to reduce or eliminate chromium volatilization from the metal seal surface (see discussion below). Tests were conducted in SLTR1 to assess two methods of pre-treating Alloy A seal cups (designated A1 and A2 in Table 18-13). The seals were tested at full scale using advanced architecture AP2k domed base pieces.

Table 18-13. Seal configuration with Alloy A pretreatment.

No.	Ceramic	Cup Material	Seal Configuration
1	AP2k	A2	10
2	AP2k	A2	10
3	AP2k	A1	10
4	AP2k	A1	10

Figure 18-62 documents the operating conditions and the leak rate over the eight cycles.

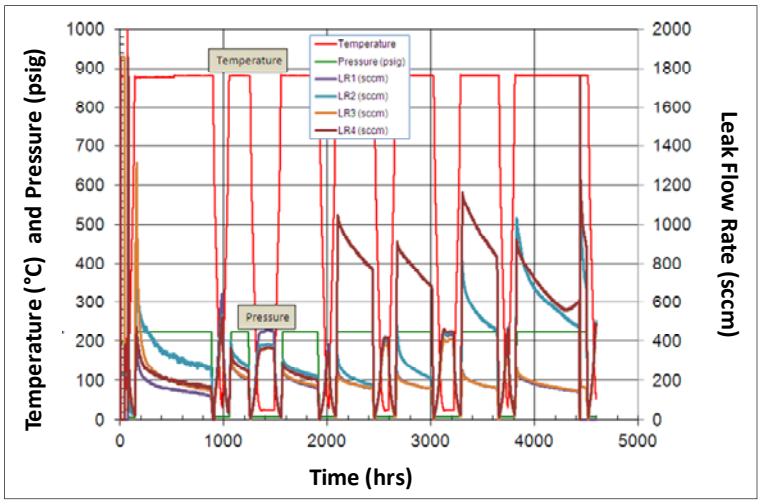

Figure 18-62. Seal performance of treated Alloy A.

All four samples performed well during the first (one month), second (one week), and third cycle, with comparatively low overall leak rates which correlate with the leak stand performance of the AP2k parts. The loss in performance from the first cycle to the second is due in part to the shorter duration of the cycle. Figure 18-63 shows the average leak rate over the eight cycles. The values reflect the average leak during the last 90 minutes of each cycle, rather than averaged over the entire cycle.

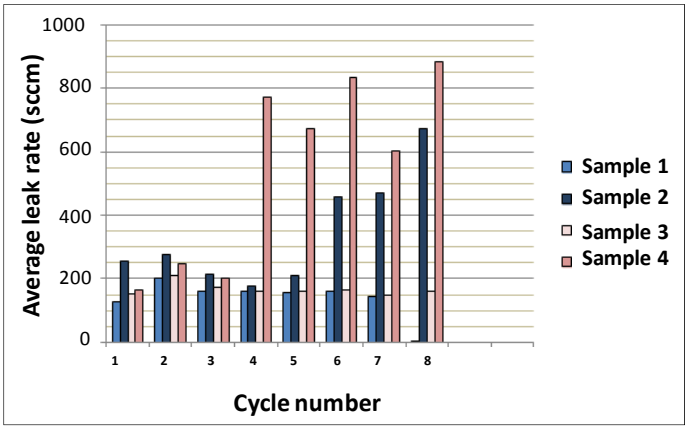

Figure 18-63. SLTR1 average seal leak rate over last part of the cycle for four pretreated A Alloy samples.

On the fourth cycle, Sample 4 developed a significant leak; similarly, Sample 2 began to leak on the sixth cycle. Both seals appeared intact upon unloading, but the bottom outer edges of both base pieces were visibly chipped over about one-eighth to one-quarter of their circumference. This suggests that the seals were not the primary cause of the leak increase.

The leak rates of Samples 1 and 3 continued to improve with time on stream. Sample 1 failed during the last cycle when an interruption in the feed air damaged the domed/base piece. There was no obvious evidence that the seal failed. In summary, this longevity test demonstrated that seal configuration No.10 held up very well under extended cycling.

Methods to reduce diffusion of seal material into the seal cup alloy at operating temperatures were investigated. Alloy A was pretreated for 12, 24 and 48 hours at a low temperature. Figure 18-64 shows the alloy surface after the pretreatment.

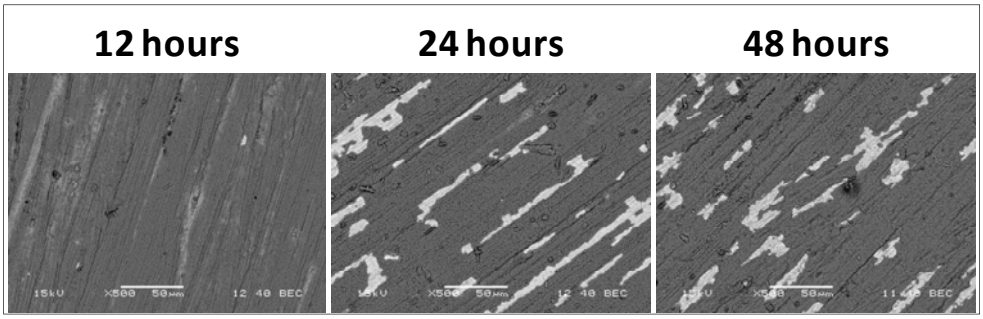

Figure 18-64. Alloy A surface after pretreatment.

The surface consisted of two regions, organized along the surface machining peaks and valleys. The samples were coupled with seal material and heated to two temperatures for four weeks. In untreated alloy, seal material diffusion appears over the whole interface. Samples pretreated for 12 and 48 hours showed greatly reduced diffusion; sSamples pretreated for 24 hours did not show any diffusion.

In a separate study, a coating was applied to Alloy A to see if diffusion could be reduced. The Alloy A samples were dip coated and left to dry overnight. The samples were coupled with seal material and heated to two temperatures for four weeks. No diffusion was found.

Diffusion couples were made with seal material and a coated alloy A to evaluate the effectiveness of the coating after heat treating to 875°C and 925°C for 10 weeks. Figures 18-65 and 18-66 show that after 10 weeks, the seal material did diffuse into the alloy.

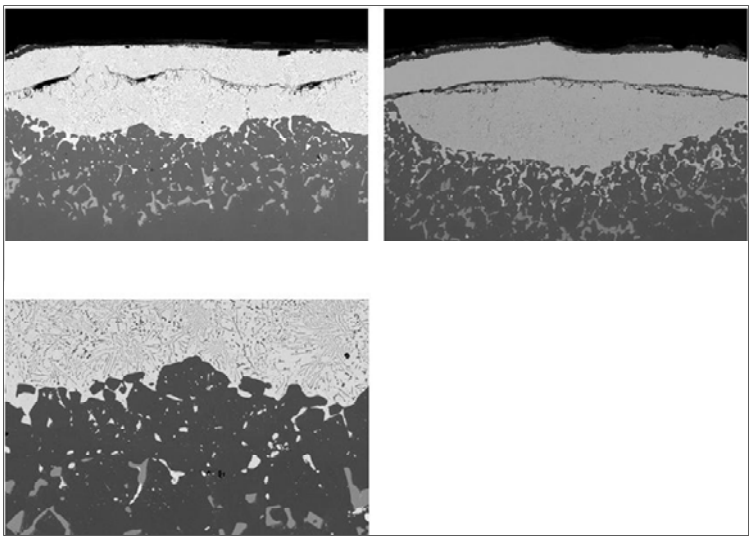

Figure 18-65. Cross section of diffusion couple made with seal material and coated Alloy A after heating to 875°C for 10 weeks.

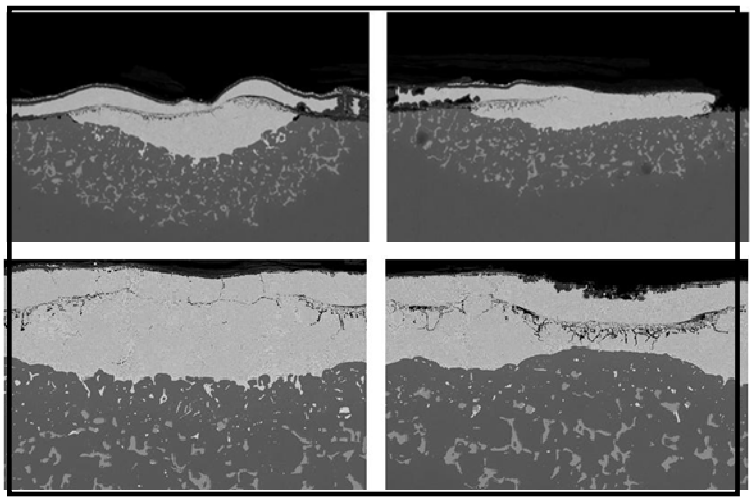

Figure 18-66. Cross section of diffusion couple made with seal material and coated Alloy A after heating to 925°C for 10 weeks.

A treated alloy A was further evaluated over 20 weeks. Initial results showed promise. Figures 18-67 and 18-68 show the samples aged over 20 weeks at 875°C and 925°C respectively. The treatment minimized seal material diffusion.

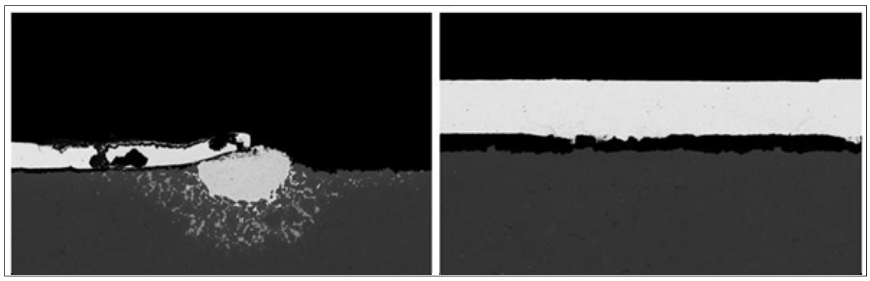

Figure 18-67. Cross section of diffusion couple made with seal material and treated alloy A after heating to 875°C for 20 weeks.

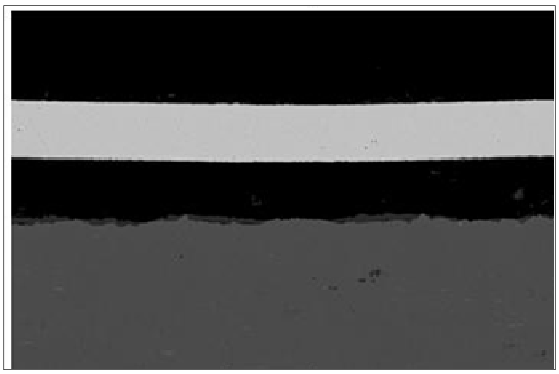

Figure 18-68. Cross section of diffusion couple made with seal material and treated alloy A after heating to 925°C for 20 weeks.

A series of experiments was initiated to look at the long-term reactivity of seal materials with the AP2K material. In the seal, two inorganic materials are in direct contact with the AP2K. The reactivity is examined by making diffusion couples consisting of a Composite Inorganic Material #1/ AP2K and a Composite Inorganic Material #2/ AP2K, applying a load to the couples to hold the interfaces in good contact and annealing at elevated temperature in air. Wafer rims were used for the ITM Oxygen ceramic parts. The Composite Inorganic Material #1/ AP2K couple was annealed for 500 hrs, then cross sectioned and examined using SEM/EDS. Figure 18-69 shows the elemental analysis of one of the composite AP2K couples after 500 hours at elevated temperature. No evidence of any interdiffusion or reaction was detected.

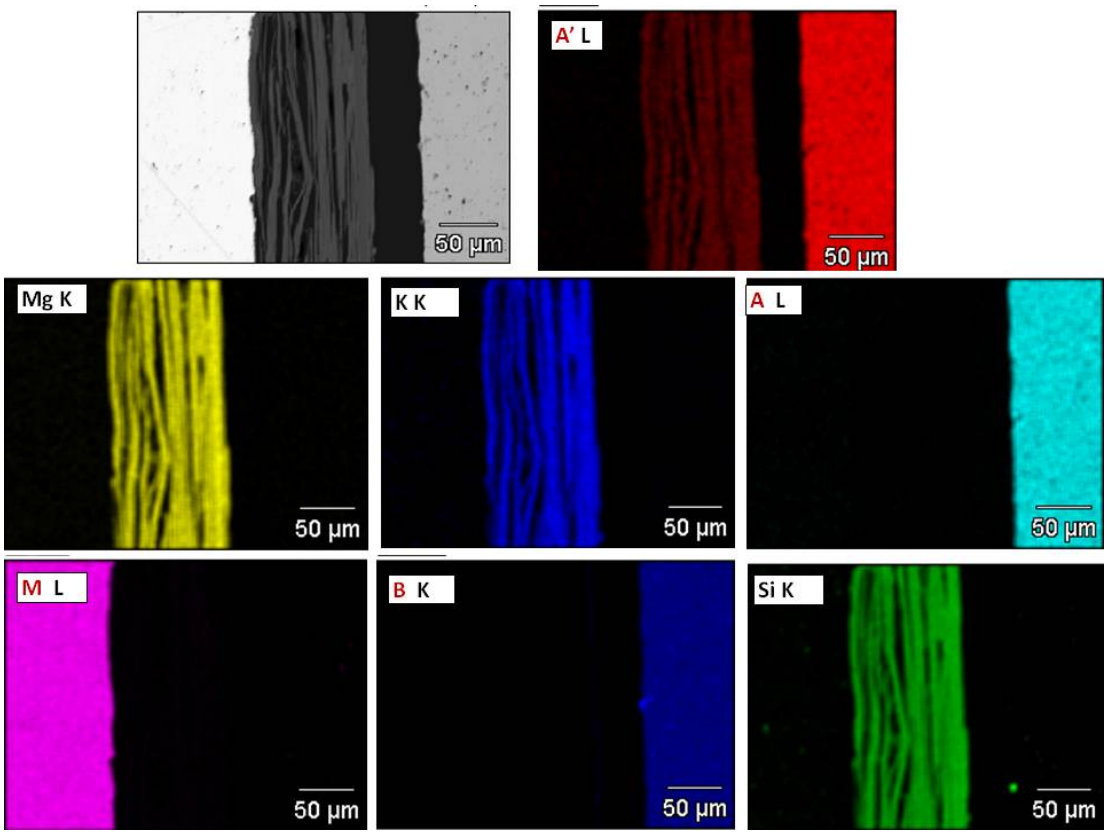

Figure 18-69. EDS elemental maps of the polished cross section of the seal material diffusion couple with the metal foil on the left and the AP2K on the right of each image. No evidence of any interdiffusion was detected. Note: M=metal; A, A' and B are the constituents of the AP2K material.

18.1.4 Module Flux Performance at High Driving Forces

Module FSM-063-1 (two wafers, low pressure-drop slot pattern) reached full temperature in the TDU and ran with a purity of 99.5% for more than 7,925 fluxing hours, which was a record for the TDU and a record run time for a full-scale module at the time. The vessel contained a prototype getter to remove chrome to provide information for getter design for the SEP and ISTU.

Flux at standard conditions was as expected and remained steady over most of the course of the run. The relatively steady flux value indicates that the getter bed was functioning well. The initial portion of the run gave flux versus feed rate data, while the later portion focused on gathering data to support modeling of module reliability.

Transitions between two permeate pressures were performed at successively faster rates with no deterioration of product purity, indicating the module sustained no damage. After successful completion of a smaller pressure interval, a larger interval was tested at successively faster rates again. Chemical expansion strains were larger at the higher intervals. Rates up to 250 times faster than typically used during startup were tested successfully and represent the fastest rates that the apparatus could perform. Some cycling of purity was noted with the permeate pressure cycles on the order of several tenths of a percent purity. However, this appears to be simple dilution of a fixed leak rate by widely varying flux rates. Figure 18-70 documents the operating conditions, leak rate and relative flux.

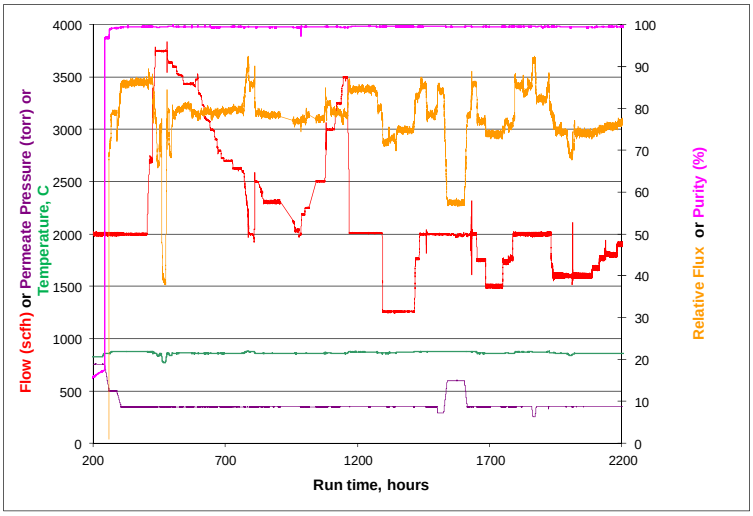

Figure 18-70. Flux, purity and process conditions for TDU run FSM-063-1.

Since no module failure occurred during this sequence, the module temperature was reduced and the sequence of permeate pressure ramps was repeated. At this lower temperature, little or no creep of the AP2K can occur so strains are not allowed to relax. The same permeate pressure ramp rates were repeated successfully as shown in Figure 18-71.

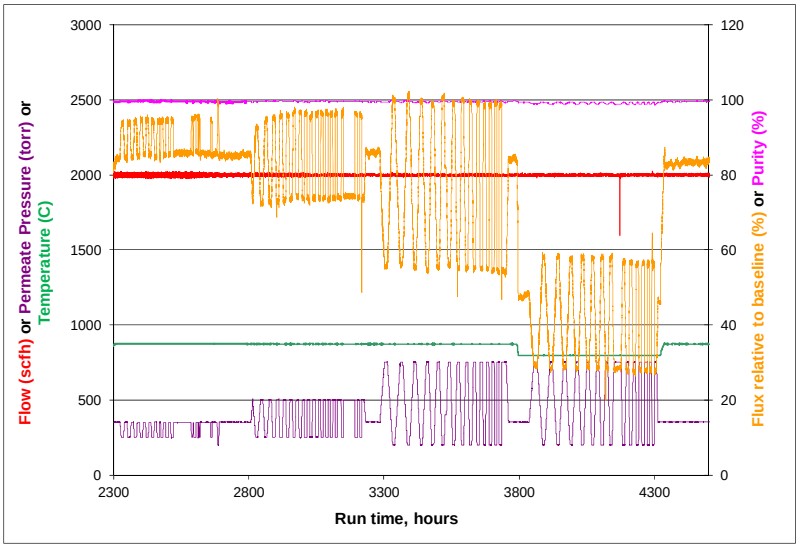

Figure 18-71. Flux, purity and process conditions for TDU run FSM-063-1.

Reliability testing then began to assess feed-side pressure changes. Five successive ramps at 10 psi per hour were run. The length of ramp was extended each time to give lower pressure targets and included 150, 125, 100, 75, and 50 psig hold pressures. The system ran fairly well through the first four ramps, with some temperature variation as the pressure changed. The ramp to 50 psig gave operational issues, with the flow control valve becoming unstable and cycling open and closed with resulting large flow swings. Despite the instability, the module survived and returned to leading-edge conditions at similar purity and flux values prior to the disturbance. Reliability of the module to both vacuum and pressure transients was very good. Figure 18-72 shows the response of flux to changes in vessel pressure.

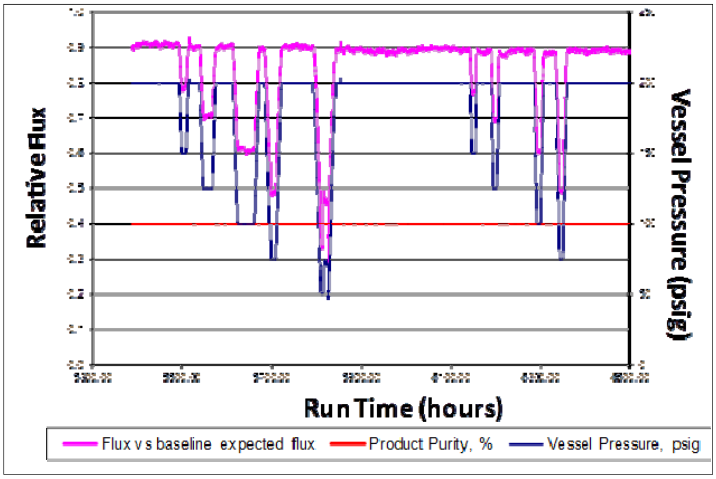

Figure 18-72. Reliability testing with pressure cycles, TDU.

Due to the length of this run, the product flowmeter became fouled. It was cleaned and recalibrated at ~7,400 hours in Figure 18-72. The process was shut down at 8,400 hours.

Wafers

During this Task, Ceramatec produced two types of wafers that differed by the geometry of the internal slot pattern. Air Products tested the two wafer types for flux performance in the Technology Development Unit (TDU). The two wafer designs were compared over a range of permeate pressures. Any significant difference in pressure drop inside the wafer slots would be manifested as a difference in measured oxygen flux rate, due to the different effective partial pressure driving forces over a portion of the active membrane surface.

The two modules were composed of a single wafer with an associated end cap and permeate tube. To account for different membrane thicknesses between the wafers, the oxygen flux was normalized to a standard under a reference set of operating conditions. A mass transfer model based on laboratory data was used to predict the flux as a function of permeate pressure. The predicted flux was also normalized to 1.0 at the reference conditions. Figure 18-73 is a plot of the normalized fluxes and the predicted flux.

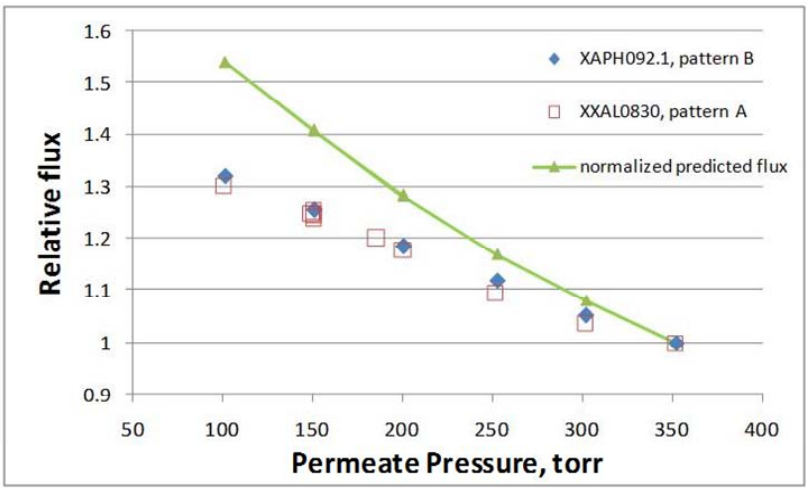

Figure 18-73. Comparisons of flux change with permeate pressure change between modules with different internal slot structures.

The two wafer types are labeled as “pattern A” and “pattern B.” At lower permeate pressure, the predicted flux increases due to a higher partial pressure ratio of oxygen across the membrane. Both of the wafer types were observed to yield measured flux values that deviated from the

expected values at lower permeate pressures. There was no significant difference between the two wafer types.

A prototype wafer module designed to improve performance in the presence of impurities was tested. The single-wafer module was loaded into the TDU and brought to full conditions, reaching a purity of 99.9% with good oxygen flux. A full study of process conditions was completed including multiple feed pressures, permeate pressures, and two temperatures. Figure 18-74 shows the measured oxygen fluxes for the improved wafer design (red symbols) along with data for the two types of internal slot geometries that were tested previously. As the plot shows, the improved wafer has a similar or better flux than the standard wafer types.

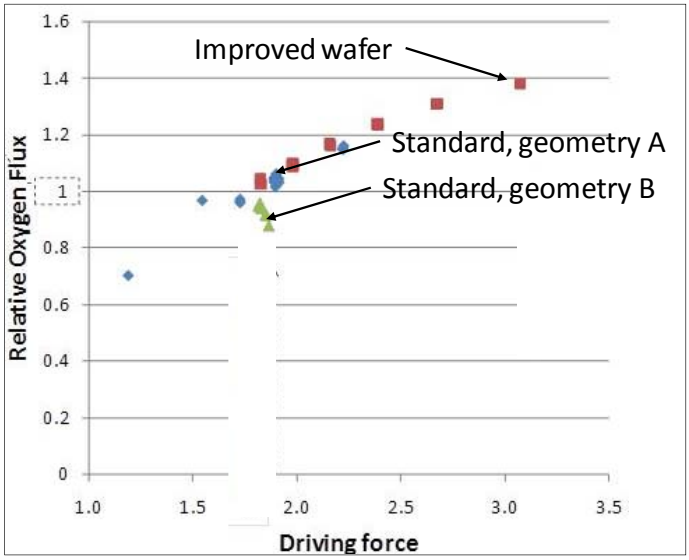

Figure 18-74. Comparisons of flux change with permeate pressure change between modules with different internal slot structures.

Another single-wafer module with a modified membrane layer was loaded into the TDU to confirm previous findings that showed no negative impact on flux from the modified membrane. The module reached leading-edge conditions with purity of 99.9% and achieved the expected flux. A full study of process conditions was done including multiple feed pressures, permeate pressures, and two temperatures as well as several feed rates. Figure 18-75 shows data for flux versus driving force.

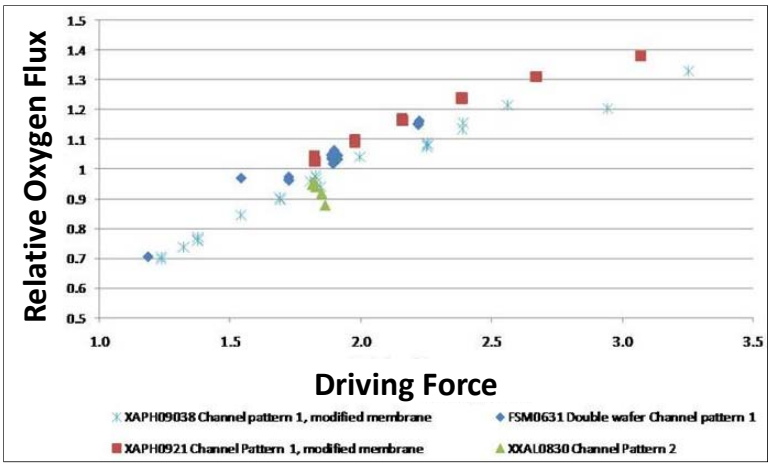

Figure 18-75. Normalized flux data versus driving force for TDU runs.

Good agreement was observed among the data generated from the one- and two-wafer modules, the wafers with different internal channel patterns, and those with and without modified membrane layers.

A two-wafer module with slot pattern #2 module was loaded into the TDU. The results after startup were good, with high purity (99.3%) and expected flux performance.

The process studies that were performed included measuring flux at a variety of feed and permeate pressures, and measuring flux versus feed flow rate. Figure 18-76 plots measured and predicted relative flux values against the driving force. The two series were obtained at different times during the run. The figure shows the temperature at each measurement point, which was very consistent.

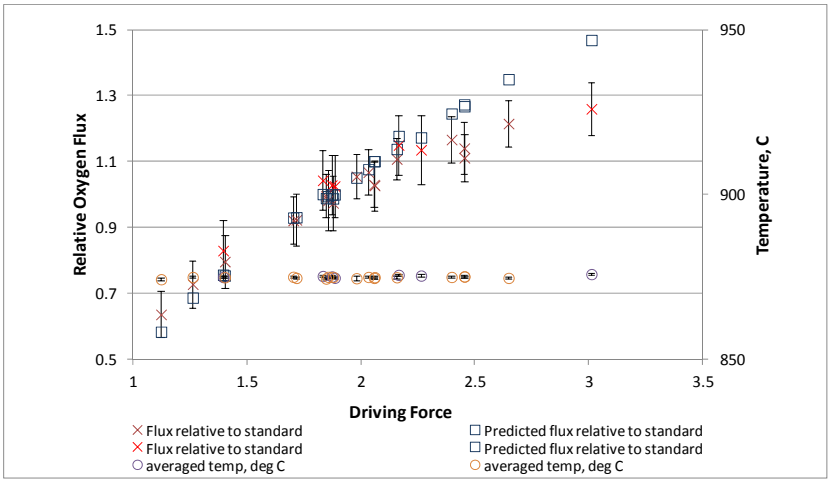

Figure 18-76. Flux versus driving force for two-wafer module.

At the expected membrane layer thicknesses, the measured flux exceeds the predicted flux at low driving force, and then falls off at high levels. The flux measured at the highest driving force/lowest permeate pressure was a record flux performance for a full-size wafer. A sudden drop in purity from over 99% to 82% occurred during a permeate pressure ramp to its lowest value. The purity improved with time and returned to nearly 98% at low driving force conditions.

This run also tested whether better insulation of the gap between the alumina internals and the TDU vessel shell reduces the bypass. Modeling work suggested that lower fluxes at low feed rates were due to bypass and depletion of oxygen in the fraction of feed in the module flow path. Flux was not observed to change with Reynolds number, as shown in Figure 18-77. Flux values were normalized to the flux at standard conditions; these values were obtained at slightly lower temperature.

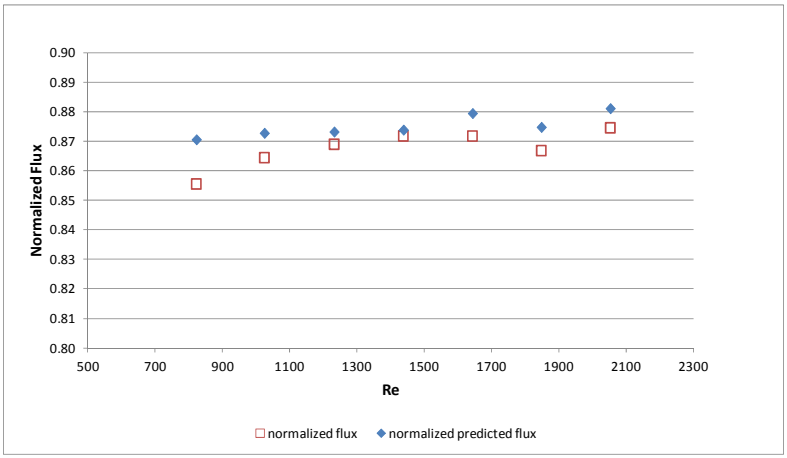

Figure 18-77. TDU flux as a function of Reynolds number for a two-wafer module.

18.1.5 Full-size Module Performance

Iso-control is a family of strategies that can be used to manage stress in ceramic components. Since AP2K exhibits both thermal and chemical expansion in response to changes in P_{O2} levels at high temperatures, P_{O2} can be intentionally manipulated to reduce chemical expansion stresses by reducing or eliminating the oxygen gradients in the material. Work on iso-control was discussed under Task 7.6.

Iso-compositional control was built into the design of the SEP for the feed system by providing two control valves for mixing nitrogen into air during cooling; however, during commissioning a third range was added. A system for sweeping the module interior with a controlled composition from 100% oxygen to nearly pure nitrogen was added so that the P_{O2} gradient across the ceramic parts could be managed.

A dry run was completed of the iso-compositional system (SEP Run 9) for controlling the atmosphere inside the modules. Installation of a mixing volume in the line helped to reduce the magnitude of transients in composition when switching between mass flow controllers.

In the following descriptions, module positions within the SEP are referenced by a letter designation, A through F. Positions A and B are side-by-side positions at the leading edge of the flow duct, followed by C and D in the middle and E and F at the trailing edge in the direction of flow.

SEP Run 10

Air Products carried out Run 10 in the SEP by successfully cycling two 0.5 TPD-scale modules from full process conditions to ambient temperature and back to full operating conditions with little decrease in flux or purity for both modules. This represented the first successful thermal cycle of full-scale modules. Advanced process controls (iso-compositional control) were used to manage the stress in the ceramic components during cooling.

Two modules were installed in the E and F positions (henceforth Modules E and F) in the SEP. Alumina injection tubes were used to distribute the permeate sweep gas to the top of the interior module volume. A bubble check during pressurization showed that initially E was not leaking but F was quite leaky.

The modified startup schedule included higher flows which were used to more evenly distribute flow over the height of the module. After heatup was complete, flow and pressure were increased. Leading-edge conditions were reached on October 19. The modules showed good performance, with the following values for product purity: E-84.1%, F-96.9%. The flux performance of F was the best yet measured for the SEP. Purity for E continued creeping up with time, reaching a maximum of 89.7%; F increased to a maximum purity of 97.2%.

A ramp on loop flow rate from 75 kscfh to 100 kscfh was done to check the impact on flux. No significant impact on flux was seen as flow rate was increased. As in previous runs, an interruption to the oxygen supply occurred due to a low supply-pressure trip. The loop O_2 level dropped very quickly, from 20.9% to 12.4%, in ~20 minutes. The oxygen supply was reestablished and the O_2 level was ramped back up over two hours. No impact on flux or purity was seen from this transient.

Iso-control was used to manage the stress in the ceramic material during cooldown. Using an understanding of the chemical expansion, the gas on the exterior of the modules was switched from air to nitrogen smoothly over a prescribed temperature range. The sweep gas for the interior of the modules was switched from oxygen to nitrogen over the same temperature range. The cooling rate was adjusted to establish control on the gas feed system. After flows were established, the cooling rate was increased. Calculations of the ceramic strains based on actual temperature and composition were monitored throughout.

There were several small process upsets during the cooldown, including a hold during the initial phase of the iso-compositional cooling and an offset from the setpoint for one of the oxygen mass flow controllers. This upset was tracked back to a zero offset due to temperature changes in the mass flow controller (MFC) cabinet. While a cabinet heater is present, it had been racked out during work in the cabinet and neglected to be turned back on. Leak flows on both modules were measured during cooldown using the hot wire probe and were found to be small.

Process heatup was initiated using the reverse process of switching from N_2 to air for feed and N_2 to O_2 for permeate during heatup. The switchover went smoothly. Upon return to full operating conditions, Module E returned to its previous values of flux and purity. Module F, while still above 90% purity, showed a decrease from values seen during the first fluxing segment. Figure 18-78 shows the purity and flux values compared to expected flux values throughout the run.

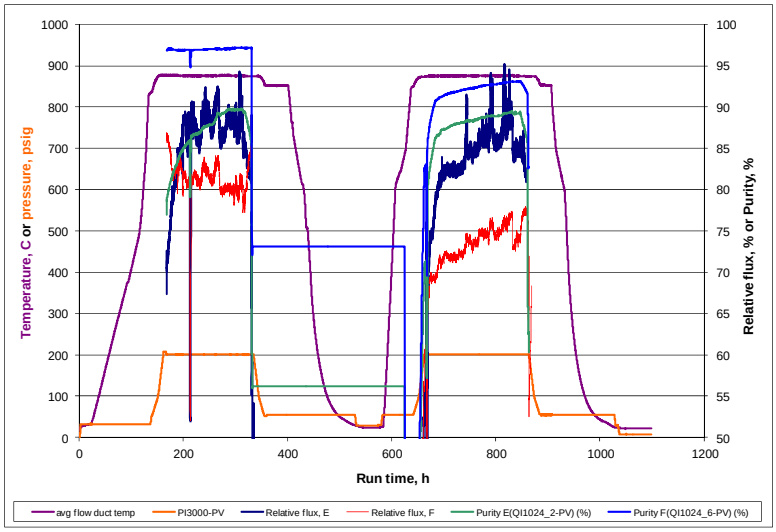

Figure 18-78. Product purity, flux and process conditions for Run 10.

While the absolute flux for Module F was higher, post-test analysis showed a thinner membrane layer, so the expected flux was even higher.

The process was cooled for a second time using the same iso-compositional schedule. Sudden increases in module internal temperatures were seen for Module F at 610°C with no accompanying change in vent flow, and for Module E at 360°C with a large change in vent flow indicative of ceramic damage. Module leak flows increased during cooling and became quite large for both modules at over 200 scfh. Based on this result, it was decided to shut the process down completely and inspect the modules.

Cycle times for heating and cooling were significantly improved by using iso-compositional methods. The heatup cycle was reduced in duration by 39%; cooling yielded even better results. Cooldown #1 with iso-control was shortened by 54% and Cooldown #2 was shortened by 61% relative to standard ramping without iso-control. Ramp durations could be further shortened but are limited by the maximum cooling rate attainable at lower temperatures during the period of simple Newtonian cooling.

The vessel was opened and the modules were found to be substantially intact, except for small cracks on both cones and hairline cracks on the bottom surface of the lowest wafer of both modules in the transverse direction. Module E had an additional crack in the lower wafer from the center manifold to the trailing edge.

SEP Run 11

SEP Run 11 was initiated by loading two 0.5 TPD-scale modules in the E and F positions. The process heatup proceeded very smoothly and reached full operating conditions with excellent initial results: Module E gave a purity of 93.3%, and F gave an unprecedented 99.9% purity.

The run completed four full thermal cycles using iso-compositional control. Table 18-14 gives the transition times from full conditions to full shutdown (30 psig and 25°C in this case) or the reverse. Times are not consistent since steps which require manual intervention are scheduled for workdays and reasonable working hours. These cycles used maximum rates of temperature and pressure change as defined by modeling and lab testing. Slower temperature ramps are used above 600°C where the atmosphere is not controlled. Cooling times are longer than heatup times due to limitations from the natural cooling rate of the system.

Table 18-14. Cycle time reductions SEP thermal cycles, Run #11.

Cycle number	Cycle time reduction, %
1 cool	50
1 heat	40
2 cool	64
2 heat	27
3 cool	63
3 heat	42
4 cool	62
4 heat	(12)

Two complete cool and reheat cycles were completed with minimal degradation of product purity. A significant decrease in Module F purity occurred after the third cycle. After completion of the third cycle, the vessel was opened to examine the modules to try to identify the source of this purity decline. Upon inspection, several small cracks in wafer surfaces were found. In addition to the wafer cracks, damage to both cones was seen.

Helium leak checking was performed by running a blend of 20% oxygen in helium (heliox) into the permeate sweep lines. The regions of high leakage were pinpointed using a helium leak detector. Areas of higher leak rate were found all around the end cap of Module E and at submodule joins of Module E. On Module F, leaks were seen at the cracks in the first wafer upper surface and at the cone.

The vessel was then closed and the process was restarted to obtain more information on the effect of cycling on module performance. Upon reaching full conditions, the purities had decreased markedly. The system was operated for several days at full conditions and then shut down again using iso-compositional control.

Figure 18-79 shows the purity performance for each module over the course of the run. Each bar represents the purity value averaged over the full time at condition, typically 50 to 80 hours. The first bar represents the initial fluxing segment after startup; the second bar is the performance after the first isocool and reheat cycle, etc.

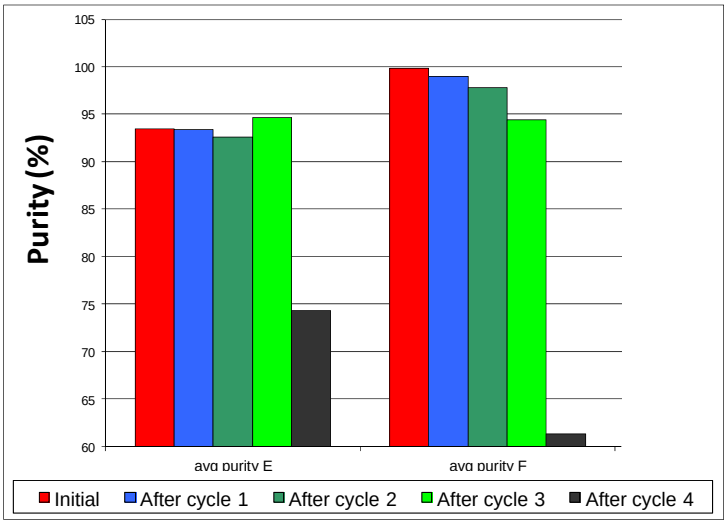

Figure 18-79. Purity by run segment for Run 11.

SEP Run 12

Two modules were loaded into the A and B positions in the SEP. Two seal configurations were tested. Two other locations in the SEP, E and F, were fitted with high-nickel alloy cones with small holes used during initial startup runs, which allow an amount of air similar to the expected oxygen flow from a module to enter the permeate system and thus obtain a relevant thermal profile in this region. The system was started up using the typical procedures. After leading-edge conditions were reached, the following product oxygen purity values were measured: Module A: 99.8% O_2, Module B: 97.5% O_2.

Flux values were as expected. Several process conditions were run during the week that the vessel was hot, including reduced permeate pressure and three temperature levels. Flux for both

modules increased each time the conditions returned to leading edge. The oxygen purity for Module A declined throughout the run, while Module B showed some variability.

The process was cooled using iso-compositional control. Feed air briefly reached 30°C and 30 psig and was then reheated again with iso-control, returning to leading-edge conditions. Conditions were held steady for nine days when another cooling cycle was begun.

A reduction in oxygen purity was seen after the first thermal cycle. Module A showed a substantially larger decrease in purity, from 99.4% to 93.6%. Module B showed a smaller purity decrease from 98.0% to 96.7

Three complete process cycles were performed where the process was cooled to ambient conditions using iso-control methods. For the first two, the minimum system pressure was 30 psig to keep the compressor from surging. For the third cycle, the pressure was reduced to ambient, and ambient humid air was introduced to check its effect on module performance. Similar declines in purity and flux were seen each time, with no significant difference seen between the third and the first two cycles.

Following the run, sections of the shutdown cycle were tested to try to identify the source of the purity decline. During portions of the cycle where the modules are not fluxing, the leak rate cannot be assessed. The results were evaluated based on purity and flux behavior after the process was returned to leading edge conditions.

Each iso-cycle consists of the following steps:

1. Increase permeate pressure to ambient.
2. Decrease system pressure and flow.
3. Decrease temperature to the desired iso-control temperature (e.g., 600°C).
4. Cool with P_{O2} change over a range of temperature.
5. Complete cooling under constant P_{O2}.
6. Reduce pressure.

A number of partial cycles were tested by isolating steps from the list above and then returning the system to leading-edge conditions. The first partial cycle (4) was only steps 1 and 2; the

second partial cycle (5) was steps 1 – 3, and the third was steps 1 through 4. A shutdown of the Sparrows Point air plant #4 required termination of the run at this point. Figure 18-80 documents the purity with cycle number.

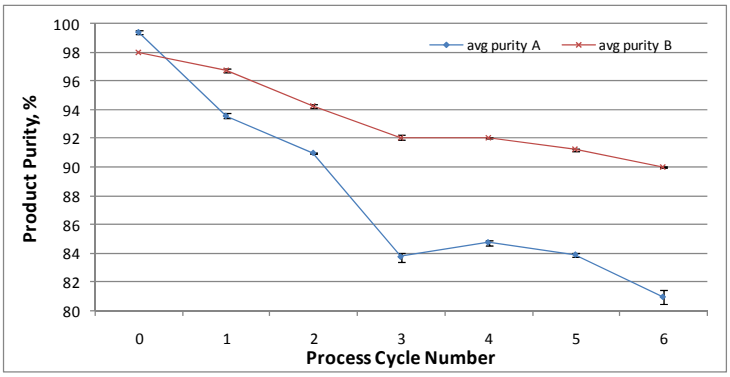

Figure 18-80. Oxygen purity for each set of process conditions for two modules, Run 12.

Process Cycle 4 appears to have had no detrimental effect on purity or flux. In fact, purity for module B increased. Purity during the time at conditions after Cycle 3 was increasing and would be expected to continue to increase with time, perhaps as the seal material crept to fill gaps in the seal region. Cycle 5 shows a small decrease, less than that seen for the full cycles. Cycle 6 shows a significant purity decline, but no change in flux was observed.

The thermocouple positioning for this run was designed to characterize the thermal profile in the region of the cones and seals. Figure 18-81 shows the temperatures at the seal level on Module A and Cone E.

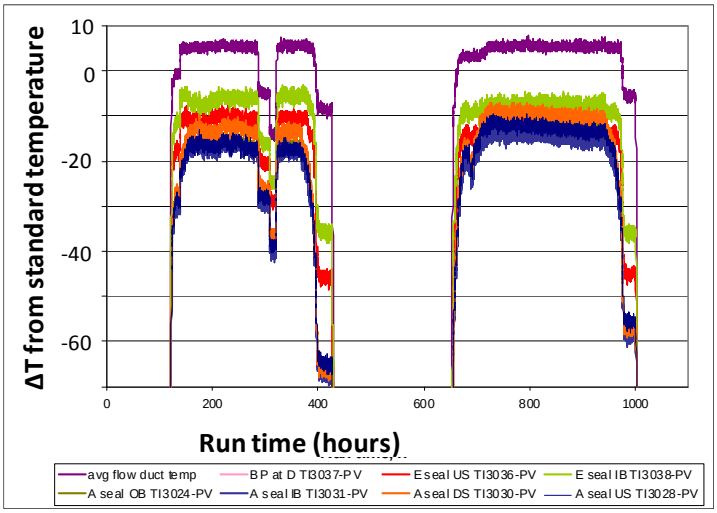

Figure 18-81. Module A and Cone E temperatures at seal level.

Several locations around the circumference of the seals were tested, with the tips of the thermocouples positioned in locator holes in the seal sub-assembly piece at the seal level. Notations on the curves are IB (inboard, toward the centerline of the flow duct), OB (outboard, toward the wall of the flow duct), or US (upstream). Similar temperatures are seen at all positions, but all are between 10 and 20°C cooler than the main part of the flow duct. All show a significant decrease at lower system pressures. For example, at 400 h, feed pressure is ~75% lower than it is at 300 h, and the temperature decrease at all positions is ~50°C instead of the 20°C drop observed at ~300 h.

Thermocouples were positioned at several heights near the cones as well on Module B and Cone F. Module B had thermocouples at low, middle, and high positions near the cones both inboard and outboard. Cone F had only inboard TCs at the same heights. Figure 18-82 shows the data from Module B TCs.

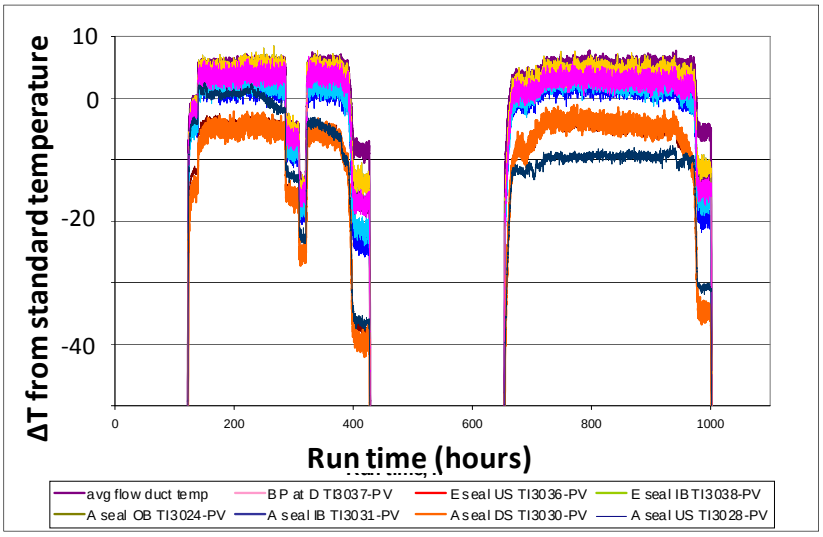

Figure 18-82. Module B and Cone F temperatures at various levels.

Examination of the figure reveals that the bottom TCs show temperatures cooler only ~5°C than the mid-level TCs, and that the top TCs are virtually at flow duct temperature. One anomalous point is the data for the TC on Bone F, IB. This starts at a higher-than-expected temperature that gradually falls off over the fluxing interval. After the thermal cycle, it ran ~5°C lower than the corresponding position for Module B.

In general, thermal gradients on the cones at full operating conditions are small but larger during startup and shutdown. These startup and shutdown gradients may be minimized by running higher pressures during heatup and cooldown.

SEP Run 13

The primary purpose of Run 13 was to investigate the effect of multiple banks of modules on flux and purity. Alternative ceramic-to-metal seal designs were also compared. The seal variants were designed to reduce the stress on the base piece. The metal receiver that supports the modules was also modified in some cases to allow better gas access to the outer surface of the module base piece. The run was started up with six modules (Figure 18-83) loaded into positions A through F. One module ("C") was damaged during installation.

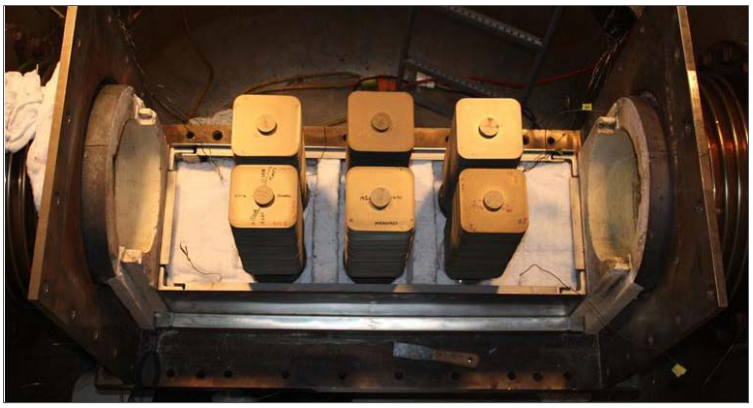

Figure 18-83. Top view of six modules loaded into the SEP for Run 13.

Full operating conditions were reached. It was found that the oxygen makeup valve could not supply enough oxygen to keep the loop at 20.9% with all six modules fluxing. The fresh air feed was maximized to keep the loop O_2 level as high as possible, but it ran in the range of 18.0 – 19.8% for most of the fluxing time.

Testing at varying vessel flow rates showed no effect on flux. Process cycles to investigate the robustness of the process were run, including:

- A depressurization cycle.
- An unexpected heater trip, which quickly brought the loop to 600°C while maintaining full pressure.
- Depressurization, reduced flow and a controlled cycle to 600°C.

Recovery from the heater trip was fairly good, with purity numbers for five of the six modules virtually unchanged. The purity of the other module decreased from 94.3% to 90.6%.

Figure 18-84 shows purity values averaged over the time at steady conditions of flow and pressure. Standard deviations for the values are indicated by error bars. During the initial fluxing time, the loop O_2 changed quite a bit as the feeds were adjusted to try to maximize oxygen supply. Later segments operated at steadier loop O_2 values and therefore show smaller standard deviations. One module achieved a record flux early in the run. Feed flow rates showed no effect on flux.

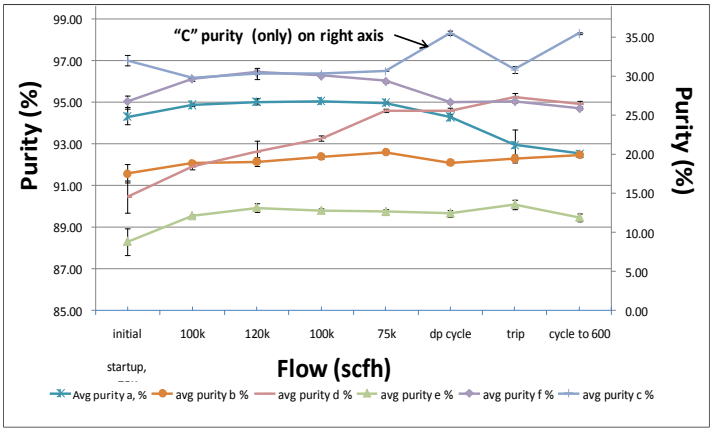

Figure 18-84. SEP Run 13 module purities.

Feed-side pressure drop for the array of modules was measured. The measurements were in agreement with predictions from a model based on literature data and computational fluid dynamics (CFD) calculations.

The system was returned to ambient temperature during a shutdown of the Air Products air separation unit. Problems with cooling control and restart issues resulted in a severe loss of purity in all the modules. An inspection of the modules after the run revealed cracking in some end caps and a few wafers, consistent with the high stresses induced in the modules during the various control problems and trips. Conical sections on most base pieces appeared to be in good shape. The base ring on most base pieces appeared to be cracked.

SEP Run 14

A new flow duct design was tested to evaluate the design concepts and manufacturing approach proposed for the ISTU vessel flow duct design. The new flow duct was also a prototype for a larger SEP duct that could house 1 TPD modules. Figure 18-85 are photographs of the old and new ducts.

Figure 18-85. SEP flow duct; old (left) and new (right).

Two 0.5 TPD-scale modules were installed. One module produced 99.5% oxygen with the expected flux, while the other produced only 50% purity. Figure 18-86 shows the uniformity of temperature throughout the interior of the flow duct.

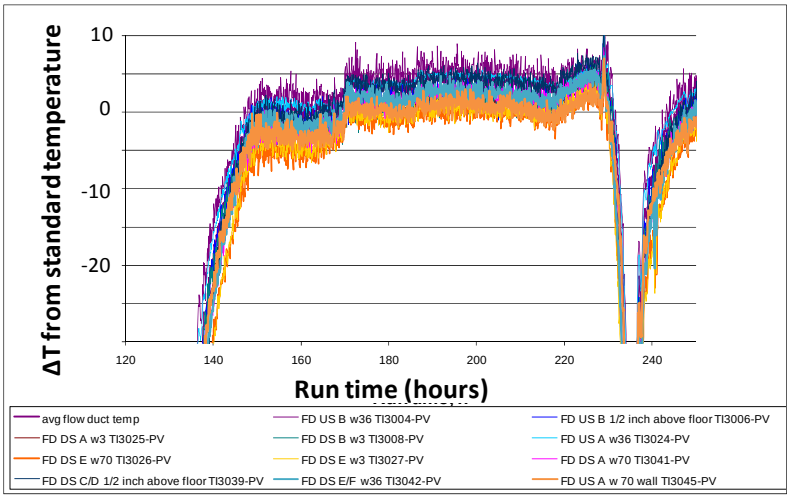

Figure 18-86. Temperatures at various points throughout the new flow duct.

The variation was quite small. The temperature excursion near the end of the run occurred when the air feed to the SEP from the Air Products air separation unit was lost.

Figure 18-87 plots the temperature on the exterior of the flow duct. Ambient temperature is shown in purple at the bottom of the chart to illustrate its impact on daily temperature swings in the process.

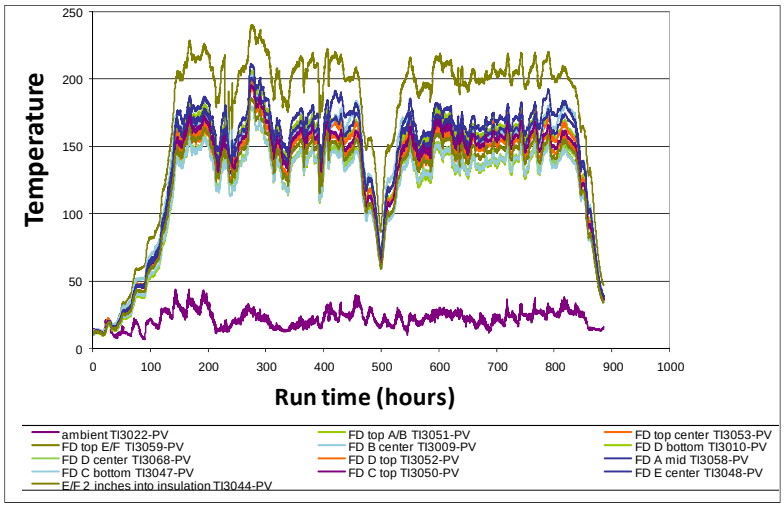

Figure 18-87. Temperatures at various points on the exterior of the new flow duct.

A thermal cycle to 300º C was performed using advanced process control techniques to minimize stresses in the ceramic. The cycle consisted of depressurizing and then cooling the system according to a specific temperature profile. A slight deviation occurred from the intended cycle. There was a slight purity decrease from 99.4 to 98.7% in the better module after the cycle.

After the run, the vessel was opened and the flow duct and modules were inspected. The flow duct was in excellent shape. The module that produced low-purity oxygen showed some damage to the conical base piece and one wafer. The other module appeared to be fully intact.

SEP Run 15

The SEP was retrofitted to accommodate 1 TPD modules, and modified bellows flanges and a flow duct were installed. Thermocouples were installed throughout the duct to enable extensive temperature mapping of the walls and gas space. Extensive alterations of the base of the duct were completed. Improvements were made to the insulation around each permeate pipe section

that penetrates the duct floor. Figure 18-88 is a photograph of the flow duct with side panels, distributor screen at the inlet, far right, and thermocouples installed.

Figure 18-88. Detail of the 1-TPD flow duct setup in the SEP.

SEP Run 15 was conducted without modules to assess the overall performance of the 1 TPD duct design. The flow duct was maintained at operating temperature for seven days over a variety of feed flow rates. Temperatures were monitored throughout the flow duct, insulation and base plate as well as the flow duct outer surface and the vessel inner surface. The pressure drop from just upstream of the distribution screen to the downstream end of the flow duct was measured. Figure 18-89 shows the process flows, pressures and average temperatures throughout the run.

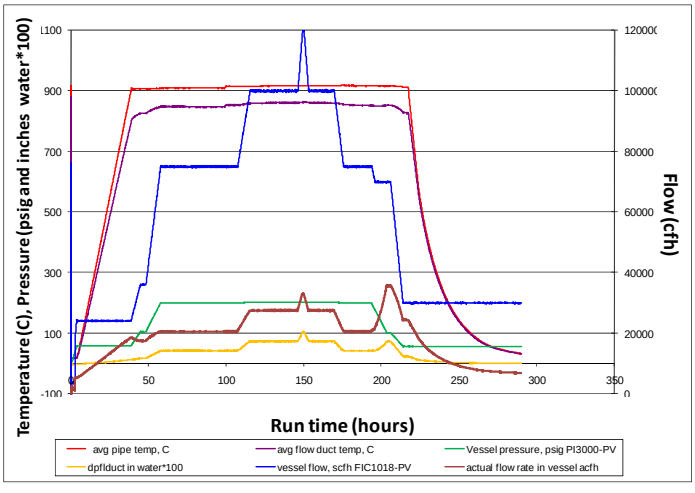

Figure 18-89. Process conditions during SEP Run 15.

When compared to previous runs, the thermocouples in the flow duct read lower temperatures at a given preheater input. The lack of modules radiating to the thermocouples may explain the difference. The temperature distribution throughout the taller flow duct was not as good as that seen for the 0.5 TPD duct. Figure 18-90 shows temperatures measured at a number of points in the downstream half of the flow duct.

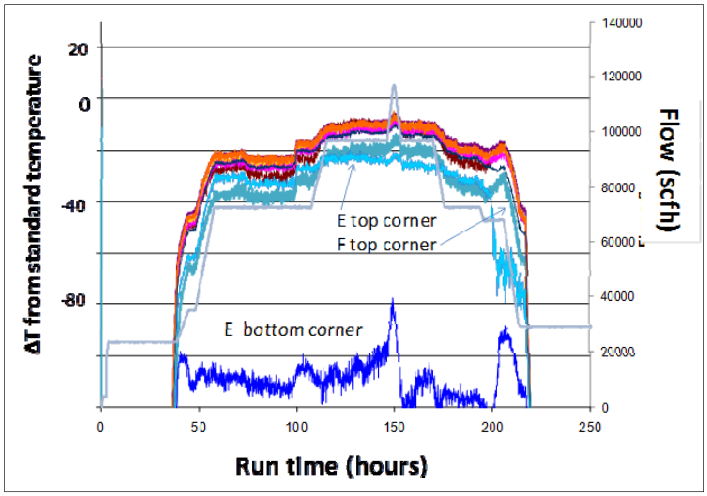

Figure 18-90. Temperature in flow duct downstream section, Run 15.

Note that the modules serve to distribute the flow, and different results were expected with and without modules. Measured temperatures on the exterior of the flow duct were on average 50°C higher for the 1 TPD flow duct, but are still reasonable. Thermocouples located in the gaps between panels showed a significant change when the flow rate was increased. When the vessel was opened for inspection, several areas on the flow duct side panels showed discoloration associated with exposure to high temperature. These issues were addressed. The pressure drop measurements tracked the actual flow rate.

Following the run, Air Products completed the delivery, installation and startup of a backup source of high-pressure air feed for the SEP to increase supply reliability (Figure 18-91).

Figure 18-91. Booster compressor placed on mounting slab.

SEP Run 16

The run objectives were to test handling fixtures and procedures for full-height modules, and determine thermal gradients when modules are installed. Two out-of-specification 1 TPD-scale modules were loaded in the A and B positions, one without a base ring and the other with a base ring.

The run used the three-part insulated flow duct that was empty in Run 15. Additional insulation was packed into spaces in the joints at the vertical corners of the flow duct to reduce any leakage in these areas. The base plate was insulated both upstream and downstream of the seal sub-assemblies, and insulation was used to surround the seal sub-assemblies. The floor was constructed with a four-layer insulation system. Insulation was installed around the lower portion of the cones, and additional insulation was used upstream of the modules to support the flow distribution screen and maintain a consistent floor height. A pressure tap was installed on the spool piece of one module. Calculations had indicated that for 1 TPD modules, the increased product flow rate would lead to significant pressure drop in the permeate line.

The objective to test handling fixtures and procedures for the large modules was successful. The new shipping/handling device worked well. Module spacing with the shipping frame (Figure 18-92) was tight but overall the shipping/handling device worked very well.

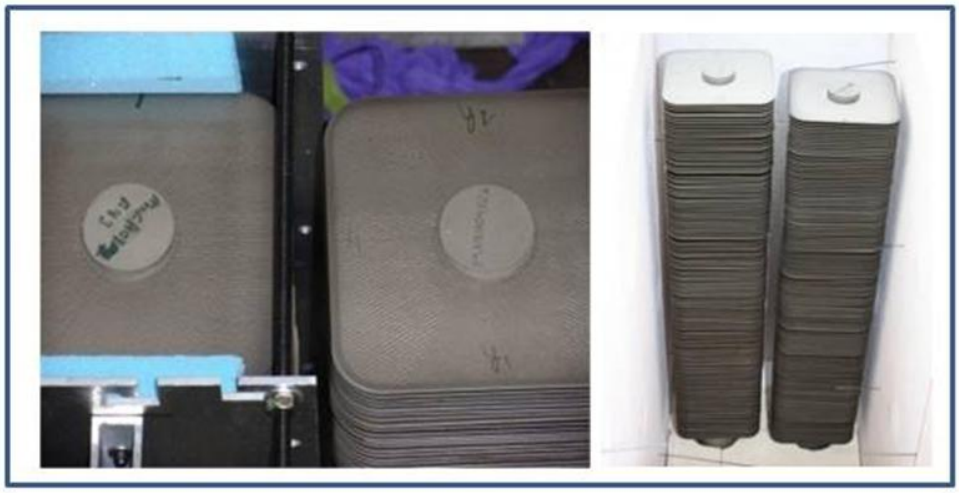

Figure 18-92. *Left*: module spacing with shipping frame; *Right*: two modules from downstream after installation of flow duct side panels.

Figure 18-93 displays the operating conditions during Run 16.

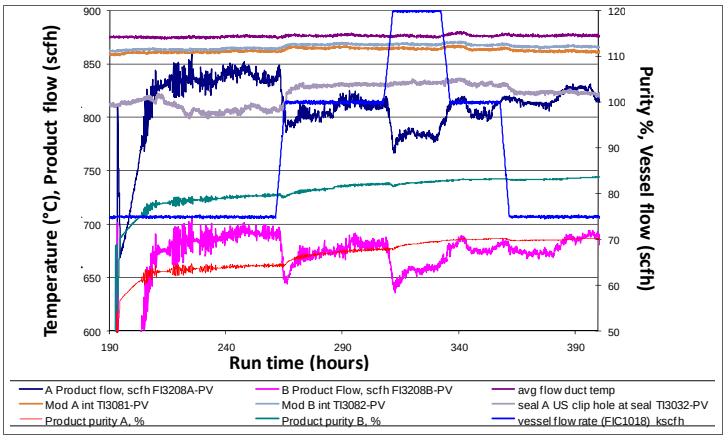

Figure 18-93. Run conditions and product flow SEP Run 16.

Oxygen purity for the out-of-spec modules was 63.2% for the module lacking the base ring and 78.0% for the module with a base ring. Purity continued to rise with run time and steadied after ~350 hours. Flux also improved over the initial portion of the run and became steady.

The second objective of SEP Run 16 was to determine the thermal gradients when modules were installed in the flow duct. Larger gradients were measured than were seen for the 0.5 TPD flow duct, but smaller than was seen for the dry run (Run 15) without modules.

Figure 18-94 shows the temperatures measured upstream of the modules.

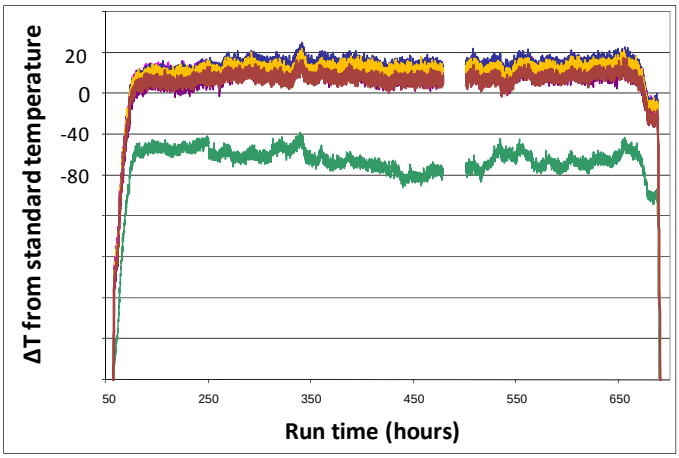

Figure 18-94. Temperatures measured upstream of modules, SEP Run 16.

The data show that there is a tight distribution of temperature upstream of the modules. Figure 18-95 shows the temperatures at the downstream end of flow duct.

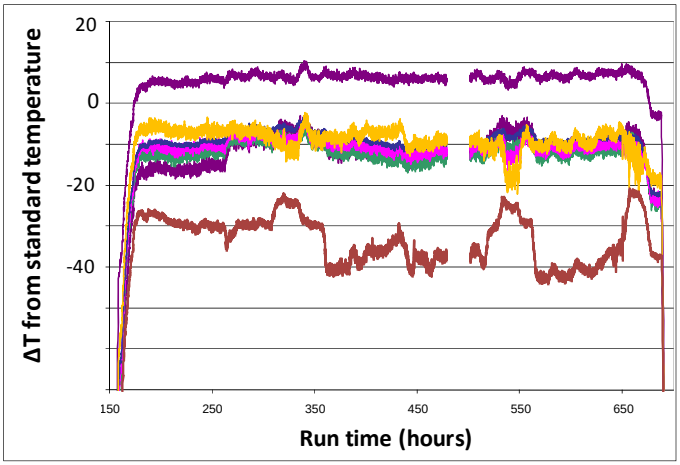

Figure 18-95. Temperatures at the downstream end of flow duct, SEP Run 16.

There was a wide variation in temperature data downstream of the modules. The coolest locations show significant changes when feed flow rates are changed. Note that the red line was low due to a faulty thermocouple.

SEP Run 18

The primary objective of Run 18 was to assess the chromium getter and the impact of flow duct modification on thermal gradients. The chromium getter used in Run 17 was re-installed, and two 0.5 TPD modules were loaded. The arrangement is shown in Figure 18-96.

Figure 18-96. Overhead view of flow duct assembly for Run #18.

To improve temperature distribution, the tight clearances and sharp corners near the module base were eliminated by moving the large upstream insulation block further from the modules and adding ramp sections to promote flow to the seal area. Reticulated foam was used as a filter upstream and as a radiation shield downstream. The downstream screen helped to distribute flow more evenly throughout the flow duct. Figure 18-97 displays the flow duct and seal temperatures during startup.

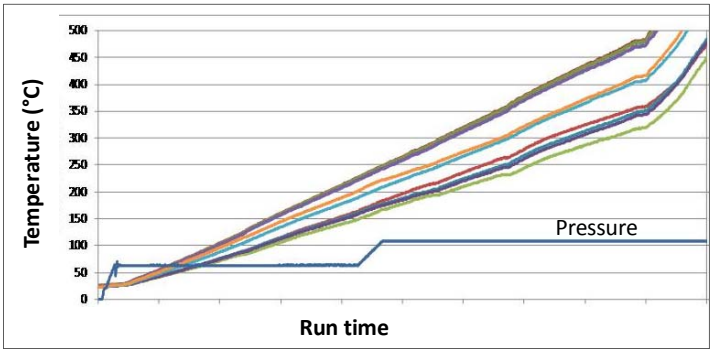

Figure 18-97. Flow duct and seal temperatures during startup, Run 18.

The thermal gradients were reduced as compared to previous runs. Temperatures throughout the flow duct are shown in the Figure 18-98.

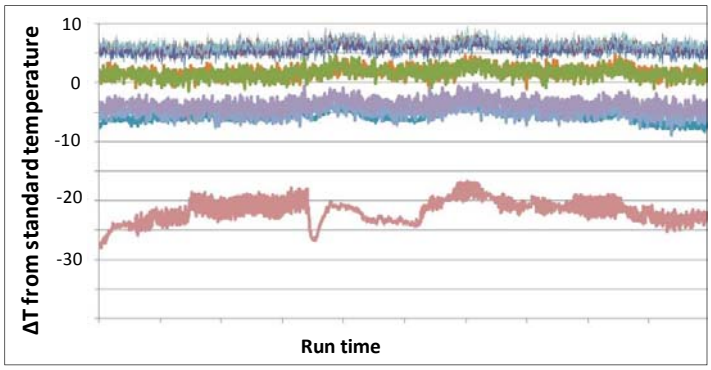

Figure 18-98. Temperature distribution in the flow duct, SEP Run 18.

The temperature distribution at leading-edge conditions for this flow duct configuration was improved compared to Run 17. The addition of the downstream radiation shield improved the temperature distribution.

The seal temperatures were still significantly lower than the flow duct temperatures. It appeared that heat transfer from the airflow in the duct to the seals did not improve significantly, despite the modifications to the module base region.

Figure 18-99 shows the process conditions and module purities during the run. A process trip occurred at 140 hours, which resulted in cooling of the flow duct but no loss of pressure. The system pressure was decreased to address the equipment issues causing the trip, and then the system was returned to leading-edge conditions at 300 hours. One of the modules was apparently damaged during this process trip.

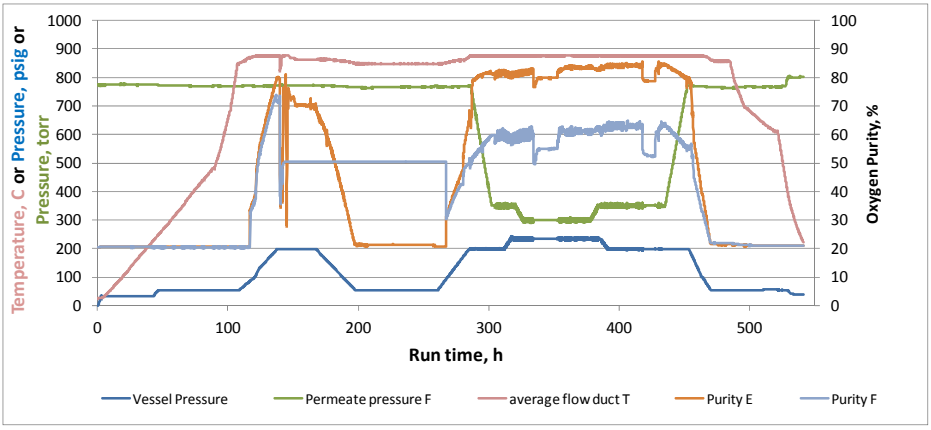

Figure 18-99. SEP Run 18 process conditions and purity.

An iso-cooling cycle was attempted to test the backup system that allows operation of the SEP from the alternate air source. Operational problems caused deviations between the actual and target P_{O2} levels. Fortunately, the strains induced by the deviations were not large (i.e., less than 300 ppm). Figure 18-100 shows the calculated strain based on the measured P_{O2}.

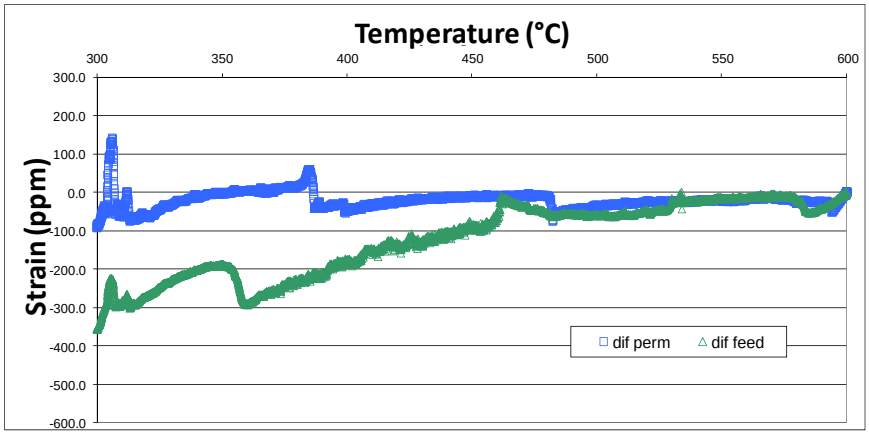

Figure 18-100. Calculated strain for AP2K in equilibrium with measured PO_2 during iso-cooling.

SEP Run 19

Changes were made to the getter position in Run 19. Also, the floor level of insulation at the modules was dropped to expose the top of the seal region, with the intent to reduce the temperature differential between the seals and the flow duct. Other modifications were implemented.

Two modules were installed in the E and F positions of the SEP. The flow duct configuration is shown in Figure 18-101.

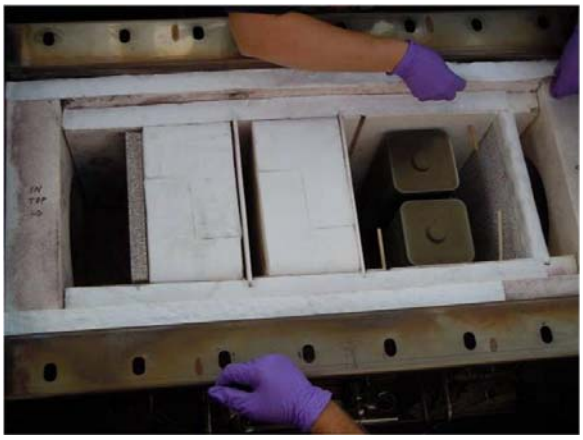

Figure 18-101. Flow duct configuration for Run 19.

After reaching operating temperature and 200 psig on the feed side, both modules produced >90% purity. After a few days of operation, the pressure was increased to 235 psig with the intent to reduce permeate pressure to 300 Torr to maximize flux.

Two upset conditions occurred during the run. In the first, the supply of high-pressure air was lost. Once operating conditions were re-established, the product purities returned to their previous values, indicating that no ceramic damage occurred. Another process trip occurred during a thermal cycle when the Air Products air separation plant lost power, resulting in a system depressurization. Once back online, the SEP pressure was ramped back to 55 psig over several hours, and the thermal cycle was completed. Averaged purities at different feed and permeate pressures are shown in Figure 18-102. The modules were at full conditions for 640 hours during Run 19, a record at that time.

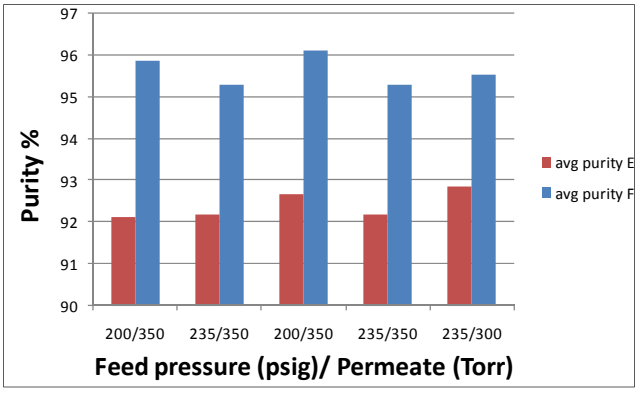

Figure 18-102. Average purity values for SEP Run 19.

Results of a test of flux at various feed oxygen levels are shown in Figure 18-103.

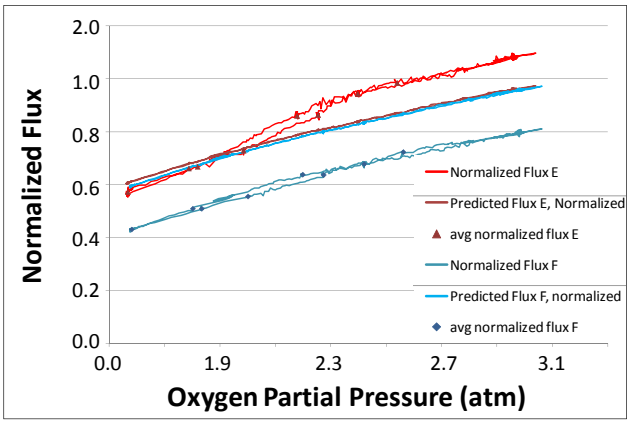

Figure 18-103. Flux versus feed PO_2 for SEP Run 19.

Predicted flux was calculated using membrane thickness based on a sampling of wafers from the same wafer lots used to build each module. In general, the model overpredicts the flux for Module F and underpredicts the flux for Module E.

SEP Run 20

Run 20 was conducted to test a flow duct prototype for the ISTU, assess the performance of two automatic shutoff valves (ASOVs) and simulate a system shutdown under iso-control. A different type of insulation was used in the flow duct, as well as a new bolting and gasketing scheme. No modules were installed for this run. The performance of the ASOV is documented in a following section.

Two ASOVs were installed. The valves were configured such that one should fail when pressurized and othe other should not. The space upstream of the excess flow valves was loaded with one bank of getter identical to that used in Run 19, except that no active getter component was used. One bank was used to produce the desired pressure drop in the flow duct. New flow duct panels were installed using high-temperature gaskets and additional bolts (roughly 50% more bolts compared to the previous design). Specified torque was applied to the bolts to reach the correct gasket stress. Great care was taken to get good alignment between the two side panels and the top to minimize any spaces between panels. Thermocouples were installed inside the flow duct, on the ASOVs, in several positions upstream and downstream of the getter, and at a number of positions on the exterior surface of the flow duct. Surface temperatures were monitored to compare the effectiveness of the a prototype ISTU insulation material with the insulation used previously.

The SEP was inspected after the ASOV test. The flow duct was reconfigured with thermal mass units (‘walls’) upstream and downstream of the getter. These walls simulate modules. Spaces between the bricks allowed flow through the walls (Figure 18-104). Total on-stream time for this run was ~1,700 hours.

Figure 18-104. Thermal mass walls installed.

A simple set point control system was originally used during iso-controlled heating and cooling. The required P_{O2} at the measured flow duct temperature was calculated based on the material database for the ITM material. There was no appreciable lag between the setpoint P_{O2} and that measured in the permeate system, but the composition in the feed system lagged the setpoint. An improved control scheme was then installed. The modified iso-control system was tested during a cooling cycle and a simulated temperature ramp. The system operated correctly, but tended to adjust to either the full -20% or +20%. Further refinements were made.

A system shutdown simulation was conducted. The permeate legs were isolated, makeup air flow was stopped, the induction heater was turned off, and the compressor was turned off, stopping flow. The process vent was closed manually to reduce the pressure loss. The temperature in the flow duct was monitored with time (Figure 18-105).

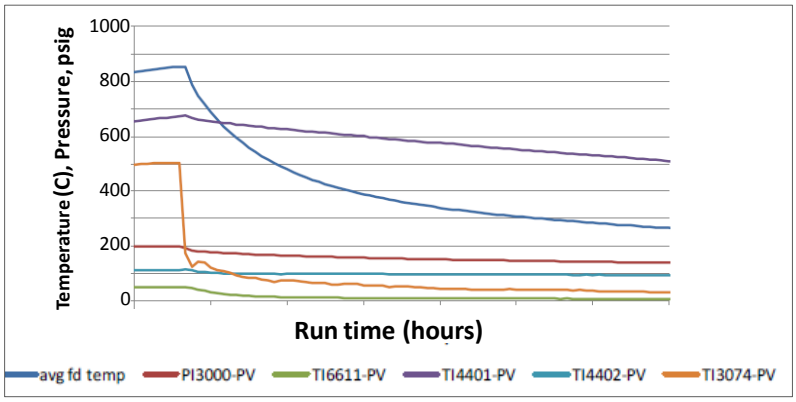

Figure 18-105. Run 20 process conditions during the system shutdown simulation.

Temperatures dropped rapidly in the flow duct, to less than 500°C in about an hour. The temperature downstream of the economizer showed a slower decline.

SEP Run 21

Two 0.5 TPD-scale modules loaded into the E and F positions in the SEP were successfully tested in Run 21, using the same ISTU prototype duct used for Run 20. These modules were low leak, and both had advanced architecture end caps and base pieces. The iso-control system was modified to incorporate feedback control. The air feed rate was adjusted to maintain proper P_{O2} based on the temperature. Nitrogen flow was adjusted to maintain total pressure. Initial purities at startup were 99.8% for Module E and 95.5% for Module F.

Purities increased as permeate pressure was ramped down. After briefly reading 100% oxygen purity, Module E suffered a sudden purity drop and product flow increased. This is indicative of ceramic damage during the first phase of the permeate pressure ramp. Operational problems occurred when power was lost. After reheating and stabilizing the process, it was determined that both modules had failed. The end caps and base pieces were intact.

The system was repressurized and reheated, then a series of different flows and pressures was run to get flow duct temperature data with the modules isolated. Vessel flow had a significant effect on the outer flow duct temperature.

SEP Run 27

In Run 27, the following two modules were installed in the flow duct:

- A standard wafer module with an original base piece and a #5 seal.
- A standard wafer module with advanced architecture end cap and base piece and a #10 seal.

Two rows of chromium getters, a particulate filter and a screen were also installed in the flow duct. An ASOV was installed in the product side of the #10 seal module.

The run objectives were:

- Evaluate the performance of the module with redesigned end cap and base piece.
- Determine the effect of percent O_2 in the feed and feed temperature on flux.
- Evaluate the modified iso controls developed during the previous run.
- Assess module performance after iso cycling.
- Evaluate the particulate filter and chromium getter.
- Intentionally trip the ASOV and evaluate aftereffects.

Figure 18-106 plots the operating conditions and the flux and purity from the wafer with a #10 seal. At full conditions, O_2 purity was 99.9+%.

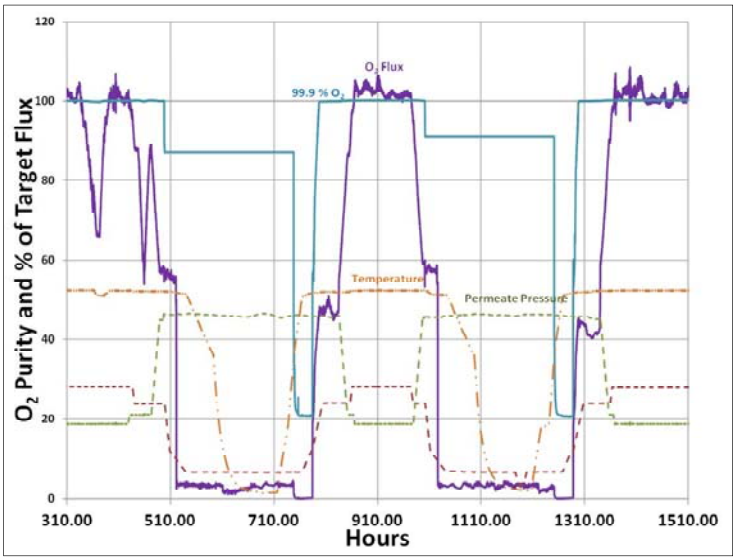

Figure 18-106. Process data, purity and flux from SEP Run 27.

After 200 hours of run time at operating conditions, a thermal and pressure cycle was performed using iso-control. After its return to full operating conditions, the module continued to flux with 99.9+% O_2 purity. After 150 hours of operation during the third cycle, the automatic shutoff valve on the module was tripped externally. The #5 seal module continued to run for an additional 100 hours following the ASOV trip.

Figure 18-107 presents the actual and theoretical flux for the module with a #10 seal. The theoretical flux matched very closely with the actual flux at almost all operating conditions.

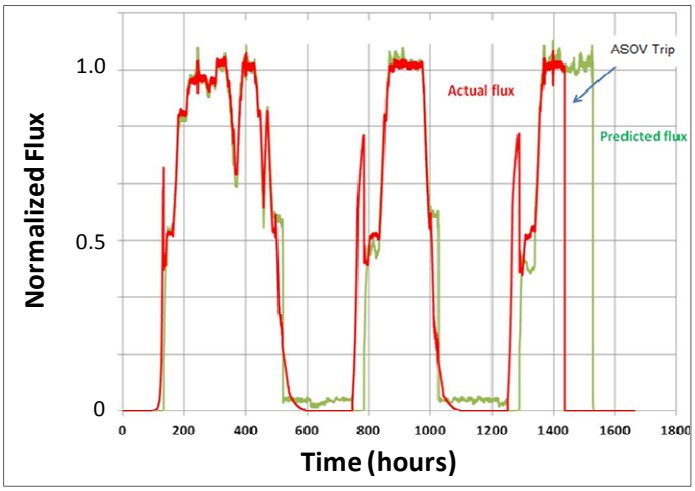

Figure 18-107. O_2 flux from #10 seal module, Run 27.

The effect of O_2 concentration in the feed air on module performance was evaluated at two different operating conditions. Figure 18-108 documents the dependence of flux on the feed O_2 concentration. The flux decreased linearly over the range of feed concentrations.

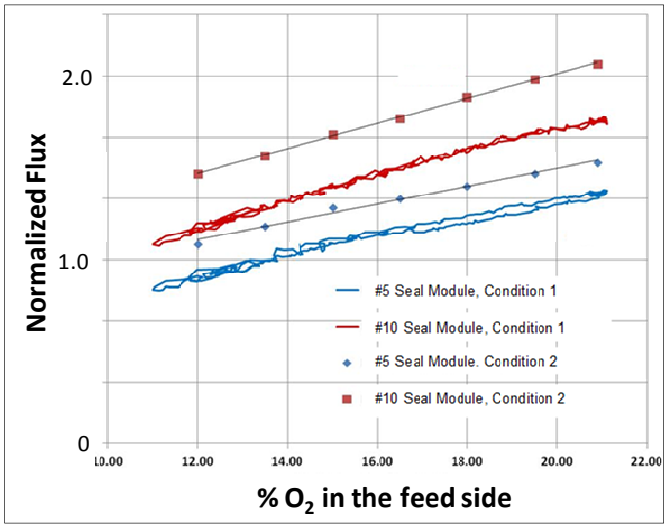

Figure 18-108. O_2 flux for #5 and # 10 seal modules vs. feed O_2 concentration for two different operating conditions.

The effect of temperature on O_2 flux and purity was also studied (Figure 18-109). Reducing the temperature did not affect the purity of the #10 seal module. The lower temperature decreased the flux from both modules.

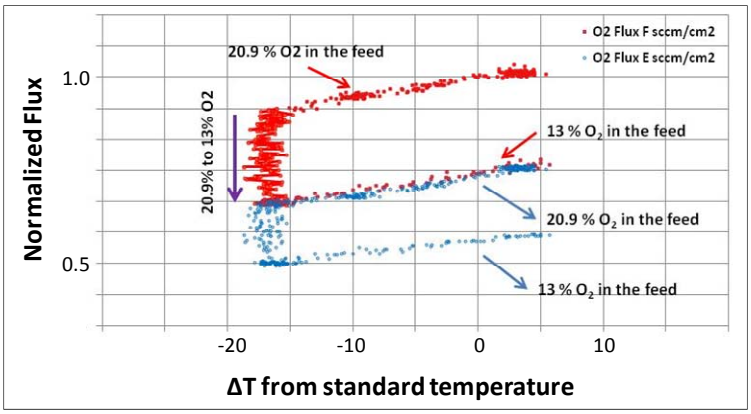

Figure 18-109. O_2 flux vs. temperature.

SEP Run 28

For Run 28, the full-size duct that had been used during Runs 15 and 16 was reused with two modifications: additional backer bars were installed on the side and the top panels of the flow duct, and the panels were re-fitted with insulation. No modules were tested. Figures 18-110 is a photograph showing the flow duct.

Figure 18-110. SEP flow duct.

One row of chromium getters was installed along with foam downstream of the flow duct. The fine particle filter was also installed. Figure 18-111 shows the process data during the run. The temperature profile in the flow duct was uniform during the run. Pressure drop was as expected.

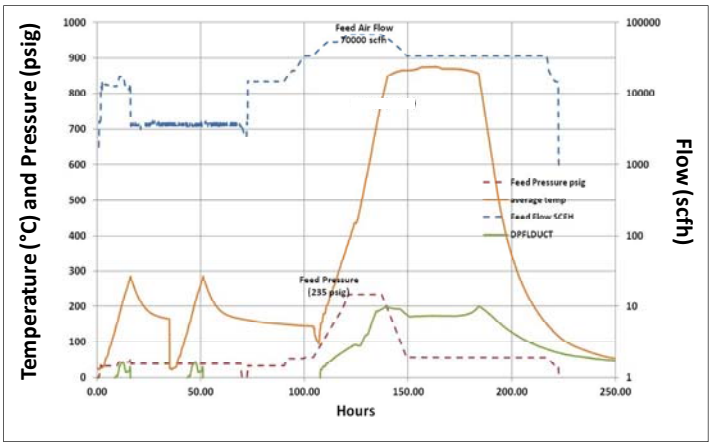

Figure 18-111. Process parameter data SEP Run 28.

SEP Run 29

Two advanced architecture 1 TPD modules were installed in positions E and F in the SEP. An ASOV was installed on one of the modules. The flow duct had one row of chromium getters and the fine particulate filter. Figures 18-112 shows the flow duct and 18-113 is a close-up of the modules prior to the run.

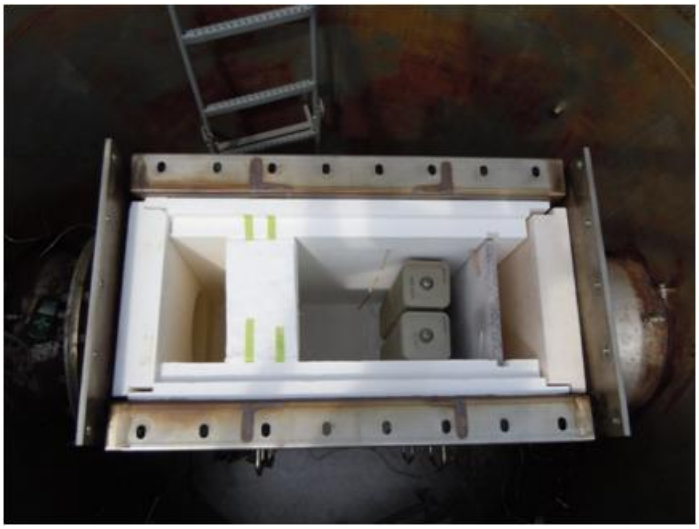

Figure 18-112. Flow duct prior to SEP Run 29.

Figure 18-113. Modules prior to SEP Run 29.

Figure 18-114 shows the process data for the run, including fluctuations that occurred when a booster compressor at the Air Products air separation plant tripped, seen at 170 hours.

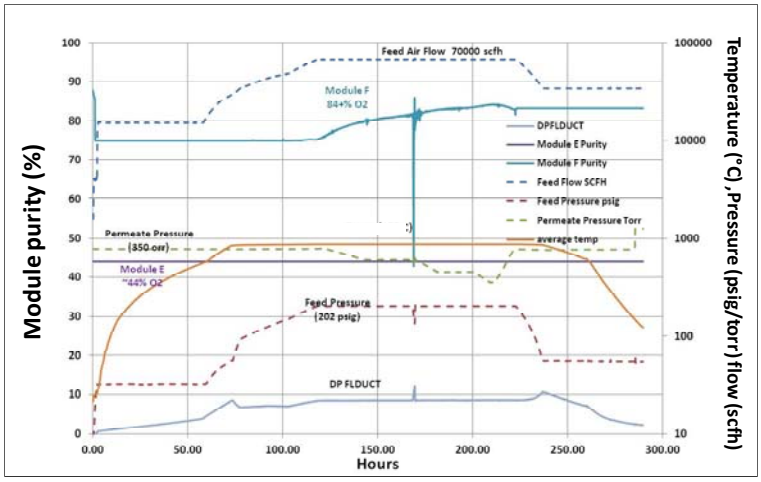

Figure 18-114. Process parameter data SEP Run 29.

SEP Relocation

Because of closure of the Sparrows Point site, the SEP skid was disassembled and transported to the Convent, Louisiana, site and subsequently reassembled. Figures 18-115, 18-116 and 18-117 are photographs showing the move.

Figure 18-115. Section A of skid on the truck at Sparrows Point.

Figure 18-116. Section B of the skid on the truck at the Convent site. ISTU is shown behind the skid.

Figure 18-117. Skid in the background and booster compressor in the foreground at the Convent site.

SEP Run 31 at Convent, Louisiana

The SEP was re-commissioned in Convent, Lousiana. Two 1 TPD-scale advanced architecture modules were loaded into the flow duct in positions C and D. A portion of the module loading apparatus designed for the ISTU was trialed and worked well. Figure 18-118 is a photograph of the modules installed in the flow duct.

Figure 18-118. Modules installed in the SEP.

One bank of getter was installed upstream of the modules, and non-fluxing modules were installed downstream of the modules (Figure 18-119).

Figure 18-119. Modules, getter and non-fluxing modules installed in the full-height flow duct of the SEP.

Figure 18-120 documents the operating parameters and Figure 18-121 shows the module performance.

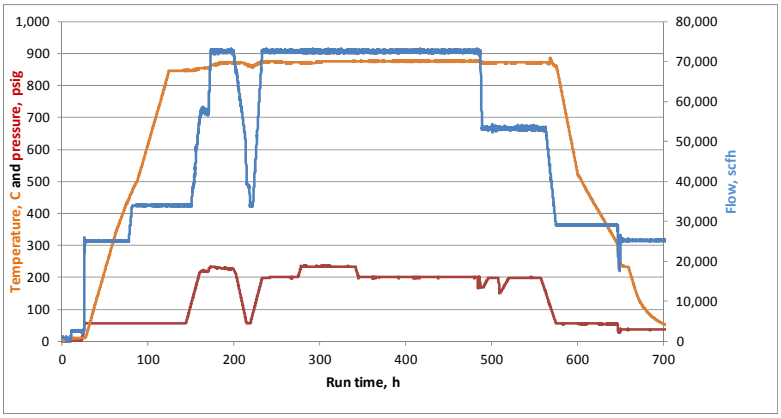

Figure 18-120. Process conditions, SEP Run 31.

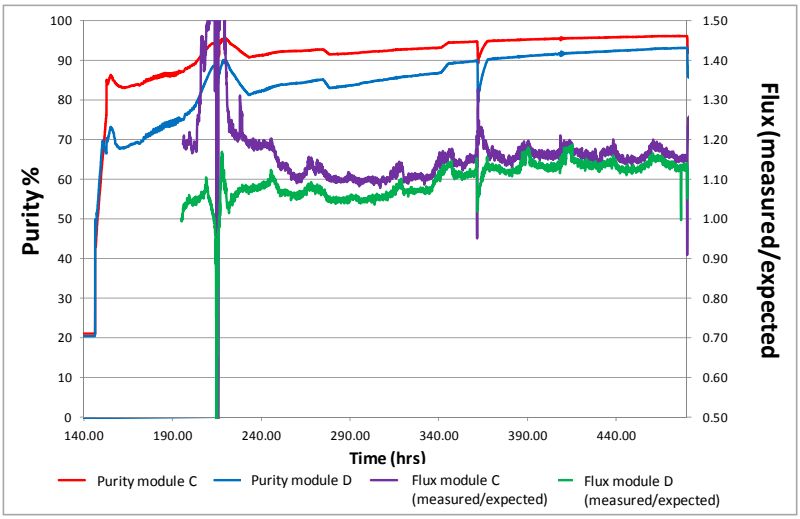

Figure 18-121. Purity and flux results, SEP Run 31.

The run was cycled down at 600 hours to repair the booster compressor. Testing resumed after the electrical connections to the booster compressor were repaired. Figure 18-122 shows the purity for each module during the second run, as well as the measured/expected flux. Some degradation of performance was seen.

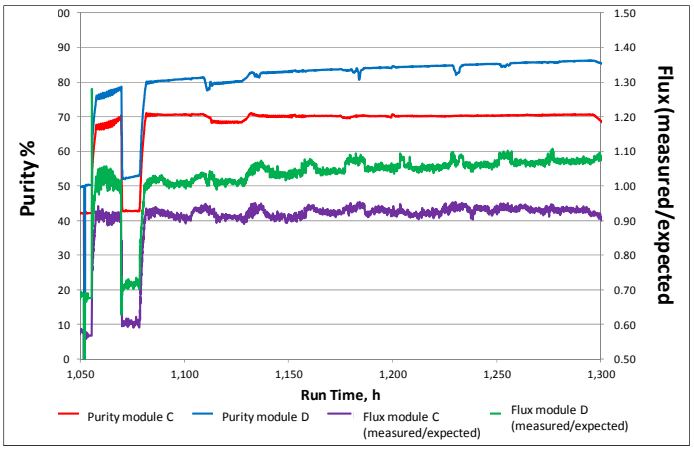

Figure 18-122. Module purity and flux results, SEP, following restart.

Automatic Shutoff Valve, Small-Scale Trials

A number of tests of the ASOV were conducted in the XVUs. In one test, a baseline pressure drop through the ASOV was established at high-temperature, high-pressure conditions. After a hold of 500 hours, the ASOV was thermally cycled. After re-heating and re-establishing the pressure drop, the unit was held at conditions for an additional 10 days. After this hold, the flow through the valve was increased until the valve tripped at a pressure drop of 3.5 times the baseline.

Four automatic shutoff valve (ASOV) tests were conducted in the XVU1 to assess the leakage through the ASOV after it is tripped. An example of the leak decay curve after an ASOV activation is shown in Figure 18-123.

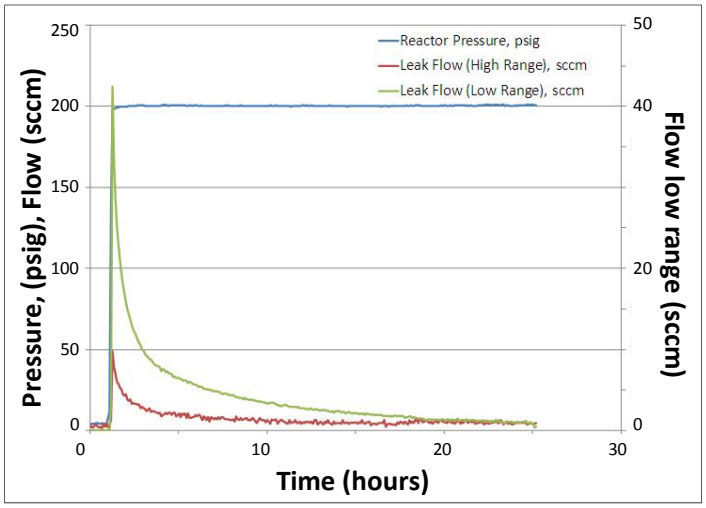

Figure 18-123. Leak decay behavior of ASOV5-2B.

The shapes of the ASOV5-2A(E) and ASOV 5-2B decay curves were very similar, but ASOV 5-2B had a lower initial leak rate. ASOV5-2C had a modest initial leak rate but a very slow leak decay. ASOV5-2D had a high initial leak rate, but it decayed much faster than for ASOV5-2C.

SEP Run 20

Run 20 was conducted to test a flow duct prototype for the ISTU, the performance of two ASOVs and to simulate a system shutdown. No modules were installed for this run.

Two ASOVs were installed. The valves were configured such that one (position E) should fail when pressurized and one (position F) should not. Figure 18-124 documents the operating parameters and module performance through the first 600 hours of operation.

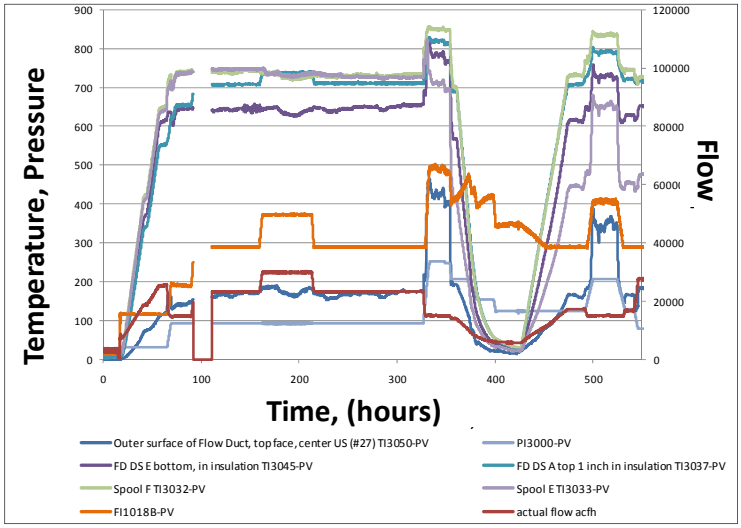

Figure 18-124. Flow duct temperatures, flows and pressure, Run 20 hours 0 through 600. The "spool" thermocouples represent the ASOV temperatures.

The permeate vent valves were closed after reaching temperature. The pressure was then increased to 95 psig and the feed flow was increased. Flow through the ASOV matched predictions. After seven days at full temperature, the permeate pressure was reduced to 310 Torr.

Pressure was ramped quickly to increase the flow through the ASOV. One ASOV tripped at the high end of the expected range. Flow abruptly decreased to zero and the permeate pressure control valve closed. The permeate vent valve was opened and a leak check was conducted. The leak was not measurable. The other ASOV did not trip.

SEP Run 25

SEP Run 25 was conducted primarily to evaluate the aftereffects following the tripping of an ASOV. Other objectives included the evaluation of the upstream particulate filter, chromium getter, module performance and the safe removal of the modules following the run. Ceramatec provided three modules with advanced architecture base pieces and end caps. Two were low-leak modules, while the third was high-leak. A No. 10 seal was installed with the high-leak module in position E . One of the low-leak modules developed cracks when the transfer frame was being removed from the module while resting on the seal sub-assembly. A module with a cone base piece and a number 5 seal was installed in its place in position F (Figure 18-125); the dissimilar heights of the module arise from the different base pieces on the two modules. An external air source was used to trip the ASOV.

Figure 18-125. Module (left) with cone base piece and a #5 seal.

The flow duct configuration is shown in Figure 18-126.

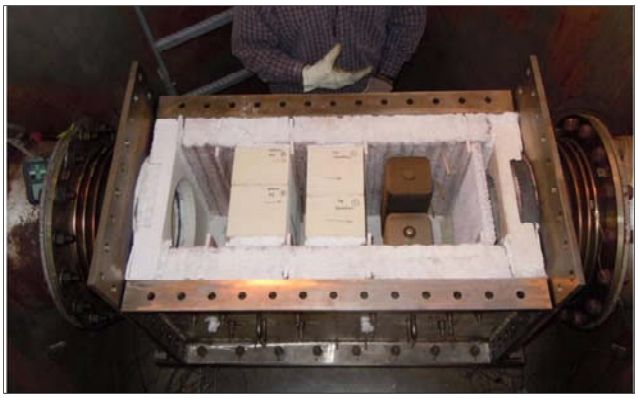

Figure 18-126. Run 25 flow duct configuration.

After 24 hours at operating conditions, the ASOV was tripped in a controlled fashion by increasing the external flow into the permeate line in small steps, shown as the red line in Figure 18-127. Once the increased flow caused the internal pressure drop to exceed the design level, the ASOV activated (at ~242.65 h in the figure). It can be seen that as the external air flow increases and mixes with the oxygen produced by flux, the measured product purity for Module F decreases. At the point where the ASOV activates, the product flow drops very quickly as the module is isolated.

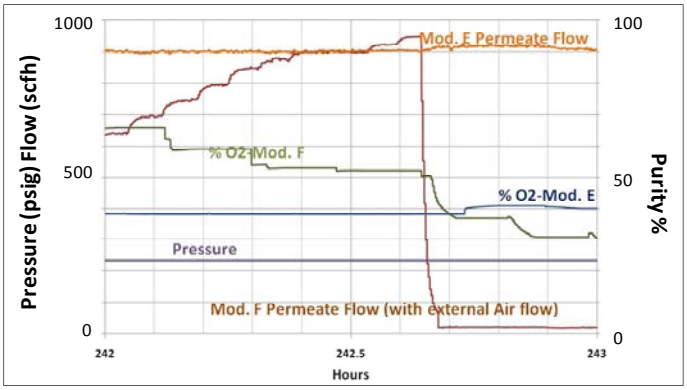

Figure 18-127. ASOV trip.

There was no indication that tripping the ASOV had any impact on the neighboring module; the purity level, pressure and flow did not change. Transients were observed in the permeate flow and O_2 purity due to a change in O_2 concentration in the recycled feed flow (due to non-fluxing of the tripped module). The transients lasted for ~20 minutes. The permeate flow through the module completely stopped with the tripped ASOV.

18.1.6 Advanced Ceramic Component Performance Testing

Components produced using advanced ceramic architecture under Task 17 were tested to quantify flux and reliability performance. Initial testing was on base pieces and end caps, and proceeded to advanced architecture wafers and modules.

Base Piece

An advanced architecture base piece was tested in the TTR utilizing the standard heating and multi-step pressurization schedule. Figure 18-128 documents the operating conditions and the base piece leak rate.

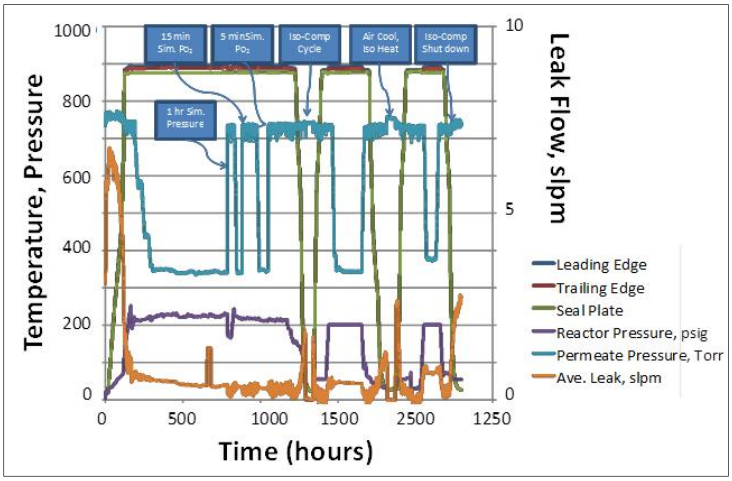

Figure 18-128. Performance of advanced architecture base piece.

A low leak rate was observed during start-up. The reactor was sequentially ramped back to baseline conditions and stabilized at baseline for 48 hours. The system was then run through a five-minute P_{O2} transient. The permeate pressure was simultaneously ramped from 350 to 760 Torr. There was essentially no change in the leak rate. The sample was then run through an iso-control shutdown and an iso-control restart back to baseline conditions. There was a slight increase in the measured leak rate after the iso shutdown and restart. After the system stabilized, the reactor was cooled using the ceramic joining cycle schedule. Nitrogen flows were initiated to the feed and permeate sides of the sample, and an iso-controlled re-start was run. After re-start, the pressure was ramped to baseline conditions. The leak rate was ~0.71 slpm after the full iso-controlled cycle. It should be noted that the sample had been on test for over 2,000 hours at this point. Previous tests of this seal configuration showed degradation at test times >1,500 hours.

End Cap and Base Piece

An advanced architecture domed end cap joined directly to an advanced architecture base piece was tested in the XVU3. This part utilized an A1 seal configuration. The initial leak rate was higher than has been seen in some of the previous tests with the A1 seal configuration. However, the leak rate decreased as the pressure vessel temperature increased.

The sample was subjected to sequential pressure cycles with cooling to 600°C; Figure 18-129 documents the data. The leak rate was essentially unaffected by the cycles and continued to improve on returning to baseline conditions.

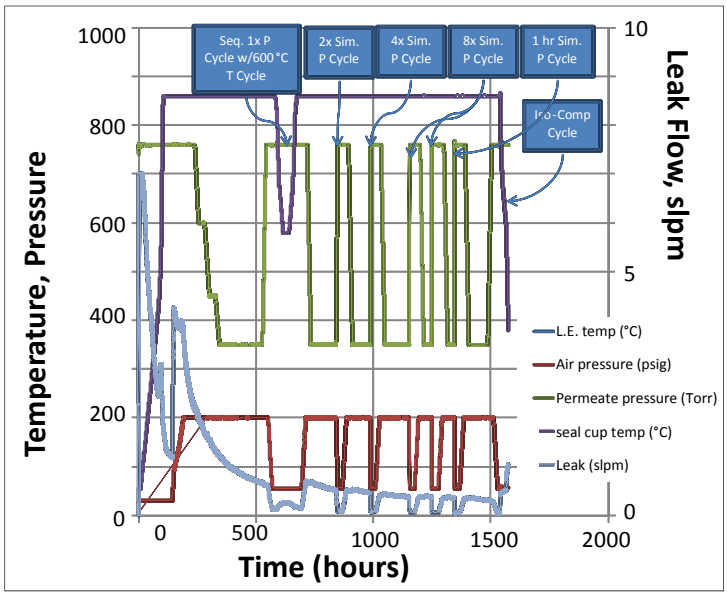

Figure 18-129. Initial results from test of domed end cap/base piece.

End Cap, Spacer and Base Piece

A test of a dome/spacer/base piece was initiated in the TTR to assess the impact of P_{O_2} cycling and high feed-side P_{O_2} on the module leak rate. An Alloy A seal plate with a #10 seal was used. The unit was pressurized and then heated using a modified joining schedule. A sequential linear pressurization schedule was followed. Figure 18-130 documents the operating conditions and the performance parameters.

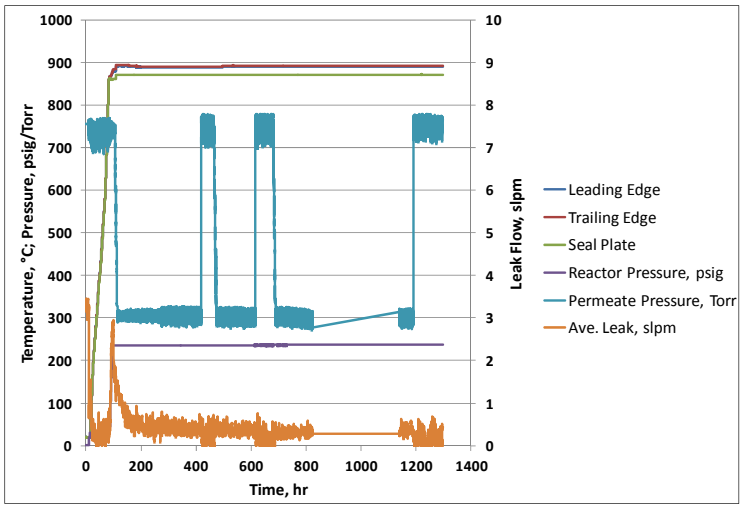

Figure 18-130. Performance of a dome/spacer/base piece (TTR).

The assembly initially showed a modest leak, which decayed rapidly during heat-up. It should be noted that the leak rate includes seal leak, sample flux, and sample leak.

The leak rate increased during the feed pressure ramp, but decayed over the permeate pressure ramp and initial hold. The assembly was held at full conditions for ~300 hours, then put through a 15-minute simultaneous feed and permeate P_{O2} ramp (i.e., a 'black plant' simulation). After approximately two days, the assembly was returned to leading-edge temperature conditions. The leak rate remained constant, indicating good reliability. The assembly was then subjected to another 15-minute P_{O2} cycle. The assembly was then subjected to a third, 15-minute 'black plant' cycle.

Wafer

The pressure drop was measured on the permeate side of advanced architecture wafers. For the initial tests, Ceramatec supplied five unjoined advanced architecture wafers. Air Products removed the edges from the circumference. The wafers were tested using the Pressure Drop Measurement Unit (PDMU). Data for the five wafers was consistent (Figure 18-131).

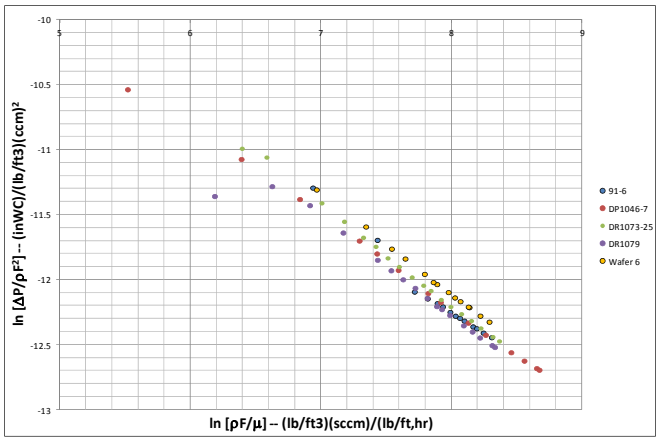

Figure 18-131. Friction factor-Reynolds number correlation of five unjoined wafers (values not dimensionless).

In previous work, it was found that the flux through single-wafer module PCL003 was substantially different than for PCL004 despite having nominally identical designs. Pressure drop measurements were conducted on both modules to determine if the difference in flux could be due to differences in pressure drop. Figure 18-132 presents the correlated pressure drop data for the two modules and the data for the unjoined advanced architecture wafers (see above).

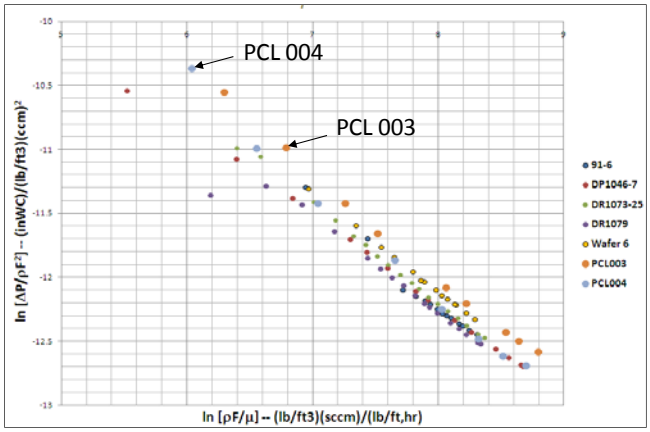

Figure 18-132. Friction factor-Reynolds number correlation, PCL003 and PCL004 (values not dimensionless).

The friction factor data for the two single-wafer modules are in line with those measured for the unjoined wafers. The curve for module PCL003 falls somewhat above that for PCL004, indicating higher pressure drop for a given flow, but the difference is not great. When the flow model is solved simultaneously with a model for oxygen flux, the resulting difference in flux is very small. Based on this result, it was concluded that the difference in pressure drop was not responsible for the difference in module performance.

TASK 19.0 TABLE OF CONTENTS

TASK 19.0 DESIGN, CONSTRUCTION AND COMMISSIONING OF THE INTERMEDIATE-SCALE TEST UNIT (ISTU).....3

19.0 SCOPE..... 3

19.0 DESIGN, CONSTRUCTION AND COMMISSIONING OF THE ISTU 3

Design 3

Feed Air Compression 4

Low- and High-Temperature Heat Exchangers (Recuperators) 5

Fired Heater 5

Permeate Cooler and Compression 6

Hot Gas Expander 6

ITM System 10

Project Execution and Construction 11

Q2-2009 11

Q4-2009 11

Q1-2010 12

Q2-2010 12

Q3-2010 13

Q1-2011 13

Q2-2011 13

Q3-2011 14

Q4-2011 14

Q1-2012 14

Q2-2012 15

Q3-2012 15

Q4-2012 16

Q1-2013 17

Q2-2013 18

Q3-2013 18

Q4-2013 18
Q1-2014 18
Q2-2014 19
Q3-2014 20
Commissioning *20*
Commissioning Run 1 20
Commissioning Run 2 21
Commissioning Run 3 23

TASK 19.0 DESIGN, CONSTRUCTION AND COMMISSIONING OF THE INTERMEDIATE-SCALE TEST UNIT (ISTU)

19.0 Scope

Air Products designs and constructs the Intermediate-Scale Test Unit (ISTU). Operating conditions are typical of commercial operation, with an oxygen capacity of 100 TPD at 99+% purity. The ISTU includes the major elements of commercial ITM Oxygen facilities and provides the first test of a working ITM-based oxygen system coupled with turbo-machinery for power generation, a fired heater and comprehensive control system.

19.0 Design, Construction and Commissioning of the ISTU

Design

Air Products began detailed design of the ITM Intermediate Scale Test Unit (ISTU) early in the budget period. At the request of the DOE, the system was originally designed to produce 150 TPD of oxygen at 99+% purity. By mutual decision between the Recipient and the DOE, the system capacity was reduced to 100 TPD and the design was modified to meet budgetary constraints.

Figure 19-1 is a block flow diagram of the ISTU process design.

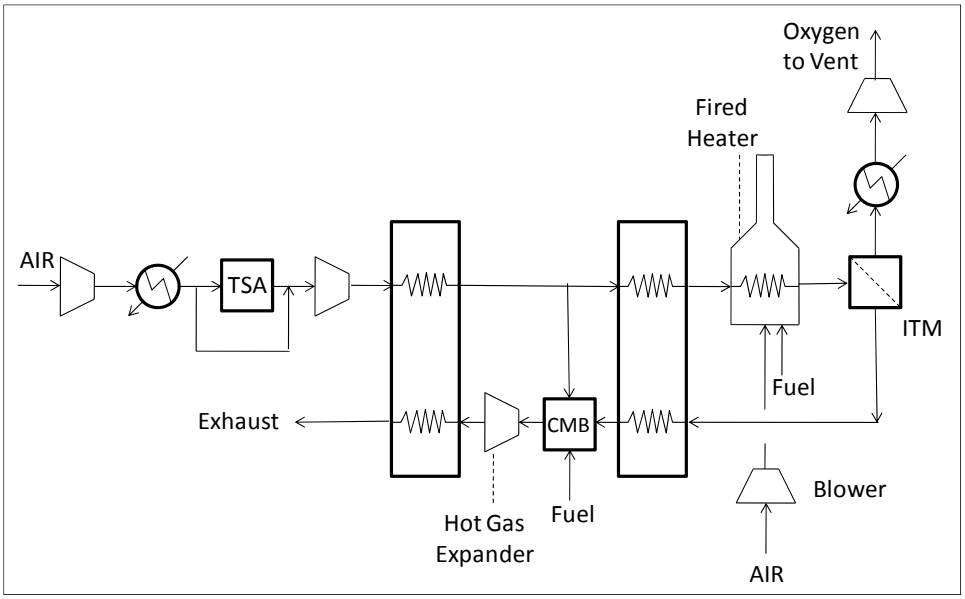

Figure 19-1. Block flow diagram of the Intermediate-Scale Test Unit (ISTU).

The system can be thought of as two processes:

- A Brayton power cycle consisting of the air compressor, temperature swing adsorption system with bypass provision, low-temperature recuperator, combustor, and hot gas expander.
- The ITM Oxygen system, consisting of a high-temperature recuperator, fired heater with air blower, ITM vessel, oxygen cooling train and oxygen blower.

On the power cycle side, the hot gas expander is coupled to a generator to co-produce power. The hot gas expander and combustor are one unit, capable of operating on the oxygen-depleted non-permeate or air, and firing natural gas to increase the power output. To minimize the fuel consumption, the power output from the expander was chosen to roughly match the power consumption of the compressor and other unit operations of the facility, so that the ISTU would be roughly neutral from a power balance.

The scheme in Figure 19-1 has advantages for further scale-up. The hot gas expander, fired heater and oxygen cooling system can all be built to significantly larger sizes. In addition, the hot gas expander-based process provides a power-flexible design that is attractive for various applications in which variable amounts of power and oxygen are required.

Feed Air Compression

Air Products determined that an in-line thermal swing adsorption (TSA) system could remove SO_2 and other sulfur species from the feed air. The ISTU team determined that a strategy for operating with dry gas with the option to switch over to "wet" gas would require the TSA to have a by-pass leg. Figure 19-2 is a schematic of the feed gas compression system.

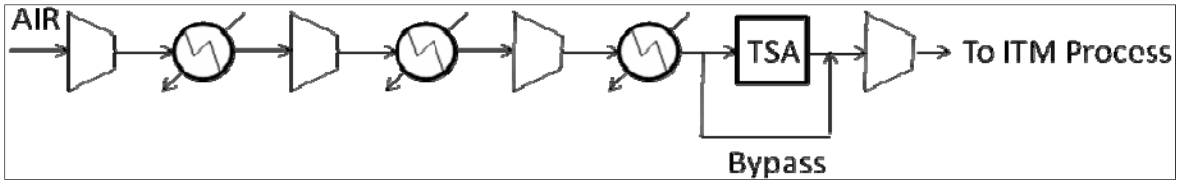

Figure 19-2. ITM feed gas compression system with thermal swing adsorption (TSA)

Three intercooled compression stages are used upstream of the TSA. A fourth stage of compression (not intercooled) brings the air to the ITM operating pressure. The TSA takes the gas stream from the third stage, treats it and passes it onto the fourth stage. The fourth stage is

not intercooled so as to utilize the heat of compression for the ITM process. Getter and filters are placed downstream of the fourth stage.

Low- and High-Temperature Heat Exchangers (Recuperators)

Process Design

The non-permeate temperature specification as feed to the hot gas expander is limited by control considerations around the hot gas expander. For example, Williams determined that a high temperature shutoff valve is required upstream of the hot gas expander to isolate the expander to avoid over-spinning the expander should it become decoupled from the generator set. Air Products identified a high-temperature valve with a maximum operating temperature of 1,000°F that serves to isolate the hot gas expander in case of a trip. As a result, the recuperative heat exchanger surface area in the non-permeate stream was specified to meet the hot gas expander inlet temperature of approximately 1,000ºF.

Mechanical Design

Air Products chose a heat exchanger supplier to design and supply the fired heater system, the high-temperature economizer and the refractory-lined piping to connect each of these units to the ITM vessel. As part of this effort, the supplier performed a piping stress analysis that included the ITM vessel and incorporated that information into its design.

Fired Heater

Process Design

Heating of the air stream to the ITM operating temperature is carried out by a combination of recuperative heat exchange and indirect firing of the partially heated air. This process was chosen over alternative developmental processes, such as post-firing the non-permeate with indirect high temperature heat exchange, because fired heaters have known operating characteristics and can be scaled up considerably.

Mechanical Design and Fabrication

Alloy A was specified for the fired heater. This decision was based on cyclic oxidation tests conducted by Air Products (see Task 15). The fired heater system consisted of an air blower, fuel control system, fire box, main heat exchange section, and flue gas stack.

Fabrication/delivery delays occurred associated with the metallurgy of the fired heater heat exchange section. The supplier evaluated several design changes to ease fabrication, and Air Products and the supplier agreed upon a path forward. New headers were successfully cast from an alternative metallurgy with a thinner wall in Q3-2013 and the equipment was delivered to site in Q1FY11 – a 21-month delay relative to the original contract delivery date.

Once installed, several mechanical design issues were identified in the heat exchanger portion of the fired heater. After extensive consultation with the vendor and internal reviews, several additional design features were added, and operating procedures were modified to maximize the service life of the equipment.

Permeate Cooler and Compression

Process Design

The process flow diagram (PFD) included a closed-loop boiler system and trim cooler for oxygen cooling.

Mechanical Design

NASA-Marshall completed high-temperature oxygen compatibility testing of prospective materials of construction for the oxygen/permeate waste heat boiler system. One of the tests demonstrated that the main material of construction upstream of the oxygen cooler is non-flammable in 100% oxygen at 870°C and one atmosphere. A test on samples of 1¼ Cr – ½ Mo demonstrated flammability at 260°C and one atmosphere, which are relevant conditions for the tubes in the oxygen waste heat boilers. Steam operating temperatures were chosen accordingly. Air Products specified specific mechanical design features for the oxygen boilers to reduce the likelihood of oxygen fires in the system.

Hot Gas Expander

Process Design

Williams International supplied the hot gas expander for the ISTU. The Williams design was based on turbo-jet components from their military and commercial products and match well with the ISTU's power requirements. The system delivered by Williams also had substantial scale-up potential.

The Williams hot gas expander concept includes an integral combustor. Concepts NREC favorably reviewed the Williams combustor design methodology and recommended that Air Products proceed with a combustor testing program proposed by Williams to validate the CFD-based design.

One aspect of the scope change agreed to by the Recipient and the DOE, which included reducing the capacity of the ISTU from 150 TPD to 100TPD, was a hot gas expander turbine inlet temperature of approximately 2,000°F to support an efficient process. The high inlet temperature to the expander resulted in a high exhaust exit temperature. Air Products developed a scheme to reduce the exit temperature by blending in ambient air with a fan. Williams evaluated an alternative design basis for their hot gas expander (i.e., lower mass flow and higher firing temperature), but concluded that a higher temperature could not be accommodated.

Combustor Development

Williams proposed a hot gas expander combustor development plan that entailed defining test points, combustor rig design, and test cell location. Williams defined the test rig P&ID, as well as a design for a ⅓-scale combustor which could be tested at three pressure levels and four oxygen concentrations. Williams was also tasked to validate CFD calculations for the combustion of natural gas at elevated pressure and temperature in oxygen-depleted air.

Williams completed construction of the combustor test rig and conducted low-pressure cold flow testing (Figure 19-3). The operation of the unit was checked at the most difficult sets of operating conditions (high temperature and low flows). The system included a nitrogen blend system to allow dynamic variation of the inlet oxygen concentration. Concepts NREC aided Air Products in the evaluation of the Williams combustor design and concluded that the approach was sound.

Figure 19-3 Williams hot gas expander combustor test unit.

Williams International conducted testing on the ⅓-scale combustor. Burner lightoff tests at various oxygen concentrations were performed at inlet temperatures of 600°F, 700°F, and 800°F, as well as several outlet temperatures, to determine the temperature dependence of the stability map. These data were extrapolated to the actual operating inlet pressure and temperature. The extrapolation suggested that the test rig would operate stably at an oxygen concentration slightly above the design concentration. Williams further predicted that the full-size combustor would be stable at oxygen concentrations below design. Given these results, the full-scale combustor became a simple scale-up of the combustor rig design (i.e., no appreciable changes). Concepts NREC compiled a stability curve for similar combustors. Figure 19-4 documents the ISTU combustor conditions relative to stable and unstable combustion conditions based on literature.

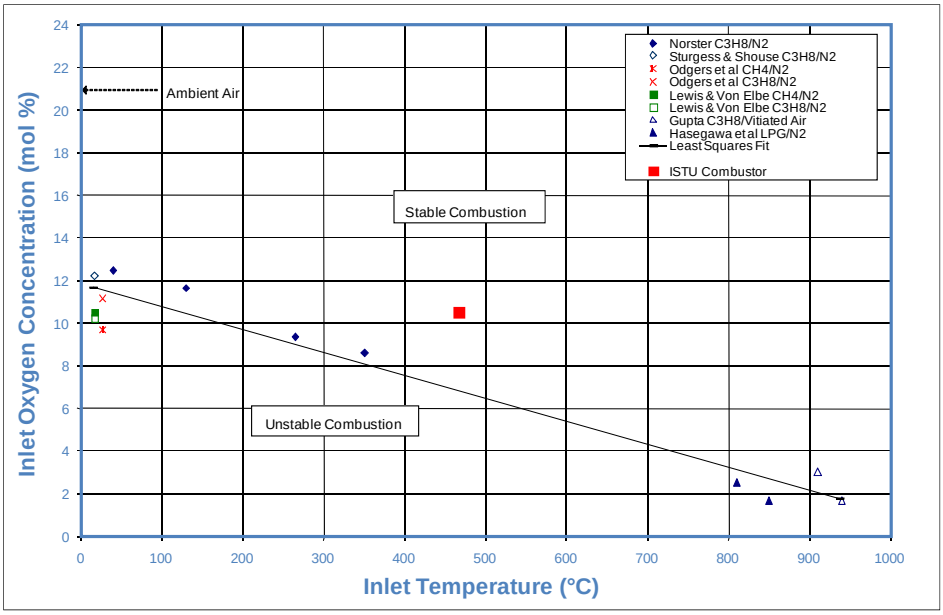

Figure 19-4. ISTU combustor conditions and stable/unstable condition.

Mechanical Design and Fabrication

P&ID development, control logic description, general arrangement drawing, scope definition, limits of operation, schedule updates, HAZOP and an updated cost estimate were completed for the hot gas expander system integrated in the ISTU. Williams began construction by ordering long-lead rotor forgings and also completed purchase-ready specifications for the turbine forgings, gearbox, lube oil system, couplings, and instrumentation and control package. The general arrangement drawing was modified to reflect the generator purchased by Air Products.

Air Products completed an FEA analysis, a redesign of the casing and inlet piping, and a determination of the allowable piping loads at the hot gas expander interface flange. Williams completed the design, analysis, and casting definition of the 3rd- and 4th-stage blades and nozzles.

Williams transitioned from design to manufacturing and began placing purchase orders for the controls, instrumentation, gearbox, and inlet pipe assembly. They fabricated the hot gas expander powerhead components, including the first-stage nozzle, and assembled the rotating equipment and verified balancing. Various sections of the static structure were fit-checked, and some components were slightly reworked. All other accessory system components arrived or were fabricated. The control system factory acceptance test was completed and witnessed by Air

Products. Final packaging of the hot gas expander was completed,and the expander skid was shipped to site and installed.

Commissioning of the hot gas expander was conducted with the Brayton Cycle section of the plant operating by only a team from Air Products, Concepts NREC, and Williams International. Once the proper light-off conditions were identified, the combustor achieved smooth ignition and stable combustion six out of six times. A series of tests was conducted to measure lean blowout performance at three different air flow rates. A post-test borescope inspection of the combustor liner found no damage or evidence of excessive temperature. During these initial tests, the hot gas expander produced 4.3 MW of 13.8kV power at approximately 90% of design flow.

ITM System

Air Products collaborated with Becht Engineering to design the ITM vessel. Concept drawings for the vessel internals were created and used to develop the specifications sent to prospective suppliers. One concept drawing is given in Figure 19-5, which shows a side view of the flow duct which houses the modules. The flow duct is located internal to the horizontal vessel.

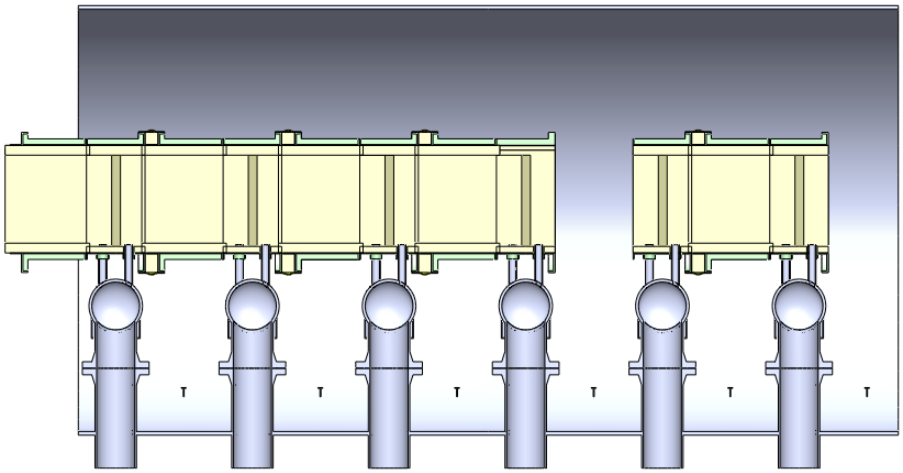

Figure 19-5. ISTU flow duct concept drawing.

In this concept, the modules are located directly over permeate manifolds. The permeate manifolds are shown in gray at the bottom of the figure. A removable piece is located between the module sections to allow access to the module section from either side. The stick figure in Figure 19-6 represents a person loading a module into the duct.

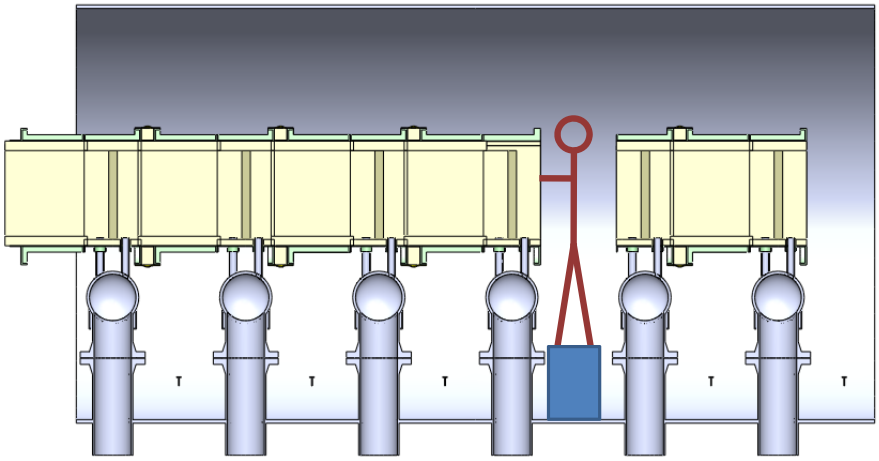

Figure 19-6. Concept of ISTU flow duct showing the flow duct and access.

The pressure-containing shell houses both the flow duct and permeate piping system. This modular approach enables good access to modules so they can be replaced easily and instrumentation can be placed around individual modules.

Project Execution and Construction

The following is a chronology of the major project execution and construction activities associated with the installation of the Intermediate Stage Test Unit.

Q2-2009

- Two Air Products sites for the ISTU were evaluated, one in Louisiana and one in Texas. The Convent, Louisiana site was chosen as it had a spare substation for power. An environmental assessment indicated that neither site would require new permits.

Q4-2009

- Process and mechanical specifications for all the major equipment were completed, and quotations were received from vendors.
- All equipment costs were tabulated. The differences in costs versus the original estimate at the beginning of Phase III were summarized and sent to DOE-NETL.
- A plot plan was developed (Figure 19-7).

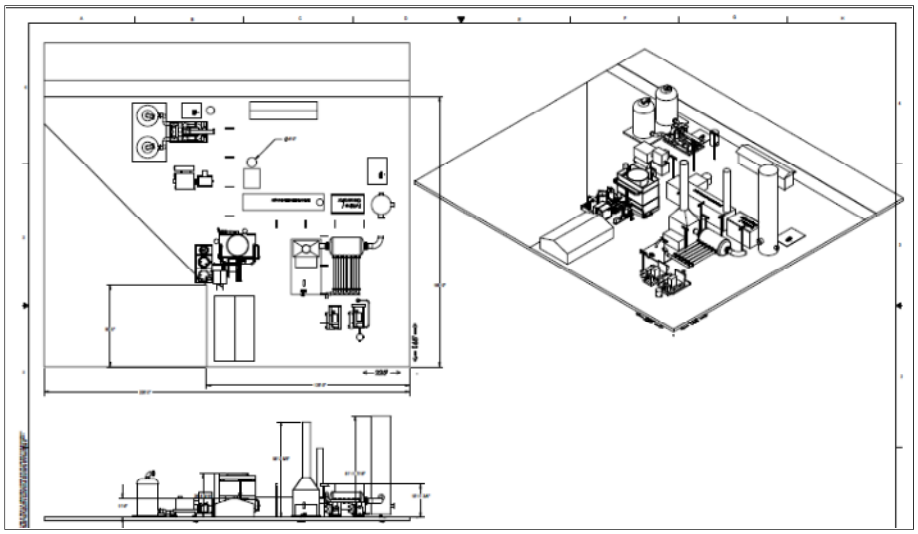

Figure 19-7. ISTU plot plan as of Q4-2009.

Q1-2010

- Project quality specifications were sent to qualified vendors.
- A detailed startup sequence was documented to define non-steady-state operability requirements for the equipment.
- Emergency trip protocols were documented for various scenarios, and the effects of emergency trip control sequences were modeled by using a dynamic modeling approach.
- Ceramatec performed detailed stress analyses for the ceramic module components during emergency trip cases.
- Equipment design requirements based on the process requirements during rapid transients were analyzed and incorporated into the equipment specifications.
- The main air compressor was ordered.
- The process and instrumentation diagram (P&ID) was completed.

Q2-2010

- The project scope was officially altered from a 150-TPD to a 100-TPD facility.
- Mechanical design details were developed for the ITM pressure vessel, oxygen coolers, fired heater, high-temperature economizer, hot gas expander and the fired heater.
- The design for a closed-loop boiler system for oxygen cooling was developed.

Q3-2010

- New process specifications were issued for all major equipment items, and revised quotes were received.
- The preliminary plot plan for the ISTU was revised to accommodate a longer, narrower footprint.
- The P&ID was updated in preparation for the update to the preliminary hazard review.
- All technical risk statements (TRSs) with risk mitigation items were completed.
- Operability and preliminary hazard reviews covering the scope changes were conducted.
- The operations staffing plan for commissioning and startup was reviewed, and the site operations lead contact for the project was identified.

Q1-2011

- The permit applications for discharge of wastewater and storm water and the air permit were submitted to the Louisiana Department of Environmental Quality (LDEQ).
- Most of the design hazards review (DHR) was completed, which generated 378 recommendations; 93 were closed out, primarily P&ID revisions.

Q2-2011

- Off-design scenarios were documented for the hot equipment and the oxygen circuit to establish design conditions.
- Oxygen backflow scenarios were evaluated to determine if the presence of oxygen could impact design conditions and materials of construction.
- A layer of protection analysis (LOPA) was conducted for the steam drum overpressure scenario.
- The environmental consultant found that the proposed site for the ISTU would be classified as wetlands, which would result in a lengthy permitting process. The plot plan was modified to avoid wetlands impact.
- The (post-DHR) P&ID was reviewed and drafted.
- Specifications for the hot control valves, hot flow meter and some relief devices were issued.
- Request for Proposal packages were distributed to several engineering firms.
- An iso-control system was designed.

- Shutdown tables were developed and reviewed.
- Over-temperature protection strategies for the refractory-lined piping runs and the ITM vessel were clarified.
- Dynamic modeling capability was upgraded, and work was begun on an alternative recovery sequence following a system shutdown trip.

Q3-2011

- A final P&ID review was completed, leading to an "approved for design" status for the flow sheet.
- The environmental applications and the DOE environmental questionnaire were resubmitted.
- The supplier submitted general arrangement drawings for the high-temperature economizer, fired heater, and interconnecting refractory-lined piping.
- The cooling water heat exchangers were ordered.
- A U.S.-based design company was chosen to perform the detailed engineering for the facility.

Q4-2011

- All major and minor piping runs, including valves, instrumentation, relief devices and vent lines, and most platforms were documented.
- The TSA was fabricated and the main air compressor was delivered to site.
- Permits were issued by the Louisiana Department of Environmental Quality, the Louisiana Department of Natural Resources, and the US Army Corps of Engineers. The DOE issued a Categorical Exclusion.

Q1-2012

- Preparation work and piling were completed (Figure 19-8).
- Civil and underground work commenced.
- The design company completed the facility model and pipe stress analysis and released "Issued for Bid" piping isometrics.
- Air Products and the design company approved the interlock table.

Figure 19-8. ISTU site preparation.

Q2-2012

- Civil work was completed.
- The mechanical contractor was mobilized.
- The cooling water exchangers and four oxygen boilers (Figure 19-9) were set in position.
- Most of the pipe rack support steel was erected, and the cooling tower was in final assembly.

Figure 19-9. Photograph of the oxygen boilers in position.

Q3-2012

- The TSA skid, high-temperature economizer, and exhaust stacks for the fired heater and expander were set in position.
- All rotating equipment (except the expander) was set in position.

- The ITM pressure vessel was shipped to the mechanical contractor for installation of the head and other late-stage fabrication steps.

Figure 19-10 is an aerial photograph of the ISTU construction site.

Figure 19-10 Aerial view of the ISTU construction site.

Figure 19-11 is a photograph of the ITM pressure vessel being prepared for shipment.

Figure 19-11. ITM pressure vessel being prepared for shipment.

Q4-2012

- The ITM pressure vessel final assembly was completed, and the vessel was set into position (Figure 19-12).

- The product nozzles were welded to the oxygen waste heat boiler and the vessel shell was welded to the saddles.
- The control room and maintenance buildings were installed, and the DCS and operation stations were placed in the control room.
- The combustion section and valve skid for the fired heater were set in place.

Figure 19-12. ITM pressure vessel being positioned at the ISTU.

Q1-2013

- The mechanical, instrumentation and electrical and insulation contractors completed the first phase of construction.
- Control loop commissioning was begun.
- All of the major machinery, including the MAC and oxygen blowers, was commissioned.
- The ITM vessel confined space entry plan was prepared and approved by ITM research and development management.

Q2-2013

- Plant construction and commissioning activities were completed except for the fired heater and hot gas expander.
- The ITM R&D team conducted the initial ITM vessel confined space entry.
- The following components were installed: chromium getter, thermal mass at the outlet end of the flow duct, non-fluxing modules, approximately 200 thermocouples, and tubing for pressure drop measurement and gas sampling.

Q3-2013

- The response to FY10 AIGCC Peer Review Milestone A1: A review of the impact of major project risks was submitted to the DOE project manager.
- The response to FY10 AIGCC Peer Review Milestone R4: A report documenting and addressing safety issues associated with handling high-temperature oxygen was submitted to the DOE project manager.

Q4-2013

- The expander skid was installed and various construction activities continued.

Q1-2014

- Air Products completed the hot gas expander installation, windmilled it to design speed and also motored it to speed. Three issues were identified: high vibrations in the expander, a significant oil leak around the high-speed shaft seal at the gearbox, and control of the balance piston.
- The initial light-off of the expander using natural gas was successful and produced 4.3 MW of power at about 90% of design flow.
- The heat exchanger portion of the fired heater was lifted into position, marking the successful installation of the final piece of major equipment. Figure 19-13 shows the heat exchanger being positioned between the fire box and the flue gas stack.

Figure 19-13. Fired heater, heat exchanger being positioned.

Q2-2014

- Modules to filter vibration signals, a vacuum pump, an oil mist detection system and new control valve trim addressed the expander deficiencies.
- Installation of the fired heater was completed. The work included the installation of specialty insulation and the refractory-lined spool piece leading to the ITM vessel inlet. Loop checks were completed for the new instrumentation.
- Modifications to the TSA and the fired expander instrumentation and control system were completed, and the final control system was validated.
- The steam system was flushed and the operational readiness inspection (ORI) was completed.
- Initial light-off of the fired heater was achieved. However, the heat-up was suspended when an atypical start-up operating condition caused two safety near-miss events (see commissioning regarding near miss).
- The site work instruction manuals (SWIMs) were updated.
- Round-the-clock engineering and start-up operator coverage began after the initial light-off of the fired heater and a multi-day refractory dry-out and cure.

Q3-2014

- All construction activities were completed.

Figure 19-14 is an aerial photograph of the completed ISTU.

Figure 19-14. Aerial photograph of the completed ISTU.

Safety

An excellent safety performance was achieved during construction:

- Total site hours worked: 96,536
- Lost time injuries: 0
- Recordable injuries: 0
- First aid cases: 1
- Near misses: 7
- Design near misses: 1

Commissioning

Commissioning Run 1

Air Products commissioned the ISTU over a series of three commissioning runs. During Run 1, the team determined that the fired heater control system allowed operation with an atypical combination of pilot versus main burner operation and low flows of combustion air. These conditions caused two different safety near-miss events, both of which were related to the burner management system (BMS) software. The initial heat-up was suspended, and a root cause analysis traced the problem back to an issue within the architecture of the safety matrix system in

the control system vendor's code. The BMS functional description, sequence flowchart and code were revised. The BMS was ultimately revalidated.

The site work instruction manuals (SWIMs) were updated. The cold plant start-up and fired heater SWIM underwent significant revisions based on the lessons learned from the root cause analysis into the BMS near misses.

Commissioning Run 2

The plant re-entered start-up mode for a two-week run. During the run:

- There were no safety incidents.
- The system achieved its design process operating temperature and reached near-design pressure and flow.
- The fired heater pilot and main burners ignited on the first attempts, and the burner was reliable throughout the run.
- Refractory dry-out and cure were completed.
- Boilout of the oxygen waste heat boilers was completed, and the system performed as designed.
- The high-temperature insulation systems in piping and equipment performed well in many areas. There were several hot spots that limited the ability to achieve design operating pressure and flow, but they were confined primarily to two general areas.
- Pressure, flow, and vacuum ramps were tuned with good success.
- The sulfur analysis system functioned well, and sulfur levels appeared to be low.

Startup Data

The pressure drops across the inertial separator and filter were measured as a function of flow, temperature and pressure. The results were compared to calculated values. The calculated values for the filter under-predicted the pressure drop, most significantly at higher velocity. The expression used to predict pressure drop sums viscous (μv) and inertial (ρv^2) terms. The calculations underestimated the relative impact of inertial forces as compared with viscous forces. Adjusting the coefficients gave a much better fit. Figure 19-15 shows the results from the revised expression.

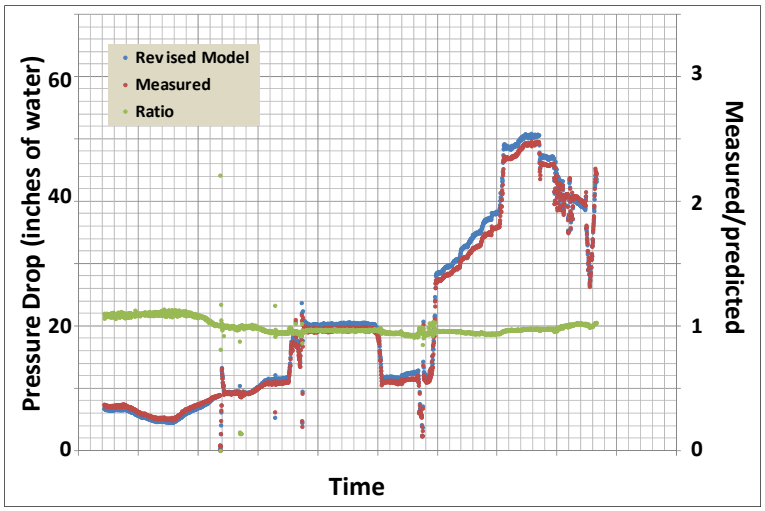

Figure 19-15. Particulate filter pressure drop as measured and as predicted with the revised model.

The previous model assumed laminar flow; the revised model assumes turbulent flow.

The inertial separator pressure drop scaled linearly with dynamic pressure. Getter pressure drop was typically about 40% of the pressure drop across the inertial separator. Figure 19-16 shows a good linear correlation between the separator data and dynamic pressure.

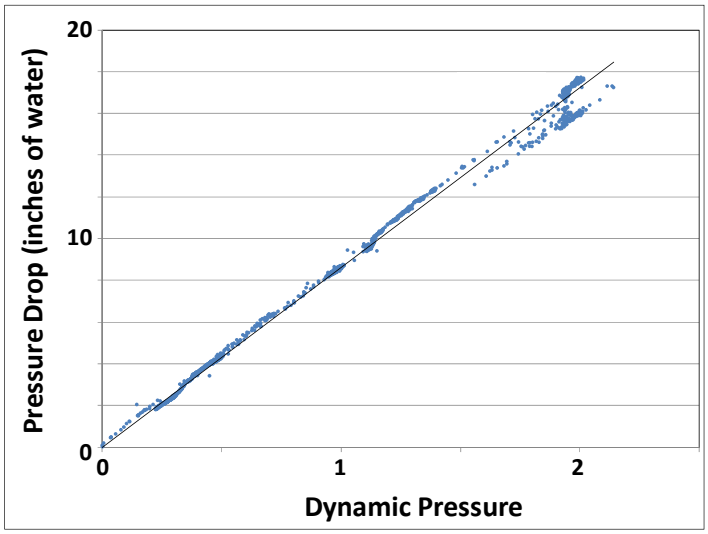

Figure 19-16. Dynamic pressure and pressure drop correlation.

ISTU Sulfur Burn-out

Sulfur dioxide levels were monitored from three sample points in the process stream as the temperature was increased. Samples were taken from a point located on the non-permeate

stream as it exits the hot recuperator. This location is downstream of most of the sulfur-containing refractory materials and therefore the most likely location to observe sulfur. The other two sample points are located in the air feed and the flow duct inside the ITM vessel. For most of the start-up, sulfur levels remained very low; higher levels were observed for short periods during process interruptions.

Commissioning Run 3

Activities focused on items resulting from Run 2, including repairs to hot spots in the refractory-lined piping as well as performing a confined space entry into the ITM vessel to relocate internal thermocouples. Following completion of these activities, the plant re-entered start-up mode for a two-week run, marked again by the onset of round-the-clock engineering and start-up operator coverage. A revised temperature and pressure schedule was used. The schedules considered the impact of pressure transients on wafer reliability observed in experiments with the TTR and XVU.

Notable accomplishments from this run include:

- Zero safety incidents.
- A modified "black plant" test to demonstrate start-up of the backup diesel generator and restart of critical equipment on that circuit.
- Achievement of full design operating conditions.
- A complete plant performance test.
- Hot spot repairs to the insulation systems. A rigorous new system was implemented to detect and manage hot spots.
- Main air compressor trip and recovery tests, as well as other planned trip tests to practice recovery procedures.
- Successful tuning of the temperature, pressure, flow, and vacuum ramps.
- Adjustments to the fired heater control system to improve operation and reliability.
- Burnout of additional sulfur.

Expander commissioning proceeded, and two light-off attempts resulted in successful operation. During the process, several adjustments were made to the sequencer that automates the control steps governing start-up, light-off, warm-up, and ramping to design temperature and pressure. The aim throughout this testing was to fully automate the sequence and achieve the optimal

conditions for the light-off and warm-up periods. After another light-off and warm-up, the system achieved near-design conditions. Power output reached the generator maximum, which exceeded the design power.

In a subsequent light-off, the combustion seemed more unstable. The system was placed in manual control, which improved combustion stability somewhat. When the system was returned to automatic temperature control, the controller called for a large step change in fuel flow, which lasted for several seconds before the control system executed an emergency trip on high temperature. An inspection of the expander found damage to some internals. The expander was sent to Williams International for an assessment of the damage. A quote for repairs was received; Air Products, in conjunction with the DOE, chose to defer repairs.

Commissioning of the ISTU was completed at the conclusion of Run 3.

TASK 20.0 INTERMEDIATE-SCALE TEST UNIT (ISTU) OPERATION

20.0 Scope

Air Products operates the ISTU with an oxygen capacity of approximately 100 TPD. The ISTU includes the major elements of a commercial ITM Oxygen facility and the operating conditions will be typical of commercial operation. The Task 20 testing establishes the basic feasibility of operations beyond the prototype scale.

Air Products subjects the ISTU to multiple test campaigns, including normal startup, steady operation, and shutdown procedures to establish an engineering design basis of an integrated commercial-scale facility. Individual equipment operations are closely monitored.

20.0 Intermediate-scale Test Unit (ISTU) Operation

ISTU Run 1

Seven modules were delivered to Convent, Louisiana, from Ceramatec in Salt Lake City, Utah. The dimensions of all of the modules were measured, and they were subsequently installed in the ISTU.

The seven ITM modules were loaded into the ISTU vessel flow duct replacing non-fluxing modules that had been used to simulate the thermal mass of an ITM module during system commissioning. Four modules were placed in Row 1 and three were placed in Row #2. Each non-fluxing module allowed air to flow into the oxygen permeate system through an orifice. At full operating conditions, each calibrated orifice controlled the flow to be equivalent to that of a fluxing module.

Air Products started the main air compressor (MAC) and dryer system (TSA). The plant was pressurized and the air flow rate ramped to an intermediate amount. The fired heater was lit and the system was heated to operating temperature. This was followed by a pressure and flow ramp.

Shortly after reaching an intermediate pressure, the system experienced significant fluctuation in feed air pressure that produced thermal fluctuations in the vessel; this ultimately caused three ITM modules to fail. The auto-shutoff valves tripped on each of the compromised modules, effectively isolating them.

Full feed-side operating conditions were achieved, and the permeate vacuum ramp was begun. The design vacuum level was reached, at which time the plant was running at full design conditions. The oxygen purity from the four remaining modules improved over time. One module achieved as high as 94.6% oxygen purity prior to a planned vacuum blower trip test. The combined oxygen product flow and air flow through the calibrated orifices resulted in an overall permeate product purity that was consistent with the expected productivity of the four fluxing modules, although this is only a rough measurement of flow.

A vacuum blower trip test was conducted whereby the vacuum blowers are turned off and isolated by means of an in-line shutoff valve, and the product vent valve upstream of the blowers is opened. In this case however, a safety interlock reacted to the high permeate vent flow rate and closed the vent valve after the blower was turned off. This caused the permeate pressure to increase rapidly to the feed-side operating pressure. Therefore, the test was much more severe than would be experienced during normal operation. The vent valve was opened manually, which brought the pressure back to atmospheric. The vacuum system was restarted and ramped back to normal operating pressure (sub-atmospheric). One ITM module recovered fully with no apparent loss of oxygen purity. The other three operating modules experienced at least some loss of purity.

Many plant trips ultimately lead to a “safe stand-by” condition. A “safe stand-by” and recovery test was conducted to establish temperature and pressure histories and thermal gradients under standby conditions in the ISTU system. The test proceeded according to plan without severe deviation from process conditions. During the return to normal operating conditions, temperature fluctuations again ensued. This ultimately caused damage to two of the four remaining ITM modules and tripped their auto-shutoff valves. As with the other two major events during this run, the best ITM module recovered fully with no apparent loss of purity. The system was shut down normally after the “safe stand-by” test.

Temperature profiles measured during the run were quite satisfactory, confirming the suitability of the flow duct design. Figures 20-1, 20-2 and 20-3 document the operating conditions in the ISTU during Run 1.

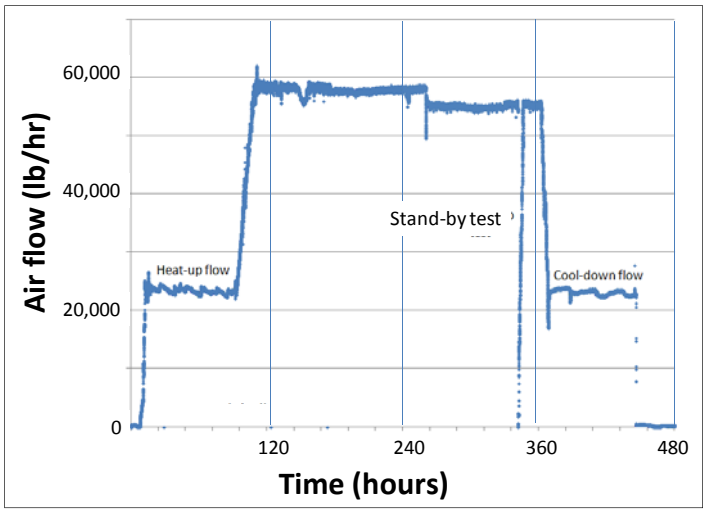

Figure 20-1. ISTU Run 1 air mass flow.

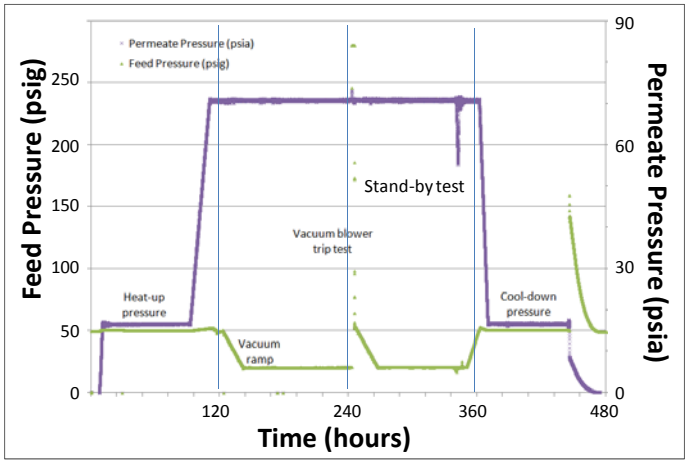

Figure 20-2. ISTU Run 1 feed and permeate pressures.

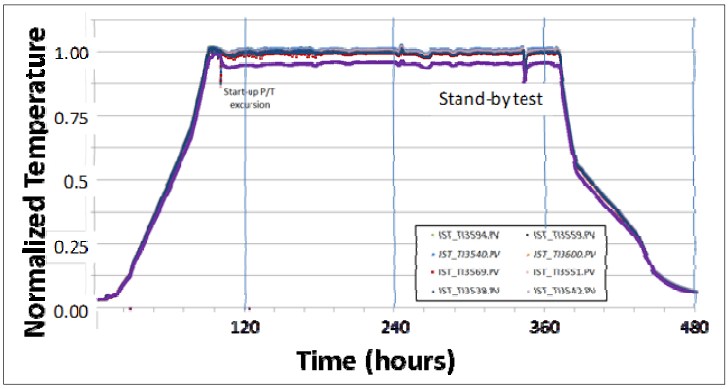

Figure 20-3. ISTU Run 1 temperature.

After Run 1 was completed, the modules were removed during a vessel entry. The flow duct was opened and the seven modules were carefully removed, along with the remaining nonfluxing modules in the first two rows of the vessel. Several modules were intact. Modules near the flow duct edge, where thermal excursions occurred, showed ceramic damage.

When the modules were unloaded, the basepieces, seals, and seal plates were inspected visually for damage. For the intact modules, no obvious cracks or other flaws in the base pieces were identified. The ceramic-to-metal seals were mostly in good shape. Some sections of the seals remained adhered to the seal plate and to the base piece and were photographed An exception was the seal on Module 16, which separated. This module was among those damaged during the initial pressure ramp event and therefore did not see full pressure load, and had only limited time at temperature and pressure. The Module 15 seal fractured, with part adhering to the base piece and part to the seal plate. The modules were removed from the vessel for further analysis.

None of the modules had any significant evidence of leak due to base piece warp. The inspection suggests that the upper and lower areas of contact on the base piece were the same, suggesting the seals were accommodating any warpage.

Wafers from modules in position 9 and 15 were analyzed using EDS. Wafers from near the top, the center, and near the bottom of each module were sampled. SEM images are shown in Figures 20-4 (Module 9) and 20-5 (Module 15).

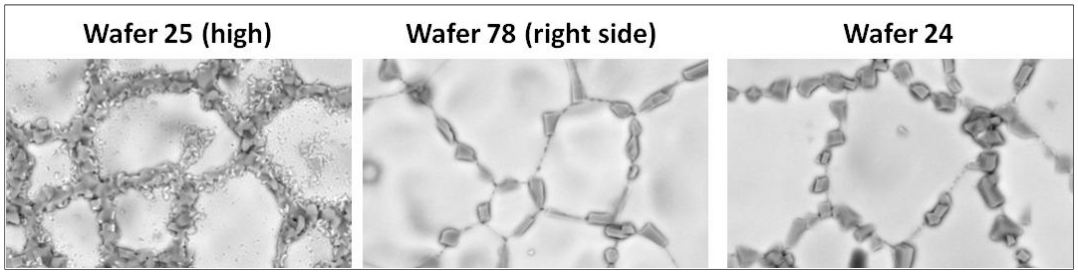

Figure 20-4. SEM images of Module 9 wafers.

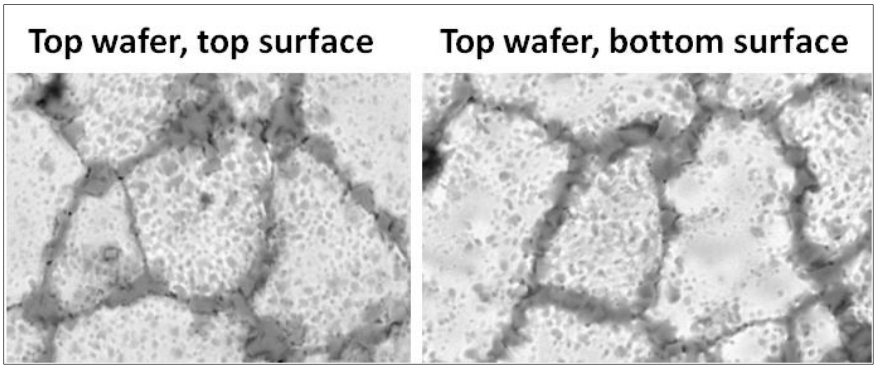

Figure 20-5. SEM images of Module 15 top wafer.

All wafers showed sulfur compounds at the grain boundaries on the outer membrane surface. Sulfur was expected to be present in the initial portion of the run because of the insulation introduced in some "hot spot" areas just prior to the run. Those areas would have undergone curing during the initial portion of the run, and would be expected to have evolved sulfur during curing. No chromium compounds were found on the wafer surfaces, indicating that the chromium getter was effective in removing chromium from the feed air.

ISTU Run 2

The objective for Run 2 was to produce tonnage oxygen from a fully-loaded module section in the ISTU without deliberate plant upsets. Prior to starting ISTU Run 2, modifications were made to the control system to address the occurrence of the temperature fluctuations seen during Run 1. Pressure fluctuations that lead to temperature fluctuations were addressed by a variety of control system responses designed to minimize temperature fluctuations in the vessel. The effectiveness of modified controls was closely monitored during Run 2.

Results Summary

The ISTU was loaded with 29 modules selected and arrayed in the pressure vessel according to a designed experiment.

ISTU Run 2 proceeded smoothly. The ISTU system operated well, as the unit experienced no large changes in process conditions during ramps like those experienced in Run 1. The ISTU was operated at full conditions for 13 days.

All 29 modules successfully started up and produced oxygen. One module produced >99.0% oxygen. Seventeen of the modules produced >90% purity during the run. The combined product purity from all modules ('header purity') remained close to 83% through most of the run. During operation, none of the modules exhibited a significant failure causing the ASOV to activate. The ISTU produced 16 tons per day of oxygen at standard conditions.

Details of the work and a further analysis of the results are presented below.

Module Shipping

A number of changes to the container and shipping procedure were implemented to minimize stresses on modules during shipping and loading/unloading from the container. Forty new module holders (rev. 3.2) were fabricated to allow for shipping of up to 47 modules at a time to the ISTU.

Ceramatec measured the dimensions, including base piece flatness, of thirty-two (32) 1 TPD-scale modules produced at Ceramatec's PDF under Task 17. The modules were packaged and shipped by Ceramatec (Salt Lake City, Utah). Modules were shipped in sets of four to a pallet in wooden crates. Modules were packed in aluminum boxes lined with foam, which in turn were supported within larger frames with springs. Figure 20-6 is a photograph of modules in spring boxes.

Figure 20-6. Modules in spring boxes.

Modules were leak tested immediately upon uncrating to confirm survival during transit. A partial view of the leak-testing apparatus can be seen in the bottom right corner of Figure 20-6.

Though there was some measurement variability, the as-received leak rates were mostly comparable to the pre-shipment leak rates. One of the modules was shipped before the flatness data was properly analyzed. Unfortunately, the module had a chip in the bottom of the base piece. Figure 20-7 shows the map of the base, as well as a photograph taken before it was loaded into the ISTU.

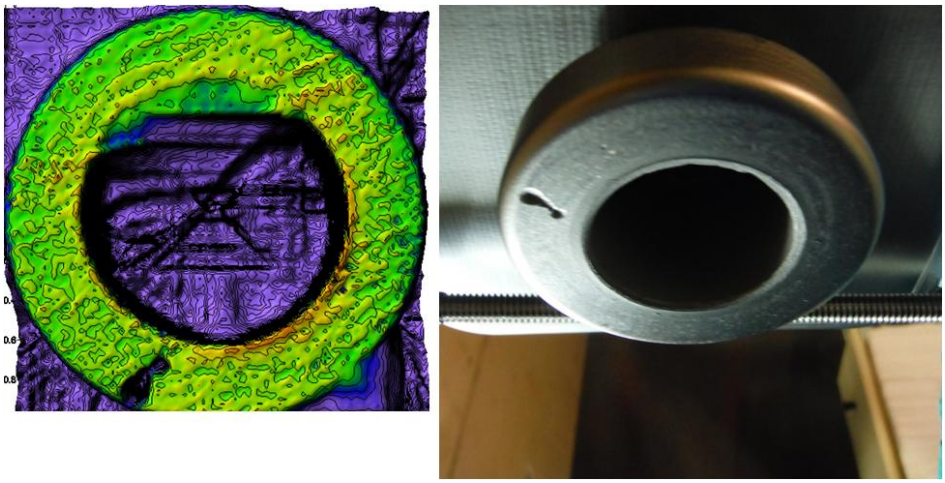

Figure 20-7. Flatness map and photograph of the bottom of the base piece of module.

The QC process has been updated to include an inspection of the base piece bottom before module loading. The defective module did, however, have an acceptable as-received leak rate.

ITM Vessel Module Load

The ISTU is equipped to allow the ability to monitor individual module purities for a select group of modules. This capability allowed for an analysis of the effect of an array of module characteristics in an experimental design. The variables included in the design were leak rate, location, seal type and base piece flatness. Output variables were module purity and reliability.

Twenty nine modules of varying quality were selected for testing. These modules comprise over 4,000 individual wafers. The entire history of testing in the SEP from 2006 through 2014 in 32 runs tested fewer wafers than this single ISTU run.

The modules and layout were selected to conduct a designed experiment to study the effects of module characteristics on purity and reliability. Thus several modules purposely were chosen that would be considered sub-par or outside module manufacturing specifications. The module section closest to where air flow enters the ITM vessel was fully loaded with AP2K modules in all 29 positions. The modules were installed using a number of fixtures designed for this purpose. Modules are hoisted to the top of the vessel in their shipping frames, then partially unloaded. The section of the frame left intact is used to support the module as it is lowered into the vessel through the top port, then installed into position on its flange and seal. The loading process proceeded more efficiently than expected, and all modules were installed in several work days. Figure 20-8 is a photograph of the loaded module section #1.

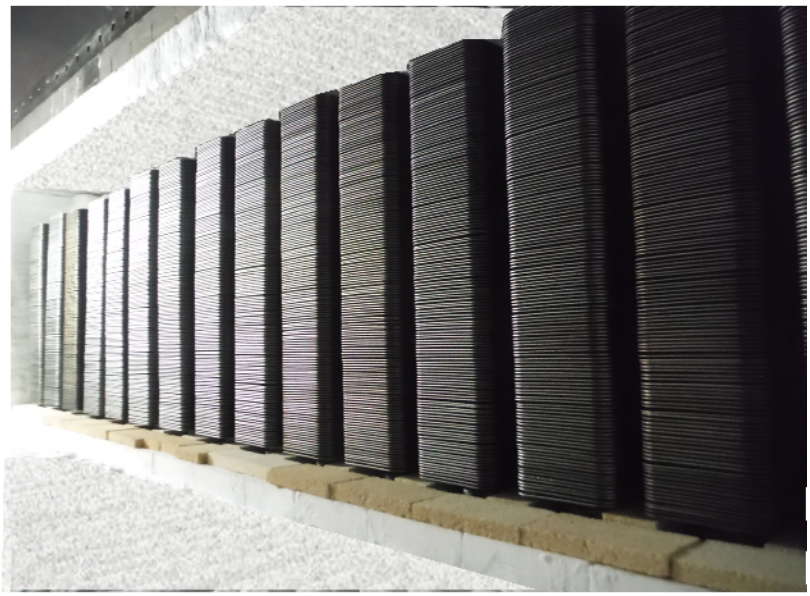

Figure 20-8. View from inlet end of module section #1 after installation.

Operating Conditions

The process was begun by first starting the main air compressor to establish flow through the vessel, followed by the initial pressurization. The fired heater was started, and the heatup was carried out per the specified procedure. Temperature was well-controlled throughout the run . Figure 20-9 documents the feed temperature, the vessel pressure and the permeate pressure. The process ran smoothly throughout the test.

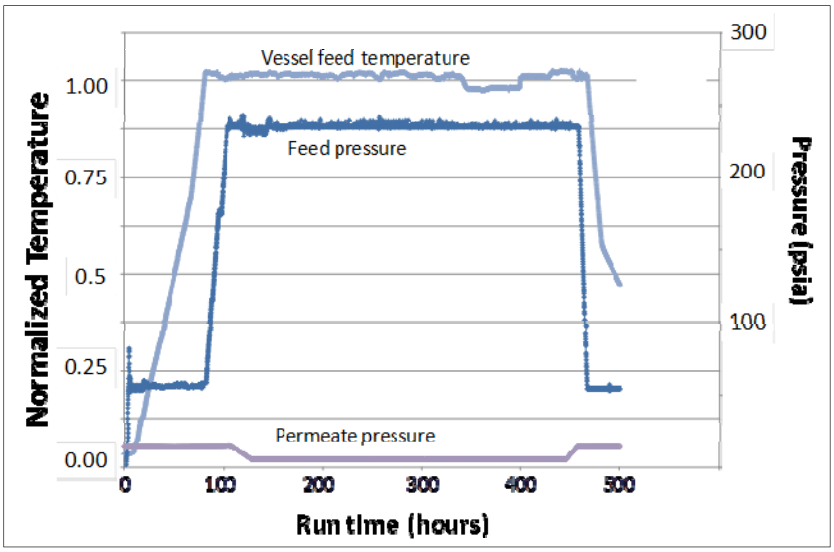

Figure 20-9. ISTU Run 2 operating temperature and pressures.

The temperature was reduced for 48 hours, returned to the baseline value for 24 hours, then increased above baseline for 24 hours before beginning the shutdown procedure. The shutdown ran smoothly. Figure 20-10 displays various process temperatures and the vessel flow rate.

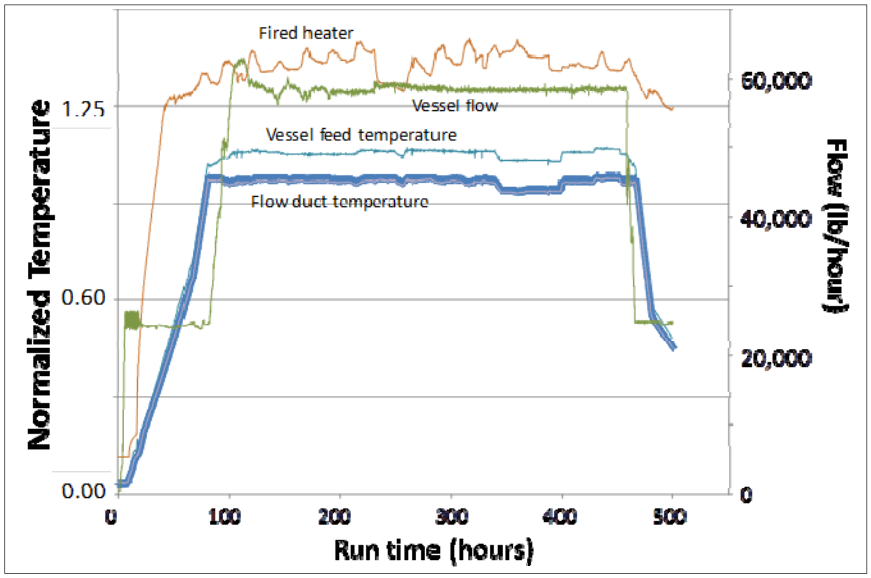

Figure 20-10. ISTU Run 2 operating temperatures and vessel flow rate.

The control system changes added after Run 1 were closely observed. The actions performed as desired, with no significant temperature fluctuations noted during testing despite some pressure fluctuations.

Flux

This was the first ISTU run featuring a module section and associated product header with a full set of modules, without non-fluxing dummy modules and orifices. As a result, there is sufficient information in the measured purities and flows to calculate an overall oxygen flux for the modules that can be compared to model predictions. The corresponding flux measurement results are plotted in Figure 20-11, along with the temperatures and pressures that affect the flux.

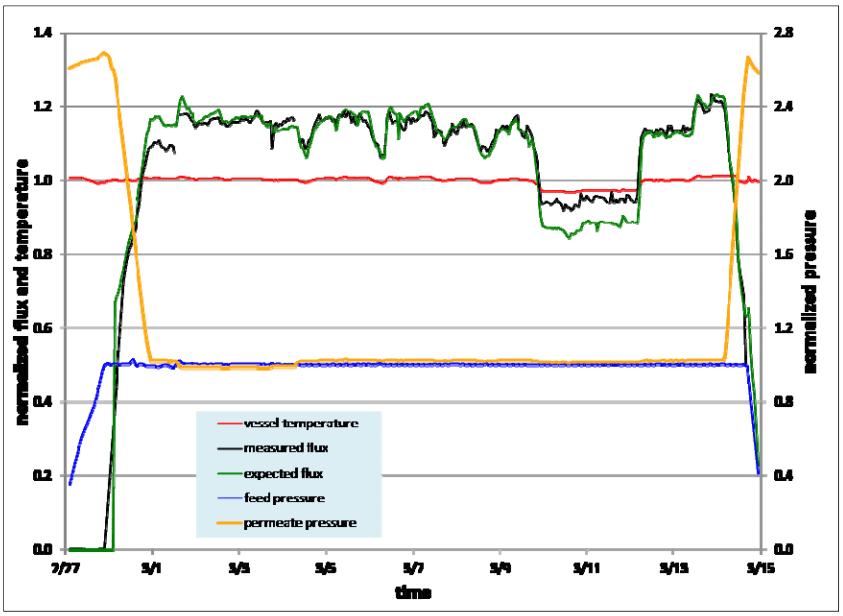

Figure 20-11. Calculated values of flux from process measurements and model predictions with corresponding temperatures and pressures.

Clearly, the flux is sensitive to fluctuations in the vessel temperature. The feed and permeate pressures were much more consistent during the steady part of the run, but the flux response to the vacuum ramps during startup and shutdown is captured well. The measured and expected fluxes agree remarkably well across most of the run. The lack of agreement early on in the run was likely due to improper calibration of the oxygen analyzer, which was corrected on 2 March.

Oxygen production was measured. Figure 20-12 documents the operating temperature, combined module purity (header purity), overall process purity and oxygen production. Dips in the header purity during the cooler portion of the run are artifacts of the data collection, not actual changes in purity. The total production from the all modules was on average 15% higher than expected based on the value corresponding to the target membrane thicknesses of the modules.

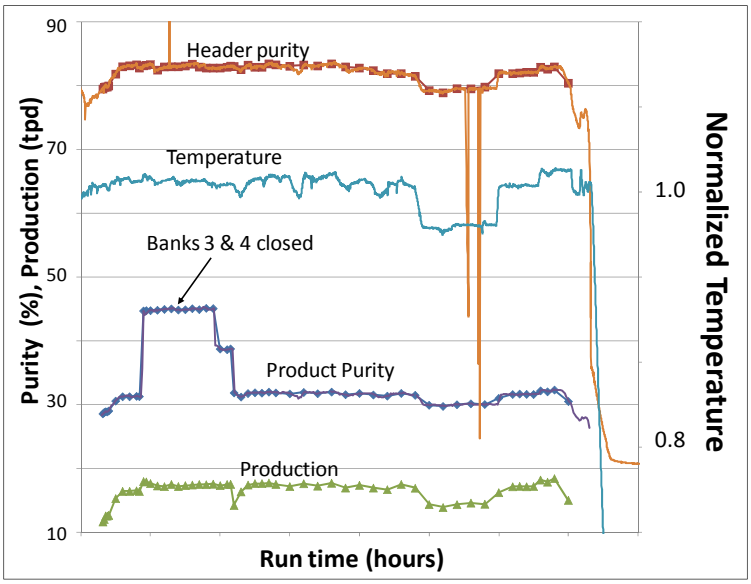

Figure 20-12. ISTU Run 2, purity, production and temperature.

Permeate from the ISTU vessel is removed through four separate lines, each representing a different section, or "bank" of the module array. The product purity in the figure is the purity of the mixed stream from all four banks. In Run 2, Banks 2, 3, and 4 were installed with nonfluxing modules with orifices that allow airflow through the product system at approximately the expected oxygen production rate for standard modules. The air from these orifices mixes with the product from Bank 1 and the flow and purity of the combined streams are measured. Banks 3 and 4 were closed off from approximately hour 150 to 200. Bank 4 was then reopened, followed by Bank 3.

While purity values are measured for each of the individual modules, there are no individual flow measurements, so there is insufficient information to directly calculate individual flux values. However, on two occasions during the run, a set of measurements was taken of the permeate-side pressure at the module base (using the module composition sample lines in a valved-off state). The measured pressures are higher than the pressure measured at the header due to the pressure drop associated with product flow from the module to the header. Using the correlation for permeate piping pressure drop, the pressure difference can be used as a crude measure of total module flow. When combined with module product purity information, the pressure drop can be translated into an estimated flux. Figure 20-13 shows these flux values for each of the modules, with different symbols used for modules with and without a porous

protective layer. Modules with a porous protective layer have flux values 9% higher than those without. Expected flux would be 7% higher at these conditions, which is reasonably consistent. Modules in Row 2 have 4% lower flux than those in Row 1 due to oxygen depletion, in agreement with theory.

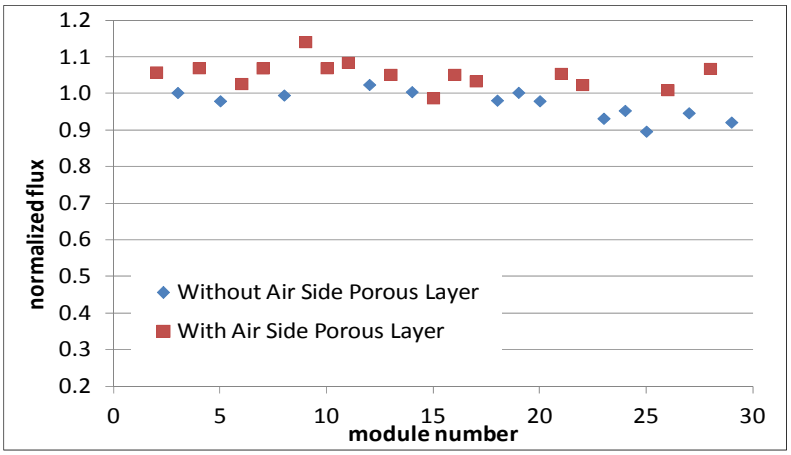

Figure 20-13. Individual module flux calculated from pressure drop measurements.

Purity

The ISTU vessel is configured with sample taps on each of the module positions in the first two rows, such that the purity of the oxygen product from each module can be measured individually. All lines run to a single analyzer, and the modules are sampled in sequence. Sampling is done on a single module for 4-5 minutes (adjustable time) to allow the reading to line out prior to switching to the next module in sequence.

All modules successfully started up and produced oxygen. A range of purity performance was seen. The best module produced >99% purity. During operation, none of the modules exhibited a significant failure causing the ASOV to activate. Seventeen of the modules produced >90% purity during the run. The combined product purity from all modules ('header purity') remained close to 83% through most of the run.

Module purities for Rows 1 and 2 are documented in Figures 20-14 and 20-15 respectively.

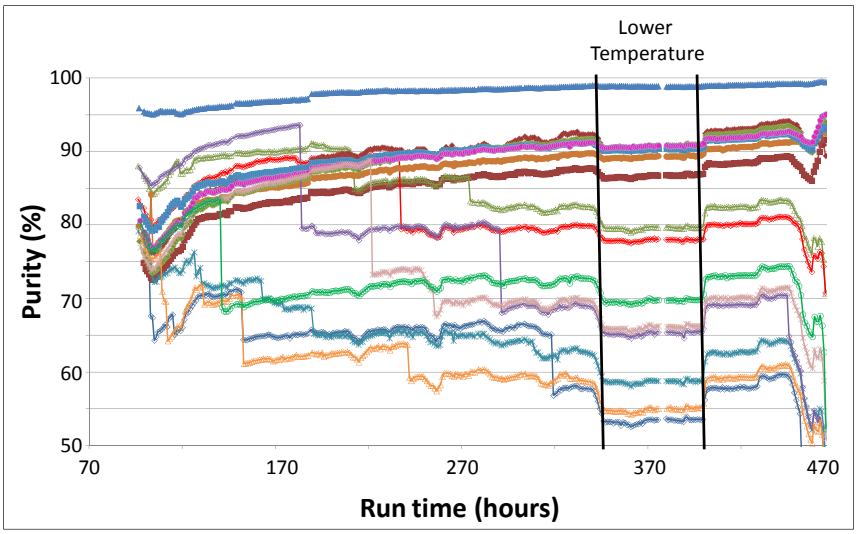

Figure 20-14. Module purity of Row 1 with run time.

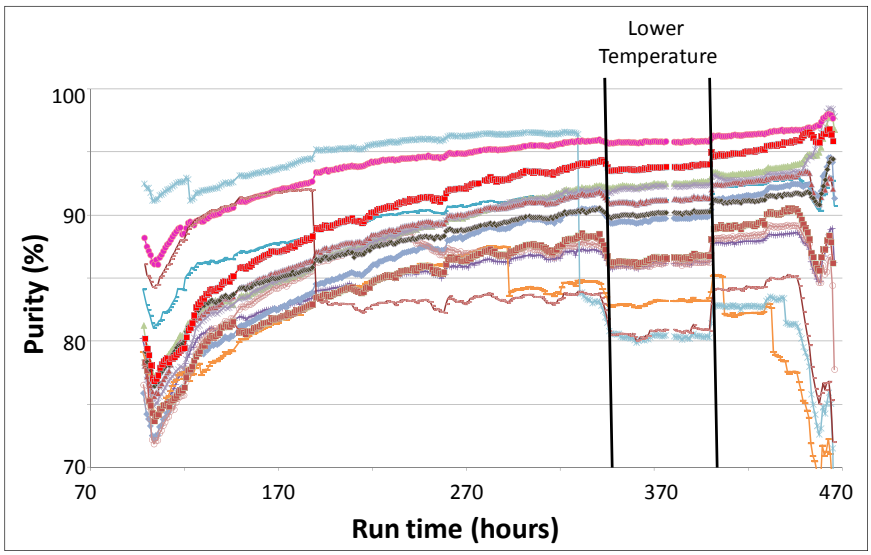

Figure 20-15. Module purity of Row 2 with run time.

The purity for a number of modules dropped while holding at steady state. This behavior was seen previously only for one module in SEP Run 32. Previous module testing always showed increasing purity with time. Module failures occasionally were seen at points where stress was increasing (e.g., process condition ramps or disturbances) in SEP testing.

To probe the cause of this observation, the temperature was reduced during hours 345 to 400, which significantly reduces thermally activated processes. None of the modules showed a drop in purity during the time at reduced temperature, though all purities were lower due to the

decreased oxygen production at lower temperature while leak flow presumably remained steady. The temperature was returned to the previous setting for 24 hours, then increased slightly for an additional 24 hours, and again several purity declines were seen. This suggested a thermally activated cause for the declines.

Performance Correlations

The following section analyzes the individual module performance against module parameters. The strongest correlations are with wafer type, submodule leak rate and module leak rate. Modules made from a particular wafer type and low leak submodules had the highest initial purities. The other variables in the experimental design were not highly correlated with initial oxygen purity. The correlation between module leak rate and module permeate purity is shown in Figure 20-16. The lowest-leak modules produced the highest permeate purities.

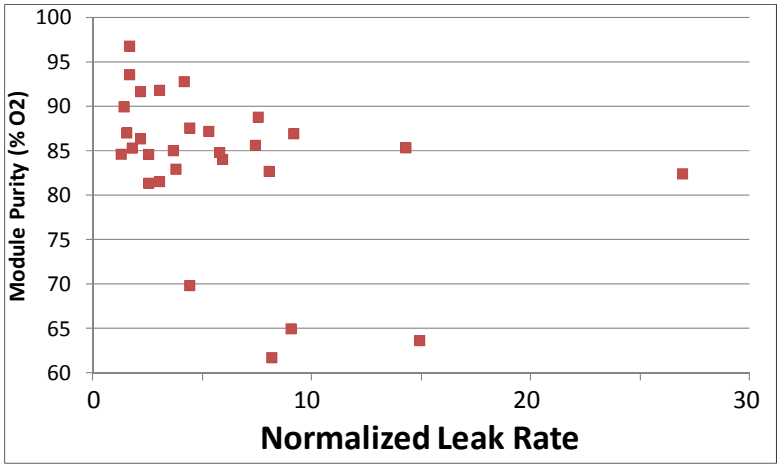

Figure 20-16. Initial module permeate purity as a function of module leak rate.

There was not a strong statistical difference between the performances of different seal types. The presence of cracked spacers, basepiece flatness or flow duct position was not correlated with initial module purity.

During the run, a number of modules suffered one or more step change decreases in permeate purity. These modules tended to have low permeate purities at the end of the run. There were three exceptions where the modules had a relatively small step decreases but all ended with purities >89%. The permeate purities of the modules which did not suffer step decreases

increased monotonically during the run. This behavior is similar to the leak rate behavior of seals tested in the lab, where leak rates decrease with time on stream.

Final module purity had a negative correlation with build date, but the effect was fairly small. Figure 20-17 is a histogram showing the number of modules achieving a purity range for modules produced from two wafers types. Wafer type A had higher purity.

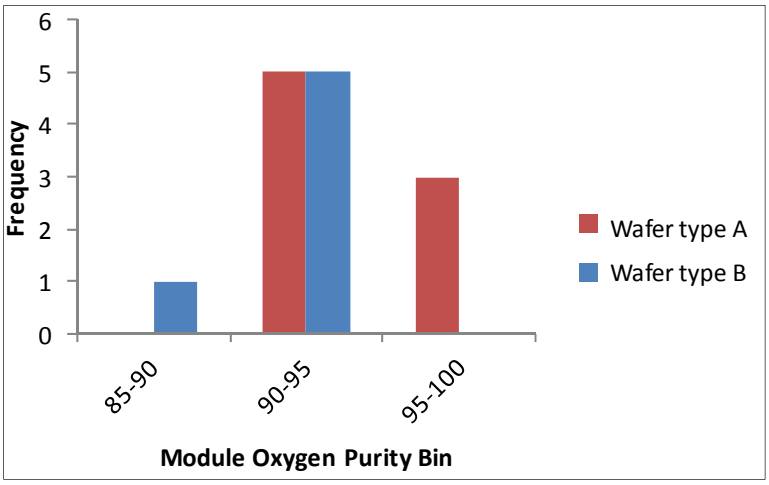

Figure 20-17. Frequency of modules made from different wafers types achieving purity ranges.

Reliability Correlations

A statistical analysis was conducted between modules that experienced a step change and the module parameters. The strongest correlation was with age, with newer modules suffering fewer step changes than older modules. The other parameter correlated with the step changes was the presence of an outer protective layer. This layer was present in all of the youngest modules but in only some of the older modules. Therefore, it is not possible to separate the effects of module age and outer protective layer on the occurrences of the step decreases seen in the modules.

Discussion of General Purity Results

The general upward progression of purity with time observed for most modules in this run is qualitatively consistent with the trends seen in our laboratory experiments in the FluX Verification and Seal Test Units (XVUs and ST-SLTRs). In these experiments, the purity trends are attributed to settling in (creep) of the ceramic-to-metal seal. Different seal types have different initial leak rates and purity improvement characteristics and respond differently to

pressure/temperature cycling, which suggests that the leak observed in these experiments is predominantly through the seals. However, in the laboratory units, leak rates drop to below target relatively quickly and improve further from there. In contrast, the leak rates for most of the modules in Run 2 were significantly higher than target.

There is no reason to expect the ceramic-to-metal seals to perform differently at the ISTU than they do in laboratory experiments. Test results from Run 2 showed a low correlation of purity with seal type or base piece flatness, which further suggests that the majority of the leak does not derive from the seals. This leaves the ceramic modules themselves as the likely majority leak source. The modules are leak-tested at atmospheric conditions. For all but the worst-leaking modules, the leak rates at full process conditions do not approximate the leak rates required to explain the observed purities.

Just as the leak rate is greater than can be reasonably explained by seal imperfections, the improvement of purity with time cannot be fully attributed to gradually improving seal performance. For example, Module 13, which is representative of modules that did not suffer a step change in purity, increased its oxygen purity from 84.2% to 92.0%. This corresponds to a decrease in leak many times the target seal leak rate, which is significantly greater than the expected seal leak or any previous improvement in seal leakage observed in the laboratory. The fact that similar leaks were not observed in XVU or TDU experiments may be explained in several ways:

- Small cracks in the ISTU modules may not be evenly distributed across all wafers; a few wafers may have caused the majority of the leak.
- When producing modules tested in our laboratory experiments, “leaky” wafers may not have been selected – either through chance or because of some heuristic approach to wafer selection.
- The large sample size of wafers in Run 2 and the fact that many of the modules were off-spec may have enabled testing of wafer/module features that are unlikely to be tested in small-campaign testing of a few wafers.

TASK 21.0 MANAGEMENT AND REPORTING

21.0 Scope

Air Products prepares and submits to DOE all required reports as specified in the Federal Assistance Reporting Checklist in the Cooperative Agreement and Amendments to the Cooperative Agreement.

21.0 Management and Reporting

Background

As an outcome of the FY12 Advanced Energy Systems (AES) Peer Review held April 23 – 27, 2012, the Review Committee provided a number of Recommendations and Actions to the program. Air Products and the Federal Project Manager agreed that three recommendations, R1, R2, and R4 would be addressed in this Final Report.

Accordingly, responses to the outstanding Peer Review recommendations from 2012 are given below.

> ***R1: Identify a plan for dealing with contaminants from the ambient air or coal-derived syngas and identify the associated costs for handling contaminants.***
>
> The project team should develop a plan to address contaminants and assess the associated costs, including an evaluation of the cost and reliability impact of the contaminant cleanup system on the overall plant. The team should consider revising the process flow diagrams of its system to include this cleanup system for the ambient air and syngas. They should also put a test program in place to check for long-term module degradation from contaminants present in the hot air (e.g., from off-gassing) and in coal-derived fuels, which should be used to define inlet gas purity specifications for the module and any necessary cleanup requirements.

Air Products has addressed potential contaminants and their effects on economics and reliability since the beginning of the program. Phase I included Task 1.2, "Lifetime Testing of the Optimized ITM Oxygen Materials," in which material reactivity with contaminants was established in long-term tests In Task 2.2, "Development and Demonstration of Contaminant Removal Method," potential contaminants were identified and mitigation approaches evaluated at the feasibility level. This work was extended in Phase II under Task 6.2, "Specification of

Allowable Process Gas Composition" in which critical levels of contaminants were established above which material degradation would proceed. The Phase II work was further extended in Phase III under Task 14.1.2, "Specification of Allowable Process Gas Composition," in which additional contaminants were identified and critical levels of exposure established, and under Task 16.4, "Contamination Mitigation Systems," in which the governing engineering design rules for mitigation systems were established. In addition, required gas clean-up steps were and are included in the process economics work under Tasks 2.6, 7.7, and 16.3. For example, under Task 2.6, a syngas clean-up step was considered to reduce sulfur to tolerable levels. This unit was costed and its effects are included in the widely cited Clearwater Coal Conference paper (V.E. Stein, E. Juwono, E.P. Demetri, "The Impact of ITM Oxygen on Economics for Coal-based IGCC," Proceedings of the 27th International Technical Conference on Coal Utilization & Fuel Systems; Clearwater, Florida, 4-7 Mar 2002.)

Subsequent analyses have included plans to avoid contaminants by indirect firing to heat the process air and to treat the process air for system-borne contaminants. Cases for indirectly heating the feed air were explicitly described in this Final Report under Tasks 7.7 and 15. Under Task 16, the Recipient developed a method and materials for removing contaminants from the hot feed gas. This system was used to treat the process air at the Intermediate Scale Test Unit (ISTU) under Task 19. The system fits inside the ITM vessel and represents <1% of the cost of the ITM vessel. The aforementioned Tasks constitute the plan requested in R1.

R2: Establish specific targets for the reliability of wafers and other components to meet a 10-year membrane lifetime.

The team should confirm that the quality assurance and quality control procedures that are currently in place are adequate to meet the required manufacturing yield in fabrication and reliability targets of membranes under IGCC operating conditions for economic viability in commercial operation.

Under Tasks 7 and 16, "Evaluation of System Reliability," Air Products and its subcontractors have established computational methods for estimating the reliability of ceramic membrane modules. The methods use as input a materials database established under Tasks 1, 6 and 14 "Measurement of ITM Oxygen Material Properties," as well as part failure statistics from testing of sample components under Tasks 7, 9, 16 and 18. Subcontractor Ceramatec has

implemented on-line and off-line quality assurance tests in the PDF that expose critical flaws introduced during the manufacturing process, including rapid thermal cycling of parts, advanced leak testing, acoustic emissions, scanning acoustic microscopy, and automated vision systems on ceramic membrane production equipment. These efforts are motivated to satisfy design criteria established for a membrane module operating life of 10 years and long-term manufacturing yield targets. Replacement of membrane modules after 10 years is included as an operating cost in economic analyses for IGCC plants.

R4: Conduct additional testing for creep and thermomechanical fatigue.

The project team should conduct additional testing to determine the extent of creep and thermomechanical issues, particularly considering that some creep and dimensional stability issues were seen on the module previously tested in the SEP. Since high temperature creep is one of the mechanisms that can lead to failure of these elements, it is essential to conduct tests on the improved architecture modules to ensure that they have creep rates acceptable for the 10-year projected lifetime. *(Addresses W4)*

Material creep of the ITM ceramic material has been well established under Tasks 6 and 14. The 10-year projected lifetime is based on the material creep of critical features in the ITM membrane wafers. In addition, accumulated creep damage (which may be considered part of the "thermomechanical fatigue" as described by the Committee) has also been measured and included in the ITM ceramic materials database. Clear guidelines and novel process control techniques for operation of ITM systems have resulted from these investigations so as to minimize creep damage. Additional work carried out under Task 28.1, "Advanced Materials and Characterization," has established creep characteristics of advanced architecture wafer structures.

In general, the term "fatigue" covers several phenomena, including cyclic fatigue, dynamic fatigue and static fatigue. Air Products notes that all of these mechanisms are related to subcritical crack growth, which has been a significant component of the work at Penn State University (PSU) under the program. The difference in these mechanisms pertains to how the stresses are applied in each case. Through testing, PSU was unable to find evidence of subcritical crack growth at elevated temperatures, although it can occur at lower temperatures in the presence of residual and applied stresses.

The work under Tasks 24 and 28 to evaluate compressive creep of advanced architecture submodules has led to a better understanding of creep deformation of those components. Accelerated compressive creep tests indicate significant deformation may occur during the expected lifetime of the modules. However, such compressive creep has not led to increased leakage or loss of reliability in the testing performed under this award, including during a 8000-hour flux test under full operating conditions. Additional work in this area is planned and is being carried out under another Cooperative Agreement.

TASK 23.0 PROCESS AND ECONOMIC EVALUATION

23.0 Scope

Air Products investigates process cycles that involve the integration of Reaction-Driven ITM technology with gasification technologies that process heavy feed stocks such as coal, biomass, petroleum coke, heavy hydrocarbon liquids, and other waste materials. These integrations also include the use of Pressure-Driven ITM technology in addition to the Reaction-Driven ITM technology. Reaction-Driven ITM performance is based on the performance of the ITM Syngas membranes developed under another DOE-funded program. Air Products uses capital and operating costs and the level of carbon dioxide emissions of the integrated facility versus those of the base case as the key evaluation criteria for any of the developed process cycles, and identifies promising integration schemes.

23.0 PROCESS AND ECONOMIC EVALUATION

Background

Ion Transport Membranes (ITMs) offer the potential to substantially reduce the capital cost associated with syngas production as well as oxygen production. The largest-scale syngas production facilities utilize an oxygen-blown syngas generation step, such as a gasifier or auto-thermal reformer (ATR). As has been shown elsewhere, the high-temperature ITM Oxygen process integrates better with such processes than a conventional cryogenic ASU. The ITM Oxygen process produces a pure oxygen product that can be fed to the syngas generator.

In contrast, an ITM-based syngas generator can both carry out air separation to produce oxygen *in situ*, while at the same time supporting the partial oxidation/reforming reactions that convert the hydrocarbon feedstock into syngas. The ITM solution is elegant and should result in a substantial reduction in capital costs. However, the technical risks are also significant. The composition of the product stream, the membrane temperature, the composition gradient through the membrane, and the very low partial pressure of oxygen at the membrane product side interface all result in a difficult material development problem. In addition to material challenges, the membrane must mechanically withstand significant pressure differentials and temperature transients. The net result is the need for a carefully-designed membrane contained within a high-pressure, high-temperature reactor.

Similar to the ITM Oxygen membranes discussed elsewhere in this report, ITM membranes for syngas generation are fabricated from non-porous, multi-component metallic oxides and operate at high temperatures (typically over 700°C) with exceptionally high oxygen flux and selectivity. Oxygen from low-pressure air permeates as oxygen ions through the ceramic membrane and is consumed through chemical reactions, thus creating a chemical driving force that pulls oxygen ions across the membrane at high rates. The oxygen reacts with a hydrocarbon fuel in a partial-oxidation process to produce a hydrogen and carbon monoxide mixture – synthesis gas. Such membranes are broadly known as "Reaction-Driven" membranes.

Although Reaction-Driven ITM increases the complexity of the ITM vessel and process requirements, it eliminates the need for an air separation plant. The economics for Reaction-Driven ITM are most attractive when a high-pressure, carbonaceous feed gas and a low-pressure air feed are used to produce a product at high pressure, matching downstream process pressures. This arrangement avoids the expenses associated with compressing the air or syngas.

In the ITM Reaction-Driven process, the permeated oxygen reacts with fuel and steam on the high-pressure product side of the membrane to form syngas. On the air side, the partial pressure of oxygen corresponds to the product of the oxygen concentration and air-side pressure, typically about one atmosphere. On the product side, even though the operating pressure is typically above 30 atmospheres, the oxygen partial pressure is very low, on the order of 10^{-16} atmospheres, due to the oxidative reforming reactions occurring at the membrane-syngas product interface. The reaction and transport mechanisms occurring on a ceramic membrane are shown in Figure 23-1.

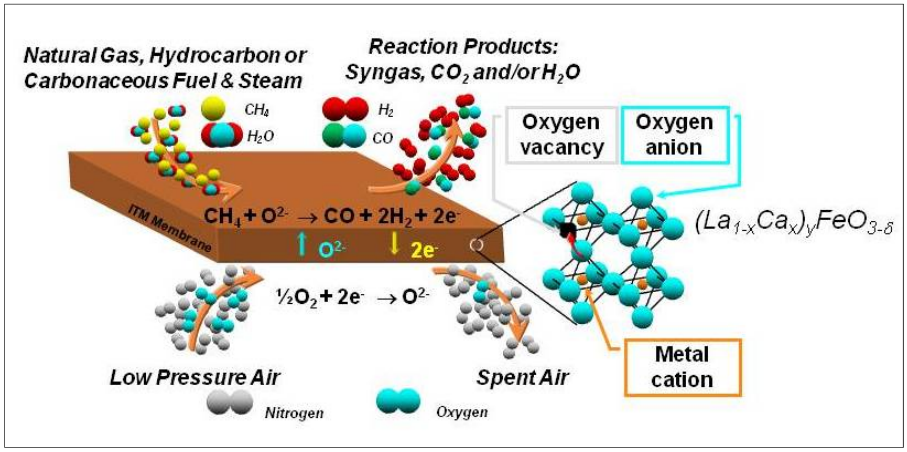

Figure 23-1. Oxygen separation with syngas production using ceramic membranes.

The ITM solution is elegant and should result in a substantial reduction in capital costs. However, the technical risks are also significant. The composition of the product stream, the membrane temperature, the composition gradient through the membrane, and the very low partial pressure of oxygen at the membrane-product interface all result in a difficult material development problem. In addition to material challenges, the membrane must mechanically withstand significant pressure differentials and temperature transients. The net result is the need for a carefully-designed membrane contained within a high-pressure, high-temperature reactor.

Previous to this cooperative agreement, Air Products and others designed and fabricated a planar, ceramic membrane structure to achieve high oxygen fluxes while withstanding the thermo-mechanical stresses encountered during operation. This membrane structure design, referred to as a "wafer," incorporates micro-channel features to reduce the thermo-mechanical stresses within the wafer assembly that are generated from pressure loads and the exothermic oxidation reactions. The micro-channels provide efficient air distribution within the wafer as high-pressure natural gas/syngas flows outside the wafer. The planar wafer design enables very efficient packing of membrane surfaces within the reactor volume.

A micrograph and schematic of the planar wafer design, showing a cross-sectional view of a section of a wafer, can be seen in Figure 23-2. The wafer consists of two thin membrane layers through which the oxygen ions diffuse. These thin upper and lower layers are supported by a slotted layer, which provides flow channels where feed air can be circulated internally within the wafer. Hot, low-pressure feed air flows through these passages, providing oxygen which passes from the feed air through the thin outer membrane layer. Hot, high-pressure hydrocarbon feed and steam flow over the outer surface of the wafer, where they react with the oxygen permeate. The wafer design also includes an outer porous layer that provides structural strength to the thin active membrane as well as diffusional resistance for feed gases reaching the active membrane surface. This resistance layer prevents runaway reactions from occurring on the syngas-side surface of the active ITM membrane. The planar wafer design makes for a very compact separation device while facilitating good gas-phase mass transfer. All of the layers contain the same ceramic material, and therefore expand and contract uniformly during temperature changes.

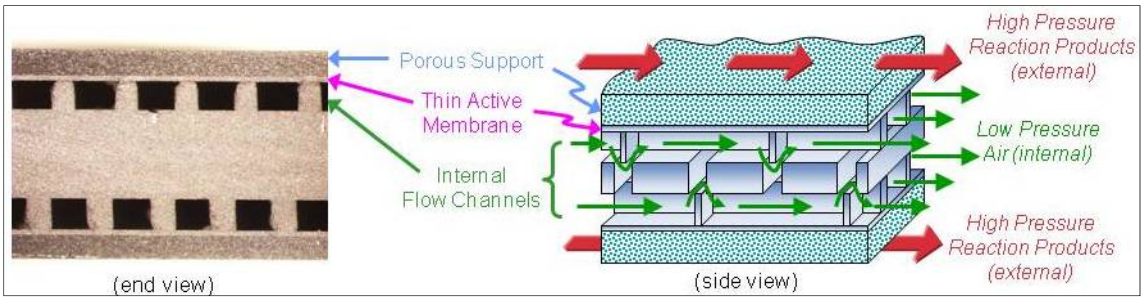

Figure 23-2. A cutaway view of a portion of a planar Reaction-Driven ITM membrane wafer. The end view (left) is an SEM micrograph of an actual wafer.

Previously, planar wafers have been scaled to their full commercial dimensions and produced in volume on a pilot production line using standard ceramic tape-casting technology. These production activities demonstrate the feasibility of achieving the low-cost production required to meet overall economic targets. Commercial-size, single-wafer modules have been constructed and successfully operated under commercially-relevant, high-temperature, high-pressure conditions in pilot-scale experiments.

Commercial-scale ITM modules may be fabricated by stacking wafers vertically. Figure 23-3 shows a photograph of a module built from four full-size, commercial-scale, ceramic wafers. Ceramic spacers are placed between the individual wafers to create channels for the flow of feed gas, steam and syngas.

Figure 23-3. Four-wafer membrane module.

An ITM-based reactor to produce syngas consists of a combination of Reaction-Driven ITM modules and a proportional amount of catalyst to balance the heat generated by the exothermic partial-oxidation reaction, with the cooling provided by the endothermic reforming reactions. Complete conversion of all feed gas requires multiple banks of Reaction-Driven ITM modules,

while secondary reforming and final syngas conversion requires only ~25% of the number of modules required for full conversion. Conceptual commercial ITM reactor systems comprise one to four vessels in series, with each vessel performing a fraction of the conversion. The final reactor section operates at the most aggressive conditions to promote complete feed gas conversion. Design concepts for commercial ITM reactors producing syngas are shown in Figure 23-4.

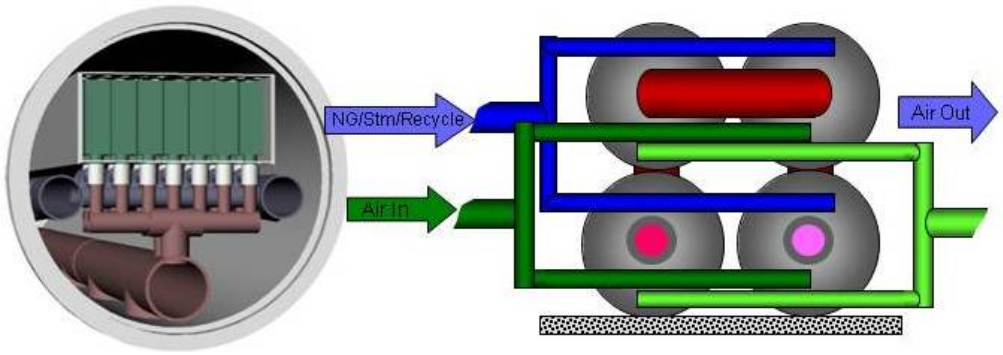

a b

Figure 23-4. Design concept for commercial ITM reactor systems. The internal arrangement is shown on the left (a) and a four-vessel arrangement is shown on the right (b).

The use of oxygen Ion Transport Membranes (ITMs) in the production of synthesis gas (syngas) has great potential to improve the efficiency and economics of such processes. Previous reports have demonstrated the benefits of using Reaction-Driven ITM to convert a natural gas feedstock to synthesis gas (Gray et al, 2009).

Under Task 23, Air Products evaluated opportunities to integrate Reaction-Driven ITM into the production of syngas or power derived from *solid* fuels. Rather than using pressure as the driving force to deliver the oxygen across the membrane to the fuel conversion process, using the thermodynamic driving force of (partial) combustion promises even greater thermodynamic efficiency, with potential benefits in overall energy efficiency and process economics.

Solid fuels such as coal, petcoke, and biomass will continue to represent an important fraction of overall US and global power production. The processes to derive power from these fuels include direct combustion and gasification to syngas followed by combined-cycle power generation. The latter offers greater promise for efficient CO_2 capture. Syngas generation by gasification is also the first step in producing liquid fuels from solid feedstocks by the Fischer-Tropsch process. An

alternative route to liquid fuels is through the pyrolysis of certain feedstocks, such as biomass or municipal solid waste, to a bio-oil, followed by hydrotreatment of the oil.

In Reaction-Driven ITM, the transport of oxygen across the membrane is driven by the difference in oxygen chemical potential between the air supply side and the process side of the membrane. The concentration (and chemical potential) on the process side is maintained at a very low level by nearly instantaneous combustion reactions, in which oxygen is consumed by reaction with gaseous fuels such as hydrogen or methane. Therefore, in order for Reaction-Driven ITM to be effective, the process environment must contain a sufficient concentration of such gaseous fuels to drive the oxygen level to near-extinction. The feedstocks under consideration are solids that must be at least partially volatilized or gasified for Reaction-Driven ITM to supply oxygen toward their further gasification or combustion. In addition, because the conditions at which the oxygen transfer occurs must be compatible with ITM materials, the process temperature and process-side composition must be taken into consideration. There is potential to extend the effective temperature range of ITM materials beyond what is possible with currently-developed ceramic compositions, but practical considerations limit how far the temperature window can be extended. Practical Reaction-Driven ITM configurations must work within this temperature window.

The potential for integrating Reaction-Driven ITM has been evaluated in four configurations:

- Direct integration of ITM into a primary gasifier.
- Secondary integration of ITM following a conventional oxygen-blown primary gasifier.
- Partial oxidation of pyrolysis product with ITM.
- Combustion of conventionally-produced syngas using ITM.

Direct Integration Of ITM Into A Primary Gasifier

In principle, replacing the oxygen delivery to a gasifier from an external source (air separation unit or pressure-driven ITM) to an internal, Reaction-Driven ITM source holds much appeal, with the potential for savings in both capital and operating costs. A conceptual flow diagram is shown in Figure 23-5.

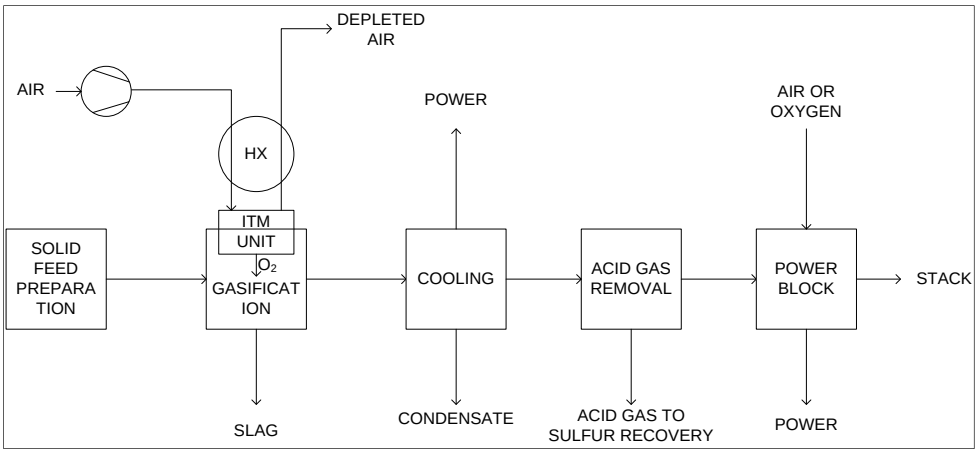

Figure 23-5. Conceptual flow diagram of an ITM unit directly integrated with a gasifier in an IGCC plant. Besides the membrane modules, the ITM-related equipment includes an air blower and a heat exchanger economizer to heat the incoming air against the hot depleted air.

Compared to a configuration using a cryogenic ASU, integrated ITM avoids the capital cost of the ASU, replacing it with the lower capital cost for the ITM system (modules, blower, and heat exchanger). It also greatly reduces the power consumption associated with oxygen delivery, since the blower power is much less than ASU air compression power.

Compared to a configuration that uses pressure-driven ITM for oxygen delivery, the Reaction-Driven ITM concept is expected to have improved efficiency. In pressure-driven ITM, the high-pressure, hot, depleted air stream represents a significant energy flow. Integration into IGCC (Stein et al, 2001)can recuperate most of this energy through the power production cycle. However, inherent efficiency can be greater if the high-pressure stream can be avoided at the outset.

While attractive on paper, full integration of a primary gasifier with Reaction-Driven ITM poses formidable challenges:

- The membrane units will be in direct proximity to the solids being gasified, as well as the slag being generated in the process. This will require membranes that are mechanically robust and resilient to plugging and coating by sticky, solid process materials. Current state-of-the-art ITM configurations cannot meet these criteria.
- The membrane will be exposed to all the contaminants and potential poisons in the solid feed, including alkali and transition metals, halides, and compounds of sulfur and

nitrogen. The ability of currently-developed ITM materials to perform in such highly-contaminated environments has not been demonstrated and is questionable.

- Gasification temperatures are typically upwards of 2000°F (1093°C) to attain the solids conversion and synthesis gas composition required for downstream operations. The combustion reactions, which would take place at the ITM membrane surface, are the source of the heat required to reach this temperature. Allowing for heat transfer, this means that the membrane units would operate at a temperature above the gasifier outlet temperature. This temperature exceeds the limits at which ITM materials have been demonstrated.
- Gasifiers require a flow of gas to interact and react with the solids. In traditional configurations, the oxygen feed represents an important part of this gas flow, especially in the entrance zone of the gasifier. In other words, oxygen plays a fluid dynamic role as well as the role of reactant. With ITM integration, the oxygen still plays the role of reactant, but does not participate in the fluid dynamic operation of the gasifier. Other configurations, possibly involving greater flows of steam or CO_2 recycling, would be required to fill this need.

Some of these challenges can be addressed by further developing ion transport membrane materials, or by developing new gasification process cycles and equipment. However, the close coupling of hot solids and liquids with ITM units in a high-temperature, high-pressure environment may be excessively demanding of ITM materials and membrane configurations in the foreseeable future. This concept is judged to be impractical in the short to medium term.

Partial Oxidation Of Pyrolysis Product with ITM

Pyrolysis is the conversion of solid organic materials such as biomass into char and a range of smaller molecules under the influence of high temperature. Rapidly heating the biomass (fast pyrolysis) yields 10-20% char, 10-15% pyrolysis gas, and 55-70% pyrolysis oil (Jones et al, 2009; Mohan et al, 2006). The pyrolysis oil results from cooling the initially-gaseous pyrolysis product, while pyrolysis gas is the fraction that is not condensed during cooling. Once cooled and condensed, the pyrolysis oil cannot be revolatilized without additional coke formation. In the production of liquid fuels, the oil can then be subjected to hydrocracking. Smaller molecules are formed in this step, and highly-oxygenated compounds such as carboxylic acids are converted in

hydrodeoxygenation and decarboxylation reactions. Without this step, the oil is unstable and unsuitable as a fuel in most applications.

Reaction-Driven ITM membranes require a gaseous fuel to consume the oxygen delivered through the membranes. Therefore, when coupling ITM and pyrolysis units, gases and condensable vapors would be processed directly; the pyrolysis product would not be cooled. Combustion of the char, which would be separated from gases and condensable vapors, may serve as the source of heat for the pyrolyzer. In the ITM unit, the pyrolysis product would be partially oxidized to produce a syngas for downstream use in power or chemicals production. A conceptual diagram is shown in Figure 23-6.

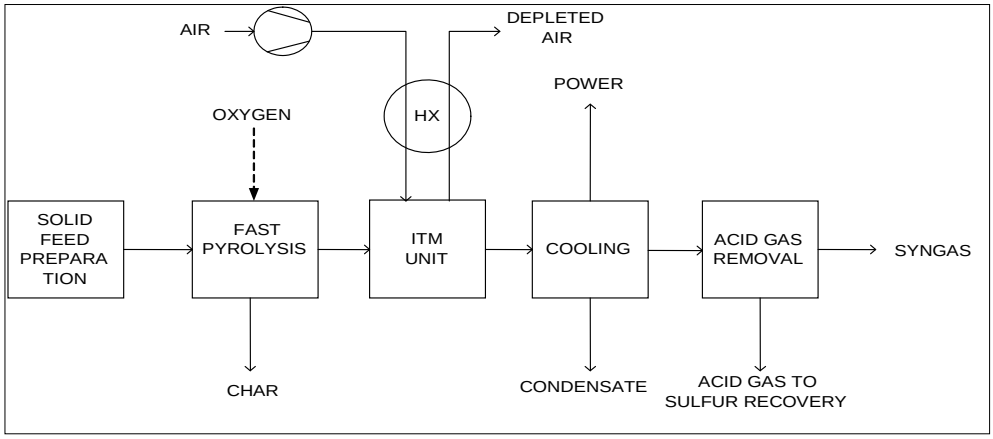

Figure 23-6. Conceptual flow diagram of an ITM unit immediately following a pyrolysis unit in a syngas production plant. The pyrolysis unit is shown with optional oxygen feed to allow for pyrolysis-gasification hybrid approaches.

The pyrolysis oil is a complex mixture comprising water and oxygenated organic compounds. Its lack of storage stability and incomplete volatility indicates a propensity for further condensation and polymerization reactions. Coke formation is a concern in further processing the vapor precursor of such an oil. The ITM unit would comprise 1) ion transport membranes, on the surface of which light fuels such as hydrogen and methane are combusted by the oxygen delivered through the membrane; and 2) reforming catalyst, which facilitates the breakdown of larger organic molecules by steam reforming. As in other reaction-driven ITM applications, the combustion processes provide the heat required by the reforming processes. Coke formation is a concern with both the membrane and the reforming catalyst. Experimental demonstrations would be required to assess the severity of coking and the effectiveness of strategies to minimize it.

Because it appears that no such experimental studies have been undertaken, a conceptual process can be proposed, but the information currently available does not support assessment of process economics.

Hybrid approaches have been proposed between pure pyrolysis and gasification, in which biomass is thermally converted in a process that includes some oxygen co-feed. The oxygen allows higher temperatures to be attained, which changes the product mixture. It is likely that fine-tuning such processes would result in intermediate pyrolysis products that can be more easily processed through ITM partial oxidation. Again, this will require additional development and demonstration.

Combustion of Syngas Using Reaction-Driven ITM

When used for power production, conventionally produced syngas (e.g., the product of an oxygen-blown gasifier) is fully combusted to provide power through steam and/or gas turbines. The oxygen required for combustion can conceptually be supplied by Reaction-Driven ITM (Figure 23-7). Depending on how acid gas removal and carbon capture are integrated into the cycle, this may yield efficiency benefits over configurations where oxygen is provided by an ASU, or where air is used in the combustion process. The primary challenge here is the high adiabatic temperature resulting from oxy-fuel combustion of the syngas, which is well above the maximum acceptable temperature for ITM membranes. The combustion process could be carried out non-adiabatically (e.g., in a steam boiler), but would yield lower power production than adiabatic combustion integrated with a gas turbine.

While this configuration represents a possible integration path for Reaction-Driven ITM into a gasification power production cycle, it is outside the scope of this report, which primarily addresses the use of Reaction-Driven ITM in the production of syngas.

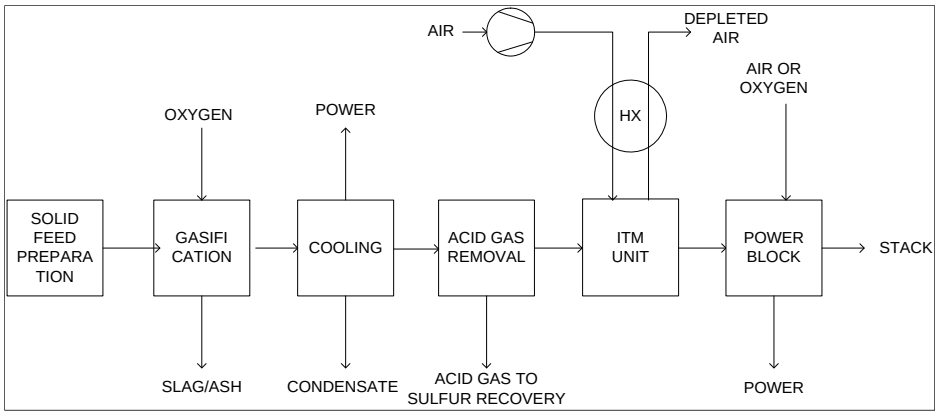

Figure 23-7. Conceptual flow diagram of an ITM unit immediately following a gasifier in an IGCC plant. Besides the membrane modules, the ITM-related equipment includes an air blower and a heat exchanger economizer to heat the incoming air against the hot depleted air.

Secondary Integration of ITM Following a Conventional Oxygen-Blown Primary Gasifier

Some of the challenges with direct integration of ITM with a primary gasifier can be avoided by maintaining an essentially conventional gasifier (with external oxygen feed) as the first stage of gasification, followed by an ITM partial-oxidation unit to complete the gasification. With this concept, the primary gasifier is chosen to operate at a lower temperature, just sufficient to fully convert the carbonaceous solids from the feed into a raw syngas. In the ITM partial-oxidation reactor, the temperature of the syngas is increased by combustion reactions using oxygen delivered through the membranes. This yields a synthesis gas suitable for downstream operations such as power generation or chemical production. The primary gasifier remains oxygen-blown and thus still requires an ASU or a pressure-driven ITM unit, but it reduces the size of the required equipment and the associated operating costs.

Compared to direct integration, this concept avoids contact between the ITM membrane units and the solid and molten phases present in the gasifier. The specific configuration selected may present other challenges, such as the presence of a wide range of contaminants and high-temperature membrane operation. This concept has been explored in more detail, as it is judged to be the most feasible of the options considered. The following sections address process configuration, equipment selection, and preliminary economic feasibility of the concept.

Choice of Gasifier

A variety of gasifier technologies have been developed since the first half of the 20th century to address the needs of different feedstocks and downstream uses. They are usually categorized into moving-bed, fluidized-bed, and entrained-bed technologies according to the gas-solid contacting pattern.

Entrained-bed designs, such as the GE, Conoco-Phillips, and Shell gasifiers, operate with the solid feedstock and the oxidizing gas in concurrent flow. This leads to a continuous rise in temperature from inlet to outlet of the gasifier. The outlet temperature is controlled to a high value to effect complete conversion of the coal, typically 2300-2700°F (1260-1982°C) upstream of the syngas quench. At these temperatures, the steam methane reforming equilibrium is driven to near completion, resulting in a syngas with very low methane concentration. To attain the high temperature, the gasifier is operated at a high oxygen-to-carbon ratio that requires high oxygen consumption. Similar considerations apply to fluidized-bed gasifiers.

In moving-bed gasifiers, the solids move downward, while the oxidizing gases move counter-currently upward. The maximum temperature occurs at an intermediate position, while both the solid ash and the syngas product exit at a lower temperature. Coal conversion can be achieved at a relatively low temperature due to the longer solid residence time compared to entrained-flow designs. The moving-bed gasification technology with by far the largest installed capacity base is the dry-ash Sasol-Lurgi gasifier. In this configuration, typical syngas exit temperatures are 700-1100°F (371-593°C). Because the exiting products are much cooler, less oxygen is required in the moving-bed gasifier, while methane levels in the syngas are significant.

The syngas from a Sasol-Lurgi gasifier can be further oxidized downstream to attain a higher temperature and a correspondingly lower methane content. This would render the syngas more suitable for IGCC with carbon capture. The deeper oxidation can, in principle, be carried out using Reaction-Driven ITM technology. The raw syngas contains sufficient hydrogen to drive the required oxygen delivery. Since the primary membrane surface reaction will be oxidation of hydrogen to steam, a downstream, adiabatic reforming unit is required to re-equilibrate the steam methane reforming reaction. Depending on the amount of oxygen required, it may be favorable to use a staged approach in which the reforming equilibrium is periodically re-established

between stages of ITM oxygen delivery. This approach will serve to keep the temperature of the syngas and the ITM membranes within the limits established by materials constraints.

Because the oxygen-to-carbon ratio of moving-bed gasifiers is much lower than for entrained-bed and fluidized-bed gasifiers, the potential for ASU oxygen savings is greater with the moving-bed designs. Therefore, a configuration integrating reaction-driven ITM with the Sasol-Lurgi gasifier was selected as the basis for the process evaluation.

Quench and cleanup configuration

The gaseous effluent from the gasifier contains gasification products generated by the combustion and gasification of char in the bottom of the reactor, as well as devolatilization products generated during heating and pyrolysis in the upper zones of the moving bed. Some of the volatile organics formed during the latter process are simple hydrocarbons which may be converted in an ITM partial-oxidation reactor. The remainder are compounds of higher molecular weight, collectively described as coal tars. The amount of tar formed in a moving-bed gasifier depends on the type of coal used and the gasifier operating conditions. The tar is removed during the downstream quench of the gasifier and may be used as a fuel or a chemical feedstock.

Further gasifying the tar volatiles in an ITM reactor is attractive from an energy standpoint. It allows a greater fraction of the caloric content of the coal to be used for downstream syngas consumption processes (such as power production), and avoids the energy penalty of a raw syngas quench followed by preheating for ITM. However, converting the tars, which contain many likely coke precursors, represents a significant challenge for developing both ITM membranes and reforming catalyst materials. Moreover, the gasifier effluent contains various inorganic contaminants (metals, nitrogen and sulfur species, etc.), the concentrations of which depend primarily on the composition of the coal. These contaminants are conventionally removed at low to moderate temperature, which requires some quench in any case. It is likely that, in the absence of a cleanup stage, at least some of the contaminant compounds would negatively affect the ITM unit performance.

For these reasons, consideration was given to the process configuration in which a Sasol-Lurgi gasifier is followed by quench, tar removal, and gas cleanup operation before reheating and

processing through a Reaction-Driven ITM system. An option that may be considered for further integration is to use part of the generated hydrogen for hydrotreating the tar stream, further processing this stream through a prereformer, and combining the resulting stream with the light gases from the gasifier to produce a combined feed to the Reaction-Driven ITM unit.

Sulfur removal may be carried out with the Selexol or Rectisol process. Both are low-temperature, physical absorption processes which result in a syngas stream with low water content. This necessitates the re-introduction of steam to drive the reforming and shift reactions toward the desired high conversions in the ITM and water-gas shift units. For the purpose of the study presented here, the inlet stream is a dry syngas at 100°F (38°C), the result of a low-temperature cleanup followed by internal heat recovery within the Selexol/Rectisol unit.

Evaluation of Process Case

As stated previously, the operating conditions and effluent composition from the gasifier depend strongly on the type of coal. For the purposes of this study, the outlet conditions modeled by Yoon et al. (1979) were used for an oxygen-blown gasifier operated with a high-activity Wyoming coal, at a pressure of 25 atm and a steam co-feed just sufficient to avoid slagging. At this mode of operation, the O_2/C ratio is 0.27, the H_2O/C ratio 1.84. The effluent gas is characterized in Table 23-1. It should be noted that some Sasol-Lurgi gasifiers are operated with higher methane concentration in the effluent gas. For these cases, other ITM control strategies would be required, but the incentive for converting the methane in a CO_2 capture case would be greater in this situation.

Table 23-1. Gasifier effluent characteristics from O_2-blown gasification of Wyoming coal (Yoon et al,1979).

Temperature °F (°C)	**CO_2 dry/wet%**	**CO dry/wet%**	**H_2 dry/wet%**	**CH_4 dry/wet%**	**Other dry/wet%**
760 (404)	26.7 / 13.0	21.7 / 10.5	41.6 / 20.2	8.8 / 4.3	1.2 / 0.6

The ITM unit is placed between the low-temperature cleanup stage, where H_2S and other contaminants are removed, and the water-gas shift converters (at least two stages, to convert the majority of the CO in the syngas to CO_2 and H_2) and operated at an inlet temperature ~450°F (232°C). Since the ITM unit itself operates at temperatures of 1500-1900°F (815-1038°C), the syngas stream must be heated to the upstream operating temperature of the ITM unit and cooled

downstream. This is accomplished using a combination of high-temperature heat recovery directly downstream of the ITM unit (to generate high-pressure steam) followed by a feed-effluent heat exchanger (recuperator). Steam must also be added to the syngas feed to reach the steam-carbon ratio required for ITM and water-gas shift operation.

Following the water-gas shift converters, the CO_2 in the product syngas is removed in an acid gas removal unit. This may be a Selexol or Rectisol unit integrated with the sulfur cleanup unit upstream of the ITM unit, or it may be an amine extraction system. The resulting hydrogen-rich product stream is used to generate power in the downstream combined-cycle power island.

A small part of the hydrogen-rich product may be diverted to the section of the ITM unit where heat from the non-permeated air is recovered into the fresh air feed to the ITM modules. The hydrogen-rich product may be combusted in the non-permeated air stream in cases where a high degree of air preheat is required. In the scenario developed for this case study, the heat management around the ITM unit does not require the combustion step.

Process conditions in the case study are based on materials constraints and catalyst operating windows. For the ITM unit, a maximum temperature of the syngas product of 1840°F (1000°C) was maintained, based on an assessment of current and projected ceramic membrane module constraints. An Aspen flowsheet was developed to model the case.

The comparison case employs oxygen from an air separation unit as the oxygen feed to an ATR. The syngas temperature at the ATR outlet was maintained at the same value as for the ITM case. Since only the source of oxygen is changing, most other conditions are unaffected.

Carbon emissions and power production from downstream operations are nearly identical for the two cases. This confines the economic comparison to the capital and operating costs associated with operation of the Reaction-Driven ITM unit vs. the air separation unit. Previously conducted, proprietary economic studies performed by Air Products and its development partners have shown significant operating and capital cost savings for the ITM case.

Task 23.1 Feedstock and Gasification Information

Information on feedstocks of interest is included in the material presented in Task 23.0 above.

Task 23.2 Integration with Gasifier and Pyrolysis Reaction Systems

Several process cycles that integrate reaction-driven ITMs with gasifier and pyrolysis reaction systems are presented in Task 23.0 above. The integration scheme where Reaction-Driven ITM is used to further process raw syngas from a primary fixed-bed gasifier was selected for further analysis, including preliminary technical and economic feasibility assessments.

Task 23.3 Nitrogen Generation

The Ion Transport Membrane (ITM) process can produce oxygen for a variety of applications. In addition to oxygen, most of these applications also require a low-oxygen purge gas for oxygen exclusion or coal drying/transporting as in IGCC or OxyCoal combustion applications. A typical application that requires 3000 MTPD of oxygen can require up to 10,000 Nm^3/HR of purge gas containing <1% oxygen at or above 7 barg. Historically, such purge gas would be produced by cryogenically separating nitrogen from air.

However, the non-permeate stream generated by the ITM process typically contains <5% oxygen. The following processes were investigated to remove excess oxygen from the ITM non-permeate stream: a second ITM stage, a reactive ITM membrane, an ambient temperature nitrogen membrane, ambient temperature pressure swing adsorption (PSA) and re-compression of the ITM combustor stream. Table 23-2 summarizes the incremental power and capital costs over the base ITM process associated with each option.

Table 23-2. Summary of incremental power and capital costs over the base ITM process for various N_2 generation options.

N2 GENERATION OPTION	INCREMENTAL POWER KW	INCREMENTAL OPERATING COSTS $MM/YR	INCREMENTAL NON-ITM CAPITAL $MM	INCREMENTAL ITM CAPITAL $MM	INCREMENTAL TOTAL CAPITAL $MM
Cryogenic ASU	2200	1	3	0	3
2 STAGE ITM	1900	0.8	0	4	4
REACTIVE ITM	1950	0.8	0	6	6
N2 PSA	3600	1.6	2	0	2
N2 MEMBRANE	2900	1.3	1	0	1
NON-PERM RE-COMPRESSION	900	0.4	1	0	1

Both the Oxygen ITM and Reactive ITM options require bypassing gas around the ITM expander and result in less power production from the ITM process. They offer limited power savings relative to cryogenic air separation, but require greater capital. Re-compression of the oxygen-depleted non-permeate stream exiting the ITM combustor provides both the lowest operating and capital costs of all options considered. This option also offers the opportunity to recover a much larger flow of purge gas with no impact on the base ITM process. However, this option can produce a pure stream that contains 0.5% oxygen at best. If significantly higher-purity nitrogen is required (<10 ppm O_2), then either the cryogenic ASU or the nitrogen PSA should be considered, depending upon the required plant capacity.

ITM Process Description. The ITM process separates compressed air into a low-pressure oxygen stream and a high-pressure, non-permeate stream by diffusing oxygen across high-temperature ceramic membranes. Figure 23-8 presents a typical schematic of the ITM process.

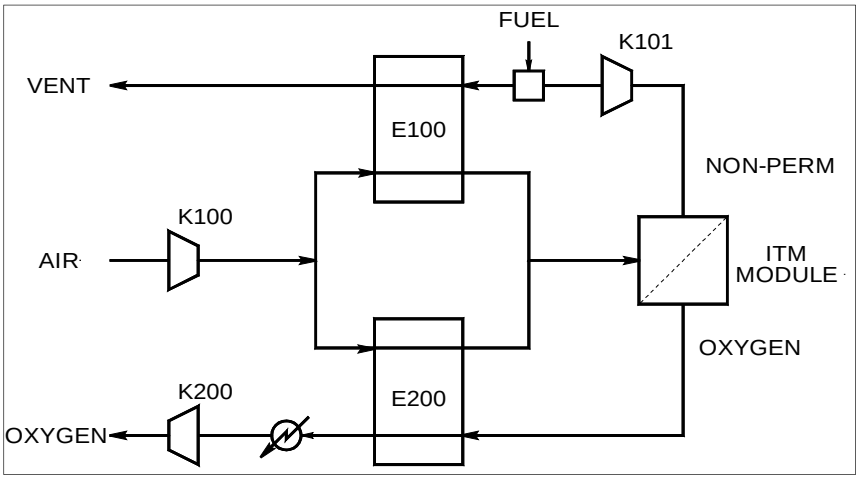

Figure 23-8. Typical ITM flow schematic.

Processing begins by compressing atmospheric air to 15 bara in the K100 main air compressor. The compressed air from the K100 is then heated to elevated temperature in the E100 and E200 exchangers. The hot air is then fed to the ITM module, which consists of banks of ceramic membranes arranged in series. The hot ceramic membranes allow oxygen to permeate while effectively blocking nitrogen or argon. To facilitate the transport across the membrane material, a vacuum is pulled on the oxygen (permeate) side of the membrane. Typically, operating pressure on the permeate side of the membrane is 0.3 bara. The low-pressure oxygen then is

cooled against incoming air in the E200 oxygen exchanger before being compressed to final use pressure in the K200 oxygen compressor.

This hot, non-permeate stream exiting the ITM module is still at high pressure and is expanded across the K101 expander to recover power. Fuel gas (hydrogen, syngas or methane) is mixed with the K101 exhaust stream and combusted to raise the non-permeate gas stream temperature high enough to heat incoming air to 800-900°C in the E100 non-permeate exchanger. It is this non-permeate stream, already depleted in oxygen, which is of interest as a feed stock to produce the purge gas for the IGCC, OxyCoal combustion and other processes.

The ITM process typically recovers 75% of the oxygen present in the air, resulting in a non-permeate stream oxygen content of 5%. This residual oxygen in the non-permeate stream is used to combust the fuel gas. Operation at higher oxygen recoveries is possible, but typically results in a less-efficient process because it requires either higher air feed pressure or lower oxygen permeate pressure.

Cryogenic ASU Process Description. Historically, nitrogen purge gas has been produced by cryogenically separating nitrogen from air in an air separation unit (ASU). To produce 10,000 Nm^3/HR of nitrogen purge gas at 7 barg, the cryogenic process would require 2200 KW of compression power. The capital cost of the equipment, including engineering but not installation, is approximately $3MM. Slightly more efficient cryogenic cycles are available at increased capital cost. The cryogenic process is not limited in the purity of the nitrogen it can produce, and can generate nitrogen purge gas with <10 ppm oxygen with negligible impact on either power or capital investment. The cryogenic cycle has been demonstrated at plant sizes up to 1,000,000 Nm^3/hr.

2-Stage Oxygen ITM Process Description. As noted earlier, the non-permeate stream exiting the ITM module typically contains 5% oxygen or less. It is possible to further process a portion of this stream in a second, smaller ITM module to produce a nitrogen purge gas with <1% oxygen. Figure 23-9 provides a simplified schematic of this process.

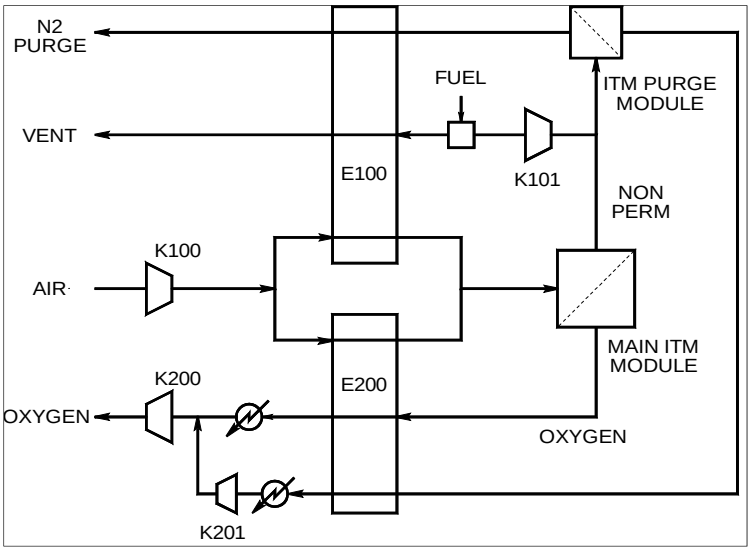

Figure 23-9. Producing N_2 purge gas with an ITM module.

Processing is the same as shown on a standard ITM flow sheet, except that a small portion of the non-permeate stream exiting the main ITM module is fed to a second, smaller ITM module which operates at a lower (<0.1 bara) oxygen permeation pressure. This allows extraction of oxygen to lower levels than the rest of the non-permeate stream. The non-permeate stream exiting the second ITM module would bypass the K101 and remain at full processing pressure while being cooled to ambient temperature for use as nitrogen purge gas.

Because the non-permeate from the second module is not expanded in the K101 expander, the expander generates 1800 KW less power than the base ITM cycle. In addition, a small amount of oxygen is recovered in the second ITM module at less than 0.1 bara instead of 0.3 bara, increasing oxygen compression power by 100 kW. The ITM process does appear to be more efficient than the cryogenic process (1900 vs. 2200 kW) in generating nitrogen purge gas. However, it comes with a capital penalty.

Although the E100 and E200 exchangers are depicted as single units in the simplified schematic, each is made up a several parallel exchangers. Therefore, keeping the N_2 purge stream and low-pressure oxygen streams separated during cooling does not significantly affect exchanger capital because one of the parallel units can be designated for these streams. However, the addition of a second ITM unit (with associated piping) would increase equipment costs by almost $3MM, and

adding a K201 low-pressure oxygen compressor would add another $1MM to the estimated costs.

It is possible to offset the power lost in the K101 expander by increasing the air flow through the ITM process. However, this would result in 6% higher fuel consumption and 4% larger heat exchanger surface area in addition to the added capital for the second ITM vessel and K201 low-pressure oxygen compressor. Taking this approach would increase estimated capital costs by another $2-3MM in addition to the $4MM for the second-stage ITM membrane.

Utilizing a second Oxygen ITM membrane limits nitrogen purity. The partial pressure of oxygen in the non-permeate stream must be greater than in the permeate stream to force oxygen across the membrane. ITM produces a nearly pure oxygen permeate. The practical lower limit of oxygen pressure on the permeate side is 0.1 bara. Assuming a normal operating pressure of 15 to 20 bara on air feed to the ITM membranes, the equilibrium oxygen content of the non-permeate is 0.6% to 0.5% oxygen (0.1/15 bara and 0.1/20 bara). Because the non-permeate oxygen partial pressure must be higher than these levels to drive oxygen across the membrane, 1.0% oxygen is the practical lower limit for nitrogen purge gas produced by an Oxygen ITM membrane.

Overall, the power savings associated with a second Oxygen ITM membrane relative to cryogenic air separation are insufficient to offset the increased capital cost of the process. In addition, the purity of nitrogen gas that can be produced by the ITM membrane is more restricted than that available from the cryogenic air separation process.

Reactive ITM Process Description. The lower limit for the oxygen content of the non-permeate stream produced in an ITM Oxygen membrane is set by the oxygen partial pressure on the permeate side. Rather than relying on a compressor to reduce the oxygen pressure on the permeate side, the Reactive ITM process consumes the permeate oxygen in a chemical reaction. This reduces the effective partial pressure of oxygen to 0.0 bara on the permeate side of the membrane. Figure 23-10 provides a simplified schematic of how a Reactive ITM membrane can be used to produce nitrogen purge gas from an ITM Oxygen process.

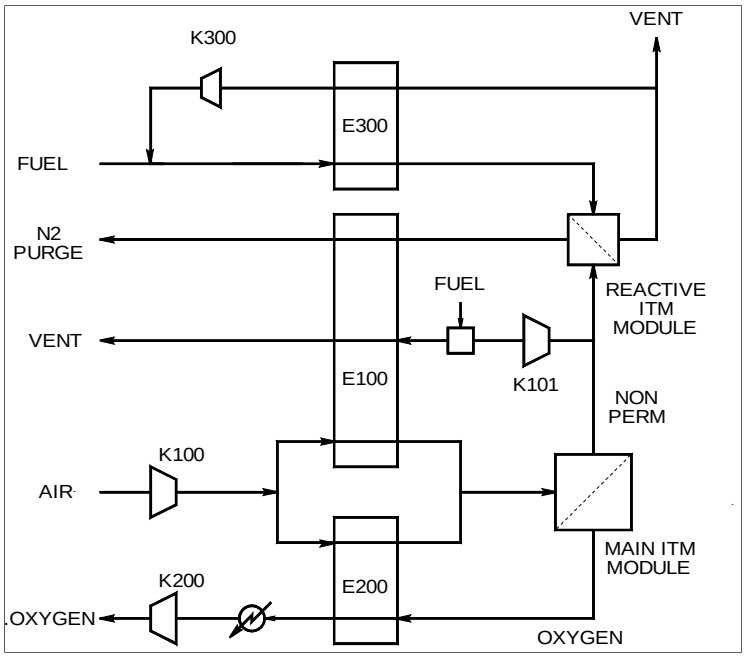

Figure 23-10. Reactive ITM production of nitrogen purge gas.

Processing is the same as shown on a standard ITM flow sheet, except that a small portion of the non-permeate stream exiting the main ITM module is fed to a second, Reactive ITM module. The non-permeate gas exiting the Reactive ITM module would bypass the K101 and remain at full processing pressure while being cooled to ambient temperature for use as nitrogen purge gas. The power penalty associated with bypassing this flow around the K101 expander is 1800 kW.

In the Reactive ITM module, fuel gas is used to consume the oxygen as it permeates across the membrane, effectively reducing the oxygen partial pressure on the permeate side of the membrane to 0.0 bara. While this option eliminates the need for the K201 low-pressure oxygen compressor, it does require additional heat exchangers to remove the heat of combustion from the Reactive ITM membrane.

Because the reaction of the permeated oxygen with fuel in the Reactive ITM membrane releases heat, the membrane temperature could elevate above its upper service limit and destroy the membrane. The fuel must therefore be diluted to moderate the temperature in the membrane. This is accomplished by compressing the cooled combustion gases from the membrane in the K300 recycle compressor to overcome the pressure drop in the system. The compressed gas is then mixed with fuel and heated to 750°C in the E300 recycle exchanger and fed to the permeate

side of the membrane. Oxygen reacts with the fuel as it permeates across the membrane, raising the membrane temperature to 950°C. Some of the combustion gas exiting the membrane is cooled to ambient temperatures in the E300 recycle exchanger, compressed and used to dilute the incoming fuel. The balance is vented directly to the atmosphere. The amount of combustion gas that must be recycled to dilute the fuel and the power required for the K300 recycle compressor depend upon the fuel available. For hydrogen fuel typically available in an IGCC facility, the Reactive ITM membrane would require 11 MMBTU/HR of hydrogen and 150 KW to operate the K300 recycle compressor.

The capital cost of the base ITM equipment is unaffected by the addition of the reactive membrane for nitrogen purge production. However, the capital costs for the Reactive ITM membrane, K300 recycle compressor and E300 recycle exchanger represent a significant increase in equipment capital over the basic Oxygen ITM process.

As with the 2-Stage Oxygen ITM membrane option, the Reactive ITM module does not offer sufficient power savings to justify the added capital expense. It also requires additional operating expenses in the form of added fuel consumption. For these reasons, the reactive ITM membrane was judged not to be a reasonable alternative to cryogenic air separation for this case.

Ambient PSA Process Description. It is possible to separate nitrogen from air in a pressure swing adsorption (PSA) unit. The unit consists of parallel beds of adsorbent sieve that remove oxygen from air at high pressure. Oxygen is adsorbed in one bed at high pressure. After the adsorbent bed is saturated, the bed is depressurized and oxygen is desorbed from the sieve. While one bed is at high pressure adsorbing oxygen, the other is at low pressure desorbing oxygen. When separating nitrogen from air, these units typically produce up to 50% of the feed air as nitrogen. These same units can process the 5% oxygen-content, ITM non-permeate stream to produce nitrogen purge gas as presented in the simplified schematic in Figure 23-11.

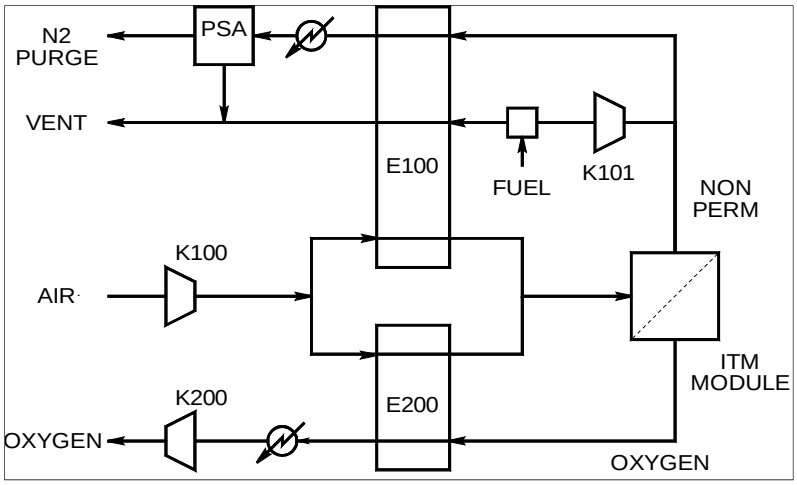

Figure 23-11. PSA processing of an ITM non-permeate stream.

For this option, a small portion of the non-permeate gas exiting the ITM module bypasses the K101 expander and is reheated to ambient temperatures in the E100 exchanger. This high-pressure stream is then processed in a conventional nitrogen PSA unit. At 50% recovery, the PSA unit requires more non-permeate gas to bypass the K101 expander than the 2-Stage Oxygen ITM option, resulting in a power loss of 3600 KW. The PSA can produce nitrogen purge gas at 10 ppm oxygen at the expense of nitrogen recovery. At 10 ppm, nitrogen recovery drops to 40%, and power would increase to 4800 KW due to the additional non-permeate flow bypassing the K101 expander.

As previously discussed, because the E100 consists of several parallel exchangers, reheating a small, high-pressure, non-permeate stream would have little impact on the capital cost of the E100 exchangers. No additional compression equipment is needed beyond the base ITM process cycle. To produce 10,000 Nm^3/hr, four parallel PSA units would be required at an estimated capital cost of $2MM.

Although the PSA unit is capable of producing high-purity purge gas similar to the cryogenic ASU, the $1MM capital reduction of the PSA option relative to the cryogenic ASU does not offset the additional 1400 KW of power needed to operate the cycle. In addition, the PSA option does not scale to higher production rates as effectively as the cryogenic option.

Ambient Nitrogen Membrane Process Description. Nitrogen is also produced from air by utilizing ambient-temperature membranes that permeate oxygen at a higher rate than nitrogen.

When separating air with 21% oxygen, these units can recover nitrogen as low as 30% at nitrogen purities below 1% oxygen. However, since the ITM non-permeate stream contains <5% oxygen, processing this stream after it has been cooled to ambient temperature results in a nitrogen recovery of 60%. The flow schematic shown in Figure 23-12 is identical to the PSA option with a nitrogen membrane substituted for the PSA unit.

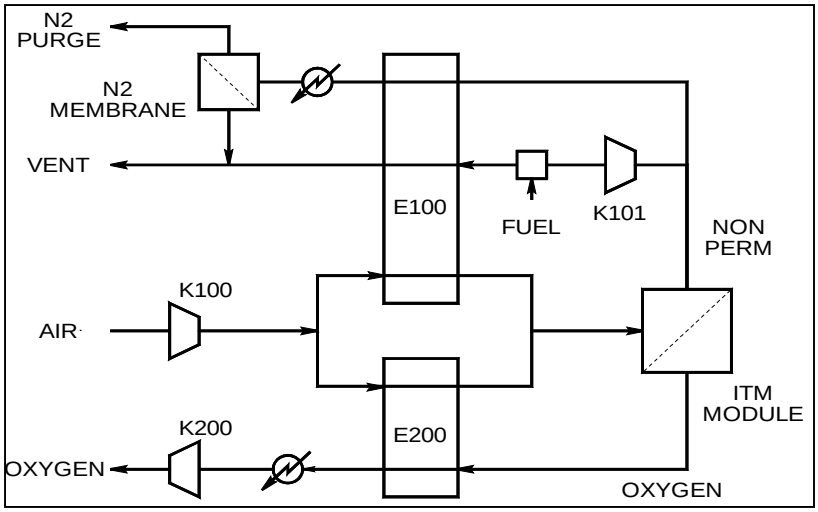

Figure 23-12 Nitrogen membrane processing of an ITM non-permeate stream.

For this option, a small portion of the non-permeate gas exiting the ITM module bypasses the K101 expander and is reheated to ambient temperatures in the E100 exchanger. This high-pressure stream is then processed in a conventional nitrogen membrane. Because the membrane unit recovers only 60% of the non-permeate gas as nitrogen, more non-permeate gas must bypass the K101 than in the 2-Stage Oxygen ITM option, resulting in a power loss of 2900 KW in the K101 Expander.

The recovery of the nitrogen membrane is strong function of the purity of the nitrogen produced. Producing nitrogen gas at 0.5% rather than 1.0% oxygen reduces nitrogen recovery from 60% to 40%. For this reason, nitrogen membranes do not appear to be a practical option for nitrogen purge gas oxygen levels below 1%.

As previously discussed, because the E100 consists of several parallel exchangers, reheating a small, high-pressure, non-permeate stream would have little impact on the capital cost of the E100 exchangers. No additional compression equipment is needed beyond the base ITM cycle.

The estimated capital cost of the nitrogen membranes needed to produce 10,000 Nm^3/hr is $1MM. If nitrogen purge gas with 1% oxygen is acceptable, nitrogen membranes should be considered due to their lower capital cost and slightly higher power consumption relative to cryogenic ASUs.

ITM Non-Permeate Recompression Description: While the high-pressure, non-permeate gas exiting the ITM module contains 5% oxygen, the low-pressure, non-permeate gas exiting the fuel combustor can be controlled to contain <1% oxygen. After cooling to ambient temperature, this low-pressure stream can then be compressed to provide purge gas as shown in Figure 23-13.

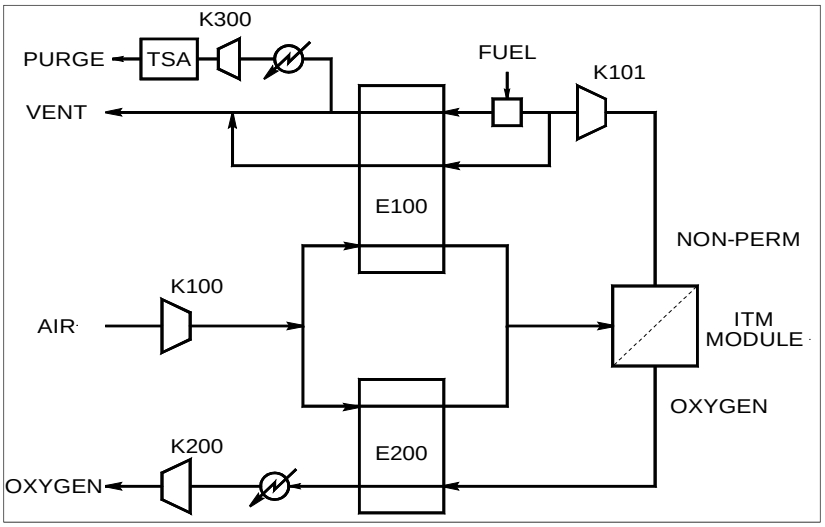

Figure 23-13. Low-pressure, non-permeate recompression.

To produce a stream with <1% oxygen, the exhaust from the K101 expander is split into two streams. One stream is fed to the fuel combustor, which consumes oxygen through the fuel gas combustion and produces a stream containing <1% oxygen. This stream is then reheated separately from the remaining 5% oxygen stream in the E100 exchanger. The cooled stream is then compressed to final use pressure. If water can be tolerated in the purge gas, then no additional processing is necessary. However, if a dry gas is required, the purge gas can be dried in a thermal swing adsorber (TSA) after compression. In either case, re-compression of the cooled non-permeate stream will require approximately 900 KW. Since all of the non-permeate stream exiting the ITM module is expanded in the K101 expander, power production from the ITM process is unaffected.

As stated before, because the E100 consists of several parallel exchangers, segregating the 5% and 1% oxygen non-permeate streams in the E100 exchangers does not affect ITM capital costs. The cost of the purge gas compressor is estimated to be $0.5MM, while the TSA dryer skid (if required) is estimated to cost $0.5MM. The non-permeate recompression option can produce a large amount of purge gas with no impact on the ITM process and offers both lower capital and operating costs than the cryogenic ASU option. However, this option should be considered only for nitrogen purge gas requirements of $\geq$0.5% oxygen to avoid contaminating the purge gas with fuel gas.

Task 23.4 Equipment Development

Equipment considerations for the secondary gasification integration scheme are discussed in Task section 23.0 above. They include the choice of gasifier and gas cleanup systems both upstream and downstream of the ITM unit.

Task 23.5 Reaction-Driven ITM Performance and Task 23.6 Operating Performance Data

The objectives of Tasks 23.5 and 23.6 were addressed simultaneously in experiments conducted in the Process Demonstration Unit (PDU). Therefore, the results for these tasks are presented in this combined section.

Research conducted at small and intermediate scales in Air Products' laboratories has established that in Reaction-Driven ITM, membrane performance (i.e., oxygen flux) depends primarily on the hydrogen concentration on the permeate side of the membrane and the membrane temperature. Other composition variables, such as the concentrations of other combustible gases on the permeate side, do not significantly affect the instantaneous high-temperature performance of the membrane, although they may affect its long-term stability and performance.
The hydrogen concentration encountered in the secondary gasification approach described in Task 23.0 (Table 23-1, 20.2 mol% on a wet basis) is within the range commonly studied with the research equipment used in this study, including Run 22 described below. This testing has demonstrated that these conditions give rise to desirable oxygen flux values.

The temperature level selected for Aspen evaluation of the secondary gasification approach was 1000°C, the temperature of the syngas leaving the ITM unit. The membrane, which is cooled by the syngas stream, will necessarily operate at a higher temperature. Heat transfer calculations

performed for operation at commercial-scale flow conditions indicate that the membrane temperature is ~20°C above the syngas temperature, so the maximum membrane temperature is 1020°C for this evaluation.

Creep strength of the inner layers has been identified as a potential weakness of the standard I4 material when operated under the expected higher operating temperatures required for reaction-driven applications. Two modules composed entirely of standard I4 material were tested in PDU Run 19. Syngas temperatures were varied throughout the run, reaching a maximum level of 885°C at high-fluxing conditions, corresponding to a trailing-edge membrane temperature of >1000°C. In post-run module testing, it was found that the inner layers became pinched at the edges of the dense ribs of the slotted layer due to preferential creep at these high-stress interfaces. Some loss of flux was observed for these modules over the course of the 92-day run, which was partially attributed to reduced accessibility of the membrane layer above the dense ribs due to the pinched inner layers.

Subsequent material testing efforts identified a potential low-creep material formulation as an alternative for selected layers within the wafer. A PDU module incorporating a wafer fabricated with this low-creep layer was built and subsequently installed in the PDU for testing during Run 22.

To demonstrate the high-temperature operability of the new membrane module configurations, PDU Run 22 was conducted between September 2010 and January 2011, completing a total of 112 days at fluxing conditions. Hydrogen concentrations were chosen both above and below the range relevant to the secondary gasification integration, with the majority of the conditions within a few mol% of the conditions of interest. During the run, thermal conditions were established that simulate expected reaction-driven operating membrane temperatures of ~1020°C. Syngas temperatures reached as high as 915°C, and, due to the lower flow rates in the PDU compared to commercial scale, the temperature difference between membrane trailing edge and syngas is much larger (according to heat transfer models at high flux, the difference exceeds 100°C). This means that the membrane temperature exceeded 1020°C during these experiments. Although direct measurement of membrane temperature is not possible with current experimental capabilities, post-test analysis of composition changes and creep deformation confirm that membrane temperatures had exceeded 1020°C during testing.

Post-run analysis of Module 3, which incorporated the low-creep material layer, indicated creep deformation of the layers over the inner slots but no densification of the low-creep material layer at the slot corners. This is a significant demonstration of the potential performance advantages of low-creep materials selectively applied within the wafer design.

Because in these tests membranes were exposed to the highest temperatures for several days, it was therefore concluded that current membrane module configurations are sufficiently robust to withstand short durations at the proposed process temperature. Longer-term stability must be demonstrated in further experiments. Membrane materials have been developed that feature higher creep strength and improved ability to withstand prolonged exposure to temperatures in the upper end of the operating range. These capabilities have been demonstrated as part of this program, as discussed in Task 24.1.

References

Gray D. et al.: Current and future technologies for gasification-based power generation, volume 2: a pathway study focused on carbon capture advanced power systems R&D using bituminous coal. DOE/NETL-2009/1389, November 2010.

Jones S.B. et al.: Production of gasoline and diesel from biomass via fast pyrolysis, hydrotreating and hydrocracking: a design case. Pacific Northwest National Laboratory report PNNL-18284, February 2009.

Mohan D., Pittman C.U., Steele P.H.: Pyrolysis of wood/biomass for bio-oil: a critical review. *Energy & Fuels* 2006, 20, 848-889.

Stein V.E., Juwono E., Demetri E.P.: Improving IGCC Economics through ITM Oxygen Integration, 18th Intl. Pittsburgh Coal Conf., 2001.

Yoon H., Wei J., Denn M.M.: Analysis of Lurgi gasification of two U.S. coals. Chem. Eng. Sci. 1979, 34, 231-237.

TASK 24.0 TABLE OF CONTENTS

TASK 24.0 REACTION-DRIVEN ITM MATERIALS 2

24.0 SCOPE 2

24.0 REACTION-DRIVEN ITM MATERIALS 2

Background 2

24.1 MATERIALS DEVELOPMENT 3

Materials Formulations with I4 3

Advanced Materials Assessment for Reactive-Driven Membranes 5

24.2 MECHANICAL PROPERTIES 7

Long-Term Creep Rupture Testing of Dense I4 in Air 7

Tensile Creep of I4 Solvent-Milled Samples 22

Dynamic Fatigue Testing of Dense I4 at 800°C in a Reducing Atmosphere 24

Aging Strengths for Dense I4 Bend Bars in a Reducing Gas 26

Elastic Moduli Property Testing 29

Additional Mechanical Property Testing of Materials and Modules 32

TASK 24.0 REACTION-DRIVEN ITM MATERIALS

24.0 Scope

Materials previously developed for ITM Syngas applications have temperature limitations and are negatively impacted by feed gas impurities and certain gas components, such as carbon dioxide. Applications integrating Reaction-Driven ITMs with gasifier and pyrolysis units will benefit from higher-temperature operation and will need to be more resistant to feed gas impurities and certain gas components.

The recipient team investigates and develops alternative materials that meet these requirements, and conduct appropriate testing in existing lab equipment at Air Products to determine the materials' capabilities. Air Products will initially conduct small-sample, non-fluxing tests, followed by fluxing tests as necessary.

The recipient team measures specific mechanical properties such as creep strength of existing and alternative materials using existing equipment. The testing conditions are dictated by the process integration schemes identified in Task 23.0. Penn State University conducts these experiments in their existing environmental tensile test rigs and evaluates creep rupture at temperatures in excess of 1,000°C. A Penn State researcher(s) subjects the samples to relevant tensile and compressive stresses at selected temperatures for extended periods and measure the sample's creep rate, time-to-failure, and strain-to-failure at simulated environment operating conditions.

24.0 Reaction-Driven ITM Materials

Background

Air Products and Penn State worked to expand the partial oxidation scope of ITM technology beyond natural gas feed. This effort investigated the potential for the ITM Reaction-Driven technology to be used in conjunction with gasification and pyrolysis technologies to provide more economical routes for producing hydrogen and synthesis gas. This task focused on developing membrane materials compatible with the gasification environment.

24.1 Materials Development

Three parallel efforts were undertaken to identify potential material options to address the temperature limitations of the current I4 ITM ceramic material previously developed for reaction-driven applications. The following routes were investigated: alternative materials with I4 to create a stronger material formulation; selective changes in structural, non-fluxing components within the ITM wafer; and identification of an entirely new ITM ceramic to replace I4. The risk and time frame associated with each alternative pathway increases when moving from one alternative to the next. Therefore, the greatest effort was focused on developing new material formulations with I4.

Materials Formulations with I4

A series of formulated disk wafers was fabricated at Ceramatec to evaluate the stability and performance of various wafer designs. The formulation does have a much higher creep resistance and strength than pure I4. It was selected primarily because it closely matches the chemical and thermal expansion properties of I4.

The stability of the formulations was evaluated by subjecting samples to high-pressure reactor tests in a CO_2 and steam environment. The samples maintained their strength and showed no indication of cracks or microstructure changes after 500 hours of testing. Figure 24-1 shows scanning electron micrographs (SEMs) of the samples both before and after the high-pressure tests.

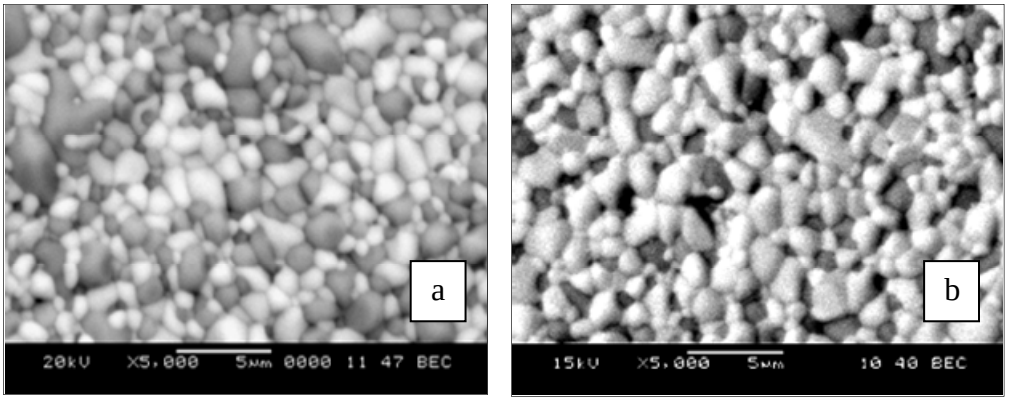

Figure 24-1 SEM of samples a) as sintered, and b)after 500 hours of exposure to high-pressure CO_2 and steam.

Fabrication of PDS Disks, Wafers and Modules

Overall, fabrication of porous-dense-slotted (PDS) disks with all layers was fairly successful, with yields varying from 15 to 90%. There was an exploratory attempt to apply reforming catalyst directly to the dense layer prior to final lamination and sintering. Unfortunately, the tested sample delaminated during the initial stages of flux testing.

PDU wafers made with formulated layers were successfully fabricated with less-than-design leak rates. Wafers made with additional layers gave encouraging results but did not pass the leak specification. The wafers were intact, achieved a good shrinkage match between all layers and were flat after sintering. Extensive work to address the PDU wafer leak rate for wafers was limited by the availability of qualified powder. Figure 24-2 shows two PDU wafers fabricated using formulated tape.

Figure 24-2. Wafers fabricated using formulated tapes.

Five PDU modules were fabricated during this program by Ceramatec and delivered to Air Products for PDU testing. All five modules were fabricated successfully, with one hermetic and four with leak rates within design specifications. The testing and performance of these modules is described in Task 23.6 of this report.

Performance Testing of PDS Disks

Tests were conducted on several disk membranes with various mixed conducting material architectures. All new disk membranes, except for the active D-layer (i.e., the dense membrane layer), performed similarly to I4-only membranes. There was no performance difference between these catalyzed and non-catalyzed membranes due to remaining surface resistances.

Similarly, non-catalyzed disks with formulated layers performed statistically the same as I4-only membranes. Post-test analysis of a disk revealed good bonding between the active I4 layer and the formulated layers, with no change in the microstructure and no evidence of any reaction between I4 and other materials. Based on the material properties and initial flux rates, formulated wafers appear to be an excellent option for Reaction-Driven ITM applications.

Advanced Materials Assessment for Reactive-Driven Membranes

After evaluating the requirements for alternative ITM materials under more aggressive operating conditions, a list of the most promising alternative materials was compiled. Both long- and short-term plans were generated to assess these alternative materials. Sixteen new compounds with expected improved thermal and chemical stability were fabricated using procedures developed to ensure that they were phase-pure. These new compounds, phase-pure alternatives to I4 materials, are expected to have improved chemical stability at elevated temperatures.

Based on literature review, three families of compositions were selected for exploration: $(La,Ce)(Ga,Fe,Al)O_{3-x}$, $(La,Sr)(Fe,Ta)O_{3-x}$ and $(La,Ca)(Fe,Ta)O_{3-x}$. The $(La,Ce)(Ga,Fe,Al)O_{3-x}$ compounds, with potential substitution of Ti and Ga on the B-site, have the potential to provide good thermodynamic stability in CO_2, high strength, and low CTE. Moderate oxygen fluxes were reported for 1 mm thick disk membranes in air/($He+H_2$) gradients at 950°C. The $(La,Sr)FeO_{3-x}$ and $(La,Ca)FeO_{3-x}$ compounds, with potential Ta or Zr substitution on the B-site, are expected to provide improved material stability. Small Ta substitution levels of ~10% are expected to have a modest impact on flux. Oxygen fluxes of 1 sccm/cm^2 were reported for 1.3 mm thick, Ta-substituted $(La,Sr)FeO_{3-x}$ membranes in air/($Ar+CH_4$) gradients at 850°C.

The critical first step in assessing alternative materials is to ensure that these new compositions are fabricated as single-phase materials for subsequent testing. XRD analysis confirmed >99% phase purity for eleven of the fabricated powders. Further work on the remaining five samples was abandoned since phase-pure materials could not be fabricated. Representative XRD patterns demonstrating the determination of phase purity for calcined $(La,Ce)(Ga,Fe,Al)O_{3-x}$ and $(La,Sr)(Fe,Ta)O_{3-x}$ are shown in Figures 24-3 and 24-4 respectively.

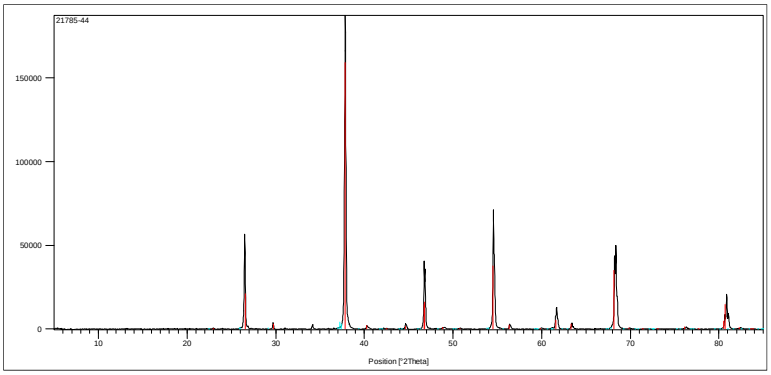

Figure 24-3. Representative pattern for calcined (La,Ce)(Ga,Fe,Al)O_{3-x}.

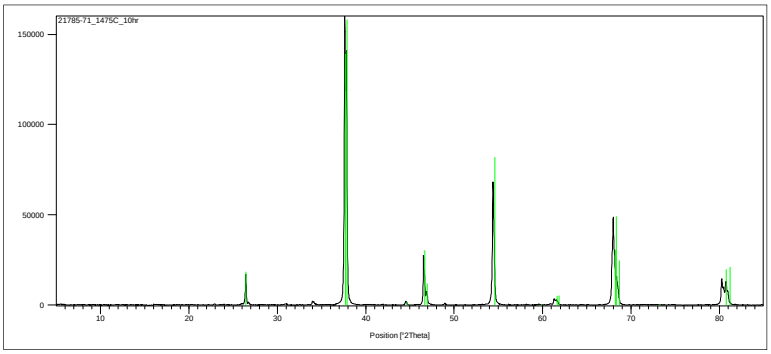

Figure 24-4. Representative pattern for calcined (La,Sr)(Fe,Ta)O_{3-x}.

A series of tests was conducted on the remaining 11 phase-pure materials as an initial screening for stability. These tests are designed to assess material phase stability in high-temperature air, reducing conditions and after exposure to CO_2. Oxygen non-stoichiometry testing was also conducted. The specific screening test conditions are listed below:

- Exposure to humidified H_2 for 500 hrs @ 900°C.
- Exposure to air for 500 hrs @ 900°C.
- Exposure to HP syngas (PCO_2 = 4 atm) for 14 days @ 850°C.
- High-temperature non-stoichiometry using TGAs.

All tested compounds were stable in both air and reducing conditions. Further evaluation for chemical and thermal expansion, flux testing and demixing, creep resistance and strength must be completed for these materials. However, preliminary screening test results have identified several materials with great potential as replacements for I4 in Reaction-Driven ITM applications.

24.2 Mechanical Properties

Creep Testing

Penn State researchers measured creep strength for various samples of existing and alternative materials. Materials were tested at aggressive operating temperatures and under both air and reducing-gas environments.

Long-Term Creep Rupture Testing of Dense I4 in Air

Penn State completed long-term creep rupture testing of I4 ITM materials in air at 900°C and 1000ºC, which are expected temperatures under reaction conditions. Two successful tests to failure were completed at 1000°C, with very similar results. The average creep rate for the samples was 1.10±0.05 $x10^{-6}$/sec. Figure 24-5 is a plot of the strain data at 1000ºC for a candidate material tested at a stress level of 62.5%.

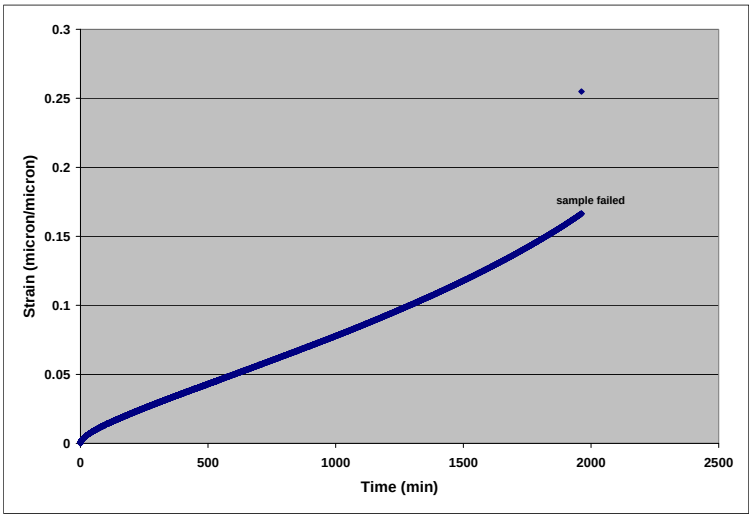

Figure 24-5. Tensile strain versus time plot for a stress rupture sample tested at 1000°C at a stress level of 62.5%.

A long-running stress rupture test on I4 tensile Sample #55 at 900°C was completed after 3.45 years when the sample failed with an applied stress of 66 MPa. Figure 24-6 shows the entire tensile creep strain versus time curve for Sample #55, exhibited an amazing 41.2% strain-to-failure. Based on the effective gage length for this test (in particular, the furnace thermal profile) the sample elongated over 7.3 mm, which was confirmed by post-test measurement using a measuring microscope. Optical microscopy measurements taken at the fracture location showed that the width of the sample decreased from an average of 0.716 mm to 0.618 mm. Similarly, the

thickness of the sample also diminished from 0.475 mm to 0.445 mm A minimum creep rate of 3.03E-09/sec was determined from the creep curve.

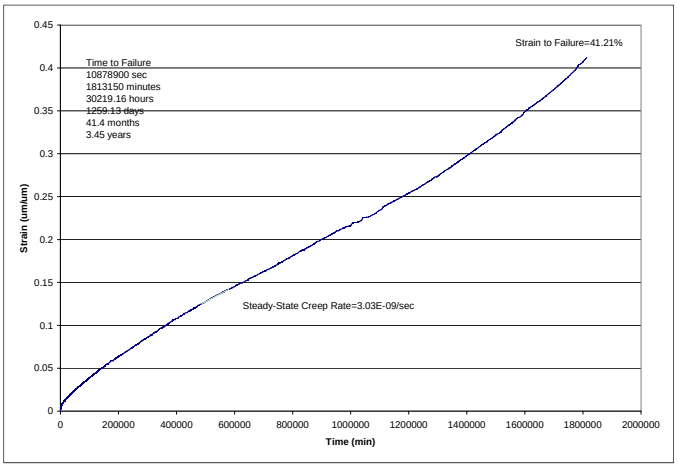

Figure 24-6. Tensile stress rupture creep strain versus time curve for I4 stress rupture sample #55 tested at 900°C with an applied stress of 66 MPa, which survived for 3.45 years and exhibited 41.21% strain-to-failure.

Energy dispersion spectroscopy (EDS) was performed in multiple locations to identify if any contaminants, such as Si or W, were present that may have reacted with I4 to increase the sample creep rate. EDS analysis of areas along the sample width and near the fracture site showed no significant levels of contamination. Close examination reveals what appears to be residual thermal insulation that is resting on the surface but has not reacted with the material.

A microstructural analysis of various regions of the sample, including the surface near the fracture site and the actual fracture surface, was conducted using scanning electron microscopy (SEM). Figure 24-7 shows a very low-magnification image of the width surface of the sample with the fracture site located on the far left of the sample. Large creep cavities extending inward from the edges of the sample are visible along the length of the sample. For the sample to elongate over 7.3 mm, one would expect to see a lot of creep cavitation. At a magnification of 200X, Figure 24-8 shows that the creep cavitation occurred not only at the edges of the sample, but also all along the surface.

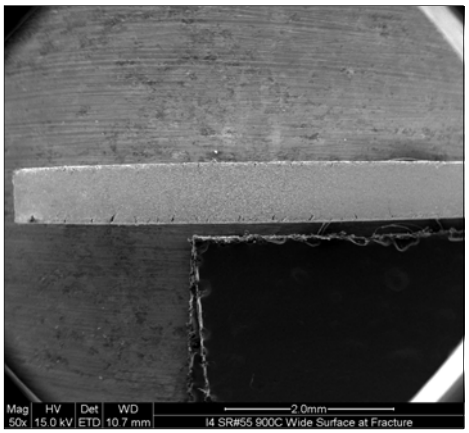

Figure 24-7. SEM low-magnification (50x) micrograph of the width surface of I4 stress rupture Sample #55 showing creep cavitation cracks along the length of the sample.

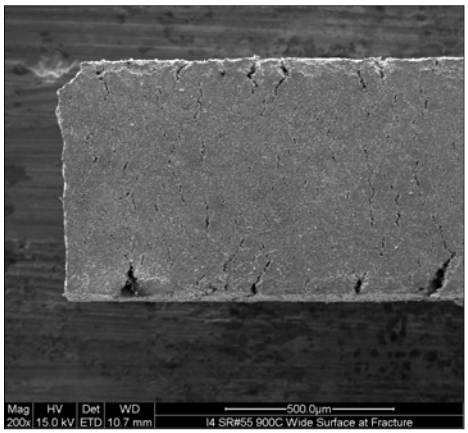

Figure 24-8. SEM micrograph (200x) of the width surface of I4 stress rupture Sample #55 showing creep cavitation cracks across the entire sample surface.

At 1500X (Figure 24-9), individual grains are visible as well as even finer-scale creep cavitation along individual grain boundaries. The sample was also oriented in the SEM to view the thickness surface of the sample. Figure 24-10 shows a 50x magnification image of the thickness surface, again with the fracture site located on the left side of the photo. As was the case for the width surface, creep cavitation is visible along the length of the sample. While the 50x image of the width surface did not reveal creep cavitation across the entire surface, cavitation is clearly visible across and along the entire surface of the thickness.

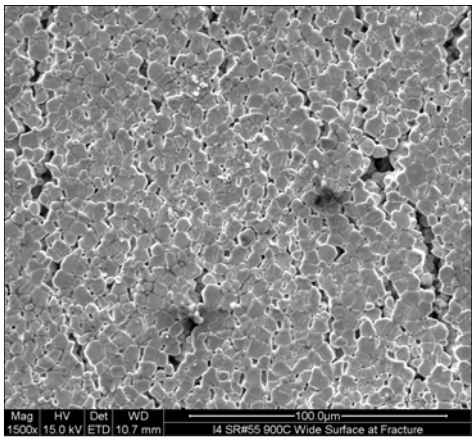

Figure 24-9. SEM micrograph (1500x) of the width surface of I4 stress rupture Sample #55 showing creep cavitation cracks as well as finer-scale nucleation of cavity along individual grain boundaries.

Figure 24-10. Low-magnification (50x) SEM micrograph of the thickness surface of I4 stress rupture Sample #55 showing creep cavitation cracks along the length of the sample.

At 200x magnification (Figure 24-11), a region is visible on the right that shows where cavitation has nearly linked to form a crack across the entire sample thickness. Also visible is more surface contamination from the furnace insulation. A 1500x close-up image of this contamination (Figure 24-12) reveals the fiber link nature of the thermal insulation. The corresponding EDS analysis indicates significant levels of Si and Mg, which is consistent with the alumino-magnesium-silicate fibers of the thermal insulation.

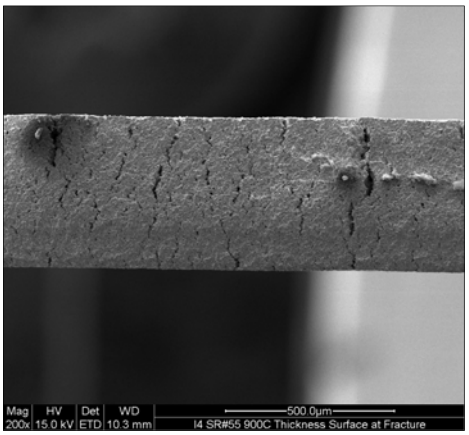

Figure 24-11 SEM micrograph (200x) of the surface thickness of I4 stress rupture Sample #55 showing creep cavitation cracks across the entire surface.

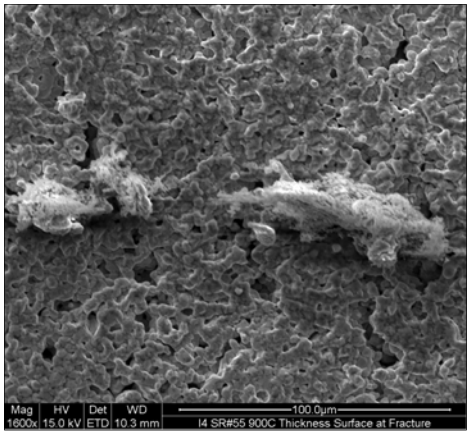

Figure 24-12. SEM micrograph (1500x) of surface contamination from furnace insulation.

Figures 24-13 and 24-14 show, respectively, 500x images taken near the fracture site (e.g., within the hot zone of the furnace) and some distance away from the hot zone. The region outside the hot zone does not show the extensive creep cavitation like the region in the hot zone. However, Figure 24-14 does show that the middle portion of the tensile sample in this region did contain some porosity. The fact that the porosity seems to be oriented parallel and not perpendicular to the tensile axis indicates that this porosity was as-processed rather than created by creep.

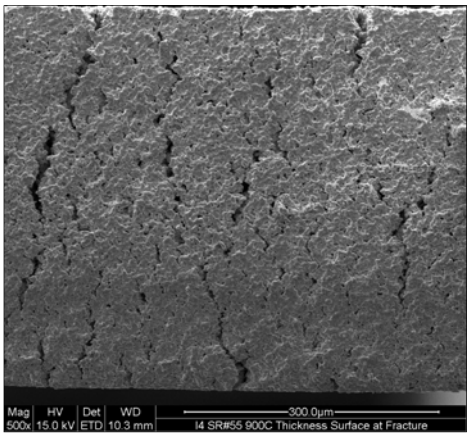

Figure 24-13. SEM micrograph (500x) of the thickness surface of I4 stress rupture Sample #55 near fracture site showing creep cavitation.

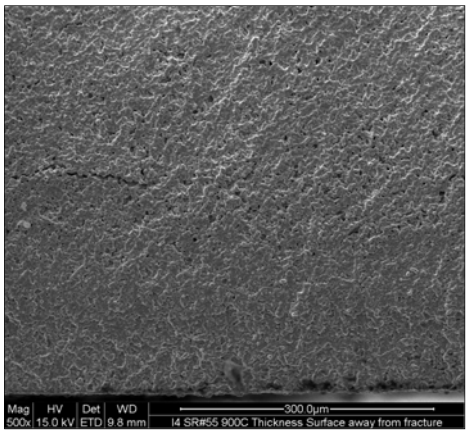

Figure 24-14. SEM micrograph (500x) of the thickness surface of I4 stress rupture Sample #55 outside of the fracture site and furnace hot zone showing no evidence of creep cavitation.

Figure 24-15 shows the fracture surface at 350x magnification of. Note that the extent of creep cavitation appears to be concentrated along the laser-cut edges of the tensile samples (Figures 24-16 and 24-17). Reduced area scans and EDS analysis of the cavitation regions along the edge show that Si is present only at the level of the background noise. Unlike the thickness and width surfaces of the sample, the fracture surface contains regions where some apparent grain growth has occurred. Figure 24-18 shows a 3000x image of the central region of the fracture surface. Regions with darker gray contrast show that grains have grown and appear less faceted than the smaller grains. This may be evidence of the grain boundary sliding to accommodate creep cavitation.

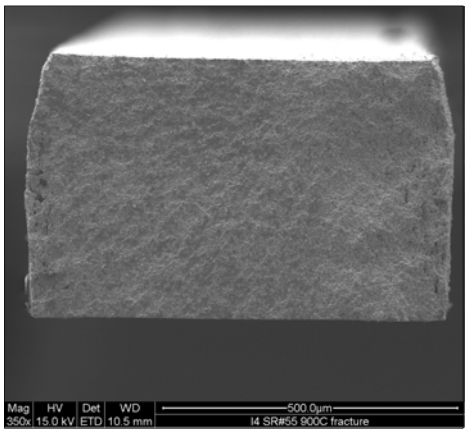

Figure 24-15. SEM micrograph (350x) of the fracture surface of I4 stress rupture Sample #55.individual grain boundaries.

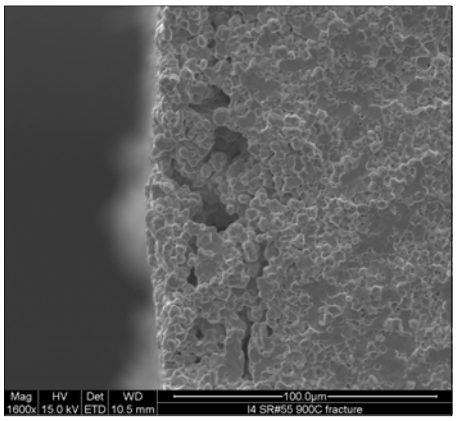

Figure 24-16. SEM micrograph (1600x) of the left side of the fracture surface of I4 stress rupture Sample #55 showing large creep cavitation cracks.

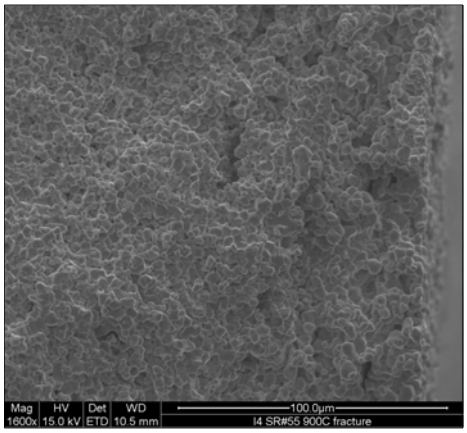

Figure 24-17. SEM micrograph (1600x) of the right side of the fracture surface of I4 stress rupture Sample #55 showing large creep cavitation cracks.

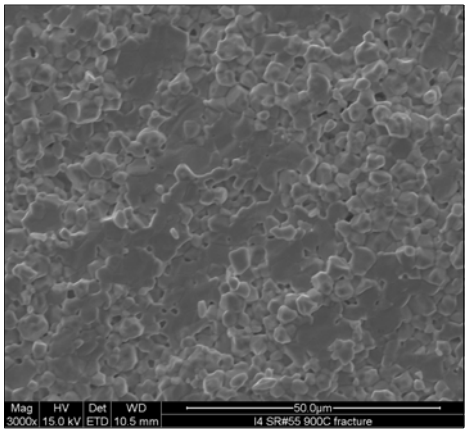

Figure 24-18. SEM high magnification (3000x) micrograph of the center region of the fracture surface showing little cavitation, but regions of grain growth.

Tensile Creep of Dense I4 in a Reducing Atmosphere

Sample pieces made from I4 were tested under reducing conditions to determine if exposure to a syngas environment impacts material creep resistance. These tests involve subjecting the samples to a series of stresses and measuring the resulting tensile creep strain rates. Samples were tested in a reducing atmosphere (4%H_2-Bal. N_2 bubbled through water at room temperature) at 950°C, 975°C and 1000°C.

A typical stress test is shown in Figure 24-19. In this example, dense I4 Sample #3 was held at a temperature of 975°C and subjected to applied stresses of 500, 1000 and 750 psi (3.45, 6.89 and 5.17 MPa). The resulting tensile creep strain rates, shown in Figure 24-19, were measured as 2.35×10^{-06}/sec, 4.42×10^{-06}/sec and 1.6×10^{-06}/sec for each test point respectively. The calculated overall creep stress exponent of 1.43 was derived from the strain rate versus stress plot shown in Figure 24-20. A summary of the eight experimental creep strain measurements at 950°C and 975°C under a reducing gas atmosphere is shown in Tables 24-1 and 24-2.

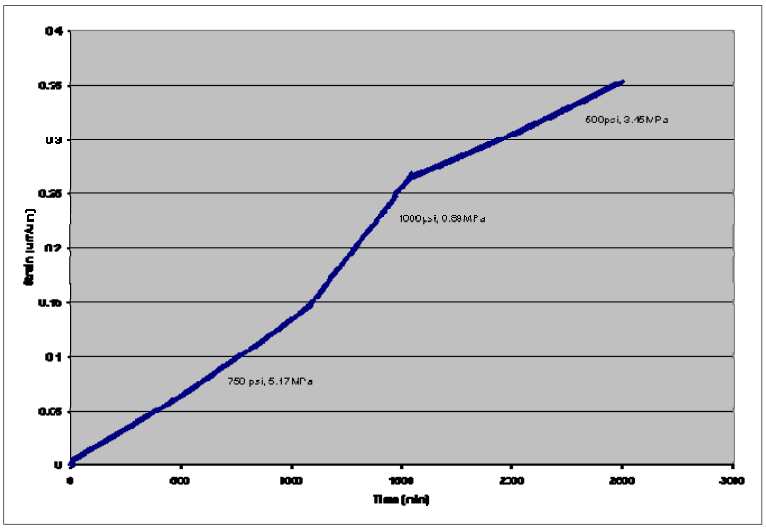

Figure 24-19. Tensile creep strain versus time curve for dense I4 Sample #3 tested at 975°C in a reducing gas atmosphere at applied stress levels of 3.45, 5.17 and 6.89MPa (500, 750, and 1000 psi).

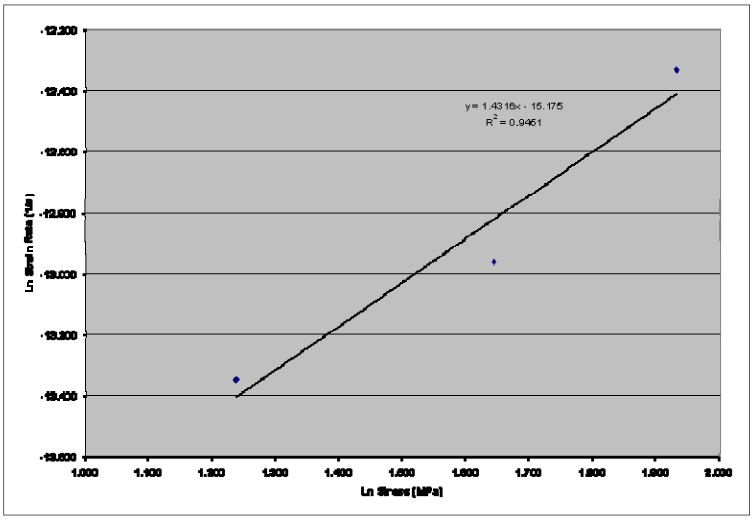

Figure 24-20. Ln creep strain rate (1/s) versus ln applied stress (MPa) plot for dense I4 Sample #3 tested at 975°C in a reducing gas atmosphere of at applied stress levels of 3.45,5.17 and 6.89 MPa (500, 750, and 1000 psi), yielding a creep stress exponent of 1.43.

Table 24-1. Tensile creep data for dense I4 tested at 950°C in a reducing atmosphere of 4% H_2 in N_2 bubbled through water at 22°C (set 1).

Sample #	AppliedStress (MPa)	Strain Rate (1/s)	Stress Exponent, n
20	6.89	1.25E-07	1.71
	13.79	4.41E-07	
	27.58	1.34E-06	
23	6.89	6.78E-08	1.82
	13.79	1.98E-07	
	20.68	5.19E-07	
25	6.89	1.16E-07	1.57
	13.79	2.82E-07	
	20.68	4.15E-07	
	27.58	1.25E-06	
15	3.45	2.62E-07	1.44
	5.17	4.18E-07	
	6.89	7.21E-07	

Table 24-2. Tensile creep data for dense I4 tested at 975°C in a reducing atmosphere of 4% H_2 in N_2 bubbled through water at 22°C (set 2).

Sample #	AppliedStress (MPa)	Strain Rate (1/s)	Stress Exponent, n
2	3.45	3.77E-07	1.54
	5.17	6.84E-07	
	6.89	1.10E-06	
3	3.45	1.60E-06	1.43
	5.17	2.35E-06	
	6.89	4.42E-06	
4	3.45	4.96E-06	1.44
	6.89	1.34E-05	
5	3.45	5.78E-06	1.42
	5.17	9.50E-06	
	6.89	1.56E-05	

Samples tested at 1000°C were more problematic. Figure 24-21 shows the creep strain versus time plot for the first test piece, where the sample experienced a total strain of nearly 39%. The sample was initially loaded to an applied stress of 6.89 MPa that was maintained overnight,

during which time the sample crept over 14% to yield a steady-state creep rate of 2.27×10^{-6}/sec. The applied stress was then increased to 13.78 MPa for 7.5 hours, yielding a steady-state creep rate of 7.49×10^{-6}/sec. When the applied stress was decreased 1.23 MPa and held overnight, the steady state creep rate was 4.05×10^{-7}/sec. As expected, these creep rates were significantly faster than for samples tested in air.

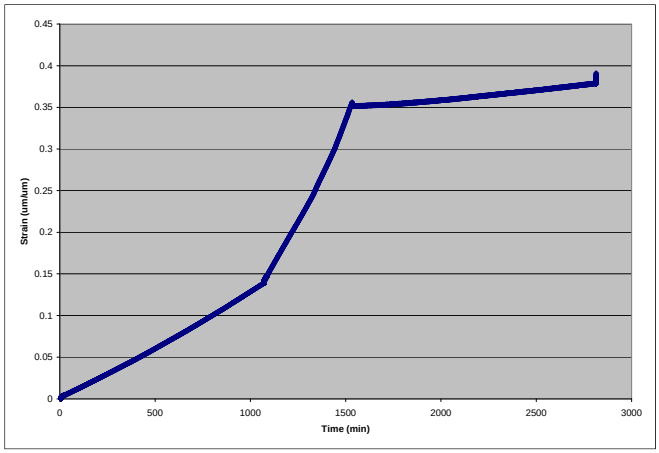

Figure 24-21. Creep strain versus time plot for a dense I4 tensile sample tested at 1000°C in a reducing atmosphere (4%H_2-Bal N_2, bubbled through water at RT).

Figure 24-22 compares an untested I4 tensile sample with a crept sample to demonstrate the extent of elongation during creep testing at 1000°C in the reducing atmosphere. The samples exhibited a reduction in width from 0.741 mm to 0.657 mm and a reduction in thickness from 0.493 mm to 0.448 mm as a result of the testing.

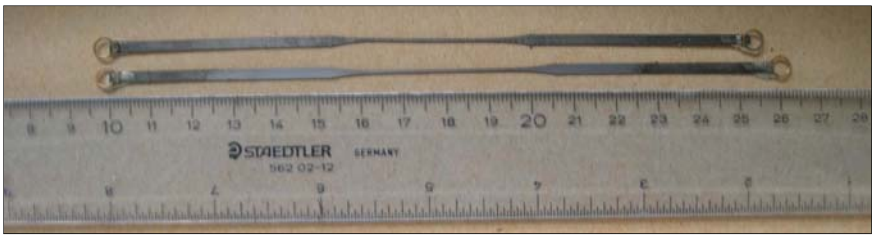

Figure 24-22. Comparison of untested (top) and creep-tested (bottom) dense I4 tensile samples showing the large amount of creep elongation the sample experienced at 1000°C in the reducing atmosphere.

When ln stress was plotted against the ln strain rate (Figure 24-23), the creep stress exponent was found to be 0.84. The data are based on stress values for the initial cross-sectional area of the sample and do not account for the reductions in width and thickness that occurred during the creep experiment.

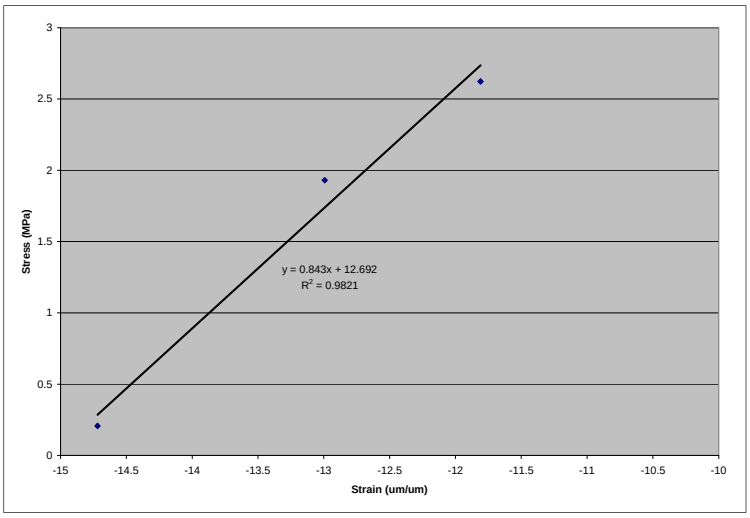

Figure 24-23. Ln stress versus Ln creep rate for dense I4 tensile sample tested at 1000°C in a reducing atmosphere to determine an incorrect stress exponent of 0.843.

Due to the fast creep rates of the I4 tensile samples at 1000°C in a reducing atmosphere, the samples tend exhibit a relatively large amount of reduction in their cross-sectional area with the reduced gage section. The reduction of the cross-sectional area yields a greater stress for the same applied constant load. Because of this, the creep stress exponent cannot be obtained simply from linear regression of the log creep strain versus log creep stress plot. Thus, follow-up tensile creep tests were performed using lower applied stresses of 0.5, 0.75, and 1 ksi to minimize the amount of creep elongation and limit the amount of reduction of the cross-sectional area within the reduced gage length of the tensile sample.

High applied stress rates sometimes resulted in unstable creep rates. Sample # 3 was tested using a constant applied stress of 13.778MPa. The sample survived for 10.86 hours prior to failing, as shown in Figure 24-24. The sample experienced 39.8% strain to failure in 652 minutes. The shape of the strain versus time curve reveals that the sample did not experience a very pronounced steady-state creep rate (e.g., no significant region of linear strain versus time), but rather a large tertiary creep region. When using the interval between 150 and 250 minutes for calculations, the steady-state creep rate was found to be 6.26×10^{-06}/sec, similar to the previous samples. Table 22-3 summarizes the tensile creep rates for six I4 samples tested at 1000°C in the reducing atmosphere.

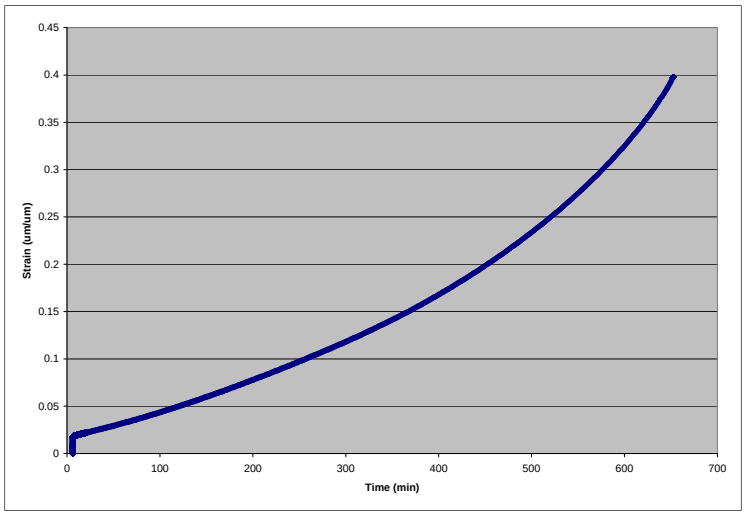

Figure 24-24. Creep strain versus time or a dense I4 tensile Sample #3 tested at 1000°C in a reducing atmosphere using an applied stress of 13.78MPa.

Table 24-3. Tensile creep data for dense I4 tested at 1000°C in a reducing atmosphere of 4% H_2-N_2 bubbled through water at 22°C.

Sample #	Applied Stress (MPa)	Strain Rate (1/s)	Stress Exponent (n)
1	1.23	4.053E-07	1.16
	6.89	2.275E-06	
	13.78	7.429E-06	
2	6.89	7.181E-06	2.80
	13.78	9.183E-06	
3	13.78	6.256E-06	
5	3.45	1.247E-06	1.66
	5.17	2.249E-06	
	6.89	3.990E-06	
	13.78	2.279E-06	
14	5.17	1.184E-05	0.97
	6.89	2.434E-05	
15	3.45	6.946E-06	0.89
	5.17	4.230E-05	

As expected, the creep rates were significantly faster for samples tested in a reducing atmosphere than for those tested in air. Since silicon contamination can increase the creep rate of I4, EDS analysis was done on two samples in the SEM. Figure 24-25 shows the results of an EDS scan from the wide side of Sample #2 within the hot zone of the furnace. No significant levels (i.e., greater than background noise) were detected for Si. Therefore, the fast creep rates for I4 in the reducing atmosphere have not been affected by Si contamination.

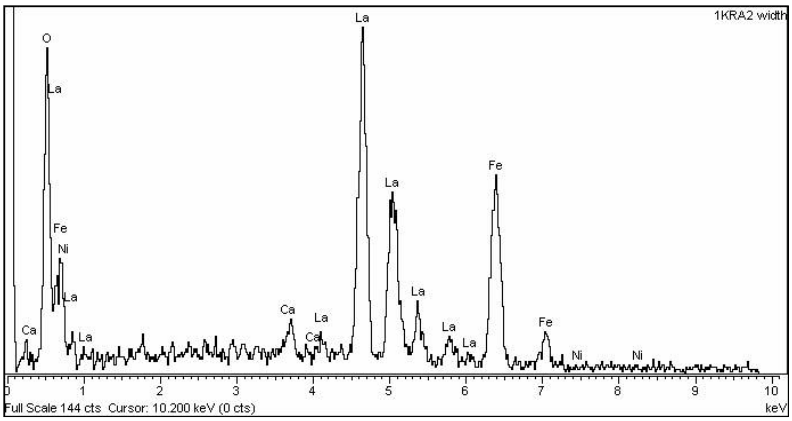

Figure 24-25. EDS spectrum of dense I4 tensile creep Sample #2 tested at 1000°C in a reducing atmosphere showing no silicon contamination.

SEM images of tensile Sample #3, tested to failure using an applied stress of 13.78MPa (2ksi), exhibited extensive creep cavitation. Figure 24-26a is a low-magnification view of the reduced gage section in the hot zone with respect to the thickness of the sample. This surface is highly decorated with large creep cavitation cracks. A higher-magnification view of the actual fracture surface (Figure 24-26b) indicates that the creep cavitation is somewhat limited to the edges of the sample.

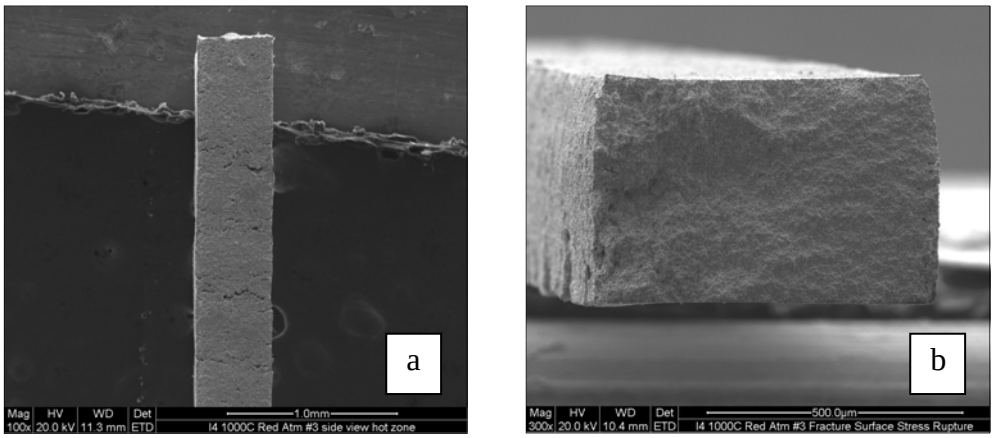

Figure 24-26. SEM images within the hot zone of tensile creep Sample #3 tested at 1000°C in a reducing atmosphere: a) thickness side of the sample; b) fracture surface.

The surface of the width region of the sample (Figure 24-27) appears to have far fewer areas of creep cavitation. However, a higher-magnification image of the wide surface of the sample (Figure 24-28a) does show significant but much smaller-scale creep cavitation. In contrast, the microstructure of the I4 sample near the tab region and outside the furnace (Figure 24-28b) shows no evidence of creep cavitation and only a small amount of porosity.

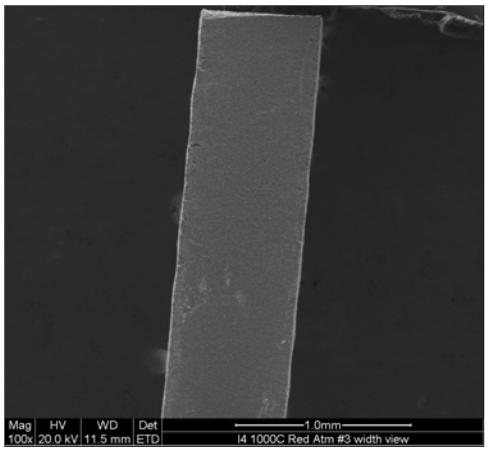

Figure 24-27. SEM image of the width side within the hot zone of tensile creep Sample #3 tested at 1000°C in a reducing atmosphere of 4%H-bal N_2 gas.

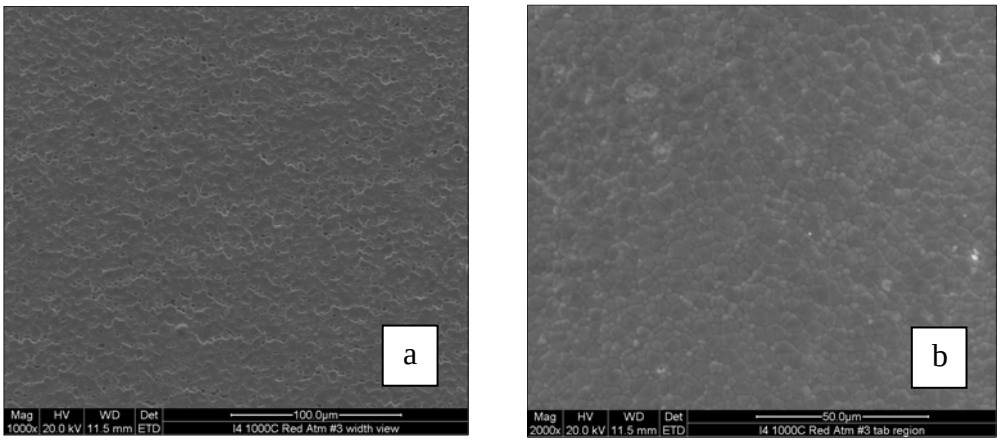

Figure 24-28. SEM image at 1000x magnification of the width side of tensile creep Sample #3 tested at 1000°C in a reducing atmosphere of 4%H-bal N_2 gas: a) within the hot zone; b) outside of hot zone.

A comparison of Figures 24-28 a) and b) shows that significant grain growth has occurred in the highly-crept region of the hot zone. The grains appear more elongated across the width of the sample and somewhat larger than the more uniformly-sized grains of the uncrept region.

The measured creep rates for Samples #14 and #15 were nearly an order of magnitude faster than the rates for previous samples. Sample #15 was tested with a smaller applied stress for the first stress level. The applied stress of 3.45 Mpa (500 psi) was held overnight, resulting in a remarkable strain of nearly 54% after almost 15 hours without failure. The stress was increased to 5.17 MPa (750 psi), quickly resulting in failure at ~55% strain (Figure 24-29).

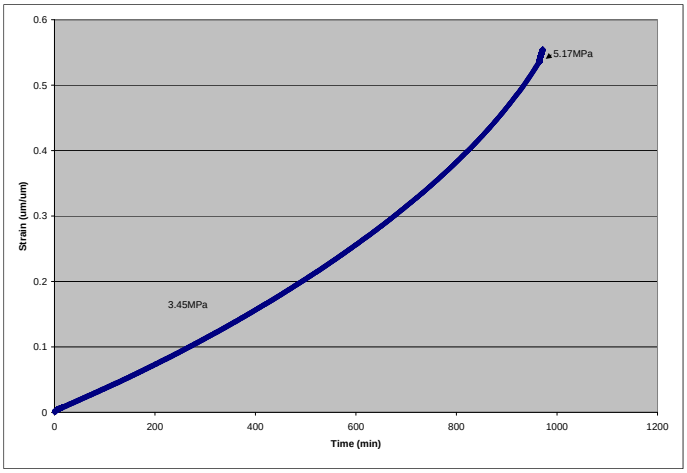

Figure 24-29 Tensile creep strain versus time curve for dense I4 Sample #15 tested at 1000°C in a reducing gas atmosphere of 4%H_2-N_2 at applied stress levels of 3.45 and 5.17MPa.

Creep strains rates of 6.94×10^{-6}/sec and 4.23×10^{-5}/sec were obtained for the 3.45 and 5.17 MPa stresses respectively. It is clear from Figure 24-29 that the sample was exhibiting signs of tertiary creep even at the 3.45 MPa stress. The evidence for tertiary creep is a non-linear, increasing creep strain curve. Although this sample did experience a rather prolonged region of tertiary creep, a creep stress exponent of 0.89 was calculated. The fact that the stress exponent is somewhat less than unity is not that surprising, given the extent of tertiary creep that the sample endured prior to failure.

SEM analysis was conducted on Sample #15 to investigate the apparent discrepancy with previous results. This sample showed an extensive amount of creep cavitation along its length. Figure 24-30 shows the regions in the lower right and left corners of the sample. These higher-magnification images reveal regions with an amorphous reaction product.

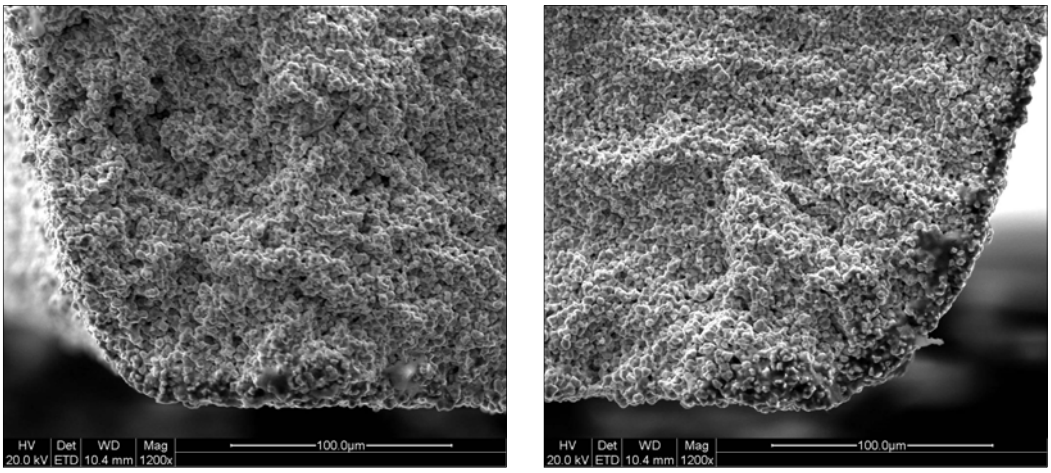

Figure 24-30. SEM images of the lower corners of the fracture surface of I4 tensile Sample #15 revealing a region of an amorphous reaction product.

EDS analysis indicated a significantly greater amount of calcium and iron in the darker, amorphous reaction phase along the left corner of the sample fracture surface than in the bulk I4 material. Contaminant peaks of Na, K, Cl and a relatively large S peak were also detected. While calcium iron oxide is known to increase the creep rate of I4, the effects these other contaminants on the creep rate of I4 is not known.

The backscatter image provides a more topographical view of the fracture surface. Creep cavities (porosity) are readily visible throughout the entire fracture surface, but appear mainly along the more heavily-cavitated regions near the edges. This is evident in the image of the lower right-hand corner of the sample in Figure 24-31. It appears that the slightly darker regions are more susceptible to creep cavitation than the lighter gray regions. EDS spectra for both the darker and lighter areas of Figure 24-31 indicated that the darker gray region contain significantly higher amounts of oxygen than the lighter gray regions.

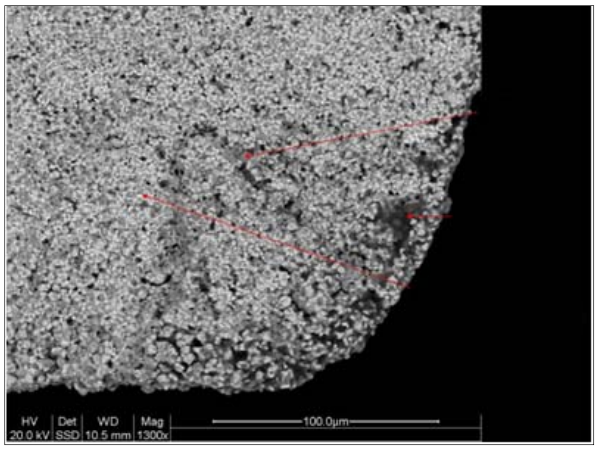

Figure 24-31. SEM image of the lower right corner of fracture surface of I4 tensile Sample #15 obtained using the solid-state backscatter detector. Red arrows indicate locations where spot mode EDS scans were obtained.

In summary, I4 tensile Samples #14 and #15 exhibited faster tensile creep rates than other samples previously tested at 1000°C in a reducing atmosphere. While some contamination (e.g., S, Na, K, and Cl) was detected using EDS, it is not known whether these contaminants affected the faster creep rates. While most pronounced creep cavitation damage was seen along the edges of the samples, SEM backscatter images revealed significant cavities through the entire sample fracture surface. Finally, the cavities seem to occur preferentially in regions which exhibited a slightly darker gray contrast in the backscatter mode. An EDS spectrum of the light and dark regions of the sample reveal a very noticeable difference in the amount of oxygen detected (i.e., the darker regions exhibited the higher oxygen levels).

Tensile Creep of I4 Solvent-Milled Samples

Tensile creep tests were conducted on samples prepared from solvent-milled powders to determine if the solvent milling process significantly affected the tensile creep behavior of the I4 samples, as compared to standard jet mill processing. The measured creep stress exponent for samples prepared from solvent-milled powders is equivalent to that obtained for earlier I4 tensile samples; however, the creep rate is slightly faster for the solvent-milled samples. The faster creep rates may be due to either the presence of a Ca_2FeO_4 second phase or a smaller grain size distribution. SEM analysis of solvent-milled crept samples did not detect any evidence of a Ca_2FeO_4 second phase. Thus, the faster creep rate is most likely due to a smaller grain size distribution for the tensile samples prepared from the solvent-milled powders than the earlier jet-

milled powders. Using only the 1000°C to 1050°C data, the creep activation energies for 6.89, 13.72, and 27.58 MPa (1, 2, and 4 ksi) stresses are -313, -306, and -359kJ/mol respectively, which is significantly lower than that of earlier I4 samples. It should be noted, however, that the I4 samples were tested at temperatures up to only 975°C.

Figure 24-32 shows a typical strain versus time curve for tensile Sample #2. Figure 24-33 shows the ln strain rate versus ln applied stress plot used to obtain the creep stress exponent from the slope of the linear regression fit to the data. Table 24-4 summarizes the measured creep rates and calculated parameters for I4 tensile samples made from the solvent-milled powders.

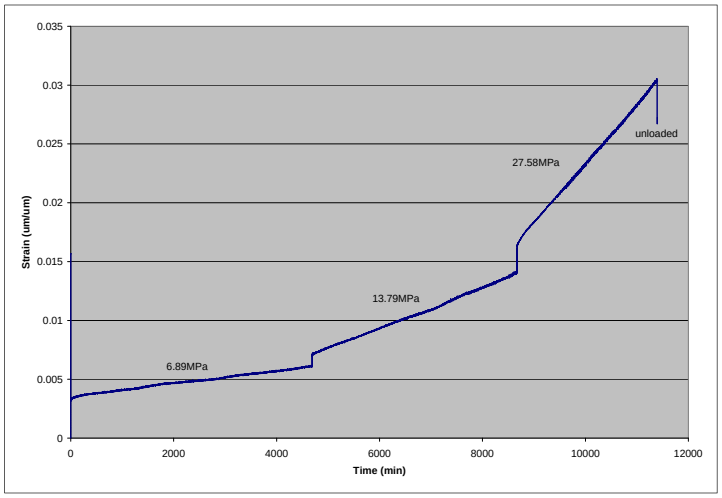

Figure 24-32. Tensile creep strain versus time curve for I4 tensile Sample #2 made from solvent-milled powder and tested at 950°C in air.

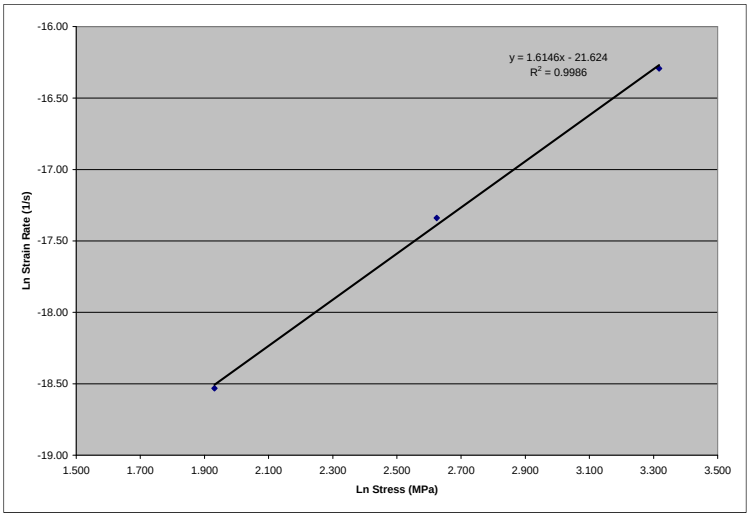

Figure 24-33. Fit of tensile creep strain and applied stress data for I4 tensile Sample #2 to calculate the creep stress exponent (1.61).

Table 24-4. Summary of creep rates and parameters for I4 tensile samples made from solvent-milled powders.

Sample #	Temp. (°C)	Stress (MPa)	Strain Rate (1/s)	Ln Stress	Ln Rate	n
1	~975	6.89	1.42E-09	1.93	-20.37	1.69
		13.79	6.47E-09	2.62	-18.86	
		27.58	1.49E-08	3.32	-18.02	
2	~975	6.89	9.10E-09	1.931	-18.51	1.61
		13.79	3.00E-08	2.624	-17.32	
		27.58	8.54E-08	3.317	-16.28	
3	~975	6.89	5.38E-09	1.93	-19.04	1.68
		13.79	1.72E-08	2.62	-17.88	
4	~975	6.89	3.27E-09	1.93	-19.54	1.34
		13.79	8.26E-09	2.62	-18.61	
		27.58	2.41E-08	3.32	-17.54	
Average	**~975**	**6.89**	**4.79E-09**		**-19.37**	**1.58**
		13.79	**1.55E-08**		**-18.17**	
		27.58	**4.14E-08**		**-17.28**	
St. Dev.	**~975**	**6.89**	**3.30E-09**		**0.79**	**0.17**
		13.79	**1.07E-08**		**0.70**	
		27.58	**3.83E-08**		**0.90**	
6	1025	6.89	1.15E-08	1.93	-18.28	1.60
		13.79	3.47E-08	2.62	-17.18	
		27.58	6.99E-08	3.32	-16.48	
7	1025	6.89	2.14E-08	1.93	-17.66	1.41
		13.79	5.94E-08	2.62	-16.64	
		27.58	1.51E-07	3.32	-15.71	
8	1025	6.89	1.50E-08	1.93	-18.02	1.46
		13.79	4.24E-08	2.62	-16.98	
		27.58	1.13E-07	3.32	-16.00	
9	1025	6.89	2.84E-08	1.93	-17.38	1.11
		13.79	4.73E-08	2.62	-16.87	
		27.58	1.32E-07	3.32	-15.84	
Average	**1025**	**6.89**	**2.16E-08**		**-17.68**	**1.33**
		13.79	**4.97E-08**		**-16.83**	
		27.58	**1.32E-07**		**-15.85**	
St. Dev.	**1025**	**6.89**	**6.72E-09**		**0.32**	**0.19**
		13.79	**8.73E-09**		**0.17**	
		27.58	**1.88E-08**		**0.14**	
11	1050	6.89	3.28E-08	1.93	-17.23	1.42
		13.79	9.57E-08	2.62	-16.16	
		27.58	2.34E-07	3.32	-15.27	
12	1050	6.89	3.74E-08	1.93	-17.10	1.43
		13.79	1.12E-07	2.62	-16.00	
		27.58	2.72E-07	3.32	-15.12	
Average	**1050**	**6.89**	**3.51E-08**		**-17.17**	**1.42**
		13.79	**1.04E-07**		**-16.08**	
		27.58	**2.53E-07**		**-15.19**	
St. Dev.	**1050**	**6.89**	**3.24E-09**		**0.09**	**0.01**
		13.79	**1.16E-08**		**0.11**	
		27.58	**2.72E-08**		**0.11**	

Dynamic Fatigue Testing of Dense I4 at 800°C in a Reducing Atmosphere

A series of tests was conducted to determine if I4 material was susceptible to slow crack growth (SCG). Dynamic fatigue testing of dense I4 bend bars using fast and slow stressing rates was completed for five samples for each stressing rate at both 750°C and 800°C, and at oxygen

partial pressures ranging from 7.2 x10^{-17} to 1.8 x10^{-18}. Figure 24-34 shows the Weibull strength distributions for the four sets of tests. Typical detailed results for fast testing at 800°C is shown in Table 24-5, with overall results summarized in Table 24-6.

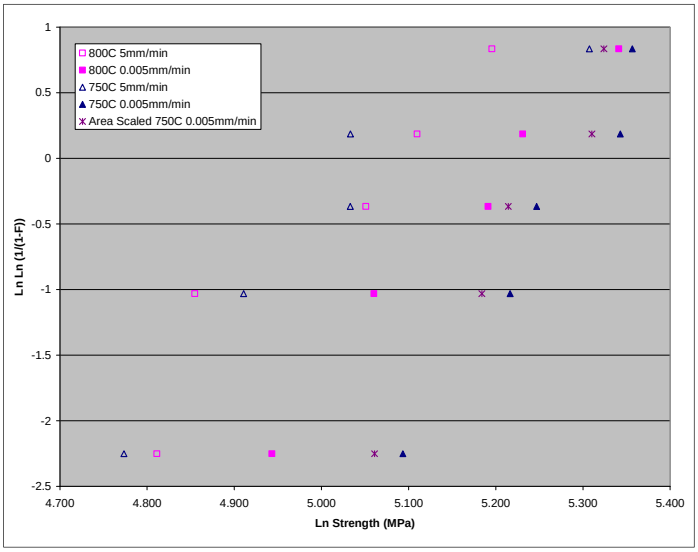

Figure 24-34. Weibull strength distribution plot for dynamic fatigue samples tested at 800°C and 750°C in a reducing atmosphere of 4%H-bal N_2.

Table 24-5. Dynamic fatigue strengths for dense I4 laminated bend bars tested at 800°C in a reducing atmosphere of 4%H-bal N_2 gas.

Dense I4					
Support Span		**40.00 mm**			
Load Span		**20.00 mm**			
Mass of Upper Fixture		**0.202 N**		**20.63 g**	
Temperature		**800 °C**		**Red Atm**	
Xhead rate		**5.000 mm/min (fast)**			
Sample #		**Width (mm)**	**Thickness (mm)**	**Load (N)**	**Stress (MPa)**
	1	4.12	2.22	105.50	156.17
	3	4.12	2.10	74.21	122.87
	4	4.15	2.20	85.73	128.35
	5	4.14	2.20	120.34	180.47
	6	4.13	2.23	113.19	165.63
Ave		**4.13**	**2.19**	**99.79**	**150.70**
StDev		**0.013**	**0.052**	**19.277**	**24.565**
ESTIMATES				**BOUNDS**	
		Biased	**Unbiased**	**Lower**	**Upper**
Weibull modulus =		8.02	5.56	2.81	11.75
Characteristic strength =		160.24	159.12	139.75	186.86

Table 24-6. Characteristic strengths for dense I4 laminated bend bars tested at 750°C & 800°C in air and a reducing atmosphere of 4%H-bal N_2 gas.

	Characteristic Strength (MPa)		
	Air	Reducing gas	
	Fast	Fast	Slow
800°C		159.12	163.37
750°C	209.43	183.73	198.23

Higher strengths were measured for samples tested at the slower stressing rate at both 800°C and 750°C. This result is contrary to what is expected for material exhibiting SCG behavior. If SCG were occurring, samples tested at a slower stressing rate would have more time for sub-critical crack growth to occur before catastrophic failure. As the sub-critical cracks grow and the stress on the sample increases, a critical crack size for a given stress is reached and the sample fails. The larger the crack size for failure, the lower the fracture stress. Therefore, samples tested at lower stressing rates should demonstrate lower fracture strengths. Based on the data for just the two stressing rates, SCG was not observed at 750°C or 800°C in a reducing atmosphere.

One possible explanation for this outcome is the inability of the equipment to measure the actual fracture stress during the fast stressing rate tests. If the peak failure load is not recorded quickly enough, it is possible that the actual failure load could be slightly higher than the recorded value, resulting in a falsely lower stress calculation. To check for this scenario, tests were performed using an intermediate stressing rate. Five samples were tested at 750°C using a stressing rate that was one order of magnitude slower than the fastest stressing rate. The five samples had an average strength of 169.38±24.25 MPa, which lies between the strengths of the fastest (150.70±24.56 MPa) and the slowest (174.64±26.53 MPa) tests. Since the strengths obtained using the middle stressing rate were not higher than those obtained for the slowest stressing rate samples, it appears that the fracture loads are being measured accurately at the fastest stressing rates.

Aging Strengths for Dense I4 Bend Bars in a Reducing Gas

A second possible explanation for the higher strengths in lower stressing rate tests is that the material exhibits stress redistribution as a result of localized creep. Creep will result in an apparent strengthening of the test sample as the stress on it is redistributed. To test this hypothesis, experiments were conducted where samples were held at temperature under reducing gas conditions prior to testing the sample at the fast rate. Tests were done at 750°C in both air

(baseline conditions) and a reducing atmosphere of 4%H_2-96%N_2 saturated with water at room temperature. The strength was determined by applying an increasing load on the sample bars at a fast crosshead rate of 5 mm/min until failure.

Baseline testing in air was conducted on 10 dense I4 bend bars. The average strength was 88.17±9.60 MPa and the Weibull modulus was 8.60. Figure 24-35 shows the Weibull strength distribution for these 10 samples assuming a single-flaw population. In addition, five dense I4 bend bar samples tested using a 2-hour hold in the reducing atmosphere yielded an average strength of 143.0±67.3MPa, while four dense I4 bend bar samples tested using a 7-hour hold in the reducing atmosphere yielded an average strength of 139.2±50.3 MPa. The results, tabulated in Table 24-7, show the measured strength and sample dimensions. Based on the limited number of samples tested and the large amount of scatter in the strength data for these tested atmospheric compositions, there does not seem to be any significant effects of gas composition or aging in a reducing atmosphere on the strength of dense I4 samples at 750°C.

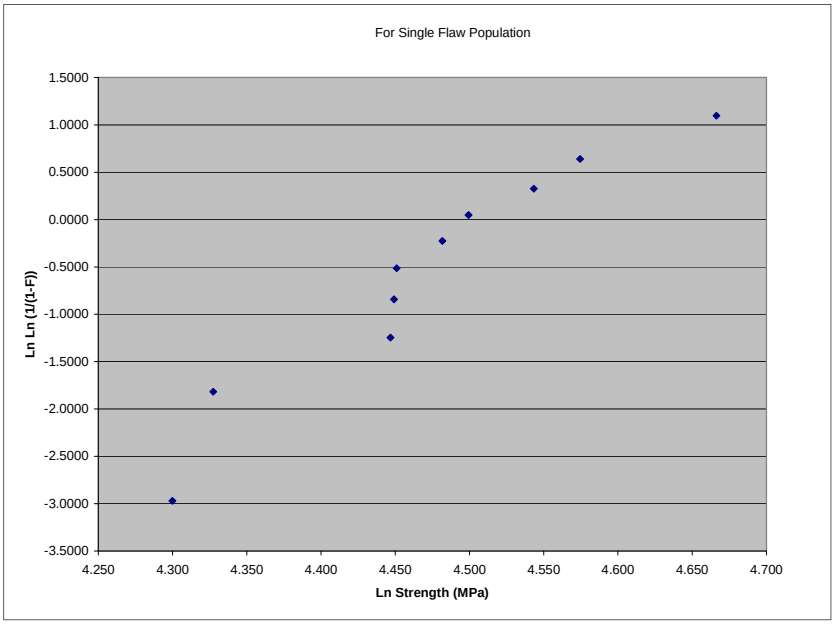

Figure 24-35. Weibull strength distribution plot for dense I4 bend bars tested at 750°C in air.

Table 24-7. Dimensions and strength data for dense I4 samples tested at 750° in air and a reducing atmosphere of 4%H_2-N_2 gas.

Sample #	Width (mm)	Thickness (mm)	Load (N)	Stress (MPa)
Dense I4 in Air at 750°C				
1	4.15	3.24	109.8	75.8
2	4.12	3.27	129.6	88.4
3	4.17	3.33	131.9	85.7
4	4.17	3.32	112.7	73.7
5	4.15	3.39	168.8	106.3
6	4.15	3.36	133.4	85.5
7	4.22	3.24	143.0	97.0
8	4.20	3.34	146.6	94.0
9	4.12	3.27	131.9	90.0
10	4.16	3.38	135.0	85.3
Average	4.16	3.31	134.3	88.2
Std. Dev.	0.031	0.056	16.7	9.6
Dense I4 in Reducing Atmosphere for 2 hrs				
1	4.16	2.26	67.8	96.0
2	4.16	2.18	118.8	180.6
3	4.15	2.24	167.2	241.2
4	4.13	2.24	53.0	77.0
5	4.17	2.30	88.2	120.2
Average	4.15	2.24	99.0	143.0
Std. Dev.	0.015	0.043	45.4	67.3
Dense I4 in Reducing Atmosphere for 7 hrs at 750°C				
2	4.19	2.20	115.5	171.2
3	4.15	2.18	61.8	94.3
4	4.23	2.32	74.5	98.4
5	4.14	2.22	131.0	192.9
Average	4.18	2.23	95.7	139.2
Std. Dev.	0.041	0.062	32.8	50.3
Support Span	40.0 mm			
Load Span	20.0 mm			
Upper Fixture Mass	0.202 N		20.6 g	
Xhead rate	5.0 mm/min			

Additional tests were performed to determine if creep is affecting the ability to measure slow crack growth behavior of dense I4 bend bars in a reducing atmosphere at 800°C. Larger-sized bend bar samples, previously checked for defects by scanning acoustic microscopy (SAM), were tested using a fast stressing rate after holding for either two or seven hours at 800°C in a

reducing atmosphere. Smaller-sized bend bar samples were also tested using the fast stressing rate after holding for seven hours at 800°C in a reducing atmosphere. The results are presented in Table 24-8. The reported strength data for the small sample bars was corrected by a factor of 0.948 to account for the Weibull scaling statistics. This allowed reporting of the strengths for the smaller samples as the equivalent strength on the same size basis as the larger samples.

Table 24-8. Results for fast stress rate tests on I4 sample bars exposed to a reducing atmosphere at 800°C.

	Creep Strength (MPa)	
Reducing Atmosphere Hold Time (hours)	Large-Size Sample Bar	Small-Size Sample Bar
2	103.9±4.8	142.9±23.3
7	72.5±10.7	

The predicted strength for all the samples held for only two hours is significantly higher than the samples held for seven hours. While the difference in strength may not point to a creep-related effect on slow crack growth, these initial results indicate that there may be some type of aging affect influencing the strength of I4 in the reducing atmosphere. Also, I4 does exhibit a phase transition near 800°C in air. Such a phase transition may also occur near 800°C in a reducing atmosphere, which could influence the strength behavior of I4.

Elastic Moduli Property Testing

The elastic moduli (shear and Young's) were measured for two different reformulated samples. Rectangular bars of each formulation are used to measure the elastic properties as a function of temperature up to 1100°C using an acoustic resonance technique.

All samples were initially tested in a room-temperature test rig. The shear modulus is obtained by contacting ends of the sample (via the length dimension) with two transducers at opposite diagonal corners. The sample is then vibrated via a frequency generator that sweeps a sine wave from 1 Hz to 35,000 Hz for five cycles, resulting in a torsional mode of vibration. The Labview computer program then performs a FFT analysis to yield a plot (amplitude versus frequency) of the resulting vibration signal from the sample. The fundamental frequency at which the sample vibrates (a high-amplitude peak) is used with the sample dimensions to calculate the shear modulus of the sample.

The sample is also vibrated in a longitudinal mode, where the two transducers are placed in the mid-width and mid-thickness locations on the lengthwise ends of the sample. The sample is then vibrated using the same 1Hz to 35000Hz frequency range to obtain the amplitude versus frequency plot. The high-amplitude peak representing the fundamental frequency of vibrates for the longitudinal mode is the used to compute the Young's modulus of the sample.

The room-temperature results for the formulated samples are shown in Table 24-9. Varying the percentage makeup of the formulation resulted in only a slight decrease in the elastic properties.

Table 24-9. Elastic moduli results for samples at room temperature.

Sample ID	Shear modulus (GPa)	Young's modulus (GPa)	Poisson's ratio
A	80.8±1.24	207.4±3.0	0.28±0.02
B	79.5±1.8	204.5±1.7	0.29±0.03

Elevated temperature tests are performed by first machining two small slits into the end of the sample, enabling suspension of the sample into a furnace by single-crystal sapphire fibers (0.007" dia). These fibers are glued to the transducers mounted above the furnace and function as wave guides to send and receive vibrations from the test sample. For longitudinal-mode tests, the slits are machined through the thickness of the sample at the mid-width location on the lengthwise ends of the sample. For the torsional mode, the slits are moved out to the opposing diagonal corners of the sample.

Samples were tested as a function of temperature by vibrating them at room temperature, 400°C, 600°C, 750°C, 850°C, 900°C, 950°C, 1000°C and 1100°C. The samples were heated to each test temperature at a rate of 1°C/min and were allowed to remain at each temperature for 10 minutes prior to vibrating the samples. Measurements were repeated at the same temperature points as the sample was cooled to room temperature using the same 1°C/min rate.

Figure 24-36 depicts the resulting shear and Young's moduli as a function of temperature. The Young's modulus decreased nearly linearly from ~209 to ~163 GPa at 1100°C. Results from cooling the sample to room temperature revealed no hysteretic behavior. Figure 24-36 also shows the results for the shear modulus as a function of temperature. The shear modulus also

exhibited linear behavior without any hysteresis and decreased from ~85 to ~65 GPa as the temperature increased from 24°C to 1100°C. The detailed data are presented in Table 24-10.

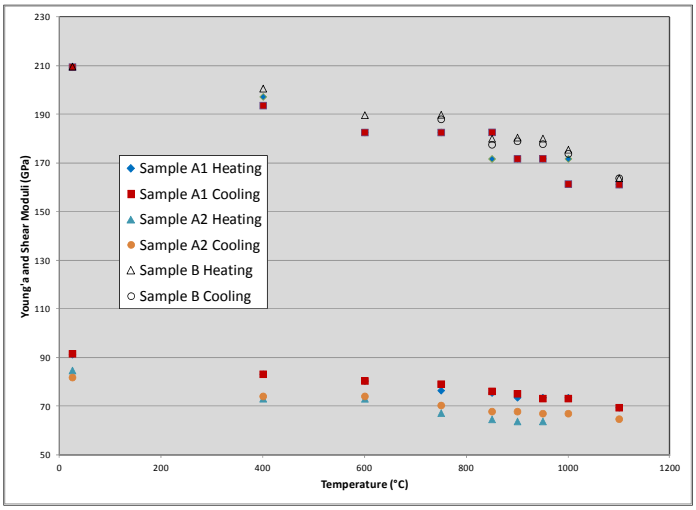

Figure 24-36. Young's and Shear moduli as a function of temperature.

Table 24-10. Young's and shear moduli as a function of temperature.

	Sample A.1		Sample A.2		Sample B	
Temperature	Shear Modulus	Young's Modulus	Shear Modulus	Young's Modulus	Shear Modulus	Young's Modulus
°C	(GPa)	(GPa)	(GPa)	(GPa)	(GPa)	(GPa)
25	91.30	209.46	84.77			209.76
400	83.24	197.30	73.19			200.71
600	80.43	182.63	73.14			189.79
750	76.50	182.70	67.28			189.95
850	75.53	171.77	64.70			180.11
900	73.59	171.80	63.85			180.56
950	73.59	171.80	63.84			180.15
1000	73.57	171.80				175.59
1100	69.46	161.23			64.77	163.82
1000	73.25	161.47			67.03	173.88
950	73.25	171.82			67.03	177.87
900	75.20	171.79			67.87	179.05
850	76.19	182.72			67.87	177.62
750	79.16	182.65			70.39	188.08
600	80.48	182.68			74.12	
400	83.24	193.70			74.12	
25	91.67	209.53			81.89	

For formulated samples "B," there is a slight indication that a phase transformation occurs ~850°C. Resonant measurements would need to be performed using smaller temperature increments to get a more accurate assessment of the transition temperature. For 100% I4

samples, this transition occurs at ~830°C. For the ”A” samples measured, there is no indication of a phase transformation. Given the limited number of samples tested, such a phase transformation cannot be ruled out. Additional testing may still detect the occurrence of a phase transformation, perhaps by using smaller temperature increments during testing.

Introducing slits into the sample for the elevated temperature testing results in a slight shift in the measured frequency, which does not have a strong affect on the measured moduli. However, a slight shift in frequencies for both the Young's and shear moduli can have a large affect on the calculated Poisson's ratio. While the room-temperature measurements (without slits) yielded a Poisson's ratio of 0.28, the elevated-temperature testing (with slits) yielded Poisson's ratios that ranged from 0.10 to 0.19.

Additional Mechanical Property Testing of Materials and Modules

Additional tests were conducted to provide data to assess the lifetime and reliability of ITM Oxygen modules, in particular to assess the creep life of ITM Oxygen modules. This data includes the creep rates of representative ITM Oxygen materials and modules under accelerated conditions. This additional testing included the following three tasks:

1) Measurement of the creep properties of ITM Oxygen membrane materials as a function of temperature and porosity
2) Measurement of the creep of a multi-wafer ITM Oxygen submodule.

The data generated in each of these tasks is needed to assess the mechanical reliability of ITM Oxygen modules under service conditions. Measurement of the creep allows the creep rates of the ITM Oxygen membrane material to be estimated under service conditions. These creep rates, coupled with the elastic properties reported under Task 14, would then in turn be used in finite element mechanical models to predict the creep performance of the modules after long-term operation. These finite element models will be developed after the end of this cooperative agreement. Measurement of the creep of multi-wafer submodules will allow comparison of the model to experimental results and further refinement of the model.

1. Measurement of the Creep Properties of ITM Oxygen Membrane Materials

The creep rates of ITM Oxygen materials were determined by measuring the creep rates of rectangular bars in flexure. Ceramatec, Inc. prepared these bars with a range of porosities so the effect of porosity on the creep rate could be determined. Porosities ranged from 0-14% open

porosity. Creep rates were measured while controlling two different parameters in the following manner: 1) three stress levels were used to assess the stress dependency of the creep rate; and 2) a range of temperatures was used to determine the activation energy of creep. Figure 24-37 shows the normalized creep rates measured at a single temperature for a range of porosities.

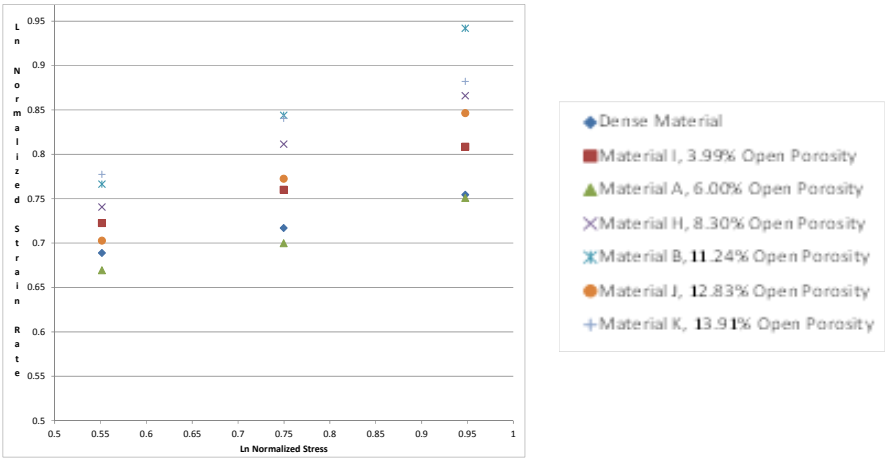

Figure 24-37. Creep rate of the ITM Oxygen material as a function of stress and open porosity. Creep rates increased with increasing stress and increasing porosity.

As expected, the creep rate increased with increasing stress level. Creep rates also accelerated with greater porosity. Figure 24-38 shows the creep rate of Material K at multiple temperatures. The measured activation energy was 337-407 kJ/mol.

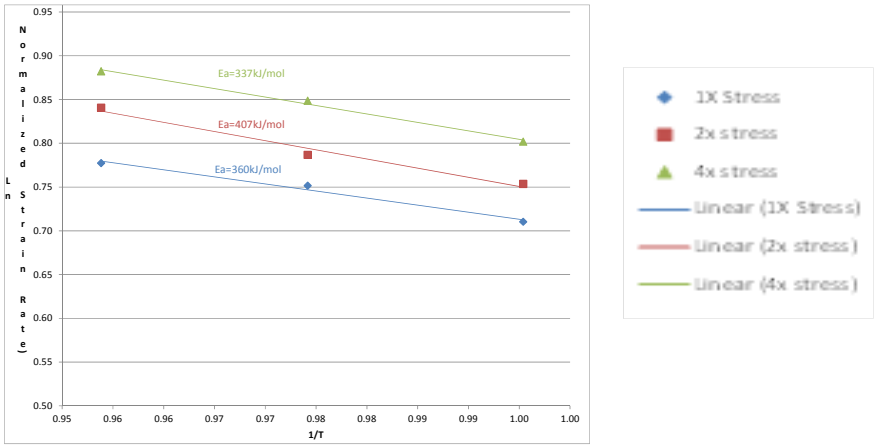

Figure 24-38. Arrhenius plot of the creep rate of Material K at three stress levels. The creep rate increased with increasing temperature with activation energy of 337-407 kJ/mol.

2. Measurement of the Creep of a Multi-Wafer ITM Oxygen Submodule

To determine how much modules would creep under service conditions, Penn State constructed an apparatus to measure the creep rate of 1-12 wafer submodules when an axial load was applied at elevated temperature. Typically, submodules consisting of 12 wafers were crept under an axial load. Ceramatec, Inc., supplied the submodules for testing. The submodule was located inside a furnace that kept the submodule at a uniform temperature. The axial load could be varied during the experiment. A typical load equaled the load that the module would experience due to the pressure exerted by the feed air pressure during service. The load was applied using an Instron®.

To accelerate the creep rate, the temperature used during creep measurement was higher than what the module would experience during actual service. The creep rate at the higher test temperature could then be scaled to the expected service temperature using the activation energy measured for the flexural bars. Extensometers contacted the submodule during creep measurement so the creep rate could be measured continuously. The submodule leak rate was measured before and after creep measurement to determine if the submodule was damaged by the creep, resulting in an increased leak rate. Figure 24-39 shows the testing apparatus with a loaded submodule.

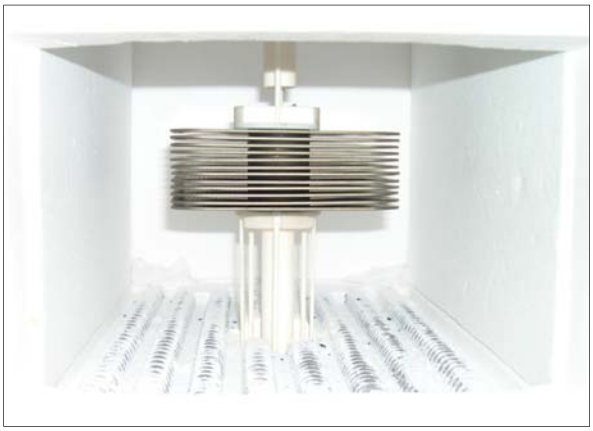

Figure 24-39. Photograph of submodule loaded into the furnace to perform compressive creep test at up to 970°C.

Figure 24-40 shows the normalized strain versus time for Submodule TMLB3148 at three stress levels and an accelerated test temperature. The measured compressive creep stress exponent was 1.45. The submodule was then cooled to ambient temperature and the leak rate was measured.

The leak rate was found to be essentially unchanged after the creep test.

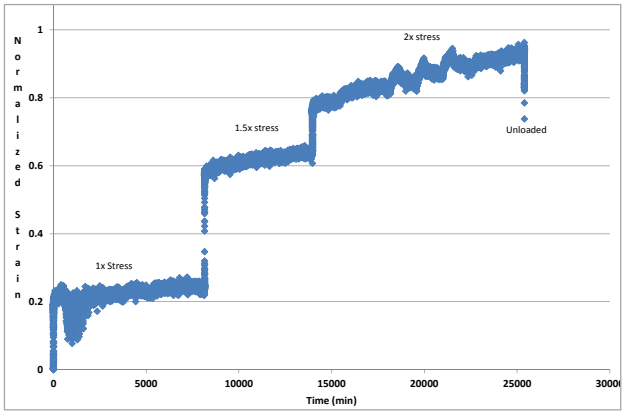

Figure 24-40. Strain as a function of time measured at three stress levels for Submodule TMLB3148. The creep rate increased with increasing stress.

Submodule TMLB3134-2 was creep tested at a higher temperature than Submodule TMLB3148. The creep strain of TMLB3134-2 versus time at a constant stress level is shown in Figure 24-41. The creep rate was fairly constant during the test. The submodule leak rate following the test was unchanged.

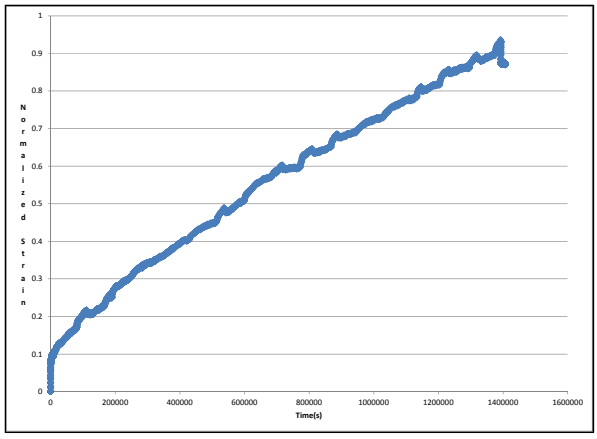

Figure 24-41. The creep rate of Submodule TLMB3124-2 at a constant stress.

Another submodule, DRBA1294, was tested under the same conditions as TMLB3134-2. The strain rate of DRBA1294 versus time at a constant stress level is shown in Figure 24-42. The experiment was repeated four times. At the end of each creep measurement, the submodule was cooled and the leak rate measured. Again, the creep rate was fairly constant during each measurement. The creep rate decreased considerably during the third and fourth measurements compared to the first two measurements. The leak rate, measured after each of the four creep

experiments, was the same – indicating that the submodule was undamaged by the creep.

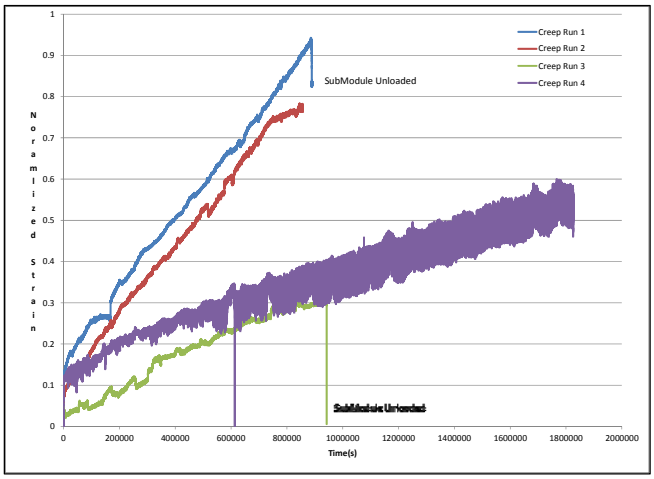

Figure 24-42. Compressive creep strain versus time curve for Submodule DRBA1294.

Three compressive creep tests under accelerated creep conditions were performed on submodule TMLB4106-02. During cooling following the third creep test, the temperature-controlling thermocouple failed at a temperature of 437°C, resulting in a more rapid cooldown to room temperature. After the furnace had cooled to room temperature, the submodule was still intact when the furnace was opened. However, thermal shock damage may have occurred.

Figure 24-43 shows a plot of the creep strain versus time plots for all three creep tests on submodule TMLB4106-02. Unlike prior creep tests of DRBA1294, submodule TMLB4106-02 did not exhibit any abrupt change in creep rate (decrease) after the second creep runs. The creep rates of TMLB4106-02 were quite consistent among the three runs.

Leak rate measurements of TMLB4106-02 after each of the first two creep runs showed an improvement by 31.6% and 54.5% relative to the starting leak rate, respectively. As expected, the leak rate after creep Run #3 was too fast to measure, most likely due to thermal shock-induced cracking caused by the furnace thermocouple failure.

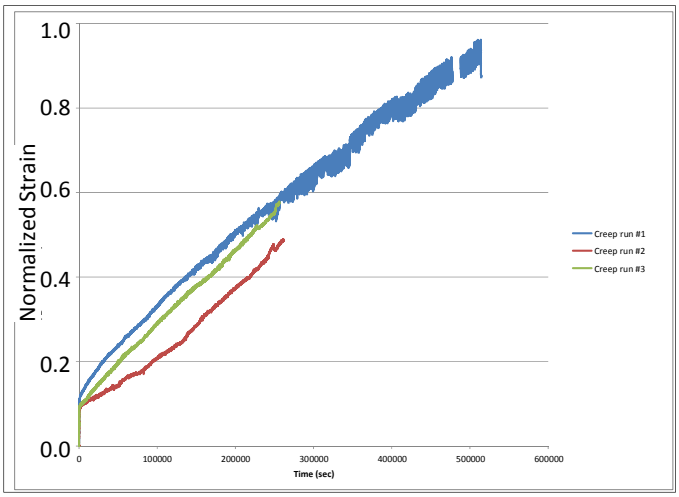

Figure 28-43. Compressive creep strain versus time plots for Submodule TMLB4106-02 tested under accelerated creep conditions for creep Runs 1, 2 and 3.

To assess changes to Submodule TMLB4106-02, such as wafer droop and wafer tilting, observations of each side of the submodule were made initially and after each creep test. Evident in the observations of the post-creep condition of the modules is modest tilting of two wafers located in the upper half of the submodule. The tilting (upward on one side, downward on the opposite side) is consistent with creep occurring at the joint under the accelerated test conditions.

TASK 25.0 TABLE OF CONTENTS

TASK 25.0 MEMBRANE AND MODULE DEVELOPMENT 2

25.0 SCOPE 2

25.0 MEMBRANE AND MODULE DEVELOPMENT 2

Background 2

Task 25.1 High-Flux Membranes 2

Task 25.2 Reliability 5

TASK 25.0 MEMBRANE AND MODULE DEVELOPMENT

25.0 Scope

The recipient team optimizes the existing planar membrane design considering gasification and pyrolysis applications. The existing planar membrane design is, in some cases, limited in oxygen flux as a result of the temperature gradients that result from the reactions on the permeate side of the membrane. The recipient fabricates test articles using existing techniques and equipment and tests these articles in lab equipment test rigs of various scales. The resulting data are used to guide the optimization and update the existing models, as required.

This task further develops methodologies to evaluate reliability and investigates the reliability impact of the operating environment imposed by the process cycles identified in Task 23.0. Non-destructive evaluation (NDE) techniques and stress modeling are employed where effectively implemented.

25.0 Membrane And Module Development

Background

Efforts to achieve and maintain high-flux membranes included minimization of contamination and changes to the ceramic wafer architecture. Feed contaminants have the potential to partially deactivate the wafer surface by either chemically reacting with the surface material or by physically shrouding or impeding gas flow to the surface.

Non-destructive testing, modeling and experimental measurements of creep were used to extend the database of known material properties to conditions pertaining to Reaction-Driven ITM for use in conversion of a broad range hydrocarbon feedstocks to syngas.

Task 25.1 High-Flux Membranes

Air Products addressed minimizing contaminants in the feed hydrocarbon feed streams by installing a bed of getter material upstream of the ITM. High-surface-area I4 was selected as the getter material since it was the most likely to remove the feed contaminants of concern to the ceramic wafer performance. Three different porous I4 getter materials were developed and fabricated for the PDU reactor syngas feed. Figure 25-1 shows the granular, cylindrical pellet and reticulated foam getter materials developed at Ceramatec. The I4 cylindrical pellets

were selected and fabricated for PDU reactor tests due to their combination of good strength and a porosity of 35 to 40%.

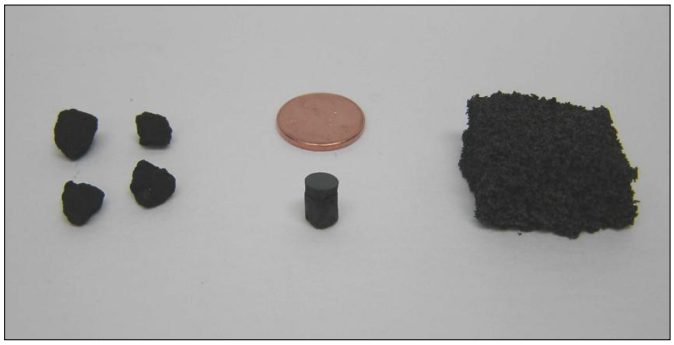

Figure 25-1. Three different I4 getter materials (left to right): granular, cylindrical pellet, and reticulated foam.

The I4 guard bed getter system was first installed in PDU Run 23. Fresh MgO guard beds were also installed on the feed air stream. Although the on-stream operating time for PDU Run 23 was not sufficient to evaluate changes in maintaining the measured oxygen flux, analytical testing was able to detect a significant change in post-run contamination levels. Post-test analyses of the modules from PDU Run 23 revealed that: a) the fresh airside MgO guard beds eliminated Cr contamination; and b) the newly installed syngas-side I4 guard significantly reduced Si contamination and eliminated Al contamination compared to the previous PDU Run 22 (Figure 25-2). Post-run guard bed analysis with inductively coupled plasma-mass spectrometry (ICP-MS) confirmed the presence of both Si and Al volatile contaminants on the used bed and its ability to scrub contaminants from the feed stream.

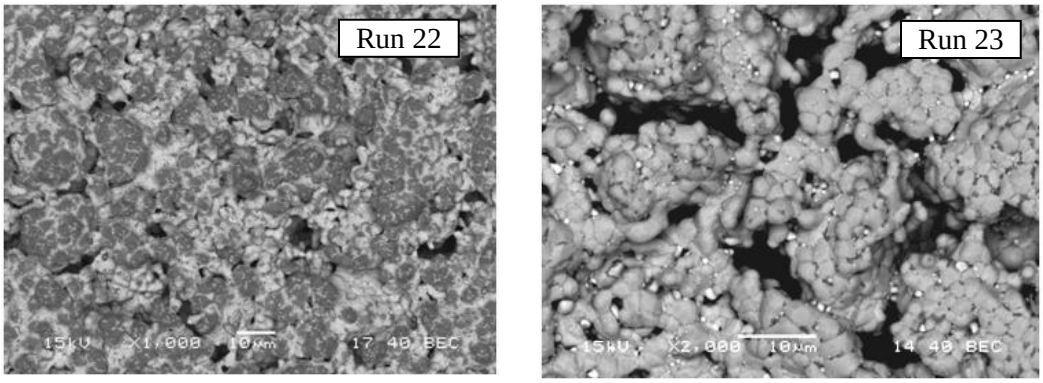

Figure 25-2. SEM images of the Housing 1 modules from Runs 22 and 23. The P-layer outer surface at the leading edge of Run 23 shows significantly reduced Si and Al contamination (dark phases) due to implementation of the syngas-side I4 guard bed

Improvements to the mixed-cell model were implemented in the effort to improve the ability of the model to predict the performance of Reaction-Driven ITM modules. A previously developed analytical model for the air-side porous layer was refined to more accurately reflect the conditions and material properties of the porous layer and the transport processes occurring within the layer. This submodel was integrated into the Fortran code of the mixed cell model, which now allows calculation of the flux enhancement due to the presence of the air-side porous layer.

The thermal phenomena described by the mixed-cell model were also reviewed, resulting in a model refinement allowing a more accurate description of the radiant heat transfer process on the syngas side. It was found that the radiation model, as well as convection parameters, greatly affects the predicted module performance and temperature profiles. The new radiant model is in closer agreement with module temperatures inferred from post-run analysis than the two radiant model options previously available in the software.

Certain aspects of actual modules, such as S1 ribs and conductive heat transfer in the axial direction, are not yet captured by the current implementation of the mixed-cell model. Some of these aspects have been previously addressed in finite element modeling using the Aspen Custom Modeler (ACM) platform; others could be addressed in similar fashion using ACM or other FEA/CFD tools. Previous work done using ACM was reviewed to determine how to integrate the insights from these studies into a design tool such as the mixed-cell model.

Although the mixed cell model doesn't accurately predict all the surface effects, it can be used to evaluate the sensitivity that proposed changes will have on wafer performance. Two such key improvements are 1) the addition of an on-membrane surface catalyst to the syngas side of the wafer, and 2) wafer modifications such as an inner porous layer.

Architectural Changes

Studies with non-catalyzed disks with various architectural modifications were done in the small-scale reactors to validate the model predictions of enhanced performance, resulting in significant flux benefits.

As reported in Task 23.3, PDU wafers and modules manufactured with additional layers were successfully demonstrated in the PDU, with results equivalent to the small-scale disk tests. Initial tests with pure I4 material resulted in high levels of material creep which, over time,

negated the initial higher oxygen flux benefit. Replacement of the I4 layer with a low-creep, porous layer formulation maintained the flux benefit with a major reduction in creep rates.

A PDU wafer module fabricated with a porous S1 layer was tested in Housing 4 of the PDU in Run 24, which began in July 2011. During initial testing, this module had an atypically high flux for a non-catalyzed module, but a more significant net flux decay. The air-side pressure drop for Housing 4 also increased with increasing flux. Post-test analysis confirmed that both the rapid flux decal and increase in airside pressure drop was due to excessive creep deformation of the porous internal S1 layers.

Task 25.2 Reliability

Task 25.2.1 Non-Destructive Evaluation (NDE) Techniques

Scanning acoustic microscopy (SAM) of green and fired PDU wafers was routinely done throughout this project to evaluate new PDU wafer designs or assembly techniques. SAM evaluation can be directly used to detect internal damage in green and fired wafers to improve the wafer yields and quality**.**

The transducer head (Figure 25-3) sends a high-frequency, ultrasonic energy pulse (typically 10 MHz and higher) into the bulk of a specimen, using water as the transfer medium. The resulting ultrasound can be reflected, scattered, absorbed, or blocked as it encounters flaws or other secondary phases. An image is generated by collecting ultrasound waves reflected back toward the transducer. Signal gating (green vertical lines in Figure 25-4) is used to discriminate ultrasound coming from different depths within the specimen.

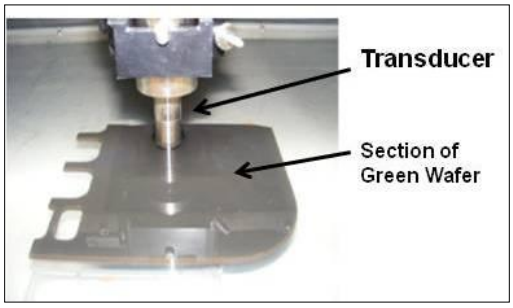

Figure 25-3. Transducer head with sample piece on a scanning acoustic microscope (SAM).

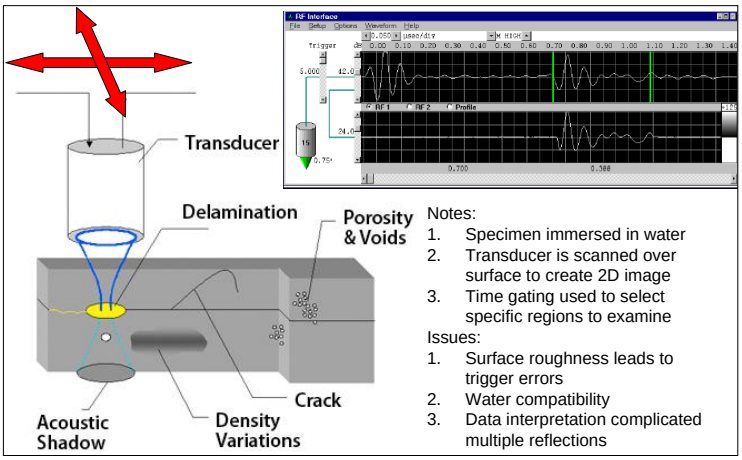

Figure 25-4. SAM sampling technique.

The most common flaws detected by SAM analysis were vertical cracks in the dense membrane layer running in the direction of the S1 slots. Figure 25-5 shows an example of these cracks in Wafer 178-19. The cracks appear as dark lines running adjacent to the ribs.

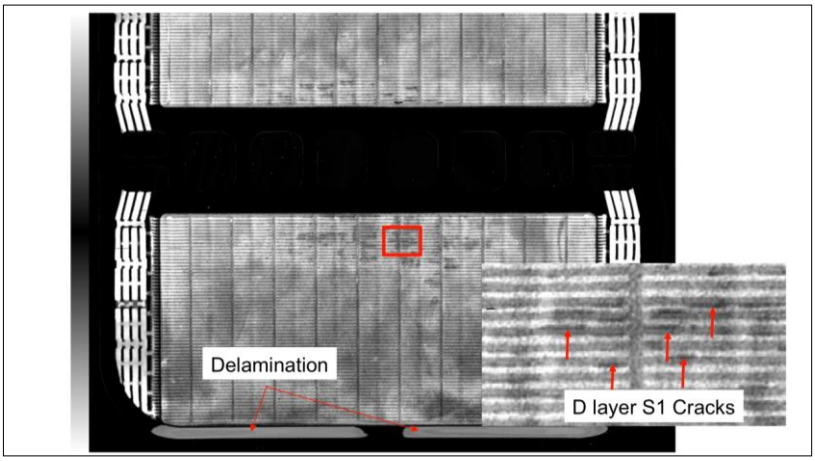

Figure 25-5. Example of S1 cracks on the air side in Wafer 178-19. The inset in the lower right represents a magnified view of the region enclosed by the red box.

Task 25.2.2 Modeling

Finite element analysis (FEA) was used to evaluate the impact of high-pressure operation on the disk wafers in the small-scale test reactors. Property data generated by Penn State (see Task 24.2) were used to develop the physical property models used in the FEA evaluation. This study evaluated the response of the baseline PDS disk to a 300 psi differential pressure using a static, linear-elastic model. The large predicted creep deformation is shown in Figure 25-6a. Figure 25-6b shows the improved creep performance achieved by increasing the S1 layer thickness

threefold, but without otherwise modifying the wafer design. Creep predictions indicate that performance can be further improved with wafer design modifications, including reorientation of the channel geometries.

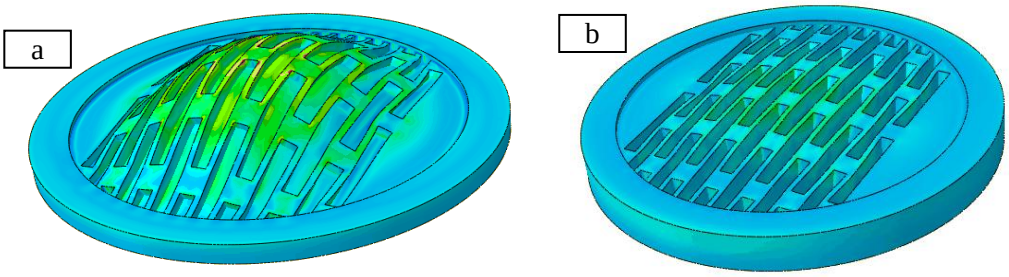

Figure 25-6. Creep deformation predictions for PDS disk wafers operating with high-pressure differentials for a) standard wafers and b) wafers with a 3X S1 layer thickness.

Several incremental model improvements were implemented in the continuing effort to enhance the ability of the mixed-cell model to predict the performance of Reaction-Driven ITM modules. The latest versions of the model still cannot quantitatively describe the fluxes observed during PDU runs, typically underpredicting the flux when the most appropriate radiation and heat transfer models are selected. The predicted oxygen vacancy void fraction sub-model was updated using input from the thermodynamic model recently developed at Penn State. The model predictions of oxygen flux have increased significantly, but it continues to underpredict oxygen flux values measured in the PDU.

Task 25.2.3 Experimental

Based on the favorable material properties and initial flux rates described in Task 24.1, formulated materials were identified as excellent candidates for Reaction-Driven ITM applications. Stronger formulated materials have the potential to address the temperature limitations of the current I4 ITM ceramic material. A series of formulated test pieces was fabricated at Ceramatec to evaluate key physical performance parameters.

Figure 25-7 shows the creep rate response to an imposed stress for a series of pure and formulated test pieces at 950°C. The creep resistance of porous I4 is ~7X lower than dense I4. However, adding 37.5% or 50% alternative material to the I4 increases the creep resistance of the porous material to a level equivalent to dense I4. This result indicates that porous formulations can be

substituted for dense I4 materials in the ITM wafer design with equivalent creep performance. In addition, the creep rate of dense formulations is about an order of magnitude less than for dense pure I4, which provides the opportunity for enhanced dense layer performance. As expected, adding alternative material at a concentration of 25%, less than the percolation threshold limit, has no significant impact on creep resistance.

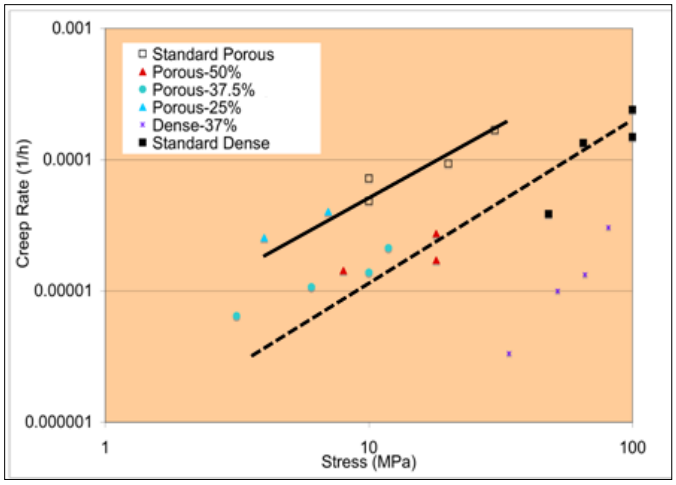

Figure. 25-7. Creep rate test results for formulated materials at 950°C.

Figure 25-8 shows the impact of added alternative materials on strength at room temperature. Adding an alternative material increases the strength of dense I4 material by 10-15%. The impact on the strength of porous materials is much more significant, increasing the strength two- to threefold.

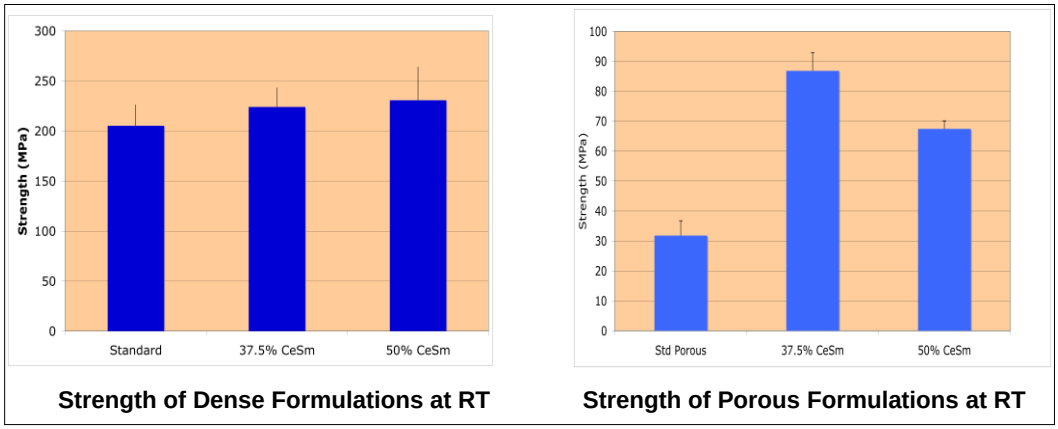

Figure. 25-8. Strength test results for formulated materials at 25°C.

TASK 28.0 TABLE OF CONTENTS

TASK 28.0 CERAMIC MATERIALS AND MANUFACTURING DEVELOPMENT FOR INDUSTRIAL AND CCS APPLICATIONS 3

28.0 SCOPE 3

28.1 ADVANCED MATERIALS AND CHARACTERIZATION 3

Background 3

28.1.1 Materials Development for Industrial and CCS Applications 3

Reactivity with CO_2 4

Phase Stability 5

Amenability to Ceramic Processing 5

28.3 Materials Characterization 6

28.1.3.1 High-temperature materials properties 6

28.1.3.3 Evaluation of materials stability in reactive environments 43

28.2 ADVANCED MODULE DEVELOPMENT 44

Background 44

28.2.1 Wafers 46

Materials Selection 46

28.2.1.1 Wafer process refinement 52

28.2.1.2 Advanced wafer process development 55

28.2.2 Submodules 65

28.2.2.1 Thermal cycle requirements 65

28.2.2.2 Joining improvement 65

28.2.3 Modules 66

28.2.3.1-2 Thermal cycle requirement and Joining improvement 66

28.3 MANUFACTURING PROCESS DEVELOPMENT AND SCALE-UP 67

Background 67

Cerfab 67

28.3.1 Materials recycling processes 68

28.3.2 Tape Casting 69

28.3.3 Advanced membrane preparation 70

Milling..... 70
28.3.4 Joining cycle time reduction..... 74
28.3.5 Module post-joining conditioning..... 75
28.3.6 High-throughput wafer inspection..... 75
28.3.7 Optimize parts cleaning processes..... 76
Kiln Furniture Cleaning..... 76

PHASE V RESULTS AND DISCUSSION

TASK 28.0 CERAMIC MATERIALS AND MANUFACTURING DEVELOPMENT FOR INDUSTRIAL AND CCS APPLICATIONS

28.0 Scope

Task 28.0 is focused on development of advanced ceramic membrane materials, characterization of those materials, and development and characterization of advanced membrane structures advantageous for applications to industrial and CCS processes.

28.1 Advanced Materials and Characterization

Background

Air Products and Ceramatec instituted quality control measurements to ensure the powder and the metal oxide blends were within specification and to analyze new materials being developed under this task. Wavelength dispersive X-ray fluorescence (WDXRF) spectroscopy was used to analyze powder samples and metal oxide blends. WDXRF is a variation of X-ray fluorescence (XRF) spectroscopy, in which X-rays incident on a sample excite photons with energies characteristic of the atoms in the sample. The WDXRF technique further splits the photon emission into characteristic wavelengths for broader and more rapid simultaneous elemental analysis of solid samples.

Dilatometry experiments were conducted to determine the differential strain between a "reference bar" and ITM component parts at various rates of temperature increase. The data were used to identify differences in component behavior, refine finite element analyses and assess changes in component geometries and structures to minimize stress. The work was instrumental in specifying the joining cycle and operational temperature ramp rates and the design of the ITM component parts.

28.1.1 Materials Development for Industrial and CCS Applications

Air Products prepared and characterized alternate ITM Oxygen membrane materials. Specific screening tests were carried out for a number of candidate compounds. Such tests include reaction with environmental contaminants, phase stability, and amenability to ceramic processing.

Reactivity with CO_2

For example, an investigation was conducted to determine the potential reactions between Material A with CO_2 by annealing its powder and pellet forms in an atmospheric gas blend of CO_2, O_2, and N_2. Two temperatures were investigated. After annealing, the powder samples were analyzed by XRD and the pellets were analyzed by SEM/EDS. The as-synthesized and heat-treated samples possessed identical diffraction patterns. There were extra satellite peaks indicating the presence of a reaction with CO_2 only at the Temperature 2 condition. The presence of reaction products (3.1% by weight of the total sample) was clear evidence that Material A reacted with CO_2. No reaction was observed at Temperature 2. Table 28-1 documents the XRD refinement data for the three samples.

Table 28-1. Compilation of the XRD refinement data of constituent phases (wt%) of the Material A samples used for CO_2 reaction study.

	As-synthesized	**Temp 1-500hrs**	**Temp 2-500hrs**
Perovskite	100	100	94.8
CO_2 rxn product	0	0	3.1
2^{nd} phase	0	0	2.1

SEM/EDS analysis was employed to examine the microstructure and chemistry of the samples. The surface of the Temperature 1 sample showed numerous nano-sized dot features. The chemistry associated with these dots could not be accurately confirmed, but XRD results indicate that the nano-sized dots were likely the CO_2 reaction products.

Another perovskite-family material was annealed in a CO_2-containing gas mixture for 500 hours. XRD spectra obtained for the annealed material showed strong characteristic peaks that were attributed to the cubic phase. Weak-intensity peaks strongly indicated the occurrence of a reaction or phase change. The constituent phases were identified and their relative weight percentages were determined. The material did not react with CO_2 but experienced a phase change. These results cast doubt on the practicability of these compositions for industrial application.

Phase Stability

The phase stability of three additional perovskite compositions was examined. The samples were annealed in ultra-pure cylinder air at Temperature 1 for 500 hrs. The air-annealed samples were subjected to XRD analysis, and results were compared with those for the starting material. The data indicated the presence of additional phases in two of the compositions, but the third composition had minimal changes in the XRD spectrogram. The improved stability of that material can be attributed to tailoring the cation stoichiometry.

A newly reported perovskite composition that had the potential for low-temperature operation was synthesized. The complex XRD patterns strongly indicated that the powders were not phase-pure, which implied a difficulty in producing phase-pure cubic material.

Amenability to Ceramic Processing

A perovskite material was screened and produced as an alternate membrane material. Tape casting techniques were used to fabricate the membrane. The samples were bisque fired to remove organic ingredients, then sintered. Figure 28-1 shows the post-sintered film.

Figure 28-1. A photograph of the pervoskite sample after sintering.

Another perovskite material in the AP2k family was screened as an alternate membrane material. To study its oxygen permeation properties, a dense and preferably thin membrane was needed. The material was sintered and a dense membrane was successfully produced (Figure 28-2).

Figure 28-2. Sintered perovskite material.

28.3 Materials Characterization

28.1.3.1 High-Temperature Materials Properties

Background

The ITM material, like most materials, expands when heated. Unlike most materials, however, at a constant temperature, the ITM material contracts with increasing oxygen partial pressure and expands with decreasing oxygen partial pressure. In the presence of an oxygen partial pressure gradient, a differential expansion can be produced that results in a mechanical stress. This is analogous to the stress produced by a temperature gradient in conventional materials. To perform mechanical analysis of membrane modules and to predict stresses in advanced membranes during operation, an understanding is needed of the expansion behavior of the ITM membrane material as a function of temperature and oxygen partial pressure.

The rate of expansion or contraction when there is a change in oxygen partial pressure is dependent upon oxygen transport properties. Conversely, the transport properties can be determined (calculated) from expansion/contraction data at various step changes in partial pressure. The ITM properties of most interest are the solid-state diffusion rate and the surface reaction rate. The solid-state diffusion rate is a function of the intrinsic properties of the material: the temperature and the diffusion length, a measure of the distance an oxygen atom travels via vacancy migration to reach a surface (e.g., dense versus porous). The length scale determines how fast a structure comes to equilibrium after a P_{O2} or temperature change.

Transport properties are most accurately determined when either the surface reaction or solid-state diffusion is the dominant resistance. There will be certain conditions of temperature and dense layer thickness where both resistances can be significant. Fitting both parameters simultaneously

is possible, but it reduces the confidence of the fit. Better estimates of the transport parameters can be made when only one parameter needs to be fitted. To determine which resistance is dominant, the solid-state diffusion resistance can be modified by changing the dense layer thickness; the surface resistance can be modified by using a porous surface layer to increase the surface area and hence the rate of the surface reaction. Under conditions where the solid-state diffusion resistance is dominant, adding a surface porous layer should not change the transient response time, and the response time should be proportional to the square of the dense layer thickness. Under conditions where the surface reaction is dominant, the transient response time should not depend on the dense layer thickness, and the addition of a porous layer to the surface should decrease the response time.

Experimental Method

Air Products conducted dilatometry experiments to determine the rate at which a sample (e.g., bar) achieved oxygen vacancy equilibrium when subjected to a step changes in oxygen partial pressure. The data were used to calculate transport properties. After the test specimen was placed underneath the measuring rods, a flow of gas with a specific composition (typically air, 99.5% nitrogen/0.5% O_2 or 100% oxygen) was started. The flow was continued and the temperature was increased to a specific (and constant) value. The specimen was allowed to reach its equilibrium expansion. The gas composition was then changed, and the change in strain was measured as a function of time.

Impact of Porosity on Length Scale

Air Products used transient dilatometry to calculate the length scales of porous ITM materials. Length scale, coupled with material strength and creep resistance, was used to select appropriate designs for the wafer, base piece and end cap.

High-open-porosity materials have smaller length scales than lower-open-porosity materials. Lower length scales and faster response times produce lower module stresses during operational transients.

Classified AP2k powder cuts were used to control sample open porosity over a range. The addition of fine powder to the classified powder reduced the open porosity. Figure 28-3 shows a microstructual comparison over a porosity range.

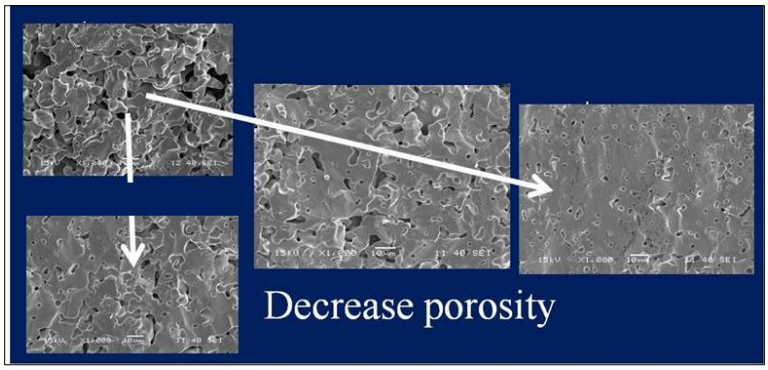

Figure 28.1-3. Examples of sample porosity.

The samples were heated to temperature and the gas was switched from 0.5%O_2/N_2 to 100% O_2. Figure 28-4 shows the transient oxidation response (switching to 100% O_2) of the samples at 300°C. At these conditions the response time scaled with open porosity. In this graph, the zero value is the sample length in 0.5%O_2/N_2. The normalized expansion is equal to the strain divided by the strain at 100% O_2.

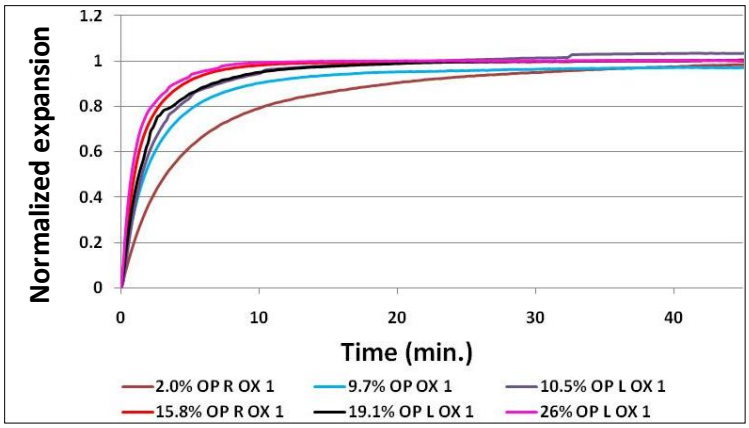

Figure 28-4. Oxidation transient response at 300°C of AP2k bars with 2%-26% porosity.

The response time during oxidation was coupled with diffusivity data at 300°C to calculate the effective diffusion length scale of the samples. Transient data at 350°C was used to calculate the length scales over the 2%-15.8% porosity range. Length scales for samples with porosity >15.8% could not be calculated because the response time was limited by the gas switching time in the dilatometer. This means the length scales were <27µm for porosities >15.8%. Figure 28-5 shows the length scales as a function of open porosity.

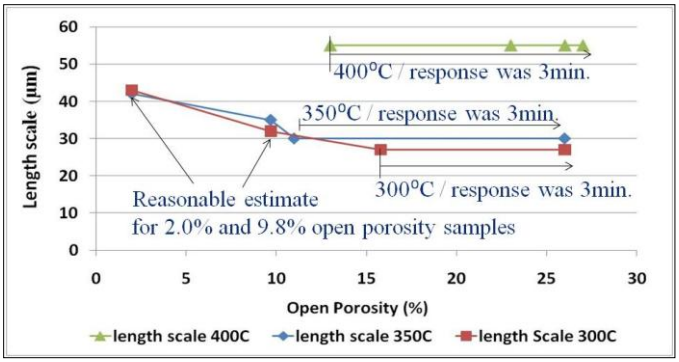

Figure 28-5. Length scale as a function of open porosity.

Impact of Geometry and Composition

Air Products performed a series of transient dilatometer experiments at various temperatures to determine the transport properties of AP2k and support the development of advanced architecture structures.

A standard series of P_{O2} step changes was performed such that the parts were subjected to alternating reduction and oxidation steps, as follows:

1. 1 atmosphere O_2 - 0.005 atmosphere O_2
2. 0.005 atmosphere O_2 - 1 atmosphere O_2
3. 1 atmosphere O_2 - 0.209 atmosphere O_2
4. 0.209 atmosphere O_2 - 1 atmosphere O_2
5. 1 atmosphere O_2 – 0.03 atmosphere O_2
6. 0.03 atmosphere O_2 - 1 atmosphere O_2
7. 1 atmosphere O_2 - 0.005 atmosphere O_2
8. 0.005 atmosphere O_2 - 1 atmosphere O_2

The seventh step is a repeat of the first step and the eighth step is a repeat of the second step. These repeats determine if any changes in transport properties occur during the experiment. The rate of change in expansion/contraction as a function of time was used to calculate the transport properties of the sample. The following are examples of some of the work performed to determine transport properties.

Figure 28-6 compares the transient response of an composite bar of porous, dense, and slotted layers following two step changes (steps 2 and 8) in P_{O2} from 0.005 atm to 1 atm (oxidation) at

300°C. In this graph, the normalized expansion is equal to 1- (strain/strain at 100% O_2). The response curves are very similar, indicating that the solid-state diffusion did not change measurably during the course of the experiment.

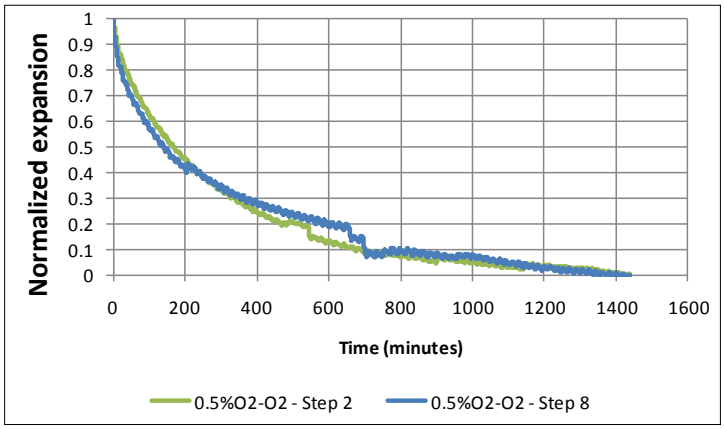

Figure 28-6. Transient response of a composite bar at 300°C to a step change in P_{O2} from 0.005 atm to 1 atm (oxidation step).

Figure 28-7 compares the transient response of three composite bars, two with combinations of porous, dense and slotted layers but differing in thickness, and one with dissimilar porous layers to that of a reference porous bar under a step change in P_{O2} from 0.005 atm O_2 to 1 atm O_2 at 350°C. In this graph, the normalized expansion is equal to 1- (strain/strain at 100% O_2).

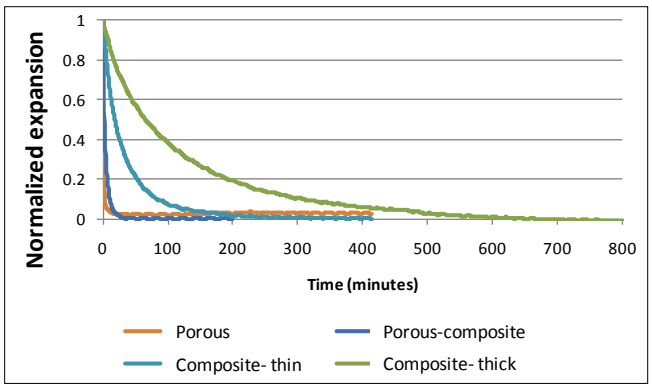

Figure 28-7. Transient response of a porous composite bar, a thick and thin porous-dense-slotted layer composite, and a porous bar at 350°C to a step change in P_{O2} from 0.005 atm to 1 atm.

The response times scaled with the square of the dense layer thickness, indicating that solid-state diffusion is the dominant resistance. The same behavior was true at 400°C (not shown).

Figure 28-8 compares the transient response of a thick composite bar and a porous bar to a step change in P_{O2} from 0.005 atm O_2 to 1 atm O_2 at 450°C. In this graph, the normalized expansion is equal to 1- (strain/strain at 100% O_2). The chemical diffusion coefficient was fitted to the transient response.

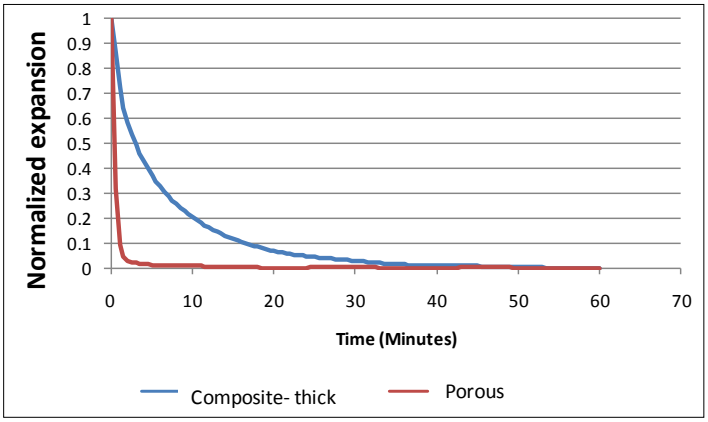

Figure 28-8. Transient response of a composite bar and a porous bar at 450°C to a step change in P_{O2} from 0.005 atm to 1 atm.

Additional work was conducted with thicker bars to allow measurement of the transport properties at 450°C and 700°C. Figure 28-9 compares the transient response of Bar H at 700°C following the step changes in P_{O2} from 1 atmosphere to lower P_{O2}. In this graph, the normalized expansion is equal to 1- (strain/strain at final O_2 concentration). Note that both strain values are negative. Of particular note is that the two steps in P_{O2} to 0.005 atmospheres produced the same result, demonstrating that no decay in transport properties occurred over the course of the experiment.

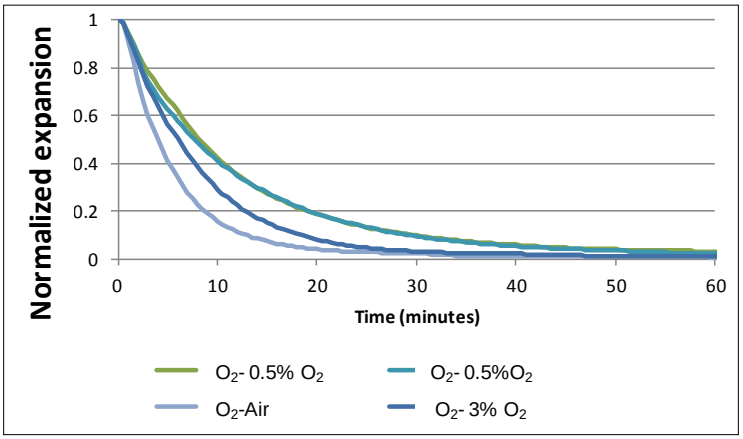

Figure 28-9. Comparison of the transient response of Bar H to step changes in P_{O2} from 1 to 0.005 atm, 0.03 atm and 0.21 atm.

Other experiments were conducted, in part, to assess the reproducibility of results. Figure 28-10 compares the calculated diffusivity of three bars of Composition D. Agreement is good, especially at the higher oxygen partial pressures.

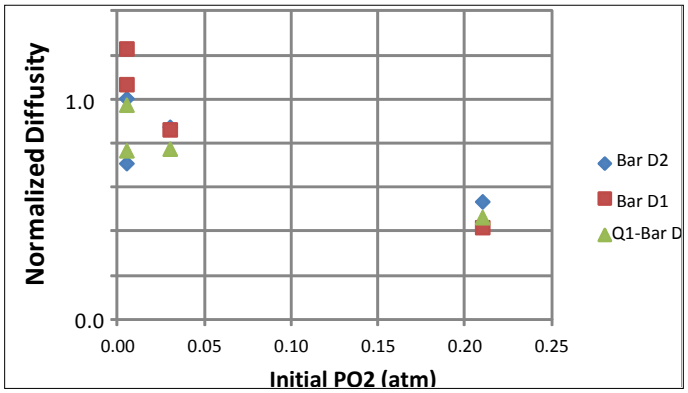

Figure 28-10. Comparison of diffusivity measured at 550°C as a function of initial P_{O2}.

The transient response of bars of different composite was measured at various temperatures. An Arrhenius plot of the calculated oxygen vacancy diffusivity, D_v, with temperature (Figure 28-11) had an excellent fit.

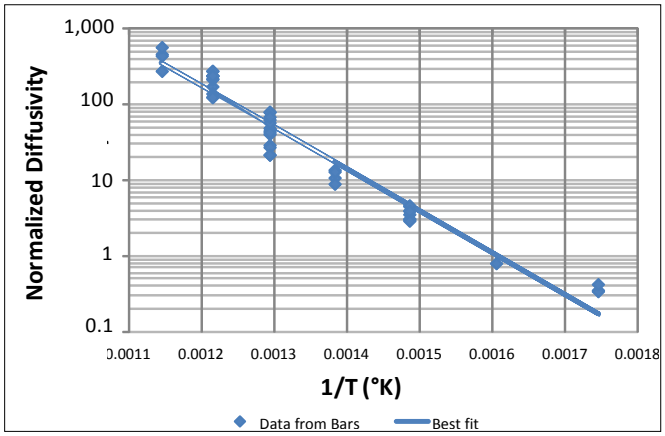

Figure 28-11. Arrhenius plot of oxygen vacancy diffusivity.

Image J Length Scale Distribution in Porous Layers

The transient dilatometer results suggest that some materials have a length scale distribution. Wafers are composed of dense, slotted and porous layers. Transient dilatometry of wafers

indicated that there was a range of length scales within a wafer. The transient response of some wafers did not fit the expansion model using a single length scale.

Public domain software called Image J is used for analyzing digital images. A large community uses the software, and there are several supporting macros. The software was used to turn SEM images of selected porous materials into simpler images amenable to analysis. The software was then used to create a network of Voronoi cells around each of the pores in the porous structure identified in the simple image. A Voronoi cell is defined here as the locus of points equidistant between the perimeters of the nearest pores. The distance between the pore boundary and the Voronoi cell boundary was considered to be the diffusion length scale. Figure 28-12 depicts the pores (solid black) and the Voronoi cells (black lines) for a hypothetical 2-D porous solid.

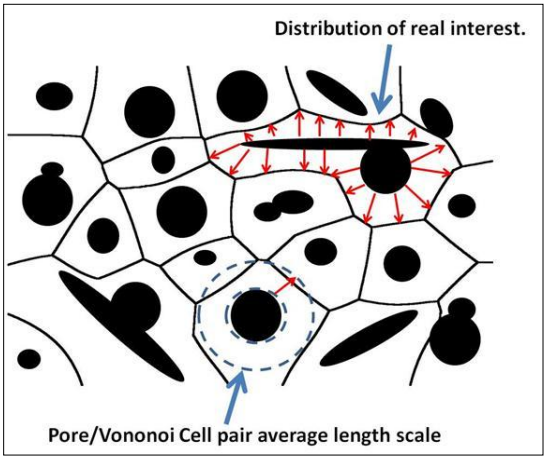

Figure 28-12. Hypothetical porous network showing the pore/Voronoi cell pair average length scale approach and a distribution of length scales that would better represent the length scale.

Figure 28-13 shows the progression for a selected porous material.

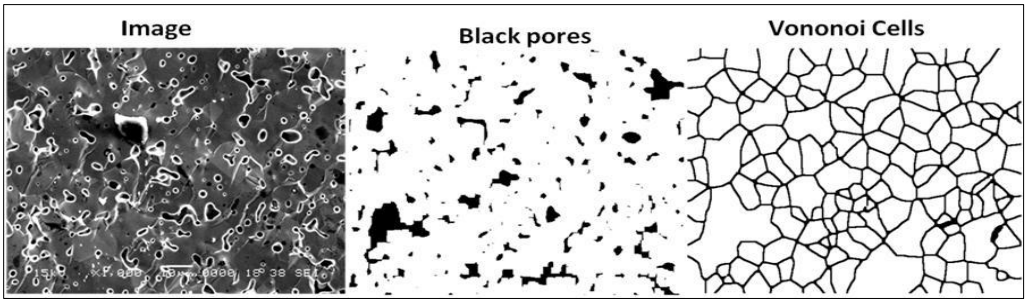

Figure 28-13. Image progression using Image J software to create a Voronoi cell network around all pores in the microstructure. The Voronoi cells were considered to be diffusion boundaries for each of the pores.

The Voronoi cell approach is a reasonable analog for diffusion length scale, as the software measures the pore area and the Voronoi cell area. If enough pore/Voronoi cell pairs are measured, a length scale distribution can be plotted. Figure 28-14 shows the length scales measured in the image shown in Figure 28-13.

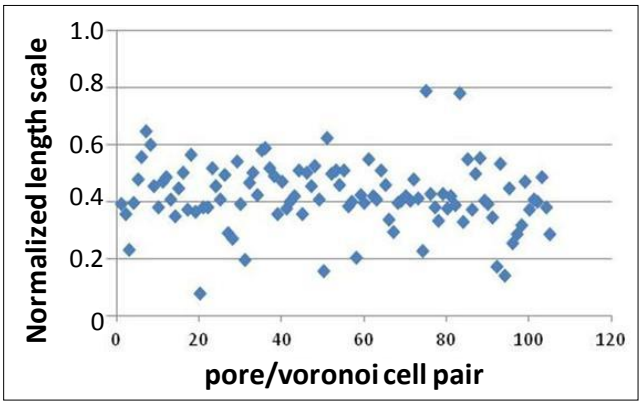

Figure 28-14. Length scale measurements for the microstructures in Figure 28-13. Each data point represents the measurement for one pore/Voronoi cell pair.

Air Products found that a processing function within Image J called "Distance" produced much better results. This function creates a grayscale image where the pixels closest to a pore would be the lightest gray and those farther away would be darkest gray. The grayscale pixel data were processed using Microsoft™ Excel, with the shades of gray assigned a corresponding diffusion distance. Figure 28-15 shows the normalized data.

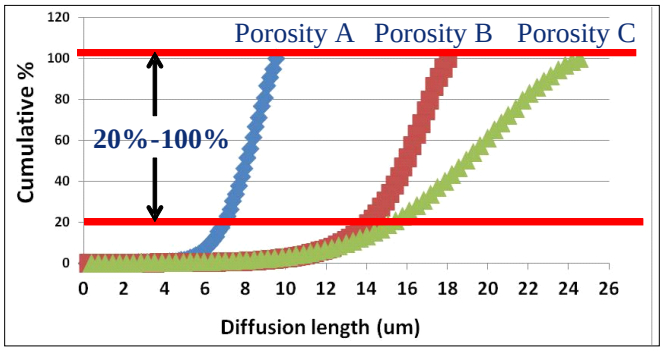

Figure 28-15. Normalized diffusion distances for materials of different porosities.

The diffusion distance scales with open porosity. The distributions were somewhat skewed, with the smaller lengths having less contribution. This makes sense spatially, since the smaller lengths

would be near the pores themselves and the pores have a finite number per image. Therefore, 20%-100% of the distribution is a reasonable range over which to determine the diffusion range.

Sample preparation was often the key to good results. The porous samples were infiltrated with Buehler cold-mount epoxy by first pulling a vacuum and then dropping the samples into the epoxy. This ensured the open porosity was fully infiltrated. The software was used to calculate the total black area in the image (open porosity). This porosity was consistent with the open porosity for the samples measured using the Archimedes method. The epoxy-filled samples were polished, and SEM images were taken in backscatter mode to accentuate the contrast between the epoxy and the AP2k.

The diffusion lengths measured using the grayscale technique were compared to the diffusion distances measured using transient dilatometry. Figure 28-16 shows the comparison.

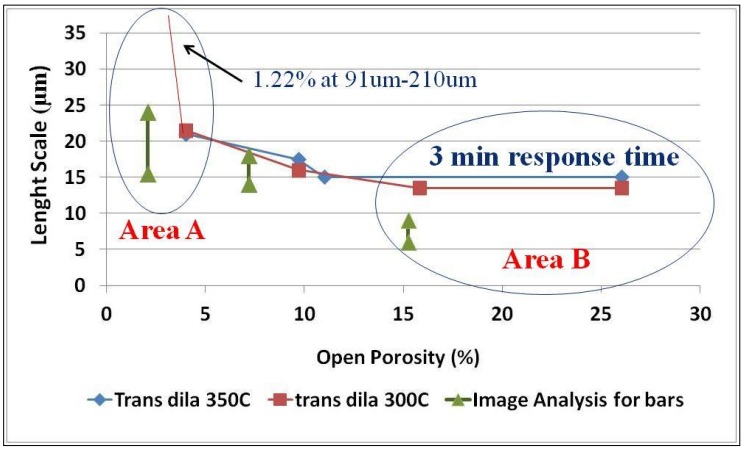

Figure 28-16. A comparison of the diffusion distances measured using Image J and transient dilatometry.

The Image J distances were less than the distances determined from transient dilatometry. The calculated distances using dilatometry may have been influenced by gas-phase mass transfer resistance for lower porosity samples (Area A), and relatively slow gas switching might have increased the measured diffusion distance for higher-open-porosity materials (Area B).

Air Products evaluated three advanced architecture control disks using imaging software, transient dilatometry and permeability testing. Figure 28-17 shows the grayscaled microstructure of the disks.

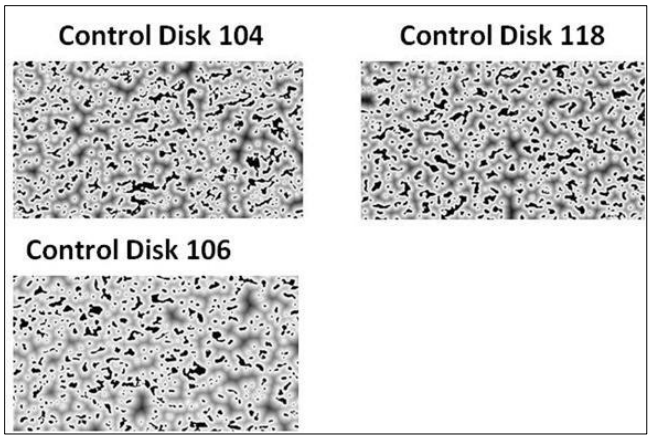

Figure 28-17. Grayscaled microstructures for disks showing the porosity.

Figure 28-18 shows the diffusion distances calculated from grayscaled Voronoi representations, and Figure 28-19 shows the corresponding pore size.

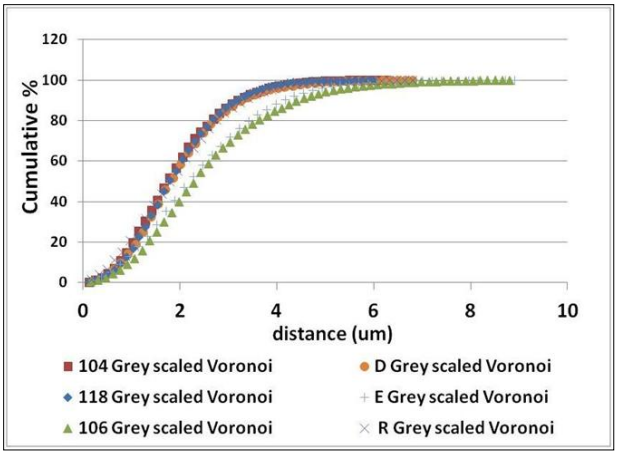

Figure 28-18. Diffusion distance comparison of control disks.

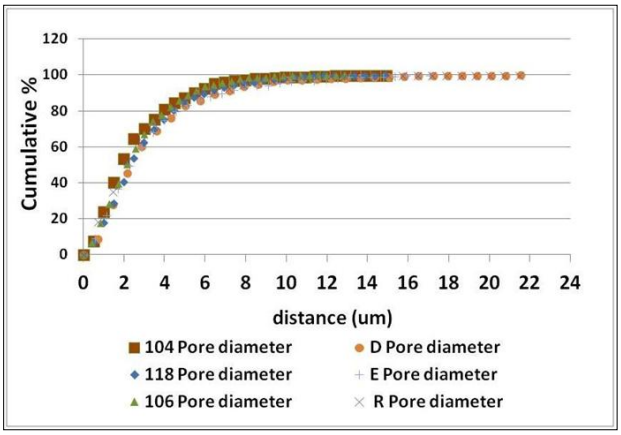

Figure 28-19. Pore size comparison of control disks.

Advanced architecture structures with porous regions (e.g., spacers, base pieces) were also characterized using imaging software and transient dilatometry. Figure 28-20 shows the grayscale microstructure.

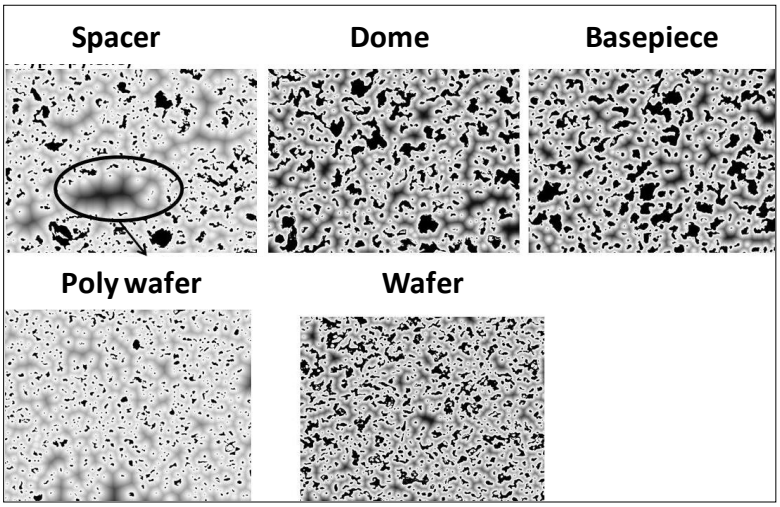

Figure 28-20. Gray-scale microstructures of porous regions within alternate structures.

Figure 28-21 shows the diffusion distance distribution.

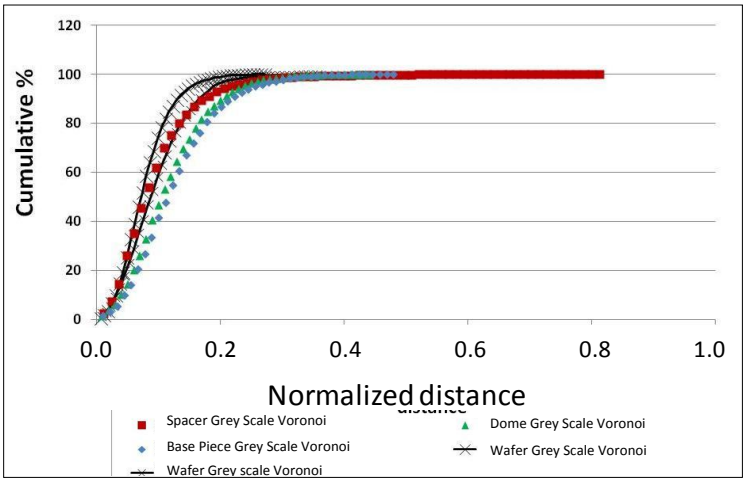

Figure 28-21. Porous region diffusion distance comparison, spacer, dome, base piece and wafers.

Figure 28-22 compares the pore diameter of the pieces.

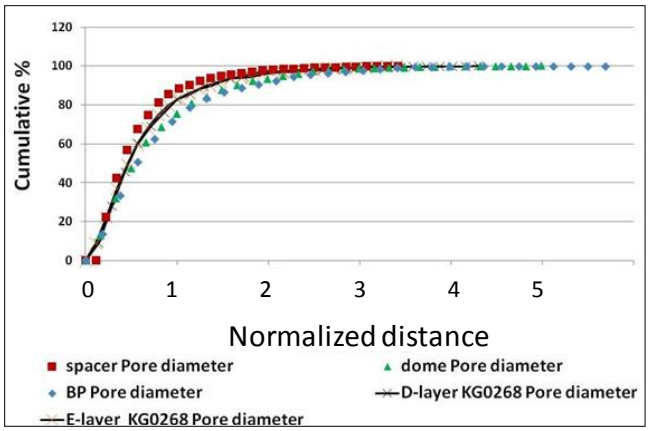

Figure 28-22. Pore diameter comparison in porous regions of spacer, dome, base piece and wafers.

Air Products performed qualifying activities with the imaging analysis protocol to ensure confidence in diffusion distance measurements in porous materials. In the analyses above, an image of the surface at a magnification of 500X was used. The images containing 800^{+} pores and the solid space between the pores was characterized by $1{,}000{,}000^{+}$ grayscale pixels. Statistical analyses were conducted to determine the number of pores required to provide a representative diffusion distance for the entire microstructure.

In the first assessment, the grayscale Voronoi distributions (length distributions) of ten different microstructural images of the same sample at 500X magnification (Figure 28-23) were plotted (Figure 28-24) and the standard deviation was calculated.

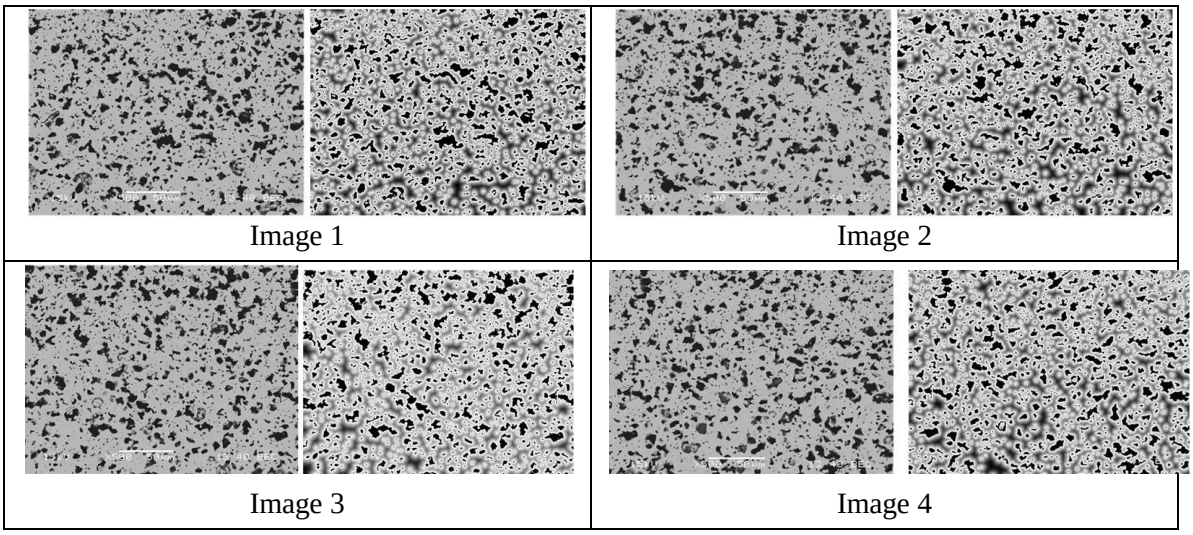

Figure 28-23. Sample images at 500X magnification.

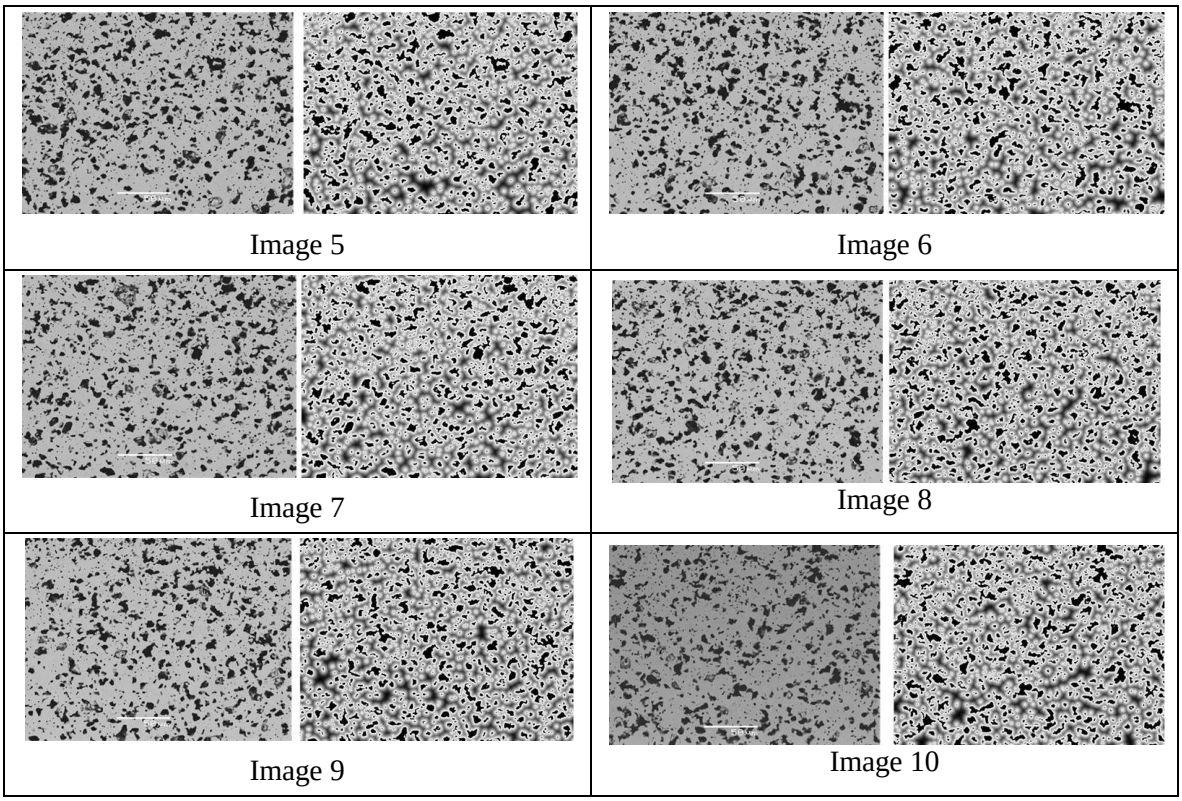

Figure 28-23. Sample images at 500X magnification (continued).

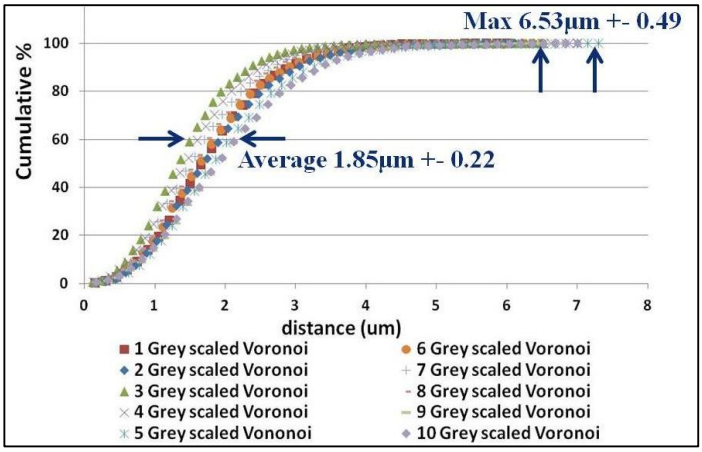

Figure 28-24. Grayscale Voronoi distribution of 10 microstructural images.

The average value at 60% cumulative "D60" was 1.85µm±0.22; the average maximum value was 6.53µm±0.49. More than 11,000 pores were included in the analysis.

Results from a sample magnified at 250X and 500X were compared. Figure 28-25 shows the initial and grayscale images, and Figure 28-26 plots the diffusion distance.

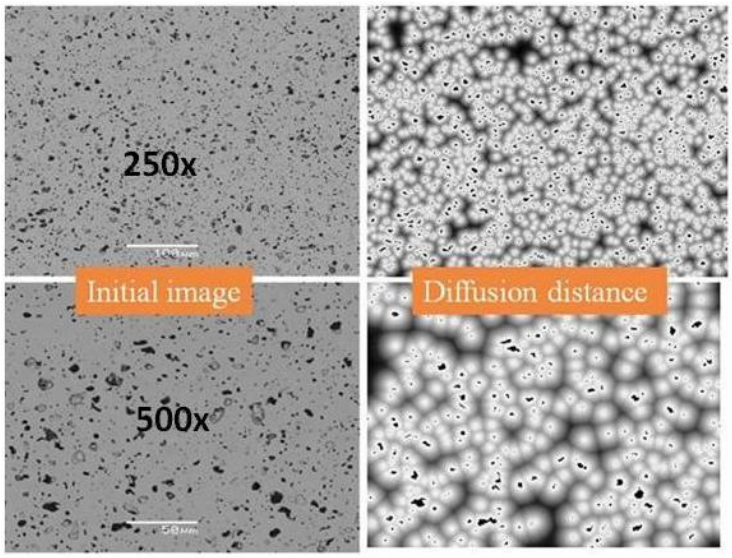

Figure 28-25. Sample A2 at 250X and 500X magnification.

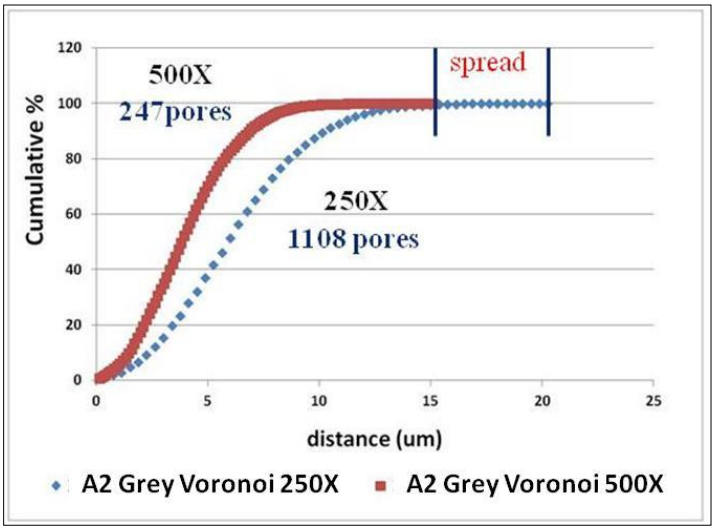

Figure 28-26. A2 Grayscale Voronoi distribution at 250X and 500X magnification.

The distributions at 250X magnification were skewed to the right as a consequence of having higher maximum grayscale distances. It was concluded that magnifications that include at least 1,100 pores are needed for grayscale imaging.

The study was expanded to identify the deviation between different magnifications. Figure 28-27 shows the visual comparison of a sample at magnifications of 250X, 500X and 800X.

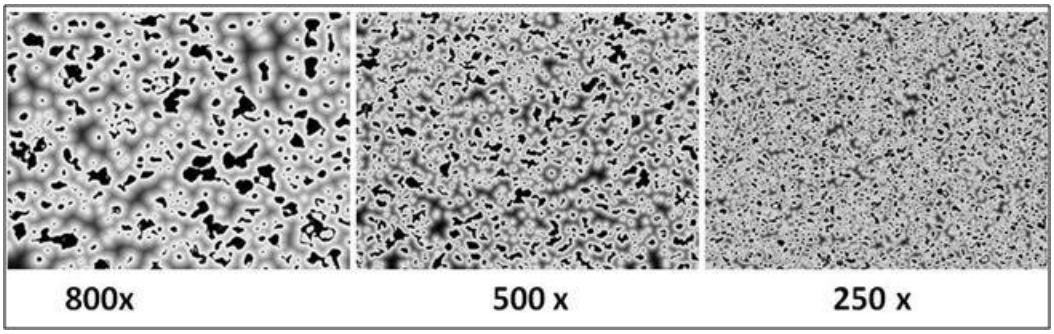

Figure 28-27. B2 images at different magnifications.

Figure 28-28 shows the grayscale Voronoi distribution for the images in Figure 28-27 and the distribution of the 10 images of Figure 28-23 (plotted in Figure 28-24).

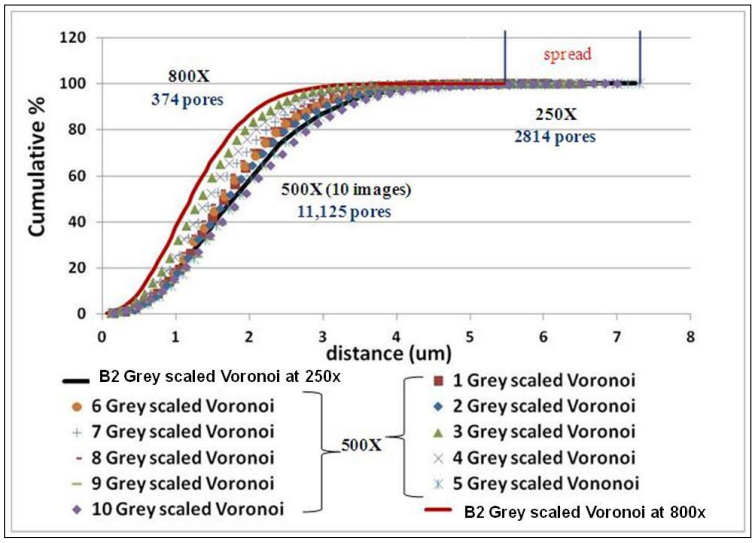

Figure 28-28. Grayscale image magnification comparison.

The 10 original images at 500X magnification collectively represented 11,125 pores. The image at 800X magnification had the lowest maximum distance and the lowest number of pores. The image at 250X magnification, with 2,814 pores, showed a distribution within the 500X magnification/10-image distribution and was shifted to the right. As magnification went up, the pore density went down. Also, as the pore count went up, the pore density went up.

It was concluded that lower magnifications/higher pore counts yielded higher grayscale distributions. Lowering the magnification increased the chance that the largest distances were represented in the analysis and would lead to a better overall microstructural representation. Pore count should be considered over magnification.

Dilatometry Measurement: Impact of Temperature Non-uniformity

Figure 28-29 is a typical setup in the large-scale dilatometry apparatus at Air Products. In this case, the expansion of a dome and an AP2k specimen are measured concurrently. It had been assumed that the temperature inside the dilatometer is uniform.

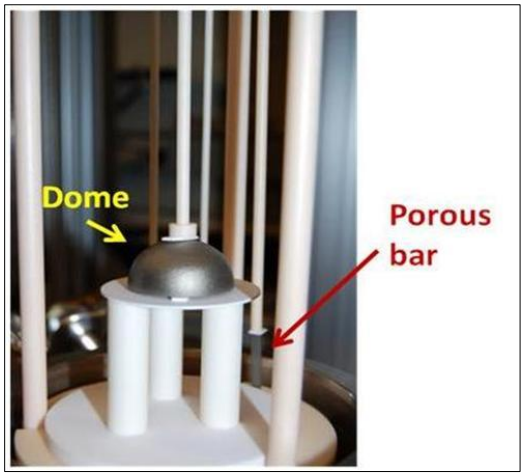

Figure 28-29. Typical large-scale dilatometer setup.

Figure 28-30 is a plot of an expansion experiment. It was noted that there was an upward slope when the temperature was greater than 700°C. This behavior was unexpected.

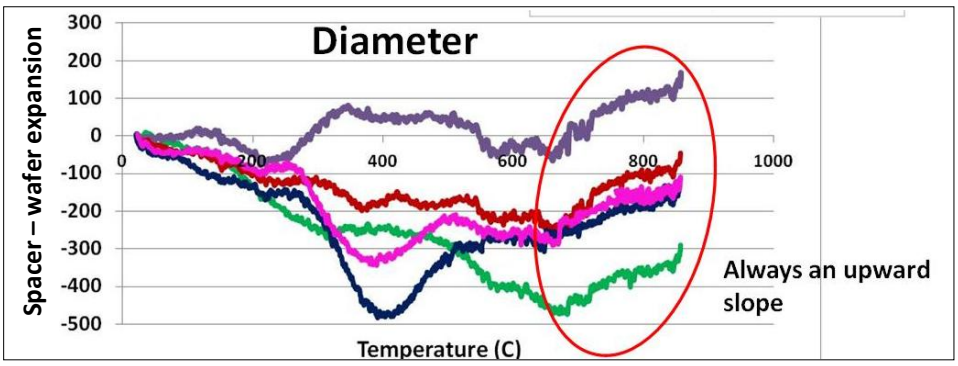

Figure 28-30. Differential expansion plot with unexpected slope.

Air Products conducted a study to determine if temperature non-uniformity in the dilatometer could explain the anomalous data. Figure 28-31 was constructed using expansion measurements for an advanced architecture wafer to understand how much differential strain would occur for a given temperature differential between the sample and the reference locations.

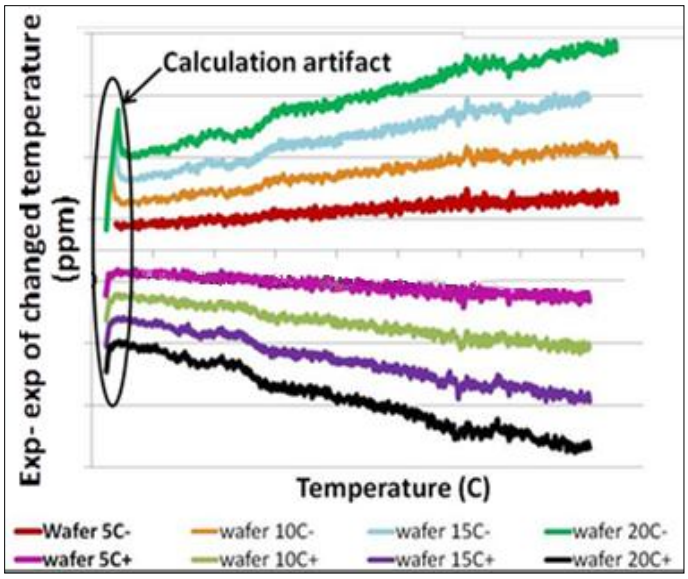

Figure 28-31. Strain difference of an advanced architecture wafer caused by a temperature difference/offset of +/-5°C, +/-10°C,+/-15°C, and +/-20°C.

The graph shows the differential strain for a temperature offset of +/-5°C, +/-10°C, +/-15°C, and +/-20°C. The expansion measurements were used to calculate the temperature difference between the stages, if the differential stain shown in Figure 28-31 was caused entirely by a temperature difference between the stages. At a higher temperature, the difference in temperature would be 4-5°C, making it a reasonable explanation for the strain change.

Parts Testing (Dilatometry at Constant Oxygen Partial Pressure)

The expansion of two modules components (e.g., wafer and spacer) as a function of temperature was measured concurrently in the dilatometers. The difference in strain was then plotted with temperature. The data were used to optimize heating and cooling cycles and to calculate induced stress. Examples are presented below.

In all experiments, the temperature of the sample and reference parts is substantially the same at any one time, thus eliminating any contribution of differences in thermal expansion in the results. Moreover, the parts are known to reach rapid thermal equilibrium with the dilatometer stage. Figure 28-32 shows the comparison in terms of the spacer expansion minus advanced architecture wafer expansion.

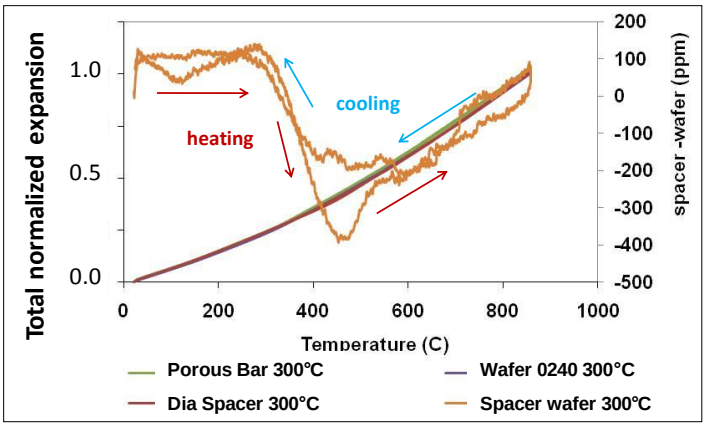

Figure 28-32. The expansion of advanced architecture wafers compared to that of a standard spacer.

The spacer-wafer line indicates the spacer lags behind the advanced architecture wafer between 300°C and 475°C, then started to expand at a similar rate at temperatures >575°C.

Other experiments were conducted to understand expansion differences between samples of different effective porosities. Figure 28-33 shows the expansion difference of the samples at heating/cooling rates of 30°C/hr and 300°C/hr.

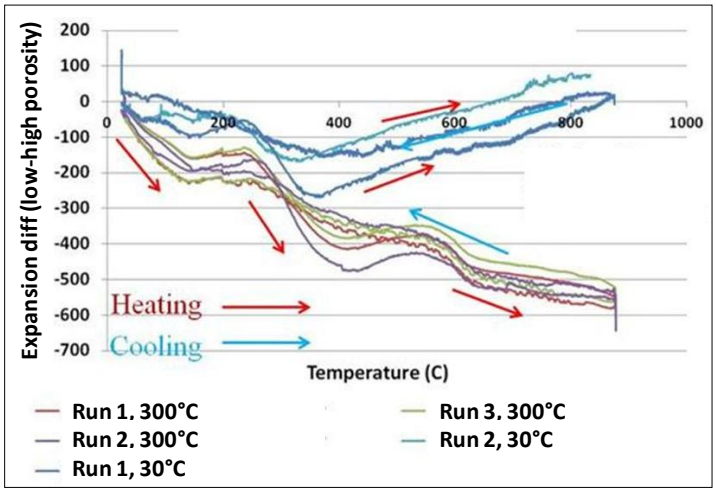

Figure 28-33. Expansion differentials of samples with different effective porosities.

For the 300°C/hr runs, the expansion of the high-porosity samples was faster compared to the lower-porosity samples, resulting in a large negative dip of 450 ppm at 450°C. The dip was shifted to a slightly lower temperature for the 30°C/hr runs, and the magnitude was only 275ppm.

The slower heating rate effectively reduced the difference since more time was given for the components to come to chemical equilibrium.

Parts Testing (Dilatometry at Constant Temperature)

Air Products determined the transient expansion response of various component designs to help guide component design work carried out by Ceramatec under Task 28.2. For example, Figure 28-34 plots the data of stacked spacers and a Rev. 2 spacer subjected to a P_{O2} partial pressure change at 500ºC. The normalized expansion is equal to the strain divided by the strain at 100% O_2.

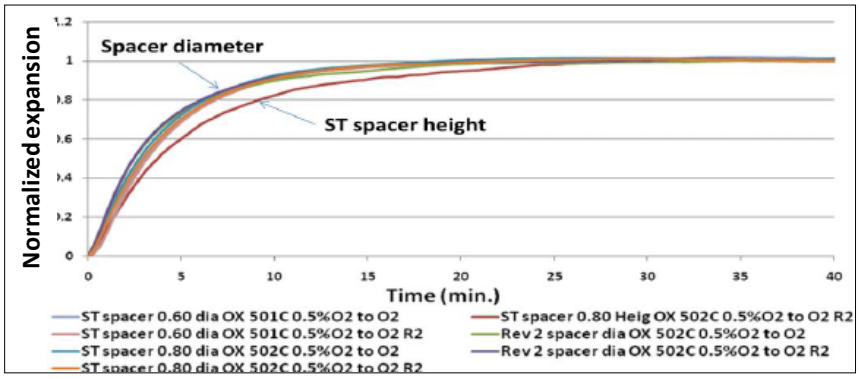

Figure 28-34. Response of ST and Rev.2 spacers at 500ºC.

The transient responses of the diameters for both the ST and Rev. 2 spacers were roughly the same. In another example, transient dilatometry measurements of base piece were conducted at 450°C. The transient response of the Rev.2 base piece was slower than the J1 basepiece suggesting the solid-state diffusion path was longer for the Rev.2 base piece.

Parts Testing for Manufacturing And Operation

When an ITM part is held at high temperature for a period of time, an equilibrium oxygen vacancy concentration is established and the expansion/strain reaches equilibrium (i.e., maximum). When the material is cooled, oxygen tries to diffuse into the material to maintain equilibrium (i.e., the equilibrium vacancy concentration decreases with temperature). If the cooling rate is too fast, equilibrium is not achieved and the part will have a locked-in (i.e., non-equilibrium) vacancy concentration and a residual strain. Restating, a locked-in vacancy concentration results from cooling at a rate faster than the vacancy concentration can equilibrate. For example, the locked-in oxygen vacancy concentration of a quickly cooled part may be equal

to the equilibrium vacancy concentration at a temperature such as 500°C. The material strain (excluding thermal expansion) would be equal to the chemical (oxygen vacancy) strain at 500°C.

When the material is reheated, the actual/locked-in vacancy concentration would initially exceed the equilibrium vacancy concentration. In the example, this will be true until a temperature of ~500°C is reached. As a result, at temperatures below 500°C, oxygen would diffuse into the part (oxidize) in an attempt to achieve equilibrium and the part would contract (negative strain). Note that the part would never return to its original pre-heating length/dimension. In contrast, a part that has not been previously heated will immediately begin to expand with a temperature increase.

Once 500°C is exceeded, the actual vacancy concentration would be lower than the equilibrium vacancy concentration (i.e., increases with temperature). Oxygen would diffuse from the part through vacancy migration (i.e., be reduced) and the part will begin to expand.

Since the expansion response is a combination of thermal and chemical expansion, it is difficult to know when there is a shift from oxidation to reduction. An understanding of this process was needed to develop heating and cooling cycles that minimize stress in the wafer and module.

Figure 28-35 organizes the various ways to heat and cool samples with respect to prior cooling and heating rates. High and low conditions were used to organize the four quadrants A-D. The table was populated with data from the heating and cooling rate schedules used for module sealing and module cycling tests.

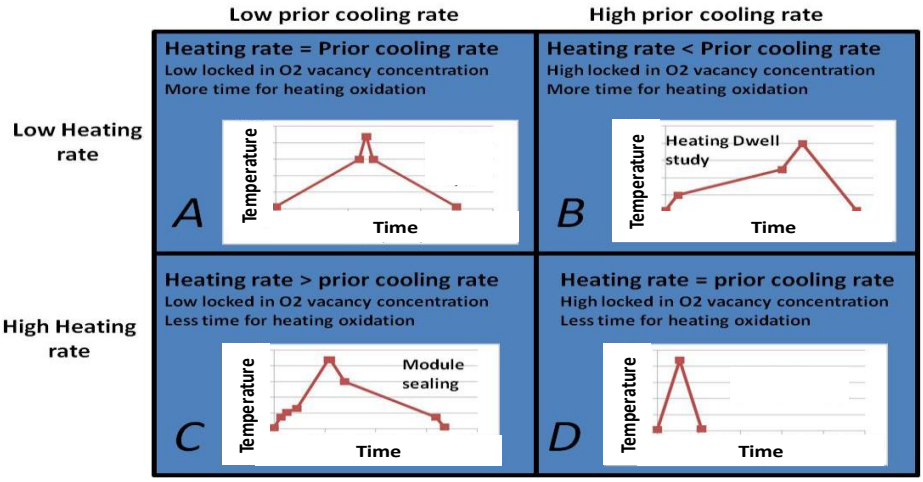

Figure 28-35. Means of heating and cooling AP2k in terms of prior cooling/heating rate.

Moving from A to D (increasing the heating and cooling rate) increased both the locked-in vacancy concentration and the maximum expansion differential between the spacer and wafer during heating (Figure 28-36).

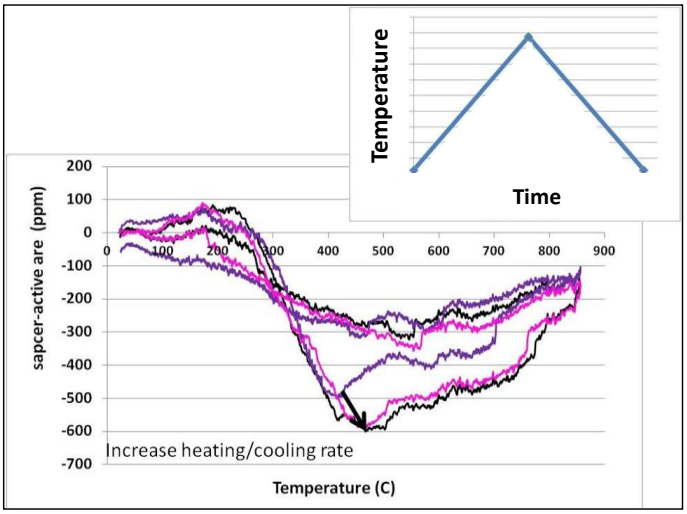

Figure 28-36. Moving from A to D in Figure 28-35.

Moving from B to A (decreasing the prior cooling rate and having a low heating rate) decreased both the locked-in vacancy concentration and the maximum expansion differential between the spacer and the wafer during heating (Figure 28-37).

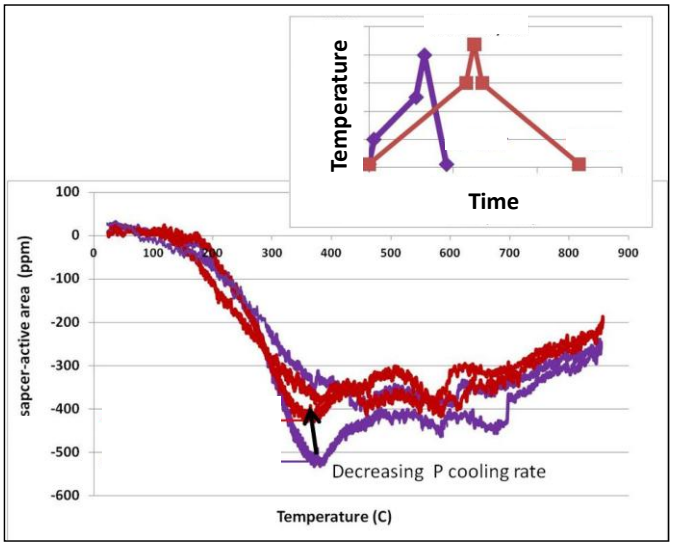

Figure 28-37. Moving from B to A in Figure 28-35.

Moving from B to D (increasing the heating rate and having a high prior cooling rate) decreased the maximum differential during heating because there is less time for oxidation (Figure 28-38).

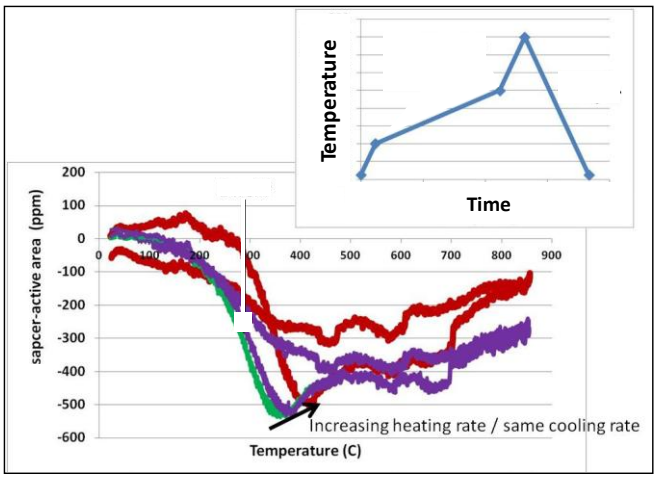

Figure 28-38. Moving from B to D in Figure 28-35.

Moving from C to D (increasing the prior cooling rate and having a high heating rate) decreased the maximum difference between the spacer and wafer during heating (Figure 28-39).

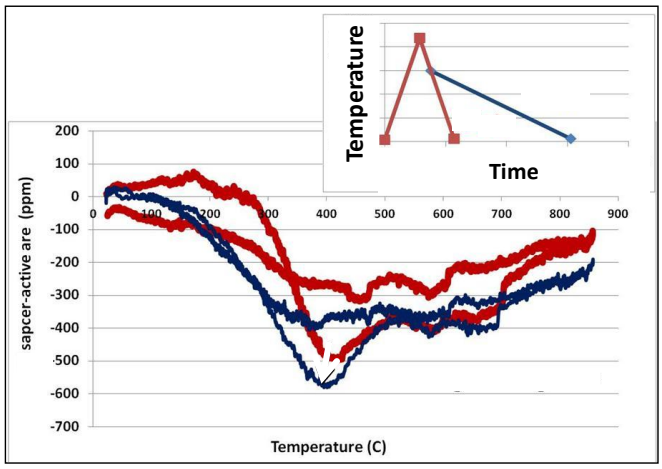

Figure 28-39. Moving from C to D in Figure 28-35.

This is contrary to the hypothesis that predicts that an increase in the prior cooling rate would increase the maximum differential, as the higher prior cooling rate would increase the locked-in vacancy concentration. The discrepancy is likely the result of complex interplay between the time needed for oxygen transport in the material and the heating/cooling rates.

Moving from A to C compares increasing the heating rate and having a low cooling rate, which decreased the maximum differential between the spacer and wafer during heating (Figure 28-40). Less time is available for oxidation, resulting in a smaller expansion differential.

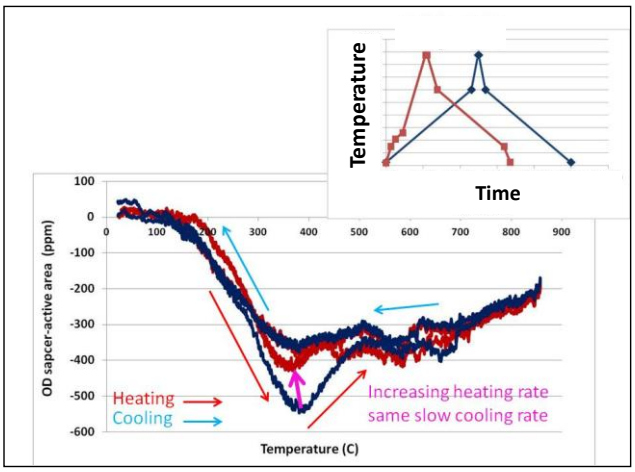

Figure 28-40. Moving from C to D in Figure 28-35.

Spacer expansion experiments demonstrated how the oxidation/reduction temperature could be determined for a cooling rate using one heating/cooling experiment. The spacer/wafer dilatometer data was used to propose an optimal heating/cooling schedule for a joined spacer/wafer. The schedule was compared to schedules used by Ceramatec. The new schedule identified two critical temperature ranges where heating/cooling must be done slowly to reduce stress. For these temperature ranges, the spacer equilibrates at a slower rate compared to the wafer. Figure 28-41 shows the spacer expansion using the proposed schedule and the expansion using the Ceramatec wafer cycling and module sealing schedules.

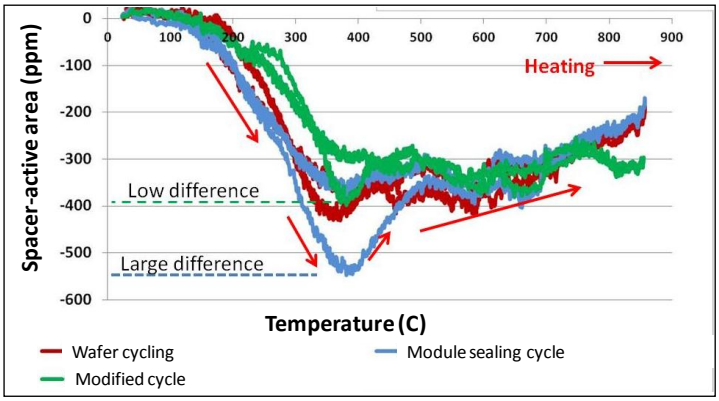

Figure 28-41. Spacer expansion: proposed schedule and existing Ceramatec schedules.

The new schedule reduced the expansion difference between the spacer and the wafer, which reduces the stress. Also, the new schedule reduced cycle time by nearly 50%. Ceramatec incorporated the new cycle into their wafer cycling experiments.

Air Products used the data above to evaluate a heating and cooling cycle to minimize the differential expansion between the spacer and an advanced architecture wafer. The heating rate was reduced during the oxidation/reduction transition temperature range. Figure 28-42 shows the height expansion results for the fast heating cycle (red) and the optimized cycle (blue).

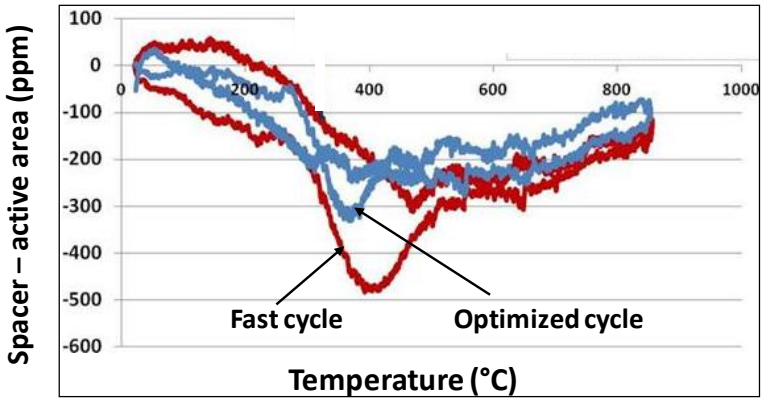

Figure 28-42. Height differential expansion of spacers, fast heating cycle (red) and the optimized cycle (blue).

The slower rate reduced the differential expansion between the spacer and the advanced architecture wafer.

Figure 28-43 shows the same comparison for the diameter expansion. The diameter showed a higher amount of differential strain compared to the height.

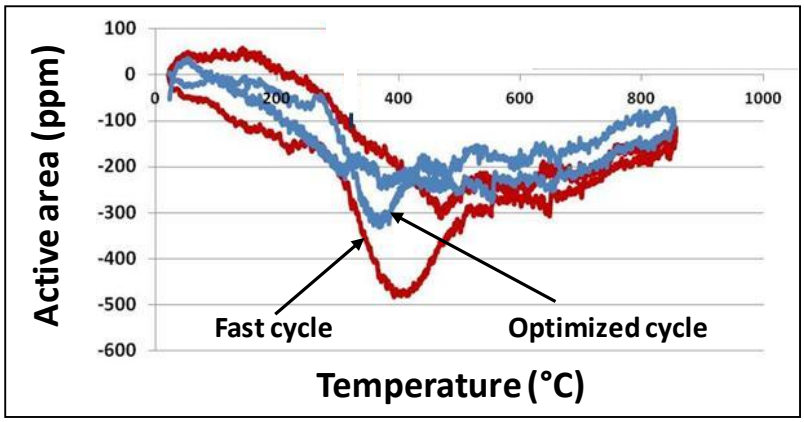

Figure 28-43. Diameter differential expansion of a spacer and an advanced architecture wafer, fast heating cycle (red) and the optimized cycle (blue).

Tests were also conducted to compare the diameter differential expansion of a module backbone when the fast and optimized cycles are used. Figure 28-44 presents the results.

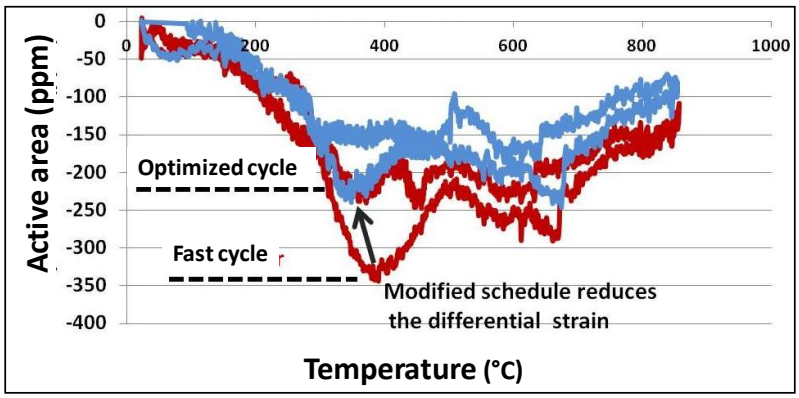

Figure 28-44. Diameter differential expansion of a module backbone, fast cycle (red), optimized cycle (blue).

Other dilatometry work discovered the following:

- The module backbone diameter expansion results indicated the module backbone has less differential strain as compared to a series of stacked spacers.
- During the height expansion cooling cycle, the wafer sections in the module backbone contracted more than the spacer. The result is less height expansion of the module backbone than assumed.
- The module backbone showed less differential strain compared to the stacked spacer sample.
- There was a substantial reduction in differential strain between the wafers and spacers when the module backbone was subjected to a modified heating and cooling schedule.

One way of understanding how strain has accumulated in a part during cooldown is to measure the expansion during heating after the sample is cooled. Figure 28-45 shows the heating expansion of the module backbone after the fast cooldown.

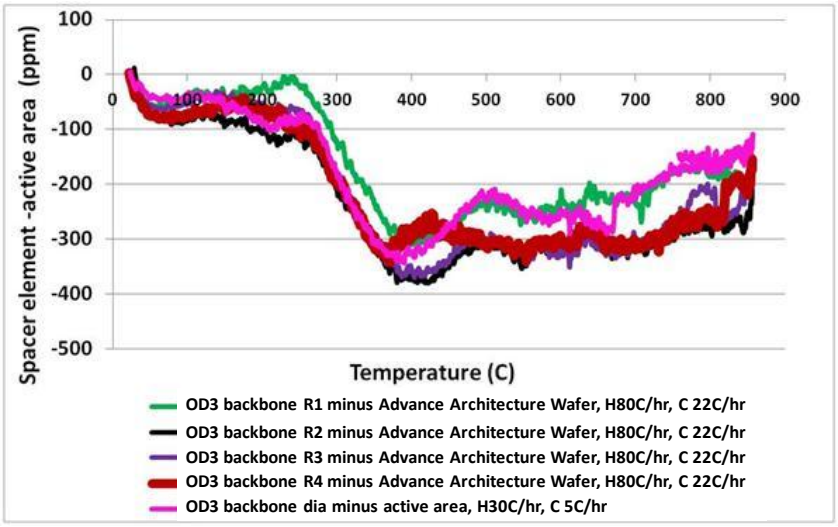

Figure 28-45. Differential expansion at different heating and cooling rates.

R1 is the expansion of the backbone after a slow cooldown; R2 and R3 are the expansions after a fast cooldown. Run 4 shows the expansion of the backbone using a slow heating rate after the backbone was fast cooled. This showed that strain could be minimized during reheating.

Composite and Poly Spacer Expansion

Air Products carried out work to determine the expansion characteristics of composite and poly spacers. Earlier work indicated that side-stage expansion of an advanced architecture wafer used as a comparative reference did not show repeatable expansion between runs. A better approach was developed. Since the composite spacer seemed to have a slower response than the poly, the poly spacer expansion was subtracted from the composite expansion data set. The poly spacer was used as a surrogate for the advanced architecture wafer. Figure 28-46 demonstrates the new approach.

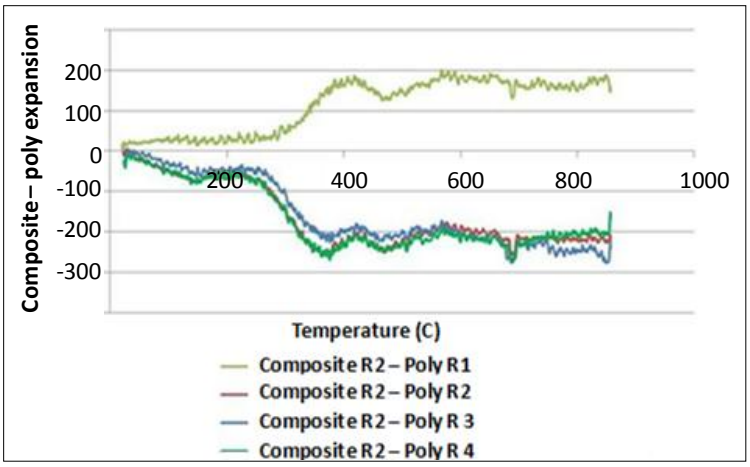

Figure 28-46. Composite minus poly spacer expansion.

Repeatability for R2-R4 was good and suggested that the composite spacer had a higher differential strain compared to the poly. Poly R1 represented the "as received" expansion and showed a higher differential strain compared to the composite R2.

High-Pressure Dilatometer

Since typical ITM Oxygen process conditions include operation with high-pressure air, knowledge is needed of the expansion behavior of the ITM membrane material at oxygen partial pressures in excess of one atmosphere. Under previous tasks, dilatometry measurements were extrapolated to high pressures to predict stress at ITM Oxygen operating conditions. To reduce technical risk in future development activities, particularly those involving a wider range of operating conditions, mechanical modeling and stress predictions at operating conditions should be done based on data obtained at the actual temperature and oxygen partial pressure conditions and not rely on extrapolations.

Commercially available dilatometers are limited to operation at relatively low pressures, typically operating with a maximum pressure of one atmosphere. To measure expansion at higher oxygen partial pressures, a dilatometer capable of operating in high-pressure air was needed. A dilatometer designed for high-pressure applications was procured to allow operation at the required conditions. The data from this unit is being used to calculate the stresses of the ITM membrane at actual process conditions anticipated in industrial and CCS applications.

The system is capability of measuring the expansion of materials at or above the ITM operating temperature and well above the ITM operating pressure. Air Products and the dilatometer supplier

collaborated to estimate the cost of the system based on a detailed scope of supply that includes dilatometer costs from the supplier and a gas handling system to be supplied by Air Products.

Air Products executed the purchase and installation of the high-pressure dilatometer. The pressure vessel consists of an upper chamber housing the electronics and a lower chamber housing the sample and heating means (Figure 28-47).

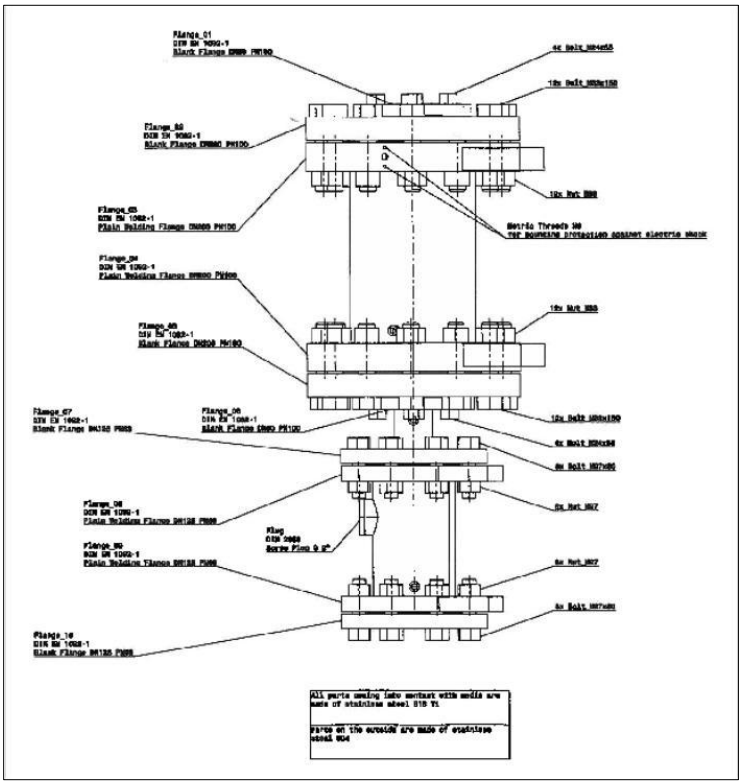

Figure 28-47. High-pressure dilatometer pressure vessel.

Air Products developed a gas-handling system to enable controlled delivery of high-pressure process gases to the device. A schematic of this system is shown in Figure 28-48.

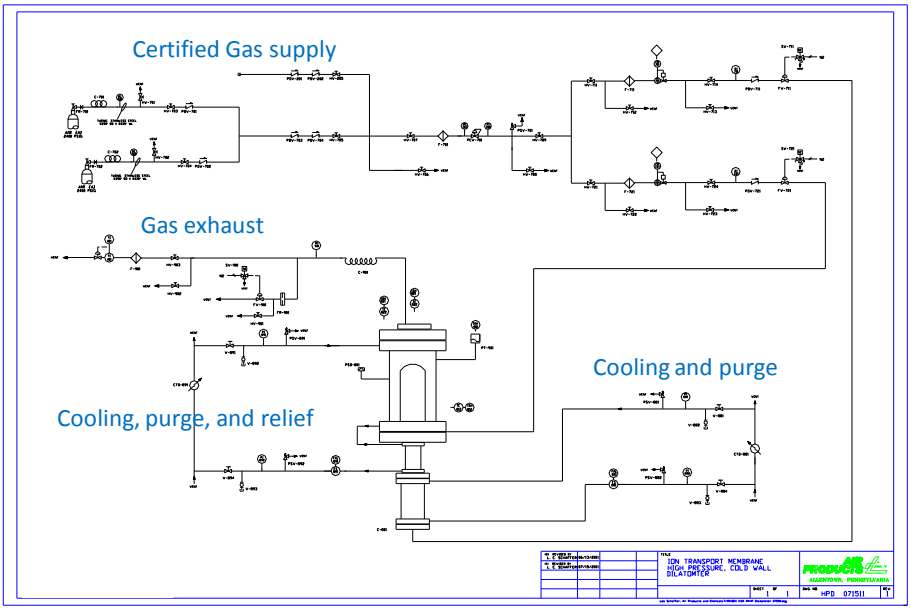

Figure 28-48. Gas-handling system for the high-pressure dilatometer system.

Air Products carried out system commissioning in a series of trials. During the first run with an AP2k sample, an alarm thermocouple broke and caused the furnace to cool. The vessel was opened, and it was discovered that the furnace tube was cracked. Figure 28-49 is a schematic of the system and shows the location of the crack.

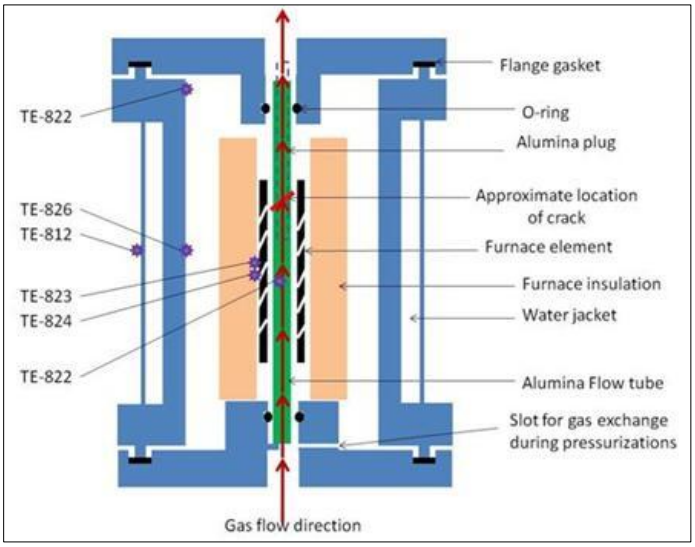

Figure 28-49. A schematic of the high-pressure dilatometer furnace showing the proximity of the break near the end of the furnace element.

The location of the break in the proximity of the furnace element suggests that thermal shock was the cause. Figure 28-50 is a photograph of the modified system showing the installed furnace with the new thermocouples and flow tube.

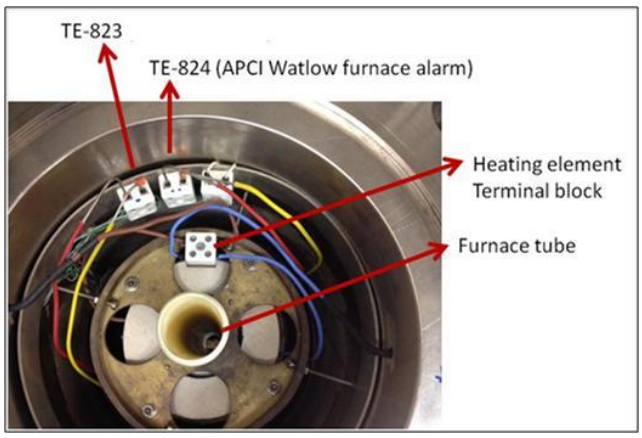

Figure 28-50. High-pressure dilatometer furnace showing newly installed thermocouples and furnace tube.

The first AP2k expansion measurements were conducted following repair of the unit. Figure 28-51 documents the raw/uncorrected expansion of AP2k at P_{O2} = 0.21 atmosphere.

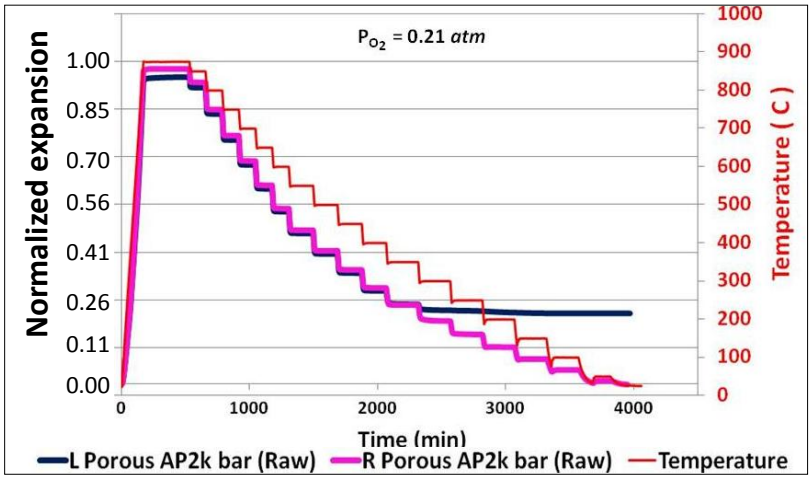

Figure 28-51. Raw expansion data for AP2k in the high-pressure dilatometer at P_{O2} = 0.21 atmosphere.

An experiment was carried out at higher oxygen partial pressure. As expected, the AP2k contracted when the P_{O2} was increased to 1.2 atmospheres. The expansion of alumina was measured using the identical heating/cooling schedules, and this data was used to subtract the background instrument expansion. The corrected data set is shown in Figure 28-52.

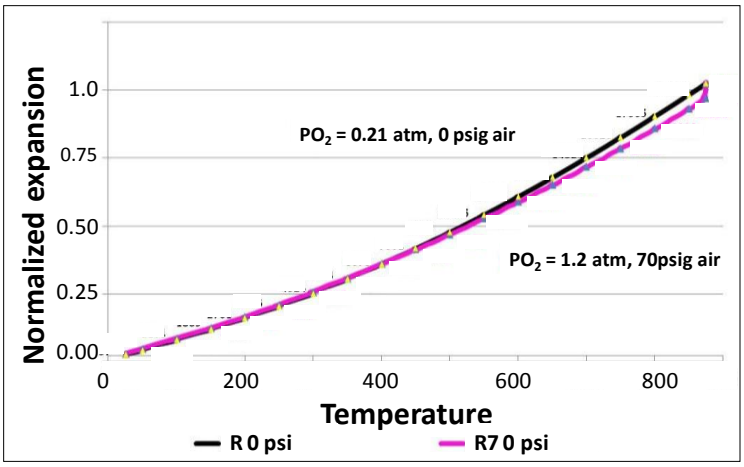

Figure 28-52. Corrected data for the high-pressure dilatometer.

A comparison of the data measured using the atmospheric and high-pressure dilatometers showed that the atmospheric-pressure dilatometer yields slightly higher expansions when extrapolated to higher pressures compared to experiments in the high-pressure dilatometer.

Modeling of Porous AP2k

The primary objective of this work was to evaluate and the define creep lifetime of modules at commercial operating conditions. Air Products evaluated creep data to develop a model describing the dependence of creep rate on temperature, stress, and porosity. Multi-linear regression was used to fit data to the expression:

$$de_c/dt = A\, f(p)\, S^N X_V^M \exp(-\Delta E/RT)$$

where de_c/dt is the creep rate (1/s), A is the pre-exponential factor (1/s), S is the stress (MPa), Xv is the oxygen vacancy fraction, ΔE is the activation energy (kJ/mole), T is the absolute temperature (K), and f(p) is a general function of the porosity, p.

In the creep experiments conducted at Ceramatec and Penn State, Xv was an independent variable in addition to stress, temperature, and porosity. However, given the limited variation in the range of this parameter, it was not possible to reliably estimate its effect on creep rate by including Xv in the linear regression. Instead, the creep rate dependence (as determined from previous tensile creep data) was assumed. The Xv dependence was then removed from the flexural creep rates data by first calculating Xv for each data point. The power law formulation relating Xv to T and P_{O2} was used for this calculation. The creep rate was then divided by the Xv term that had been

estimated previously using the tensile creep data. The creep rate stress dependency, as reflected by the N value, was consistently smaller for the flexure tests. This difference is likely due to the fact that the response of the flexure bar is dictated by both compression and tensile creep. Because the former typically exhibits a lower stress dependency, the resulting stress exponent for flexure creep falls between the two values.

The regression analyses of the Penn State data yielded values of A, ΔE, and N that were in relatively good agreement with corresponding values determined from the tensile data set. Therefore, the Penn State parameters were used to model the creep of the porous and dense layers in a wafer.

Bars

Penn State conducted flexural creep tests on three samples at temperatures of 875°C, 900°C, and 925°C. Due to the faster creep rates at 925°C, the length transducer exceeded its travel limit before sufficient data could be recorded for the 27.6MPa applied stress. Therefore, the creep rates for applied stresses of only 6.9 and 13.8MPa were obtained.

The flexural creep activation energy was determined from the slope of the data. The calculated creep activation energy was 438kJ/mol for both applied stresses of 6.9 and 13.8 MPa (1 and 2 ksi). For the highest applied stress of 27.6MPa (4ksi), a much lower creep activation energy of 315kJ/mol was obtained. The travel limit problem of the length transducers during the 27.6MPa (4ksi) at 925°C creep condition may have skewed the activation energy to a lower value.

Wafers and Submodules

Ceramatec used COMSOL to predict the creep deformation occurring in a wafer due to pressure differentials between the outside and inside of the wafer, chemical stresses and axial loading along the backbone. A simple 2D axis-symmetric model consisting of a wafer, spacer, and a ceramic joint was prepared. In some cases, a creep rate multiplication factor was applied to represent the fact that some layers were not continuous but contained slots. Only a portion of the wafer was modeled, as the focus was to examine the creep occurring in the vicinity of the backbone.

To validate the model, the creep compaction arising from just the axial load was predicted for both standard and advanced architecture wafers. The results were compared to the deflection-time curves measured previously using backbone specimens prepared from submodules. The deflection-time behavior of each specimen type was measured at elevated temperature and 1,000 N for ~420 hours. As shown in Figure 28-53, the compaction rate of the advanced architecture wafer was more than 5X greater than that of the standard wafer.

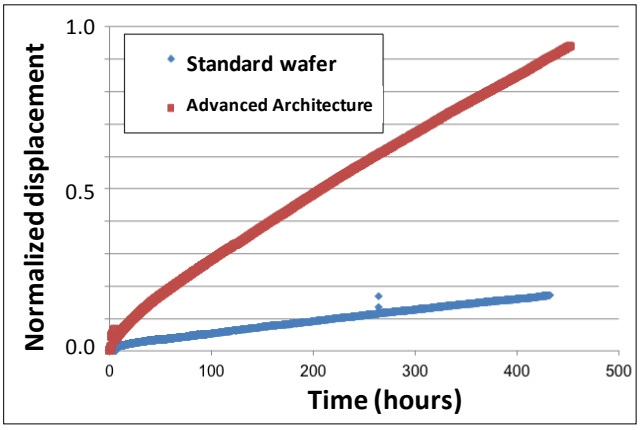

Figure 28-53. Predicted deflection-time curves for standard and advanced architecture wafers.

Significant deformation occurred in the vicinity of the joint. This is expected, since the axial stresses would be greatest in the component with the smallest cross-sectional area. The COMSOL models were used to predict the deflections of standard and advanced architecture wafers. The results, presented in Figure 28-54, indicate that the current model is somewhat conservative in its ability to predict deflections.

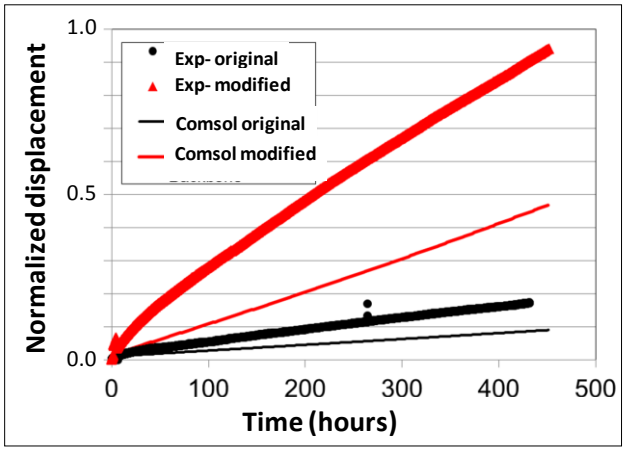

Figure 28-54. Comparison of experimental deflection-time curves versus model.

The discrepancy may have been due to the inability of the model to account for the creep of some components. A second potential reason for the discrepancy is that the model assumed that the joints were perfectly aligned in the axial direction. In reality, the joint is not perfectly aligned, which leads to additional deflection due to bending.

Wafers

Penn State conducted a creep experiment on advanced architecture wafers at an elevated temperature and a stress level of 410psi (a load of 969N). During the loading process, two cracking events occurred that coincided with a temporary drop in load at 544N and 946N (Figure 28-55).

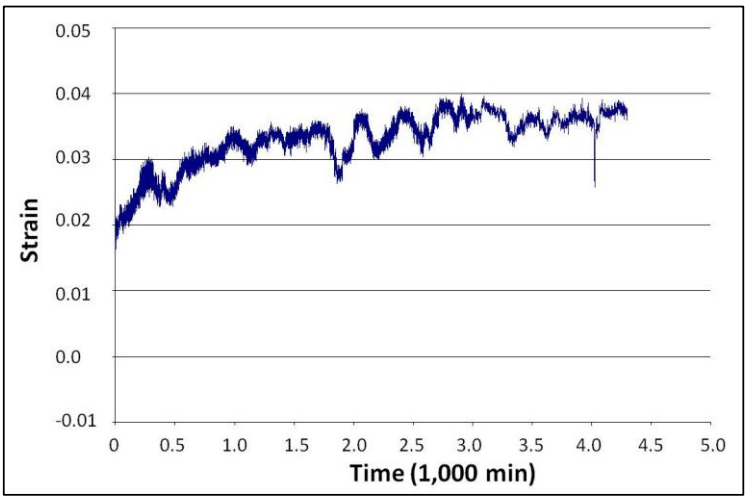

Figure 28-55. Compressive creep strain plot for an advanced architecture wafer.

This extended period of primary creep probably contained some creep flattening of the advanced architecture wafer.

Submodules

Ceramatec joined a set of submodules using a wider joining layer compared to the baseline width to study the effect on creep of submodules and modules. Figure 28-56 compares results of the first two submodule runs with previous runs of baseline parts. While there is much scatter in the data, the trend does suggest that the wider joining layer reduced creep. The data are compared with additional data collected by Penn State, extending the data reported under Task 24. Figure 28-57 is a photograph of the PSU test rig.

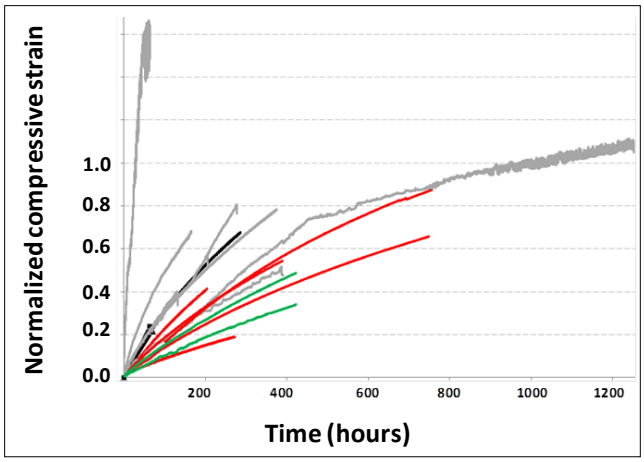

Figure 28-56. Submodule creep. Black and red: baseline wafers. Green: wafers with thicker joining layers. Gray: Penn State data under different conditions.

Figure 28-57. Submodule creep rig installed on an Instron 5866 load frame.

Wafer Stress with Temperature Change

Ceramatec investigated the effects of an abrupt temperature change on wafer stress and strain. Two approaches were used: a simple 2D COMSOL model, and a convection oven to rapidly heat or cool the wafer between 200°F and 300°F.

The COMSOL model estimated the temperature and stress distributions arising from the 100°F transition during both heating and cooling. Relevant properties of the flowing air (heat capacity, density, and thermal conductivity) were extracted from existing property tables for air at 250°F. Figures 28-58 plots the predicted tensile stress along the wafer surface during heating. Figure 28-59 shows the predicted stress data during cooling.

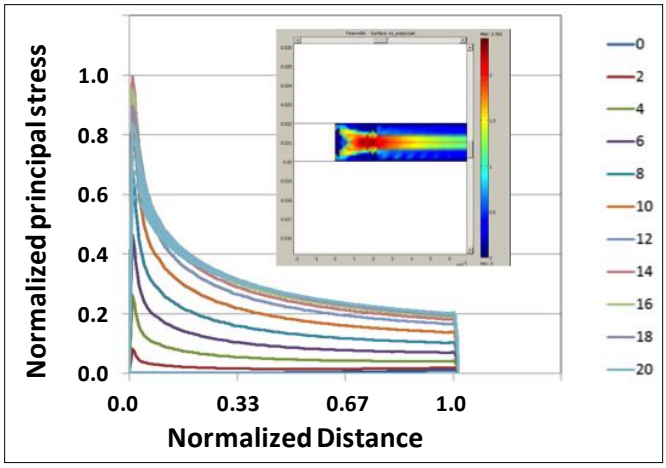

Figure 28-58. First principal stress profiles generated during heating. Values on the right are time in minutes.

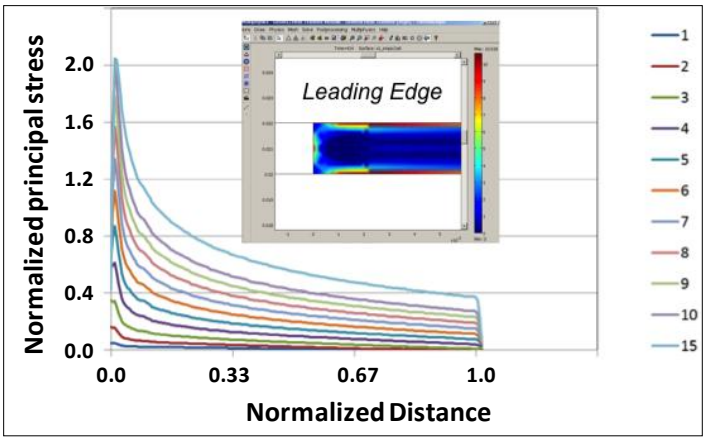

Figure 28-59. First principal stress profiles generated during cooling. Values on the right are time in minutes.

Ceramatec used a second approach used to examine wafer reliability during short temperature transitions by rapidly heating or cooling wafers between 200°F and 300°F in a convection oven. As shown in Figure 28-60, a single wafer was supported at the oven mid-span using alumina fixtures. A fan in the rear of the oven forced heated or cooled air over the surfaces of the wafer.

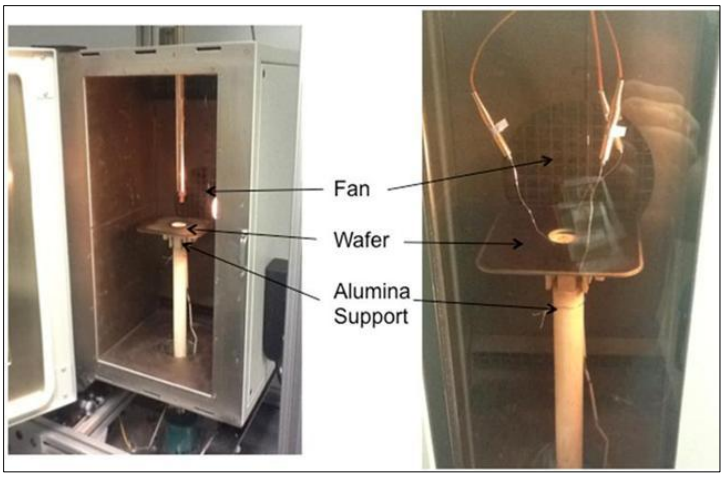

Figure 28-60. Oven setup used to rapidly heat and cool single wafers.

The oven door was left ajar to facilitate air flow during cooling; and one to three thermocouples were used to measure temperature. Three wafers were tested. The first wafer failed sometime during the cooling segment of the second cycle. A second wafer survived rapid heating and cooling cycles (Figure 28-61).

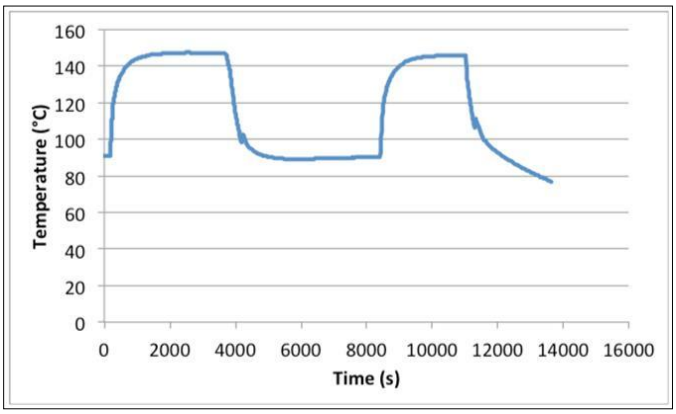

Figure 28-61. Temperature-time profiles measured during the second wafer test.

28.1.3.3 Evaluation of Materials Stability in Reactive Environments

Air Products conducted testing to establish the effects of impurities on the lifetime of an ITM material in the presence of a hydrogen-rich stream. The chosen impurities were those typically found in refractory materials used to insulate the high-temperature equipment associated with the ITM process. Baseline performance was first measured to obtain the flux in a clean environment. For the second test, a fresh membrane was first exposed for one week to an atmosphere containing a vapor-phase contaminant. The oxygen flux through the membrane was then

measured at four temperatures. This experiment was repeated a second time. Figure 28-62 compares the oxygen flux of the uncontaminated sample with that of the two contaminated samples.

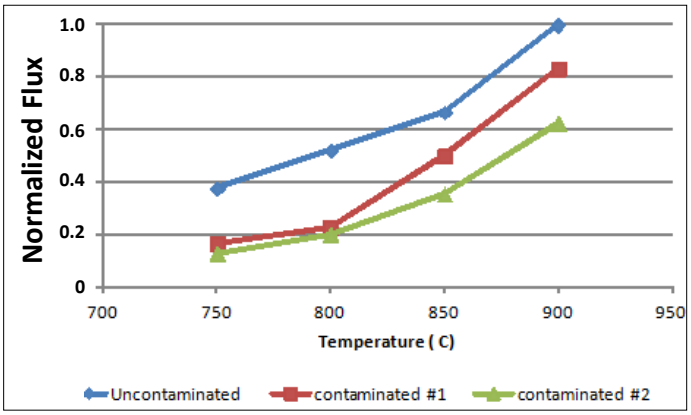

Figure 28-62. Flux of uncontaminated and contaminated membranes in a reactive environment.

The contaminated samples had lower flux, especially at the lower temperatures. Post-test analysis confirmed that the vapor-phase contaminant had reacted with the surface of the membrane.

28.2 Advanced Module Development

Background

As part of previous tasks, finite element analysis (FEA) was used to determine optimum module architectures that would minimize stresses that arise in the structures during operation. In addition to conventional mechanical stress generated by pressure, hydrodynamic flow, gravity, etc., ITM Oxygen materials are susceptible to stresses created by mismatched chemical expansion within the material due to oxygen concentration gradients caused by mass transport limitations. An assumption was made that the greatest overall reliability would be provided by designing structures that evolve minimal stress during unplanned transients. Although these structures may or may not be optimally designed for startup conditions, these conditions can be controlled to minimize stress. Controlled startup and cycling have been demonstrated repeatedly in the Subscale Engineering Prototype (SEP).

The results of the FEA-driven analysis indicated that advanced structures that minimize oxygen concentration gradients experience the lowest stresses during unplanned cooldown scenarios. An illustration of this is shown in Figure 28-63, where the stresses experienced by a 5-wafer module

during a typical cycle in the SEP facility are compared for standard and advanced model architectures.

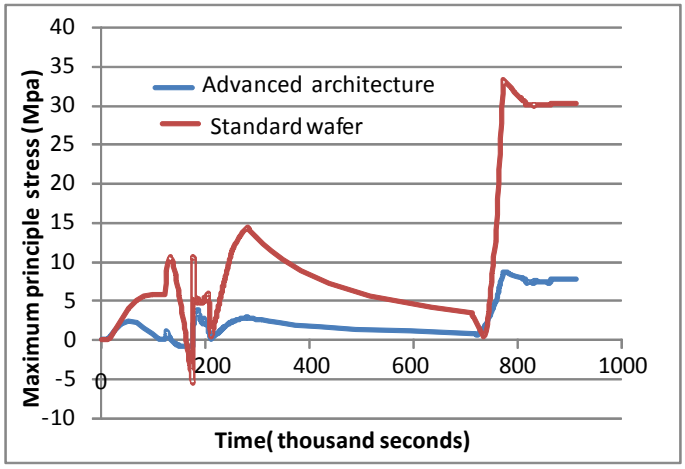

Figure 28-63. Comparison of stresses in standard and advanced modules during an operational cycle.

At the time that these results were generated, processing methods for fabricating the advanced components required for ITM Oxygen modules were not practiced at Ceramatec. Subsequently, a method to form them was developed under Task 17 to make module structural components that met the requirement that sufficiently low leak rates be used in modules. Ceramatec utilized the results of the FEA-driven analysis and advanced architecture component performance to guide development of improved components for ITM Oxygen modules. Under Task 28.2, Ceramatec conducted work on wafer, submodule, and module components to reduce module cost, increase module performance, and increase module durability based primarily on advanced architecture designs.

Based on the approaches used to fabricate structural components for ITM modules under Task 17, similar processes were applied to the fabrication of advanced architecture wafers. There are many similarities between fabricating a standard wafer and an advanced architecture wafer, as well as a few subtle differences. For example, both types of wafer involve producing ITM powder by solid-state reaction of precursors, followed by particle size reduction processes to obtain particles capable of densifying via solid-state diffusion (sintering).

The forming methods used for both wafers are identical: tape casting, tape featuring, and lamination. Two parallel approaches for applying the membrane layer to advanced architecture

wafers were investigated, one in which the membrane is applied as a single layer (single-application), and another in which the membrane is first applied to other layers and then applied to the balance of the wafer. After wafer fabrication, the methods of building submodules and modules from advanced architecture wafers are the same as has been practiced for standard components.

Due to the ability of the advanced architecture components to equilibrate more rapidly with the surrounding environment, much lower stresses are induced in these types of structures due to oxygen concentration gradients within the material. Subsequently, the durability of advanced architecture components is anticipated to be greater than that of components made with the standard architectures. This durability will also manifest in higher production yields that will reduce manufacturing costs and broaden the allowable operating conditions, which will improve performance.

28.2.1 Wafers

Advanced architecture wafer (AAW) development focused on the production of wafers with a sufficiently low leak rate to produce high-purity oxygen during operation.

Materials Selection

Initial investigation of advanced architecture wafers indicated that the material and structures had to be engineered to simultaneously meet requirements of product purity, chemical and thermal equilibration, and manufacturing. The desired material and structures must be strong enough to handle the load required during assembly processes, yet must achieve the benefits of significantly reduced chemical expansion-induced residual stress relative to standard structures. In addition, there is a concern that the materials may creep excessively during joining and possibly over the desired operational lifetime. To address these issues, studies were undertaken to develop processes capable of adjusting the morphology of the material and its corresponding properties. An investigation of the effect of processing on morphology and the resulting strength, creep behavior, shrinkage rates, elastic properties, thermal properties, and chemical expansion behavior was conducted. The starting powder properties and the effect of sintering temperature were characterized to allow engineering of the appropriate wafer powder stream and processing conditions.

Another constraint on advanced architecture materials is that they must be compatible with achieving an intact outer membrane. As described earlier, this can be accomplished either by fabricating a support structure that is amenable to application of a membrane that can subsequently be densified onto the support, or by fabricating a structure that undergoes transformations along with the outer layer. Ceramatec investigated both approaches for wafer fabrication.

Support structures were selected for the One Step route based on results of previous research under Task 17. The supports were made from powder that was processed to create the desired powder morphology. The powder morphology and process was chosen because it had been used to make advanced structures for module end caps (domes) and base peices earlier in Task 17 and had the mechanical and chemical properties which appeared to be adequate for those applications.

Selecting the powder morphology and processes for making parts with the Two Step method required additional experimental testing. The effect of starting powder, tape processing conditions, and sintering temperature on the physical properties of standard control samples were measured. The following is a summary of the test parameters:

Starting material for porous layers: Several different materials were examined and compared to the material source used to produce internal support layers in standard wafers, since they are known to be compatible with the membrane layer. These formulations were based on a powder produced by milling calcined powder so that it passes through mesh screens, followed by additional particle size reduction and mixing. Some powders were mixed with higher-surface-area powder to study the effects of powder mixtures in controlling material properties.

Tape Processing: Three basic processes were compared – the on-line production process for making tapes, small-scale batching and casting using a laboratory-scale tape caster, and the blending of powders and organic materials using commercial dispersing equipment. All laboratory-scale casts were batched using the same formulations as on the on-line production process. Formulations were also studied that used disperser which generally adjusts tape properties relative to those achieved with simple mixing.

Sintering Temperature: Control samples were sintered over a range of temperatures. Samples were held at for temperature several hours to achieve near-final density.

The study indicated that a substantial amount of control over material layer properties could be exerted by selecting the correct particle morphology and sintering temperature. The sintering temperature was subsequently fixed at a temperature known to provide densification of the membrane layer and was desirable from the perspective of kiln operating and maintenance costs.

Figure 28-64 shows the effects of different starting powders (designated 200-series powders and one 500-series powder) on open porosity as a function of sintering temperature for a variety of different powder morphologies.

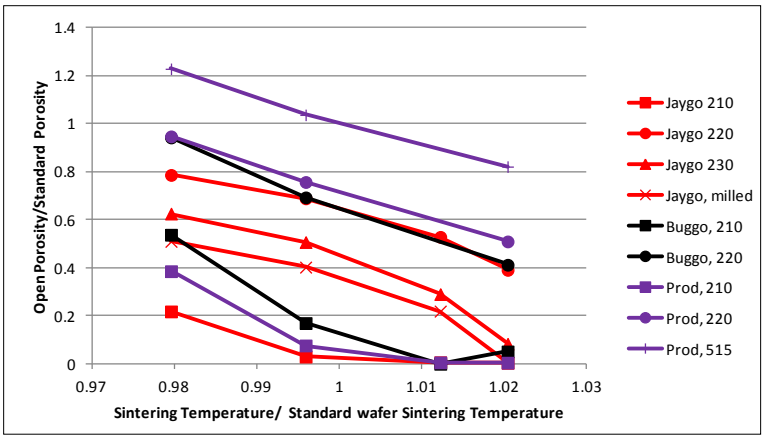

Figure 28-64. Open porosity vs. sintering temperature for tapes made with different powders and with different equipment.

As can be seen, the choice of starting powder can control part porosity, ranging from the porosity of standard wafers to no measurable open porosity. The data show tapes from different processing routes using a range of powders.

As mentioned earlier, the shrinkage of the tapes for the inner layers must be compatible with the membrane tape shrinkage. Figure 28-65 shows the shrinkage for the tapes shown in Figure 28-64 and shows that all of the tapes with higher porosities have much lower shrinkages.

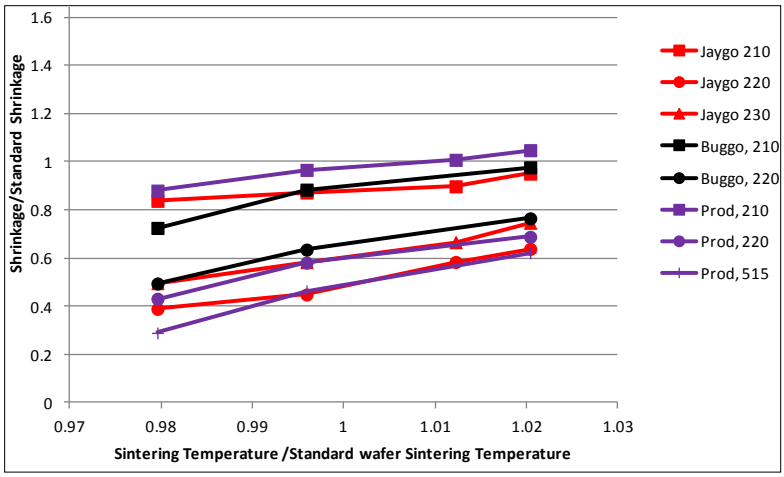

Figure 28-65. Shrinkage vs. sintering temperature for various tapes made with different powders and with different equipment.

For comparison, the porosity values for a series of tapes made for a support layer in standard wafers are shown in Figure 28-66.

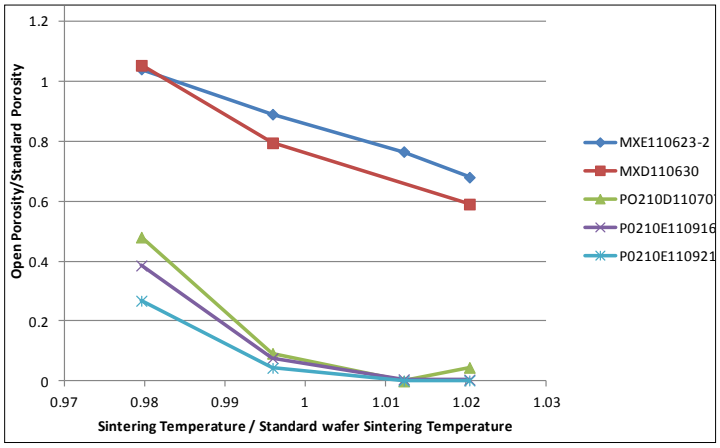

Figure 28-66. Open porosity as a function of sintering temperature for tape lots made with two types of powders (MX and PO).

This figure shows typical variation from lot to lot. Also shown are the results for three tapes made with similar starting powders. The shrinkage of the tapes is shown in Figure 28-67.

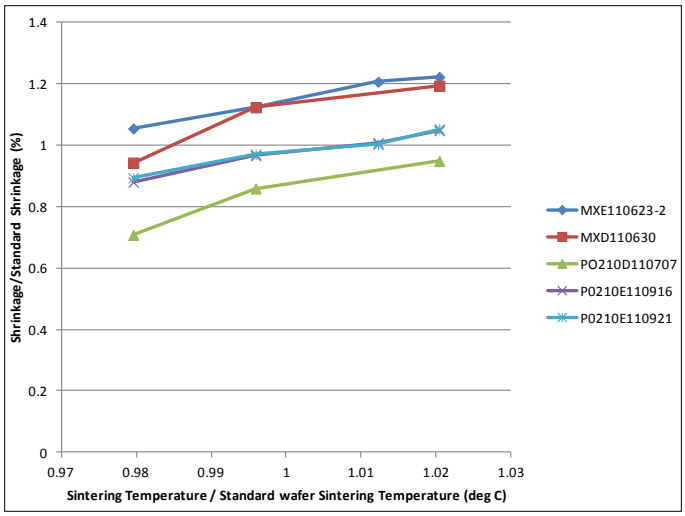

Figure 28-67. Shrinkage as a function of sintering temperature of cast tapes.

Based on these results, it is fairly clear that the 210 series material is the best fit to co-sinter with membrane tapes. It should be noted that the 210 series powder has a particle size distribution similar to the screened powder produced for standard wafers. A comparison was made of the particle size distributions between several 210 series powder lots and several typical lots from the screened powder source after being milled as per procedure and cast into tape (Figure 28-68). The only real difference is a distribution of finer powder, which has only a minor effect on tape sintering properties.

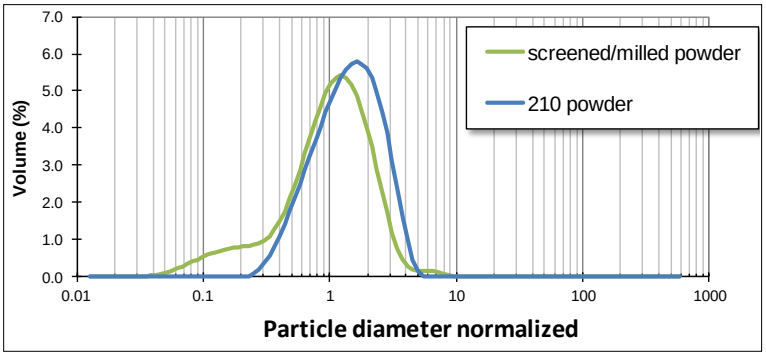

Figure 28-68. Overlay of the PSDs of milled screened powder and 210 series powder, showing similar particle sizes except for some fine particle distribution.

Finally, one option available to control layer properties is to alter the particle morphology. To this end, a baseline of the 210 and 220 series powders was selected and additions of 0, 10 and 20% fine powders were made. Figure 28-69 shows the effects of different levels of fines addition to the 210 series powder.

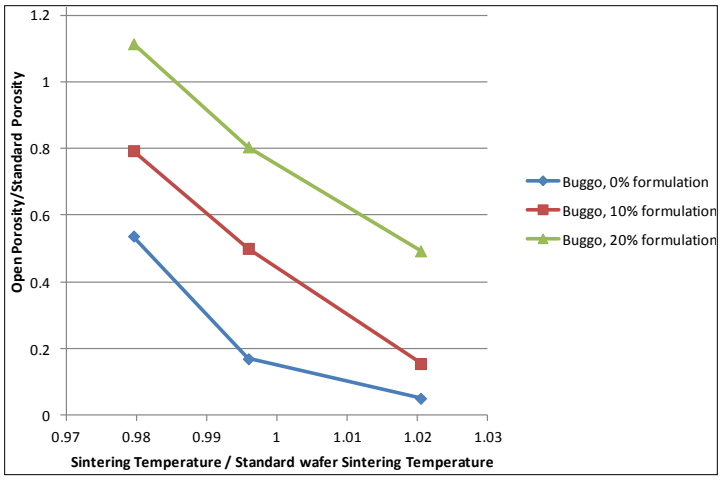

Figure 28-69. Open porosity vs. sintering temperature for lab-scale cast tapes made from 210 series powder for different fines loading.

The data show that adjusting the fines content is effective in adjusting the porosity. Figure 28-70 shows the shrinkage as a function of fines loading for 210 series powders.

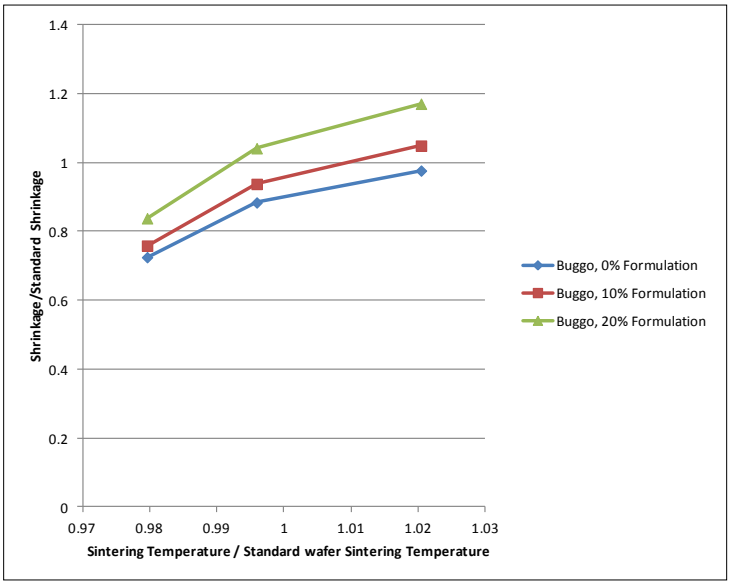

Figure 28-70. Shrinkage vs. sintering temperature for lab-scale cast tapes made from 210 series powder for different fines loading.

Figures 28-71 and 28-72 show that the addition of finer powder has a lesser effect on porosity than anticipated. In particular, the effects on shrinkage were minimal, likely due to the improved packing of a bi-modal distribution of powders.

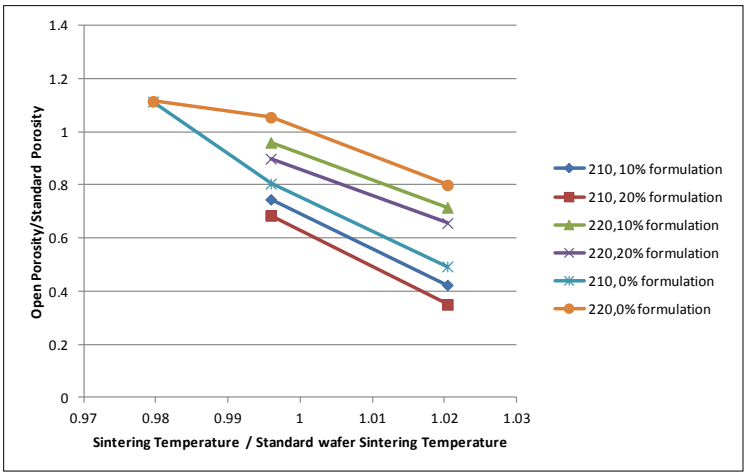

Figure 28-71. Open porosity vs. sintering temperature for 210 and 220 series powders cast with various amounts of fine powder additions.

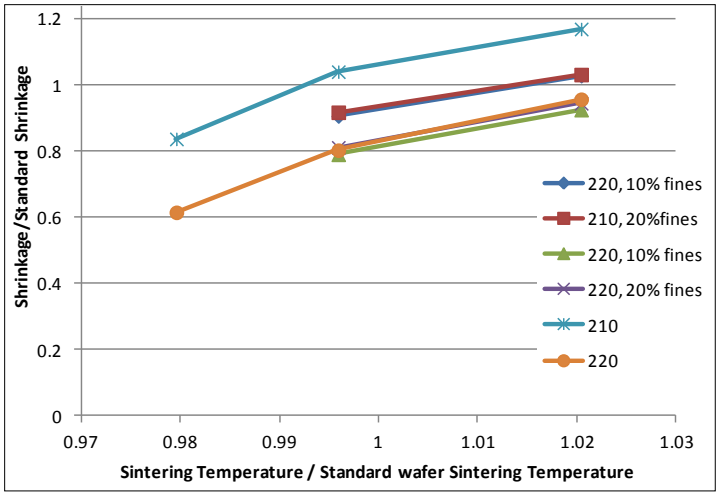

Figure 28-72. Shrinkage vs. sintering temperature for tapes with 210 and 220 series powder cast with varying amounts of fine powder additions.

From these data, the 210 series powder was selected as the best powder for production of wafers, although the results indicate that some slip re-formulation may be optimal.

28.2.1.1 Wafer Process Refinement

Ceramatec produced over 74,500 kg of powder in support of advanced architecture wafer (AAW) development (Task 28) and, under Task 17, to produce ISTU modules. Figure 28-73 shows the overall powder production at Ceramatec by quarter in blue, and production at the CerFab (Task 30) by quarter in red.

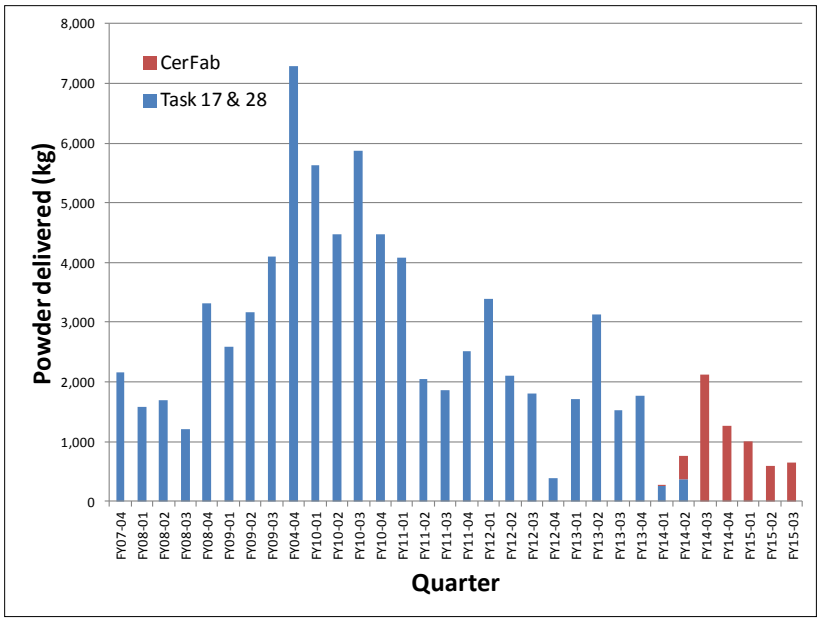

Figure 28-73. Powder production (blue bars) in support of experimental wafer fabrication during Phase 3 (Task 17) and Phase 5 (Task 28) by quarter.

Ceramatec utilized the powder produced to make 70,200 feet of ceramic tape for casting experimental advanced architecture wafers (Task 28) and wafers for use in the ISTU (Task 17). Figure 28-74 shows the overall tape production at Ceramatec by quarter.

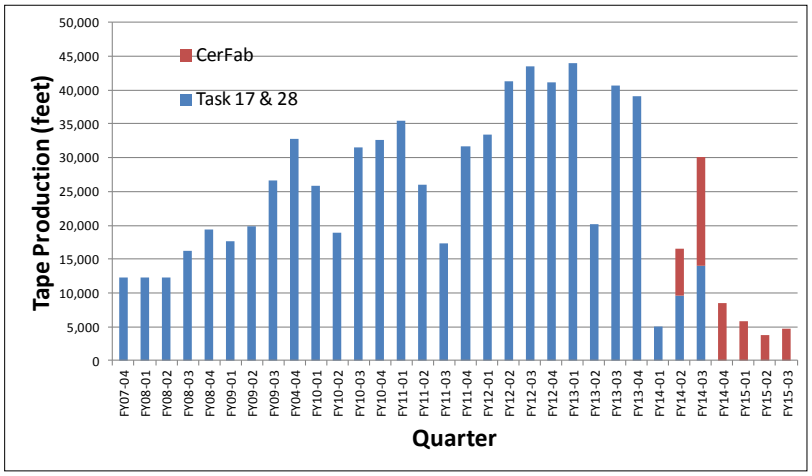

Figure 28-74. Tape production (blue bars) in support of experimental wafer fabrication during Phase 3 (Task 17) and Phase 5 (Task 28) by quarter.

Tape was converted to over 790,000 featured parts, as shown in Figure 28-75**.** These parts were included in experimental AAWs (Task 28) and for ISTU module construction (Task 17).

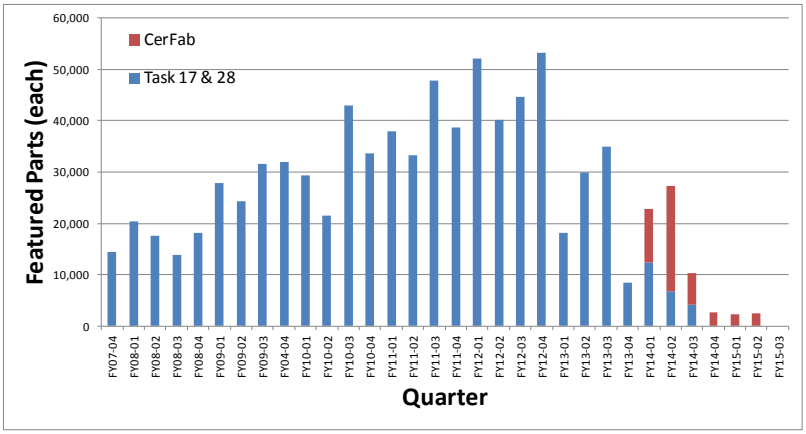

Figure 28-75. Featured parts production (blue bars) in support of experimental wafer fabrication (Task 28) and module production (Task 17) by quarter.

Figure 28-76 documents the number of wafers sintered through the time frames of Tasks 17, 28, and 30. Over this period, a total of nearly 110,000 wafers were sintered. The production for Task 30, done at the CerFab, is included for reference in the figure through Q2FY15 but not included in these totals.

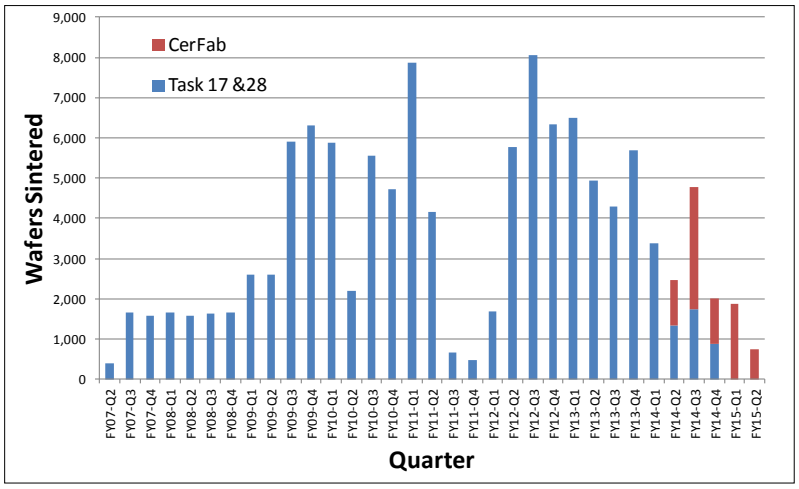

Figure 28-76. Wafers sintered by quarter.

Figure 28-77 documents submodule production during Tasks 17, 28 and 30. A total of almost 4,400 submodules were fabricated over this period. The production for Task 30, done at the CerFab, is included for reference in the figure but not included in the total.

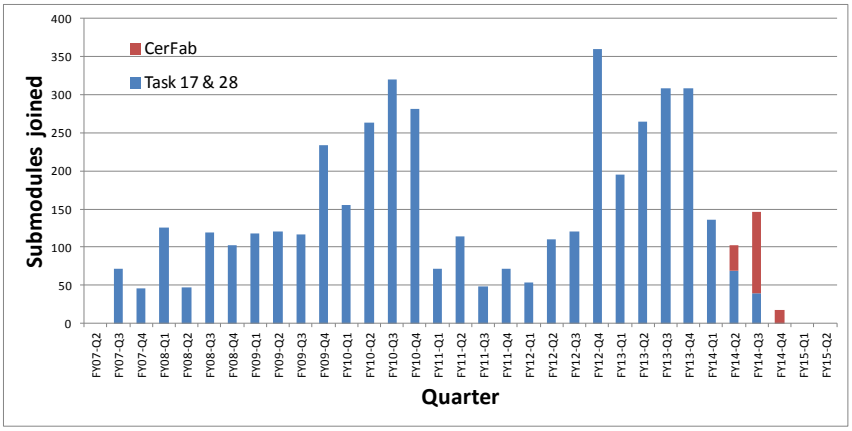

Figure 28-77. Submodule production from Tasks 17, 28 and 30 by quarter.

28.2.1.2 Advanced wafer process development

Validation Testing

Ceramatec cycled two 12-wafer stacks of advanced architecture wafers and two 12-wafer stacks of standard wafers in a laboratory furnace from room temperature to 900°C and back to room temperature at 20°C/hour. All of the advanced architecture wafers survived this cycle, but over half of the standard wafers fractured (Figure 28-78).

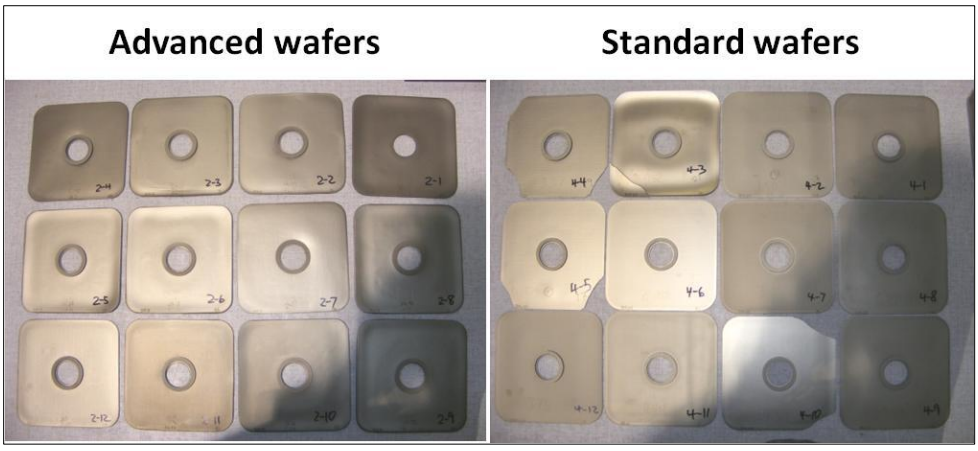

Figure 28-78. Photographs of advanced architecture and standard wafers after cycling at 20°C/h to 900°C.

In another validation test, stacks consisting of three joined advanced architecture wafers were heated, then power to the furnace was turned off to simulate an uncontrolled cooldown in a hot vessel. The experiment was performed twice without any observable degradation to the stack, as monitored by acoustic emissions. The results of these validations confirm the ability of the

advanced architecture wafers to cycle more rapidly than standard wafers due to their ability to equilibrate with the environment and maintain uniform oxygen concentration in the material.

Process Development for the Advanced Architecture Wafers and Modules

Subsequent to the selection of the materials for advanced architecture wafers, viable processes for producing these wafers had to be developed. A manual system for executing the One Step process was designed and used by operators to produce ~2,000 wafers. At the same time, lab-scale work was directed at investigations of the Two Step process using a similar methodology. Multiple thermal cycles were used to achieve a leak tight component. The lab-scale work produced the best results for wafers.

As efforts continued, the results indicated that the Two Step approach was more successful than the One Step approach. This is not surprising because there is a higher probability for defects to occur during the One Step process. Typical leak rate distributions for wafers made by the One Step process are shown in 28-79. Therefore, a decision was made to focus efforts only on wafers made with the Two Step process.

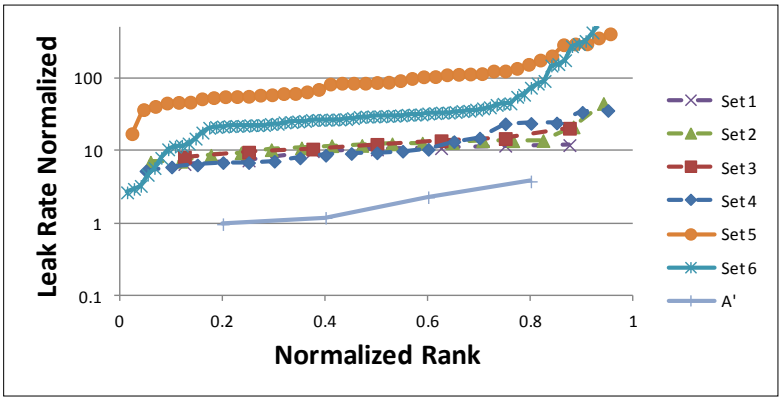

Figure 28-79. Leak rate distributions for wafers made by the One Step process.

As mentioned earlier, initial wafers were made using a screened powder and processes for making the standard wafer internals because they were known to have good compatibility with the membrane. However, the morphology of the screened powder was not ideal for advanced architecture wafers because it leads to low-strength materials.

Measurements were made of both the strength and compressive creep rate of wafers made using the screened powder process. Although wafers equilibrated rapidly during thermal cycles and

could be joined successfully, several wafers cracked during joining. In addition, the using the screened powder process for making powder and slip for these wafers was labor-intensive and inefficient.

Wafers using the screened powder process were fabricated because they met leak rate specifications and could be made in reasonable quantities by production operators. Work conducted in laboratory-scale experiments demonstrated that equivalent or better yields of "in-specification" wafers could be obtained by the Two Step method with a relatively low number of thermal cycles. After the desired 210 series powder stream was identified, wafers were made with the improved Two Step method. The combination of the 210 powder and the appropriate thermal cycles proved successful, as equivalent or higher yields of in-specification wafers were obtained as compared to wafers made from screened powder.

A full factorial experimental test matrix was completed (64 wafers) to understand the interplay of various parameters affecting the One Step process. The evaluation parameters were membrane thickness and average leak rate. The measured leak rates did not meet specifications, but were good enough to draw some direction. In parallel, Ceramatec processed several hundred wafers through the PDF to gain experience with high-volume fabrication. In general, the wafer leak rates were too high to produce high-purity oxygen during operation. However, some wafers with sufficiently low leak rates were produced, which demonstrates the feasibility of this approach. Most leaks occurred around the edges of wafers, as opposed to the membrane area (Figure 28-80).

Figure 28-80. Bubbles from a submerged, internally pressurized wafer showing sources of leaks as small holes around wafer edges.

A procedure to reduce edge leakage was developed. Three of five laboratory wafers produced using the procedure met the specifications for producing >99.5% pure oxygen, and the remaining two wafers meet specification for producing >97% pure oxygen. Despite the manual nature of the work, the edge quality was generally high (Figure 28-81).

Figure 28-81. Photograph of the sintered edge of an advanced architecture wafer treated with a preferred method to address edge leakage.

In other laboratory studies, testable wafer yields of over 85% were achieved using the edge treatment.

Two types of spacers were processed with the Two Step wafers: improved standard spacers, referred to as the OD2 spacer, and advanced architecture spacers. Six out of six three-wafer stacks using the OD2 spacer survived joining. Thirty out of 33 submodules survived joining when the advanced architecture spacer was used. Submodules were used to build two 1 TPD modules and one 0.5 TPD module. Joining of the 0.5 TPD module was unsuccessful primarily due to processing parameters. As a result, the joining parameters for the two 1 TPD modules were altered *in situ*, and both 1 TPD modules were joined successfully. An image of one of the modules in the assembly furnace is shown in Figure 28-82.

Figure 28-82. One of the first 1 TPD modules made entirely from advanced architecture wafers in the assembly furnace.

The "210" series powder stream and a process for making it were selected, and the Two Step process for producing advanced architecture wafers was further developed. The selected powder was modified to be compatible with the tape cast membrane. Yields of wafers meeting the leak-rate specification using the modified 210 powder increased. A set of three submodules produced with Two Step wafers and the 210 powder were joined using standard procedures and materials and with reduced thermal cycling time. All three submodules were successfully joined, with leak rates lower than the sum of the starting wafers.

Wafer Flatness

Ceramatec measured the flatness of the joining surfaces of advanced architecture wafers to determine the optimal cycle to produce the flattest surface. Advanced architecture wafers were less flat than standard wafers (Figure 28-83)

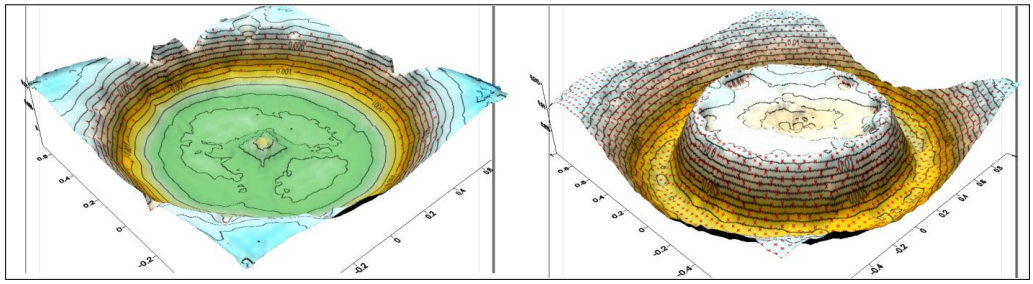

Figure 28-83. Profilometer measurement of an advanced architecture wafer.

The distortion was thought to be due to differential equilibration between the spacer and wafer. The data indicated that refined joining methods were required. Further assessment was made of the flatness of the joining surfaces of various types of wafers. The wafer types showed similar deflection of the wafer during cycling.

Parallelism

Ceramatec measured the parallelism of 30 advanced architecture submodules. Figure 28-84 documents the average variation in submodule height. The results were comparable to the parallelism seen in standard submodules.

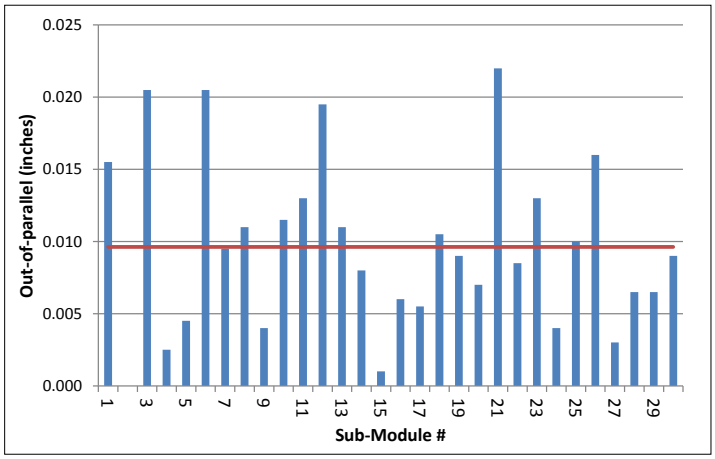

Figure 28-84. Advanced architecture submodule out-of-parallelism.

The submodules discussed above were part of a larger study in which Ceramatec adjusted the strength of the internal layers and studied joining efficiency with AAWs. The following is a summary of this work.

Wafer Type 1

- Without spacers:
  - One of approximately 18 survived with no visible cracks
  - All wafers had high leak rate
- With spacers:
  - No attempts

Wafer Type 2

- Without spacers:

- One of three submodules survived with no visible cracks
- All wafers had high leak rate

- With spacers (standard architecture):
  - All six 3-wafer submodules fabricated with no signs of cracking
  - All wafers had high leak rate
- With spacers (advanced architecture):
  - Thirty of 33 submodules survived with no visible cracks
  - All wafers had high leak rate

Wafer Mechanical Testing

Ceramatec mechanically tested a variety of different wafer types using four test methods:

- Wafer ring-on-ring: Loads a wafer with two offset o-rings on either side.
- Wafer c-ring: Pulls a sectioned wafer in tension to failure.
- Wafer tensile testing: Pulls a spacer/wafer/spacer sub-component apart in the axial direction.
- Wafer deflection: Measures the allowed loading on the edge of a wafer before failure.

An image of each test method is shown in Figure 28-85.

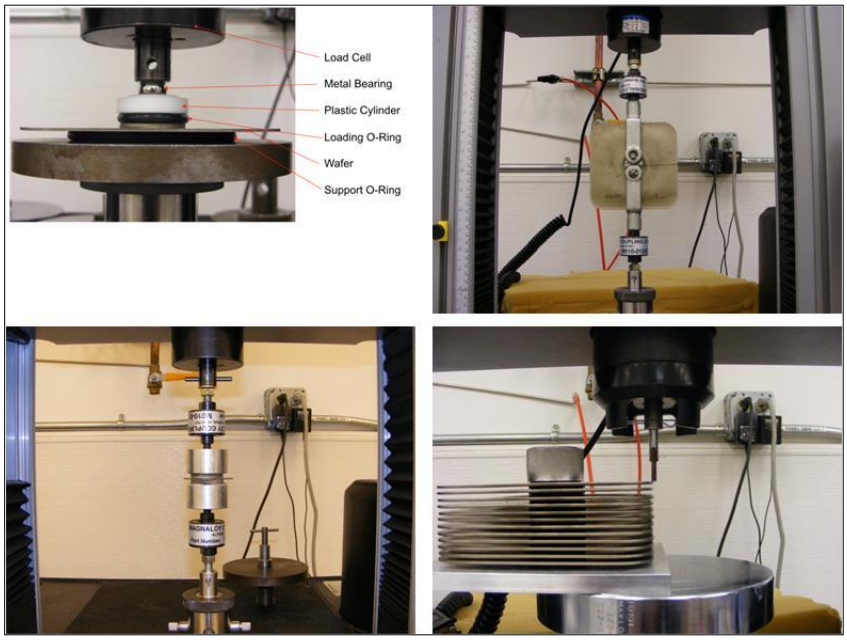

Figure 28-85. Four testing methods used to test the mechanical properties of wafers. From left to right, top to bottom: wafer ring-on-ring, wafer c-ring, wafer tensile testing (wafer broken off), and wafer deflection testing.

Table 28-1 presents the ring-on-ring and c-ring test results.

Table 28-1. Wafer ring-on-ring and c-ring test results.

	Failure Loads (N)			
	Ring-on-ring		C-ring	
	Mean	SD	Mean	SD
With spacers				
Advanced Architecture A	68.1	13	131.1	15.2
Advanced Architecture B	72.4	14	114.4	7.6
Advanced Architecture C	76	11.3	126.1	11.3
Advanced Architecture D	79.6	6.1	130.5	28.8
Advanced Architecture E	73.7	12.4	132.2	28
Advanced Architecture F	70.8	12.2	130.4	14.6
Advanced Architecture G	78.3	9.8	154.9	7.3
Original	71	2.2	106.2	11.1
With no spacers				
Original	27.8	5	-	-
Advanced Architecture H	54.9	4.2	141.4	14.1
Standard A	30.6	1.1	-	-
Standard B	31.3	2.8	54.2	3.6

The table is divided into wafers tested with spacers, and wafers without spacers. For wafers with spacers, there was very little difference in the strengths as measured by ring-on-ring. Without spacers, the wafers were notably weaker in both test methods, with the exception of advanced architecture wafer H, which performed remarkably well.

Wafer Deflection Testing

Wafer deflection tests were conducted in both the direction of their crept "droop" during thermal processing and in the opposite direction ("anti-droop"). The results are presented in Figure 28-86.

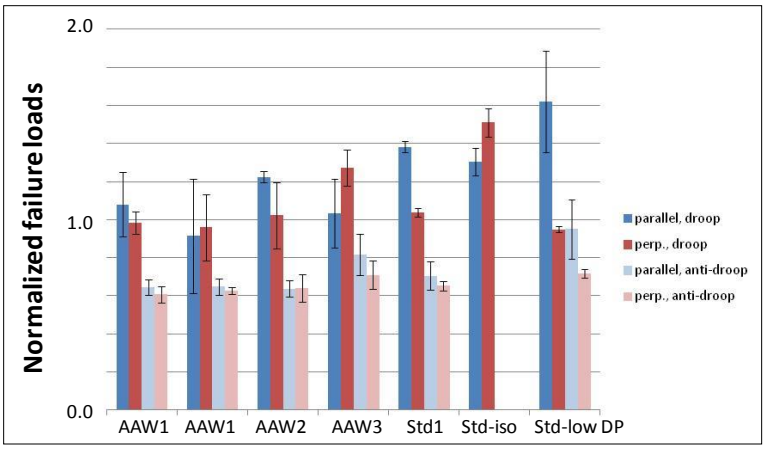

Figure 28-86. Failure loads for crept wafers.

Strength was controlled by the direction of testing relative to the "droop" of the wafer caused by creep. When loaded opposite to this droop, the strength was notably lower. There was no significant strength penalty between the different types of advanced architecture wafers. In some cases, the advanced architecture wafers outperformed their standard wafer counterparts.

Poly Wafer Development

Poly wafers are an advancement of the processing methods used to make advanced architecture wafers. Early experimental casts of the poly wafer had shown variable adhesion properties to the casting substrate. Two options to resolve this issue were investigated: a coating formulation with a lower release point, and casting modifications which would allow the use of the current substrate. Tape cast using a new coating formulation showed significant promise. Also, the formulation and casting conditions were adjusted.

Another area of emphasis was the improvement of the spacer-wafer joint and its effect on leak rate. Ceramatec measured leak rates from wafers joined to spacers for trial poly wafers. The results are shown in Figure 28-87. The leak rates declined due to the correction or elimination of manufacturing-related issues.

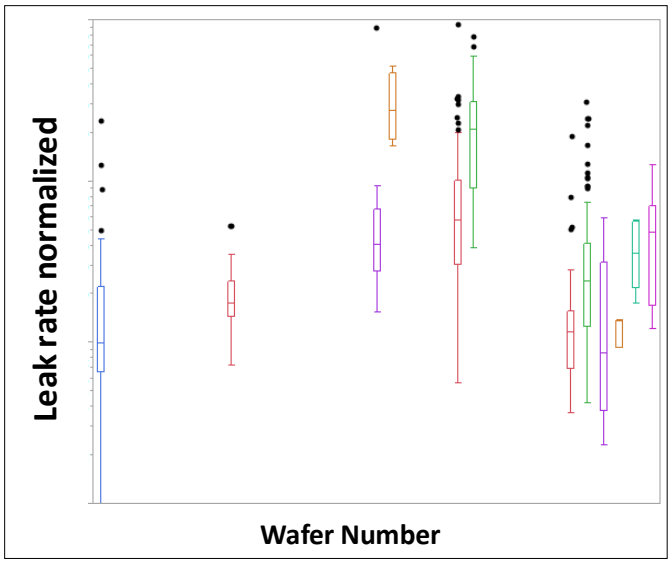

Figure 28-87. Poly wafer leak rates from experimental trials.

Spacers

Ceramatec developed a method to prepare the spacers by first producing the core of the spacer and then adding outer layers by lamination. Spacers can be adhered directly to an outer tape cast layer as shown in Figure 28-88.

Figure 28-88. Photograph of an advanced architecture spacer that was directly adhered to a tape cast layer.

Ceramatec explored a powder press processing method to develop spacers for use with advanced architecture wafers. The success of this method depended on several factors, including shrinkage compatibility with the green wafer and of making a low-leak joint.

A study was undertaken to determine the proper loads during pressing. It is important to press in the loading regime so as to avoid deleterious spring-back, which causes cracking. If double-pressing were employed, it would be vital that the first press be done in the loading regime where spring-back of the pressed part is bypassed. The study also provided a good extrapolation to other powder formulations. Pellets were pressed to determine green density as a function of loading. Figure 28-89 presents the test results.

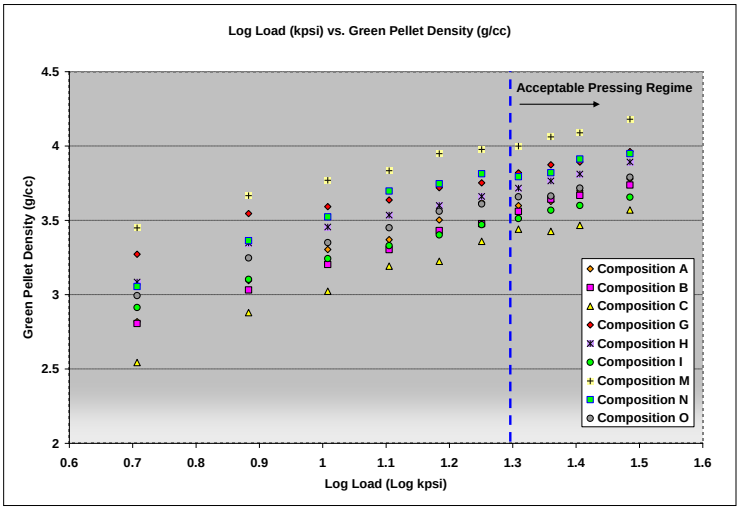

Figure 28-89. Acceptable and non-acceptable loading regimes based on pressing experiments with pellets.

The deleterious spring-back regime (unacceptable loading) transitions smoothly into the non-deleterious spring-back regime (acceptable loading). The blue dotted line separates the two regimes. The pellets were fired and subsequently tested for shrinkage and fired density. Compositions C and I were the only viable candidate formulations.

28.2.2 Submodules

28.2.2.1 Thermal Cycle Requirements

28.2.2.2 Joining Improvement

Cracking occurred in many AAW submodules with a standard spacer, so various approaches were taken to eliminate the cracks. It was theorized that the cracking was due to differential equilibrium, and Ceramatec conducted experiments to test this theory. The kiln fixtures were set up differently to reduce constraints. The results were positive: 29 of the 31 submodules were successfully joined without any signs of cracking in the wafers or spacers. The data in red (Figure 28-90) represent the improved spacer. The other data represents the historical trend going back

12+ months. The decline in yield shown by the blue data after Run 433618 was eventually traced to a bad component lot that caused a defect to propagate through to the assembled structures. Figure 28-90 documents trends in submodule yields and the number of submodules joined for on-line process and experimental trials during Tasks 17 and 28.

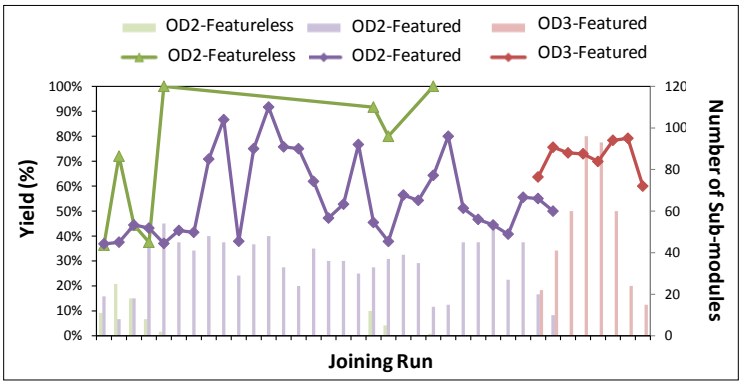

Figure 28-90. Yield trends during submodule joining. Yields are shown with points connected by lines.

28.2.3 Modules

28.2.3.1-2 Thermal Cycle Requirement and Joining Improvement

Testing and development of submodule and module assembly methods were conducted concurrently with work on materials selection and component development. Ceramatec carried out the first attempt to join AAW submodules into modules with 30 submodules produced in the submodule joining experiments (see section 28.2.2.2), and attempted to build two 1 TPD module and one 0.5-TPD module. The two 1 TPD modules were processed fully intact (Figure 28-91); the 0.5-TPD module had one cracked submodule.

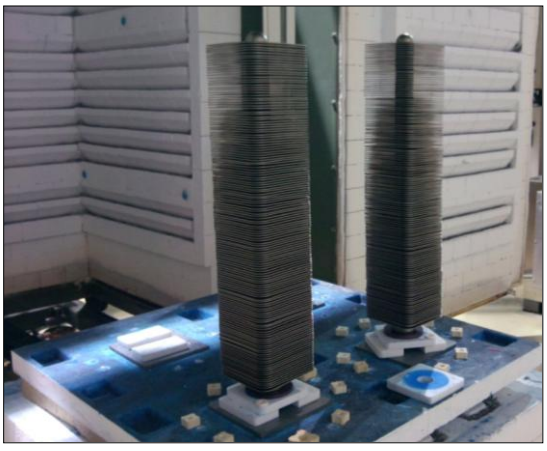

Figure 28-91. Advanced architecture modules.

The two 1 TPD modules were built with methods developed under Task 17 per standard procedure for building standard modules to enable good alignment. The overall alignment of the advanced architecture modules was comparable to the alignment seen in standard modules.

A number of attempts were made to join wafers using standard spacers. All attempts at joining advanced architecture wafers without spacers had unacceptably high levels of cracking. In contrast, three submodules were made for another study using the same wafer type, the same process conditions, and with spacer/wafer coupled. This method yielded three out of three good submodules.

A new oven was used to prepare five of 32 modules for joining. Modifications to the oven were made based on the initial trials of two modules. The oven cart, which rolls in and out of the oven, was put on rails to provide smoother and more stable motion. The top of the cart was modified to allow up to 12 fixtures, secured and leveled so it could be easily removed to transfer the modules for joining. The arrangement was used to prepare additional modules which were subsequently joined. Module alignment was measured and found to be comparable to that achieved previously.

28.3 Manufacturing Process Development and Scale-up

Background

Cerfab

The Process Development Facility (PDF) at Ceramatec provided a test bed for the development of most engineering specifications for the CerFab equipment. In some instances, the equipment procured for the CerFab was a newer version of the same equipment used at the PDF. Examples of specification development for the main process manufacturing areas at the CerFab are presented below, along with some background on the effects of AAW development on the eventual CerFab design.

Because advanced architecture modules were likely to achieve superior results in both manufacturing and operation, implementation of advanced architecture manufacturing was incorporated into the CerFab design from its conceptual inception. Equipment was specified for the CerFab with a goal for the facility to be capable of accomplishing all process steps required to fabricate modules with advanced components. Specific equipment requirements and operating procedures to fabricate such modules in the CerFab required additional component and process

development. The team was successful in achieving the required project schedule and the development activities in parallel.

The team traveled to numerous vendor sites to complete the specification for and selection of the eventual suppliers to the CerFab. Various types of equipment or variations produced by different vendors were evaluated, and engineering comparisons were made of the options available. These developmental and engineering activities enabled creation of specifications and selection of over 120 major equipment items that make up the facility.

28.3.1 Materials Recycling Processes

Experiments were conducted at Ceramatec to evaluate the potential to recover powder from tape scrap and, later, sintered wafers. Two stream methods of recycling tape cast material were investigated. The "A Stream" involved re-dissolving scrap tape that would be re-solvated and then casting the redisolved slip. The "B Stream" was developed for scrap that contained more than one starting powder, or that had been affected by various processing conditions. The "B stream" involved heating the material to temperatures high enough to remove all the organics, recovering the powder, and re-milling the recovered powder to the desired particle size.

A shredder was purchased and installed to develop a process to break down green tape, laminates and scrapped wafers into a feed stock that could be fed into slip batching systems or a kiln. Initial trials to develop the B Stream were done in batch kilns using stainless steel pans to remove the binder at elevated temperature. This later led to the purchase of a small laboratory rotary kiln to run trials on developing a more continuous and energy-efficient means to convert green scrap to powder that could be either be calcined alone or blended with virgin (raw) AP2k constituent powders prior to calcination. Qualification of this stream (referred to as "B"), mixing it with virgin material prior to calcination, was completed.

Re-solvating tape (A Stream) was also found to have potential. This process was qualified for making wafers with older designs. However, the process for wafers with advanced designs required isolation of scrap per tape formulation, and was abandoned to simplify the process to burnout all scrap green tape and wafers.

Ceramatec recommended that the same shredder vendor be used for the CerFab, but with a larger HP motor to reduce the potential of clogging the equipment. Based on experimentation with the

laboratory rotary kiln and predictions of scrap rates and the required throughput, the rotary kiln was scaled accordingly and a method to inject the feedstock into the tube was recommended to the vendor to avoid material buildup at the tube entrance.

28.3.2 Tape Casting

Experience with tape casting under Task 17 provided the starting point to select the tape casting equipment for the CerFab. The Air Products/Ceramatec team selected a tape casting approach for the CerFab with the same configuration as that used in the PDF. The scale of both casters is not materially different; that is, each could achieve the tapes and rates required for larger-scale production. However, the operability, control, and instrumentation of the caster at the CerFab needed to be significantly different and better.

Several suppliers provided bids for the CerFab caster. The final choice was made by conducting tests at the suppliers' facilities to confirm the ability of the caster to make the required tapes and provide the necessary operability and control flexibility. The equipment chosen enabled rapid turnaround time in transitioning between tape layer production needs. The sensors and controls in the drying sections provided a consistent base from which to produce the required tapes.

Tape casting development and equipment specifications were based on casting the various layer thicknesses. Critical parameters included not only drying conditions to generate defect-free substrates, but also consideration for release parameters from the carrier, lamination characteristics, and featuring such as laser cutting, or punching while achieving target shrinkages, porosities and densities.

In evaluating suppliers for casters, material (powder, solvents, organics additives and/or slip) was sent to evaluate caster coating thickness control along with drying control. Safety controls were also reviewed. Tests included coating using a high-viscosity slip. The vendors proved that they were able to successfully dry and have consistent coating thickness. A low-viscosity, thin-layer coating was tested successfully: consistent coating thickness and a dry membrane layer were produced.

Based on this work, Ceramatec fully specified the tape caster to the CerFab engineering team working under Task 30.

28.3.3 Advanced Membrane Preparation

Milling

Ceramatec conducted a test of a high-amplitude particle size reduction mill using ITM powder. The goal was to determine whether the mill could be used in the CerFab (Task 30) directly or if the resulting powder would require additional classification. Each test, regardless of variable settings, generated the lower bound on particle size before the upper bound was reached. Thus, classification of the milled powder was required to achieve the desired particle size distribution (PSD). One mill chosen for the study had significant advantages, including simple operation, low maintenance, excellent mixing homogeneity and low energy consumption. The tests matrix was composed of six separate tests where the powder weight and process parameters were adjusted. Samples were pulled at defined intervals from each test. Each sample was tested for PSD and powder surface area (PSA). Least squares analysis of PSA showed that all of the parameters documented in Table 28-2 were significant. However, least squares analysis of the upper and lower bound on the PSD showed that the only significant factors were powder weight and milling time.

Table 28-2. Parameter estimates for PSA.

Term	Estimate	Std Error	t Ratio	Prob>|t|
Intercept	0.4857003	0.022248	21.83	<.0001*
Var. 1	-0.001997	0.000347	-5.76	<.0001*
Powder WT (Kg)(7.5,15)	-0.122244	0.013383	-9.13	<.0001*
Time (min)	0.0018575	9.682e-5	19.19	<.0001*
(Var 1)*Powder WT (Kg)	0.0011917	0.000347	3.43	0.0023*
(Var 2)*(Time (min)-137.5)	-2.053e-5	2.231e-6	-9.20	<.0001*
Powder WT (Kg)*(Time (min)-137.5)	-0.001139	0.000102	-11.14	<.0001*

The test model predictive curves suggested optimal conditions. Two more tests were conducted at 5 kilogram and 7.5 kilogram. The 7.5 kilogram sample was run for 960 minutes, and the 5 kilogram sample was sampled periodically at a test completion of 47 hours. This second test resulted in a multimodal distribution. Both the PSD and PSA shifted well below their respective desired ranges. The time verses particle size curve fit suggests that most of the size reduction occurs in the first 4-10 hours of milling (Figures 28-92 and 28-93).

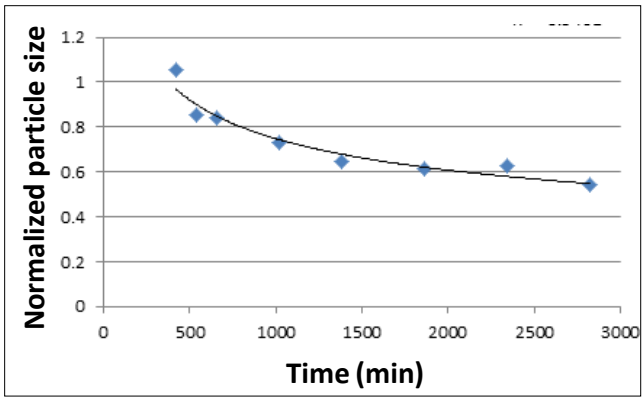

Figure 28-92. Plot of upper bound on the normalized particle size distribution as a function of milling time.

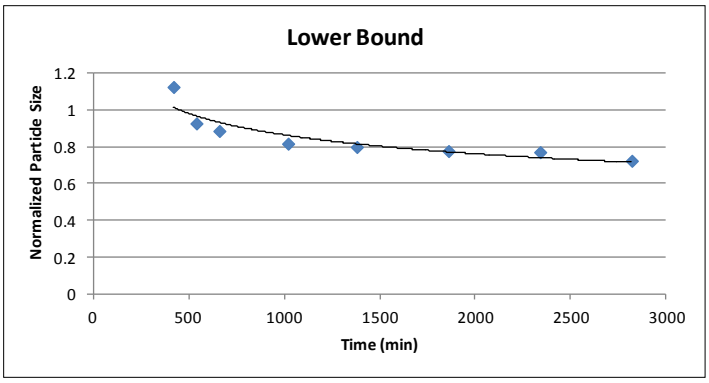

Figure 28-93. Plot of lower bound on the particle size distribution as a function of milling time.

The difference between the time in which the PSD lower bound is reached and time in which the PSD upper bound is reached was negative in every test. This means that the PSD will drop below the lower bound before it reaches the upper bound. It was concluded that the desired PSD cannot be achieved using this mill without using classification.

A mixer which mixed, dried and granulated the powder was tested to determine its ability to produce manifold component powder. AP2K manifold powder was successfully generated (50% yield). Twenty-five percent of the remaining powder was larger than the desired size, and 25% was smaller. Domes manufactured from the powder showed no variation from the normal production domes.

A planetary mixer was tested to assess its ability to produce the powder. The resulting powder was more uniform and flowed better than the manually produced powder (Figure 28-94).

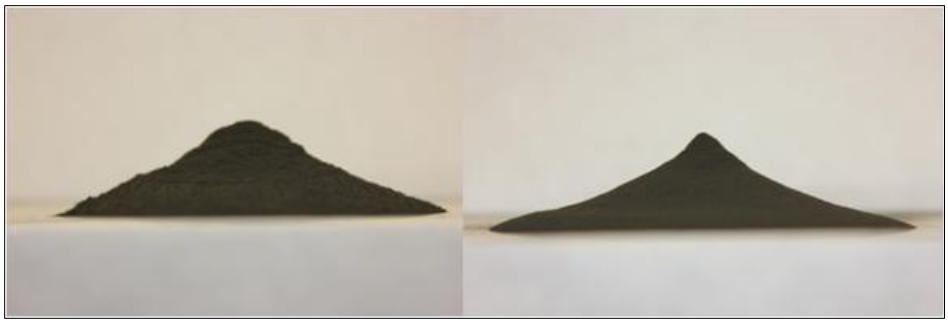

Figure 28-94. Granules made by hand (left), and in planetary mixer (right).

As a result, a used planetary mixer was ordered, delivered and modified so that it met all safety requirements.

An additional series of tests was conducted to improve the powder yields from the planetary mixer. Adjusted variables in the formulation were systematically studied, and the resulting powders were classified into three size ranges (A, B, and C). The yield results are presented in Figure 28-95.

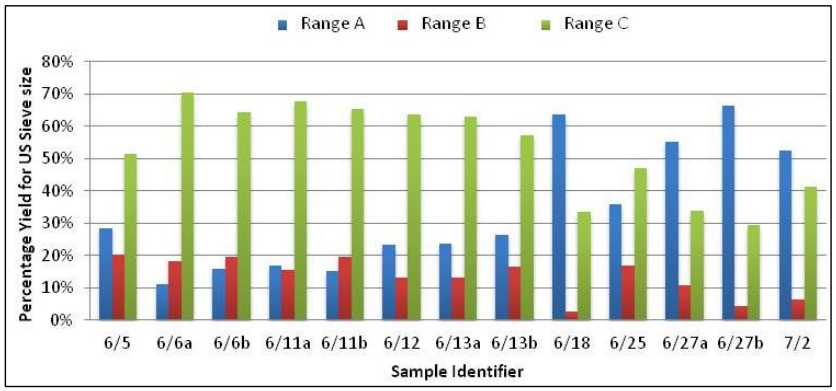

Figure 28-95. Planetary miller powder size distribution.

Only one variable had a significant effect on yield. Additional tests were run using an additive to see if it would increase the yield. The results were very favorable.

Additional tests using a planetary mixer were conducted at custom milling shop. The test system included a helical dual planetary mixer. Powder from this process flowed nicely. By repeating the process, all of the powder could eventually be converted to the desired powder size distribution.

Table 28-3 is a comparison of four milling methods.

Table 28-3. Milling methods comparison.

	Pros	Cons	Capital Costs	Labor (kg/hr)	Yield
Milling Method A	• Easy to operate • Low maintenance • Energy Efficient • Low level of contamination. • Robust process	• Requires additive • Long mill times (24 hrs) • Unable to produce much smaller PSDs in a reasonable time frame.	4	200	100%
Milling Method B	• Short grind times (6 hrs) • Capable of producing smaller PSDs	• High maintenance (pump head will require replacement on a regular basis) • High labor • Requires solvent • Must be operated in Class I Div. I Group C zone. • Temperamental process. Power loss during cycle or pump failure during cycle results in significant down time • Higher risk of contamination • Requires adjustment of solvents following grinding process.	2	60	100%
Incumbent	• Current baseline Capable of producing multiple PSD fractions • Once the process is established, easy to operate. • Minimal Contamination	• Hi energy consumption. • Less than 100% yield.	3	250	90%
Milling Method C	• Low energy consumption • Low initial cost	• Very labor intensive (least efficient of all options) • Requires significant repetitive motion (would eventually need to provide a manipulator to prevent injury) • Requires solvents • Equipment must be Class I Division I group C • Minimal control of PSDs • Requires significant hazardous rated floor space. • Greatest risk of higher variability.	1	19	100%

The capital cost of Milling Method A was found to be too high to justify its use. Milling Method B would be very difficult to operate due to pumping problems. The abrasive nature of the ceramic powder results in high wear of the circulating pump bearings, seals and displacement contact surfaces. If the pump shuts down during the milling process, the powder will settle out and plug pipes, the pump, and the bowl with a concrete-type solid. Disassembly and cleaning would take significant time. This milling method would require about four times the labor to keep running as compared to the Incumbent and Milling Method C.

Method C has the lowest equipment capital costs. However, the process is labor-intensive when compared to the other options. Also, there is little flexibility in adjusting the width of the PSD and there is a high risk of batch-to-batch variation. The incumbent method provides the greatest flexibility, and very narrow cuts of powder can be generated.

Ceramatec used the information above to specify the CerFab powder processing area final design; all of the above tests were beneficial in the decision. In addition, the team visited the third-party tolling operations that had provided the in-specification powder used at the PDF and surveyed their equipment. Ceramatec recommended specifications based on much of the powder processing equipment operated by the third parties that was already successfully providing powder for program needs. Testing with the raw materials was also performed at the suppliers' facilities to confirm that the newer equipment would provide the desired results.

28.3.4 Joining Cycle Time Reduction

Ceramatec optimized the thermal process for manufacturing wafers. A shortened firing schedule showed no evidence of reduced wafer yield. A short-duration schedule was designed to maintain the mass loss rate within a band (Figure 28-96).

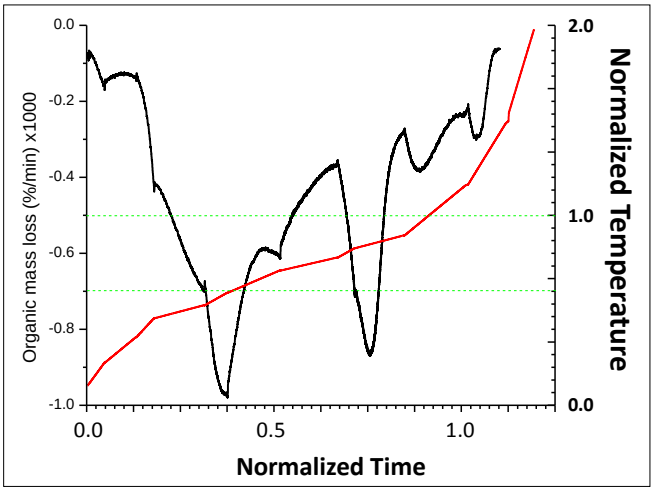

Figure 28-96. Organic mass loss rate (black), short-duration sintering cycle.

Figure 28-97 plots the organic mass loss rate for an experimental slip additive, with the well-optimized additive as reference. These data suggest that the binder removal rate can be accelerated.

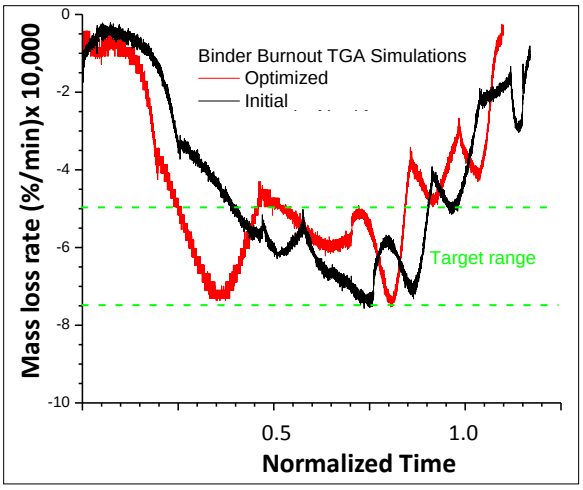

Figure 28-97. Comparison of the initial and optimized burnout profiles.

The evolution of cycle time reduction included new designs for kiln furniture and fixtures. Each of these developments improved the individual process cycle times by 15%, which has a direct impact on production capability and rate. Consistent application of the new methods and fixtures, along with revised thermal profiles in the kilns, also drove yield improvements at the PDF. These improvements all were transferred to the specifications for the CerFab process for immediate use in the design and eventual production techniques.

28.3.5 Module Post-Joining Conditioning

Prior to development of the advanced wafer design, several approaches were investigated to enhance the startup time and cyclability of modules. One of these methods was to condition the modules in a separate thermal cycle after joining. Due to the conditions of the proposed post-joining cycle, separate kilns were determined to be the most cost-effective means to implement this approach in manufacturing. A single-wafer module was sent to a potential kiln vendor and subjected to the proposed conditioning treatment. The treatment was shown to improve the allowable heating rate of the parts. Fortunately, development of the advanced wafer designs was timely and eliminated the need for this process.

28.3.6 High-Throughput Wafer Inspection

Ceramatec projected the cycle time and amount of labor needed for 100% inspection of wafers prior to submodule assembly; the estimates indicated that a large staff was required to support

inspection. The manual process to leak test, measure wafer size (X,Y), and sort based on leak rate and size, including the handling, took significant time per part.

Ceramtec's experience with the vision system on the WAM (Task 17) showed that with significant resolution on wafer image capture and test time, the wafer size (X/Y) could be captured within seconds. Using an outside integrator, a system was designed and tested to perform X-Y sizing, leak testing, and sorting with a rapid cycle time, which was sufficient for the CerFab required throughput. Ceramatec specified the design to the CerFab team under Task 30.

28.3.7 Optimize Parts Cleaning Processes

Kiln Furniture Cleaning

Ceramatec operated a parts cleaning machine under Task 17 that conveys the kiln furniture that supports the wafers during sintering through a fixed-gap abrasive wheel. The fixed gap allows parts only within a specific thickness range to be effectively cleaned. This presented two options: buffing the parts based on size bins, or setting a specification for part thickness. Binning parts requires accurate measurement and batch processing, but allows for surface-damaged parts to be resurfaced and put back into service. Resurfacing is not possible if a single part thickness is specified. Based on a few initial trials with a random selection of parts, tens of bins would be needed considering the current stock variance.

One hundred parts were processed/cleaned for use in the Cerfab. Originally, the parts were only planarized, making it difficult to manage consistent resurfacing with the abrasive resurfacer. The project allowed for the benchmarking of the new Cerfab part surface grinder tooling prior to ramp-up. The initial part surface grinding step was optimized to ensure a consistent surface. Parts were surface ground parallel, as envisioned for Cerfab, and a series of thermal treatments were conducted to define the thermal work window for surface restructuring. The surface restructuring was conducted with and without the presence of sintered wafers to determine the effect of simultaneous restructuring and seasoning.

An initial time-temperature surface restructuring scoping study was also completed. The new initial surface restructuring step appeared to produce a surface similar to a well-seasoned tenth-thermal-cycle part (Figure 28-98).

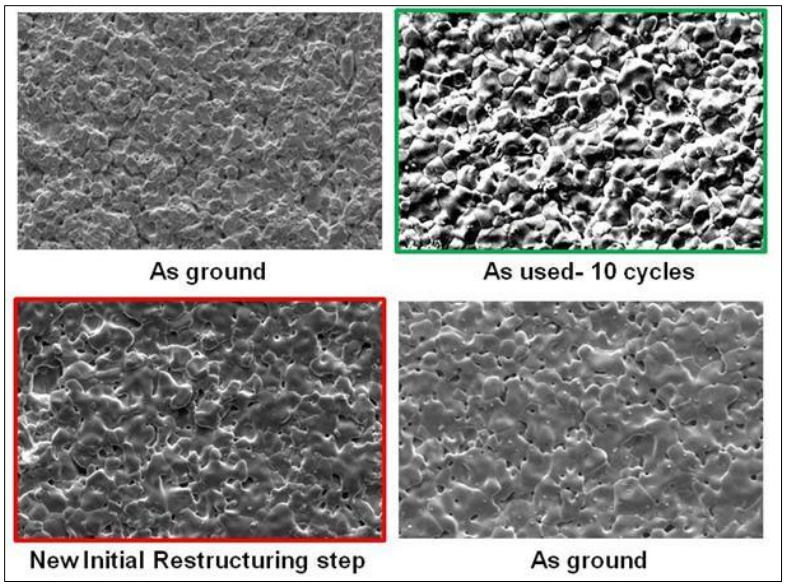

Figure 28-98. Kiln furniture surfaces: as ground, as used (10 cycles) and a new initial restructuring step.

Ceramatec also considered the removal of debris and contamination. After a review of rejected parts, it was determined that parts should be resurfaced if contamination is found. Parts are rejected for three main causes: warp, reaction with kiln constituents, and AP2k buildup. Surface grinding is required to remove warp and reaction products. A buffing/washing step is probably sufficient to remove AP2k buildup.

Materials Handling Development

Material handling involves moving process parts from one operation to the next. Ceramatec proposed a revised CerFab facility layout to ensure effective workflow from raw material handling to green material fabrication and featuring through the final thermal operations required to complete the modules. Specialized fixtures and handling devices were developed. For example, a fixture to maintain alignment of the green wafers during submodule assembly was developed based upon observation of the fixtures and methods used at the PDF. Compared to previous options, the new fixture maintains the alignment better and allows the assembly operation to be performed more consistently.

TASK 29.0 TABLE OF CONTENTS

TASK 29.0 ENGINEERING DEVELOPMENT FOR INDUSTRIAL AND CCS APPLICATION **2**

29.0 SCOPE **2**

29.1 CONCEPTUAL ENGINEERING DEVELOPMENT **2**

29.1.1 Process Development for Industrial and CCS Applications *2*

29.1.1.1 Process cycle and process economics 2

29.1.1.2 Equipment Development 4

29.1.2 Process Development for the ITM Oxygen Development Facility *6*

29.1.2.1 Process cycle development 6

29.2 DETAILED ENGINEERING DEVELOPMENT **19**

29.2.1 Identification of a preferred process scheme for testing ITM Oxygen at the 2000 TPD scale *19*

29.2.1.1 Performance model development 19

29.2.1.2 Operating profile development 22

29.2.2 Identification of a suitable site for the ITM Oxygen Development Facility *22*

29.2.3 Development of project-specific information for the ITM Oxygen Development Facility *24*

29.2.3.1 Equipment specification development 24

29.2.3.2 Budgetary cost estimate model 25

TASK 29.0 ENGINEERING DEVELOPMENT FOR INDUSTRIAL AND CCS APPLICATION

29.0 Scope

Task 29.0 focused on engineering development of specific implementations of ITM Oxygen technology for oxygen/power production and had two components: work on processes that feature or achieve low carbon dioxide emissions, and work on a 2000 TPD test unit design. Air Products carried out detailed process modeling of the ITM Oxygen Development Facility. The preferred process scheme for producing 2,000 TPD of oxygen from a developmental ITM Oxygen system was based on simulations of system and equipment performance. A suitable site for the facility was identified, detailed equipment specifications were developed and a project-quality cost estimate based on site-specific information prepared.

29.1 Conceptual Engineering Development

29.1.1 Process Development for Industrial and CCS Applications

29.1.1.1 Process Cycle and Process Economics

A number of industrial and CCS applications for ITM oxygen were investigated during the initial work under Task 29.0. Examples are described below.

Natural Gas Combined Cycle (NGCC)

Natural gas-fired combined cycles will be an important source of power in the US. The CO_2 in the NGCC flue gas is at a low partial pressure, making it uneconomical to capture by conventional absorption methods. Oxygen can be used to convert natural gas into a fuel that is more amenable to CO_2 capture. The oxygen is best sourced from an ITM membrane that, in turn, is integrated with the gas turbine. Many gas turbine integration variants are possible, and they are detailed in prior work under Tasks 2, 7, and 15.

Vacuum Residual Gasification for Chemicals, Power or Steam

There is a large inventory of vacuum residuals, a heavy by-product of crude oil refining. As crude oil gets heavier, this inventory is growing. There is commercial interest in monetizing this potential feedstock for chemicals, steam or power. If carbon capture is required, the most economical way to extract value from these residuals is through gasification, which requires

significant amounts of oxygen. ITM Oxygen would be integrated with the gasification and syngas processes.

Methanol or Gas-to-Liquids (GTL)

Both the manufacture of methanol (MeOH) and GTL fuels such as Fischer-Tropsch liquids require large quantities of oxygen that are used to convert gaseous, liquid or solid carbonaceous fuels to syngas. The conversion process is conducted at high temperatures and can be conveniently integrated with ITM Oxygen, which is also a high-temperature process. For example, the current technology for methanol manufacture from a natural gas (NG) feedstock involves "combiforming." That is, steam reforming of the NG in a primary reformer, followed by oxygen secondary reforming such that a stoichiometric mix of H_2 and COx is obtained:

$$(y_{H2} - y_{CO2})/(y_{CO} + y_{CO2}) = 2$$

where y_i is the mole fraction of species i. Syngas of this composition is converted practically to extinction to methanol, ensuring there is no surplus gas being vented/wasted. In MeOH manufacture, there is typically no "process CO_2," as all the process-side carbon leaves within the MeOH molecules. Carbon dioxide is, however, emitted in the flue gas from the primary reformer, which is typically fired with NG, along with purge gas from the MeOH synthesis reactor loop.

The hot syngas exiting the secondary reformer at 1,742-1,922°F is typically quenched in a fire-tube boiler, raising steam. There is a desire to use this high-grade heat more efficiently. For example, it has been proposed to use a "gas-heated reformer" (GHR) in lieu of the fired primary reformer. The approach would make better use of the high-grade heat, and emit no CO_2. In the ITM Oxygen integration case, part of the high-grade heat would be used to heat ITM feed air, either in lieu of or in parallel with the GHR. Also, the synloop purge gas would be used as fuel to fire the ITM or the turbine.

Ammonia

Currently ammonia is manufactured from carbonaceous fuels (such as NG) by combiforming, first with steam in a primary reformer, followed by an air secondary reformer. Air is used instead of O_2, as the N_2 is a reactant in the manufacture of NH_3: $N_2 + 3H_2 = 2\ NH_3$. There may be value in using O_2-enriched air in a single auto-thermal reforming step and eliminate the

primary fired reformer and thereby its flue gas. In this way, all CO_2 is "process CO_2" that is readily captured.

Hybrid Cryo / ITM Oxygen

The current standard for oxygen production is the cryogenic air separation unit (ASU), which is power-intensive. It would be synergistic to have the ITM Oxygen plant manufacture part of the O_2, and meet the power requirements for the ASU, which would produce the balance of the O_2 and any required pure N_2 and/or Ar. It has been well established that ITM Oxygen is produced more efficiently than oxygen from a cryo-ASU. Therefore, this should therefore result in an accompanying decrease in the CO_2 emissions, even assuming that the over-the-fence purchased power is NG. Additionally, in view of the fact that the majority of U.S. power generation is coal based, the NG-fired ITM process would have an even lower CO_2 burden.

Steel

Air Products is currently pursuing technology wherein O_2-enrichment of blast furnace air raises the calorific content of the off-gases for easier combustion in a gas turbine. ITM Oxygen power integrations can be added to these schemes to increase the overall efficiency of the process and therefore reduce the carbon footprint.

29.1.1.2 Equipment Development

29.1.1.2.1 Turbo-machinery

The focus of the work used the Siemens' model SGT-800 gas turbine, which has been the basis of study of the Task 29 work pertaining to the ODF flowsheet development. Siemens carried out a study in conjunction with Air Products to evaluate the assumptions made by Air Products in its ODF study on the integration between the SGT-800 and the ITM Oxygen process. The study included modeling work involving combustor design and modification, core engine design and modification, process integration and controls in conjunction with the ITM system, and factors affecting the reliability and maintenance of the resulting system.

The study found that a combustor could be developed that would accept the vitiated air from the ITM process. Siemens identified a lower limit for the oxygen content in the vitiated air but it is in line with previously published data and the assumptions made in the ODF study. The evaluation of other fuel streams for flexibility also showed promise. Another phase of work with

substantial equipment development work will be required to progress this work toward demonstration.

The integration of the ITM process with the gas turbine was also reviewed. Much consideration was dedicated to the protection systems required for both the ITM and gas turbine equipment to prevent damage during off-design conditions that would occur from system faults and various shutdown conditions. Several trip scenarios for the gas turbine and ITM system were considered, including a full-load trip of the turbine and various potential turbine overspeed scenarios caused by ITM system faults. The work found that the equipment could, in fact, be protected from damage with some modification to the existing systems.

The gas turbine system maintenance philosophy was evaluated relative to the existing maintenance plans used today on SGT-800 systems. The changes to the plan would be associated with the changes to the components of an ITM-integrated turbine relative to today's model. The primary differences would be in the hot section of the turbine, specifically the burner and combustion chamber components. Much of the maintenance is performed based upon operating hours and/or number of equipment cycles, whichever occurs first. This philosophy was not deemed to require change based upon the integration with the ITM system.

29.1.1.2.2 Heat Exchange and Process Heating

GTPRO was used to design the HRSG systems within the flowsheet. Various programming adjustments were needed to accommodate the required unusual configuration. First, the GT exhaust was augmented with exhaust from the fired heater (the fired heater is described in Section 29.2 below). This was accomplished by eliminating the GT in the GTPRO simulation and running the HRSG only with flue gas input at the admixed mass and enthalpy. Second, the two HRSGs raise their respective steams, which are combined to feed a single steam turbine. For purposes of simulation, the HRSG was simulated at double the single-train size/flow to yield double the single-train steam flows that fed the steam turbine. Steam is raised at two pressure levels, and GTPRO optimizes and natively handles the two pressure levels with injections into the appropriate stages of the steam turbine (per is standard power plant design and practice). The steam generated in the oxygen coolers from both trains is also injected into the second stage of the ST – something which GTPRO is capable of handling natively.

Compact heat exchangers and fired heaters were investigated and used within this effort. Work reported under Task 15 examined several alloy materials for mechanical life viability in the operating environment for ITM. This work then guided the quotation process to ensure appropriate material was quoted for the heat exchange equipment within the flowsheet. Much of this effort was built from the experience in design and fabrication of the heat exchange equipment associated with the ISTU under Task 19.

29.1.1.2.3 ITM Vessel

The basis for this estimate comes from the Task 19 design work associated with the ISTU facility. It was decided to split the ITM based oxygen production between two vessels. This provided the right balance between cost, pressure drop management for power consumption and flow distribution.

29.1.1.2.4 Contaminant Mitigation

The proposed ODF process does not use a conventional TSA front-end dryer as would a cryogenic ASU. While most of the moisture is knocked out before the booster, the residual moisture level in the air stream extracted from the gas turbine is still substantially higher than the dew point achievable with a TSA. The increased partial pressure of water may leach out increased amounts of Cr and Si as various oxide and hydroxide species. It is difficult to completely avoid Si from refractory, and Cr is a component of many high-temperature alloys such as those used within various heat exchangers. These species will harm the ITM material and thus need to be removed (gettered) from the ITM feed. Various getters materials made have been explored (see Task 14). The chosen material was based upon the work performed for ISTU design activities (Task 19) and new work on getter systems (Tasks 14, 16 and 18) following completion of the ISTU design.

29.1.2 Process Development for the ITM Oxygen Development Facility

29.1.2.1 Process Cycle Development

Work up to Decision Point 2 was focused mainly on Task 29.1.1.1 (“Process cycle and process economics development”) and identifying applications that require carbon reduction. Work after Decision Point 2 focused primarily on the 2000 TPD test unit design, Task 29.1.2.1.

Hybrid - General

One option for the Oxygen Development Facility (ODF) is a "hybrid" facility that combines both a cryogenic air separation unit (ASU) and an ITM Oxygen plant where the ITM unit supplies the power requirement for the cryogenic plant. Prima facie, it may appear somewhat quixotic that a hot ITM unit can coexist synergistically with a super-cold cryogenic unit. Nevertheless, the concept has advantages. ITM Oxygen configurations may generate excess power through expansion of the pressurized, hot vitiate. It is also well known that a cryogenic ASU requires power to drive the separation and refrigeration processes. Air Products developed a conceptual facility that overall makes 2,000 TPD of gaseous oxygen (GOX), ~36% of the which is furnished by the ITM unit. The hot, high-pressure ITM vitiate generates a net surplus of power, which is used by the cryogenic ASU to make the remaining 64% of the GOX product. The overall facility is *karmaneutral* – that is, there is no net import or export of electric power. (Note: From the Sanskrit, one meaning of *karma* is "work.") This particular facility was also configured to export pressurized gaseous nitrogen (GAN) and liquid argon (LAR) from the cryogenic ASU. However, the ASU can easily be configured to vent crude nitrogen and argon as gases at near-ambient conditions to reduce capital and operating cost.

Having a facility that is *karmaneutral* offered an advantage in siting because the combined system does not require an external customer for the cogenerated power. Further, the cryogenic unit backs up the ITM unit should the ITM unit need to be shut down for routine maintenance or by an unplanned event. Cryogenic technology is mature and has on-stream factors greater than 98%. The ITM test unit may be expected to have the operating profile of a new technology, namely, more frequent startups and shutdowns than a plant based on the incumbent cryogenic technology. A commercial customer facility for oxygen at this scale would need a reliable supply. Thus, having a cryogenic ASU as backup provides an alternative to a pipeline. The cryogenic facility can also be configured to have a liquefier and provide liquid storage for a few days, which provides further backup. The multiple gaseous and liquid products from the cryogenic ASU may also have commercial value.

The typical product requirement from the facility is a nitrogen-to-oxygen ratio of either 0.5 or 1.0. Four cases were considered in the initial assessment (Table 29-1).

Table 29-1. Product requirements assumed for cases of a combined cryogenic-ITM Oxygen facility.

Case	ITM GOX (NM^3/hr)	ITM GAN (NM^3/hr)	CRYO GOX (NM^3/hr)	CRYO GAN (NM^3/hr)	Power Export	GAN/GOX
1	40,000	0	60,000	50,000	~0	0.5
2	40,000	0	60,000	100,000	~0	1.0
3	80,000	0	20,000	50,000	>0	0.5
4	50,000	0	50,000	100,000	>0	1.0

Note: 30 NM3/hr are approximately equal to 1 TPD.
GAN = Gaseous Nitrogen; GOX = Gaseous Oxygen

It was assumed that the cryogenic unit will use feed pressures of 6–20 bar, extendable to 30 bar, whereas the ITM feed pressures are 12-20 bar to match gas turbine requirements. Multiple parallel trains were considered for operability. In the case of an unplanned shutdown of one train, the problem train could be isolated so that the associated turbo-machinery in the ITM could continue operating to supply the cryogenic unit with power.

Table 29-2 documents the preliminary estimate of the relative utility consumption of a 2,000 TPD hybrid system relative to a cryogenic-only system. Both facilities produce identical amounts of oxygen and nitrogen at typical projected power and natural gas prices. The cryogenic-only system only requires electricity. The hybrid system only requires natural gas. The fuel-to-electricity conversion is 57% on a lower heating value (LHV) basis, which is typical for a natural gas combined cycle (NGCC) plant.

Table 29-2. Product flow and power input for an example hybrid cryo-ITM system

	CRYO Only	CRYO-ITM Hybrid
GOX, Nm^3/h	58,380	58,380
GAN, Nm^3/h	29,220	29,220
LAR, Nm^3/h	2,005	1,060
5 yr power cost	$138 MM	- $1 MM
5 yr fuel cost	$0.8 MM	$71 MM
Total 5 yr utility cost	$139 MM	$70 MM

Efficiency

There are several ways to compute the efficiency of a hybrid cycle. One could simply divide the ITM-side net power by its net fuel (i.e., natural gas) consumption, but this does not give any credit to the work of O_2 separation performed by the ITM. One could credit the ITM with the thermodynamic minimum work of O_2 separation, but this is not sufficient since the other components in the plant (compressors, cryogenic ASU) are not operating at their thermodynamic minima. Rather, it is appropriate to credit ITM Oxygen with the actual amount of work consumed by a state-of-the-art, cryogenic ASU cycle, which is greater than the minimum thermodynamic work. There is a conceptually easy way to do this. The cryo-ITM system consumes natural gas to produce oxygen. The identical product slate can alternately be generated by a bigger, cryogenic-only ASU which will consume electric power plus a small amount of fuel. Therefore, the ITM O_2 technology can be assessed based on equivalent fuel requirement. For example, the electric power consumed by the cryogenic-only facility could be sourced from a combustor-expander without ITM, which would consume only fuel/natural gas. In the discussions below, this is referred to as "oxy-equivalent" efficiency.

Karmaneutrality versus Power Export

It is illustrative to compare the *karmaneutrality* case with an ITM process which exports power. Figure 29-1 profiles efficiency versus the amount of power export for constant GOX production (2,000 mTPD from the ITM side and 6,250 mTPD total).

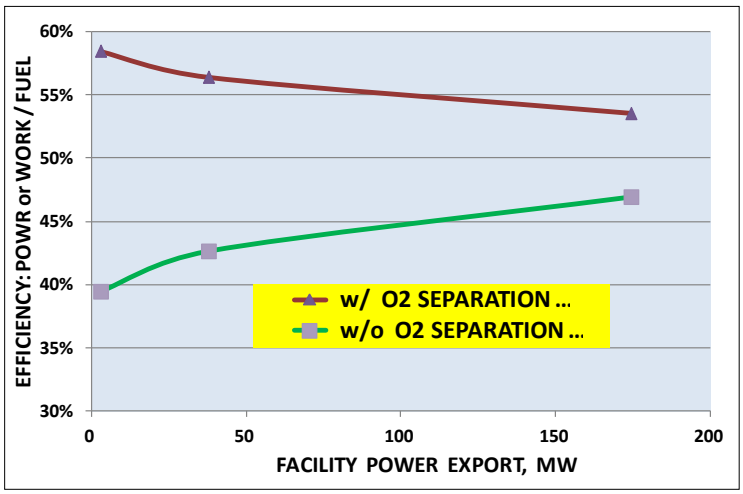

Figure 29-1. ITM+combustor-expander efficiency (30-bar operation).

There are two profiles. The bottom (green) profile computes efficiency as net power export from the facility relative to natural gas consumption and gives no credit for the work of O_2 separation. As discussed above, this is an inadequate representation. The top (burgundy) profile computes efficiency and takes both O_2 separation work and fuel into account (O_2-equivalent efficiency). As power export becomes larger, both curves asymptotically approach 51.9% efficiency. As power export approaches zero, the O_2-equivalent efficiency increases to 58.5%. This suggests that the most efficient way to use power is to utilize it as work to separate oxygen from air.

Integrated Combustor/Expander (ICE)

Air compression configuration is a critical part of the process design. A conventional gas turbine compresses air adiabatically, fires it with fuel in an integrated combustor, and then expands the hot pressurized offgas in an integral expander mounted on the same shaft as the compressor. The heat of compression is preserved at the cost of increased compression power. In contrast, the main air compressor (MAC) of a cryogenic ASU typically attempts to simulate isothermal compression by employing several intercooled stages of compression. The intent is to minimize compression power at the cost of low-grade heat rejection into a cooling media. One of the potential benefits of an integrated cryo-ITM hybrid facility is the possible integration of air compression, benefiting from economy of scale and higher efficiencies. Thus, an ITM configuration employing staged-intercooled (SI) compression was investigated. This scheme would bifurcate a conventional gas turbine into its constituent parts, as the adiabatic compression portion would be replaced with a separate SI compressor. Only the pressurized combustor(s) and the turbine/expander need be retained in a so-called "combustor-expander." Figure 29-2 depicts one possible combustor-expander configurations of an ITM O_2 plant. In this case, the ITM plant would generate about 720 TPD of oxygen.

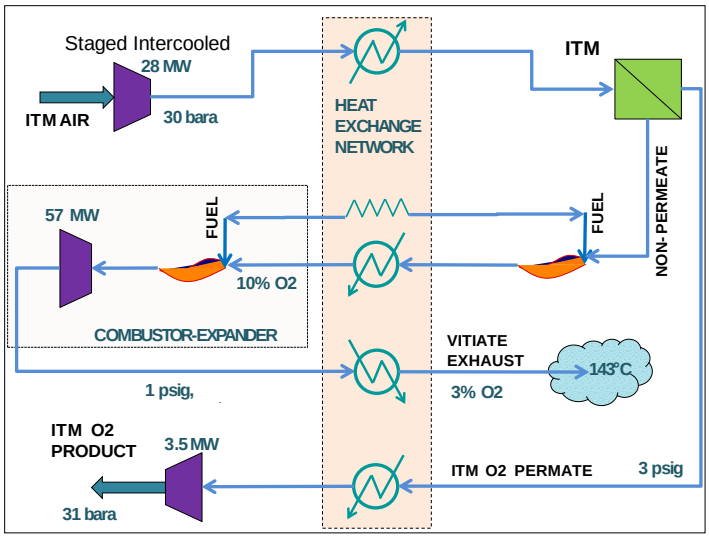

Figure 29-2. ITM Oxygen flow schematic with a staged/intercooled compressor and a separate combustor-expander.

Ambient air is compressed to 30 bara in an SI compression train, as discussed above. It is then preheated indirectly by heat exchange and routed to the ITM unit. The oxygen is collected off of the ITM at 3 psig. The ITM oxygen is cooled by heat exchange, then compressed to the product pressure of 31 bara.

The non-permeate from the ITM is fired with a modest amount of fuel in a pressurized combustor to provide the majority of the high-grade heat required to preheat the ITM feed air. The resulting non-permeate has an oxygen concentration of ~10%, which is sufficient to ensure a stable flame and provide the oxygen needed to combust the fuel fed to the combustor of the combustor-expander system. The expander exhaust heat is recovered by heat exchange against incoming air before being vented through a stack. In the example flowsheet, the oxygen/permeate is drawn off at 3 psig. To maintain a reasonable driving force, the feed pressure was boosted to 30 bar.

A review of commercially available expanders (i.e., the turbine portion of a gas turbine) revealed a limited supply of machines suitable for the above operating conditions. As a result, it was decided to explore 18 bar flowsheets, as there is a greater supply of turbo-machinery in this pressure range. Surprisingly, the 18-bar cycle has a slightly higher efficiency (52.5%) than the 30-bar (51.9%) case. While more power is generated at 30 bar, more power is consumed in (isothermal) air compression, and more heat is rejected from the intercoolers. The expander exhaust is cooler in the 30-bar cycle (1,009°F) than the 18-bar cycle (1,177°F). In both cycles,

the expander inlet temperature was assumed to be 2,400°F after the combustor exhaust is mixed with side-drawn air used to cool machine internals.

The integrated combustor/expander (ICE) cycle was further refined to include:

- Blade cooling.
- Updated heat exchangers with discrete equipment.
- The elimination of fuel preheat.
- Updated efficiencies and losses.

Some of these refinements impact "pure-power" (non-ITM) ICE cycles as well. The original ICE cycle did not employ blade cooling, but feedback from turbine manufacturers indicates that some blade cooling is necessary. In the ITM case, the expander feed is cooled by the ITM non-permeate before being direct fired. Using the non-permeate as a coolant reduces efficiency by 2.2 percentage points. Compressed air could be used, but this further impacts efficiency by 0.9 percentage points. In the compressed air case, the coolant air is preheated to facilitate heat recovery from the expander exhaust. Blade coolant requirements impact both ITM and non-ITM cycles, and thus do not affect the oxy-equivalent efficiency advantage the hybrid cycles have over a pure cryogenic cycle.

Heat leak appeared to have the greatest impact on efficiency. There is a 3.3% loss relative to the theoretical case with no heat leaks, and a 2.4% loss relative to what was previously assumed. The estimated heat leak is comparable to that of other high-temperature processes. Heat leak and pressure drops are the two biggest differentiators between non-ITM and ITM-integrated systems.

Gas Turbine Combined Cycle

Figure 29-3 depicts the process configuration for a hybrid system which incorporates a gas turbine.

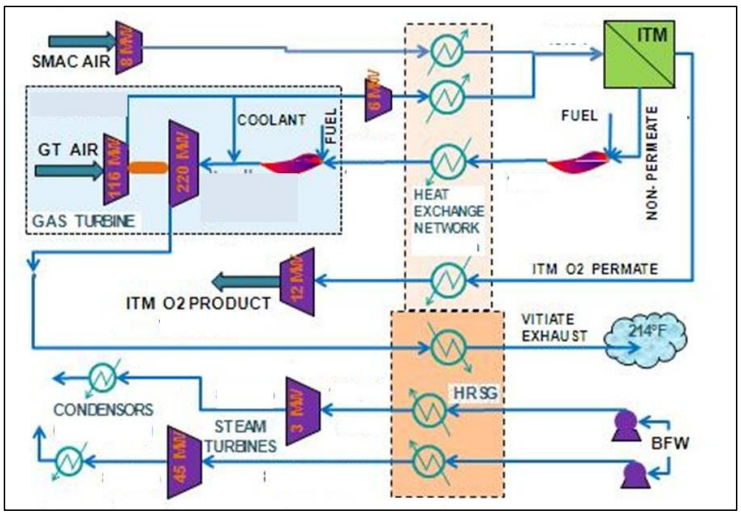

Figure 29-3. Base case simulation flowsheet with a GTCC.

The base simulation extracts gas turbine compressor air and supplements it with air compressed in an external compressor. The ITM non-permeate returns a mass-matched oxidant flow to the turbine combustor. A hot booster was used on the extracted air to compensate for the pressure losses in the ITM system.

One constraint on oxygen production is the maximum amount of air extractable from the turbine air compressor that can be sent to the ITM system. A portion of the air from the compressor is used for turbine blade cooling, burner cooling and other purposes. An alternative source for these utilities is vitiated air from the ITM unit adjusted to match the temperature and pressure of the air extracted from the turbine air compressor. This has the potential to increase the ITM oxygen production by almost 30% as compared to the base simulation, depending upon the ability to increase the air extraction rates from a given model of gas turbine versus the current uses of the gas turbine air stream as noted above.

In a specific evaluation of the ITM/ASU O_2 co-production cycle based on the GTCC configuration, the plant generated 84 MW of net power for export to a state-of-the-art cryogenic ASU plant that makes 5,200 TPD of 99.5% oxygen at 37 bara, and a small amount of nitrogen. The cycle assumes 100% air extraction from the gas turbine. The GTCC-ITM system was sized to export 2,000 mTPD of oxygen and generates just enough power for the cryogenic ASU. Air is compressed adiabatically, fully extracted, further preheated and fed to the ITM unit. The ITM unit extracts

oxygen at 350 Torr and 99.5% nominal purity. The 2,000 mTPD of oxygen is cooled by heat exchange with cooling water and compressed to 37 bara.

The non-permeate from the ITM unit is direct-fired with natural gas and used to preheat the ITM feed air. This gas is then used in the gas turbine combustor. The vitiate from the combustor is routed to the turbine section, where it expands to generating shaft power. The shaft is directly coupled to the adiabatic compressor and an electric generator. Heat in the turbine exhaust is recovered in a HRSG, then discharged to atmosphere. The steam turbines exhaust at 1.1 psia.

The system was modified from a two-steam to a single-steam system wherein the steam turbine inlet had no liquid. It was found that the stack gases could not be cooled below 350°F, and the efficiency dropped to 58.6%. An examination of the heat exchanger network suggested that a dual-pressure steam system would be beneficial in this case. Stack temperature was reduced to 239°F, and efficiency was 59.9%. The *karmaneutral* hybrid oxy-equivalent efficiencies of 58.6% to 60.7% are about five percentage points higher than that of the non-ITM cycle at 53.9%.

ICE and GTCC Comparisons

More detailed comparisons between the integrated combustor/expand (ICE) and a gas turbine combined cycle (GTCC) with 100% air extraction were conducted. Neither cycle was coupled with an ITM system, and both were configured for power generation. In the GTCC simulation, the pressure at the combustor inlet was the same as the ICE cycle. Other factors such as the combustor outlet temperature and expander efficiencies were also constant. The GTCC cycle had both a heat recovery steam generator (HRSG) section to raise steam and a condensing steam turbine. The ICE cycle was fully recuperated, and the steam flow rate and turbine inlet conditions were optimized for maximum power. Table 29.1-3 presents the results.

Table 29-3. Comparison of ICE and GTCC cycles for pure power.

POWER BALANCE	**IsoCompExp**	**GTCC**
Gross Expander Power, MW	143	115
Steam Turbine Power, MW		27
Compression Power, MW	59	57
Net Power Export, MW	**84**	**84**
THERMAL LOSSES		
Stack Temperature, °F	295	197
Stack Losses, MMBtu/hr	132	107
Inter/After Coolers, MMBtu/hr	178	0
Steam Condenser, MMBtu/hr	0	189
Total Thermal Losses (excl heat leaks)	311	295
EFFICIENCIES		
Compressor Thermo Efficiency	88% polytropic	91% isentropic
Electromechanical Efficiency	94%	99%
Process Cycle Efficiency (Power/Fuel, LHV)	**52.5%**	**54.5%**
Oxy Equivalent Cycle Efficiency, LHV basis	**51.9%**	**53.9%**

For the GTCC case, roughly 19% of the power comes from the steam turbine. For the ICE case, all the power comes from the vitiate air expander. Since all other conditions are substantially equal, the ICE has to handle more air and vitiate flow. Thus, the compression power for both cases is roughly the same, even though iso-compression requires less work than adiabatic compression.

The process cycle efficiency (Net Power Export/LHV Fuel) is 52.5% for ICE, and 54.5% for GTCC. The difference comes primarily from compression efficiency. Motor and gear losses contribute to the efficiency loss for the ICE case. The GTCC case benefits from direct coupling, which would eliminate part of a steam system and all its concomitant equipment. There are also differences in thermodynamic efficiency. The ICE cycle uses polytropic efficiency for each of the stages, whereas the gas turbine compressor uses isentropic efficiency. The ICE case would benefit substantially if the compressor were directly coupled to the expander.

One of the advantages of the ICE family of cycles is increased flexibility in the choice of machines due to a wider range of possible operating pressures and flow rates. The advantages and disadvantages of the ICE cycle and the GTCC are summarized in Table 29-4.

Table 29-4. ICE and GTCC comparison.

ICE	GTCC
More Flexible: Higher air extraction, flow rates, pressure	Less flexible
Machine requires development	Low extraction machines exist High extraction machines require development
More integration with a Cryo-ASU Air compression, O_2 pressurization	Less integration with a Cryo-ASUO_2 pressurization
Needs air heater recuperator	Needs steam system and turbines Requires SMAC, BAC
Machine coupling inefficiencies (ElectroMechanical)- need management	Direct drive but EM inefficiency in coupling to Cryo-ASU- needs management

Hybrid- Hot Gas Expander, Gas to Liquid (GTL)

The use of ITM for GTL production was investigated due to a high interest in the application. The target ratio for GOX/GAN is 6.5. There is very little need for GAN and no need for GAR. The overall production targets for several representative GTL applications are summarized in Table 29-5.

Table 29-5. Requirements for GTL.

Parameter	Value
GOX/GAN ratio	6.5
LAR, LOX, LIN	Zero
GOX pressure	37 bara
GOX Purity	99.5%
GAN pressure	37 bara
GAN purity	<5 ppm O2

The evaluated system is depicted in Figure 29-4.

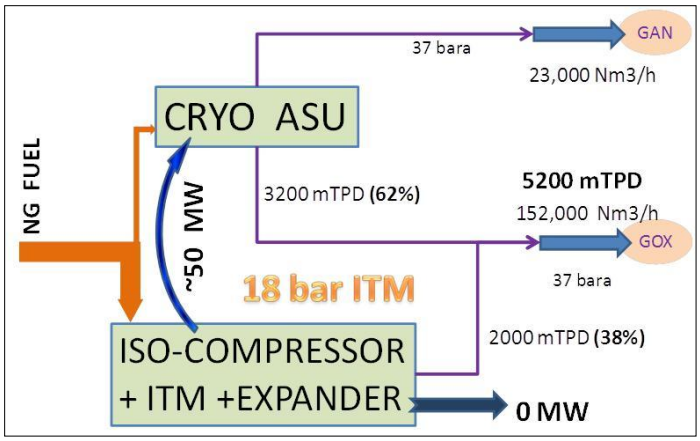

Figure 29-4. Gas-to-liquid hybrid *karmaneutral* configuration.

The ITM generates 2,000 mTPD GOX and supplies all power required by the cryogenic ASU. The cryogenic ASU is intentionally sized to consume exactly 50 MW of power and thereby generate an additional 3,200 mTPD of GOX. It also generates all the required GAN. There is no power imported from or exported to the combined facility; it is *karmaneutral*. The only utility imported is natural gas (NG), the majority of which is consumed in the combustion operations used to heat the air for the ITM and to fire the expander. For this case, an O_2-equivalent efficiency of 57.3% is achieved when work is measured and valued in its ability to yield GOX.

In the cryogenic-only ASU, the electric power consumed could be sourced from a combustor-expander without ITM. This cycle obtains an efficiency of 51.9% after consideration for an additional small amount of fuel. It is convincingly apparent that when GOX separation work is valued, an ITM-cryo hybrid has the capability to enhance efficiency by 5+ percentage points (57% vs. 52%).

It can be argued that the required power could be purchased from the grid versus being produced in a combustor-expander. In this case, a utility cost comparison is needed (Table 29-6).

Table 29-6. Relative utility comparison at 18 bar (high power).

	Cryogenic Only	Cryo + Exp + ITM
GOX mtpd	5,200	5,200
GAN/GOX ratio (molar)	0.154	0.154
5 year Power Cost (relative)	314	0
5 year Fuel Cost (relative)	0	161
Total 5 year Utility Cost	314	161

The cryogenic-only ASU must purchase power at a market rate from the grid, incurring a relative utility cost of 314 units over five years versus the hybrid at 161. Thus, there is a 5-year savings of 153 units or ~50%. This difference would roughly offset the purchase of additional equipment for the hybrid cycle, including the compressors, ITMs, combustor-expanders and heat exchangers.

A comparison (for the above GTL conditions) was conducted for an ITM operating at 18 bar and 3 psig permeate pressures, 18 bar and 350 Torr permeate pressure and 30 bar and 3 psig permeate pressure (Table 29-7).

Table 29-7. Comparison of ITM at different feed and permeate pressures.

Nominal Pressure	**30 bar**	**18 bar**	**18 bar**
ITM GOX, mTPD	2,000	2,000	1,900
Overall GOX Product, mTPD	6,250	5,200	5,200
Power Import/Export, MW	0	0	0
Power Transfer ITM-CE to Cryo ASU, MW	~70	~50	~55
O2 Equivalenced Hybrid Efficiency	58.5%	57.2%	59.9%
Permeate Pressure	3 psig	350 Torr	3 psig
Est. relative Cost of Key equipment	*17*	0	9
Overall 5-yr Utilities, relative	*8*	4	0

The 2,000 mTPD ITM unit at 30 bar has a higher power surplus, which required a larger cryogenic ASU to consume the power and keep the facility *karmaneutral*. Thus, the 30-bar facility exports approximately 6,250 mTPD GOX, about 20% more than the 18-bar facility. Although this makes it difficult to the compare capital costs (i.e., the data in bold in Table 29-3), it is nevertheless legitimate to compare the other numbers. The 30-bar case operates with a permeate pressure of 3 psig and does not need an O_2 vacuum. This makes it more efficient (58.5%) relative to the 18-bar case at 350 Torr. It is possible to operate the 18-bar case at 3 psig for the best efficiency (59.9%), but with a steep increase in the ITM surface area and cost. Even though operating at 350 Torr requires a blower and has higher utility costs, a quick comparison of the significant cost numbers justifies the choice of 350 Torr operation.

Ammonia from Syngas from Coal

Coal gasification is typically oxygen-blown, which generates a substantially N_2-free syngas. The CO-rich syngas from the gasifier is shifted to be substantially H_2-rich by using "sour gas shift" technology. The shifted syngas is cleaned, and the acidic gases (e.g., H_2S and CO_2) are removed in an acid gas removal (AGR) unit, such as Rectisol. The treated gas has residual CO and CH_4, so care must be taken if the syngas is used for ammonia production. Because CO will poison the NH_3 synthesis catalyst, it must be removed to ppm levels. CH_4 is an inert gas that can build up in the NH_3 synthesis loop and have a detrimental effect on the economics.

There are several ways to remove CO, and also CH_4 if necessary. The first employs H_2 PSA technology, which generates pure H_2 at pressure. Typical H_2 recoveries are 85-90%. Alternately, impure H_2 can be washed with liquid N_2, which preferentially dissolves CO and CH_4. In this case, H_2 recovery is much higher. The purified H_2 is compressed into the NH_3 synthesis loop. Compression is usually required, since NH_3 synthesis loops operate at 90-200 bara while gasifiers are typically limited to 40-60 bara. Table 29-8 indicates potential for ITM integration into this process. There is a small but significant power savings (~4%) in the ITM scheme.

Table 29-8. Ammonia from coal gasification process analysis.

	CRYO Only	**CRYO + ITM Hybrid**
COAL CONSUMED, mTPD	7,200	7,200
NH_3 PRODUCTION, mTPD	5,000	5,000
GOX from ITM, mTPD	0	1,100
GOX from CRYO, mTPD	4,450	3,350
POWER CONSUMPTION	Baseline	-4% relative to Baseline

29.2 Detailed Engineering Development

29.2.1 Identification of a Preferred Process Scheme for Testing ITM Oxygen at the 2,000 TPD Scale

29.2.1.1 Performance Model Development

Air Products screened a number of different process cycles as the basis for the 2,000 TPD test facility (ODF). Air Products considered only hybrid cycles consisting of a 2,000 TPD ITM plant together with a 3,000 TPD cryogenic ASU supplying the gaseous products to a GTL facility. Some options did not consider any further integration beyond power export from the ITM plant

to the cryogenic plant. Others options look at various levels of equipment/process integration. In addition, the ITM cycles themselves can be of the iso-compression-expansion (ICE) type or with adiabatic compression as described above. The ICE type employs multi-staged, intercooled compression of feed air and a hot gas expander (HGE). The adiabatic compression occurs in a gas turbine (GT) with high extraction and gas return capabilities.

A key consideration in the hybrid cycle was power export. Machinery available from today's suppliers drives the ITM plant to export power, which increased the size of the cryogenic plant that consumes the power (i.e., to remain *karmaneutral*). It was decided that the overall GOX production was to be fixed consistent with the application need and to export varying amounts of power from the GT/expander. Gas turbine suppliers were engaged to assess potential operating conditions for the turbine.

Permeate was cooled by raising steam, which was blended with the steam produced in the HRSG section in the GT cases.

Five ITM-ASU integration schemes based on the two alternative technologies (i.e., gas turbine or hot gas expansion) were evaluated. Detailed process simulations were developed and used to generate a preliminary equipment list and preliminary operating/capital cost estimates. Air Products developed a mechanical integration scheme for the accompanying air separation unit (ASU) for each cycle. Preliminary process and machinery details were determined, and an initial financial analysis and technical risk assessment were performed. Key objectives included capital and operating cost minimization, identification of the most commercially favorable option, and assurance of a reasonable technical risk profile. Based on these criteria, a gas turbine case with no mechanical ASU integration was chosen for the project development Phase. Figure 29-5 shows a simplified representation of the chosen scheme.

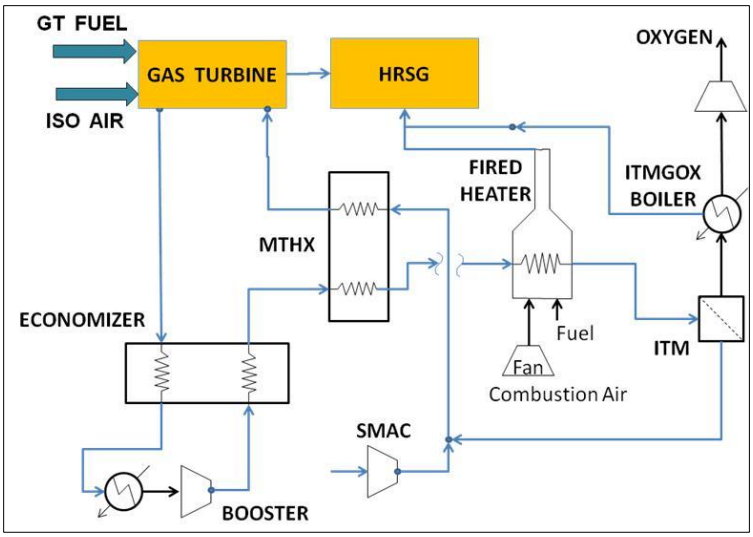

Figure 29-5. ITM process schematic chosen for the development phase.

The process cycle is based on two gas turbines (GTs), each exhausting into their own heat recovery steam generation (HRSG) system. Steam, raised at two pressure levels, is fed to a single condensing steam turbine (ST). The fuel is natural gas. Air extracted from the gas turbine compressor section furnishes the feed to the ITM section. Oxygen is extracted as permeate, and the oxygen-depleted retentate (non-permeate) is returned to the gas turbine combustor. There are two ITM trains, each mated to a gas turbine. Each ITM system produces nominally 1,000 metric tonnes per day (mTPD) of oxygen to meet the overall requirement of 2,000 mTPD of gaseous oxygen (GOX).

The two gas turbines and common steam turbine generate a net power surplus. To reduce power export, a 3,000 mTPD cryogenic GOX plant was included in the design. Under the original design conditions based on a hot gas expander cycle, aan ir separation unit (ASU) of this size would have rendered the overall facility *karmaneutral*. The 3,000 mTPD ASU will increase the availability of the facility and could furnish co-products such as nitrogen (N_2) and argon (Ar). For example, a gas-to-liquid (GTL) or coal gasification facility would require a small amount of N_2, and a steel facility would require Ar. The ASU can also generate small amounts of liquid product for the merchant market. Some liquid oxygen (LOX) can also be generated and stored onsite, which further increases overall facility availability. Power make from the system is increased by use of two waste heat streams from the ITM in the HRSG: 1) the hot flue gas from fired heater augments the turbine exhaust stream to raise additional steam; 2) the steam generated

in the oxygen coolers (GOX boilers) is added to the steam loop, resulting in additional power make by the ST. The plant is designed such that the GT/HRSG/ST train operates independently of the ITM system. Power is a revenue source, so it is advantageous to maximize its availability.

The ITM feed air, extracted from the GT, undergoes a pressure drop through the ITM train. This pressure drop, which would reduce the power output from the turbine, was avoided by including an auxiliary compressor in each train. The compressors boost the pressure of the extracted air stream by an amount approximately equal to the pressure drop in the ITM circuit. The boosted air is heated in stages to the ITM operating temperature. The main heat source is a fired heater.

The ITM permeate is collected under vacuum from each module and flows through a network of collectors to the discharge piping. The hot permeate is cooled in boilers and then compressed from vacuum to atmospheric pressure with low-pressure compressors. The ambient-pressure oxygen stream is then compressed to the GOX product pressure with a common medium- and high-pressure compressor.

29.2.1.2 Operating Profile Development

29.2.2 Identification of a Suitable Site for the ITM Oxygen Development Facility

A generic Gulf Coast location was chosen for the plant site. Such a site would be expected to have a sufficient low-cost natural gas fuel supply and power export options. The proposed plot plan (Figures 29-6 and 29-7) minimizes runs of hot piping and high-voltage electrical lines and maintains a sufficient distance from the control room to the plant area.

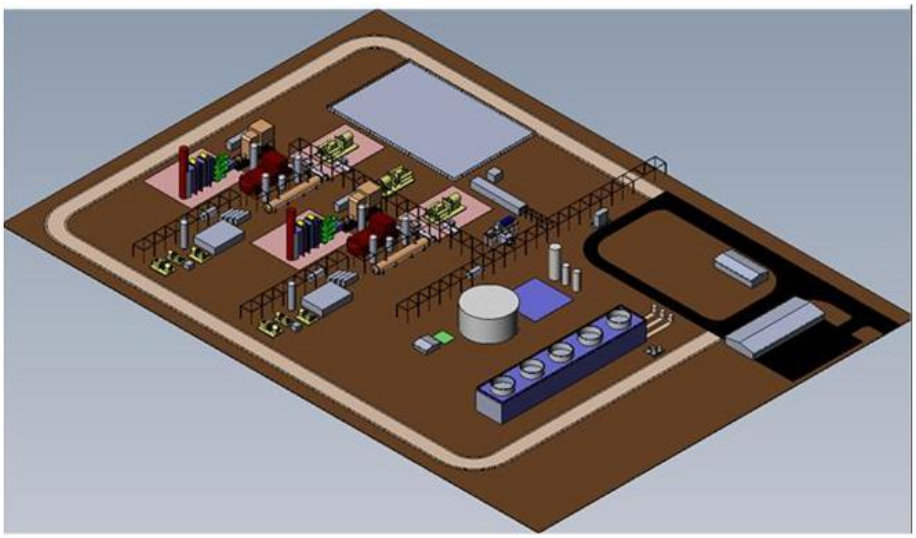

Figure 29-6. Oxygen Development Facility (ODF) proposed plot plan.

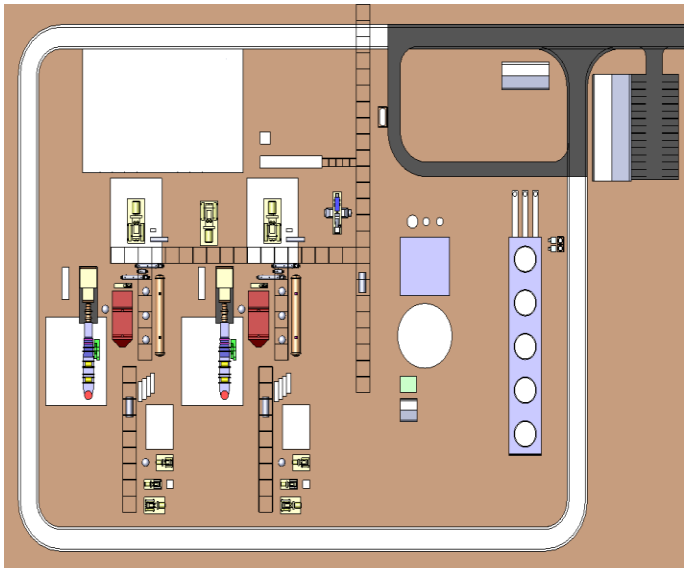

Figure 29-7. Oxygen Development Facility (ODF) proposed plan overhead.

Referring to the above figures, there are two identical process trains on the top left, each fed with its GT (housed inside its brown "building") and exhausting into its own HRSG (resting on the larger pink pads in Figure 29-6). Steam, raised at two pressure levels, is fed to a single condensing ST common to both ITM trains.

Air extracted from each gas turbine compressor section furnishes the feed to the ITM section. Oxygen is extracted as permeate, and the oxygen-depleted retentate is returned to the gas turbine combustor. The ITM modules are located in the ITM vessels (the two light brown horizontal cylinders). The ITM permeate is collected under vacuum from each module and flows through a network of collectors to the discharge piping. The hot permeate is cooled in boilers, then compressed from vacuum to atmospheric pressure with low-pressure compressors. The ambient-pressure oxygen stream is then compressed to the GOX product pressure with a common medium- and high-pressure compressor. The oxygen compressors (yellow machines on the other two pink pads towards the rear in Figure 29-6) are enclosed in safety barriers, but are close to the ITM vessels (dark brown horizontal cylinders) to minimize the length of refractory piping under vacuum. The control room (top right corner) is located a minimum distance from the plant to minimize personnel risk. There is one ITM train, embedded with one ITM vessel, mated to each gas turbine. Each ITM system produces nominally 1,000 mTPD of oxygen to meet the overall requirement of 2,000 mTPD of ODF-generated GOX.

The ITM feed air, extracted from the GT, passes to the two auxiliary compressors that boost the pressure of the extracted air stream by an amount approximately equal to the pressure drop in the ITM circuit. The boosted air is heated in stages to the ITM operating temperature. The main heat source is a fired heater (the two large dark brown L-shaped boxes), again juxtaposed to the ITM vessel to minimize the length of refractory piping.

The 3,000 mTPD (GOX) cryogenic plant is not included in this plot plan, but is treated as a separate "over-the-fence" entity for costing purposes.

The five cooling towers are readily apparent in the foreground of Figure 29-6. The off-white, large cylindrical tank is for demineralized water. The large cooling water lines are underground, as are the high-voltage power lines. The NH_3-fed SCR system is included for NO_X control, as is continuous emission monitoring system-quality instrumentation. Other features visible are a storage building next to the control room (for spare parts), an electrical switchyard (rearmost rectangle next to the circular road), four pipe racks and piping modules to maximize shop labor and minimize field labor.

29.2.3 Development of Project-Specific Information for the ITM Oxygen Development Facility

The initial PFD, equipment list, and a preliminary plot plan concept for the ODF were developed. PFDs documenting all major equipment, design temperatures, pressure breaks, and fundamental/primary controls are being developed. Decisions were made on equipment count and the redundancy of major equipment. Preliminary control strategies were developed to address normal operation, start-up/shutdown and upset conditions. These efforts led to the start of P&ID development. The Air Products team evaluated material suitability based on the services, design pressures, design temperatures, and process sensitivities to certain material elements.

29.2.3.1 Equipment Specification Development

Siemens calculated thermodynamic stream variables for cases of integrated ITM processes and the SGT-800 gas turbine in both static and dynamic modes. Effects of a redesigned SGT-800 were determined. The re-design achieved a reasonable flow pattern and also improves the combustor cooling inlet and flow symmetry. Extensive design iterations were done for the

central casing and incorporated into flow calculations. Effects from various transients and simulated equipment failures were also assessed.

The standard SGT-800 burner was successfully fired on natural gas using low-oxygen-content combustion air. Nitrogen was fed into the combustion air before the air heater to achieve a low-oxygen-content stream. The nitrogen-diluted air stream simulates the non-permeate stream. Hydrogen was also tested at various concentrations with nitrogen and natural gas.

These data informed the choice of operating conditions for air extraction and vitiated air re-insertion, including impacts on performance. Preliminary designs were proposed for the heat recovery steam generator (HRSG) and the associated steam turbine.

Additional input was obtained from fired heater suppliers and heat exchanger suppliers to complete the specification process.

29.2.3.2 Budgetary Cost Estimate Model

The project-quality cost estimation was completed. The majority of the cost estimation work was focused on developing equipment costs for those portions of the plant devoted to the production of oxygen from the ITM. Preliminary operability and hazard reviews were conducted, and estimates were obtained for instruments and valves, including the higher-temperature control valves. The GT and HRSG costs were based on Air Products data.

The plant and plot plan were reviewed for constructability and maintainability and served as the starting point for the construction cost estimate. The plot plan was further optimized to minimize runs of refractory-lined piping and oxygen-conveying ducts. Development costs of the site and installation costs for setting, connecting and commissioning equipment were developed. Construction costs were estimated based on a US Gulf Coast location.

The breakdown of cost allocation to the major parts of the facility is shown in Figure 29-8.

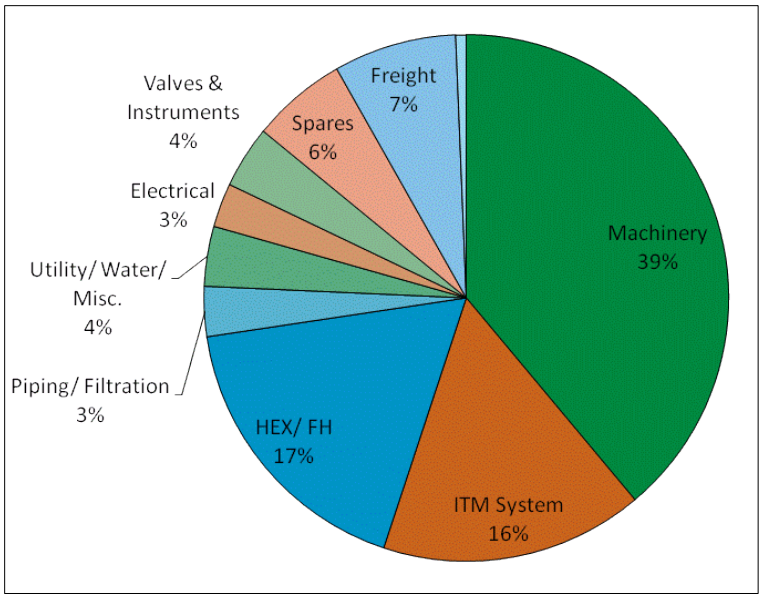

Figure 29-8. Oxygen Development Facility (ODF) cost allocation (%).

The largest capital cost areas are associated with the heat exchange and thermal equipment, the ITM system, and the machinery. Each of these three areas was expected to represent the majority of the capital cost for the facility. It is estimated that the total cost for this facility would be in the $400MM to $500MM range. This facility produces a total of 5,000 TPD of oxygen, with 2,000 TPD coming from ITM technology and the rest from a cryogenic ASU. A net of 80 MW of power is available for export after the power required for the cryogenic ASU is considered. More work is planned for a future program that will use this work as a starting point.

TASK 30.0 TABLE OF CONTENTS

TASK 30.0 CERAMIC MEMBRANE MODULE FABRICATION FACILITY 2

30.0 SCOPE 2

30.1 DESIGN, CONSTRUCTION AND COMMISSIONING 2

30.1.1 Conceptual Process Design Development 2

30.1.1.1 Performance Model Development 2

30.1.1.2 Operating Profile Development 3

30.1.2 Site Development 6

30.1.2.1 Building Specification and Site Selection 6

30.1.2.2 Site Procurement 8

30.1.2.3 Preliminary Equipment Specification and Modified Process Scheme 9

30.1.2.4 Preliminary Safety Review 10

30.1.3 Detailed Process Design Development 10

30.1.3.1 Permitting 10

30.1.3.2 Equipment Specification 12

30.1.3.3 Project-Quality Cost Estimation 12

30.1.3.4 Project Schedule and Execution Plan Development 14

30.1.4 Manufacturing Facility Construction and Commissioning 15

30.1.4.1 Equipment Procurement and Installation 16

30.1.4.2 Building Infrastructure Installation 17

30.1.4.3 Safety Review 19

30.1.4.4 Equipment Commissioning 21

30.1.4.5 Process Commissioning 23

30.2 OPERATION AND PROCESS ASSESSMENT 23

30.2.1 Production of 1-TPD modules 23

30.2.2 Process Quality and Efficiency Assessment 26

TASK 30.0 CERAMIC MEMBRANE MODULE FABRICATION FACILITY

30.0 Scope

In Task 30.0, Air Products identifies a ceramic manufacturing process and specifications for a manufacturing facility, and designs, builds, and operates a ceramic manufacturing facility (the "CerFab") capable of supplying a 2000 TPD ITM Oxygen test unit. Air Products is assisted by subcontractor Ceramatec in this process.

30.1 Design, Construction and Commissioning

30.1.1 Conceptual Process Design Development

30.1.1.1 Performance Model Development

The processing scheme was sized to meet the overall objective for the facility to supply a conceptual 2000 TPD ITM Oxygen Development Facility. To meet this goal, Air Products considered typical equipment delivery times in the industry and took into account the expected yield of the CerFab in its early years of operation.

The target annual module production from the CerFab at mature (commercial) overall process yield was developed based specifically on 1) prevailing equipment delivery times in the industrial gas industry, and 2) with the expectation that the ITM Oxygen Development Facility would likely undergo a staged startup consisting of a preliminary operating period at reduced oxygen production rate followed by a longer-term operating period at the full oxygen production rate. This production target allows for an overall ceramic process yield that is lower during the early years as the process matures while still producing enough modules to fully supply the ITM Oxygen Development Facility within the delivery period typical of the other equipment in the facility. The overall process yield is expected to range from ~30% first year yield to 80% by the time the process reaches maturity, which is typical of ceramic processing industry standards. However, the yield comprises both individual yields of the processing steps that lead to "green" (unfired) components and a thermal processing yield that consists of the sintering and joining steps necessary to make finished ceramic parts. Off-spec parts generated during the fabrication of the green component are assumed to be fully recycled; thus the overall processing yield of the

process is more accurately characterized by the thermal processing steps, which are projected to achieve an approximate overall yield of $\geq$90%.

Using the above assumptions, Ceramatec identified appropriate processing equipment to meet the production target. Major equipment items include large wafer sintering kilns, submodule and module joining kilns, punches and laser cutters for featuring, a powder calcining kiln and a tape caster. The process bottleneck was found to be in the sintering and joining kilns. Based upon a provisional simulation of the proposed manufacturing process for the ceramic membrane manufacturing facility ("CerFab"), Ceramatec developed a preliminary facility layout to determine the manufacturing floor space required for the CerFab. This layout was based on quotations received for specific machinery selected for the proposed fabrication processes. Office and support space requirements were also developed based on personnel requirements (both technical and production staff) developed to support the fabrication process. Overlayed on the preliminary facility layout were utility requirements (positions and routings) needed to support the fabrication process equipment, including electrical, natural gas, chilled water, nitrogen, compressed air and exhaust/ventilation requirements. The equipment layout planning effort determined that a 65,000 sq. foot facility would be adequate to house the facility.

30.1.1.2 Operating Profile Development

The conceptual ceramic manufacturing process scheme was devised to handle both standard and advanced wafer architectures. The process consists of 12 sequential batch or semi-batch processing steps to convert the raw ITM powders into completed modules. A simplified process schematic is presented in Figure 30-1

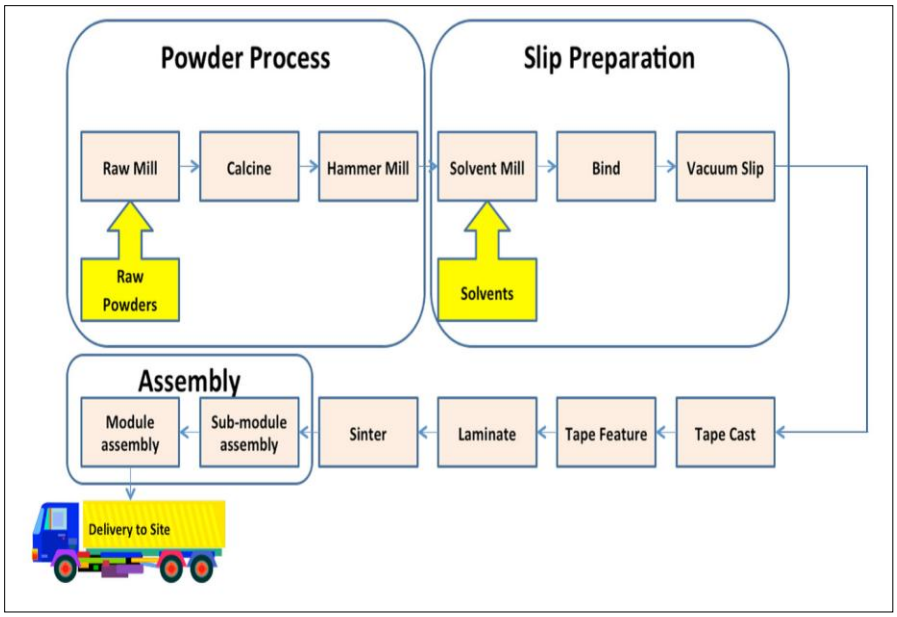

Figure 30-1. Simplified CerFab process.

Powder Processing

The first three steps, Powder Processing operations, are performed on the raw ITM powder. In the raw milling step, constituent powders are mixed dry and reduced in particle size to improve reactivity during the subsequent calcining step. In the calcining step, the components are reacted together at high temperature to form the required perovskite lattice structure. Hammer milling crushes the material from the calcining furnace into a material that is more easily processed downstream. The ITM material is then fine milled to provide the particle size required for the ceramic component for which the powder will be used.

Slip Preparation

The next three steps in the process prepare the slip that will be fed to the tape casting operation. During slip preparation, the powder is mixed with solvents, organic binders and plasticizers to form a pourable slip of the correct viscosity and composition.

Materials for both dense and porous layers are prepared in the solvent mill. For dense layers, milling produces a particle size distribution that will fully densify during sintering and maintain the same shrinkage as the porous layers. For porous layers, the aim is to select a particle size range that will remain porous during sintering and shrink in the same way as the dense layers.

In the bind step, the ceramic/solvent slurry is mixed with binder and plasticizer. A vacuum is then applied to remove air from the slip and adjust its viscosity by removing solvents.

Tape Casting

Batches of slip are cast in Step 7 to form continuous thin sheets of "green" tape by depositing the slip on a plastic carrier film on a moving-belt tape casting machine. Most of the solvents are extracted in the dryer section of the tape caster, which leaves a dried tape that can be handled in downstream processing steps. Both the standard and advanced architecture wafers use the same tape casting process.

Tape Featuring

Various cutting methods are used to form the different layers of the ITM wafer structure. These methods form the eighth step in the process. Slots are cut into the internal wafer layers to allow oxygen flow. The internal layers are then washed to remove any debris. Both the standard and advanced architecture green wafers use the same featuring processes.

Lamination

Following tape featuring, the different wafer green layers are bonding together using combinations of solvents, temperature and pressure. The laminated wafers are trimmed (punched) to form the required final wafer size.

Thermal Processing

The thermal processing steps are carried out in high-temperature furnaces where the assembled green wafers are first sintered to densify the ceramic materials and subsequently assembled into sub-modules. These completed modules ready for packaging.

In the sintering step, wafers are loaded onto setter plates and placed in one of the large wafer sintering furnaces. Although both the standard and advanced architecture wafers use this step, cycle times differ for the two wafer types. After sintering, all wafers are inspected for leaks to determine the grade and quality of wafers produced. The inspection machine that tests for leak rate was successfully developed and used in this program.

In submodule assembly, wafers of similar leak rates are stacked together with a ceramic joint between each wafer, loaded into one of the identical submodule kilns, and subjected to a thermal

cycle. Joining times differ for the two wafer types. All submodules are leak checked to determine quality.

In the module assembly step, 12 submodules with similar leak rates are stacked together with a ceramic joint between each submodule, loaded into one of the identical module kilns, and subjected to a thermal cycle. Joining times differ for the two submodule types. All modules are leak checked to determine quality.

The flowsheet was further revised to include a wafer finishing step for the processing of the green wafers. In this step the spacer is applied to the laminated wafer and, in the case of the advanced architecture wafer, the green spacer-wafer couple is fully sealed to ensure leak tightness prior to sintering. The revised schematic is presented in Figure 30-2.

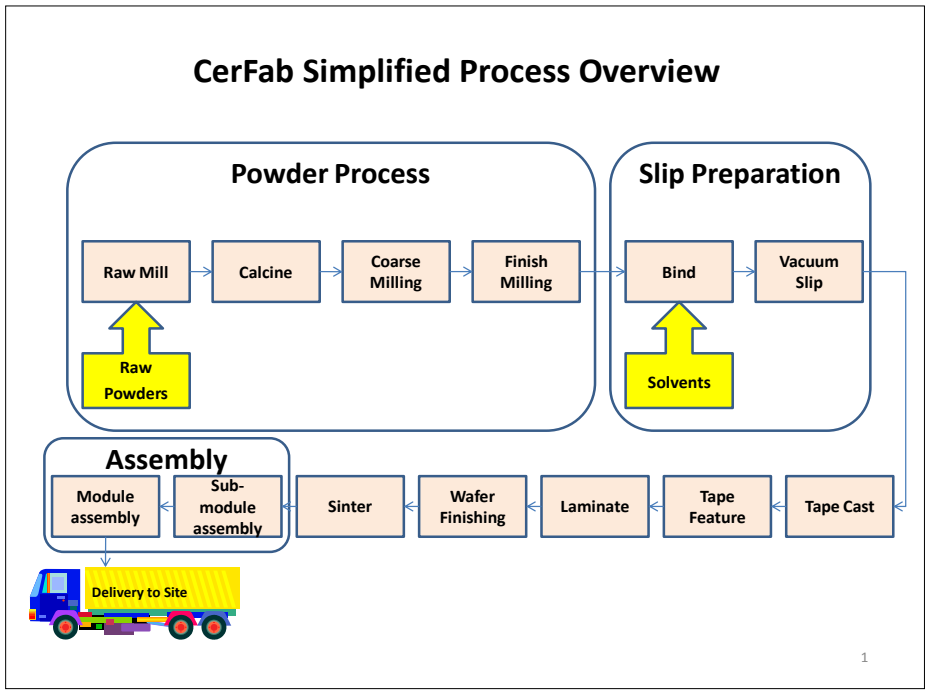

Figure 30.2 Revised CerFab simplified process overview.

30.1.2 Site Development

30.1.2.1 Building Specification and Site Selection

Ceramatec developed a preliminary facility layout to determine the manufacturing floor space required by CerFab. The layout was based on quotations received for specific machinery selected for the proposed fabrication processes. Office and support space requirements were also

developed based on staffing requirements. Overlayed on the preliminary facility layout were utility requirements needed to support the fabrication process equipment, including electrical, natural gas, chilled water, nitrogen, compressed air and exhaust/ventilation requirements.

A detailed building project definition was drawn up to act as a general document to specify all aspects of the building needed to house the proposed fabrication process. Key criteria included:

- **Location:** Sites near Ceramatec, Inc., Salt Lake City, Utah, were given highest consideration.
- **General building description:** Building codes were was specified, as were specific requirements in terms of square footage, expected occupancy rates, utility requirements including backup power infrastructure, roof characteristics, flooring, and HVAC.
- **Space allocations:** Space allocations, including specific area requirements, were generated for the various functional areas of the ceramic processing line.
- **Engineering requirements:** Requirements for building structure, flooring, HVAC, roofing, plumbing, fire protection, electrical, telecommunications, and security were generated that are specific to the needs of the intended ceramic processing line.

A representative schematic of the fabrication facility floor plan, including major equipment, was generated to help assess building fit.

Based upon the above information, engineer/procure/construct contracting companies (EPCs) in the Salt Lake City area were asked to bid on the facility based on two options: new building construction and rehabilitation of an existing leased building. Results of the bid process confirmed a cost penalty for new construction, and bidders provided valuable feedback on optimizing the facility layouts to minimize overall cost. Air Products worked with a commercial property realtor to identify suitable properties available for lease in the general Salt Lake City area. Twenty initially identified properties were narrowed down to five facilities for detailed review. A property in Tooele, Utah within a 40-minute drive of Salt Lake City was selected as the most suitable based on the following attributes:

- A modern, well-planned and well-constructed facility that would meet existing building codes with minimum modifications
- Sufficient installed power with installed step-down transformers and switch gear.

- A good, heavy-duty HVAC system with humidity control.
- An open, useable factory layout with sufficient ceiling heights and column spacing.
- Appended offices, reception, lunchroom, server room and maintenance workshop, all with appropriate size and location.
- Installed air compressors and distribution piping.
- Modern sprinkler and fire detection systems.
- An installed LAN for machine locations and an installed PA system.
- All drawings for the original building project that are available electronically for re-use.
- Located in an area with the fewest permitting barriers.
- Located within a 40-minute drive of the existing Ceramatec facility.

The following upgrades were required to meet the CerFab needs:

- Power cabling for the kilns and an upgrade to the power feed above its current rating.
- Emergency back-up generators.
- HVAC system modifications to exactly meet the CerFab process requirements.
- Additional utilities (nitrogen, chilled water, and natural gas).
- Installation of a clean rooms for specific production processes.
- Floors drains for equipment washdown with drainage to a central sump for analysis prior to discharge to local sewage treatment.

30.1.2.2 Site Procurement

The Tooele location was chosen from a list of 20 available properties in the Salt Lake City region. The site includes a building with some existing required manufacturing infrastructure, office space, and various supporting utilities. The site was judged based on criteria determined for the facility through an assessment of the ceramic manufacturing process requirements, including required floor space, power, heating, ventilation and cooling. Air Products also assessed the expected ease of obtaining the required environmental permits. The selected site meets or exceeds all of the CerFab requirements, and a long-term lease for the facility was negotiated.

30.1.2.3 Preliminary Equipment Specification and Modified Process Scheme

Process Equipment Layout

A preliminary process equipment layout (Figure 30-3) was proposed based on the Tooele facility.

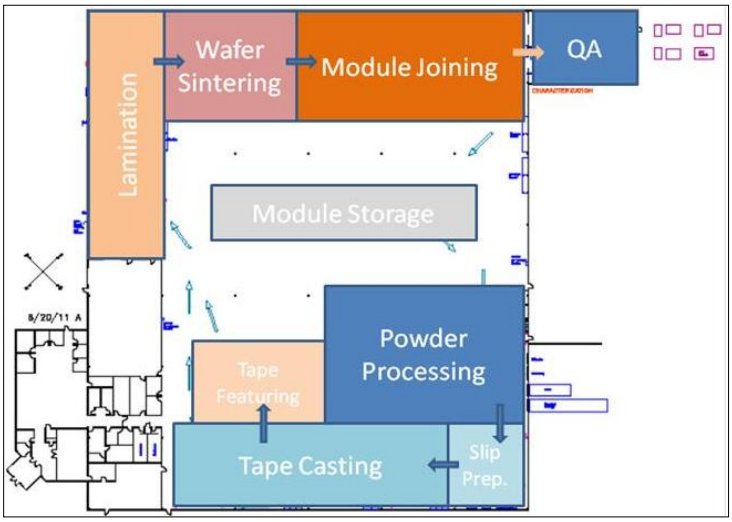

Figure 30-3. Preliminary process equipment layout for the CerFab based upon the selected Tooele facility. Flow of material is roughly clockwise, as shown by the arrows in the figure.

This layout was based on quotations received for specific machinery selected for the proposed fabrication processes and took into account additional equipment needed to produce advanced architecture wafers. This proposed arrangement considered of the following and sometimes conflicting criteria:

- Efficiency. All materials flow clockwise around the building from the receiving/material storage area to completely assembled modules ready for storage/preparation for shipping.
- Safety. Applicable safety requirements included space allocation, segregation of hazardous materials, distance to escape routes, etc.
- Building refurbishment costs. The layout needed to minimize the refurbishment costs for the needs of Task 30. For example, furnaces are located close to the incoming electrical power to minimize the high cost of running electrical power to these high energy consumers.
- Building constraints. The layout considers the restrictions of the existing building and the need to eliminate any demolition/reconstruction of the main building structure, factors considered as both a condition of the building lease and a requirement for minimizing the potential for any environmental concerns.

The layout was again modified (Figure 30-4) to accommodate the addition of the wafer finishing system. The revised layout was based on updated quotations.

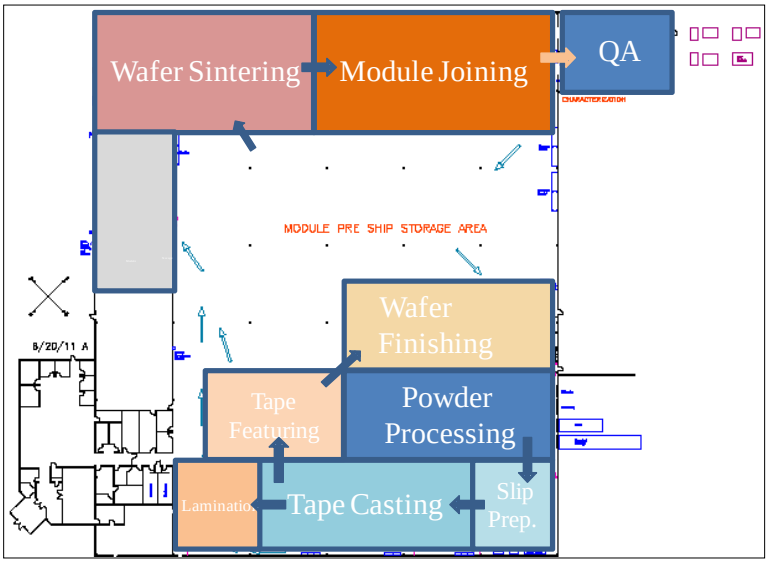

Figure 30-4. Updated process equipment layout for the CerFab including membrane application.

30.1.2.4 Preliminary Safety Review

Specifications were updated and budgetary quotes obtained based on changes identified during the HAZOP for the CerFab. Preliminary safety reviews were conducted for most of the major equipment items, and action items resulting from these reviews were completed. Safety and hazards reviews continued as the detailed equipment drawings became available from the manufacturers.

30.1.3 Detailed Process Design Development

30.1.3.1 Permitting

Summary of the Environmental Approvals Required

Ceramatec calculated the expected material flows in and out of the process and assisted Air Products in preparing the required NEPA questionnaire. The following permitting requirements were expected:

- U.S. DOE National Environmental Policy Act (NEPA) review.
- Air Emissions - Utah DEQ, Division of Air Pollution.
- Wastewater - City of Tooele Uniform Zoning Code, Title 7, Chapters 5, 6, 7, and 8.

- Solid and Hazardous Waste – Utah DEQ, Division of Solid and Hazardous Waste.
- Spill Prevention, Control, & Countermeasure Plan – Utah DEQ Division of Water Quality.

Air Products pursued a comprehensive stakeholder engagement process to ensure concerns were heard and addressed through the approval, construction and operating phases of the project. Stakeholders include the U.S. DOE, Air Products, the City of Tooele, the State of Utah, and the owner of the leased property.

General environmental control strategies were developed and included air and water emission controls necessary to comply with all regulatory limits and to protect the environment. A Best Available Control Technology (BACT) analysis was also completed to determine if any additional emission controls were required. Various administrative controls (spill prevention, training, environmental compliance management system, incident investigation, etc.) were implemented to further reduce the likelihood of environmental impacts from the construction and operation of the CerFab facility. The required permits that were issued are documented in Table 30-1.

Table 30-1. Permit approvals completed.

Permit/Approval [Agency]	**Reason**
National Environmental Policy Act, Categorical Exclusion B3.6	NEPA Section 102
Utah Department of Environmental Quality, Division of Air Pollution	UDEQ Rule 307-101.
Wastewater Discharge Permit, City of Tooele	Uniform Zoning Code, Title 7, Chapters 5, 6, 7, & 8.
Small Quantity Solid Waste Generator Registration UDEQ/USEPA	40 CFR Part 261
Spill Prevention, Control, and Countermeasure Plan – UDEQ	40 CFR 112

Drawings were submitted to the City of Tooele in support of a request for a building permit. A revised air permit was submitted and approved for the facility following commissioning to account for a change in solvents used in the revised manufacturing process. All of the required permits were issued and have been maintained throughout Task 30.

30.1.3.2 Equipment Specification

Final specifications for the majority of the major equipment were submitted for purchase order placement. Three CO_2 laser cutter suppliers were evaluated, a vendor was selected, and an order was placed.

Ceramatec evaluated two particle size analyzers. The two instruments were statistically comparable in performance, but the analyzer from Vendor A was selected because it was far more "user-friendly."

From the three casting line vendors selected from the initial request for bid, two were evaluated for more detailed consideration. Vendor A's equipment was installed at Ceramatec as part of Task 17. Vendor C conducted a two-day trial and produced visually acceptable tape. The tape roll was then shipped back to Ceramatec and used to produce wafers. Wafers fabricated from this tape cast during the trial were leak tested. The leak rates were as good as or better than the control wafers. Vendor C was chosen.

30.1.3.3 Project-Quality Cost Estimation

Air Products completed a detailed cost estimate for the CerFab equipment and the overall project. The equipment contained in the process layout (see above) was costed based on equipment vendor quotations and/or engineering estimates. Costs and quotations were collected and tabulated.

Firm quotations were obtained for large and/or specialty equipment items (60% of the equipment total), while budgetary quotes were obtained for off-the-shelf items (32%). Engineering costs were estimated by Air Products and Ceramatec. Approximately 8% of the equipment scope was estimated based on engineering judgment. The majority of these items fall into the category of tooling and are smaller-value items.

Construction Costs

Overall project costs for the CerFab were updated and estimated to be slightly lower than the estimate at the time the definitized contract was put in place. Firm quotes were obtained from three contractors to establish the cost of building modifications. Significant reductions in cost were realized because of the selection of the Tooele building, which already had a substantial amount of installed infrastructure. Accordingly, building remodeling and facility equipment

costs were lower. In addition, the facility design emphasis on advanced architecture component fabrication reduced the capacity or need for some process equipment.

Firm quotations were obtained for large and/or specialty equipment items, and budgetary quotes were obtained for off-the-shelf items. Some equipment costs increased, most notably for tape casting, wafer sintering, and engineering. Tape casting costs increased as the tape casting specification was further developed. Sintering costs increased as a result of the use of advanced architecture technology, which requires more sophisticated and thorough thermal processing. Increases in engineering costs resulted mainly from the emphasis on advanced architecture technology, which necessitated a re-work of the facility to enable full production and additional specialty equipment as determined by the work under Task 28.2. Additional engineering staff was added relative to the original budget to manage commissioning. Despite these changes, the final facility cost was ultimately slightly below the original estimate for the completed facility.

Commissioning and Operating Costs

Air Products estimated the commissioning and operating costs based on the commissioning plan described under Task 30.1.3.4 below and the requirement for a quarter-year operating campaign under Task 30.2 to meet the Phase 5 objectives. Operating and material costs were developed based on power and labor requirements for the tasks within the plan. In addition, Air Products increased engineering activities associated with commissioning the custom equipment in the CerFab that were unknown when the Phase 5 contract modification (adding the CerFab scope of work) was definitized. Table 30-2 is a summary breakdown of estimated costs for commissioning and operation. The actual costs were consistent with this estimate.

Table 30-2. Summary of commissioning and operating costs.

Period	**Cost, $000's**
Commissioning	*$ 3,915*
Operation	*$ 2,517*
Grand Total	***$6,432***

Budget Trade-Offs

The CerFab process was optimized to limit overall costs while meeting the project objectives and balancing the technical risk. The process emphasizes advanced architecture wafer production, but retains the ability to produce standard architecture modules.

The capacity of the CerFab facility was based on a normal material supply schedule for the air separation industry. Some variance in schedules exists under typical conditions. Thus, there is some ability to vary the facility's final capacity while still achieving the important objective of the work scope: to construct a facility capable of supplying membrane modules to a 2,000 TPD ITM Oxygen plant.

Additional process equipment was added to reduce risk in certain parts of the process. For example, the process has been designed with sufficient thermal processing equipment to address technical risk.

30.1.3.4 Project Schedule and Execution Plan Development

Gantt Chart

A summary of the detailed schedule developed after Decision Point 2 is shown in Table 30-3. This schedule was updated as the project continued and was used to track the almost 700 tasks that made up the nearly 24-month schedule from DP3 to the beginning of operations under this phase. The project schedule included staffing requirements and was adjusted based on periodic meetings between the Air Products and Ceramatec. The final overall schedule was extended by six months from DP2 as CerFab project resources were shifted to Task 17 to complete ISTU module production in the PDF at Ceramatec for eventual use in the ISTU.

Table 30-3. Simple Gantt chart for the CerFab.

ID	Task Name	Duration	Start	Finish
1	APCI Approvals	242 days	Fri 1/7/11	Mon 12/12/11
4	DOE Approvals	85 days	Tue 12/6/11	Mon 4/2/12
15	Real Estate	120 days	Fri 1/14/11	Thu 6/30/11
23	Environmental	335 days	Mon 8/8/11	Mon 11/19/12
37	R&D (Phase 5 Execution Basis Finalized)	50 days	Mon 3/5/12	Mon 5/14/12
39	Engineering	475 days	Mon 1/17/11	Mon 11/12/12
110	Equipment Specified by Air Products	189 days	Mon 3/12/12	Thu 11/29/12
130	Equipment Specified by Ceramatec	630 days	Wed 8/3/11	Tue 12/31/13
536	Materials Management	150 days	Mon 4/23/12	Mon 11/19/12
553	Construction	381 days?	Tue 9/6/11	Tue 2/19/13
595	Commissioning	190 days	Mon 11/19/12	Mon 8/12/13
637	3 month Operations (Task 30.2)	60 days	Mon 8/12/13	Fri 11/1/13
640	DOE final reports	2 mons	Mon 11/4/13	Fri 12/27/13

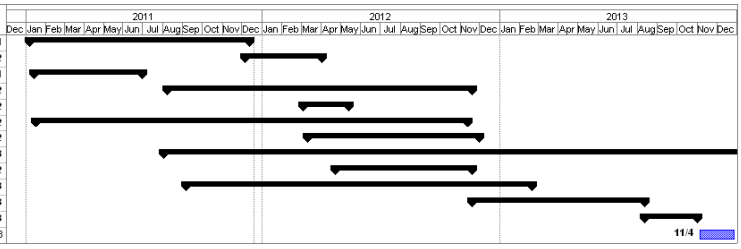

Air Products applied its standard Technical Risk Management Process (TRMP) to the CerFab project. The process was used to identify technical and project risks, to weigh their ramifications and probability of occurrence, and to assign each risk a monetary valuation which reflects the weighted expectation of the additional expenditure associated with each risk. A risk assessment was carried out at the onset of the project, then updated with new information based on the added

emphasis on advanced architecture wafer technology and with feedback from equipment suppliers. This process continued until all of the identified risk items were mitigated.

Project Schedule Critical Path

DOE authorized the release of funding prior to Decision Point 3 so purchase orders could be issued for both the tape casting and powder processing equipment. These items were identified as procurement critical-path, long-lead items relative to the overall project schedule. Additional early-release funds were used to begin fabricating the kiln furniture required as part of the wafer sintering process.

Decision Point 3 (DP 3)

Air Products completed an assessment of the mitigating actions required to reduce the uncertainty in the likelihood and impact of the major technical risks in the program. The information was presented to the DOE during the Decision Point 3 review meeting. The DOE authorized Air Products to proceed with the facility construction following Decision Point 3.

30.1.4 Manufacturing Facility Construction and Commissioning

Air Products provided overall project management for CerFab equipment development, specification, procurement and installation out of Air Products' Allentown, Pennsylvania headquarters. The majority of the engineering work was performed by both Ceramatec and Air Products based upon development activities from other parts of the program. Air Products provided a Project Manager, who was responsible for the day-to-day management of all aspects of the project including schedule, quality, safety, engineering design, cost control, procurement and engineering services.

The Project Manager was assisted by an execution team, including Project Technicians and Project Services, which were responsible for the performance, monitoring and coordination of all activities. The Project Management team was supported by project-specific lead discipline engineers using well-proven company practices for project execution. Regularly-scheduled meetings held with the project team members promoted good communications within the team and allowed the early identification of actions necessary to maintain the project quality, schedule, development activities, and performance targets. Many of these meetings were held (respectively) at the CerFab and at the offices of Ceramatec in Tooele and Salt Lake City, Utah.

Table 30-4 is a synopsis of the execution plan.

Table 30-4. Project execution after DP3 (18 months).

Schedule Task	Plan Date	Completion Date
DOE Definitization		April 2011
DP-1 Approval of Site Selection		April 2011
DP-2 Process Criteria Fixed		Sept 2011
DP-3 Budget Approval (DE, Permits complete)	March 2012	March 2012
Air Permit Issued	Feb 2012	Feb 2012
EPC Contract Award	Apr 2012	April 2012
Equipment Purchase Initiated	Sept 2012	Sept 2012
Design Hazard Review Conducted	Apr 2012	April 2012
Building Improvements Complete	Mar 2013	March 2013
Equipment Installation Complete/Start Commission	Sept /Oct 2013	Sept/Oct 2013
DP-4 Commissioning Complete	Mar/Apr 2014	March 2014

Equipment procurement and installation began in March 2012. From that time through September 2013, over 120 major pieces of equipment were specified and procured, and over 130 U.S. companies provided equipment and support to the CerFab. Approximately 80,000 man-hours of engineering, procurement, and construction and installation activities were safely executed in completion of this sub-task.

30.1.4.1 Equipment Procurement and Installation

All long-lead equipment was ordered early in the process; equipment installation bids were reviewed, and purchase orders issued. As equipment began to arrive (Figure 30-5), installation was initiated.

Figure 30-5. Cerfab equipment deliveries.

Per the project execution schedule, ~95% of the equipment was received in a single calendar quarter and 80% was installed. Vendor representatives completed systems checks on most of the larger equipment items. The tape caster was delivered on schedule, installed and passed the installation check by the supplier. Several factory acceptance tests were completed, the SCADA system was installed, and the raw material for the ceramics was received.

A final Davis-Bacon audit was completed with the DOE in Q4-2013 to ensure local craft wage rates were applied during the construction and installation period. The final commissioning and operating plan was also reviewed with DOE program management after completing the Davis-Bacon audit.

30.1.4.2 Building Infrastructure Installation

Ceramatec prepared the building refit package prior to the start of equipment installation. Building infrastructure installation was initiated early in the project. Air Products provided the construction site supervisor, and the Air Products Construction Engineering group managed the installation project. The design definition and preliminary design reviews for the building refit were completed, and the building retrofit EPC contract was awarded.

The existing building was cleaned, and utility systems were upgraded to handle the CerFab process equipment. Duct work and a thermal oxidizer were added to accommodate the clean room services and emissions associated with ceramic module production. Figure 30-6 shows the progress of the building cleanup and start of retrofit activities. Figure 30-7 shows the interior where much of the power and ductwork was completed and the interior rooms fitted with drywall.

Figure 30-6 Cerfab interior after clean up and preparation.

Figure 30-7. Cerfab interior with most power, ductwork and drywall installed.

Two of the four existing bag houses were removed as the particulate collection volumes from CerFab operations did not warrant the available capacity. Exterior concrete pads were installed to accommodate the solvent storage required for CerFab operations. These systems were all designed in compliance with the air permit and the categorical exclusion received at the time of DP3. Communications and security systems were upgraded to bring the building into compliance with Air Products' standards and to fulfill the needs of an operating facility. An exterior photograph of the facility is shown in Figure 30-8.

Figure 30-8. The main entrance to the CerFab.

The clean room was further expanded mid-project to meet NFPA guidelines for minimum safe distance from the tape caster for non-explosion-proof equipment, and to provide more flexibility for the tape caster footprint. Figure 30-9 is a photograph showing the clean room.

Figure 30-9. Cerfab clean room during construction.

Building infrastructure installation was substantially finished in 2013. The only remaining activity was to complete the clean room ceiling, which was finished once the final drawings were issued for the major equipment to be used in this room.

Figure 30-10 shows before-and-after photographs of the clean room area as an example of the activities completed following the Decision Point 3 (DP3).

Figure 30-10. The clean room before (left) and after (right) DP3.

30.1.4.3 Safety Review

The project team followed a formalized, proprietary hazard analysis process to ensure effective multidisciplinary reviews occurred at appropriate times during the evolution of the CerFab project and its transition into operations. These reviews provided checks on the decisions made by individual engineering groups and ensured that the safety and operability of the total integrated system was clearly addressed. The safety reviews that were conducted for the CerFab Project are outlined below.

In specific reviews, processes underwent rigorous, systematic analyses for potential hazards. Modifications to the system design and/or operating procedures to achieve process safety were identified by the review team, or further studies were initiated when justified by the nature of the problem. Reviews were carried out in three distinct phases: Design Hazards Review (DHR), Design Verification Review (DVR) and Operational Readiness Inspection (ORI).

The hazard review included a thorough check of the P&ID using the HAZOP methodology concentrating on the safety aspects of the process. For equipment where there was a previous standard or repeat design element, the review took place against a generic HAZOP template to confirm that all hazards had been addressed and that safeguards exist. Exceptions were noted, and recommendations were then made and documented to cover any deficient areas. Personnel at Ceramatec's PDF with experience operating equipment similar to that at the CerFab provided input to the HAZOP process.

At the completion of the design phase, a DVR was performed. The purpose of this review ensured that the design criteria developed during the previous hazard reviews have been incorporated into the final design. The document generated from this review was used during the construction phases of the project to ensure that each design item identified for safety had been incorporated into the facility during construction.

An ORI was conducted immediately prior to start-up of a facility. The purpose of this inspection was to ensure that all safety and health-related details discussed and agreed upon during the design stages had been incorporated into the facility construction and operation. This review also verified that all the design recommendations identified during the hazards reviews had, in fact, been incorporated into the plant during construction. The existence of complete safety emergency procedures, operator training, site EHS management systems and plant operating manuals for the facility were also verified during the ORI.

The hazard review documentation summarized, on an exception basis, the hazard issues that needed to be addressed and tracked the resolution of all recommendations made in the review. This process continued until all of the open items had been addressed by the team. Over 330 items were identified during the HAZOP process. The process was executed in multiple meeting sessions over a two-week period with project, operations, process, design, and research teams

contributing to the effort. Follow-up activities on the project continued to the beginning of the commissioning phase. No items identified in the DHR remained open by the end of commissioning.

The DHR team documented over 830 cause-and-consequence pairs during the process. From this work, over 1,250 safeguards and over 120 additional recommendations were implemented at the facility.

The major equipment items were inspected by the end of the installation phase. In addition, much of the equipment was put through a dry run by both the Operations team and the equipment suppliers' support teams brought in to assist with the start-up activities.

30.1.4.4 Equipment Commissioning

Equipment commissioning began on 30 September 2013. The first activities were facility safety training of the Cerfab Operations staff (a team of Air Products and Ceramatec employees) and completion of the final safety reviews for all equipment. The final ORI was organized on-site and led by a Process Safety representative, with the Operations team participating in their respective process areas. The team reviewed, inspected, and verified that the equipment was installed properly and that the function testing was completed. Any deficiencies were documented, classified and corrected.

After the ORI approval by facility management, raw materials were brought into the process areas. This was done in parallel in the powder processing and tape casting areas by using the existing stock of raw powders and a production lot of AP2K materials from Ceramatec's Salt Lake City facility specially prepared for this purpose. This allowed a faster start for two of the most critical process areas at the facility. All useable materials were sent to downstream process operations, providing material for tuning the process controls and confirming that each apparatus operated within its respective specifications. Suppliers were brought in for initial startup of some of the equipment.

The operational methods and procedures for each processing area were documented, and the team successfully completed the equipment commissioning task. The process areas were free of operational issues other than typical debugging of instrumentation and controls associated with new processes and equipment. The primary exception was the mechanical operation of the kiln

used for manufacturing the AP2K powder. In-specification powder was obtained quickly, but the mechanical reliability was not what was expected. The kiln supplier worked with the team to improve the mechanical performance of the equipment. The kiln was loaded with "dummy" mass and the thermal profile was tuned. As a result, in-specification AP2K material was produced and used in the downstream processes. The kiln produced approximately 3,700 kg of ITM ceramic powder during the commissioning period.

All other processes in the Powder Preparation room ran well, and this room was commissioned. Suppliers provided the final training for the operations team and assisted in initial operation of the equipment.

Most of the green component processing areas were fully operational toward the end of commissioning. The slip preparation area was commissioned, and controls programming was completed. Loop checks and functional tests were completed, and a commissioning plan was developed for the solvent storage and delivery systems. The solvent totes were safely charged. Several batches of slip were produced and moved to the tape caster for processing. The solvent storage and dispensing systems functioned well.

Supplier representatives completed the setup, testing, and commissioning of the tape caster and regenerative thermal oxidizer (RTO). All open HAZOP items were closed, and ORI action items were cleared. Several faults were encountered during the first cast of tape. This was expected given the complexity of the tape caster, the drying zones, the measurement systems, and the RTO systems. The system reacted appropriately to each fault, and all were fixed. The tape caster produced tape that was used in downstream processes. The clean room and all associated equipment were commissioned, and operating protocols were implemented to restrict the ingress of contaminants. All featuring and lamination systems were commissioned and operated as expected.

Analytical equipment was commissioned in the Characterization Lab, which is used for quality control to ensure the raw materials, AP2K powder, and various components that make up a module were within specification. The X-ray-based spectrometer supplier presented a radiation safety program and conducted radiation safety training to support operation of the spectrometers.

The supplier also performed a radiation survey of the XRD and XRF units. Both were acceptable.

Out-of-specification green wafers were sintered in a kiln to begin thermal processing. The wafers showed de-lamination, which was expected given that the materials from the upstream processes for this batch did not meet specifications.

With successful operation of the kilns, the ceramic manufacturing process equipment was deemed commissioned.

30.1.4.5 Process Commissioning

In parallel with the commissioning of the ceramic manufacturing process equipment, work was also done to commission the overall process. Because the process is sequential and generally done in batch operations, commissioning was first completed on the processes furthest upstream following equipment commissioning in those areas. Process commissioning of the powder processing, tape casting, featuring and lamination, wafer sintering and sub-module assembly areas was completed sequentially. The remaining downstream module assembly thermal processes were then commissioned.

30.2 Operation and Process Assessment

30.2.1 Production of 1-TPD modules

The Decision Point 4 application was approved by the DOE, signifying the transition from commissioning to operations at the CerFab. Operations were initiated following commissioning of the equipment and processes. A major challenge in this effort was to produce intermediate products (powders, slips, tapes) meeting QA targets while operating equipment and processes on a much larger scale than was done in the Ceramatec PDF.

An initial goal was to produce a large amount of powder to charge the front end of the facility to begin production work. The powder production team blended, milled and calcined 4,000 kilograms of raw materials to the required specification. The AP2k powder was used to produce slip for the tape casting operations, resulting in 2,600 meters of tape. The tape was featured and cut to produce over 27,000 featured parts and module component parts. The wafers and module components were sintered and then sent to the module assembly operations. Several in-

specification wafers were produced. Submodules were produced and a module was assembled. The components used in this module did not meet the quality control requirements, so the assembled module was not testable. Figure 30-11 is a photograph of the first module produced at the CerFab.

Figure 30-11. First module produced at CerFab.

During the first three months of continuous operations, the powder processing area blended, milled and calcined 5,900 kg of raw materials and AP2k powder streams to the required specifications. Tape casting operations produced 9,300 meters of finished green tapes during this time.

All of the green wafers and module components were sintered, and all output was taken to the module assembly operations. Several submodules and 1 TPD-scale modules were produced. The modules did not meet the quality control requirements and were not testable, but established that intact ceramic devices could be built in the process.

A number of wafers and three-wafer submodule test assemblies were produced to specification. Additional testable wafers were reserved. All other useable parts were processed through the entire CerFab manufacturing system to stabilize the last thermal processing steps. The testable yields exceeded 50%. The equipment performed well, with the exception of some mechanical issues with the calcining kiln. The supplier provided warranty service to resolve the issues.

Based on advances under Task 28 to support more reliable and creep-resistant modules, process operations were subsequently modified to improve advanced architecture wafer production for module reliability and yield.

Developmental operations were started using a new formulation. The green material reclaim process was commissioned, and reclaimed powder was used for some tape production. Several equipment mechanical issues were addressed. The calcining kiln supplier completed design modifications, which were reviewed and approved. Several of the wafer kilns were taken offline to complete minor warranty repairs. Lastly, the supplier of the wafer finishing equipment made several changes to the mechanical hardware and PLC programming to improve the quality of parts produced by these machines.

The CerFab team produced single-wafer modules suitable for testing in the XVU. The testing of these modules is discussed under Task 31.

The Q1-2015 CerFab operational summary is documented in Table 30-5, representing efforts toward improving yields of advanced architecture wafers with the reformulated materials.

Table 30-5. Q1-2015 CerFab operating data.

Process Description	Oct. 14	Nov. 14	Dec. 14	Total	Unit of Measure
Powder calcined	140	166	926	1,232	kg
Tape cast	584	461	359	1,404	m

Work was carried out to assess the process variability of the new formulation of tape casting slip. Control discs of porous materials were fabricated from the tapes. Density and porosity measurements are shown in Table 30-6.

Table 30-6. Lot 35 control disc density and porosity.

Lot	% of Theoretical Density	% Open Porosity
35C	84.1	8.0
35D	89.1	0
35E	84.2	5.78
35E'	85.9	2.43

The control discs in Lots 35E and 35E' differed in porosity because of the different manufacturing methods used to make them. These data were used in the specifications of powder, slip and tape casting operations to enable fine control of porosity in specific layers.

Operations expanded in Q2-2015 with advances in understanding made with the reformulated materials. The CerFab operational summary is documented in Table 30-7.

Table 30-7. Cerfab operating data for Q2-2015.

Process Description	Jan-15	Feb-15	Mar-15	TOTAL	Unit of Measure
Powder Calcined	1375	1528	0	2,902	kg
Calcining Kiln Operation	195	217	0	412	h
Slip Batches processed	27	38	28	93	each
Tape Cast	137	602	634	1,373	m
Wafers sintered	138	333	273	744	each
Wafer Kiln Runs	2	5	4	11	each

30.2.2 Process Quality and Efficiency Assessment

Through the commissioning and operations periods, each of the unit operations was shown to have the required capacity to produce the parts and components necessary to meet the overall facility production goals. Operation at capacity was limited, as developmental work using the CerFab equipment was chosen as a priority in consultation with DOE Program Management. In addition, operation at capacity while pursuing yield improvement is not an effective use of materials.

TASK 31.0 TABLE OF CONTENTS

TASK 31.0 CERAMIC COMPONENT TESTING.....2

31.0 SCOPE..... 2

31.0 CERAMIC COMPONENT TESTING..... 2

Background..... 2

Technology Development Unit (TDU)..... 3

FluX Verification Unit (XVU)..... 3

Vacuum Permeate Short Loop Test Rigs (VP-SLTRs)..... 5

Transient Test Rig (TTR)..... 7

31.1 Performance Testing of Industrial and CCs Membrane Prototypes..... 8

31.2 Performance Testing of Advanced Module Designs..... 11

End Caps and Base Pieces..... 11

Modules..... 13

31.3 Performance Testing of Modules Produced with the CerFab..... 24

TASK 31.0 CERAMIC COMPONENT TESTING

31.0 Scope

In Task 31.0, Air Products carried out limited performance tests of optimal membrane formulations in support of Task 28. Tests of module performance were carried out in laboratory pilot-scale apparatus and small pilot units. Tests of oxygen flux, purity, and reliability were conducted in high-pressure, high-temperature rigs. Ceramic-to-metal seal performance for both advanced module designs and CCS-optimized modules will be assessed.

31.0 Ceramic Component Testing

Background

Ceramic modules comprising one or more planar wafers, spacer rings between each wafer, an oxygen flow tube and an end cap, were built and tested in specially designed pilot-scale rigs for assessing oxygen flux and purity under commercially relevant, high-temperature, high-pressure conditions. In general, the rigs are composed of a heated pressure vessel to house the ceramic module, a compressed air source, an air heater, and an oxygen collection system consisting of an oxygen control valve for controlling the oxygen pressure at the membrane, an oxygen pump, and a downstream flow meter and purity analyzer. A simple pictorial arrangement of these components is shown in Figure 31-1. A variety of rigs is used for different purposes; each is briefly explained in the experimental section of the report.

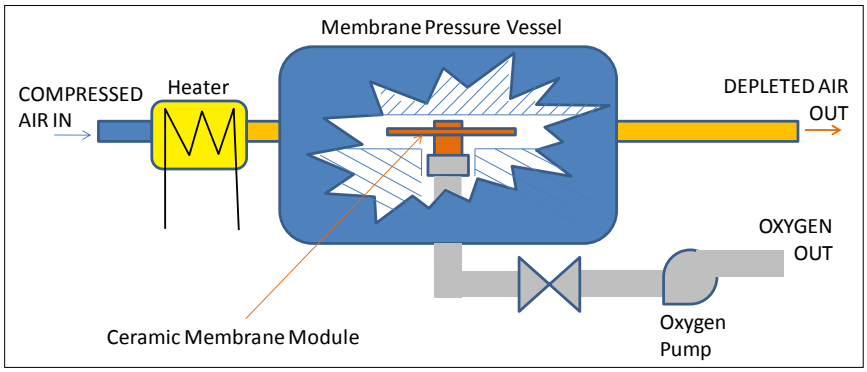

Figure 31-1. Simple schematic of a pilot-scale test rig for assessing oxygen flux performance and purity from ceramic membrane modules.

Technology Development Unit (TDU)

The TDU comprises all the components mentioned above, including a horizontal vessel with an 8- inch internal diameter. The test module can comprise one to 12 wafers and is contained in a dense alumina flow duct which channels the flow around the wafers. A chromium getter resides in the inlet of the vessel and is made up of a bundle of getter tubes. Product oxygen exits through a support tube which passes through the vessel flange where it is cooled. The product flows through a pressure control valve, a vacuum pump and a flowmeter before being vented to atmosphere. Slip streams of product as well as non-permeate are plumbed to an oxygen analyzer for measurement of oxygen content. The TDU is fitted with a direct-fired combustor upstream of the vessel. Modules capable of producing up to 0.1 TPD of oxygen were tested for flux and purity. Figure 31-2 shows photographs of the TDU and the module.

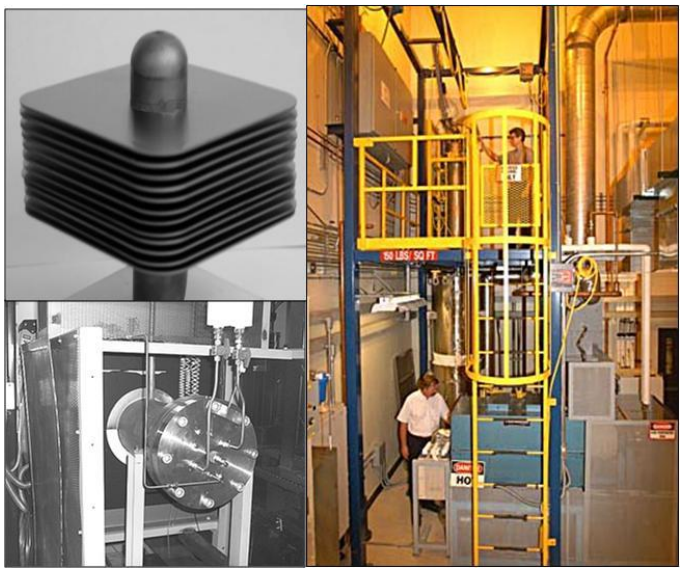

Figure 31-2. The Technology Development Unit (TDU). *Upper left:* ceramic module capable of producing up to 0.1 TPD. *Lower left:* TDU pressure vessel and associated heater. *Right*: A wide-angle view of the rig; the blue box in the foreground is the TDU vessel heater.

FluX Verification Unit (XVU)

The ITM oxygen flux verification units (XVU1, XVU2, and XVU3) are designed to verify the oxygen flux capability of a full-size single wafer module (Figure 31-3).

Figure 31-3. FluX Verification Unit (XVU).

Compressed air is supplied to each of the three XVUs at 500 psig from a remotely located compressor to a high-pressure manifold located above the XVUs. Air from the manifold is reduced in pressure through a pressure regulator and its flow is controlled via a mass flow controller for each unit. The controlled flow of air then enters a preheater coil that heats the air to the required process temperature before entering the pressure vessel that houses the ITM module. Both the preheater and the vessel are located inside a large, electrically heated furnace. After entering the vessel, the high-pressure air goes through the horizontal inlet section of the vessel that channels flow to a slot located in the wafer. The oxygen-depleted (non-permeate) air then flows out of the vessel through an identical slot 180º opposite the first. The non-permeate then flows through the outlet section of the vessel and exits. A slip stream of the non-permeate is analyzed for O_2 content using paramagnetic oxygen analyzer.

After oxygen permeates through the membrane, it travels down a support tube at 0.2-1.0 atm (absolute) pressure to the bottom of the vessel to the connecting flange. The oxygen product stream cools rapidly by losing heat to ambient air. The oxygen then flows through a dry-seal, diaphragm-based vacuum pump and is exhausted into the vent. A slip stream is sent to a paramagnetic oxygen analyzer for purity measurement.

While the flow systems for XVU1, XVU2, and XVU3 are very similar, the flow systems for XVU2 and XVU3 have special provisions to conduct iso-compositional (or "iso-strain") thermal cycling. Iso-compositional methods enable changing of the gas composition, on both the air and permeate sides of the membrane, to manage the composition-dependent chemical expansion that is characteristic of the ceramic material. As such, either XVU2 or XVU3 can be optionally

connected to the ISU unit, a cart-mounted flow control system that manages the blending of air and N_2 on the air feed side and O_2 and N_2 on the permeate side.

The XVU vessel is "T" shaped and constructed of high-nickel alloy. The vessel is ASME coded and dually-rated at 250 psig/1650°F, 450 psig/1525°F. The vessel includes a section of alloy tubing wrapped around the horizontal section that is used as an air preheater. A flange is attached to the bottom of the vertical section. There is also a mating blind flange fitted with three thermocouple ports and a tube inserted inside the vessel. The tube supports the module and acts as the permeate flow tube, connecting to the permeate system on the outside of the mating blind flange. The portion of vessel that houses the module and the preheater tubing section is enclosed in a furnace. XVU1 has a slightly different vessel design than XVU2 and XVU3. The upstream side-arm of XVU1 has been extended outside of the furnace, where it terminates at a bolted flange closure. This allows for a guard bed to be loaded into the sidearm to remove impurities from the hot air stream before contacting the ITM module.

Vacuum Permeate Short Loop Test Rigs (VP-SLTRs)

The Vacuum Permeate Short Loop Test Rigs are designed to investigate the oxygen flux response of small prototype membrane modules as a function of time, temperature, pressure, and feed gas composition (Figures 31-4 and 31-5).

Figure 31-4. VP-SLTR housing, closed, and open showing subscale wafer.

Figure 31-5. VP-SLTRs showing moisture addition system at bottom.

The four VP-SLTR systems are similarly configured, although they vary somewhat in their feed composition capabilities. The heart of a VP-SLTR system is a furnace, in the hot zone of which a sub-scale ITM module is mounted inside a magnesium oxide flow path with an integral permeate tube. The sub-scale ITM module features a single planar disk wafer with approximately one twentieth the surface area of a single full-size wafer, which allows meaningful flux results to be obtained at feed air throughputs easily attained at the laboratory scale. The flow duct receives pressurized air as feed, optionally modified with potential contaminants such as water vapor, carbon dioxide, or sulfur dioxide. The oxygen permeate from the membrane (as well as any leak) is withdrawn from the interior of the sub-scale module using a vacuum pump. The permeate flow is measured using a mass flow meter, and its oxygen concentration determined using a zirconia-cell oxygen analyzer. These measurements allow characterization of the oxygen flux during the experiment. Air is fed from the shared compressor system. Using auxiliary feed systems (liquid water feed system, pure CO_2 feed system, ppm-level SO_2 feed system), low-percentage concentrations of CO_2 and/or water, and ppb-level concentrations of SO_2 can be established in the inlet gas.

In a typical experiment, the oxygen flux is first evaluated at baseline operating conditions, after which its immediate and long-term responses to changes in operating conditions are evaluated, typically over a duration of several weeks to months.

Transient Test Rig (TTR)

The Transient Test Rig (TTR) is designed to evaluate the response of ITM Oxygen modules when subjected to transients in temperature, pressure, and oxygen concentration (Figure 31-6).

Figure 31-6. Transient Test Rig (TTR).

The reactor portion of the TTR consists of an internally heated pressure vessel. The module is contained within a magnesium oxide-lined, high-nickel alloy retort. The vessel heating element is imbedded in a cast ceramic split cylinder unit. The interior of the vessel and the outside of the heating element unit are filled with vacuum-formed ceramic insulation and purged with nitrogen during operation.

The process feed gas is a mixture blended from nitrogen, air, oxygen, and CO_2, all at high pressure. These gases have independent pressure and flow controls to permit process feed gas compositions spanning the range from pure nitrogen to pure oxygen at pressures from 0 to 300 psig. In the vicinity of the module, the feed is transitioned to a MgO pre-heater/getter bed to equilibrate the feed gas to the reactor temperature while also acting as a getter to remove

chromium and other contaminants from the process gas feed. The process feed gas is fed across the module through an MgO-lined flow path. The non-permeate stream then exits the reactor.

The vessel is purged with nitrogen which has independent pressure and flow control. The purge stream enters through the vessel wall and exits through the bottom blind flange. The purge exit stream is combined with the non-permeate stream after exiting the reactor. A back-pressure controller acts on the combined stream to regulate the vessel pressure. A check valve arrangement maintains the purge gas pressure at a slightly higher value than the process gas within the reactor.

The module can be purged, if desired. The module purge feed gas is a mixture blended from nitrogen and oxygen. These gases have independent pressure and flow control to permit module purge feed gas compositions ranging from pure nitrogen to pure oxygen at pressures from sub-atmospheric to ~10 psig. The module purge feed gas enters the reactor through the bottom blind flange. Permeate pressure is regulated by a pressure control valve. The permeate gas stream can be at sub-atmospheric pressure as it runs through a vacuum pump system.

31.1 Performance Testing of Industrial and CCs Membrane Prototypes

ITM membranes must exhibit stable oxygen flux over their lifetime. An experiment studying long-term flux stability of a non-catalyzed Type A membranes that have application in carbon, capture, and storage (CCS) applications was completed after 4,000 hours of continuous operation. The oxygen flux degradation rates generally increased with decreasing temperature and decreasing partial pressure of the hydrogen fuel. Stable flux was achieved at one temperature condition for 500 hrs.

Experiments have shown that that aging thin and thick Type A membranes under reducing conditions cause flux degradation. A catalyst was applied to the fuel-side surface of Type A membranes after they were aged for several months under reducing conditions. The catalyst reduces the surface kinetic resistance on the fuel side of the membrane. The flux performances of aged and non-aged membranes are shown in Figures 31-7 (thick) and 31-8 (thin).

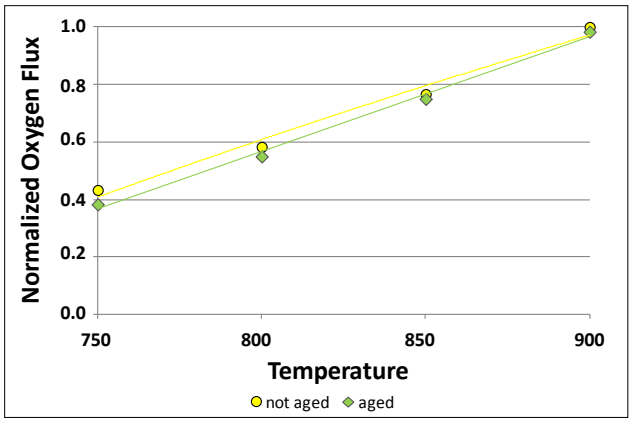

Figure 31-7. Flux performance of two thick Type A membranes: non-aged, and aged in fuel and catalyzed.

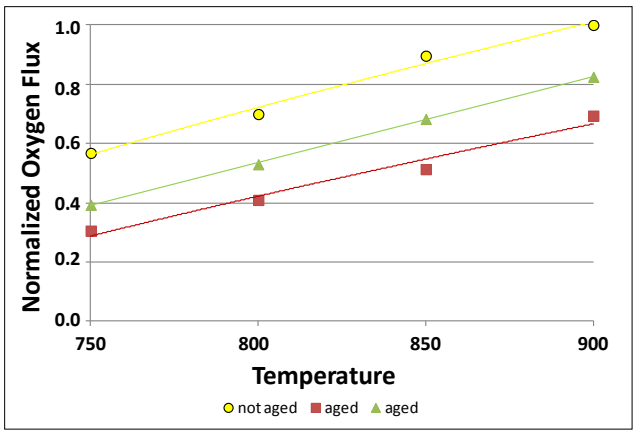

Figure 31-8. Flux performance of two thin Type A membranes: non-aged, and aged in fuel and catalyzed.

The thicker membranes exposed to syngas (and subsequently catalyzed) had a slightly lower flux than the non-aged membranes (Figure 31-7). Exposure of the thin membranes to syngas (and subsequently catalyzed) adversely affected their performance (Figure 31-8). The thinner Type A membranes have an overall higher fraction of syngas-side surface kinetic resistance than the thicker membranes. This suggests that the surface kinetic resistance is increasing with time.

An improved composition with better flux stability was prepared. This composition, Type B, has superior thermodynamic stability compared to Type A. Figures 13-9 and 13-10 compare the flux performances of Type A and Type B membranes at two different membrane thicknesses. Performance of the thick Type A and B membranes was nearly equivalent. The thin Type B membranes outperformed the Type A membranes.

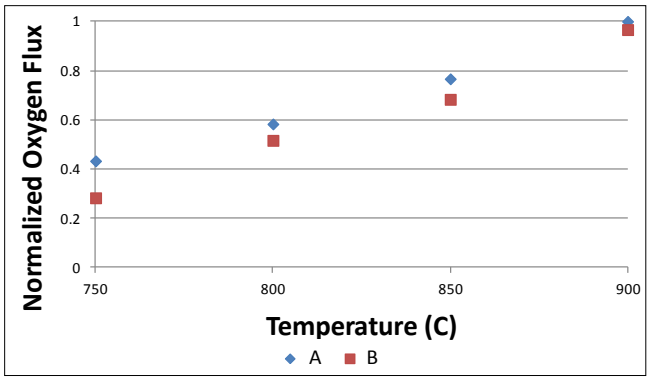

Figure 31-9. Flux performance of non-aged, catalyzed, thick Type A and B membranes.

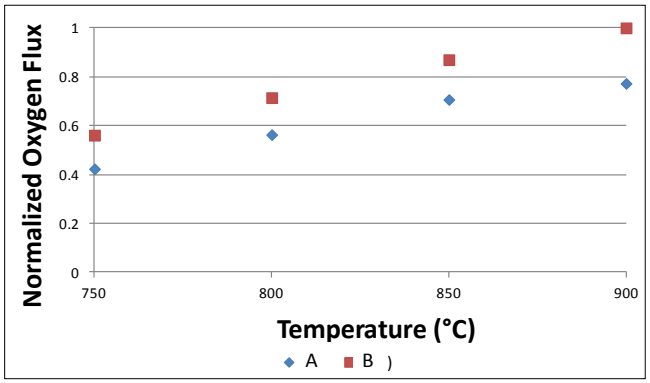

Figure 31-10. Flux performance of non-aged catalyzed thin Type A and B membranes.

Type B membranes were aged in fuel for several months and then catalyzed. Figures 31-11 and 31-12 show that the membranes did not suffer flux degradation during the aging in fuel.

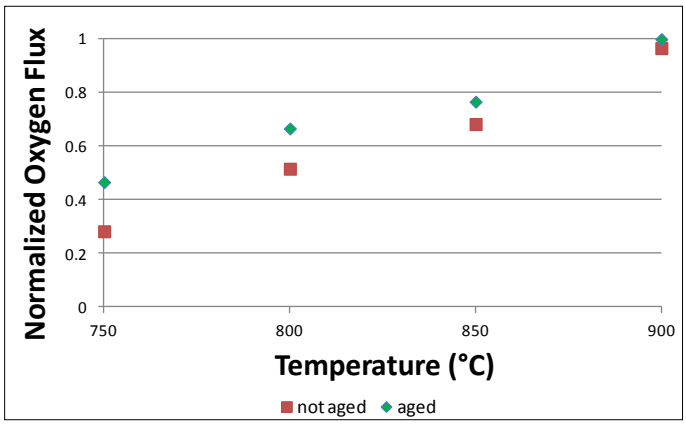

Figure 31-11 Flux performance of non-aged and aged-in-fuel and catalyzed thick Type B membranes.

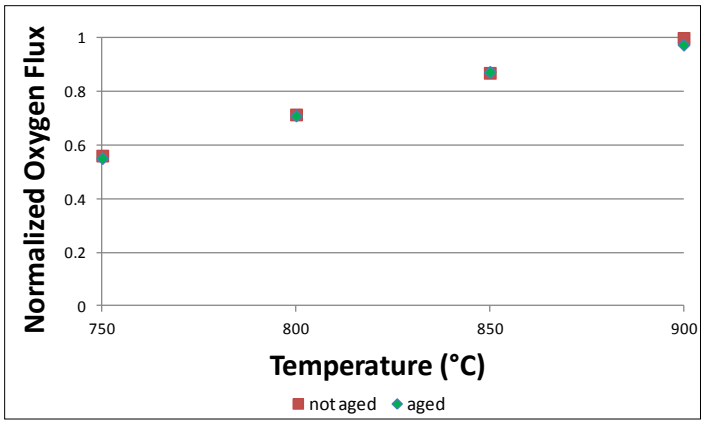

Figure 31-12 Flux performance of non-aged and aged-in-fuel thin and catalyzed Type B membranes.

31.2 Performance Testing of Advanced Module Designs

End Caps and Base Pieces

TTR

Testing of a redesigned dome/base piece was conducted in the Transient Test Rig (TTR). The sample was mounted on an Alloy A seal plate with a #10 seal. A higher-than-usual leak rate observed at the start of the test decreased by about 50% during heat-up (see Figure 31-13).

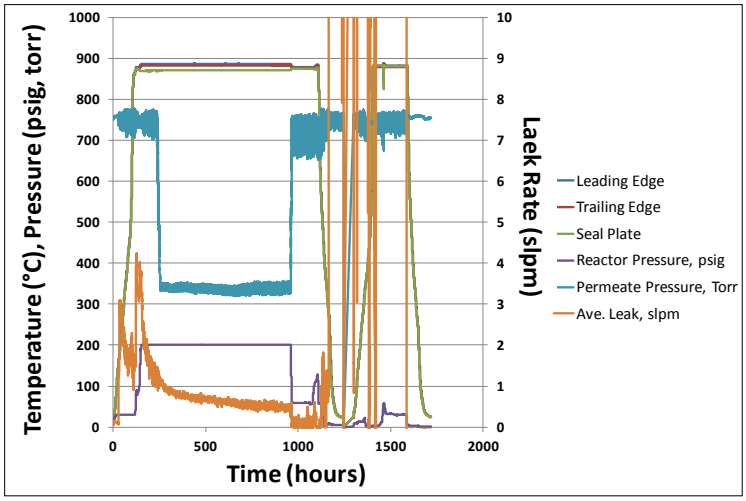

Figure 31-13. Results for redesigned dome/base piece tested in the TTR.

The leak rate increased again during the feed pressure ramp. The leak rate was seen to decay once a stable feed pressure was attained.

After holding at feed and permeate pressure for 500 hours, the sample was subjected to a decreasing pressure ramp and then returning to operating pressure to complete a cycle. After initiating an increasing pressure ramp, it was discovered that the reactor could not be pressurized. A decision was made to shut down the reactor and determine the cause(s) of the problems.

In other work, testing of an advanced architecture dome/spacer/base piece was conducted in the TTR to assess the impact of P_{O2} cycling and high feed-side P_{O2} on the module leak rate. An Alloy A seal plate with a #10 seal was used. Figure 31-14 documents the operating conditions and leak performance.

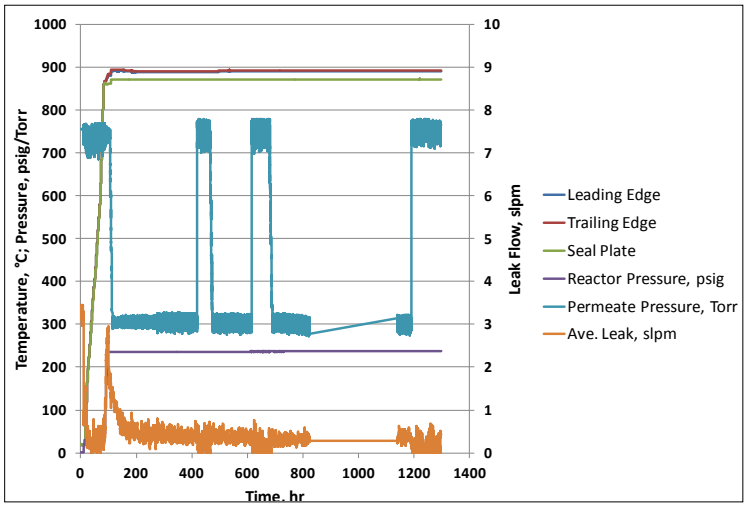

Figure 31-14. TTR operating condition and leak rate of a dome/spacer/base piece.

The unit was pressurized to an intermediate value and then heated using a modified joining schedule. A sequential linear pressurization schedule was followed. The assembly initially showed a modest leak, which decayed rapidly during heat-up. It should be noted that the leak rate includes seal leak, sample flux, and sample leak.

The leak rate increased during the feed pressure ramp, but decayed over the permeate pressure ramp and initial hold. The assembly was held at full conditions for approximately 300 hours, then put through a 15-minute simultaneous feed and permeate P_{O2} ramp (i.e., a 'black plant' power failure simulation). After approximately two days, the assembly was returned to leading-edge temperature conditions. The leak rate remained constant, indicating good reliability. The assembly was then subjected to another 15-minute P_{O2} cycle. After a delay, the P_{O2} was increased by adding oxygen to the air feed while maintaining the feed pressure. The assembly

was then subjected to another 15-minute 'black plant' cycle. The leak rate remained low throughout, indicating good resistance to damage of the advanced architecture ceramic part, even during fast transients.

Modules

TDU

Testing of advanced architecture wafer (AAW) modules was initiated in the TDU. The first tests were conducted on a single AAW with a redesigned dome and base piece with a #15 seal. Figure 31-15 shows the actual O_2 flux and purity.

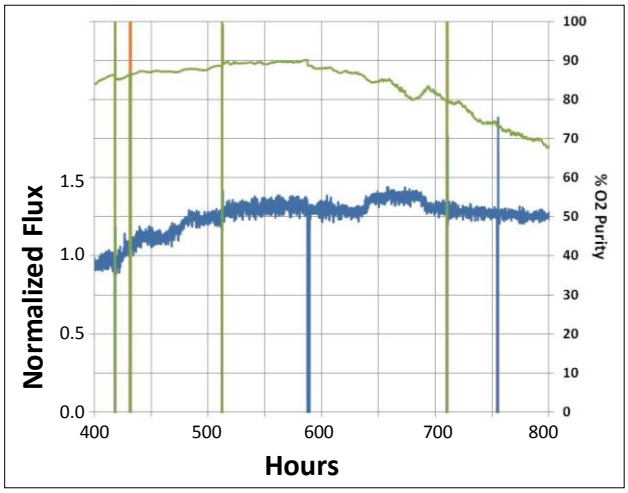

Figure 31-15. O_2 flux and purity with a single-wafer module in the TDU.

A purity of 90% and the target flux were reached at operating conditions. A decrease in purity was observed at 600 hours. At 640 hours, the feed pressure was increased for 36 hours, during which time the flux increased. However, the purity continued to deteriorate at a higher rate. The pressure was reduced and held for another 100 hours. The purity continued to decrease and reached 68% at 800 hours, with no change in the measured flux. The actual flux exceeded the theoretical flux throughout the experiment. (Note: flux was corrected for the leak rate.)

Upon unloading, this first advanced architecture wafer tested in the TDU was found to be intact. Despite the use of a Cr getter, there was a Cr-containing phase on the upstream section associated with a thermocouple positioned upstream. To minimize Cr contamination, the thermocouple was moved and the exposed surface area has also been eliminated.

A 12-wafer advanced architecture wafer module with a #10 seal was tested in the TDU. Figure 31-16 shows the module before it was loaded into the TDU.

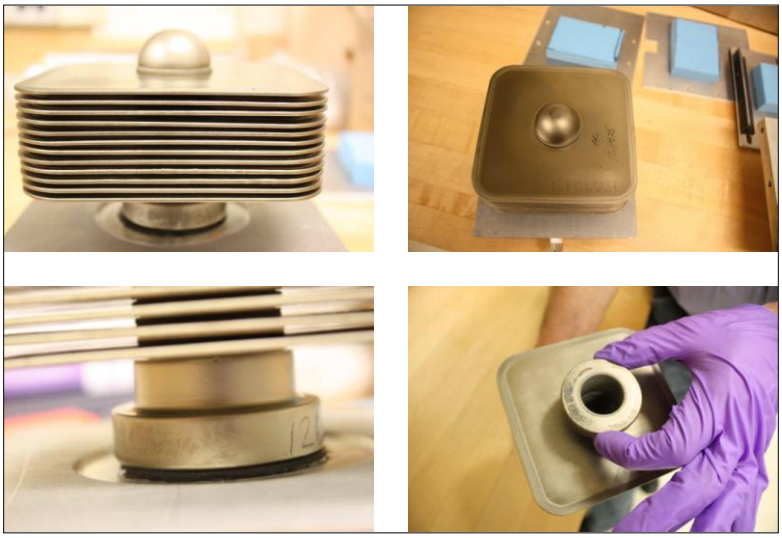

Figure 31-16. Wafer module being tested in the TDU.

After ~40 hours at operating conditions, a power failure caused the coolant flow to stop. The process recovered to pre-trip conditions and was held at operating conditions for more than 1,000 hours. Figure 31-17 shows the measured flux and purity and the theoretical flux.

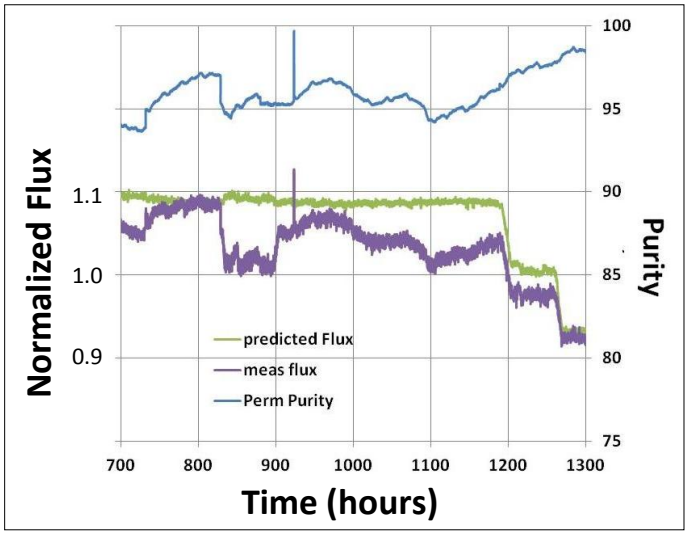

Figure 31-17. Module flux and purity during TDU run.

The measured flux is within 10% of the theoretical flux. The large variation seen at 800-900 hours is associated with a lower feed flow. After 1,200 hours, the feed pressure was decreased to evaluate performance at a lower oxygen partial pressure.

The ability for wafers and modules to thermally cycle without the use of iso-control greatly simplifies the process flowsheet and process controls. To confirm the ability of advanced architecture wafers and modules to cycle under air, a 12-wafer advanced architecture module (12PCL045) with a #10 seal was tested in the TDU starting in March 2013. Figure 31-18 shows a photograph of module loading.

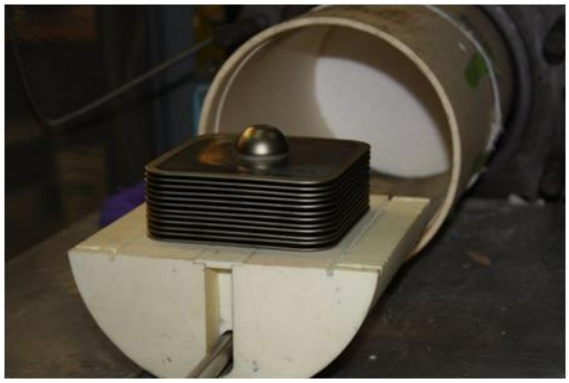

Figure 31-18. Advanced architecture module being loaded into the TDU.

The prescribed start-up procedure was used to take the module to leading-edge conditions, at which point the permeate purity was 98.4% and the flux was as predicted. Figure 31-19 shows the process data over the first 2,700 hours.

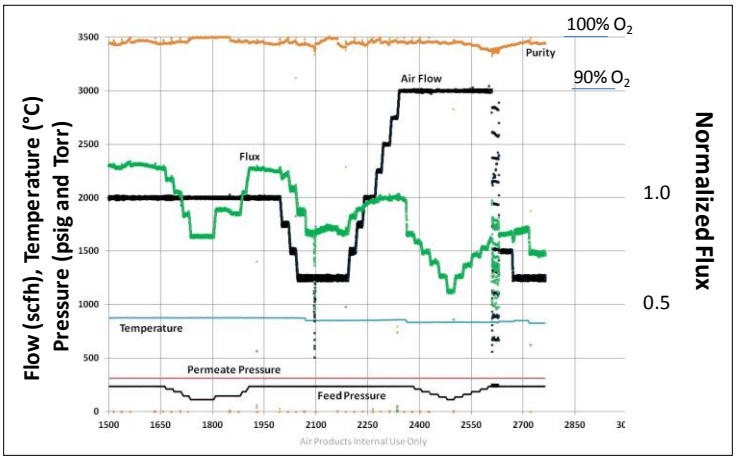

Figure 31-19. TDU process conditions, leak and flux of an advanced architecture module for first 2,700 plus hours.

Flow and feed pressure surveys were carried out, and lower-than-standard temperatures were also evaluated. Flux decreased by ~20% when the flow was decreased by ~35%. The flux did not increase appreciably at air flow rates above the standard. The decrease in flux at lower flow rates may be partially due to bypass around the module in the flow box. A pressure survey was conducted. The observed flux was very close to the expected flux under the experimental conditions. Module performance at lower temperatures was measured. Results were in close agreement with expectations. The decrease in the flux at lower temperatures was the same at two different pressures.

The TDU is fed by two compressors in a parallel configuration. One of the two compressors shut down at 2,600 hours; the other was unable to sustain the set flow rate. Flow and pressure oscillations occurred over a 20-hour period, causing oscillations in temperature and flux. This process upset did not cause any damage to the module. A second full thermal and pressure cycle was then completed. Flux returned to previous values and the purity continued to run > 99%.

A loss in power to the building interrupted the feed flow at hour 4,165. The system went into a failsafe mode in which heat to the vessel continued, and outlet valves were closed. Temperature was maintained, but pressure slowly dropped over 20 hours. Flow was reestablished, the system was re-pressurized, and flux and purity returned to their previous levels. This condition is similar to what may occur during plant upsets and at the ISTU, and provides good verification of ceramic reliability under this scenario. After the unanticipated shutdown, the system ran at steady flux and purity for an additional 2,000 hours before being shut down for a scheduled building-wide power outage. Figure 31-20 documents the operating conditions, purity and module flux for hours 4,000 through 6,000.

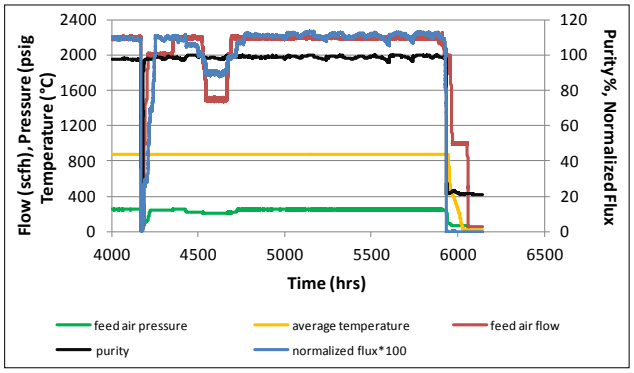

Figure 31-20. TDU operating conditions, module flux and leak (ongoing).

After completion of the maintenance work, the process was restarted using an accelerated schedule. There was no decline in performance on restart. The module experienced more than 8,000 hours at full operating temperatures under Task 31 and showed no degradation in purity or flux. Figure 31-21 documents the operating conditions, purity and flux during Task 31 operation.

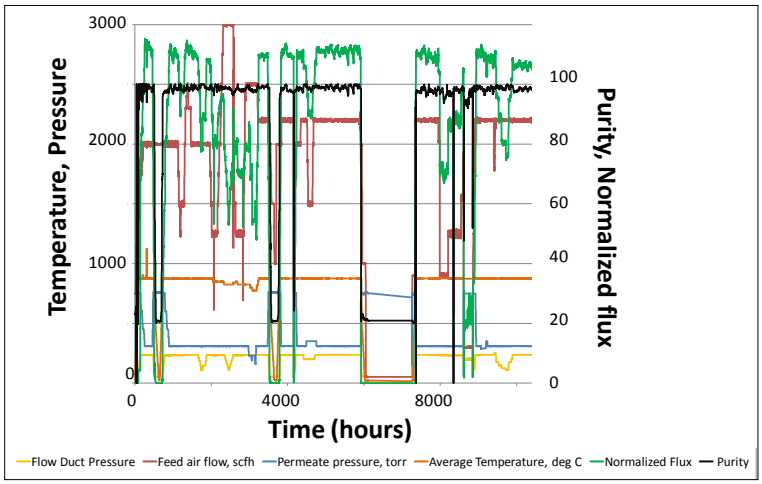

Figure 31-21. TDU operating conditions, module flux and leak over entire test period (ongoing).

Testing will continue under another contract until sufficient time at temperature has elapsed such that extrapolated creep data would project that measurable creep deformation of the internal wafer layers has occurred. After that time, a postrun analysis of the actual creep deformation will be completed.

Flux versus temperature at a standard set of conditions was measured during the run. The data are presented in Figure 31-22.

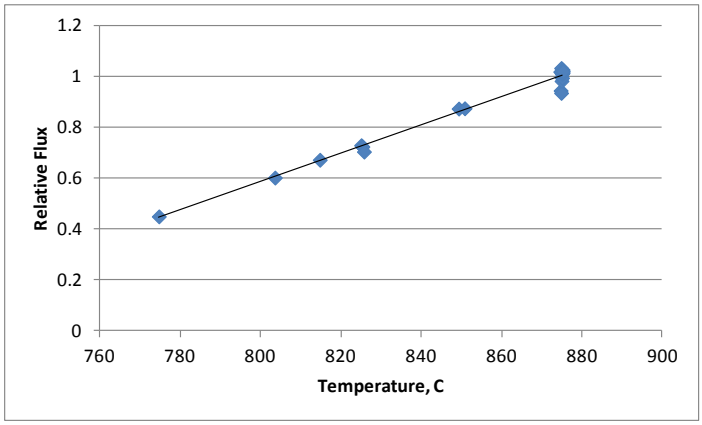

Figure 31-22. Flux versus temperature.

Flux was measured versus pressure at two temperatures as a function of P_{O2}. Figure 31-23 shows the result.

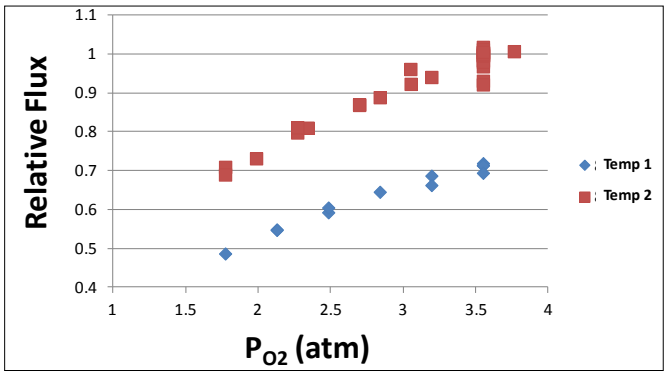

Figure 31-23. Flux versus oxygen partial pressure.

A scan of flux at various feed pressures was also completed. The measured flux agrees well with expected values (Figure 31-24).

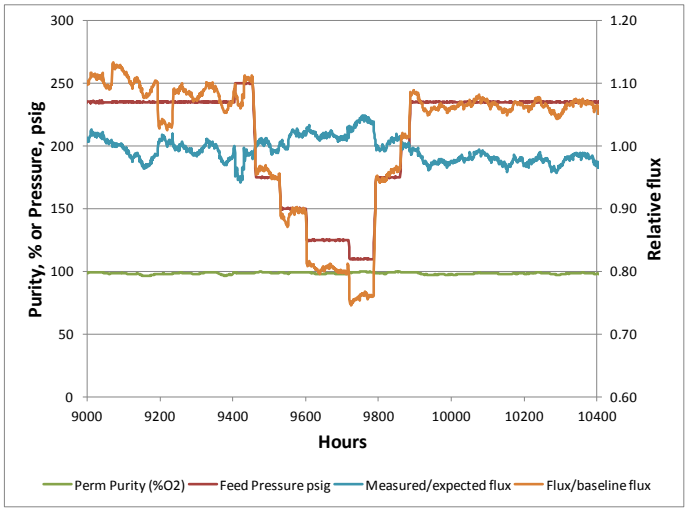

Figure 31-24. Purity and flux during testing at a variety of feed pressures.

XVU Testing

Extensive testing was conducted in the XVUs to determine flux and leak rate behavior over extended periods at operating conditions, module reliability and performance changes resulting from transients. Flux was also determined as a function of process parameters. The primary focus of the work was to establish the expected operating characteristics of advanced architecture wafers.

Figure 31-25 is an example of a test to assess performance over extended periods at operating conditions. The data reflect the operation of a single advanced architecture wafer.

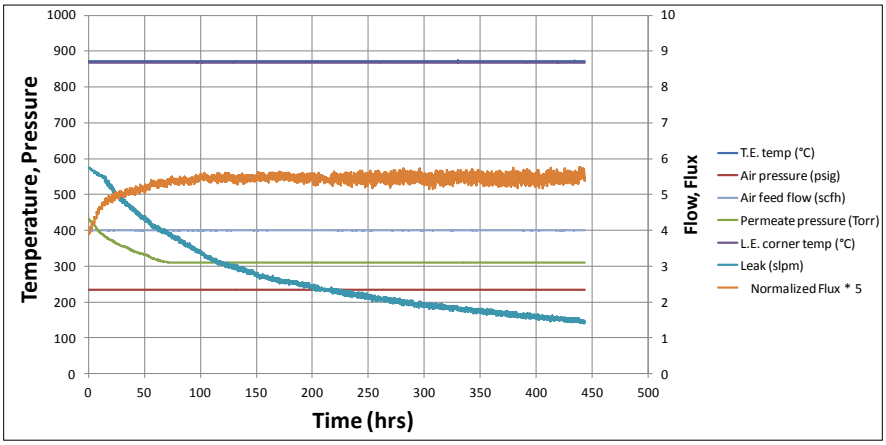

Figure 31-25. XVU test conducted at operating conditions.

Figure 31-26 is an example of a test to assess performance and reliability when the module is subjected to pressure cycles (transients).

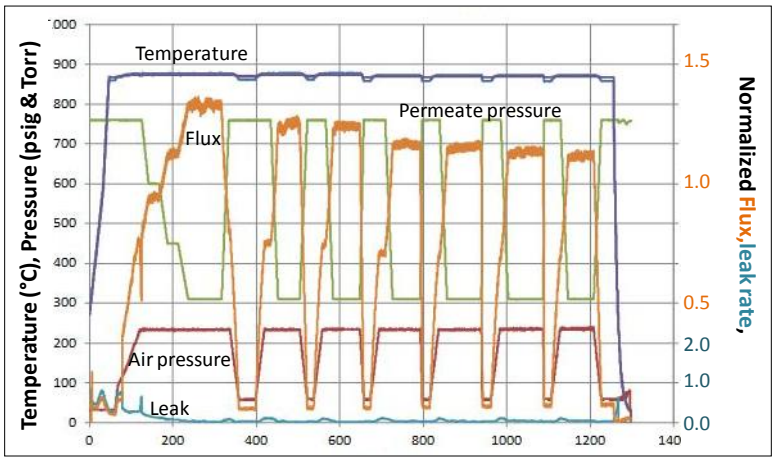

Figure 31-26. XVU2-2 test, pressure cycles (transients).

Figure 31-27 is a photograph of the wafer after being subjected to pressure cycles in XVU3-1. XVU3 is not fitted with a chromium getter, so some chromium deposition from the unit is evident on the wafer surface; discoloration is evident on the leading edge of the wafer in the photograph. Despite the contamination, the module appeared intact and crack-free upon removal from the reactor.

Figure 31-27. Module after test XVU3-1, pressure cycles.

Figure 31-28 is an example of a test to assess performance and reliability when the module is subjected to pressure and thermal cycles (transients). Leakage is quite low during the testing, which comprised multiple thermal and pressure cycles.

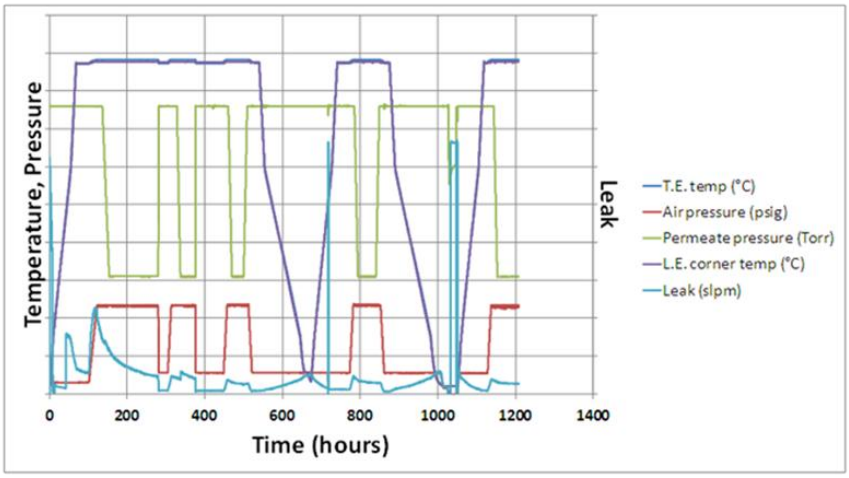

Figure 31-28. XVU2-5 test, pressure and thermal cycles (transients).

Figure 31-29 is an example of a test to determine the influence of feed and permeate pressure on module flux. Flux was very high at the beginning of the run, but declined to a level closer to the expected level after 1500 h on stream.

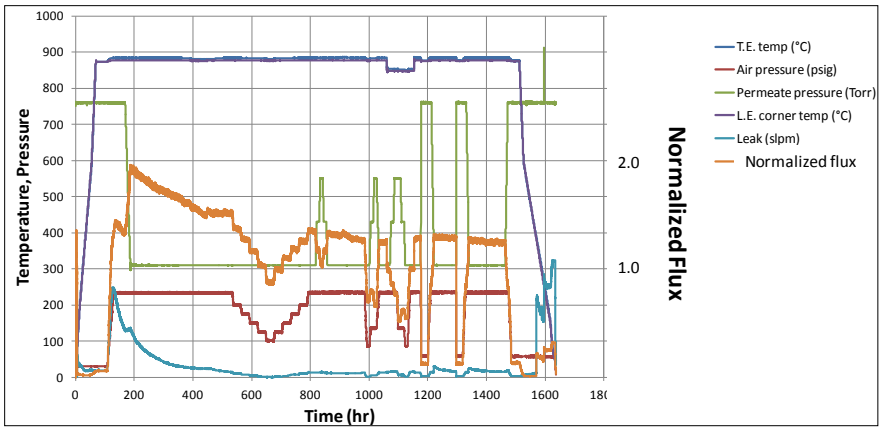

Figure 31-29. XVU2-7 test, feed and permeate pressure survey.

Figure 31-30 plots the measured relationship between flux and feed pressure from the XVU2-7 test. The effect of the flux change with time on stream is evident in the data.

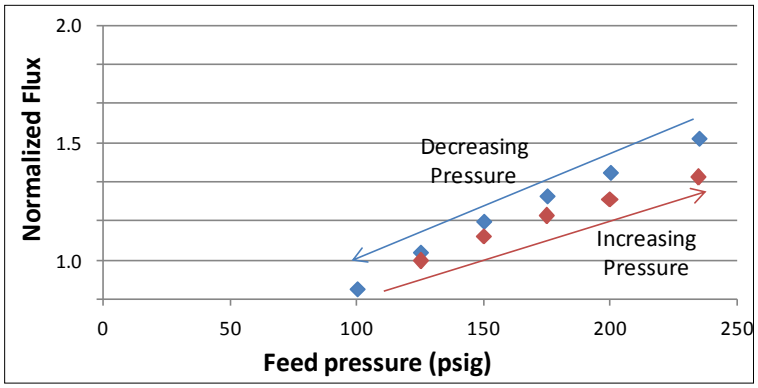

Figure 31-30. XVU2-7 test, flux versus feed pressure.

Figure 31-31 plots the measured relationship between flux and permeate pressure.

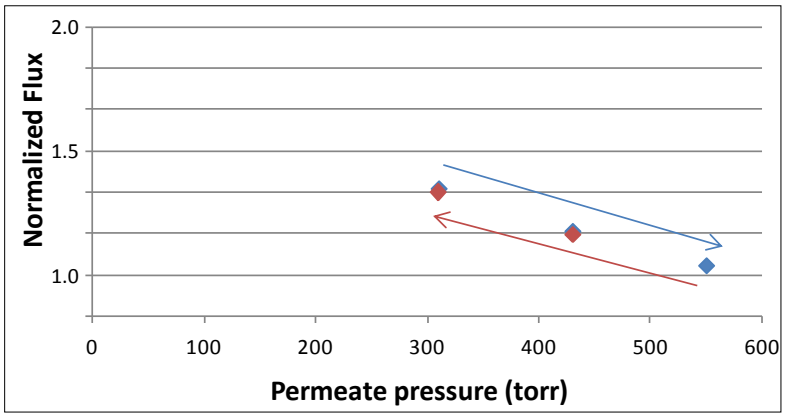

Figure 31-31. XVU2-7 test, flux versus permeate pressure.

Figure 31-32 is an example of a test to determine the influence of feed and permeate pressure and temperature on module flux.

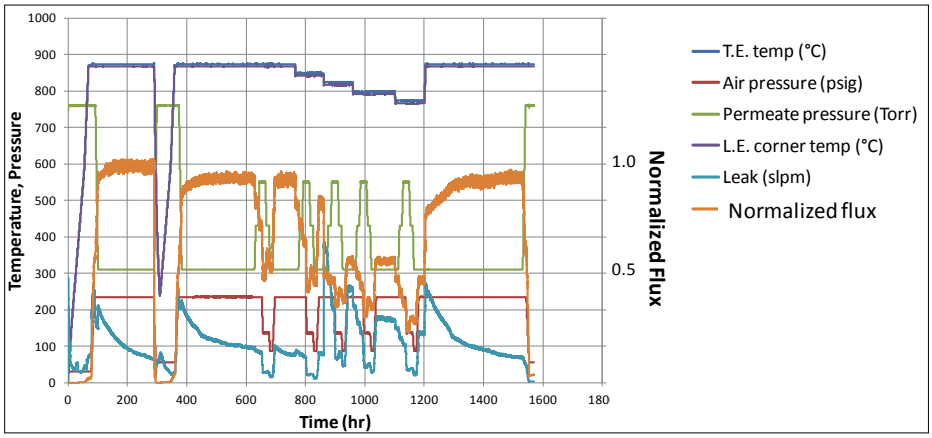

Figure 31-32. XVU1-1 test, pressure and thermal cycles (transients). Leak flow rate is not reflected in the axes.

Figure 31-33 plots the measured relationship between flux and temperature at various feed and permeate pressures.

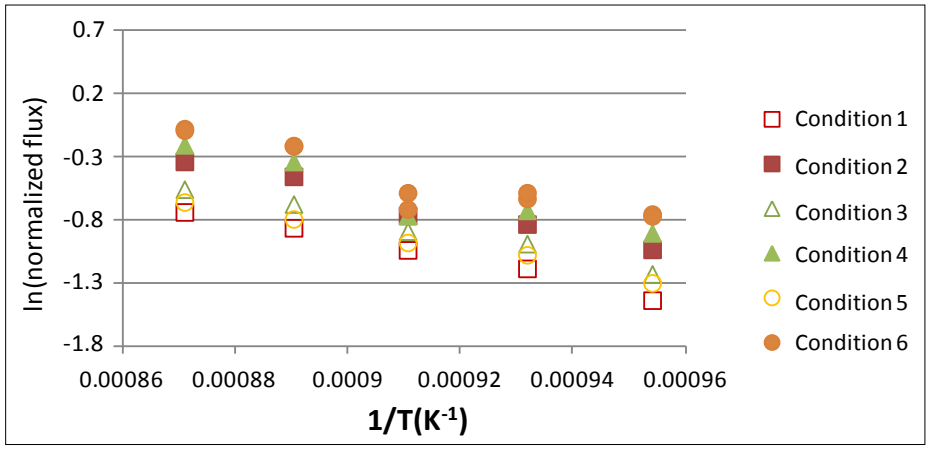

Figure 31-33. XVU1-1 test, flux versus temperature at various feed and permeate pressures.

Table 31-1 summarizes all of the tests conducted in the XVU. The listing is in chronological order.

Table 31-1. Summary of XVU tests on advanced architecture components.

Unit	Seal	Time (hrs)	Test Conditions	Comments
XVU2-1	A10	1,400	Operating conditions	New Endcap Flux approximately 0.5, Leak lower than target Wafer failure, ops issue
XVU3-1	A11 coated	1,100	Pressure cycles	Flux, from 1.0 to 0.8, leak at target, leak declined at operating conditions
XVU2-2	A11	1,300	Pressure cycles	Very low leak rate Wafer crack, ops issue
XVU2-3	A10	900	Pressure cycles	Flux decline from 1.2 to 0.5 Leak lower than target
XVU3-2	A10	1,400	Pressure cycles	Stable Flux, leak at target, leak declined at operating conditions
XVU3-3	A19			Wafer failure, ops issue
XVU3-4	A10			Ops problems test ended
XVU2-4	A10	1,300	Pressure cycles	Leak lower than target Wafer failed during cooldown
XVU2-5	A10 coated	1,200	Pressure cycles 2 thermal cycles	Good purity Leak lower than target
XVU3-5	A10	700	Pressure cycles	Leak lower than target, declined at operating conditions
XVU3-6	A10			Permeate rupture disc failure. Test stopped
XVU3-7				Experimental wafer failed at 500°C
XVU2-6	A10		Pressure cycles, 3 thermal cycles	Leak declined at operating conditions Wafer failed during 3rd thermal cycle
XVU2-7	A10	1,600	Flow and pressure surveys	Very low leak rate Slow decline in flux, surface contamination found
XVU2-8	A10	2,400	Flow, pressure and temperature surveys	Flux started above 1.0 then declined, possible chromium contamination
XVU1-1	A10	1,600	Pressure and temperature survey	Stable Flux See Figure 31-33 for relationships
XVU2-9	A10	1,400	Pressure and temperature survey	Flux started above 1.0 then declined
XVU1-2	A10			High leak rate, test stopped
XVU1-3	A10	450	Operating conditions	Flux >1.0 and stable Leak >target but declined
XVU2-10	A26	500+	Operating conditions	Flux >>1.0 but declining Leak at target and declining
XVU1-4	ISTU-type	1,700	Operating conditions	Cerfab wafer Flux >1.0 Leak >target, declined to < target 2 upsets, no damage, see Figure 31-36
XVU2-11	Other	725	Operating conditions	Flux >1.0, declining, Cr and S contamination found Ops issue caused wafer failure (Figure 31-38) Leak greater than target but declining

Wafer-to-Wafer Flux Variation

SEM analysis was performed on wafer sections from four previously tested modules. Modules 1, 2 and 3 were tested in the XVU2 and XVU3 and exhibited higher-than-expected flux values. Module 4 was tested in the XVU1 and showed expected flux. All system checks (flow rates, pressures, oxygen analyzers) indicated nominal performance for the three reactors. No irregularities were discovered in the powder formulations. Analysis of Module 4 indicated some of the fine channels had very tapered sides that could have restricted flow. Also, some fine channels were partially filled with material. This material could be a result of debris left in the slots from cutting. This is illustrated in Figures 31-34 and 31-35.

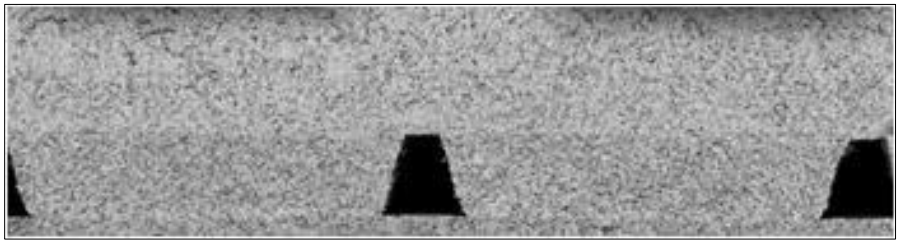

Figure 31-34. Cross-section of Module 4 with clear fine channels.

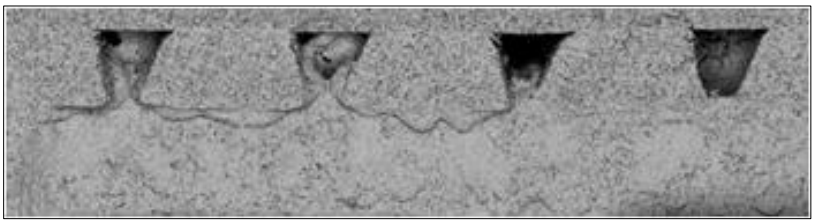

Figure 31-35. Cross-section of Module 4 with debris-filled fine slots.

31.3 Performance Testing of Modules Produced with the CerFab

Two CerFab-produced modules were tested, one in the XVU1 and the other in the XVU2. XVU1 has a chromium getter upstream of the test module, while XVU2 does not. The XVU1 module utilized the same seal that was used in the ISTU Run #2 (Task 20). The operating conditions, leak rate and flux are documented in Figure 31-36.

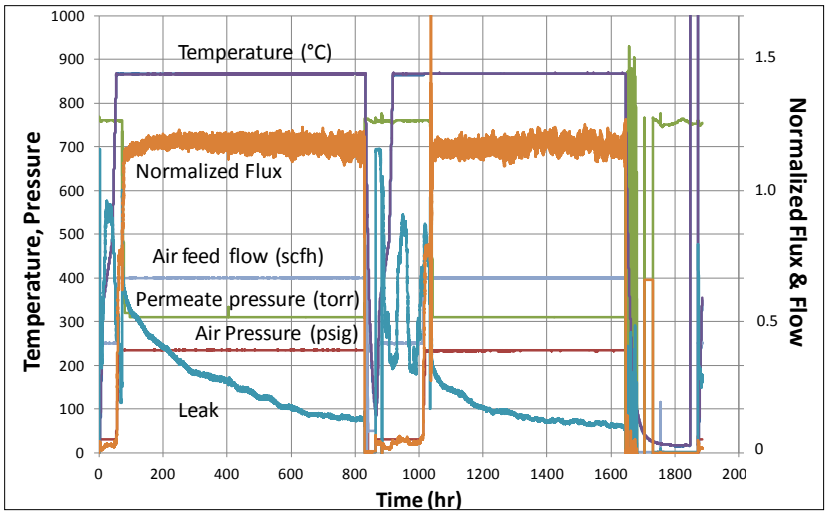

Figure 31-36. Test results for CerFab-produced single-wafer module in XVU1.

The initial startup went well. The flux quickly stabilized, and the normalized leak rate steadily declined. At about hour 825, a facilities upset led to a system shutdown. The restart went well other than some fluctuating leak behavior. Once full conditions were re-established, steady flux resumed and the leak rate again showed a steady decline. At ~1,640 hours, a PLC power supply failure led to a second system shut-down. The re-start was unsuccessful due to high leak flow. The module was removed. No cracks or other damage was visible on the module. The module was leak tested and found to have essentially the same leak rate as in the as-received condition. Figure 31-37 show photographs of the module in its original state and after 1,600 hours of operation.

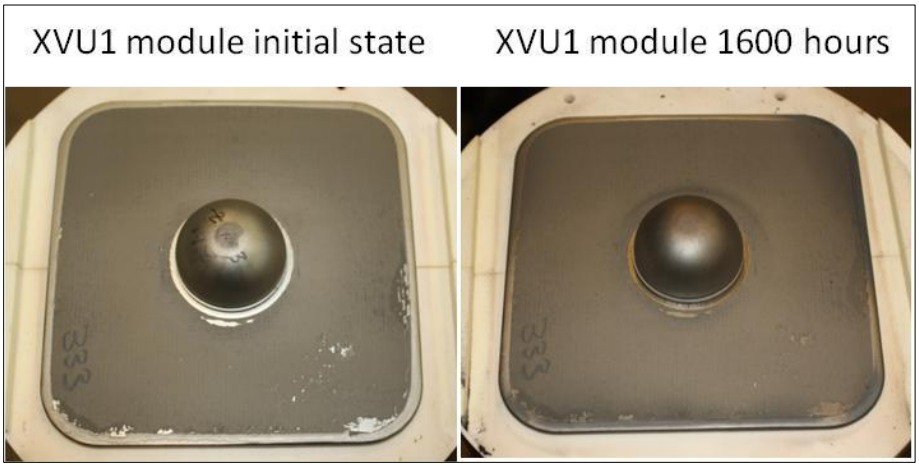

Figure 31-37. XVU1 module in original state and after 1,600 hours of operation.

The seal plate and the bottom of the module base piece were cleaned, a new seal was installed and the module was reloaded. The initial leak rate was modest and lower than the previous leak rate.

The XVU2 module utilized another seal configuration. Problems with the permeate pressure control valve complicated the startup of the reactor, so early leak data was not reliable. The operating conditions, leak rate and flux are documented in Figure 31-38.

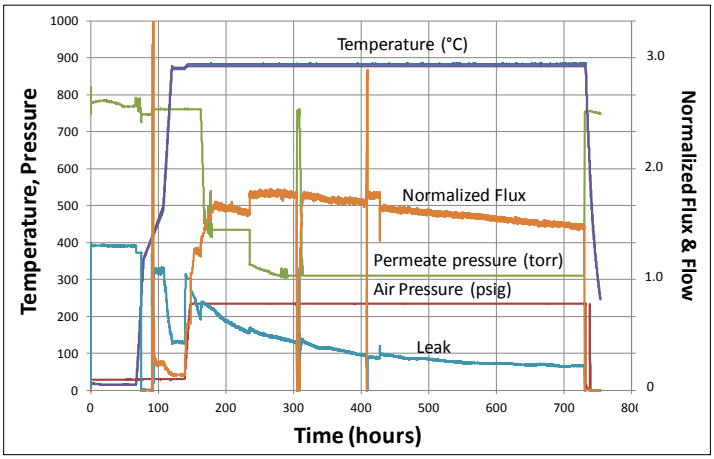

Figure 31-38. Test results for CerFab-produced single wafer module in XVU2.

The leak rate showed a steady decline after the process reached full conditions. After ~50 hours at full conditions, the flux began to decline. At ~720 hours, the facilities upset noted above resulted in a rapid shutdown of the XVU2. The module could not be restarted due to high leak, and when the reactor was disassembled the module was found to have fractured. Post-test analysis found significant chromium and sulfur contamination of the surface of the wafer.

ACRONYMS AND ABBREVIATIONS

∆P	Pressure drop or pressure loss
(A,A'A")(B,B'B")O3	Mixed metal oxygen perovskite material
ABO3	Generic ITM oxygen perovskite material
ACM	Aspen Custom Modeler
AGR	Acid gas removal
AP2k	ITM material
ASOV	Automatic shut-off valve
ASU	Air separation unit
Atm	Atmosphere
ATR	Autothermal reformer
Bara	Pressure in bar absolute
BBL	Barrels
BFD	Block flow diagram
BPD	Barrels per day
CFD	Computational fluid dynamics
cm	Centimeter
CTE	Coefficient of thermal expansion
DCS	Digital control system
EDAX	Energy dispersive X-ray
EDS	Energy dispersive spectroscopy
FEA	Finite element analysis
FFT	Fast Fourier Transform
FT	Flow transition
F-T	Fischer-Tropsch
GBD	Gram bulk density
GHR	Gas-heated reformer
GPa	Giga Pascals
GTCC	Gas turbine combined cycle
GTL	Gas-to-liquid
HHV	High heating value
HMB	Heat and material balance
HPTGA	High-pressure thermal gravimetric analyzer
HX	Heat exchanger
I4	Standard LaCaFeO ceramic material used for Reaction-Driven ITM
ICP-MS	Inductively coupled plasma mass spectrometry
ID	Inside diameter
IGCC	Integrated gasification combined cycle

In-lb	Inch pounds
ISTU	Intermediate-scale test unit
ITM	Ion transport membrane
keV	Kilo-electron volt
kg	Kilogram
kN	Kilo-Newton
Ksi	1,000 pounds per square inch
KW	Kilowatts
KWH	Kilowatt hours
Lb	Pound
LBO	Lean blow-out
LHV	Lower heating value
mm	Millimeter
MM	Millions
MMBTU	Millions of BTUs
MMSCFD	Millions of standard cubic feet per day
MT/D	Metric tons per day
MPa	MegaPascals
MW	Megawatts
MWe	megawatt electric
MWt	megawatt thermal
n	Stress exponent in material creep tests
NG	Natural gas
Nm^3/hr	Normal cubic meters per hour
NOx	nitrogen oxide
OD	Outside diameter
ODF	Oxygen development facility
ORI	Operational readiness inspection
Pa	Pascal
PDS	Porous-dense-slotted
PDF	Process Development Facility
PDU	Process Development Unit
PID	Piping and instrumentation diagram
PNNL	Pacific Northwest National Laboratory
P_{O2}	Oxygen partial pressure
ppb	Parts per billion
ppm	Parts per million
ppmv	Parts per million volume
PSA	Pressure swing adsorption
PSDF	Power systems development facility
psi	Pounds per square inch

psia	Pounds per square inch absolute
psig	Pounds per square inch gauge
PTCR	Process temperature control rings
P&ID	Process and instrumentation diagram
QA	Quality assurance
Re	Reynolds number
RMS	Root mean square
RT	Room temperature
SAM	Scanning acoustic microscope
sccm	Standard cubic centimeters per minute
Scfh	standard cubic feet per hour
SCG	Slow crack growth
SAM	Scanning acoustic microscopy
SEI	Siemens Energy, Inc.
SEM	Scanning electron microscopy
SEP	Subscale engineering prototype
slpm	Standard liters per minute
SLTR	Short loop test rig
SMR	Steam methane reformer
SPC	Statistical process control
TGA	Thermogravimetric analysis
TPD	Tons per day
TDU	Technology development unit
TRS	Technical risk statement
TSA	Temperature swing adsorption
TTR	Transient testing rig
V	Volts
(V)IGV	(variable) inlet guide vane
VP-SLTR	Vacuum-permeate short loop test rig
µm	Micrometer
UTS	Ultimate tensile stress
WDXRF	Wavelength dispersive X-ray fluorescence
wsw	Wafer-starts-per-week
XPS	X-ray photoelectron spectroscopy
XRD	X-ray diffraction
XV	Vacancy fraction
XVU	fluX verification unit
YS	Yield stress